

Limin Jia · Yong Qin · Baoming Liu ·  
Zhigang Liu · Lijun Diao · Min An ·  
*Editors*

# Proceedings of the 4th International Conference on Electrical and Information Technologies for Rail Transportation (EITRT) 2019

Novel Traction Drive Technologies of Rail  
Transportation

# Lecture Notes in Electrical Engineering

## Volume 638

### Series Editors

Leopoldo Angrisani, Department of Electrical and Information Technologies Engineering, University of Napoli Federico II, Naples, Italy

Marco Arteaga, Departament de Control y Robótica, Universidad Nacional Autónoma de México, Coyoacán, Mexico

Bijaya Ketan Panigrahi, Electrical Engineering, Indian Institute of Technology Delhi, New Delhi, Delhi, India  
Samarjit Chakraborty, Fakultät für Elektrotechnik und Informationstechnik, TU München, Munich, Germany  
Jiming Chen, Zhejiang University, Hangzhou, Zhejiang, China

Shanben Chen, Materials Science and Engineering, Shanghai Jiao Tong University, Shanghai, China  
Tan Kay Chen, Department of Electrical and Computer Engineering, National University of Singapore, Singapore, Singapore

Rüdiger Dillmann, Humanoids and Intelligent Systems Laboratory, Karlsruhe Institute for Technology, Karlsruhe, Germany

Haibin Duan, Beijing University of Aeronautics and Astronautics, Beijing, China

Gianluigi Ferrari, Università di Parma, Parma, Italy

Manuel Ferre, Centre for Automation and Robotics CAR (UPM-CSIC), Universidad Politécnica de Madrid, Madrid, Spain

Sandra Hirche, Department of Electrical Engineering and Information Science, Technische Universität München, Munich, Germany

Faryar Jabbari, Department of Mechanical and Aerospace Engineering, University of California, Irvine, CA, USA

Limin Jia, State Key Laboratory of Rail Traffic Control and Safety, Beijing Jiaotong University, Beijing, China

Janusz Kacprzyk, Systems Research Institute, Polish Academy of Sciences, Warsaw, Poland

Alaa Khamis, German University in Egypt El Tagamoa El Khames, New Cairo City, Egypt

Torsten Kroeger, Stanford University, Stanford, CA, USA

Qilian Liang, Department of Electrical Engineering, University of Texas at Arlington, Arlington, TX, USA

Ferran Martín, Departament d'Enginyeria Electrònica, Universitat Autònoma de Barcelona, Bellaterra, Barcelona, Spain

Tan Cher Ming, College of Engineering, Nanyang Technological University, Singapore, Singapore

Wolfgang Minker, Institute of Information Technology, University of Ulm, Ulm, Germany

Pradeep Misra, Department of Electrical Engineering, Wright State University, Dayton, OH, USA

Sebastian Möller, Quality and Usability Laboratory, TU Berlin, Berlin, Germany

Subhas Mukhopadhyay, School of Engineering & Advanced Technology, Massey University,

Palmerston North, Manawatu-Wanganui, New Zealand

Cun-Zheng Ning, Electrical Engineering, Arizona State University, Tempe, AZ, USA

Toyoaki Nishida, Graduate School of Informatics, Kyoto University, Kyoto, Japan

Federica Pascucci, Dipartimento di Ingegneria, Università degli Studi “Roma Tre”, Rome, Italy

Yong Qin, State Key Laboratory of Rail Traffic Control and Safety, Beijing Jiaotong University, Beijing, China

Gan Woon Seng, School of Electrical & Electronic Engineering, Nanyang Technological University, Singapore, Singapore

Joachim Speidel, Institute of Telecommunications, Universität Stuttgart, Stuttgart, Germany

Germano Veiga, Campus da FEUP, INESC Porto, Porto, Portugal

Haitao Wu, Academy of Opto-electronics, Chinese Academy of Sciences, Beijing, China

Junjie James Zhang, Charlotte, NC, USA

The book series *Lecture Notes in Electrical Engineering* (LNEE) publishes the latest developments in Electrical Engineering - quickly, informally and in high quality. While original research reported in proceedings and monographs has traditionally formed the core of LNEE, we also encourage authors to submit books devoted to supporting student education and professional training in the various fields and applications areas of electrical engineering. The series cover classical and emerging topics concerning:

- Communication Engineering, Information Theory and Networks
- Electronics Engineering and Microelectronics
- Signal, Image and Speech Processing
- Wireless and Mobile Communication
- Circuits and Systems
- Energy Systems, Power Electronics and Electrical Machines
- Electro-optical Engineering
- Instrumentation Engineering
- Avionics Engineering
- Control Systems
- Internet-of-Things and Cybersecurity
- Biomedical Devices, MEMS and NEMS

For general information about this book series, comments or suggestions, please contact [leontina.dicecco@springer.com](mailto:leontina.dicecco@springer.com).

To submit a proposal or request further information, please contact the Publishing Editor in your country:

#### **China**

Jasmine Dou, Associate Editor ([jasmine.dou@springer.com](mailto:jasmine.dou@springer.com))

#### **India, Japan, Rest of Asia**

Swati Meherishi, Executive Editor ([Swati.Meherishi@springer.com](mailto:Swati.Meherishi@springer.com))

#### **Southeast Asia, Australia, New Zealand**

Ramesh Nath Premnath, Editor ([ramesh.premnath@springernature.com](mailto:ramesh.premnath@springernature.com))

#### **USA, Canada:**

Michael Luby, Senior Editor ([michael.luby@springer.com](mailto:michael.luby@springer.com))

#### **All other Countries:**

Leontina Di Cecco, Senior Editor ([leontina.dicecco@springer.com](mailto:leontina.dicecco@springer.com))

**\*\* Indexing: The books of this series are submitted to ISI Proceedings, EI-Compendex, SCOPUS, MetaPress, Web of Science and Springerlink \*\***

More information about this series at <http://www.springer.com/series/7818>

Limin Jia · Yong Qin · Baoming Liu ·  
Zhigang Liu · Lijun Diao · Min An  
Editors

# Proceedings of the 4th International Conference on Electrical and Information Technologies for Rail Transportation (EITRT) 2019

Novel Traction Drive Technologies of Rail  
Transportation



Springer

*Editors*

Limin Jia  
State Key Laboratory of Rail Traffic  
Control and Safety  
Beijing Jiaotong University  
Beijing, China

Baoming Liu  
National Innovation Center  
of High Speed Train  
Qingdao, China

Lijun Diao  
Beijing Jiaotong University  
Beijing, China

Yong Qin  
State Key Laboratory of Rail Traffic  
Control and Safety  
Beijing Jiaotong University  
Beijing, China

Zhigang Liu  
Beijing Jiaotong University  
Beijing, China

Min An  
School of Science, Engineering  
and Environment  
University of Salford  
Salford, UK

ISSN 1876-1100

ISSN 1876-1119 (electronic)

Lecture Notes in Electrical Engineering

ISBN 978-981-15-2861-3

ISBN 978-981-15-2862-0 (eBook)

<https://doi.org/10.1007/978-981-15-2862-0>

© Springer Nature Singapore Pte Ltd. 2020

This work is subject to copyright. All rights are reserved by the Publisher, whether the whole or part of the material is concerned, specifically the rights of translation, reprinting, reuse of illustrations, recitation, broadcasting, reproduction on microfilms or in any other physical way, and transmission or information storage and retrieval, electronic adaptation, computer software, or by similar or dissimilar methodology now known or hereafter developed.

The use of general descriptive names, registered names, trademarks, service marks, etc. in this publication does not imply, even in the absence of a specific statement, that such names are exempt from the relevant protective laws and regulations and therefore free for general use.

The publisher, the authors and the editors are safe to assume that the advice and information in this book are believed to be true and accurate at the date of publication. Neither the publisher nor the authors or the editors give a warranty, expressed or implied, with respect to the material contained herein or for any errors or omissions that may have been made. The publisher remains neutral with regard to jurisdictional claims in published maps and institutional affiliations.

This Springer imprint is published by the registered company Springer Nature Singapore Pte Ltd.  
The registered company address is: 152 Beach Road, #21-01/04 Gateway East, Singapore 189721,  
Singapore

# Contents

<b>Study on Ball Screw Wear Model Considering the Influence of Abrasive Particles .....</b>	1
Qiujin Li, Ying Liu, Genbao Zhang and Yan Ran	
<b>Electrical Transformation to Improve Energy-Stored Experimental Capability of Rail Transit Test Line of Tongji University .....</b>	13
Liwei Dong, Haiquan Liang, Jingtai Hu and Yufei Chen	
<b>E-Field Simulation and Voltage Withstand Test Analysis of Solid Insulators for AC GIS Used in High-Speed Railway Traction Substation .....</b>	23
Shiling Zhang	
<b>Research on Train Energy-Saving Optimization Based on Parallel Immune Particle Swarm Optimization .....</b>	33
Shibo Li, Wang Dai, Lichao Fang, Yong Zhang and Zongyi Xing	
<b>Research on Comprehensive Evaluation Method of Optimized Charging .....</b>	45
Liye Wang, Lifang Wang, Wenjie Zhang and Yuwang Zhang	
<b>Study on Key Metrics of Maintenance of Cascade-Utilized Battery Storage System's Consistency .....</b>	55
Na Li, Kai Bai, Kairang Wang, Yinchi Shao, Yu Gong, Jia Diao and Yaqi Zhao	
<b>Reverse Characteristic Model of SiC MPS Diode .....</b>	71
Qiwen Du and Xuehui Tao	
<b>Stochastic Simulation of Traction Load for Urban Rail Transport Based on Dynamic Train Headway .....</b>	81
Zhenhai Sun, Hui Liu, Jinping Fang and Shaobing Yang	

<b>Transient Direct Current Control of Single-Phase Cascaded H-Bridge Rectifier Without Phase-Locked Loop .....</b>	93
Juxia Ding and Qunzhan Li	
<b>A Design of Ground Auto-Passing Neutral Section Logical Control System .....</b>	103
Lintong Li and Baodi Xiao	
<b>Parallel Control of Auxiliary Inverter Based on Virtual Synchronous Generator .....</b>	117
Lei Lu, Xuefei Li, Yang Kuang, Jie Chen and Ruichang Qiu	
<b>Application of Improved PSO Algorithms in Train Energy Consumption Optimization .....</b>	127
Binhui Yang, Jing Zhang, Yong Zhang and Zongyi Xing	
<b>Design of LRC Filter for High-Power Inverters .....</b>	135
Zongju Cai, Jie Yang and Zhijie Zhang	
<b>Research on a Secondary Pulsation Active Power Filter for Single-Phase PWM Rectifier .....</b>	143
Yuxi Zhang, Fujun Peng, Qiyang Xu, Lailai Shen and Jie Chen	
<b>An Improved Shunt Hybrid Active Power Filter Based on Cascaded H-Bridge Converter and Its Generalized Inverse System Decoupling Control .....</b>	151
Xin Li, Ruoqiong Li and Bo Li	
<b>Research on Motor Bearing Fault Detection Method Based on Cyclic Autocorrelation Function Analysis .....</b>	163
Peng Wang, Chidong Qiu, Xinbo Wu and Zhengyu Xue	
<b>Double-Loop Control Strategy for Buck/Boost-CLLLC Two-Stage Bidirectional DC/DC Converter .....</b>	171
Linghang Huang, Jie Chen, Ruichang Qiu and Zhigang Liu	
<b>Research on Motor Bearing Fault Detection Method Based on Teager-Kaiser Energy Operator .....</b>	183
Yuan Gao, Chidong Qiu, Changqing Xu and Zhengyu Xue	
<b>Research on Active Power Factor Correction Technology .....</b>	191
Yuan Sun, Jie Chen, Fei Meng, Ruichang Qiu and Zhigang Liu	
<b>Fault Diagnosis of Induction Motor Bearing Based on Multitaper Spectrum and Support Vector Machine .....</b>	199
Xinchao Zheng, Zhengyu Xue and Chidong Qiu	

<b>A Simplified Method Based on LM Algorithm for Electrochemical–Thermal Coupling Model of Tram Supercapacitor . . . . .</b>	209
Xueting Fu, Chaohua Dai and Yun Du	
<b>Review and Research Progress of Energy Bidirectional Feed ICPT System . . . . .</b>	221
Junjie Wang, Ruqiong Li and Xin Li	
<b>Sensorless Control for IPM Synchronous Motor Using Disturbance Observer . . . . .</b>	233
Yikun Wang, Xizheng Guo and Donghui Cao	
<b>A U2P-Miner-Based Method to Identify Critical Energy-Consuming Parts of Urban Rail Operation System . . . . .</b>	245
Mingtao Wu, Yanhui Wang, Shuai Lin, Boyan Hao and Pengfei Sun	
<b>Cascade–Parallel Structure Application of Converters for AC–DC–AC Traction Substation . . . . .</b>	257
Linwei Li and Mingli Wu	
<b>Influence of Air Gap on Electric Field of the EMU Roof Cable Terminal . . . . .</b>	277
JiXing Sun, QingYun Zhi, Jin Li and Qi Dai	
<b>Research on Reactive Power Optimization Scheme of Metro Medium Voltage Power Supply Network Based on the Medium Voltage Energy Feeding Device . . . . .</b>	285
Lingmin Meng, Dawei Song, Jie Chen, Fuqiang Mu and Zhigang Liu	
<b>Research and Application on Electric Vehicle Charging Communication Protocols Compatibility Detection . . . . .</b>	295
Sixiang Zhao, Zhenyu Jiang, Di Han, Hanji Ju, Yachao Wang and Chenwei Zhang	
<b>Hybrid Energy Storage Trolley System Configuration Optimization Method Taking into Account the Whole Life Cycle Cost of the Whole Vehicle . . . . .</b>	305
Qi An, Fangli Shi, Beiyu Liu, Chaohua Dai and Weirong Chen	
<b>Review of Energy-Efficient Train Trajectory Optimization and Intelligent Control . . . . .</b>	317
Jie Yang, Biao Wang, Limin Jia and Kuan Zhu	
<b>Influence Analysis on the CRH2 EMUs Vehicle Bodies Voltage Fluctuation Considering Isolated Rail Joint Discharge . . . . .</b>	327
Ying Lu, Ying Wang, Yanlong Shen, Xiaoqiang Chen and Yanming Lu	

<b>Hydrogen Consumption Minimization for Fuel Cell Trains Based on Speed Trajectory Optimization . . . . .</b>	335
Zheng Huang, Chaoxian Wu, Shaofeng Lu and Fei Xue	
<b>Simulation of Permanent Magnet Synchronous Motor Based on Dual PWM . . . . .</b>	347
Huawei Wang, Xilian Wang, Daqiang Bi and Yanhua Li	
<b>Analysis and Implementation of High Efficiency High Power Density Battery Charger for Electric Vehicle . . . . .</b>	357
Jie Yang, Zhijie Zhang, Zongju Cai, Yu Yao, Fei Li and Wei Yang	
<b>Simulation of Power Supply System Considering Inverter Feedback Device in Urban Rail Transit . . . . .</b>	367
Liping Zhao, Feng Wang, Sheng Lin and Xiaohong Lin	
<b>Study on Stray Current Distribution of the Metro Depot . . . . .</b>	377
Liping Zhao, Junyi Li, Sheng Lin and Aimin Wang	
<b>Active Fault-Tolerant Control Strategy of ANPC Three-Level Inverter Based on Sliding Mode Control . . . . .</b>	387
Qinyue Zhu, Zhaoyang Li, Xitang Tan, Wei Dai, Dabo Xie and Sha Liu	
<b>A Survey: Learning-Based Energy Management Strategy for Heterogeneous Multi-energy Drive System . . . . .</b>	399
Xiaoyu Ren, Xinyue Zhang, Dangwei Duan and Lijun Diao	
<b>Feed-Forward Compensation Strategy for Suppressing Beat Phenomenon in Railway Traction System . . . . .</b>	407
Xueyan Ma, Dongyi Meng, Yaru Xue and Lijun Diao	
<b>Dead-Band Optimization for ZVS in Inductive Power Transfer System . . . . .</b>	417
Bing Li, Daomeng Cai, Xuemei Diao, Lei Wang and Lijun Diao	
<b>Research on the Improved Fault-Tolerant Control of ANPC Three-Level Converter . . . . .</b>	425
Qinyue Zhu, Chen Wang, Xitang Tan, Pengcheng Zhang and Qingwen Fan	
<b>Reliability Analysis of Metro Traction Substation Based on Bayesian Network . . . . .</b>	439
Guangtao Cong, Wen Xu and Zongyi Xing	
<b>Study on Steady-State Output Characteristics of Three-Level Boost Converter . . . . .</b>	451
Chengwei Kang, Wei Wang, Guoqin Zhang and Huiqing Du	
<b>Optimization of Magnetic Coupling for Small and Medium Power Wireless Charging System . . . . .</b>	461
Xuemei Diao, Chunhui Miao, Bing Li, Weiyao Mei and Lijun Diao	

<b>Dynamic Programming in Energy Management Strategy for Optimizing Multi-energy Drive System . . . . .</b>	471
Xinyue Zhang, Xiaoyu Ren, Caihui Zheng, Yue Yuan and Lijun Diao	
<b>Research on Principle and Control Method of Totem-Pole PFC . . . . .</b>	481
Chunjiang Liu, Chao Li, Weiyao Mei, Chunmei Xu and Lijun Diao	
<b>Pure Electric Brake of the Train with Speed Sensorless Vector Control . . . . .</b>	489
Qiya Wu, Shaobo Yin, Dangwei Duan, Chunmei Xu and Lijun Diao	
<b>Rule-Based Energy Management Strategy for Multi-energy Drive System . . . . .</b>	499
Yue Yuan, Rongjia He, Haibo Zhao, Enlong Li, Xuekun Li and Chunmei Xu	
<b>Vector Control Optimization of Traction Motors Based on Online Parameter Identification . . . . .</b>	507
Xitang Tan, Dabo Xie, Qinyue Zhu, Zhaoyang Li, Wei Dai and Quanpeng Wu	
<b>T-Type Equivalent Circuit of Double-Sided Long Primary Linear Induction Motor Considering the Backward Traveling Wave . . . . .</b>	519
Jiefang Ma, Huijuan Liu and Qian Zhang	
<b>Optimal Matching of High-Speed Pantograph Parameters Considering Catenary Suspension Irregular Point and Wind Damping . . . . .</b>	527
Yulong Liu, Ying Wang, Li Cao, Xiaoqiang Chen and Zhengqing Hao	
<b>Dynamic Power Threshold Control Strategy of Wayside Hybrid Energy Storage System Based on Battery SOC Tracking . . . . .</b>	537
Mingcheng Ai, Zhongping Yang, Fei Lin and Qiangqiang Qin	
<b>Research on Key Technologies of Energy Storage in Photovoltaic/Battery MicroGrid . . . . .</b>	547
Jun Zhou, Tao Yang, Wen Xuan Wang, Yalou Chen and ZhaoRui He	
<b>Performance Evaluations of DCAT Position for the Floating DCAT System in DC Railways . . . . .</b>	557
Miao Wang, Xiaofeng Yang, Trillion Q. Zheng, Menghan Ni and Wei Guo	
<b>Negative Impedance Converter for Reducing Rail Potential in Urban Rail Transit . . . . .</b>	569
Wei Guo, Xiaofeng Yang, Jingda Gu and Trillion Q. Zheng	
<b>Distributed Cooperative Absorption Method of Braking Energy for Urban Rail Transit . . . . .</b>	579
Shenyi Liu, Lei Wang, Ming Li, Yanqin Wang and Lei Zhang	

<b>Lifetime Prediction Model of IGBT Modules in EMU . . . . .</b>	591
Benchao Zhu, Lei Wang, Lei Zhang, Ming Li and Yanqin Wang	
<b>Research on Medium Voltage MMC Fault-Tolerant Optimized Control Strategy . . . . .</b>	601
Qinyue Zhu, Qingwen Fan, Xitang Tan, Zhaoyang Li, Wei Dai and Dabo Xie	
<b>Energy Storage System Design for Catenary Free Modern Trams . . . . .</b>	613
Li Wang, Qinghua Zhao, Hongliang Duan and Changqing Liu	
<b>Modeling and Simulation of Multi-Vehicle DC Traction Power Supply System Based on MATLAB/Simulink . . . . .</b>	623
Hui Liu, Zhenhai Sun, Jinping Fang and Zihui Hao	
<b>Research on Eddy Current Braking Control Strategy of 600 km/h High-Speed Maglev Train . . . . .</b>	635
Hongfeng Qi, Wenjin Hao and Jianqiang Liu	
<b>Extended Kalman Filter Observer Based on the Induction Motor Model Considering Iron Loss . . . . .</b>	645
Leiting Zhao, Chengguang Huang, Shaobo Yin, Dongyi Meng and Kan Dong	
<b>Online Fault Protection Method and Its Implementation Based on Control Bus for Electromechanical Composite Transmission Bench Test System . . . . .</b>	655
Lei Guo, Gen Zeng and Yaoheng Li	
<b>Research on Transformer Core Loosening Fault Diagnosis Based on VMD . . . . .</b>	671
Yuzhi Liu, Kuankuan Zhai, Xiaorui Kang, Wei Guo and Xinyu Zhang	
<b>Braking Energy Harvesting Strategy of High-Speed Maglev System . . . . .</b>	683
Dong Yang, Rong Wei and Pengkun Sun	
<b>Research on the Improved Time-Sharing Control Strategy with MPPT Algorithm . . . . .</b>	691
Yi Fan, Fan Lu, Tao Yang, Wenzuan Wang and Mingxiang Liu	
<b>Research on Power Conversion System Based on Multiple DC/DC Converter . . . . .</b>	701
Wenzuan Wang, Tao Yang, Jun Zhou, Yi Fan and Zhaorui He	
<b>Simulation Analysis and Experimental Verification of High-Speed Train Electromagnetic Disturbance . . . . .</b>	711
Jun Yu	

<b>Research on a PMSM Control Method Based on Model Prediction Control . . . . .</b>	721
Yalou Chen, Jun Zhou, Wenxuan Wang, Tao Yang and Zhaorui He	
<b>Research of the Three-Phase Input High Efficiency and Low Harmonic Battery Charging Power Supply . . . . .</b>	731
Chunhui Miao, Jie Yang, Sen Yang, Yu Yao, Zhijie Zhang, Fei Li and Wei Yang	
<b>Analysis and Suppression of Bearing Electric Erosion in the Metro Traction Motors . . . . .</b>	741
Erle Yang, Ruifang Liu, Qincong Zhao and Zhiwei Zheng	
<b>Hardware-in-the-Loop Real-Time Simulation Platform Design for Electric Rail Traction System . . . . .</b>	751
Zhen Zhao, Jialu Liu, Leiting Zhao and Weizhi Liu	
<b>Control Strategy of Rail Transit High-Power Permanent Magnet Synchronous Motor and Verification of Semi-physical Platform . . . . .</b>	761
Zhenzhong Liang, Qubo Xie and Xuepu Li	
<b>Research on PWM Modulation Strategy of High-Power Permanent Magnet Synchronous Traction System . . . . .</b>	769
Qubo Xie, Zhenzhong Liang and Wen Wang	
<b>Optimization Control of Energy-Efficient Driving for Trains in Urban Rail Transit Based on GA-PSO Algorithm . . . . .</b>	777
Lidan Zhao, Junqin Peng, Jiaxing Wang and Yonghua Zhou	
<b>Impact of Inverter's DC Virtual Resistance on Braking Energy Flow in Urban Rail Transit . . . . .</b>	787
Dongsheng Xu, Gang Zhang, Fengjie Hao and Yong Wang	
<b>Grey Prediction Method for Cylinder Wear Extent of Automobile Engine . . . . .</b>	797
Zheng-Wei Fan	
<b>Modeling Analysis and Control of Bidirectional DC/DC Converter in Hybrid EMU System . . . . .</b>	805
Wang Li, Miaoxin Jin and Libing Fan	
<b>Research on Energy Configuration and Characteristics of Hybrid EMU Power System . . . . .</b>	819
Yunxin Fan, Wang Li, Miaoxin Jin and Qingmin Qin	
<b>Dynamic Imitation Real Platform of Urban Rail Transit Traction Power Supply System for PHM . . . . .</b>	829
Jianmin Wen, Kaikang Wang, Fei Ye, Bin He and Jiangtao Wu	

<b>Design Method of Fuzzy Controller for Speed Control of Heavy-haul Train . . . . .</b>	839
Jiao Dong, Youneng Huang and Huazhen Yu	
<b>Design of Wireless Data Transmission System for Vehicle Energy Storage Components Based on STM32 . . . . .</b>	849
An Zhang, Yan kun Li, Yan ru Zhang and Ding hong Chen	
<b>The Charging Control Scheme of On-board Battery Energy Storage System in Tram . . . . .</b>	859
Dangwei Duan, Caihui Zheng, Zhanguo Wang and Fulai An	
<b>SOC Estimation of All-Vanadium Redox Flow Battery via Parameters Identification and UKF Algorithm . . . . .</b>	867
Guobin Sun, Yufu Hao, Zhenghao Li, Li Wang and Kun Fang	
<b>The Control Strategy of Hybrid Energy Storage System of Tramcar Based on Parallel Interleaving Bidirectional DC/DC Converter . . . . .</b>	877
Zhexu Zhang, Yang Cui, Qinkun Zhao, Bin Zhou and Zhenghao Li	
<b>Vehicle Propulsion System of New MBTA Orange Line Trains . . . . .</b>	891
Caihui Zheng, Hang Yin, Haifeng Hong and Changqing Liu	

# Study on Ball Screw Wear Model Considering the Influence of Abrasive Particles



Qiujin Li, Ying Liu, Genbao Zhang and Yan Ran

**Abstract** Wear is the main cause of the failure of the ball screw pair, which seriously affects its accuracy and service life. Therefore, it is necessary to build and analyze the wear model of ball screw pairs based on analyzing wear mechanism in depth. At present, the study of ball screw wear model mostly adopts the theory of adhesion wear. It is believed that the wear amount during normal wear period is proportional to time. But in fact, this conclusion cannot express the change of the whole wear process. Based on the wear mechanism of the ball screw pair, this paper deeply analyzes the influence of abrasive wear on the ball screw during the entire life cycle. And according to the Archard wear theory, a wear model considering the impact of abrasive particles is established. In this model, the wear of the ball screw pair is exponentially related to time. The experiments verify the applicability and accuracy of the model set out in this paper, which provides a theoretical foundation for the following research on the accuracy maintenance of ball screw pairs.

**Keywords** Ball screw · Abrasive wear · Adhesive wear · Wear model

## 1 Introduction

Ball screw pairs play an important part in CNC machine tools and other mechanical equipment, but domestic ball screw pairs always have problems such as poor accuracy retention and fast wear failure. These problems are due to wear and tear caused by the relative movement of the ball with the screw and nut, respectively. At present, ball screw pairs are developing toward high speed and high precision, so it

---

Q. Li · Y. Liu · G. Zhang · Y. Ran (✉)

School of Mechanical Engineering, Chongqing University, Chongqing 400044,  
People's Republic of China

e-mail: [ranyan@cqu.edu.cn](mailto:ranyan@cqu.edu.cn)

G. Zhang

School of Mechanical and Electrical Engineering, Chongqing University  
of Arts and Sciences, Chongqing 402160, People's Republic of China

is important to study the wear law of ball screw pairs. The wear analysis of ball screw pairs needs to be based on the surface contact friction model. Early scholars such as Greenwood [1] put forward a random model assuming that the contact surface was composed of hemispheres, which reflects the contact condition of the friction surface. Based on of volume conservation of plastic deformation, Chang [2] proposed a micro-model of rough contact surface, which was further extended by Horng [3] to make it suitable for various contact surfaces. However, the calculation of these wear models is rather complicated. Scholars have proposed using Archard model to study the wear of ball screw pairs. For example, Zhong [4] used Archard wear theory to analyze the wear process of ball linear guide pair and established a calculation model of slider displacement to predict the wear amount of ball linear guide pair. Xu [5] established the wear model of ball screw pair based on the incremental form of Archard model. The wear law of ball screw pair during normal wear period was obtained by numerical method and verified by experiment. Liu [6] also used Archard model to find out the friction coefficients of ball screw pairs by the same material under different loads and sliding speeds. However, these studies have their own emphases and seldom considering the effect of abrasive particles on the whole wear process. Ball screw pair is a closed friction pair. The number of abrasive particles in the ball screw pair will accumulate over time. A large number of abrasive particles will aggravate the wear condition. Ignoring the influence of abrasive particles in the raceway will inevitably lead to errors between theoretical calculation and actual results. Olofsson's [7] tests on spherical roller bearings also showed that the wear amount is obviously affected by the wear particles falling off the contact surface over a long period of time.

At present, the calculation formulas of life and dynamic load rating of ball screw pairs used in the national standard are based on the mechanical model of ball bearing. The calculation results themselves have deviation. Moreover, the wear research of ball screw pairs focuses on fatigue wear and adhesion wear, which is not conducive to the rapid development of ball screw pairs to high speed and high precision. Therefore, it is necessary to study the effect of abrasive particles on the wear of ball screw pairs. In this paper, the wear mechanism of ball screw pair is deeply analyzed, and according to the actual wear condition of ball screw pair, the wear model considering the effect of abrasive particles is established. The correctness of the model is verified by an example. The relationship between wear depth and time of ball screw raceway determined by this model can be helpful for the study of precision degradation and life prediction of ball screw pairs.

## 2 Wear Mechanism and Model

Wear is a complicated failure mode of surface damage. Domestic scholars classified wear into four categories: adhesive wear, abrasive wear, fatigue wear, and corrosive wear to the different failure mechanism and wear characteristics of the friction surface [8]. In the actual wear phenomenon, there are usually several forms of wear

at the same time, and one kind of wear often induces other forms. For example, wear debris generated by fatigue wear can cause abrasive wear. Under different working conditions, the main and secondary wear modes are different.

The phenomena of adhesive wear are as follows. In contact area, the materials under contact load form adhesion point due to adhesion effect. When relative sliding occurs, shear fracture happens at the adhesion point, and the sheared surface material migrates from one surface to another or falls off into abrasive debris. Archard [9] did a lot of research on adhesion wear, and on this basis, a calculation model of adhesion wear was proposed. Archard considered that the wear volume of materials is proportional to the slip distance and normal contact load, but inversely proportional to the yield limit of materials. Therefore, the formula for calculating the adhesive wear volume is as follows:

$$W = K \frac{Ns}{H} \quad (1)$$

In the formula,  $W$  is the wear volume;  $K$  is the wear coefficient, the probability of producing abrasive particles;  $N$  is the normal load;  $s$  is the sliding distance;  $H$  is the hardness of the weaker material. The formula is widely used as the basic formula for studying material wear.

Abrasive wear is materials migration or shedding caused by hard particles or hard bumps on the friction surface during the friction process. Rabinovich [10] proposed a quantitative formula for abrasive wear based on micro-cutting theory. The formula shows the relationship between abrasive sharpness and wear rate:

$$\frac{dW}{ds} = P \frac{\tan \theta}{\pi \cdot H} \quad (2)$$

In the formula,  $dW$  is the increment of wear volume;  $ds$  is the increment of sliding distance;  $P$  is the load on the abrasive grain;  $\theta$  is the angle between the conical surface of the abrasive grain and the horizontal surface of the metal. Archard also gave a formula for calculating abrasive wear [11]:

$$\frac{dW}{ds} = K \frac{N}{H} \quad (3)$$

$K$  refers to abrasive wear constant, which is determined by factors such as abrasive hardness, shape, and number of abrasive particles. The diagrams of adhesion wear and abrasive wear are shown in Fig. 1.

Compared with the first two wear forms, the quantitative formulas of the other two wear forms are seldom studied. Fatigue wear is pitting or spalling on the friction surface caused by plastic deformation and fatigue of surface material under alternating contact stress. Bayer [12] also believed that the fatigue of materials is the basic factor causing the wear of materials under sliding friction. Archard directly gave the same formula of fatigue wear as adhesive wear, in which  $K$  was given a new meaning;  $1/K$  was equal to the number of stress cycles that cause fatigue

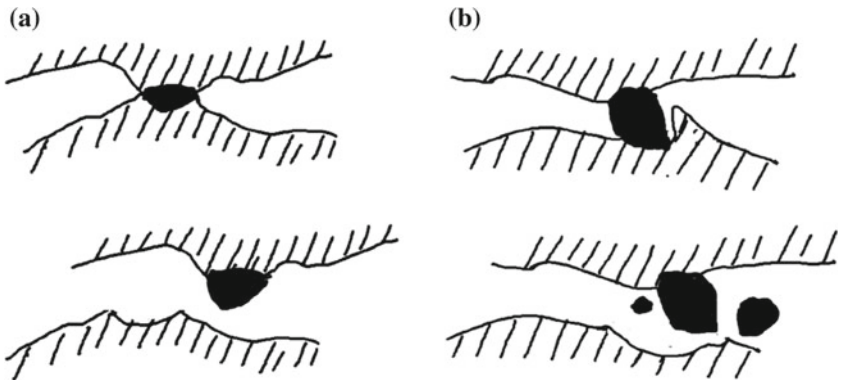


**Fig. 1** **a** Adhesive wear diagram and **b** abrasive wear diagram

failure. Corrosion wear is the surface damage caused by chemical or electrochemical reaction between metal and surrounding medium. Corrosion wear is greatly affected by environmental factors, such as acid, alkali, and salt. Archard gave the same formula for calculating corrosion wear, in which  $K$  represents the coefficient related to the thickness of corrosion film.

At present, most of the wear formula of ball screw pairs is based on Archard adhesive wear model. Although the calculation formulas of various wear models are the same, the values of coefficient  $K$  have different meanings. From the perspective of adhesive wear alone, the corresponding  $K$  values of different wear forms and operating environments are also different [6, 13]. Therefore, the adhesive wear model is difficult to accurately represent the wear condition of the ball screw.

### 3 Wear Model of Ball Screw Pair

Macroscopically, the whole wear process of ball screw pair includes three stages: running-in wear period, normal wear period, and severe wear period. During the running-in wear period, the surface defects of wear pairs caused by processing and assembling lead to too excessive peak pressure on the contact surface that abrasion is intense and irregular. After that, the convex peak of the wear pair is flattened, the contact area increases, and the wear rate decreases sharply, thus entering a stable wear period. Previous research suggests that, in the normal wear period, the wear rate is constant [8], and the wear rate is approximately proportional to the time when other operating conditions are determined. But for closed wear pairs such as ball screw pairs, there are two main types of wear during the stable wear period, adhesive wear and abrasive wear. With the increase of abrasive particles, abrasive wear becomes more serious, the wear rate should have increased. Through a large number of experiments, SKF Bearing Manufacturing Company concluded that the

fatigue life of rolling bearings can be prolonged to 10–50 times by removing 2–5 micron solid particles in lubricating oil [14]. Therefore, the influence of the number of abrasive particles should not be neglected when considering the wear model.

There are two main wear forms of ball screw pairs in the process of low load wear, which should be considered in two parts when calculating wear amount. The first part is adhesive wear, which can directly adopt the commonly used adhesive wear formula of ball screw [5]:

$$\frac{dW}{ds} = k_s \frac{F_N}{3\sigma_s} \quad (4)$$

In the formula,  $k_s$  is dimensionless wear constant, and take  $10^{-9}$  when lubrication is good.  $F_N$  is the normal force acting on a single bonding point.  $\sigma_s$  is the compressive yield limit of softer material between rolling element and raceway.

The second part is abrasive wear. From the microscopic point of view, the influence of abrasive particles on contact surface has two parts. One is the large abrasive particles which are directly squeezed into the softer material, which causes the friction surface to produce wear marks and new abrasive particles under the furrow action; the other is the small particles which are directly attached to the frictional surface to form a peak. The role of this part of abrasive particles is similar to adhesion wear, which also produces grooves and more debris. For closed wear pairs, this is a vicious cycle process, which means the wear increment per unit time should be positively correlated with the number of abrasive particles involved in the wear process. Therefore, the abrasive wear formula under closed condition can be written as follows:

$$\frac{dW}{ds} = k \frac{F_N}{3\sigma_s} \cdot \frac{W}{\bar{V}} \quad (5)$$

In the formula,  $\bar{V}$  is the average volume of debris produced,  $W/\bar{V}$  is the number of abrasive grains, and  $k$  is a dimensionless constant, which is related to the proportion, hardness, and shape of abrasive particles actually involved in the wear process. Combining these two parts, the wear model of ball screw pair can be obtained:

$$\frac{dW}{ds} = ks \frac{F_N}{3\sigma_s} + k \frac{F_N}{3\sigma_s} \cdot \frac{W}{\bar{V}} \quad (6)$$

Assuming that the area of the contact surface between two friction pairs is  $\Delta A$ , the wear depth on the contact area is  $\Delta h$ ; then,  $dW/\Delta A = \Delta h$ , and  $\Delta t$  is unit time, and then, the relative sliding velocity of ball and raceway is  $v = ds/\Delta t$ . Divide the two sides of Eq. (6) by  $\Delta A$  and  $\Delta t$  at the same time; then, the relationship between wear depth and time is obtained as follows:

$$\frac{dh}{\Delta t} = k_s \frac{F_N \cdot v}{3\sigma_s \Delta A} \cdot \left( 1 + \frac{k}{k_s} \cdot \frac{\Delta A}{V} \cdot h \right) \quad (7)$$

Formula (7) is a differential equation, and the initial condition is  $t = 0$  and  $h = 0$ . An approximate model for calculating the wear depth of ball screw can be obtained by solving the differential equation:

$$h = \frac{k_s \bar{V}}{k \Delta A} \cdot \exp \left( k \frac{F_N \cdot v}{3\sigma_s \bar{V}} \cdot t \right) - \frac{k_s \bar{V}}{k \Delta A} \quad (8)$$

Compared with the wear model of ball screw in literature [5]:

$$\frac{dh}{\Delta t} = k_s \frac{F_N \cdot v}{3\sigma_s \Delta A} \quad (9)$$

When the operating conditions such as load and lubrication conditions are determined, the right side of Eq. (9) is a constant. This shows the wear depth of the original model has a linear relationship with the running time. However, the new model is exponential. The accuracy of the new model will be verified by the experimental data in reference [5], and the estimation of the correlation coefficient will be obtained.

## 4 Verification of Ball Screw Wear Model

In reference [5], the wear data of ball screw pair under general conditions were obtained by testing a certain type of ball screw pair made in China. The experiment was conducted on a vertical test stand, and the axial load was simulated by means of the counterweight applied under the test bench. The structural parameters and operating conditions of the ball screw pair are given in Table 1.

In the initial of the experiment, the sample is in the running-in period and the measured value changes greatly. Therefore, the ball screw pair will run for 50 h to enter a stable wear period. During the test, the measurement was made every 50 h, and the initial measurement value was taken as the reference value. Then, the difference between the measured value and the initial value was taken as the measurement value of wear. In order to eliminate the interference of human factors, the average values of the data obtained from the three groups of experiments were taken as the final experimental results. The experimental data are shown in Table 2.

The parameters  $k/\bar{V}$  related to abrasive wear coefficient and average volume of debris in the new model cannot be measured. Therefore, the correctness of the model cannot be proved directly by comparing the calculated data of the new model with the experimental data. However, according to the trend of test data and considering the possible actual relationship between wear rate and time, the

**Table 1** Structural parameters and operating conditions of ball screw pairs

Parameter	Unit	Value
Lead angle $\varphi$	°	3.64
Pitch diameter of lead screw $D_{pw}$	mm	40
Ball diameter $D_w$	mm	4.763
Curvature radius of screw raceway $r_s$	mm	2.477
Curvature radius of nut raceway $r_n$	mm	2.477
Initial contact angle $\alpha_0$	°	45
Total effective balls $N$		100
Modulus of elasticity $E_1, E_2$	GPa	207
Poisson ratio $\mu_1, \mu_2$		0.3
Yield limit of bearing steel under compression $\sigma_s$	MPa	1617
The sum of preload and axial load $F_a$	$N$	6000
Speed of screw $n$	r/min	100
Running time $\Delta t$	h	310
Studio temperature	°C	20 ± 1
Lubricating oil type		L-FC 32

**Table 2** Measured value of wear amount of ball screw pairs

Running time (h)	Effective displacement variation (μm)	Relative wear depth (μm)
50	8.64	0.00
100	8.97	0.33
150	9.20	0.56
200	9.42	0.78
250	9.70	1.06
300	10.98	2.34
350	18.96	10.32

proportional model, power function model, and exponential model are selected to fit the test data. The fitting results obtained by the least square method using Origin are shown in Fig. 2.

The coefficient  $R^2$  of goodness of fit for proportional relation, power relation, and exponential relation is 0.4718, 0.9747, and 0.9936, respectively. The results show the fitness of the exponential model is the highest. Therefore, when the confidence level is 0.05, there is a 99.36% probability that the relationship between wear rate and wear time is exponential. This means the new model is in the right form. And the exponential fitting model of test data is as follows:

$$y = A1 * \exp(x/t1) + y0 \quad (10)$$

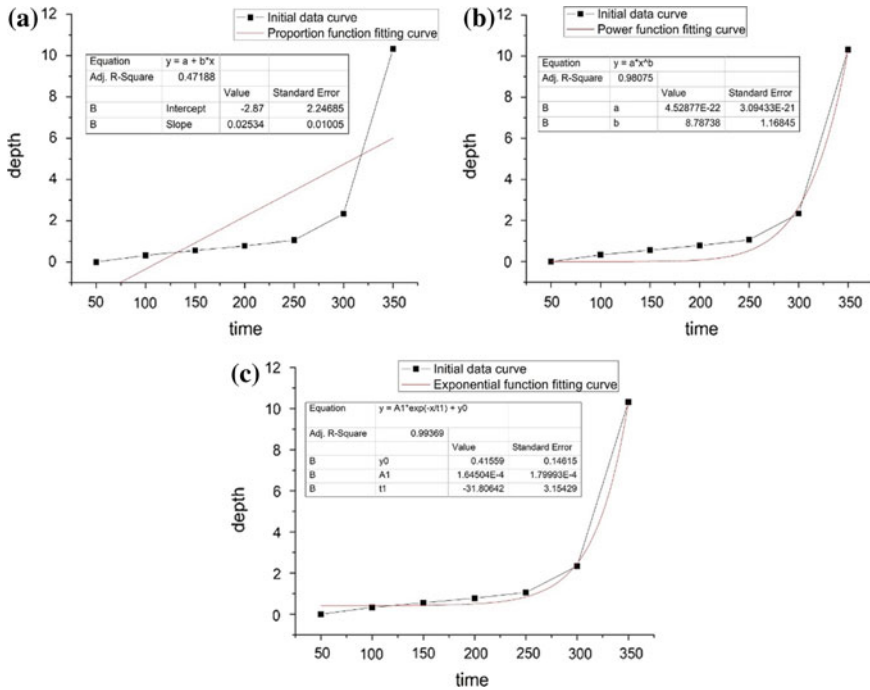


**Fig. 2** Fitting results: **a** proportional relationship, **b** power relationship, and **c** exponential relationship

To further verify the correctness of the new model theory, the unknown parameters in the new model can be estimated by using the coefficient  $1/t1$  of shape determination in the fitting equation. After the estimated values of unknown parameters are obtained, the theoretical values of wear can be calculated by the new model. Then, the theoretical calculation values of the original model and the new model are compared with the experimental measurements, respectively. Comparing the new model with the fitting equation, the relationship between the parameters can be obtained as follows:

$$\frac{1}{t1} = k \frac{F_N \cdot v}{3\sigma_s \bar{V}} \quad (11)$$

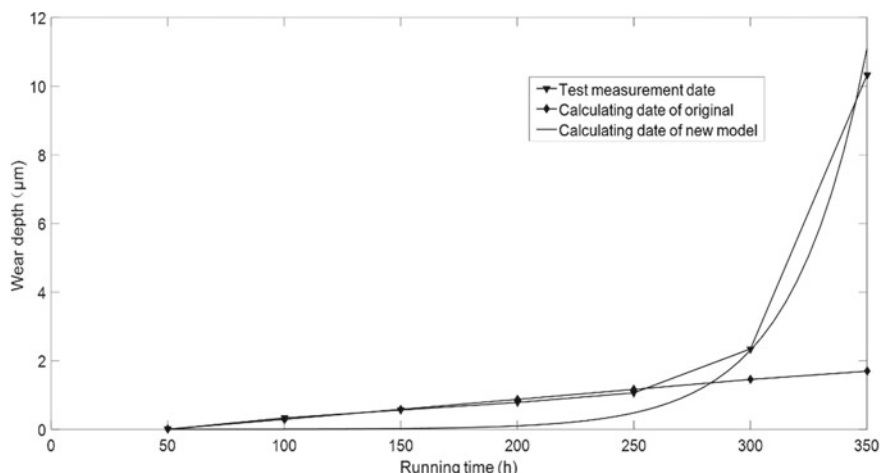
Therefore, the formula for calculating unknown parameters is as follows:

$$\frac{k}{\bar{V}} = \frac{3\sigma_s}{F_N \cdot v \cdot t1} \quad (12)$$

Then, according to Hertz elastic contact characteristics and kinematics analysis, the deformation, contact angle, and relative sliding speed of the contact points

**Table 3** Measured values of wear of ball screw pairs and calculated data of original model

Running time (h)	Measured relative wear ( $\mu\text{m}$ )	Calculating relative wear amount by original model ( $\mu\text{m}$ )	Calculating relative wear amount by new model ( $\mu\text{m}$ )
50	0.00	0.00	0.0000
100	0.33	0.29	0.0034
150	0.56	0.58	0.0197
200	0.78	0.87	0.0984
250	1.06	1.16	0.4772
300	2.34	1.45	2.3016
350	10.32	1.96	11.0884

**Fig. 3** Comparison of experimental data with model data

between ball and screw raceway, ball and nut raceway can be calculated. The concrete calculation formula can be referred to reference [5]. The calculation results are directly used here. The wear amount of the new model corresponding to the time can be calculated by adding the calculated parameters into Eq. (8). The calculation data of the original model and the new model are compared, as shown in Tables 3 and Fig. 3.

According to the formula of correlation coefficient test method:

$$R^2 = \left[ \sum_{i=1}^n (X_i - \bar{X})(Y_i - \bar{Y}) \right]^2 / \left[ \sum_{i=1}^n (X_i - \bar{X})^2 \sum_{i=1}^n (Y_i - \bar{Y})^2 \right] \quad (13)$$

The correlation coefficients of the original model and the new model are  $R_1^2 = 0.6973$  and  $R_2^2 = 0.9962$ , respectively. Therefore, we can draw the following

conclusions: (1) The estimated values of unknown parameters in the new model are reasonable, and the theory of the new model is correct. (2) The new model is better than the adhesive wear model in expressing the relationship between wear rate and time. However, there are some deviations between the calculated data of the new model and the experimental data in the early stage of operation. This is because the irregular wear in the running-in stage produces a certain amount of debris, and the initial wear value is not zero. On the whole, the new model considering the effect of abrasive particles can better reflect the wear condition of ball screw during the whole operation process.

## 5 Conclusion

Based on the traditional study of ball screw pair wear, this paper analyzes the wear mechanism of closed pairs and builds a wear model considering the effect of abrasive particles. The model shows that the debris generated by the closed wear pair during operation will aggravate the wear process, and the wear amount and time are exponentially related. The rationality and accuracy of the model are verified by wear experiments of ball screw pairs. The model provides a theoretical basis for predicting the precision degradation law and service life of ball screw pairs. At the same time, the model proposed in this paper can also be applied to other closed wear pairs such as bearings. However, the model needs to solve the following problems. One is to determine the effective value of the average volume of debris produced in the wear process. The other is to determine the value of abrasive wear coefficient  $k$ . These parameters need a lot of experiments to determine, which also point out the direction for the future work.

**Acknowledgements** This work is supported by the National Natural Science Foundation, China (No. 51835001; 51705048); the National Major Scientific and Technological Special Project for “High-grade CNC and Basic Manufacturing Equipment,” China (2018ZX04032-001).

## References

1. Greenwood JA, Williamson JBPP (1996) Contact of nominally flat surfaces. Proc Roy Soc A Math Phys Eng Sci 295(1442):300–319
2. Chang WR, Etsion I, Bogy DB (1987) An elastic-plastic model for the contact of rough surfaces. ASME J Tribol 109(2):257–263
3. Horng JH (1998) An ellipticity elastic-plastic asperity microcontact model for rough surfaces. ASME J Tribol 120:82–88
4. Zhong Y, Tao WJ, Han J (2003) Research on precision loss model of ball linear guide pair. Modular Mach Tools Autom Process Technol (12):33–36 (2003) (in Chinese)
5. Xu XH, Tang WH, Yu T (2016) Ball screw wear prediction based on Archard theory. Combination Mach Tools Autom Process Technol 2:54–59 (in Chinese)

6. Liu CH, Chen XY, Gu JM (2009) High-speed wear life-time analysis of instrument ball bearings. *Proc Inst Mech Eng Part J: J Eng Tribol* 223(3):497–510
7. Olofsson U (1997) Characterization of wear in boundary lubricated spherical roller thrust bearings. *Wear* 208(1–2):194–203
8. Wen SZ, Ping H (2012) Principles of tribology (2nd edn). Tsinghua University Press, Beijing, pp 301–340 (in Chinese)
9. Archard JF (1953) Contact and rubbing of flat surfaces. *J Appl Phys* 24(8):981–988
10. Rabinowicz E, Dunn LA, Russell PG (1961) A study of abrasive wear under three-body conditions. *Wear* 4(5):345–355
11. Gui CL (1990) Archard's wear design calculation model and its application method. *Lubr Eng* 1:12–21 (in Chinese)
12. Bayer RG, Clinton WC, Sirico JL (1964) A note on the application of the stress dependency of wear in the wear analysis of an electrical contact. *Wear* 7(3):282–289
13. Gao HQ, Cai HJ, Cai M (2018) Finite element analysis of angular contact ball bearing wear based on archard modified model. *Mach Tool Hydraul Pressure* 46(15):159–164 (in Chinese)
14. Wang N (2008) Physical characteristics of wear faults of low-speed bearings based on fractal-wavelet analysis. Northeast University (in Chinese)

# Electrical Transformation to Improve Energy-Stored Experimental Capability of Rail Transit Test Line of Tongji University



Liwei Dong, Haiquan Liang, Jingtai Hu and Yufei Chen

**Abstract** The application of regenerative braking energy storage system is one of the development directions of rail transit energy traction technology, which conforms to the concept of energy saving and environmental protection. In order to carry out relevant research and experiments, the electrical transformation of the rail transit test line of Tongji University was carried out. Based on the analysis of the main wiring of traction substation, a scheme of adding a new DC feeder cabinet on the DC side is proposed, and the electrical components in the cabinet are designed. At last, a simulation model of lithium-ion supercapacitor energy storage system is established based on the transformed test line. The simulation results show that the transformed rail transit test line has a good ability of energy-storage-related experiments, and the expected goal has been achieved.

**Keywords** Rail transit · Traction substation · DC feeder cabinet · Energy storage system · Supercapacitor

## 1 Introduction

Due to the short distance between urban rail transit stations, the vehicles start and stop frequently, and considerable braking energy is generated during the braking process. The supercapacitors have the advantages of high power density, fast charge and discharge speed, long cycle life, and high efficiency. Therefore, they are very suitable for urban rail transit braking energy recovery system [1, 2].

---

L. Dong · H. Liang (✉) · J. Hu  
Institute of Rail Transit, Tongji University, No. 4800 Cao'an Highway,  
Jiading District, Shanghai, China  
e-mail: lhq@tongji.edu.cn

Y. Chen  
College of Electronic and Information Engineering, Tongji University,  
No. 4800 Cao'an Highway, Jiading District, Shanghai, China

To improve the performance of traditional supercapacitors, scholars and experts in the industry mainly improve their energy density and monomer voltage through chemical research on electrode materials and electrolyte materials of supercapacitors [3], thus deriving a series of more excellent supercapacitors, including lithium-ion supercapacitors. In addition to materials, the research of supercapacitor model [4, 5], management system [6, 7], and mixed use with other energy storage components [8, 9] are also the hotspots in the application of supercapacitors.

Lithium-ion supercapacitor combines the advantages of supercapacitor and lithium-ion battery and has higher energy density and monomer voltage. It is necessary to conduct research on the application of lithium-ion supercapacitor in urban rail transit. In order to build a lithium-ion supercapacitor energy recovery system, research on regenerative braking with energy stored and related experimental preparations are carried out. On the one hand, a transformation scheme is proposed based on the analysis of existing traction substation. A new DC feeder cabinet is reasonably designed and installed to ensure the safe operation of the energy recovery system. On the other, energy recovery system is simulated based on test line parameters, and the simulation results show that energy-stored experimental capability of test line is effectively improved.

## 2 Research Methods

### 2.1 Overview of Traction Substation

There is a traction substation in the rail transit test line. The traction substation obtains electric energy from the regional substation and transforms it into the required voltage level of the test vehicle by step-down and rectification. Figure 1 shows the main wiring of the traction substation. Electric energy is fed through 10 kV GIS incoming cabinet and is sent to two sets of 750 V 12-pulse rectifier units through the autotransformer. The autotransformer can adjust the 10 kV voltage through the voltage regulating switch to meet the relevant experimental requirements. The two sets of rectifier units switch the connection state through a pair of self-locking isolating switches. Equivalent 750 V voltage is output in parallel, and 1500 V voltage is output in series. The DC traction electric energy is input to the positive bus through the rectifier, and then flows to the catenary through the DC feeder cabinet; the running test vehicle is subjected to the electric bow to obtain electric energy from the catenary, and the generated current flows back to the negative bus through the rail and the return line, thereby completing one complete traction reflow process.

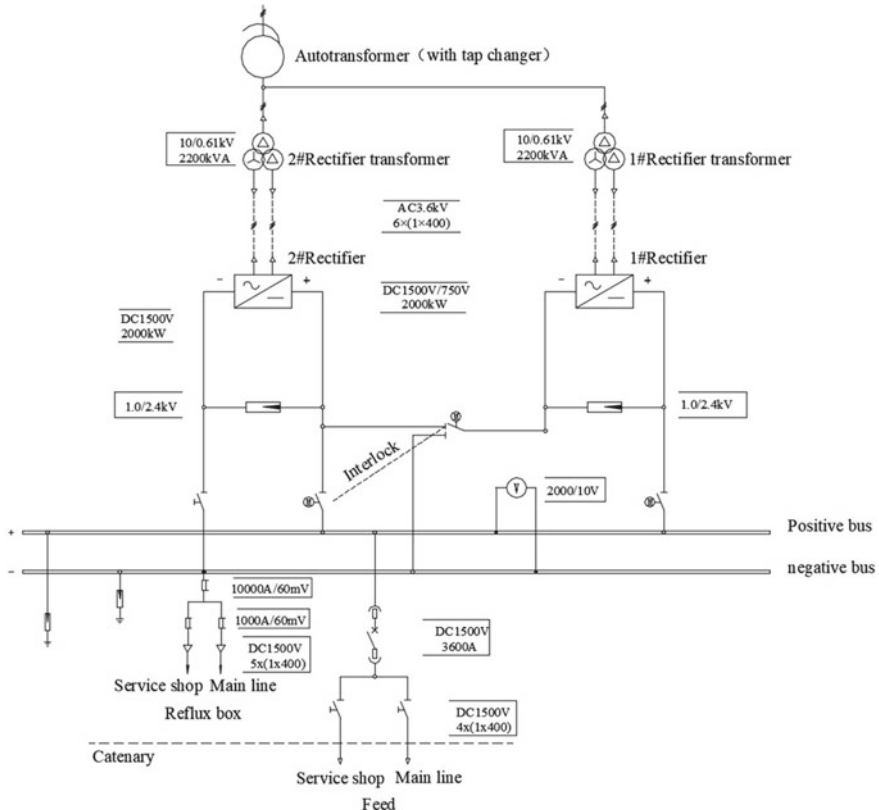


**Fig. 1** Main wiring diagram of traction substation

## 2.2 Electrical Transformation

Our school undertakes the project funded by Shanghai Science and Technology Commission. The project content is the engineering demonstration of lithium-ion supercapacitor energy recovery system, namely realizing the intermodulation of lithium-ion supercapacitor system, DC-DC converter, and the network terminal on the rail transit test line, and verifying the feedback response of energy recovery system including in overload protection, short-circuit protection, and other working conditions by connecting with the existing real-time signal detection system. In this project, the stationary supercapacitor energy storage system is selected, and lithium-ion supercapacitor bank is needed to be connected in traction substation. At the same time, corresponding protection should be provided for energy storage equipment and DC feeder section. Based on this requirement, the traction substation should be transformed. A new 1500 V DC feeder cabinet is added to the DC part in the dotted frame, as shown in Fig. 2. The negative of it is introduced into the DC

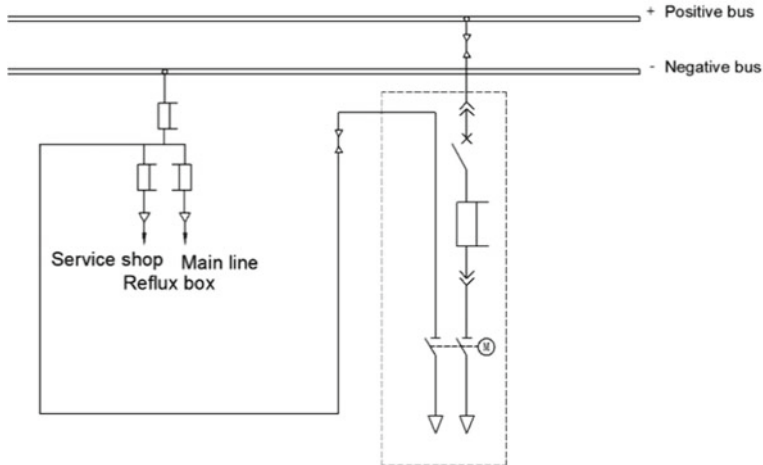


**Fig. 2** Scheme of main circuit of DC feeder cabinet

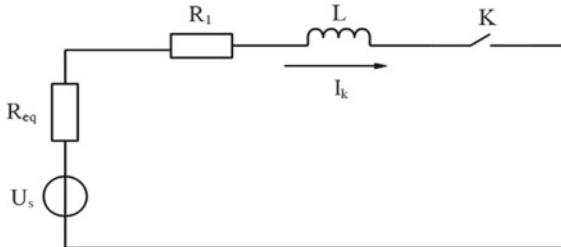


**Fig. 3** Equivalent circuit of traction power supply system

switch cabinet, and the new feeder cabinet is connected with the energy storage equipment through the disconnector.

The traction power supply system can be equivalent to the circuit shown in Fig. 3.

When the switch K is on, short-circuit fault of DC feeder circuit can be simulated. The mathematical model of short-circuit system is as shown in (1).

$$L \frac{di}{dt} + (R_{eq} + R_1) I_k = U_s \quad (1)$$

where  $L$  is equivalent inductance of DC feeder circuit,  $R_{eq}$  and  $R_1$  are equivalent internal resistance of traction substation and resistance of DC feeder circuit, respectively,  $I_k$  is short-circuit current, and  $U_s$  is an ideal voltage source equivalent to traction substation.

The expression of  $I_k$  can be obtained by solving (1):

$$I_k = \frac{U_s}{R_{\text{eq}} + R_1} \left( 1 - e^{-\frac{R_{\text{eq}} + R_1}{L} t} \right) = \frac{U_s}{R_{\text{eq}} + R_1} - \frac{U_s}{R_{\text{eq}} + R_1} e^{-\frac{R_{\text{eq}} + R_1}{L} t} = I_p - I_{\text{ap}} \quad (2)$$

$I_k$  consists of  $I_p$  and  $I_{\text{ap}}$ .  $I_p$  is the component of steady-state short-circuit current.  $I_{\text{ap}}$  is the component of transient short-circuit current, and it decreases exponentially with time.

According to (2), the maximum value of  $I_k$  is  $I_p$ . And  $I_p$  is inversely proportional to the sum of  $R_{\text{eq}}$  and  $R_1$ . The maximum short-circuit current  $I_k$  may appear near the traction substation, and  $R_1$  can be seen as zero at this time. So  $I_{k\max}$  can be calculated as shown in (3).

$$I_{k\max} = \frac{U_s}{R_{\text{eq}}} \quad (3)$$

The relationship between ideal voltage source and rated voltage of traction substation is shown in (4).

$$R_{\text{eq}} = (U_s - U_n)/I_n \quad (4)$$

where  $U_n$  is the rated voltage of DC side and  $I_n$  is rated current of traction substation.

Considering that two sets of rectifiers in series or in parallel correspond to DC voltage output of 1500 V or 750 V, respectively, DC feeder cabinet and equipment in cabinet should meet the requirements of two voltage modes at the same time. The internal insulation level of DC feeder cabinet is designed according to DC 1500 V system. The maximum short-circuit current of two sets of rectifier units operating in parallel with the output voltage of 750 V is much larger than that in series, so the breaking capacity of circuit breaker should be designed according to the working condition of 750 V in parallel. The equivalent internal resistance  $R_{\text{eq}}$  of traction substation is calculated as shown in (5).

$$R_{\text{eq}} = K_r \frac{U_d \%}{100} \times \frac{U_n^2}{0.9nS_T} \quad (5)$$

where  $K_r$  is internal resistance coefficient,  $U_d \%$  is the ratio of short-circuit impedance voltage to rated voltage of rectifier transformer,  $n$  is the number of traction rectifier unit, and  $S_T$  is the capacity of rectifier transformer.

From (3), (4), and (5), it can be estimated that the maximum short-circuit current  $I_{k\max}$  which may occur in the circuit connecting the energy storage equipment is 62.485 kV.

The model of DC feeder cabinet is selected as WDQ-1500. Considering the possible maximum short-circuit current, the rated switching current of DC circuit

**Table 1** Main electrical components of DC switch cabinet

Electrical components	Model	Number
DC circuit breaker	WLDS1-2500	1
DC disconnector	HD18-3000	1
Microcomputer protection device	ST700	1
Splitter	FL-2 3000 A/60 mV	1
Voltage isolation transmitter	P42001D3	1
Current isolation transmitter	P41066D1	1
Fault detection device	WL-JC	1
DC voltmeter	6C2-V	1
DC ammeter	6C2-A	1

breaker is selected as 80 kV, and the model of it is selected as WLDS1-2500. During the selection process, the rated current of DC disconnector should be larger than that of circuit breaker. Otherwise, it may occur that when the circuit breaker does not reach its maximum load current and is not disconnected, the disconnector will be burnt because of the excess of the maximum current, and then, the arc will produce overvoltage, which will endanger other equipment. Therefore, the model of DC disconnector is selected as HD18-3000. The main electrical components in the DC feeder cabinet are shown in Table 1.

The setting range of tripping current of selected circuit breaker is 3200–8000 A. The tripping current setting is selected as 8000 A to verify the operation time of circuit breaker.

When one set of 750 V 12-pulse rectifier units works alone, short-circuit current at the end of DC feeder circuit is calculated as (6).

$$I_{k1} = \frac{U_s}{R_{eq} + R_1} \left( 1 - e^{-\frac{R_{eq} + R_1}{L} t} \right) = \frac{U_s}{R_{eq} + rd} \left( 1 - e^{-\frac{R_{eq} + rd}{ld} t} \right) \\ = \frac{783.435}{0.0251 + 0.03 \times 0.1} \left( 1 - e^{-\frac{0.0251 + 0.03 \times 0.1}{2.5 \times 10^{-3} \times 0.1} t} \right) = 27,880 (1 - e^{-112.4t}) \quad (6)$$

where  $r$  is unit resistance of DC feeder circuit and the value is 0.03  $\Omega/\text{km}$ .  $l$  is the unit inductance of DC feeder circuit, and the value is 2.5 mH/km.  $d$  is length of cable in DC feeder circuit, and the value is 0.1 km.

When two sets of 750 V 12-pulse rectifier units work in parallel, short-circuit current at the end of DC feeder circuit is calculated as (7).

$$I_{k2} = \frac{783.435}{0.0125 + 0.03 \times 0.1} \left( 1 - e^{-\frac{0.0125 + 0.03 \times 0.1}{2.5 \times 10^{-3} \times 0.1} t} \right) = 50,544 (1 - e^{-62t}) \quad (7)$$

When two sets of 750 V 12-pulse rectifier units work in series, short-circuit current at the end of DC feeder circuit is calculated as (8).

$$I_{k3} = \frac{1566.87}{0.0502 + 0.03 \times 0.1} \left( 1 - e^{-\frac{0.0502 + 0.03 \times 0.1}{2.5 \times 10^{-3} \times 0.1} t} \right) = 29,452(1 - e^{-212.8t}) \quad (8)$$

By introducing the tripping current setting into (6), (7), and (8), the operation time calculated is 3, 2.8, and 1.5 ms, respectively. It shows that the selected circuit breaker can quickly disconnect the DC feeder circuit when short-circuit occurs in different working modes.

### 3 Research Validity

After the electrical transformation of the rail transit test line, a simulation model of lithium-ion supercapacitor energy recovery system is built according to the requirements of the project undertaken. The parameters of supercapacitors take the supercapacitor bank purchased of the test line as reference; the lithium-ion supercapacitor bank is shown in Fig. 4. The relevant simulation data are collected during the whole running process of the test vehicle. Figure 5 is the voltage comparison of the catenary before and after adding the energy storage system. Figures 6 and 7 are the voltage and current curves of lithium-ion supercapacitor bank, respectively.

From the analysis of Fig. 5, it can be concluded that:

1. After adding energy storage system, the fluctuation of catenary voltage decreases from 1200–1750 V to 1300–1650 V, and the fluctuation range decreases by 36%.
2. When the vehicle is switched from acceleration mode to uniform mode/from uniform mode to braking mode, the catenary voltage rises suddenly, which causes impact on the catenary. After adding the energy storage system, the catenary voltage increases slowly to about 1450 V/1650 V.



**Fig. 4** Lithium-ion supercapacitor bank

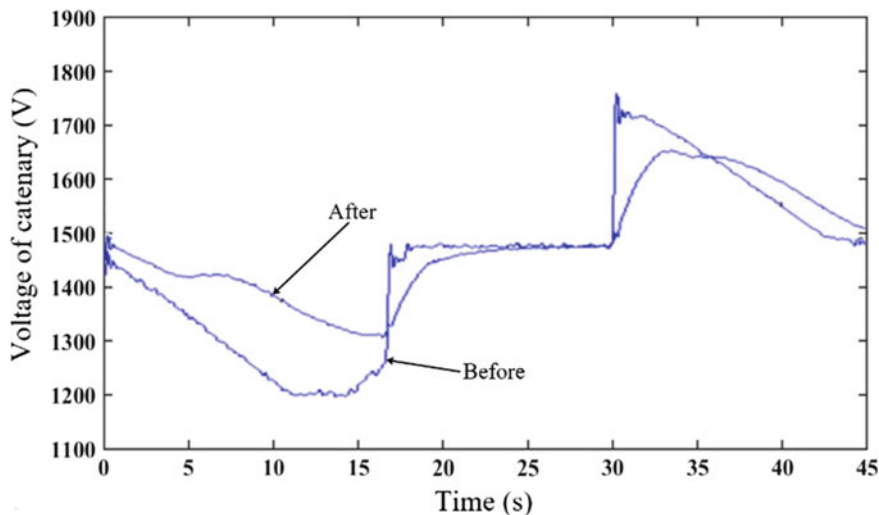


Fig. 5 Voltage comparison of catenary

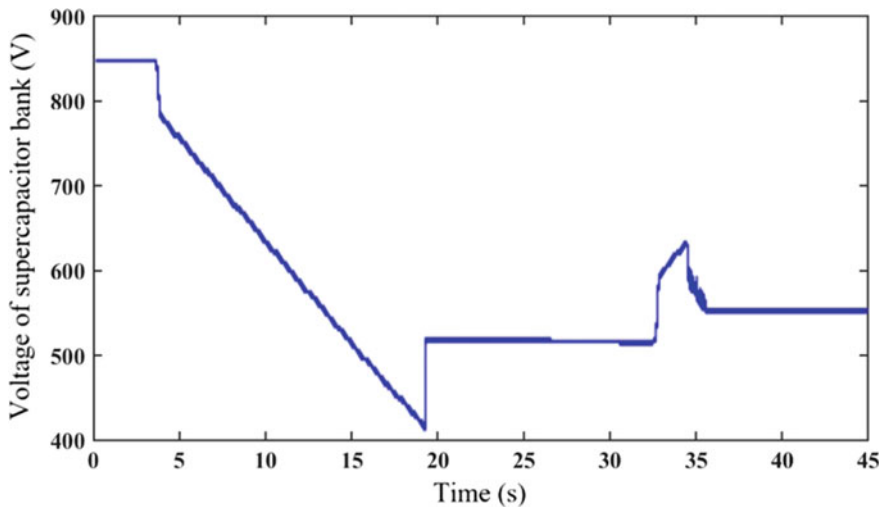
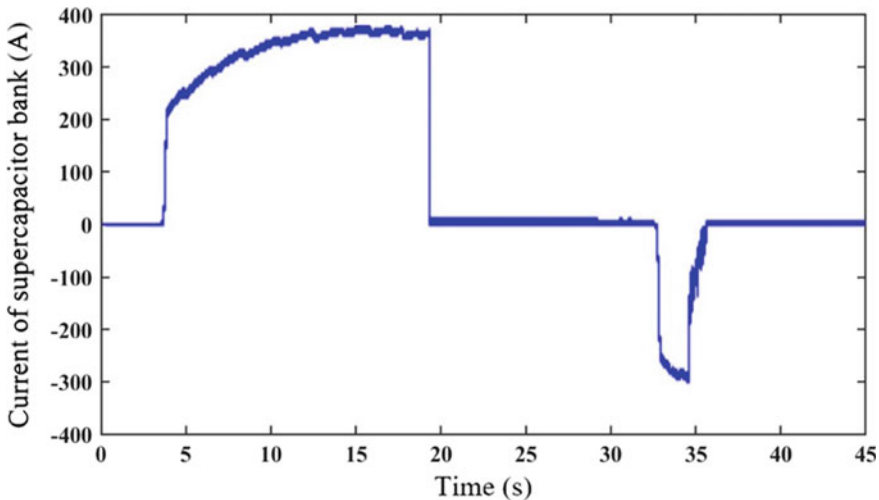


Fig. 6 Voltage curve of lithium-ion supercapacitor bank

3. In the process of vehicle braking, the energy storage system limits the maximum voltage of the catenary to less than 1650 V, the braking resistance is not started, and the energy storage system absorbs all regenerative braking energy.



**Fig. 7** Current curve of lithium-ion supercapacitor bank

From the analysis of Figs. 6 and 7, it can be concluded that:

1. During vehicle traction, the voltage range of lithium-ion supercapacitor bank is 850–405 V, and the discharge current range is 0–390 A. The energy released by the energy storage system is calculated to be 3108 kJ;
2. During vehicle braking, the voltage range of lithium-ion supercapacitor bank is 520–645 V, and the charging current range is 0–300 A. The energy absorbed by energy storage system is calculated to be 221 kJ.

## 4 Conclusion and Future Work

Regenerative braking with energy stored is one of the development trends of urban rail transit. The rail transit test line of Tongji University adopts the above scheme to carry out electrical transformation. At present, the laying of cable grooves and basic embedded parts of DC feeder cabinet and the transformation of main wiring of traction substation have been completed. The simulation model of lithium-ion supercapacitor energy recovery system based on the transformed test line runs well, which can reduce the fluctuation range of catenary voltage, and can effectively recover and reuse train braking energy. It has been successfully applied to the project “Lithium-ion supercapacitor rail energy recovery system engineering demonstration” supported by Shanghai Science and Technology Commission, which can be used as a reference for the application of regenerative braking with

energy stored in the actual operation of metro. The next research direction is to carry out the experiment of energy recovery system to verify its practical application effect.

**Acknowledgements** This work is supported by the Fundamental Research Funds for the Central Universities (22120180530) and the Fund of Shanghai Science and Technology Commission (No. 15DZ1201203).

## References

1. Zhao Y, Liang H, Zhang Y (2012) Review and expectation of modeling research on electrochemical supercapacitor. *Trans China Electrotechnical Soc* 27(3):187–195 (in Chinese)
2. Ma L, Liao W, Gao Z (2015) Research on AC side series supercapacitor regenerative braking energy storage system control strategy of railway vehicle. *Trans China Electrotechnical Soc* 30 (1):63–68 (in Chinese)
3. Tran C, Singhal R, Lawrence D et al (2015) Polyaniline-coated freestanding porous carbon nanofibers as efficient hybrid electrodes for supercapacitors. *J Power Source* 293(10):373–379
4. Logerais PO, Camara MA, Riou O et al (2015) Modeling of a supercapacitor with a multibranch circuit. *Int J Hydrogen Energy* 40(39):1–12
5. Tevi T, Takshi A (2015) Modeling and simulation study of the self-discharge in supercapacitors in presence of a blocking layer. *J Power Source* 273(10):857–863
6. Zhang Y, Guo Y, Zhu J et al (2015) Power and energy management of grid/PEMFC/battery/ supercapacitor hybrid power sources for UPS applications. *Electr Power Energ Syst* 67(9):598–612 (in Chinese)
7. Wang W, Cheng M, Wang Y et al (2014) A novel energy management strategy of onboard supercapacitor for subway applications with permanent-magnet traction system. *IEEE Trans Veh Technol* 63(6):2578–2588 (in Chinese)
8. Amin, Bambang RT, Rohman AS et al (2014) Energy management of fuel cell/battery/ supercapacitor hybrid power sources using model predictive control. *IEEE Trans Ind Informatics* 10(4):1992–2002
9. Mendis N, Muttaqi KM, Perera S (2014) Management of battery-supercapacitor hybrid energy storage and synchronous condenser for isolated operation of PMSG based variable-speed wind turbine generating systems. *IEEE Trans Smart Grid* 5(2):944–953

# E-Field Simulation and Voltage Withstand Test Analysis of Solid Insulators for AC GIS Used in High-Speed Railway Traction Substation



Shiling Zhang

**Abstract** The solid insulators are widely used in alternating current gas-insulated switchgear (GIS) equipment in high-speed railway traction substation. They have both mechanical support and electrical insulation functions. AC withstand voltage test is required before they are put into operation. In this paper, the series resonant circuit is theoretically analyzed, and the transient voltage change process of GIS solid insulators during sudden flashover is simulated and analyzed in the MATLAB/Simulink computing environment. The 3D electric field simulation of basin insulators and typical solid insulators with insulation support is carried out by using ANSYS electric field simulation platform. The withstand voltage test of the real interval of GIS is carried out to obtain the opening of circuit breaker. The relationship curves between  $Q$ ,  $I$  and applied voltage  $U$  of solid insulator under two operating conditions are obtained. The results show that after flashover of solid insulators in series resonant circuit, the arc will be extinguished immediately after high voltage drop, and the recovery voltage will be established for a long time. The typical electric field distribution of solid insulators has concentrated area of local electric field, and flashover in field withstand voltage test starts in high field strength area. The research results of this paper provide some theoretical support for the field voltage withstand test of solid insulators used in AC GIS with series resonant circuit.

**Keywords** Solid insulator for GIS · Series resonant circuit · MATLAB/simulink · Pot insulator · Voltage withstand test

---

S. Zhang (✉)

State Grid Chongqing Electric Power Company Chongqing Electric Power Research Institute, Chongqing 401123, People's Republic of China

## 1 Introduction

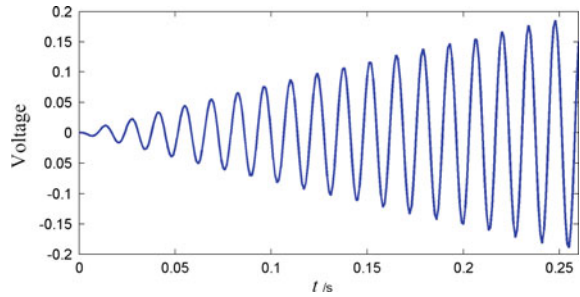
The GIS equipment is widely used in substations of various voltage levels, which has advantages such as less space occupation, easy maintenance and high reliability [1]. Field operation experience of GIS shows that external impurities such as metal particulate matter and burrs, bubbles and cracks on the surface of solid insulators in GIS pipelines can lead to operation accidents of GIS equipment [2, 3]. The role of typical solid insulators in GIS is to support the metal pipe bus of GIS and realize the electrical isolation between the high-voltage pipe bus and the geopotential GIS pipe. Insulators withstand high voltage and high current, so GIS solid insulators are the weak link of insulation. Insulation state detection should be strengthened after installation and operation of GIS. At present, main detection methods focus on partial discharge and SF<sub>6</sub> gas decomposition products [4, 5]. The above methods are applied to the operation of GIS equipment. However, before GIS pipeline is put into operation, AC voltage withstand test should be carried out on the GIS pipeline to check whether there are insulation defects in the solid insulators of GIS.

AC withstand voltage test is mainly realized by series resonance method, and partial discharge of GIS pipeline is monitored during AC withstand voltage test. Starting from the basic principle of AC withstand voltage test, this paper attempts to simulate the AC withstand voltage test device under the environment of MATLAB/Simulink and obtain the transient voltage change process of GIS solid insulators during the sudden flashover. On this basis, the model of solid insulators is established, and the AC voltage is applied to insulators. The three-dimensional electric field simulation of the basin insulators and typical solid insulators with insulating support is carried out by using ANSYS electric field simulation platform. The voltage withstand test of the true spacing of GIS is carried out, and the circuit quality factor  $Q$ , circuit current  $I$  and the outside of the solid insulators are obtained when the circuit breaker is opened or disconnected. The research results of this paper can provide some theoretical support for the application of series resonant circuit in the field voltage withstand test of solid insulators for AC GIS used in high-speed railway traction substation.

## 2 Theory and Numerical Modeling Analysis of Series Resonant Circuit

The voltage withstand test of solid insulators for GIS is carried out by using the high-voltage AC series resonance equipment. If the insulating defects of solid insulators occur flashover, the recovery voltage  $u_{0-1}$  after arc extinguishing can be characterized by Formula (1) [6, 7]:

**Fig. 1** Typical waveform of recovery voltage  $u_{0-1}$  after flashover



$$u_{0-1} = \cos(\omega t) - [\cos(\beta t) + \alpha \sin(\beta t)/\beta] \exp(-\alpha t) \quad (1)$$

$\beta = \sqrt{1/(LC) - R^2/(4L)^2}$ ,  $\alpha = R/(2L)$ . Thus, circuit resistance  $R$  is mainly the equivalent resistance caused by corona loss of the resonant circuit,  $L$  is the equivalent inductance of resonant circuit, and  $C$  is the equivalent capacitance of the resonant circuit (Fig. 1).

$$\beta = \sqrt{\omega^2 - [\omega^2/(4Q^2)]} = \omega \sqrt{1 - 1/(4Q^2)} \approx \omega \quad (2)$$

$$\alpha = R/(2L) = \omega/(2Q) \quad (3)$$

Therefore, Formula (1) can be rewritten to Formula (4):

$$u_{0-1} = \cos \omega t - [\cos \omega t + \sin \omega t/(2Q)] \exp[-\omega t/(2Q)] \quad (4)$$

Because  $1/(2Q)$  is small, Formula (4) can be further rewritten to Formula (5):

$$u_{0-1} \approx \{1 - \exp[-\omega t/(2Q)]\} \cos \omega t \quad (5)$$

### 3 Theory Numerical Modeling and Analysis of Series Resonance Circuit

The theoretical analysis of series resonant circuit includes many assumptions. In order to accurately analyze the voltage transient process of GIS solid insulators in withstand voltage test, MATLAB/Simulink module is used to simulate the voltage waveform after sudden flashover in series resonant circuit test. Topology of MATLAB/Simulink computing environment is shown in Fig. 2, including test power supply, excitation transformer, reactor, equivalent resistance, capacitor voltage divider and test sample, in which the test sample is considered as pure capacitance.

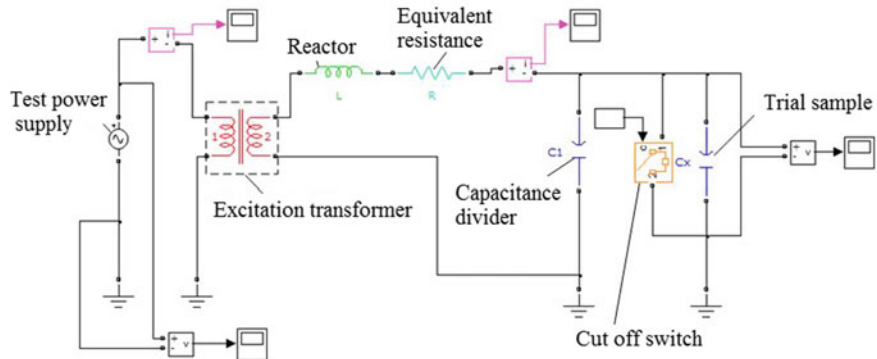


**Fig. 2** MATLAB/Simulink numerical modeling

The function of the test switch is to simulate the sudden flashover during the test. The excitation transformer is considered as a linear transformer, the rated capacity is set to 240 kVA, and rated voltage is 40 kV/340 V. In the simulation, the calculation time is set to 20 power frequency cycles, assuming that the first nine cycles flashed over suddenly, lasted for 1 ms and then returned to normal until flashover occurred again in fourteenth cycle and lasted for 1 ms. In transient process, attention is paid to reactor and test voltage as shown in Fig. 3.

**Fig. 3** Voltage of key equipment in flashover transient process

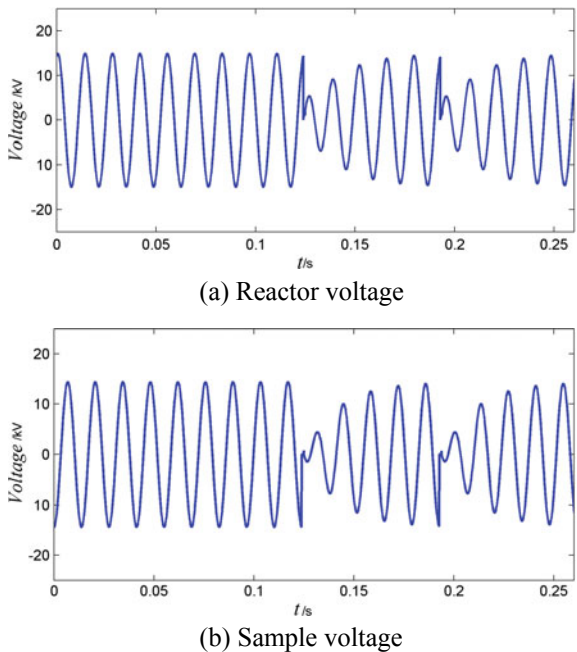
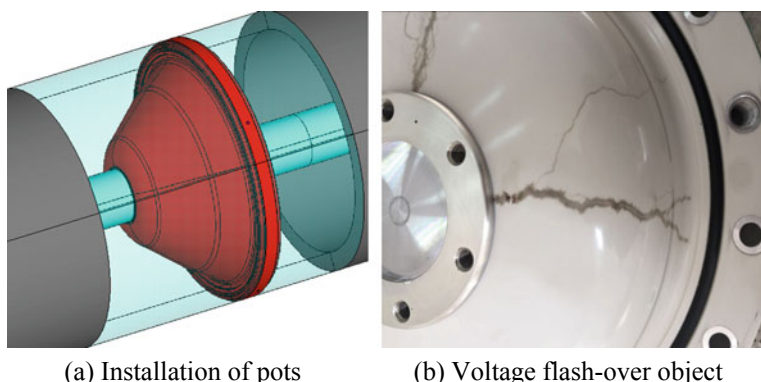


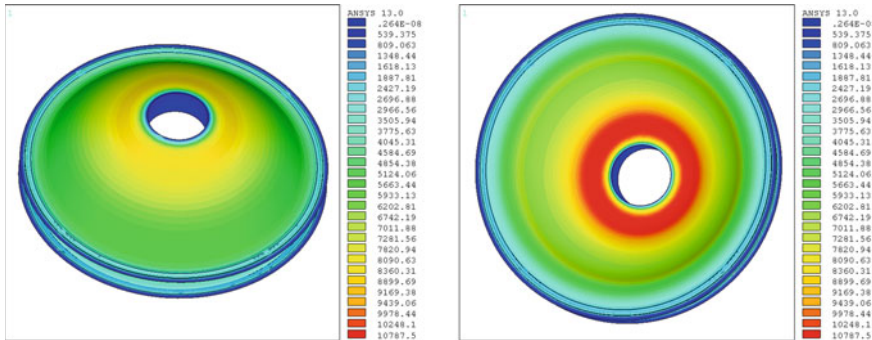
Figure 3 shows that the peak voltage on the power side is about 400 V. The peak voltage generated by series resonance device on reactor and test sample is about 14.4 kV, and the voltage amplitude increases about 36 times. The transient voltage waveform on reactor and test sample shows that the peak voltage on reactor and test sample is the same, and the voltage phase is different. When the test sample flashes, the high voltage drops, the arc is extinguished immediately, and the recovery voltage is built. The vertical process is longer, and repetitive breakdown can be avoided. There is no overshoot in the process of voltage recovery.

#### 4 AC Electric Field Simulation of Solid Insulator for GIS Circuit

The solid insulators used in GIS include pot insulators, insulation support and other typical structures. The series resonant circuit is used to test the insulation performance of the above typical structures [8]. Taking pot insulators as an example, the installation of pot insulators in GIS and the physical objects after voltage flashover are introduced, as shown in Fig. 4. Figure 4a shows that the basin insulator achieves electrical isolation between the central conductor of GIS and the grounding flange, and withstands the full voltage value between the central conductor and the grounding flange. Therefore, basin insulator is required to have good electrical insulation performance, and the AC withstand voltage test is applied to verify [9, 10]. Figure 4b shows that in the voltage withstand test by series resonance method, there are remarkable discharge marks between the center conductor of the basin and the metal flange, and the flashover starting point is located at the interface between the epoxy resin solid material and the metal center guide rod. Three-dimensional simulation analysis of AC electric field distribution of basin insulators for GIS is carried out, as shown in Fig. 5.



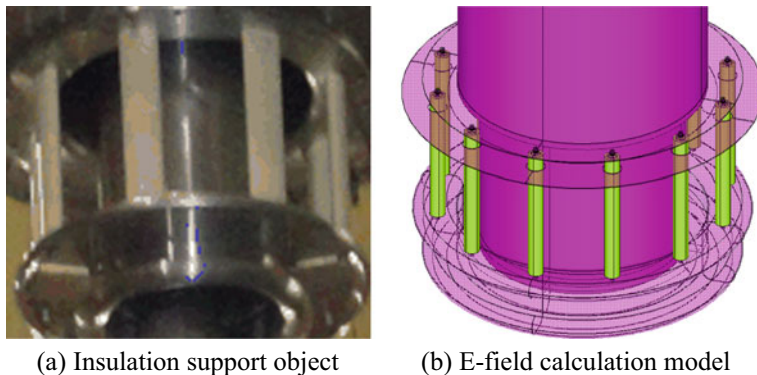
**Fig. 4** Field installation and flashover of pot insulators



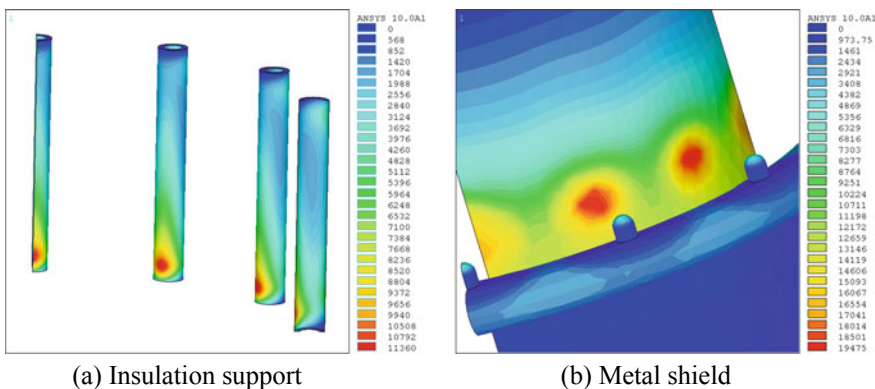
**Fig. 5** Electric field distribution on the surface of pot insulators

Figure 5 shows that the maximum field strength of the basin insulator is near central guide rod. Compared with the convex and concave surface of the basin, the maximum field strength appears at the concave surface of the basin about 10.8 kV/mm, which is consistent with the starting position of the flashover point of the basin in Fig. 4b. The surface electric field of the metal shielding cover of the basin insulator is high. Because of the metal shielding effect, a low electric field area is formed at the interface between the basin insulator and the central conductor, and the electric field intensity is about 12.08 kV/mm. The results of field strength analysis show that the weak part of the pot insulator during the withstand voltage test is the interface between the pot and the central conductor. Therefore, it should be noted there should be no metal foreign body, metal protrusion and other insulation defects at interface between the pot insulator and the metal, so as to avoid flashover accident shown in Fig. 4b. GIS outgoing sleeve is an important part of GIS equipment. Its function is to connect the central conductor with overhead conductor. Compared with the coaxial structure of GIS pipeline, the insulation structure of GIS outgoing sleeve is more complex, which mainly includes internal double-layer metal shielding, and the insulation support is connected through insulation support. The insulation support object is shown in Fig. 6a, and the double-layer metal shielding of GIS outgoing sleeve is more complex. The three-dimensional finite element model of the insulation support is shown in Fig. 6b. Figure 7 shows that the insulating support is arranged in a circular shape between the two shielding layers. The end of the insulating support is embedded in the metal shielding flange to ensure that the end of the insulating support is in the low field strength area.

The potential difference between the two shielding layers is applied to both ends of the insulation support. Figure 8 shows the distribution of electric field on the surface of insulating support and metal shielding. It can be seen that the distribution of electric field on the surface of insulating support is not uniform. The maximum electric field intensity appears near the side of metal shielding, and the electric field



**Fig. 6** Physical and electric field calculation model of insulation support



**Fig. 7** Electric field distribution on insulating support and metal shielding surface

intensity is about 11.36 kV/mm. Local high field intensity region appeared at the corresponding position of suspension shielding surface, and field intensity was about 19.48 kV/mm.

## 5 Series Resonant Loop Used in Practical GIS Voltage Resistance Test

The voltage withstand test of the true spacing of GIS is carried out, which includes the circuit breaker, disconnector, lightning arrester, voltage and current transformer. The maximum voltage of the series resonant voltage withstand device can be



**Fig. 8** True interval of actual GIS

increased to 680 kV with rated current of 1.2 A. The series resonant device adopts SF<sub>6</sub> gas insulation and generates high voltage from the resonant circuit. Its frequency can be adjusted in the range of 18–300 Hz. The true spacing of GIS is shown in Fig. 8.

Figure 8 is a real spaced circuit breaker of GIS. In the actual withstand voltage test, the grounding switches are all disconnected. At the same time, the arrester, voltage transformer and GIS pipe are separated by the disconnector. When the circuit breaker is on and off, the voltage withstand test is carried out for the whole true interval of GIS. During the test, the resonance frequency  $f$ , the circuit quality factor  $Q$  and the current value  $I$  of the whole series resonant circuit are emphasized. Two-stage boost technology is used in the test process: After the power frequency 220 V, voltage is raised to 10 kV by distribution transformer, and the voltage is raised to  $10Q$  kV by series resonance technology. The actual value of power frequency voltage is 212.8 V, and the reactance value in series resonant circuit is  $L = 720$  Hz. The voltage applied to the true interval of GIS is 20–110 kV, and the step-up is 10 kV. Through actual withstand voltage test, it is found that when the circuit breaker closes, the whole circuit reaches resonance state frequency  $f_1 = 123.11$  Hz, and when the circuit breaker is disconnected, the circuit reaches resonance state frequency  $f_2 = 136.83$  Hz. When series resonant circuit reaches resonance state, the relationship between reactance value  $L$ , capacitance value  $C$  and resonance frequency  $f$  is characterized by Formula (6):

$$C = (2 * \pi * f)^{-2} L^{-1} \quad (6)$$

The values of  $L$  and  $F$  are substituted into Formula (6) to calculate  $C_1 = 2.3212 \text{ nF}$  when the circuit breaker is closed and  $C_2 = 1.8791 \text{ nF}$  when the circuit breaker is disconnected. Because the current  $I_c$  of the high voltage side of the excitation transformer and the series reactor is calculated by Formula (7), that is:

$$I_c = I_L = 2 * \pi * f * C_x * U_s \quad (7)$$

The voltage value of GIS pipeline has a linear relationship with the loop quality factor  $Q$ . The  $Q$  value varies between 20 and 45. Because  $U_c/Q = U$ , where  $U$  is the output voltage value of the excitation transformer, it shows that the output voltage value of the excitation transformer is basically constant. The difference between the circuit breakers is that the circuit load capacitance value is different under the conditions of interruption and closure. With the increase of GIS pipeline voltage, the low-voltage side current value of excitation transformer shows an increasing trend, and there is a saturation effect.

## 6 Conclusion

- (1) Based on the MATLAB/Simulink computing environment, the transient voltage change process of GIS solid insulators during sudden flashover can be simulated and analyzed. After flashover of solid insulators in series resonant circuit, the arc will be extinguished immediately, and it takes 4–5 power frequency cycles to rebuild the recovery voltage.
- (2) The high field strength region of the basin insulator is located at the interface between the central conductor and the bulk insulating material, and the high field strength region of the supporting insulator is located near the end of the insulator. The flashover initiation position in the power frequency withstand voltage test is consistent with the above high field strength region.
- (3) Series resonance circuit is applied to the real simulation interval of GIS. Field test data show that the voltage of GIS pipeline is linearly related to the quality factor of the circuit, the current value of low-voltage side of excitation transformer is positively correlated with the voltage value of GIS pipeline, and there is saturation effect.

**Acknowledgements** The paper is supported by technology project Chongqing Research Program of Fundamental Science and Advanced Technology (cstc2018jcyjAX0486), and Science and Technology Project of Chongqing Power Company (2018 Science and Technology Project of Chongqing Power Company 4#).

## References

1. Jyothi NS, Ramu TS, Manoj M (2010) Temperature distribution in resin impregnated paper insulation for transformer bushings. *IEEE Trans Dielectr Insul* 7:931–938
2. Monga S, Gorur RS, Hansen P, Massey W (2006) Design optimization of high voltage bushing using electric field computations. *IEEE Trans Dielectr Insul* 13:1217–1224
3. Hesamzadeh MR, Hosseinzadeh N, Wolfs P (2008) An advanced optimal approach for high voltage AC bushing Design. *IEEE Trans Dielectr Insul* 15:461–466
4. Champion JV, Dodd SJ (2001) Inter-foil electrical breakdown in high voltage ERIP condenser bushings. In: 2001 IEEE 7th international conference on solid dielectrics, pp 329–332
5. Platek R, Sekula R, Lewandowski B (2010) Fluid influence on dynamic characteristics of transformer-bushing system using Fluid Structure Interaction (FSI) approach. *IEEE Trans Dielectr Insul* 17:408–416
6. Ko C, Zhang S (2009) Improved transient hot-spot temperature calculation method of high voltage bushings. *IEEE Trans Power Deliv* 24:1295–1301
7. Wang Q, Wang H, Peng Z, Liu P, Zhang T, Wei H (2017) 3-D coupled electromagnetic-fluid-thermal analysis of epoxy impregnated paper converter transformer bushings. *IEEE Trans Dielectr Insul* 24(1):630–638
8. Wang Q, Yang X, Tian H, Liu P, Peng Z (2017) A novel dissipating heat structure of converter transformer RIP bushings based on 3-D electromagnetic-fluid-thermal analysis. *IEEE Trans Dielectr Electr Insul* 24:1938–1946
9. Zhang S, Peng Z, Liu P (2014) Inner insulation structure optimization of UHV RIP oil-SF<sub>6</sub> bushing using electro-thermal simulation and advanced equal margin design method. *IEEE Trans Dielectr Electr Insul* 21:1768–1777
10. Zhang S, Peng Z, Liu P, Li N (2015) Design and dielectric characteristics of 1100 kV UHVDC wall bushing in China. *IEEE Trans Dielectr Electr Insul* 22:409–419

# Research on Train Energy-Saving Optimization Based on Parallel Immune Particle Swarm Optimization



Shibo Li, Wang Dai, Lichao Fang, Yong Zhang and Zongyi Xing

**Abstract** Aiming at the optimization problem of subway train energy conservation, this paper proposes a train energy-saving optimization method based on parallel immune particle swarm optimization. The parallel immune particle swarm optimization algorithm is used to optimize the train energy saving in two stages: firstly, the running time of each interval is fixed, the algorithm is used to search for the optimal working condition switching point, and then, the train running time is optimized under the premise of constant running time. Finally, using the real data of Beijing Yizhuang line to simulate, verify the feasibility of the model and algorithm.

**Keywords** Urban rail transit · Train energy conservation · Parallel immune particle swarm · Two-step optimization

## 1 Introduction

Urban rail transit is an important mode of transportation in China. Due to its frequent operation and large traffic volume, the power consumption of trains is very large, so it is of great significance for energy-saving optimization of urban rail transit trains.

Experts at home and abroad have made some research on the energy-saving optimization of trains. For the first time, Chang C S et al. [1] used genetic algorithm to optimize the coasting control strategy in ATO mode. XiuLing H et al. [2] comprehensively considered the change of the following metro's tracking interval based on the moving occlusion interval and optimized the energy-saving operation problem of the tracking train by genetic algorithm. Xin Y et al. [3] has studied a

---

S. Li · W. Dai · L. Fang · Y. Zhang (✉) · Z. Xing

School of Automation, Nanjing University of Science and Technology, Nanjing, China

timetable optimization algorithm to make the regenerative braking energy generated by the braking train can be used to the maximum extent.

This paper proposes a train energy-saving optimization method based on parallel immune particle swarm optimization [4].

## 2 Analysis of Train Operating Conditions

The train has four different operating conditions: traction, cruise, coasting and braking under different external forces [5]. Therefore, each optimization scheme can be regarded as different combinations of four operating conditions [6].

## 3 Parallel Immune Particle Swarm Optimization Algorithm

In this paper, the parallel-improved artificial immune particle swarm optimization algorithm is studied.

### 3.1 Algorithm Introduction

Firstly, the initial population is divided into two subpopulations,  $Y$  and  $N$ . In the  $Y$  population, high-quality particles with high fitness and low particle concentration are stored, and the  $N$  population stores the inferior particles with the relatively low concentration of the remaining particles. The high-quality particles in the  $Y$  population are updated according to the particle swarm updating formula to ensure that the particles of the entire population are approaching the optimal position. The particles in population  $N$  are immunized to reproduce high-quality particles in the population and renew inferior particles. The number of particles of the two subpopulations is adjusted according to the concentration of the particles.

When the particle in the particle swarm algorithm is regarded as an antibody, the value  $X_{ik}$  of the  $k$ th dimension of the  $i$ th particle in the particle swarm algorithm corresponds to the  $k$ th decision cluster [7] of the  $i$ th antibody in the immune algorithm. Then, according to the Euclidean distance formula, the Euclidean distance of the antibody  $X_i$  and the antibody  $X_j$  is:

$$\text{Distance}(X_i, X_j) = \sqrt{\sum_{k=1}^D (X_{ik} - X_{jk})^2} \quad (1)$$

Then, the similarity between the two antibodies can be expressed as:

$$\text{Similar}(X_i, X_j) = \frac{1}{\sqrt{\sum_{k=1}^D (X_{ik}, -X_{jk})^2}} \quad (2)$$

The greater the similarity of the antibody, the greater the antibody concentration value, and the antibody concentration can be expressed as:

$$\text{Density}(X_i) = \frac{1}{M} \left( \sum_{j=1}^M \text{Similar}(X_i, X_j) \right) \quad (3)$$

Among them,  $M$  is the total number of populations.

The affinity of the antibody and antigen is expressed as:

$$\text{Affinity}(X_i) = \sqrt{\sum_{i=1}^D (X_i - F_i)^2} \quad (4)$$

Among them,  $F_i$  is the spatial representation of the objective function.

The particle number expressions for population  $Y$  and population  $N$  are:

$$\text{number}(Y) = d_{\max} M \quad (5)$$

$$\text{number}(N) = M - d_{\max} M \quad (6)$$

In order to enhance the diversity of particles, the number of particles in the  $N$  population should be increased and the number of particles in the  $Y$  population should be reduced. While ensuring that high-quality particles fly in  $Y$ , another part of the particle continues to search for the optimal solution in its certain neighborhood. Therefore, automatically adjusting the number of particles in the two populations can effectively improve the diversity of the population particles [8], so that the algorithm can find the global optimal solution.

## 4 Two-Step Optimization of Train Energy Saving Based on Parallel Immune Particle Swarm Optimization

### 4.1 Algorithm Introduction

Train timing energy-saving optimization includes two steps: model building and solving.

#### 4.1.1 Establishment of Train Timing Energy-Saving Model

In this paper, energy consumption indicators, on-time indicators and precise parking indicators are used as objective functions to establish a model.

Taking the punctual indicator as an objective function, it can be expressed as:

$$f_T = \left| \frac{T_{\text{all}} - T_p}{T_p} \right| \quad (7)$$

$$T_{\text{all}} = T_I + T_H + T_{III} + T_{IV} \quad (8)$$

$T_{\text{all}}$  is the actual running time and  $T_p$  is the planned running time;  $T_I$ ,  $T_H$ ,  $T_{III}$  and  $T_{IV}$  are the running time of the vehicle in various working conditions.

The instantaneous traction power  $P(t_n)$  of the train at  $t_n$  time can be expressed as:

$$P(t_n) = F(t_n) \cdot v(t_n) \quad (9)$$

Among them,  $F(t_n)$  is the traction force of the train at  $t_n$  time.

The traction energy consumed during the  $\Delta t$  time is:

$$E(t_n) = F(t_n) \cdot v(t_n) \cdot \Delta t \quad (10)$$

Therefore, the full-line traction energy consumption  $E_{\text{all}}$  is:

$$E_{\text{all}} = \int_{t_0}^T E(t_n) dt_n = \int_{t_0}^T F(t_n) \cdot v(t_n) dt_n \quad (11)$$

When the train starts to braking, it only receives basic resistance and braking force, and the total energy is the kinetic energy of the train. From the start of braking to the stop of the train, the train's kinetic energy is divided into three parts: running resistance consumption, braking force consumption and regenerative braking energy feedback. Therefore, taking the energy consumption index (actual energy consumption) as an objective function can be expressed as:

$$f_E = E_s = E_{\text{all}} - E_{\text{reg}} \quad (12)$$

Among them,  $E_{\text{reg}}$  is the regenerative braking energy.

Obviously, the objective function of the timing energy-saving optimization model can be expressed as:

$$\min F\{f_E, f_T\} = \alpha \left( \frac{E_s - E_p}{E_p} \right) + \beta \cdot \left| \frac{T_{\text{all}} - T_p}{T_p} \right| \cdot \gamma \quad (13)$$

Among them,  $\alpha$  and  $\beta$  are the weight of the on-time indicator and the weight of the energy consumption indicator, respectively, and  $\alpha + \beta = 1$ .  $\alpha$  and  $\beta$  are determined based on the accept or reject between the two indicators.  $\gamma$  is the time penalty factor.

In this paper, safety indicator, comfort indicator, speed limit indicator, etc., are used as constraints to establish a model. In summary, the train timing energy-saving model is established as follows:

$$\begin{aligned} & \min\{f_E, f_T\} \\ s.t. : & \left\{ \begin{array}{l} g_s = |S_n - (S_I^n + S_{II}^n + S_{III}^n + S_{IV}^n)| \leq \Delta S \\ g_{K_V} = K_V = 0 \\ g_a = |a| \leq a_{\max} \\ a'_{\min} \leq g_{a'} = |a'| \leq a'_{\max} \\ v(S_0) = v(S_T) = 0 \\ 0 \leq v \leq V_{\text{line}} \\ 0 \leq F(t) \leq F_{\max}(t) \\ 0 \leq B(t) \leq B_{\max}(t) \\ S_{qx}^i < S_{xd}^i < S_{dz}^i \\ \mu_f \in [0, 1], \mu_b \in [0, 1], t \in N^* \end{array} \right. \end{aligned} \quad (14)$$

Among them,  $S_I$ ,  $S_{II}$ ,  $S_{III}$  and  $S_{IV}$  are the distance traveled by the train in various working conditions.

#### 4.1.2 Model Solving Based on Improved Immune Particle Swarm Optimization Algorithm

The specific application process of the algorithm is shown in Fig. 1.

## 4.2 Optimization of Train Running Time

Optimization of train running time includes two steps: model building and solving.

#### 4.2.1 Establishment of Train Timing Energy-Saving Model

The objective function is the total energy consumption of the interval operation, expressed as:

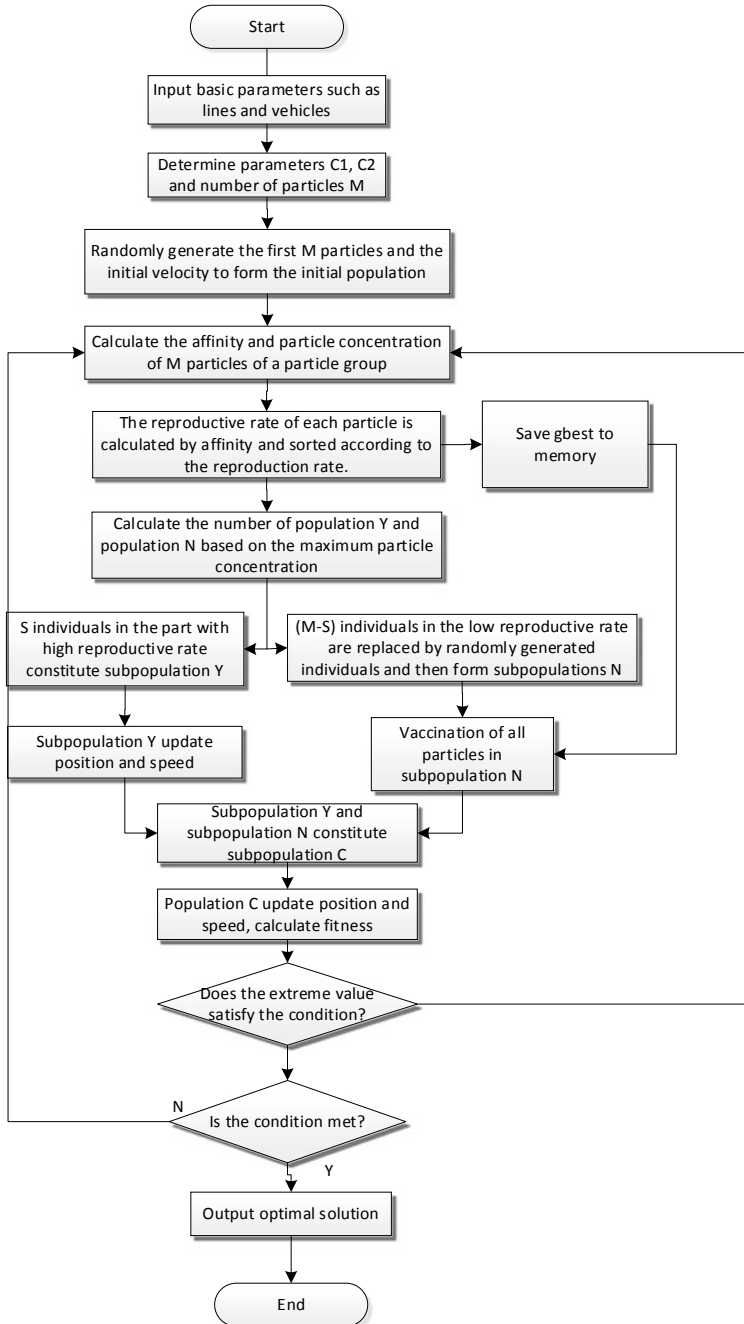


**Fig. 1** Flowchart of the solution of the timing energy-saving model

$$\min F(E_i) = \sum_{i=1}^n E_i \quad (15)$$

Among them,  $E_i$  is the energy consumption of the  $i$ th interval.

The constraints are expressed as:

$$T_i^s \geq T_i^{\min} \quad (16)$$

$$\sum_{i=1}^n T_i^s \leq \sum_{i=1}^m T_i^{\text{plan}} \quad (17)$$

Among them,  $T_i^s$  is the actual running time of the  $i$ th interval;  $T_i^{\min}$  is the minimum running time of the  $i$ th interval; and  $T_i^{\text{plan}}$  is the planned running time of the  $i$ th interval.

In summary, the train running time optimization model is established as follows:

$$\begin{aligned} \min F(E_i) &= \sum_{i=1}^n E_i \\ s.t. : & \begin{cases} T_i^s \geq T_i^{\min} \\ \sum_{i=1}^n T_i^s \leq \sum_{i=1}^m T_i^{\text{plan}} \end{cases} \end{aligned} \quad (18)$$

#### 4.2.2 Model Solving Based on Improved Immune Particle Swarm Optimization Algorithm

Based on the improved immune particle swarm optimization algorithm, this paper solves the train running time optimization model. The specific application process of the algorithm is shown in Fig. 2.

## 5 Simulation Analysis

### 5.1 Simulation Background

In order to verify the accuracy of the model and the rationality of the algorithm, this section is based on the actual data of the Beijing Yizhuang line for simulation research. The Yizhuang line has a total of 14 stations with a total length of 22.73 km, including 8 underground stations, with a total length of 13.81 km and 6 underground tunnels, with a total length of 8.92 km. The interval “Rongjing East Street—Wanyuan Street” is selected for simulation. The specific line data of the interval is given in Tables 1 and 2.

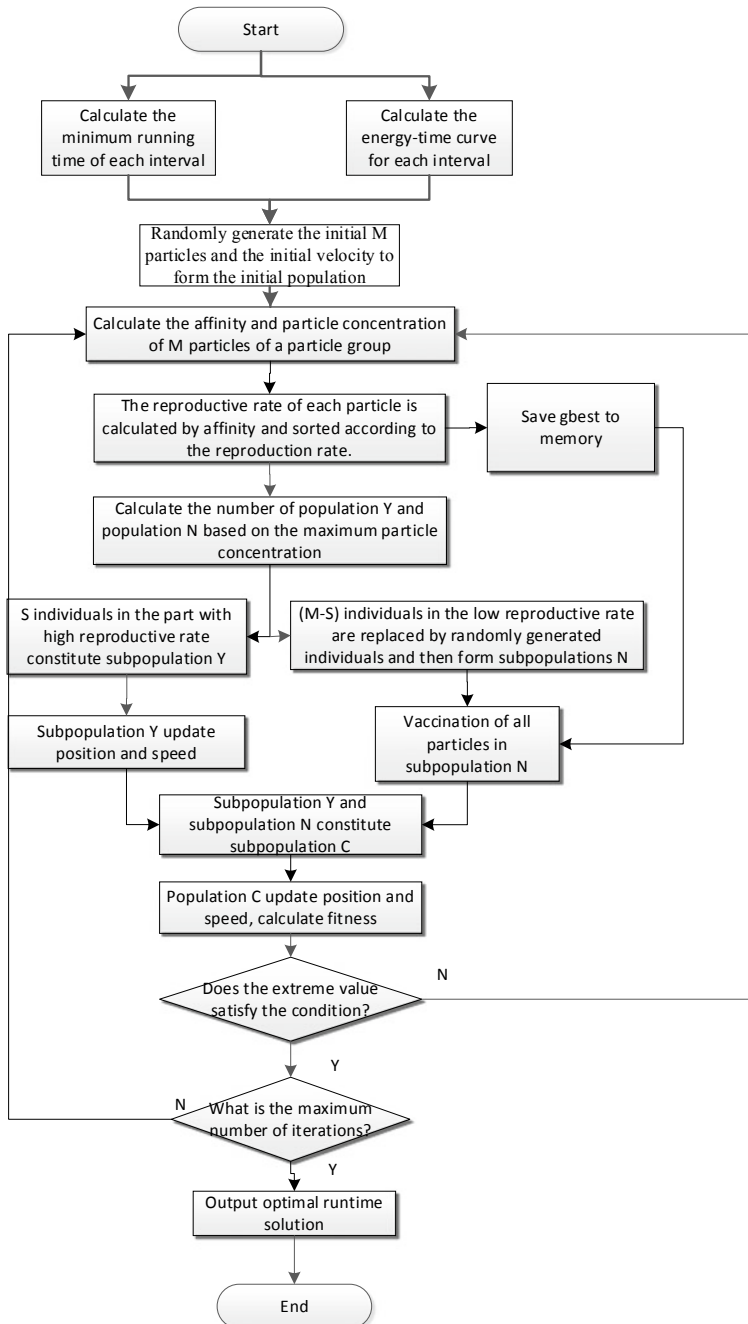


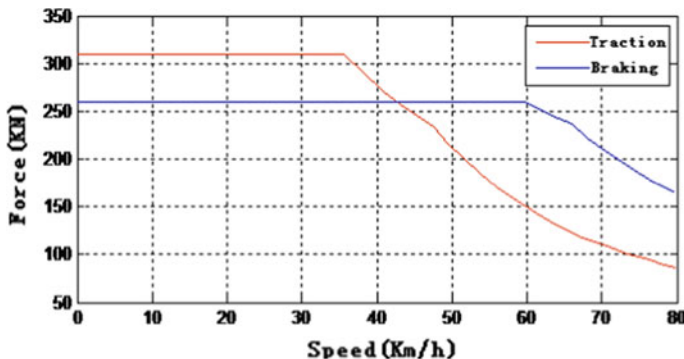
**Fig. 2** Solution flowchart of time optimization model

**Table 1** Slope parameters of Rongjing East Street to Wanyuan Street

Starting point position (m)	End point position (m)	Line gradient (%)
0	159	0
159	197	-1
197	236	-2
236	506	-3
506	543	-2
543	567	-1
567	612	0
612	648	1
648	1078	2
1078	1137	1
1137	1280	0

**Table 2** Speed limit parameters of the line from Rongjing East Street to Wanyuan Street

Starting point position (m)	End point position (m)	Line gradient (km/h)
0	131	56
131	1095	80
1095	1280	56

**Fig. 3** Traction and braking force characteristics of the Yizhuang line train

The Beijing Yizhuang line train is in the form of three movements and three tows. The net weight of the train is 194.295t. Under the condition of the AW2, the total weight of the train is 284.055t, and the maximum running speed is 80 km/h.

The traction and braking force characteristics of the Yizhuang line train are shown (Fig. 3).

## 5.2 Simulation Result

Combined with the line data and vehicle conditions, through the simulation optimization of the train running curve, the  $v\text{-}s$  curve and  $v\text{-}t$  curve of the subway train in the “Rongjing East Street—Wanyuan Street” section are shown in Figs. 4 and 5.

According to the above simulation figure, after optimization, the three best working condition turning points in the interval are: 261.3 m, 685.3 m and 1027.2 m.

After the running time optimization, the optimization results of the partial interval of Yizhuang line are given in Table 3.

**Fig. 4** Train running  $v\text{-}s$  curve

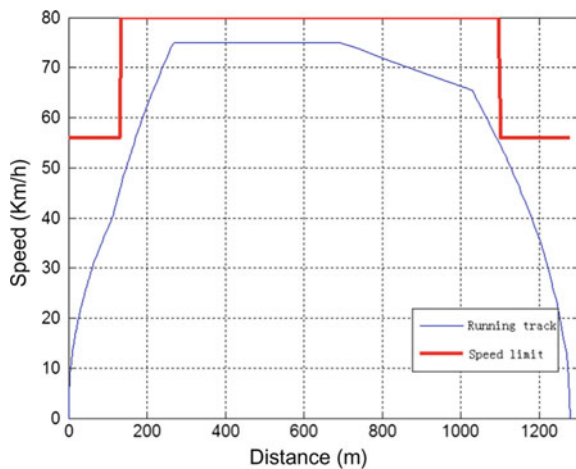


**Fig. 5** Train running  $v\text{-}t$  curve

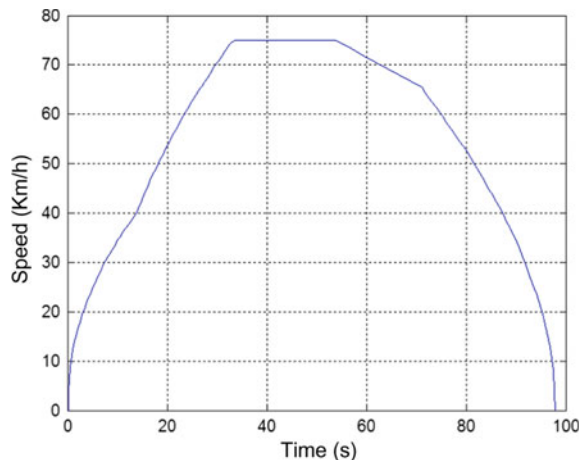


**Table 3** Results of the running time optimization

Station	Planned running time/s	Optimized running time/s	Pre-optimization energy consumption/kw * h	Optimized energy consumption/kw * h
Yizhuang Railway Station to Ciqu	110	112	27.156	23.641
Ciqu to Ciqu South	100	99	10.683	8.299
Ciqu South to Jinghai Road	141	145	18.296	16.365
Jinghai Road to Tongji South Road	150	147	20.561	17.854
Tongji South Road to Rongchang East Street	162	160	16.956	13.696
Rongchang East Street to Rongjing East Street	103	108	12.652	10.845
Rongjing East Street to Wanyuan Street	101	96	9.959	8.656
Total	867	867	116.263	99.356

Available from the above table, after the running time optimization, the total running time of the train is unchanged, and the operating energy consumption is 99.356 kW \* h, which is 14.54% lower than the 116.263 kW \* h pre-optimized.

## 6 Conclusion

In this paper, a train energy-saving optimization method based on parallel immune particle swarm optimization algorithm is proposed to solve the multi-objective train energy-saving optimization problem. The actual simulation data of Beijing Yizhuang line is taken as an example. Firstly, the immune particle swarm optimization algorithm is used to search for the optimal operating conditions. Then, the train running time is optimized. The simulation results are close to the actual operation, indicating the actual reliability of the algorithm.

**Acknowledgements** This work is supported by National Key R&D Program of China (2017YFB1201004).

## References

1. Chang CS, Sim SS (1997) Optimising train movements through coast control using genetic algorithms. *J IEE Proc Electr Power Appl* 144(1):65–73
2. XiuLing H, ChangLin W (2009) Simulation on train automatic operation based on moving automatic block. *J Railway Comput Appl* 18(10):5–10 (in Chinese)
3. Xin Y, Xiang L, ZiYou G et al (2013) A cooperative scheduling model for timetable optimization in subway systems. *J IEEE Trans Intell Trans Syst* 14(1):438–447
4. WenJu T, DeQiang H, HeLiang W (2017) Research on energy-saving optimization of subway train based on immune particle swarm optimization. *J Locomotive Electr Drive* (2):94–95 (in Chinese)
5. Ping L, Qiong T (2012) Analysis of traction energy consumption of urban rail transit trains. *J Shandong Sci* 25(3):7–11 (in Chinese)
6. KunFei L (2014) Research on energy saving optimization method for multi-train collaborative control. Beijing Jiaotong University, Beijing (in Chinese)
7. DeChun W, KePing L, Xiang L (2012) Multi-target train energy-saving scheduling model and fuzzy optimization algorithm. *J Sci Technol Eng* 12:2869–2873 (in Chinese)
8. WengBin H, YongBo W, JianGuo L (2013) Optimize subway timetable to reduce energy consumption of train braking resistor. *J Urban Rail Transit Res* 11:90–94 (in Chinese)

# Research on Comprehensive Evaluation Method of Optimized Charging



Liye Wang, Lifang Wang, Wenjie Zhang and Yuwang Zhang

**Abstract** The characteristics of the power battery determine the performance of the electric vehicle, and the charging time of the power battery is much longer than the traditional fuel vehicle, which has become one of the key factors limiting the development of the electric vehicle. At present, the research focuses on improving the traditional Constant Current Constant Voltage charging method and pulse charging method by optimal charging of power batteries, and few studies have been done on the evaluation of charging methods. Therefore, this paper evaluates the performance of the proposed optimal charging method from three aspects: polarization voltage characteristics, charging efficiency and charging temperature rise. The verification results show that these three optimized charging methods have better performance than the traditional charging methods.

**Keywords** Evaluation method · Battery · Optimized charging · Voltage characteristics

## 1 Introduction

The electric energy replenishment time of electric vehicles is much larger than that of traditional fuel vehicles, and it has become one of the key factors limiting the development of electric vehicles [1–3]. At present, the vehicle-to-pile ratio of electric vehicles and charging facilities in China is still relatively large, and it still cannot meet the charging demand of electric vehicles. Effective measures to solve the problem of electric vehicle charging in addition to vigorously building electric vehicle charging equipment and improving the utilization rate of charging equipment [2–5], the development of fast charging technology has become an urgent need.

---

L. Wang (✉) · L. Wang · W. Zhang · Y. Zhang

Key Laboratory of Power Electronics and Electric Drive, Institute of Electrical Engineering, Chinese Academy of Sciences, Beijing, China

e-mail: [wangliye@mail.iee.ac.cn](mailto:wangliye@mail.iee.ac.cn)

At the same time, in the process of electric vehicle promotion, charging safety accidents frequently occur, and how to ensure the safety of charging has attracted more and more attention [6]. Therefore, achieving fast and efficient optimized charging under the premise of ensuring safety is the development direction of electric vehicle charging technology. At present, research on optimized charging of power batteries focuses on the improvement of the conventional Constant Current Constant Voltage (CCCV) charging method and the pulse charging method [7–10]. The improvement of CCCV usually adopts intelligent control methods such as fuzzy control and grayscale prediction. The heat generation, charging time and charging efficiency of the power battery are used as optimization conditions to improve the different charging phases of CCCV to achieve the purpose of optimizing charging.

At present, there are few studies on the evaluation of charging method. Therefore, this paper evaluates the performance of the proposed optimized charging method from three aspects: polarization voltage characteristics, charging efficiency and charging temperature rise. Among them, in the aspect of polarization voltage characteristics, the equivalent charge rate factor is proposed as the evaluation parameter. In the aspect of charging efficiency, the proposed principal component analysis method is used for evaluation. In terms of charging temperature rise, the experimental data of the power battery charging temperature rise is developed. The evaluation was carried out using the proposed temperature rise rate factor.

## 2 Evaluation of Optimized Charging Method Based on Polarization Voltage Characteristics

In order to quantitatively analyze the polarization characteristics of the power battery of different charging method, the power battery polarization voltage multiplying factor  $\varphi_{U_{dl}}$  is set as the evaluation parameter in this paper. The formula is as follows:

$$\begin{cases} \Phi_{U_{dl}}^{SOC} = \int_0^1 U_{dl}(SOC)dSOC \\ \varphi_{U_{dl}} = \frac{\Phi_{U_{dl}}^{SOC}}{C_{eq}} \end{cases} \quad (1)$$

where  $\Phi_{U_{dl}}^{SOC}$  is an integral value of the power battery polarization voltage and SOC, and  $C_{eq}$  is an equivalent charging magnification. The physical meaning of  $\varphi_{U_{dl}}$  is the average value of the polarization voltage in the full SOC range of the power battery caused by the unit charge rate. The smaller the value, the more reasonable is the corresponding charging method.

Table 1 shows the integration of polarization voltage and rate factor of power battery under different operating temperatures and charging methods. Among them, the optimized charging method 1 is an optimized charging method based on the

**Table 1** Integration of polarization voltage and rate factor of power battery under different operating temperatures and charging methods

Temperature	0 °C			10 °C			25 °C			40 °C		
Charging method	Integral value	Rate factor										
Optimized charging method 1	0.0899	0.2983	0.0676	0.1848	0.0624	0.1484	0.0580	0.1337				
Optimized charging method 2	0.0423	0.1956	0.038	0.1130	0.0495	0.1300	0.0482	0.1140				
0.2C-CCCV	0.0498	0.2926	0.041	0.2272	0.0345	0.1852	0.0363	0.1900				
0.5C-CCCV	0.0776	0.2872	0.0646	0.1791	0.0589	0.1456	0.0564	0.1352				
0.8C-CCCV	0.1003	0.3656	0.0859	0.2239	0.0874	0.1795	0.0648	0.1285				
Optimized charging method 1 (Inflection point)	0.0770	0.2353	0.0604	0.1355	0.0545	0.1125	0.0531	0.1099				
Optimized charging method 2 (Inflection point)	0.0382	0.1304	0.0322	0.0869	0.0417	0.0959	0.0437	0.0951				
0.2C-CCCV (Inflection point)	0.0458	0.2420	0.0339	0.1739	0.027	0.1396	0.0316	0.1608				
0.5C-CCCV (Inflection point)	0.0737	0.2262	0.0574	0.1312	0.051	0.1101	0.0515	0.1114				
0.8C-CCCV (Inflection point)	0.0963	0.2890	0.0787	0.1657	0.0795	0.1375	0.0599	0.1041				

comprehensive evaluation of the charging efficiency of the power battery, and the optimized charging method 2 is based on the optimized charging method for the continuous peak power capability of the power battery, from the data in the table, shows that the polarization voltage multiplying factor of the optimized charging method based on the continuous peak power capability of the power battery at different operating temperatures has reached a minimum value.

Figure 1 shows the diagrams of the equivalent charging rate and the polarization voltage multiplying factor of the different SOC ranges of the power battery. The following conclusions can be drawn: (1) The equivalent charging rate of different power battery charging method is significantly affected by the operating temperature and gradually increases with the increase of operating temperature. (2) Within the operating temperature range of 0–40 °C with the increase of temperature, the equivalent charging rate of the optimized charging method based on the continuous peak power capability of the power battery gradually approaches the equivalent charging rate of the CCCV charging method with 0.5 C constant current charging rate. (3) At 0–40 °C in the operating temperature range, based on the polarization voltage multiplying factor of the charging method as the evaluation parameter, the optimized charging method based on the continuous peak power capability of the power battery is superior to other CCCV charging methods with different constant current charging rates.

### 3 Evaluation of Charging Efficiency Based on Principal Component Analysis Method

Since the power battery charging rate efficiency is a description of the charging ability of the conventional CCCV charging method in the constant current phase, in this paper, only the charging efficiency  $\eta_c$ , the charging energy efficiency  $\eta_e$  and the charging time efficiency  $\eta_t$ , the power battery at 25 °C will be used. The charging method is optimized to evaluate the charging efficiency.

The CCCV charging method of 0.2, 0.5 and 0.8 C constant current charging magnification was selected as a control group for optimizing the charging efficiency evaluation of the charging method. Table 2 shows the charging efficiency statistics for different charging methods. It can be seen that the optimized charging methods 1 and 2 cannot simultaneously optimize the three charging efficiency parameters compared with other CCCV charging methods, so the principal component analysis method is used for comprehensive evaluation.

The index parameter matrix is constructed by the charging efficiency of different charging methods:

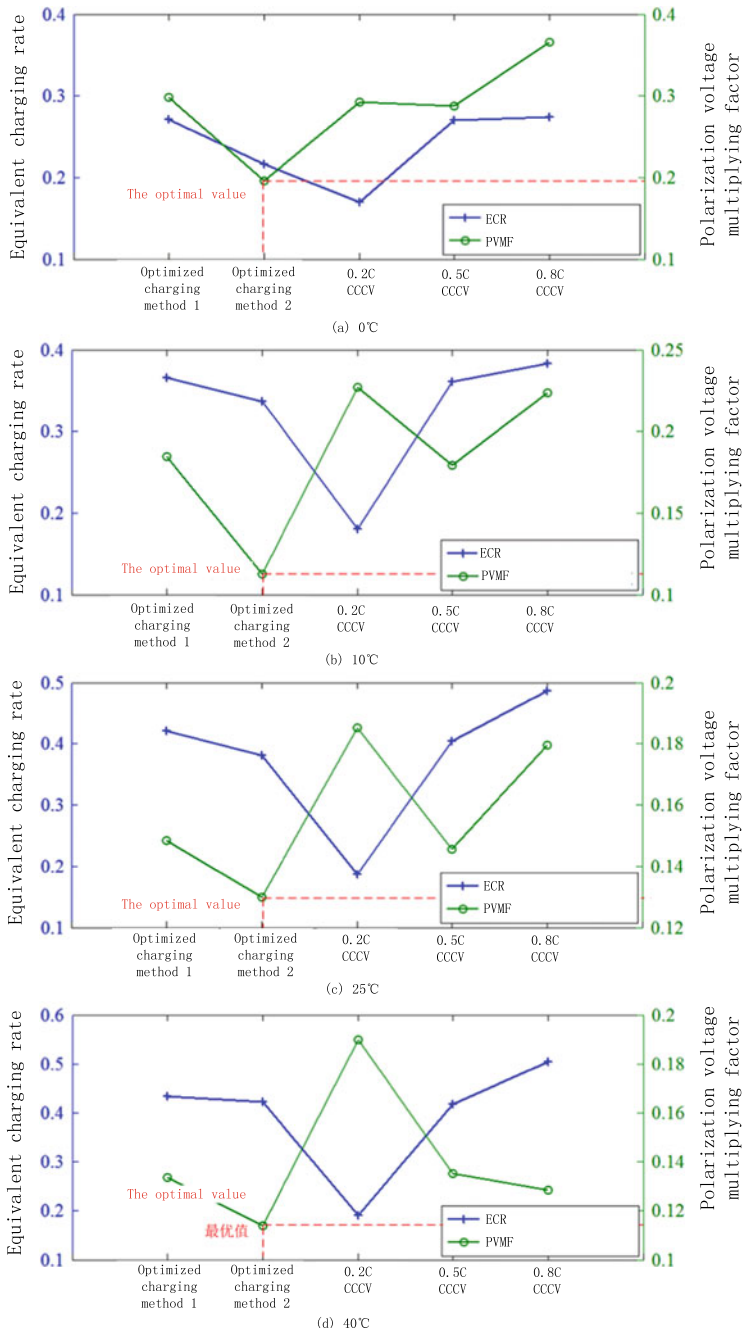


**Fig. 1** Equivalent charging magnification and polarization voltage multiplying factor of power battery under different operating temperatures and charging method

**Table 2** Charging efficiency statistics for different charging methods at 25 °C

Method	Efficiency		
	Charge efficiency	Energy efficiency	Time efficiency
Optimized charging method 1	0.9987	0.8409	1.1675E-04
Optimized charging method 2	0.9987	0.8565	1.0574E-04
0.2C-CCCV	0.9984	0.8414	5.1753E-05
0.5C-CCCV	0.9982	0.8262	1.1238E-04
0.8C-CCCV	0.9955	0.7913	1.3524E-04

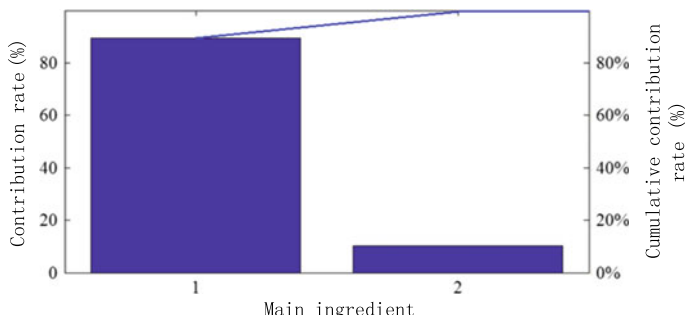
$$\mathbf{X} = (\boldsymbol{\eta}_c \boldsymbol{\eta}_e \boldsymbol{\eta}_t) = \begin{pmatrix} 0.9987 & 0.8409 & 1.1675E - 04 \\ 0.9987 & 0.8565 & 1.0574E - 04 \\ 0.9984 & 0.8414 & 5.1753E - 05 \\ 0.9982 & 0.8262 & 1.1238E - 04 \\ 0.9957 & 0.7913 & 1.3524E - 04 \end{pmatrix} \quad (2)$$

Using principal component analysis, the eigenvector and unit eigenvector  $\mathbf{a}_j (j = 1, 2, 3, 4)$  of the (2) correlation coefficient matrix are calculated as follows:

$$\boldsymbol{\lambda} = (\lambda_1, \lambda_2, \lambda_3)^T = (2.6835 \quad 0.3056 \quad 0.0109)^T \quad (3)$$

$$\left\{ \begin{array}{l} \mathbf{a}_1 = (0.6072 \quad 0.5716 \quad 0.5519)^T \\ \mathbf{a}_2 = (-0.1104 \quad -0.6272 \quad 0.7710)^T \\ \mathbf{a}_3 = (0.7868 \quad -0.5291 \quad -0.3178)^T \end{array} \right. \quad (4)$$

There is only one feature root greater than 1, and the variance contribution rate of the first principal component is 89.45%, indicating that the first principal component value can adequately represent the information of the three charging efficiency indicators, and the first and second principal component variance contributions. The rate statistics are shown in Fig. 2. Therefore, comparing the first

**Fig. 2** Statistical graph of the contribution rate of the first and second principal components variance

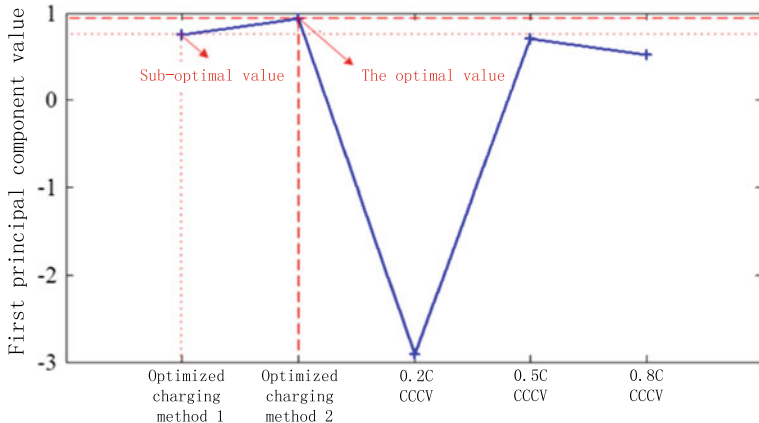


**Fig. 3** First principal component score of charging efficiency for different charging methods

principal component scores of the power battery charging efficiency can evaluate the charging efficiency of the charging method.

Figure 3 shows the first principal component scores for the charging efficiency of different charging methods. It can be seen that the optimized charging method based on the continuous peak power capability of the power battery has the best performance in the comprehensive evaluation of the charging efficiency of the power battery.

#### 4 Optimize the Charging Method Temperature Rise Experimental Evaluation

The temperature rise of the power battery under different charging method is an important factor to evaluate the quality of the charging method. For this reason, different charging methods are applied to the power battery in this section. The operating environment temperature is 25 °C. Acquisition was performed using a thermal imager. Figure 4 shows the temperature rise thermal imaging of the power battery with different charging methods. The temperature sampling point is marked with “ $\times$ ,” and the temperature rise of the power battery is characterized by the average temperature of the sampling point. Table 3 shows the temperature rise of the power battery under different charging methods. In order to quantitatively analyze the effect of different charging methods on the temperature rise of the power battery, the temperature rise rate factor  $\varphi_T$  is proposed as the evaluation parameter.

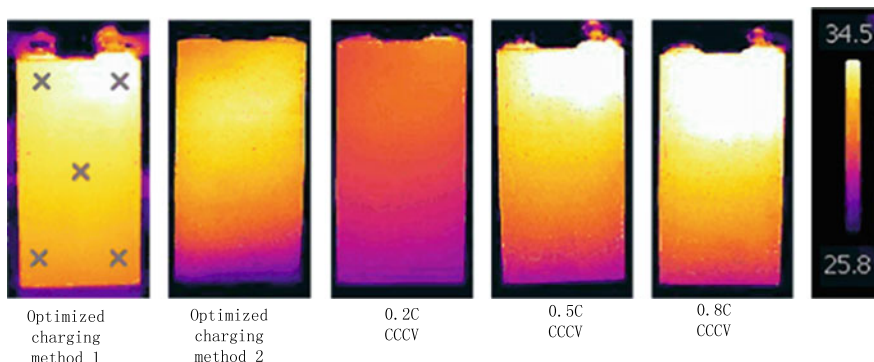


**Fig. 4** Temperature rise thermal imaging of the power battery with different charging method

**Table 3** Temperature rise statistics of power batteries for different charging methods

Method	Optimized charging method 1	Optimized charging method 2	0.2C-CCCV	0.5C-CCCV	0.8C-CCCV
Temperature rise (°C)	5.1	4.6	2.5	5	6.2
Temperature rise rate factor	12.48	12.08	13.41	12.36	12.73

$$\varphi_T = \frac{\Delta T}{C_{eq}} \quad (5)$$

where  $\Delta T$  is the difference between the average surface temperature of the power battery and the ambient temperature, and  $C_{eq}$  is the equivalent charging rate. The physical meaning of  $\varphi_T$  is the surface temperature rise of the power battery caused by the unit charge rate, and the smaller the value, the better is the performance of the corresponding charging method. From the data in Table 3, it is known that the optimized charging method based on the continuous peak power capability of the power battery has the best performance.

## 5 Conclusion

In summary, the optimized charging method based on the continuous peak power capability of the power battery has better performance in the three aspects of polarization voltage characteristics, charging efficiency and charging temperature rise than the conventional CCCV charging method. The optimized evaluation of the

optimized charging method is still a CCCV charging method, although it has better performance in terms of charging efficiency compared to other constant current charging ratios, and the CCCV charging method does not have the best polarization voltage characteristics and charging temperature rise performance.

**Acknowledgements** This study is sponsored by the National Key Research and Development Program of China (2017YFB0102102).

## References

1. Whittingham MS (2004) Lithium batteries and cathode materials. *Cheminform* 104(10):4271
2. Scrosati B (2015) Conducting polymers: advanced materials for new design, rechargeable lithium batteries. *Polym Int* 47(1):50–55
3. Xu J, Deshpande RD, Pan J et al (2015) Electrode side reactions, capacity loss and mechanical degradation in lithium-ion batteries. *J Electrochem Soc* 162(10):2026–2035
4. Veldman E, Verzijlbergh RA (2015) Distribution grid impacts of smart electric vehicle charging from different perspectives. *Smart Grid IEEE Trans* 6(1):333–342
5. Rivera S, Wu B, Kouro S et al (2015) Electric vehicle charging station using a neutral point clamped converter with bipolar DC bus. *IEEE Trans Industr Electron* 62(4):1999–2009
6. Anseán D, Dubarry M, Devie A et al (2016) Fast charging technique for high power LiFePO<sub>4</sub> batteries: a mechanistic analysis of aging. *J Power Sources* 321:201–209
7. Ryu HS, Guo Z, Ahn HJ et al (2009) Investigation of discharge reaction mechanism of lithium|liquid electrolyte|sulfur battery. *J Power Sources* 189(2):1179–1183
8. Jiang Z, Qu Z (2016) Lattice Boltzmann simulation of ion and electron transport in lithium-ion battery porous electrode during discharge process. *Energy Procedia* 88:642–646
9. Zhang WJ (2011) Structure and performance of LiFePO<sub>4</sub> cathode materials: a review. *J Power Sources* 196(6):2962–2970
10. He H, Xiong R, Zhang X et al (2011) State-of-charge estimation of the lithium-ion battery using an adaptive extended Kalman filter based on an improved Thevenin model. *Veh Technol IEEE Trans* 60(4):1461–1469

# Study on Key Metrics of Maintenance of Cascade-Utilized Battery Storage System's Consistency



Na Li, Kai Bai, Kairang Wang, Yinchi Shao, Yu Gong, Jia Diao  
and Yaqi Zhao

**Abstract** When power battery is applied to storage system after decommissioned, compared to traditional new battery storage power station, the divergence problem of battery consistency is even more prominent which increases the maintenance difficulty. In this paper, we discussed the reason and manifestation of the divergence of battery consistency and conducted a sample test and data analysis toward the decommissioned LiFePO<sub>4</sub> battery module of pure electric bus. We analyzed the reason of battery module's capacity deterioration from the aspect of consistency, suggested some consistency metrics that are closely related to usable capacity and concluded a method for determining key metrics of maintenance of cascade-utilized battery consistency, and the method's effectiveness has been verified via tests.

**Keywords** Cascade-utilized battery · Storage system · Consistency · Maintenance

## 1 Preface

When battery capacity is below 80%, usually we consider it no longer suitable for use in electric vehicles. But it will be a great waste of resources if we decommission such battery directly. As an effective way of solving the issue of new energy consumption, power storage is not commercially available due to its high cost. While there is an idea that cascade using power battery to power storage that possibly can solve this problem. According to expectations of research institutions [1], our national power lithium battery recycling market will reach 5 billion yuan to 2018, and power battery market demand will reach 125 GW·h and scrapped quantity 32.2

---

N. Li (✉) · K. Bai · K. Wang · Y. Shao · Y. Gong  
Corporation Key Laboratory, Grid-connected Operation Technology  
for Wind-Solar-Storage Hybrid System State Grid, Beijing 100045, China  
e-mail: [qiboer@163.com](mailto:qiboer@163.com)

J. Diao · Y. Zhao  
State Grid Xinyuan Zhangjiakou Wind, Photovoltaic, Storage and Transmission  
Pilot Power Station Co. Ltd., Zhangjiakou 075000, China

GW·h which is about  $50 \times 104$ t. On December 1, 2016, MIIT issued *Interim Measures for the Administration of Recycling of Power Batteries for New Energy Vehicles* (Draft) to further identify liability subject of each market segment in battery recycling. Cascade utilized power battery has become a research hotspot.

Many countries are actively engaged in experimental research and engineering applications of cascade utilized power battery, among which Japan, US and Germany are pioneers. Those countries already have some demonstrating application of engineering and commercial projects. Several cases of demonstrating application projects of cascade utilized power battery across the world are listed in Table 1.

Based on capacity and purpose, there are mainly two classes of cascade-utilized battery storage system as applied to civil and commercial use of electricity and applied to power grid, respectively. For the first class, its capacity ranges from several kWh to tens of kWh. It also can run in conjunction with solar distributed power generation and be used for standby and charging power. The capacity of the second class ranges from hundreds of kWh to several MWh, some are installed on wind farms and photovoltaic power plants to stabilize new energy fluctuations,

**Table 1** Typical cases abroad of cascade-utilized battery storage system

Country	Company or institution	Projects and operated date	Battery source	Purpose
Japan	4R Energy	20 kW\50 kW\100 kW \200 kW household \commercial modular products, in 2012	Nissan leaf decommissioned batteries of pure EV	Standby power, portable power
	Nissan	XStorage, 4.2 kWh, in 2016	12 leaf decommissioned battery modules	Household electricity
Germany	BWM, BOSCH, Vattenfall	Container type 2 MW $\times$ 2 h cascade-utilized battery storage system, in the end of 2015	BWM i3, ActiveE decommissioned batteries	Improve PV output characteristics
	Daimler, GETEC and REMONDIS	13 MWh cascade-utilized battery storage station, in earlier 2016	Smart fort two decommissioned batteries	Maximize output of new power station
	Daimler, The Mobility House	15 MWh cascade-utilized battery storage station, under construction	Smart fort two decommissioned batteries	Grid peaking and frequency modulation
The USA	General Motors Corporation	The US milford data center kWh level of cascade utilized pilot project, in 2012	5 suit of Chevrolet Volt decommissioned battery systems	Household/commercial electricity
	FreeWire	48 kWh mobile charging car, in 2014	AESC factory test out batteries	Mobile charging for EVs

(continued)

**Table 1** (continued)

Country	Company or institution	Projects and operated date	Battery source	Purpose
China	State Grid, Beijing Jiaotong University	Beijing Daxing EV charging station 100 kWh cascade utilized demonstration project, in 2012	MGL electric bus decommissioned batteries	Single-pass system of power station
		Zhengzhou Jianshan true type transmission line test site 140 kWh cascade utilized demonstration project, in 2014	Huanyu electric bus decommissioned batteries	Micro-power grid
		National wind and light storage demonstration power station 1.2 MWh pilot project, in 2016	BYD K9 electric bus decommissioned batteries	Provide wind and light power generation with schedulability

Note 0/100/162 represents times of cycle

while some are directly used for power grid peaking and frequency modulation. In recent years, Germany has made great progress in the application of the cascade utilized large capacity battery storage which the system capacity has increased from several MWh to tens of MWh.

State Grid has started related researches to cascade utilized power battery storage in 2012. In 2014, such systems have been applied in Beijing Daxing EV Charging Station and Micro-Grid Demonstration Project in Zhengzhou Jianshan Test Site, both capacities are hundreds of kWh, and in those sites, we initially studied the technologies of decommissioned battery screening and match. In 2015, State Grid started the research of MWh level cascade-utilized battery storage and successfully developed pilot system of 1.2 MWh which has been put into trial operation in National Wind and Light Storage Demonstration Power Station. It is also the first MWh level cascade-utilized battery storage system that our country developed.

Many research institutions at home and abroad have conducted related studies on technologies of cascade-utilized battery, mainly focusing on its external characteristics, screening, matching and management. Reference [2] aimed at the problem of inconsistent recession of characteristics of cascade utilized Li-ion power battery and proofed that cascade-utilized battery storage system is suitable for application in small rate charge and discharge storage conditions through analyzing such battery's internal resistance characteristics of capacity by a series of charge and discharge tests. References [3, 4] took decommissioned battery of one kind of EV as test sample and studied the reason of battery's deterioration failure and the performance trends as cascade-utilized battery's recycling numbers increased. Based on results of electrochemical impedance spectroscopy, reference [5] built an electrochemical impedance model of cascade utilized Li-ion battery and studied the change characteristics of impedance model parameters as battery charge status and

aging condition changing. Reference [6] studied how power battery's decommissioned interface properties will impact on its economy when applied to power market. Reference [7] built a model between battery life and cascade utilized Li-ion battery's capacity recession and energy efficiency reducing and studied the quantified relationships between battery performance and reduction of CO<sub>2</sub> emission. Reference [8] studied the change pattern of impedance of each part in battery system with the numbers of cycling and conducted characterization analysis toward surface morphology of positive and negative electrode of different cycles. Reference [9] analyzed the degradation mechanism of 18650 retired lithium iron phosphate battery, established battery life prediction model. Reference [10] analyzed the energy storage system which reconstructed from the retired power battery, it's performance is close to the Energy storage system composed of new batteries. The echelon energy storage system is applied to photovoltaic power station, which improves the photovoltaic output, and reduces the cost of optical storage system.

Those research findings mentioned above are mainly based on single battery or battery module to access its status and life in laboratory's environment and provide theoretical basis for battery's cascade utilization. While some test data also showed that compared to traditional storage systems, the maintenance of cascade-utilized battery storage system is much harder. And the maintenance method of cascade-utilized battery storage system cannot just replicate that of new battery storage station because the establishment of new battery storage station's operation and maintenance is based on two foundations: one is that battery systems from the same batch of same production line have better consistency, and the other is that those battery's failure rate is extremely low as they are in the first half of their life cycles. However, the sources of cascade utilized batteries are all different, and their production and consumption all vary. When integrated nonlinearly, internal and external parameters and their recession patterns are more dispersed and easier to mutate than new batteries; meanwhile, since battery producers have little concerns about decommissioned battery's performance change, there is no reference experience to cascade-utilized battery's performance changing pattern when individually or massively integrated which leads to operational defects and high risks of failure. By studied existed demonstration projects of cascade-utilized battery storage systems, we found that massive maintenance work in demonstration projects has already restricted the normal operation of those stations, thus, we need figure out a way to effectively maintain the cascade-utilized battery storage system and one of the maintenance purposes is the consistency between batteries. In this paper, we focused on how to design an effective method to maintain consistency to improve the maintenance efficiency and reduce labor costs after power station put into operation by sampling tests before storage power station put into operation.

## 2 Study on Consistency Dispersion Reasons of Cascade-Utilized Battery Module

Battery parameters' inconsistency is mainly caused by two factors [11–13], one is that there are deviations in technical control and differences in materials in battery production that leads to same type of batteries with different capacity and impedance. The other is that during the match and operation process, due to different position and connection methods the temperature, SOC using interval in the process of using are totally different which exacerbates the initial state of inconsistency.

Reduction of usable capacity caused by inconsistency of battery module can be eased by maintenance. For the perspective of maintaining, the issue of inconsistency can be divided into two kinds [14–16]: (1) Internal resistance difference of single battery. The external characteristic of different internal recession of single battery is different internal resistance. In series structures, the battery with large internal resistance gets higher voltage and reach maximum voltage threshold prior to others when charging; in parallel structure, different internal resistance with different current, thus, when each single battery is working under different charge-discharge rate, the battery module's life is affected. Single battery with large internal resistance will lose more energy and generate more heat with temperature rising faster during use process. If the battery module's heat transfer condition is poor which means heat cannot emission timely and the temperature of battery will continue to rise, it probably can cause the deformation of battery and even serious consequence as explosion. In the maintenance of storage station, for battery module with large internal resistance inconsistency, we typically choose to change those batteries. (2) The SOC using interval of each single battery is different. The inconsistency of each single battery's capacity and self-discharge rate in battery module will make the module's maximum and minimum working voltage determined by battery with smaller capacity or cross determined by several single batteries. When charging, battery with small capacity will be fully charged prior to others to reach cutoff charge voltage which prevent the battery module from charging to reduce the total storage capacity of the battery module; when discharging, battery with small capacity will be discharged prior to others too and reach cutoff discharge voltage which prevent the battery module from discharging to make the capacity and energy of the battery module not fully utilized. The inconsistency of single battery's SOC using interval will cause inefficient capacity and energy utilization, and decrease the efficiency and operational economy of storage system. This kind of issue is the key point of storage station's maintenance and inconsistency of SOC using interval can be eased by maintaining.

To study the consistency dispersion reasons and the methods of maintenance of cascade-utilized battery module, we randomly pick two groups of decommissioned battery modules for one certain pure electric bus as testing samples: LiFePO<sub>4</sub> battery module of 300 Ah, module's internal connecting type is 6 parallel and 4 series, 6 batteries of 50 Ah are individually paralleled to form a minimum parallel unit then 4 minimum parallel units connected in series to form the entire battery module.

The interface parameters of those two battery modules when decommissioned are showed below (see Table 2). No. 1 Battery module's residual capacity is 68.2% and No. 2 is 67.6%. The Ohm resistance and polarization resistance of No. 4 single battery in both two battery modules are increased massively and energetic efficiency of two battery modules are both above 95%.

To connect No. 1 and No. 2 battery modules in series, and the minimum parallel units in No. 1 battery module are numbered as 1-1, 1-2, 1-3 and 1-4 while the minimum parallel units in No. 2 battery module as 2-1, 2-2, 2-3 and 2-4. And conduct cycling test under the condition with charge rate as 0.5C, discharge rate as 1C and charge and discharge depth as 100%. During the test, we focused on battery module's parameters like residual capacity and ohm resistance to study the impacts of inconsistency of ohm resistance and SOC using interval on capacity.

Firstly, we observed the internal resistance's change in each single battery during the cycling test. We took charging ohm resistance and discharging ohm resistance under 50% SOC as evaluating indicator. Figure 1 shows the distribution of charge and discharge ohm resistance and residual capacity of battery modules under different numbers of cycles. From this, we can observe that except 1-4 and 2-4 batteries that their ohm resistance increases as number of cycles increases, other batteries' ohm resistance did not change as number of cycles increases nor represent dispersive trend. For removable battery module, replace 1-4 and 2-4 batteries can achieve the purpose of maintenance. However, presently, the mainstream domestic EV battery modules are all laser welding structure that cannot be disassembled. If we must replace batteries, we have to replace the entire battery modules.

Secondly, we studied the relationship between single battery's capacity and battery module's capacity. To represent the inconsistency of battery capacity, the standard deviation of 8 single batteries capacity is:

$$s = \sqrt{\frac{\sum_1^8 (s_i - \bar{s})^2}{8}} \quad (1)$$

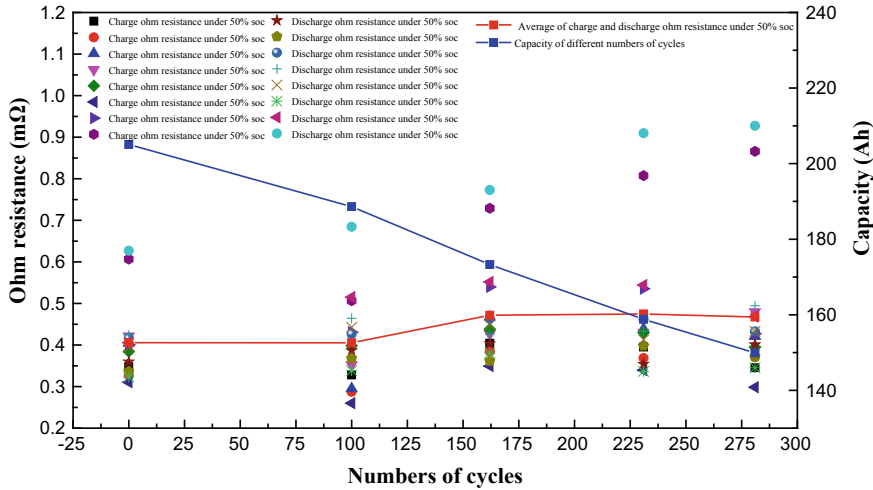
In above formation:  $s_i$  is residual capacity of No.  $i$  battery and  $\bar{s}$  is average residual capacity of 8 single batteries.

Figure 2 shows that the changing trends of the capacity of 8 single batteries in No. 1 and No. 2 battery modules as the number of cycles increases. We can observe that the residual capacity of 8 single batteries is decreasing as the number of cycles increases and represent a dispersive trend while capacity standard deviation increases as the number of cycles increases. Figure 3 shows the curve of variation curve of battery module's capacity decay rate and standard deviation with the number of cycles increases. From which we can observe a significant correlation between inconsistency of battery capacity and residual capacity of battery module.

According to above research, in the cycling process, the tested decommissioned batteries' ohm resistance did not show significant rising trends and capacity decay is mainly caused by inconsistency of single batteries' capacity.

**Table 2** Interface parameters of two decommissioned battery modules of pure electric bus

No.	Charge capacity/ (Ah)	Discharge capacity/ (Ah)	Residual capacity Rate, %	Charge energy/ (Wh)	Discharge energy/ (Wh)	Energetic efficiency, %	Ohm resistance z50%)/mΩ	Rp/mΩ
No. 1 battery module	1-1	203.70	204.50	68.20	2736.00	2599.00	0.38	0.67
	1-2						0.36	0.70
	1-3						0.37	0.78
	1-4						0.64	2.25
No. 2 battery module	2-1	198.90	202.80	67.60	2678.00	2577.00	0.42	0.81
	2-2						0.31	0.67
	2-3						0.45	0.67
	2-4						0.83	3.84



**Fig. 1** Distribution of Ohm resistance of single battery in battery module as number of cycles increases

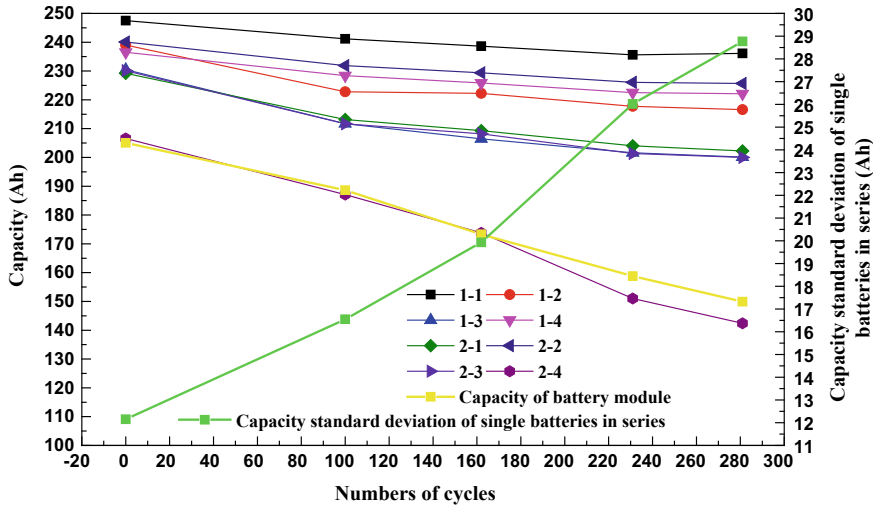


**Fig. 2** Capacity and standard deviation of single batteries in series with different numbers of cycles

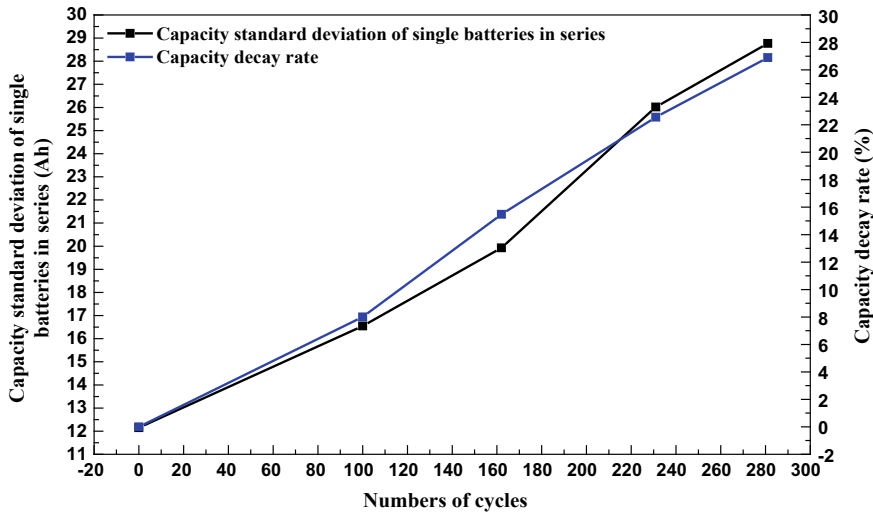


**Fig. 3** Battery module's capacity decay rate and standard deviation with different numbers of cycles

### 3 Determining Methods for Using Battery Consistency to Maintain Key Metrics

Fully charging and discharging storage unit over and over again with battery module that reached cutoff condition first balanced or replaced is a common method for consistent maintenance of conventional storage power station. For storage unit of large extent of consistency divergence, workload and time costs of maintenance are higher, as higher workload of maintenance is inevitable for cascade using battery storage system.

#### 3.1 Method Summary

A sampling test-based determining method of cascade using battery storage system to maintain key metrics is proposed in this paper (see Fig. 4), especially for battery module of similar working condition in vehicle using stage, for example, decommissioned battery of pure electric bus in charging and change mode.

- Step 1: In the batch of decommissioned battery, module of sampling battery and sampling ratio can be determined by test capacity, as ratio higher than 1/1000 is recommended.
- Step 2: Carrying out cycling test on sampling battery module, as test working condition can be taken properly according to occasions of the following

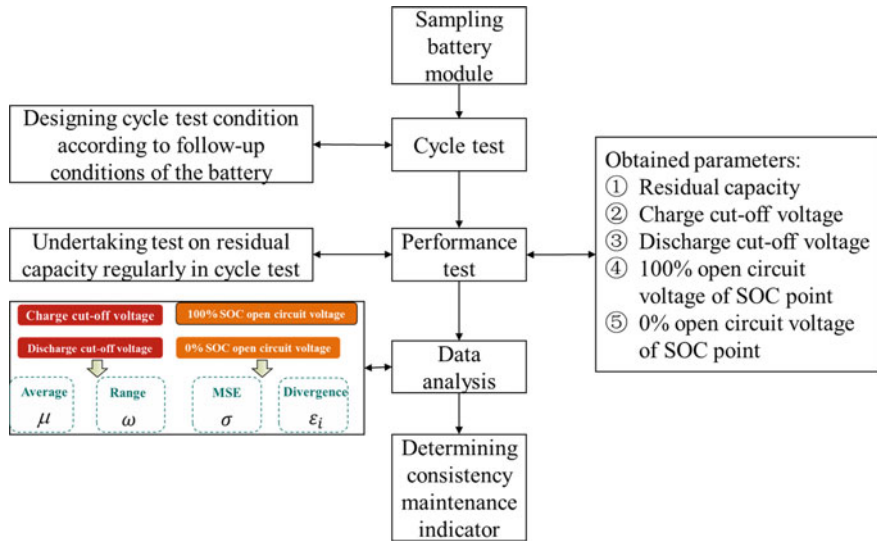


**Fig. 4** Flowchart of determining method of cascade using battery storage system to maintain key metrics

cascade using battery. For example, moderate conditions shall be taken for battery applied in power storage, with charge and discharge rate less than 0.5C and workspace of SOC less than 10–90%.

- Step 3: Undertaking capacity test for every 100 cycles, namely, 3 number of fully charging and discharging cycle, so that residual capacity of the battery can be average discharging capacity measured in 3 number, with voltage data of single battery in the test process obtained simultaneously.
- Step 4: Calculating charge cutoff voltage, discharge cutoff voltage, 100%SOC point open-circuit voltage and 0%SOC point open-circuit voltage (standing for 1 h) of single battery in different number of cycle, and using corresponding average  $\mu$ , range  $\omega$ , MSE  $\sigma$ , and battery divergence of single battery to describe inconsistency of voltage of individual battery with average voltage of battery. The method to calculate range  $\omega$  is:

$$\omega = \max x_i - \min x_i \quad (2)$$

Range of charging voltage refers to the difference between unit voltage maximum and minimum at the end of charging, range of discharging voltage refers to the difference between unit voltage maximum and minimum at the end of discharging.

MSE  $\sigma$  represents the degree of deviation of individual battery voltage from the average level, MSE of charging cutoff voltage is the quadratic

sum of difference between individual battery voltage and average voltage at the end of charging and calculation of MSE of discharging cutoff voltage is in similar, with the specific method as:

$$\sigma = \sqrt{\frac{1}{N} \sum_{i=1}^N (x_i - \mu)^2} \quad (3)$$

Calculation of divergence  $\varepsilon$  is:

$$\varepsilon_i = (E_i - E)/E \quad (4)$$

where  $\varepsilon$  is individual divergence of the battery pack;  $E_i$  is end voltage of the  $i$ th individual battery;  $E$  is average voltage of the battery pack.

Step 5: Calculating the relationship between residual capacity and charge cutoff voltage, discharge cutoff voltage, open-circuit voltage of 100%SOC point and that of 0%SOC point, and then calculating the relationship between residual capacity and range, MSE and divergence of above index separately. The calculation of correlation coefficient is:

$$R = \rho_{xy} = \frac{\sum_{i=1}^N (X_i - \bar{X})(Y_i - \bar{Y})}{\sqrt{\sum_{i=1}^N (X_i - \bar{X})^2} \times \sqrt{\sum_{i=1}^N (Y_i - \bar{Y})^2}} \quad (5)$$

In the equation above,  $X$  and  $Y$  are two variables,  $\bar{X}$  and  $\bar{Y}$  are the mean value of  $X$  and  $Y$ .  $\rho_{xy}$  is the correlation coefficient of  $X$  and  $Y$ . The more  $\rho_{xy}$  gets close to 1, the higher the degree of fitting is.

Step 6: Working out the indicator with highest correlation to residual capacity as indicator of consistency maintenance.

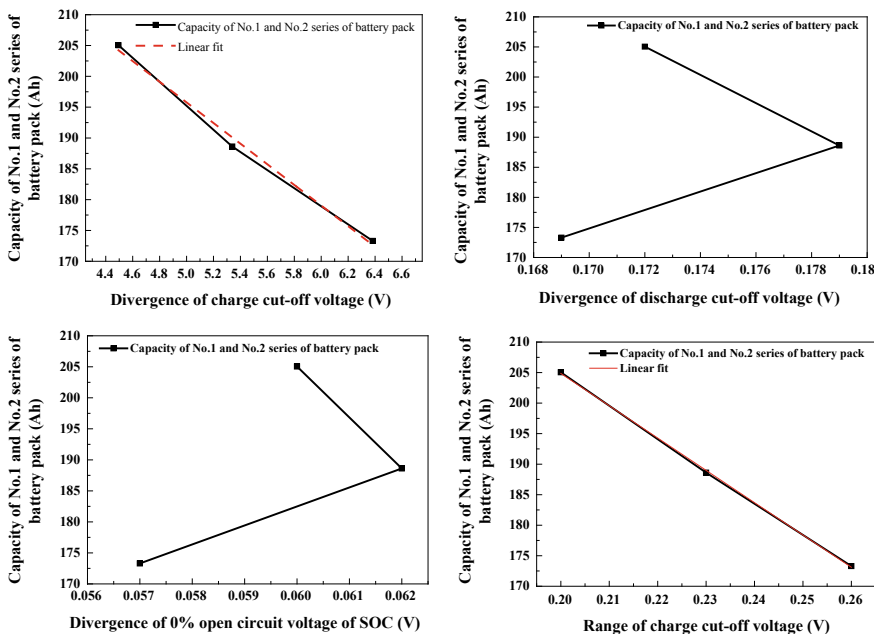
### 3.2 Case Study

Based on the data from sampling battery module cycle test, charge and discharge cutoff voltage, charge and discharge cutoff open-circuit voltage of each unit in the battery module in different number of cycle, and average  $\mu$ , range  $\omega$ , MSE  $\sigma$  and divergence  $\varepsilon_{max}$  shall be worked out. Range and MSE of charge and discharge cutoff voltage of 8 individuals in series increase along with cycle number, and open-circuit voltage of 100%SOC point and 0%SOC point is also ascendant (see Table 3).

For calculating correlation between each indicator of battery pack with available capacity in different times of cycle, analytical curve of correlation between 4 indicators with available capacity is shown in Fig. 5, as it is summarized that the correlation between divergence of charge cutoff voltage and charge range and available capacity is higher.

**Table 3** Parameter of each individual battery in different number of cycle

Battery	Charge cutoff voltage (V)			Discharge cutoff voltage (V)			Charge cutoff open-circuit voltage (V)			Discharge cutoff open-circuit voltage (V)		
	0	100	162	0	100	162	0	100	162	0	100	162
1-1	3.45	3.42	3.39	3.15	3.180	3.20	3.349	3.347	3.338	3.195	3.213	3.159
1-2	3.45	3.43	3.39	3.13	3.150	3.14	3.352	3.348	3.345	3.170	3.194	3.193
1-3	3.47	3.45	3.41	3.04	3.080	3.02	3.354	3.351	3.346	3.099	3.108	3.028
1-4	3.46	3.44	3.40	3.12	3.150	3.14	3.353	3.341	3.345	3.168	3.195	3.104
2-1	3.49	3.45	3.40	3.03	3.100	3.01	3.370	3.361	3.358	3.078	3.116	3.038
2-2	3.47	3.42	3.39	3.15	3.170	3.16	3.357	3.358	3.349	3.158	3.200	3.112
2-3	3.50	3.46	3.42	3.04	3.030	2.90	3.362	3.359	3.357	3.070	3.110	3.183
2-4	3.65	3.65	3.65	2.50	2.500	2.50	3.363	3.364	3.367	2.921	2.939	2.916
$\mu$	3.49	3.47	3.43	3.02	3.045	3.01	3.358	3.354	3.351	3.107	3.134	3.092
$\omega$	0.20	0.23	0.26	0.65	0.68	0.70	0.021	0.023	0.029	0.274	0.274	0.277
$\sigma$	0.07	0.08	0.09	0.22	0.226	0.23	0.007	0.008	0.009	0.089	0.091	0.094
$e_{\max}$	4.50	5.4	6.38	0.17	0.18	0.17	0.002	0.003	0.005	1.313	1.271	2.711

**Fig. 5** Correlation of different parameters with residual capacity of battery Module

In order to find the parameter of the highest linear correlation with capacity of the battery pack between charge cutoff voltage divergence and charge cutoff voltage range, relevant coefficient of the two parameters with residual capacity can be

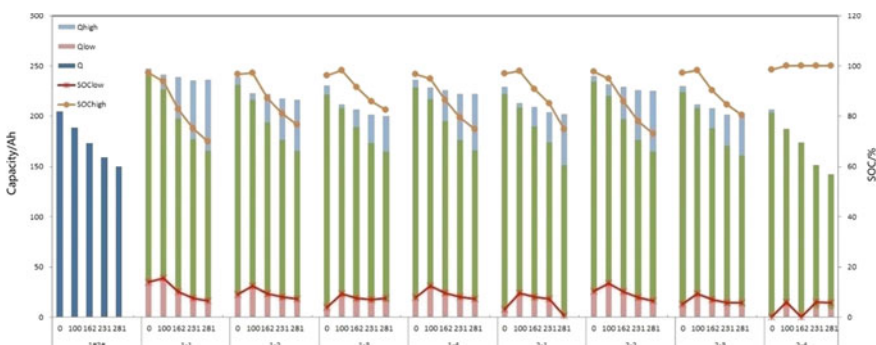
**Table 4** Correlation coefficient of different parameters with residual capacity of the battery module

Correlation coefficient	No. 1 and No. 2 series
Divergence of charge cutoff voltage	0.98677
Range of charge cutoff voltage	0.99959

worked out, as shown in Table 4. It reveals that charge cutoff voltage range has the highest correlation with capacity, as the battery module with largest capacity recession can be picked out via charge cutoff voltage range in engineering practice.

### 3.3 Test Verification

Through data analysis, it is believed that capacity recession is caused by inconsistency of using high-end SOC interval, as SOC using interval of each individual battery is tested in different number of cycle to verify the conclusion. The method lies in carrying out capacity test on each individual battery to test residual capacity at both high and low end and capacity of charging and discharging fully after cutoff of charge and discharge of battery module. Figure 6 shows residual capacity of battery module and individual battery and SOC using interval in different number of cycle (where:  $Q_{\text{high}}$  represents chargeable power at high end after fully charging the battery pack,  $Q_{\text{low}}$  represents dischargeable power at low end after fully discharging the battery pack, Q represents capacity of the battery pack,  $\text{SOC}_{\text{low}}$  represents residual capacity of SOC at low end and  $\text{SOC}_{\text{high}}$  represents residual capacity of SOC at high end). It is shown that capacities of high-end SOC area of 1-1, 1-2, 1-3, 1-4, 2-1, 2-2 and 2-3 are yet to be used, and residual capacities at high end will

**Fig. 6** Capacity of battery module and individual battery and SOC using interval in different number of cycle

increase along with the number of cycle, as results of data analysis are verified with relatively good inconsistency at low end. When applying the battery module in power storage system, use at SOC high end shall be avoided and SOC high end shall be maintained in maintenance work as a highlight.

## 4 Conclusion

This paper sorts out problems and research status quo of cascade using battery storage system maintenance, takes a set of decommissioned battery as test sample, studies methods to determine cascade using battery storage system inconsistence to maintain metrics and verifies by test, with conclusions shown as follows:

- ① Compared with conventional battery storage system, cascade using battery storage system inconsistence to maintain consumes more labor and time, as inconsistency maintenance method needs to be adjusted.
- ② Main causes and parameter features of cascade using battery inconsistence divergence are analyzed.
- ③ A sampling test-based determining method of cascade using battery storage system to maintain key metrics is proposed in this paper, and effectiveness of the method is verified with test.
- ④ A set of pure electric bus decommissioned battery is taken as sample, as Ohm impedance consistence has no significant change in the later cycle of the battery module, but SOS using space shows significant change, especially SOC capacity utilization at high end declines with the increase of cycle number with available capacity of the battery module affected, deserving attention in maintenance.

**Acknowledgements** This work is supported by Science and Technology Project of State Grid (52018K16005V).

## References

1. The Storage Industry Technology Alliance in Zhongguancun. White Paper of Energy Storage Industry Research 2016 (in Chinese)
2. Li X, Chen Q, Guan Y et al (2013) Testing characteristic analysis of cascade using of lithium-ion battery. Power Supply Technol 11:1940–1942
3. Xu J (2014) Research on cascade using of lithium-ion battery capacity and resistance change characteristics. Beijing Jiaotong University (in Chinese)
4. Y Zou (2014) Modeling and parameter estimation of capacity, resistance and state of charge based on decommissioned lithium-ion battery. Central South University
5. Zhang C, Jiang J, Zhang W et al (2013) Cascade using of lithium-ion battery electrochemical impedance model and characteristic parameters analysis. Power Syst Autom 37(1):54–58

6. Viswanathan VV, Kintner-Meyer M (2011) Second use of transportation batteries: maximizing the value of batteries for transportation and grid services. *IEEE Trans Veh Technol* 60(7)
7. Ahmadi L, Fowler M (2014) Energy efficiency of Li-ion battery packs re-used in stationary power applications. *Sustain Energy Technol Assessments* 8:9–17
8. Zhang W, Feng P, Liu P et al (2015) Research on electrochemical impedance model in EIS lithium iron phosphate battery cycle. *Power Technol* 39(1):54–57
9. Liu Z (2014) Research on inconsistency of lithium-ion battery pack and thermal management simulation. Tianjin University (in Chinese)
10. Tong SJ, Same A (2013) Off-grid photovoltaic vehicle charge using second life lithium batteries: an experimental and numerical investigation. *Appl Energy* 104:740–750
11. Gao F, Yang K, Dong H, Li D (2013, February) Analysis of power of storage lithium iron phosphate battery cycle life. *Proc CSEE*41–45
12. Zhao S, Feng W, Zidong W (2009) Research on lithium iron phosphate battery operation mode cycle performance. *Electron Compon Mater* (011):43–47 (in Chinese)
13. Wang Z, Fengchun S, Cheng L (2016) Analysis of influence of inconsistency on battery pack service life. *J Beijing Inst Technol* 26 (7th Session of 2016)
14. Lin C, Wang J, Chen Q (2014) Principle and utilization of SOC estimation for electric vehicle. *Battery* (2014) (in Chinese)
15. Ma Y, Chen Q, Zhu Y (2001) Exploration on definition method of battery charge state under PMW. *Battery* (2001) (in Chinese)
16. Gong M, Wang Z, Ma Z, Guo H, Yu WF (2013) SOE estimation method of series battery pack. *J Beijing Jiaotong Univ* 37 (2th Session of 2013)

# Reverse Characteristic Model of SiC MPS Diode



Qiwen Du and Xuehui Tao

**Abstract** In this paper, the effects of applied voltage, temperature and structural parameters of MPS diodes on the reverse leakage current of these diodes are studied. A new analytical model for merged PiN Schottky (MPS) diodes is also developed to analyze and predict the reverse characteristics of these diodes. The model of the surface electric field is approximately solved by using the 2D Poisson equation. The reverse leakage current model of MPS diodes is analyzed and solved from the four parts of the thermionic emission, namely the leakage, tunneling, depletion and diffusion currents, based on the surface electric field model. The validated model and experimental results show good agreement.

**Keywords** SiC · MPS diode · Reverse characteristic · Surface electric field

## 1 Introduction

Material quality is an important factor that affects the performance of power devices. The high thermal conductivity, electron mobility, breakdown electric field and electron saturation drift speed of silicon carbide (SiC) make this material suitable for high-temperature, high-power and high-frequency applications [1–3]. SiC has also become an ideal material for manufacturing the next-generation power devices. Increasing the switching frequency of the system is a long-term requirement for the development of power systems. Therefore, the switching characteristics of the rectifier must be improved [4, 5]. In 1984, Baliga and Wiliamovski proposed the junction barrier Schottky (JBS) diode, which simultaneously implements the superior blocking characteristics of the PN junction diode and the low turn-on voltage drop of the Schottky diode [6, 7]. The MPS is obtained by modifying the P trap of the JBS [8, 9].

---

Q. Du · X. Tao (✉)  
Soochow University, Suzhou, Jiangsu Province 210000, China  
e-mail: [xhtao@suda.edu.cn](mailto:xhtao@suda.edu.cn)

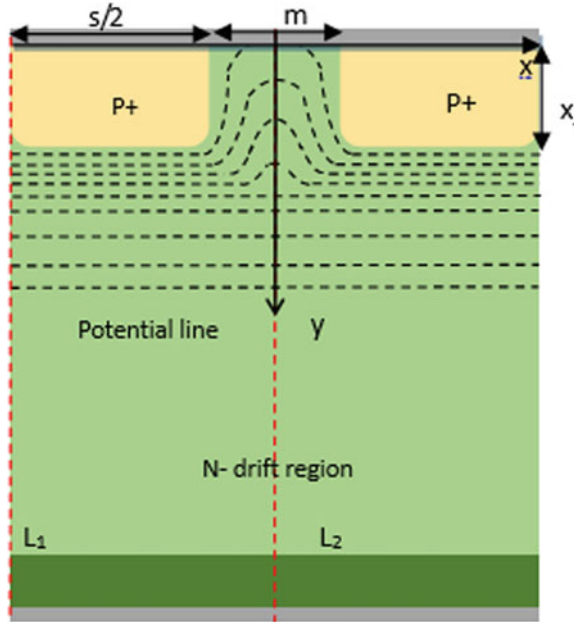


**Fig. 1** Basic unit cell of a MPS diode

The JBS and MPS diodes have a similar structure as shown in Fig. 1. However, JBS uses a low Schottky barrier metal with a low turn-on voltage for low-voltage systems while the MPS diode has a thick drift region and strong reverse-blocking capability for high-voltage applications. In terms of its reverse characteristics, the proposed MPS diode model is not comprehensive and ignores the effects of the transverse electric field and tunnel current [10]. Although a mature inverse characteristic model of JBS diodes has been developed [11], the structure of JBS diodes is different from that of MPS diodes, thereby rendering this model inapplicable for MPS diodes. In addition, MPS diodes have a thick drift region, have a leakage current in their depletion region, and do not show any breakdown. The model of JBS diodes also ignores the leakage current in the depletion region and observes an avalanche breakdown phenomenon.

MPS diodes have good application prospects, and their performance is influenced by their reverse characteristics. This paper initially analyzes such feature from two dimensions given its special working mechanism. The surface electric field model of Schottky contact is established by considering the influences of lateral voltage, device parameters and applied voltage.

## 2 Reverse $I-V$ Model

The reverse leakage current of MPS diodes comprises four parts, namely the thermionic emission leakage current, tunneling current, current generated by the depletion region and diffusion current.

### 2.1 Surface Electric Field

An increase in the surface electric field increases both the image force barrier reduction effect and the leakage current generated by the thermionic emission. The barrier width of the Fermi level is determined by the surface electric field, which can significantly influence the tunneling effect. The electric field at the Schottky contact interface is a key parameter in determining the thermionic emission current and tunneling current of the MPS.

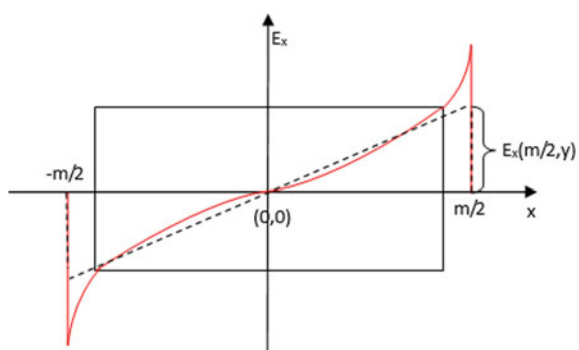
The coordinate system is established as shown in Fig. 1. The surface electric field of the Schottky metal can be obtained by solving the 2D electric field distribution of the Schottky contact region.

$$\frac{\partial^2 \phi}{\partial x^2} + \frac{\partial^2 \phi}{\partial y^2} = -\frac{qN_d}{\varepsilon} \quad (1)$$

$$\frac{\partial E_x}{\partial x} + \frac{\partial E_y}{\partial y} = \frac{qN_d}{\varepsilon} \quad (2)$$

where  $\phi$  is the potential distribution in the diode,  $E_x$  and  $E_y$  are the intensities of the horizontal and vertical electric fields, respectively, and  $N_d$  is the doping concentration of the drift region. To achieve a vertical electric field distribution, the horizontal electric field distribution of different depths must be obtained. The distribution of the horizontal electric field in the middle portion of the Schottky contact zone linearly increases as indicated by the red curve in Fig. 2 and is approximated by the black dotted line in the same figure.  $V(0, y)$  can be expressed as

**Fig. 2** Electric field distribution of MPS diodes



$$V(0, y) = \frac{1}{2} \cdot \frac{m}{2} \cdot E_x\left(\frac{m}{2}, y\right) \quad (3)$$

The horizontal electric field strength at  $x = 0$  can be expressed as:

$$\frac{\partial E_x}{\partial x}|(0, y) = \frac{E_x\left(\frac{m}{2}, y\right)}{m/2} = \frac{8}{m^2} V(0, y) \quad (4)$$

By substituting Eq. (4) to Eq. (2), the vertical electric field strength at  $x = 0$  can be expressed as:

$$\frac{\partial E_y}{\partial y}|(0, y) = \frac{qN_d}{\epsilon} - \frac{8}{m^2} V(0, y) \quad (5)$$

By taking the derivative of Eq. (5), the following is obtained along line  $y$ -axis:

$$E_y'' = \frac{8}{(m)^2} E_y \quad (6)$$

The solution of Eq. (6) is as given below.

$$E_y = C_1 e^{\frac{2\sqrt{2}}{m}y} + C_2 e^{-\frac{2\sqrt{2}}{m}y} \quad (7)$$

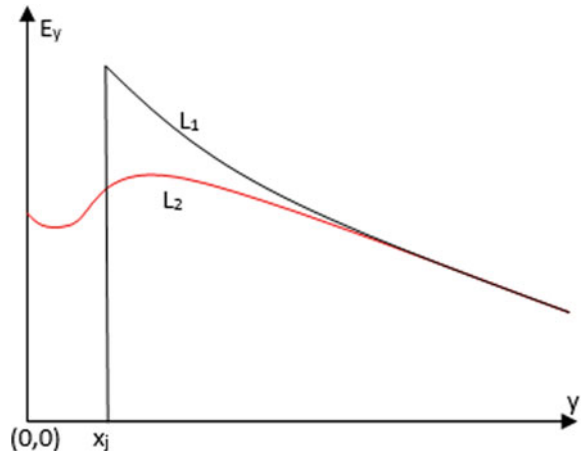
where  $C_1$  and  $C_2$  are constants that are determined by the boundary conditions. Equation (7) is the electric field distribution along the line  $L_2$  ( $y$ -axis).  $\partial E_y / \partial y$  is set to  $qN_d/\epsilon$  at  $y = 0$  because the vertical electric field at  $y = 0$  is not affected by the lateral PN junction depletion layer. The vertical electric field distribution of the MPS diodes [12] is shown in Fig. 3, and the slope of the vertical electric field intensity  $E_y$  of the drift region tends to be  $-qN_d/\epsilon$  when  $y > x_j + w$ . The values of  $C_1$  and  $C_2$  can be obtained from the slope of the vertical electric field strength at  $y = 0$  and  $y = x_j + w$ . The relationships of the MPS Schottky metal surface potential  $E_s$  with the junction depth  $x_j$ , the distance between adjacent zone  $P$  and reverse bias voltage  $V_F$  can be expressed as

$$E_s = \frac{qmN_d e^{\frac{2\sqrt{2}}{m}(x_j + w)} + e^{-\frac{2\sqrt{2}}{m}(x_j + w)} - 2}{2\sqrt{2}\epsilon} \quad (8)$$

where  $w$  is the depletion layer width, and  $m$  is the distance between of adjacent zone  $P$ .

$$w = \sqrt{\frac{2\epsilon}{qN_d} (V_{bi} - V_F)} \quad (9)$$

**Fig. 3** Electric field distribution of MPS diodes



## 2.2 Current of Each Part

Given the image power reduction effect, the thermionic emission current can be expressed as

$$J_{LTE} = \frac{m}{m+s} A * T^2 \exp\left(-\frac{q\phi_{Bn}}{kT}\right) \exp\left(\frac{q\Delta\phi}{kT}\right) \quad (10)$$

where  $\Delta\phi$  is a barrier that is reduced by the mirror force effect which can be expressed by a Schottky metal surface potential.

$$\Delta\phi = \sqrt{\frac{qE_s}{4\pi\epsilon_s}} \quad (11)$$

The tunneling current can be expressed as follows:

$$J_{LT} = \frac{m}{m+s} \frac{A.T \cdot E_s^2}{q\phi_{Bn}} \exp\left(-\frac{B.T \cdot (q\phi_{Bn})^{3/2}}{E_s}\right) \quad (12)$$

where  $A.T$  and  $B.T$  are given by [13, 14], respectively.

The concentration of electrons and holes in the space charge region is equal to 0, and the recombination center level produces electrons and holes when the applied bias voltage of the MPS is negative. These electrons and holes attempt to re-establish a heat balance, and the generation of electron and hole pairs in a semiconductor is affected by the generation rate.

$$U = \frac{n_i}{\tau} \quad (13)$$

$\tau$  denotes the life of space charge. These carriers are generated in the entire space charge region, which in turn generates an electric current.

$$J_U = \frac{qn_iw}{\tau} \quad (14)$$

$w$  denotes the space charge zone width,  $n_i$  is the intrinsic carrier concentration, and the relationship between  $n_i$  and temperature can be expressed as (15).

$$n_i = 4.9 \times 10^{15} \times \left[ \frac{m_{de}^* m_{dh}^*}{m_0^2} \right]^{\frac{3}{4}} M_C^{\frac{1}{2}} T^{\frac{3}{2}} \exp\left(-\frac{E_g}{kT}\right) \quad (15)$$

where  $k$  is the Boltzmann constant,  $T$  is the thermodynamic temperature,  $m_0$  is the electron mass and  $M_C$  is the number of effective states of the conduction band bottom, which is equivalent to 12 for 4H-SiC. In addition,  $m_{de}^*$  and  $m_{dh}^*$  represent the state density effective masses of electrons and holes, respectively, and  $E_g$  is the forbidden bandwidth. Its relationship with temperature can be expressed as [5]

$$E_g(T) = E_g(300K) - 3.3 \times 10^{-3} \times (T - 300K) \quad (16)$$

The diffusion current is related to the generation of electron–hole pairs in the neutral region. The minority generated at the edge of the depletion region is swept into the bottom of the drift region by the electric field to generate a diffusion leakage current. The diffusion current obtained by the bipolar transport equation is

$$J_p = \frac{qD_p n_i^2}{L_p N_d} \quad (17)$$

where  $D_p$  denotes the hole diffusion coefficient and  $L_p$  represents the hole diffusion length. The total reverse leakage current of MPS diodes can then be expressed as

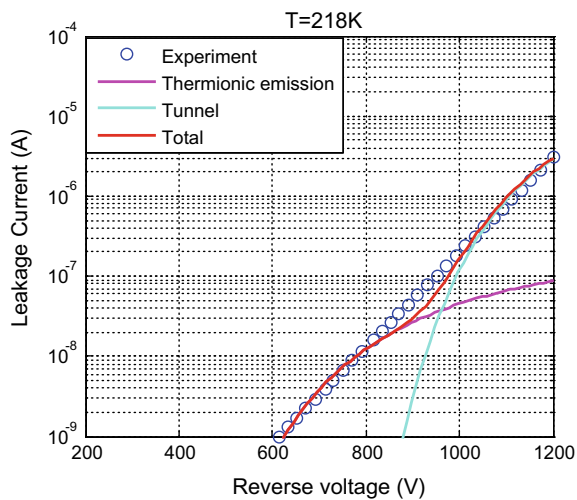
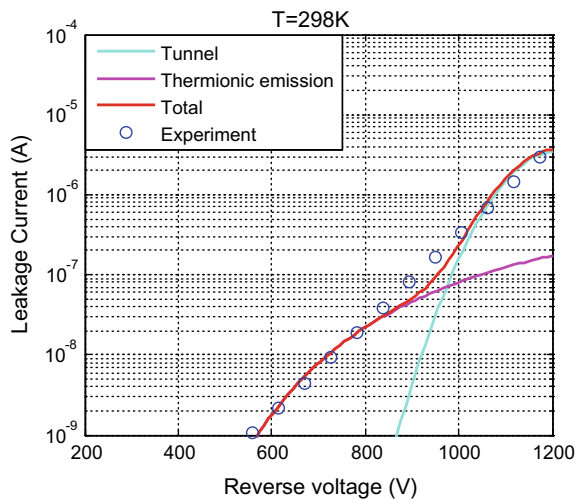
$$J_R = J_p + J_U + J_{LTE} + J_{LT} \quad (18)$$

### 3 Model Verification and Analysis

The reverse leakage current of the MPS diode IDM10G120C5 was simulated by the reverse  $I$ – $V$  characteristic model described above and was compared by using the results measured in the IDM10G120C5 data sheet. The parameters required in the model are given in Tables 1; [15].

**Table 1** MPS diode parameters

Parameter	Value	Unit
$N_a$	$1 \times 10^{19}$	$\text{cm}^{-3}$
$N_d$	$1.2 \times 10^{16}$	$\text{cm}^{-3}$
$x_j$	$1 \times 10^{-4}$	cm
$s$	$10 \times 10^{-4}$	cm
$m$	$10 \times 10^{-4}$	cm

**Fig. 4** Modelling performances of reverse characteristics ( $T = 218$  K)**Fig. 5** Modelling performances of reverse characteristics ( $T = 298$  K)

**Fig. 6** Modelling performances of reverse characteristics ( $T = 373$  K)

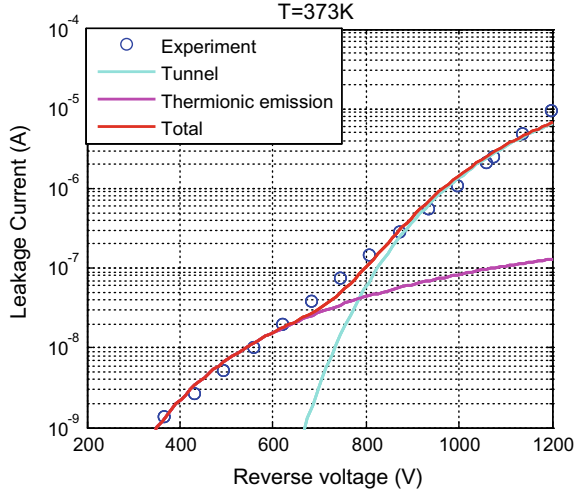
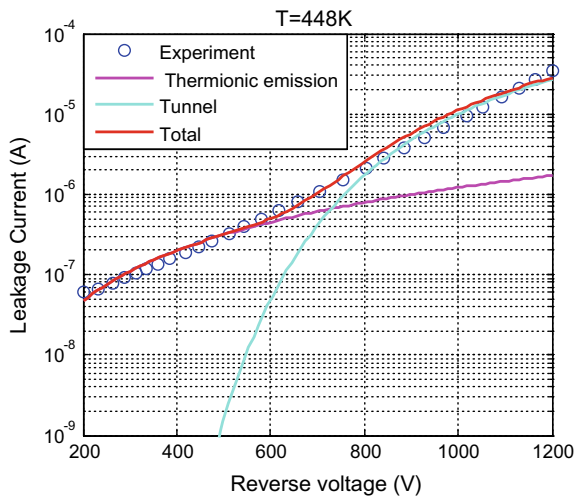


**Fig. 7** Modelling performances of reverse characteristics ( $T = 448$  K)



where  $N_a$  is the doping concentration of the  $P+$  region. Figures 4, 5, 6 and 7 show the relationship between the leakage current and the reverse bias voltage in logarithmic coordinates. In this figure, the blue curve denotes the test value of the total leakage current, the red curve denotes the model value of the total leakage current, the purple curve denotes the model value of the current generated by the thermionic emission, and the cyan curve denotes the model value of the current generated by the tunneling effect. Figures 4, 5, 6 and 7 are obtained by substituting the parameters listed in Table 1 into Eqs. (10), (12) and (18) at  $T = 218, 298, 373$  and  $448$  K, respectively. This figure also shows that the calculated values are consistent with the measured values, thereby validating the accuracy of the model.

Figures 4, 5, 6 and 7 also show that the leakage current of MPS diodes which is mainly generated by the thermionic emission and tunneling effects (the sum of the generated current and diffused current in the depletion region ranges between 10 and 20 and is thereby not shown in the figure). When the reverse bias voltage is small, the total leakage current is similar to the current generated by the thermionic emission effect, but when the reverse bias voltage increases, the total leakage current is similar to the current generated by the tunneling effect. In sum, the thermionic emission effect plays a major role in the reverse characteristics of the MPS diode when the reverse bias voltage is small. By contrast, when the reverse bias voltage is large, the tunneling effect plays a major role in the reverse characteristics of the MPS diode.

The total leakage current and the leakage current of each component increase along with voltage and temperature, whereas the surface potential of the Schottky contact increases along with the reverse bias voltage. In this case, the mirror force barrier reduction effect is strengthened, thereby increasing the leakage current generated by the thermionic emission effect. Moreover, given that the gradient of the conduction band energy of MPS diodes in the Schottky contact region increases along with the reverse voltage which leads to an increase in the range of the tunneling, and the leakage current generated by the tunneling effect also becomes larger. Therefore, the total leakage current increases as the reverse bias voltage increases.

## 4 Conclusion

This paper establishes a reverse characteristic model of 4H-SiC MPS diodes for simulating MPS diodes. This model is validated by comparing its results with the test results. Only slight differences are observed between these two sets of values. The surface electric field model of the Schottky contact is established by analyzing the 2D electric field of MPS diodes. The proposed model is used to analyze the leakage currents of MPS diodes and can accurately predict the reverse characteristics of these diodes within the range of their operating voltage and operating temperature. The main factors that affect MPS diodes are also analyzed. The reverse leakage current and its various components increase along with temperature and reverse bias, the leakage current is mainly generated by the thermionic emission effect when the voltage is low, and the leakage current is mainly caused by the tunneling effect when the voltage is high.

**Acknowledgements** This work is supported by the National Natural Science Foundation of China under (No.51307113) and Natural Science Foundation of Jiangsu Province (No. BK20130307). Xuehui Tao is the corresponding author.

## References

1. Hefner AR, Singh R Jr, Lai J-S, Berning DW, Bouché S (2001) SiC power diodes provide breakthrough performance for a wide range of applications. *IEEE Trans Power Electron* 16(2):273–280
2. Amairi M, Mtimet S, Salah TB, Morel H (2018) Temperature dependence of silicon and silicon carbide power devices: an experimental analysis. In: IEEE mediterranean electrotechnical conference, pp 97–98
3. Starzak L, Stefanskyi A, Zubert M (2018) Improvement of an electro-thermal model of SiC MPS diodes. *IET Power Electron*, pp 660–667
4. Mantooth HA, Peng K (2015) Modeling of wide bandgap power semiconductor devices—part I. *IEEE Trans Electron Dev* 62(2):423–426
5. Jiang Y, Sung W, Song X, Ke H, Liu S, Baliga BJ, Huang AQ, Van Brunt E (2016) 10 kV SiC MPS diodes for high temperature applications, pp 43–46
6. McNutt TR, Hefner AR (2004) Silicon carbide PiN and merged PiN Schottky power diode models implemented in the saber circuit simulator. *IEEE Trans Power Electron* 19(3):573–575
7. Miao Y, Zhang Y (2004) Merged PiN Schottky Diodes: a new power switching diode. *Microelectron Inst* 34(2):117–118 (in Chinese)
8. Niu Xinjin, Zhang Yuming, Zhang Yimeng (2003) Analysis of power dissipation characteristics of MPS based on SiC. *Res Progr SSE* 23(2):194–196 (in Chinese)
9. Haihong X (2017) Simulation and design of 1200 V MPS diode. Shenyang University of Technology, pp 5–24 (in Chinese)
10. Neamen DA (2013) Semiconductor physics and devices basic principles. Publishing House of Electronics Industry, pp 77–289
11. Zhu Lin, Chow T Paul (2008) Analytical modeling of high-voltage 4H-SiC Junction Barrier Schottky (JBS) rectifiers. *IEEE Trans Electron Dev* 55(8):1857–1861
12. Ren Na, Sheng Kuang (2014) An analytical model with 2-D effects for 4H-SiC trenched junction barrier Schottky diodes. *IEEE Trans Electron Dev* 61(12):4158–4162
13. Lenzlinger M, Snow EH (1969) Fowler-Nordheim tunneling into thermally grown SiO<sub>2</sub>. *Appl Phys* 40(1):278–283
14. Weinberg ZA (1982) On tunneling in metal-oxide-silicon structures. *Appl Phys* 53(7):5052–5056
15. Palanisamy S, Fichtner S, Lutz J, Basler T, Rupp R (2016) Various structures of 1200 V SiC MPS diode models and their simulated surge current behavior in comparison to measurement. In: Proceedings of the IEEE ISPSD. Prague, pp 235–238

# Stochastic Simulation of Traction Load for Urban Rail Transport Based on Dynamic Train Headway



Zhenhai Sun, Hui Liu, Jinping Fang and Shaobing Yang

**Abstract** Traction load modeling for urban rail transport is a fundamental work, which is a necessary technique of energy consumption statistics, energy saving analysis and equipment evaluation. Dynamic train headway is the decisive factor of traction load level. The train headway in the morning peak and evening peak is the shortest, which leads to two peak loads. This paper analyzes the distribution characteristics of the headway, then based on the cosine function, it proposes a method of describing the headway on the operating day. By nonlinear curve fitting, the local volatility of the headway with the Cauchy distribution is determined. What is more, the sliding time window method is proposed to output the simulation time, train position and its load. According to the analysis of an actual case, the stochastic simulation method, we propose can accurately describe the fluctuation characteristics and probability distribution characteristics of the traction load.

**Keywords** Urban rail transport: traction load · Stochastic simulation · Dynamic train headway · Statistical characteristics

---

Z. Sun · J. Fang

Beijing Subway Power Supply Branch, Beijing 100082, China

e-mail: [s1618@sohu.com](mailto:s1618@sohu.com)

J. Fang

e-mail: [fipyy2003@163.com](mailto:fipyy2003@163.com)

H. Liu (✉)

Beijing Subway Operation Technology Centre, Beijing 102208, China

e-mail: [630288235@qq.com](mailto:630288235@qq.com)

S. Yang

Beijing Jiaotong University, Beijing 100044, China

e-mail: [shbyang@bjtu.edu.cn](mailto:shbyang@bjtu.edu.cn)

## 1 Introduction

With the advantages of strong transport capacity, low energy consumption, green environmental protection and high energy efficiency, urban rail transit has been developed rapidly in recent years. Compared with the countries with developed rail transit in the world, rail transit in China is still of broad application prospects, especially in suburban and inter-city traffic. With the increase of train traffic and speed, the impact of traction load on urban power grid which cannot be ignored has attracted wide attention. In many related studies, traction load simulation is a basic and necessary technical means.

At present, traction load modeling technology can be classified as three methods: constant power method, average traffic method and operation diagram method. Obviously, the constant power (or current) method is the simplest, but the dynamic characteristics of traction load cannot be reflected. So, it is generally used for a rough load assessment. The average traffic method is a calculation method based on statistical and probabilistic calculation methods. It is simple and convenient to use, but the calculation error is usually big, which is more than 20%. Train operation diagram method is the most detailed and accurate among three methods. Operation diagram method is the most detailed and accurate calculation method, which describes the train load and its movement process through dynamics and timetable. There are two shortcomings: one is that the calculation process is complicated and expensive; the other is that it cannot reflect random behaviors during train operation process. The load curve obtained by the operation diagram method is still of significant deviation from the measured data [1, 2].

In China and abroad quality standards, the probability method is generally used to evaluate the stochastic load. For example, China national standard specifies the limit value of voltage fast fluctuation, harmonic and three-phase unbalance as the 95% probability values. Therefore, stochastic simulation of traction load and probabilistic power flow calculation are hot issues [3]. Compared with the operation diagram method, the stochastic method has many advantages. Firstly, it can reveal the distribution characteristics of traction load more comprehensively, and then analyze its average level, the most serious situation and other working conditions. Secondly, the stochastic method can provide a basis for more reasonable planning of system capacity and evaluation of power supply capacity. What is more, the stochastic model can construct the actual measured model of existing lines by parameter identification, which makes the simulation results closer to the actual data.

However, it is difficult to construct a stochastic model that is accurate, reliable and practical. Literature [4] obtained the mathematical formula of daily load curve by piecewise curve fitting, which can describe the change of load more accurately. But due to the diversity of load curve, the formula needs to be modified according to the actual measurement in application. Literature [5] established the simulation algorithm of train flow based on train working condition and motion equation. The algorithm can accurately generate train operation results, but it is too complex for power supply load analysis.

This paper proposes stochastic simulation based on dynamic train headway, in which the position of train is described by probability method. The data of train power comes from traction calculation or measured data. There are two reasons for it: one is that there are many factors affecting train power to create an accurate mathematical model, so it is difficult to build an accurate mathematical model, but it is more convenient and reliable to use traction calculation results or measured data; the other is that there are few parameters describing dynamic train headways, which can reduce the difficulty of parameter identification and improve the practicability of the model. At first, this paper studies the statistical characteristics of dynamic train headways based on the actual measurement and puts forward the mathematical model. Secondly, the method and process of power supply interval load synthesis are given in detail and the identification method of model parameters is introduced. Finally, the specific application examples of the model are introduced through the case.

## 2 Statistical Characteristics of Train Headways and Mathematical Modeling

Rules of people's daily travel are closely related to time, including working days, rest days, different periods of the day, etc. According to the actual arrival time of a train at a subway station in Beijing, changes of the train headways are shown by the red curve in Fig. 1. It is obvious that the traffic density in the morning and evening is the highest, and the traffic density from 11 a.m. to 4:30 p.m. is much lower. By large number of field measurements, it is found that the working days are similar, and the fluctuation trend is consistent [6].

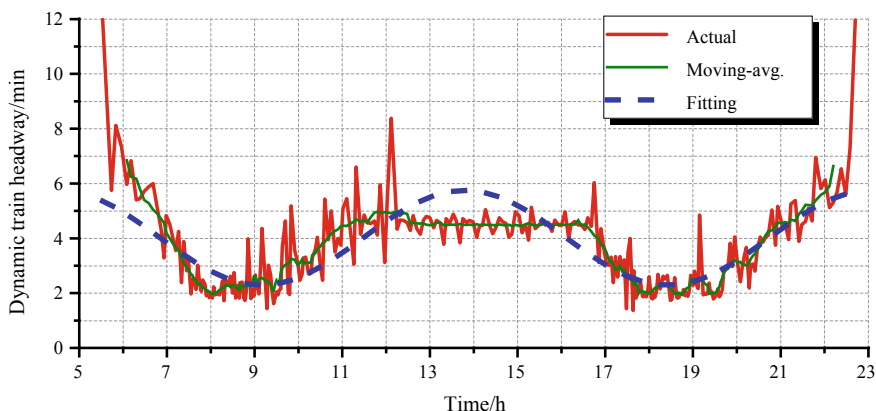


**Fig. 1** Field test data of weekday headways

Because of the slight migration of different working days on the time boundary, considering the complexity of the model, a cosine function is used to describe the fluctuation of the train headways. It is expressed as follows:

$$\delta(t) = \delta_0 - A \cdot \cos\left(2\pi \frac{t - t_1}{t_2 - t_1}\right), \quad t \in [5, 23] \quad (1)$$

where  $t$  is the time which the unit is hour, and  $\delta_0$  is the average value of the departure interval every day.  $t_1$  and  $t_2$  are the corresponding time of morning and evening peak and  $A$  is the gain, which represents the difference of the departure interval between the peak time and the idle time.

According to the measured samples to fit nonlinear curve in Fig. 1, parameters can be identified as:  $[\delta_0, A, t_1, t_2] = [4.0, 1.7, 9.1, 18.4]$ . It can be seen that the average departure interval is 4 min. The peak value of the morning peak corresponds to 09:06, and the peak value of the evening peak corresponds to 18:24. The fitting curve is shown in the blue dotted line in Fig. 1. It can be seen that the mean absolute percentage error (MAPE) of all samples is less than 20%, the moving average MAPE of 10 samples is less than 15%, and the average error of the whole sample is only 2.7%. From above, it can be thought that this function can better describe the trend of train headway.

According to the measured samples, the statistical characteristics of the fluctuation amplitude of the train headways can be expressed as follows.

$$\Delta h = z(t) - \delta(t) \quad (2)$$

where  $z(t)$  represents the measured train headways corresponding to time  $t$ . As shown in Fig. 2, the probability density of the fluctuation amplitude basically shows positive and negative symmetric fluctuations. Cauchy distribution can well describe the fluctuation characteristics by nonlinear curve fitting, shown as follows.

$$C(\Delta h) = \frac{1}{\pi} \cdot \frac{\gamma}{(\Delta h - \mu)^2 + \gamma^2} \quad (1.3)$$

In the equation,  $\mu$  represents the position parameters, and  $\gamma$  indicates the scale parameters. According to Eq. (1.3), the position parameter is  $-0.35$  and the scale parameter is  $0.64$ , which are identified by fitting a nonlinear curve-based measured data in Fig. 2. The determination coefficient of the fitting effect is more than 0.97, which indicates a good matching. The headway fluctuations described in Eq. (1.3) is applicable to all-day periods and independent of the specific moment.

Urban rail transit is of high traffic density and uniform interval. Owing to the short distance and strong control, the trains can almost arrive at the station on time. Therefore, it is appropriate to describe the deviation of train headway with Cauchy distribution. On the contrary, the long interval distance and more complex situations of inter-city railway make it better to adopt normal distribution.

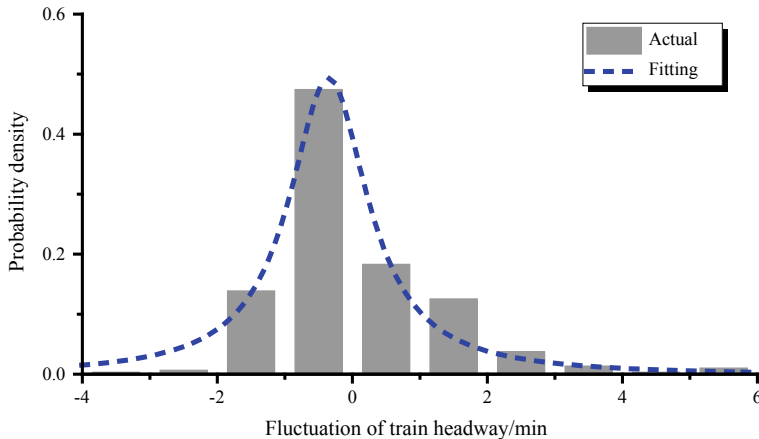


**Fig. 2** Histogram of headway fluctuations computed by (2)

### 3 Method and Steps of Power Supply Interval Load Synthesis

#### 3.1 Method of Generation of Stochastic Train Headways

Before load simulation, train headways should be generated for all trains (except the first train) in the simulation period, which is the time interval between the train and the front train when entering the power supply area.  $t$  is set as the entry time of the first train, and the following train headways are obtained as follows:

1. Input  $t$  into Eq. (1) to get the train headway  $\delta$  at this moment;
2. Generate random fluctuation values  $\Delta h$  subjecting to Cauchy distribution;
3. Record the train headway  $\delta + \Delta h$  of the current train;
4. Set  $t = t + (\delta + \Delta h)$ , and turn back to step 1 to get the train headway of the next train.

Through the steps above, the train operation diagram of all trains passing through the power supply section one day can be obtained, which has stochastic properties. In order to get the total traction load, superposition calculation should be performed based on the results of traction calculation or measured data.

In the second step above, random numbers subject to Cauchy distribution should be generated. According to the probability theory, the inverse function method can be obtained by the following steps:

1. Generate  $N$  random numbers which uniformly distributed in  $(0, 1)$  as  $U_k$ ,  $k \in [1, N]$ ;
2. Input  $U_k$  into Cauchy inverse function, as follow equation;

$$\Delta h = \gamma \cdot \tan \left[ \left( U_k - \frac{1}{2} \right) \pi \right] + \mu \quad (4)$$

### 3.2 Steps of Traction Load Synthesis

The results of train traction calculation and the measured data can be both indexed by time. Therefore, load synthesis can be accomplished by creating an array indexed by time. As shown in Fig. 3, it takes 480 s for a single train to pass through the power supply section. The current is shown in the red curve, where the negative value represents the regenerative braking feedback current and the blue triangle indicates the train running to the right.

In this paper, the sliding time window method as shown in Fig. 4 is used to determine the position, time and load of the train. In Fig. 4,  $T$  expresses the total time of sliding time window duration, which is the length of time that a single train passes through the power supply section. The number of trains passing through the sliding time window in one day is  $N$ . And  $N$  represents the total number of trains passing through the power supply section on a whole day. Let  $T$ , be the total time the sliding time window slides in a day, which is the total running time of the train in the power supply section. Let  $u_k$  be the  $k$ th train, which is the first train outside the time window. There are  $n$  trains in the sliding time window and  $d$  suggests the cumulative time of the last train entering the section. Record the traction calculation results of a single train as structural arrays  $[x, l, I]$ , which indicates the length of the train after entering the section, the kilometer mark and the load current, respectively.

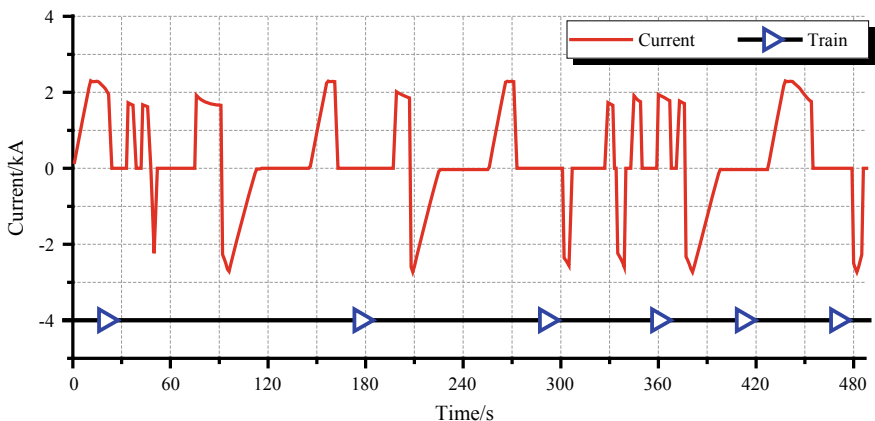


**Fig. 3** Illustration of superposition of train loads

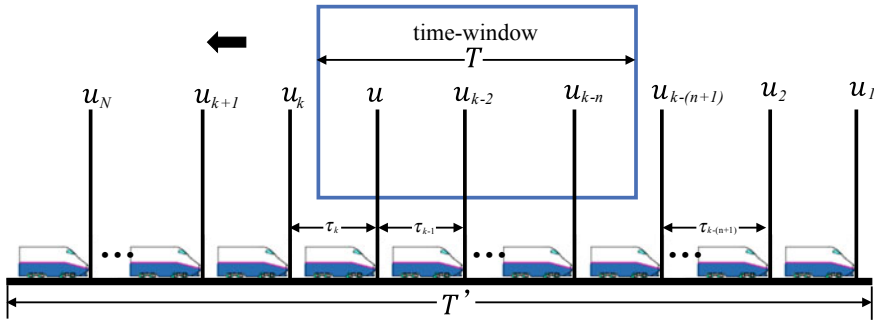


**Fig. 4** Illustration of the sliding time window method

The specific operation steps are shown as follows:

Since the results of train traction calculation and the measured data can be both indexed by time, the total load at a certain moment is the superposition of all the train loads in the time window at that time.

In application, the up train and the down train can be considered as running independently. In addition, the identification parameters of Eq. (1) are obtained from a certain station. The time scale corresponding to the calculated load distribution should take into account the time difference between the station and the power supply area.

## 4 Specific Study on Case

Taking Beijing Changping Metro Line as an example, distance between two traction substations (*A* and *B*) is 6 km. Double-ended power supply mode is adopted. Supposing the voltage of DC bus of the two stations is constant and the influence of adjacent substations is not taken into account. The average weight of trains is set at 280 t and the group is 4M2T. The departure interval parameters are set as  $[\delta_0, A, t_1, t_2] = [4.5, 1.5, 9.1, 18.4]$ . The regenerative braking power is consumed by the ground resistance device. According to the traction calculation results, the train position and the current taken corresponding to each simulation moment are calculated by the foregoing steps, and then the output power of the substation is obtained through power supply calculation. For example, the average power for substation *A* is shown in Fig. 5. Solid line indicates simulated power, and dot line indicates measured power. It can be seen that there are two load peaks in the peak time of morning and evening flow, which are in good agreement with the measured curve. The MAPE is only 5.6%. Obviously, it can accurately describe the power change. It is found that the peak load of the evening peak is significantly higher. That is because the downward operating condition in the evening peak is heavy-load climbing and the upward operating condition in the morning peak is heavy-load downhill.

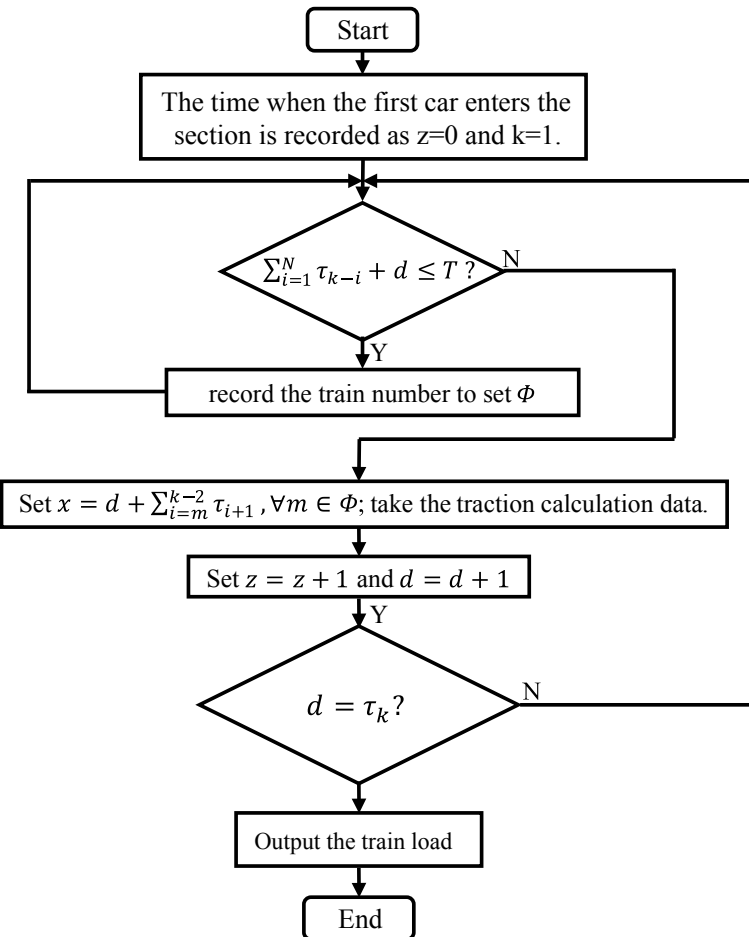


**Fig. 5** Flowchart of the siding window method operation

In most cases, change of the train density is tiny in off-peak period, so the description of dynamic train headway which adopts the cosine function brings some deviation. As shown in Fig. 5, the measured load curve from 10:00 am to 16:00 pm is relatively flat, while the simulated load curve is of obvious decline, with a deviation of nearly 13% at 13:00. Since the load evaluation usually focuses on the maximum value, the 95% probability value and the average value, the application of the proposed model is not influenced by the deviation in the low load range.

In order to verify the validity of dynamic train headway, the average power of substation A during the operating hour is calculated as shown in Fig. 6. It can be seen that the simulation results are in good agreement with the measured results. Probability density distribution of simulated power of substation A is shown in Fig. 7. There is a peak value near 0.5 MW in the measured probability histogram,

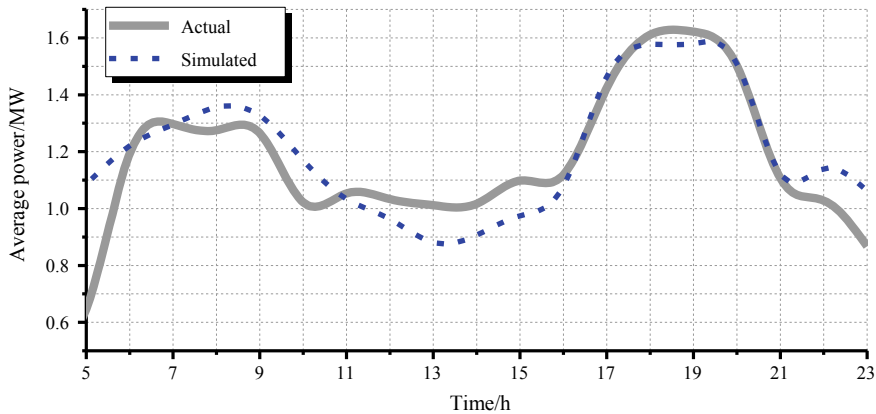


**Fig. 6** Comparison of average power between measurement and simulation for substation A

**Table 1** Statistics of measured and simulated power load of substation A

Statistics items	Measured (MW)	Simulation (MW)	Error (%)
Maximum value	2.004	1.969	-1.75
Average value	1.174	1.173	-0.09
95% probability value	1.680	1.705	1.49

which is caused by the unloaded traction load during non-operational periods (including the dynamic load). From above, it can be calculated that the absolute value error is less than 2% as shown in Table 1; (Figs. 7 and 8). We also simulate relationship between power and time. Figure 8 shows power varies with time during a period time. It accords with the fact well.

## 5 Conclusion

Train traction calculation is widely used in traction load simulation of urban rail, and parallel operation diagrams are often adopted to describe train movement. This simplified processing will lead to a single traction load model, which cannot fully analyze the load distribution and fluctuation. In this paper, the distribution characteristics of train headway of metro trains are analyzed, and then a new method with cosine function is proposed to describe the tracking headways. The advantages are as follows:

1. The model accurately describes the distribution characteristics of traction load of urban rail and indicates the significant impact of load on passenger flow level.
2. The proposed model is of simple structure and clear meaning of parameters, which makes the model easy to use.

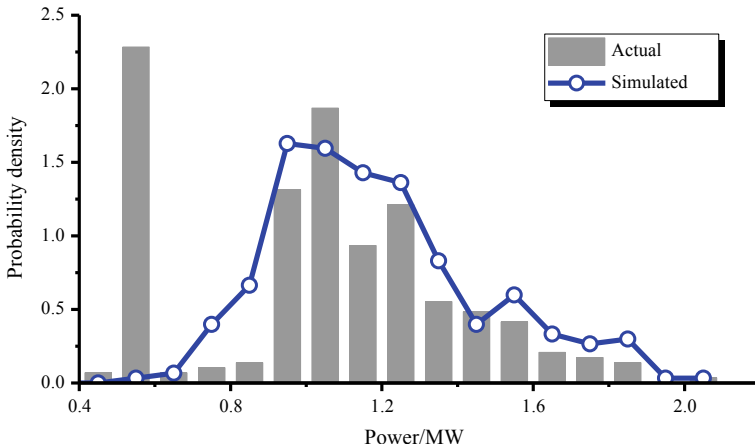


**Fig. 7** Histogram and fitting result of simulated power of substation A

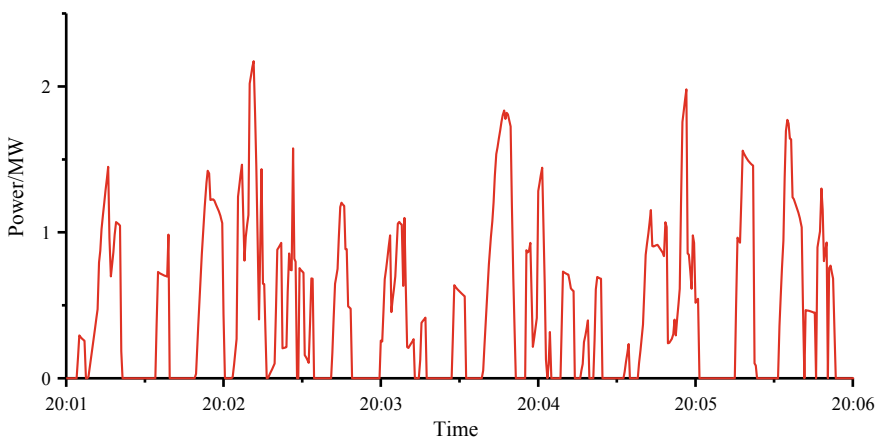


**Fig. 8** Simulated power load profile of substation A

3. The proposed model is of clear application steps and independent functions. It can embed the train traction calculation program or directly read the measured data of the train load to output random load samples.

Usually, traction load is the superposition of multiple trains, and the overall level of train load is determined by the number of trains. Therefore, the description of headway is very important, which determines the accuracy of load simulation. The proposed model takes random factors into consideration. With more realistic and comprehensive evaluation of load conditions, it is of good application prospect.

**Acknowledgements** This work is supported by research project of Beijing Subway Operation Company Limited in 2018, “Development of Data Analysis and Computing Software for Subway Power Supply System” (No. 2018000504000002). Hui Liu is the corresponding author.

## References

1. Heng C, Wei X (2015) Analysis of difference between calculated load and actual traction load of urban rail transit and countermeasures. *Urban Mass Transit* 18(05):128–129 + 134 (in Chinese)
2. Bao ming H, De wei L, Bo W, Ming hui Z (2013) Calculation and improvement of urban rail transport capacity. *Urban Mass Transit* 16(04):38–43 (in Chinese)
3. Yu bing M (2015) Research on regenerative braking energy utilization scheme in urban rail system. *J Southwest Jiaotong Univ* (in Chinese)
4. Meng rong G (2013) Metro power system design and simulation. *J Southwest Jiaotong Univ* (in Chinese)
5. Hang fei H (2018) Models and algorithms for urban rail transit timetable optimization. *J Beijing Jiaotong Univ* (in Chinese)
6. De long G (2016) Analysis of the operation load characteristics at DC traction station. *Urban Mass Transit* 19(02):79–82 (in Chinese)

# Transient Direct Current Control of Single-Phase Cascaded H-Bridge Rectifier Without Phase-Locked Loop



Juxia Ding and Qunzhan Li

**Abstract** The traction drive system without industrial frequency transformer is the trend and effective lightweight solution of high-speed train in the future. Cascade H-bridge rectifier has become the preferred solution for the front end of this technology due to its modular structure and simple control. In this paper, the working principle of single-phase cascaded H-bridge rectifier is analyzed, and an improved transient direct current control method without phase-locked loop (PLL) is proposed. The command current signal is calculated by the relation of instantaneous power to voltage and current in the two-phase stationary coordinate system to realize the tracking control of the grid current to the voltage. On this basis, aiming at the DC-link voltage imbalance caused by unbalanced loads, a voltage balancing control method without PLL is proposed. Simulation results show the effectiveness of the proposed method.

**Keywords** Single-phase · Cascaded H-Bridge rectifier · Transient direct current control · Phase-locked loop (PLL) · Voltage balancing control

## 1 Introduction

In order to meet the requirements of energy saving and environmental protection, lightweight is an inevitable trend in the future development of high-speed train. However, the industrial frequency transformer is an important part of the traction drive system of high-speed train; due to its large size, high cost, low efficiency, and excessive space occupied, it seriously restricts the power and speed of train traction drive system [1, 2]. Because of its modular design, simple control, easy realization of high voltage output and high reliability, cascaded H-bridge rectifier has become a research hotspot of the front end of the traction drive system without industrial frequency transformer [3, 4].

---

J. Ding (✉) · Q. Li

Department of Electrical Engineering, Southwest Jiaotong University, Chengdu, China  
e-mail: [northdingding@163.com](mailto:northdingding@163.com)

There are two main control targets for single-phase cascaded H-bridge rectifier. One is that the grid current is the same frequency and phase as the grid voltage, so that the system unit power factor operates, and the other is that the DC-link voltages are stable and balanced. The grid current control treats the cascaded H-bridge as a whole, and the DC-link voltage needs to be independently controlled. The overall control of cascaded H-bridge rectifier currently uses a double closed-loop control method of voltage outer loop and current inner loop [5–9]. For the DC-link voltage balance problem, the voltage balancing algorithm based on power feedback [5], the voltage balancing algorithm for changing modulation ratio in real time [6], and the improved algorithm based on proportional-integral adjustment [7] are proposed, respectively. On this basis, the Ref. [8] proposed a SVPWM method that can quickly balance the DC-link voltages, and the Ref. [9] proposed an improved voltage balancing control method to solve the load difference. However, all the above studies are under the ideal grid voltage, and all require PLL.

In this paper, a transient direct current control method for single-phase cascade H-bridge rectifier without PLL is improved. According to the relation of instantaneous power to voltage and current in the two-phase stationary coordinate, the current command signal in phase with the grid voltage and the voltage equalizing command signal of each cell can be obtained without PLL. Thus, the single-phase cascade H-bridge rectifier can work in the unit power factor, and the DC-link voltages remain balanced and stable. Moreover, the method has clear physical meaning and is simple to implement.

## 2 The Principle of Single-Phase Cascade H-Bridge Rectifier

Figure 1 shows the topology of single-phase cascade H-bridge rectifier. In the diagram,  $u_s$  and  $i_s$  are the grid voltage and current;  $L_s$  and  $R_s$  are the equivalent AC inductance and AC resistance;  $L_2$  and  $C_2$  are the inductance and capacitance of resonance filter;  $C_{di}$ ,  $R_i$ , and  $U_{di}(i = 1, 2, \dots, n)$  are, respectively, the DC-link capacitance, equivalent load resistance, and the DC-link voltage of each cell;  $u_{ab}$  is the AC side voltage of single-phase cascade H-bridge rectifier. If the DC-link voltage of each cell is the same, there will be  $C_{d1} = C_{d2} = \dots = C_{dn} = C_d$ .

For the convenience of analysis, the on-off state of each switch is defined as

$$T_{ij} = \begin{cases} 1 & T_{ij} \text{ is open} \\ 0 & T_{ij} \text{ is close} \end{cases} \quad i = 1, 2, \dots, n; j = 1, 2, 3, 4 \quad (1)$$

The switch functions  $S_i$  is defined with  $T_{ij}$  as follows

$$S_i = T_{i1} - T_{i3} \quad i = 1, 2, \dots, n \quad (2)$$

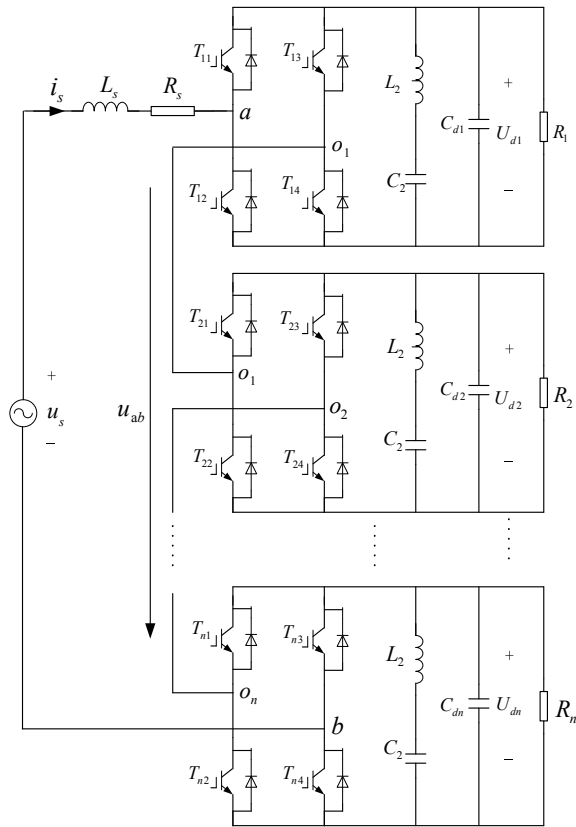


**Fig. 1** Topology of the single-phase cascaded H-bridge rectifier

Neglecting  $R_s$  and using the switch function  $S_i$ , the mathematical model of the topology is as follows.

$$\begin{cases} u_s - L_s \frac{di_s}{dt} = \sum_{i=1}^n S_i U_{di} = u_{ab} \\ C_i \frac{du_{di}}{dt} = S_i i_s - \frac{u_{di}}{R_i} \end{cases} \quad (3)$$

### 3 Transient Direct Current Control of Single-Phase Cascaded H-Bridge Rectifier Without PLL

#### 3.1 Transient Direct Current Control Without PLL

For single-phase cascade H-bridge rectifier, since the current through the connected units is the same, it is usually regarded as a single-phase single-stage rectifier.

According to Eq. (3), the mathematical formula of the transient direct current overall control method is

$$\begin{cases} I_s^* = T_p \left( \sum_{i=1}^n U_{di}^* - \sum_{i=1}^n U_{di} \right) + \frac{1}{T_i} \int \left( \sum_{i=1}^n U_{di}^* - \sum_{i=1}^n U_{di} \right) dt \\ u_{ab} = u_s(t) - \omega L_s I_s^* \cos \omega t - T_p [I_s^* \sin \omega t - i_s(t)] \end{cases} \quad (4)$$

where  $I_s^*$  is the reference grid current value,  $U_{di}^*$ ,  $U_{di}$  are, respectively, the reference voltage value and actual voltage value of the  $i$ -th cell, and  $T_p$ ,  $T_i$  are the proportional and integral parameter of the PI controller.

It can be seen from Eq. (4) that the key of the method is the accurate tracking of the grid current to the voltage, thereby obtaining the grid current command signal  $I_s^* \sin \omega t$  and  $I_s^* \cos \omega t$ , which are, respectively, in phase and orthogonal to the grid voltage, and then, the AC side voltage, that is, the total modulation wave  $u_{ab}$ , is calculated.

According to the instantaneous power theory of three-phase circuit, the three-phase voltage  $u_{sa}$ ,  $u_{sb}$ ,  $u_{sc}$  and the current  $i_{sa}$ ,  $i_{sb}$ ,  $i_{sc}$  are transformed into a two-phase orthogonal coordinate system  $\alpha - \beta$  to obtain  $u_{s\alpha}$ ,  $u_{s\beta}$  and  $i_{s\alpha}$ ,  $i_{s\beta}$ , such, the instantaneous active power and instantaneous reactive power are

$$\begin{bmatrix} p \\ q \end{bmatrix} = \begin{bmatrix} u_{s\alpha} & u_{s\beta} \\ u_{s\beta} & -u_{s\alpha} \end{bmatrix} \begin{bmatrix} i_{s\alpha} \\ i_{s\beta} \end{bmatrix} \quad (5)$$

For the single-phase circuit, there are

$$\begin{bmatrix} p \\ q \end{bmatrix} = \frac{1}{3} \begin{bmatrix} u_{s\alpha} & u_{s\beta} \\ u_{s\beta} & -u_{s\alpha} \end{bmatrix} \begin{bmatrix} i_{s\alpha} \\ i_{s\beta} \end{bmatrix} \quad (6)$$

Suppose that  $p^*$  and  $q^*$  are the given instantaneous active and reactive power value, and  $i_{s\alpha}^*$  and  $i_{s\beta}^*$  are the command signals of the grid current on the  $\alpha$ ,  $\beta$  axis, then

$$\begin{bmatrix} i_{s\alpha}^* \\ i_{s\beta}^* \end{bmatrix} = \frac{3}{u_{s\alpha}^2 + u_{s\beta}^2} \begin{bmatrix} u_{s\alpha} & u_{s\beta} \\ u_{s\beta} & -u_{s\alpha} \end{bmatrix} \begin{bmatrix} p^* \\ q^* \end{bmatrix} \quad (7)$$

To achieve unity power factor control,  $q^* = 0$ , suppose  $K = \frac{3u_{s\alpha}}{u_{s\alpha}^2 + u_{s\beta}^2}$ , then

$$i_s^* = i_{s\alpha}^* = \frac{3u_{s\alpha}}{u_{s\alpha}^2 + u_{s\beta}^2} p^* = K \cdot p^* \quad (8)$$

As can be seen from Eq. (8), the denominator  $u_{s\alpha}^2 + u_{s\beta}^2$  is a constant value, and  $p^*$  is also a constant value. Therefore, the frequency and phase of the command

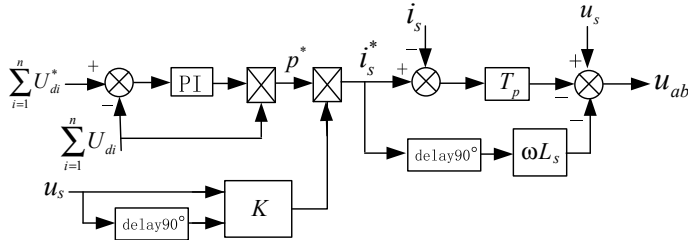


**Fig. 2** Diagram of the transient direct current control without PLL

signal  $i_s^*$  are consistent with the frequency and phase of the real-time detected voltage, thus realizing the real-time tracking of the grid current to the voltage.

According to above approximation, the control block diagram of the improved method without PLL is shown in Fig. 2.

### 3.2 The DC-Link Voltage Balancing Control Without PLL

Due to the loss of each cascade submodule, the delay of the control signal, and the difference of load, the DC-link voltage of each cell is unbalanced, which affects the stable operation. So, it is necessary to equalize the DC-link voltage of each cell.

In this paper, first, the load balance of each cell is assumed and the same modulation ratio  $d$  is adopted; then, the corresponding modulation ratio increment  $\Delta d_i$  is obtained according to the difference of output voltage of each cell; finally, the modulation ratio  $d_i$  of each cell is reconfigured through increment, so as to realize the equalization control of the capacitor voltage of each cell.

The block diagram of the DC-link voltage balancing control without PLL is shown in Fig. 3. In the structure, the DC-link voltage  $U_{di}$  is measured and then compared to the reference voltage value  $U_{di}^*$ , the error is regulated by a PI controller, the output of the PI controller is multiplied by the reference voltage value  $U_{di}$ , and then, the result is multiplied by  $K$ . In order to obtain the modulation ratio increment  $\Delta d_i$ , the result of the product is divided by  $U_{di}^*$ ; thus, the modulation ratio  $d_i$  of each cell is obtained by adding  $\Delta d_i$  to  $d$ .

## 4 Simulation

In order to verify the correctness and effectiveness of the proposed method, a single-phase two-element cascade H-bridge rectifier is taken as an example for simulation research under the nonideal grid voltage and load imbalance. The simulation parameters are as given in Table 1.

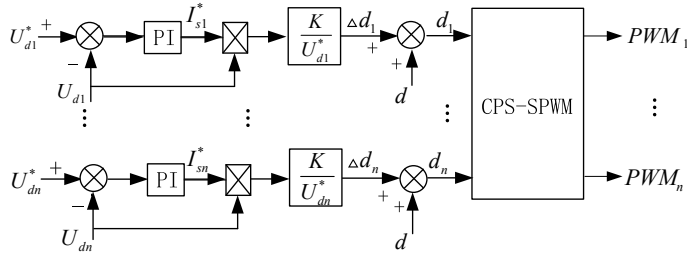


**Fig. 3** Diagram of the DC-link voltage balancing control without PLL

**Table 1** Simulation parameters

Parameters	value
Effective value of grid voltage $U/V$	100
Equivalent AC inductance $L_s/mH$	2
Inductance of resonance filter $L_2/mH$	0.84
Capacitance of resonance filter $C_2/mF$	3
DC-link capacitance $C_d/mF$	3
The DC voltage reference $U_d^*/V$	100
Switching frequency $f_c/Hz$	2.5 k
load resistance $R_1/\Omega$	3
load resistance $R_2/\Omega$	5

#### 4.1 The Grid Voltage Amplitude Fluctuation

Assume that the grid voltage decreases to 90 V at 0.3 s, recovers at 0.6 s, and suddenly rises to 110 V at 0.9 s. The simulation results are as (Fig. 4).

Figure 4a is the simulation result of the grid voltage and current. It can be seen that the grid current is in phase with the grid voltage, which indicates a unit power factor. Figure 4b is simulation result of the two DC-link voltages; although the loads are unbalanced, the two voltage waveforms overlap after a short period of fluctuation and stable at 100 V, which shows the two DC-link voltages with the

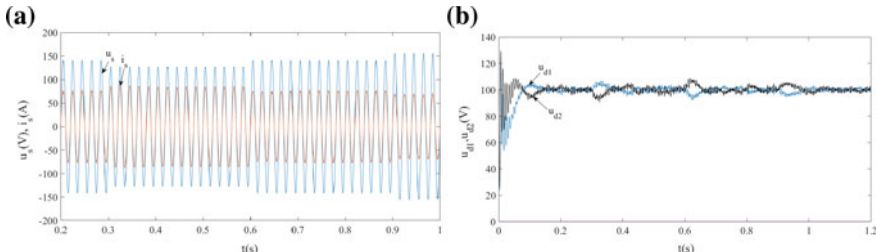


**Fig. 4** Simulation waveforms with the voltage amplitude fluctuation

voltage balancing control. It demonstrates that the proposed method can deal with the voltage amplitude fluctuation.

## 4.2 The Grid Voltage Frequency Offset

It is assumed that the frequency of the grid voltage is offset to 49.5 Hz at 0.4 s, returns to normal at 0.6 s, and then fluctuates to 50.5 Hz at 0.8 s.

Figure 5a and b show the waveforms of the grid voltage, the grid current, and the DC-link voltages, respectively. As shown in Fig. 5, the current waveform is the same frequency and phase as the voltage waveform after less than one cycle, and the two voltage waveforms overlap quickly. Thus, the rectifier operates at unit power factor, and the DC-link voltages reach equilibrium and stability. It is shown that the method has good dynamic control performance for the grid voltage frequency offset.

## 4.3 The Grid Voltage Phase Mutation

Assume that the grid voltage phase is changed from  $0^\circ$  to  $60^\circ$  at 0.4 s. The simulation results are as (Fig. 6).

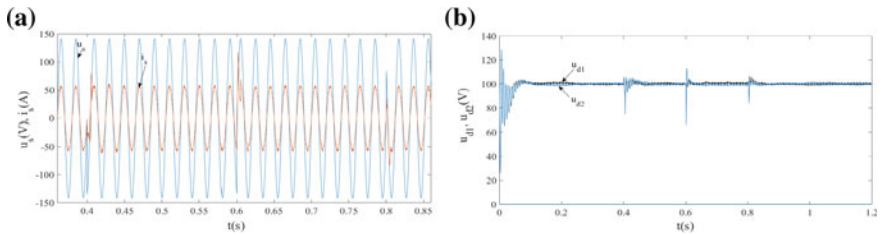


**Fig. 5** Simulation waveforms with the voltage frequency offset

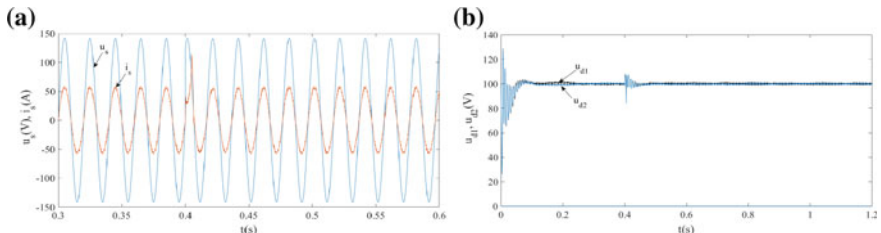


**Fig. 6** Simulation waveforms with the voltage phase mutation

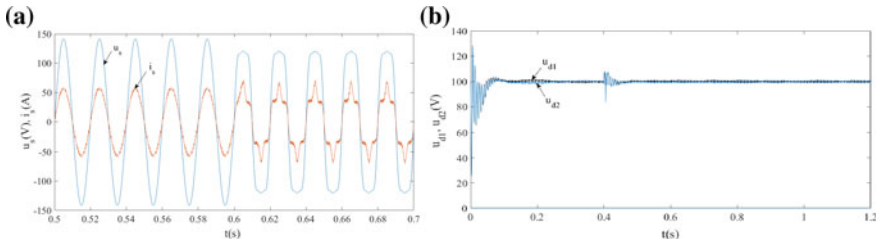


**Fig. 7** Simulation waveforms with the voltage distortion

Figure 6a is the grid voltage and current waveforms, and Fig. 6b is the DC-link voltage waveforms. As can be seen from Fig. 6, when the voltage phase changes, the current waveform can still be in the same frequency and phase with the voltage waveform after less a short fluctuation, and the two voltage waveforms overlap quickly. So, the rectifier can operate at unit power factor, and the DC-link voltages can reach equilibrium and stability. It indicates that the method is effective for the voltage phase mutation.

#### 4.4 The Grid Voltage Distortion

Suppose that the grid voltage is distorted at 0.6 s, superimposing 20% of the 3rd harmonic and 5% of the 5th harmonic. The simulation results are as (Fig. 7).

It can be seen from the waveform voltage and current in Fig. 7a, when the voltage waveform is distorted, although the current waveform is also distorted at the same time, it can still maintain the same phase and frequency with the grid voltage waveform. The DC-link voltage waveforms in Fig. 7b also overlap and stabilize quickly. It proves that the proposed method can cope well with the grid voltage distortion.

## 5 Conclusion

In this paper, based on the analysis of the control principle of the single-phase cascaded H-bridge rectifiers, according to the instantaneous power theory of three-phase system, the power and current relationship of the single-phase cascade H-bridge rectifier is obtained by using the virtual coordinate axis, so that the current command signal in phase with the grid voltage can be obtained without PLL. Based on this, an improved control method without PLL is improved and simulated. The simulation results show that the proposed method has better control effect under the nonideal grid voltage and load imbalance.

## References

1. Drábek P, Peroutka Z, Pittermann M et al (2011) New configuration of traction converter with medium-frequency transformer using matrix converters. *IEEE Trans Ind Electron* 58(11):5041–5048
2. Zhao C, Dujic D, Mester A et al (2014) Power electronic traction transformer medium voltage prototype. *IEEE Trans Ind Electron* 61(7):3257–3268
3. Cecati C, Dell'Aquila A, Liserre M et al (2003) Design of H-bridge multilevel active rectifier for traction systems. *IEEE Trans Ind Appl* 39(5):1541–1550
4. Tiefu Z, Gangyao W, Bhattacharya S et al (2013) Voltage and power balance control for a cascaded H-bridge converter-based solid-state transformer. *IEEE Trans Power Electron* 28(4):1523–1532
5. Xinghua T, Yongdong L, Min S (2011) Voltage balancing control algorithm for cascaded H-bridge rectifier based on active power feedback. *J Tsinghua Univ Sci Technol* 51(7):903–908 (in Chinese)
6. Xinghua T, Yongdong L, Min S (2011) A novel DC-link voltages balancing control method for cascaded H-bridge rectifier. *Trans China Electrotech Soc* 26(8):85–89 (in Chinese)
7. Xinghua T, Yongdong L, Yichao S, Lei SH (2012) Improved DC-link voltage balancing method for cascaded H-bridge rectifier. *High Volt Eng* 38(2):505–512 (in Chinese)
8. Shunliang W, Wensheng S, Xiaoyun F (2016) A SVPWM method with capacitor voltages balancing control for single phase cascaded H-bridge rectifiers. *J China Railway Soc* 38(7):26–33 (in Chinese)
9. Xiang L, Xizheng G, Xiaojie Y et al (2017) An Advanced DC voltage balance strategy for cascaded H-bridge rectifier. *Trans China Electrotech Soc* 32(4):66–75 (in Chinese)

# A Design of Ground Auto-Passing Neutral Section Logical Control System



Lintong Li and Baodi Xiao

**Abstract** The development history of passing neutral section technology was introduced, and the advantages of ground auto-passing neutral section technology were analyzed. By analyzing the working principles and system compositions of the ground auto-passing neutral section system, problems such as no backup system and poor reliability were found. A design scheme of ground auto-passing neutral section logical control system was proposed which based on double 2-vote-2 redundant structure and used microprocessor as the arithmetic unit and depended on the mature technology of the secure computer platform. This article analyzed the hardware components of the system, the working logic in the software design, and system reliability. After field testing, the system has verified the output information, added the backup system, reduced the failure rate of the ground auto-passing neutral section system, enhanced the reliability of the locomotive auto-passing neutral section, improved the locomotive operating efficiency, and achieved the requirements of the design.

**Keywords** Auto-passing neutral section · Logical control · Double 2-vote-2 · Reliability

## 1 Introduction

The power supply contact network of China's railway adopts the single-phase AC traction power supply mode. In order to balance the load of the three-phase AC system used in the power system, it is necessary to supply power to the electric locomotive by using different phases to supply power to the locomotive on the line. It is necessary to set a section of nonelectric neutral section between adjacent

---

L. Li (✉) · B. Xiao

School of Automation and Electrical Engineering Academy, Lanzhou Jiaotong University, Lanzhou, China

different phases to prevent the short circuit of the contact net. The process of passing the locomotive through the neutral zone is called passing neutral section. The traditional passing neutral section method is the operation of the locomotive driver. According to the indication of the ground power-off mark, the main circuit breaker of the locomotive is operated in a split-and-close manner, so that the train passes through the power-off and coasting mode to pass the electric phase separation. This method has high requirements for the operation of the driver and safety hazards; once the operation is wrong, it will cause the locomotive to cross the phase, which will cause a major accident of burning the traction power supply network. With the development of auto-passing neutral section technology, the operating efficiency of the locomotive has been effectively improved, and the hidden troubles have been reduced [1–3].

Up to now, the most widely used auto-passing neutral section schemes mainly include in-vehicle equipment control schemes, on-column switch control schemes, and ground switch control schemes [4]. It is known from the literature that compared with the former two schemes, the ground control method has the following advantages:

- (1) The locomotive does not have to disconnect the main circuit breaker of the locomotive during the over phase separation process, avoiding the switching of the onboard equipment and reducing the maintenance cost.
- (2) The locomotive has a short power loss time, which reduces the locomotive loss due to the locomotive over phase separation process. The speed loss caused by taxiing can solve the danger of heavy-duty locomotive climbing or sliding.
- (3) The control equipment is installed on the ground phase separation, easy to maintain. Based on in-depth study of ground auto-passing neutral section technology scheme, a design scheme of ground auto-passing neutral section logic control system is proposed. The hardware design and software logic of the module are discussed, and the module reliability is analyzed.

## 2 Ground Auto-Passing Neutral Section System

### 2.1 System Composition

The composition of the ground automatic over phase system is shown in Fig. 1. The system is mainly composed of the following four subsystems: remote monitoring subsystem, logic control subsystem, operation execution subsystem, and locomotive position detection subsystem.

As the core of the whole control system, the logic control subsystem controls the opening and closing action of the vacuum load switch in the operation execution subsystem, which directly determines the safe operation of the entire ground auto-passing neutral section system. The logic control system performs information

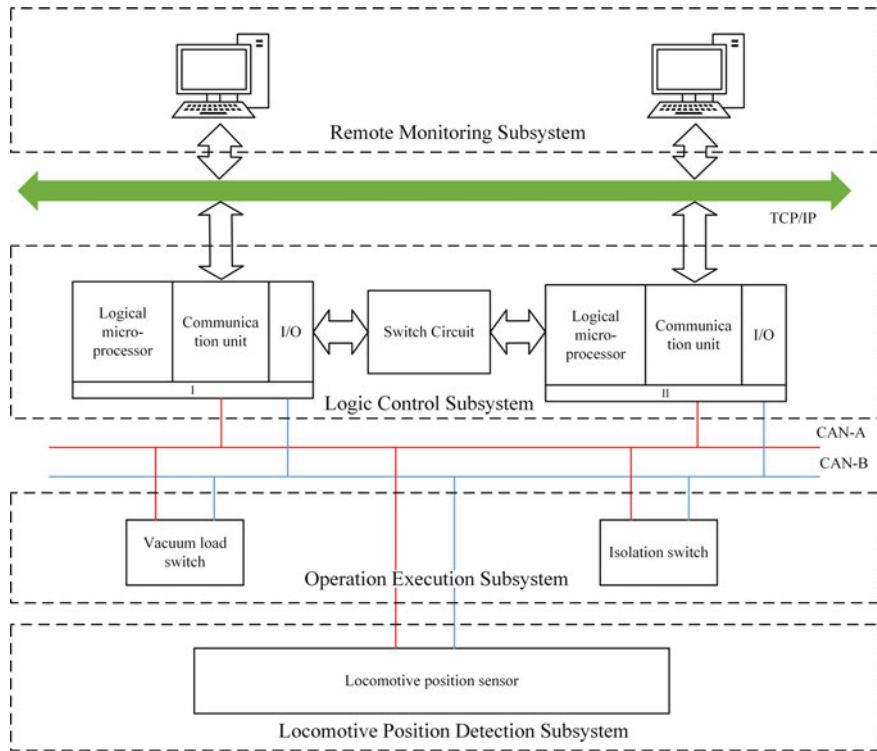


**Fig. 1** System composition block diagram

processing and logic judgment and continuously judges the working state of the acquisition unit and the execution unit and issues data commands to the execution unit. Therefore, it is necessary to design a logic control system that satisfies the reliability requirement. At present, the logic control unit of the ground control auto-passing neutral section system uses the industrial control PLC as the control core and directly accesses the system operation in a single series mode. There are many shortcomings in this method. For example, there is no backup system, manual operation of the faulty system is required, the output information cannot be recalibrated, and the equipment fault is easy to cause short-circuit tripping of the phase separation. For the above problems, the mature technology of the secure computer platform is used for reference. This paper chooses the microprocessor as the logic operation host instead of PLC [5] and puts forward the idea of using hardware-level double 2-vote-2 redundancy design and designs a new ground auto-passing neutral section logic control system.

## 2.2 System Working Principle

The ground auto-passing neutral section system is based on the feedback information of the ground locomotive position-sensing device and then controls the vacuum load switch to realize the automatic over phase separation of the locomotive. The whole process does not require the movement of the train equipment, all of which are the phase separation device on the ground performs information processing and the opening and closing operation of the vacuum load switch of the phase separation. By studying the auto-passing neutral section process, a scheme of series-parallel vacuum load switch is proposed. The design of redundant is adopted to ensure that the vacuum load switch does not affect the normal operation of the system in the event of failure. The main wiring of the ground control auto-passing neutral section system is shown in Fig. 2.

The system keeps the standby state: The isolating switches QS1, QS2, and QS3 are closed, the vacuum load switches QF1 and QF2 are closed, and the vacuum load switches QF1X, QF3, QF2X, and QF4 are disconnected. QF1X and QF2X are the main circuit breakers. The QF1X and QF2X are opened and closed to realize the auto-passing neutral section of the locomotive in the case of no fault. If the main switch QF1X has a refusal to close, QF3 is used instead of the closing operation. If the main switch QF1X refuses to open, then use QF1 instead of the opening operation; switch QF2X has the same similar fault resolution with QF1X. This design solves the problem that the vacuum load switch is faulty and there is no standby switch, which causes the locomotive to stop in the neutral section or short circuit.

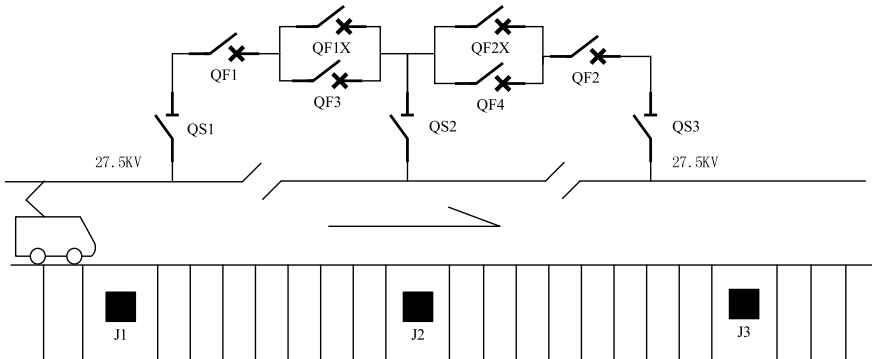


**Fig. 2** System main wiring diagram

### 3 Hardware Design

The logic control subsystem collects train position signals through the I/O unit and inputs the data to the computing host. The data is synchronized and logically operated according to the set program, the accuracy of the operation is compared by the comparator, and then, the control unit is sent to execute the subsystem operation through the I/O unit. The module is designed with redundant and independent “2-vote-2” structure, which realizes the “fail-safe” of the module. The reliability of the module is also improved based on enhancing the security of the module [6–8]. The logic control system can mainly realize the following functions: perform logical operation on the collected information, control the vacuum load switch through the I/O to perform the opening and closing operations, and judge the state after the operation is completed.

- (1) Judging the status of the sensor and the circuit breaker through the information collected in real time and uploading the backup.
- (2) Capable of self-testing the module, judging the status of the module, and outputting a test report.
- (3) The fault processing logic is automatically converted if there is an incorrect operation.
- (4) After the ground control auto-passing neutral section system is invalid, the switch of the traction substation can be quickly disconnected to ensure the safe passage of the train.

#### 3.1 Module Structure

The logic control system adopts the design of double 2-vote-2 redundant structure, which consists of two parts: I and II. Safety is ensured by using 2-vote-2 units in each series. The output results in the same system are compared by means of logical “and”. If the comparison result is the same, then output the data, or not output. If the output is different and the diagnosis is faulty, the alarm will be out of operation and the two series will be switched. I and II are hot standby. Under normal working conditions, I work for the main system, and II is the standby system. In the fault state, the system automatically switches to II. At this time, II is the main system. After the fault is removed, I reenters the system and becomes the standby system. The state information is synchronized by real-time communication between the two parts, so that after the main part works abnormally, the spare part can perform undisturbed and fast switching, realize state synchronization, and improve the availability and reliability of the control system. The logic control system is shown in Fig. 3. It is mainly composed of logic microprocessor, comparison circuit, binary switch, communication unit, and I/O module.

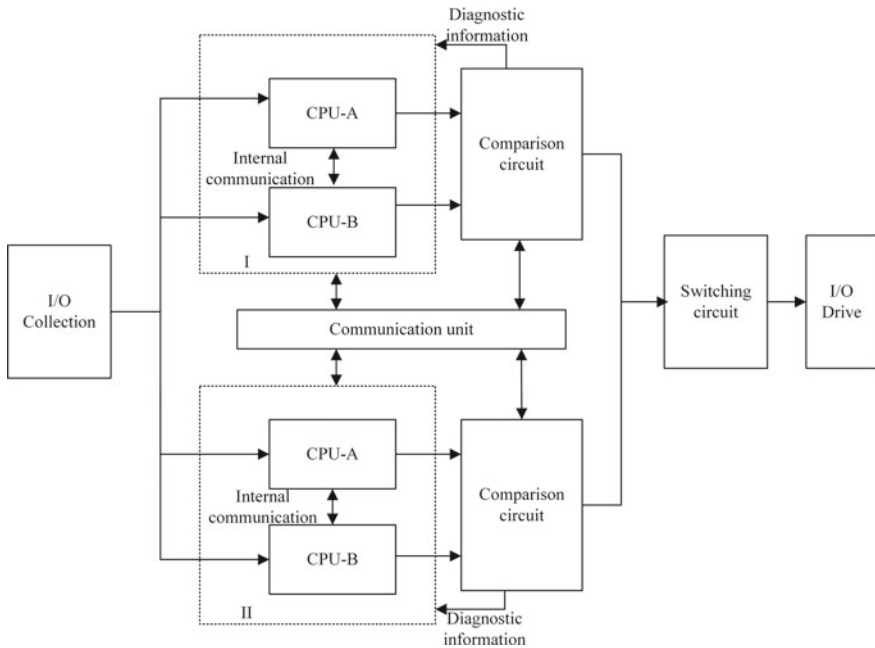


**Fig. 3** Logic control module

### 3.2 Logical Microprocessor

The microprocessor selects the AT91SAM9X25 chip based on ARM architecture as the central processing unit (CPU) to realize the logic processing function of the control system. In order to realize the hardware-level double 2-vote-2 design, each control unit contains two main operations. The CPU unit performs simultaneous calculation on the input information, performs real-time synchronization through internal communication transmission, and performs 2-vote-2 on the input data and commands, and if the output data is inconsistent, it leads to the secure side [9].

### 3.3 Comparison Circuit

The comparison circuit adopts the 2-vote-2 design, synchronously receives the operation results of the two CPUs, and compares the results. If the operation results are consistent, the drive command is output through the comparison circuit. If not, the data is not output, the operation is determined to be an error, and the operation is recalculated.

### **3.4 Two-Pass Switch**

The two parts of the host adopt the dual-system hot standby structure. The mutual switching is based on the fault diagnosis of the two parts of the CPU and the calculation result of the data. The conditions for switching between I and II are automatically performed according to the program: The standby system constantly obtains the data from the main system and compares with itself. If the output commands are consistent, continue to operate in the current mode and perform state synchronization. If the output command is inconsistent and the diagnosis is the main system failure, it is converted to the standby system output. The main system exits the operation, and the alarm waits for maintenance. At this time, the standby system becomes the main system to work. If the output commands are inconsistent and it is determined that the standby system has a fault, the main system maintains the current running state, and the standby system alarm waits for maintenance.

### **3.5 Communication Unit**

The communication unit is designed based on the ARM architecture. It mainly realizes the communication between the logic microprocessors, the communication with other IO modules, the information exchange between the comparators, and the communication scheduling function between other communication devices. Each communication unit contains a rich communication interface, which realizes the acquisition of input information and the release of output instructions. The communication unit alleviates the time spent on communication control and enhances the communication control capability of the logic control system.

### **3.6 I/O Module**

The I/O module is divided into two parts: acquisition and drive. It mainly adopts two-two redundancy technology to realize fail-safe. The module consists of two CPUs, which, respectively, receive the information of different code bits uploaded from the bus CAN for comparison and jointly control the safety power supply and safety logic “and” output circuit to achieve safe driving. The two CPUs are independent of each other and form corresponding response information, thus achieving safe information collection. The module also uses active fail-safe technology to detect and diagnose faults in the hardware of the module, detects hardware faults in a timely manner, and performs fault-safe processing. At the same time, the I/O module also adopts address data security processing design, communication security design, independence clock design, and other security design techniques to ensure the collection and drive security of I/O modules.

## 4 Software Design

The main function of the system software design is to complete the data logic calculation and information verification of the CPU and finally drive the I/O interface output command, complete the control of the over phase device, realize the automatic over phase of the locomotive, and the whole process does not require manual intervention. In addition to the hardware design in strict accordance with the principle of “2-vote-2”, the software design of the logic control system also needs to be designed in strict accordance with the requirements of safety and reliability and meets the corresponding technical standards.

As the core of the logic control system software design, the logic program design determines the current device status and output control commands by processing and calculating the information input by the position sensor and other devices. The design of the logic program mainly includes the following four aspects: the main logic program, power outage maintenance program, fault logic program, and self-test program.

### 4.1 Main Logic Program

When the locomotive passes through the phase separation section normally, the main logic program is adopted. The program flow is as shown in Fig. 4. When the locomotive is far away from the phase separation section, the system is always in the standby state, and the system remains in standby state: isolation switches QS1, QS2, and QS3 are closed, vacuum load switches QF1X and QF2X are disconnected. When the locomotive travels to a certain distance J1 from the neutral section, the ground position detecting device detects that the locomotive is about to cross the phase and controls the vacuum load switch QF1X to close, the neutral section connected to the left power supply arm, the locomotive is charged into the neutral section. When the locomotive travels to J2, the vacuum load switch QF1X is disconnected, the vacuum load switch QF2X is closed, the neutral section is connected to the right power supply arm, and the locomotive is electrified to drive out of the neutral section. When the locomotive drives out J3, the vacuum load switch QF2X is disconnected. At this time, the neutral section is not connected to the left and right power supply arms and is in a state of no power. When the initial state is restored, the locomotive realizes a complete auto-passing neutral section.

### 4.2 Power Outage Maintenance Program

When the equipment in the over phase system fails, in order to ensure the safety of the maintenance personnel, it is necessary to enter the power-off maintenance mode

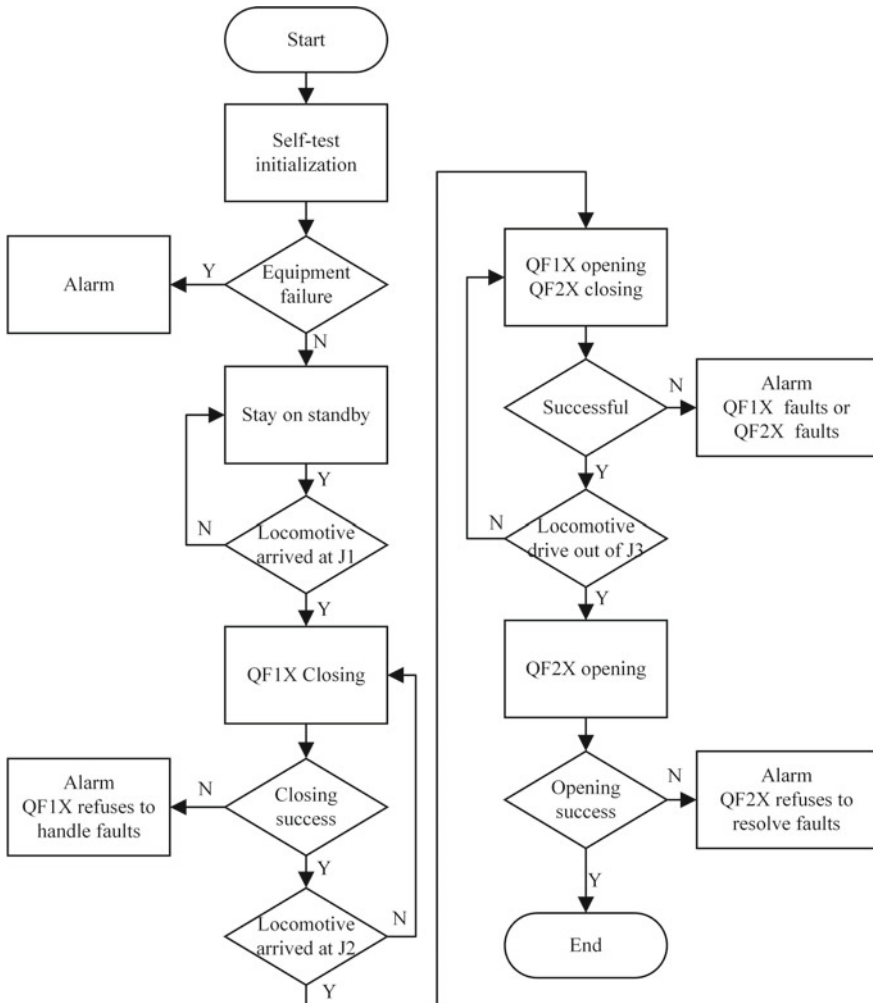


**Fig. 4** Main logic program flow chart

to repair the system equipment. The program flow is shown in Fig. 5. When it is determined that no car enters the phase separation section, manually turn on the power failure maintenance mode for equipment maintenance. In the state of power failure maintenance, in order to ensure the safety of the software lockout conditions, the operation of the isolating switch can only be carried out without load.

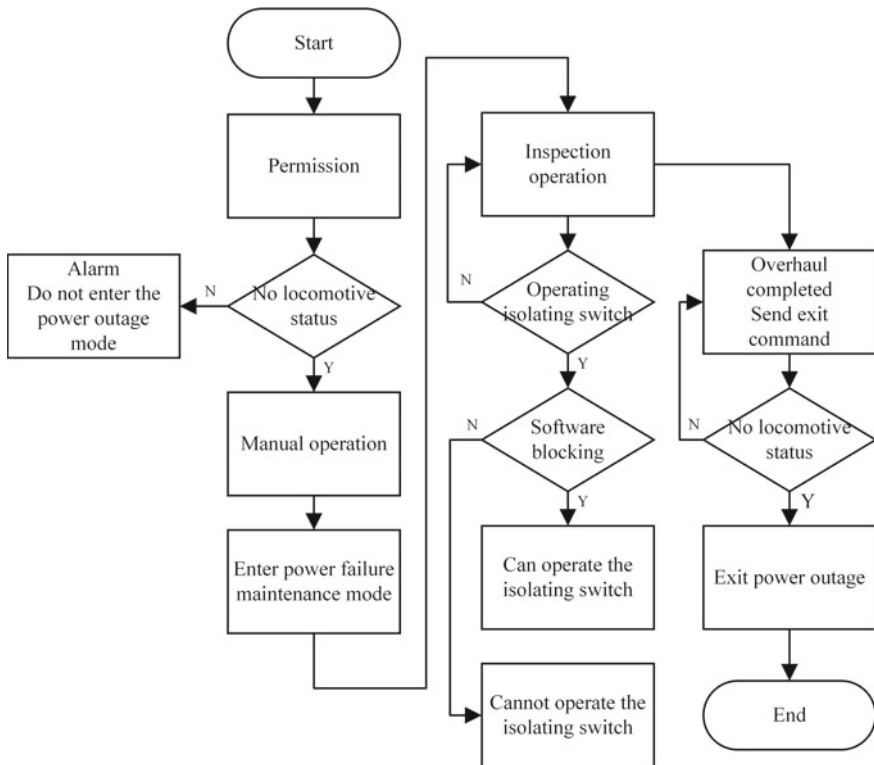


**Fig. 5** Power failure maintenance flow chart

### 4.3 Fault Logic Program

If the vacuum load switch refuses to open or refuse during the system operation, the logic processing flow automatically switches to the process of the fault-handling program, and the automatic transfer switch operates to ensure that the locomotive safely passes through the phase separation zone. Taking the switch QF1X reject fault as an example, the fault logic processing flow is shown in Fig. 6. After the fault is processed, it is automatically merged into the main logic program.

### 4.4 Self-Test Program

When the auto-passing neutral section system is operated for a long period, in order to ensure the function of the control system equipment is normal, the working condition of the equipment will be checked from time to time. Because the manual inspection is time-consuming and labor-intensive, a self-test program is designed.

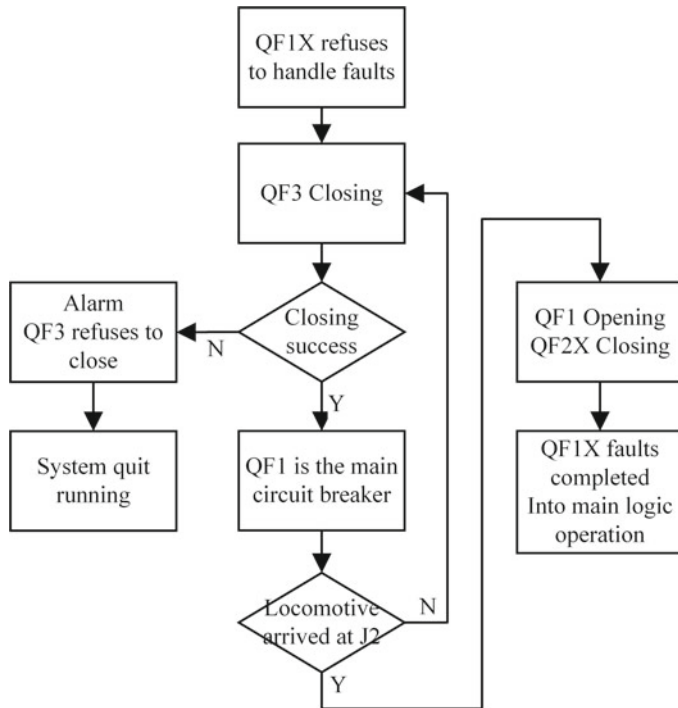


**Fig. 6** Fault logic flow chart

The program flow is shown in Fig. 7. The self-test operation can only be performed when the system is in the state of power failure maintenance, which improves the maintenance efficiency of maintenance personnel.

## 5 Reliability Analysis

The auto-passing neutral section logic control system is an important device to realize the safety of the locomotive through the phase-separated section. Its reliability directly affects the operation safety and efficiency of the locomotive. The reliability of the module refers to the ability to complete the specified function in the non-faulty state [10]. According to GJB/Z299C-2006 “Electronic Equipment Reliability Prediction Manual” for the relevant specifications of various electronic components reliability index parameters and fault failure rate model calculation method, the AT91SAM9X25 chip selected in this paper belongs to imported components. Therefore, the formula for calculating the work failure rate is as shown in Eq. (1):

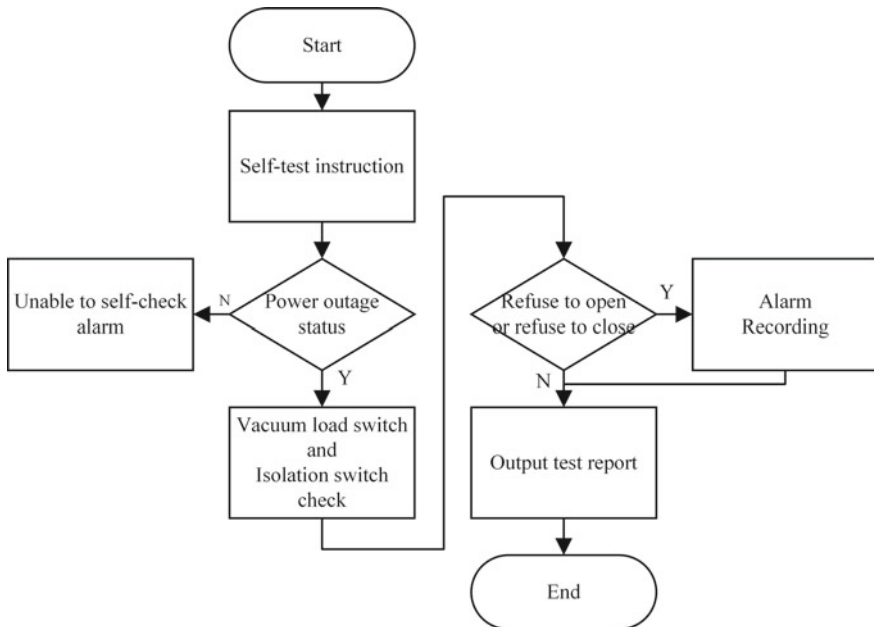


**Fig. 7** Self-test flow chart

$$\lambda_a = (C_1\pi_T + C_2\pi_E)\pi_Q \quad (1)$$

The reliability of the module is:

$$R_a(t) = e^{-\lambda_a t} \quad (2)$$

The average time between failures MTBF<sub>I</sub> (the average running time of the fault) is:

$$\text{MTBF}_I = \int_0^{\infty} \left(1 - (1 - R_a(t))^2\right) dt \quad (3)$$

The relevant parameters are selected as follows:

$\lambda_a$ —the work failure rate of the chip, the unit is:  $10^{-6}/\text{h}$ ;

$C_1$ —the chip internal circuit complexity failure rate, take 0.0088;

$\pi_T$ —the temperature stress coefficient, choose 37, take 0.190;

$C_2$ —the failure rate of the package, take 0.0076;

$\pi_E$ —the environmental coefficient, select GF<sub>1</sub>, take 1.8;

$\pi_Q$ —the quality factor, select the civilian chip of the B-3 military standard test, take 4;

Therefore, the module failure rate is:

$$\lambda = \frac{1}{\text{MTBF}_i} = 0.40939 \times 10^{-6}/\text{h}, \text{ meet the design requirements.}$$

## 6 Conclusion

The design of ground auto-passing neutral section logic control system uses the structure of 2-vote-2 to correct the data of the logical operation input and output to ensure the accuracy of the control instructions. The dual-system hot standby structure realizes the hot standby switching when the module is faulty, which ensures the reliability of the system and meets the expected design requirements.

In the process of trial operation, the process of auto-passing neutral section of the locomotive is very stable, and the power loss time of the electric locomotive is reduced to 150–200 ms, which reduces the power supply zero zone, greatly improves the transportation efficiency, and enhances the reliability of the system. It has been applied to the phase separation system and has the value of promotion and application.

## References

1. Qinyue H (2018) Research of ground automatic convert technology. Southwest Jiaotong University (in Chinese)
2. Yi C, Hong L, Ma L (2014) Research on electric locomotive auto-passing neutral section. In: Fourth international conference on intelligent systems design & engineering applications
3. Wang R, Zheng TQ, Xiong L, et al (2011) Research on power electronic switch system used in the auto-passing neutral section with electric load. In: International conference on electrical machines & systems
4. Hongquan T (2015) Advantage of auto-passing neutral section with ATP. Railway Signal Commun
5. Penuche Z (2009) Development of locomotive auto-passing neutral section device based on onboard monitoring device. China Railway Sci 30(2):141–144
6. Kim H, Lee H, Lee K (2005) The design and analysis of AVTMR (all voting triple modular redundancy) and dual-duplex system. Reliability Eng Syst Saf 88(3):291–300
7. Pengcheng Z (2017) Study on a new type ground switch passing neutral section. Railway Locomotive Car 37(03):72–75 + 103 (2017) (in Chinese)
8. Mei C, Yueqian W, Yongxian Z, Kai G (2018) Research on synchronization mechanism in double 2-out-of-2. Microcontrollers Embedded Syst 18(03):10–12 + 18
9. Guangwu C, Duowang F, Zongshou W et al (2010) All Electronic Computer Interlocking System Based on Double 2-Vote-2. China Railway Sci 31(4):138–144
10. Li L, Youpeng Z (2017) Reliability analysis of time synchronization system of railway ground signal equipment. Journal of Lanzhou Jiaotong University 36(04):138–144

# Parallel Control of Auxiliary Inverter Based on Virtual Synchronous Generator



Lei Lu, Xuefei Li, Yang Kuang, Jie Chen and Ruichang Qiu

**Abstract** As an important part of electric multiple units (EMU), the auxiliary power supply system plays an important role in the normal operation of the vehicle. In order to improve the reliability of the auxiliary power supply system, the virtual synchronous generator (VSG) technology is applied to the parallel control system of auxiliary inverter. The essence of VSG technology is to control the inverter to simulate the working principle of synchronous generator, so as to obtain similar operation characteristics of synchronous generator. The auxiliary inverter controlled by VSG technology can avoid the disadvantage of hard external characteristics of power electronic devices. Its rotating inertia can obviously prevent frequency fluctuation, and the system has high stability and reliability. In this paper, the frequency and voltage of the auxiliary inverters are controlled independently with VSG technology, so that the output voltage can be controlled stably and the power quality can be improved. Finally, the MATLAB simulation results show that the parallel control of auxiliary inverter based on VSG achieves the expected goals.

**Keywords** Auxiliary inverter · Virtual synchronous generator · Parallel control

---

L. Lu (✉) · J. Chen · R. Qiu

School of Electrical Engineering, Beijing Engineering Research Center of Electric Rail Transportation, Beijing Jiaotong University, Beijing 100044, China  
e-mail: [17121476@bjtu.edu.cn](mailto:17121476@bjtu.edu.cn)

J. Chen

e-mail: [jiechen@bjtu.edu.cn](mailto:jiechen@bjtu.edu.cn)

R. Qiu

e-mail: [rchqiu@bjtu.edu.cn](mailto:rchqiu@bjtu.edu.cn)

X. Li · Y. Kuang

CRRC Changchun Railway Vehicles Co., Ltd., Changchun 130062, China  
e-mail: [13844090307@163.com](mailto:13844090307@163.com)

Y. Kuang

e-mail: [kuangyang@cccar.com.cn](mailto:kuangyang@cccar.com.cn)

## 1 Introduction

With the rapid development of rail transit in China, the EMU has become an important choice for people to travel. EMU has the advantages of high security, high speed, energy saving, large transportation volume and so on [1]. As an important part of EMU, the duty of auxiliary inverters is to provide a stable AC supply for the medium-voltage loads on the vehicle, including air conditioning units, air compressors, ventilation devices, train wireless, car sockets, etc.

Parallel auxiliary inverters can ensure that the failure of an inverter or regular maintenance will not cause power outage, which improves the reliability and flexibility of power supply [2]. In current control methods of parallel inverters, droop control based on active and reactive power has been used [3]. Compared with VSG control [4], droop control cannot avoid the drawbacks of hard external characteristics in power electronic devices, such as the lack of rotating inertia and excitation transient characteristics of synchronous generator, which results in large fluctuation of frequency and poor system stability and reliability. This is the difference between droop control and VSG strategy proposed in this paper.

This paper studies the parallel control technology of auxiliary inverters based on VSG [4], sets up the simulation model of auxiliary inverters system. The frequency and voltage of auxiliary inverters are controlled independently by using VSG control method, so the output voltage quality of the inverters and the reliability of power supply can be improved.

## 2 Principle of Virtual Synchronous Generator Control

The essence of VSG technology is to control the inverter to simulate the synchronous generator, so as to obtain similar operation characteristics with synchronous generator. Figure 1 is the topology of VSG circuit.

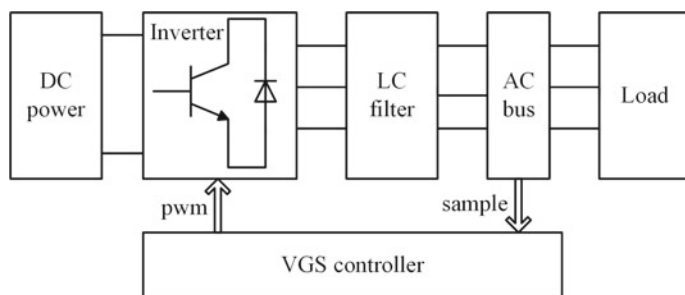


**Fig. 1** Circuit of VSG

According to Fig. 1, VSG topology mainly includes the main circuit and VSG controller. The main circuit is a conventional inverter topology, including DC power supply, inverter, LC filter circuit, load and so on.

VSG controller is the key to VSG technology. Figure 2 is schematic diagram of VSG controller.

VSG controller includes  $P$ - $f$  controller,  $Q$ - $U$  controller, rotor equation and stator equation. Rotor equation and stator equation mainly simulate the electromagnetic relationship and mechanical movement of synchronous generator from the mechanism, while  $P$ - $f$  controller and  $Q$ - $U$  controller mainly simulate the characteristics of active frequency regulation and reactive voltage regulation of synchronous generator from the external characteristics [5–8].

$P$ - $f$  controller is to provide the given mechanical power for the rotor equation, which is shown as Formula (1).

$$P_m = P_{ref} + K_\omega (\omega_{ref} - \omega) \quad (1)$$

where  $P_{ref}$  is reference active power,  $K_\omega$  is frequency adjustment parameter,  $\omega_{ref}$  is reference angular frequency,  $\omega$  is fundamental angular frequency,  $P_m$  is mechanical power.

$Q$ - $U$  controller is to provide the excitation voltage amplitude for the stator equation, which is shown as Formula (2).

$$E = V_{ref} + K_e (Q_{ref} - Q) \quad (2)$$

where  $V_{ref}$  is reference voltage amplitude,  $K_e$  is voltage adjustment parameter,  $Q_{ref}$  is reference reactive power,  $Q$  is output reactive power,  $E$  is excitation voltage amplitude.

Rotor equation is used to describe the motion of synchronous generator rotor. When  $\omega$  is near the synchronous speed  $\omega_0$ , the rotor equation can be described as Formula (3).

$$J \frac{d(\omega - \omega_0)}{dt} = T_m - T_e - D(\omega - \omega_0) = \frac{P_m}{\omega} - \frac{P_e}{\omega} - D(\omega - \omega_0) \quad (3)$$

where  $J$  is rotational inertia parameter,  $T_m$  is mechanical torque,  $T_e$  is output torque,  $D$  is damping parameter,  $P_e$  is output active power,  $\omega_0$  is the synchronous speed.

According to Formula (3), we can get the following Formula (4).

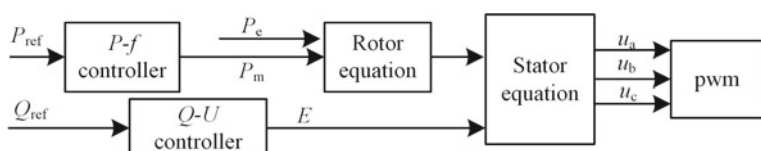


**Fig. 2** Schematic diagram of VSG controller

$$\omega = \int \frac{1}{J} \left[ \left( \frac{P_m - P_e}{\omega} \right) - D(\omega - \omega_0) \right] dt + \omega_0 \quad (4)$$

According to Formula (4), the control block diagram of the rotor equation is obtained as shown in Fig. 3.

Stator equation of VSG is shown as Formula (5).

$$U = E - I(R_a + jX_d) \quad (5)$$

where  $R_a$  is armature resistance,  $X_d$  is synchronous reactance,  $I$  is output current,  $U$  is the output of stator equation.

The main core of VSG controller of parallel auxiliary inverters is to generate system terminal voltage  $U$ , which is used as reference voltage for pulse width modulation.

### 3 Parallel Control of Auxiliary Inverter

In auxiliary inverters, Synchronous Reference Frame Phase-Locked Loop (SRF-PLL) [9] is often used to extract phase, frequency and amplitude information of AC bus voltage. Its control block diagram is shown in Fig. 4.

Referring to the quasi-synchronous parallel mode of the synchronous generator, the VSG parallel control method is proposed, in which the pre-synchronous part is the key technology [10–12], as shown in Fig. 5.

The specific operation steps are as follows. Firstly, cut into SRF-PLL and get the information of bus voltage amplitude, phase and frequency. Secondly, when the

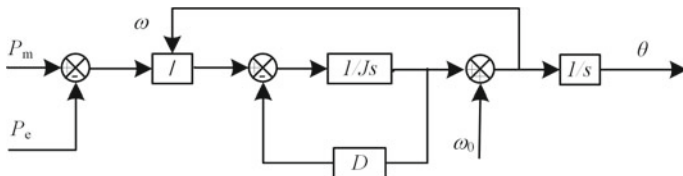


**Fig. 3** Block diagram of the rotor equation

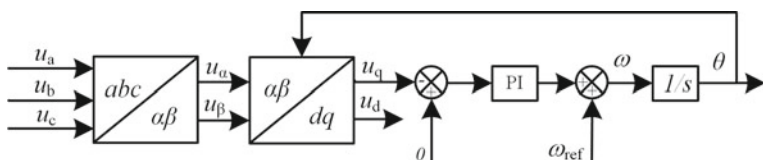


**Fig. 4** Block diagram of SRF-PLL

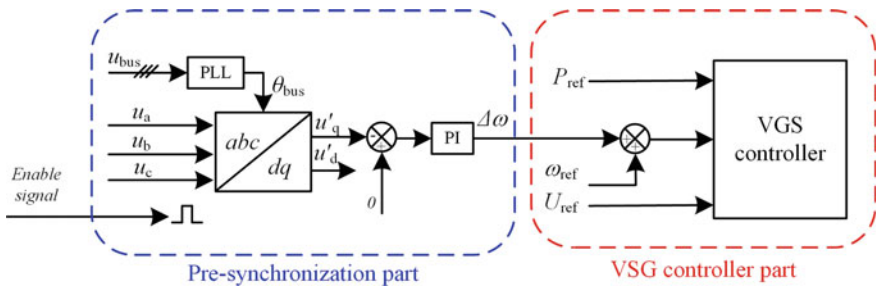


**Fig. 5** Block diagram of VSG parallel control

pre-synchronization enabling signal arrives, the reference angular frequency is switched from  $\omega_{ref}$  to  $\omega_{bus}$ , and the reference voltage is switched from  $V_{ref}$  to  $V_{bus}$ , and the pre-synchronization part is started,  $u'_q$  is adjusted to zero gradually, and the output voltage of VSG is controlled to synchronize with bus voltage. Thirdly, when the pre-synchronization control reaches steady state, the absolute value of the deviation between reference value 0 and  $u'_q$  is less than the allowable error threshold  $u_{erms}$ , which basically realizes the synchronization between the output voltage of VSG and the bus voltage. Finally, the adjustment  $\Delta\omega$  is set to 0 and the parallel switch can be closed to realize the seamless switching from island mode to parallel mode of inverter.

Parallel inverters based on VSG are connected to auxiliary power supply system, which makes parallel inverters simulate the operation characteristics of synchronous generators in terms of external characteristics, overcomes the shortcomings of inertia and damping, prevents the current impact caused by the too fast response of power electronic devices and improves the dynamic characteristics of auxiliary power supply system.

## 4 Simulation Result

This paper using S-Function in MATLAB/Simulink, by setting the interrupt similar to DSP with C language, to construct a virtual DSP control system, better simulate main circuit and the discrete control system of the actual operation of the inverter.

Figure 6 is simulation model of two virtual synchronous generators. The DC side provides 1650 V DC voltage. Through inverters, transformer and LC filter, the output is 380 V AC voltage. The two virtual synchronous generators work in parallel to supply power to the load. The simulation parameters are shown in Table 1.

The two VSG-controlled inverters supply power to 15 kW three-phase load. In the initial state, the phase difference between the two parallel inverters is set to 72°. In order to facilitate the analysis, the phase A voltage waveform is taken as an example to illustrate.

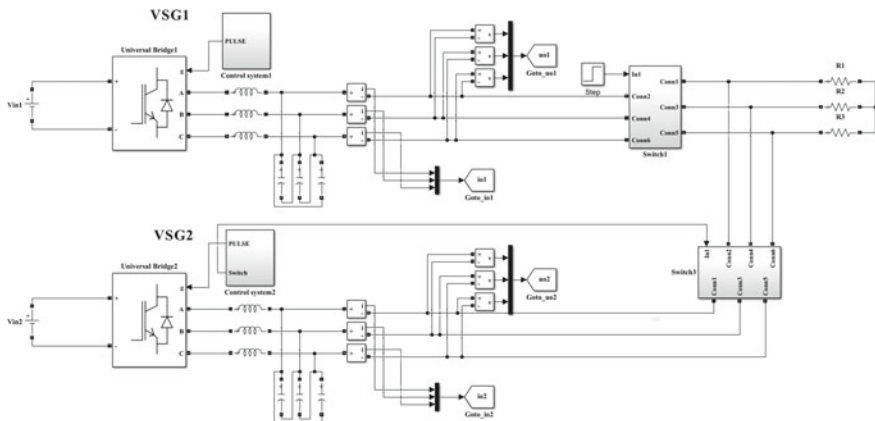
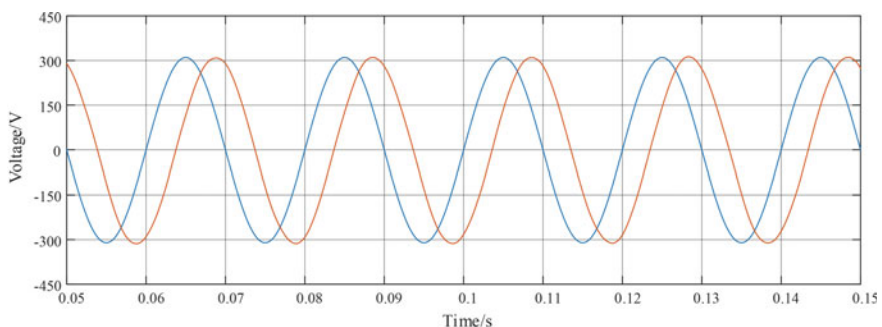


**Fig. 6** Simulation model of two virtual synchronous generators

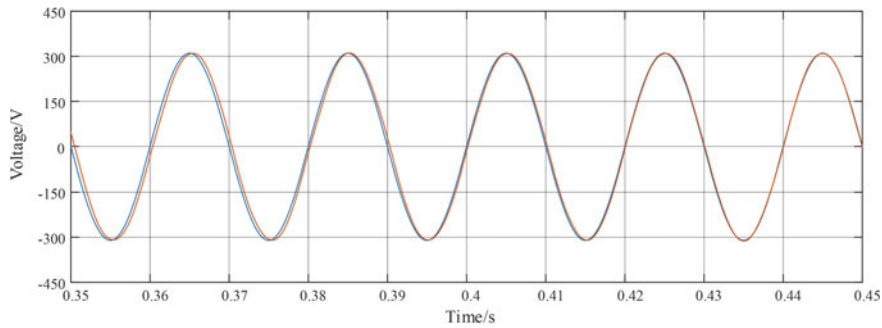
**Table 1** Parameters of simulation

Parameters	The setting value	Parameters	The setting value
$R_d/\Omega$	2	$X_d/\Omega$	2.512
$K_\omega$	3858	$K_e$	0.1
$J$	3	$D$	0.1

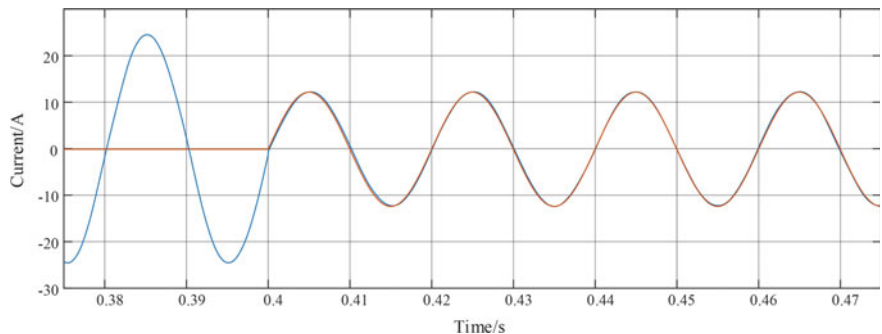
Figures 7 and 8 are the simulation waveforms of phase A voltage of two inverters at the start and end time of pre-synchronous part. It can be seen from the figure that the phase difference at the start-up moment is  $72^\circ$ , and that in the end of pre-synchronization part, the phase difference is near to  $0^\circ$ . After 0.4 s, the phases of the two inverters are basically the same, and the parallel switch is closed to realize the parallel operation.



**Fig. 7** Phase A voltage waveform of two inverters when pre-synchronous started



**Fig. 8** Phase A voltage waveform of two inverters when pre-synchronous finished



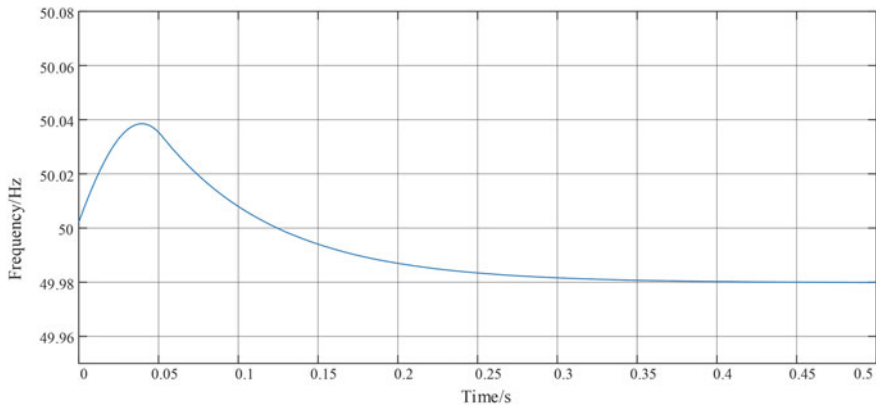
**Fig. 9** Phase A current waveform of two inverters

Figure 9 is the simulation waveform of phase A current of two inverters. From the figure, the phase of the two inverters is synchronized at 0.4 s, and the parallel switch is closed. From the current sharing process of the two inverters in parallel system, it can be seen that the current of the two inverters is basically the same, the load current is equalized, and the current sharing characteristic is good.

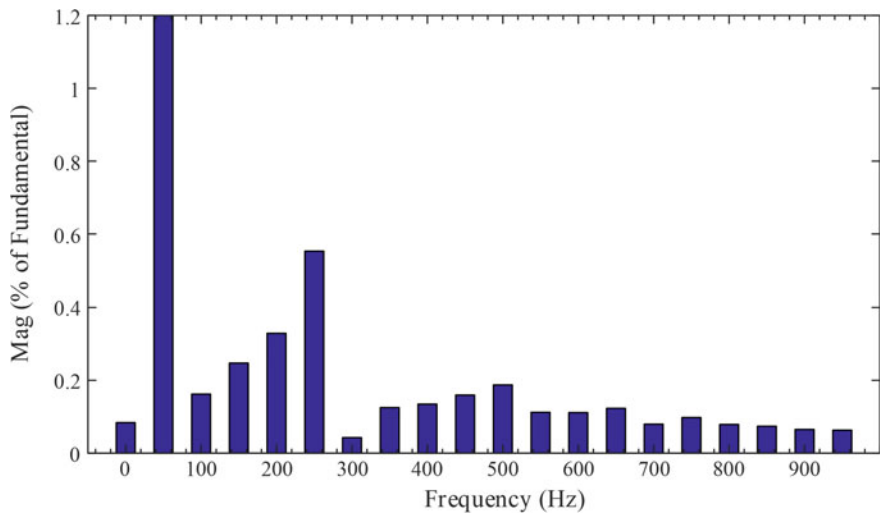
Figure 10 is phase A frequency waveform of inverter. Because of the phase difference between the output voltages of the two inverters, the PI regulator will raise the frequency instantaneously with a peak value of 50.04 Hz and the minimum frequency is of 49.98 Hz.

Figure 11 is FFT analysis in phase A voltage of the inverter. The output voltage amplitude is 301 V and THD is 0.83%. By FFT analysis, it shows that the output voltage waveform is of good quality.

It can be seen that the output voltage waveform of parallel inverters based on VSG control is not obviously distorted, and there is no large impulse voltage and current at the moment of parallel connection. The frequency error meets the requirement within 0.5 Hz.



**Fig. 10** Frequency waveform of inverter



**Fig. 11** FFT analysis in phase A voltage

## 5 Conclusion

In this paper, two parallel auxiliary inverters of EMU are simulated and analyzed. The frequency and voltage of the auxiliary inverters are controlled independently by using VSG control technology. Through above simulation and analysis, it can be seen that the proposed parallel control design of auxiliary inverters based on VSG is stable, which also ensures good output voltage quality of the parallel inverters.

**Acknowledgements** This work is supported by the National Key Research and Development Program (2016YFB1200502-04).

## References

1. Wu D, Guo Z, Sha D et al (2012) Parallel-connected three-phase inverters for railway auxiliary power supply without sensing output currents. In: The twenty-seventh annual IEEE applied power electronics conference and exposition (APEC), pp 136–140
2. Jie C, Huiqing D, Lei W et al (2015) Parallel control strategy for auxiliary systems with complex load characteristics. Proc CSEE 35:213–219 (in Chinese)
3. Jie C, Mingwa L, Xin C et al (2018) Wireless parallel connection and circulation suppression technology of inverters based on droop control. Trans China Electro-Tech Soc 33(07):1450–1460 (in Chinese)
4. Sakimoto K, Miura Y, Ise T (2011) Stabilization of a power system with a distributed generator by a Virtual Synchronous Generator function. In: 2011 IEEE 8th international conference on power electronics and ECCE Asia (ICPE & ECCE). IEEE, pp 1498–1505
5. Liu J, Miura Y, Bevrani H et al (2016) Enhanced virtual synchronous generator control for parallel inverters in Microgrids. IEEE Trans Smart Grid, 1–10
6. He J, Li YW (2011) Analysis, design, and implementation of virtual impedance for power electronics interfaced distributed generation. Ind Appl IEEE Trans On 47(6):2525–2538
7. Chen Y, Smedley K (2005) Parallel operation of one-cycle controlled grid connected three-phase inverters. In: Fourtieth IAS annual meeting. Conference record of the 2005. Industry applications conference, 2005, vol 1. IEEE, pp 591–598
8. Li Z, Li Y, Wang P et al (2008) Three-phase PWM inverters with three-phase output transformer and three-phase filter inductor. In: International conference on electrical machines and systems, 2008. ICEMS 2008. IEEE, pp 1116–1121
9. Guerrero JM, Vasquez JC, Matas J et al (2009) Control strategy for flexible microgrid based on parallel line-interactive UPS system. IEEE Trans Ind Electron 56(3):726–736
10. Zhong QC, Nguyen PL, Ma Z et al (2014) Self-synchronized Synchronverters: inverters Without a Dedicated Synchronization Unit. IEEE Trans Power Electron 29(2):617–630
11. Wang W, Zhu Y (2011) The space vector PWM scheme for a novel three-level inverter with two parallel three-phase full-bridges. In: 2011 International conference on electrical and control engineering (ICECE). IEEE, pp 903–906
12. Garralda D, Marroyo L, Gubia E (2014) A method for modelling the power flow in train auxiliaries fed by two inverters set in parallel. In: 2014 17th IEEE mediterranean electrotechnical conference (MELECON). IEEE, pp 115–121

# Application of Improved PSO Algorithms in Train Energy Consumption Optimization



Binhui Yang, Jing Zhang, Yong Zhang and Zongyi Xing

**Abstract** Aiming at the optimization of energy management for energy storage trams, an improved PSO algorithm based on classical PSO algorithm is proposed in this paper. On the premise of determining the operation strategy and operating conditions, the dynamic analysis of tramcar is carried out, the energy-saving model of tramcar is established, its objective function and constraints are analyzed, the model is solved by improved PSO algorithm, and the simulation results are compared with the actual energy consumption. The results show that the PSO algorithm of competition mechanism can improve the convergence of the algorithm, effectively find the turning point of the energy-saving model, reduce the energy consumption of tramcar operation, and improve the safety, precision parking, and comfort of operation.

**Keywords** Tram · Operating conditions · Energy-saving model · PSO algorithm

## 1 Analysis of Tram Operation Strategy

There are two main types of tram operation strategies: time-saving operation strategy and energy-saving operation strategy [1].

Time-saving operation strategy: The tram has the maximum running capacity during the running process. When this running strategy is adopted, the running time in the interval is the least, but the energy consumption is large.

Energy-saving operation strategy: In the operation process, when a certain speed is reached, the inert working condition is added, and the energy consumption in the interval is minimized under the premise that the tram reaches the safety and on-time indicators.

---

B. Yang · J. Zhang · Y. Zhang · Z. Xing (✉)  
Nanjing University of Science and Technology, Nanjing, China  
e-mail: [xingzongyi@163.com](mailto:xingzongyi@163.com)

## 2 Analysis of Energy-Saving Operation Conditions of Trams

The operating conditions of trams are mainly divided into three types: full traction, cruising, and full braking [2]. The direct impact on the energy-saving effect of the tram is the cruising condition. At this stage, the train runs at a constant speed or in a combination of traction inert conditions [3].

As shown in Fig. 1, the trams are operated in a combination of uniform speed and traction inert conditions during the cruise phase [4].

Assuming that braking energy recovery is not considered, the trams in two modes are  $x_1 \sim x_2$ . The kinetic energy theorem is analyzed in the interval, as shown in Eqs. (1) and (2):

$$\frac{1}{2}m(v_2^2 - v_1^2) = W_t + W_c + W_0 + W_g + W_h \quad (1)$$

$$\frac{1}{2}m(v_2'^2 - v_1'^2) = W_t + W_c + W_0 + W_g + W_h \quad (2)$$

In the formula,  $v_1^2$  and  $v_2^2$  representing the speed of tram at the starting point  $x_1$  and ending point  $x_2$ ,  $w_t$ ,  $w_c$ ,  $w_0$ ,  $w_g$ ,  $w_h$  are represented, respectively, the traction energy consumption, braking energy consumption, basic resistance work, additional resistance work, and potential energy work in the cruise interval.

According to the basic resistance formula of the tram, you can get [5–7]:

$$\int_{x_1}^{x_2} v^2(x) dx \geq s \times v_0^2 \quad (3)$$

It can be known from Eq. (3) that the tram runs at a constant speed in the cruise operating range.

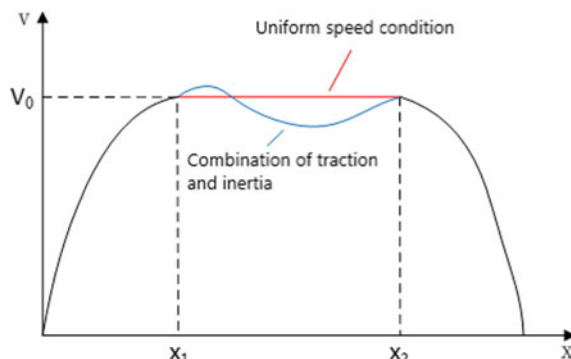


**Fig. 1** Comparison of tram conditions

### 3 Tramway Energy-Saving Optimization Model

Energy storage type tram energy optimization model is shown in (4).

$$\begin{aligned} \min J &= \int_{x_0}^{x_s} u_f(x)f(v)dx \\ \text{s.t. } &\left\{ \begin{array}{l} \frac{dv}{dx} = \frac{u_f(x)f(v) - u_b(x)b(v) - r(v) - w(x)}{Mv(x)} \\ \frac{dt}{dx} = \frac{1}{v(x)} \\ \int_{x_0}^{x_s} \frac{1}{v(x)} dx = T, v(x_0) = 0, v(x_s) = 0 \\ v(x) \leq V(x), u_f(x) \in [0, 1], u_b(x) \in [0, 1] \end{array} \right. \end{aligned} \quad (4)$$

In the formula,  $j$  is the mechanical energy consumption of the traction work, referred to as the traction energy consumption;  $u_f(x)$  is traction usage factor;  $u_b(x)$  is the coefficient of use of braking force;  $f(v)$  is the maximum traction force;  $b(v)$  is the maximum braking force;  $M$  is the total mass of the train;  $v(x)$  is the speed limit corresponding to the train;  $T$  is a given train running time;  $r(v)$  is the basic resistance of train operation;  $w(x)$  is the added ramp resistance of the train [8].

Solving the above model according to the Pontryagin's maximum principle, the train's energy-saving maneuvering strategy is:

- $u_f(x) = 1, u_b(x) = 0$ , the train is fully pulled;
- $u_f(x) \in (0, 1), u_b(x) = 0$  or  $u_f(x) = 0, u_b(x) \in (0, 1)$ , the train maintains a constant speed;
- $u_f(x) = 0, u_b(x) = 0$ , the train is idle;
- $u_f(x) = 0, u_b(x) = 1$ , the train is fully braked.

#### 3.1 Model Constraints

On-time indicator related objective function  $g_1(x)$  :

$$g_1(x) = T - T_0 \leq \Delta t \quad (5)$$

Equation (5) indicates that the error between the actual running time of the tram and the time specified in the timetable is less than  $\Delta t$ .

Precise parking indicator related constraints  $g_2(x)$ :

$$g_2(x) = |S - S_p| \leq \Delta s \quad (6)$$

Equation (6) indicates that the error between the actual parking position of the tram and the specified position is less than  $\Delta s$ .

Safety indicator related constraints  $g_3(x)$ :

$$g_3(x) = 0 \quad (7)$$

Equation (7) indicates that the actual running speed of the tram is not exceeded. Comfort index related constraints  $g_4(x)$ :

$$g_4(x) = 0 \quad (8)$$

Equation (8) indicates that the auxiliary equipment of the tram is working properly [9].

## 4 PSO Algorithm Based on Competition Mechanism

In the competitive PSO optimization algorithm, the paired competitive particle update strategy replaces the optimal solution update particle strategy in the classical PSO algorithm, so that the optimization problem can be processed efficiently [10].

The position and velocity update formula of the competitive particles after the  $k$ th competition is as follows:

$$v_{1,k}^{t+1} = \omega \times v_{1,k}^t + R_{ik}^t (x_{1,k}^t - x_{w,k}^t) + R_{2k}^t (x_k^{-t} - x_{w,k}^t) \quad (9)$$

$$x_{id}^{t+1} = x_{id}^t + v_{id}^{t+1} \quad (10)$$

Among them,  $k = 1, 2, \dots, m/2$ ;  $t$  is the number of iterations;  $\omega$  is the inertia factor;  $R_{ik}^t, R_{2k}^t$  are the random number in  $(0,1)$  interval;  $x_k^{-t}$  is the average of the position of all particles in the population at  $t$  iteration and  $K$  competition [11].

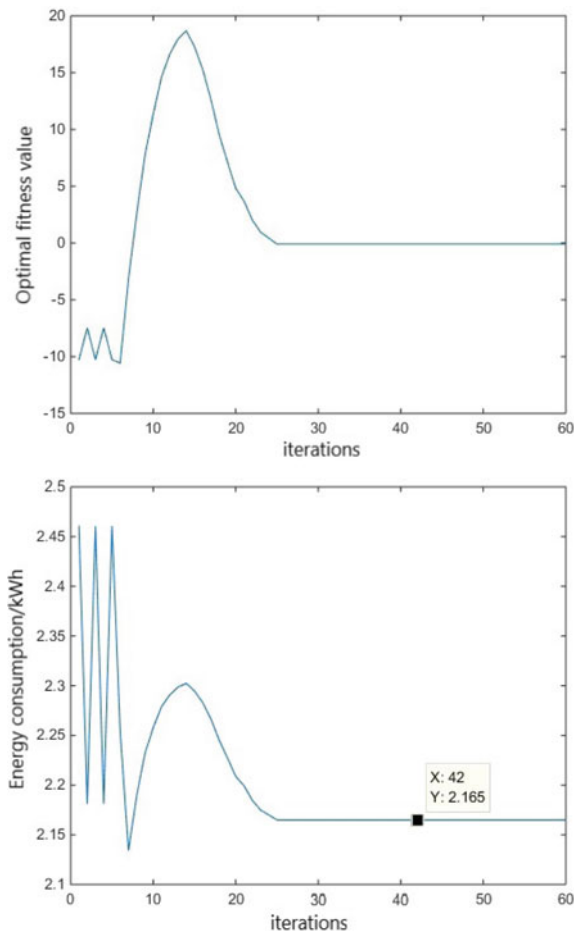
## 5 Simulation and Analysis

The energy optimization model given above is simulated and solved by the competition-based PSO optimization algorithm. The simulation data is measured by the thz1 line of Guangzhou–Zhuhai tram. The particle group related parameters are set as shown in Table 1.

After simulation, the optimal solution curve and energy consumption iteration curve of the particle swarm adaptive value in the running interval are shown in Fig. 2.

**Table 1** Particle swarm algorithm parameter setting table

Parameter name	Settings
Maximum number of iterations $n$	60
$\omega$	0.8
$R_1, R_2$	Random number between [0,1]
$V_{\max}$	5
$V_{\min}$	5
Particle swarm size	6
Particle swarm initial value	0, 10, 20, 30, 40, 50

**Fig. 2** Exhibition Center—exhibition west range adaptation value optimal solution and traction energy consumption iteration diagram

It is observed that at the beginning of the algorithm, the optimal fitness value and energy consumption value jump up and down, and the global search ability is strong. As the number of iterations increases, the wireless approaches the optimal value of the timing energy-saving operation strategy [12].

The train energy consumption data and the line data are simulated to get Fig. 3.

Compare the energy optimization results with the actual results and obtain the runtime consumption comparison Table 2.

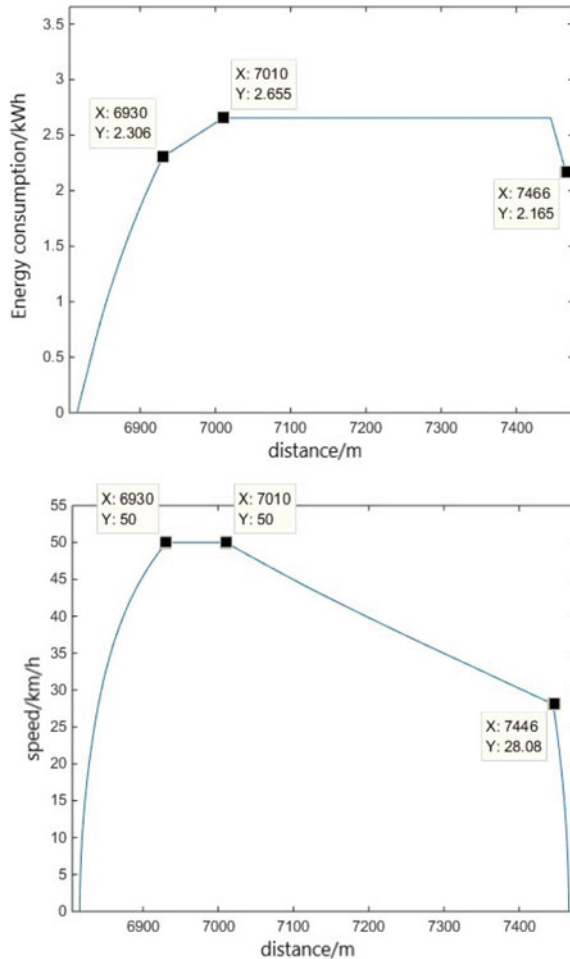


**Fig. 3** Exhibition Center—exhibition west section energy consumption and speed distance curve

**Table 2** Comparison of simulated energy consumption and actual energy consumption

Operating interval	Actual time consumption / s	Simulation time consumption / s	Actual energy consumption / kwh	Simulation energy consumption / kwh	Energy consumption optimization ratio /100%
Convention and exhibition center	62.5	62.4	3.23	3.03	6.2

## 6 Conclusion

The results show that the PSO algorithm of the competitive mechanism can improve the convergence of the algorithm, effectively find the turning point of the energy-saving model working condition, save the tram traction energy consumption, and enable the tram to operate according to the predetermined time node.

**Acknowledgements** This work is supported by National Key R&D Program of China (2017YFB1201004).

## References

1. Scholten J, Steiner M (2005) Energy Storage on board of railway vehicles. In: Proceedings of european power electronics conference, pp 632–637
2. Steiner M, Scholten J (2006) Improving overall energy efficiency of traction vehicles. In: WCRR, pp 377–382
3. Lacote F (2005) Alstom-future trends in railway transportation. Japan Railway Transp Rev 42:4–9
4. Zhang W, Wang H (2009) Analysis of parameter selection strategy for stability of particle swarm optimization algorithm. J Syst Simul 21(14):4339–4350 (in Chinese)
5. Cheng R, Jin Y (2015) A competitive swarm optimizer for large scale optimization. IEEE Trans Cybern 45(2):191
6. Eckart Z, Deb K (2000) Comparison of multi-objective evolutionary algorithms:empirical result. Evolutionary Computation 8(2):173–195
7. Szenasy I (2008) Improvement the energy storage with ultracapacitor in metro railcar by modeling and simulation. In: IEEE vehicle power and propulsion conference, VPPC'08, pp 3–5
8. Barrero R, Tackoen X, Van Mierlo J (2008) Analysis and configuration of supercapacitor based energy storage system on-board light rail vehicles. In: 2008 13th power electronics and motion control conference, EPE-PEMC. pp 1512–1517
9. Sun Central (2005) Practical tutorial for train traction calculation procedures. China Railway Publishing House, Beijing (in Chinese)
10. Miyatake M, Matsuda K (2008) Optimal speed and charge/discharge control of a train with onboard energy storage devices for minimum energy operation. In: SPEEDAM, pp 1211–1216

11. Dewei W, Kun Z, Shenrong W, Zhongping Y, Xiaojie Y (2011) Power distribution control strategy of on-board supercapacitor energy storage system of railway vehicle. In: 2011 International conference on materials for renewable energy& environment
12. Ogasa M, Taguchi Y (2007) Power flow control for hybrid electric vehicles using trolley power and on-board batteries. QR RTRI 48(1):30–36

# Design of LRC Filter for High-Power Inverters



Zongju Cai, Jie Yang and Zhijie Zhang

**Abstract** To solve the problem of vibration and noise of high-power motor, LRC filter is usually added at the output of large-capacity inverters to reduce the harmonic content of the output voltage, so the selection of cut-off frequency of the filter is particularly important. If the cut-off frequency of the filter is not designed properly, the output filter resonance will damage the filter, which affects the stability and reliability of the whole power system. In this paper, a kind of LRC filter is designed, fully considering the factors such as volume, weight and filtering characteristics. The fundamental reason for resonance is analyzed theoretically from the aspect of modulation and control. A criterion is proposed for designing cut-off frequency parameters. The criterion has a certain guidance and reference for the design and use of the filter.

**Keywords** Inverter · LRC filter · Resonance · Filter design

## 1 Introduction

### 1.1 Brief Introduction of LRC Filter

At present, the switching frequency of power switching devices in high-power inverters is getting higher and higher, and  $dv/dt$  on the motor side is also rising, which poses a great threat to the winding insulation of the motor. At the same time, the large harmonic content in the output voltage will seriously affect the vibration and noise performance of the system [1, 2]. Usually, a filter is added at the output of large-capacity inverters to eliminate most harmonics higher than the cut-off frequency and reduce the total harmonic in the output voltage so as to get a better sinusoidal output voltage [3, 4]. But if the parameters of the filter are not designed

---

Z. Cai (✉) · J. Yang · Z. Zhang  
Systems Engineering Research Institute, Feng xian dong Road 1st,  
Hai dian District, Beijing 100094, China  
e-mail: [18911990408@163.com](mailto:18911990408@163.com)

properly, the output voltage will not converge and resonance may occur. Large resonance current will degrade the performance of the filter, even damage the power components of the filter, and ultimately affect the reliability of the whole system.

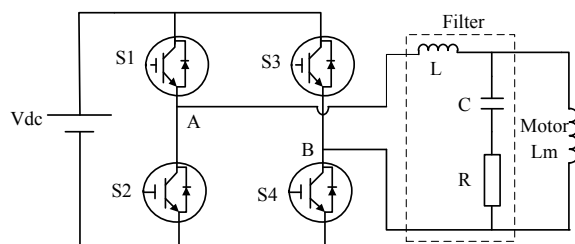
In reference [5], the maximum switching frequency is up to 1 kHz due to IGCT device in the design of H-bridge high voltage converter output filter. Considering the limitation of volume and weight, the cut-off frequency is as high as possible, but the upper limit is lower than the switching frequency. In reference [6], the cut-off frequency and LRC parameters are determined by calculating the rise time of the motor  $dv/dt$ . Reference [7] improves the inductance design of LRC filter, divides the positive and negative poles of the filter inductance equally, realizes the symmetry of the filter characteristics, effectively eliminates the distortion of the output voltage of the conventional LRC filter and thus suppresses the peak of the output voltage better. In reference [8], the parameters of passive damped filter are optimized to minimize the active and reactive power losses of RC branch. In summary, when designing cut-off frequency, the switching frequency should be taken into account. The cut-off frequency and parameters of the filter can also be calculated by specific indicators such as  $dv/dt$  and branch loss. However, at present among most of them the resonant reason of the filter is not analyzed with modulation and control technology, and effective guidance cannot be provided for the design of engineering parameters.

In this paper, LRC filter is adopted. The factors such as volume weight, filtering characteristics and resonance of the filter are fully considered. The design criterion of filter cut-off frequency and parameters is put forward. The engineering optimization of cut-off frequency design is carried out. The reasons for the resonance problem of the inverter filter are analyzed through experiments. Finally, filtering performance and reliable reality are obtained in the application.

## 2 Characteristic Analysis of LRC Filter

The single-phase H-bridge inverters are used in the inverters. Each H-bridge drives an open-end winding of the motor independently. The electrical topology of H-bridge inverter is shown in Fig. 1. The output pulse voltage of H-bridge inverter is filtered by LRC filter.

**Fig. 1** Electrical topology of single-phase H-bridge Inverter



The stator of motor is usually equivalent to inductance  $L_m$ , so the transfer function of LRC filter is

$$G(s) = \frac{RCs + 1}{LCs^2 + RC\left(1 + \frac{L}{L_m}\right)s + \left(1 + \frac{L}{L_m}\right)} \quad (1)$$

The inductance value of motor winding is millihertz, and the inductance of filter is microhertz. Therefore,  $L_m \gg L$ , the upper formula can be simplified as follows

$$G(s) = \frac{RCs + 1}{LCs^2 + RCs + 1} \quad (2)$$

The cut-off frequency of the LRC filter is as follows

$$f_o = \frac{1}{2\pi\sqrt{LC}} \quad (3)$$

Damping Ratio of LRC Filter is as follows

$$\zeta = \frac{R}{2} \sqrt{\frac{C}{L}} \quad (4)$$

### 3 Design Criteria of LRC Filters

The design of cut-off frequency of LRC filter is closely related to switching frequency and output frequency of the inverter. The cut-off frequency should be designed according to the following principles:

$$f_{out} < f_o < \frac{f_s}{n} \quad (5)$$

Among them,  $f_{out}$  is rated frequency of output voltage of H-bridge of the inverter,  $f_s$  is switching frequency of the inverter and  $n$  is natural number.

When designing the cut-off frequency of the filter, it is necessary to find a balance between the effect of harmonic filtering, volume/weight and loss. Lower cut-off frequency can filter out more frequency harmonics, and there is enough room for larger volume reactance and capacitance. At this time,  $n$  can be selected as a larger natural number. When the power density of the equipment must be high or the space of the equipment is limited,  $n$  should be chosen as a smaller natural number. By increasing the cut-off frequency of the filter, volume and weight can be decreased.

In addition, if the cut-off frequency is directly designed in the frequency band of  $f_s/n$  and its vicinity, the output voltage of the inverter will lead to the resonance of the filter in some cases. At the start moment, the output current of the inverter is

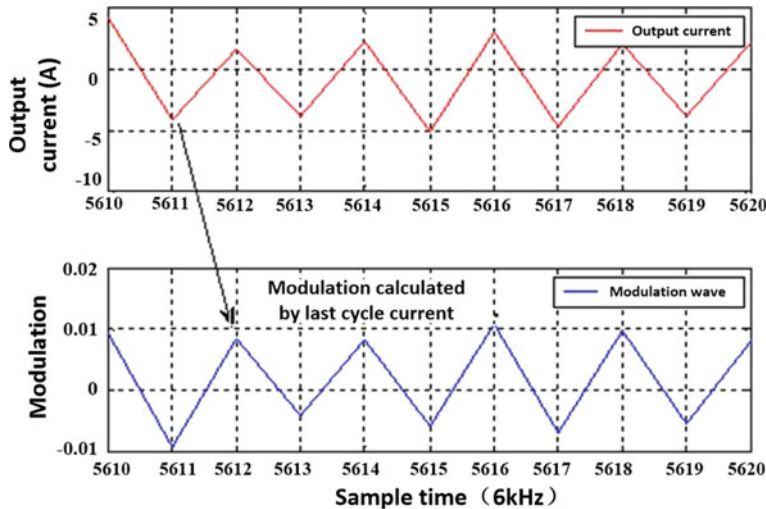


**Fig. 2** Output current and modulation wave of filter resonance

very small, nearly zero. Due to the sampling error of the current sensor and the external disturbance, sampled current values between adjacent switching cycles are in the opposite direction, as shown in Fig. 2. If the switching period is 6 kHz, when the current sampled in this period is negative, the next period modulation calculated by current closed-loop is positive. Similarly, the next periodic current sample is positive, and the modulation wave obtained by closed-loop calculation is negative, so the feedback current is amplified by the closed-loop controller to form a positive feedback of 3 kHz resonant current. The resonant current output by the inverter is the excitation source which directly causes the resonant of the output filter. Closed-loop current control enlarges the output current amplitude, which makes the output current of the inverter oscillate between positive and negative at a frequency of 3 kHz.

Therefore, in order to ensure the normal operation of the filter, the cut-off frequency should be avoided from  $f_s/n$  and its adjacent frequency band. Usually, the switching frequency of high-power converter is much larger than the rated frequency of output voltage, so the cut-off frequency can be selected according to the following formula:

$$10f_{\text{out}} < \frac{f_s}{n+1} < f_o < \frac{f_s}{n} \quad (6)$$

The design steps of LRC filter are as follows.

- (1) Design the appropriate cut-off frequency according to the formula.
- (2) The inductance value is calculated according to the fundamental voltage drop and selected according to volume/weight.

- (3) The capacitance value is calculated by cut-off frequency formula and inductance value.
- (4) The resistance value is determined according to the damping ratio.

## 4 Simulation and Experiment

The rated frequency of the output fundamental wave voltage of a high-power inverter is  $f_o = 18$  Hz and the switching frequency  $f_s = 6$  kHz. According to filter design criteria, the center frequency of 2, 3 and 6 kHz and the frequency band nearby should be avoided when designing the cut-off frequency. The cut-off frequency is selected 4.5 kHz.

Generally, inductance accounts for more than 75% of the weight of the whole filter, so the selection of capacitance and inductance should be considered comprehensively. The inductance can be calculated according to the requirement of fundamental voltage drop and volume/weight. The inductance can be calculated through the following calculation. The fundamental voltage drop  $\Delta U \leq 6$  V and the rated current 310 A.

$$L = \frac{\Delta U}{2\pi f_o I} \leq \frac{6}{2 * 3.14 * 18 * 310} = 171 \mu\text{H} \quad (7)$$

The selected inductance value is 170  $\mu\text{H}$ . Then, the capacitance value is calculated by the cut-off frequency.

$$C = \frac{1}{L(2\pi f_o)^2} = 7.4 \mu\text{F} \quad (8)$$

In order to prevent voltage overshoot and get smaller overshoot, the damping ratio is 1.4, and the resistance value is calculated.

$$R = 2\zeta\sqrt{\frac{L}{C}} = 2 * 1.4 * \sqrt{\frac{170}{7.4}} = 13.4 \Omega \quad (9)$$

The parameters of a set of filters are obtained as follows:  $L = 170 \mu\text{H}$ ,  $C = 7.4 \mu\text{F}$ ,  $R = 13.4 \Omega$ . Through MATLAB simulation, the Bode Diagram is obtained as shown in Fig. 3.

The experimental waveform of the filter is as shown in Fig. 4. No. 1 (blue) is the H-bridge output voltage, No. 2 (green) is the motor voltage and No. 3 (red) is the output current. It can be seen that the motor voltage sinusoidal degree is good, and the output current resonance does not appear.

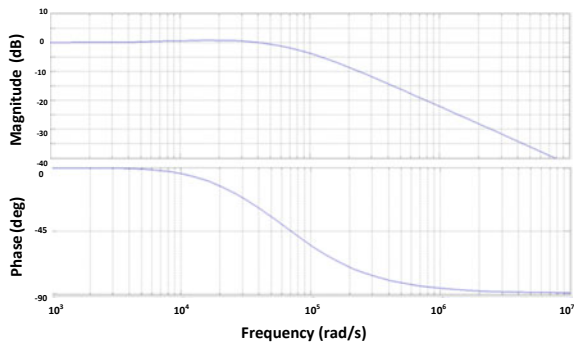


**Fig. 3** Filter bode diagram

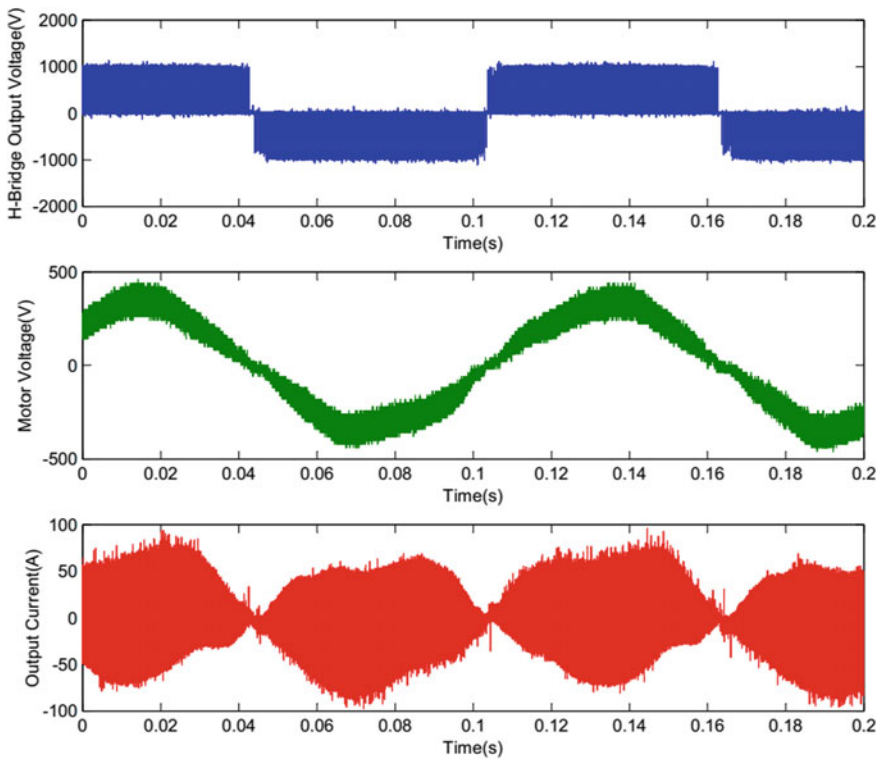


**Fig. 4** Experimental waveform of filter

If the capacitor is  $10 \mu\text{F}$ , the inductance remains unchanged, the resonant frequency is  $3.05 \text{ kHz}$  and the switching frequency is  $6 \text{ kHz}$ , and the resonant frequency is in the frequency band near  $f_s/2$ . When the inverter starts, the output current oscillates, and the output current waveform is as follows (Figs. 5 and 6).

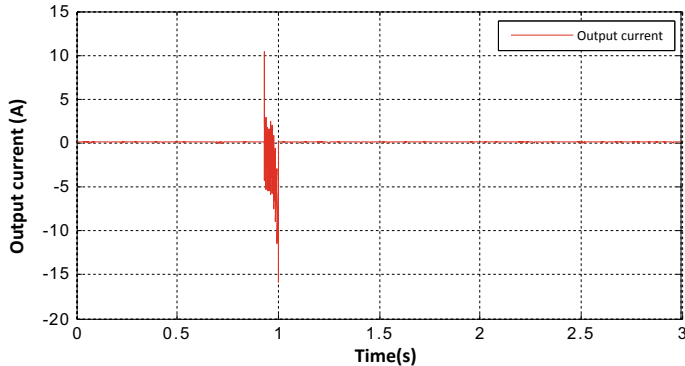


**Fig. 5** Output current of output filter in resonance

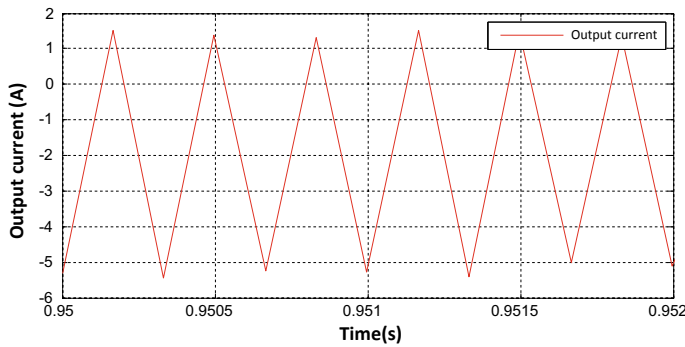


**Fig. 6** Details of output current of output filter in resonance

In summary, it can be inferred that the direct cause of output filter resonance is that the resonant frequency of the filter is at the  $f_s/2$  of the inverter. When the output current is near zero, due to the deviation of current detection, the feedback current and the current closed-loop controller form positive feedback, which results in the output current of the inverter fluctuate at  $f_s/2$ . If the resonant frequency of the output filter is also near  $f_s/2$ , the oscillatory excitation source of the inverter output will cause the output filter to resonate, thus burning the filter.

## 5 Conclusion

For H-bridge inverters, it is a common method to reduce THD of output power supply by adding LRC filter on the output side. However, the selection of resonant frequency of the filter is closely related to the switching frequency. Because the

filter has a certain resonance bandwidth, in order to avoid filter resonance, the resonant frequency of the output filter should be designed to avoid  $f_s/n$  and the frequency band nearby, so as to ensure the normal operation of the filter.

## References

1. Wu W, Sun Y, Lin Z (2014) A modified LLCL filter with the reduced conducted EMI noise. *IEEE Trans, Power Electron* 29(7):3393–3401
2. Wu W, Sun Y, Lin Z (2014) A new LCL-filter within series parallel resonant circuit for single-phase grid-tied inverter. *IEEE Trans, Power Electron* 61(9):4640–4643
3. von Jouanne A, Prasad N (1997) Design considerations for an inverter output filter to mitigate the effects of long motor leads in ASD applications. *IEEE Trans Ind Appl* 33(5):1138–1145
4. Yan B, Chen X (2002) The engineering design of VVVF output RLC sine-wave filter. *Electr Mach Control* 6(3):256–260 (in Chinese)
5. He Y (2010) Design of output filter for high voltage inverter based on H-bridge. *Power Electron* 44(5):84–85 (in Chinese)
6. Tian J, Ding Z (2013) Design of dv/dt Filter for Frequency Converter. *Mar Electr* 33(7):3–6 (in Chinese)
7. Ai S, Ren Q, Wang H, Zeng Q (2016) Asymmetry of the output filter structure of twelve-phase H-bridge converter and its improvement. *Power Capacit & React Power Compens* 37(5):0026–0030 (in Chinese)
8. Baoquan L, Hua G, Yixin Z (2017) Analysis and design of a passively damping lcl filter in three-phase converters. *Trans China Electrotech Soc* 32(2):195–205 (in Chinese)

# Research on a Secondary Pulsation Active Power Filter for Single-Phase PWM Rectifier



Yuxi Zhang, Fujun Peng, Qiyang Xu, Lailai Shen and Jie Chen

**Abstract** The single-phase PWM rectifier has a second harmonic current and a corresponding ripple voltage on the DC side. The low-frequency harmonic current is usually eliminated by a resonant circuit composed of a large-capacity capacitor and an inductor in the DC bus, but the LC brand reduces the power density of the entire system. To this end, a secondary pulsation active power filter based on a bidirectional boost–buck converter (bidirectional buck/boost) is proposed to suppress the DC bus voltage secondary pulsation. The compensation current equation when the filter fully compensates the pulsating power is derived, and a voltage loop and current loop control strategy is proposed based on this. Based on MATLAB/Simulink simulations and experiments demonstrate the effectiveness of the scheme, it can also reduce the volume and improve the power density of the system.

**Keywords** Single-phase PWM rectifier · Bidirectional buck/boost · Active power filter · Secondary pulsation

---

Y. Zhang (✉) · L. Shen · J. Chen

School of Electrical Engineering, Beijing Engineering Research Center  
of Electric Rail Transportation, Beijing Jiaotong University, Beijing 100044, China  
e-mail: [18121547@bjtu.edu.cn](mailto:18121547@bjtu.edu.cn)

L. Shen  
e-mail: [181117017@bjtu.edu.cn](mailto:181117017@bjtu.edu.cn)

J. Chen  
e-mail: [jiechen@bjtu.edu.cn](mailto:jiechen@bjtu.edu.cn)

F. Peng · Q. Xu  
Hohhot Urban Rail Transit Construction Management Co., Ltd., Hohhot, China  
e-mail: [546810488@qq.com](mailto:546810488@qq.com)

Q. Xu  
e-mail: [379400798@qq.com](mailto:379400798@qq.com)

## 1 Introduction

The problem of secondary pulsation exists in single-phase PWM rectifier. Secondary pulsating loads and power grids can cause damage. For example, a pulsating voltage generates a low-frequency harmonic current on the stator windings of the motor, resulting in an increase in electromagnetic losses, an increase in temperature expenditures, and a low-frequency pulsation and mechanical noise [1]. The solution is to use LC resonant branch to absorb the pulsation power. However, it increases the volume and weight of the traction converter, reduces the power density and increases the cost [2]. When the parameters of LC resonant circuit are seriously mismatched with the harmonic frequency, a large second harmonic cycle will be generated, which reduces the stability of the system [3].

Active power filter (APF) is using active transformation circuit pulse energy into the energy storage elements such as inductor, capacitor. Due to the energy storage components are not directly connected to the DC bus, APF can realize energy storage volume decreases and the power density increase [4]. The literature [5] proposes that the bridge arm of the low-voltage side of the APF is connected with the AC side of the rectifier. This scheme requires modification of the conventional rectifier structure, which is complicated. In the literature [6], the traditional boost-type bidirectional DC/DC circuit is used as the APF topology. Multiple sensors are required to collect multiple single-phase rectifiers and load side information in real time to obtain APF control reference signal, which is complicated to implement. The literature [7] and literature [8] use a current-breaking APF topology based on the buck circuit, which increases the hysteresis loss of the inductor, generates heat in the core and has serious electromagnetic interference. The literature [9] uses the buck circuit. The voltage resistance of the switching device is the same as that of the rectifier module. It is easy to design. The filter capacitor voltage command is the secondary pulsating current, and the secondary pulsating power is absorbed by the storage capacitor. The control scheme is simple, and four pulsations are introduced to the busbar. When the power of the rectifier becomes large, the filtering effect is deteriorated, which limits the application range. According to the shortcomings of scheme in literature [9], based on the half-bridge bidirectional buck/boost topology, using the capacitor as the energy storage component, the expression of the APF inductor current is derived, and a control strategy of the voltage loop plus current loop is proposed. Firstly, this paper describes the working principle of the APF and derives the target current expression of APF when the pulsating power is fully compensated; then, the control strategy of secondary pulsation APF is introduced; finally, simulation and experimental results demonstrate the effective filtering scheme of the secondary pulsation APF.

## 2 Secondary Pulsation Power Analysis

Figure 1 is a single-phase PWM rectifier system. From the aspect of the rectifier power to analyze the working principle of secondary pulsation APF, the voltage and current of the AC power supply are assumed to be sinusoidal input of power frequency, as shown in Eq. (1):

$$\begin{cases} u_s = U_s \sin(\omega t) \\ i_s = I_s \sin(\omega t - \phi) \end{cases} \quad (1)$$

In Eq. (1),  $\phi$  is the power factor angle of the supply voltage and current. In practical operation, the single-phase PWM rectifier can realize the same phase of the voltage and current at the network side, that is, the power factor is 1.  $\phi = 0$ , then the input power on the AC side  $p_{in}$  is described in Eq. (2).

$$p_{in} = u_s i_s = \frac{U_s I_s}{2} - \frac{U_s I_s}{2} \cos(2\omega t) \quad (2)$$

The energy of the input inductance is usually not negligible, so the input power of the rectifier after the input inductance  $p_L$  is described in Eq. (3).

$$p_L = i L_s \frac{di_s}{dt} = \frac{\omega L_s I_s^2}{2} \sin(2\omega t) \quad (3)$$

The input power of the rectifier  $p_s$  includes constant active power  $p_o$  and pulsating power  $p_r$ ,  $p_s$  and  $p_r$  are described in Eqs. (4) and (5).

$$p_s = p_{in} - p_L = \frac{U_s I_s}{2} - \left[ \frac{U_s I_s}{2} \cos(2\omega t) + \frac{\omega L_s I_s^2}{2} \sin(2\omega t) \right] \quad (4)$$

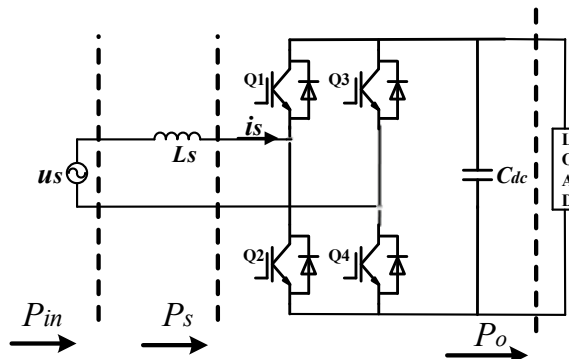


**Fig. 1** Single-Phase PWM rectifier system

$$p_r = \sqrt{\frac{U_s^2 I_s^2}{4} + \left(\frac{\omega L_s I_s^2}{2}\right)^2} \sin\left(2\omega t + \arctan \frac{U_s}{\omega L_s I_s}\right) = p_{r-\text{peak}} \sin(2\omega t + \gamma) \quad (5)$$

Therefore, the pulsating power will cause a corresponding pulsation on the DC supporting capacitor.

### 3 Secondary Pulsation Active Power Filter

The method in this paper is based on capacitive energy storage type parallel DC active power filter. The topology of the whole system is shown in Fig. 2.

When the pulsating power in Eq. (5) is completely absorbed by the capacitor, the capacitor current satisfies the following Eq. (6).

$$i_{cs} L_{cs} \frac{di_{cs}}{dt} = p_{r-\text{peak}} \sin(2\omega t + \gamma) \quad (6)$$

The capacitance instruction current  $i_{cs}^*$  can be calculated as Eq. (7).

$$i_{cs}^* = \frac{P_{r-\text{peak}} \sin(2\omega t + \gamma)}{\sqrt{(P_{r-\text{peak}}/C_s \omega)(k - \cos(2\omega t + \gamma))}} \quad (7)$$

In Eq. (7),  $k$  is constant, and  $k > 1$ .

When the secondary pulsation APF completely compensates the pulsating power, the average value of the compensation capacitor charging/discharging power of the secondary pulsation APF is 0 in a period of the double-frequency ripple component. When the current command is greater than 0, the secondary pulsation APF charges the storage capacitor; otherwise, the secondary pulsation APF operates in the boost mode to discharge the storage capacitor and transfer the energy stored in the capacitor to the DC bus.

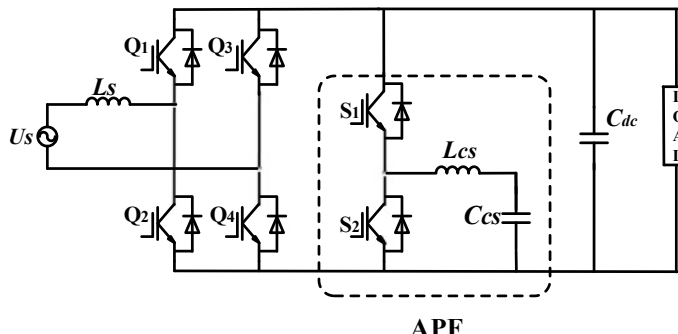


**Fig. 2** Rectifier-APF system topology

## 4 Control Strategy Design

This paper adopts current closed-loop control and voltage closed-loop control. The control strategy includes instruction current calculation, compensation voltage control and compensation current control. Instruction current calculation is shown in Fig. 3. Control block diagram of secondary pulsation APF is shown in Fig. 4.

Compensation capacitance control and compensation current control are the core of control. PI controller is used for closed-loop control of direct voltage flow of energy storage capacitor, and the obtained output is superimposed with current instruction. PR controller is used for current loop. PR controller can realize sinusoidal signal tracking without static difference. The transfer function is described in Eq. (8).

$$G_{PR}(s) = K_p + \frac{2K_f\omega_c s}{s^2 + 2\omega_c s + \omega^2} \quad (8)$$

The proportional coefficient  $K_p$  affects the dynamic response speed of the system, and the integral coefficient  $K_f$  changes the attenuation degree of the resonant

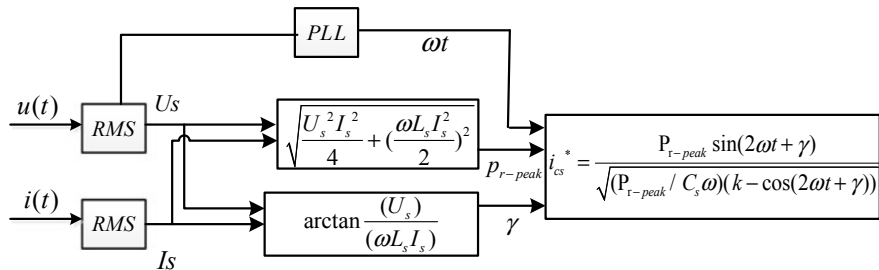


**Fig. 3** Current instruction acquisition

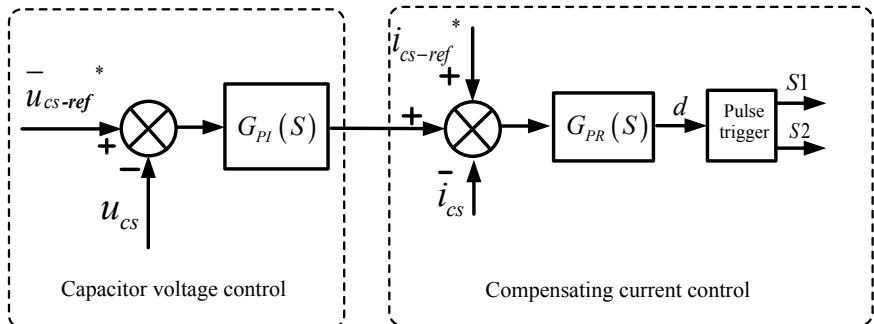


**Fig. 4** Control block diagram of secondary pulsation APF

controller to other frequency signals,  $\omega_c$  is the cut-off frequency, which is proportional to the system bandwidth.

## 5 The Simulation Result

In order to verify the effectiveness of the control scheme described in this paper, a digital control platform was built based on MATLAB/Simulink simulation environment through S function to simulate the front-stage rectifier of traction system and secondary pulsation APF system. According to the energy balance relationship during secondary pulsation APF filtering, the compensation capacitor  $C_{cs}$  is determined by factors such as the compensation capability of secondary pulsation APF and the amount of change in capacitance voltage. In order to obtain a better filtering effect, the actual inductance needs to be able to track the current instruction. The selection of the inductance value of the filtering inductance  $L_{cs}$  is related to the amplitude of the compensating pulsation power, the intermediate DC voltage and the compensating capacitor voltage. The basic parameters of the simulation system are shown in Table 1.

In Table 1,  $P_e$  is rated power,  $T_s$  is sampling time,  $f_{switch}$  is frequency of rectifier and secondary pulsation APF,  $L_s$  is rectifier inductance,  $L_{cs}$  is filtering inductance,  $C_{cs}$  is energy storage capacitor,  $C_{dc}$  is direct current capacitor,  $U_{dc}$  is DC bus voltage,  $U_{cs}$  is storage capacitance voltage.

In order to verify the effectiveness of the secondary pulsation APF, the operating condition simulation before and after the secondary pulsation APF is put into operation is carried out, and the simulation results are as (Figs. 5 and 6).

It can be seen from Figs. 5 and 6 that the secondary pulsation peak after the secondary pulsation APF input is significantly decreased, and the DC voltage THD is lowered, thereby effectively improving the waveform quality.

## 6 The Experimental Result

This paper is based on the traction converter ground experiment platform construction for experimental verification; test parameters and simulation are consistent. The experimental waveform is as Fig. 7.

**Table 1** Parameters table

$P_e$	$T_s$	$f_{switch}$	$L_s$	$L_{cs}$	$U_{dc}$	$U_{cs}$	$C_{cs}$	$C_{dc}$
300 KW	1e-5 s	1 kHz	2.08 mH	1 mH	1500 V	1100 V	2 mF	4 mF

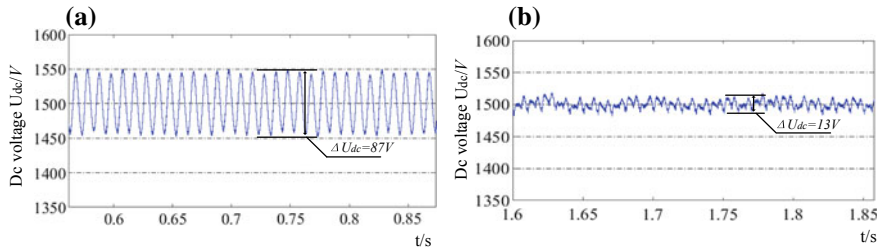


**Fig. 5** Waveform of secondary pulsation APF before and after input

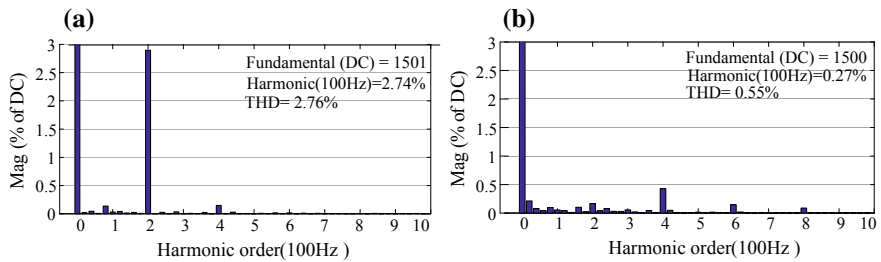


**Fig. 6** FFT analysis of DC voltage

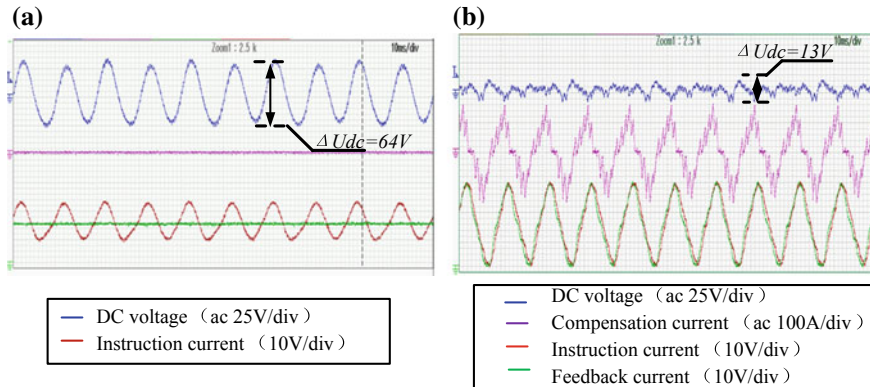


**Fig. 7** Waveforms before and after secondary pulsation APF input

As can be seen from (a) of Fig. 7, before the secondary pulsation APF is input, the voltage pulsation is about 64 V, and there is a significant secondary pulsation. After the filter device is started, as shown in (b), the voltage ripple is reduced to 13 V. In order to compensate the current command, the current after the actual

filtering can prove the effectiveness of the control strategy in this paper. The compensation current can track the current command, the secondary component is basically eliminated, and the voltage ripple is obviously suppressed.

## 7 Conclusion

This paper deals with the problem of secondary DC voltage ripple in single-phase PWM rectifier system. A secondary pulsation active power filter based on current closed-loop control and voltage closed-loop control strategy is designed, and the feasibility of the scheme is verified by simulation and experiment. This scheme can basically achieve the same effect as the passive filter and can replace the traditional secondary resonance link, effectively reducing the volume and weight of the system and improving the power density of the system.

**Acknowledgements** This work is supported by the National Key Research and Development Program (2017YFB1200802-01).

## References

1. Klima J, Chomat M, Schreier L (2008) Analytical closed-form investigation of pwm inverter induction motor drive performance under dc bus voltage pulsation. *IET Electr Power Appl* 2 (6):341
2. Yujie L, Caifei S, Fei L et al (2010) Harmonic analysis of power grid-side for high speed train. *Electric Drive* 40(1):33–37 (in Chinese)
3. Yanping C, Li X, Zhonghao L (2010) Research on the secondary resonant circuit of single-phase voltage-pulse rectifier. *Electr Drive Locomot* 2:28–32 (in Chinese)
4. Krein PT, Balog RS (2009) Cost-Effective hundred-year life for single-phase inverters and rectifiers in solar and LED lighting applications based on minimum capacitance requirements and a ripple power port. In: IEEE applied power electronics conference & exposition. IEEE
5. Shimizu T, Fujita T, Kimura G et al (2015) Unity-power-factor PWM converter with DC ripple compensation. *Electr Eng Jpn* 123(1):51–62
6. Wenjiao G, Chunguang R, Lei W et al (2016) Control method of bidirectional AC/DC converter with unbalanced voltage in hybrid micro-grid. *Power Syst Technol*
7. Wang R, Wang F, Boroyevich D et al (2011) A high power density single-phase PWM rectifier with active ripple energy storage. *IEEE Trans Power Electron* 26(5):1430–1443
8. Wang R, Wang F, Lai R et al (2009) Study of energy storage capacitor reduction for single phase PWM rectifier
9. Chao KH (2009) New control methods for single phase PWM regenerative rectifier with power decoupling function. In: International conference on power electronics and drive systems, Taipei, Taiwan (2009–11). IEEE

# An Improved Shunt Hybrid Active Power Filter Based on Cascaded H-Bridge Converter and Its Generalized Inverse System Decoupling Control



Xin Li, Ruoqiong Li and Bo Li

**Abstract** In this paper, a novel improved shunt hybrid active power filter (SHAPF) is presented based on cascaded H-bridge converter to compensate the harmonics on the grid. This improved structure of SHAPF can significantly reduce the 5th and 7th harmonics which mainly affect the power quality on the grid. H-bridge converter and passive power filter (PPF) are connected in series to compensate the harmonics together, passive power filter is mainly used to compensate 5th and 7th harmonics, and the other harmonics are compensated by the cascaded H-bridge converter. Furthermore, based on the generalized inverse system, a decoupling control method is proposed for the nonlinear and strong coupling characteristics of the 2-input 2-output improved SHAPF. After using an interactive algorithm and analyzing based on the operating principle, it is verified that the improved SHAPF model is reversible. The improved SHAPF-generalized inverse system is obtained, which is decoupled by the generalized inverse system theory after forming a composite system in series with the original system. Finally, by using an additional PI controller, the first pseudo-linear system that controls decoupling can achieve performance tuning of the subsystem. The effectiveness of this decoupling method is proved by MATLAB simulation that the decoupling subsystem has good performance, both dynamic and static.

**Keywords** Improved shunt hybrid active power filter · Cascaded H-bridge inverter · Decoupling method · Harmonic suppression

---

X. Li (✉)

School of New Energy & Power Engineering, Lanzhou Jiaotong University,  
Anning District, Lanzhou, China  
e-mail: [lxfp167@163.com](mailto:lxfp167@163.com)

R. Li · B. Li

School of Automation & Electrical Engineering, Lanzhou Jiaotong University,  
Anning District, Lanzhou, China

## 1 Introduction

In recent years, with the advancement of power systems, increasingly nonlinear electrical compensators have appeared in our daily lives, which have brought a lot of harmonics that affect the quality of power, causing damage to the power system. Therefore, new types of equipment are needed to eliminate the harm caused by harmonics and reactive power and improve the power quality of the grid.

Active power filter (APF) is a traditional power electronic device that can suppress dynamic harmonics and compensate reactive power. But the applications of traditional two-level topology are limited in some situations because of its low-voltage operation and low volumes [1–3]. To solve this problem, a cascaded H-bridge inverter is used in the case of high voltage output, which makes APF applicable to high power situations [4–7].

In this paper, the traditional H-bridge structure circuit is improved by adding a parallel passive power filter (PPF), so we can achieve the target that H-bridge inverter and passive power filter can compensate the harmonics together.

But the coupling relationship between the three-phase compensated current of improved SHAPF based on H-bridge cascade inverter seriously affects its compensation effect [8–10]. The scholars mainly use feedforward decoupling control strategy to solve the problem, now in literatures [11–13]. This strategy requires high precision of the system model, it does not have robustness to parameter perturbation, what is more, it is morbid when it involves the reversibility of the system, and it is not effective in dynamic compensation. So, it is difficult to apply to reality.

To solve the problem, in this paper, a new generalized inverse system decoupling control scheme is proposed for the strong coupling relationship between the three-phase compensation currents. The mathematical model of the modified SHAPF based on H-bridge cascade inverter is firstly proposed. Then, by using interactor algorithm based on the analysis of operation principle, the modified SHAPF based on cascade H-bridge inverter is verified to be invertible. Finally, we get the generalized inverse system and then concatenate it with the original system. Decoupling can transform the strongly coupled nonlinear composite system with two outputs and two inputs into two easily controllable first linear subsystems.

## 2 Basic Principle of SHAPF

The main components of shunt hybrid active power filter (SHAPF) are main circuit (PWM converter), drive circuit, control circuit, command current calculation circuit and so on. The system component of SHAPF is shown in Fig. 1 [14].

The harmonic current on the grid is first detected, and the compensation current signal  $i_{c*}$  is calculated by the compensation amplifier circuit.  $i_c$  is the actual compensation current calculated by low-pass filter. Then, the difference between  $i_c$  and  $i_{c*}$  is used as input for the current tracking circuit. The PWM signal is generated by

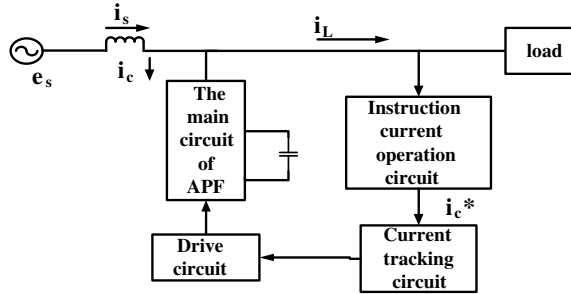


**Fig. 1** System components of SHAPF

a hysteresis comparator, and the compensation current generated by the PWM converter can cancel the harmonic current. And, the load current finally obtained is very close to the sine wave signal. Insulated-gate bipolar transistor (IGBT) is the core device of the SHAPF main circuit. DC power can be converted to AC by IGBT, and its high frequency, pressure and current resistance are outstanding. It is widely used in inverters [15, 16].

### 3 Mathematical Model of Improved SHAPF

The structure of the modified SHAPF based on single cascaded H-bridge inverter is shown in Fig. 2a.

The parallel passive filters (PPF) are used to compensate for the 5th and 7th harmonics generated by the grid. The cascaded H-bridge inverter structure is used to compensate for other subharmonics and reactive power.  $i_{L_a}$ ,  $i_{L_b}$ ,  $i_{L_c}$  are the current in grid side.  $v_{ca1}$ ,  $v_{ca2}$ ,  $v_{cb1}$ ,  $v_{cb2}$ ,  $v_{cc1}$ ,  $v_{cc2}$  are the branch voltage of PPF.  $v_{La}$ ,

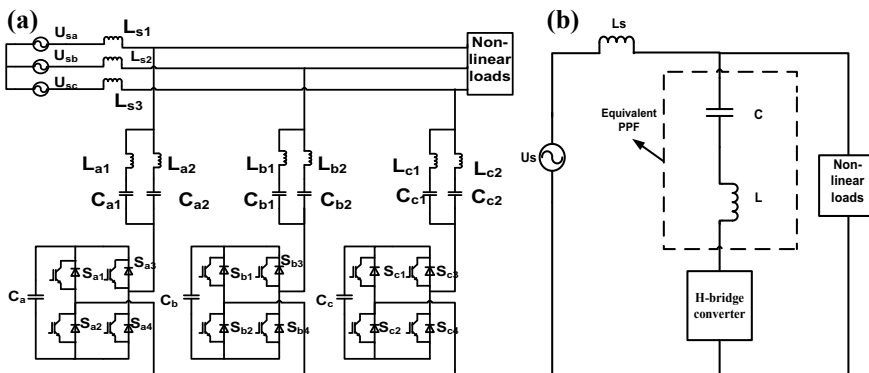


**Fig. 2** a Mathematical model of improved SHAPF based on H-bridge converter and b single-phase equivalent mode

$v_{Lb}$ ,  $v_{Lc}$  are the voltage at the common coupling point.  $i_a$ ,  $i_b$ ,  $i_c$  are the compensation current of H-bridge inverter.  $L_s$  is the equivalent inductance in grid side.  $V_{dc}$  is the DC-side capacitance voltage of H-bridge inverter.  $R$  is the internal resistance of each phase and all other losses. The switching function of each phase of H-bridge inverter is equivalent to  $S_a$ ,  $S_b$ ,  $S_c$ .

For the predigestion of the mathematical model, the parallel-positive power filters of each phase are equivalent to a LC-positive filter, equivalent capacitance of each phase is  $C_a$ ,  $C_b$ ,  $C_c$ , and capacitor voltage is  $v_{ca}$ ,  $v_{cb}$ ,  $v_{cc}$ . The single-phase equivalent model is obtained as shown in Fig. 2b.

The mathematical expression of improved SHAPF in a–b–c coordinate system is:

$$v_{dc} \cdot S_a + L \frac{di_a}{dt} + Ri_{ca} + v_{ca} = v_{La} \quad (1)$$

$$v_{dc} \cdot S_b + L \frac{di_b}{dt} + Ri_{cb} + v_{cb} = v_{Lb} \quad (2)$$

$$v_{dc} \cdot S_c + L \frac{di_c}{dt} + Ri_{cc} + v_{cc} = v_{Lc} \quad (3)$$

$$C \frac{dv_{dc}}{dt} = \frac{1}{3} (i_{ca} \cdot S_a + i_{cb} \cdot S_b + i_{cc} \cdot S_c) \quad (4)$$

$$i_{ca} + i_{cb} + i_{cc} = 0 \quad (5)$$

Providing that  $\begin{bmatrix} x_1 \\ x_2 \\ x_3 \end{bmatrix} = \begin{bmatrix} i_d \\ i_q \\ v_{dc} \end{bmatrix}$  is the state variables of SHAPF system,  $\begin{bmatrix} S_d \\ S_q \end{bmatrix}$  is the control variable of SHAPF system, and  $\begin{bmatrix} y_1 \\ y_2 \end{bmatrix} = \begin{bmatrix} i_d \\ i_q \end{bmatrix}$  is the output variable of SHAPF system. The improved SHAPF formula in  $d$ – $q$  coordinate system is:

$$x_3 S_d + L \frac{di_1}{dt} + Rx_1 - \omega L x_2 + v_{cd} = v_{Ld} \quad (6)$$

$$x_3 S_q + L \frac{di_2}{dt} + Rx_2 + \omega L x_1 + v_{cd} = v_{Lq} \quad (7)$$

$$C \frac{dx_3}{dt} = \frac{1}{3} (x_1 S_d + x_2 S_q) \quad (8)$$

In the above formula,  $\omega$  is the fundamental angular frequency. In other words, it is the rotational angular velocity of the  $d$ – $q$  coordinate axis. In  $d$ – $q$  coordinates,  $i_d$  and  $i_q$  are the compensation currents of SHAPF.  $v_{Ld}$  and  $v_{Lq}$  are the voltages at the junction between AC and SHAPF.  $S_d$  and  $S_q$  are switching function control quantities. From (6)–(8), the formula can be obtained as follows:

$$x'_1 = (-Rx_1 + \omega Lx_2 - x_3 \cdot S_d + v_{Ld} - v_{cd})/L \quad (9)$$

$$x'_2 = (-Rx_2 - \omega Lx_1 - x_3 \cdot S_q + v_{Lq} - v_{cq})/L \quad (10)$$

$$x'_3 = \frac{1}{3C}(x_1 \cdot S_d + x_2 \cdot S_q) \quad (11)$$

From formulas (9), (10) and (11), it is easy to see that the compensation current ( $x_1, x_2$ ) in  $d-q$  coordinate system has strong coupling and nonlinear relationship, so it is difficult to design the controller for the two input and two output system, and it is impossible to compensate the current precisely. The coupling relationship of the improved SHAPF can not be ignored.

## 4 Generalized Inverse System Decoupling Method for Improved SHAPF

### 4.1 Inverse System and Method of Generalized Inverse System Decoupling

Generating an  $\alpha$ th integral inverse system is the central idea of the inverse system decoupling method, and the system then feeds back according to the mathematical model of the controlled object. The inverse system is connected in series with the original system. Thinking of the two systems as a composite system, the composite system will become a decoupled system with a linear transfer relationship by changing the input of the composite system, and by this way, the linear system design theory can be used to design the pseudo-linear system. But there are also some shortcomings that the inverse system method has. For example, the inverse method can not configure the poles of the subsystems, making it difficult to tune the performance of the subsystems.

In order to solve this problem, this paper proposes a generalized inverse system method based on inverse system method. In the inverse system, its input vector is  $\varphi = y'$ . The output vector is  $[y_1 \ y_2]^T$ , and the state feedback vector is  $[x_1 \ x_2]^T$ . In a generalized inverse system, the input vector becomes

$$\varphi_j = \alpha_{j0}y_0 + \alpha_{j1}y'_1 + \alpha_{j2}y''_2 + \dots + \alpha_{jn}y_n^{(n)}. \quad (12)$$

Obviously, the generalized inverse system adds some parameters compared to the inverse system. By adjusting the generalized inverse parameters, the poles of the pseudo-linear system can be configured to any position. So, it is easy to bridle the frequency characteristics of the pseudo-linear system to achieve the desired effect.

## 4.2 Invertible Analysis

In this section, we analyze the reversibility of the improved SHAPF by the inverse system. Deriving the output equations of SHAPF system until the equations contain the control variable  $[S_d \ S_q]$ . From Eqs. (9) and (10), we can get the following equation:

$$\begin{bmatrix} y'_1 \\ y'_2 \end{bmatrix} = \begin{bmatrix} \frac{-Rx_1 + \omega Lx_2 - x_3 \cdot S_d + v_{Ld} - v_{cd}}{L} \\ \frac{-Rx_2 - \omega Lx_1 - x_3 \cdot S_q + v_{Lq} - v_{cq}}{L} \end{bmatrix}$$

Now, the output equation contains the control variables by once derivation. The Jacobi matrix is  $\begin{bmatrix} 0 & -\frac{v_{dc}}{L} \\ -\frac{v_{dc}}{L} & 0 \end{bmatrix}$ .

The Jacobi matrix is non-singularity. The system's relative degree vector is  $\alpha = [\alpha_1, \alpha_2]^T = [1, 1]^T$ . For  $\alpha_1 = \alpha_2 = 1$ ,  $\alpha_1 + \alpha_2 = 2$ , the order is smaller than the order of the improved SHAPF system (third); thus, demonstrating that the improved SHAPF system is reversible.

## 4.3 Generalized Inverse System of Improved SHAPF Based on Cascaded H-Bridge Three-Level Converter

In this section, ordering the input vector  $\varphi$  of improved SHAPF system is:

$$\varphi_1 = a_{11}y'_1 + a_{10}y_1 \quad (13)$$

$$\varphi_2 = a_{21}y'_2 + a_{20}y_2 \quad (14)$$

Transforming Eqs. (13) and (14) into:

$$y'_1 = (\varphi_1 - a_{10}y_1)/a_{11} \quad (15)$$

$$y'_2 = (\varphi_2 - a_{20}y_2)/a_{21} \quad (16)$$

From Eqs. (9) and (10), we can get the expression of  $S_d$  and  $S_q$ :

$$S_d = (v_{Ld} - Rx_1 + \omega Lx_2 - v_{cd} - Ly'_1)/x_3 \quad (17)$$

$$S_q = (v_{Lq} - Rx_2 - \omega Lx_1 - v_{cq} - Ly'_2)/x_3 \quad (18)$$

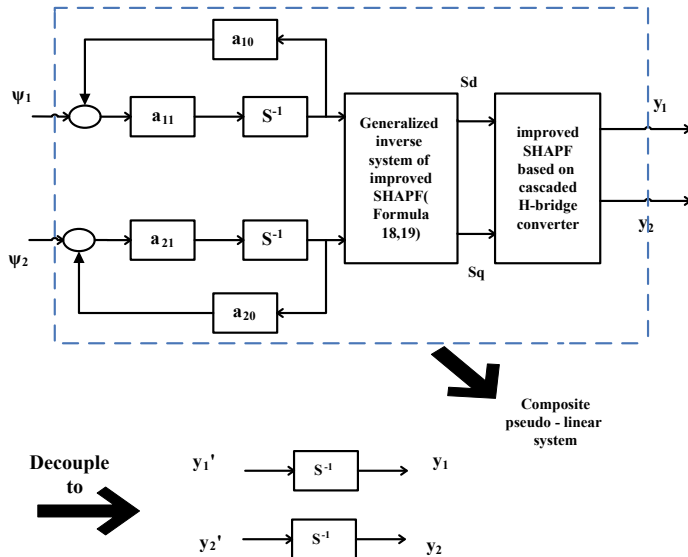


**Fig. 3** Decoupling and feedback linearization of SHAPF by generalized inverse system method

Substituting Eqs. (15) and (16) into Eqs. (17) and (18):

$$S_d = (v_{Ld}a_{11} - Rx_1a_{11} + \omega Lx_2a_{11} - v_{cd}a_{11} + L\alpha_{10}x_1 - L\varphi_1)/(a_{11}x_3) \quad (19)$$

$$S_q = (v_{Lq}a_{21} - Rx_2a_{21} + \omega Lx_1a_{21} - v_{cq}a_{21} + L\alpha_{21}x_2 - L\varphi_2)/(a_{21}x_3) \quad (20)$$

Equations (19) and (20) are the duty cycle functions of the PWM inverters of the new generalized inverse system. In order to control the compensation current, we achieve this by revising the duty cycle of the PWM inverter. The new input vector of the system is  $\varphi$ , and the new system is called generalized inverse system. The composite system is obtained by the series connection of the generalized inverse system and the original system, and the decoupling of the improved SHAPF composite system based on the generalized inverse system theory is realized. SHAPF uses the generalized inverse system method for feedback linearization and decoupling, as shown in Fig. 3. The control of the improved SHAPF system is converted to the control of two linear systems, and the control of the first linear system can be realized by the PI controller.

#### 4.4 Design of Controller of Pseudo-Linear System

In this paper, the performance of the decoupling subsystem is improved by two PI additional controllers, which reduces the system steady-state error and correctly

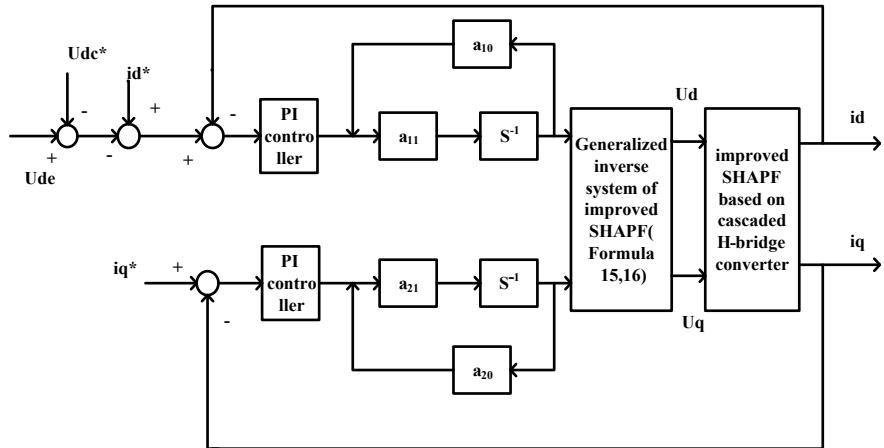


**Fig. 4** Generalized inverse PI control system

deploys the poles. The two decoupled first pseudo-linear systems are controlled by two PI controllers. The device simultaneously controls the capacitor on the DC side. The decoupling control structure is shown in Fig. 4.

The transfer function can be easily derived from the above figure. The composite system was found to be stable because the pole distribution of the composite system was found by calculation and was on the left side of the s-plane. Chen Boshiin proved an optimal damping ratio [15]. In order to achieve the maximum operating frequency range and the system that has the best overall dynamic performance, the generalized inverse system parameters ( $a_{10}$ ,  $a_{11}$ ,  $a_{20}$ ,  $a_{21}$ ) can be set. The damping ratio which is calculated by the transfer function  $\delta$  of the system is close to 0.707. In Fig. 4,  $i_{Fd}$  and  $i_{Fq}$  are actual compensation current, and  $i_{Fd}^*$  and  $i_{Fq}^*$  are reference current theoretically.

## 5 Simulation Research

In this paper, MATLAB is used for simulation. The effectiveness of the generalized inverse system decoupling strategy for improved SHAPF based on H-bridge inverter is verified. The feedforward decoupling and inverse system decoupling methods are compared. The system parameters of the simulation are shown in Table 1.

By constructing an improved SHAPF model and applying a controller, the resulting load current waveform is shown in Fig. 5.

It is obvious that all of the decoupling methods can improve the grid quality, but the load compensation current waveform using the generalized inverse system method is the closest to the sine wave, so the generalized inverse decoupling strategy is better than the other decoupling strategies. The spectrum analysis of each decoupling method is shown in Fig. 6.

**Table 1** Comprehensive parameter

Comprehensive parameter	Value
Virtual value of grid voltage ( $V_m$ ) and frequency	220 V/50 Hz
Internal resistance of each phase and all other	0.01 $\Omega$
DC-side capacitor ( $C_{dc}$ ) and its voltage ( $V_{dc}$ )	0.1 F/680 V
Parameters of PPF $L_{a1} L_{a2} C_{a2} C_{a2}$	1.2 mH/1.2 mH/340 F/170 F
PI controller parameter of generalized inverse subsystem ( $k_p k_i k_p k_i$ )	300/100,300/100
Generalized inverse parameter ( $a_{11}, a_{10}, a_{21}, a_{20}$ )	1, 1.41, 1, 1.41
PI controller parameter in DC side ( $k_p k_i$ )	0.01/0.002
Three-phase bridge load	15 $\Omega$ /5 mH

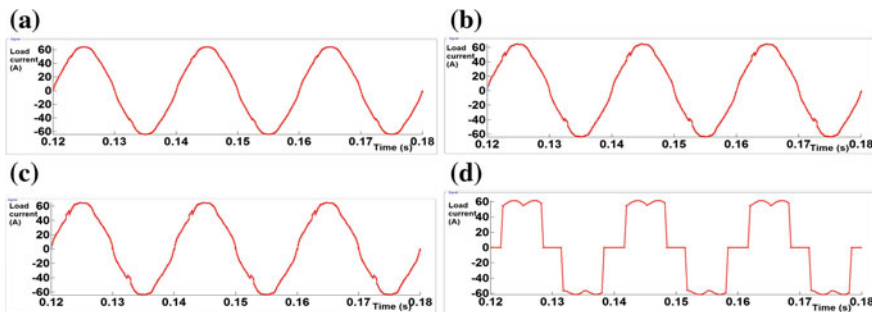


**Fig. 5** Comparison of load current waveforms using different decoupling methods **a** generalized inverse system decoupling method, **b** inverse system decoupling method, **c** feedforward decoupling method and **d** without decoupling method

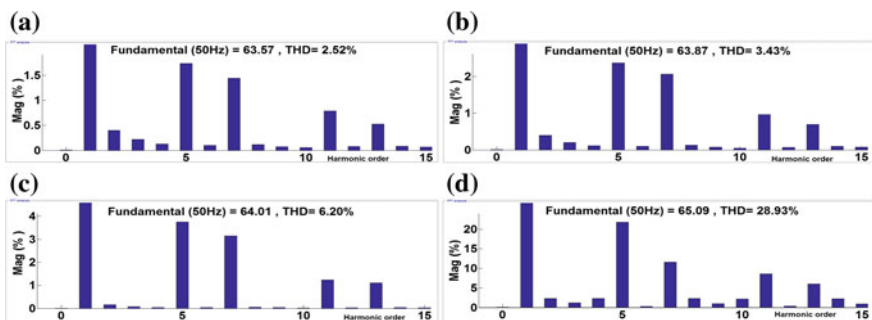


**Fig. 6** Comparison of spectrum analysis using different decoupling methods **a** generalized inverse system decoupling method, **b** inverse system decoupling method, **c** feedforward decoupling method and **d** without decoupling method

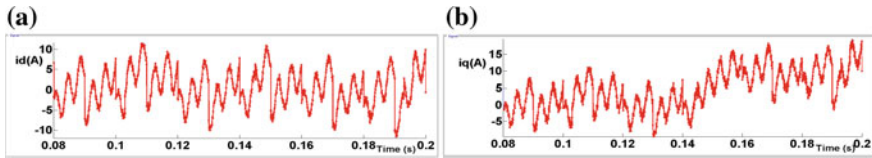


**Fig. 7** Compensated current  $i_d$  and  $i_q$

In Fig. 6, the THD of the system with generalized inverse system decoupling method is 2.52%, and the 5th harmonic and the 7th harmonic can suppress THD below 2% of the basic value by the generalized inverse decoupling method, so that the effect is the best in the above method.

By analyzing the waveform obtained by applying the disturbance step signal to the  $i_d$  at 0.153 s of the simulation, it can be verified whether the system is completely decoupled. The  $i_d$  and  $i_q$  waveforms are shown in Fig. 7.

In Fig. 7, it is obvious that the step signal of  $i_d$  does not interfere with  $i_q$ . So, the complex system is completely decoupled. The analysis proves that the decoupling method proposed in this paper is effective.

## 6 Conclusion

In this paper, a novel improved shunt active power filter (SHAPF) is presented to achieve the goal of reducing the harmonic distortion rate on the grid. The linearization and decoupling control of the improved SHAPF system model are realized using the generalized inverse system control method. The closed-loop controller for two decoupling current subsystems is designed by using linear system theory, which ensures the dynamic and static performance of the system. It turns out that the decoupling effect of the generalized inverse system is better than the traditional feedforward decoupling method and inverse system decoupling method, which can improve the power quality better. This method will be achieved in the practical application of the project for further research.

**Acknowledgements** The author is very grateful to the reviewer for his review of the manuscript and proposing valuable suggestions and supported by the National Natural Science Foundation of China, 51776015, Gansu Natural Science Foundation of China, 18JR3RA117 and the National Key Laboratory of Large Electric Drive Systems, SKLLDJ022016015.

## References

1. Jian L (2006) Research on SAPF based on cascade H-Bridge five-level converter. *Trans China Electrotech Soc* 21(2):79–83 (in Chinese)
2. Ying Z, Chong L (2011) Three-level H-Bridge cascade type multi-level inverter. *Trans China Electrotech Soc* 26(5):78–82 (in Chinese)
3. Zhi L, Li Z (2012) A novel three-phase-bridge cascaded PWM converter. *Power Syst Protect Control* 40(24):131–138 (in Chinese)
4. Xiu L (2014) Research on key techniques of cascaded H-Bridge static var generator. Hebei University of Technology, Hongqiao, pp 11–18 (in Chinese)
5. Farvar G, Hredzak B, Agelidis V (2015) Decoupled control system for cascaded H-bridge multilevel converter based STATCOMA. *IEEE Trans Industr Electron* 63(1):322–331
6. Serban I (2015) Power decoupling method for single-phase H-Bridge inverters with no additional power electronics. *IEEE Trans Industr Electron* 62(8):4805–4813
7. Bertoluzzo M, Buja G, Dashora H (2017) Design of DWC system track with unequal DD coil set. *IEEE Trans Transport Electrification* 3:380–391
8. Xin L (2013) Research on modeling of traction control system and control strategy based on train communication network. Lanzhou Jiaotong University of Automation, Lanzhou, pp 25–34 (in Chinese)
9. Wei L, Chun L (2013) Inverse system method based decoupling control of shunt hybrid active power filter. *Control Theory Appl* 30(9):1145–1152 (in Chinese)
10. Xin D (2004) Neural network inverse control method for multivariable nonlinear systems. Science Press, Beijing, pp 71–84 (in Chinese)
11. Gao H (2014) Study on static var generator based on cascade H-Bridge. Harbin University of Science and Technology, Nangang, pp 30–40 (in Chinese)
12. Tao L (2015) Research on APF based on cascaded H-bridge converter. China University of Mining, Beijing, pp 10–17 (in Chinese)
13. Wen L (2014) Research on active power filter based on cascaded H-Bridges. Shanghai Jiao Tong University, Shanghai, pp 23–41 (in Chinese)
14. Zhao W, Jin L (2015) Harmonic suppression and reactive power compensation, 3rd edn. China Machine Press, Beijing, pp 333–341 (in Chinese)
15. Aboulouifa A, Giri F, Lachkar I (2014) Cascade nonlinear control of shunt active power filters with average performance analysis. *Control Eng Practice* 26(1):211–221
16. Bo C (2003) Electric power drag automation control system-motion control system, 4th edn. China Machine Press, Beijing, p 65 (in Chinese)

# Research on Motor Bearing Fault Detection Method Based on Cyclic Autocorrelation Function Analysis



Peng Wang, Chidong Qiu, Xinbo Wu and Zhengyu Xue

**Abstract** In the case of motor bearing failure, aiming at the weak bearing fault characteristics in stator current, this paper takes advantage of the sensitivity of cyclic autocorrelation function for initial fault characteristics and proposes a motor bearing fault detection method based on cyclic autocorrelation function analysis. Firstly, according to the torque fluctuation model, the stator current expression of bearing outer raceway fault is deduced. Then, the current expression is added to the cyclic autocorrelation function, and the result shows that the proposed method can not only demodulate the fault characteristic frequency, but also the amplitude of the fault characteristic signal will be maximized by selecting the appropriate slicing position, which is beneficial to the fault identification. Finally, the experimental platform is built, and the fault characteristics are extracted effectively by using the proposed method, and its performance is obviously better than that of the traditional power spectrum analysis.

**Keyword** Induction motor · Bearing · Fault · Cyclic autocorrelation function

## 1 Introduction

Rolling bearings are key components of modern industrial equipment and one of the wearing parts. Therefore, it is very significant for condition monitoring of the motor bearings. In the research process of motor bearing fault diagnosis technology, diagnosis methods based on signal include: vibration, current, acoustic emission, stray flux and other methods [1]. Since most of the bearings are often subjected to environmental interference such as noise and vibration, causing detection signal at the initial stage of the failure unstable, then the current detection method is preferable in this case. For these reasons, the research on detecting bearing fault

---

P. Wang · C. Qiu (✉) · X. Wu · Z. Xue

College of Marine Electrical Engineering, Dalian Maritime University,  
Dalian 116026, China

e-mail: [qiuchidong@dltu.edu.cn](mailto:qiuchidong@dltu.edu.cn)

based on motor stator current signal has attracted more scholars, and a variety of effective detection methods have been proposed, such as using power spectrum to estimate the severity of the fault [2], discrete wavelet transform analysis signal [3] generalized likelihood ratio test [4], qualitative analysis combined with infrared thermography [5], using 1D convolutional neural network to extract fault features [6].

Due to the very low signal-to-noise ratio of the fault feature, if the ordinary power spectrum is used to process the current signal, the weak fault signal is often submerged in the strong background noise. And if the artificial intelligence technology is used, the detection depends heavily on the learning phase, which requires a large amount of different operating state data for training [4]. Based on cyclic autocorrelation function analysis, this paper reveals the nature of the initial fault and the weak fault features concealed in the noise, effectively demodulates the fault feature frequency from the current signal, and choosing the proper slice position can maximize the amplitude of fault feature signal, so as to effectively identify the fault.

## 2 Theoretical Analysis

### 2.1 Cyclic Autocorrelation Function

Bearing fault signal is a non-stationary signal characterized by periodic stability, which is called cyclic stationary signal [7]. The time-varying autocorrelation function of the cyclic stationary signal  $x(t)$  is defined as:

$$R_x(t, \tau) = E[x(t + \tau/2)x^*(t - \tau/2)] \quad (2.1)$$

where  $\tau$  is time delay,  $\tau = (\tau_1, \tau_2, \dots, \tau_{k-1})$ ,  $E[\cdot]$  is referred to as statistical expectation,  $*$  refers to taking conjugation.

For the second-order cyclic stationary signal, the time-varying autocorrelation function  $R_x(t, \tau)$  is expanded with Fourier series. Take the  $R_x(t, \tau)$  Fourier expanded coefficient, which can be expressed as  $R_I(\tau, \alpha)$ :

$$R_x(\tau, \alpha) = \frac{1}{T} \int_{-T/2}^{T/2} R_x(t, \tau) e^{-j2\pi\alpha t} dt \quad (2.2)$$

The  $\alpha = m/T$  is the cyclic frequency in formula (2.2), and  $T$  is the time-varying autocorrelation function period of the second-order cyclic stationary signal,  $m \in \mathbb{Z}$ .  $R_x(\tau, \alpha)$  is called a cyclic autocorrelation function, a binary function with respect to the time delay  $\tau$  and the cyclic frequency  $\alpha$  as variables. The second-order cyclo-stationary characteristic of the signal can be exhibited when the cycle frequency is non-zero.

## 2.2 The Effect of Torque Ripple on Stator Current

Blödt proposes that the resistance to the rolling element will change when it passes the fault point, and the load torque will fluctuate. The fluctuation frequency is the periodic pulse signal  $f_c$  [8]. The load torque equation is:

$$T_l(t) = T_0 + T_c \sin(\omega_c t) \quad (2.3)$$

Formula (2.3) only considers the fundamental component,  $T_l(t)$  is the total load torque,  $T_0$  is a constant torque,  $\omega_c$  is the angular frequency of the fault feature, and  $T_c$  is the amplitude of the motor load torque fluctuation caused by the bearing fault.

According to the torque equilibrium equation, the expression of the mechanical angle position of the rotor is:

$$\theta_r(t) = T_c \cos(\omega_c t) / (J\omega_c^2) + \omega_{r0}t \quad (2.4)$$

where  $J$  is the moment of inertia of the system;  $\omega_{r0}$  is the constant part of the angular frequency.

When the mechanical position of the rotor changes, the rotor magnetomotive force is affected. At this time, the rotor magnetomotive force in the stator coordinate system can be expressed as:

$$F_r^S(\theta, t) = F_r \cos[p\theta - \omega_s t - \beta \cos(\omega_c t)] \quad (2.5)$$

where  $F_r$  is the magnitude of the change in rotor magnetomotive force,  $p$  is the pole number of the motor,  $\omega_s$  is the angular frequency of the power supply, and  $\beta$  is the modulation index,  $\beta = T_c / (n\omega_c)^2$ .

Since the rotor magnetomotive force  $F_r$  affects the variation of the air gap flux density of the motor, the magnetic flux density  $B$  can be solved by Eq. (2.5), and then the surface integral is solved for  $B$ , and the magnetic flux  $\phi(t)$  is obtained, which is substituted into the stator voltage equation of the motor  $V(t) = RI(t) + d\phi(t)/dt$ , the stator current expression can be obtained:

$$I(t) = I_1 \sin[\omega_s t + \beta \cos(\omega_c t)] \pm I_2 \cos[\omega_s t + \beta \cos(\omega_c t) \pm \omega_c t] \quad (2.6)$$

It can be seen from Eq. (2.6) that the stator current of the bearing fault is a form of phase modulation, and superposition of fundamental and multi-frequency harmonics, where  $I_1$  represents the amplitude at the fundamental frequency and  $I_2$  represents the harmonic amplitude. When a pit-like fault occurs in the outer ring of the motor bearing, the stator current frequency is in the form of phase modulation of the modulation frequency by the power frequency as the carrier frequency and the fault characteristic frequency.

### 2.3 Characteristic Frequency Analysis in Current

The modulation index  $\beta$  is a value between (0, 0.1), so the influence of  $I_2$  can be ignored, and according to the Jacobi-Anger series  $e^{j\beta \sin \varphi} = \sum_{m=-\infty}^{\infty} J_m(\beta) e^{jm\varphi}$ , Eq. (2.6) can be simplified to obtain:

$$I(t) = I_1 J_k(\beta_1) \cos(\omega_s t + k\omega_c t) \quad (2.7)$$

Similarly,  $I(t + \frac{\tau}{2})$  and  $I^*(t - \frac{\tau}{2})$  can be obtained

$$I\left(t + \frac{\tau}{2}\right) = I_1 J_k(\beta_1) \cos(2\pi f_s t + \pi f_s \tau + 2k\pi f_c t + k\pi f_c \tau) \quad (2.8)$$

$$I^*\left(t - \frac{\tau}{2}\right) = I_1 J_h(\beta_1) \cos(2\pi f_s t - \pi f_s \tau + 2h\pi f_c t - h\pi f_c \tau) \quad (2.9)$$

where  $f_s$  represents the power frequency and  $f_c$  represents the fault characteristic frequency, which can be taken into Eq. (2.1) to obtain the time-varying autocorrelation function of the stator current expression when the motor bearing fails.

$$\begin{aligned} R_I(t, \tau) &= I_1^2 J_k(\beta_1) J_h(\beta_1) \cos(2\pi f_s t + \pi f_s \tau + 2k\pi f_c t + k\pi f_c \tau) \\ &\quad \times \cos(2\pi f_s t - \pi f_s \tau + 2h\pi f_c t - h\pi f_c \tau) \end{aligned} \quad (2.10)$$

Bring Eq. (2.10) into (2.2) and obtain the cyclic autocorrelation function expression of the stator current according to the trigonometric function prosthaphaeresis and the Euler's formula:

$$\begin{aligned} R_I(\tau, \alpha) &= \frac{1}{4T} I_1^2 J_k(\beta_1) J_h(\beta_1) \\ &\quad \int_{-\frac{T}{2}}^{\frac{T}{2}} \left[ e^{\pm j[2\pi f_s \tau + (k+h)f_c \tau]} h(t) + e^{\pm j[(k-h)\pi f_c \tau]} g(t) \right] dt \end{aligned} \quad (2.11)$$

In Eq. (2.11),  $h(t)$  and  $g(t)$  are:

$$h(t) = \cos[2(k-h)\pi f_c t \mp 2\pi \alpha t] + j \sin[2(k-h)\pi f_c t \mp 2\pi \alpha t] \quad (2.12)$$

$$\begin{aligned} g(t) &= \cos[4\pi f_s t + 2(k+h)\pi f_c t \mp 2\pi \alpha t] \\ &\quad + j \sin[4\pi f_s t + 2(k+h)\pi f_c t \mp 2\pi \alpha t] \end{aligned} \quad (2.13)$$

It can be seen from Eq. (2.11) that the bearing fault signal is an amplitude modulated signal with the frequency of the fault characteristic frequency multiplied as the modulation frequency, and the amplitude of the modulation frequency is

related to the coefficient developed by the Jacobi-Anger series. Solving the cyclic autocorrelation function is equivalent to slicing the  $R_I(\tau, \alpha)$ .

The real part of the cyclic autocorrelation function  $R_I(\tau, \alpha)$  represents the magnitude, and the imaginary part only represents its phase. In the actual bearing failure analysis, only the magnitude of its amplitude is considered. According to the periodic characteristics of the cosine function, only when  $\alpha = \pm(k - h)f_c$ , the result of  $h(t)$  in Eq. (2.12) is equal to 1, and the cyclic autocorrelation function  $R_I$  has a solution; similarly, only when  $\alpha = \pm[2f_s \pm (k + h)f_c]$ , the result of  $g(t)$  in Eq. (2.13) is equal to 1, and the function  $R_I$  has a solution. Equation (2.9) can be simplified as:

$$R_I(\tau, \alpha) = \begin{cases} 0 & \alpha = \text{Others} \\ \frac{1}{4T} I_1^2 J_k(\beta_1) J_h(\beta_1) e^{\pm j[(k-h)\pi f_c \tau]} & \alpha = \pm(k - h)f_c \\ \frac{1}{4T} I_1^2 J_k(\beta_1) J_h(\beta_1) e^{\pm j[2\pi f_s \tau + (k+h)\pi f_c \tau]} & \alpha = \pm[2f_s \pm (k + h)f_c] \end{cases} \quad (2.14)$$

The results of Eq. (2.14) reveal that the cyclic frequency of the frequency modulation signal caused by the bearing fault occurs mainly in the peak area of the two parts. On the one hand, the modulation frequency  $f_c$  of the fault and the frequency peak of its multiplication; on the other hand, side-frequency signal with amplitude of  $2f_s + f_c$ . Side-frequency signal is the modulation frequency with twice power carrier frequency as the center and characteristic frequency as the interval.

The cyclic autocorrelation function can effectively utilize the demodulation performance, separate the fault characteristic signal from the carrier signal, and retain the modulation characteristic of the original signal at twice carrier frequency. The cyclic autocorrelation function analysis method has the characteristics of intuitive analysis and can be used to verify each other by using the information of modulation and demodulation.

### 3 Experimental Validation

The fault detection platform of induction motor bearing built in this paper is composed of two parts: the motor drive system and the current signal acquisition system. The schematic diagram of the experimental platform is shown in Fig. 1.

Working principle of the experimental platform: Firstly, the three-phase alternating current is connected to the voltage regulator to facilitate the AC motor speed control by terminal voltage, so that the motor runs at the optimal detection speed. Then, the three-phase AC is passed through a three-phase bridge rectifier circuit, and the rectified AC is input to the IPM module. The PWM signal is generated by the FPGA to control the IPM peripheral drive, and the DC power is input to the induction motor after being inverted. Finally, The Hall sensor measures the motor running current of the faulty bearing installed, transmits the measurement signal to the NI data acquisition card, and analyzes the collected current signal in the host computer.

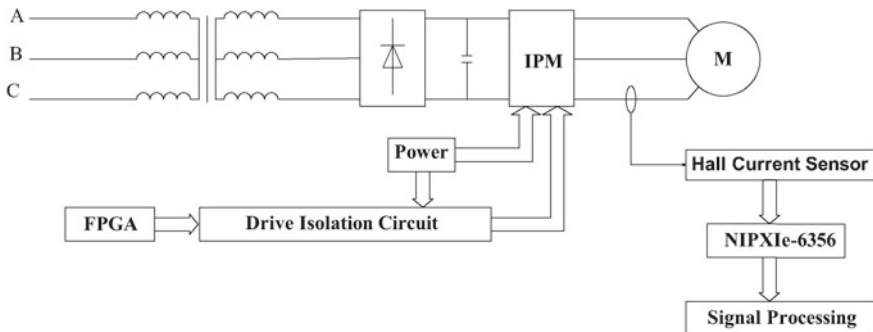


**Fig. 1** Experimental platform

The motor drive system of the experimental platform selects Mitsubishi's IPM, the model is PM75CL1A120, the rated current is 75 A, the maximum voltage AC is 400 V, the maximum switching frequency is 20 kHz, and the controller selects the FPGA of Intel company Altera's Cyclone IV series, the model is EP4CE15F17C8N.

The IT 60-S Hall Current sensor of LEM Company is adopted for current signal acquisition, with measurement range 0 to  $\pm 60$  A, and measurement accuracy  $\pm 3$  to  $\pm 12$  ppm.

The NIPXIE-6356 data acquisition card parameters are: 8 synchronous analog inputs, sampling rate 1.25 MS/s, digital converter resolution is 16 bits.

The motor parameters are: voltage is 380 V, current is 5.03 A, power is 2.2 kW, speed is 1430 r/min, number of pole-pairs is 2.

The fault bearing model is SKF6206, the number of balls is 9 and the pitch diameter is 46 mm, the diameter of the ball is 9.6 mm. The sparking machine is used to make pitting faults in the outer raceway. The bearing fault is shown in Fig. 2.

The collected stator current signal was analyzed in MATLAB. According to Ref. [9], the characteristic frequency of the bearing fault is obvious when the power

**Fig. 2** Outer raceway fault of bearing



supply frequency is 20 Hz. Therefore, this paper mainly chooses the power supply frequency of 20 Hz for verification analysis.

According to the above analysis process based on the cyclic autocorrelation function, the health bearing and the fault bearing are respectively installed on the motor for running measurement, the rotation speed is  $n = 591 \text{ r/min}$ . The collected stator current signal is analyzed by slicing, and the spectrum diagram of cyclic autocorrelation function is made by using fixed time delay  $\tau$ . A comparison of the current spectra of the two is shown in Fig. 3.

As shown in Fig. 3, the spectrum diagram of the bearing fault includes the power carrier frequency  $f_s$  and the multiplier, and the fault characteristic frequency  $f_c$  and the frequency multiplication demodulated by the cyclic autocorrelation function. And a frequency component  $2f_s \pm f_c$  means that the fault characteristic frequency and the even multiple of the power supply frequency  $f_s$  are mutually modulated. However, the current characteristic spectrum of the healthy bearing is similar to the variation trend of fault bearing, but it can also be seen that the frequency amplitude at  $f_c$  and  $2f_s - f_c$  is significantly higher than that of healthy bearing.

In this paper, the power spectrum is used to analyze the collected current signals. The frequency spectrum diagram is shown in Fig. 4.

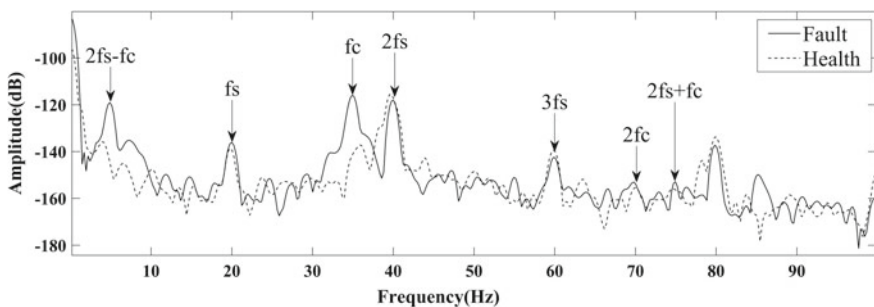


**Fig. 3** Comparison diagram of spectrum analysis of bearing fault and health

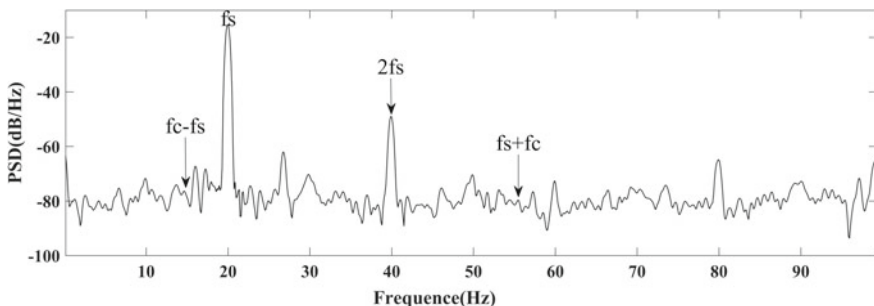


**Fig. 4** Bearing fault frequency spectrum diagram based on power spectrum PSD analysis

Comparison between Figs. 3 and 4 reflects that when the stator current signals with the same frequency, the same voltage and the same speed are used for data processing, the cyclic autocorrelation slice has great advantages over the traditional power spectrum analysis (PSD). In the PSD analysis spectrum, there is no obvious damaged frequency information, and the characteristic frequency is submerged in the noise harmonics.

## 4 Conclusion

For the stator current signal during motor bearing fault, the cyclic autocorrelation function slice analysis is carried out. The demodulated fault characteristic frequency can be observed effectively, which can avoid noise's impact on the side frequency. At the same time, the modulation signal with twice carrier frequency and fault characteristic frequency appearing in the spectrum has further verified the validity of cyclic autocorrelation function analysis.

**Acknowledgements** The research work was supported by National Natural Science Foundation of China under Grant No. 51279020. The support is greatly appreciated.

## References

- Tian J, Morillo C, Azarian MH, Pecht M (2016) Motor bearing fault detection using spectral kurtosis-based feature extraction coupled with k-nearest neighbor distance analysis. *IEEE Trans Ind Electron* 63(3):1793–1803
- Kang M, Kim J, Jeong IK, Kim JM, Pecht M (2016) A massively parallel approach to real-time bearing fault detection using sub-band analysis on an FPGA-based multicore system. *IEEE Trans Ind Electron* 63(10):6325–6335
- Ghods A, Lee HH (2016) Probabilistic frequency-domain discrete wavelet transform for better detection of bearing faults in induction motors. *Neurocomputing* 188:206–216
- Trachi Y, Elbouchikhi E, Choqueuse V, Benbouzid MEH, Wang TZ (2017) A novel induction machine fault detector based on hypothesis testing. *IEEE Trans Ind Appl* 53(3):3039–3048
- Picazo-Ródenas MJ, Antonino-Daviu J, Climente-Alarcon V, Royo-Pastor R, Mota-Villar A (2015) Combination of noninvasive approaches for general assessment of induction motors. *IEEE Trans Ind Appl* 51(3):2172–2180
- Ince T, Kiranyaz S, Eren L, Askar M, Gabbouj M (2016) Real-time motor fault detection by 1-D convolutional neural networks. *IEEE Trans Ind Electron* 63(11):7067–7075
- Chen J, Dong GM (2013) Cyclostationary theory and method for mechanical fault feature extraction. In: Hai S (ed) Shanghai Jiao Tong University Press, pp 40–43 (in Chinese)
- Blodt M, Jérémie R, Jean F (2009) Distinguishing load torque oscillations and eccentricity faults in induction motors using stator current Wigner distributions. *IEEE Trans Ind Appl* 45(6): 1991–2000
- Patela VN, Tandonb N, Pandey RK (2013) Vibration studies of dynamically loaded deep groove ball bearings in presence of local defects on races. *Procedia Eng* 64:1582–1591

# Double-Loop Control Strategy for Buck/Boost-CLLLC Two-Stage Bidirectional DC/DC Converter



Linghang Huang, Jie Chen, Ruichang Qiu and Zhigang Liu

**Abstract** This paper adopts Buck/Boost and CLLLC cascade topology. Buck/Boost-CLLLC two-stage bidirectional DC/DC converter topology and its control strategy are suitable for medium and high-power applications with large fluctuation range of input voltage and bidirectional flow of power and have the advantages of wide input voltage range and high efficiency. Aiming at Buck/Boost-CLLLC two-stage bidirectional DC/DC converter, the working principle of bidirectional Buck/Boost converter and bidirectional CLLLC resonant converter is analyzed. The small-signal model of bidirectional Buck/Boost converter and bidirectional CLLLC resonant converter is built. A dual-loop control strategy for two-stage DC/DC converter is proposed, and a dual-loop controller is designed. Finally, the simulation model is built to verify. The validity of double-loop control strategy of Buck/Boost-CLLLC two-stage bidirectional DC/DC converter in wide input voltage range is verified. And the bidirectional power flow of Buck/Boost-CLLLC two-stage bidirectional converter is verified.

**Keywords** Bidirectional DC/DC converter · Bidirectional buck/boost converter · Bidirectional CLLLC resonant converter · Double-loop control

---

L. Huang (✉) · J. Chen · R. Qiu · Z. Liu

School of Electrical Engineering, Beijing Engineering Research Center of Electric Rail Transportation, Beijing Jiaotong University, Beijing 100044, China  
e-mail: [17121441@bjtu.edu.cn](mailto:17121441@bjtu.edu.cn)

J. Chen  
e-mail: [jiechen@bjtu.edu.cn](mailto:jiechen@bjtu.edu.cn)

R. Qiu  
e-mail: [rchqiu@bjtu.edu.cn](mailto:rchqiu@bjtu.edu.cn)

Z. Liu  
e-mail: [zhgliu@bjtu.edu.cn](mailto:zhgliu@bjtu.edu.cn)

## 1 Introduction

With the wide application of high-power bidirectional DC/DC converters in rail transit, the research of bidirectional DC/DC converters has become a hot spot. Common bidirectional DC/DC converters are divided into two types: non-isolation and isolation. Non-isolated bidirectional DC/DC converters [1, 2] include Buck/Boost, Boost/Buck, Cuck, Zera, etc. Isolated bidirectional DC/DC converters [3–5] include bidirectional forward and flyback DC/DC converters, bidirectional push-pull DC/DC converters, bidirectional half-bridge DC/DC converters, bidirectional full-bridge DC/DC converters, etc.

In this paper, the Buck/Boost and CLLLC cascade topology is adopted. The open-loop frequency-fixed control strategy is adopted for the rear CLLLC resonant converter. The output voltage of the DC/DC converter is adjusted by controlling the duty cycle of the front Buck/Boost converter. Buck/Boost-CLLLC two-stage bidirectional DC/DC converter topology and its control strategy are suitable for medium- and high-power applications with large fluctuation range of input voltage and bidirectional power flow.

## 2 Topology and Working Principle of Buck/Boost-CLLLC Two-Stage Bidirectional Converter

### 2.1 Topological Structure

The topology of two-stage bidirectional DC/DC converter is shown in Fig. 1. In the main circuit structure,  $T_1-T_2$  is two switching transistors of Buck/Boost converter;  $S_1-S_8$  is eight switching transistors of CLLLC resonant converter;  $D_{S1}-D_{S8}$  are anti-parallel parasitic diodes of switching transistors;  $C_1-C_8$  are parasitic capacitors of switching transistors;  $V_1$  is DC bus side voltage;  $V_2$  is battery side voltage. The first stage is Buck/Boost converter and the second stage is CLLLC resonant converter. Two-stage bidirectional DC/DC converter is connected with 375 V DC bus (voltage fluctuation range is 250–500 V) and 110 V battery.

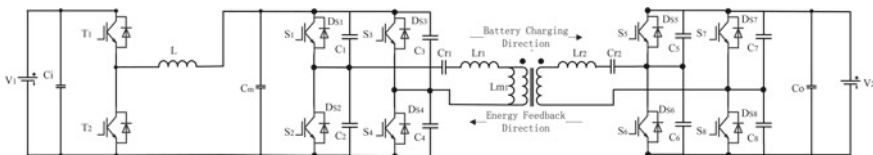


**Fig. 1** Buck/Boost-CLLLC two-stage bidirectional DC/DC converter

## 2.2 Working Principle

**Working Principle of Bidirectional Buck/Boost Converter.** When the bidirectional DC/DC converter absorbs energy, the bidirectional Buck/Boost converter operating in Buck mode controls the energy flow from the DC bus to the battery. The equivalent circuit is shown in Fig. 2. In this case, the bidirectional Buck/Boost converter can be equivalent to a Buck converter.

When the bidirectional DC/DC converter releases energy, bidirectional DC/DC converter controls battery discharge, and bidirectional Buck/Boost converter operating in Boost mode controls energy flow from battery to DC bus. The equivalent circuit is shown in Fig. 3.

**Working Principle of Bidirectional CLLLC Converter.** The main circuit structure of the bidirectional CLLLC resonant converter is completely symmetrical. When the bidirectional DC/DC converter absorbs energy, the CLLLC resonant converter works in the forward mode. When the bidirectional DC/DC converter releases energy, the CLLLC resonant converter works in the reverse mode. The CLLLC resonant converter has two resonant frequencies, and its working process is divided into three working states: resonant working point ( $f_s = f_{r1}$ ), super-resonant region ( $f_s > f_{r1}$ ) and sub-resonant region ( $f_{r2} < f_s < f_{r1}$ ).

**Fig. 2** Buck mode equivalent circuit diagram

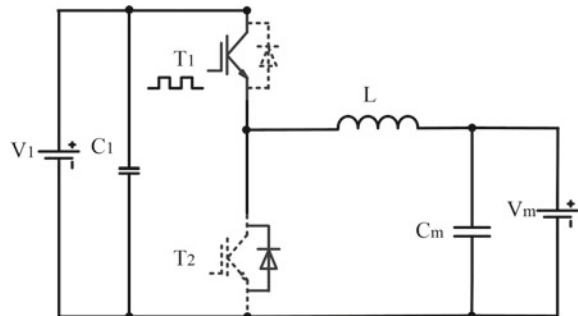
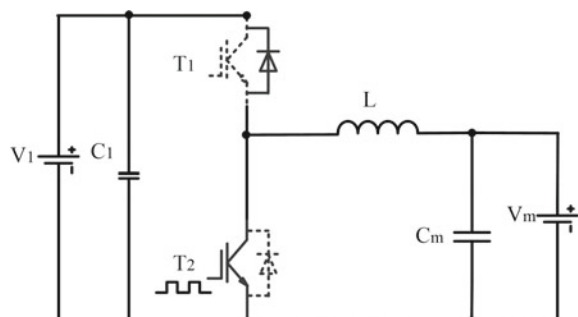


**Fig. 3** Boost mode equivalent circuit diagram



The two resonant frequencies are respectively:

$$f_{r1} = \frac{1}{2\pi\sqrt{L_{r1}C_{r1}}} \quad (1)$$

$$f_{r2} = \frac{1}{2\pi\sqrt{(L_{r1} + L_m)C_{r1}}} \quad (2)$$

$f_s$  is switching frequency. When the switching frequency operates in the sub-resonant region and the resonant operating point, that is  $f_{r2} < f_s \leq f_{r1}$ , the converter can realize ZVS of the power switches and ZCS of the rectifier parasitic diodes, which reduces the switching loss.

### 3 Small-Signal Modeling and Double-Loop Control Strategy of Buck/Boost-CLLLC Two-Stage Converter

When two-stage bidirectional DC/DC converter works in forward mode, the converter is equivalent to Buck-CLLLC two-stage converter; when the converter works in reverse mode, the converter is equivalent to CLLLC-Boost two-stage converter.

#### 3.1 Small-Signal Modeling and Double-Loop Control Strategy of Buck-CLLLC Two-Stage Converter

**Small-Signal Modeling of Buck Converter.** According to the state space averaging method [1, 6], it is easy to deduce the small-signal model and transfer function of Buck converter. The transfer function of output capacitor voltage to duty cycle of Buck converter is:

$$G_{vd\_bck}(s) = \frac{\hat{v}_m}{\hat{d}} = \frac{V_1}{LC_m s^2 + \frac{L}{Z_{LLC}} s + 1} \quad (3)$$

$$G_{i_L d}(s) = \frac{\hat{i}_L}{\hat{d}} = \frac{V_1(sC_m + \frac{1}{Z_{LLC}})}{LC_m s^2 + \frac{L}{Z_{LLC}} s + 1} \quad (4)$$

Among them,  $V_1$  is the DC bus side voltage,  $C_m$  is the output capacitance of Buck converter,  $L$  is the inductance of Buck converter, and  $Z_{LLC}$  is the input impedance of the later stage converter.

**Small-Signal Modeling of CLLLC Resonant Converter.** The method is used to build the small-signal model of CLLLC resonant converter, according to Refs. [7, 8].

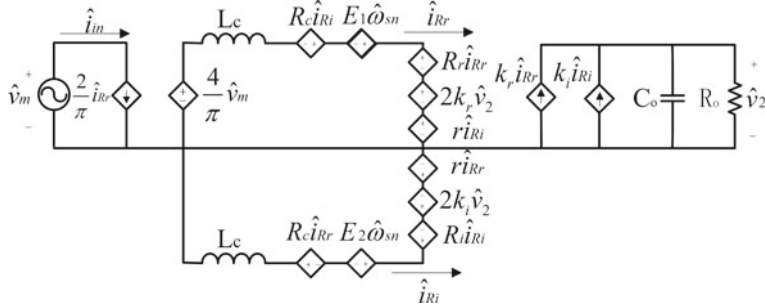


**Fig. 4** Third-order small-signal model of CLLLC resonant converter

The third-order small-signal model of CLLLC resonant converter can be obtained, as shown in Fig. 4.

According to the third-order small-signal model of CLLLC resonant converter, the expressions of input voltage to output voltage transfer function and input impedance of CLLLC resonant converter are as follows.

$$G_{vg\_LLC}(s) = \frac{\hat{v}_2}{\hat{v}_m} = \frac{4R_o(k_rR_{eq} - k_iR_c + k_lL_c s)}{\pi[L_c^2R_oC_o s^3 + L_c(L_c + R_{eq}R_oC_o)s^2 + (2L_cR_{eq} + R_c^2R_oC_o)s + (R_{eq}^2 + R_c^2)]} \quad (5)$$

$$Z_{LLC}(s) = \frac{\pi^2[L_c^2R_oC_o s^3 + L_c(L_c + R_{eq}R_oC_o)s^2 + (2L_cR_{eq} + R_c^2R_oC_o)s + (R_{eq}^2 + R_c^2)]}{8L_cR_oC_o s^2 + 8(L_c + R_iR_oC_o)s + 8R_{eq}} \quad (6)$$

**Double-loop Control Strategy of Buck-CLLLC Two-Stage Converter.** The double-loop control block diagram of Buck-CLLLC two-stage converter is shown in Fig. 5. The two-stage converter adopts double-loop control strategy, the output voltage of CLLLC resonant converter is used as voltage outer loop, the inductance current of Buck converter is used as current inner loop, and the CLLLC resonant converter adopts fixed-frequency open-loop control strategy.

Current loop PI controller parameters:

$$G_{ic}(s) = k_{ip} + \frac{k_{ii}}{s} = 1.182 \times 10^{-2} + \frac{9.8}{s} \quad (7)$$

After adding the current loop controller, the system's traversing frequency is 2 kHz, the phase margin is 88.5%, the amplitude margin is infinite, and the system is stable. Voltage loop PI controller parameters:

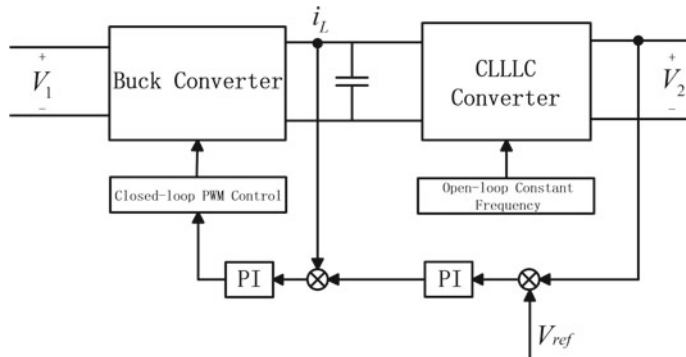


**Fig. 5** Double-loop control block diagram of Buck-CLLLC two-stage converter

$$G_{vc}(s) = k_{vp} + \frac{k_{vi}}{s} = 0.459 + \frac{380.2}{s} \quad (8)$$

The open-loop transfer function  $G_{vo}$  of the system before adding the controller, the transfer function  $G_{vc}$  of the controller, and the open-loop transfer function  $G_v$  of the system after adding the controller are shown in Fig. 6. After adding the voltage loop controller, the system's traversing frequency is 100.8 Hz, the phase margin is 107%, and the amplitude margin is 30.9 dB. The system is stable.

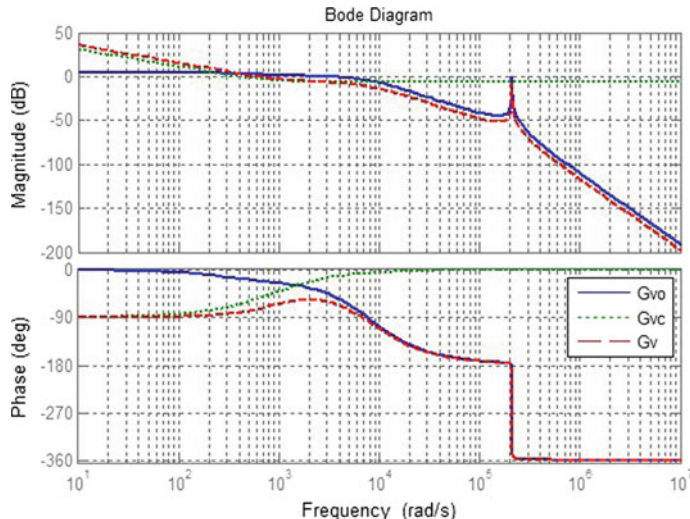


**Fig. 6** Bode diagram of Buck-CLLLC two-stage converter control system

### 3.2 Small-Signal Modeling and Double-Loop Control Strategy of CLLLC-Boost Two-Stage Converter

**Small-Signal Modeling of Boost Converter.** According to the state space averaging method [1, 6], it is easy to deduce the small-signal model and transfer function of Boost converter. The transfer function of output capacitor voltage to duty cycle of Boost converter is:

$$G_{vd\_boost}(s) = \frac{\hat{V}_1}{\hat{d}} = \frac{(1 - D)V_1 - sLI_L}{LC_i s^2 + \frac{L}{R_i} s + (1 - D)^2} \quad (9)$$

The transfer function of inductance current to duty cycle of Boost converter is:

$$G_{i_L d}(s) = \frac{\hat{i}_L}{\hat{d}} = \frac{V_1 \left( \frac{2}{R_i} + sC_i \right)}{LC_i s^2 + \frac{L}{R_i} s + (1 - D)^2} \quad (10)$$

Among them,  $V_1$  is DC bus side voltage,  $C_i$  is DC bus side capacitance,  $L$  is Boost converter inductance,  $R_i$  is DC bus side equivalent resistance.

**Double-loop Control Strategy of CLLLC-Boost Two-Stage Converter.** The double-loop control block diagram of CLLLC-Boost two-stage converter is shown in Fig. 7. Two-stage converter adopts double-loop control strategy, the output voltage of Boost converter is used as voltage outer loop, the inductance current of Boost converter is used as current inner loop, and CLLLC resonant converter adopts fixed-frequency open-loop control strategy.

The Bode diagram of the open-loop transfer function  $G_{vo}$  of the system before adding the controller, the transfer function  $G_{vc}$  of the controller and the open-loop transfer function  $G_v$  of the system after adding the controller are shown in Fig. 8.

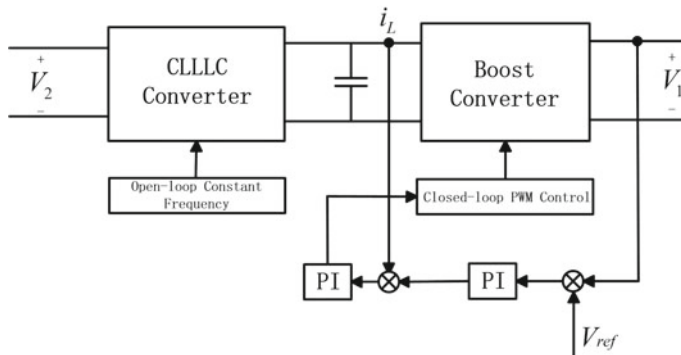


**Fig. 7** Double-loop control block diagram of CLLLC-Boost two-stage converter

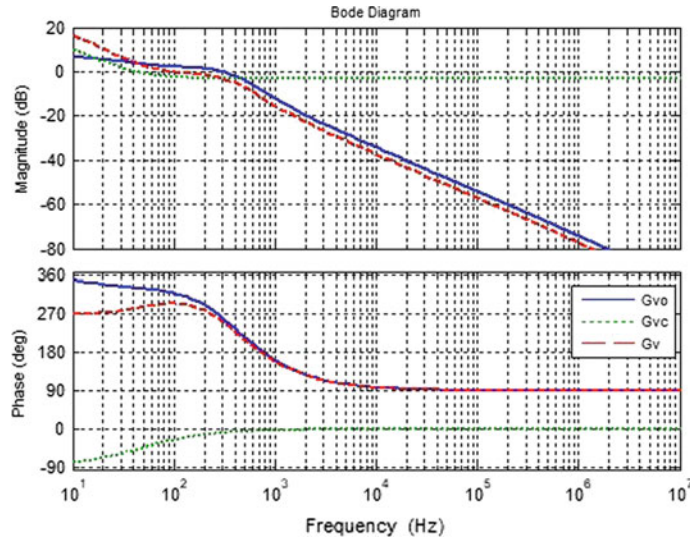


**Fig. 8** Bode diagram of CLLLC-boost two-stage converter control system

After adding voltage and current loop controller, the system's traversing frequency is 99 Hz, phase margin is 114%, and amplitude margin is 11.5 dB. The system is stable.

Current loop PI controller parameters:

$$G_{ic}(s) = k_{ip} + \frac{k_{ii}}{s} = 1.322 \times 10^{-2} + \frac{3.8}{s} \quad (11)$$

Voltage loop PI controller parameters:

$$G_{vc}(s) = k_{vp} + \frac{k_{vi}}{s} = 0.694 + \frac{199.5}{s} \quad (12)$$

## 4 Simulation Verification

A simulation model is built to verify the proposed dual-loop control strategy for two-stage bidirectional DC/DC converter and the bidirectional power flow of two-stage bidirectional DC/DC converter. The simulation parameters are follows: DC bus voltage is 375 V(250–500 V), converter output voltage is 110 V, inductance of Buck/Boost converter is 400  $\mu$ H, switching frequency of Buck/Boost converter is 20 kHz, turn ratio of transformer is 15/11, magnetizing inductance is 4.9  $\mu$ H, primary side resonant inductor is 0.49  $\mu$ H, secondary-side resonant inductor is 0.265  $\mu$ H, primary resonant capacitor is 5.175  $\mu$ F, secondary-side

resonant capacitor is 9.57  $\mu\text{F}$ , switching frequency of CLLLC resonant converter is 100 kHz.

#### 4.1 Forward Working Mode Simulation

In Fig. 9a, it can be seen that the power switches realize zero voltage switching on (ZVS). In Fig. 9b, it can be seen that the diodes achieve zero current switching off (ZCS). In Fig. 9c, the resonant inductance currents of the primary and secondary sides are approximately sinusoidal, and the CLLLC resonant converter achieves resonant operation. In Fig. 9d, it can be seen that when the input voltage (DC bus side voltage  $V_1$ ) is 375 V, the output voltage (battery side voltage  $V_2$ ) of the two-stage converter is stable at 110 V, and the output voltage ripple is 0.9%, which meets the requirements.

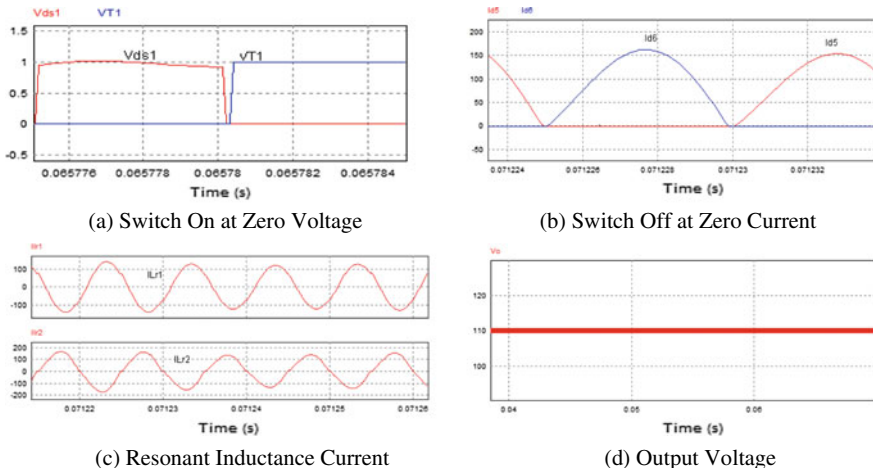


**Fig. 9** Waveform diagram of forward working mode simulation

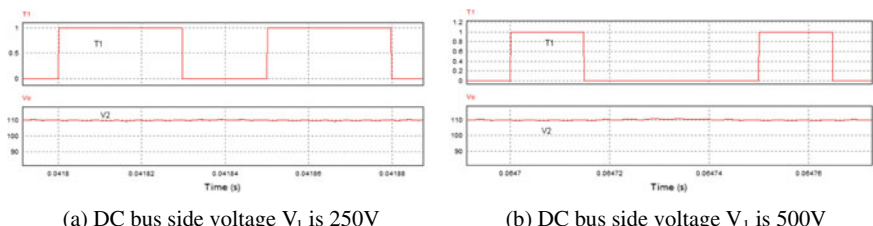


**Fig. 10** Simulation of output voltage waveform in forward mode

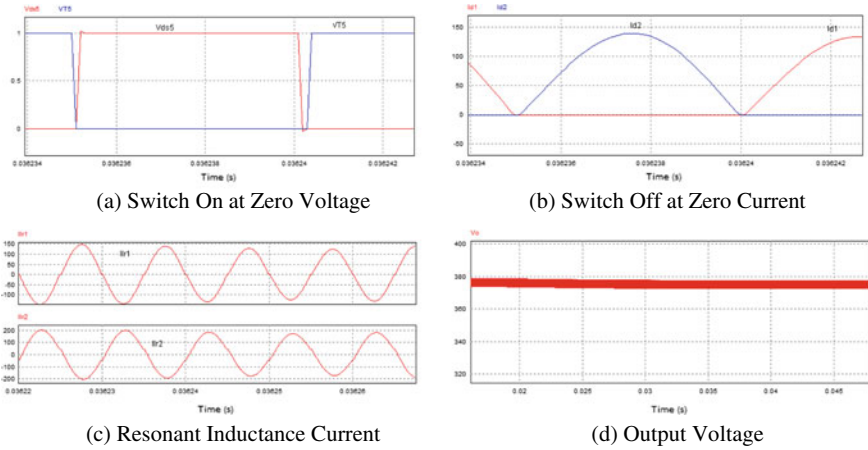


**Fig. 11** Waveform diagram of reverse working mode simulation

In Fig. 10, when the input voltage (DC bus side voltage  $V_1$ ) changes, the output voltage waveform of the two-stage converter can be kept unchanged by adjusting the duty cycle of the power switch of the Buck converter. It can be verified that the two-stage converter double-loop control strategy is correct in wide input voltage range.

## 4.2 Reverse Mode Simulation

In Fig. 11a, it can be seen that the power switches realize zero voltage switching on (ZVS). In Fig. 11b, it can be seen that the diodes achieve zero current switching off (ZCS). In Fig. 11c, the resonant inductance currents of the primary and secondary sides are approximately sinusoidal, and the CLLLC resonant converter achieves resonant operation. In Fig. 11d, it can be seen that when the input voltage (battery side voltage  $V_2$ ) of the two-stage converter is 110 V, the output voltage (DC bus side voltage  $V_1$ ) is stable at 375 V, and the output voltage ripple is 0.8%, which meets the requirements.

## 5 Conclusion

This paper introduces the small-signal modeling of Buck/Boost-CLLLC two-stage bidirectional converter, proposes a dual-loop control strategy for wide input voltage range Buck/Boost-CLLLC two-stage bidirectional converter, and designs a dual-loop controller. The simulation model is built to verify the correctness of the

double-loop control strategy of Buck/Boost-CLLLC two-stage bidirectional converter in wide input voltage range, and the bidirectional power flow of Buck/Boost-CLLLC two-stage bidirectional converter is verified.

**Acknowledgements** This work is supported by the National Key Research and Development Program (2016YFB1200502-04).

## References

1. Liu C, Zhang X, Jiang TY, Wang FS (2017) Buck-LLC two-stage DC/DC converter dual-loop frequency control strategy. *Power Electron Technol* 51(10):11–13 (in Chinese)
2. Luo Y (2013) Research on bidirectional DC/DC converter and battery energy management system. Huazhong University of Science and Technology (in Chinese)
3. Chung SH, Cheung WL, Tang KS (2004) A ZCS bidirectional flyback DC/DC converter. *IEEE Trans Power Electron* 19(6):1426–1434
4. De Souza EV, Barbi I (2011) Bidirectional current-fed flyback-push-pull DC-DC converter. In: 2011 Brazilian Power Electronics Conference (COBEP), IEEE, pp 8–13
5. Daneshpajoh H, Bakhshai A, Jain P (2011) Optimizing dual half bridge converter for full range soft switching and high efficiency. In: 2011 Energy Conversion Congress and Exposition (ECCE), IEEE, pp 1296–1301
6. Zhou GH, Xu JP, Wu SR (2016) Modeling, analysis and control of switching converters. Science Press, Beijing (in Chinese)
7. Tian KZ (2016) Research on LLC Resonant bidirectional full bridge DC/DC converter. Yanshan University (in Chinese)
8. Zhou GJ (2016) Research on multi-module input-series-output parallel system based on Boost + LLC resonant converter. Huazhong University of Science and Technology (in Chinese)

# Research on Motor Bearing Fault Detection Method Based on Teager–Kaiser Energy Operator



Yuan Gao, Chidong Qiu, Changqing Xu and Zhengyu Xue

**Abstract** For the weak fault characteristics in the external stray magnetic field when the motor bearing faults, this paper proposes a fault detection method based on Teager–Kaiser energy operator. Firstly, it is theoretically analyzed that the application of the Teager–Kaiser energy operator to the stray magnetic field can not only demodulate the fault characteristic frequency, but also enhance the amplitude of the weak fault characteristic frequency, thereby improving the fault detection capability. Experimental test with artificial bearing defect was conducted by measuring stray magnetic field; the experimental results verify that the proposed method can effectively extract weak fault features in stray magnetic field.

**Keywords** Induction motor · Bearing · Stray magnetic field · Teager–Kaiser energy operator

## 1 Introduction

Among all machine fault causes, the bearing fault ratio is about 35–55% [1, 2]. Immovilli proposed the bearing fault is up to 90% for small machines [3]. Therefore, fault detection, especially at the beginning of fault, is particularly important to avoid complete damage or even unexpected downtime.

Bellini et al. divided the fault detection method into five different methods: temperature detection, mechanical vibration detection, chemical detection, partial discharge detection, and electrical characteristic detection [4]. Electrical characteristic detection is widely used also typical electrical quantities include current, magnetic flux, and electromagnetic torque. Compared with motor current signal

---

Y. Gao · C. Qiu (✉) · C. Xu · Z. Xue  
College of Marine Electrical Engineering, Dalian Maritime University,  
Dalian 116026, China  
e-mail: [qiuchidong@dltu.edu.cn](mailto:qiuchidong@dltu.edu.cn)

analysis (MCSA), although stray magnetic field analysis cannot distinguish different faults such as eccentricity in some cases, it is more sensitive, reliable, and robust and does not appear that assembling, disassembling, reassembling, and debugging the motor may change the current spectrum [5]. So it is more suitable for initial fault detection of induction motors.

In recent years, some studies have focused on external magnetic field measurements to detect faults in low and medium power motors [6]. The analysis results show that the characteristic frequency cannot be seen in the current magnetic field spectrum [7]. On the contrary, only the harmonic components with lower amplitude (side frequency) can be seen, which is easily submerged in the clutter. In the actual measurement, the collected motor external magnetic field signal is surrounded by a high noise background. For the identification of weak characteristic signals in the background of strong noise, the Teager–Kaiser energy operator is applied to the stray magnetic field. The method based on Teager–Kaiser energy operator can directly observe the fault characteristic frequency from spectrogram. Besides, the method can also improve the signal-to-noise ratio of fault characteristics.

## 2 Theoretical Analysis

### 2.1 Stray Magnetic Field for Motor Bearing Fault

There are studies have shown that the motor air-gap length variations and torque vibrations are the two most obvious effects of motor bearing faults [8]. Schoen considers that the bearing fault will vary the motor air-gap length, which will cause the magnetomotive force of the motor to be amplitude modulated [9]. Blodt considers that the bearing fault will cause the motor torque vibration, which will lead to the magnetomotive force of the motor to be phase modulated [10]. Trajin has experimentally demonstrated that a single-point defect mainly causes torque vibration [11]. This paper will refer the torque vibration model proposed by Blodt to deriving the stray magnetic field characteristic frequency at an outer bearing raceway defect.

Under a bearing fault, the load torque as a function of time can be described by a constant component  $\Gamma_0$  and an additional component varying at the characteristic frequency  $f_c$  [10]. For simplification, only the fundamental term is considered. So, the load torque after Fourier series expansion can be expressed as:

$$\Gamma_{\text{Load}}(t) = \Gamma_0 + \Gamma_c \cos(\omega_c t) \quad (1)$$

where  $\Gamma_c$  is the amplitude of the bearing fault-related torque variations, and  $\omega_c = 2\pi f_c$  is the vibration characteristic frequency of the bearing fault.

The transformation between the rotor and stator reference frames is defined by

$$\theta' = \theta - \frac{\omega_s(1-s)}{p}t - A_c \cos(\omega_c t) \quad (2)$$

where  $\theta'$  is the mechanical angle in the rotor reference frame,  $\omega_s$  is supply frequency,  $s$  is the motor slip rate,  $p$  is pole pairs,  $A_c = \Gamma_c / (J\omega_c^2)$  is the amplitude of the angle variations,  $J$  is the total inertia of the system machine load. So, the rotor magnetomotive force in the stator reference coordinate system is

$$F_r(\theta, t) = F_r \cos(p\theta - \omega_s t - \beta_1 \cos(\omega_c t)) \quad (3)$$

where  $F_r$  is the amplitude of the rotor magnetomotive force,  $\beta_1 = pA_c$  represents the modulation index.

According to  $B = F\Lambda$ , assuming that the air-gap length and magnetic permeance  $\Lambda$  are constant, i.e.,  $\Lambda = \Lambda_0$ , the expression of the magnetic field induced by the rotor fundamental magnetomotive force at the end of the stator winding is:

$$B(\theta, t) = F_r(\theta, t)\Lambda_0 = F_r\Lambda_0 \cos(p\theta - \omega_s t - \beta_1 \cos(\omega_c t)) \quad (4)$$

And then it is expanded into a Fourier series by the first Bessel function, ignoring the rotor angular frequency, which is simplified as follows:

$$B(t) = B_0 \cos(\omega_s t + \theta) + \frac{1}{2}\beta_1 B_0 (\cos((\omega_s + \omega_c)t + \theta) + \cos((\omega_s - \omega_c)t + \theta)) \quad (5)$$

where  $B_0 = F_r\Lambda_0$ .

## 2.2 Analysis for Stray Magnetic Field Characteristics Based on Teager–Kaiser Energy Operator

The Teager–Kaiser energy operator was originally used to track the energy of a linear undamped oscillator by using its modulation [12]. Later, this method was also widely used in communications, bearing faults detection, etc. This paper will refer to the torque vibration model, the TKEO algorithm is used to demodulate the magnetic field signal, improve the traditional power spectrum analysis, and extract the weak characteristic frequency from the magnetic field signal [13]. On the other hand, the proposed method will strengthen its amplitude and improve the variability of the fault characteristic frequency.

The continuous form of the TKEO applied to the continuous time signal  $x(t)$  is

$$\psi(x(t)) = \dot{x}(t)^2 - x(t) \cdot \ddot{x}(t) \quad (6)$$

where  $\dot{x}(t) = dx/dt$ ,  $\ddot{x}(t) = d^2x/dt^2$ .

The TKEO applied to discrete signals (such as the sampling motor magnetic field) is

$$\psi(x[n]) = x[n]^2 - x[n-1] \cdot x[n+1] \quad (7)$$

Under the disturbance of the periodic fault signal, such as the bearing outer raceway fault, apply (6) to the fault magnetic field signal (5),  $\beta_1 \ll 1$ , so  $\beta_1^2$  is a smaller number, then the term containing  $\beta_1^2$  is ignored

$$\begin{aligned} \psi(B(t)) &\approx B_0^2 \omega_s^2 + \frac{1}{2} B_0^2 \beta_1 (4\omega_s^2 + \omega_c^2) \cos(\omega_c t) \\ &+ \frac{1}{2} B_0^2 \omega_s^2 \beta_1 [\cos((2\omega_s - \omega_c)t + 2\theta) + \cos((2\omega_s + \omega_c)t + 2\theta)] \end{aligned} \quad (8)$$

where  $\omega_c = 2\pi f_o$ ,  $f_o$  is determined by the fault type. This paper studies an outer raceway defect of the induction motor bearing, so

$$f_o = \frac{1}{2} N_b \left( 1 - \frac{D_b}{D_c} \cos \beta \right) f_r \quad (9)$$

In (9),  $\beta$  is the contact angle,  $f_r = n/60$ ,  $n$  is the motor rotation speed,  $N_b$  is the number of ball,  $D_b$  is the diameter of ball, and  $D_c$  is the pitch or cage diameter of ball. In (8), compared to the amplitude of the main magnetic field, the fault harmonics is very low due to the modulation component  $\beta_1$ . In order to suppress the influence of the supply harmonic (the constant term) in (8) on the analysis, the equation is normalized to lead to a new signal  $B_{TK}(t)$  as

$$B_{TK}(t) = \frac{\psi(B(t)) - \overline{\psi(B(t))}}{\overline{\psi(B(t))}} \quad (10)$$

Replacing (8) in (10), the original signal  $B(t)$  becomes:

$$\begin{aligned} B_{TK}(t) &\approx \frac{1}{2} \left( 4 + \left( \frac{\omega_c}{\omega_s} \right)^2 \right) \beta_1 \cos(\omega_c t) \\ &+ \frac{1}{2} \left( \frac{\omega_c}{\omega_s} \right)^2 \beta_1 [\cos((2\omega_s - \omega_c)t + 2\theta) + \cos((2\omega_s + \omega_c)t + 2\theta)] \end{aligned} \quad (11)$$

By analyzing the previous theoretical results, a demodulated characteristic frequency and the sideband components can be seen in (11). In addition, the amplitude of the characteristic frequency is obviously enhanced. The instantaneous frequency of the signal can be given by deriving the phase in (11)

$$f_B = f_c \text{ or } f_B = 2f_s \pm f_c \quad (12)$$

where  $f_c$  is the vibration characteristic frequency of an outer bearing raceway defect,  $f_s$  is the power supply frequency,  $f_B$  is the magnetic field characteristic frequency of an outer bearing raceway defect. In the  $B_{TK}(t)$ , the characteristic frequency is demodulated. On the contrary, in the original signal  $B(t)$  only contains the sideband components. Theoretically, this method improves the legibility of the fault characteristic frequency.

### 3 Experimental Results

According to the literature [14], when the power supply frequency is 20 Hz, the characteristic frequency of the bearing fault is obvious. Based on the conditions required for the measurement, the experimental platform of induction motor bearing fault detection is built in laboratory.

The experimental platform consists of two parts: the motor control system and the data acquisition system. The schematic diagram of the experimental platform is shown in Fig. 1.

The equipment parameters of experimental platform:

Induction motor: power 2.2 kW, rated voltage 380 V, frequency 50 Hz, rated current 5.03 A, rated speed 1450 r/min, pole pairs 2.

The FPGA is EP4CE15F17C8N; The IPM is PM75CL1A120: rated current 75 A, maximum voltage 400 V, maximum switching frequency 20 kHz.

The magnetic sensor is HMC6042: working voltage 2.7 to 3.6 V, magnetic field range -6 to 6 Oe, resolution 0.12 milligauss (RMS), sensitivity 0.8 to 1.25 mV/V/gauss.

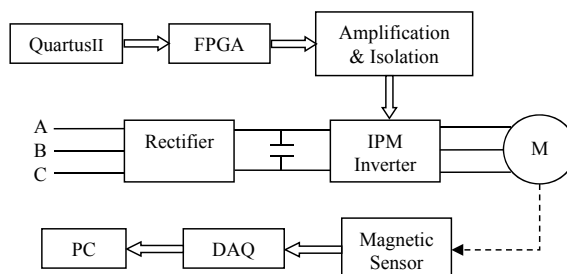


**Fig. 1** Experimental platform



**Fig. 2** Photograph of bearings with an outer raceway single-point defect

The data acquisition (DAQ) device is mainly composed of LabVIEWs NI PXIe-1071, data acquisition card NI PXIe-6356 and embedded controller NI PXIe-8135. It can implement the acquisition, conversion and storage of signal data. Its digital-to-analog conversion accuracy is 16 bits.

Use the electric spark drilling machine to create a single-point defect on the outer raceway of the 6206 bearing, as shown in Fig. 2.

Based on the above experimental platform, the power supply frequency is set at 20 Hz by the FPGA; meanwhile, the actual speed is 596 r/min. The magnetic field signal under a single-point defect of the bearing outer raceway is measured and collected. According to the bearing parameters, the characteristic frequency is  $f_c \approx 35$  Hz based on Eq. (9).

Applying the proposed method to spectral estimate, the fault signal is shown in the solid line in Fig. 3. The characteristic frequency 35 Hz and the sideband components 5, 75 Hz can be clearly seen Fig. 3. However, it must be noted that the

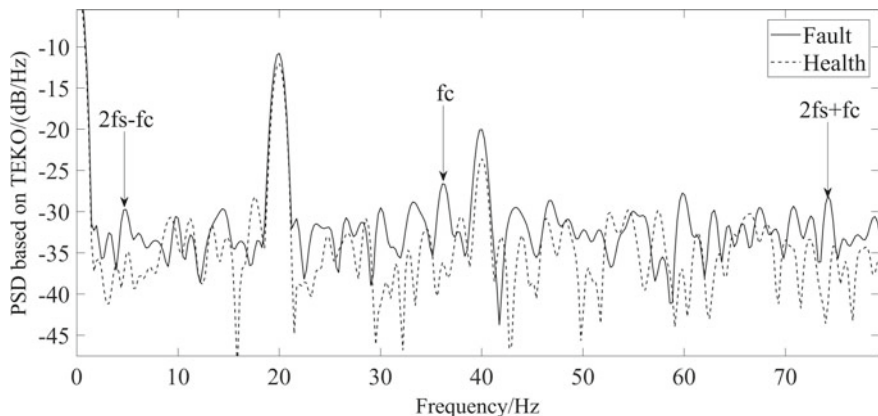


**Fig. 3** Comparison diagram of fault and health bearing based on TKEO

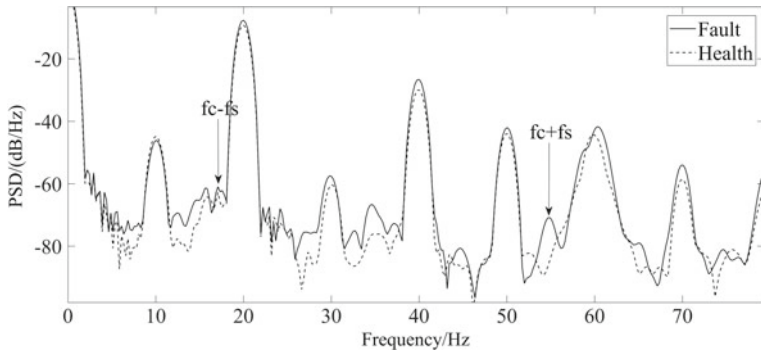


**Fig. 4** Comparison diagram of fault and health bearing based on traditional PSD

amplitude is obviously higher than the clutter. Therefore, the proposed method not only successfully demodulates the fault characteristic frequency, but also strengthens the amplitude of the characteristic frequency.

In the same way, the spectral estimation results of the healthy bearing are shown in the dotted line of Fig. 3. Comparing the fault and health, the amplitude of the fault is obviously higher at the characteristic frequency  $f_c$ , which proves the correctness of the method from experiments. And it also shows the same result at the two sideband components. So, the experimental results have validated the previous theoretical results.

For the same data, results of traditional PSD analysis are shown in Fig. 4. It can be seen from the figure that the sideband components are mixed in the clutter, especially at 15 Hz, which affects the accuracy of the characteristic frequency identification. It means the proposed method has good demodulation performance.

## 4 Conclusion

The fault detection method of motor bearing based on stray magnetic field is studied in this paper. The method based on Teager–Kaiser energy operator can successfully demodulate the characteristic frequency from the magnetic field signal, thus improving the identifiability of the characteristic frequency. The experiment verifies the prominent performance of the detection method based on Teager–Kaiser energy operator in extracting weak feature signals with strong noise background.

**Acknowledgements** The research work was supported by National Natural Science Foundation of China under Grant No. 51279020. The support is greatly appreciated.

## References

1. Negrea MD (2006) Electromagnetic flux monitoring for detecting faults in electrical machines. Helsinki University of Technology, Laboratory of Electromechanics, Helsinki, Finland. ISBN 951-22-8477-4 (2010)
2. Jiang C, Habetler TG (2015) Static eccentricity fault detection of the BLDC motor inside the air handler unit (AHU). In: 2015 IEEE International Electric Machines & Drives Conference (IEMDC), pp 1473–1476
3. Immovilli F, Bellini A, Rubini R, Tassoni C (2010) Diagnosis of bearing faults in induction machines by vibration or current signals: a critical comparison. *IEEE Trans Ind Appl* 46 (4):1350–1359
4. Bellini A, Filippetti F, Tassoni C, Capolino GA (2008) Advances in diagnostic techniques for induction machines. *IEEE Trans Industry Electron* 55(12):4109–4126
5. Obaid RR, Habetler TG, Stack JR (2003) Stator current analysis for bearing damage detection in induction motors. In: Proceedings of the 4th IEEE International Symposium on Diagnostics for Electric Machines Power Electronics and Drives, pp 182–187
6. Jiang C, Li S, Habetler TG (2017) A review of condition monitoring of induction motors based on stray flux. In: Energy Conversion Congress and Exposition (ECCE), pp 5424–5430
7. Vitek O, Janda M, Hajek V, Bauer P (2011) Detection of eccentricity and bearings fault using stray flux monitoring. In: 8th IEEE Symposium on Diagnostics for Electrical Machines Power Electronics & Drives, pp 456–461
8. Cameron JR, Thomson WT, Dow AB (1986) Vibration and current monitoring for detecting air-gap eccentricity in large induction motors. *IEE Proc B Electr Power Appl* 133(3):155–163
9. Schoen RR, Habetler TG, Kamran F, Bartheld RG (1995) Motor bearing damage detection using stator current monitoring. *IEEE Trans Ind Appl* 31(6):1274–1279
10. Blodt M, Chabert M, Regnier J, Faucher J (2006) Mechanical load fault detection in induction motors by stator current monitoring. *IEEE Trans Ind Appl* 42(4):1454–1463
11. Trajin B, Regnier J, Faucher J (2010) Comparison between vibration and stator current analysis for the detection of bearing faults in asynchronous drives. *IET Electr Power Appl* 4 (2):90–100
12. Teager H (1980) Some observations on oral air flow during phonation. *IEEE Trans Acoust Speech Signal Process* 28(5):599–601
13. Manuel PS, Rubén PP, Martín RG (2013) Application of the Teager–Kaiser energy operator to the fault diagnosis of induction motors. *IEEE Trans Energy Convers* 28(4):1036–1044
14. Trajin B, Regnier J, Faucher J (2008) Indicator for bearing fault detection in asynchronous motors using stator current spectral analysis. In: IEEE International Symposium on Industrial Electronics, pp 570–575

# Research on Active Power Factor Correction Technology



Yuan Sun, Jie Chen, Fei Meng, Ruichang Qiu and Zhigang Liu

**Abstract** Current harmonic seriously endangers the safety of power facilities and power grid. Power factor correction (PFC) technology can effectively solve the problem of harmonic pollution. In this paper, the working principle of the full-bridge PFC converter based on the average current control is introduced in detail. The small-signal model of the full-bridge PFC converter under the current continuous mode is established based on the space state average method. The MATLAB simulation model of the system under the current continuous mode is built, and the control algorithm is verified by simulation. According to the characteristics of DSP, the system software is designed. Based on the test of the prototype with an output voltage of 400 V and a switching frequency of 100 kHz, the experimental results obtained verify the correctness of the design.

**Keywords** Active power factor correction · Double closed-loop control · Control strategy

## 1 Introduction

After rectifying and filtering, the nonlinear load distorts the input current waveform, and the input current appears as a pulse waveform, containing a large number of harmonic components, making the power factor very low [1]. Power factor correction is to adjust the distortion current to sinusoidal current and make it phase with voltage, so that the power factor is close to 1 [2].

---

Y. Sun (✉) · J. Chen · R. Qiu · Z. Liu

School of Electrical Engineering, Beijing Engineering Research Center of Electric Rail Transportation, Beijing Jiaotong University, Beijing 100044, China  
e-mail: [18121493@bjtu.edu.cn](mailto:18121493@bjtu.edu.cn)

F. Meng

Hohhot Urban Rail Transit Construction Management Co. Ltd., Hohhot, China  
e-mail: [mengfei\\_124@163.com](mailto:mengfei_124@163.com)

At present, PFC technology can be divided into active PFC and passive PFC. Active PFC mainly uses power electronic switching devices with higher frequency and appropriate control strategy to achieve the purpose of reducing harmonic content and improving power factor [3]. The size of active PFC circuit is small and the efficiency is high.

The traditional boost PFC circuit cannot improve the efficiency of the whole machine fundamentally because of the rectifier bridge. Especially in the case of low voltage and high current, the loss of the rectifier bridge is particularly serious. Compared with traditional boost PFC, full-bridge PFC circuit reduces the conduction loss of rectifier bridge and has high efficiency [4].

## 2 Full-Bridge PFC Working Principle

The topology of the full-bridge PFC converter is shown in Fig. 1, AC is AC 220 V power supply,  $L_1$  is voltage booster inductor,  $S_1$ ,  $S_2$ ,  $S_3$ , and  $S_4$  are MOSFET switching tube,  $D_1$ ,  $D_2$ ,  $D_3$ , and  $D_4$  are body diodes,  $C$  is filter capacitor, and  $R_L$  is load.  $S_1$  and  $S_2$  are power-frequency working tubes and  $S_3$  and  $S_4$  are high-frequency working tubes. Figure 2 shows the specific working process of the full-bridge PFC converter.

Specific working process of full-bridge PFC circuit:

- (1)  $[0 \ t_1]$ ,  $S_1$  and  $S_4$  charge the inductor  $L_1$  through the power supply.
- (2)  $[t_1 \ t_2]$ ,  $S_1$  conducts,  $S_4$  switches off, and  $S_3$  has not yet conducted. It can only supply power to the load through the volume diode  $D_3$  of  $S_3$ .
- (3)  $[t_2 \ t_3]$ ,  $S_1$  and  $S_3$  lead to the load power supply.
- (4)  $[t_4 \ t_5]$ ,  $S_1$  is switched off and  $S_3$  is on, and the current can only pass through the body diode  $D_1$  of  $S_1$ .
- (5)  $[t_5 \ t_6]$ ,  $S_2$  and  $S_3$  charge the inductor  $L_1$  through the power supply.
- (6)  $[t_6 \ t_7]$ ,  $S_2$  on,  $S_3$  off,  $S_4$  is not on, it can only supply power to the load through the body diode  $D_4$  of  $S_4$ .
- (7)  $[t_7 \ t_8]$ ,  $S_2$  and  $S_4$  lead to the load power supply.

**Fig. 1** Full-bridge PFC converter circuit

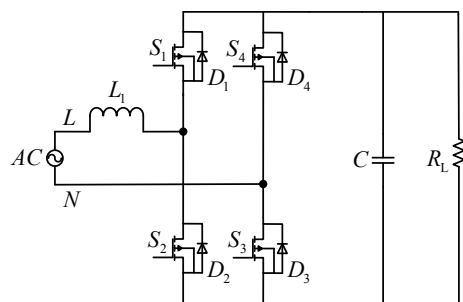
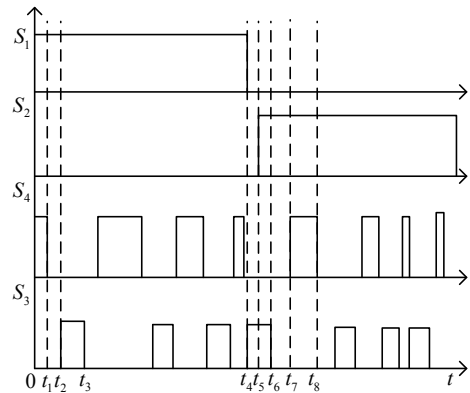


**Fig. 2** PWM driver waveform



Compared with other topological boost PFC circuits, the devices on the bridge arm of the full-bridge PFC circuit are MOSFET. It has simple structure, flexible control, high efficiency, and small EMI. But the cost is high and the control method is complex.

### 3 Control Strategy of Full-Bridge PFC Converter

This design adopts the average current control strategy based on DSP control to control the PFC algorithm. There are two main digital closed-loop control:

- (1) Voltage outer-loop control: the output voltage is sampled and calibrated to achieve stable output voltage.
- (2) Current inner loop control: the input current is sampled and calibrated to make the input current follow the input voltage waveform into a standard sine quantity, so as to reduce the harmonic of the input current [5].

In this design, the state space average method is adopted to analyze and establish the mathematical model of the converter. The main steps are as follows:

- (1) Establish the state equation in stages to solve the static working point.
- (2) Add external disturbance to the static working point, analyze, and build a small-signal model.
- (3) Remove the second-order small-signal and linearize the equation of state [6].

The transfer function controlling to the output is derived:

$$\hat{V}_o(s) = \frac{V_o^2(V_{in}R - sL\frac{V_o}{V_{in}})}{s^2LCRV_o^2 + sLV_o^2 + RV_{in}^2} \hat{D}(s) \quad (1)$$

The transfer function of the duty cycle disturbance to the inductive current:

$$I_L(s) = \frac{V_o(sRC + 2)}{s^2LCR + sLV_o^2 + RV_{in}^2} \hat{D}(s) \quad (2)$$

Input to output control functions:

$$\frac{\hat{V}_o(s)}{\hat{V}_{in}(s)} = \frac{D'R}{D'^2R + s^2CLR + sL} \quad (3)$$

$V_{in}$  is the input voltage,  $V_o$  is the output voltage,  $R$  is the load resistance,  $L$  is the input inductance,  $C$  is the output capacitance, and  $D$  is the duty cycle of PWM,  $D' = 1 - D$ .

Figure 3 is the control block diagram of the current loop of the full-bridge PFC converter. In the double closed-loop digital control process, the current loop makes the input current track the given sinusoidal current reference value, making the input current sinusoidal.  $G_{co}(s)$  represents the transfer function of the compensation link of the current loop PI controller, and  $H_m(s)$  is the corresponding magnification of DSP conversion.  $K_s(s)$  is the current sampling coefficient,  $G_{id}(s)$  is the transfer function from duty cycle to inductive current, and  $F_m(s)$  is the transfer function of the switch.

The open-loop transfer function of the system current inner loop is:

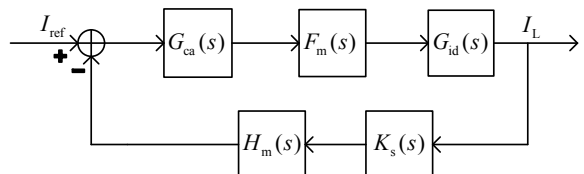
$$G_{co}(s) = F_m(s)K_s(s)H_m(s)G_{id}(s) \quad (4)$$

Uncompensated Bode graph is shown in Fig. 4, and the system is in conformity with the stable condition, but the system cutoff frequency is more than 100 kHz. There is no way to filter the current ripple generated by the switching frequency in the 100kHz circuit, so there is a need to design PI controller to compensate current loop control circuit, and compensation transfer function expression is:

$$G_{ca}(s) = K_{ip} + \frac{K_{ii}}{s} \quad (5)$$

MATLAB is used to assist the design of the current control loop, and the compensated Bode Fig. 5 is obtained. Get PI parameters of the current loop:  $K_{ip} = 0.0007$  and  $K_{ii} = 0.72$ . After the addition of compensation, the phase margin

**Fig. 3** Current loop control block diagram



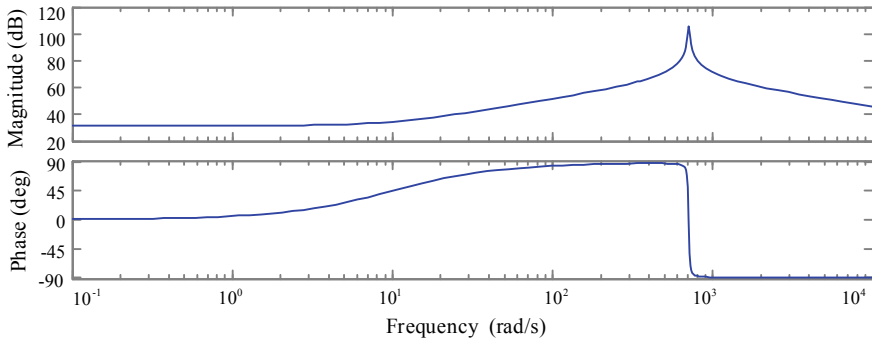


**Fig. 4** Open-loop Bode diagram before current loop compensation

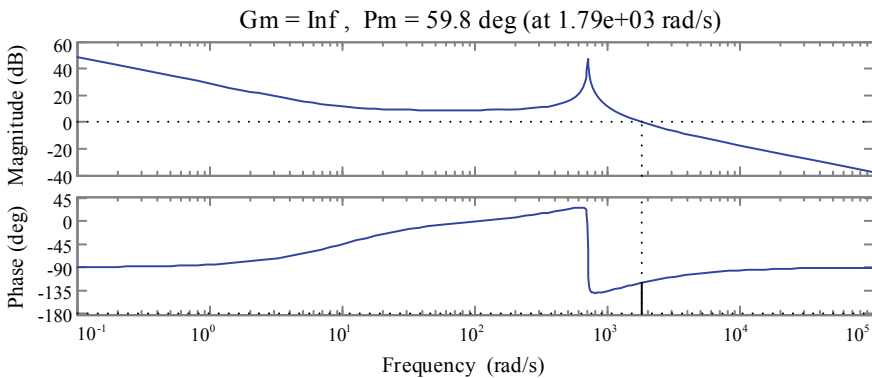


**Fig. 5** Open-loop Bode diagram after current loop compensation

of the open-loop Bode graph of the current inner loop at its cutoff frequency is 59.8 degrees. The PI compensation design of the current loop meets the requirements [7].

Similarly, PI parameters of the voltage loop are obtained:  $K_{pv} = 0.27$  and  $K_{iv} = 11.57$ .

## 4 MATLAB Simulation and Prototype Test of Full-Bridge PFC Converter

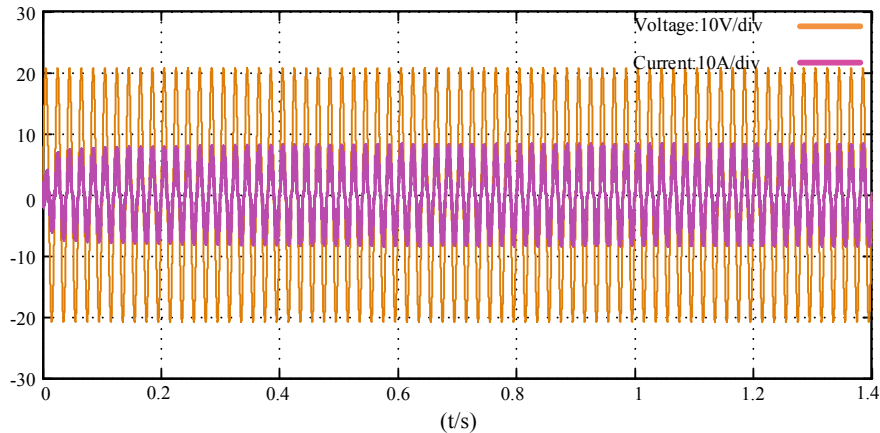
The objective parameters of this design as shown in Table 1.

### 4.1 Full-Bridge PFC Circuit MATLAB Simulation and Result Analysis

Figure 6 is the input voltage and current waveform of the full-bridge PFC circuit. In order to facilitate the observation, the design reduces the amplitude of the input

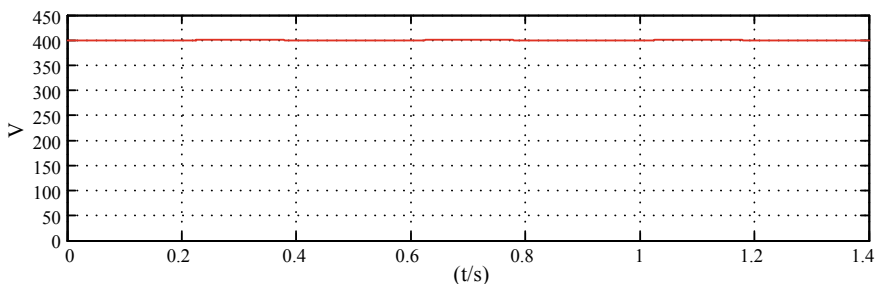
**Table 1** Design objective parameters

Type	Value	Type	Value
Input power frequency	50 Hz	Output power	1 kW
Working frequency	100 kHz	Output voltage	DC 400 V
The input voltage	AC 220 V	Input inductance	150 $\mu$ H
Filter capacitor	1200 $\mu$ F	Load	160 $\Omega$

**Fig. 6** Input voltage and current waveforms

voltage by 15 times. It can be seen from the figure that the input current tends to be stable soon after experiencing a very short period of fluctuation. The waveform of input current follows the waveform of input voltage with good sinusoidal characteristics, and so it achieves the purpose of power factor correction and verifies the correctness of the design.

Figure 7 shows the output voltage waveform. It can be seen from the figure that the output voltage pulsates at 400 V, meeting the design requirements.

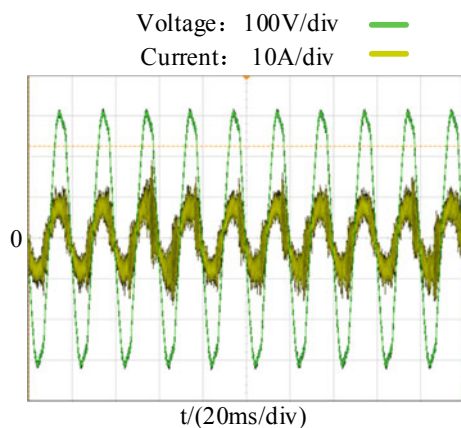
**Fig. 7** Output voltage waveform

## 4.2 Prototype Test Results

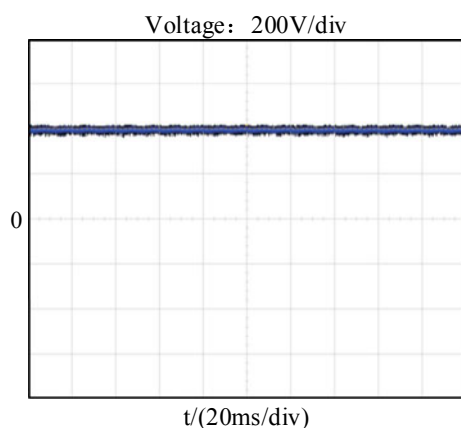
According to the simulation, a 1 KW full-bridge PFC prototype is built and tested.

Figure 8 shows the input voltage and current waveforms tested by the experimental prototype. The results show that the input current waveform is sinusoidal waveform and well follows the input voltage [8]. Therefore, the PFC prototype test shows that the power factor correction function required by the system design has been completed to a certain extent and the operating efficiency of the system has been improved. Figure 9 shows the output voltage waveform. The output voltage is basically stable and meets the design requirements.

**Fig. 8** Input voltage and current waveforms



**Fig. 9** Output voltage waveform



## 5 Conclusion

This paper analyzes the cause and harm of harmonic pollution in power electronic devices and then introduces the characteristics of full-bridge PFC converter and double closed-loop control strategy. The small-signal model of the full-bridge PFC converter is established based on the space state average method, and the modeling and simulation of the full-bridge PFC control system using MATLAB/Simulink tool based on the above theory are carried out to verify the correctness of the control algorithm. Finally, the prototype is tested and analyzed according to the experimental results.

**Acknowledgements** This work is supported by the National Key Research and Development Program (2017YFB1200802-01).

## References

1. Mahmud MWB, Alam AHMZ, Rahman DA (2018) Improvement of active power factor correction circuit for switch mode power supply using fly back and boost topology. In: 2018 7th International conference on computer and communication on engineering, pp 437–440
2. Yuan J, Zechang S, Haifeng D, Nan W (2016) The design and optimization of bridgeless power factor correction for vehicle battery. Mechatronics 28–34 (in Chinese)
3. Xiao L, Hongbo M, Liang P (2018) Research and design of bridge-less Boost PFC converter based on SiC MOSFET. Adv Technol Electr Eng Energy 37(10):65–70 (in Chinese)
4. Binghua J, Chao G, Xuelong H, Jingwei Z (2018) A new bridgeless double Boost PFC converter. Power Electron 52(12):129–132 (in Chinese)
5. Juan S, Jiebin C, Qiancao X (2006) Modeling and analysis of PFC circuit based on Boost converter topology. Mod Electron Technol 28(15):71–73 (in Chinese)
6. Xiaolu M, Yabin X (2018) Simulation research on boost PFC circuit of dual-closed-loop PI control. Electron World 1:147–149 (in Chinese)
7. Wei T (2017) Structure and algorithm implementation of BOOST PFC control based on DSP control (in Chinese)
8. Shigao H, Endian H, Xiaojun D et al (2014) Design of digital switching power supply based on DSP control. Manufact Autom 11:112–115 (in Chinese)

# Fault Diagnosis of Induction Motor Bearing Based on Multitaper Spectrum and Support Vector Machine



Xinchao Zheng, Zhengyu Xue, and Chidong Qiu

**Abstract** This paper focuses on bearing fault detection in induction machines based on stator currents analysis. The method for extracting and identifying bearing fault information of induction motor based on multitaper spectrum combined with support vector machine is proposed in this paper. This approach relies on two steps: the stator current of motor is preprocessed based on multitaper spectrum analysis in order to extract the fault information of motor bearing. Afterward, the support vector machine is employed. Five parameters including kurtosis, skewness, crest factor, clearance, and shape factor are extracted from the spectrum analysis and formed the support vector machine feature vector. By means of optimizing experimental parameters of the kernel function, the bearing fault is identified. The proposed method is used for bearing fault detection in induction motor under the condition of the bearing outer raceway damage. Experimental results show that the proposed method has relatively simple calculation complexity and better performance in identifying bearing fault of motor effectively.

**Keywords** Induction motor · Bearing · Fault diagnosis · Multitaper spectrum · Support vector machine

## 1 Introduction

Bearing failures accounts for more than 40% of all induction motor failures [1], and it is especially important to detect them for troubleshooting them. The motor current signature analysis (MCSA) is widely used in motor fault diagnosis. At present, scholars at home and abroad have done a lot of research on fault diagnosis of induction motor based on MCSA. There are many methods to solve the problem of extracting motor bearing fault information. Fast Fourier transform (FFT) [2] is a very simple and fast frequency domain analysis method. However, due to the low

---

X. Zheng · Z. Xue (✉) · C. Qiu

College of Marine Electrical Engineering, Dalian Maritime University, Dalian 116026, China  
e-mail: [xuezy@dlmu.edu.cn](mailto:xuezy@dlmu.edu.cn)

vibration energy caused by motor bearing failure, the fault signal is often covered by the strong noise background of the power system [3]. The wavelet and wavelet packet [4] methods require a large amount of computation. Due to frequency analysis range of the wavelet decomposition sub-band covers a certain frequency segment, a large deviation occurs when dealing with weak characteristic signals of bearing faults [5]. The phenomenon of empirical mode decomposition modal aliasing appears frequently, and the denoising process is too rough [6]. The multitaper spectrum solves the problem of extracting the bearing fault characteristic signal under the condition of low signal-to-noise ratio by selecting the window function, and the calculation is relatively small. As far as the ideas of identifying extracted fault information are concerned, some traditional method diagnosis results are not intuitive and low accurate, thus machine learning being more and more used in fault diagnosis. The traditional neural network [7] method has limited generalization ability and requires a large amount of data to practice, and the meta-parameters and network topology selection are difficult. Especially, the neural network will not work properly when the data is insufficient [8]. In fact, it is difficult to obtain a large number of samples in industrial production processes. Support vector machine (SVM) [9] has great advantages in solving small sample data, which has strong ability to improve algorithm generalization performance and solve high-dimensional problems and nonlinear problems. In order to design low-cost and less calculation devices for online monitoring of bearing faults in induction motors, this paper proposes a new method based on multitaper spectrum combined with SVM to realize motor bearing fault diagnosis. The fault information is extracted by means of multitaper spectrum. Since a single feature is easily interfered by external conditions, the sensitivity of different features to different faults is different. In the vibration monitoring of rolling bearings, the bearing state is evaluated only according to a certain feature quantity, so as to ensure that the identifying method is sensitive and robust to the faults. The kurtosis, skewness, crest factor, clearance, and shape factor which extracted from multitaper spectrum are formed as the support vector machine feature vectors. The kernel function parameters are optimized by experiments to realize bearing fault identification.

## 2 Theoretical Analysis

### 2.1 Bearing Outer Raceway Damage Fault Characteristic Frequency

According to Blodt's theory [10], the single-point fault of the motor bearing is divided into four types: outer raceway, inner raceway, ball damage, and cage damage.

The motor rotor vibration frequency of the outer raceway damage is

$$f_c = \frac{n}{2} f_r [1 - (B_D/P_D) \cos \beta] \quad (1)$$

where  $n$  is the number of balls,  $f_r$  is the mechanical rotating frequency,  $B_D$  is the diameter of the ball,  $P_D$  is the pitch diameter of the rolling bearing, and  $\beta$  is the contact angle between the ball and the raceway.

Due to outer raceway damage defect on the bearing, motor torque variations are produced and lead to characteristic frequencies appearance in the current spectrum. According to the characteristic frequency of the motor bearing vibration, the corresponding current characteristic frequency can be calculated as

$$f_{CF} = |f_s \pm mf_c| \quad (2)$$

where  $f_{CF}$  is the stator current characteristic frequency under bearing fault conditions,  $f_s$  is the power supply frequency,  $f_c$  is the vibration frequency of the bearing, and  $m$  is a positive integer,  $m = 1, 2, 3, 4, \dots$ , with  $m = 1, 2, 3$  only in this paper.

## 2.2 Feature Extraction Based on Multitaper Spectrum

In order to extract the bearing fault characteristics, Welch's method is used. This method divides the same stationary random signal into  $K$  segments. Each segment data is windowed to calculate the periodic graph, and the total average period graph is obtained. Different resolution effect is obtained by using different window functions. The Blackman window is selected because the sidelobe attenuation speed is large, and the bearing fault signal is extracted more effectively. The calculation formula for Welch is as follows:

Set  $x_i(n)$  is the motor current signal,

$$x_i(n) = x(iD + n)\omega(n) \quad \text{s.t.} \quad 0 \leq n \leq L - 1, \quad 0 \leq i \leq K - 1 \quad (3)$$

$\omega(n)$  is a Blackman window function of length  $L$ , which is 4096.

$$\begin{aligned} \omega(n) &= \left[ 0.42 - 0.5 \left( \cos \frac{2\pi n}{N} \right) + 0.08 \left( \frac{4\pi n}{N} \right) \right] R_N(n) \\ R_N(n) &= \begin{cases} 1, & 0 \leq n \leq N - 1 \\ 0, & \text{otherwise} \end{cases} \end{aligned} \quad (4)$$

D is the offset, and the period diagram of in the  $i$ th segment is

$$S_{x,i}(\omega) = \frac{1}{L} \left| X_i(e^{j\omega}) \right|^2 = \frac{1}{L} \left| \sum_{n=0}^{L-1} X_i(n)(e^{-j\omega n}) \right|^2 \quad (5)$$

Then, the Welch spectrum analysis is

$$S_x(\omega) = 1/KL \sum_{i=0}^{K-1} \left| X_i(e^{j\omega}) \right|^2 \quad (6)$$

The current characteristic frequencies  $f_{\text{CF}}$  of the considered bearing are calculated as explained in formula (2). The energy density of a specific interval, which contains a characteristic fault frequency as center frequency, is extracted. Considering energy leakage, each characteristic frequency is expressed in the 2 Hz band. That is,

$$[f_{\text{CF}} - 1, f_{\text{CF}} + 1] \quad (7)$$

Five parameters including kurtosis ( $x_{\text{kr},k}$ ) [11], skewness ( $x_{\text{sk},k}$ ), crest factor ( $x_{\text{cr},k}$ ), clearance ( $x_{\text{cl},k}$ ), and shape factor ( $x_{\text{sh},k}$ ) are selected to form the feature matrix. Each feature parameter is defined as follows:

$$x_{\text{kr},k} = \frac{1}{l} \sum_{i=1}^l (y_k(i) - \frac{1}{l} \sum_{i=1}^l y_k)^4 \Bigg/ \left( \frac{1}{l} \sum_{i=1}^l \left( y_k(i) - \frac{1}{l} \sum_{i=1}^l y_k \right)^2 \right)^2 \quad (8)$$

$$x_{\text{sk},k} = \frac{1}{l} \sum_{i=1}^l \left( y_k(i) - \frac{1}{l} \sum_{i=1}^l y_k \right)^4 \Bigg/ \left( \sqrt{\frac{1}{l} \sum_{i=1}^l (y_k(i) - \frac{1}{l} \sum_{i=1}^l y_k)^2} \right)^3 \quad (9)$$

$$x_{\text{cr},k} = \max(y_k(i)) \Bigg/ \sqrt{\frac{1}{l} \sum_{i=1}^l y_k^2} \quad (10)$$

$$x_{\text{cl},k} = \max(y_k(i)) \Bigg/ \frac{1}{l} \sum_{i=1}^l \sqrt{y_k^2} \quad (11)$$

$$x_{\text{sh},k} = \sqrt{\frac{1}{l} \sum_{i=1}^l y_k^2} \Bigg/ \frac{1}{l} \sum_{i=1}^l |y_k(i)| \quad (12)$$

$y_k$  is the spectral density value of the multitaper spectrum corresponding to the frequency in the interval of the formula (7), and the support vector machine input feature matrix X contains the statistical values for each extracted frequency interval is as follows:

$$X = \begin{bmatrix} x_{kr,1} & x_{sk,1} & x_{cr,1} & x_{cl,1} & x_{sh,1} \\ x_{kr,2} & x_{sk,2} & x_{cr,2} & x_{cl,2} & x_{sh,2} \\ x_{kr,3} & x_{sk,3} & x_{cr,3} & x_{cl,3} & x_{sh,3} \\ x_{kr,4} & x_{sk,4} & x_{cr,4} & x_{cl,4} & x_{sh,4} \\ x_{kr,5} & x_{sk,5} & x_{cr,5} & x_{cl,5} & x_{sh,5} \\ x_{kr,6} & x_{sk,6} & x_{cr,6} & x_{cl,6} & x_{sh,6} \end{bmatrix} \quad (13)$$

## 2.3 Classification Based on Support Vector Machine

SVM is a two-class classification method based on statistical learning theory. For n-dimensional space, the input data  $x_i$  ( $i = 1, \dots, k$ ) belongs to class 1 or class 2. For class 1, the associated label is  $-1$ . For class 2, the associated label is  $+1$ . If the input data is separated by superplanar linear classification, the separation of the hyperplane equation is given by

$$\omega x_i + b = 0 \quad (14)$$

Where  $x_i$  represents the training vector,  $\omega$  represents the normal vector, and  $b$  represents the offset of the hyperplane. Adding a slack variable  $\xi_i$  to the constraint, the maximum interval hyperplane at this time is called the generalized optimal classification hyperplane. Then, the constraint is  $y_i(\omega x_i + b) \geq 1 - \xi_i$ . In order to obtain the optimal separation hyperplane that distinguishes the samples and maximizes the classification interval, the following optimization problems need to be considered:

$$\min \phi(\omega) = \frac{1}{2} (\omega^T \omega) + C \sum_{i=1}^l \xi_i \quad \text{s.t.} \quad y_i(\omega x_i + b) \geq 1 - \xi_i \quad (15)$$

where  $C$  is the penalty coefficient, and  $\xi_i$  is the slack variable.

In this paper, the training sample set of bearing fault diagnosis is linearly inseparable, and the Lagrangian multiplier  $\alpha_i$  and KKT condition are introduced. By deriving the appropriate inner product kernel function in the optimal hyperplane, the linear indivisible problem is transformed into a high-dimensional space. Therefore, the maximization problem becomes

$$\text{MaxL}(\omega, b, \alpha) = \sum_{i=1}^l \alpha_i - \frac{1}{2} \sum_{i=1}^l \alpha_i \alpha_i y_i K(x_i, x_i) \quad (16)$$

$$\text{s.t. } 0 \leq \alpha_i \leq C \sum_{i=1}^l \alpha_i y_i = 0$$

This paper RBF kernel function is used,

$$K(x_i, x_j) = \exp(-\|x_i - x_j\|^2 / 2\sigma^2) \quad (17)$$

Therefore, the classification decision letter is as follows:

$$f(x) = \text{sign} \left( \sum_{i=1}^l \alpha_i y_i \exp(-\|x_i - x_j\|^2 / 2\sigma^2) + b \right) \quad (18)$$

The hyperplane equation is as follows:

$$\sum_{i=1}^l \alpha_i y_i \exp(-\|x_i - x_j\|^2 / 2\sigma^2) + b = 0 \quad (19)$$

Definitions are as follows: the class of normal bearings is called positive class, the class of fault bearing is called negative class, TP: the positive class is predicted as a positive class, FN: the positive class is predicted as a negative class, FP: the negative class is predicted as a positive class, and TN: the negative class is predicted as a negative class. The evaluation indicators are accuracy (A), precision (P), and recall (R).

$$\begin{cases} A = (\text{TP} + \text{TN}) / (\text{TP} + \text{FP} + \text{TN} + \text{FN}) \\ P = \text{TP} / (\text{TP} + \text{FP}) \\ R = \text{TP} / (\text{TP} + \text{FN}) \end{cases} \quad (20)$$

### 3 Experiment Results for Bearing Faults Detection

#### 3.1 Experimental Setup Description

The experiment adopts an induction motor with rated voltage of 380 V, rated current of 5.03 A, rated power of 2.2 kW, rated speed of 1430 r/min, and frequency of 50 Hz. The parameters of the bearing 6206 are: the number of balls  $N = 9$ , the pitch diameter  $P_D = 46$  mm, and the ball diameter  $B_D = 9.6$  mm. Electric spark



**Fig. 1** Outer raceway damage bearing

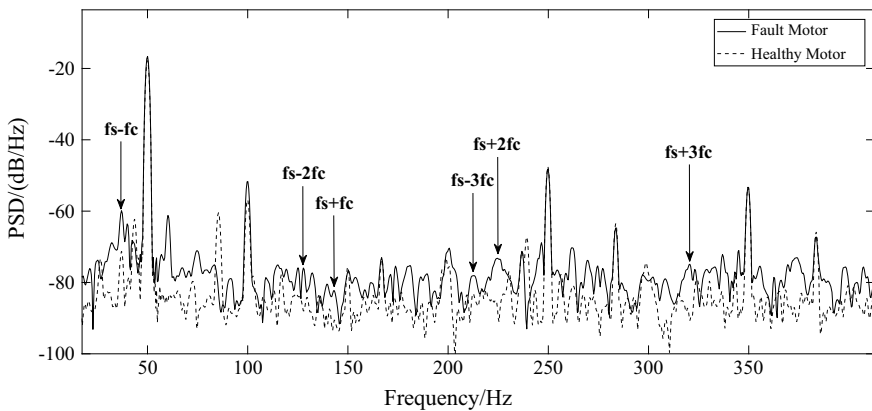


**Fig. 2** Comparison diagram of multitaper spectrum analysis of bearing fault and health

hole punching machine is used for artificial drilling, and the outer track damage fault bearing is manufactured. The damage degree of the fault bearing is shown in Fig. 1.

The current signal acquisition adopts the Hall sensor of IT 60-S model, the measurement range is 0–60 A, the measurement accuracy is  $\pm 3$  to  $\pm 12$  ppm, and the sampling frequency is 10 kHz. 50 sets of bearing fault stator current data and normal motor current data are collected, respectively, 100 sets in total, with 10,000 points in each set of samples. The 8192 data points are used for each analysis. The Blackman window function is used, and the window length is 4096. The comparison between the normal motor and the bearing fault motor using multitaper spectrum analysis is shown in Fig. 2.

**Table 1** Bearing fault diagnosis results

Fault type	Label	Number of training samples	Number of testing samples	Accuracy rate	Precision rate	Recall rate
Healthy	0	38	12	95%	100%	92%
Fault	1	42	8			

### 3.2 Diagnosis Based on SVM

The original data set  $D$  is divided into five mutually exclusive subsets, and each subset  $D_i$  is randomly sampled from  $D$ . The union of four subsets is used as the training set, and the remaining subset is used as testing set per time. The test data is used for evaluation data. Then, by changing the group alternatively for evaluation, five successive accuracy rates are obtained, and the average accuracy rate is calculated. The experimental adjustment can ensure the under-fitting and over-fitting of the feature data set. The above said process is repeated for different values of  $C$  and  $\gamma$ . As a result, the values 1.0 and 0.2 were adopted for  $C$  and  $\gamma$ , respectively. Table 1 shows the results of fault diagnosis.

It can be clearly seen from the diagnosis that the average accuracy, average precision, and average recall are over 92%. And these test set samples are independent of the training set.

Compared with other methods that include wavelet packet method, empirical mode decomposition method and so on, the proposed method has relatively simple calculation complexity. Therefore, the proposed method has strong generalization ability.

## 4 Conclusion

A bearing faults detection method based on multitaper spectrum combined with SVM is proposed in this paper. These experimental results show that the proposed method has a satisfactory performance for motor bearing fault diagnosis. And the method has the advantages of low cost and short data processing time.

**Acknowledgements** The research work was supported by National Natural Science Foundation of China under Grant No. 51279020. The support is greatly appreciated.

## References

1. Ben Abid F, Zgarni S, Braham A (2018) Distinct bearing faults detection in induction motor by a hybrid optimized SWPT and aiNet-DAG SVM. In: IEEE Trans Energy Convers 33 (4):1692–1699
2. Aimer AF, Boudinar AH, Benouzza N, Bendiabdelah A (2015) Simulation and experimental study of induction motor broken rotor bars fault diagnosis using stator current spectrogram. In: Presented at the IEEE 3rd international conference on control engineering & information technology, Tlemcen, Algeria, 25–27 May 2015
3. Deng W, Zhang S, Zhao H, Yang X (2018) A novel fault diagnosis method based on integrating empirical wavelet transform and fuzzy entropy for motor bearing. IEEE Access 6:35042–35056
4. Guo H, Liu M (2018) Induction motor faults diagnosis using support vector machine to the motor current signature. In: 2018 IEEE industrial cyber-physical systems (ICPS), St. Petersburg, pp 417–421
5. Elbouchikhi E, Choqueuse V, Amirat Y, Benbouzid MEH, Turri S (2017) An efficient Hilbert-Huang transform-based bearing faults detection in induction machines. IEEE Trans Energy Convers 32(2):401–413
6. Osman S, Wang W (2016) A morphological Hilbert-Huang transform technique for bearing fault detection. IEEE Trans Instrum Meas 65(11):2646–2656
7. Wen L, Li X, Gao L, Zhang Y (2018) A new convolutional neural network-based data-driven fault diagnosis method. IEEE Trans Ind Electron 65(7):5990–5998
8. Yagami Y, Araki C, Mizuno Y, Nakamura H (2015) Turn-to-turn insulation failure diagnosis of stator winding of low voltage induction motor with the aid of support vector machine. IEEE Trans Dielectr Electr Insul 22(6):3099–3106
9. Pandarakone SE, Mizuno Y, Nakamura H (2017) Distinct fault analysis of induction motor bearing using frequency spectrum determination and support vector machine. IEEE Trans Ind Appl 53(3)
10. Blodt M, Granjon P, Raison B, Rostaing G (2008) Models for bearing damage detection in induction motors using stator current monitoring. IEEE Trans Ind Electron 55(4):1813–1822
11. Mbo'o CP, Hameyer K (2016) Fault diagnosis of bearing damage by means of the linear discriminant analysis of stator current features from the frequency selection. In: IEEE Trans Ind Appl 52(5):3861–3868

# A Simplified Method Based on LM Algorithm for Electrochemical–Thermal Coupling Model of Tram Supercapacitor



Xueting Fu, Chaohua Dai and Yun Du

**Abstract** In order to reduce the complexity and shorten the solution time of the tram supercapacitor electrothermal coupling model when solving the heat conduction problem, according to the relationship between charge and discharge current and supercapacitor heat generation, a simplified method based on Levenberg–Marquardt algorithm for tram supercapacitor electrochemical–thermal coupling model was proposed. Firstly, aiming at the tram operating parameters, the supercapacitor electrochemical–thermal coupling model was constructed based on the high temperature and high current operating conditions. Secondly, in order to solve the high complexity of the multiphysics finite element software calculating the heat conduction problem, by correlating COMSOL and MATLAB, the Levenberg–Marquardt algorithm was used to solve the inverse heat conduction problem, and the electrochemical–thermal coupling model was simplified and simulated to verify its effectiveness. The results showed that under the same condition, the simplified model can predigest the electrochemical–thermal multiphysics heat conduction problem to a single physics problem, and the calculation result error was less than 0.65% and the solution speed increased 97.5%.

**Keywords** Tram · Supercapacitor · Electrochemical–thermal coupling model · Simplified method

## 1 Introduction

Compared with traditional power batteries, supercapacitor is widely used in tram energy storage systems because of its high-power density, excellent low temperature endurance, rapid charge and discharge and having no thermal runaway [1, 2], then supercapacitor played an important role not only as a power supplement but

---

X. Fu (✉) · C. Dai · Y. Du

Department of Electrical Engineering, Southwest Jiaotong University,  
No. 999, Xi'an Road, Pidu District, Chengdu, Sichuan, China  
e-mail: [blue\\_sky0022@163.com](mailto:blue_sky0022@163.com)

also in recovering braking energy, and it is one of the cores of high-power rail vehicles such as tram. However, the temperature rise of the supercapacitor is significant, and the temperature changes drastically during operation, resulting in a large temperature gradient between the monomers then accelerates the attenuation of performance [3–5]. Therefore, the study of its thermal behavior had attracted extensive attention from scholars at home and abroad. In [6], the finite element method was used to accomplish the three-dimensional model improved thermal model solution of cylindrical wound supercapacitor. Literature [7] adopted the finite element analysis method to analyze the internal temperature distribution field of stacked supercapacitors in the working process. Both literature [8] and [9] adopted the method of combining finite element simulation analysis and experiment. The difference was that literature [8] established the ultracapacitor thermal model based on the finite difference method and studied the steady and transient temperature distribution of ultracapacitors. Literature [9] studied the temperature field distribution of ultracapacitors under different ambient temperatures and current densities. However, most of the above researches on thermal behavior were focused on ultracapacitor monomers or modules composed of a small number of monomers, and few researches have been conducted on the actual running conditions of trams. However, trams require a lot of energy in actual operation, and the ultracapacitor modules adopted have high-energy density, large volume and high thermal production. When the finite element method was used to study thermal behavior, the model calculation complexity was higher and the solution speed was slower.

In order to solve the high complexity of the multiphysics finite element software calculating the heat conduction problem, by correlating COMSOL and MATLAB, the Levenberg–Marquardt algorithm was used to solve the inverse heat conduction problem, and the electrochemical–thermal coupling model was simplified and simulated to verify its effectiveness. This simplified model laid a foundation for the subsequent study of the thermal management problem of tram supercapacitor.

## 2 Supercapacitor Electrochemical–Thermal Coupling Model

In this paper, the 2.7 V, 3000 F symmetrical winding supercapacitor unit and supercapacitor module (48 V module composed of 18 monomers) of model BCAP3000 were studied.

## 2.1 Introduction to Tram Conditions

The data of the tram condition data of a demonstration line in Tangshan were selected for simplified simulation. The output power and current conditions of the supercapacitor in one cycle (120s) were obtained and its characteristic interval ignored. The actual operation of the supercapacitor voltage was 1.35–2.7 V, and its current–voltage curve during the charge and discharge cycle is shown in Fig. 1.

## 2.2 Physical Model

### 2.2.1 Supercapacitor Electrochemical Model

The supercapacitor is mainly composed of a current collector, a porous electrode, an electrolyte and a separator, and the one-dimensional electrochemical model was shown in Fig. 2.

A mathematical model for simulating the electrochemical process of a supercapacitor was established based on the material transport process.

The supercapacitor porous electrode is a mixed material having an electrode phase and an electrolyte phase; electrodes and pore electrolytes conform charge conservation and mass conservation. Conservation of mass:

$$\frac{\partial c_i}{\partial t} = -\nabla \cdot N_i \quad (1)$$

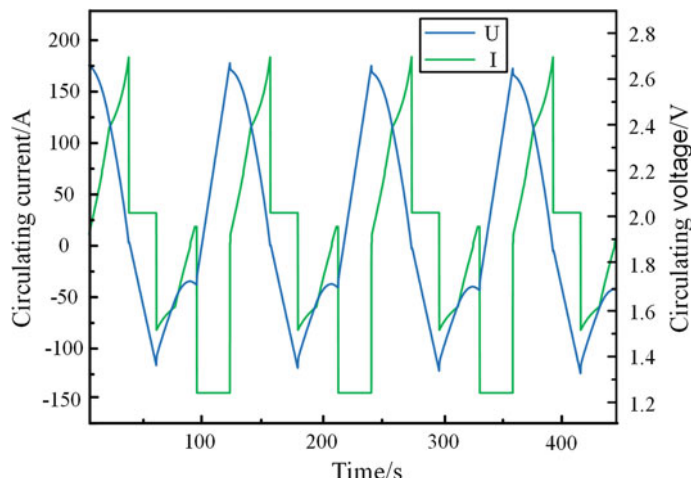
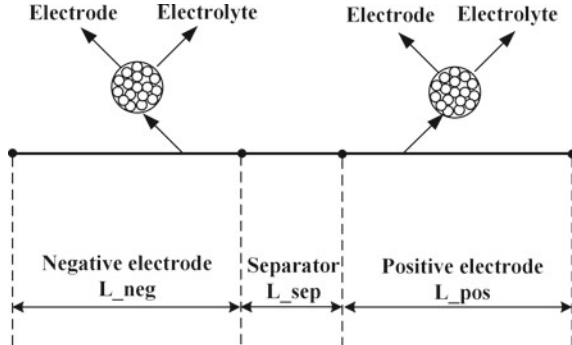


**Fig. 1** Charge and discharge curve under working conditions

**Fig. 2** Supercapacitor electrochemical model



where  $N_i$  is the total flux of the substance.  $c_i$  is the concentration of the substance  $i$ .

During the cyclic charge and discharge process, the flux in the electrolyte can be described by the Nernst–Planck equation, and the diffusion, migration and convection are, respectively, the three terms on the right side of the equation below.

$$N_i = -D_i \nabla c_i - z_i u_{m,i} F c_i \nabla \phi_l + c_i u \quad (2)$$

where  $D_i$  is the diffusion coefficient.  $z_i$  is the price of the substance.  $u_{m,i}$  is the mobility.  $F$  is the faraday constant.  $\phi_l$  is the electrolyte potential.  $u$  is the velocity vector.

The electrolyte and the porous electrode remain electrically neutral, and the current density vector expression in the electrolyte is as follows:

$$i_l = -F^2 \sum z_i^2 u_{m,i} c_i \nabla \phi_l \quad (3)$$

The electron conduction in the electrode is modeled using Ohm's law, and the current density vector is as follows:

$$i_s = -\sigma_s \nabla \phi_s \quad (4)$$

The charge conservation equation is obtained from the continuity of the current:

$$\nabla i_l + \nabla i_s = 0 \quad (5)$$

The Joule heat generation rate of the one-dimensional electrochemical model is as follows:

$$q^{(1)} = -i_l \nabla \phi_l - i_s \nabla \phi_s \quad (6)$$

where  $\sigma_s$  is the conductivity.  $\phi_s$  is the potential. The superscript “(1)” represents a parameter or variable in a one-dimensional model.  $q^{(1)}$  is the Joule heat generation rate.

### 2.2.2 Supercapacitor Thermal Model

The supercapacitor generated reversible heat and irreversible heat during cyclic charging and discharging, and the heat transfer equation of the supercapacitor core heat producing zone is

$$\begin{cases} \rho^{(3)} c_p^{(3)} \frac{\partial T^{(3)}}{\partial t} + \nabla \cdot q^{(3)} = Q^{(3)} \\ q = -k^{(3)} \nabla T \end{cases} \quad (7)$$

Wherein, the superscript “(3)” represents a parameter or a variable in the three-dimensional model.  $\rho$  is the density of the active material.  $c_p$  is the equivalent atmospheric heat capacity.  $T$  is the thermodynamic temperature.  $k$  is the thermal conductivity, and  $Q$  is the heat source.

Assuming that the supercapacitor is exposed to the air, heat is transferred to the surrounding environment through natural convection. The heat convection equation can be obtained by Newton's law of cooling.

$$q_0 = h(T_s - T_{\text{ext}}) \quad (8)$$

Since this paper studied the electric double layer supercapacitor that stores energy through polarized electrolyte, no chemical reaction occurred during charging and discharging, and the Faraday effect was not considered. Therefore, the main form of internal heat generation was the irreversible Joule heat generated by the equivalent series internal resistance. The Joule heat of the supercapacitor in the three-dimensional thermal model was expressed as

$$q = I^2 R_{\text{req}} \quad (9)$$

where  $T_s$  is the surface temperature of the supercapacitor.  $T_{\text{ext}}$  is the external ambient temperature.  $h$  is the convective heat transfer coefficient.  $R_{\text{req}}$  is the equivalent series internal resistance.

### 2.2.3 Supercapacitor Electrochemical–Thermal Coupling Model

The supercapacitor electrochemical–thermal coupling model is a coupling between a one-dimensional electrochemical model and a three-dimensional thermal model. Using the temperature and average of the generated heat to couple the electrochemical model and the thermal model, (10) is the coupling process [10].

$$\begin{cases} T^{(1)} = T_{\text{avg}}^{(3)}|_{r=r_0} \\ Q^{(3)} = Q_{\text{avg}}^{(1)} \end{cases} \quad (10)$$

The thermal properties of the supercapacitor are determined by the coupled model, (11) is the constant pressure heat capacity of the core region.

$$\begin{cases} C_p = \frac{C_{\text{pos}}L_{\text{pos}} + C_{\text{neg}}L_{\text{neg}} + C_{\text{sep}}L_{\text{sep}}}{L_{\text{batt}}} \\ L_{\text{batt}} = L_{\text{neg}} + L_{\text{sep}} + L_{\text{pos}} \end{cases} \quad (11)$$

Similarly, (12) is the equivalent density of the core region.

$$\begin{cases} \rho = \frac{\rho_{\text{pos}}L_{\text{pos}} + \rho_{\text{neg}}L_{\text{neg}} + \rho_{\text{sep}}L_{\text{sep}}}{L_{\text{batt}}} \\ L_{\text{batt}} = L_{\text{neg}} + L_{\text{sep}} + L_{\text{pos}} \end{cases} \quad (12)$$

Since the supercapacitor is a symmetrical cylinder, the heat transfer is equal in the  $X$ -axis and  $Y$ -axis. In polar coordinates, (13) and (14) are the thermal conductivity along the axial and radial directions.

$$K_{r,\theta} = \frac{L_{\text{batt}}}{L_{\text{pos}}/k_{\text{pos}} + L_{\text{neg}}/k_{\text{neg}} + L_{\text{sep}}/k_{\text{sep}}} \quad (13)$$

$$K_z = \frac{L_{\text{pos}}k_{\text{pos}} + L_{\text{neg}}k_{\text{neg}} + L_{\text{sep}}k_{\text{sep}}}{L_{\text{batt}}} \quad (14)$$

Wherein,  $C$  represents the constant pressure heat capacity.  $L$  indicates the thickness.  $k$  expresses the thermal conductivity.

### 3 Simplified Process

#### 3.1 Simplified Method

When supercapacitor operated under high current conditions, once the model, initial state of charge and initial temperature were determined, the heat generated can be determined as the irreversible Joule heat generated by the energy storage core region, and when the equivalent series internal resistance was known and the current was constant, the heat generation can be calculated by the formula. Due to the time-varying working current, the heat production cannot be calculated directly according to the formula, and the constant current obtained by finding the root mean square value according to the working condition current had a larger error than the simulation result under the original working condition current. Therefore, it is necessary to find an equivalent constant current that can guarantee the accuracy of the calculation result to calculate the heat production. Therefore, the above process is transformed into an inverse problem of heat conduction using an electrochemical-thermal coupling model. The simplification method was shown in Fig. 3.

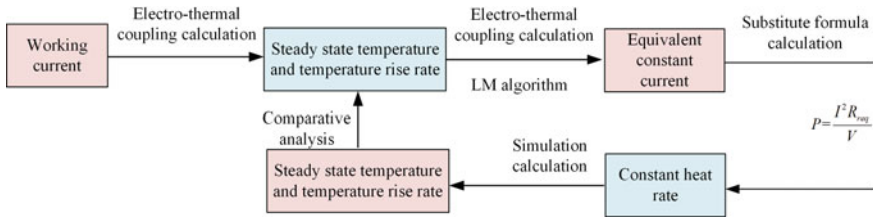


**Fig. 3** Simplified method flow

When solving the positive heat conduction problem, the operating current is known, and the unknown amount to be solved is the steady state temperature and the temperature rising rate of the supercapacitor. While in the inverse problem analysis, the equivalent constant current is the unknown parameter, and it can be solved by an inversion method according to the steady state temperature and the temperature rise rate.

### 3.2 Research on Inverse Heat Conduction Problem Based on LM Algorithm

By correlating COMSOL and MATLAB [11], the finite element method and the Levenberg–Marquardt algorithm were used to solve the inverse heat conduction problem. The parameter that needs to be determined for the inverse heat conduction problem is the equivalent charge and discharge current  $I_h$ , and the parameter to be determined is represented by a variable, then there is

$$f(x) = I_h \quad (15)$$

Minimize Eq. (16) by iterating through constantly changing estimates

$$J[f(x)] = \sum_{i=0}^{3600} [T_i - Y_i]^2 = U^T U \quad (16)$$

where  $T_i$  is the supercapacitor transient weighted average temperature calculated by Eq. (7) based on the estimated value  $f_0(x)$  of  $f(x)$ .  $Y_i$  is the reference value (the weighted average temperature of the supercapacitor at different times under the operating current);  $t$  is time. Let formula (16) take the minimum value, by deriving we can get

$$\frac{\partial J}{\partial f(x)} = \sum_{t=0}^{3600} (\partial J / \partial f(x))(T_i - Y_i) = 0 \quad (17)$$

Equation (17) performs Taylor series expansion on  $T(f(x))$  and removes high-order terms, and the parameter  $\mu^n$  is added to the result to adjust the convergence speed. The LM calculation method is as follows [12]

$$f^{n+1} = f^n + [\phi^T \phi + \mu^n I]^{-1} \phi^T [T - Y] \quad (18)$$

where  $I$  is the identity matrix.  $\phi$  is the Jacobian matrix, defined as

$$\phi = [\partial T / \partial f]^T \quad (19)$$

When  $\mu^n = 0$ , it is the Newton iteration method; when  $\mu^n \rightarrow \infty$ , it is the gradient descent method. In order to improve the convergence speed, the iterative starts to adopt the gradient descent method and then reduces the value of  $\mu^n$  to obtain the inverse problem solution by Newton method. The convergence condition of Eq. (18) is

$$J[f_g(x)] < \varepsilon \quad (20)$$

where  $\varepsilon = 0.001$ .

### 3.3 Heat Conduction Inverse Problem Solving Process

The current cycle of a working condition is 120 s, and the total duration of the transient calculation is 3600 s (30 cycles) with a step size of 10s.

1. Based on the structural characteristics and operating mechanism of the supercapacitor, the geometric model of the supercapacitor was established based on the finite element software.
2. Set the material and define the corresponding physical parameters.
3. Added a physics field and set the initial conditions.

The one-dimensional electrochemical model used the “three-current distribution” physics interface. For the electrochemical behavior of the supercapacitor, the boundary conditions such as grounding, electrode current density and no flux were set as shown in Table 1.

Where,  $i_{app}(t)$  is the electrode current density under the condition of current charging and discharging cycle.

**Table 1** Boundary conditions

$\phi_S _{x=0}$	$i_S _{x=L_{neg} + L_{sep} + L_{pos}}$	$i_S _{x=0} = i_S _{x=L_{neg}} = i_S _{x=L_{cng} + L_{sep}}$	$i_l _{x=0} = i_l _{x=L_{cng} + L_{neg} + L_{pos}}$
0 V	$-i_{app}(t)$	0 A	0 A

**Table 2** Initial value setting

$\varphi_S _{0 \leq x \leq L_{\text{neg}} + L_{\text{sep}}} (t = 0)$	$\varphi_S _{0 \leq x \leq L_{\text{neg}} + L_{\text{sep}} \leq x \leq L_{\text{neg}} + L_{\text{sep}} + L_{\text{pos}}} (t = 0)$	$\varphi_t _{0 \leq x \leq L_{\text{neg}} + L_{\text{sep}} + L_{\text{pos}}}$	$T _{t=0}$	$c_d _{t=0}$
0 V	2.7 V	0 V	315.5 K	1 mol/L

Assumed that the supercapacitor is fully charged at the initial moment, and the initial value setting was shown in Table 2.

The three-dimensional thermal model adopted the “heat transfer” physics interface. It was assumed that the heat generated by the supercapacitor module was used for the temperature rise, ignoring the heat flux of the supercapacitor and the outside, so the boundary condition was set as thermal insulation.

The initial value  $f_0(x)$  of iteration is set according to the working current  $I_g$ , and the calculation method of  $f_0(x)$  is as follows:

$$f_0(x) = \sqrt{\frac{\sum I_g^2}{1200}} \quad (21)$$

4. Meshing the solution domain.
5. Transient solution and post-processing.
6. Bring the simulation results into the formula to calculate the heat consumption.

## 4 Simplify Results and Discussion

Set the weighted average temperature of the supercapacitor at different times under the condition of current circulating current and discharge as the initial reference condition. The inverse problem was solved by LM algorithm, and the solution  $I_h$  of the inverse problem was 110.15 A.

The simplified model was evaluated in four aspects: weighted average temperature deviation, supercapacitor temperature rise, model complexity and calculation time. In order to observe the change trend of the T-S curve (time vs. weighted average temperature curve) more intuitively, three time periods of the curve are, respectively, intercepted, as shown in Fig. 4. The T-S curve (time and weighted average temperature curve) of the supercapacitor under operating conditions was taken as the reference, and the reference T-S curve was nonlinear. This is because the time variability of the operating current makes the temperature at different times fluctuate to some extent, but the T-S curve with constant heat consumption rate was always within the range of 0–0.5 K from it, indicating that the error of the model obtained by the simplified method was small compared with the calculation results of the original model, which also verifies the reliability of the solution results of the reverse heat conduction problem of LM to some extent.

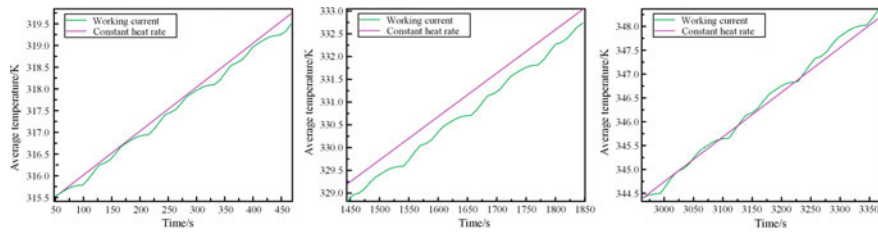


**Fig. 4** Partly weighted average temperature

Under the T-S curve at a constant heat rate, degree of deviation will have a small increase with time increase. It should be noted that once the deviation is too large, the simplified model with a constant heat rate is not able to accurately reduce the heat generation process of the supercapacitor under the current charge and discharge. Therefore, the weighted average temperature deviation of the constant heat rate needed further calculation and analysis.

The T-S curves of the operating current and the constant heat rate were linearly fitted to obtain the slope and intercept as shown in Fig. 5. The  $k_1$  of the  $y_1$  curve is 0.00991,  $b_1 = 314.78345$ , and  $k_2$  of the  $y_2$  curve is 0.00983, and  $b_2 = 315.1084$ .

In order to investigate the variation of the weighted average temperature deviation of constant heat rate with time, when calculating the time of 1200, 2400 and 3600 s (100, 200, 300 working current cycles), the weighted average temperature deviation of the supercapacitor at a constant heat rate is 0.635, 1.595 and 2.555 K. It can be seen that for every 100 cycles increase, the deviation degree increased by about 1 K. However, the deviation degree was within an acceptable tolerance relative to the overall temperature of the supercapacitor.

Electrochemical module and heat transfer module should be set up to study the thermal conductivity in COMSOL. The electrochemical module was used to

**Fig. 5** Weighted average temperature over time

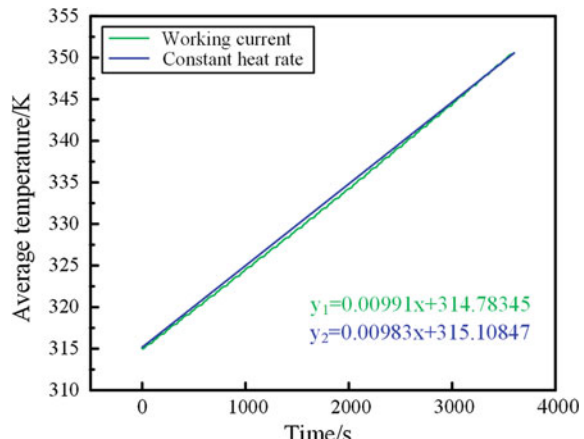


**Table 3** Solution results

Temperature rise	Working current (K)	Equivalent current (K)	Relative error (%)	Constant heat rate (K)	Relative error (%)
$T_{av}$	35.634	35.716	0.23	35.4	0.65
$T_{max}$	35.939	36.038	0.27	35.749	0.52
$T_{min}$	35.442	35.522	0.22	35.23	0.59

**Table 4** Solution speed

Heat production condition	Physics field	Solution time	Solving speed increase ratio
Working current	Electrochemical and heat transfer	1 h 9 min	–
Constant heat rate	Heat transfer	1 min 44 s	97.5%

simulate the heat generated by the change of supercapacitor concentration in the charging and discharging process, namely the heat source in the heat transfer module. During the coupling process of the module, the heat production rate was constantly changing. And by solving an inverse heat conduction problem, on the basis of coupling model to solve the supercapacitor as a heat source of heat production rate constant of the equivalent, so just settings were applied to solve the heat transfer module to produce thermal dissipation, and other parameters settings were consistent with the coupling model, adopted finite element method to solve the model, the solving result and solving speed as shown in Tables 3 and 4.

The data in Tables 3 and 4 show that the equivalent constant current obtained by the inverse heat conduction problem has a small error compared with the reference result and can be used to calculate the constant heat rate. A simplified model with a constant heat rate as a heat source can simplify the electrochemical–thermal multiphysics problem to a single physics problem, simplifying the complexity of the electrochemical–thermal coupling model and improving the computational efficiency on the basis of ensuring the solution results accuracy. And the solution time is shortened by 97.5%.

## 5 Conclusion

In this paper, a simplified method was presented based on the Levenberg–Marquardt algorithm for the tram supercapacitor electrochemical–thermal coupling model, and its effectiveness is verified by simulation. Under the same conditions, the simplified model can simplify the electrochemical–thermal multiphysics heat conduction problem to a single physics problem, the calculation result error exceeded within 0.65%, and the solution speed increased by 97.5% at the same time. This simplified model can be used to study the tram supercapacitor thermal management problem.

**Acknowledgements** This work is supported by National Key R&D Program of China (No. 2017YFB1201004, 2017YFB1201003). Xuetong Fu is the corresponding author.

## References

1. Zhixiong C (2014) Analysis of catenary-free technology applied in modern trams. *Urban Mass Transit* 17(4):117–121 (in Chinese)
2. Chengying L (2015) Research on quick charge technology at urban traffic intersection. *Chin J Power Sour* 39(11):2487–2488 (in Chinese)
3. Omar N, Gualous H, Salminen J et al (2014) Electrical double-layer capacitors: evaluation of ageing phenomena during cycle life testing. *J Appl Electrochem* 44(4):509–522
4. Mejdoubi AE, Oukaour A, Gualous H et al (2016) Experimental investigation of aging calendar parameters for supercapacitors. In: Renewable & sustainable energy conference. IEEE
5. Gualous H, Gallay R, Alcicek G et al (2010) Supercapacitor ageing at constant temperature and constant voltage and thermal shock. *Microelectron Reliab* 50(9–11):1783–1788
6. Yansong L, Meina Z, Yunfei S et al (2016) Study on thermal behavior influences of spiral wound supercapacitors with package units structure. *Proc Chin Soc Electr* 36(17):4762–4770 (in Chinese)
7. Wang K (2013) The thermal analysis on the stackable supercapacitor. *Energy* 59:440–444
8. Gualous H, Louahlia-Gualous H, Gallay R et al (2007) Supercapacitor thermal characterization in transient state. 2007 IEEE industry applications annual meeting. IEEE
9. Meina Z, Yansong L, Jun L et al (2016) Research on supercapacitor's coupling of thermology and electrochemistry. *Chin J Power Sour* 40(7):1382–1384 (in Chinese)
10. Li Z, Yinghua J, Kai W (2013) Thermal analysis on the working process of spiral wound supercapacitors. *Proc CSEE* 33(9):162–166 (in Chinese)
11. Ozana S, Pies M, Docekal T (2016) Case studies on optimization problems in MATLAB and COMSOL multiphysics by means of the livelink. In: International conference of numerical analysis & applied mathematics
12. Huang CH, Chao BH (1997) An inverse geometry problem in identifying irregular boundary configurations. *Int J Heat Mass Transfer* 40:2045–2053

# Review and Research Progress of Energy Bidirectional Feed ICPT System



Junjie Wang, Ruqiong Li and Xin Li

**Abstract** The traditional rail transit traction power supply system is susceptible to extreme environmental conditions, resulting in a decrease in its safety and reliability. The contactless power supply technology solves the problems caused by the contact between the electric locomotive and the traction network and provides significant advantages for the new rail transit power supply technology. Inductively coupled power transfer (ICPT) technology has become the best choice for contactless power supply technology for rail transit because of its large transmission power and suitable transmission distance. The bidirectional ICPT system solves the traditional traction power supply problem, and can also return the regenerative braking energy of the electric locomotive to the traction net to achieve peak cutting and valley filling, and achieves energy-saving operation. This paper reviews the commonly used topologies, control methods, modeling and optimization methods and looks forward to the application of these key technologies in rail transit applications at the future.

**Keywords** Transfer rail transit · Contactless power supply · Inductively coupled power transfer · Energy bidirectional feed · Segmented power supply · Traffic energy internet introduction

## 1 Introduction

With the continuous development of wireless energy transmission (WPT) technology, more and more wireless devices appear in our daily life. WPT mainly has three types: radiation type, electric field coupling type and electromagnetic coupling

---

J. Wang · R. Li (✉)

School of Automation & Electrical Engineering, Lanzhou Jiaotong University,  
Anning District, Lanzhou, China  
e-mail: [liruoqiong26@163.com](mailto:liruoqiong26@163.com)

X. Li

School of New Energy & Power Engineering, Lanzhou Jiaotong University,  
Anning District, Lanzhou, China

type. Compared with other methods, the transmission gap of ICPT technology is not the largest, but the high-power and high efficiency features are suitable for powering cars and electric locomotives. The bidirectional ICPT technology is derived from the traditional unidirectional ICPT technology and inherits many advantages [1]. Its energy bidirectional feed characteristics can be used for the feedback utilization of the regenerative braking energy of rail transit and can also be applied to V2G scenes. Both have great significance for building a transportation energy Internet, so it is valuable to study bidirectional ICPT technology.

Its typical topology is shown in Fig. 1, after the rectification and DC–DC conversion, the AC power on the grid side becomes DC power through the full-bridge high-frequency inverter of S11–S14 in the topology, then passes SS-type compensation and transmits energy by coupling the magnetic field of the transmitting coil and the receiving coil. Finally, the S21–S24 on the load side is synchronously rectified and supplies energy to the load. The bilateral controllers, respectively, collect the voltage and current signals of the primary and secondary sides and then determine the bilateral working state through real-time signal transmission. Finally, the bilateral converters are controlled by the switching signals.

In this paper, the topology of bidirectional ICPT is introduced in Sect. 2. Then, the control strategy and model optimization of bidirectional ICPT system are reviewed in Sects. 3 and 4, respectively. The thesis is summarized and prospected in Sect. 5.

## 2 Topology

At present, the research on the topology of energy bidirectional feed ICPT system is mainly for the research of resonant compensation structure and the research of power electronic converter. The role of the resonant compensation link is to

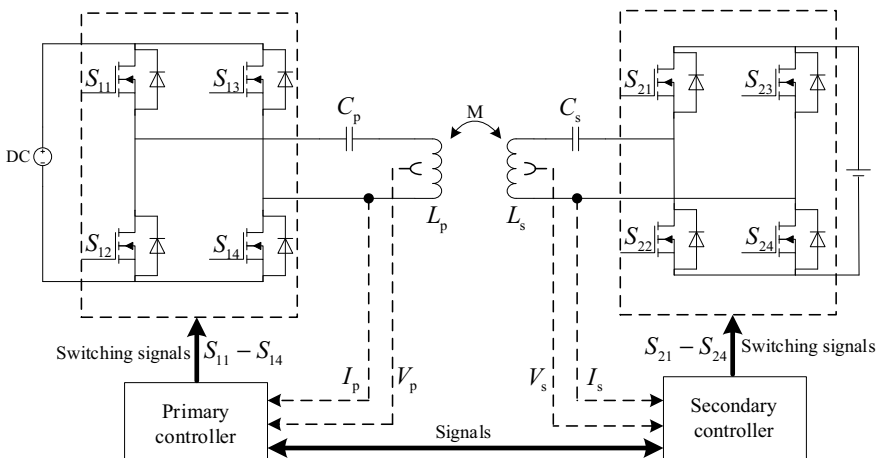


**Fig. 1** Typical topology of a bidirectional ICPT system

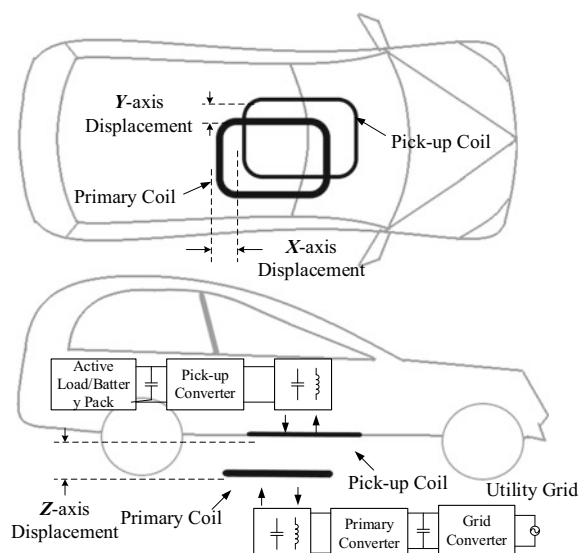
compensate the reactive power of the system to improve the transmission power and overall efficiency of the system [2]. On the research of power electronic converters, one is to improve the voltage stress and power level by changing the structure of the high-frequency inverter, so that it is convenient for high-frequency operation, reducing control difficulty and switching loss. The second is to simplify the topology and reduce the cost by means of direct-crossing converters, but this method has higher requirements for the application environment.

## 2.1 Resonance Compensation Structure

Traditional compensation structures such as SS, SP, PS, PP or bilateral LCL have been analyzed by many literatures, and the effects of various parameters in these structures on frequency characteristics have been obtained through modeling analysis, simulation and experiment [3–7]. In recent years, new compensations structure has been proposed.

Professor Udaya K. Madawala's team proposed a hybrid compensation structure for V2G technology in the early years. The effect of no effect on the quantity achieves 100 mm horizontal displacement and 40 mm vertical displacement of the electric vehicle charging pad [8]. Based on this structure, the team applied this structure to the three-phase bidirectional electric vehicle charging system and verified its feasibility and applicability [9]. Then, the hybrid compensation structure is improved, the high fault tolerance capability of the electric vehicle charging pad 3D misalignment is realized [10], and Fig. 2 is a model diagram when the charging pad is misaligned and charged. To extend the transmission distance of electric

**Fig. 2** Typical V2G system



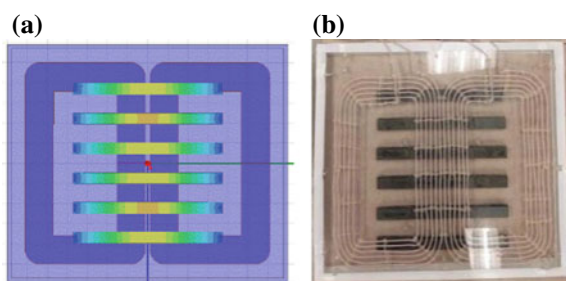
vehicle wireless charging system and improve its fault tolerance and energy feedback capability and power transmission efficiency, a new topology with the relay circuit is proposed [11]. Considering the simultaneous transmission of energy and signal, Ref. [12] proposes a single-coil double-resonance structure, achieving 354 W power transmission and 19.2 kbps signal transmission rate when the air gap is 100 cm.

The above is mainly to improve the fault tolerance of the system from the perspective of the characteristics of the compensation structure. In addition, considering the influence of the coil itself on the magnetic field coupling, the University of Auckland in New Zealand proposed a magnetic structure of a tripolar pad consisting of a circular pad and a bipolar pad as a secondary pad. The optimization of the primary current of the pole plate improves the effective coupling coefficient in the conventional topology, especially when the current is out of regulation, and the leakage flux is kept below the international standard [13]. In Ref. [14], based on the eight-polarized DD pad structure, an optimized magnetic design method based on the finite element method (Fig. 3) is developed. The method is universal and suitable for different power levels, air gap levels, resonance, frequency and pad structure.

## 2.2 Power Electronic Converter

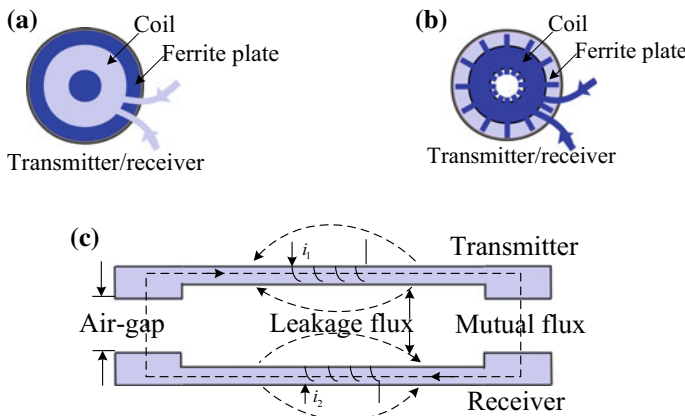
The structure of the current bidirectional ICPT system has been introduced. The high-frequency inverter is the most important part of the whole system. The University of Hong Kong has reviewed the resonant circuits of wireless power transfer and analyzed and compared various types of inverters from the aspects of voltage stress, power level, high-frequency operation, control difficulty, switching loss and effective cost [4]. The specific content is shown in Table 1. Professor Akshay Kumar's team is closely related to V2G technology and proposes a topology based on current-fed half-bridge converter and CCL-LC resonant network. It has the characteristics of current sharing and voltage doubling. No matter how the load side changes, the inverter can always achieve soft switching, and the efficiency is as high as 92%, which is consistent with the experimental expectation [6, 15].

**Fig. 3** DD pad  
**a** three-dimensional finite element analysis of DD liner  
**b** optimized DD pad



**Table 1** Comparison of power electronic variators in wireless power transfer

Type	Voltage stress	Power level	High-frequency operation	Control different	Switching loss	Effective cost
Single-phase AC–AC converter	Low	Low	Medium	Medium	Low	Medium
Three-phase AC–AC converter	Medium	Medium	Medium	High	Medium	Medium
DC-fed energy injection converter	Low	Low	High	Medium	Low	Low
Class E resonant inverter	High	High	High	Low	Low	Low
Class D resonant inverter (full-bridge)	Medium	High	Medium	Medium	Medium	Low
Class DE resonant inverter	Low	Medium	High	Medium	Low	Medium
Class EF <sub>2</sub> resonant inverter	Low	Medium	High	Low	Low	Low

**Fig. 4** Round pad and UU pad

Reference [15] also compares the advantages and disadvantages of the three pad structures, and in Fig. 4a a circular pad is developed with solid ferrite plate, Fig. 4b pad for improved structure of electric vehicle application, Fig. 4c shows a UU-type IPT pad. Reference [16] uses three half-bridge inverter brackets to design a dual-channel dual-pickup structure that can individually control the size and direction of each power flow. In addition, there are multi-level converters with

selective harmonic distortion modulation [17] and relatively rare multi-module topologies [18].

In an ICPT system, power is processed through multiple power transfer stages, resulting in reduced efficiency and increased cost. These limitations can be significantly offset by the use of direct AC converters. Reference [19] proposes a novel ICPT topology using a full-bridge current-fed direct-transfer converter, which is a topology derived from boost, whose input is a current source and uses a double closed-loop control strategy to ensure high quality of the source current, and the soft switching can still be achieved in the region of the lagging power factor; THD is about 4.5%, fully in line with the specified standard of IEEE 519-1992. Reference [20] proposes an AC matrix converter that can implement soft switching and considers the practical application environment of V2G, which can be used in bidirectional ICPT systems.

### 3 Control Strategy

The control strategy is mainly composed of the controlled object, the purpose of the control and the control method adopted. Common control objects are mainly voltage [21], current and their respective phases. Commonly used control methods are as follows: Method 1, add a DC–DC link on the grid side or load side [2, 22]; Method 2, use phase shift control measures on the grid side [23–27]; Method 3, the “energy injection, free oscillation” control measures are adopted on the grid side [28, 29]. Method 4 uses pulse width modulation [22, 30]. All of the above control methods have been developed more maturely and continue to be innovative. Tokyo University of Science considers that the previous control methods are not efficient or the control methods are complex and versatile and proposes a high efficiency control method considering the amplitude of the primary and secondary voltages and the phase difference between the primary and secondary voltages [30]. Reference [31] studies the influence of parameter changes on output power by introducing relative gain array (RGA) and designs a PID controller. Reference [32] proposes a self-resonant PWM controlled bidirectional air gap electric vehicle charger with an air gap of 12–20 cm for constant frequency operation. Reference [22] realizes a 22 kW high-power electric vehicle charging device, which has a higher charging rate than the conventional 1–5 kW system, and the efficiency is as high as 97.4%. The use of Sic-MOSFETs bilaterally enables the system to achieve bidirectional power transmission (Fig. 5).

At present, there are some shortcomings in the control strategy of bidirectional ICPT system: First, the control method needs to be innovated. Professor Zhao Zhengming’s team from Tsinghua University analyzed the three control degrees of the output phase between the original and secondary side control signals, the phase angle  $\gamma$  and the original and secondary converter phase shift angles  $\alpha$  and  $\beta$ , respectively. After the influence of overall efficiency, a multi-degree of freedom combination control strategy to optimize the efficiency of bidirectional wireless

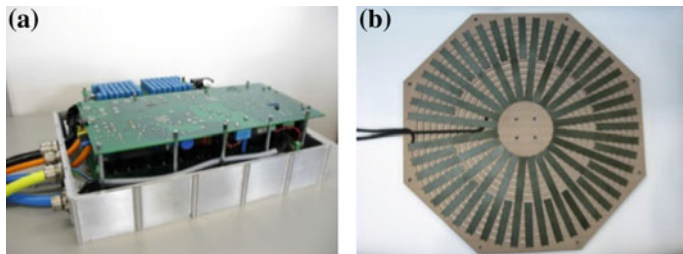


**Fig. 5** **a** a 22 kW bidirectional IPT system experimental device setup **b** transmission coil setting ( $60 \times 60\text{cm}$ )

power transfer (BWPT) system is proposed [33]. Compared to traditional control methods, this control strategy can further improve the overall efficiency of the BWPT system when operating over a wide load range. Professor Udaya K. Madawala's team also innovatively proposed a controller for bidirectional wireless power transfer. This controller is different from the previous bilateral controllers. It can be realized by using only one controller on the pickup side. In the absence of additional communication, the power flow and the reactive power in the resonant network are measured to adjust the power flow, while providing synchronization in both directions [34]. As shown in Fig. 6a, the frequency of the pickup switch is locked by a voltage-controlled oscillator (VCO) so that the phase difference between the calculated power phase angle and the reference point is zero. At the same time, after comparing the measured power  $P_s$  with the expected power  $P_{ref}$ , the error signal is transmitted to the PI module, and the variable  $\varphi_s$  for adjusting the power flow can be generated, as shown in Fig. 6b.

Second, most of the results achieved so far are focused on the technology itself, focusing only on technical issues such as coil offset, power flow and phase control. Considering the actual application scenario of the technology, the control strategy formulated in consideration of the actual situation of the grid and the load is extremely rare.

Third, there is still a lack of research on the simultaneous operation of multiple loads in a bidirectional ICPT system, whether it is a multi-load energy flow problem or a multi-load. There are few studies on the control issues when switching. Southeast University studied the bidirectional wireless power transfer system with  $(k + 1)$  energy transmission units. The method utilizes the relationship between the amplitude of the exit voltage of the bidirectional converter of each loop unit and the phase angle, which reduces the control difficulty of the system power flow direction and power distribution [35, 36].

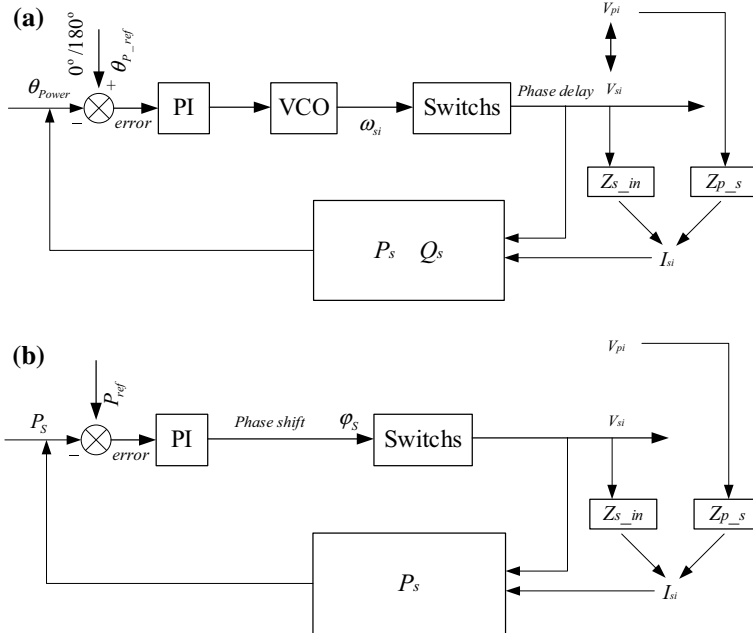


**Fig. 6** Control block diagram

## 4 Modeling and Optimization

Accurate and efficient models can predict and optimize performance. Compared with unidirectional systems, bidirectional ICPT systems have more system parameters, more complex working modes and wider application applications. These characteristics explain the significance of their modeling and optimization work.

The most common models are circuit models and mathematical models. The mathematical model is currently the most commonly used modeling method for bidirectional ICPT systems, including various modeling methods such as static and dynamic models, continuous and discrete time models, linear and nonlinear models which are suitable for bidirectional ICPT multi-parameter, multi-modal features. In the mathematical model, the object of modeling is flexible, and it can be parameters in the system such as voltage [37], current [38], power [39], harmonic [40–42] or coils in a broad range [43], and the offset trajectory of the picking pad is also modeled and analyzed, in particular, the use of physical finite element knowledge for modeling and simulation [44]. Reference [45] proposes a two-dimensional finite element model of bidirectional WPT based on physical principles. The model is also a steady-state analytical model and proves its expandability.

To optimize the overall performance of the system, modeling and improvement of the model need to be considered from multiple perspectives. Considering the influence of the dead zone effect in the operation of the high-frequency inverter on

the bidirectional ICPT system, Li Mengyi believes that the dead zone will have a large interference to the phase shift control, causing the voltage and current waveform distortion, thereby reducing the system efficiency and stability. The influence of dead zone on various parameters of the system under  $120^\circ$  phase shift control is studied. The influence coefficient of each electrical quantity dead zone is given, and the dead zone effect is accurately quantified [46]. Professor Udaya K. Madawala's team compared the reliability of a typical BWPT system with a segmented multi-track BWPT system based on the reliability of the system. The reliability parameters of the two systems are compared, such as failure rate and mean time between failures (MTBF). An optimization model of electric vehicle charging plan based on nonlinear programming is proposed [47].

## 5 Conclusion

In view of the four aspects mentioned above, the outlook is made here. Combined with the development of rail transit, electric locomotives are more suitable for segmented power supply to achieve long-distance wireless power supply and regenerative braking energy feedback. In addition to the normal load position detection, the main difficulty of its control is how to control the coil so that its working mode can be switched according to the different needs of the two sides of the vehicle. The influence of the system on both sides of the vehicle when the coil is switched also needs to be studied. Besides, the modeling of multi-load or multi-case conditions should take into account the integrity and accuracy of the model. At present, there is a lack of nonlinear mathematical models and modeling analysis of non-resonant states. The above issues need further study.

**Acknowledgements** The authors would like to thank the editors and the anonymous referees for their constructive comments and careful proof, which were helpful in the improvement of the manuscript. This work was supported by the National Natural Science Foundation of China under Project 51767015, the Gansu Provincial Natural Science Foundation of China (Gansu Provincial Science and Technology Plan) under Project 18JR3RA117.

## References

1. Lin S, Zheng Y et al (2017) Advances in inductively coupled power transfer technology for rail transit. CES Trans Electr Mach Syst 1(4):383–396
2. Huan Z (2017) Research on current sourced bi-directional inductively coupled power transfer system. Chongqing University, pp 1–12 (in Chinese)
3. Kai C, Zheng Z, Fang L et al (2017) Analysis of resonant topology for bi-directional wireless charging of electric vehicle. Autom Electr Power Syst 41(02):66–72 (in Chinese)
4. Jiang C, Chau K, Liu C et al (2017) An overview of resonant circuits for wireless power transfer. Energies 10(7):894

5. Artur M, Rafal M (2014) Bidirectional inductive contactless energy transfer system topology for electric vehicles. In: IEEE international electric vehicle conference, pp 1–7
6. Suvenu S, Akshay R, Duleepa T (2017) Bidirectional current-fed Half-Bridge (C) (LC)–(LC) configuration for inductive wireless power transfer system. *IEEE Trans Ind Appl* 53 (4):4053–4062
7. Lei Z, Duleepa JT, Udaya KM (2014) A comparison of LCL and LC bi-directional inductive power transfer systems. In: 2014 international power electronics and application conference and exposition, pp 766–771
8. Lei Z, Duleepa JT, Udaya KM (2015) A hybrid bi-directional IPT system with improved spatial tolerance. In: 2015 IEEE 2nd International Future Energy Electronics Conference (IFEEC), pp 1–6
9. Yuan S, Udaya KM, Duleepa JT (2016) LCL and CL compensations for wireless three phase bi-directional EV charging systems. In: 2016 IEEE 2nd annual southern power electronics conference, pp 1–6
10. Lei Z, Duleepa JT, Udaya KM (2017) Hybrid bidirectional wireless EV charging system tolerant to pad misalignment. *IEEE Trans Ind Electron* 64(9):7079–7086
11. Xia C, Wang W, Liu Y (2017) A bidirectional wireless power transfer system for an electric vehicle with a relay circuit. *Turkish J Electr Eng Comput Sci* 25:3037–3051
12. Li J, Li W, Cheng L, Shu L (2019) Simultaneous Wireless power and bidirectional information transmission with a single-coil, dual-resonant structure. *IEEE Trans Ind Electron* 66(5):4013–4022
13. Seho K, Grant C, John B (2017) Tripolar pad for inductive power transfer systems for EV charging. *IEEE Trans Power Electron* 32(7):5045–5057
14. Mohamed A, Marim A, Mohammed O (2017) Magnetic design considerations of bidirectional inductive wireless power transfer system for EV applications. *IEEE Trans Magnet* 53(6):1–5
15. Rathore A, Samanta S, Thrimawithana D (2017) Analysis and design of current-fed Half-Bridge (C)(LC)-(LC) resonant topology for inductive wireless power transfer application. *IEEE Trans Ind Appl* 53(4):3917–3926
16. Iqbal SM, Thrimawithana DJ, Madawala UK et al (2013) A bi-directional inductive power transfer system with individually controlled tracks and pick-ups. In: IEEE ECCE Asia Downunder, pp 1059–1064
17. Sarangga W, Udaya KM, Duleepa JT (2015) A closed loop controlled bidirectional contactless grid interface with a soft DC-link. In: IEEE 13th Brazilian power electronics conference and 1st Southern power electronics conference, pp 1–6
18. Nguyen BX, Vilathgamuwa D, Foo G, Wang P et al (2015) A multilevel converter topology based bidirectional inductive power transfer system with improved characteristics. In: 9th international conference on power electronics and ECCE Asia, pp 1673–1677
19. Suvenu S, Akshay R (2018) A new inductive power transfer topology using direct AC–AC converter with active source current wave shaping. *IEEE Trans Power Electron* 33(7):5565–5577
20. Masood M, Arif S (2018) Single-Phase soft-switched AC–AC matrix converter with power controller for bidirectional inductive power transfer systems. *IEEE Trans Ind Appl* 54 (4):3760–3770
21. Li G, Ke Z, Wen Z, Zhi W et al (2013) Design of energy feedback mode wireless charging system for electric vehicles. In: IEEE 8th conference on industrial electronics and applications, pp 1827–1831
22. Johannes T et al (2014) A practical investigation of a high power, bidirectional charging system for electric vehicles. In: 16th european conference on power electronics and applications, pp 1–7
23. Yi Z, Fan H, Fang L et al (2016) Comparison of two bidirectional wireless power transfer control methods. In: Asia-Pacific international symposium on electromagnetic compatibility, pp 68–70

24. Johannes T et al (2015) Comparison of different control strategies for series-series compensated inductive power transmission systems. In: 17th European conference on power electronics and applications, pp 1–8
25. Jian L, Yue S, Xin D (2012) Modeling and control of an LCL bi-directional inductive power transfer system. *J Chongqing Univ* 35(10):117–123 (in Chinese)
26. Bac N et al (2015) An efficiency optimization scheme for bidirectional inductive power transfer systems. *IEEE Trans Power Electron* 30(11):6310–6319
27. Lei Z, Duleepa JT, Udaya KM (2015) Performance optimization of LC bi-directional inductive power transfer system. In: IEEE 13th Brazilian power electronics conference and 1st Southern power electronics conference, pp 1–6
28. Fang Y, Yue S, Xin D (2012) Simulation of multi-load inductive coupled power bi-directional transfer mode. *J Central South Univ (Nat Sci Edn)* 43(10):3865–3871 (in Chinese)
29. Xin D, Hui S, Yue S (2013) An LCL composite resonant-type bi-directional contactless power transfer mode. *J Southwest Jiaotong Univ* 48(3):487–493 + 519 (in Chinese)
30. Ryosuke O, Kengo K, Nobukazu H, Daiki S (2017) Maximum efficiency control scheme and design method for resonant circuit of Bi-directional inductive power transfer system. In: 19th European conference on power electronics and applications, pp 1–9
31. Akshya S, Srikanth D, Udaya KM (2014) Modeling sensitivity analysis, and controller synthesis of multi pickup bidirectional inductive power transfer systems. *IEEE Trans Ind Inf* 10(2):1372–1380
32. Jun L, Byung H (2015) A bidirectional wireless power transfer EV charger using self-resonant PWM. *IEEE Trans Power Electron* 30(4):1784–1787
33. Fang L, Kai C, Ye J, Zheng Z (2019) Research on the overall efficiency optimization of the bidirectional wireless power transfer system. *J Electr* 34(05):891–901 (in Chinese)
34. Yun T, Yi C, Udaya KM et al (2018) A new controller for bidirectional wireless power transfer systems. *IEEE Trans Power Electron* 33(10):9076–9087
35. Lin T, Chang Y, Zhi L, Xue H et al (2017) Analysis of multi-unit coupling bi-directional wireless power transfer system and its control scheme. *Autom Electr Power Syst* 41(02):38–45 (in Chinese)
36. Chang, Y (2017) Modeling and control of wireless power transfer system with bidirectional energy interaction. Southeast Univ, pp 1–8 (in Chinese)
37. Dian R, Meng L, Gang Y et al (2018) Mathematical analysis of bidirectional LCL-IPT system. *Power Syst Clean Energy* 34(01):15–20 (in Chinese)
38. Udaya KM, Duleepa JT (2011) A bidirectional inductive power interface for electric vehicles in V2G systems. *IEEE Trans Ind Electron* 58(10):4789–4796
39. Ahmed M, Alberto B, Osama M (2017) Experimental validation of comprehensive steady-state analytical model of bidirectional WPT system in EVs applications. *IEEE Trans Veh Technol* 66(7):5584–5594
40. Duleepa JT, Udaya KM, Michael N (2013) A steady-state analysis of bi-directional inductive power transfer systems. In: IEEE international conference on industrial technology, pp 1618–1623
41. Ahmed M, Alberto B, Osama M (2015) Power Flow Modeling of Wireless Power Transfer for EVs Charging and Discharging in V2G Applications. In: IEEE vehicle power and pro-pulsion conference, pp 1–6
42. Meng L, Gang Y, Li Z et al (2016) Harmonic analysis of bidirectional LCL-IPT system. In: IEEE 2nd annual southern power electronics conference, pp 1–5
43. Yuan S, Udaya KM, Duleepa JT (2015) Cross coupling effects of poly-phase bi-directional inductive power transfer systems used for EV charging. In: IEEE 2nd international future energy electronics conference, pp 1–7
44. Filippo P et al (2015) Efficiency optimization in bi-directional inductive power transfer sys-tems. In: International conference on electrical systems for aircraft, railway, ship propulsion and road vehicles, pp 1–6

45. Ahmed M, Alberto B, Osama M (2016) Physics-based FE model and analytical verification of bi-directional inductive wireless power transfer system. In: IEEE/ACES international conference on wireless information technology and systems, pp 1–2
46. Meng L, Gang Y, Zhi Y, Li Z (2018) Research on dead zone effect in bidirectional inductive power transfer systems. Power Electron 52(09):5–9 (in Chinese)
47. Iqbal SMA, Udaya KM, Duleepa JT et al (2013) Reliability analysis of an LCL tuned track segmented bi-directional inductive power transfer system. In: IECON 2013 39th annual conference of the IEEE industrial electronics society, Vienna, pp 1217–1222

# Sensorless Control for IPM Synchronous Motor Using Disturbance Observer



Yikun Wang, Xizheng Guo, and Donghui Cao

**Abstract** The interior permanent magnet synchronous motor (IPMSM for short) has been widely used in many fields, such as rail transport, robot and even the aerospace. The research on the vector control strategy of permanent magnet synchronous motor has attracted much attention. The traditional vector control strategy needs to obtain the position information of the rotor through the position sensor. However, the position sensor has a series of shortcomings such as high cost and poor stability. Therefore, the research on the sensorless sensor has gained more and more attention. In the front research, we have put forward many different kinds of methods on sensorless control, but there are some obvious disadvantages. This paper introduces a sensorless control method in the full speed range. The motor is started by  $I/f$  control. When the motor is in the middle and high-speed stage, this paper uses the method based on disturbance observer to estimate the rotor position, and it achieved good results.

**Keywords** Permanent magnet synchronous motor · Sensorless control · Disturbance observer ·  $I/f$  control · Extended electromotive force

## 1 Introduction

In recent years, the sensorless control method has received extensive attention. According to the current literature, there is no control method that can achieve sensorless control in the full speed range [1], so sensorless control method can be classified into the two kinds: control method in the low-speed range and a control method in the medium and high-speed range, and if we want to achieve sensorless control at the full speed range, we should combine these two kinds of methods to achieve the full speed control.

---

Y. Wang (✉) · X. Guo · D. Cao

School of Electrical Engineering, Beijing Jiaotong University, Beijing, China  
e-mail: [16121536@bjtu.edu.cn](mailto:16121536@bjtu.edu.cn)

In the low-speed range, high-frequency voltage injection has been widely used, but this method is complicated and the filter will affect the position estimation [2], so many scholars put forward the V/f control (variable voltage and variable frequency) method [3, 4]. This method keeps the ratio of voltage and frequency constant to start up the motor smoothly. This control method does not depend on motor parameters; however, the method is prone to over-current during starting up. The  $I/f$  control method can be applied to the starting-up of the motor. The  $I/f$  control method is a method keeping the value of  $I/f$  constant. Compared with V/f control,  $I/f$  control has a smoother current during the starting process, and there is no sudden change in current and torque [5]. In this passage, we use  $I/f$  open-loop method to start up PMSM.

In the high-speed range, the main method of estimating the rotor position is to estimate back electromotive force of motor [6], which contains the position angle. According to the literature, the commonly used methods are sliding mode observer (SMO) method, but the electromotive force we estimate has lots of high-frequency noises, so we need filter to filter out the noises, but the filter will result in the phase shift of electromotive force, which makes the error of the position estimation. In this paper, we use disturbance observer to estimate the extended electromotive force of IPMSM [7]. This method is based on the current state equation, constructing the disturbance observer with extended electromotive force (EEMF) as the disturbance, so we can use disturbance observer to observe the EEMF. Compared to the sliding mode observer, the disturbance observer does not need to process EEMF through low-pass filtering, which can cause the phase shift of EEMF.

## 2 Sensorless Method Using Disturbance Observer

In this section, we first propose a concept of EEMF based on the mathematical model of the IPMSM. Then, the linear state equation of the disturbance observer is proposed by mathematical model of the salient machine, and the disturbance observer which estimates the extended electromotive force of the IPMSM is designed according to the state equation [8].

### 2.1 EEMF Mathematical Model

The voltage equation of IPMSM on  $d$ - $q$ -axis is

$$\begin{bmatrix} v_d \\ v_q \end{bmatrix} = \begin{bmatrix} R + pL_d & -\omega_{re}L_q \\ \omega_{re}L_d & R + pL_q \end{bmatrix} \begin{bmatrix} i_d \\ i_q \end{bmatrix} + \begin{bmatrix} 0 \\ \omega_{re}K_E \end{bmatrix} \quad (1)$$

In Eq. (1),  $R$  stands for stator resistance of the motor;  $L_d$ ,  $L_q$  stand for inductances of  $d$ -axis and  $q$ -axis;  $K_E$  stands for back electromotive force constant;  $\omega_{re}$  stands for electric angular velocity of the motor.

The equation that (1) transformed into fixed coordinate  $\alpha - \beta$  is:

$$\begin{bmatrix} v_\alpha \\ v_\beta \end{bmatrix} = R \begin{bmatrix} i_\alpha \\ i_\beta \end{bmatrix} + pL_0 \begin{bmatrix} i_\alpha \\ i_\beta \end{bmatrix} + \omega_{\text{re}} K_E \begin{bmatrix} -\sin \theta_{\text{re}} \\ \cos \theta_{\text{re}} \end{bmatrix} + pL_1 \begin{bmatrix} \cos 2\theta_{\text{re}} & \sin 2\theta_{\text{re}} \\ \sin 2\theta_{\text{re}} & -\cos 2\theta_{\text{re}} \end{bmatrix} \begin{bmatrix} i_\alpha \\ i_\beta \end{bmatrix} \quad (2)$$

In Eq. (2), it contains the component  $\theta_{\text{re}}$  and  $2\theta_{\text{re}}$ , which can make it difficult to extract the rotor position. Therefore, we should eliminate the monomial that contains  $2\theta_{\text{re}}$ . In the IPMSM, the Eq. (2) can be transformed into the Eq. (3) by coordinate transforms. The Eq. (3) is shown below:  $2\theta_{\text{re}}$

$$\begin{bmatrix} v_d \\ v_q \end{bmatrix} = \begin{bmatrix} R + pL_d & \omega_{\text{re}} L_q \\ -\omega_{\text{re}} L_q & R + pL_d \end{bmatrix} \begin{bmatrix} i_\alpha \\ i_\beta \end{bmatrix} + \begin{bmatrix} 0 \\ (L_d - L_q)(\omega_{\text{re}} i_d - i_q) + \omega_{\text{re}} K_E \end{bmatrix} \quad (3)$$

We will transform Eqs. (3–4), which is on  $\alpha - \beta$ -axis. In Eq. (4),  $e = (L_d - L_q)(\omega_{\text{re}} i_d - i_q) + \omega_{\text{re}} K_E$ .

$$\begin{bmatrix} v_\alpha \\ v_\beta \end{bmatrix} = R \begin{bmatrix} i_\alpha \\ i_\beta \end{bmatrix} + \begin{bmatrix} pL_d & \omega_{\text{re}}(L_d - L_q) \\ -\omega_{\text{re}}(L_d - L_q) & pL_d \end{bmatrix} \begin{bmatrix} i_\alpha \\ i_\beta \end{bmatrix} + e \begin{bmatrix} -\sin \theta_{\text{re}} \\ \cos \theta_{\text{re}} \end{bmatrix} \quad (4)$$

## 2.2 Composition of Disturbance Observer

According to the previous description, we can construct a disturbance observer by a linear state equation of the motor and a linear state equation. According to the voltage model of the motor and the equation of electromotive force, if the current and electromotive force form a space vector of the state equation, the voltage equation becomes:

$$pi = -\frac{R}{L_d} Ii + \frac{\omega_{\text{re}}(L_d - L_q)}{L_d} Ji - \frac{1}{L_d} e + \frac{1}{L_d} v = A_{11}i + A_{22}e + B_1v \quad (5)$$

In (5),  $v = [v_\alpha \ v_\beta]^T$ ,  $i = [i_\alpha \ i_\beta]^T$ ,  $e = [e_\alpha \ e_\beta]^T$ , it is the input quantity of the observer, the state quantity and the amount of interference that needs to be observed. Then, we got the differential of  $e$  from (5).

$$pe = \{(L_d - L_q)(\omega_{\text{re}} \dot{i}_d - \ddot{i}_q) + \omega_{\text{re}} K_E\} \begin{bmatrix} -\sin \theta_{\text{re}} \\ \cos \theta_{\text{re}} \end{bmatrix} + \omega_{\text{re}} Je = A_{22}e + W \quad (6)$$

(5) and (6) are summarized to state equation of the disturbance observer. Assuming that the time constant of the system is very small and velocity is constant, the equation of state of the disturbance observer is:

$$p \begin{bmatrix} i \\ e \end{bmatrix} = \begin{bmatrix} A_{11} & A_{12} \\ 0 & A_{22} \end{bmatrix} \begin{bmatrix} i \\ e \end{bmatrix} + \begin{bmatrix} B_1 \\ 0 \end{bmatrix} v + \begin{bmatrix} 0 \\ W \end{bmatrix} \quad (7)$$

According to the literature, when the disturbance is changing slowly, the equation of the reduced-order disturbance observer can be written as:

$$\dot{\hat{e}} = G(A_{12}\hat{e} - A_{12}e) \quad (8)$$

In the real situation,  $\dot{e} = \omega_{\text{re}}Je$ , so in this situation, we can get the estimation equation in Eq. (9):

$$\dot{\hat{e}} = G\tilde{A}_{11}i + (G\tilde{A}_{12} + \tilde{A}_{22})\hat{e} + G\tilde{B}_1v - Gi \quad (9)$$

The differential of current appears in (9), which causes noise of current and affects the performance of observer. To eliminate the differential of current, you can construct intermediate variables  $\xi$ :

$$\xi = \hat{e} + Gi \quad (10)$$

In Eq. (10),  $G$  is the gain matrix of the equation. The equations can be simplified according to (9) and (10):

$$\dot{\xi} = (G\tilde{A}_{12} + \tilde{A}_{22})\xi + G\tilde{B}_1v + (G\tilde{A}_{11}I - G\tilde{A}_{12}G - \tilde{A}_{22}G)i \quad (11)$$

When we obtain  $\xi$  in Eq. (11), we can estimate EEMF  $\hat{e}$  in (12):

$$\dot{\hat{e}} = \xi - Gi \quad (12)$$

### 2.3 Adaptive Estimator

The velocity  $\hat{\omega}_{\text{re}}$  is obtained by adaptive observer. According to the adaptive algorithm, the adaptive observer consists of three parts: reference model, estimation model and adaptive law. The reference model is disturbance observer mentioned above. The estimation model consists of EEMF model and EEMF feedback loop. The adaptive law is to let the reference model and the estimation mode become more coincident by adjusting the parameter of the estimation model.

The reference model of the estimator is:

$$\dot{\hat{e}}_n = \omega_{\text{re}} J \hat{e}_n \quad (13)$$

The estimation model of the estimator is:

$$\dot{\tilde{e}}_n = \hat{\omega}_{\text{re}} J \tilde{e}_n + G' (\tilde{e}_n - \hat{e}_n) \quad (14)$$

The adaptive law of the observer is designed by Popov's theory of hyperstability, so the estimation error may converge to zero. The adaptive law of the adaptive system can be derived as the following equation:

$$\hat{\omega}_{\text{re}} = \left( k_p + \frac{k_I}{s} \right) (e^T J \tilde{e}_n) \quad (15)$$

Based on the above model and related equations, we can build related models. In IPMSM, we use MTPA vector control strategy, and the block diagram is shown in Fig. 1.

### 3 Zero-Low-Speed Start Method

In the process of starting up the motor, there are two steps to start up: Detect the initial position of the motor, and start up the motor. The method we use to detect the initial method is pre-positioning method, and then we use *I/f* open-loop method to

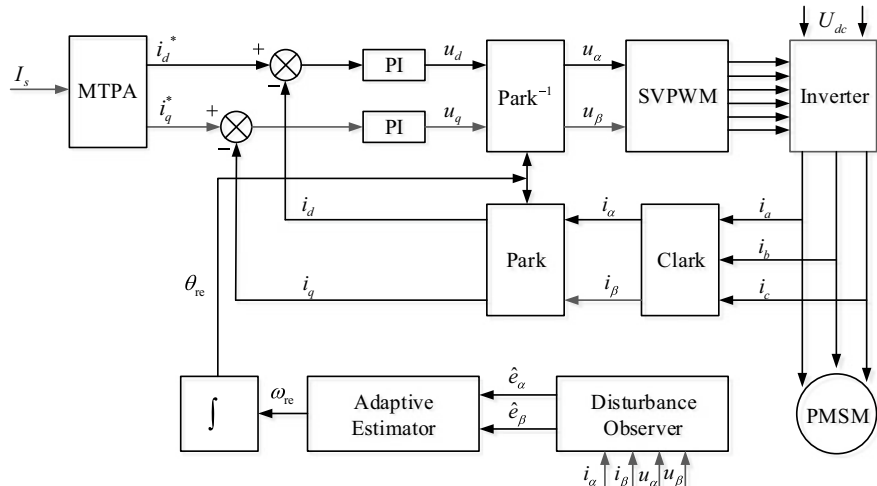


**Fig. 1** Block diagram of sensorless control at high-speed range

start up the motor. In this paragraph, we will describe the starting-up method we use in this passage.

### 3.1 Initial Position Detecting

In this passage, we use pre-positioning method for rotor positioning. The schematic diagram of the pre-positioning method is shown in Fig. 2. We inject the current vector in two stators *A* and *B*, stators will generate a synthetic magnetic field to position the rotor at a predetermined position [9]. In the Fig. 2, the (a) in the Fig. 2 shows the stator position before injecting. The (b) in the Fig. 2 shows the staror position after injecting. The (c) in the Fig. 2 shows the blind zone of the pre-positioning.

When the angle between the current vector and the rotor position is too small, the torque of the motor is not enough to overcome the original torque, resulting in positioning failure. This angle can be defined as the limit angle. The limit angle can be expressed as:

$$\theta_{\text{lim}} = \sin^{-1} \frac{2T_0}{3pI_s\psi_f} \quad (16)$$

The area where the motor cannot be positioned is called positioning blind zone. The positioning blind zone is shown in Fig. 3. When the rotor rotates to area *d-e*, the rotor error is always maintained at  $180^\circ$ , motor cannot be started, so we can inject vector  $I_{s2}$  after injecting  $I_{s1}$ . The blind zones of the two positionings will not coincide, so that at least one of the two positioning processes can cause the rotor to rotate for positioning.

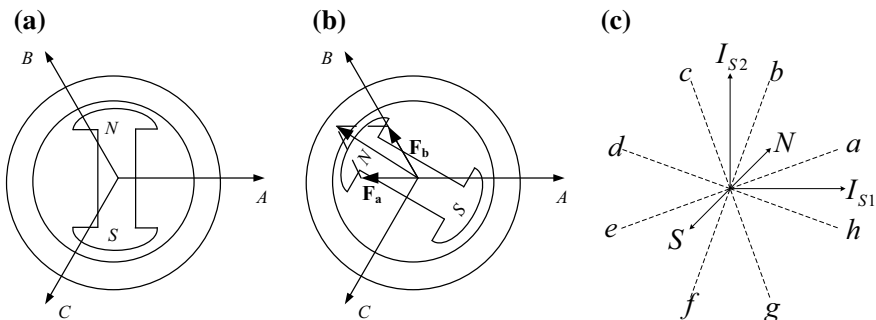


**Fig. 2** Schematic diagram of pre-positioning method and blind zone. **a** Before pre-positioning, **b** after pre-positioning and **c** diagram of pre-positioning blind zone

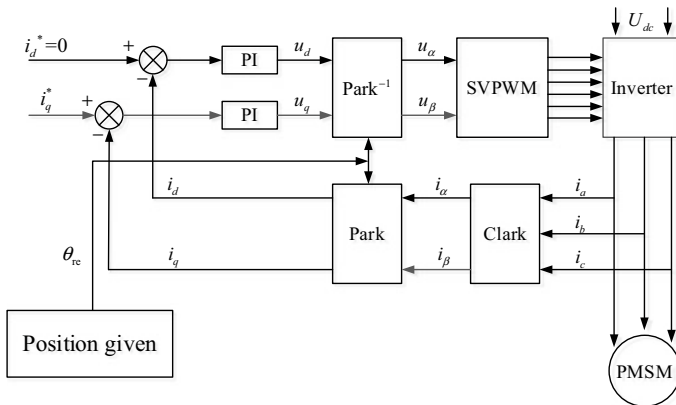


**Fig. 3** Diagram of  $I/f$  control method

### 3.2 $I/f$ Flow Frequency Ratio Open-Loop Start Method

After the initial position of the rotor is successfully positioned, the motor will start. In this paper, the starting method we use is  $I/f$  open-loop starting method. This method is not affected by the motor parameters. The  $I/f$  control is compared to the open-loop start method as shown in Fig. 3.

As we can see from Fig. 3, the currents  $i_d$  and  $i_q$  are controlled by current loop, and speed loop is replaced by the open-loop position angle generator. We give the

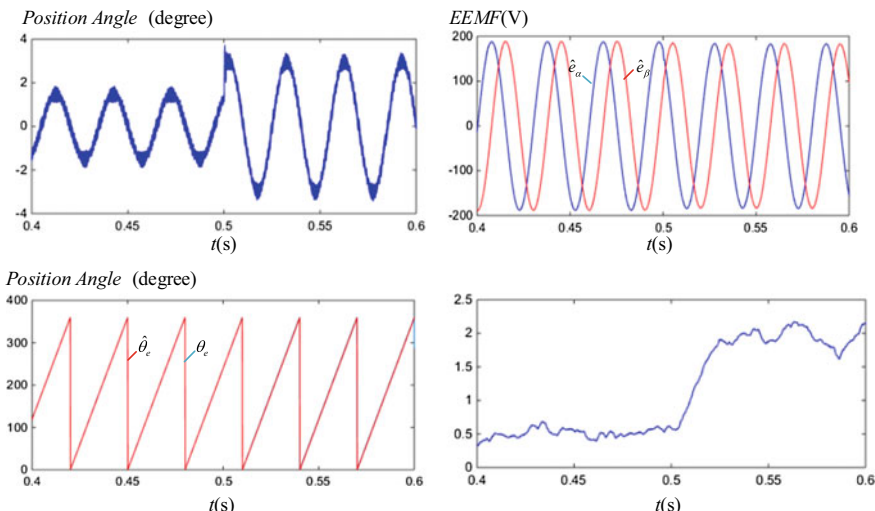


**Fig. 4** Simulation results of the model when current is abrupt

angle command to accelerate the current vector. We assume the rotor acceleration is  $a$ , the initial position is  $\theta_0$ , and the angle command  $\theta_{\text{open}}$  can be shown in (17).

$$\begin{cases} \theta_{\text{open}} = \theta_0 + \int \omega^* dt \\ \omega^* = \int a dt \end{cases} \quad (17)$$

In order to avoid the starting failure, there are limitations on speed acceleration, we can set the acceleration of the speed within a range, and it is shown in (18).

$$a < \frac{p}{J} \left( \frac{3}{2} p \psi_{PM} i_{q^*} - T_L \right) \quad (18)$$

## 4 Simulation Results

In order to verify the correctness of this sensorless control method, we built a sensorless control model in MATLAB. The simulation model adopts 3 kW PMSM experiment platform, and the motor parameters are shown in Table 1. The step size of the simulation is 1e-6s. The PI regulator of the simulation adopts inertia regulation. The main parameters of the simulation is shown in the Table 1.

### 4.1 Simulation Results in High-Speed Range

When the current command is abrupt from 1.5 to 3 A, the velocity of motor is 500 rpm, and the switching frequency is 10 kHz. The simulation results are shown in Fig. 4.

From Fig. 4, we can draw a conclusion that when current is abrupt, the error of the rotor position will increase from 0.5 degrees to 2°, but the control system can maintain the good angle tracking performance. When the current changes, the amplitude of EEMF changes too. From this, we can see that when the load of the

**Table 1** Parameter of IPMSM

Parameter	Numerical value
Rated voltage/V	380
Rated torque/N · m	15
Pole pairs/ $p$	4
Stator resistance/ $\Omega$	2.85
$d$ -axis inductance/mH	24.75
$q$ -axis inductance/mH	80.51
Flux linkage/Wb	0.85

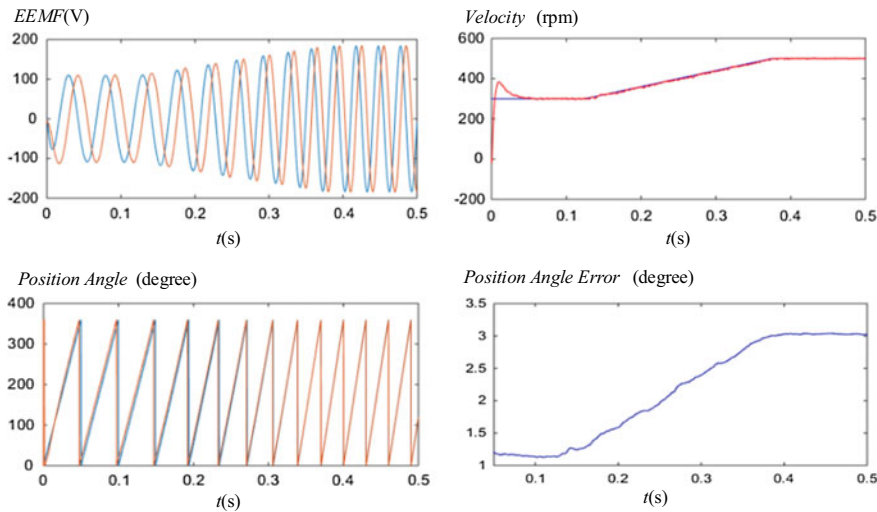


**Fig. 5** Simulation results of the model when velocity increases

motor changes, the EEMF also changes. When velocity is linear grown from 300 to 500 rpm and current command is 3 A, the simulation results are shown in Fig. 5.

In Fig. 5, we can see that when the velocity increases, the error increases from  $1.2^\circ$  to  $3^\circ$ , but it still keeps the good control performance, and when the velocity increases linearly, the amplitude of EEMF also increases linearly, which is consistent with Eq. (4).

From the simulation above, we can draw the conclusion that the method based on the disturbance observer has a good performance on motor control in high-speed range, and the adaptive improvement can widen the speed range.

## 4.2 Simulation Results in Low-Speed Range

In the low-speed range, we should locate the rotor position first. We built a model based on pre-positioning method in MATLAB, the initial angle is 150 degree, and then it mutates to  $240^\circ$  when  $t$  is 0.5 s. The simulation results of pre-positioning are shown in Fig. 6.

From Fig. 6, we can infer that the pre-positioning can locate rotor to the pre-determined location.

After locating the initial position, we will start up the motor by  $I/f$  open-loop method. We have built  $I/f$  control method model in MATLAB, and the simulation results are shown in Fig. 7.

From Fig. 7, we can find that  $I/f$  control can start up the motor smoothly, and the actual speed can keep up with command speed.

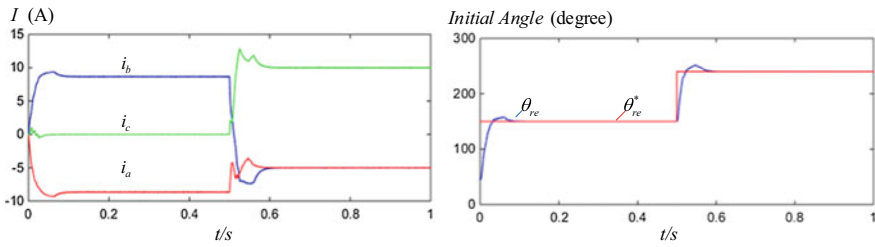


**Fig. 6** Pre-positioning simulation results

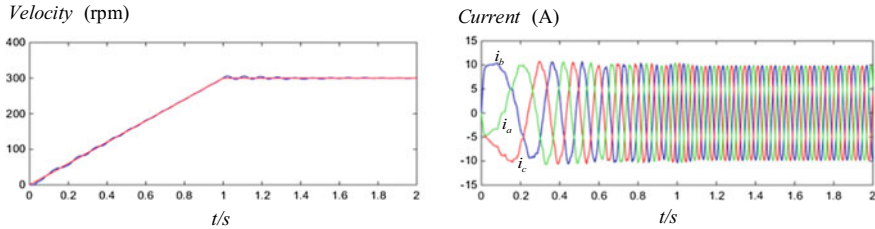


**Fig. 7** Simulation results of  $I/f$  control

From simulation in this section, we can find that the method based on  $I/f$  control in the low-speed range and the method based on the disturbance observer in the high-speed range both have a good performance in controlling the motor.

## 5 Conclusion

In this paper, we proposed a sensorless control method using disturbance observer. First, in the low-speed range, we used the  $I/f$  open-loop control to start up the motor. In high-speed range, the method using disturbance observer is used to control the motor. We have designed the disturbance observer to estimate EEMF. Then, we designed the velocity estimator using EEMF to estimate the velocity and position of the rotor based on the adaptive model.

Finally, we use the MATLAB to simulate the operation of the sensorless control method in this paper. From the simulation results in MATLAB, we can draw a conclusion that whether the motor is in low-speed range or in the high-speed range, and the sensorless control has the good performance.

## References

1. Liyong Y, Xiaofeng X, Zhigang C (2016) Study on sensorless control of PMSM based on back EMF PLL method. *Power Electron* 50(12):88–90 (in Chinese)
2. Gang Q, Bin L (2019) Improvement of sliding mode observer for position sensorless position estimation of PMSM. *Electr Eng* 20(04):67–71 (in Chinese)
3. Xinyi X (2015) Exploration of PMSM speed sensor based on extended synovial controller. *Electron Test* 2015(05):4–6 (in Chinese)
4. Zhibin R, Lujia W, Bin X, Wei W (2019) A new method and implementation of position sensorless control for brushless DC motor. *Micromotor* 52(03):26–30 + 36 (in Chinese)
5. Hamasaki S, Uchino N, Tsuji M (2004) Novel method for line current detection type active filter using the disturbance observer. In: 30th annual conference of Industrial Electronics Society, IECON 2004, IEEE
6. Hwang JK, Oh KH, Song CK (2005) Sliding mode control with disturbance observer for antilock braking systems. In: Proceedings of IEEE/ASME international conference on advanced intelligent mechatronics, 2005
7. Liu Y, Zhou B, Sichen F (2009) Sliding mode control of PMSM based on a novel disturbance observer. In: 4th IEEE Conference on Industrial Electronics and Applications, ICIEA 2009
8. Jian Z, Hexu S, Zhaoming L, Tao L (2007) A design method of sliding mode controller based on disturbance observer. In: 2007 Chinese control conference, CCC 2007
9. Jian Z, Hexu S, Zhaoming L, Tao L (2007) A design method of sliding mode controller based on disturbance observer [P]. In: 2007 Chinese control conference, CCC 2007

# A U2P-Miner-Based Method to Identify Critical Energy-Consuming Parts of Urban Rail Operation System



Mingtao Wu, Yanhui Wang, Shuai Lin, Boyan Hao and Pengfei Sun

**Abstract** Urban rail system is one of the most energy-consuming and highest costing public sectors in cities, and its energy efficiency has great potential to improve on the system level. The aim of this study is to introduce a novel method for identifying key energy-consuming parts based on univariate uncertain data pattern miner (U2P-miner) in order to improve the energy efficiency of urban rail system and to apply it in a real urban rail system. Firstly, an energy consumption association network model is constructed based on the operation energy consumption by analyzing the association among the energy use during operation. Secondly, a method for identifying critical nodes using U2P-miner algorithm is presented, which consider both topological and energy-consuming attributes of nodes. Finally, the proposed method is applied in Beijing Subway to help operator make better choices in energy efficiency improvement.

**Keywords** Urban rail operation system · Energy efficiency · Network model · Critical part identification · Univariate uncertain data pattern miner

---

M. Wu (✉) · Y. Wang · S. Lin

State Key Laboratory of Rail Traffic Control and Safety, Beijing Jiaotong University,  
Beijing 100044, China  
e-mail: [17120770@bjtu.edu.cn](mailto:17120770@bjtu.edu.cn)

Research and Development Center of Transport Industry of Technologies  
and Equipments of Urban Rail Operation Safety Management,  
MOT, PRC, Beijing, China

Y. Wang  
e-mail: [Wangyanhui@bjtu.edu.cn](mailto:Wangyanhui@bjtu.edu.cn)

S. Lin  
e-mail: [13114253@bjtu.edu.cn](mailto:13114253@bjtu.edu.cn)

M. Wu · S. Lin · B. Hao · P. Sun  
School of Traffic and Transportation, Beijing Jiaotong University,  
Beijing 100044, China  
e-mail: [17120809@bjtu.edu.cn](mailto:17120809@bjtu.edu.cn)

P. Sun  
e-mail: [17120967@bjtu.edu.cn](mailto:17120967@bjtu.edu.cn)

## 1 Introduction

Urban rail transportation, as the most important public transportation of urban transportation, has become one of the most energy-consuming and highest costing public sectors in cities of developing and developed countries both. For instance, in the European Union (EU) [1], urban rail transportation releases almost 25% of the total CO<sub>2</sub>. In fact, energy costs of urban rail transportation have accounted for almost 40% of operating costs, and the amount is still showing a rapid upward trend: In 2012, the electricity consumption of Beijing Subway was 853 million kWh, and in 2017 it reached 1.13 billion kWh. In order to conserve energy, China has proposed to build a faster, safer and more reliable urban rail system with higher volumes and energy efficiency in the 13th Five-Year Plan [2]. Therefore, how to effectively implement energy saving and emission reduction, improve energy efficiency and avoid high energy consumption points during the operation phase has become an important scientific and technical issue.

A large number of literatures research the energy efficiency management and energy-saving measures of each profession and each subsystem for the rail transit system. For regenerative braking, Boizumeau [3] utilized braking energy recovery system to save significant energy up to 14%. For energy efficiency comfort function of infrastructure, Fong [4] proposed some dynamic control strategies with less investments but more energy saving in heating, ventilation, and air conditioning (HVAC) system. A coupling effect among subsystems and devices of the rail transit system reduces the energy efficiency in nature, while this coupling relationship is not taken into account in the existing methods. Therefore, in order to improve system energy efficiency, there is an urgent need to solve how to assess the holistic system energy from the perspective of the system as a whole.

## 2 Energy-Associated Network Model

The system energy efficiency is the ability to minimize the energy consumption through the full utilization of existing technologies under the premise of the demand and service level of urban rail transit passengers, reflecting the energy utilization efficiency. The level of system energy efficiency, which is the emergence characteristics of component interaction, is determined by the behavior, associated relationships and emerging behaviors of the energy-consuming devices that make up the system. According to the definition of system energy efficiency, it is closely related to the structure of the system which is suitable to be represented by topological network. Therefore, in this paper we construct an EAN with subsystems as components and connections among them as edges.

## 2.1 Components

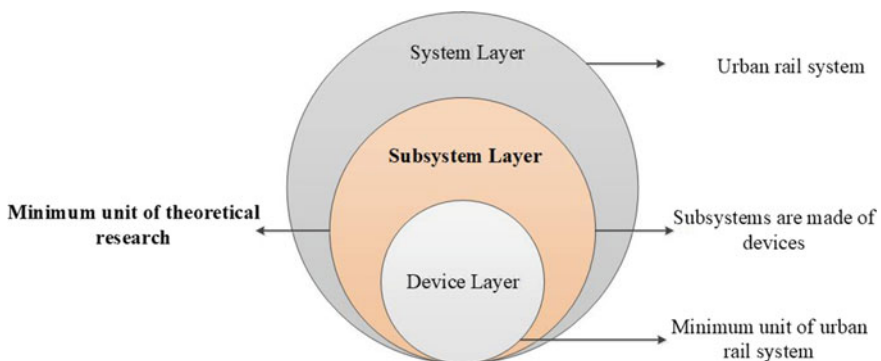
The urban rail system could be decomposed into limited manageable energy-consuming subsystems or devices from the perspective of maintenance and management. That is, it can be divided into three layers including system, subsystem and device layer (Fig. 1).

In theory, though the energy-consuming device is the minimum unit of urban rail system, it is impossible to access to energy-consuming data of every single device with limited cost. Hence, in this paper, the subsystems, which consist of devices with similar or identical functions, are regarded as the components, i.e., the minimum units of theoretical research. In other words, when components are selected, the following conditions also should be satisfied:

1. Computability: The energy consumption of components could be calculated according to the data in Table 1 which we attain from Beijing Subway.
2. Functionality: The component should have a specific function and a whole behavior, and could participate in the energy consumption process of the system as a whole.

## 2.2 Connection Among Components

There are two types of connections among components that is the mutually reinforcing or inhibiting relationship. Mutually reinforcing relationship refers to that one component promotes the energy consumption of another component and vice versa. Also, mutually inhibiting relationship refers to that one component reduces the energy consumption of another component and vice versa. Pearson correlation coefficient [5] is used to find out the correlation between component energy

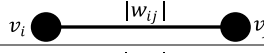
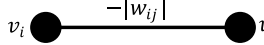


**Fig. 1** Hierarchy division of urban rail system

**Table 1** Part of the energy-consuming data obtained from Beijing Subway

Year	Month	Traction system	Elevator and escalator system	HVAC system	Lighting system	Other system
2016	January	63192419	7050922	17123667	8085221	7864142
	February	55930394	4708305	11434456	10588367	9503925
	...	...	...	...	...	...
	December	61465086	7409108	17993549	8796269	3427689
2017	January	58941636	5970386	14499509	6393935	10600356
	February	55270453	5329943	12944148	6303970	7841619
	...	...	...	...	...	...
	December	62819086	6990293	16976425	6435240	5185789

**Table 2** Connection among components

Connection among components	Network representation
Mutually reinforcing relationship	
Mutually inhibiting relationship	

consumption data. In Table 2,  $|w_{ij}|$  is the absolute value of Pearson correlation coefficient between  $v_i$  and  $v_j$ . If  $v_i$  and  $v_j$  have mutually reinforcing relationship, their connection should be represented by  $|w_{ij}|$ . Otherwise, their connection should be represented by  $-|w_{ij}|$ .

### 2.3 Energy-Associated Network Model of Urban Rail System

According to network theory, the structure of urban rail system may be abstracted as a directed network, where the components are regarded as nodes, and the connections between components are abstracted as edges. Taking into account the strength of topological indicators and energy-consuming characteristics, an analytical model is called as energy-associated network (EAN) model and defined as Eq. (1):

$$EAN = G(V, E, T_V, EC_V)$$

$$\begin{cases} V = \{v_1, v_2, v_3, \dots, v_n\} \\ E = \{e_{ij} | i, j \in n\} \\ T_V = \{\text{DC}(v_i), \text{BC}(v_i), \text{CC}(v_i), \dots | v_i \in V\} \\ EC_V = \{\text{EC}(v_i) | v_i \in V\} \end{cases} \quad (1)$$

where  $V$  is a set of nodes, the number of nodes is  $n$ , and each node  $v_i$  represents the energy-consuming subsystem;  $E$  is a set of association, and  $e_{ij}$  represents the association relationship between  $v_i$  and  $v_j$ ;  $T_V$  is the set of topology properties of nodes, including  $DC(v_i)$ ,  $BC(v_i)$ ,  $CC(v_i), \dots$ ;  $DC$ , weighted degree centrality of a node, is defined as the sum of the weight of edges in the network that are directly connected to the node  $v_i$  [6];  $BC$  is the betweenness centrality of node  $v_i$ , and it represents the ratio of the number of edges existing between this node  $v_i$  and its neighbor nodes in the network to the total number of possible edges [7];  $CC(v_i)$  is the clustering coefficient of node  $v_i$ , and it reflects the tightness of the connection between the node  $v_i$  and its neighbor node [8].  $EC_V$  is average consumption of electricity consumed by the subsystem during a statistical period which could be yearly, monthly or daily, depending on the available operation energy-consuming data. It is average consumption of electricity consumed by the subsystem during a statistical period which could be yearly, monthly or daily, depending on the available operation energy-consuming data. Besides, average consumption means it is the ratio of total energy consumption to passenger flow in order to fully considering the impact of operations on energy efficiency.

### 3 Critical Energy-Consuming Node Identification Method Based on U2P-Miner

In this section, we propose a U2P-miner [9, 10]-based method to identify critical energy-consuming parts, and those steps which are illustrated in Fig. 2 in the proposed method are explained as follows:

*Step 1.* Construct the energy-associated network model  $EAN = G(V, E, T_V, EC_V)$  of an actual urban rail system according to Sect. 2.3.

*Step 2.* Calculate interval numbers of the association structure attributes for nodes which include  $DC$ ,  $BC$  and  $CC$ , and energy-consuming attribute which is  $EC$ . Suppose an attribute  $A_j, j \in J$  in a node  $v_i$  is associated with a quantitative interval  $I_j$  and a probability density function  $P_A$  that assigns a probability to each value in the interval, where a node in the *EAN model* constructed in *Step 1* comprises four non-repeated attributes, denoted by  $J = \{1, 2, 3, 4\}$ , that capture the essential features of every node, and all should be taken into account in identification process. Therefore,  $DC$ ,  $BC$ ,  $CC$  and  $EC$  are represented by  $A_1, A_2, A_3$  and  $A_4$ , and  $I_j$  with a range from  $m$  to  $n$  is represented by  $I_j = \{m, n\}$ , whose type is univariate uncertain model.

(1) Association structure attributes. Association structure attributes of a node are constant values, since the topological structure of the *EAN model* is definite and unchangeable. Therefore, interval numbers of association structure attributes are  $I_j = \{m, m\}, j = \{1, 2, 3\}$ , and the probability density functions  $P_A$

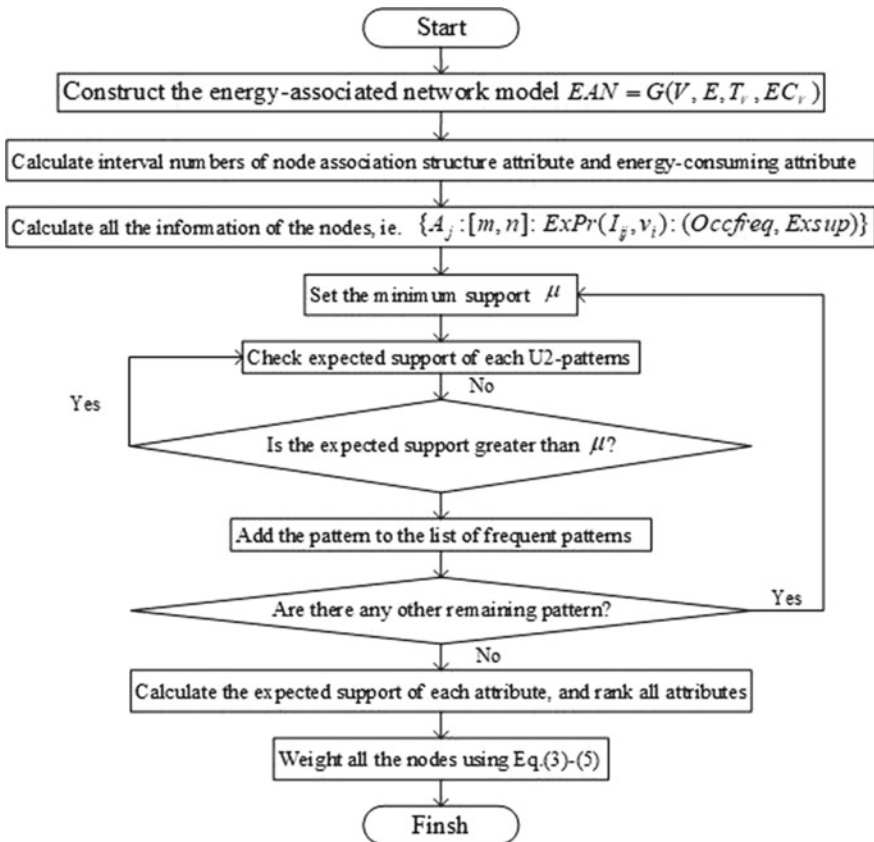


**Fig. 2** Procedures for the proposed method

associated with  $I_j$  can be considered as a uniform distribution function, which means the probability that  $I_j$  is assigned  $m$  is 100%.

- (2) Energy consumption attribute. A large amount of operational energy consumption data is collected and recorded by the energy metering system of urban rail system every day, which means we usually have a number of energy consumption data of nodes. In order to fully consider the impact that the values of energy consumption of subsystems and the actual situation of the operation have on the node, interval number of energy consumption attribute is represented as  $I_4 = \{\min, \max\}$ , where  $\min$  is the minimum ratio of total energy consumption of the node to passenger flow of the system during the statistical period which depends on the energy monitoring conditions for urban rail system, and  $\max$  is the maximum ratio under the same condition. Besides, the probability density functions  $P_A$  associated with  $I_4$  can also be considered as a uniform distribution function, since there is little research on the feature of operational energy-consuming data of each subsystem.

*Step 3.* A U2-pattern is frequent if its expected support exceeds the minimum support determined in advance, and the more frequent U2-pattern indicates the interval numbers of the attribute where the actual values locate with higher probability. Besides, the existential probability of  $I_{ij}$ ,  $\text{ExPr}(I_{ij}, v_i)$  denotes the integral of the density over  $I_{ij}$ , which can be considered as the possibility that the values in the  $I_{ij}$  appear in *EAN model*. In this step, we calculate expected support of the given U2-pattern  $U$  which is outlined by Eq. (2), where  $|V|$  denotes the numbers of nodes in *EAN model*.

$$\text{ExSup}(U) = \sum_{i=1}^{|V|} \left[ \prod_{x \in v_i} \text{in}_{\text{EAN}} \text{ExPr}(x, v_i) \right] \quad (2)$$

*Step 4.* Calculate all the information of the nodes in *EAN model*, and these will be used in the following steps. The consequential information of a node in *EAN model* can be represented by  $\{A_j : [m, n] : \text{ExPr}(I_{ij}, v_i)\} : (\text{Occfreq}, \text{Exsup}) \text{ExPr}(I_{ij}, v_i)$ ,  $\text{ExSup}$  has been introduced in Step 3, and the rest of terms are defined below:

- (1) Base element  $\{A_j : [m, n] : \text{ExPr}(I_{ij}, v_i)\}$

For the interval  $I_j$  of the attribute  $A_j$ , there are many values acting as lower or upper bounds, which are more consequential than those that do not, and each pair of consecutive bound can form directly a base interval, which is denoted by  $BI_k : [m, n]$  showing the base interval  $k$  with a range from  $m$  to  $n$ . Besides, the base element which is built by each base interval abided by  $\text{ExPr}(I_{ij}, v_i)$  is denoted by  $\{A_j : [m, n] : \text{ExPr}(I_{ij}, v_i)\}$ .

- (2) Occurrence frequency Occfreq

Occurrence frequency is defined as the number of attributes that contain the base element.  $\{A_j : [m, n] : \text{ExPr}(I_{ij}, v_i)\}$  and its Occfreq are contained in a node in the U2P-tree which compresses the attributes of *EAN model* into a tree structure.

*Step 5.* Construct a U2P-tree for frequent U2-patterns enumerating. In this step, all the information of attributes of *EAN model* is compressed into a tree structure. In other words, every interval is decomposed into base intervals. A node in the U2P-tree contains the information of attributes, denoted by  $\{A_j : [m, n] : \text{ExPr}(I_{ij}, v_i)\} : (\text{Occfreq}, \text{Exsup})$ .

*Step 6.* Enumerate frequent U2-patterns using the constructed U2P-tree. The patterns including the final base interval of the last nodes in the *EAN model* are enumerated first, and so does the next. The partial expected support of the tree node is attained by multiplying Occfreq by the value of the existential probability of its base interval. Then, for each U2-pattern,  $\text{ExSup}(U)$  is derived by summing the partially expected supports that are containing that base interval of the nodes in the U2P-tree. Finally, the list of U2-pattern will be attained after enumerating.

*Step 7.* Compare  $\text{ExSup}(U)$  with the minimum support  $\mu$ . If  $\text{ExSup}(U)$  is larger than or equal to  $\mu$ , then the pattern is considered as a frequent pattern; in the other way, if  $\text{ExSup}(U)$  is less than  $\mu$ , then the pattern is not considered as a frequent pattern.

*Step 8.* Rank the attributes by using the attained total expected supports of the attributes which is used to attain the importance of the nodes in *EAN model*. The less the total expected support of attribute  $j$ , denoted by  $T_j$ , the more important the attribute is. In other words, the most important attribute is the one with smallest total expected support.

*Step 9.* Weight the nodes using the method represented by Eq. (3).

$$w_j = \frac{100(n+1-r)}{n}, j \in J \quad (3)$$

where  $w$  is the weight of the nodes,  $J$  is the set of attributes,  $r$  is the rank of the attributes, and  $n$  is the number of attributes.

*Step 10.* Convert interval data into single-value data using Eq. (4).

$$I_{i4} = w_4 I_L + (1 - w_4) I_R \quad (4)$$

where  $I_L$  and  $I_R$  are the lowest and highest limits of the interval.

*Step 11.* Calculate the weight of the node using the method represented by Eq. (5).

$$N_k = \sum w_k I_{kj}, k \in K, j \in J \quad (5)$$

where  $N_k$  is the weight of the nodes and  $K$  is the set of nodes. The more value the  $N_j$  is, the more important the node will be.

## 4 Case Study and Discussion

### 4.1 Network Model of Beijing Subway

Beijing Subway is one of the most important operators of the urban rail system in China, and it operates 15 lines and 234 stations up to December 2018. Beijing Subway consists of many energy-consuming subsystems according to the data

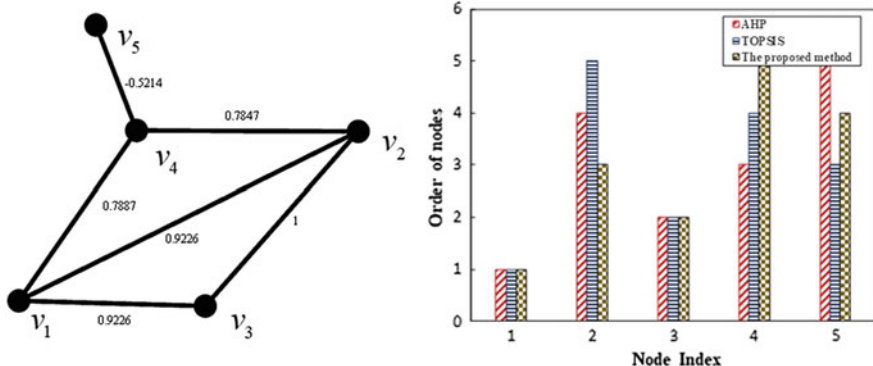


**Fig. 3** (Left) EAN of Beijing Subway, (right) comparison of the order of nodes using AHP, TOPSIS and the proposed method

achieved by detailed survey with engineers from Beijing Subway as shown in Table 1.

Using the network construction procedure in Sect. 2.3, the EAN model for Beijing Subway is shown in Fig. 3 (left). In EAN model, nodes from  $v_1$  to  $v_5$  represent traction system, elevator and escalator system in the station, HVAC system, lighting system and other systems, separately, and the weights of the edge are available in EAN model. Besides, the normalized attributes originated from EAN are shown in Table 3.

## 4.2 Results and Analysis

Using the method in Sect. 3, the final U2P-tree is shown in Fig. 4. Afterward, let the minimum support be 2, and the rank of attributes is  $T_4 = 66.003$ ,  $T_1 = 22$ ,  $T_3 = 19$ ,  $T_2 = 11$ . Then, apply Eqs. (3) to (5) to get the nodes' order. The ranks for nodes by AHP, TOPSIS and the proposed method are shown in Fig. 3 (right). The common features of these three approaches are that nodes  $v_1$  and  $v_3$  are the most important nodes in *EAN model*, which means the traction system and the HVAC system are the critical energy-consuming parts. Therefore, the proposed method can

**Table 3** Normalized attributes originated from EAN

Node	<i>DC</i>	<i>BC</i>	<i>CC</i>	<i>EC</i>	
				Max	Min
$v_1$	2.6339	1	0.6667	0.5107	0.652
$v_2$	2.7073	1	0.6667	0.1281	0.21
$v_3$	1.9226	0	1	0.311	0.51
$v_4$	2.0948	3	0.3333	0.1719	0.3099
$v_5$	0.5214	0	0	0.0091	0.3647

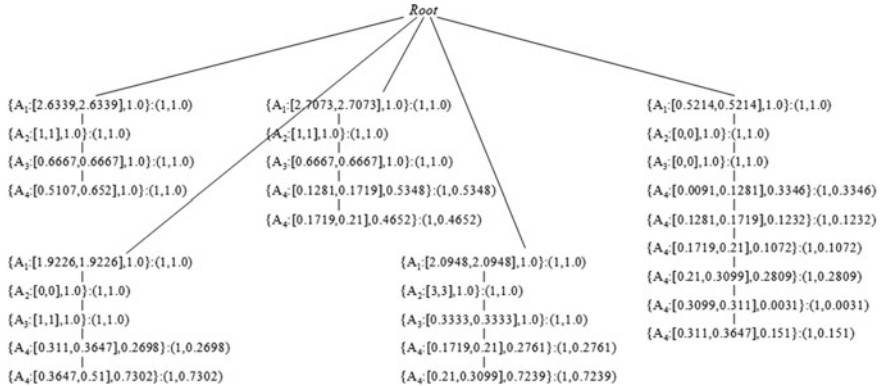


**Fig. 4** Final U2P-tree

be used to identify the critical energy-consuming parts in urban rail operation system, and the improvement of the systematic energy efficiency can be achieved by the reduction of energy consumption of the traction system and the HVAC system in station.

## 5 Conclusion

In urban rail system, there are complex interactions between subsystems and it is hard to analyze the energy efficiency association among them. Therefore, energy efficiency has a large potential to improve on the system level, which is a paramount problem for operators. In this paper, an energy-associated network (EAN) model is constructed based on the operation energy consumption by analyzing the association among the energy use. Besides, critical node identifying method using U2P-miner algorithm is presented, which considers both topological and energy-consuming attributes of nodes in EAN model. Finally, the method is applied in Beijing Subway to solve the intricate interaction mechanism of energy efficiency, and the result indicates that the improvement of the systematic energy efficiency can be achieved by the reduction of energy consumption of the traction system and the HVAC system in the station, which are the critical energy-consuming parts of Beijing Subway.

**Acknowledgements** The authors gratefully acknowledge the support from “the Fundamental Research Funds for the Central Universities” (Grant No.2018YJS198).

## References

1. European Commission (2019) Roadmap to a single European transport area—towards a competitive and resource efficient transport system. <https://eur-lex.europa.eu/LexUriServ/LexUriServ.do?uri=COM:2011:0144:FIN:en:PDF>. Last accessed 21 July 2019
2. China State Council (2019) “13th five-year plan” energy saving and emission reduction comprehensive work plan. [http://www.gov.cn/zhengce/content/2017-01/05/content\\_5156789.htm](http://www.gov.cn/zhengce/content/2017-01/05/content_5156789.htm). Last accessed 21 July 2019
3. Boizumeau JR, Leguay P, Navarro E (2011) Braking energy recovery at the Rennes metro. In: Workshop on braking energy recovery systems—ticket to Kyoto project. Bielefeld, Germany
4. Fong KF, Hanby VI, Chow TT (2006) HVAC system optimization for energy management by evolutionary programming. *Energy Build* 2006(38):220–231
5. Ahlgren P, Jarneving B, Rousseau R (2003) Requirement for a cocitation similarity measure, with special reference to Pearson’s correlation coefficient. *J Am Soc Inform Sci Technol* 54(6):550–560
6. Swami I, Timothy K, Bala S (2013) Attack robustness and centrality of complex networks. *PLoS ONE* 8(4):e59613
7. Goh K-I, Oh E, Kahng B (2003) Betweenness centrality correlation in social networks. *Phys Rev E Stat Nonlinear Soft Matter Phys* 67(2):017101
8. Saramaki J, Kivela M, Onnela JP (2006) Generalizations of the clustering coefficient to weighted complex networks. *Phys Rev E Stat Nonlin Soft Matter Phys* 75(2):027105
9. Liu YH (2012) Mining frequent patterns from univariate uncertain data. *Data Knowl Eng* 71(1):47–68
10. Golpíra H (2018) A novel multiple attribute decision making approach based on interval data using U2P-Miner algorithm. *Data Knowl Eng* S0169023X17302872

# Cascade–Parallel Structure Application of Converters for AC–DC–AC Traction Substation



Linwei Li and Mingli Wu

**Abstract** The topology of a converter-based traction substation is proposed in this paper to solve the power quality problems in traditional power supply systems (TPSSs). Its series–parallel structure is suitable for traction applications. The topology of power circuit is presented, and its working principle is analyzed in depth. For the cascade–parallel structure, constraints for its stable operation are given. The DC voltage sharing performance of the active front end (AFE)-based cascade inverters is analyzed. In the control of the rectifier, the DC feedforward control is adopted to improve the dynamic performance. The mathematical model is established for the parallel structure at the output, and the active and reactive power decoupling control strategy based on shared synchronous bus is proposed. Moreover, the calculation method of the active power and the reactive power is introduced. The basic functions of the system and the performance of cascade–parallel structure at the output side are validated based on MATLAB/Simulink.

**Keywords** Cascade–parallel structure · Electric railway · Power quality · AC–DC–AC traction substation · Current sharing control

## 1 Introduction

In China, the problem of the negative sequence becomes more prominent than before due to the rapid development of electrified railway [1–3]. Besides, the neutral sections inserted result in the loss of train speed and traction force, and also cause the voltage fluctuation and flicker of the traction network. Aiming at these problems, referring to German mode, an advanced traction power supply system

---

L. Li · M. Wu (✉)

School of Electrical Engineering, Beijing Jiaotong University,  
No. 3 Shang Yuan Cun, Hai Dian District, Beijing, China  
e-mail: [mlwu@bjtu.edu.cn](mailto:mlwu@bjtu.edu.cn)

L. Li

e-mail: [15117378@bjtu.edu.cn](mailto:15117378@bjtu.edu.cn)

was proposed in [4]. AC–DC–AC power conversion is employed to convert three-phase AC power to single-phase AC power, presented in Fig. 1. This power supply system can solve the power quality problems of electric railways thoroughly, and it is a superior traction power supply system.

For this converter-based traction power supply mode, the topology of traction substation has been studied in many literatures. Due to the large current and high voltage characteristics of the electrified railways, the traditional single two-level or tri-level converter can no longer meet the requirements, so large-capacity converter must be adopted. The neutral point clamped (NPC)-based structure [5–7] and MMC [8–11] have been proposed to apply in the electric railways, and NPC-based structure has been put into engineering application. Cascade structures [12–14] have extensive applications in static var generator (SVG), active power filter (APF) and solid-state transformers (SSTs). Series–parallel connected converters [15–17] are widely used in DC–DC converter system today. Series structure can increase the levels of the voltage, and it can be applied in high voltage occasions. At the same time, parallel structure can reduce the current stress of the switch devices with the capacity expansion. So, it is suitable for high voltage and high power occasions. The above structures provide a reference for the topology selection in this work.

This paper proposes a main circuit topology of AC–DC–AC traction substation based on cascade–parallel structure of converters. The cascade structure can increase the output voltage, and the parallel structure can enlarge the output current. It can deal with the power quality problems in TPSSs thoroughly, and the neutral sections can also be omitted totally. The topology of the converter-based traction substation is studied in this paper in depth. It is indicated that the design of AFE improves the voltage sharing problem inherited in the cascade structure. In addition, the inductors are inserted into the output side of the cascade inverters, and the active and reactive power decoupling control method based on shared synchronous bus is proposed to solve the current sharing problem of parallel structure. These are all verified in the simulations.

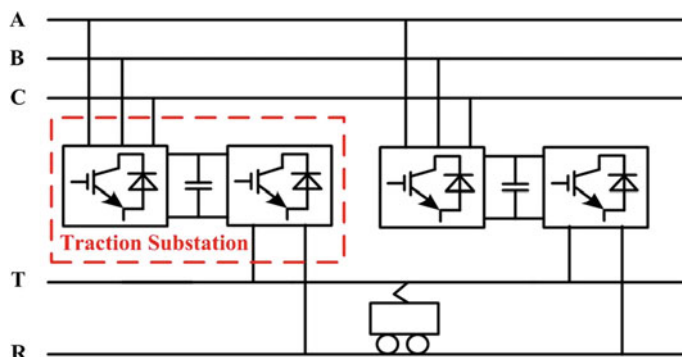


**Fig. 1** Schematic diagram of advanced power supply system

## 2 Topology of the Traction Substation and the Analysis

### 2.1 Topology of the Traction Substation

The topology proposed in this paper is presented in Fig. 2. In this topology, a cascade-parallel structure of back-to-back converters is adopted to obtain the single-phase AC power from the three-phase power grid through AC–DC–AC power conversion.

For this structure, we analyze it from the following three aspects:

- (1) Three single-phase transformers are used at the input side to match the grid voltage to reduce voltage stress of power devices. The primary side of the transformer is connected in Y-type, so there is no coupling in the structure and control of the three phases. Therefore, each phase can be controlled independently. As can be seen from the single-phase structure, the input side adopts multiple structures, and each secondary winding is connected with a back-to-back converter. Using appropriate control algorithm and phase-shifting modulation strategy, the harmonics of the source current in the primary side of the transformer can be eliminated. Because each module is independent and uniform in structure and control, the input side only needs to control the single-phase PWM rectifier and cooperate with the carrier phase shift sinusoidal pulse-width modulation (CPS-SPWM) strategy to achieve the control targets.
- (2) AC–DC–AC power conversion is the main part of this structure. It is responsible for converting the three-phase AC power of the public grid to the single-phase AC power of the traction network. It mainly includes the rectifier

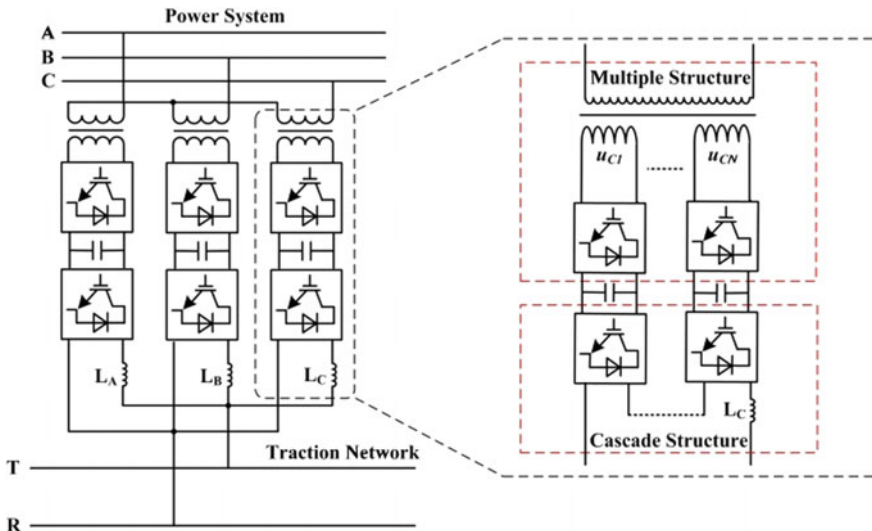


**Fig. 2** Main circuit topology of the traction substation

and the inverter. The rectifier conducts three-phase AC power to DC power conversion. The PWM rectifier deals with the source current regulation and realizes high power factor operation. Therefore, the power quality of point common coupling (PCC) is improved. The energy generated by braking can be returned to the power grid by the four-quadrant characteristic of the PWM rectifier. So, the energy utilization is increased. The rectifier controls DC voltage around the reference value, so as to ensure that the energy absorbed from three-phase power grid can be transferred to traction load. DC-link decoupled the rectifier and the inverter in structure and control, so they can be controlled independently. Inverter deals with the DC power to single-phase AC power conversion. In addition, the magnitude and frequency of the output voltage can be controlled, so neutral sections can be removed totally.

- (3) The cascade converters can obtain the high output voltage with low voltage stress switching devices, and the parallel topology can achieve the large output current with low current stress switching devices. Therefore, the cascade-parallel structure reduces the loss and the cost of the system.

## 2.2 Constraints for the Stable Operation of Cascade-Parallel Structure

This section describes the constraints of the cascade-parallel structure during the steady state, illustrated in Fig. 3, where  $i_1$ ,  $i_2$ ,  $i_3$  and  $i_0$  represent the output current of phase-A, phase-B, phase-C and the load current, respectively.  $P_A$ ,  $P_B$ ,  $P_C$  and  $P_L$  represent the active power of phase-A output, phase-B output, phase-C output and the load, respectively.  $Q_A$ ,  $Q_B$ ,  $Q_C$  and  $Q_L$  represent the reactive power of phase-A output, phase-B output, phase-C output and the load, respectively.

In order to obtain the stable operation for the cascade-parallel structure, the following equations should be met.

$$U_{dca1} = U_{dca2} = \dots = U_{dcaN} = U_{deb1} = \dots = U_{debN} = U_{dec1} = \dots = U_{decN} \quad (1)$$

$$i_1 = i_2 = i_3 = \frac{1}{3}(i_1 + i_2 + i_3) \quad (2)$$

or

$$\begin{cases} P_A = P_B = P_C = \frac{1}{3}(P_A + P_B + P_C) \\ Q_A = Q_B = Q_C = \frac{1}{3}(Q_A + Q_B + Q_C) \end{cases} \quad (3)$$

In other words, the DC-links among modules should be balanced, and the currents or power of three phases should be shared.

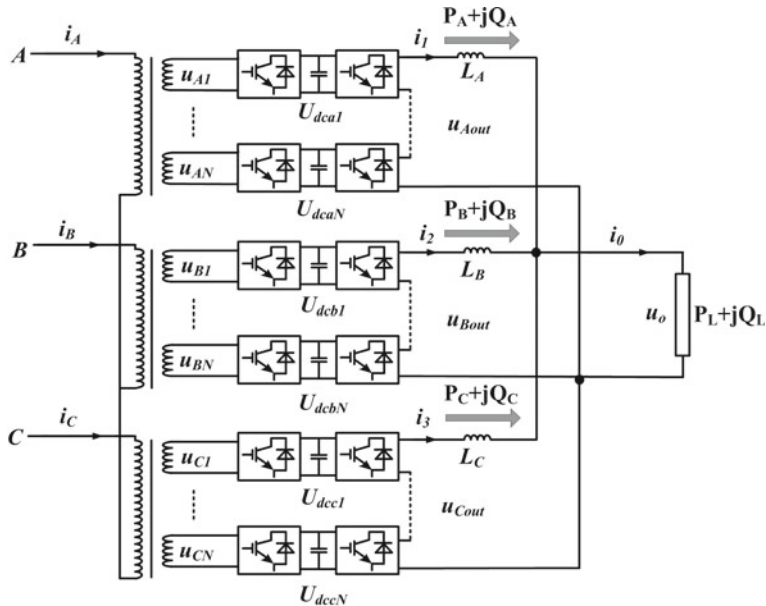


**Fig. 3** Schematic diagram of the overall topology

### 2.3 Analysis of Unbalance Among DC-Links of Different Modules

In back-to-back structure, PWM rectifier can be equivalent to a DC voltage source to feed the inverter, as shown in Fig. 4.

The DC voltages all operate at the reference value during the steady state in theory, so the values of all DC voltages are the same. There is little voltage unbalance among the DC-links, which will be verified in the simulation. So, in this structure, current sharing of the parallel structure should be focused on.

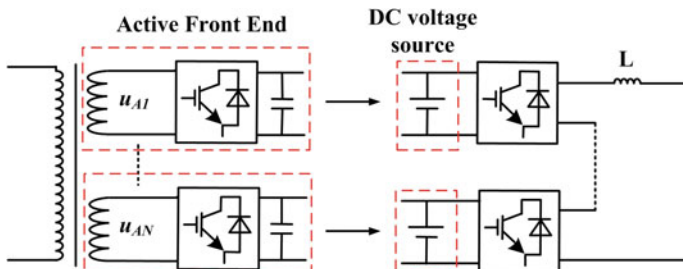


**Fig. 4** Equivalent circuit of the PWM rectifier

## 2.4 The Structure of the Single-Phase Back-to-Back Converter

Figure 5 shows the back-to-back converter in this topology. It is composed of two H-bridge (HB) converters sharing the common DC-link.  $L_N$  is the inductance,  $R_N$  represents the equivalent resistance of inductance and the switching loss, and  $C$  is DC capacitance.

## 3 Control of the Proposed Structure

Before introducing the control strategy, we should determine the control targets first.

### 3.1 Control Targets

The target of the structure is dealing with the power quality problem of electric railway and removing the neutral sections. DC-link should be regulated to guarantee the power transmission between the grid and traction load. The source current should be controlled to realize the high power factor operation, so that the power grid and the load only exchange the active power. In addition, there should be the low harmonic content in the grid current. The output voltage needs to be controlled to ensure the normal operation of the train. And above all, since the output side of the topology employs the parallel structure, current sharing must be achieved to obtain a good performance.

### 3.2 Control of the PWM Rectifier

Based on the analysis in Sect. 2, it needs to control the single-phase H-bridge PWM converter at the input side and cooperate with the carrier phase shift modulation

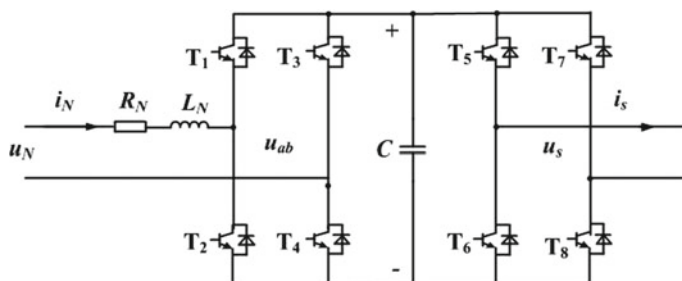


**Fig. 5** Structure of back-to-back converter

strategy to achieve DC voltage control and the source current regulation. The circuit structure of single-phase PWM rectifier is shown in Fig. 6, and the mathematical model is presented in (5).

$$\begin{cases} L \frac{d i_N}{d t} = u_N - R i_N - u_{ab} \\ C \frac{d u_{dc}}{d t} = i_{dc} - \frac{u_{dc}}{R_L} \end{cases} \quad (4)$$

The control strategy of the rectifier is shown in Fig. 7, which adopts direct current control, and DC load current feedforward is employed to eliminate the influence of the train on the public grid. It includes three components.

### (1) Control for DC-link voltage

DC voltage should be regulated to trace the reference value. Due to the single-phase traction load, DC-link contains 100 Hz component. We should take some steps to

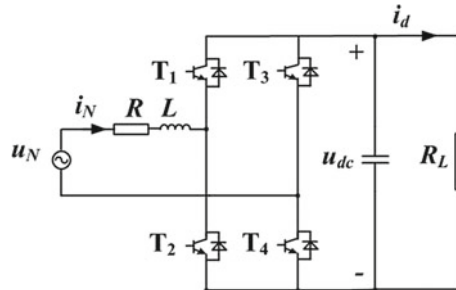


**Fig. 6** Structure of single-phase rectifier

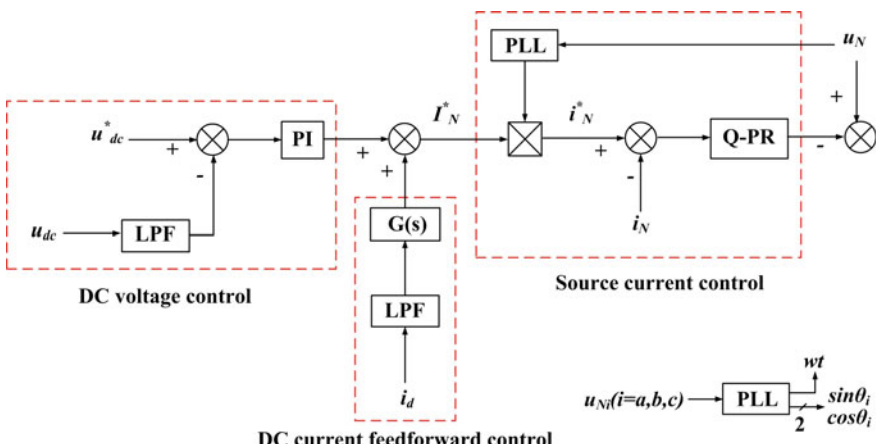


**Fig. 7** Control for the single-phase rectifier

remove it, or third-order harmonic will be introduced to source current. In Fig. 7, low-pass filter (LPF) is adopted to eliminate the 100 Hz component. Proportional integral (PI) controller contains DC internal model, so it can make DC voltage to track the reference value without steady-state error.

### (2) DC feedforward control

In back-to-back converter, the inverter can be equivalent to the resistance, as presented in Fig. 7. The train is an impact load, and the change of its operation state will degrade the system performance. DC feedforward control can alleviate this effect.  $G(s)$  is the transfer function of DC feedforward control, and

$$G(s) = K_i(T_i s + 1) \quad (5)$$

$K_i$  is proportional coefficient, and  $T_i$  is the time of differential link, which includes filtering and modulation delay, source current control delay, etc. According to the power balance between public grid and traction load, (6) can be obtained

$$\frac{U_N I_N}{2} = U_d I_d \quad (6)$$

where  $I_d$  is DC component which contains no double-frequency ripple. Thus, the proportional coefficient of  $G(s)$  is

$$K_i = \frac{I_N}{I_d} = \frac{2U_d}{U_s} \quad (7)$$

### (3) Control for the source current

We carry out the sum of output of the voltage loop and DC feedforward link, and it is taken as the amplitude reference value for the source current. Phase-locked loop (PLL) is adopted to follow the phase of the source voltage; thus, unity power factor operation can be achieved. The current loop adopts the quasi-proportional resonance (Q-PR) regulator, and it can control AC component with better dynamic performance and no steady-state error.

## 3.3 Control of the Input Side

According to multiple structures at the input side, the carrier phase shift sinusoidal pulse-width modulation (CPS-SPWM) strategy should be employed to eliminate the harmonic content of the source current in the primary winding of the transformer. Therefore, the overall control structure of the input side is shown in Fig. 8. The carrier phase difference between adjacent modules is  $\pi/2N$ .

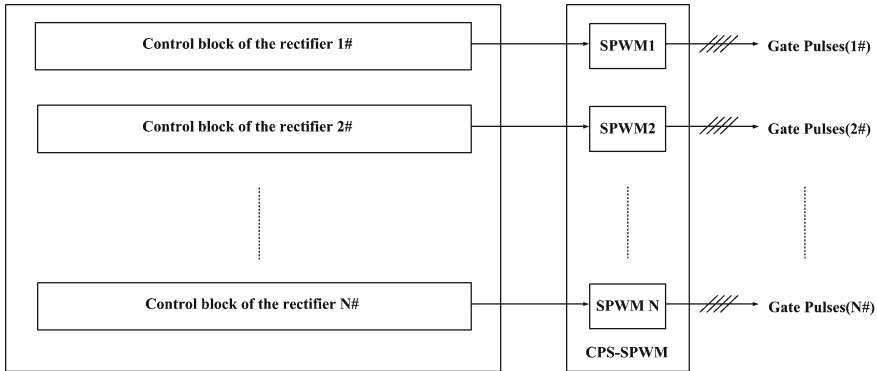


**Fig. 8** Overall control system of the input side

### 3.4 Control Strategy of the Output Side

The control strategy of the output includes two parts: control of the cascade inverters and control of current sharing among inverters.

#### The Parallel Model and the Circulation Current Analysis for the Cascade Inverters

In this topology, the parallel structure can be equivalent to the parallel connection of the single-phase power supply. The analysis of circulation mechanism is conducted by taking two parallel operation inverters as an example, as displayed in Fig. 9.

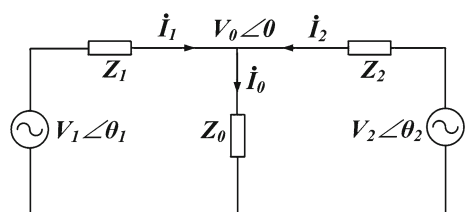
$V_1\angle\theta_1$ ,  $V_2\angle\theta_2$  are the output voltages of two inverters, respectively, while  $I_1$ ,  $I_2$  represent the output currents of two inverters, respectively.  $Z_1$ ,  $Z_2$  ( $Z_1 = r_1 + jX_1$ ,  $Z_2 = r_2 + jX_2$ ) denote the output equivalent impedances of two inverters, respectively, while  $Z_0$  is the load impedance. The load voltage is taken as the reference, and its phase angle is set as 0.

According to Fig. 9, we can obtain

$$\begin{cases} V_1 - Z_1 I_1 = V_0 \\ V_2 - Z_2 I_2 = V_0 \end{cases} \quad (8)$$

Assuming that  $Z_1 = Z_2 = Z$ , (9) can be derived

**Fig. 9** Equivalent circuit of two inverters in parallel



$$\begin{cases} I_1 - I_2 = \frac{V_1 - V_2}{Z} \\ I_1 + I_2 = \frac{V_1 + V_2 - 2V_0}{Z} \end{cases} \quad (9)$$

Thus,

$$\begin{cases} I_1 = \frac{V_0}{2Z_0} + \frac{V_1 - V_2}{2Z} \\ I_2 = \frac{V_0}{2Z_0} - \frac{V_1 - V_2}{2Z} \end{cases} \quad (10)$$

As presented in (10), only if the output voltages of the parallel inverters have no difference, the output currents of them are the same. We define that the expression of the circulating current is

$$I_H = \frac{I_1 - I_2}{2} \quad (11)$$

In Fig. 9, the complex power provided by  $n\#$  ( $n = 1, 2$ ) inverter is

$$S = V_0 I_n^* = V_0 \left( \frac{V_n \cos \theta_n + j V_n \sin \theta_n - V_0}{R_n + j X_n} \right)^* \quad (12)$$

Thus, the expression of active and reactive power can be written as

$$\begin{cases} P_n = \frac{V_0 R_n (V_n \cos \theta_n - V_0) + V_0 V_n X_n \sin \theta_n}{R_n^2 + X_n^2} \\ Q_n = \frac{V_0 X_n (V_n \cos \theta_n - V_0) - V_0 V_n R_n \sin \theta_n}{R_n^2 + X_n^2} \end{cases} \quad (13)$$

Since the series inductor is inserted into the output side of the inverter, the resistance component can be ignored. In addition, the phase angle difference between the output voltage of the inverter and that of the load voltage is very small, so  $\sin \theta \approx \theta$ ,  $\cos \theta \approx 1$ . Therefore, (13) can be rewritten as

$$\begin{cases} P_n = \frac{V_0 V_n \theta_n}{X_n} \\ Q_n = \frac{V_0 X_n (V_n - V_0)}{X_n} \end{cases} \quad (14)$$

As shown in (14), we can see that the active power of the single inverter mainly depends on the difference of the phase angle among inverters, and the reactive power mainly lies on the difference of the voltage amplitude among inverters. Therefore, active power can be used to adjust the phase, while reactive power can be used to regulate the amplitude to achieve the parallel operation of the inverters.

It is indicated in [18] that the circulating current generated by the difference of phase angle is much larger than that of the amplitude when AC power supplies are running in parallel. So, the uniform phase reference is provided for each cascade inverter. Then, the phase and amplitude are slightly adjusted by decoupling active and reactive power control to achieve parallel operation and power sharing of the inverters.

Since the phase angle is not easy to detect, we use the frequency instead. The relationship between active power and frequency, and the relationship between reactive power and the amplitude can be expressed as

$$\begin{cases} f = f_{\text{ref}} - (K_{\text{Pf}} + K_{\text{If}}/s)(P - P_{\text{ref}}) \\ V = V_{\text{ref}} - (K_{\text{PV}} + K_{\text{IV}}/s)(Q - Q_{\text{ref}}) \end{cases} \quad (15)$$

where  $V_{\text{ref}}$ ,  $f_{\text{ref}}$  are the uniform given amplitude and phase references. The proportion integral (PI) controller is adopted to regulate DC component.

### Calculation of Active and Reactive Power

The traditional active and reactive power theory is based on the average value, and it can only be used on the condition that the voltage and current are all sine waveforms. Moreover, it is conducted once per period. When the switching frequency is much higher than the fundamental frequency, this method reduces the precision and degrades the dynamic performance of the system. The instantaneous reactive power theory is defined on the basis of the instantaneous value. It can quickly and accurately detect the magnitude of instantaneous active and reactive power, so as to ensure the nice dynamic response of control system. But the instantaneous reactive power theory is based on the three-phase system, and it cannot be used in the single-phase circuit directly. If a three-phase system is constructed based on the voltage and the current of the single-phase circuit, the instantaneous reactive power theory can be applied.

Assume that  $u_0$ ,  $i_0$  are the instantaneous values of the voltage and the current and provide that  $u_a = u_0$ ,  $i_a = i_0$ . Thus,  $u_b$  can be obtained by delay  $u_0$  with a phase angle of  $\pi/3$ , and  $u_c$  can be obtained by delay  $u_0$  with a phase angle of  $2\pi/3$ . Similarly,  $i_b$  and  $i_c$  can be constructed. Transform the three-phase voltage and the three-phase current to  $\alpha-\beta$  frame.

$$\begin{bmatrix} u_\alpha \\ u_\beta \end{bmatrix} = C_{32} \begin{bmatrix} u_a \\ u_b \\ u_c \end{bmatrix} \quad \begin{bmatrix} i_\alpha \\ i_\beta \end{bmatrix} = C_{32} \begin{bmatrix} i_a \\ i_b \\ i_c \end{bmatrix} \quad (16)$$

where

$$C_{32} = \sqrt{\frac{2}{3}} \begin{bmatrix} 1 & -1/2 & -1/2 \\ 0 & \sqrt{3}/2 & -\sqrt{3}/2 \end{bmatrix} \quad (17)$$

The instantaneous active power and reactive power are expressed as

$$\begin{cases} p = u_\alpha i_\alpha + u_\beta i_\beta \\ q = u_\alpha i_\beta - u_\beta i_\alpha \end{cases} \quad (18)$$

## Control of the Output

Control for the output of the topology is shown in Fig. 10. It consists of two parts, the calculation for the active and reactive power reference, and control of the parallel operation, presented in Fig. 11a, b. In Fig. 11a, the voltage and current signals are sent to the power calculation to obtain the active power and reactive power of each phase. We calculate the sum of active and reactive power of the inverters, and then they are divided by the number of inverters as the reference value.

## 4 Simulink Results and Analysis

The simulation was conducted in MATLAB/Simulink, while the parameters are presented in Table 1. The magnitude of output voltage, load voltage and grid voltage is zoomed out to 1/100, 1/100 and 1/1500 of the original ones, respectively.

We set two branches where each one is  $20\ \Omega$  resistance, and  $2\text{ mH}$  inductance was connected in parallel as the load to carry out the verification of the dynamic performance. The switch of phase-A, that of phase-B and that of phase-C are closed at 0 s, 0.2 s and 0.4 s, respectively. One load switch is closed at 0.6 s, and the other branch is put into operation at 1.2 s.

### (1) The simulation results for the basic functions

When the AC–DC–AC traction substation supplies the load, the grid currents are symmetrical and synchronize the voltage, so the unity power factor operation is achieved, as presented in Fig. 12a, b. In addition, the total harmonic distortion

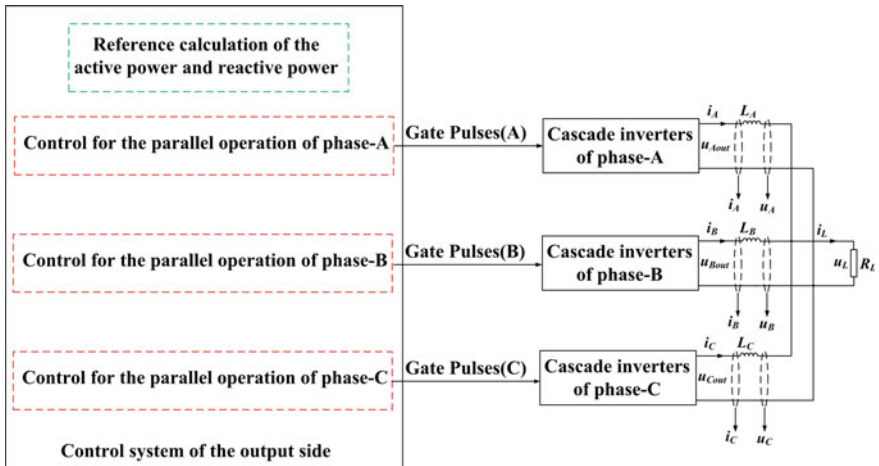


**Fig. 10** Control of the output

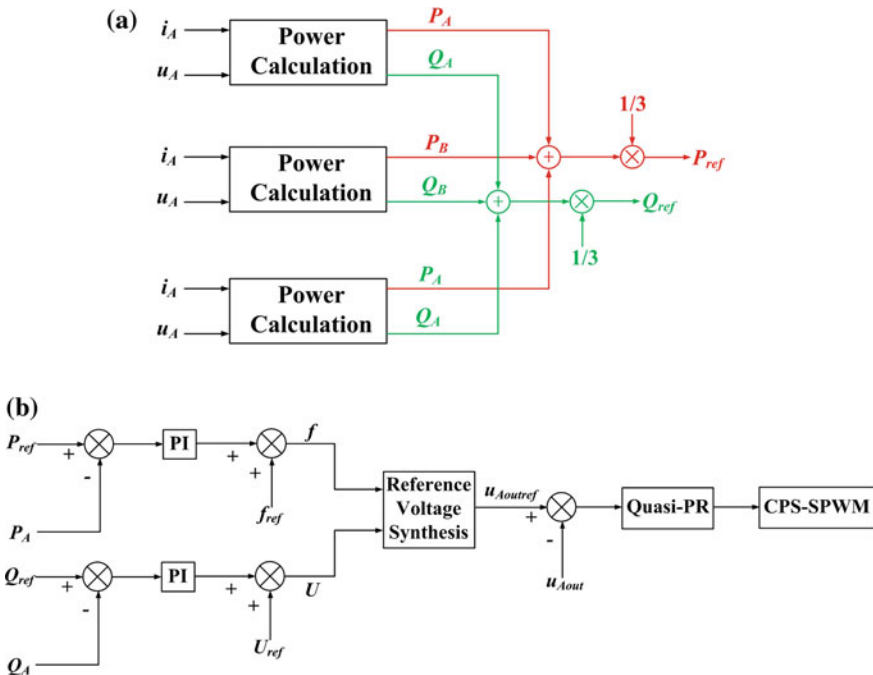


**Fig. 11** a Calculation for the active and reactive power reference and b the control of the parallel operation

**Table 1** Main simulation parameters

Parameters	Value
Nominal primary voltage of multi-winding transformer	110 kV
Nominal secondary voltage of multi-winding transformer	1530 V
DC capacitor	3000 $\mu$ F
DC voltage reference	2800 V
Phase modulation inductance of each module	2.1 mH
Switching frequency (input side/output side)	500 Hz
Number of modules	15
Smoothing inductor of each phase (output side)	6.4 mH
Nominal capacity	15 MVA
Nominal output voltage	10 kV

(THD) is very low. Thus, the power quality of PCC is good. The load voltage can be stable at 10 kV, and the load voltage contains harmonics due to the nonlinear load, but the THD is very low, which is shown in Fig. 12c. Moreover, the dynamic response of the system is rapid when the load mutates.

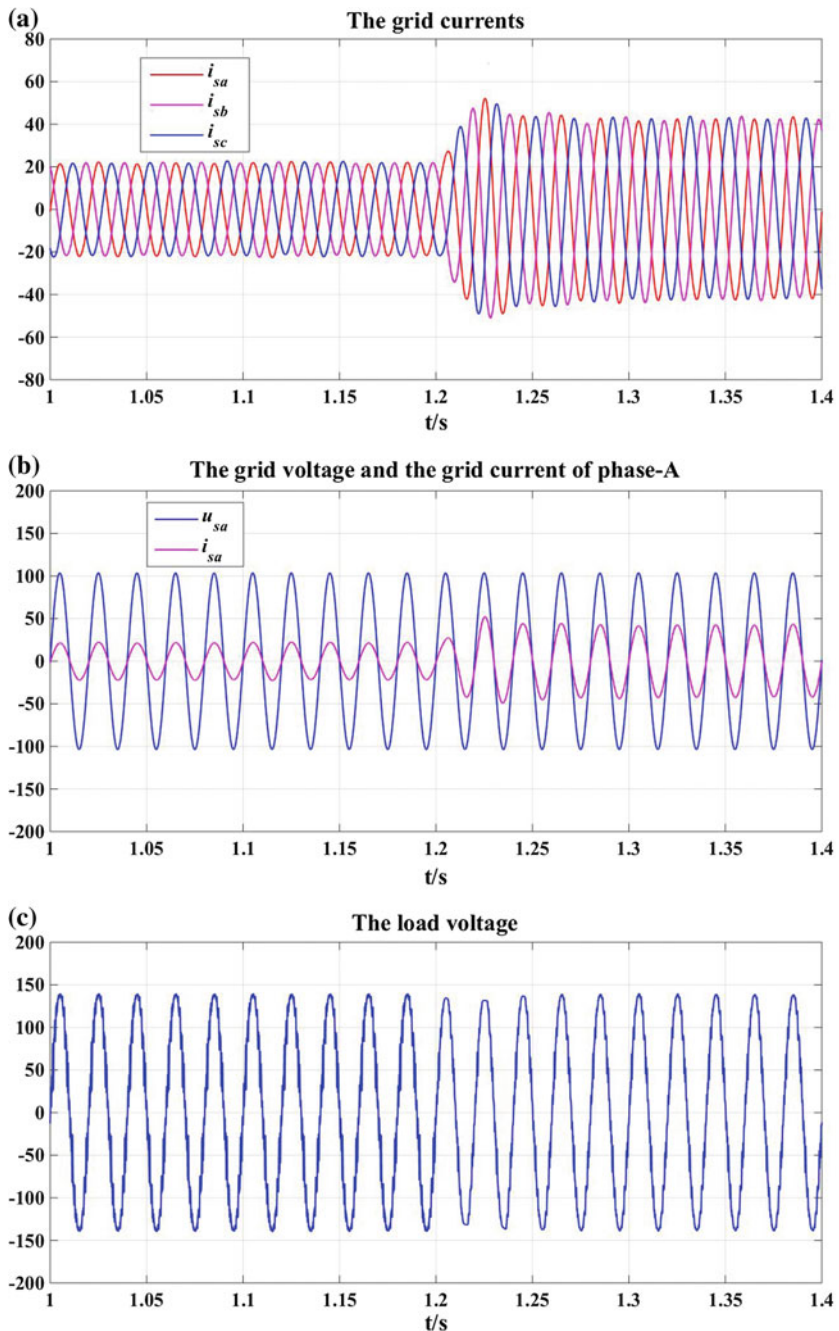


**Fig. 12** **a** Grid currents, **b** the grid voltage and current, **c** the load voltage

## (2) Simulation results for the DC voltage unbalance among modules

Figure 13a, b presents the voltage sharing performance in one phase and among different phases. It can be seen that whether DC voltages in one phase or among different phases can all be stable around 2800 V, and they do not diverge when the load mutates.

## (3) The current sharing simulation results

As can be seen from Fig. 14a, the amplitude and the phase of three-phase output currents are almost the same. The amplitude of the circulating current is around 5 A, presented in Fig. 14b. Compared with the rated current of each phase in which value is 500 A, the circulating current is small that it will have little effect on the normal operation of the system. The active and reactive power sharing is achieved, as presented in Fig. 14c, d.

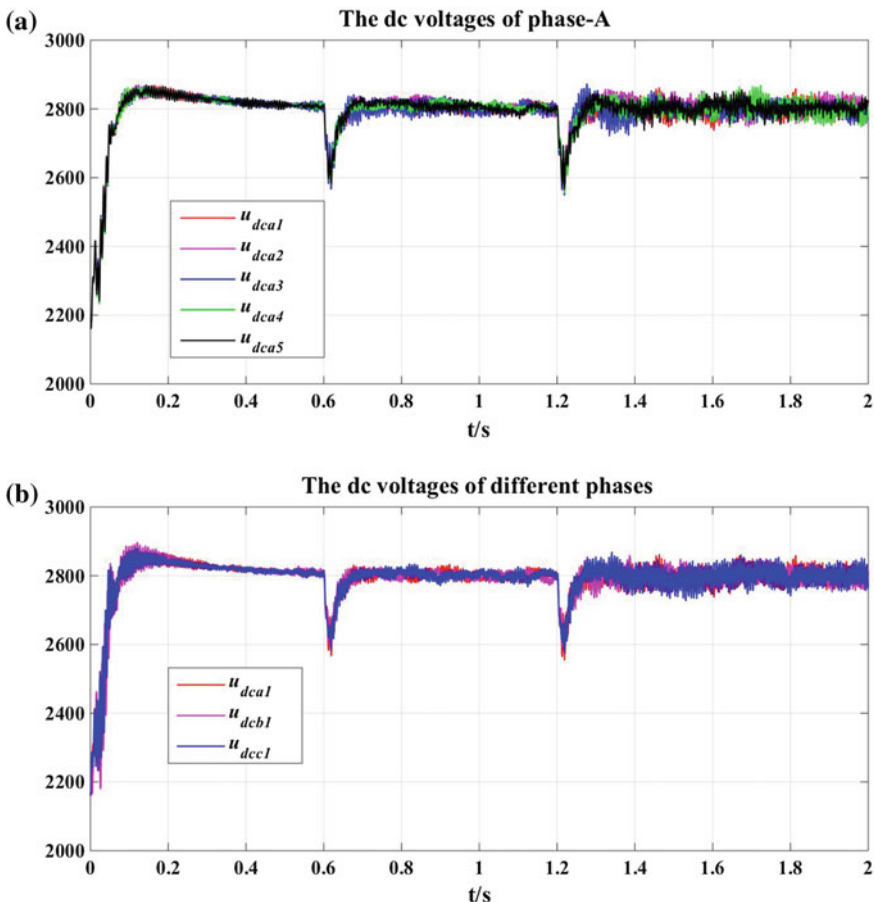


**Fig. 13** **a** DC voltages in the same phase and **b** the DC voltages among different phases

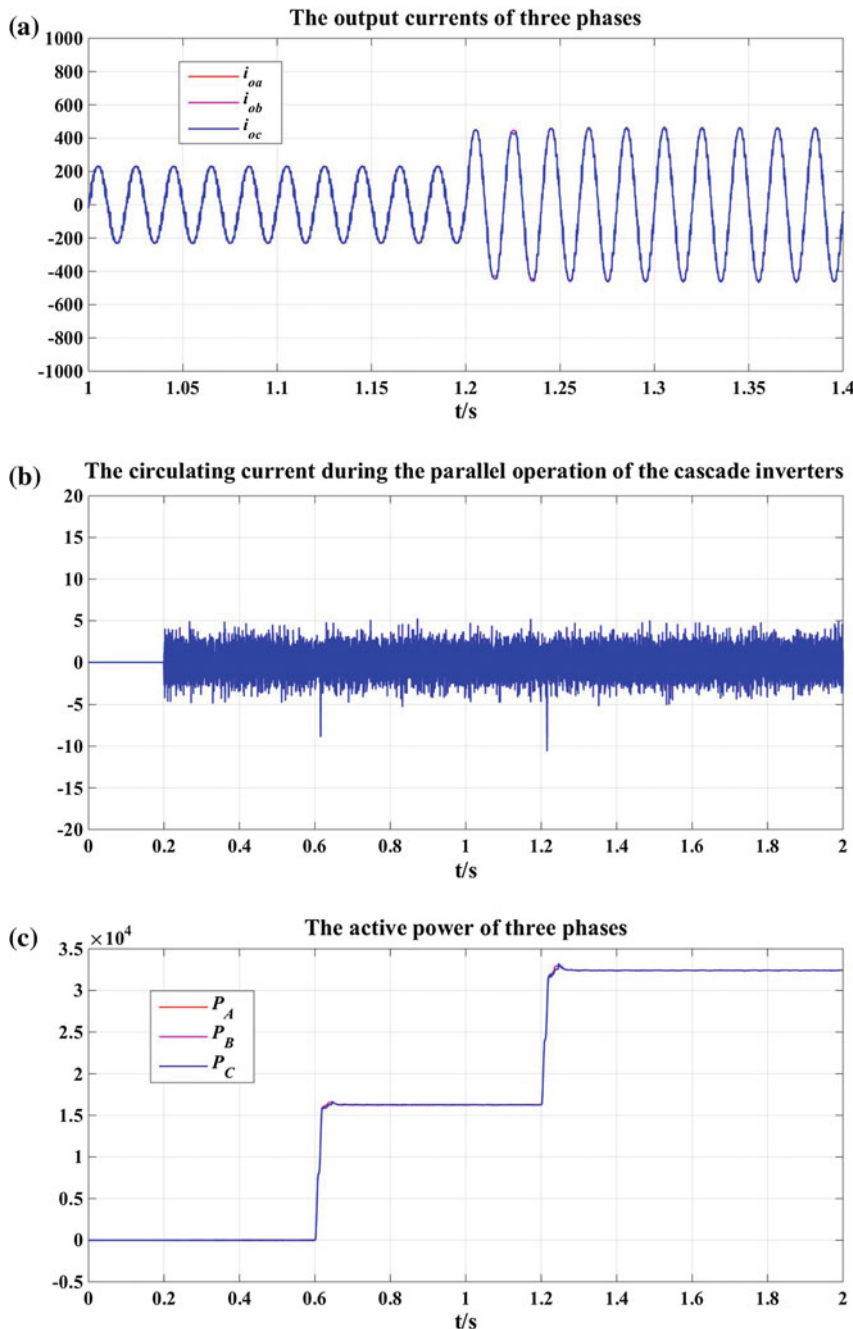


**Fig. 14** **a** Output currents of three phases, **b** the circulating current, **c** the active power of three phases, **d** the reactive power of three phases

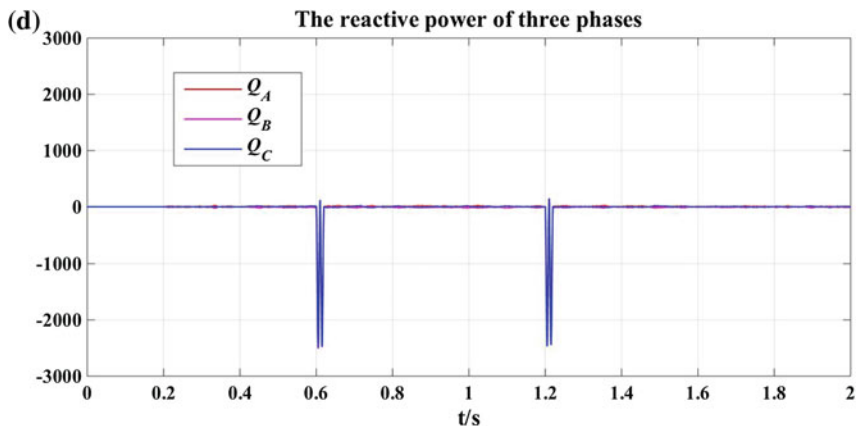


**Fig. 14** (continued)

#### (4) The simulation results for the output voltage

It can be seen from Fig. 15 that the cascade inverters with five modules can achieve 11 levels of the output voltage, and its sine degree is so much better than the traditional two-level output voltage, so the harmonic content of the output voltage can be effectively decreased and the burden of the filter is reduced.

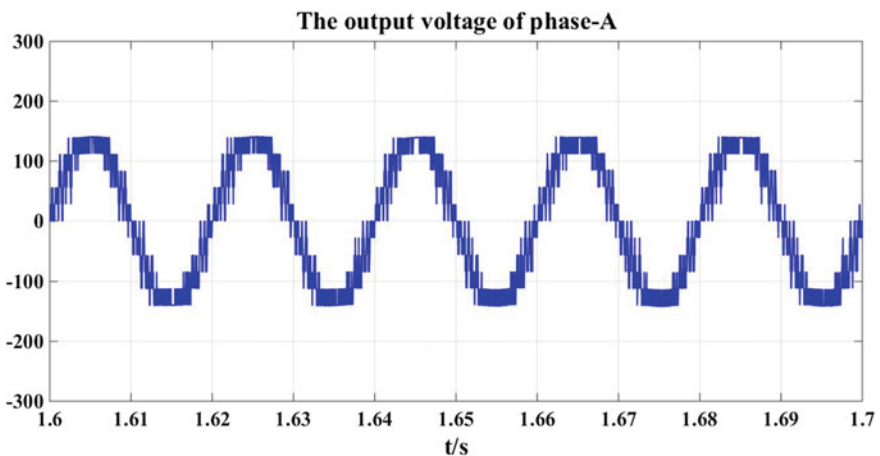


**Fig. 15** Output voltage of phase-A

## 5 Conclusion

- (1) This paper proposes a power circuit topology of AC–DC–AC traction substation based on cascade–parallel structure. It can not only deal with power quality problems in TPSSs, but also the neutral sections can be removed totally.
- (2) From the topology aspect, the three-phase decoupling and symmetrical structure provides advantages in solving negative sequence. The AFE improves the DC voltage sharing performance, so there is no need to design a voltage sharing algorithm or circuit. The series–parallel structure makes it suitable for high voltage and large-capacity applications, and the capacity expansion is obtained easily.
- (3) From the control perspective, the decoupling structure of the input and output side, as well as the back-to-back converter based on H-bridge, makes the control simple to implement. In addition, parallel current sharing control at output side is easy to be realized in practical application.

**Acknowledgements** This work was supported by the Fundamental Research Funds for the Central Universities (2018JBZ101).

## References

1. Zeliang S, Shaofeng X, Qunzhan L (2011) Single-phase back-to-back converter for active power balancing, reactive power compensation, and harmonic filtering in traction power system. *IEEE Trans Power Electron* 26(2):334–343
2. Dinghua Z, Zhixue Z, Weian W et al (2016) Negative sequence current optimizing control based on railway static power conditioner in V/v traction power supply system. *IEEE Trans Power Electron* 31(1):200–212
3. Xu T, Qirong J, Yingdong W (2012) Research on novel uninterruptible phase-separation passing scheme in electrified railways. *Power Syst Protect Control* 40(21):14–18 (in Chinese)
4. Qunzhan L (2010) On some technical key problems in the development of traction power supply system for high speed railway in China. *J China Railw Soc* 32(4):119–124 (in Chinese)
5. Wrede H, Umbricht N (2009) Development of a 413 MW railway power supply converter. In: 2009 35th annual conference of IEEE industrial electronics. IEEE, Porto, pp 3587–3592
6. Xiaoqiong H, Zeliang S, Xu P (2014) Advanced cophase traction power supply system based on three-phase to single-phase converter. *IEEE Trans Power Electron* 29(10):5323–5333
7. Xiaoqiong H, Zeliang S, Xu P (2015) A traction three-phase to single-phase cascade converter substation in an advanced traction power supply system. *Energies* 8(9):9915–9929
8. Fei C, Zhongping Y, Fei L (2016) A new traction power supply system based on modular multilevel converter (I). *J China Railw Soc* 38(12):41–46 (in Chinese)
9. Fei C, Zhongping Y, Fei L (2017) A new traction power supply system based on modular multilevel converter (II). *J China Railw Soc* 39(2):39–43 (in Chinese)
10. Winkelkemper M, Korn A, Steiner P (2010) A modular direct converter for transformerless rail interties. In: 2010 IEEE international symposium on industrial electronics. IEEE, Bari, pp 562–567

11. Schrader T, Heising C, Staudt V et al (2012) Multivariable control of MMC-based static converters for railway applications. In: 2012 electrical systems for aircraft, railway and ship propulsion. IEEE, Bologna, pp 1–6
12. Rui L, Yingjie H, Jinjun L (2018) Research on the unbalanced compensation of delta-connected cascaded H-Bridge multilevel SVG. *IEEE Trans Ind Electron* 65(11):8667–8676
13. Jianghao H, Min L, Yabin L (2018) DC side voltage balancing control for the medium voltage cascaded H Bridge APF. In: 2018 37th Chinese control conference (CCC). IEEE, Wuhan, pp 286–291
14. Xueyin Z, Yonghai X, Yunbo L (2019) Hybrid-frequency cascaded full-bridge solid-state transformer. *IEEE Access* 7:22118–22132
15. Marco B, Luigi C, Massimo V (2016) Series-parallel PV arrays: a comparison between the performances of two algorithms for strings with an equal or with a different number of PV modules. In: 2016 IEEE international power electronics and motion control conference (PEMC). IEEE, Varna, pp 1269–1274
16. Kasemsan S, Michael W, Kenneth C (2007) Uniform voltage distribution control for series connected DC-DC converters. *IEEE Trans Power Electron* 22(4):1269–1279
17. Zhenghai L, Dazheng W, Jinli R (2016) An optimized fading fault localization method applied in series-parallel photovoltaic array. In: 2016 international conference on smart grid and clean energy technologies (ICSGCE). IEEE, Chengdu, pp 182–186
18. Kawabata T, Higashino S (1988) Parallel operation of voltage source inverters. *IEEE Trans Ind Appl* 24(2):281–287

# Influence of Air Gap on Electric Field of the EMU Roof Cable Terminal



JiXing Sun, QingYun Zhi, Jin Li and Qi Dai

**Abstract** The semi-rigid cable terminal of high-speed EMU will inevitably generate air gap during the production process. The air gap can cause partial discharge during the normal operation of the train, which would deteriorate the internal insulation and cause terminal explosion failure in severe cases. This paper has studied this kind of problem, analyzed the internal composition of the cable terminal, and simulated the distribution characteristics of the electric field when the air gap at different internal positions. The results showed that the internal insulation layer and the stress layer were more likely to cause insulation breakdown failure when the air gap existed. The air gap length had little effect on the electric field distribution. And the depth of the air gap along the insulation layer can influence the electric field. The weak points in the cable terminal manufacturing process have proposed.

**Keywords** Cable terminal · Air gap defect · Electric field distribution

## 1 Introduction

The semi-rigid cable terminal was located at the junction of the roof pantograph and the cable of the high-speed EMU. It ensured the support of the cable and also transmitted the power obtained by the pantograph to the roof transformer. Therefore, the normal operation of the cable terminal is extremely important for the safe operation of the EMU and the power supply in the train. However, in the manufacturing process, the cable terminal needs to be stripped of the shielding layer, and the manufacturing process is imperfect, resulting in a very uneven electric field distribution inside the cable terminal. Then, partial discharge would occur in a place where the local electric field was very high, causing breakdown of the internal insulation of the cable terminal, making the internal core to be directly

---

J. Sun · Q. Zhi (✉) · J. Li · Q. Dai

School of Electrical Engineering, Beijing Jiaotong University, Beijing 100044, China  
e-mail: [18121553@bjtu.edu.cn](mailto:18121553@bjtu.edu.cn)

grounded, causing the cable terminal to explode, interrupting the internal power supply of the EMU, and affecting the operation of the line. According to relevant survey data, the failure of cable accessories accounts for about 70% of the total cable failure.

A lot of research work has been done at China and abroad for the air gap defects of cable terminals. Literature [1] simulated the 35 kV cold shrink cable terminal and analyzed the stage characteristics of partial discharge; as for the problem of air gap of main insulation air of 10 kV XLPE cable terminal, literature [2–6] has simulated the electric field distribution of defect condition and proposed the necessity to adjust the cable terminal structure. Literature [7–11] studied the internal field strength distribution of cross-linked polyethylene under four typical defects and carried out experimental verification. However, the semi-rigid cable termination in the trains was formed by heat-shrinking multiple layers of different insulating materials. The manufacturing technology determined that the air gap can exist in different layers inside, and the influence of air gap distribution on the internal electric field needs to be considered.

In this paper, the roof semi-rigid cable terminal of high-speed EMU with the voltage class of 27.5 kV was taken as an example. The cable terminal model was established by COMSOL, simulated the electric field in several different situations, analyzed the reason why the air gap affects the electric field distribution, and proposed the weak points of semi-rigid cable terminations and key considerations in the manufacturing process.

## 2 Simulation Model Establishment and Parameter Setting

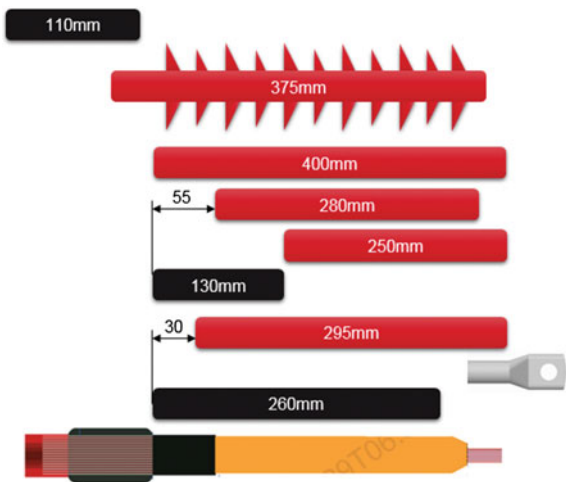
### 2.1 Semi-rigid Cable Terminal Internal Structure

The roof high-voltage cable is mainly connected to the pantograph and the entire EMU to provide the required electric energy for the traction motor and the vehicle. The cable termination adopts a semi-rigid cable termination, which is distributed at the pantograph or straddle connection. It is mainly composed of an outer shed, an outer insulation layer, a stress layer, an inner insulation layer, a semiconductor layer, and a cable core. The composition diagram was shown as follows.

### 2.2 Simulation Model

Because of the cable termination is a highly symmetrical structure, the electric fields of each section along the core 360° are the same, so the simulation model of the two-dimensional model can be established to analyze the internal field strength of the actual cable terminal. Furthermore, the actual terminal voltage of the roof cable is 27.5 kV single-phase AC, so the simulation of the simulation model can be performed by electrostatic field simulation of 50 Hz amplitude voltage.

**Fig. 1** Internal composition of cable terminal



According to the actual structure of the 27.5 kV cable termination, the axisymmetric simulation model is established according to the 1:1 ratio. As shown in Fig. 1, the air gap is set to air, and the remaining layers are set according to the actual material. At the same time, according to the simulation conditions of the electrostatic field, the potential of the inner boundary of the insulation layer in the simulation is set to 38.8 kV, and the ground plane side of the shield layer and the infinity outer plane of the terminal are set to the ground potential.

### 2.3 Simulation Calculation Method

After applying a voltage at the core of the cable terminal, an electric field is generated in and around various layers of the cable termination; for a semi-rigid cable termination, since it is a cylindrical structure, its electric field analysis can be listed by the following formula:

$$E = \frac{U}{r \ln \frac{r_i}{r_0}} \quad (1)$$

$E$  represents the electric field strength at the point,  $U$  is the voltage applied to the cable termination,  $r$  is the distance from the point to the core,  $r_i$  is the radius of the layer at which the point is located, and  $r_0$  is the radius of the inner semiconducting layer.

However, the internal structure of the cable structure is complicated. The calculation amount of the above analytical formula is very large. Therefore, this paper uses COMSOL software to perform finite element analysis. It is mainly calculated according to Maxwell's equations (Fig. 2; Table 1):

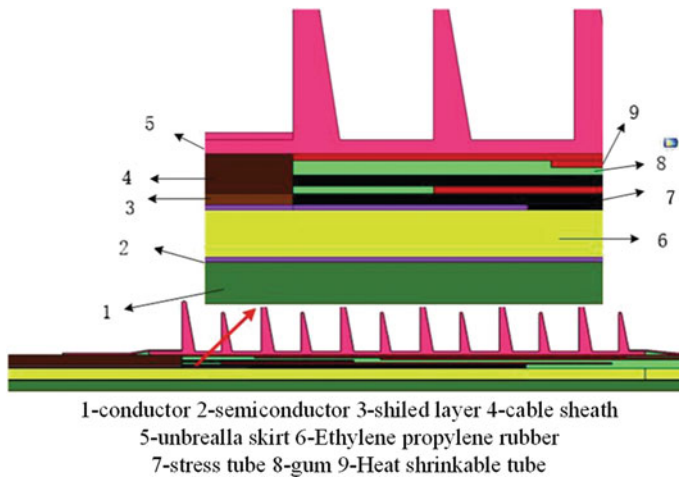


**Fig. 2** Simulation model

**Table 1** Relative dielectric constant of cable termination materials

Material	Relative permittivity
EPR	2.50
Stress tube	25.3
Heat-shrinkable tube	3.34
Umbrella skirt	3.34
Cable sheath	3.07
Gum	7.70
Air	1.00

$$\begin{aligned} \nabla \times H &= J + \frac{\partial D}{\partial t} \\ \nabla \times E &= 0 \\ \nabla \cdot B &= 0 \\ \nabla \cdot D &= \rho = 0 \end{aligned} \quad (2)$$

### 3 Simulation Results and Analysis

#### 3.1 Electric Field Distribution During Normal Cable Operation

As shown in Fig. 3, it is the electric field distribution diagram of the cable terminal during normal operation; it can be seen that the electric field in the left half of the internal insulation layer is higher, because it has no grounded shielding layer in the

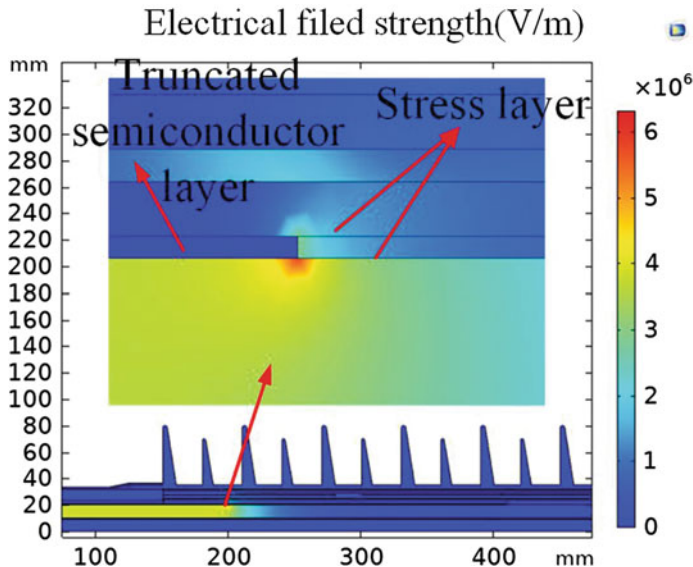


**Fig. 3** Electric field distribution of the cable terminal during normal operation

radial direction, so the electric field is higher; at the same time, it can be seen from the figure that the electric field is distorted near the cut-off portion of the semiconductor layer, and the highest field strength can reach 6.5 MV/mm. This is because the semiconductor layer and the shield layer are connected to be grounded, but the surrounding layers are not grounded, so the electric field distribution is very uneven near the truncated semiconducting layer.

### 3.2 Influence of Air Gap Position on Electric Field Distribution Inside Cable Termination

As shown in Fig. 4, an air gap of 2 mm in length and 0.5 mm in width is constructed in different layers inside the cable terminal. The simulation model is shown in the above figure, and the electric field simulation is carried out to obtain the electric field distribution cloud diagram as shown in the figure. It can be seen from the figure that when the air gap is between the inner insulation layer and the stress tube, the electric field distortion is obvious, and the highest part field strength is as high as 7 MV/mm, which far exceeds the air breakdown field strength of 3 MV/mm, and the air gap will be breakdown produces partial discharge, causing damage to internal insulation.

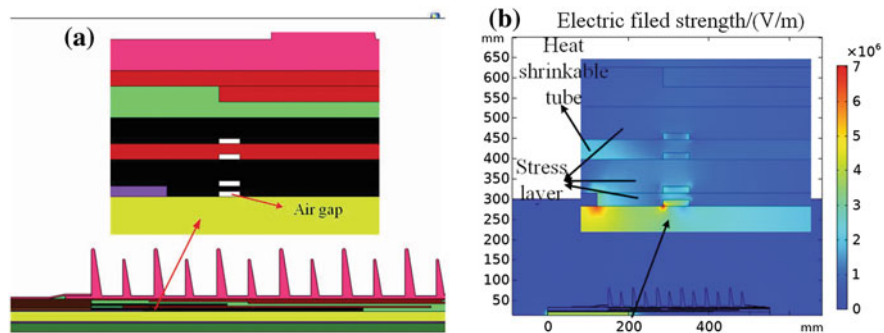


**Fig. 4** Simulation model and results of cable terminal with air gap in different layers

### 3.3 Influence of Air Gap Length and Distance from Joint on Electric Field Distribution Inside Cable Terminal

In order to determine the influence of the air gap depth, the length of the air gap, and the distance from the intercepting semiconductor on the distribution of the electric field strength, an air gap was established at  $d = 5, 35, 65$ , and  $95$  mm from the truncated semiconductor, and then get its electric filed by simulation. As it was shown in the picture, when the air gap is  $35$  mm away from the truncated semiconductor, the electric field intensity distortion is most obvious, and the air gap length is not obvious to the electric field intensity distortion around the air gap. However, the depth of the air gap affects the electric field strength along the depth of the insulating layer. The deeper the air gap is along the inner insulating layer, the smaller the electric field strength around the air gap (Figs. 5 and 6).

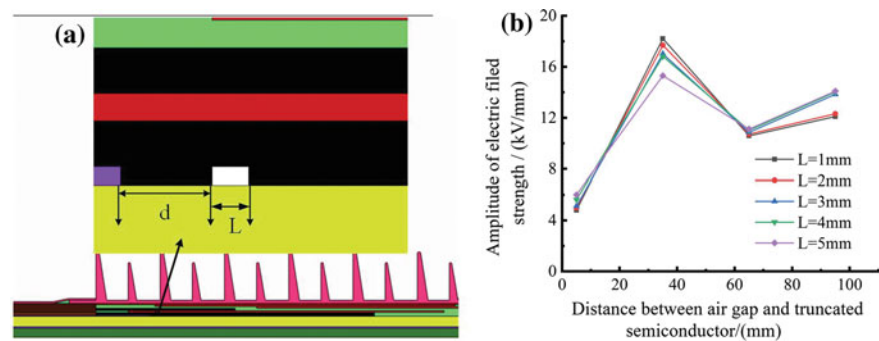


**Fig. 5** Simulation model and results of cable terminations with different air gap lengths

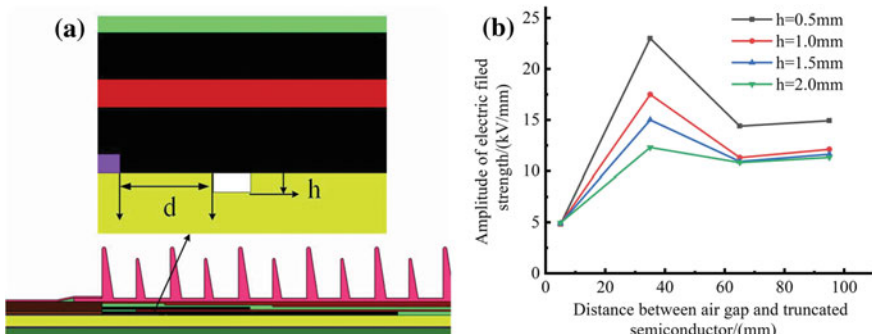


Fig. 6 Simulation model and results of cable terminal with different air gap depths

### 3.4 Analysis of Simulation Results

As a result, when the cable terminal does not contain an air gap, the electric field is distorted near the cut semiconductor layer because the semiconductor layer is connected to the grounded shield layer and its potential is low; when the cable terminal contains an air gap and when the air gap is located at the junction of the stress tube and the inner insulating layer, the electric field distortion is the most serious. The reason is that the inner insulating layer is connected to the core, and the air gap is farther from the high-voltage end than the other layers. And the distance between the air gap and the truncated semiconductor layer has a great influence on the degree of electric field distortion, when the air gap is 35 mm away from the truncated semiconductor layer, and the electric field intensity has a maximum value, which may be caused by the tip effect of the semiconductor being cut-off. The truncated semiconductor is directly connected to the stress tube, which produces a tip effect that may cause the effect of the length of the air gap on the electric field strength to be inconspicuous. As for the electric field strength at an angle of 95 mm from the semiconductor, the analysis can be considered that the tip effect is weakened due to the distance too far, and the air gap is close to the high voltage of the other end, causing the increase of electric filed. The deeper the air gap is along the inner insulating layer, the smaller the electric field strength around the air gap is. The analysis considers that the width of the air gap increases, causing the radial radius of the air gap to increase, resulting in a decrease in electric field strength.

## 4 Conclusion

In this paper, the internal air gap defect of the semi-rigid cable terminal was simulated and analyzes the electric field distribution of cable terminal with the air gap. The main conclusions are as follows:

- (a) Due to the stripping of the shielding layer inside the cable terminal, the electric field distribution of the electric field at the stripping portion is extremely uneven, and at the same time, when there is an air gap inside the cable terminal, partial discharge would be generated.
- (b) When there is air gap between the inner insulation layer and the stress layer of the cable terminal, the electric field distribution is more likely to be uneven. The length of the air gap is not obvious to the electric field strength distortion. The electric field strength distortion is the most serious at 35 mm from the truncated semiconductor; the deeper the gap along the inner insulating layer, the distortion of the electric field strength will be reduced.
- (c) The presence of an air gap between the inner insulating layer and the stress layer is more likely to cause electric field concentration, causing insulation discharge and breakdown, and the manufacturing process should improve the link.

**Acknowledgements** The article is grateful to the China Railway Science Research Institute Group Co., Ltd. Research and Development Fund Project (2018YJ009) for its support.

## References

1. Li W, Kai Z, Xutao L et al (2014) The mechanism of partial discharge development of air gap in cable termination based on electric field characteristics. *High Voltage Eng* 40(12):3709–3716 (in Chinese)
2. Lijun Z, Yuan L, Longlei B et al (2019) Partial discharge characteristics and failure mechanism of vehicle-mounted flexible cable terminals in alpine regions *High Voltage Technol* 01:189–195 (in Chinese)
3. Uchida K, Tanaka H, Hirot Su K (1996) Study on detection for the defects of XLPE cable lines *IEEE Trans Power Deliv* 2(11):663–668
4. Zhigang L, Juan C (2012) Experiment of main insulation with air gap of 10 kV crosslinked polyethlencable terminal *High Voltage Eng* 38(3):678–683 (in Chinese)
5. Chao W, Yigang L, Gang L et al (2007) Analysis of stress cone defects in cable terminations by finite element method. *High Voltage Eng* 33(5):152–155 (in Chinese)
6. Yasha L, Yaping D, Xu H et al (2018) The influence of impurities on electric field and space charge distribution in XLPE cable. *Trans China Electrotech Soc* 33(18):4365–4371 (in Chinese)
7. Wagenaars P, Wouters P, Van Der Wielen P et al (2008) Accurate estimation of the time-of-arrival of partial discharge pulses in cable systems in service. *IEEE Trans Dielectr Electr Insul* 15(4):1190–1199
8. Shuai1 H, Baojun H, Mingli F et al (2018) Performance evaluation for XLPE extruded insulation HVDC cable and space charge measurement under operating condition with temperature difference. *High Voltage Eng* 44(5):1467–1474 (in Chinese)
9. Huuva R, Englund V, Gubanski SM et al (2009) A versatile method to study electrical treeing in poly- meric materials. *IEEE Trans Dielectr Electr Insul* 16(1):171–178
10. Fan Y, Qi Y, Peng C et al (2017) Characterization method of insulation degradation under air gap discharge defects in cable joints. *Trans China Electrotechn Soc* 02:24–32 (in Chinese)
11. Chao W, Yigang L, Gang L et al (2007) Analysis of faults on cable terminal stress cone based on finite element method. *High Vol Eng* 33(5):152–155 (in Chinese)

# Research on Reactive Power Optimization Scheme of Metro Medium Voltage Power Supply Network Based on the Medium Voltage Energy Feeding Device



Lingmin Meng , Dawei Song, Jie Chen, Fuqiang Mu  
and Zhigang Liu

**Abstract** The metro power supply system has a low power factor during low load rate operation. In order to save the investment of reactive compensation devices and compensate the reactive power for the metro medium voltage power supply network in the most reasonable and economical way, the reactive power optimization scheme based on the medium voltage energy feeding device is studied. The reactive power optimization model of the metro medium voltage power supply network is built and the particle swarm optimization (PSO) is used to solve the problem. In order to verify the proposed scheme, taking a metro medium voltage power supply line as an example, PSO is applied to reactive power optimization with the objective of minimizing active power loss. The simulation results show that the reactive power compensation based on the optimization results can effectively reduce the active power loss, which verifies the feasibility, rationality, and economy of the proposed scheme.

**Keywords** Metro power supply system · Reactive power optimization · Medium voltage energy feeding device · PSO

---

L. Meng  · J. Chen · Z. Liu

School of Electrical Engineering, Beijing Engineering Research Center of Electric Rail Transportation, Beijing Jiaotong University, Beijing 100044, China  
e-mail: [17121481@bjtu.edu.cn](mailto:17121481@bjtu.edu.cn)

J. Chen

e-mail: [jiechen@bjtu.edu.cn](mailto:jiechen@bjtu.edu.cn)

Z. Liu

e-mail: [zhgliu@bjtu.edu.cn](mailto:zhgliu@bjtu.edu.cn)

D. Song

Hohhot Urban Rail Transit Construction Management Co., Ltd., Hohhot, China  
e-mail: [772117871@qq.com](mailto:772117871@qq.com)

F. Mu

Beijing Qiansiyu Electric Co., Ltd., Beijing 100082, China  
e-mail: [mufuqiang@163.com](mailto:mufuqiang@163.com)

## 1 Introduction

The centralized power supply mode of the metro power supply system refers to the power transmission from urban power grid to the metro power supply system through the main substation. The transformer in the main substation converts the high voltage such as 110 kV introduced from the urban power grid to the medium voltage such as 35 kV, and supplies electric energy to the traction substations and the step-down substations through the medium voltage power supply network. Medium voltage cables have large capacitance to the ground, when the load rate is low, such as night outage, the capacitive reactive power generated by the medium voltage cables can not be fully consumed, the power factor of the metro power supply system is low, and the power factor at the billing point can not meet the lower limit, which will impose huge fines on the metro. Therefore, it is necessary to compensate the reactive power for the metro medium voltage power supply network.

Reactive compensation devices mainly include synchronous condenser, static capacitor, static Var compensator (SVC) and static Var generator (SVG) [1]. SVG is a reactive compensation device based on voltage source converter [2]. It has many advantages, such as fast adjustment speed and wide adjustment range. The core equipment of the medium voltage energy feeding device is high power PWM converter. It is basically the same as SVG in the main circuit topology and operating principle [3]. It can realize four-quadrant operation, and the power factor can be controlled arbitrarily. Therefore, the medium voltage energy feeding device can be used for reactive power compensation.

Particle swarm optimization (PSO) is a group intelligent optimization algorithm, which is inspired by the bird predation process and obtains the optimal solution through the exchange of information among the whole group and the accumulation of individual experience. So far, it has been applied in multiple areas such as power system optimization [4, 5], automatic control system parameter design [6], and job shop scheduling [7]. In this paper, PSO is applied to the reactive power optimization of metro medium voltage power supply network.

## 2 Reactive Power Compensation Scheme

The key equipment of medium voltage energy feeding device includes transformer and high power PWM converter. The high power PWM converter has the characteristics of controllable power factor, stable DC voltage, and bidirectional energy transmission. When the train brakes, the PWM converter works in the mode of inverter and feeds the regenerative braking energy back to the medium voltage network, which has a good energy-saving effect. In the traction substation, the medium voltage energy feeding device operates in parallel with the diode rectifier unit. The main structure of traction substation is shown in Fig. 1.

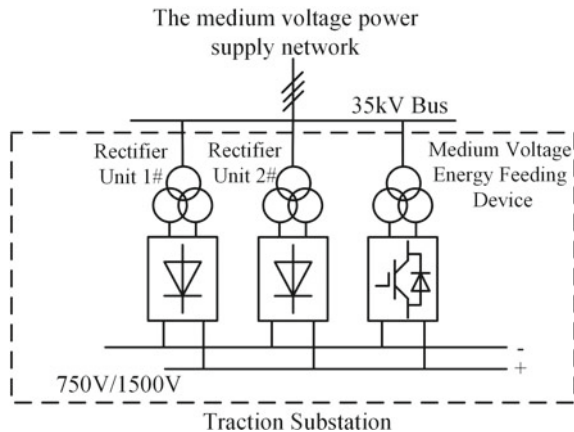


**Fig. 1** Main structure of traction substation

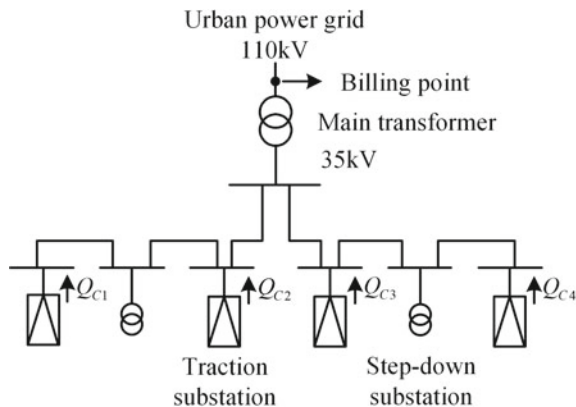


**Fig. 2** Schematic diagram of reactive power compensation scheme based on the medium voltage energy feeding device

In the case where the medium voltage energy feeding device is arranged in each traction substation, it can realize the zonal compensation and improve the reactive power distribution of the metro medium voltage power supply network, thereby improving the power factor of the entire power supply system. The schematic diagram of reactive power compensation scheme for the metro medium voltage power supply network based on the medium voltage energy feeding device is as Fig. 2.

In the process of implementation, it is necessary to reasonably determine the reactive power output of the medium voltage energy feeding device and ensure that the power factor at the billing point meets the requirements of the grid.

### 3 Reactive Power Optimization Model

The reactive power transmission will cause active power loss and voltage fluctuation on the transmission line. The reactive power optimization of metro medium voltage power supply network is to improve the reactive power distribution of the metro medium voltage power supply network by adjusting the reactive power output of medium voltage energy feeding device, reduce the active power loss in transmission, and ensure that the power factor and the voltage satisfy the requirements. In this paper, the reactive power optimization model is established with the objective of minimizing active power loss.

The objective function is as below:

$$P_{\text{loss}} = \sum_{k \in N_k} G_k (V_i^2 + V_j^2 - 2V_i V_j \cos \theta_{ij}) \quad (1)$$

where  $N_k$  is the collection of branches included in the system,  $G_k$  is the branch conductance,  $V_i$  and  $V_j$  are the voltage amplitudes at both ends of the branch, respectively,  $\theta_{ij}$  is the phase difference of the voltage at both ends of the branch.

The reactive power output of medium voltage energy feeding device  $Q_c$  is taken as the control variable, the node voltage amplitude  $V$  and the power factor at the billing point  $\lambda$  are regarded as the state variables.

The equality constraints are as below:

$$0 = P_i - V_i \sum_{j \in N_i} V_j (G_{ij} \cos \theta_{ij} + B_{ij} \sin \theta_{ij}) \quad i \neq S \quad (2)$$

$$0 = Q_i - V_i \sum_{j \in N_i} V_j (G_{ij} \sin \theta_{ij} - B_{ij} \cos \theta_{ij}) \quad i \in N_{pq} \quad (3)$$

The inequality constraints are as below:

$$\begin{cases} Q_{ci \min} \leq Q_{ci} \leq Q_{ci \max} & i \in N_c \\ V_{i \min} \leq V_i \leq V_{i \max} & i \in N_{pq} \\ \lambda_{\text{std}} \leq \lambda & \end{cases} \quad (4)$$

Where  $N_i$  is the set of nodes associated with node  $i$  in the system including itself,  $S$  means slack bus,  $N_{pq}$  is the set of PQ nodes,  $P_i$  and  $Q_i$  are the active power and reactive power injected into node  $i$ , respectively,  $N_c$  is the set of reactive compensation nodes based on the medium voltage energy feeding device,  $Q_{ci \min}$  and  $Q_{ci \max}$  are determined by the maximum reactive power output of medium voltage energy feeding device,  $V_{i \min}$  and  $V_{i \max}$  are determined by the allowable voltage offset, and  $\lambda_{\text{std}}$  is the required power factor at the billing point.

The extended objective function of the reactive power optimization model constructed by penalty function method [8] is proposed as Eq. (5).

$$\begin{aligned}
G = & P_{\text{loss}} + \delta \sum_{i \in N_{pq}} [\max\{0, -(V_i - V_{i\min})\}]^2 \\
& + \delta \sum_{i \in N_{pq}} [\max\{0, -(V_{i\max} - V_i)\}]^2 \\
& + \delta [\max\{0, -(\lambda - \lambda_{\text{std}})\}]^2
\end{aligned} \tag{5}$$

$\delta$  is a penalty, and it should take a sufficiently large value.

## 4 Particle Swarm Optimization

Particle swarm optimization (PSO) is inspired by the bird predation process. It is initialized with a population of particles in the search space. Every particle in the population has attributes of position, velocity, and fitness. The fitness is used to judge the performance of the particle and PSO records the best position found by all particles and the individual best positions found by each particle in the search process.

For an optimization in the  $d$ -dimensional search space, the position and velocity of every particle in the population are  $d$ -dimensional vectors and the position represents a potential solution. In the iteration process, each particle updates its position and velocity according to Eqs. (6) and (7).

$$v_{i,j}(t+1) = \omega v_{i,j}(t) + c_1 r_1(p_{i,j}(t) - x_{i,j}(t)) + c_2 r_2(g_j(t) - x_{i,j}(t)) \tag{6}$$

$$x_{i,j}(t+1) = x_{i,j}(t) + v_{i,j}(t+1) \tag{7}$$

where  $t$  means the number of iterations,  $v_{i,j}(t)$  is the velocity of individual  $i$  on dimension  $j$ ,  $x_{i,j}(t)$  is the position on dimension  $j$ ,  $p_{i,j}(t)$  is the individual best position on dimension  $j$ ,  $g_j(t)$  is the best position among all the particles on dimension  $j$ ,  $c_1$  and  $c_2$  are learning factors,  $r_1$  and  $r_2$  are the random numbers within the range of  $[0, 1]$ , and  $\omega$  is the inertia weight. To avoid blind searching, the data on each dimension of position vector and velocity vector has upper and lower bounds.

The inertia weight  $\omega$  reflects the ability to inherit the previous velocity. When  $\omega$  is large, PSO has strong global search ability. On the contrary, the local search ability is better. In order to balance the global search and the local search, it is adopted that the strategy of linearly decreasing the inertia weight. In the initial stage of iteration,  $\omega$  is large, which makes the exploration range of particles wide. As the number of iterations increases,  $\omega$  decreases linearly and the local search ability of PSO increases gradually. In the later stage of iteration, it is advantageous for PSO to search around the optimal solution carefully.

The formula for calculating inertia weight is as follows:

$$\omega = \omega_{\max} - \frac{\omega_{\max} - \omega_{\min}}{T} t \quad (8)$$

where  $T$  is the maximum number of iterations,  $t$  is the current number of iterations,  $\omega_{\max}$  is the initial inertia weight, and  $\omega_{\min}$  is the inertia weight when reaching the max iterations.

When the particle position exceeds the boundary, the boundary processing method adopted is as follows:

$$\begin{aligned} & \text{if } x_{i,j} > x_{j\max} \text{ or } x_{i,j} < x_{j\min} \\ & x_{i,j} = x_{j\min} + r \cdot (x_{j\max} - x_{j\min}) \end{aligned} \quad (9)$$

Where  $x_{j\min}$  is the lower bound of the position on dimension  $j$ ,  $x_{j\max}$  is the upper bound of the position on dimension  $j$ , and  $r$  is the random number within the range of  $[0, 1]$ .

This method is equivalent to re-initializing the particle in the search space, avoiding the particle falling into the local optimum near the boundary and enhancing the variability of the particle.

In this paper, the PSO is used to solve the reactive power optimization of metro medium voltage power supply network.

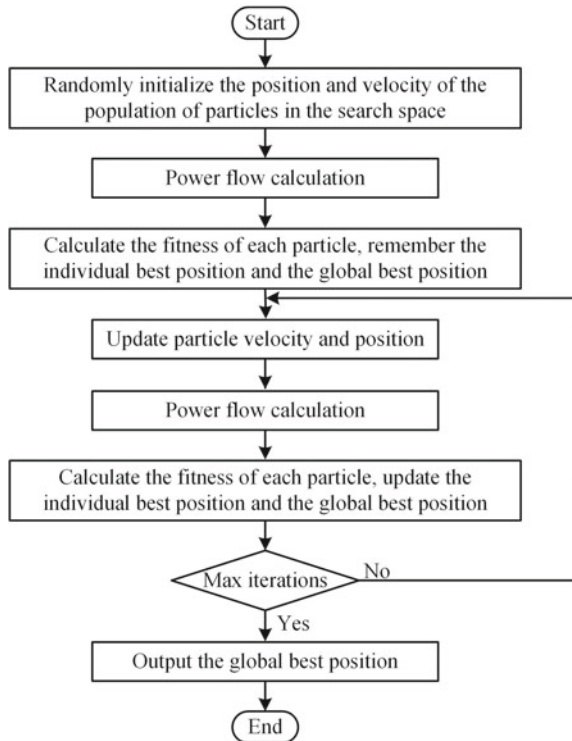
## 5 Reactive Power Optimization of Metro Medium Voltage Power Supply Network

### 5.1 Reactive Power Optimization Procedure

Assuming that the number of the medium voltage energy feeding devices is  $m$  in the system, the dimension of PSO is  $m$  and particle position can be expressed as  $X = [Q_{c_1}, Q_{c_2}, \dots, Q_{c_{(m-1)}}, Q_{c_m}]$ . Before the implementation of PSO, it is necessary to determine the swarm size and the maximum number of iterations. For the problem in a non-high-dimensional search space, the swarm size is generally set between 20 and 50, and the maximum number of iterations can be determined according to the convergence rate of the problem.

The flow chart for reactive power optimization is as Fig. 3. In the process of reactive power optimization, the state variables of the system can be determined by power flow calculation [9] based on the potential solution provided by the particle position. The fitness of particle is calculated according to Eq. (5). Particle velocity and position are updated according to Eqs. (6) and (7). At the end of the calculation, the global best position is taken as the optimal solution.

**Fig. 3** Flow chart for reactive power optimization



## 5.2 Reactive Power Optimization Example and Analysis

In order to verify the proposed reactive power optimization model and the process, the metro medium voltage power supply line in Fig. 4 is used as the test line. As shown in Fig. 4, there are 15 stations under the main substation. Taking the line within the 1# main transformer power supply as an example, the structure is as Fig. 5.

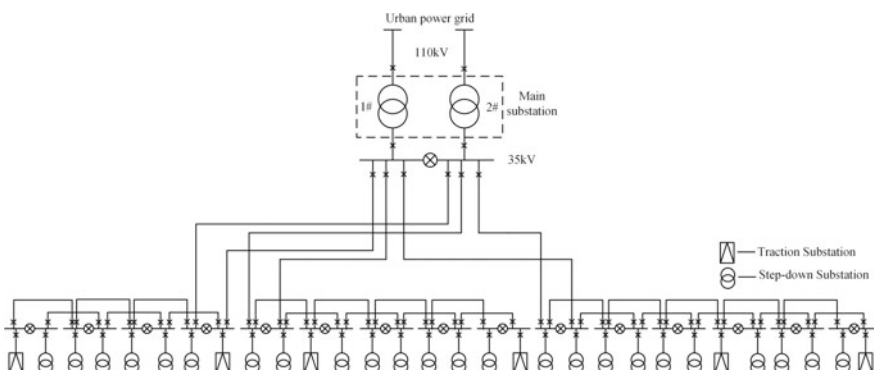


**Fig. 4** A metro medium voltage power supply line

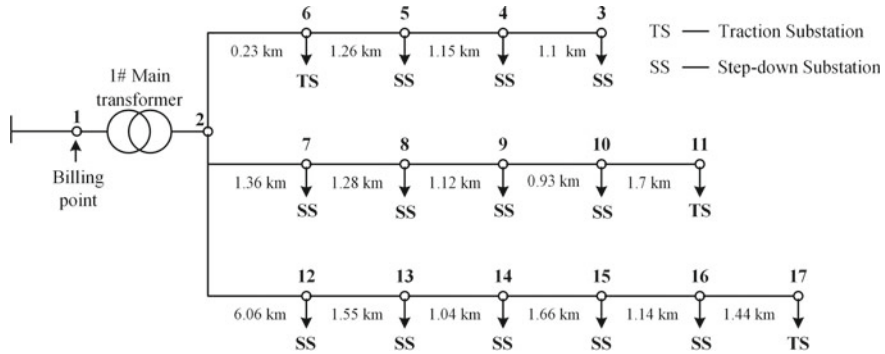


**Fig. 5** Structure diagram of the line within the 1# main transformer power supply

In Fig. 5, node 1 is a slack bus and it is required that the power factor at node 1 is not less than 0.95. The other nodes are regarded as PQ nodes, allowing  $\pm 5\%$  voltage offset.

In the traction substation, the capacity of the medium voltage energy feeding device is 2 MW and the capacity of the diode rectifier unit is 4 MW. For non-operational hours, there is no traction load, only part of the power and lighting load. Therefore, the load of each station is set as 60 kW with power factor of 0.8.

The capacity of 1# main transformer is 25 MVA, rated voltage is 110/35 kV, short circuit impedance is 10.52%, and short circuit loss is 118 kW. The distance of each station is shown in Fig. 5. The resistance of the cable is  $0.159 \Omega/\text{km}$ , the reactance is  $0.187 \Omega/\text{km}$ , and the admittance is  $80.038 \times 10^{-6} \text{ S/km}$ .

Based on the above line conditions, the power flow calculation is carried out. Without reactive power compensation, the active power loss is 1.3 kW, and the power factor at node 1 is 0.49. The calculated active power loss includes the active power loss of the medium voltage cables and the active power loss caused by the resistance of the windings on both sides of the main transformer, but does not include the no-load loss of the main transformer.

The PSO parameters are as follow:

The maximum number of iterations is 60, the swarm size is 30, the dimension is 3,  $c_1$  and  $c_2$  are set as 2,  $\omega_{\max}$  is set as 0.9, and  $\omega_{\min}$  is set as 0.4.

Optimizing by the PSO and the genetic algorithm (GA) provided by MATLAB optimization toolbox, the results are shown as Table 1:

**Table 1** Reactive power optimization results of PSO and GA

Algorithm	Active power loss (kW)	Optimal solution (Mvar)
PSO	0.4791	[0.8309, 0.203, 0.4436]
GA	0.4791	[0.829, 0.204, 0.445]

**Fig. 6** The evolution curves of the best fitness of GA and the PSO

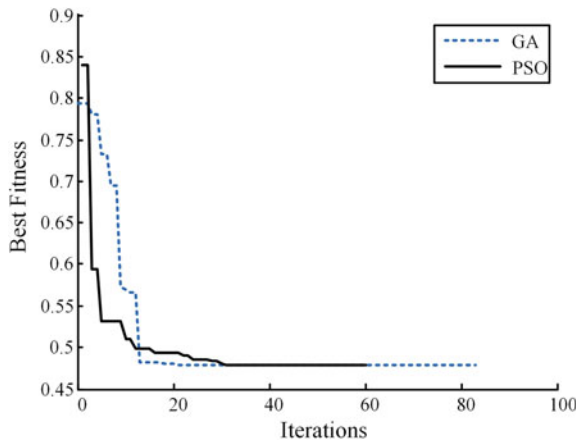


Figure 6 shows the evolution curves of the best fitness of GA and the PSO, which reflects the variation of the best fitness with the number of iterations.

The optimization results of the PSO and GA are similar. Compared with GA, the PSO converges quickly and the result is reliable. The PSO has good performance.

According to the optimal solution, 0.8309, 0.203, and 0.4436 Mvar inductive reactive power are, respectively, injected at node 6, node 11, and node 17. The active power loss is 0.4791 kW, and the power factor at the billing point is 0.99. The voltage amplitude of each node is within the allowable offset.

Comparing with the case without reactive power compensation, the active power loss decreases by 63.1%, and the power factor increases from 0.49 to 0.99. The proposed reactive power optimization model and the process can reduce the active power loss effectively and ensure that the power factor at the billing point meets the requirement of the grid.

## 6 Conclusion

In the simulation, the PSO converges rapidly and the optimization results are reliable. The simulation results show that the proposed reactive power optimization model and the process can effectively reduce the active power loss and meet the requirements of the grid. Therefore, the reactive power optimization scheme of metro medium voltage power supply network based on the medium voltage energy feeding device proposed in this paper is feasible and economical.

**Acknowledgements** This work is supported by the National Key Research and Development Program (2017YFB1200802-17).

## References

1. Wang X (2006) Statement and development trend of reactive power compensation equipment. *Appl Energy Technol* 4:31–32 (in Chinese)
2. Zheng S, Yan H, Chen L et al (2013) Research on static VAR generator with direct current control strategy. In: Industrial electronics & applications. IEEE
3. Zhang G (2010) Study on key techniques of energy-fed traction power system for urban mass transit. Beijing Jiaotong University (in Chinese)
4. Smita P, Vaidya BN (2012) Particle Swarm Optimization based Optimal Power Flow for reactive loss minimization. In: Electrical, electronics & computer science. IEEE
5. Shuqin S, Bingren Z, Jun W et al (2013) Power system reactive power optimization based on adaptive particle; swarm optimization algorithm. In: World congress on intelligent control & automation. IEEE
6. Kiree C, Kumpanya D, Tunyasirut S et al (2016) PSO-based optimal PI(D) controller design for brushless DC motor speed control with back emf detection. *J Electr Eng Technol* 11 (3):715–723
7. Zhang G, Shao X, Li P et al (2009) An effective hybrid particle swarm optimization algorithm for multi-objective flexible job-shop scheduling problem. *Comput Ind Eng* 56(4):1309–1318
8. Hou Y, Lu L, Xiong X et al (2004) Enhanced particle swarm optimization algorithm and its application on economic dispatch of power systems. *Proc Chin Soc Electr Eng* 24(7) (in Chinese)
9. He Y, Wen Z (2002) Power system analysis. Huazhong University of Science & Technology Press (in Chinese)

# Research and Application on Electric Vehicle Charging Communication Protocols Compatibility Detection



Sixiang Zhao, Zhenyu Jiang, Di Han, Hanji Ju, Yachao Wang  
and Chenwei Zhang

**Abstract** Electric vehicles are gradually favored by people for the advantages of low energy consumption, high energy efficiency, and zero emission. Whether charging facilities can properly charge electric vehicles is one of the factors that affect the electric vehicles travel. Communication compatibility issues of DC chargers will lead to failure of charging, which affect the user experience. In this paper, the communication protocol compatibility detection device of electric vehicle charger is proposed and designed. When the products in operation are in communication compatibility problem, the charging process can be directly detected to identify the problem. Compared with the previous independent testing of chargers and vehicles, it is more convenient and quick to use and is suitable for on-site operation and maintenance.

**Keywords** Electric vehicle · Communication protocols · Compatibility · Detection

## 1 Background

In recent years, the energy crisis and environmental pollution have become serious problems facing economic and social development. The advantages of low energy consumption, high energy efficiency, and pollution-free of electric vehicles are gradually favored by people. In 2018, the production and sales volume of new

---

S. Zhao (✉) · Z. Jiang · D. Han · H. Ju · Y. Wang  
State Grid Jibei Electric Power Company Limited Power Research Institute,  
Beijing 100045, China  
e-mail: [zhaosx0518@126.com](mailto:zhaosx0518@126.com)

North China Electric Power Research Institute Co. Ltd., Beijing 100045, China

C. Zhang  
Beijing Jiaotong University, Beijing 100044, China

energy vehicles in China exceeded 1.25 million units, a year-on-year increase of 60%. The rapid growth of the number of new energy vehicles has gradually become a national focus.

As one of the key factors directly affecting the promotion and application of electric vehicles, the charging piles are also developing rapidly. According to the data from China Charging Alliance, there were 285,000 public charging piles till October 2018. According to the “Electric Vehicle Charging Infrastructure Development Guide (2015–2020),” the number of charging stations will reach 12,000 by 2020, and the number of charging piles will reach 4.5 million.

With the explosive growth of electric vehicle charging facilities, in order to interconnect electric vehicles and charging facilities, the state has compiled and released a series of electric vehicle charging interfaces and communication protocol standards [1–4]. However, charging failures caused by communication compatibility problems occur frequently in actual charging. Mainly because (1) Some electric vehicle factories and charging facility manufacturers have deviations from the understanding and implementation methods of communication protocols, which results in compatibility problems. (2) Some vehicles and charging piles were produced earlier and did not adopt the latest national standards. (3) The new version debugging work is not done in the process of updating and upgrading the program of electric car and charging pile.

Charging communication compatibility problems will cause charging failures which directly affect the user experience. Charging failures also affect the stable operation of the charging infrastructure and may cause indirect damage to the power quality of the grid and the service life of the power battery [5].

At present, there are researches on testing of chargers [6–8] and electric vehicles [9]. It is mainly applicable to the detection method in the laboratory environment before the product is put into operation. The vehicle or pile is tested separately, focusing on the quality evaluation of the equipment. There is less research on detecting the compatibility problems and fault location.

This paper proposes and designs an electric vehicle charging post communication protocol compatibility detection device, which can directly detect the charging process and locate the compatibility problem. Compared with the previous testing approaches of charging piles and vehicles, it is easy and suitable for field testing, and it can improve the quality and efficiency of operation and maintenance work and provide better services to users.

## 2 Hardware Design

### 2.1 Schematic Diagram of Detection System

The detection system designed in this paper analyzes the acquired communication messages and locates the problem without affecting the communication between the off-board charger and the battery management system (BMS) of electric vehicle.

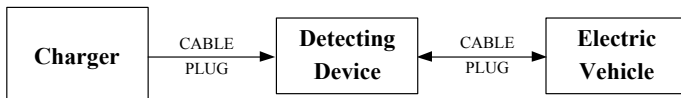


**Fig. 1** Schematic diagram of the detection system

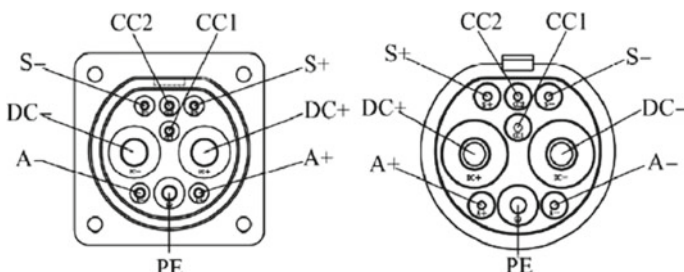
The charging communication protocol compatibility detecting device is connected in series between the charging pile and the vehicle to collect and acquire communication messages. The messages are transmitted to the host computer for further analysis and result preservation. Figure 1 is the schematic diagram of the system design.

## 2.2 Communication Messages Acquiring

Communication based on controller area network (CAN) has the advantages of strong real-time performance, strong anti-electromagnetic interference capability, long transmission distance, and low cost. In the current electric vehicle industry, the CAN bus technology is applied in the charging communication between the battery management system and the charger during charging.

When a node on the CAN bus transmits data, it broadcasts to all nodes of the network in the form of messages. Each node can receive the message whether the data are sent to it or not. Therefore, the broadcast characteristics can be utilized by adding a node between the charging pile and the electric vehicle for receiving the communication messages sent by the electric vehicle and the charging pile so as to obtain the communication messages.

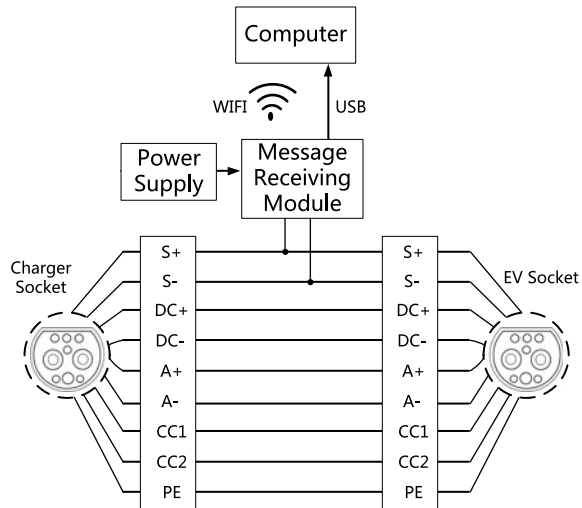
The cable assembly is used between the electric vehicle and the charging pile and connected by the vehicle plug and the vehicle socket to realize information interaction and power transmission during charging. The arrangement of the vehicle plug and the vehicle socket is as shown in Fig. 2. The contact identification and its function definition are shown in Table 1 [2].



**Fig. 2** Arrangement of the vehicle connector and vehicle socket

**Table 1** Contact identification and function definition

Contact identification	Function definition
DC+	Positive DC power supply, connecting DC power supply with battery positive
DC-	Negative DC power supply, connecting DC power supply with battery negative
PE	Protective earthing
S+	Charging communication CAN_H
S-	Charging communication CAN_L
CC1	Charging connection confirmation
CC2	Charging connection confirmation
A+	Low voltage auxiliary power supply positive
A-	Low voltage auxiliary power supply negative

**Fig. 3** Hardware structure

The functions of the S+ contact and the S- contact of the vehicle plug and socket are, respectively, the charging communication CAN\_H and CAN\_L, which are communication lines connecting the off-board charger and the electric vehicle. Without affecting the original working state, the S+ contact and the S- contact can simultaneously acquire the message sent to the other part by the electric vehicle and the charging pile. The main power supply circuit (DC+, DC-), auxiliary power supply circuit (A+, A-), connection confirmation (CC1, CC2), and protective earth (PE) are directly connected. The hardware structure is shown in Fig. 3.

## 2.3 Other Parts Design

### ① Message Receiving Module

The communication message receiving module is connected to the CAN bus, and the internal CAN transceiver converts the received differential signal into a logic level signal to realize reception of the CAN signal. The CAN core implements the reception of CAN protocol information frames. The controller is responsible for the control of message reception. The acceptance filter is responsible for filtering the information. And the receiving buffer is responsible for the acceptance of the error-free information. In order to facilitate on-site implementation, the message receiving module is equipped with a variety of transmission data interfaces. The message can be sent to the computer via wireless mode (WIFI) or wired mode (USB) for subsequent message preservation and analysis (Fig. 4).

### ② Wire Selection

The detection device is connected to wires between the charging pile and the electric vehicle, and the socket size is designed according to the national standard of China. The cable cross section of the vehicle socket needs to meet the relevant standards [1]. According to the rated current of each contact of the socket, the appropriate type is selected for each wire, and a certain value is reserved in consideration of the possibility of over-rated operation. The nominal cross section of each wire design is shown in Table 2.

**Fig. 4** Schematic diagram of message receiving module

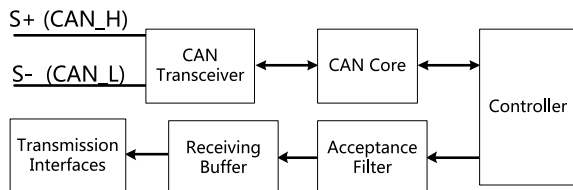


**Table 2** Contact electrical reference value and wire selection

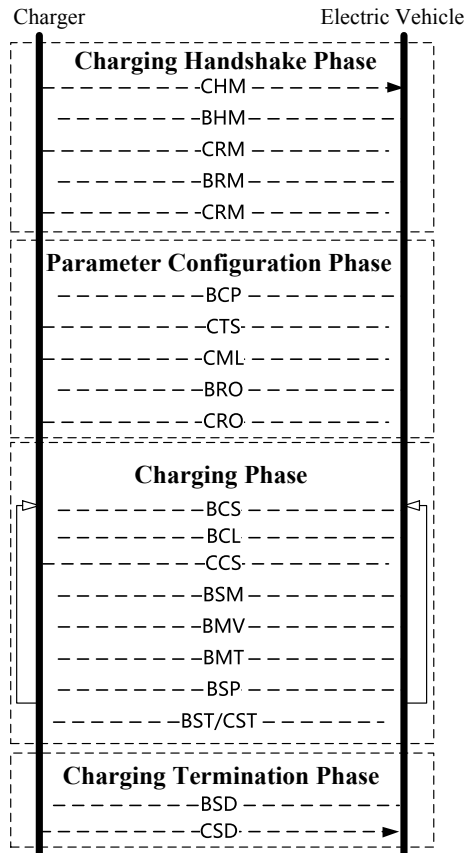
Contact ID	Electrical reference value	Wire cross section area (mm <sup>2</sup> )
DC+	750 V, 250 A	100
DC-	750 V, 250 A	100
PE	/	25
S+	5 V, 2 A	1.0
S-	5 V, 2 A	1.0
CC1	12 V, 2 A	1.0
CC2	12 V, 2 A	1.0
A+	12 V, 10 A	1.5
A-	12 V, 10 A	1.5

The cable assembly connecting the detection device and the electric vehicle meets the national standard. The maximum rated current is 250 A, and the line length is 50 cm, which can meet the requirements under most conditions.

### 3 Software Design

The national standard stipulates normal charging state flow chart [3], describes the specific message interaction timing of the charger and the electric vehicle and the message format requirements [4]. The charging process consists of six phases: physical connection, low voltage auxiliary power-on, charging handshake phase, charging parameter configuration phase, charging phase, and charging termination phase. The communication message interaction starts from the handshake phase and ends at the end of the charging phase. The message interaction timing is shown in Fig. 5.

**Fig. 5** Message mutual sequence



Firstly, the software detects the communication rate and frame format, protocol data unit, network address, etc., and determines whether the communication conforms to the specifications of the physical layer and the data link layer.

The message classification is then determined according to the parameter group number (PGN). Check whether the timing and period of the charging interaction message are normal. According to the PGN, the message format and content are parsed according to the standard and displayed by text, which is convenient for analyzing whether the charger and the electric vehicle are charging according to the standard process.

When the BMS or the charger detects an error, it sends an error message (BEM or CEM), analyzes the content of the error message, and analyzes the interactive message before the error, which can determine the cause of the compatibility problem.

During the test, the user can read the current charging demand of the electric vehicle, the actual output of the charger, and the message interaction in the process. When the test is over, the report can be generated automatically.

## 4 Test Verification

The communication protocol compatibility detection device was used to test the charging process of the electric vehicle and the charging pile. And the following problems were found.

### 4.1 Address Problem and Period Problem

In the communication process between the electric vehicle and the charging pile, there are problems with the message address, period, etc. Table 3 shows the problem message address. The device obtains the communication message between the charger and the BMS, according to the standard, the charger communication address (56H), and the electric vehicle BMS communication address (F4H). The charging station sends an incorrect address (E5H) message, which will interfere with normal communication and increase the charging hazard.

As shown in Table 4, the standard period of the CRM message issued by the charger is 250 ms, and the actual period is 249 ms. Some vehicles have strict

**Table 3** Address problem message

Receiving time identifier	Frame ID	CAN raw data	Problem
14:42:15.834.0	0 × 1801f4e5	64 00 00 00 33 34 35 36	Address problem
14:42:16.085.0	0 × 1801f4e5	64 00 00 00 33 34 35 36	Address problem

**Table 4** Period problem message

Receiving time Identifier	Frame ID	CAN raw data	Message code
16:14:02.866.0	0 × 1826f456	01 01 00	CHM
16:14:03.018.0	0 × 182756f4	4c 1d	BHM
16:14:03.023.0	0 × 1801f456	00 64 00 00 00 ff ff ff	CRM
16:14:03.272.0	0 × 1801f456	00 64 00 00 00 ff ff ff	CRM

**Table 5** Content problem message

Frame ID	CAN raw data	Message code	Parsed message content
0 × 100af456	00	CRO	Charger charging preparation not ready
0 × 100956f4	aa	BRO	BMS charging preparation ready
0 × 100af456	00	CRO	Charger charging preparation not ready
0 × 100956f4	aa	BRO	BMS charging preparation ready
0 × 081ff456	fc f0 c0 fc	CEM	Charger error message

detection of the message period. When charged by this charger, communication failure will occur, resulting in charge failure.

## 4.2 Content Problem Message

Sometimes, the compatibility problem analysis is based on the parsed message content and the interaction timing.

As shown in Table 5, the BMS completes the charging preparation and sends the BRO message, and the charger does not complete the charging preparation. The reason for the charging failure is that the charger is faulty. The BEM (BMS charging error) message should be sent by the electric vehicle, and the content is “Receiving the charger to complete the charging preparation message timeout.”

However, in this example, the electric vehicle did not send the BEM charging error message, and the charger sent the CEM (car charging error) message, which did not meet the standard requirements. At the end of charging, there is no CST/BST (car/BMS stop charging) message to abort the charging. Both the charger and the electric vehicle have problems.

## 5 Conclusions

This paper studies the communication detection methods between chargers and electric vehicles and develops a communication protocol compatibility detection device, which can perform compatibility detection and locate faults without

opening the facilities. It is suitable for normal operation and maintenance work and inspection of charging equipment after software updating. The device may ensure the interconnection of charging and facilitate the use of electric vehicle users, which will avoid the waste of huge social resources caused by incompatibility.

**Acknowledgements** This project was supported by The National Key Research and Development Program of China (2016YFB0900500).

## References

1. GB 20234.1-2015, Connection set for conductive charging of electric vehicles—Part 1: General requirements (in Chinese)
2. GB 20234.3-2015, Connection set for conductive charging of electric vehicles—Part3: DC charger coupler (in Chinese)
3. GB/T 18487.1-2015, Electric vehicle conductive charging system—Part 1: General requirements (in Chinese)
4. GB/T 27930-2015, Communication protocols between off-board conductive charger and battery management system for electric vehicle (in Chinese)
5. Carlos Gómez J, Morcos MM (2003) Impact of EV battery chargers on the power quality of distribution systems. *IEEE Trans Power Deliv* 18(3):975–981
6. Zhi-xiang Y (2018) Method for detecting DC charging communication consistency of electric vehicle. North China Electric Power University (in Chinese)
7. Bin Z, Guoliang M, Jianguo W et al (2017) Design of the automatic testing platform for electric vehicle dc chargers. *Power Syst Clean Energy* 33(11):120–127 (in Chinese)
8. Xiulan L, Yuan J, Shuang Z et al (2017) Research and design of portable charging equipment detection system. 44(9):48–53(in Chinese)
9. Ru-peng D, Bai-xia W, Chuan L et al (2017) Design and problem analysis for EV charging protocol testing system. *Auto Electric Parts* 2017(12):5–8 (in Chinese)

# Hybrid Energy Storage Trolley System Configuration Optimization Method Taking into Account the Whole Life Cycle Cost of the Whole Vehicle



Qi An, Fangli Shi, Beiyu Liu, Chaohua Dai and Weirong Chen

**Abstract** In order to configure the parameters of the hybrid energy storage system (HESS), based on the typical working conditions of the trolley, a matching optimization method of the hybrid energy storage trolley system considering the whole life cycle cost of the whole vehicle is proposed. The method establishes a multi-objective and multi-constrained configuration optimization model with the lowest life cycle cost (LCC) and the smallest volume as the objective function of the energy storage system. The enumeration method is used to solve the multi-objective and multi-constraint model to obtain the Pareto frontier. The recommended scheme with acceptable volume and economy is given. The simulation results show that the configured hybrid system can meet the design requirements. After optimizing, the power system cost during the whole vehicle life cycle decreases from 3.85 million yuan to less than 1.5 million yuan, which has important reference value for designing and operating the hybrid energy storage tram.

**Keywords** Hybrid energy storage tram · LCC · Pareto front

## 1 Introduction

The hybrid energy storage tram has high density both in energy and in power which can be nicely used in some complicated rail transit working conditions. This environmental-friendly system can recover a large amount of regenerative braking energy and improve energy utilization. It also has broad application prospects in the field of rail transit [1, 2]. In current hybrid energy storage tram researches, the life cycle cost and operating electricity cost of the energy storage system are optimized, and the optimal configuration scheme was solved by genetic algorithm [3]. Besides, an optimal configuration method considering the cost of the ground charging station

---

Q. An (✉) · F. Shi · B. Liu · C. Dai · W. Chen  
School of Electrical Engineering, Southwest Jiaotong University,  
No. 999, Xi'an Road, Pidu District, Chengdu, Sichuan, China  
e-mail: [784014410@qq.com](mailto:784014410@qq.com)

is proposed [4]. In [5], the advantages and disadvantages in the conditions of using battery, supercapacitor, and battery–supercapacitor combination are compared in city bus. In [6], the economics and dynamics of electric vehicles are optimized by using NSGA-2 algorithm. However, the above researches do not give the basis for the selections of power system size and expenses. In real operations of the tram, the choosing of parameters needs to meet the requirements of space size and operation cost. Therefore, a method is needed to optimize the matching parameters of the hybrid power system, and the system space size and cost under the premise of meeting the train power performance requirements are satisfied by the user.

## 2 Hybrid Energy Storage Tram Model

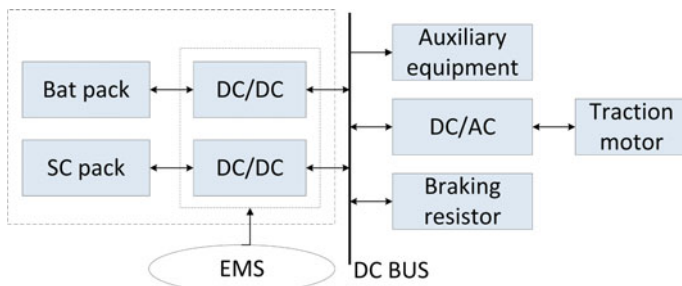
### 2.1 HESS

The hybrid energy storage tram in this paper uses lithium batteries and supercapacitors as power sources. The battery and the supercapacitor are connected to the DC bus through a bidirectional DC/DC converter, respectively. When the tram is on the state of starting, accelerating, and cruising phase, the lithium battery and the supercapacitor provide energy for the load together. When the tram is in the deceleration and braking phase, both the lithium battery and the supercapacitor get the feedback braking energy from the bus. Its topology is shown in Fig. 1.

The vehicle adopts two-moving and one-drag grouping. The main parameters are as shown in Table 1 [7].

### 2.2 Energy Management Strategy

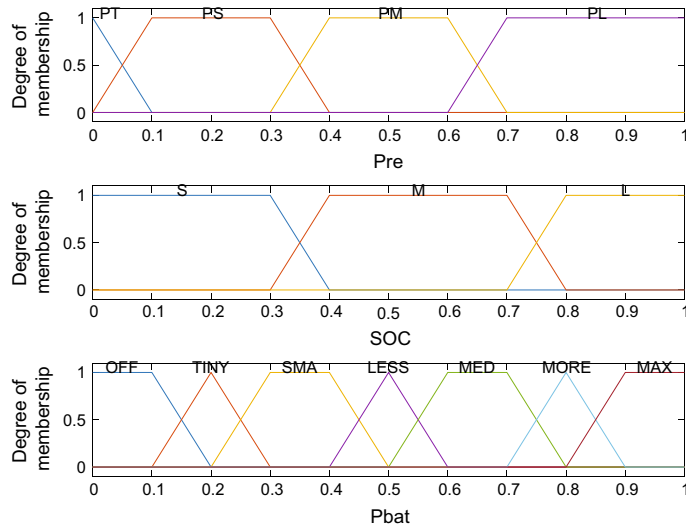
The energy management strategy (EMS) of the hybrid system distributes the load demand power among different power sources. The EMS studied in this paper is the fuzzy logic energy management strategy [8, 9]. In this strategy, the locomotive



**Fig. 1** Topology of hybrid energy storage tram

**Table 1** Parameters of hybrid energy storage tram

Parameter	Numerical value
Application ambient temperature (°C)	-25 to 42
Bus voltage (V)	750
Vehicle grouping	Mc-T-Mc
Axle weight (t)	10.5
Maximum operating speed (km/h)	70
Maximum slope (m)	5‰
Train length (m)	30.19
Train width (m)	2.65
Train weight (t)	51.06
Trainer/person	267
Acceleration (m/s <sup>2</sup> )	1.2
Driving range (km)	30

**Fig. 2** Fuzzy distribution of input and output variables

demand traction power  $P_{re}$  and the battery state of charge (SOC) are selected as the input variables of the fuzzy logic controller. The output power  $P_{bat}$  of the lithium battery is selected as the output of the fuzzy logic controller. The corresponding fuzzy distribution figure and fuzzy control rule table are shown in Fig. 2 and Table 2.

**Table 2** Parameters of hybrid energy storage tram

PW	OFF	OFF	OFF
PL	Tiny	SMA	SMA
PH	Tiny	Less	MED
PH	SMA	More	Max

### 3 Multi-objective Optimization Model of HESS

#### 3.1 Hybrid Energy Storage System Long Circle Cost Model

LCC is the total cost associated with the HESS within N years of vehicle design life, including acquisition costs, replacement costs, and maintenance costs [10].

##### Lithium Battery Long Circle Cost Model

###### 1. Acquisition cost

$$\text{Bat\_my} = (f_d P_{d,b} + n_b C_b f_b) \cdot \text{CRF} \quad (1)$$

In Eq. 1, Bat\_my is the acquisition cost.  $C_b$ ,  $n_b$ , and  $f_b$  are the rated capacity, the number, and the capacity unit price of the single lithium battery, respectively; CRF is the capital recovery coefficient.

###### 2. Replacement cost

$$\text{Bat\_cy} = N_b n_b C_b f_b \cdot \text{CRF} \quad (2)$$

In Eq. 2, Bat\_cy is the replacement cost.  $N_b$  is the number of replacement cycles of the lithium battery. It is necessary to estimate its equivalent cycle life by rain flow method. The following are the different discharge depths of lithium batteries corresponding to the number of cycles as shown in Table 3.

Estimating the current  $n$ th cycle period and the depth of discharge be  $D_n$ , the expression of the equivalent cycle life  $N_{Dn}$  is:

$$N_{Dn} = \frac{N_{ctf}(D_1)}{N_{ctf}(D_n)} \quad (3)$$

**Table 3** Lithium battery discharge depth and cycle times

Depth of discharge	Cycle life	Depth of discharge	Cycle life
0.1	280,000	0.6	23,200
0.2	124,000	0.7	17,200
0.3	72,400	0.8	13,200
0.4	47,200	0.9	10,000
0.5	32,400	1.0	7500

Then, the number of cycles  $N$  of the lithium battery in one working cycle is:

$$N_b = \sum_{n=1}^{n=i} \frac{N_{ctf}(D_1)}{N_{ctf}(D_n)} \quad (4)$$

where  $i$  is the number of cycles in the battery during one duty cycle. When  $N = N_{ctf}(D_1)$ , the lithium battery needs to be replaced.

### 3. Maintenance cost

$$\text{Bat\_ry} = m_b T (f_d P_{d.b} + n_b C_b f_b) \quad (5)$$

where  $m_b$  represents the lithium battery maintenance cost factor.  $\text{Bat\_ry}$  is the maintenance cost.

## Supercapacitor Long Circle Cost Model

### 1. Acquisition cost

$$\text{SC\_my} = (f_d P_{d.s} + n_s C_s f_s) \cdot \text{CRF} \quad (6)$$

where  $C_s$ ,  $n_s$ , and  $f_s$  are the rated capacity, number, and capacity unit price of a single supercapacitor module, respectively.

### 2. Replacement cost

$$\text{SC\_cy} = N_s n_s C_s f_s \cdot \text{CRF} \quad (7)$$

In Eq. 7,  $N_s$  is the number of times that the supercapacitor is replaced by the life cycle. Unlike lithium batteries, the number of times of supercapacitor cycle life is not affected by the depth of discharge. The number of cycles can reach millions of times, so it is not necessary to calculate the equivalent cycle life.

### 3. Maintenance cost

$$\text{SC\_ry} = m_c T (f_d P_{d.s} + n_s C_s f_s) \quad (8)$$

where  $m_c$  is the supercapacitor maintenance cost factor.

## 3.2 Objective Function

Hybrid power system configuration optimization involves not only maximizing the economic benefits of the vehicle service cycle, but also considering the space size of the system. Therefore, using  $n_b$  and  $n_c$  as optimization variables, a multi-objective function as shown below is established.

The objective function  $F = \{F_1, F_2\}$ :

$$\begin{cases} F_1 = C_{b\_cost} + C_{sc\_cost} \\ F_2 = a_b n_b v_b + a_s n_s v_s \end{cases} \quad (9)$$

where  $C_{b\_cost}$ ,  $C_{sc\_cost}$  are the life cycle cost of lithium battery and supercapacitor, respectively,  $a_b$ ,  $a_s$  respectively represent the proportional coefficient between monomer and system, while  $v_b$ ,  $v_s$  represent the volume of single lithium battery and supercapacitor module, respectively.

### 3.3 Constraints

In order to meet the requirements of the dynamic and safety of HESS, the following constraints should be satisfied in the system configuration:

- (1) Maximum power constraint: The output power of power system should be able to meet the maximum power demand during train operation.
- (2) Energy constraints: The power system should meet the energy requirements of the full range of trams.
- (3) Power source power constraints: Lithium battery and supercapacitor output power should be within the set range.
- (4) SOC constraint: The SOC of the battery and supercapacitor should be within the setting range; otherwise, it will affect the lifespan of the energy storage system.
- (5) Maximum space constraint: The total volume of lithium batteries and supercapacitors cannot exceed the maximum value of the system.

In summary, the constraint formula is as follows:

$$\left\{ \begin{array}{l} P_{max} \leq \eta_{d1} \eta_b n_b P_b + \eta_{d2} \eta_s n_s P_s \\ E_{max} \leq w_1 \int_0^t P_{re} dt = w_1 (\eta_{d1} \eta_b n_b E_b + \eta_{d2} \eta_s n_s E_s) \\ P_{b\_min} \leq P_b \leq P_{b\_max} \\ P_{s\_min} \leq P_s \leq P_{s\_max} \\ SOC_{b\_min} \leq SOC_b \leq SOC_{b\_max} \\ SOC_{s\_min} \leq SOC_s \leq SOC_{s\_max} \\ V_{max} \geq a_b n_b v_b + a_s n_s v_s \end{array} \right. \quad (10)$$

In equation groups 10,  $P_{max}$  represents the maximum power value of the driving process;  $E_{max}$  represents the energy demand of the tram driving the whole line;  $P_{b\_min}$ ,  $P_{b\_max}$ ,  $P_{s\_min}$ ,  $P_{s\_max}$  respectively represent the upper and lower limits of the output power of the lithium battery and the supercapacitor; other parameters like  $SOC_{b\_min}$ ,  $SOC_{b\_max}$ ,  $SOC_{s\_min}$ ,  $SOC_{s\_max}$  represent the upper and lower limits of

the lithium battery and supercapacitor SOC, respectively;  $V_{\max}$  represents the maximum spatial size of the system;  $w_1$  represents the engineering margin set for the sake of performance and safety reasons.

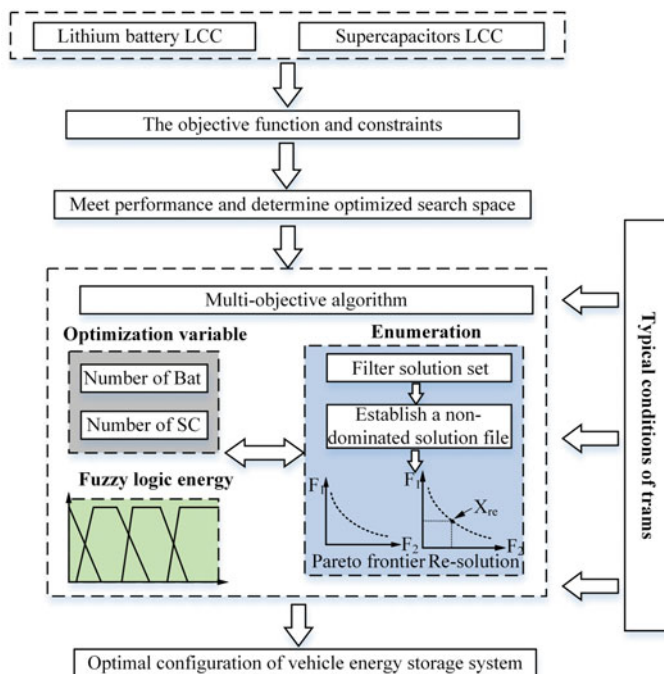
## 4 Multi-objective Model Solving

In this paper, the enumeration method is used to solve the problem. The optimized variables are the number of lithium batteries and supercapacitors, which appear as integers, where each set of solutions needs to meet the constraints above. The specific solution process is shown in Fig. 3.

## 5 Case Analysis

### 5.1 Recommended Configuration Scheme

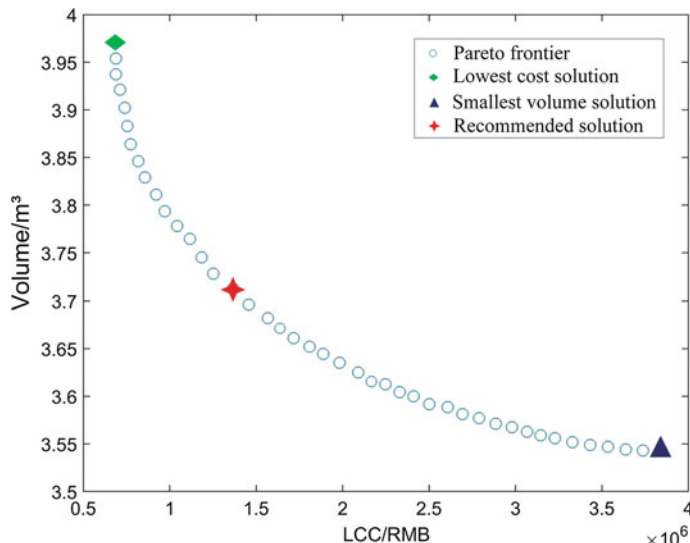
In this paper, the typical working conditions of the hybrid energy storage trolley are simulated. The vital parameters of the simulation platform are shown in Table 4.



**Fig. 3** Specific solution process

**Table 4** Main parameters

Parameter	Numerical value	Parameter	Numerical value
Lithium battery rated voltage	2.4 V	Supercapacitor rated capacity	165 F
Lithium battery rated capacity	26 Ah	Supercapacitor capacity unit price	30,400 yuan/kwh
Lithium battery capacity unit price	3800 yuan/kwh	Supercapacitor volume	0.0145 m <sup>3</sup>
Lithium battery volume	0.00064 m <sup>3</sup>	Engineering margin $w_1$	1.3
Supercapacitor rated voltage	48 V	Vehicle life	20 years

**Fig. 4** Pareto front

According to the solution method in the third section above, the cost-volume Pareto front can be obtained as shown in Fig. 4.

Figure 4 shows three configuration schemes, which are the recommended configuration scheme, the lowest cost configuration scheme, and the configuration with smallest volume; each of the scheme details is shown in Fig. 4 (Table 5).

It can be seen that when the life cycle cost is the lowest, the system volume is the largest. Compared with the system, when volume is the smallest, the life cycle cost is greatly increased. Therefore, the recommended scheme is selected for the next simulation verification.

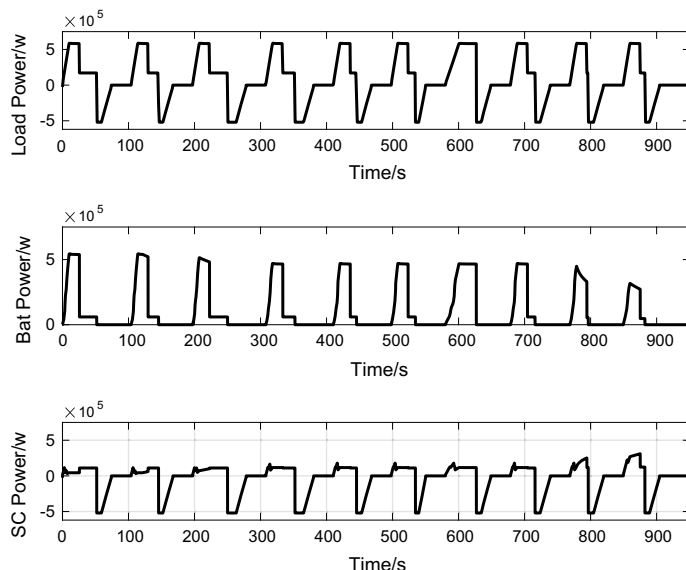
**Table 5** Configuration

Matching scheme	Number of lithium batteries	Number of supercapacitors
Recommended solution	179 series 5 parallel	13 series 7 parallel
Lowest cost plan	203 series 4 parallel	20 series 5 parallel
Minimal solution	178 series 6 parallel	12 series 7 parallel

## 5.2 Running Simulation

In this paper, the fuzzy logic energy management strategy is adopted. According to the above-recommended configuration scheme, the hybrid energy storage type tram is simulated and verified under typical working conditions. To make it clearer, the output power and the actual load power are obtained as shown in Fig. 5. The output voltage, output current, SOC of the lithium battery, and supercapacitor are shown in Figs. 6 and 7.

In Fig. 5, the lithium battery bears the main energy supply task. The supercapacitor has the responsibility of providing peak power and recovering the braking energy. The combinations of these two output powers meet the load demand power. Meanwhile, in Fig. 6 as well as Fig. 7, the voltage, current, and SOC of both lithium battery and the supercapacitor are maintained within a limited interval. The hybrid system configuration solution can meet all design requirements.

**Fig. 5** Load demand power and power source output power

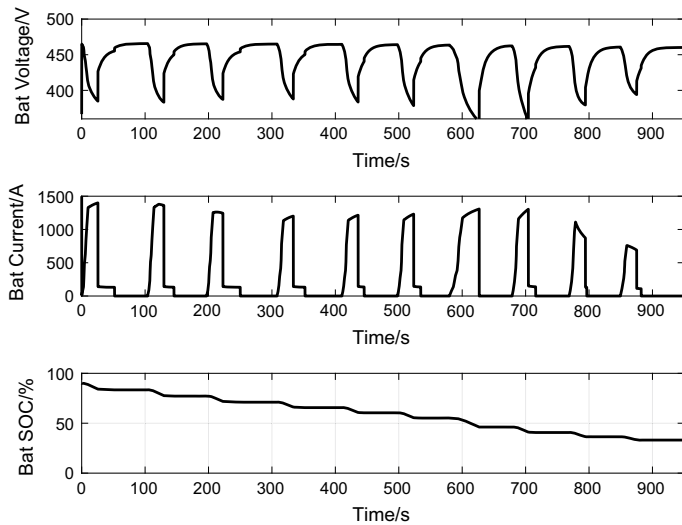


**Fig. 6** Lithium battery output curve

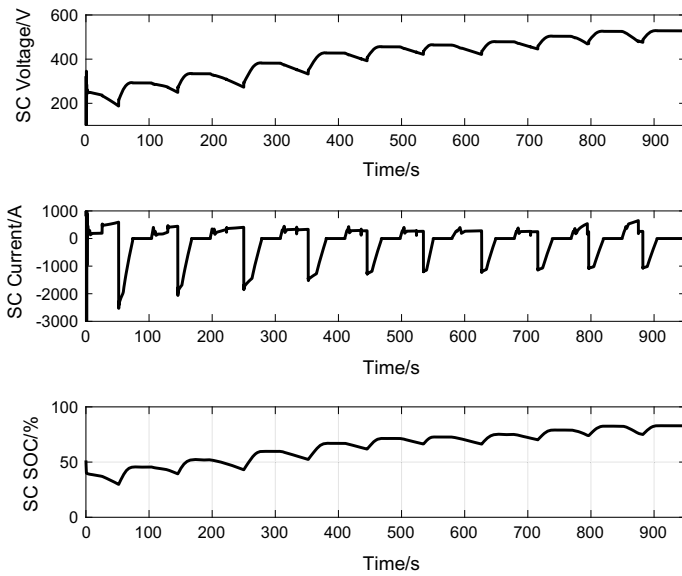


**Fig. 7** Supercapacitor output curve

## 6 Conclusion

In this paper, a multi-objective and multi-constrained optimization model for hybrid electric energy storage vehicle hybrid system configuration is established. The model considers the acquisition cost, replacement cost, and maintenance cost of the energy storage system over the life of the tram. Multiple constraints are related to the operating power, energy, power source parameters, volume, etc. Considering the above constraints, the enumeration method is used to solve the Pareto frontier to describe the non-dominated relationship between the life cycle cost and volume of the energy storage system. It can provide decision-making basis for users. By running simulation, the proposed configuration optimization scheme is verified, which has parametric value for the design of hybrid energy storage tram system.

**Acknowledgements** The authors would like to thank the National Key Research and Development Program of China (2017YFB1201005) as well as the program of CRRC Tangshan Locomotive & Rolling Stock Co. Ltd (R-91802) for their support in this research. Qi An is the corresponding author.

## References

1. Luo X, Wang J, Dooner M et al (2015) Overview of current development in electrical energy storage technologies and the application potential in power system operation. *Appl Energy* 137:511–536
2. Li Q, Chen W, Liu Z et al (2015) Development of energy management system based on a power sharing strategy for a fuel cell-battery-supercapacitor hybrid tramway. *J Power Sour* 279:267–280
3. Herrera V, Milo A, Gaztanaga H et al (2016) Adaptive energy management strategy and optimal sizing applied on a battery-supercapacitor based tramway. *Appl Energy* 169:831–845
4. Wei S, Jiang J, Cheng L et al Optimal sizing model of the energy storage type tramway considering the integration of on-board energy storage and off-board energy supply. *Trans China Electrotechn Soc* 1–10 (in Chinese)
5. Ostadi A, Kazerani M (2015) A comparative analysis of optimal sizing of battery-only, ultracapacitor-only, and battery-ultracapacitor hybrid energy storage systems for a city bus. *IEEE Trans Veh Technol* 64(10):4449–4460
6. Deng T, Lin S, Li Y et al (2015) A multi-objective optimization method for energy management control of hybrid electric vehicles using NSGA-II algorithm. *J Xi'an Jiaotong Univ* 49(10):143–150 (in Chinese)
7. Wei C, Pu Q, Liu Z et al (2016) Power system design for a fuel cell hybrid power tram. *J Southwest Jiaotong Univ* 51(03):430–436 (in Chinese)
8. Lv Y, Yuan H, Liu Y et al (2010) Fuzzy logic based energy management strategy of battery-ultracapacitor composite power supply for HEV. In: First international conference on pervasive computing. IEEE Computer Society
9. Yin H, Zhou W, Li M et al (2016) An Adaptive fuzzy logic based energy management strategy on battery/ultracapacitor hybrid electric vehicles. *IEEE Trans Transp Electrification* 2 (3):300–311
10. Xiang Y, Wei Z, Sun G et al (2015) Life cycle cost based optimal configuration of battery energy storage system in distribution network. *Power Syst Technol* 39

# Review of Energy-Efficient Train Trajectory Optimization and Intelligent Control



Jie Yang, Biao Wang, Limin Jia, and Kuan Zhu

**Abstract** With the increasing attention of the society to the green, security and intelligence, the train trajectory optimization and intelligent control is becoming one of the hot points of research. In this paper, the existed research, recent progress, and research trends of speed profile optimization and train speed tracking control are introduced in this paper. The references cover most well-known institutions, research groups, and researchers in this field. This paper provides a detailed reference for the study and research of the students and researchers in this field to know the relevant history, present situation, and future work.

**Keywords** Energy-saving · Intelligent control · Trajectory optimization · Speed tracking · Rail traffic

## 1 Introduction

Rail transit has the advantages of large volume, fast speed, low energy consumption, low pollution, high safety, punctuality, and other advantages. Rail transit is also gradually becoming more and more important to national economy and the public traffic. At the same time of efficient service, railway consumes a lot of energy. The energy-saving and emission reduction work of rail transit is very important both for economic benefit and for ecological environment protection. Especially, energy-saving trajectory optimization has important academic significance and engineering application value.

---

J. Yang (✉) · B. Wang · L. Jia · K. Zhu

School of Electrical Engineering and Automation, Jiangxi University of Science and Technology, Ganzhou 341000, China

e-mail: [yangjie@jxust.edu.cn](mailto:yangjie@jxust.edu.cn)

L. Jia

School of Electrical Engineering, Beijing Jiaotong University, Beijing 100044, China

State Key Laboratory of Rail Traffic Control and Safety, Beijing Jiaotong University, Beijing, China

The railway also consumes a lot of energy while bringing more and more convenient and efficient services. As of the beginning of 2019, China's national railway energy consumption was converted to 16.224 million tons of standard coal [1]. The energy conservation and emission reduction work of rail transit is very important for both economic benefits and ecological environmental protection. The methods of energy saving and efficiency improvement of railway systems are as follows [2]:

- Reduce the energy consumption of urban rail transit systems through regenerative braking technology, including optimizing train schedules and using on-board energy storage systems.
- Energy-saving driving technology is adopted for the train, including optimizing the speed displacement curve and the train speed tracking controller, and installing the vehicle driving suggestion system.
- Improve train traction drive efficiency, including reducing energy loss in distribution networks, optimizing vehicle traction equipment efficiency and lightweight vehicle body materials.
- Improve the energy saving of the vehicle's environmental control system, including vehicle operation, parking, and environmental protection and energy reduction in the station.
- Energy monitoring management technology for renewable energy generation and intelligent power management.

This paper mainly reviews the speed curve optimization of train energy-saving operation according to the different research methods. Jing et al. [3] reviewed the optimization methods of train energy-saving manipulation according to analytical methods, numerical methods and simulation methods; Gerben et al. [4] reviewed the energy-saving operation control and timetable optimization of trains; Hui et al.

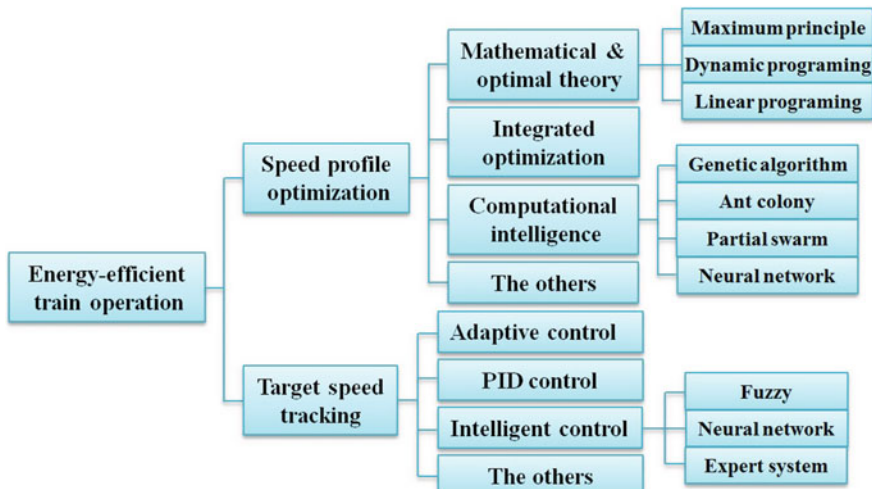


**Fig. 1** Methodology tree of energy-efficient train operation

[5] reviewed the train speed control methods. Methodology tree can be briefly combed as shown in Fig. 1.

## 2 Speed Profile Optimization

### 2.1 Maximum Principle

Mathematical methods based on maximum principle are the most well-studied and most matured methods. Milroy [6] was the first one to research energy-efficient train operation problem and attempt to solve the optimization problem of minimal consumption between two stations in his dissertation. With his result, the South-Australia established Scheduling and Control Group (SCG). The group had the highest theoretical level of the team in currently filed, trained Cheng, Howlett, Pudney, Vu, Albrecht, and other well-known scholars during 30 years of development and heritage. The results are also directly or indirectly adopted in the algorithm design of Energymiser and the other system.

Albrecht et al. [7, 8] used the disturbance analysis to prove the convexity of the local energy function, the uniqueness of the optimal switching point in the steep slope segment, and the uniqueness of the global optimal. Albrecht et al. [9] aimed at tracking the operation for two trains on straight road, discussed how to adjust the interval between existing train timetables in order to achieve both energy efficiency and safety objectives. And they also discussed the mathematical modeling of the train operation, the typical optimal control mode, the existence of the best switching point, the best strategy under the speed limit, etc. (2016) [10].

The principle of maximum is the classical optimization method, with strict mathematical derivation and proof process. However, this kind of method has a strong dependence on the mathematical model, and it is difficult to deal with complex constraints and multi-objective, and the process is complex and difficult to understand, it is harmful for the engineering staff to the popularize the method.

### 2.2 Dynamic Programming

Lu et al. [11] aiming at the energy-saving operation of train, for the energy management problem of diesel EMU train, the dynamic programming algorithm is used to solve the energy optimization configuration of several independent drive systems, and the nonlinear programming online optimization issues. Lu et al. [12, 13] proposed the establishment of distance-based discrete optimization model by using dynamic programming, ant colony algorithm, and genetic algorithm to optimize the target speed curve of the train. And taking in-depth comparison of the optimization results analysis is to point out some new ideas and ideas for research and development in the filed.

Jørgen et al. [14] considered a novel solution method for generating improved train speed profiles with reduced energy consumption. The solution method made use of a time-space graph formulation which could be solved through dynamic programming. Instead of using uniform discretization of time and space as seen previously in the literature, they relied on an event-based decomposition that drastically reduced the search space.

The optimization method based on dynamic programming divides the running task into several sections, and searches for feasible strategies under the constraint condition of speed limit and planned run time. The convergence of this kind of method is uncertain, and the relationship between the optimization effect and the computation time is often balanced.

### **2.3 Mathematical Planning**

Lu et al. [15] aimed at the problem of regenerative use of brake energy for train besides adopting the research of dynamic programming and nonlinear programming methods described in the previous section, applied the Bellman-Ford algorithm and the linear programming algorithm to the optimization problem of train braking curve, and thus, the regenerative braking energy obtained by the optimization algorithm was obviously better than the braking curve of constant deceleration. Lu et al. [16] further proposed a mathematical model suitable for the mixed integer programming algorithm, which can quickly solve the time and position coordinates of the train speed point under the condition of speed monotonic hypothesis.

Su [17, 18] aimed at ATO energy-saving driving strategy, took energy consumption as a constraint to ensure the accuracy of the train station time error under the premise of a set of iterative algorithm, to optimized train speed curve and running schedule by extending the idle distance and reducing traction energy consumption. A numerical algorithm is proposed to reverse the distribution of the given traveling time to different sections, to obtain the optimal controlling sequence, and to reduce the switching mode and the speed fluctuation.

Mathematical program optimizes the target equation, solves secondly, and makes the decision by establishing the mathematical mode of research objects. In addition, in order to obtain the analytical expression of the model, it is often necessary to simplify the complex engineering problems and add the non-convex characteristic of most engineering problems. But such algorithms always cannot guarantee the optimality of the solution.

### 3 Computational Intelligence

#### 3.1 Genetic Algorithm

Jiao and others [19] using multi-population evolutionary algorithm to optimize the train's energy saving. Based on elitism preservation and immigrant strategies, the optimization process is rapidly converged and the stability is enhanced.

Liang and others [20] in order to provide more comprehensive optimization and accurate reference of running curve for automatic train operation system, they adopted the multi-objective optimization strategy of genetic algorithm to optimize from five aspects: speeding (safety), parking accuracy, punctuality, energy consumption, and comfort. In order to increase the convergence speed of genetic algorithm to the optimal solutions, we propose a modified genetic algorithm, which the penalty function method is added into the fitness objective function.

Genetic algorithm does not need accurate mathematical modeling of constraints and optimization objects. The adaptability is strong, but the search is random and easy to fall into local optimum. The optimality cannot be guaranteed. At the same time, in order to ensure the smooth operation of the train and reduce the mechanical and electrical losses of the train, the adjustment of the train handle position must be continuous and infrequent, but the genetic algorithm can not solve this problem well.

#### 3.2 Particle Swarm Algorithm

Cucala and others [21], Domínguez [22] synthetically used the search function of particle swarm optimization and genetic algorithm, as well as fuzzy logic on the target characteristics of a reasonable description, the timetable optimization of high-speed trains and energy-saving driving overall consideration. The fuzzy linear programming is used to model the train timetable optimization and the driver's response, and the genetic algorithm is used to optimize the scheme. Rodriguez, Cucala, and others [23] proposed a method to improve the robustness of ATO systems based on multi-objective particle swarm optimization.

Huang and others [24] used the particle swarm optimization algorithm to optimize the train speed sequence and obtain the satisfactory strategy of energy-saving driving. Optimization task is divided into two stages: the station running time constant energy-saving driving strategy; multi-station total running time constant energy-saving driving strategy. Li Zhuoyue, Ren Xiaoyu, Sun Qisheng, Li Lingyu, and so on using the particle swarm algorithm for similar research work and achieved some results.

Particle swarm algorithm can solve all the problems that can be solved by genetic algorithm in theory and get a better balance in convergence and optimization effect, but the amount of calculation will be great when search precision is high.

### 3.3 Ant Colony Algorithm

Ant colony algorithm is an evolutionary algorithm for finding the optimal path, proposed by Dr. Dorigo in 1992, and gradually gained more and more widely used. Ke and others [25] take the train's running code as a control variable, and the ant colony algorithm is used to search the optimal speed profile of the train. In this paper, Yu [26] proposed a two-stage optimization algorithm for train energy-saving optimization by using the discrete combination optimization model and using the maximum and minimum ant system algorithm. The two-stage optimization algorithm is a comprehensive search with low-density discretization method and then is further optimized by high-density discretization. Dou Wen-wen, Feng Xiaofang, Fan Liqian based on the ant colony algorithm, the paper has carried on the similar research to the energy-saving operation of the train and has made certain achievements.

The ant colony algorithm is similar to the genetic algorithm and the particle swarm algorithm in the optimization effect. In the early optimization of the convergence rate slightly better, but with the advance of the iteration, fine search ability is unsatisfactory.

### 3.4 Neural Network

Artificial neural network is a kind of computing model which imitates the connection method of human brain neurons; it has learning ability. Acikbas and Soylemez [27] proposed a new algorithm for idler optimization based on neural networks and genetic algorithms. Chuang and others [28] used neural networks to design the optimal idling speed and energy-saving optimization method for urban rail trains. Feng et al. [29] based on the analysis of the main factors affecting the traction energy consumption; a prediction model of traction energy consumption based on neural network is proposed.

Neural networks have the characteristics of self-learning. You can build a mapping relationship for objects that cannot be accurately modeled; it usually requires a lot of effective data for training and often used in combination with other algorithms.

## 4 Train Speed Tracking Control

### 4.1 PID Control and Adaptive Control

Liu [30] analyzed rail transportation system of its nonlinear, the clock skew, and external interference. In view of the shortcomings of traditional PID, fuzzy adaptive PID algorithm is used to design the control system, and the tracking control effect of the speed curve is achieved.

Zhang and Xu [31] aimed at the strong coupling, the nonlinear train system model and uncertain characteristics, strategies for the design of adaptive fuzzy sliding mode controller based on the adaptive fuzzy system, approximation model in upper bound of uncertainties and interconnections.

Wang et al. [32] introduced the parameter adaptive mechanism and used the adaptive terminal sliding mode control to train the parking algorithm design to improve the robustness, adaptability, and comfort of the train control system.

PID control has the advantages of simple structure, fast convergence, strong robustness, and so on. However, the timeout setting is relatively difficult to suppress; it is also difficult to apply to time-delay systems and nonlinear systems and it is often used in combination with other algorithms to improve its proper range of dynamic and static characteristics.

## 4.2 Intelligent Control

Yin and Chen [33] design to make full use of the advantages of artificial driving in ATO, with combining expert knowledge and data mining algorithm based on an intelligent train control algorithm. Based on the summary of expert experience, a knowledge base is constructed to ensure safety and comfort in the first step. Then, the regression algorithm and ensemble learning method are used to mine useful information from historical travel data.

Yang et al. [34, 35] studied the vehicle speed tracking control based on MM-FPID (multi-modal FPID) in view of the large lag and nonlinear characteristics of train system. The intelligent control technology system of train operation, such as fuzzy logic and neural network, is discussed and perfected.

Intelligent control is not dependent on accurate mathematical model; it is easy to deal with complex targets which are difficult to be formally described, and some prior knowledge can be set as control rules, and intelligent processing is carried out. However, the amount of computation of intelligent control is often large, and the optimality is not guaranteed.

## 5 Summaries and Expectation

With the stage of overall automation improving in the world's railway industry, the automatic train operation is general trend (the small part of high-speed train and urban rail line have used firstly). However, for the existing line of high-speed railway has more complex line conditions, the performance of existing ATO system cannot achieve the need of automatic driving; intelligent control core algorithm should be proved. The development direction of this field in the future is as follows (limited level or biased, urge your criticism):

- (1) Improve the computational efficient: As stated above, existing algorithms cannot be applied generally largely owing to the improvement of computation speed, optimization effect and adaptability in variety of complex constraints. The work of research in the future needs to further improve the optimization algorithm of speed profile and takes engineering treatment based on existing theories. To ensure computing precision, in order to create conditions of the train online real-time optimization control, the computation of single-speed profile should be optimized or the computation time of dynamical adjusting should within three seconds.
- (2) Successive scarp: Existing algorithms of the optimization effect of successive scarp still have the space to improve. It is hard to find effective solutions based on mathematical methods. Especially, when it comes to over mountain (steep ascent appears immediately after steep descent) or over the valley (steep descent appears immediately after steep ascent), there is not enough non-steep slope to local adjust, which needs to regulate the assignment of whole process. The research work in the future needs to further analyze to enhance algorithm's scope of application, accuracy, robustness, intelligence in this problem.
- (3) Collaborative optimization of train groups: In the actual operation of the train, especially the mixed line of passenger and cargo, a long time to avoid parking is more common, seriously affecting the production efficiency. By the method collaborative optimization of train groups, it could adjust running time of local section with keeping the smooth operation, to make the full use of existing facilities, to decrease or eliminate parking time, to improve operation efficiency and achieving the minimum energy consumption in interval network or even entire network.
- (4) The new ATO system based on artificial intelligence: In one of the most challenging games of intelligence—O, the AlphaGo of Google defeated Lee Sedol and Kejia who are the world's top professional players, has attracted the attention of the world. For control angle, many complex operations and machines have not exceeded the manual manipulation. In terms of train driving, good drivers have accumulated a lot of valuable experience in long-time transport production. In engineering research, these valuable experiences need to be shown by priori knowledges. Meanwhile, it is necessary for us to research a new generation of smart railway system to unite latest practices, such as artificial intelligence, big data, Internet of Things, cloud computing, etc., and make it have the function of comprehensive perception, autonomic learning, self-perfection, and intelligent decision.

**Acknowledgements** The authors would like to thank all reviewers for their help and valuable comments and the contributions of Wenyu He, Chen Huang, Heng Shi and Tianlu Zhang for this paper. This work was supported by the National Key R&D Program of China (Project No. 2017YFB1201105-12).

## References

1. China National Railway Administration Railway Statistics Bulletin (2019) (in Chinese)
2. González-Gil A, Palacin R, Batty P, Powell JP (2014) A systems approach to reduce urban rail energy consumption. *Energy Convers Manag* 80:509–524
3. Jing X, Xin Y, Yihui W, Kunfei L (2014) A survey of optimization methods for train energy saving operation. *J China Railway Soc* 36(04):14–20 (in Chinese)
4. Scheepmaker GM, Goverde RMP, Kroon LG (2017) Review of energy-efficient train control and timetabling. *Eur J Oper Res* 257:355–376
5. Hui Y, Tingya F (2018) A survey of train operation modeling and speed control methods. *J East China Jiaotong Univ* 35(05):1–8 (in Chinese)
6. Milroy IP (1980) Aspect of automatic train control. Loughborough University, Loughborough Leicestershire, UK
7. Albrecht AR, Howlett PG, Pudney PJ, Vu X (2013) Energy-efficient train control: from local convexity to global optimization and uniqueness. *Automatica* 49:3072–3078
8. Albrecht AR, Howlett PG, Pudney PJ, Vu X, Zhou P (2015) Energy-efficient train control: the two-train separation problem on level track. *J Rail Transp Plann Manag* 5:63–182
9. Albrecht A, Howlett P, Pudney P, Vu X, Zhou P (2016) The key principles of optimal train control—part 1: formulation of the model, strategies of optimal type, evolutionary lines, location of optimal switching points. *Transp Res Part B: Methodol* 94:482–508
10. Albrecht A, Howlett P, Pudney P, Vu X, Zhou P (2016) The key principles of optimal train control—Part 2: existence of an optimal strategy, the local energy minimization principle, uniqueness, computational techniques. *Transp Res Part B: Methodol* 94:509–538
11. Lu S, Hillmansen S, Roberts C (2011) A power-management strategy for multiple-unit railroad vehicles. *IEEE Trans Vehic Technol* 60:406–420
12. Lu S (2011) Optimising power management strategies for railway traction systems. Doctor thesis, University of Birmingham, UK
13. Lu S, Hillmansen S, Ho TK, Roberts C (2013) Single-train trajectory optimization. *IEEE Trans Intell Transp Syst* 14:743–750
14. Haahr JT, Pisinger D, Sabbaghian M (2017) A dynamic programming approach for optimizing train speed profiles with speed restrictions and passage points. *Transp Res Part B: Methodol*, vol 99
15. Lu S, Weston P, Hillmansen S, Gooi HB, Roberts C (2014) Increasing the regenerative braking energy for railway vehicles. *IEEE Trans Intell Transp Syst* 15:2506–2515
16. Lu S, Ming Q, Paul W, Chen S, Yang J (2016) Partial train speed trajectory optimization using mixed integer linear programming. *IEEE Trans Intell Transp Syst* 10:2911–2920
17. Su S, Li X, Tang T, Gao Z (2013) A subway train timetable optimization approach based on energy-efficient operation strategy. *IEEE Trans Intell Transp Syst* 14:883–893
18. Su S, Tang T, Chen L, Liu B (2015) Energy-efficient train control in urban rail transit systems. *Proc Inst Mech Eng Part F: J Rail Rapid Transit* 229:446–454
19. Jiao Y, Liu S, Huang H, Ma X, Liu S (2016) Energy-saving operation optimization of middle-low-speed Maglev train based on genetic algorithm. In: 12th World Congress on Intelligent Control and Automation (WCICA), Guilin, pp 1803–1807
20. Liang Y, Liu H, Qian C, Wang G (2019) A modified genetic algorithm for multi-objective optimization on running curve of automatic train operation system using penalty function method. *Int J Intell Transp Syst Res* 17(1):74–87
21. Cucala AP, Fernández A, Sicre C, Domínguez M (2012) Fuzzy optimal schedule of high speed train operation to minimize energy consumption with uncertain delays and driver's behavioral response. *Eng Appl Artif Intell* 25:1548–1557
22. Domínguez M, Fernández A, Cucala A, Pecharromán R (2012) Energy savings in metropolitan railway substations through regenerative energy recovery and optimal design of ATO speed profiles. *IEEE Trans Autom Sci Eng* 9:496–504

23. Fernández-Rodríguez A, Fernández-Cardador A, Cucala AP, Domínguez M, Gonsalves T (2015) Design of robust and energy-efficient ATO speed profiles of metropolitan lines considering train load variations and delays. *IEEE Trans Intell Transp Syst* 16:061–2071
24. Huang YN, Shao-feng GONG, Yuan CAO (2016) Optimization model of energy-efficient driving for train in urban rail transit based on particle swarm algorithm. *Journal of Transportation Systems Engineering and Information Technology* 16:118–124 and 142(2016)
25. Ke BR, Lin CL, Yang CC (2012) Optimisation of train energy-efficient operation for mass rapid transit systems. *IET Intell Transp Syst* 6:58–66
26. YU X (2012) Energy—saving optimization and energy evaluation of train in urban rail transit. Beijing Jiaotong University, Beijing (in Chinese)
27. Açıkbas S, Soylemez MT (2008) Coasting point optimisation for mass rail transit lines using artificial neural networks and genetic algorithms. *IET Electr Power Appl* 2:172–182
28. Chuang HJ, Chen CS, Lin CH, Hsieh CH, Ho CY (2009) Design of optimal coasting speed for MRT systems using ANN models. *IEEE Trans Ind Appl* 45:2090–2097
29. Feng J (2014) Train behavior optimization of urban rail transit system considering energy saving. Beijing Jiaotong University, Beijing (in Chinese)
30. Liu Y (2013) Optimized research of ATO based on fuzzy self-adaptive PID. *Electron Meas Technol*
31. Zhang M, Xu H, Zhang Y (2015) Automatic stop method for high speed train based on adaptive fuzzy sliding mode control. *Inf Control* 44:223–229 (in Chinese)
32. Wang Q, Wu P, Feng X, Zhang Y (2016) Precise automatic train stop control algorithm based on adaptive terminal sliding mode control 38:56–63
33. Yin J, Chen D, Li Y (2016) Smart train operation algorithms based on expert knowledge and ensemble CART for the electric locomotive. *Knowl-Based Syst* 92:78–91
34. Yang J, Jia L, Fu Y, Luo Y (2016) Energy-efficient freight train operation-part II: combined control of speed tracking 38:23–31
35. Yang J, Jia L, Lu S, Fu Y, Ge J (2016) Energy-efficient speed profile approximation: an optimal switching region-based approach with adaptive resolution. *Energies* 9:762

# Influence Analysis on the CRH2 EMUs Vehicle Bodies Voltage Fluctuation Considering Isolated Rail Joint Discharge



Ying Lu, Ying Wang, Yanlong Shen, Xiaoqiang Chen  
and Yanming Lu

**Abstract** In this paper, the voltage fluctuation issue of the train body caused by the discharge phenomenon between the wheel-set and rail when the CRH2 electric multiple units (EMUs) runs through the rail insulation section is studied. Firstly, the working grounding and protection grounding systems of CRH2 EMUs are introduced, and then, we established the equivalent model of CRH2 EMUs grounding system and confirmed its parameters. Meanwhile, insulating section discharge model is also established. Secondly, the simulation results show all the car body voltages as wheel-rail discharge phenomenon occurs, and we analyze CRH2 EMUs grounding system structure itself. Finally, we come to the conclusion that the change of value of the grounding resistor shall make CRH2 EMUs train body electric potential difference at the time of isolated rail joint discharge phenomenon lower than before.

**Keywords** Electric multiple units (EMUs) · Isolation rail joint discharge · Train body voltage · Grounding optimization

## 1 Introduction

With the rapid development of high-speed railways, the safe and stable operation of electric multiple units (EMUs) has received much attention. The EMUs frequently pass through the insulated rail joints; especially, when passing through the side line traction reflux cutoff point, the insulating joint is prone to arc phenomenon and carbonized burning loss of insulation. In several cases, the surface of the rail may have obvious potholes [1]. This will cause the electric potential fluctuation of the

---

Y. Lu · Y. Wang (✉) · Y. Shen · X. Chen · Y. Lu

School of Automation and Electrical Engineering, Rail Transit Electrical Automation Engineering Laboratory of Gansu Province, Lanzhou Jiaotong University, No. 88 West Anning Road, Lanzhou, China  
e-mail: [wangying01@mail.lzjtu.cn](mailto:wangying01@mail.lzjtu.cn)

EMUs and the uneven distribution of the electric potential of each segment [2]. It is unfavorable for the safe and stable operation of the EMUs.

To solve the above problems, the relationship between the body potential of EMU and rail potential was studied [3]. The vehicle body voltage distribution parameter model is established, its impedance characteristics are analyzed and the stray flow characteristics of the rail are discussed based on the finite element model [4]. The main reasons affecting rail potential were studied [5]. The reasons for the increase in the difference between the vehicle body and the track potential were analyzed based on the special grounding mode of specific models [6]. It was found that the overvoltage of the vehicle body was mainly caused by inadequate grounding technology setting, and based on this, an optimization scheme for the protection grounding of the EMU was designed [7]. The causes of appearing train body overvoltage about Japanese AC locomotive were analyzed in [8]. And combining with experiment, improved methods were discussed to avoid extreme overvoltage phenomenon. PSpice was used to establish a simulation model of overvoltage of the vehicle body when lightning strikes the contact network, and the influence of the grounding resistance parameters on the overvoltage of the vehicle body was analyzed quantitatively in [9]. CRH380BL EMU as an example to study the effect of electrical coupling on overvoltage and grounding circulation of the car body was analyzed in [10].

In conclusion, the systematic analysis of the effect of rail insulation section arc and its potential on the body of the EMU is not enough. This paper studies the changes of body potential caused by discharge phenomena between wheel-sets and rails of CRH2 EMUs. It is obtained that the body potential difference can be significantly reduced by changing the resistance of the original ground resistor when the isolated rail joint discharge occurs and analyzes the overvoltage distribution characteristics of the vehicle body caused by the rail insulation section arc.

## 2 Equivalent Modeling

China CRH2 EMUs adopt the method of grouping 8 vehicles, among which the vehicle bodies 2, 3, 6 and 7 are bullet trains, and the rest are trailers (motor vehicles are represented by MC, and trailers are represented by TP). It can be divided into 2 power units. Two traction transformers are placed on vehicles no. 2 and no. 6, respectively. No. 2, 3, 6 and 7 bullet trains are equipped with traction converter and traction motor, which are used to provide traction power for the EMUs. The pantograph is mounted on the top of vehicle body no. 4 and vehicle body no. 6, and the pantograph on the top of vehicle body no. 4 is the spare pantograph, as shown in Fig. 1. There are two main kinds of train body ground methods, i.e., working ground and protection ground. Ground layout of reconnected CRH3 train body is depicted in Fig. 1.

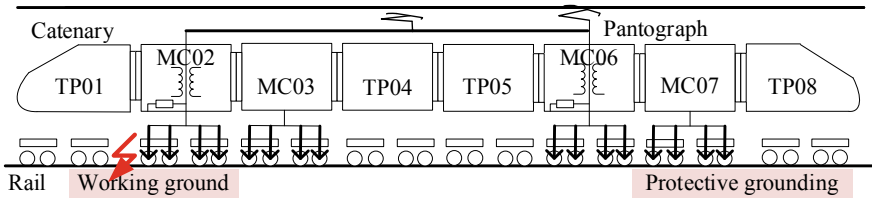


**Fig. 1** EMUs grounding diagram

## 2.1 CRH2 EMUs Vehicle Body Modeling

CRH2 EMUs adopt multi-point simultaneous grounding to disperse the traction backflow into the earth, so as to reduce the current flowing through the grounding carbon brush and avoid excessive loss of the carbon brush. Each vehicle body is equipped with a grounding resistor, which is connected to the bearing ground ring. Such a structure enables the grounding resistor to prevent the current from flowing into the vehicle body, so that there is no circulation in the vehicle body.

In Fig. 2, the model mainly includes the high-voltage cable model, the vehicle body impedance model, the EMUs working grounding model, the protection grounding impedance model and the rail impedance model. Figure 2 shows the equivalent circuit model of the vehicle body reflux system of EMUs under normal conditions. The AC voltage source represents the traction substation. Since the high-voltage cable above the EMUs has a shielding layer, the traction current is normally shielded and its coupling effect on the vehicle body is very small, so the high-voltage cable can be equivalent to the transmission wire.  $T_1$  and  $T_2$ , respectively, represent the onboard traction transformer on vehicle no. 2 and vehicle no. 6, and  $R_1$  and  $R_2$ , respectively represent the equivalent resistance on the secondary side of the onboard traction transformer.  $R_{c2.2}$ ,  $R_{c2.3}$ ,  $R_{c3.1}$ ,  $R_{c3.2}$ ,  $R_{c3.3}$ ,  $R_{c6.1}$ ,  $R_{c6.2}$ ,  $R_{c6.3}$ ,  $R_{c7.1}$  and  $R_{c7.2}$ , respectively, represent the equivalent

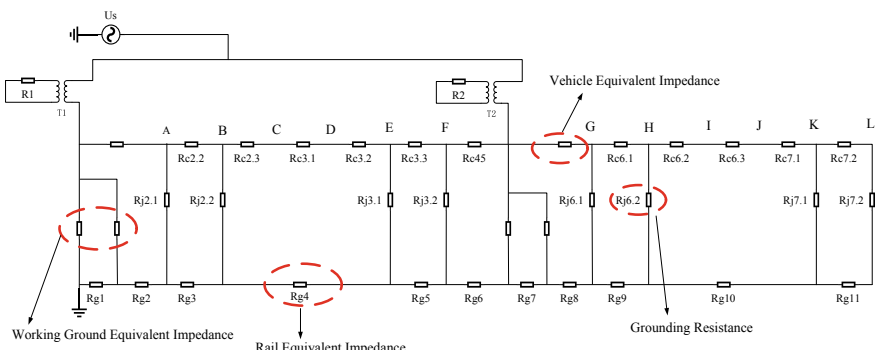


**Fig. 2** Equivalent circuit model of vehicle body system

impedance of vehicle body no. 2, 3, 6 and 7.  $R_{c45}$  refers to the sum of the impedances of vehicle body no. 4 and vehicle body no. 5 and the impedances between their bodies.  $R_{j2.1}$ ,  $R_{j2.2}$ ,  $R_{j3.1}$ ,  $R_{j3.2}$ ,  $R_{j6.1}$ ,  $R_{j6.2}$ ,  $R_{j7.1}$  and  $R_{j7.2}$ , respectively, are the grounding resistors of vehicle no. 2, 3, 6 and 7.

## 2.2 Determination of Model Parameters

In the equivalent model, the traction substation is represented by an equivalent power frequency of 27.5 kV single-phase AC power supply. Since the grounding device is installed in the vehicle body of no. 2–7, the model of these six vehicle bodies is detailed. According to the position of bogie in each vehicle body, each vehicle body is divided into three sections. The length of each bar is 8.33 m, and single body impedance  $R_c$  is 0.047  $\Omega$ . Grounding system impedance  $R_j$  is 0.05  $\Omega$ . The impedance of the 4th and 5th vehicles and the sum of the impedances between the vehicles  $R_{c45}$  are 0.124  $\Omega$ . The electrical resistance of the steel rail is about 0.2  $\Omega/km$ , and EMU single section body length is 26.5 m, so  $R_{g3} = R_{g4} = R_{g5} = R_{g9} = R_{g10} = R_{g11} = 0.005 \Omega$ ,  $R_{g1} = R_{g2} = R_{g7} = R_{g8} = 0.001 \Omega$ ,  $R_{g6} = 0.01 \Omega$ . There are 12 voltage measuring points A~L in the specific model, as shown in Fig. 2, and the corresponding model parameters are depicted in Table 1.

## 2.3 Isolated Rail Joint Arc Discharge Modeling

According to the energy balance of arc column in (1), an isolated rail joint arc discharge model is established, and the differential equation of arc conductance  $g$  is used to describe the arc in air:

**Table 1** Specific electrical parameters of the equivalent model

Parameter	Value	Parameter	Value
$U_s$	27,500 V	$R_{c2.3}$	15.667e-3 $\Omega$
$R_{j2.1}$	0.05 $\Omega$	$R_{c3.1}$	0.03 $\Omega$
$R_{j2.2}$	0.05 $\Omega$	$R_{c3.2}$	15.667e-3 $\Omega$
$R_{g3.1}$	0.05 $\Omega$	$R_{c3.3}$	15.667e-3 $\Omega$
$R_{g3.2}$	0.05 $\Omega$	$R_{c45}$	0.124 $\Omega$
$R_{g6.1}$	0.05 $\Omega$	$R_{c6.1}$	15.667e-3 $\Omega$
$R_{g6.2}$	0.05 $\Omega$	$R_{c6.2}$	15.667e-3 $\Omega$
$R_{g7.1}$	0.05 $\Omega$	$R_{c6.3}$	0.03 $\Omega$
$R_{g7.2}$	0.05 $\Omega$	$R_{c7.1}$	15.667e-3 $\Omega$
$R_{c2.2}$	15.667e-3 $\Omega$	$R_{c7.2}$	15.667e-3 $\Omega$

$$\frac{dg}{dt} = \frac{1}{\tau}(G - g) \quad (1)$$

where  $\tau$  is the arc time constant,  $g$  is instantaneous arc conductance,  $G$  is stationary arc conductance, and it is defined as:

$$G = \frac{|i_{\text{arc}}|}{u_{\text{st}}} \quad (2)$$

where  $i_{\text{arc}}$  is instantaneous arc current,  $u_{\text{st}}$  is stationary arc voltage,  $u_0$  is characteristic arc voltage,  $r_0$  is characteristic arc resistance, and  $u_{\text{st}} = u_0 + r_0 \cdot |i_{\text{arc}}|$ .

Meanwhile, parameters  $u_0$  and  $r_0$  are related to arc length  $l_{\text{arc}}$ , which can be calculated by the formula obtained from arc measurement:

$$u_0 = 0.9 \frac{kV}{m} \cdot l_{\text{arc}} + 0.4 \text{ kV} \quad (3)$$

$$r_0 = 40 \frac{m\Omega}{m} \cdot l_{\text{arc}} + 8 \text{ m}\Omega \quad (4)$$

The arc current  $i_{\text{arc}}$  can be expressed as follows

$$i_{\text{arc}} = \frac{g \cdot v_{\text{th}}}{1 + g \cdot r_{\text{th}}} \quad (5)$$

The above differential equation is solved using Laplace transform to obtain  $g$ :

$$g(s) = \frac{1}{1 + \tau \cdot s} \cdot G(s) \quad (6)$$

The voltage across the arc  $v_{\text{guess}}$  is estimated. Using this value, an estimated isolated rail joint arc current is calculated:

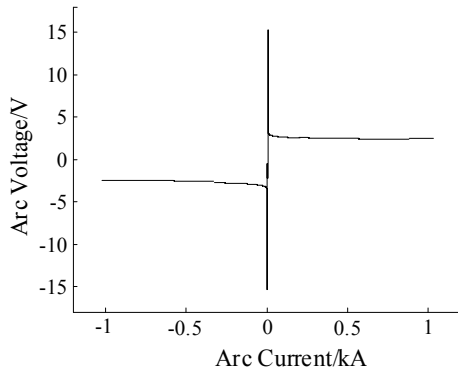
$$i_{\text{arc}} = g \cdot v_{\text{guess}} \quad (7)$$

Figure 3 is a simulation of the model built by the above formula. It can be seen that the volt–ampere characteristics of the volt–ampere characteristic and the general AC arc are similar.

### 3 Analysis of Vehicle Body Voltage

By introducing the rail arc model into the above equivalent circuit model, we can obtain the voltage value of each test point when the arc is ignited at different rail insulation joints. The voltage values of each measuring point when the EMUs

**Fig. 3** Simulated arc volt–ampere characteristic curve



normal run, inter-rail discharge between vehicle body no. 2 and vehicle body no. 3, discharge in the working ground of vehicle body no. 2, discharge in the protective ground of vehicle body no. 2, inter-rail discharge between vehicle body no. 4 and vehicle body no. 5 can be, respectively, obtained by simulation calculations.

Figure 4 shows the voltages of 12 voltage measurement bits  $A \sim L$  under the above-mentioned working conditions. We can see that when the train passes through the rail insulation section normally, the maximum potential of the car body is always kept less than 0.5 V. When the train passes through the insulation section of the rail and discharges, the results of discharges between different wheel-sets are different. When the arc discharge occurs at the rail insulation joint between no. 2 and no. 3, the vehicle body no. 3 voltage increases to 1.5 V. When the discharge occurs in the working ground of no. 2, the voltage of all vehicle bodies increases by about 1.5 V compared with the normal operation. When the discharge occurs between the protection ground of no. 2, the voltage of each vehicle body also increases, but the increase in amplitude is not large. When the discharge occurred at the rail insulation joint between no. 4 and no. 5, the vehicle body voltage surged to 3.3 V. It can be found that when the train is discharged through the insulation

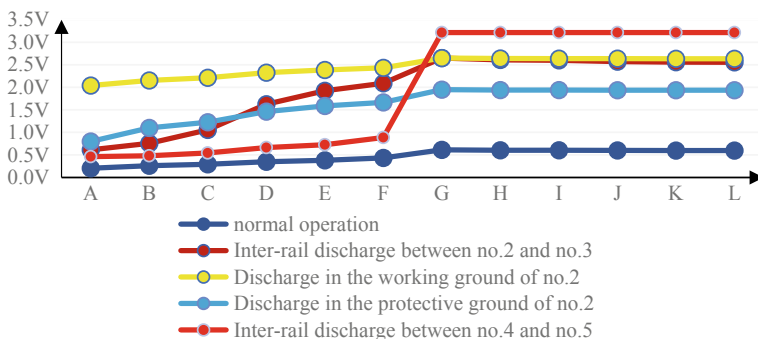


**Fig. 4** Each test point potential under different working conditions before suppression measure

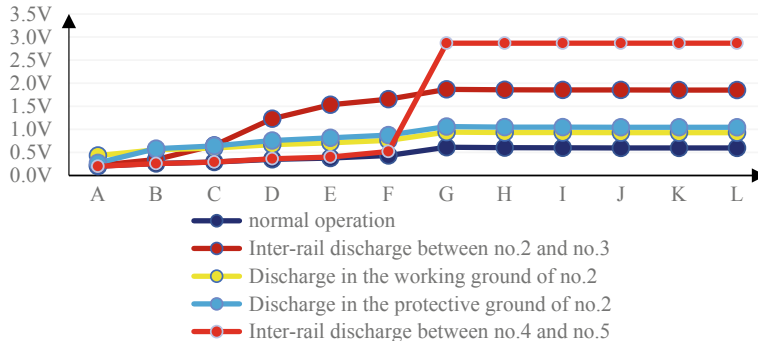


**Fig. 5** Each test point potential under different working conditions after suppression measure

section, the potential of the vehicle body will rise. The increase of the potential difference will cause electric corrosion to the CRH EMUs bearing, so it is very necessary to reduce the vehicle body potential difference.

In Fig. 5, considering the influence of the grounding resistor on the vehicle body voltage, the CRH2 EMUs vehicle body voltage is reduced by changing the value of the grounding resistor. We can change the value of grounding resistor to  $0.01 \Omega$ . When the CRH2 EMUs pass through the insulation section normally, the highest potential of the vehicle body is always kept below 0.5 V. When the arc discharge occurs between no. 2 and no. 3, the body voltage of the no. 3 increases to 1.2 V. When the arc discharge occurs in the working ground of no. 2, the train body voltage rises to about 1 V, and when the arc discharge occurs on the rail between no. 4 and no. 5, the vehicle body voltage remains below 3 V.

By comparing the influence of changing the value of the grounding resistor on the voltage of each vehicle body, it can be seen that the potential difference decreases greatly. Therefore, changing the value of the grounding resistor has a good inhibitory effect on the voltage of the vehicle body.

## 4 Conclusions

In this paper, the phenomenon of arcing discharge and the sudden change of vehicle body electric potential that may occur in the rail insulation joint of CRH2 EMUs are mainly addressed. PSCAD software is used to simulate and calculate the distribution of vehicle body voltage when discharge occurs at different positions, and the corresponding optimization measures are proposed from the perspective of changing the resistance value of grounding resistor. The following conclusions are drawn:

- When the isolated rail joint arc discharge occurs between no. 4 and no. 5, the overall voltage of the latter power unit rises greatly, and the potential of each test point on it is similar.
- Aiming at the CRH2 EMUs, the voltage of the first power unit is higher than that of the second power unit, regardless of whether or not discharge occurs and where it occurs.
- Changing the resistance value of the grounding resistor has an obvious suppression effect on two of the four discharge conditions, but the inhibitory effect is not obvious for the remaining two conditions.

**Acknowledgements** This work was supported by the Natural Science Foundation of Gansu Province Science and Technology Department (18JR3RA111), the National Natural Science Foundation of China (51767013), the Science and Technology Research and Development Plan of China Railway Corporation (2017J012-A), the Natural Science Foundation of Gansu Province Education Department (2017A-020) and the Program for Excellent Team of Scientific Research in Lanzhou Jiaotong University (201701).

## References

1. Ying W, Zhigang L, Xiuqing M et al (2016) An extended Habedank's equation-based EMTP model of pantograph arcing considering pantograph-catenary interactions and train speeds. *IEEE Trans Power Delivery* 31(3):1186–1194
2. Ying W, Fengyang G, Xiuqing M et al (2017) Analysis of EMUs vehicle body voltage caused by pantograph-catenary off-line arc. EITRT 2017, Lecture Notes in Electrical Engineering, 20–22 October, Changsha, China
3. Ahmad A, Thomas D WP, Christopoulos C et al (2008) Effects of homogenous soil characteristics to the transient responses of a single long horizontal ground conductor mod-el. Power and Energy Conference, 2008. PECon 2008. IEEE 2nd International. IEEE, pp 367–371
4. Hill RJ, Carpenter DC (1991) Determination of rail internal impedance for electric railway traction system simulation. In: IEE proceedings B-electric power applications, vol 138, no 6. IET Digital Library, pp 311–321
5. Dong WJ (2009) Research on integrated grounding system of high-speed passenger dedicated line. Master's thesis of southwest Jiaotong university (in Chinese)
6. Yin YH (2013) Fault analysis and solution of shaft temperature sensor for CRH380BL EMU 1:33–36 (in Chinese)
7. Li XJ, Wang JG, Wu HB et al (2013) Optimization research of the earthing design for CRH380BL EMU. *Electr Locomot Mass Transit Veh* 36(5):19–26 (in Chinese)
8. Hatsukade S (2009) Reduction method of surge voltage on AC railcar body. *Q Rep RTRI* 50 (2):70–75
9. Baojiang C, Yue Z, Guoqiang G et al (2018) Analysis and repressive methods of high-speed EMU carriage overvoltage caused by lightning strike on catenary. *J China Railw Soc* 40 (6):44–49 (in Chinese)
10. Ye C, Zhigang L, Ke H et al (2018) Study on electrical coupling effect of traction network loop circuit on vehicle body earth loop circuit of electric multiple unit based on ATP-EMTP. *J China Railw Soc* 40(4):43–51 (in Chinese)

# Hydrogen Consumption Minimization for Fuel Cell Trains Based on Speed Trajectory Optimization



Zheng Huang, Chaoxian Wu, Shaofeng Lu and Fei Xue

**Abstract** To make rail transport much greener, the fuel cell system has been applied in some train vehicles. The paper is aimed at establishing an integrated mixed-integer linear programming (MILP) model to optimize operations of the trains with the fuel cell system. Train motion analysis and physical constraints setup are given to illustrate the model. The main power-efficiency characteristic of the fuel cell system is also modeled in the research. The optimal train speed trajectory is obtained by applying the proposed approach, where the hydrogen consumption of the fuel cell is minimized. To prove the robustness of the model, the power profiles of scenarios with normal and extreme power-efficiency characteristics are compared, and the results show influences of these characteristics on the train operations.

**Keywords** Fuel cell · Power-efficiency characteristic · Train speed trajectory optimization · Hydrogen consumption minimization

---

Z. Huang · C. Wu · S. Lu (✉) · F. Xue

Department of Electrical and Electronic Engineering,  
Xi'an Jiaotong-Liverpool University, Suzhou 215123, China  
e-mail: [Shaofeng.Lu@xjtu.edu.cn](mailto:Shaofeng.Lu@xjtu.edu.cn)

Z. Huang

e-mail: [Zheng.Huang15@student.xjtu.edu.cn](mailto:Zheng.Huang15@student.xjtu.edu.cn)

C. Wu

e-mail: [Chaoxian.Wu@xjtu.edu.cn](mailto:Chaoxian.Wu@xjtu.edu.cn)

F. Xue

e-mail: [Fei.Xue@xjtu.edu.cn](mailto:Fei.Xue@xjtu.edu.cn)

Z. Huang · C. Wu

Department of Electrical Engineering and Electronics, University of Liverpool,  
Liverpool L69 3BX, UK

## 1 Introduction

Air pollution is steadily aggravated as the growing vehicle fleet. It is reported that the transport sector compromised 24.7% of global CO<sub>2</sub> emissions from fuel combustion in 2015 [1]. Hydrogen fuel cells, for its pollution-free characteristic, are regarded as a promising power source of trains.

Many types of studies have been done to improve the fuel economy of fuel cell hybrid electric vehicles (FCHEVs). Fletcher et al. [2] uses stochastic dynamic programming (SDP) controller to minimize the total running cost of the fuel cell both considering fuel consumption and degradation. In [3], the equivalent consumption minimum strategy for FCHEV powered by the fuel cell, battery, and supercapacitor is derived based on sequential quadratic programming (SQP). A comprehensive model of a generic FCHV architecture and a specification independent control strategy is developed and integrated with the optimization algorithm to find optimal control strategy [4]. Other research such as [5] investigates the effects that hydrocarbon instead of hydrogen will bring, and [6] provides a critical analysis of the fuel cell membrane material.

Optimization on train speed trajectory is a traditional way to save traction energy, and it is usually achieved through seeking optimal speed profile. The optimal train speed trajectory can be found by maximum principle based on optimal control theory [7–9]. The solution can be obtained through numerical algorithm by determining the cruising regimes and connecting two consecutive constant speed regimes with traction, coasting, or braking operation. Mathematical programming is also used to find the optimal speed profile, and [10] proposes a speed-based model to optimize the partial speed trajectory during speed-varying processes such as accelerations and decelerations for recovering more regenerative energy. The work is extended in [11], and it proposes a distance-based model which replaces the speed with the energy.

As shown above, the fuel cell system is one type of emerging technologies applied in the railway system, while the research on the integrated operation of both the fuel cell and train operations is still rare in this area. However, without changing any existed infrastructure, better speed trajectory can help reduce the hydrogen consumption for fuel cell trains. As such, the main contribution of this paper is that an integrated mathematical model for the fuel cell trains without battery is established, which can minimize the hydrogen consumption through locating the optimal speed trajectory.

## 2 Methodology

This section will introduce the formulation of the distance-based speed trajectory optimization problem based on mixed-integer linear programming (MILP), which owns advantages in high extendibility as proposed in [11, 12], as well as the modeling of fuel cell system characteristic.

## 2.1 Train Motion Analysis and Physical Constraints Setup

In the distance-based model, the track length of a single inter-station journey is discretized into several distance segments. Provided that the entire track length is  $D$ , and it can be divided into  $N$  segments with the value of  $\Delta d_i$  respectively, the expression is shown in (1).

$$D = \sum_{i=1}^N \Delta d_i \quad (1)$$

The elapsed time  $\Delta t_i$  for each  $\Delta d_i$  can be calculated by (2), where  $v_{i,\text{ave}}$  denotes the average speed in  $i$ th segment. Total journey time  $T$  is the summation of  $\Delta t_i$ , as expressed in (3).

$$\Delta t_i = \frac{\Delta d_i}{v_{i,\text{ave}}} \quad (2)$$

$$T = \sum_{i=1}^N \Delta t_i \quad (3)$$

For  $N$  distance segments, there are  $N+1$  speed points  $v_i$  where  $i = 1, 2, 3 \dots N+1$ . The train is assumed to do uniformly accelerated or decelerated motion between two adjacent speed points  $v_i$  and  $v_{i+1}$ ; thus, we have

$$a_i = \frac{v_{i+1}^2 - v_i^2}{2\Delta d} \quad (4)$$

where  $a_i$  is the acceleration or deceleration in each distance segment. The precision of the model can be guaranteed if there are sufficiently small distance segments.

The maximum acceleration  $\overline{a_a}$  and deceleration rate  $-\overline{a_d}$  of the train limits  $a_i$  as in (5).

$$-\overline{a_d} \leq a_i \leq \overline{a_a} \quad (5)$$

The average drag force applied to the train can be derived by (6), where  $A$ ,  $B$ , and  $C$  are the Davis coefficients.

$$F_{i,\text{drag}} = A + Bv_{i,\text{ave}} + Cv_{i,\text{ave}}^2 \quad (6)$$

In each distance segment, the train consumes the traction energy  $E_i$ , which then experiences the motor efficiency  $\eta_t$  and is transferred into the internal energy, the potential energy, and the kinetic energy, as shown in (7).

$$E_i \eta_t - F_{i,\text{drag}} \Delta d - Mg \Delta h_i - \frac{1}{2} M (v_{i+1}^2 - v_i^2) \geq 0 \quad (7)$$

where  $M$  is the total mass of the train,  $g$  is the local gravity acceleration, and  $\Delta h_i$  is the altitude change in the segment.

Both the maximum traction effort  $F_m$  and maximum traction power  $P_{\max}$  of the motor limit the traction energy consumed within a single segment, as in (8) and (9).

$$0 \leq E_i \leq \frac{1}{\eta_t} F_{\max} \Delta d_i \quad (8)$$

$$0 \leq E_i \leq P_{\max} \frac{\Delta d_i}{v_{i,\text{ave}} \eta_t} \quad (9)$$

## 2.2 Linearization of the Speed-Related Constraints

Piecewise linear (PWL) can represent a nonlinear function with a number of nonnegative variables called special-ordered set type 2 (SOS2), among which only two adjacent ones can be greater than 0 and the total sum of all variables equal to 1 [13]. In order to linearize the nonlinear constraints in (2), (6), and (9), a series of ascending key speed points  $V_1, V_2, \dots, V_K$  are selected to represent any speed within the range from  $V_1$  to  $V_K$ . Hence, the decision variables  $v_i^2$  can be expressed by (10). The approximation of the speed  $v'_i$  and the average speed  $v'_{i,\text{ave}}$  can be obtained by (11) and (12). We can further approximate  $\frac{1}{v'_{i,\text{ave}}}$  and  $v'^2_{i,\text{ave}}$  as in (13) and (14).

$$v_i^2 = \sum_{k=1}^K V_k^2 \cdot \alpha_{i,k} \quad (10)$$

$$v'_i = \sum_{k=1}^K V_k \cdot \alpha_{i,k} \quad (11)$$

$$v'_{i,\text{ave}} = \frac{v'_i + v'_{i+1}}{2} = \sum_{k=1}^K V_k \cdot \beta_{i,k} \quad (12)$$

$$\frac{1}{v'_{i,\text{ave}}} = \sum_{k=1}^K \frac{1}{V_k} \cdot \beta_{i,k} \quad (13)$$

$$v_{i,\text{ave}}^2 = \sum_{k=1}^K V_k^2 \cdot \beta_{i,k} \quad (14)$$

where  $\alpha_{i,k}$  and  $\beta_{i,k}$  are variables of two sets of SOS2 in each distance segment.

## 2.3 Modeling of Fuel Cell System Characteristic

This paper uses the power-efficiency characteristic to model the fuel cell system. The solid blue line in Fig. 1 represents the actual fuel cell power-efficiency characteristic [14]. In order to adapt this power-efficiency characteristic to the current linear model, the actual curve is linearized to three sections as illustrated in Fig. 1. To distinguish different sections, the logical variables are introduced; thus, in each distance segment, the efficiency of the fuel cell  $\eta_i$  can be formulated by (15).

$$\eta_i = \begin{cases} f_1\left(\frac{P_i}{P_f}\right) & \text{for } \left[0 \leq \frac{P_i}{P_f} < 0.1\right] \Leftrightarrow [\lambda_i = 1] \\ f_2\left(\frac{P_i}{P_f}\right) & \text{for } \left[0.1 \leq \frac{P_i}{P_f} < 0.5\right] \Leftrightarrow [\mu_i = 1] \\ f_3\left(\frac{P_i}{P_f}\right) & \text{for } \left[0.5 \leq \frac{P_i}{P_f} \leq 1\right] \Leftrightarrow [v_i = 1] \end{cases} \quad (15)$$

$$\lambda_i + \mu_i + v_i = 1 \quad (16)$$

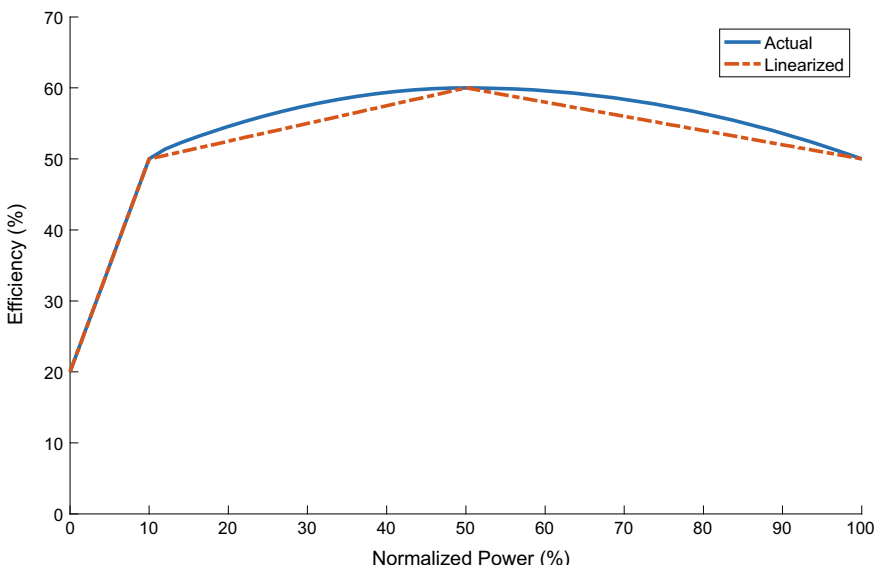


**Fig. 1** Fuel cell system normalized power versus efficiency

$$\lambda_i, \mu_i, v_i \in \{0, 1\} \quad (17)$$

where  $\lambda_i$ ,  $\mu_i$ , and  $v_i$  are the logic variables,  $f_1$ ,  $f_2$ , and  $f_3$  represent the functions of three linearized sections,  $P_i$  is the power of the fuel cell system in each distance segment, and  $P_f$  denotes the maximum fuel cell power.

To coordinate the fuel cell system with the train speed trajectory optimization model, we assume that there is no transmission loss; thus, the output power of the fuel cell system equals the received power of the motor. Furthermore, we can relate the power with the product of the traction energy and the average speed as in (18).

$$P_i = \frac{E_i}{\Delta t_i} = \frac{1}{\Delta d_i} E_i \cdot v_{i,\text{ave}} \quad (18)$$

This nonlinear constraint can be converted into a separable form as in (19) by introducing two new variables  $y_{1,i}$  and  $y_{2,i}$  as shown in (20) and (21).

$$P_i = \frac{1}{\Delta d_i} \left( y_{1,i}^2 - y_{2,i}^2 \right) \quad (19)$$

$$y_{1,i} = \frac{1}{2} (E_i + v_{i,\text{ave}}) \quad (20)$$

$$y_{2,i} = \frac{1}{2} (E_i - v_{i,\text{ave}}) \quad (21)$$

A series of ascending numerical values  $Y_1, Y_2, \dots, Y_Q$  are selected to represent the values of  $y_{1,i}^2$  and  $y_{2,i}^2$ , and then (19) can be reformulated as (22).

$$P_i = \frac{1}{\Delta d_i} \left( \sum_{q=1}^Q Y_q^2 \gamma_{i,q} - \sum_{q=1}^Q Y_q^2 \delta_{i,q} \right) \quad (22)$$

where  $\gamma_{i,q}$  and  $\delta_{i,q}$  are the variables of two sets of SOS2 in each  $\Delta d_i$ .

Since the relationship between power and efficiency of the fuel cell system has been introduced in (15), we can further deduce the mass of hydrogen  $M_i$  consumed in each  $\Delta d_i$  by (23).

$$M_i = \frac{1}{H} E_i \cdot \frac{1}{\eta_i} \quad (23)$$

where  $H$  is the combustion heat of hydrogen. One thing should be emphasized is that only the efficiency of the fuel cell is considered during the process of generating electrical energy.

Similarly, the product of traction energy and reciprocal of efficiency is transformed by (24). A series of ascending numerical values  $Z_1, Z_2, \dots, Z_R$  are selected

to represent the values of  $z_{1,i}^2$  and  $z_{2,i}^2$ , and then (23) can be reformulated as (25), where  $\varepsilon_{i,r}$  and  $\zeta_{i,r}$  are the variables of two sets of SOS2 in each  $\Delta d_i$ .

$$E_i \cdot \frac{1}{\eta_i} = z_{1,i}^2 - z_{2,i}^2 = \left( \frac{E_i + \frac{1}{\eta_i}}{2} \right)^2 - \left( \frac{E_i - \frac{1}{\eta_i}}{2} \right)^2 \quad (24)$$

$$M_i = \frac{1}{H} \left( \sum_{r=1}^R Z_r^2 \varepsilon_{i,r} - \sum_{r=1}^R Z_r^2 \zeta_{i,r} \right) \quad (25)$$

The objective of the model is to minimize the hydrogen consumption during the entire journey. Therefore, we conduct the optimization shown in (26) based on MILP.

$$\text{Minimize : } M_h = \sum_{i=1}^N M_i \quad (26)$$

Subject to : (1) – (25)

This type of model can be solved by commercial optimizers such as CPLEX, Gurobi. The solution, which locates the optimal train speed, the power profiles, and the hydrogen consumption, can be obtained by solving the objective function shown above.

### 3 Results and Discussion

Polymer electrolyte membrane (PEM) fuel cells are suited for small capacities (2–200 kW), e.g., transportation [15]. Therefore, a 200 kW PEM fuel cell is chosen as the power source of the train, and we assume that hydrogen is sufficient to support the entire journey. Modeling parameters for a typical fuel cell train are given in Table 1. The following sections will display scenarios with different power-efficiency characteristics, i.e., normal and extreme ones.

#### 3.1 Optimization with the Normal Power-Efficiency Characteristic

The normal power-efficiency characteristic of the fuel cell system in Fig. 1 is applied in this optimization. The results are shown in Table 2, and the speed, power and efficiency profiles are illustrated in Fig. 2. Note that the fuel cell system efficiency is 20% without any load.

**Table 1** Modeling parameters for a typical fuel cell train during a journey

$M(t)$	$P_{\max}$ (kW)	$F_{\max}$ (kN)	$\eta_t$	$P_f$ (kW)	$H$ (MJ/kg)	$D(m)$	$T(s)$
50	120	60	0.6	200	119.96	1000	150

**Table 2** Results with normal power-efficiency characteristic

Type	Total traction energy (MJ)	Traction time (s)	Average normalized traction power	Optimal hydrogen consumption (kg)
Normal	5.06	29.48	85.82%	0.0933

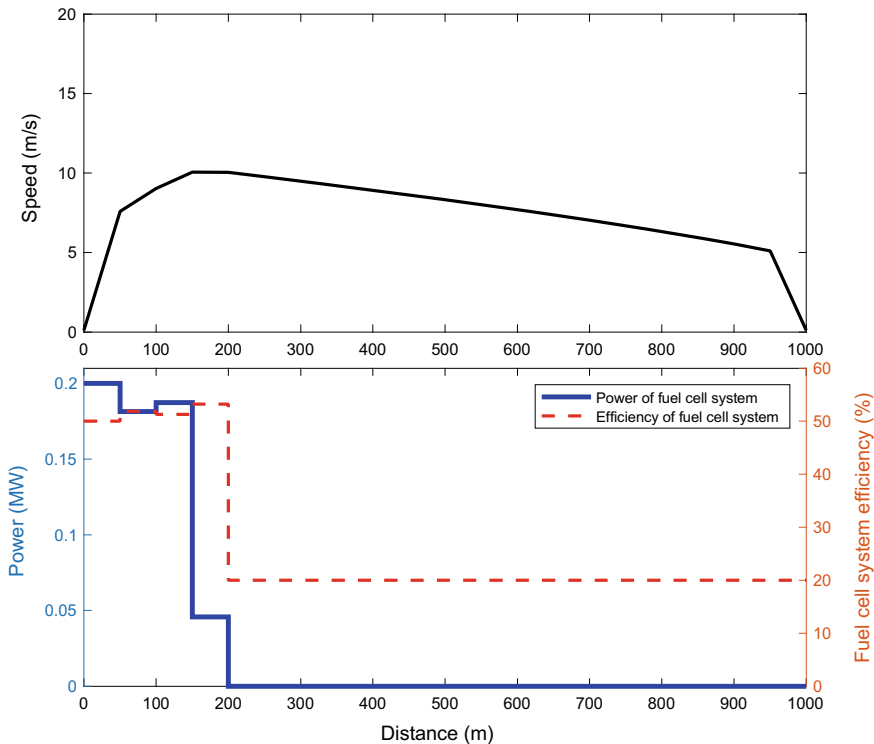
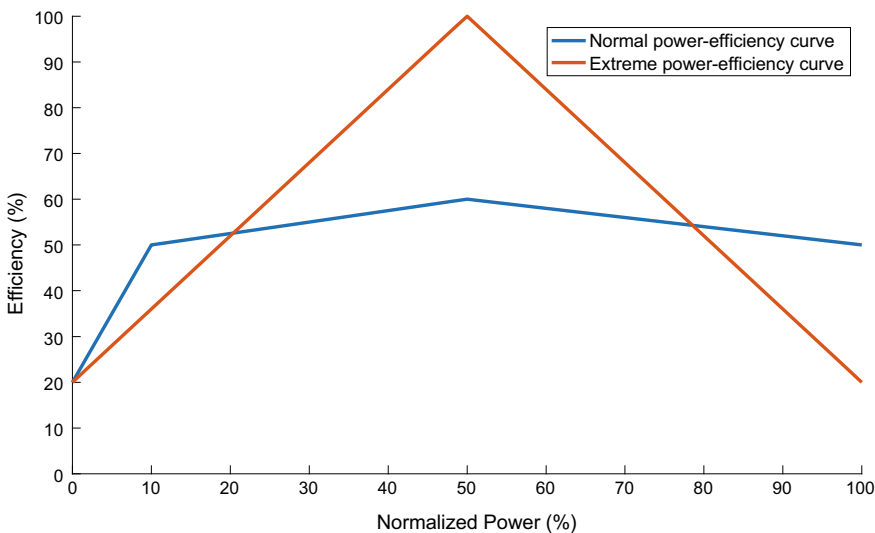
**Fig. 2** Speed, power and efficiency profiles

Figure 2 demonstrates that the train always runs in high efficiency above 50%. According to the normal power-efficiency characteristic in Fig. 1, when  $P_i > 10\% P_f$ , i.e.,  $P_i > 0.02$  MW, the efficiency of the fuel cell system has only seen small variations with the power; hence, there is no significant finding in this scenario.

### 3.2 Optimization with the Extreme Power-Efficiency Characteristic

The robustness and effectiveness of the model can be verified by comparing the optimization result with different power-efficiency characteristic. An imaginary characteristic with extremely high gradient is used and plotted together with the normal one in Fig. 3. We have made a comparison under the same journey, and the optimization results are shown in Table 3 and Fig. 4.

Table 3 and Fig. 4 show that compared to using the normal power-efficiency characteristic, the train with the extreme one operates at lower start-up power for the benefit of higher efficiency, and it also owns an approximately 4 s longer traction time. It is notable that the train with normal power-efficiency characteristic cruises between the distance segments 150 and 200 m, while that with the extreme one prevents the appearance of low-power cruising.



**Fig. 3** Normal and extreme power-efficiency characteristics

**Table 3** Results with normal and extreme characteristics

Type	Total traction energy (MJ)	Traction time (s)	Average normalized traction power	Optimal hydrogen consumption (kg)
Normal	5.06	29.48	85.82%	0.0933
Extreme	5.18	33.44	77.45%	0.0895

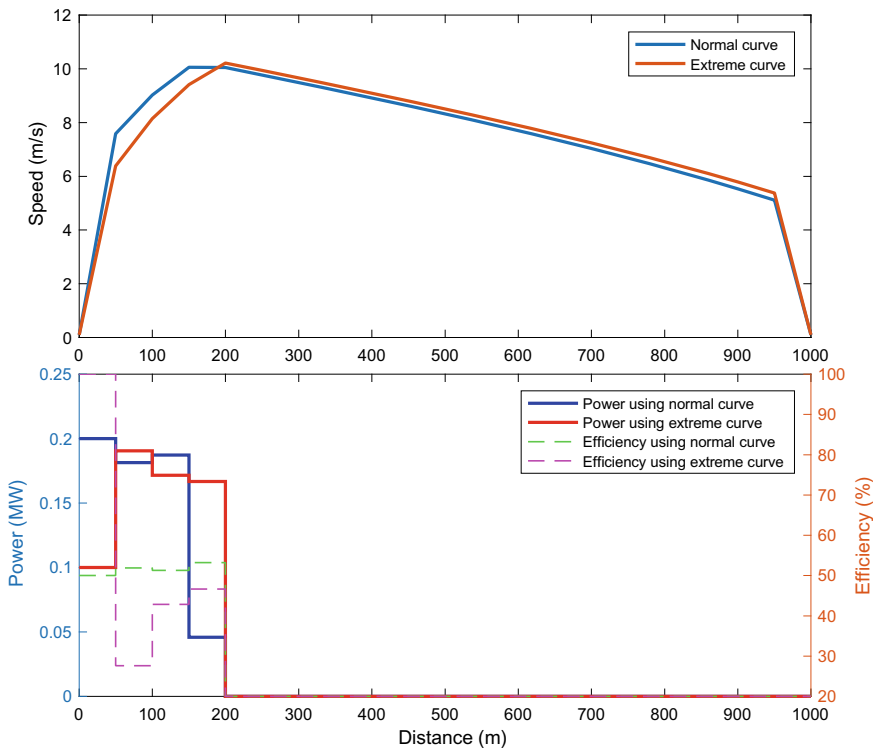


**Fig. 4** A comparison of speed, power and efficiency profiles

## 4 Conclusion and Future Work

This paper focuses on minimizing the hydrogen consumption of fuel cell trains based on the speed trajectory optimization. By linearizing the power-efficiency characteristic of the fuel cell system and other constraints mentioned, the optimal hydrogen consumption and the corresponding speed trajectory are finally found by MILP. Scenarios with normal and extreme power-efficiency characteristics are displayed and analyzed. Optimization results show that the train tends to operate with powers in high efficiency in order to save the hydrogen.

In the future, the effect of the power-efficiency characteristic could be further examined, e.g., compared to a model without the fuel cell system. A hybrid power system for a train could also be considered to explore more in this area.

## References

1. IEA-UIC (2017) Railway handbook 2017
2. Fletcher T, Thring R, Watkinson M (2016) An energy management strategy to concurrently optimise fuel consumption and PEM fuel cell lifetime in a hybrid vehicle. *Int J Hydrogen Energy* 41(46):21503–21515
3. Li H, Ravey A, N'Diaye A, Djerdir A (2018) A novel equivalent consumption minimization strategy for hybrid electric vehicle powered by fuel cell, battery and supercapacitor. *J Power Sources* 395:262–270
4. Sorrentino M, Cirillo V, Nappi L (2019) Development of flexible procedures for co-optimizing design and control of fuel cell hybrid vehicles. *Energy Convers Manag* 185:537–551
5. Mohammed H, Al-Othman A, Nancarrow P, Tawalbeh M, El Haj Assad M (2019) Direct hydrocarbon fuel cells: a promising technology for improving energy efficiency. *Energy* 172:207–219 (2019)
6. Ogungbemi E et al (2019) Fuel cell membranes—Pros and cons. *Energy* 172:155–172
7. Khmelnitsky E (2000) On an optimal control problem of train operation. *IEEE Trans Autom Control* 45(7):1257–1266
8. Albrecht A, Howlett P, Pudney P, Vu X, Zhou P (2016) The key principles of optimal train control—Part 1: formulation of the model, strategies of optimal type, evolutionary lines, location of optimal switching points. *Transp Res Part B: Methodol* 94:482–508
9. Albrecht A, Howlett P, Pudney P, Vu X, Zhou P (2016) The key principles of optimal train control—Part 2: existence of an optimal strategy, the local energy minimization principle, uniqueness, computational techniques. *Transp Res Part B: Methodol* 94:509–538
10. Lu S, Wang M, Weston P, Chen S, Yang J (2016) Partial train speed trajectory optimization using mixed-integer linear programming. *IEEE Trans Intell Transp Syst* 17(10):2911–2920
11. Tan Z, Lu S, Bao K, Zhang S, Wu C, Yang J, Xue F (2018) Adaptive partial train speed trajectory optimization. *Energies* 11(12):3302
12. Wu C, Zhang W, Lu S, Tan Z, Xue F, Yang J (2018) Train speed trajectory optimization with on-board energy storage device. *IEEE Trans Intell Transp Syst* 1–11
13. Bisschop J, Roelofs M (2006) AIMMS—The user's guide. Paragon Decision Technology, Haarlem
14. Jeong K, Oh B (2002) Fuel economy and life-cycle cost analysis of a fuel cell hybrid vehicle. *J Power Sources* 105(1):58–65
15. Argonne National Laboratory (2008) Fuel cycle comparison of distributed power generation technologies

# Simulation of Permanent Magnet Synchronous Motor Based on Dual PWM



Huawei Wang, Xilian Wang, Daqiang Bi and Yanhua Li

**Abstract** This paper presents a new method for the simulation of permanent magnet synchronous motor (PMSM), which is the electronic load structure based on dual PWM converter. In this method, according to the characteristics of PMSM, the input PWM converter adopts hysteresis control mode to make its output current, speed, torque and other characteristics consistent with the actual motor. The output PWM converter stabilizes the voltage value of the DC link and achieves grid connection through double closed-loop control mode of voltage and current. In MATLAB/Simulink, the simulation model of PMSM was built and compared with the PMSM model in Simulink library to verify the correctness of the established model.

**Keywords** PMSM · PWM converter · Hysteresis control · Double closed-loop control

## 1 Introduction

PMSM has incomparable advantages such as simple structure, small size, light-weight, small loss and high efficiency, so it is widely used in national defense, industry, life and other application scenarios [1]. However, at present, most experimental researches on the control of PMSM use actual motors for testing. During the experiment, the research cost is high, the power loss is large, and it is inconvenient to adjust different motor parameters. Aiming at the above problems, this paper presents a simulation method of PMSM based on dual PWM converter.

Power electronic load is a kind of power electronic device which uses converter to simulate the port voltage and current characteristics of real load. It is widely used in various power supply performance testing occasions due to its flexibility and

---

H. Wang · X. Wang (✉) · Y. Li  
Beijing Jiaotong University, No. 3 Shang Yuan Cun, Hai Dian District, China  
e-mail: [xlwang1@bjtu.edu.cn](mailto:xlwang1@bjtu.edu.cn)

D. Bi  
Tsinghua University, No. 30 Shuang Qing Road, Hai Dian District, China

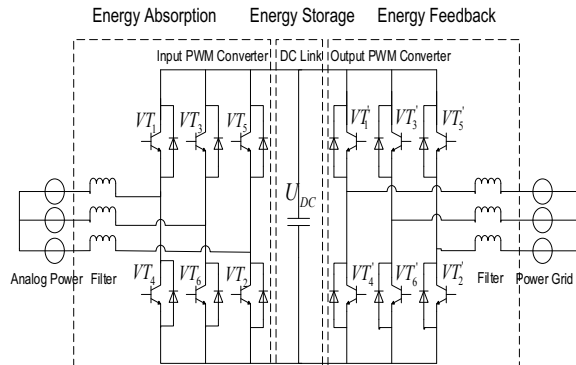
changeability, including uninterrupted power supply (UPS), DC power supply and factory test of frequency conversion power supply [2–4]. Literature [5] designed a separate control AC-DC-AC power load simulator. The AC-DC-AC part was responsible for simulating the volt-ampere characteristics of the power load and stabilizing the DC voltage. The direct-alternating part adopts unit power factor control to feed power back to the grid. However, only the constant load or slowly changing load is simulated, and the impact load is not studied. In literature [6], a new method is proposed for power simulation of asynchronous motors, but the grid-connected control of the analog motors is not fully considered, and the unification of inverter side and grid phase cannot be considered when the power grid fluctuates. In reference [7], it is proposed that the amplitude-phase control is used to take charge of the inverter grid-connection part, but the initial value of the capacitor voltage of the DC link is directly set at 800 V, and the initial phase angle of the grid-connection process is set at 0°.

The output characteristics of PMSM are simulated by using PWM converter, and the DC side voltage is stabilized. At the same time, PLL module is used in the grid-connected inverter to realize the same frequency and phase of the inverter side with the power grid. The establishment of the experimental platform of simulated motor provides a guarantee for future research.

## 2 Topology of Electronic Loads

The main circuit of power electronics load is composed of a set of PWM converters back to back and energy storage capacitor modules in the middle of the converters. The power supply is frequency converter, the rectifier side simulates port characteristics under a different input quantity [8], and the PWM converter on the inverter side connects to the three-phase power grid to realize inverter grid connection. Its circuit structure is shown in Fig. 1.

**Fig. 1** Main circuit structure of electronic load



### 3 Mathematical Model of PMSM

The size of the flux linkage in the mathematical model varies with the relative position of the stator and rotor of the PMSM [9]. Therefore, the voltage equation and the flux linkage equation of the motor are nonlinear time-varying equations, which are more complicated. The mathematical model of PMSM in two-phase rotating coordinate system is selected [10]. Its motor equations include voltage equations, flux equations, torque equations and equations of motion.

$$\begin{cases} u_d = R_s i_d + \frac{d\psi_d}{dt} - \omega_e \psi_q \\ u_q = R_s i_q + \frac{d\psi_q}{dt} - \omega_e \psi_d \end{cases} \quad (1)$$

Here,  $u_d$ ,  $u_q$  is the stator cross-axis voltage,  $R_s$  is the stator winding resistance,  $i_d$ ,  $i_q$  is the stator cross-axis current, and  $\omega_e$  is the rotor electrical angle.

$$\begin{cases} \psi_d = L_d i_d + \psi_f \\ \psi_q = L_q i_q \end{cases} \quad (2)$$

By arranging the above two equations, the current state equation can be obtained:

$$\begin{cases} \frac{di_d}{dt} = -\frac{R_s}{L_d} i_d + \frac{1}{L_d} u_d + \omega_e i_q \frac{L_q}{L_d} \\ \frac{di_q}{dt} = -\frac{R_s}{L_q} i_q + \frac{1}{L_q} u_q - \omega_e i_d \frac{L_d}{L_q} - \frac{1}{L_q} \psi_f \omega_e \end{cases} \quad (3)$$

$$T_e = P[\psi_f i_q + (L_d - L_q) i_d i_q] \quad (4)$$

$$J \frac{d\omega_r}{dt} = T_e - T_L - F \omega_r \quad (5)$$

Here,  $J$  is the moment of inertia,  $\omega_r$  is the mechanical angular velocity of the rotor,  $T_L$  is the load torque, and  $F$  is the damping coefficient. According to the above-related motor equation, the mathematical model of PMSM can be built.

### 4 Hysteresis Current Control

For the three-phase PWM rectifier side, the stator current simulated by the rectifier is required to quickly and accurately track the current reference command value. The principle of hysteresis current control is through the hysteresis comparator, so that the difference between the actual collected current and the given current is greater than the hysteresis width given by the hysteresis comparator, the power switch tube switches, and the current is adjusted to reduce the error [11] (Fig. 2).

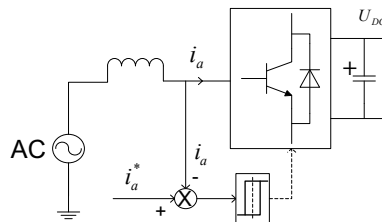


**Fig. 2** Principle of hysteresis current control

## 5 Inverter Control Scheme Comparison

For the three-phase PWM inverter, it is necessary to maintain the stability of the DC bus voltage first, and then to control the phase and amplitude of the AC side voltage to achieve grid connection. In this paper, amplitude and phase control and voltage and current double closed-loop control are compared and analyzed [12].

### 5.1 Amplitude-Phase Control

Firstly, the reference value of DC voltage is subtracted from the actual voltage, and the reference value of active current is added to the reference value of active current after the PI link as the instruction value of active current. When the power factor angle is given, the instruction value of reactive current is obtained. The voltage of phase angle is taken as SPWM modulation reference voltage to control PWM converter.

### 5.2 Double Closed-Loop Control

The double closed-loop control principle relies on a phase-locked loop to track the grid voltage phase  $\theta$ . Real-time acquisition of the three-phase current output from the grid side, combined with the phase-locked angle obtained by the PLL module, is obtained by coordinate transformation to obtain the cross-axis current  $i_d$ ,  $i_q$ . The DC bus voltage  $U_{DC}$  is collected and connected to the grid through double loop control, and its principle is shown in Fig. 3.

## 6 The Simulation Modeling

In the MATLAB/Simulink simulation environment, the electronic load is modeled and simulated. The principle block diagram of the simulation model is shown in Fig. 4.

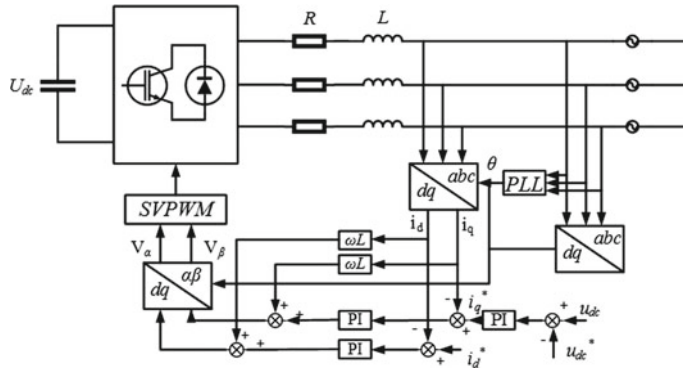


**Fig. 3** Principle of double loop control

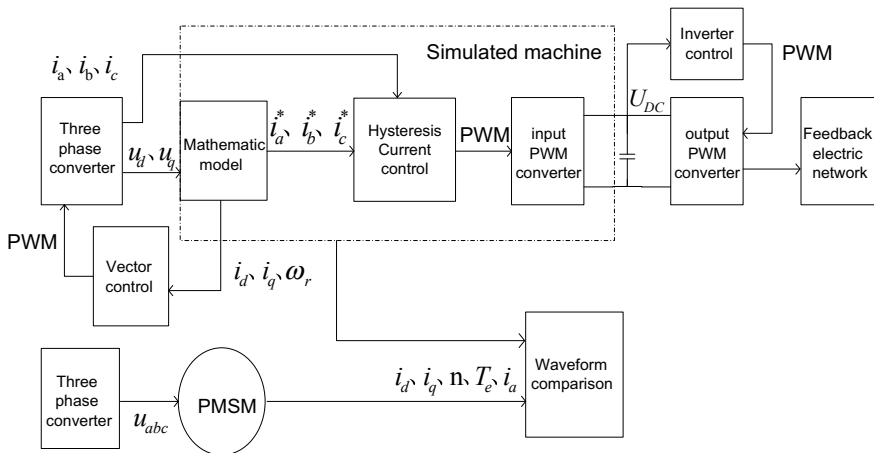


**Fig. 4** Principle of simulation mode

In the figure, the two analog power supplies are three-phase converters with adjustable amplitude and frequency. The output of the analog motor and the actual motor, such as current, speed, torque and rotor angle, is fed back to the converter through vector control, adjust the output three-phase current or output after coordinate transformation, respectively, drive the two motors to run.

## 7 Analysis of Simulation Results

The selected motor parameters in this experiment are shown in the following Table 1.

**Table 1** Motor parameters

Name of parameter	Symbols for parameter	Numerical value (unit)
Stator resistance	$R_s$	2.875 ( $\Omega$ )
q-axis inductance	$L_q$	0.0085 (H)
d-axis inductance	$L_d$	0.0085(H)
Rotor flux	$\psi_f$	0.175 (Wb)
Rotational inertia	$J$	0.0008 ( $\text{kg m}^2$ )

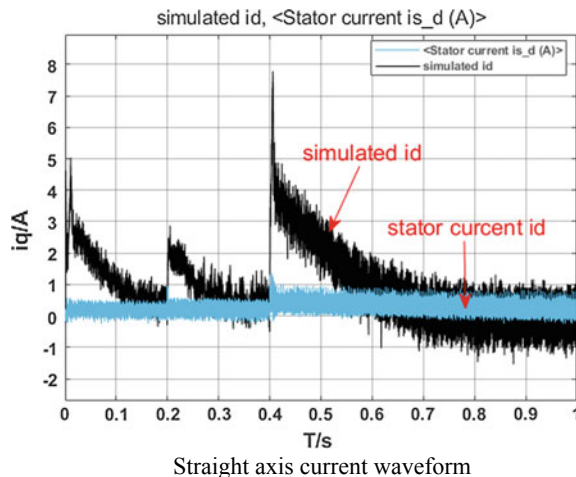
The parameter table shows that the rated speed of the motor is 750 rpm.

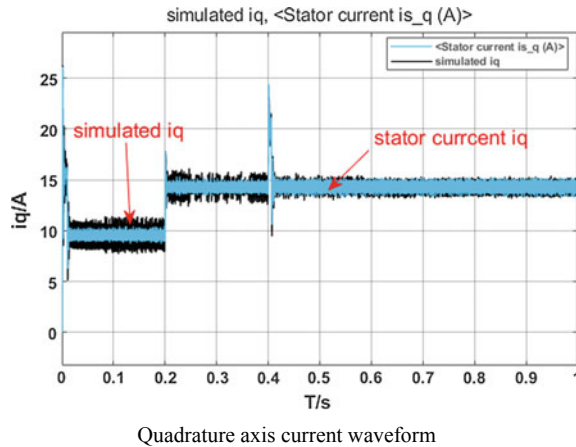
The parameters of the AC side filter reactor are:  $0.05 \Omega$ ,  $10 \text{ mH}$  on the rectifier side and  $0.01 \Omega$ ,  $5 \text{ mH}$  on the inverter side. DC side capacitor selection is  $7500 \mu\text{F}$ ; DC bus reference voltage  $U_{DC}^* = 800 \text{ V}$ .

The total simulation time for setting the simulation is 1 s. The initial torque of the two motors is  $10 \text{ N*m}$ , and the initial speed is 750 rpm. The load torque was changed to  $15 \text{ N*m}$  at 0.2 s and 1200 rpm at 0.4 s. Compare the output of the simulated motor with the motor model that comes with the Simulink library into the oscilloscope.

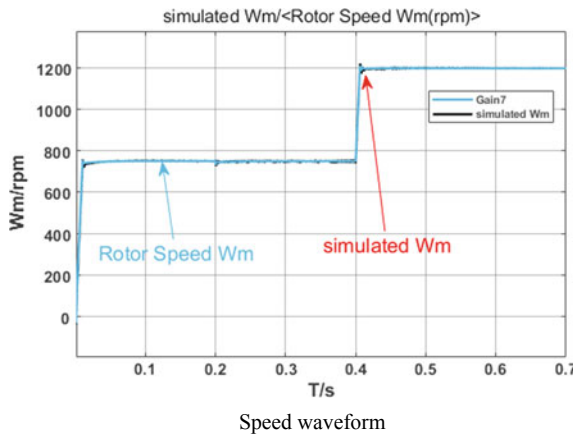
It can be seen from the above simulation comparison results that the simulated motor model built by the experiment can be compared with PMSM in MATLAB/Simulink from start-up to variable load operation to variable speed operation. The experiment proves the correctness of the model built. The comparison results are shown in Figs. 5, 6, 7, and 8.

In the above simulation process, the sudden torque and sudden speed are simulated, respectively. It can be seen that the output current, speed, torque and other characteristics of the simulated motor module are basically consistent with the

**Fig. 5** Straight axis current waveform



Quadrature axis current waveform

**Fig. 6** Quadrature axis current waveform**Fig. 7** Speed waveform

model in MATLAB library in terms of values and changing trends. At 0.2 s, the load torque increases from 10 to 15 N\*m, the direct axis current returns to zero after 0.1 s, and the oscillation amplitude remains at  $\pm 1$ A. The load torque rises rapidly to 15 N\*m, the amplitude of oscillation is  $\pm 2$  N\*m, and the change of quadrature axis current is synchronous with the change of torque. At 0.4 s, the rotation speed increases from 750 to 1200 rpm, and after the rapid increase, the oscillation attenuates and the rotation speed is stable. At the same time, the current  $i_d$  and the current  $i_q$  oscillate. It can be seen that when the speed increases, the current  $i_d$  oscillates more and the stabilization time is longer. In general, there is still a problem that the vibration of the motor simulator is slightly larger than that of the

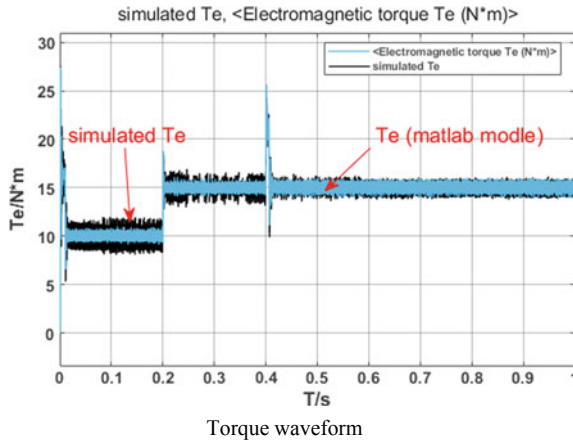


**Fig. 8** Torque waveform

self-built motor model in the simulation, but the simulation of the motor has been basically realized.

The simulation results of the DC link of the two grid-connected schemes are shown in the following Figs. 9 and 10.

It can also be seen from the figure that the two control schemes can achieve the stability of DC side voltage at about 800 V, but the amplitude and phase control adopts the PLL phase-locked loop. When facing the power grid fluctuation, the maximum deviation reaches 10 V, the oscillation attenuation is slow and the stabilization process is long, so it is impossible to accurately track the given voltage, and the control effect becomes worse. The control effect of double closed loop is obviously better than that of amplitude and phase control. The real-time acquisition

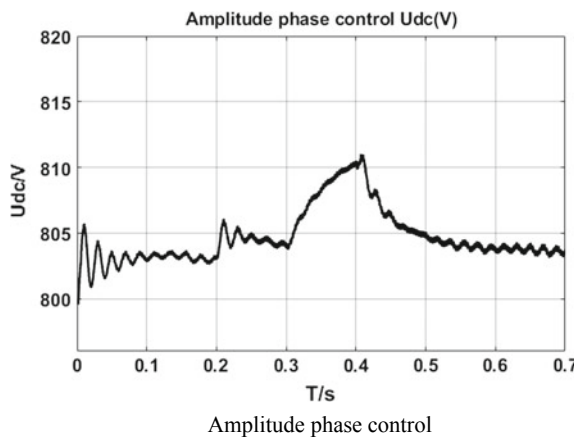
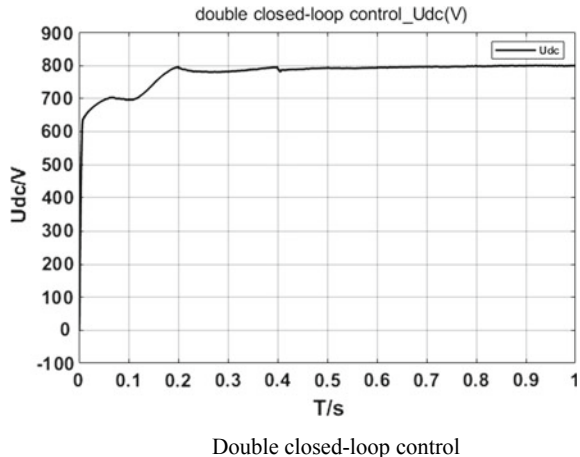


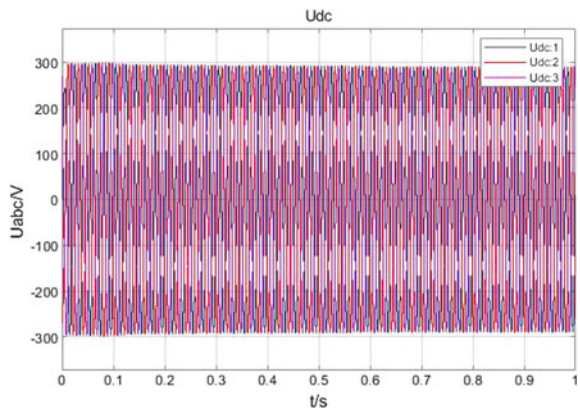
**Fig. 9** Amplitude phase control

**Fig. 10** Double closed-loop control



Double closed-loop control

**Fig. 11** Waveform of energy feedback part



of voltage phase of the power grid takes about 0.2 s to achieve stability and timely tracking and control in the process of sudden loading and sudden torque. So double closed-loop control is better.

The waveform of the subsequent power feedback section is shown below. It can be seen from the waveform in the figure that electrical energy feedback to the grid (Fig. 11).

## 8 Conclusion

The new power simulation method that replaces the actual motor with power electronic structure is practical and feasible.

Direct current control is carried out on PWM converter by taking the calculated current of the mathematical model as the instruction to accurately track the current instruction.

The inverter side compares the amplitude-phase control and double closed-loop control to achieve DC voltage stability and AC side feed grid connection.

In conclusion, the simulation scheme of permanent magnet synchronous motor based on dual PWM converter is feasible.

## References

1. Tang R (2006) Theory and design of modern permanent magnet motors. Mechanical Industry Press (in Chinese)
2. Chaturvedi DK, Mali OP (2008) Neurfuzzy power system stabilizer. IEEE Trans on Energy Conversion 23(3):887–894
3. Mithulananthan N, Canizares CA, Reeve J et al (2003) Comparison of PSS SVC, and STATCOM controllers for damping power system oscillations. IEEE Trans on Power Syst 18 (2):786–792
4. Mishra S (2006) Neural-network-based adaptive UPFC for improving transient stability performance of power system. IEEE Trans Neural Netw 17(2):461–470
5. Zhang B, Yao J (2006) Power load simulator based on PWM technology. Power Electron 40 (4):111–113 (in Chinese)
6. Chen Z (2007) Digital simulation of asynchronous motor based on PWM converter and its load characteristics. Huazhong University of Science and Technology, Wuhan (in Chinese)
7. Jin Y (2014) Research on analog permanent magnet synchronous motor based on dual PWM converter. Sichuan University, Sichuan (in Chinese)
8. Huang Q, Sun M, Zou X, Liu L, Xiong W (2014) Design of power electronic load system for simulating motor port characteristics. Autom Electr Power Syst 38(3):71–77 (in Chinese)
9. Yang J, Yang G, Li T (2010) Modeling and vector control of dual three-phase permanent magnet synchronous motors. J Electr Mach Control 14(6):1–7 (in Chinese)
10. Zhang C, Wang F, Li S, Yang D (2011) Vector control of permanent magnet synchronous motor based on MATLAB/Simulink. J Suzhou Univ 31(3):63–67 (in Chinese)
11. Zhou H, Bian X, Zhang Y (2017) SVPWM control and current hysteresis control of permanent magnet synchronous motor based on simulink. Equip Manuf Technol 10:45–47 (in Chinese)
12. Yu T, Wang C, Meng Y (2019) Design and research of energy—fed dc electronic load. Sci Technol Innov Inf (11):3–5(in Chinese)

# Analysis and Implementation of High Efficiency High Power Density Battery Charger for Electric Vehicle



Jie Yang, Zhijie Zhang, Zongju Cai, Yu Yao, Fei Li and Wei Yang

**Abstract** This paper presents a circuit structure for electric vehicle battery chargers. The AC-DC stage employs boost APFC circuit which can convert 220 V AC voltage to 400 V DC voltage with very low-input THD. In order to convert 400 V DC voltage to 44–64 V, an improved phase-shift full-bridge soft switching ZVS PWM converter added by two clamping diodes and one resonant inductor is presented. All main switches of the improved converter can achieve ZVS at full load variation, and the oscillation and voltage spikes across the output rectifier diodes at the secondary side of the transformer can be significantly reduced. Thus, the charger system has high efficiency and compact structure merits. Performance of the proposed circuit is verified by experimental results for a 1.5 kW prototype.

**Keywords** High efficiency · High power density · Battery charger · DC-DC converter · Soft switching

---

J. Yang  
Naval University of Engineering, Wuhan, Hubei, China

J. Yang · Z. Zhang (✉) · Z. Cai  
CSSC Systems Engineering Research Institute, Haidian District, Beijing, China  
e-mail: [07zhangzhijie@163.com](mailto:07zhangzhijie@163.com)

Y. Yao  
Shandong Vocational College of Industry, Zibo, China

F. Li  
Zibo Electric Power Company. Shandong Electric Power Company, Zibo, China

W. Yang  
School of Electrical Engineering and Automation, Harbin Institute  
of Technology, Harbin, China

## 1 Introduction

Onboard battery chargers play a major role in the development of electric vehicles [1]. An onboard EV battery charger can charge a depleted 120 Ah battery pack in about 6–7 h from a single-phase 220 VRM AC supply. For the conventional onboard battery chargers, an AC-DC converter with power factor correction followed by a DC-AC converter is usually employed [2]. And according to the requirement, the battery charger system must have some special qualities such as reliable performance, high efficiency and low-cost. Topology shown in Fig. 1 whose DC-DC stage used phase-shifted full-bridge (PSFB) converter is the most common topology for onboard battery chargers. It has ZVS of power switches with the pulse width modulation (PWM) for DC-DC stage. However, this traditional PSFB converter has some drawbacks such as narrow ZVS range of its lagging leg, severe voltage spikes and oscillations across output rectifier diodes. To extend ZVS range of lagging leg, either auxiliary switches with saturated inductance [3] or additional circuits [4] is utilized. Nevertheless, these methods cannot solve the trade-off between power-loss savings by the extended ZVS range and power losses by the auxiliary circuits. Also, these solutions did not focus on the severe voltage spikes and oscillations across output rectifier diodes. In [5], an LC network is added to the lagging bridge; it can easily achieve ZVS under light load conditions, yet it has complicated calculation and still cannot solve the voltage spikes and oscillations across output rectifier diodes. Snubber circuits [6] and [7] have been suggested to relieve the effect of the voltage oscillations.

Although these methods can reduce the voltage stresses of output diodes, circuit components and overall cost are increased. It is not desirable for the practical design of onboard EV battery chargers. This paper presents a preferable charger topology shown in Fig. 2, which includes the APFC AC-DC converter and the improved phase-shift full-bridge soft switching ZVS PWM DC-DC converter added by two clamping diodes and one resonant inductor. This new DC-DC topology can not only achieve ZVS easily under whole load condition but also significantly reduce the voltage spikes and oscillations across output rectifier diodes. Moreover, through connecting the transformer with the lagging leg, the clamping diode only conducts once during one switching cycle. Thus, further improved efficiency of the charger

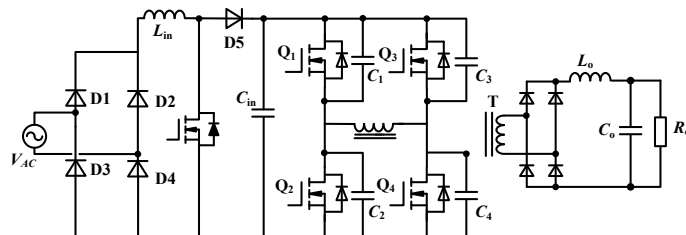


**Fig. 1** Traditional topology for onboard battery chargers

system can be obtained. Also, a charging strategy is suggested and implemented. The performance of the new charger system is verified by simulated and experimental results for a 1.5 kW prototype circuit.

## 2 Circuit Configuration

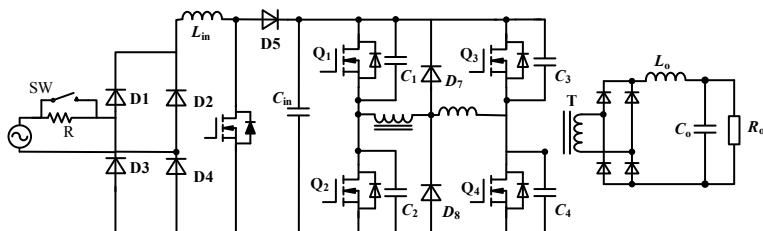
Figure 2 shows the circuit topology of the charger system. A soft-start circuit is connected to limit line current at the turn-on power. The APFC boost converter is used to convert the AC voltage to unchanged DC voltage, meanwhile achieve low THD. An improved phase-shifted full-bridge soft switching PWM converter is employed to regulate the output voltage. The leakage inductance of the transformer, the resonant inductor and the junction capacitance of power MOSFET are utilized to achieve ZVS for power switches. The clamping diodes are used to weaken voltage spikes and oscillations across output rectifier diodes.

## 3 System Analysis and Operation Principle

To analyze the improved PSFB-ZVS converter, the AC-DC converter is eliminated from Fig. 2. Like Fig. 3, this fraction is focused on the analysis of the improved PSFB-ZVS converter.

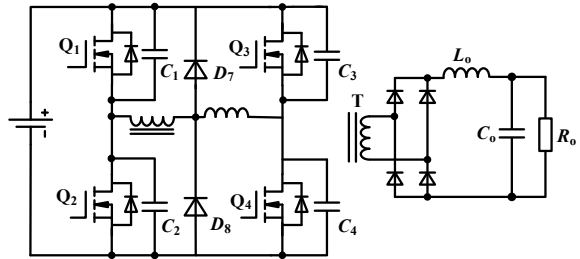
As shown in Fig. 3,  $Q_1-Q_4$  is the main switches of the improved PSFB-ZVS converter. Among the main switches,  $Q_1, Q_2$  is the lagging leg switches and  $Q_3, Q_4$  is the leading leg switches of the converter.  $C_1-C_4, D_7, D_8$  is the clamping diodes.  $T$  is the transformer which connects with the lagging leg of the converter.

Figure 4 shows the principle waveforms of the improved converter which includes switch driving waveform, current waveform of the transform ( $i_p$ ), resonant inductance ( $i_{L_r}$ ) and clamping diodes ( $i_{D7}, i_{D8}$ ), waveform of the midpoint voltage between the bridge ( $V_{AB}$ ) and voltage waveform of the transformer's second winding ( $V_{rect}$ ).

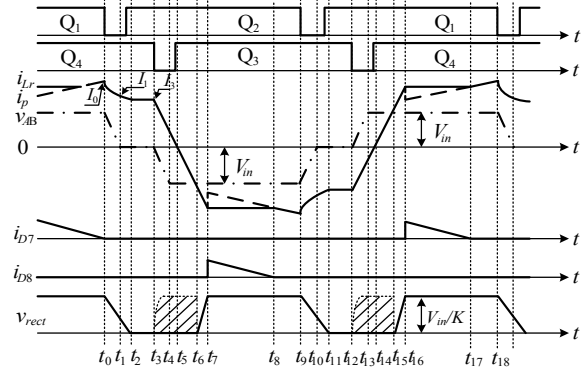


**Fig. 2** Presented charging system

**Fig. 3** New improved PSFB-ZVS converter



**Fig. 4** Principle waveforms of the improved converter



## 4 Circuit Design Consideration

### 4.1 APFC AC-DC Converter Design

The technical indicators of APFC AC-DC converter are as follows:

Input voltage: AC 220 V ( $\pm 10\%$ )/50 Hz; output voltage: DC 390 V  $\pm 10$  V; full load power: 1.5 kW.

For APFC AC-DC converter, the designing of the boost inductance is related to the effect of the input current correction. Thus, it is important to design the boost inductance. This AC-DC converter works under continuous current mode, so the principle for designing of the inductance includes current pulse rating principle, limiting current zero distortion principle and volume weight principle. Here, the first principle is chosen to design the inductance since it can improve the power density of the inductance.

According to the principle, the boost inductance should meet the following formula:

$$L > \frac{U_{iPKmin} D_{max}}{\delta_{max} I_{iPKmax} f_s} \quad (1)$$

$I_{iPKmax}$  is the maximum peak value of the input current, and it can be obtained by the following formula:

$$I_{iPKmax} = I_{imax} + \frac{1}{2} \delta_{max} I_{imax} \quad (2)$$

$\delta_{max}$  is the maximum current ripple rate, which 20% is chose.

$D_{max}$  is the maximum duty cycle, and it can be obtained by

$$D_{max} = \frac{U_o - U_{iPKmax}}{U_o} \quad (3)$$

In order to achieve higher efficiency meanwhile reduce the size of the circuit, the switch frequency  $f_s$  is chosen to be 70 kHz.

According to Formula (1–3), the value of inductance can be obtained.

There are two ways to select the output capacitance: limiting the output voltage ripple and holding time principle. On the basis of the principle of holding time, the output capacitance can be chosen

$$C_{out} = \frac{2P_o \cdot \Delta t}{U_o^2 - U_{omin}^2} \quad (4)$$

Through comparison, the control method of the AC-DC APFC converter is average current control mode, and UCC3854 control chip is utilized to achieve this control method. The design of the control circuit is not described in this paper.

## 4.2 DC-DC Converter Design

The technical indicators of DC-DC converter are as follows:

Input voltage: DC 390 V  $\pm$  10 V; output voltage: DC 44 V–64 V; output current: 0–25A; maximum output power: 1.5 kW; switch frequency: 50 kHz.

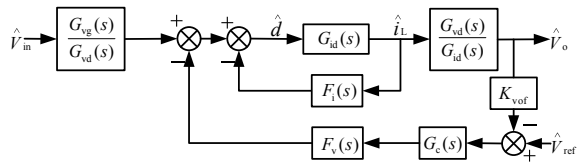
In order to improve the efficiency and reduce the volume of the charge system, the value of the resonant inductance should meet the formula:

$$\frac{1}{2} L_r I^2 = \frac{3}{4} C_{mos} V_{in}^2 \quad (5)$$

The control circuit is designed on the basis of peak current control mode. The control block diagram of the peak current control mode is shown in Fig. 5. The transfer function of the peak current control mode DC-DC converter is

$$G_o(s) = F_v(s) G_c(s) K_{vof} \cdot \frac{G_{vd}(s)}{1 + F_v(s) G_{id}(s)} \quad (6)$$

**Fig. 5** Block diagram of the peak current control mode



The close loop amplitude-frequency and phase-frequency feature through a suitable PI controller is shown in Fig. 6.

The traditional control chip UCC2895 is utilized to implement the control circuit.

## 5 Implementation of Charging Strategy

This charge system is designed to charge lead-acid battery, and an advanced five-state charging curve is adopted, as shown in Fig. 7. This strategy contains five states: precharging state (S1), constant current charging state (S2), constant voltage charging state (S3), trickle charging state and float charging state (S4). This charging strategy is implemented by PIC18F2480.

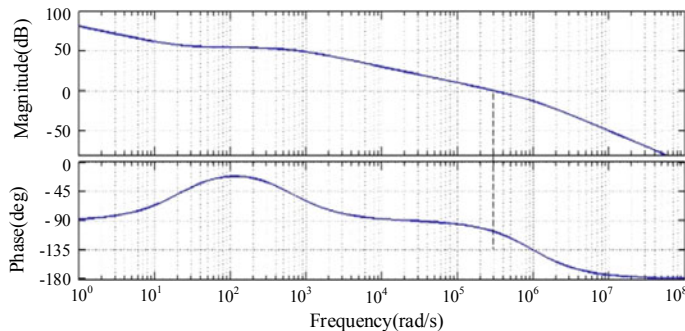


**Fig. 6** Close loop amplitude-frequency and phase-frequency feature

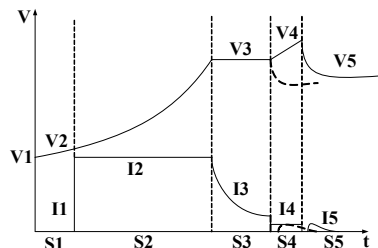


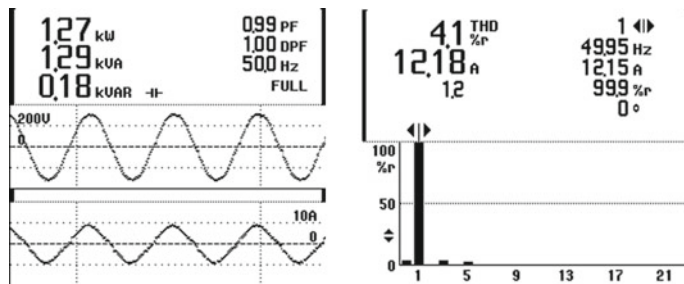
**Fig. 7** Five-state charging curve

## 6 Experiment Results

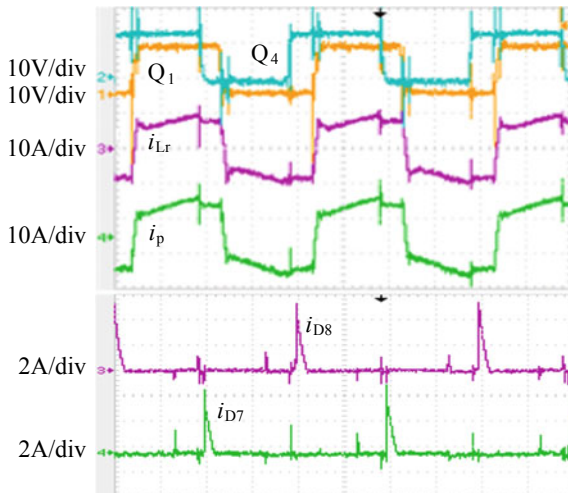
Based on the analysis and designing above, a laboratory prototype was built to verify the performance of the charging system with the following operation:  $V_i = 220 \text{ V} \pm 22 \text{ V}$ .  $V_o = 44\text{--}64 \text{ V}$ .  $I_o = 0\text{--}25 \text{ A}$ . The experimental waveforms of the charging system are shown in Figs. 8, 9, 10 and 11.

Figure 8 gives the results of the APFC AC-DC converter. It can be seen that at 1.27 kW conditions, the THD of the input current is 4.1%.

Figure 9 shows the performance of the DC-DC converter at full load condition. From the waveforms, we can see that the clamping diodes conducts only once during one switch cycle. Figure 10 reveals the soft switching conditions of the leading and lagging leg under full load conditions. Figure 11 shows the efficiency and temperature curve of the system under complete charging cycle. From Fig. 11, we can conclude the following: (1) This system needs 6 h 45 min to complete



**Fig. 8** Waveforms of the APFC AC-DC converter



**Fig. 9** Waveforms of the improved DC-DC converter

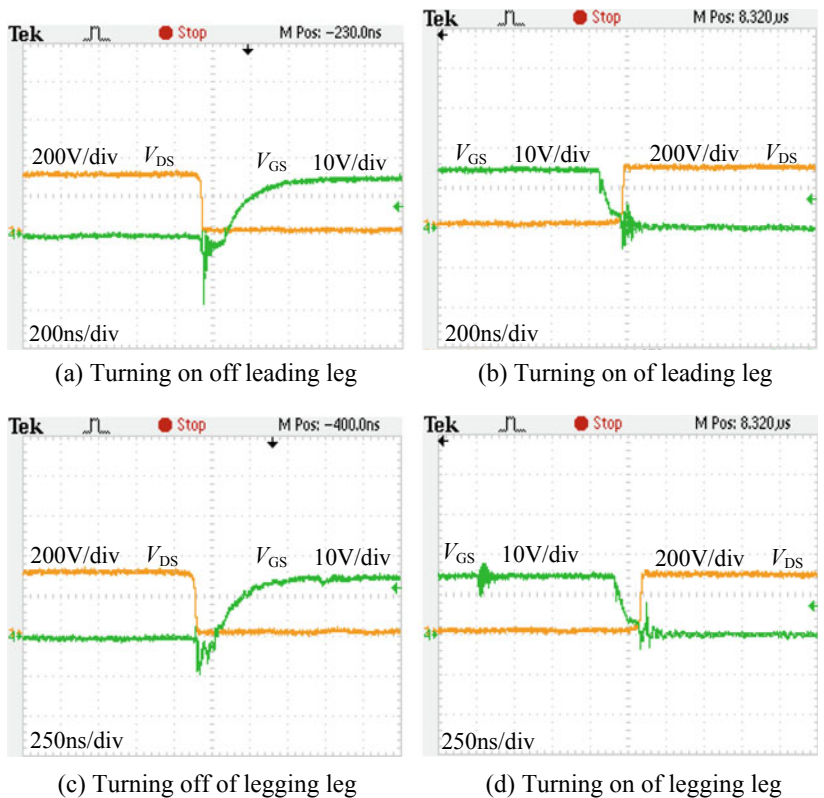


**Fig. 10** ZVS conditions of the improved DC-DC converter

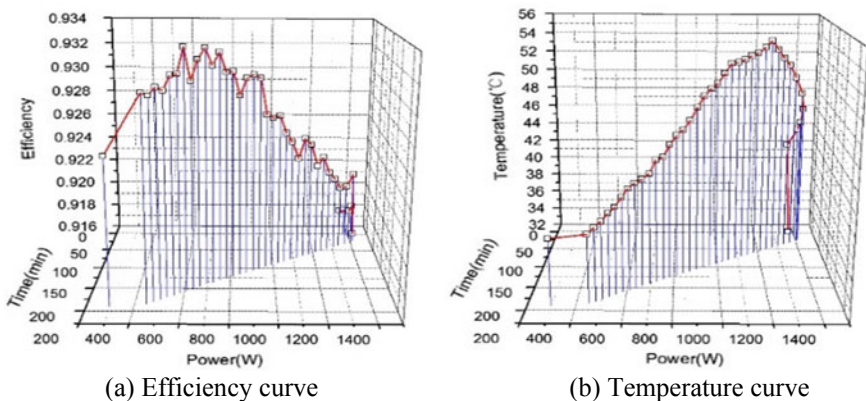


**Fig. 11** Efficiency and temperature curve of the improved DC-DC converter

charging the 120 Ah battery pack. (2) Its maximum efficiency is 93.2% and minimum efficiency is 91.6%. (3) The maximum temperature of the system is 53 °C when ambient temperature is 30 °C.

## 7 Conclusion

According to the analysis and experimental results of the charging system, the advantages of the presented charging converter have been verified. (1) The APFC AC-DC converter can make the THD of the input current below 5%, and the PF is approximately equal to 1. (2) The new presented improved PSFB-ZVS DC-DC converter can further improve the system efficiency (maximum 93.4%) and reduce the working temperature (maximum 54.4 °C). (3) The new charging strategy can not only increase the charge speed, reducing charge time (6 h 45 min to complete charging the 120 Ah battery pack), but also can provide more comprehensive protection in order to increase system reliability. (4) The charging system has a high power density.

## References

1. Kamble AS, Swami PS (2018) On-board integrated charger for electric vehicle based on split three phase induction motor. In: IEEE international conference on emerging trends and innovations in engineering and technological research (ICETIETR), Ernakulam, India, pp 1–5
2. Yang M-K, Cho H-S, Lee S-J (2013) High-efficiency soft-switching PWM DC-DC converter for electric Vehicle battery chargers. In: IEEE energy conversion congress and exposition, Denver, CO, USA, pp 1092–1095
3. Shu L, Chen W, Ma D, Ning G (2018) Analysis of strategy for achieving zero-current switching in full-bridge converters. *IEEE Trans Ind Electron* 65(7):5509–5517 (2018)
4. Jain PK, Kang W, Soin H, Xi Y (2002) Analysis and design consideration of a load and line independent zero voltage switching full bridge dc/dc converter topology. *IEEE Trans Power Electron* 17(5):649–657 (2002)
5. Niu R, Zhang W, Chen W, Shu L, Ning G, Ma D (2018) A novel ZCS full-bridge PWM converter with simple auxiliary circuits. In: IEEE international power electronics and application conference and exposition (PEAC), Shenzhen, China, pp 1–6
6. Lee IO, Moon GW (2013) Phase-shifted PWM converter with a wide ZVS range and reduced circulating current. *Trans Power Electron* 28(2):908–919
7. Ting Y, de Haan S, Ferreira JA (2013) The partial-resonant single active bridge DC-DC converter for conduction losses reduction in the single active bridge. In: IEEE ECCE conference proceedings, Melbourne, VIC, Australia, pp 987–993

# Simulation of Power Supply System Considering Inverter Feedback Device in Urban Rail Transit



Liping Zhao, Feng Wang, Sheng Lin and Xiaohong Lin

**Abstract** At present, with the rapid development of urban rail transit, the design requirements of urban rail power supply system are getting higher and higher. This paper mainly studies the simulation of urban rail transit power supply system with inverter feedback device, in order to provide data support for power supply system design and energy consumption analysis from the aspects of system modeling and simulation. First of all, the model of traction substation is established, including rectifier unit and inverter unit, and the calculation principles and algorithm implementation process of DC network power flow calculation and AC network power flow calculation are also analyzed next. Finally, the power flow distribution and energy utilization effect of the power supply system considering inverter feedback device are evaluated. The results show that the inverter feedback device installed in traction substation plays an important role in reducing traction network voltage, improving energy efficiency and saving operation cost.

**Keywords** Power supply system · Inverter feedback device · AC and DC power flow calculation

## 1 Introduction

The metro train will produce a lot of regenerative braking energy in the braking process. A lot of tests show that the braking energy of the metro train accounts for about 30% or more of the traction energy of the train [1, 2]. An excellent way to use this part of the energy is to install the inverter feedback device in the traction substation to feed back the excess regenerative braking energy. The literature [3] designed a double closed-loop control strategy with a hysteresis comparator and applied it to the three-phase grid inverter system; the literature [4] built a simplified

---

L. Zhao · F. Wang · S. Lin (✉) · X. Lin  
School of Electrical Engineering, Southwest Jiaotong University,  
No. 999, Xi'an Road, Chengdu 611756, China  
e-mail: [slin@swjtu.edu.cn](mailto:slin@swjtu.edu.cn)

power system model containing regenerative inverters and trains, and the impact of operating characteristics on the amount of regenerative braking energy and its distribution is analyzed; the literature [5] designed the control system of the inverter and the SVPWM midpoint voltage balance control method based on capacitive charge balance control through modeling and analysis, and verified the function of the feedback system through simulation; the literature [6] proposes a structure that is capable of suppressing unbalanced voltage, and the control strategy based on the resonant controller is proposed. Then, the experimental results fully demonstrate the excellent performance of the comprehensive control strategy; the literature [7] establishes the mathematical model of the inverter feedback system and discusses the main circuit parameter design and system switching principle. The structure and control mode of the inverter are analyzed in the above literature, but the influence and results of the inverter on the power flow distribution in the urban rail power supply system are not or simply analyzed.

In the early stage, the traction calculation of metro train is studied, and the running characteristic curve of metro train is obtained. The AC side and DC side of the power supply system are modeled, including rectifier units and inverter feedback devices, and the alternating iteration method is used to calculate AC and DC power flow in power supply system. The train running characteristic curve is supplemented by the departure strategy as the input of power flow calculation. Then, the power flow distribution and the energy-saving effect of power supply system considering inverter feedback device are quantitatively evaluated in the end.

## 2 Modeling of Traction Substation

Most of the rectifier units used in urban rail transit traction substations are 24 pulse rectifier units. In the DC side power flow calculation of urban rail transit, the rectifier unit is regarded as DC power supply.  $U_s$  and  $R_{eq}$  represent the ideal voltage source and equivalent internal resistance in Thevenin equivalent circuit of rectifier unit, respectively.

$$U_s = \frac{12}{\pi k} \int_{-\frac{\pi}{24}}^{\frac{\pi}{24}} \sqrt{6} U_a \cos \omega t d(\omega t) = \frac{2.44 U_a}{k} \quad (1)$$

$$R_{eq} = \frac{3X_c}{2\pi} \quad (2)$$

Among them,  $X_c$  is the commutation reactance;  $U_a$  represents AC side phase voltage [8, 9].

The inverter feedback device installed in urban rail traction substation is a three-phase inverter composed of IGBT switching elements, in which the voltage

inverter feedback device has a good operation effect in many domestic metro lines, and it is not easy to fail [10].

The control strategy of fixed phase angle  $\delta$  or fixed modulation M is adopted. When calculating the equivalent input power  $P_a$  and  $Q_a$  of the AC system in this control strategy,  $U_a$  or the reactive power  $Q_a$  injected into the AC system is controlled at the given value, and the voltage  $U_d$  or the power  $P_d$  of the DC system is the known quantity. That is to say, when the inverter feedback unit of traction substation is working on the above control strategy, the traction substation can be regarded as a voltage source with constant voltage value in the DC side, and the voltage value is equal to the starting voltage of the inverter device. The power calculation model of the inverter feedback device is as follows [2]:

$$P_a = U_d I_d \quad (3)$$

$$Q_a = U_d I_d \tan \varphi \quad (4)$$

$$\cos \varphi \approx \frac{U_d}{U_{d0}} = \frac{U_d \pi k}{3\sqrt{2} U_a} \quad (5)$$

Among them,  $P_a$  and  $Q_a$  represent active power and reactive power of the AC side;  $U_d$  and  $I_d$  represent voltage and current of the DC side, while  $U_{d0}$  represents no-load voltage;  $k$  represents the transformer ratio.

### 3 Simulation Calculation of AC and DC Hybrid Power Flow

#### 3.1 *Simulation Calculation of DC Side Power Flow*

The DC side network of power supply system is a complex time-varying network. However, at a certain running time, it can be considered that the power and position of the train and the voltage of the traction network are constant. The current vector iterative method can be used to solve the DC side node voltage equations and obtain the power flow distribution of the DC side network. At a certain time, the schematic diagram of the DC side section of the power supply system is shown in Fig. 1.

In Fig. 1,  $R_{tn}$ ,  $R_m$  and  $G_{rn}$  represent the equivalent resistance of traction network, rail equivalent resistance and rail leakage conductivity of the corresponding section n;  $U_{di}$  and  $R_{eqi}$  represent the output no-load voltage and equivalent internal resistance of traction substation  $i$ ;  $P_{sxm}$  and  $P_{xxm}$  represent the uplink train m driving power and the downlink train m driving power.

The DC side network of the power supply system shown in Fig. 1 can be expressed by the following node voltage equations.

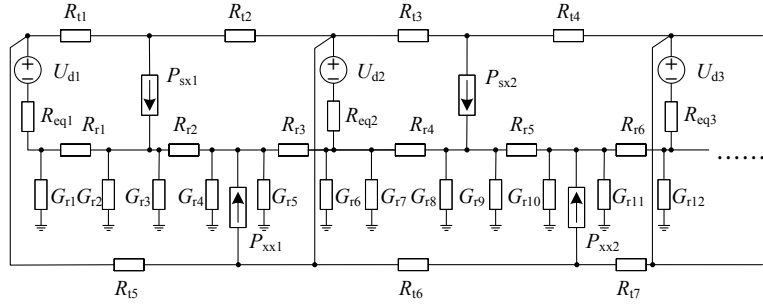


**Fig. 1** Schematic diagram of DC side section of power supply system

$$[G][U]^{(k+1)} = [I]^{(k)} \quad (6)$$

In Formula (6),  $[G]$  represents the node admittance matrix, which is obtained from the DC side network structure, and  $[I]^{(k)}$  is the current column vector composed of the injection current of each node during the  $k$ th iteration.  $[U]^{(k+1)}$  is the voltage column vector composed of the voltage of each node to be calculated at the  $k$ th iteration. During the  $k$ th iteration, the injection current of each train node can be obtained from the power of the corresponding train and the corresponding node voltage, as follows:

$$I_{\text{sxm}}^{(k)} = P_{\text{sxm}} / U_{\text{sxm}}^{(k)} \quad (7)$$

$$I_{\text{xxm}}^{(k)} = P_{\text{x xm}} / U_{\text{x xm}}^{(k)} \quad (8)$$

First of all, it is assumed that the voltage of each node in the traction network is 1500 V, and the voltage of each node on the rail is 0 V. Continuously update the voltage of each node according to Formula (6) until the accuracy requirements are met.

### 3.2 Simulation Calculation of AC Side Power Flow

Calculation of AC side power flow is done by using the method of “forward and backward” iteration. This method is easy to operate and has good convergence.

Urban rail transit power supply system is a hybrid AC and DC power supply system. Traction substation is the link between AC system and DC system to realize the connection of AC side and DC side power flow calculation. The calculation of AC and DC hybrid power flow process is shown in Fig. 2.

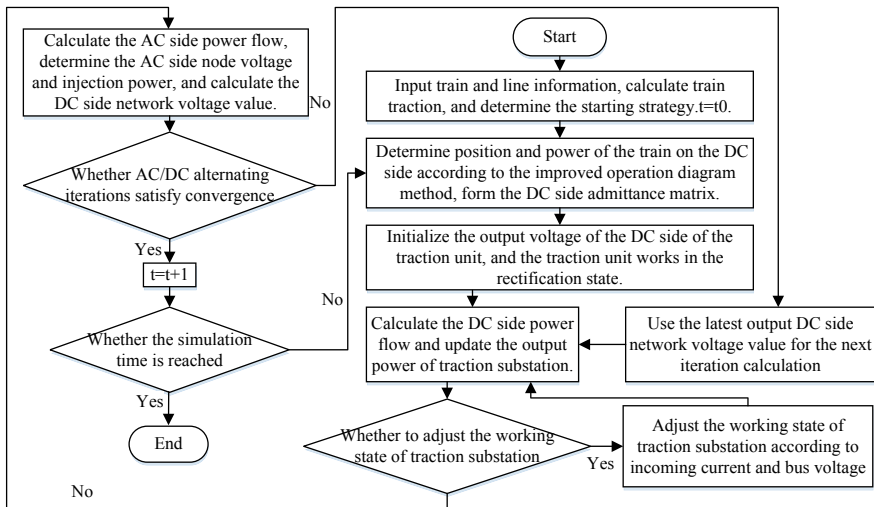


**Fig. 2** Flow chart of AC/DC hybrid power flow calculation

#### 4 Simulation Example

The simulation calculation of the power supply system of a metro line is carried out, and the power supply network structure of the metro line is shown in Fig. 3.

The location of each station on the line and the parameters of the components of the power supply system are shown in Tables 1 and 2, respectively.

Through the analysis of the train traction simulation calculation, the traction simulation calculation of the metro train running on the line is carried out. It is assumed that the stop time of each station is 30 s, and when the train is running on the line, the traction simulation results of the uplink and downlink trains are shown in Fig. 4.

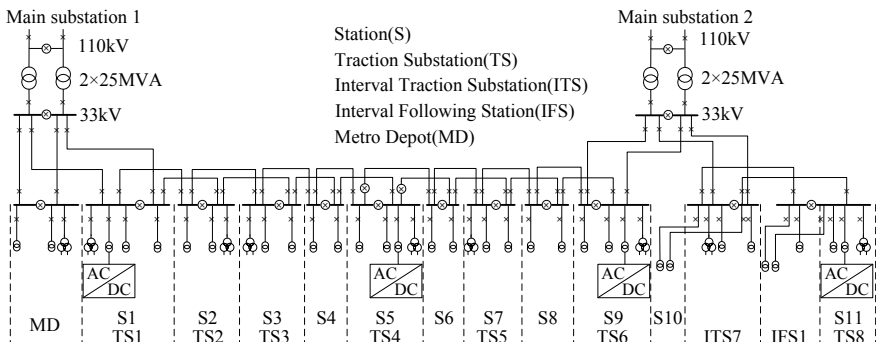


**Fig. 3** Power supply network structure diagram of a metro line

**Table 1** Location of metro stations

Station	S1	S2	S3	S4	S5	S6
Position (m)	0	2595	4815	6053	7227	9094
Station	S7	S8	S9	S10	S11	–
Position (m)	10,730	12,142	13,517	14,915	19,147	–

**Table 2** Parameters of components of power supply system

Designation	Parameters	Designation	Parameters
Equivalent resistance of traction network	0.008 Ω/km	Equivalent admittance of main transformer	j0.00002S
Rail equivalent resistance	0.02 Ω/km	Medium voltage cable impedance	0.17 + j0.402 Ω/km
Rail leakage conductivity	0.0967 S/km	Medium voltage cable admittance	j2.78 × 10 <sup>-6</sup> S/km
Equivalent power supply of urban power network	115.83 kV	Traction transformer impedance	12 + j100 Ω
Equivalent impedance of urban power network	2.08 + j0.48 Ω	Traction transformer admittance	j0.00001S
Equivalent impedance of main transformer	j12 Ω		

The output result of the train traction simulation calculation is supplemented by the departure strategy to obtain the train operation diagram of the metro line. The choice of departure strategy is a five-minute departure interval, and the first uplink train leaves at 6:00 am, while the first downlink train leaves six minutes later than the first uplink train, and all stop at 10:00 pm.

Taking the output results of the traction calculation as the input of the simulation calculation of the power supply system, the power flow of the power supply system is simulated. The definition  $\eta$  represents the ratio of the energy fed by the traction substation to the traction energy of the traction substation. The definition  $\mu$  represents the proportion of the total traction energy of the four traction substations with inverter feedback devices to the total regenerative braking energy of all trains. The starting voltage of the selected inverter is 1730 V. At a certain time, the power flow simulation results of the power supply system are shown in Fig. 5, and Fig. 5a shows the voltage distribution of the whole line when the inverter feedback device is installed in the traction substations 1, 4, 6 and 8, while Fig. 5b shows the voltage distribution of the whole line without the inverter feedback device. The full-day energy consumption of the metro line is shown in Table 3, where  $P$  is the full-day traction energy and  $B$  is the full-day feedback energy of the traction substation.

As can be seen from Table 3, the  $\eta$  of traction substation 1 has reached 51.84%, which may be due to the fact that traction substations 2 and 3 are not equipped with

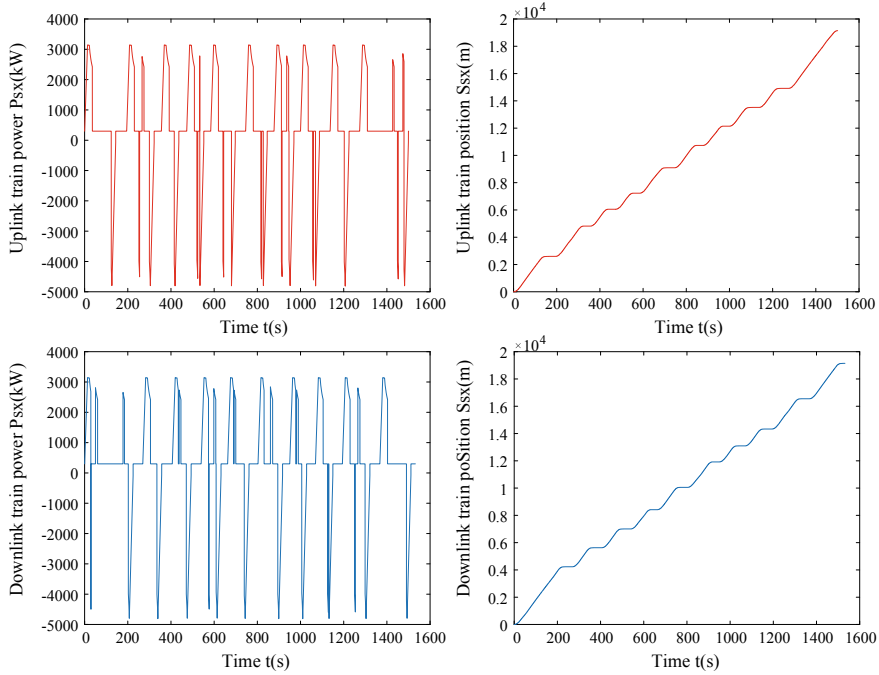


**Fig. 4** Results of traction simulation

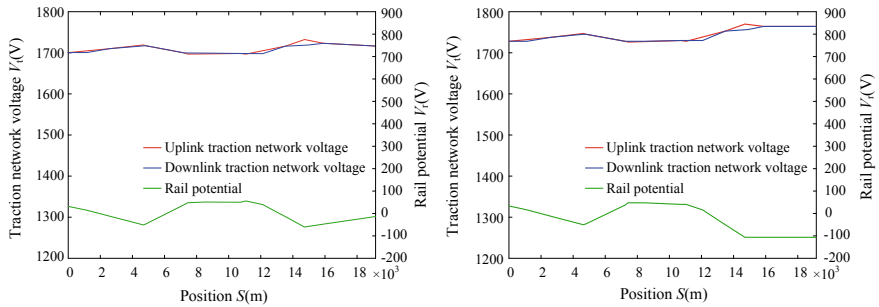


**Fig. 5** Simulation results of power flow at some time

inverter feedback devices. Because the traction substations 2 and 3 are not equipped with inverter feedback device, it is more likely to cause the increase of traction network voltage at traction substation 1 during train braking, which triggers the inverter feedback device, and makes the  $\eta$  of traction substation 1 on the high side.

**Table 3** Statistics of daily energy consumption of full-line traction substation

Serial number	P/kWh	B/kWh	$\eta$ (%)	$\mu$ (%)
TPS1	9285.96	4780.28	51.48	—
TPS2	9871.13	0	0	—
TPS3	9476.00	0	0	—
TPS4	9064.05	3250.03	35.86	—
TPS5	15,466.49	0	0	—
TPS6	10,907.30	2607.95	23.91	—
TPS7	9506.63	0	0	—
TPS8	7358.19	2883.12	39.18	—
Total amount	80,935.74	13,521.38	16.71	19.65

## 5 Conclusion

In this paper, the simulation results show that when the train is in the state of regenerative braking, the traction network voltage will increase and the rail potential will decrease. If the traction substation is equipped with inverter feedback device, the excessive increase of traction network voltage and the excessive decrease of track potential can be effectively avoided. The traction network voltage or rail potential of a traction substation without inverter feedback device is at risk of exceeding the voltage or potential limit. Therefore, the installation of inverter feedback device is very necessary for the safe and reliable operation of power supply system.

The regenerative braking energy of the train will not only be absorbed and utilized by other trains running on track, but also part of the energy will be inverted back to the AC power grid of the traction substation equipped with inverter feedback device. According to the charging method of 0.75 yuan per kilowatt-hour of industrial electricity, the metro line can save about 3,701,477.78 yuan in electricity cost in a whole year, so the installation of inverter feedback device in traction substation is of great significance to save energy and emission reduction and save urban rail operation cost.

**Acknowledgements** This research is sponsored by the National Natural Science Foundation of China (No. 51677153) and Sichuan Science and Technology Program (2018GZ0020).

## References

1. He W, Gao S, Wang L (2011) Traction power supply and transformation technology of rail transit. Southwest Jiaotong University Press, Chengdu (in Chinese)
2. Xu L (2017) Optimal system design of inverter feedback device for urban rail. Southwest Jiaotong University, Chengdu (in Chinese)

3. Lou Y, Liu W, Cui H, Ye X (2018) Study on improved double closed loop control strategy for urban rail inverter feedback system. In: 2018 IEEE transportation electrification conference and expo, Asia-Pacific
4. Zhang G, Tian Z, Tricoli P, Hillmansen S, Wang Y, Liu Z (2019) Inverter operating characteristics optimization for DC traction power supply systems. *IEEE Trans Veh Technol* 3400–3410
5. Huang K (2016) Simulation study on regenerative braking energy feedback system of urban rail transit. China University of Mining and Technology, Jiangsu (in Chinese)
6. Chen J, Diao L-J, Wang L, Du H, Liu Z (2016) Distributed auxiliary inverter of urban rail train—the voltage and current control strategy under complicated load condition. *IEEE Trans Power Electron* 1745–1756
7. Zhou J (2018) Study on inverter feedback regenerative braking of urban rail transit. Southwest Jiaotong University, Chengdu (in Chinese)
8. Wu X (2013) Research on modeling of DC traction substation in AC/DC power flow calculation. Beijing Jiaotong University, Beijing (in Chinese)
9. Guo D, Zhou Y, Tian L (2016) Application of regenerative braking energy absorption inverter in Chongqing rail transit. *Freq Convert World* 11:59–61 (in Chinese)
10. Lu Y, Zhao X, Zhao Y (2014) Application of regenerative braking energy absorption device in Beijing Metro. *Urban Express Rail Transit* 04:105–108 (in Chinese)

# Study on Stray Current Distribution of the Metro Depot



Liping Zhao, Junyi Li, Sheng Lin and Aimin Wang

**Abstract** In order to provide guidance for the protection and mitigation of stray current at the metro depot, the distribution of stray current of the metro depot is studied in this paper. A simulation model including the metro depot and line is established on CDEGS. The distribution of rail potential, ground potential, current of the single conductor device, and stray current are analyzed under different conditions that the trains operate in metro depot and on mainlines. Simulation results show that the stray current could penetrate to the metro depot and then back to the mainline through the single conductor device when the trains operate on the mainlines. The distribution characteristic of the stray current provides a foundation of new guidance for stray current mitigation in the metro depot.

**Keywords** Stray current · Distribution characteristic · Single conductor device

## 1 Introduction

With the development of metro, the buried metal structure corrosion caused by stray current, the earth potential uplift, and the DC bias of transformers are becoming increasingly serious. As the depot is an indispensable part of the metro system, it is very necessary to study the stray current distribution of the metro depot [1, 2].

Most of the domestic researches on stray current focus the stray current effect of the mainline [3]. However, there are few studies on the security of the metro depot, which are mainly reflected in the causes of stray current and the monitoring of stray current of the metro depot [4]. The protection and management of the metro depot depend on the single conductor device and the influence of the single conductor device on stray current [5, 6]. Under different operating conditions, the stray current circulation path is different, and the current of the single conductor device is

---

L. Zhao · J. Li · S. Lin (✉) · A. Wang

School of Electrical Engineering, Southwest Jiaotong University, No. 999, Xi'an Road,  
611756 Chengdu, China

e-mail: [slin@sjtu.edu.cn](mailto:slin@sjtu.edu.cn)

constantly changing, so there is a lack of specific research on the actual working condition.

In order to provide guidance for the protection and suppression of stray current at the metro depot, this paper studies the distribution of stray current at the metro depot. The metro depot was built based on current distribution, electromagnetic field, grounding and soil structure analysis (CDEGS) software by the simulation model of the single conductor device connection to the mainline. We analyze the traction substation power supply rail potential distribution and leakage current. According to simulation results, we calculate the single conductor device under various operating conditions in the conduction of research under various operating conditions train surface potential distribution. Based on the analysis of the above calculation results, stray current analysis and security management for the metro depot and the specific usage of the single conductor device provide the reference.

## 2 Research on Modeling Methods

The CDEGS railway model in this paper mainly consists of two parts: mainline and rolling stock metro depot.

### 2.1 Model Architecture

In this model, the distance between the upper and lower lines of the rail transit is set as 3.6 m. The geometric center of the rolling stock grounding network is located at 3 m underground of the rolling stock center. The ground potential is considered to be zero at infinity. Based on this idea, we extend the ground grid as far as possible; the grounding network is inserted into the 23 m underground at 9 points. The calculation includes the potential and the longitudinal current of the conductor and the leakage current. When the single conductor device is considered, there is a positive current flow, it is greater than the diode threshold, the single conductor device will be on, and vice versa [7, 8]. The model profile is shown in Fig. 1. The cross section is shown in Fig. 2.

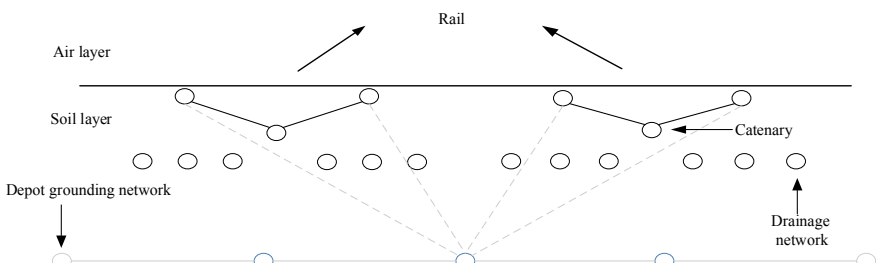


**Fig. 1** Sectional view of subway model

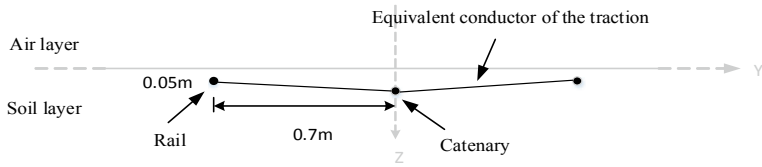


**Fig. 2** Cross section of subway model

## 2.2 Model Parameter

The relevant parameter tests of the rolling stock metro depot show that the overall insulation resistance of the rolling stock metro depot track to the ground is relatively low, and the insulation resistance of the mainline is about 50 times of it.

Traction substations at metro depot are usually directly connected to the ground. We adopt a single resistance of  $0.02 \Omega/\text{km}$  structural steel simulation grounding system, and the structural steel resistivity is set are less than the rolling stock metro depot rail and the drainage network, traction substation internal resistance. Table 1 shows the settings of basic parameters of simulation.

## 2.3 Single Conductor Device Description

The nature of a single conductor device is equivalent to a rectifier diode, plus a partial protection device, a disconnecting switch, and a monitoring device. In general, the diode threshold used in metro is 0.7 V, which is its own pressure drop.

**Table 1** Basic parameters of the model [9, 10]

Parameter	Numerical value
Tunnel length L	3000 m
The power supply mode	The mainline adopts bilateral power supply, the rolling stock metro depot adopts unilateral power supply, and the traction dc is 1000 A.
Reflow rail resistance R	$0.04 \Omega/\text{km}$ , diameter of 0.07 m
Track insulation thickness h	0.01 m
Rail insulation resistivity $\rho_1$	$450,000 \Omega/\text{km}$
Soil resistivity $\rho_2$	$200 \Omega/\text{km}$
Structural steel	Single resistance $0.02 \Omega/\text{km}$ , diameter of 0.02 m
The grounding net is buried deep	10 m above the ground
Row of drift	Single resistance $0.64 \Omega/\text{km}$ , diameter 0.018 m
Both streamline	Single resistance $0.016 \Omega/\text{km}$ , diameter of 0.07 m
The observation plane	400 observation points at the surface

In this simulation modeling, we adopt  $0.04 \Omega/\text{km}$ ,  $0.07 \text{ m}$  diameter insulation materials to simulate single conductor device.

When the potential difference between the two ends of the single conduction device is less than the threshold value, the single conduction device will be off. At this time, the single conduction device should be replaced by the  $200 \Omega \text{ m}$  resistivity of the soil, and then, the simulation of other data is carried out to ensure that the simulation model conforms to the actual situation.

## 2.4 Observation Surface

In order to cover the whole model, the observation surface was set as an area with a length of  $4000 \text{ m}$  and a width of  $200 \text{ m}$ , and an observation point was set at every  $10 \text{ m}$ , with a total of 400 points, to calculate the surface potential.

## 3 Simulation Calculation and Analysis

In the CDEGS software, we regard the injection current  $1000 \text{ A}$  as the acceleration condition of the train and call it  $+1000 \text{ A}$ . The drawn current  $1000 \text{ A}$  is regarded as the braking condition of the train, which is recorded as  $-1000 \text{ A}$ . There are 36 train operating conditions in this study.

Case 1: Fig. 3 shows the rail potential and rail current of the metro depot. Figure 3a indicates that the current flows from the rail to the traction substation at  $-6 \text{ m}$  when the train is accelerating. At this time, the current in the single conductor device is  $0.78 \text{ A}$ , and the current cannot reach the diode threshold, so the single conductor device has no effect. In Fig. 3b, at  $-6 \text{ m}$ , the rail current measured is  $1995 \text{ A}$ . Within this interval, the leakage current of the metro depot itself is  $5 \text{ A}$ . However, the current flowing into the single conductor device is almost 0 after the negative pole of the traction substation, indicating that the stray current leaked by the train itself flows back through the grounding grid.

Figure 4 surface potential shows that, due to the presence of the catenary, the stray current generated by the train operation of the metro depot is collected by the catenary at  $-206 \text{ m}$  and flows back to the traction substation at  $-6 \text{ m}$ , which is consistent with the data in Fig. 3b. The rail and ground transition resistance of the metro depot itself is small, and its stray current has a serious impact.

For the mainline model of substation (reversible) power supply, we simulate the acceleration and braking situation of the train at various positions.

Case 2: Both the upper and lower trains are speeding up at a position of  $750 \text{ m}$ . The rail potential of the positive line is negative and lower than the rail potential of the metro depot, the pressure drop on both sides of the single guide device is greater than its threshold value, and the single conduction device will be on.

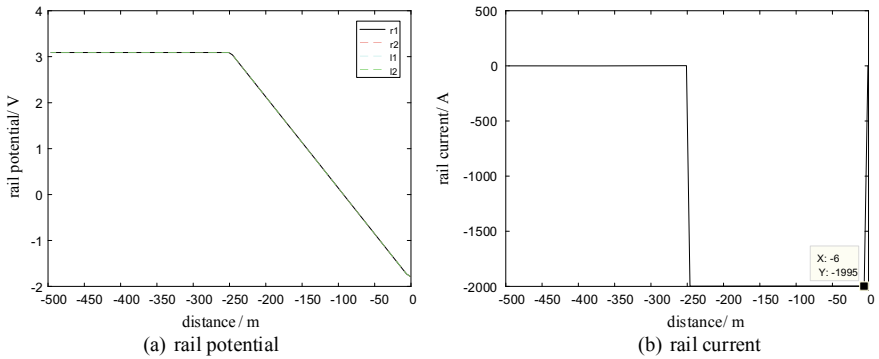


**Fig. 3** Rail data of metro depot

**Fig. 4** Ground potential of case 1

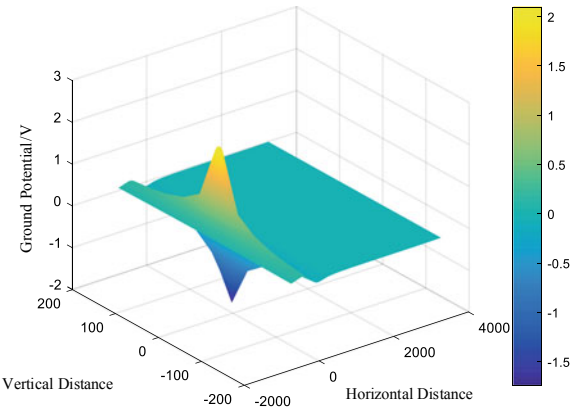
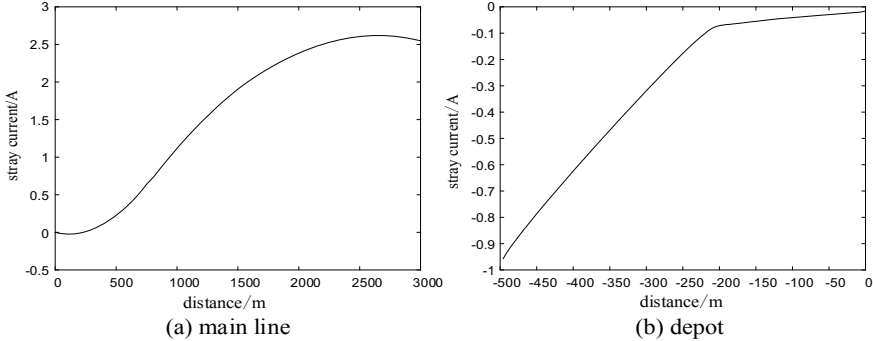
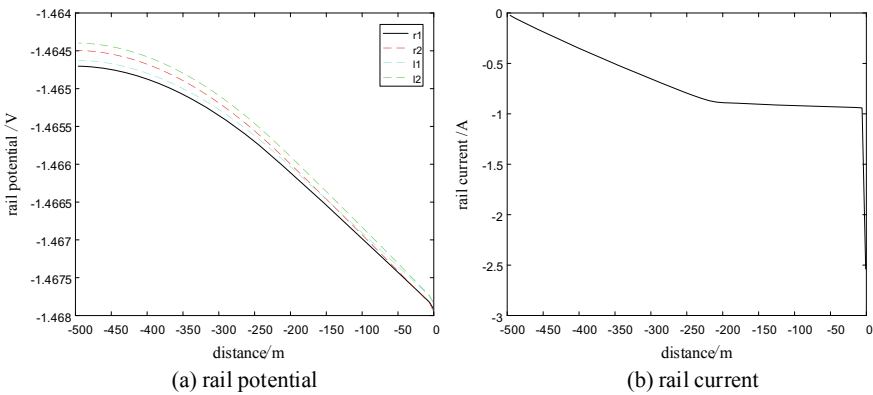


Figure 5 shows the stray current curve of mainline and the metro depot. Figure 5a shows that on the mainline 0–120 m area, stray current is negative. It suggests that current from the soil into the rail. Within the area in 120–2640 m, 120 m curve slope is positive and the slope is 0, in this period of interval rail of leakage current, the stray current is positive, after 2640 m curve slope is negative, the rail absorbs current from the earth, and it indicates the negative reflow to the distal traction substation.

Figure 5b of the metro depot stray current also shows that all stray current is negative, and the rail of the metro depot absorbs current from the ground. As the grounding grid is located in the area of -6 to -206 m, part of stray current flows back to the rail through the grounding grid, resulting in a sudden increase in the slope of the curve at -206 m and accelerated current return. At last, it flows back to the negative pole of the positive traction substation through the single conductor device.



**Fig. 5** Stray current curve of case 2



**Fig. 6** Rail data of metro depot

Conductor current and rail potential of the metro depot are shown in Fig. 6. In Fig. 6a, rail potential gradually decreases from  $-500\text{ m}$  to the origin, which conforms to the principle that the current flows from the top of the potential to the bottom. Due to the existence of the average flow line at the metro depot entrance, the potential of each rail will tend to be consistent with the direction of stray current mentioned above. Figure 6b shows that the incoming current in the rail conductor section increases gradually from  $-500\text{ m}$  to the origin, and the negative value at this moment indicates the direction, indicating the current flows to the positive line. At the position of  $-206\text{ m}$ , most stray current enters the ground grid, resulting in the reduction of stray current absorbed by the rail, so the slope of the curve becomes slowly. At the position of  $-6\text{ m}$  is an electrical connection between rail and grounding grid, the previous grounding grid absorbed stray current into the rail, resulting in a sudden increase in the total stray current of the rail, and Fig. 5 shows that the movement of the stray current curve in the same direction, confirming the final stray current through single conductor device back into the mainline.

Figure 8a is the surface potential of the whole model, and the blue part is the potential of the metro depot return point, which is extremely low and negative, indicating that the current flow in the soil is mainline to the metro depot. Especially at -206–0 m, the grounding grid absorbs a large amount of stray current flowing to the metro depot. The electric potential is also in line with the trend of the spurious current curve in Fig. 5.

Case 3: When the up line train accelerates at 750 m and the down line train decelerates at 1500 m, the impact of stray current on the metro depot is different from scenario 4. Considering that the ascending train is a large current release source, the descending train is a large current absorption source.

Figure 7 shows the stray current curve of the model metro depot and the positive line. Figure 7a shows that although the rail on the mainline has leakage or reflow current everywhere, the current at the origin is 0.0002 A, which is close to 0. As for the stray current of the metro depot, the curves at -206 and -6 m in Fig. 7b have a sudden change. This is because the stray current at -206 m starts to flow back through the grounding grid and returns to the rail at -6 m. However, the current value is too small to reach the diode threshold and the single conductor device will be off. At this time, the rail potential change of the metro depot is less than 0.01 V, which has less influence on stray current generated by the positive line of scenario 1.

Figure 8b is a surface potential under this condition, the potential near the metro depot is less than that near the metro depot on the positive line, but the potential difference value is too small, and the single conductor device will be off. In the range of 2000 m, the ground potential is negative, and most of the stray current flows to the far end of the positive line. At 3000 m, the surface potential is again close to the value of 0, indicating that the stray current flows back to the negative pole of the traction substation at the far end of the train operating range. Compared with case 2, the impact on the metro depot is reduced.

We can get some information from the above case. As the subway accelerates, it draws current from the catenary, and the current flows back through the rails. The

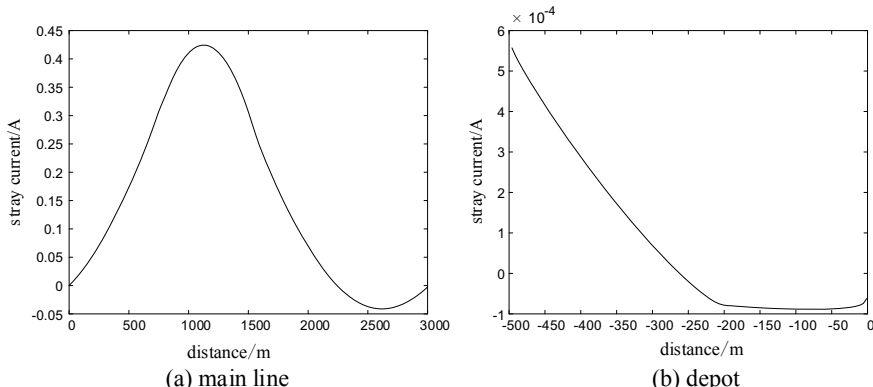
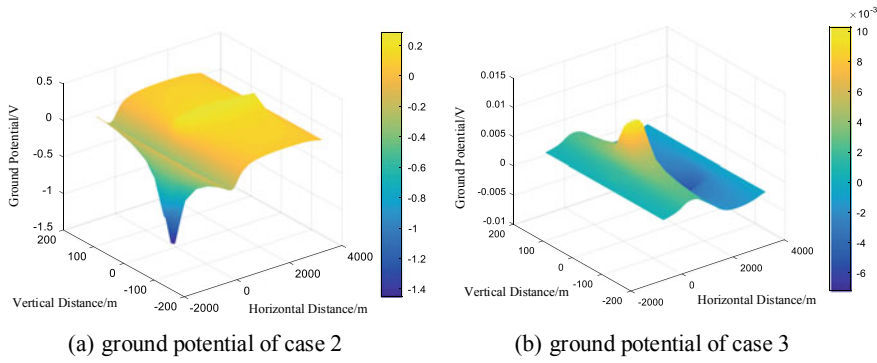


Fig. 7 Stray current curve of case 3



**Fig. 8** Ground potential

**Table 2** State of single conductor device in each situation

Scenario	The upside position (m)/current (A)	The downside position (m)/current (A)	Conduction situation
# 1	750/+1000	750/+1000	Is
# 2	750/+1000	750/-1000	No
# 3	750/+1000	1500/+1000	Is
# 4	750/+1000	1500/-1000	No
# 5	1500/+1000	750/+1000	Is
# 6	1500/+1000	750/-1000	No
# 7	1500/+1000	1500/+1000	Is
# 8	1500/+1000	1500/-1000	No
# 9	-250/+1000	-250/+1000	No
# 10	-250/+1000	-250/-1000	No

rail potential is positive, the ground is negative, and current leaks from the rails into the soil. At the negative pole of traction substation, the rail potential is negative and the ground is positive, so the leakage current flows from the ground to the rail and finally back to the traction substation negative pole. The direction of leakage current when the train slows down is opposite to that when the train accelerates. Table 2 shows some typical operating conditions. When stray current in the soil enters the depot from the mainline, the single conductor device will be on.

## 4 Conclusion

This paper describes the flow direction of stray current and the state of single conductor device of stray current, analyzing the distribution of stray current through the actual analysis. Here is the conclusion of the simulation results. (1) The positive

or negative direction of the mainline traction current determines the on or off of the single conductor device. (2) For the traction, substation is beside the single guide device; when the train runs in the depot, single conductor device will be off. (3) There is no obvious relationship between the working state of the single conductor device and the train running position on the mainline. (4) In subway operation, no matter whether there are trains running in the depot, there is stray current in the depot.

The model can effectively considering main metro stray current distribution of the metro depot and provide new ideas for mitigation of stray current metro depot.

**Acknowledgements** This research is sponsored by the National Natural Science Foundation of China (No. 51677153).

## References

1. Yu Z (2017) Analysis and protection of stray current characteristics of metro depot. *Urban Rail Transit Res* 20(10):44–47 (in Chinese)
2. Yu Y (2019) Analysis and treatment scheme for stray current problems of metro depot. *China Sci Technol Inform* 01:90–92 (in Chinese)
3. Liao J, Liu W, Xu L, Wang P, Zheng J, Wu W (2017) Stray current measurement and analysis of metro parking lot and metro depot. *Urban Rail Transit Res* 20(08):64–68 (in Chinese)
4. Liu S, Li C, Shi Y, Qian C, Liu L (2017) Calculation of dc current of traction transformer for electrified railway caused by dc grounding pole. *High Voltage Technol* 43(07):2161–2166 (in Chinese)
5. Liu J, Shen S, Zhou M, Wang H (1992) Analysis of the influence of single guide-pass device on stray current. *Urban Fast Rail Transit* 29(04):116–120. 6. Cox DR (1992) Regression models and life: tables, breakthroughs in statistics. Springer, New York, pp 527–541 (in Chinese)
6. Yan Dafeng, Liu Naiyong, Yuan Pengbin, Shu Jiang, Li Yuee (2013) Corrosion of buried steel pipeline by stray current in subway maintenance base and protective measures. *Corrosion Protect* 34(08):739–742 (in Chinese)
7. Yang J, Chen H (2017) Simulation analysis and optimization of the influence of single guide device on stray current. In: Automation Committee of China Railway Association (in Chinese)
8. Yu K, Zhu F, Liu G, Gou J (2014) Simulation research on stray current of subway based on CDEGS. *Electr Railw* 06:44–48 (in Chinese)
9. Liu M (2018) Study on dynamic characteristics of metro stray current based on CDEGS. Southwest Jiaotong University, Chengdu (in Chinese)
10. Yu K (2018) The simulation of metro stray current based on CDEGS. Southwest Jiaotong University, Chengdu (in Chinese)

# Active Fault-Tolerant Control Strategy of ANPC Three-Level Inverter Based on Sliding Mode Control



**Qinyue Zhu, Zhaoyang Li, Xitang Tan, Wei Dai, Dabo Xie  
and Sha Liu**

**Abstract** In order to solve the fault-tolerant problem of open-circuit fault of power switching devices in each arm in active neutral point clamped (ANPC) three-level inverter, an active fault-tolerant control (FTC) strategy based on sliding mode (SM) control is proposed. First, on the basis of establishing the state-space model of the inverter system, the fault characteristic signal is extracted and introduced. Then, the fault-tolerant controller using SM is designed to adjust the output voltage control signal in real time by reconstructing the SM control law after the fault. Based on the above strategy, the SVPWM control algorithm is adjusted to reconstruct the voltage space vector, which further changes the vector sending sequence. Consequently, the stable operation of inverter after FTC is realized and verified by simulation. Results show that the closed-loop FTC method with SM controller has better dynamic and steady-state response characteristic than open-loop control method, which meets the requirements of higher control accuracy. The proposed active FTC strategy achieved the expected goals in terms of effectiveness and feasibility.

**Keywords** ANPC three-level inverter · Active fault-tolerant · Sliding mode · Control law reconfiguration · Space vector sequence reconstruction

## 1 Introduction

Neutral point clamped (NPC) three-level traction inverter is widely used in electric multiple units (EMUs). The topology of NPC three-level inverter is stable, but the loss of power devices is not balanced enough, which will adversely affect the reliability of the traction inverter after long-term operation. In recent years, ANPC three-level inverter proposed by T. Bruckner has become the mainstream due to its

---

Q. Zhu · Z. Li · X. Tan (✉) · W. Dai · D. Xie · S. Liu  
School of Electronics Information and Engineering, Tongji University,  
Shanghai 201804, People's Republic of China  
e-mail: [xtan@tongji.edu.cn](mailto:xtan@tongji.edu.cn)

stable performance and more flexible balance control of loss. Hence, applications of ANPC three-level inverter in high-speed EMUs have attracted the attention of scholars [1, 2]. However, the topology and control strategy of ANPC three-level inverter are both more complicated compared with the NPC three-level inverter, resulting in a significant increase in failure probability of internal devices, especially for power switches such as IGBTs [3, 4]. If the fault cannot be processed in time, it will cause overload of other components, which will further affect the overall output performance of the system. Therefore, FTC after the failure of ANPC three-level inverter is momentous.

At present, researches of FTC of NPC three-level inverter mainly focus on hardware redundancy control [5, 6], which implements FTC by adding redundant bridge arms and devices to reconstruct the hardware topology of the inverter. This method is an ideal FTC scheme for NPC three-level inverter. However, the input of redundant devices to ANPC three-level inverter will further increase the size and cost of the inverter, which makes the system more complicated and less reliable [7]. Hence, it is especially necessary to use the active FTC method without adding redundant devices to quickly recover the operational performance of the system.

The existing research on active FTC mainly aimed at sensor faults in inverter system, as well as actuator failures and sensor faults in aerospace electromechanical system, and active FTC is greatly achieved by using SM control method [8–10]. At present, the fault-tolerant method for ANPC three-level inverter is to establish the FTC table under different fault modes through fault analysis [11], which is still passive FTC essentially. Therefore, more extensive and in-depth research on the active FTC for ANPC three-level inverter should be carried out.

Based on the existing topology and modulation strategy of ANPC three-level inverter, this paper designs a SM fault-tolerant controller and SVPWM fault-tolerant controller, and adjusts the output voltage control signal in real time by reconstructing the SM control law. Then, the SVPWM control strategy is adjusted to reconstruct the space vector sequence, which realizes the fast switching and reconstruction of FTC laws under different faults of power switches in single-phase bridge arm.

## 2 Active FTC Method of ANPC Three-Level Inverter

### 2.1 Mathematical Model of ANPC Three-Level Inverter

Each phase bridge arm of ANPC inverter with RL loads contains six power switches  $S_{x1} \sim S_{x6}$  and six antiparallel diodes  $VD_{x1} \sim VD_{x6}$  ( $x = a, b, c$ ). According to the topology, the switch states of the bridge arms can be divided into three types: “P”, “O”, and “N”.

By defining the state variable  $\mathbf{x}$  as a three-phase load current vector and the control input  $\mathbf{u}$  as a three-phase load voltage vector, state-space model can be obtained

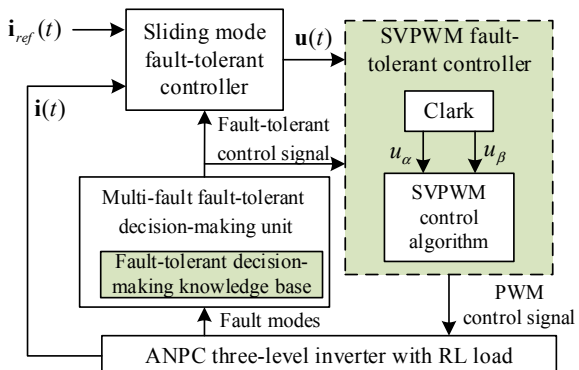
$$\begin{cases} \dot{\mathbf{x}} = \mathbf{Ax} + \mathbf{Bu} \\ \mathbf{y} = \mathbf{Cx} \end{cases} \quad (1)$$

where  $\mathbf{x} = [i_a \ i_b \ i_c]^T$ ,  $\mathbf{u} = [u_{an} \ u_{bn} \ u_{cn}]^T$ ,  $\mathbf{y} = [i_a \ i_b \ i_c]^T$ ,  $\mathbf{A} = \text{diag}(-R/L, -R/L, -R/L)$ ,  $\mathbf{B} = \text{diag}(L, L, L)$ ,  $\mathbf{C} = \text{diag}(1, 1, 1)$ .

## 2.2 Design of Active FTC System

The active fault-tolerant closed-loop control system is formed by adding a SM controller to the original inverter system, and then the input voltage signal of SVPWM fault-tolerant controller can follow the change of the load current in real time whether the device is faulty or not, which achieves the goal of fast tracking control. As shown in Fig. 1, the active FTC system mainly includes three parts: multi-fault fault-tolerant decision-making unit, SM fault-tolerant controller, and SVPWM fault-tolerant controller. The FTC idea is: Firstly, a knowledge base of fault-tolerant decision-making is established according to normal mode and various failure modes when the system is offline, which mainly includes the mapping tables of  $\theta_i \sim i$ ,  $\phi_i \sim i$ , where  $\theta_i$  represents the system output signals after fault,  $\phi_i$  represents SVPWM voltage vector set that cannot be output normally after fault, and  $i = 0, 1, 2, \dots$  corresponds to normal mode, failure mode 1, failure mode 2, ..., respectively. Secondly, the multi-fault fault-tolerant decision-making unit performs fault-tolerant switching control according to the system operation state (normal or certain fault mode) when the system is running. Finally, the active FTC in multiple fault modes can be implemented by outputting a control signal to the unit that needs to perform fault-tolerant reconstruction.

**Fig. 1** Structure diagram of active FTC



Consequently, there are two units in this system which need to be fault-tolerant reconstructed: SM fault-tolerant controller and SVPWM fault-tolerant controller.

### 3 Design of Sliding Mode Fault-Tolerant Controller

According to the fault characteristic signal and the state-space model after the fault, the SM control law and output voltage control signal are both reconstructed, and then the reference voltage is given for the adjustment of SVPWM FTC strategy.

#### 3.1 The Extraction of Fault Characteristic Signal

It can be known from the mathematical model of the inverter deduced in Sect. 2.1 that the open-circuit fault of a power switch in the inverter will change the working state of the system directly, thereby affecting the three-phase load voltage  $u_{xn}(x = a, b, c)$ . If a three-phase fault characteristic signal  $\mathbf{f}(t) = [f_a, f_b, f_c]^T$  is introduced, the state-space model of the inverter after the fault becomes

$$\begin{cases} \dot{\mathbf{x}} = \mathbf{Ax} + \mathbf{B}(\mathbf{u} + \mathbf{f}) \\ \mathbf{y} = \mathbf{Cx} \end{cases} \quad (2)$$

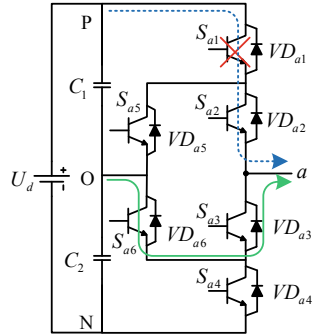
The fault characteristic signal must be considered in the design of SM fault-tolerant controller since the SM controller design is based on the state-space model of the inverter. In order to facilitate the design of the SM fault-tolerant controller, the following takes the open-circuit fault of the power switch  $S_{a1}$  as an example to study the extraction method of the fault characteristic signal in different fault modes.

As shown in Fig. 2, the current path from the inverter to the load indicated by the dotted line in the figure will be cut off due to the open-circuit fault of  $S_{a1}$ . On the other hand, the switch  $S_{a6}$  is turned on at this time, so the current forces the diode  $VD_{a3}$  to conduct, forming the current path shown by the solid line in the figure. Hence, the output terminal is at zero level; that is, the switch state of  $a$ -phase bridge arm after the fault changes from “P” to “O”. Therefore, the actual value of the output voltage of the fault phase will differ from the expected value since the switch state of the inverter does not match the actual situation.

In this fault mode, the difference between the output voltage of  $a$ -phase bridge arm after the fault ( $u'_{ao}$ ) and the output voltage before the fault ( $u_{ao}$ ) is

$$\Delta u_{ao} = u'_{ao} - u_{ao} = -U_d/2 \quad (3)$$

**Fig. 2** Current flow path after the fault



The difference between the output voltage of the non-fault phase (*b*- and *c*-phase) is

$$\begin{cases} \Delta u_{bo} = u'_{bo} - u_{bo} = 0 \\ \Delta u_{co} = u'_{bo} - u_{co} = 0 \end{cases} \quad (4)$$

From the above equation, the difference between the three-phase load voltage after and before the fault can be further obtained [4], which is

$$\Delta \mathbf{u} = \mathbf{u}' - \mathbf{u} = [-U_d/3 \quad U_d/6 \quad U_d/6]^T \quad (5)$$

It can be seen that  $\Delta \mathbf{u}$  of each phase is a periodic function in a fundamental frequency period, so it can be approximated as

$$\Delta \mathbf{u} = \begin{cases} [-U_d/3 \quad U_d/6 \quad U_d/6]^T, & nT < t \leq (2n+1)T/2 \\ [0 \quad 0 \quad 0]^T, & (2n+1)T/2 < t \leq (n+1)T \end{cases} \quad (6)$$

where  $n$  is a nonnegative integer and  $T$  is the fundamental period.

Perform Fourier transform on the difference signal of *a*-phase load voltage. If we ignore its DC component, it can be represented as follows according to its parity.

$$\Delta u_a(t) = -\frac{U_d}{3\pi k} \sum_{k=1}^{\infty} (1 - \cos k\pi) \sin k\omega t \quad (7)$$

The calculation process of *b*-phase and *c*-phase is similar. For the convenience of analysis, only three-phase fundamental frequency component is selected as the three-phase fault characteristic signal, and the geometric mean value is taken as its amplitude, which is  $F_m = \sqrt{(-2U_d/3\pi)^2 + (U_d/3\pi)^2 + (U_d/3\pi)^2} = \sqrt{6}U_d/3\pi$ . In this way, the three-phase fault characteristic signal can be expressed as

$$\begin{cases} f_a(t) = -(\sqrt{6}U_d/3\pi) \sin(\omega t) \\ f_b(t) = -(\sqrt{6}U_d/3\pi) \sin(\omega t - 2\pi/3) \\ f_c(t) = -(\sqrt{6}U_d/3\pi) \sin(\omega t + 2\pi/3) \end{cases} \quad (8)$$

The fault-tolerant reconstruction of SM controller can be designed based on  $\mathbf{f}(t)$ .

### 3.2 Fault-Tolerant Reconstruction of Sliding Mode Controller

In order to simplify the design of the SM controller, the parameters of the SM controller are transformed from abc coordinate system to dq dynamic coordinate system.

Based on the design principle of SM controller, the fault-tolerant reconstruction design process of SM controller is as follows.

#### (1) Construction of sliding surface

The SM control target is selected as the sliding surface, which is

$$\begin{cases} s_d = i_d - i_{d\_ref} \\ s_q = i_q - i_{q\_ref} \end{cases} \quad (9)$$

#### (2) Reconstruction of control law

SM index approach law  $\dot{s} = -\varepsilon \text{sgn}(s) - qs$ ,  $\varepsilon > 0, q > 0$  is selected to determine the SM control signal (control law), where  $\text{sgn}(\cdot)$  represents a symbolic function.

$$\begin{cases} u_d = -\varepsilon_d \text{sgn}(s_d) - q_d s_d - f_d \\ u_q = -\varepsilon_q \text{sgn}(s_q) - q_q s_q - f_q \end{cases} \quad (10)$$

#### (3) Adjustment of controller parameters

According to the defined Lyapunov function  $V = s^2/2$  and satisfying the reachability requirement  $\lim_{s \rightarrow 0} \dot{s}\dot{s} < 0$ , the sliding surface variation law can be obtained, which is

$$\begin{cases} \dot{s}_d = -(R s_d + \varepsilon_d \text{sgn}(s_d) + q_d s_d + f_d + R \dot{i}_{d\_ref} + L \ddot{i}_{d\_ref})/L \\ \dot{s}_q = -(R s_q + \varepsilon_q \text{sgn}(s_q) + q_q s_q + f_q + R \dot{i}_{q\_ref} + L \ddot{i}_{q\_ref})/L \end{cases} \quad (11)$$

Hence, the SM control parameters  $\varepsilon$  and  $q$  can be adjusted according to Eq. (12).

$$\begin{cases} \varepsilon_d = |Ri_{d\_ref} + L\dot{i}_{d\_ref} + f_d|, & q_d > 0 \\ \varepsilon_q = |Ri_{q\_ref} + L\dot{i}_{q\_ref} + f_q|, & q_q > 0 \end{cases} \quad (12)$$

### 3.3 Analysis of Voltage Output Control Performance

By performing coordinate transformation to  $\mathbf{f}(t)$  in Eq. (8), we can obtain

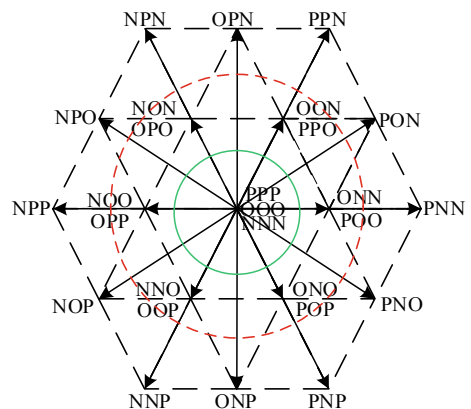
$$\begin{cases} f_d(t) = 0 \\ f_q(t) = \sqrt{6}U_d/3\pi \end{cases} \quad (13)$$

Then, the control laws after  $S_{a1}$  fault can be obtained from Eqs. (10) and (13):

$$\begin{cases} u_d = -e'_d \operatorname{sgn}(s_d) - q'_d s_d - 0 \\ u_q = -e'_q \operatorname{sgn}(s_q) - q'_q s_q - \sqrt{6} U_d / 3\pi \end{cases} \quad (14)$$

The control laws shown in Eq. (14) are control signal output to SVPWM fault-tolerant controller. We can see that the amplitude of the voltage control signal is reduced by  $\sqrt{6}U_d/3\pi$  after the fault. Therefore, the space vector distribution map of the voltage control signal shown in Fig. 3 can be obtained, wherein the dotted outer circle is the trajectory of the voltage control signal before the fault, and the solid inner circle is the trajectory of it after the fault. Obviously, the original SVPWM control strategy must be adjusted in real time to achieve FTC.

**Fig. 3** Space vector distribution map



## 4 Design of SVPWM Fault-Tolerant Controller

If an open-circuit fault occurs in a single power switch of ANPC three-level inverter, the corresponding fault-tolerant reconstruction control strategy is as follows:

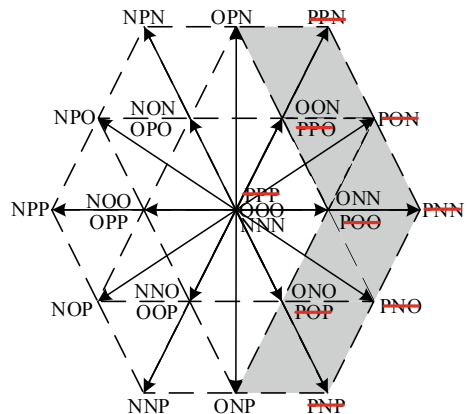
Step 1: The basic SVPWM control algorithm is used to determine the corresponding voltage space vector and its action time based on the voltage control signal.

Step 2: Voltage space vectors that cannot be output normally in the fault mode are determined by analyzing the mapping relationship of  $\phi_i \sim i$ , which are deleted in the space vector set generated by step 1. Then, new voltage space vector set is constructed on the basis of keeping output voltage and current still three-phase symmetrical.

Step 3: Based on new voltage space vector set, SVPWM algorithm is reconfigured and original seven-segment space vector sending sequence is adjusted to a five-segment vector sending sequence to generate PWM control signal. The action time and PWM signal distribution mode are the same as those in normal operation.

It is assumed that an open-circuit fault occurs in switch  $S_{a1}$ , and we can know that nine vectors cannot be output normally from fault-tolerant decision-making knowledge base. The corresponding space vector distribution is shown in Fig. 4. In order to ensure that the fundamental wave of output voltage is still sinusoidal, the reconstructed voltage space vector should be distributed in the small hexagonal region, which means that the inverter needs to operate at a reduced rate. Based on this, the original SVPWM algorithm is reconstructed to adjust the voltage space vector sending sequence, and then original seven-segment sequence is adjusted to five-segment sequence.

**Fig. 4** Space vector distribution after  $S_{a1}$  failure



## 5 Simulation Verification

In order to validate the effectiveness of the proposed active FTC strategy, this paper builds a closed-loop control model of ANPC three-level inverter based on SM on Simulink platform. Then, the open-loop redundant FTC model is built. Lastly, the fault-tolerant performance of the inverter in closed-loop and open-loop control modes is compared and analyzed. The simulation parameters are as follows: DC bus voltage is  $U_d = 1500$  V, switching frequency is  $f_s = 10$  kHz, RL loads are  $R = 15 \Omega$ ,  $L = 33$  mH, modulation ratio is  $m = 0.8$ , and parameters of SM controller are  $q_d = 1000$ ,  $q_q = 130$ .

### 5.1 Simulation Analysis of Active FTC

It is assumed that an open-circuit fault of  $S_{a1}$  occurs at  $t_f = 0.04$  s, and the simulation waveforms are shown in Fig. 5. It can be seen that the output waveforms are distorted as soon as the open-circuit fault occurs, and then the system is in faulty operation stage. After less than half of the fundamental frequency period, the system adjusts and gradually enters a new steady state through the action of the SM fault-tolerant controller and the SVPWM fault-tolerant controller, and then the system is in fault-tolerant operation stage. Meanwhile, it can be further found that the amplitude of the system output voltage and current signals are reduced to half of the original while the phase remains unchanged, which indicates that the inverter operates at a reduced rate under the action of active FTC strategy, so as to keep the signal three-phase symmetrical and achieve FTC. The result is consistent with the above theoretical analysis.

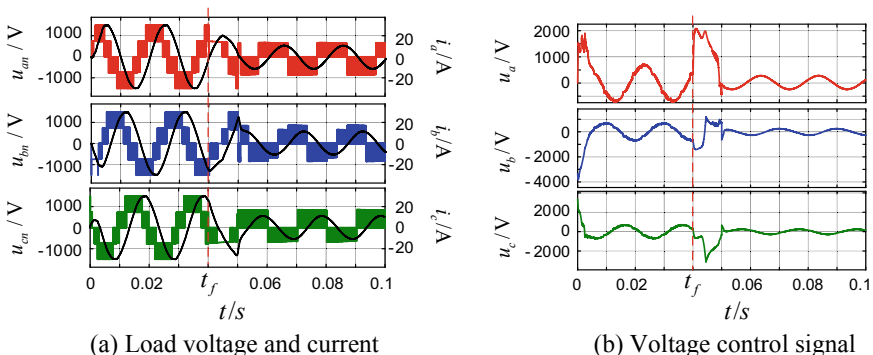


**Fig. 5** Simulation waveforms in the case of open-circuit fault of  $S_{a1}$

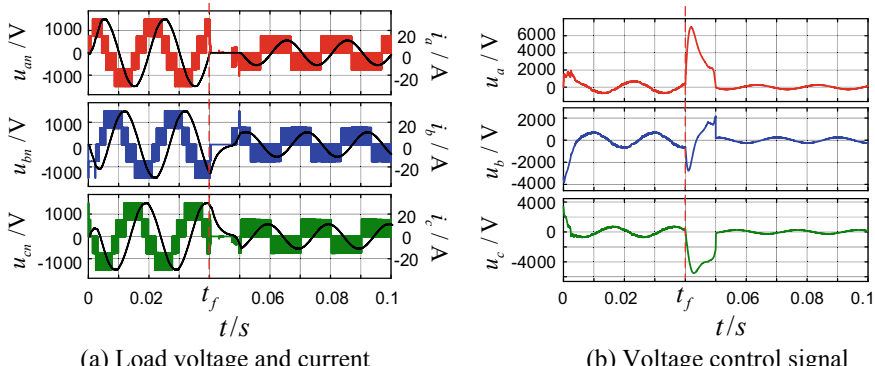


**Fig. 6** Simulation waveforms in the case of open-circuit fault of  $S_{a2}$

We assume that an open-circuit fault of  $S_{a2}$  occurs at  $t_f = 0.04$  s, and simulation waveforms are shown in Fig. 6. A similar analysis of Fig. 6 shows that the above active FTC strategy is also applicable to open-circuit fault of single-bridge arm inner tube.

## 5.2 Simulation Analysis of Fault Tolerance Performance

This section further builds an ANPC three-level inverter open-loop FTC model [12] and performs comparative analysis of FTC performance from the aspects of output waveform quality, FTC dynamic, and steady-state response performance.

FFT module is used to analyze the waveform quality of the load current signal. The total harmonic distortion (THD) is shown in Table 1. By comparison, THD of output current after closed-loop FTC remains at a low level, while THD of output current after open-loop FTC increases significantly. It can be seen that quality of waveform based on active FTC is obviously better than that under open-loop FTC.

**Table 1** FFT analysis results of load current

Open-circuit fault type	Output signal	THD (%) before fault		THD (%) after fault	
		Closed-loop	Open-loop	Closed-loop	Open-loop
$S_{a1}$	$a$ -phase current	1.08	1.45	1.75	2.85
$S_{a2}$	$a$ -phase current	1.08	1.45	1.92	2.46

**Fig. 7** Response curve under the fault of  $S_{a1}$

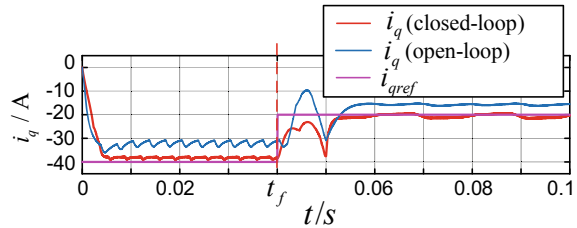


**Fig. 8** Response curve under the fault of  $S_{a2}$

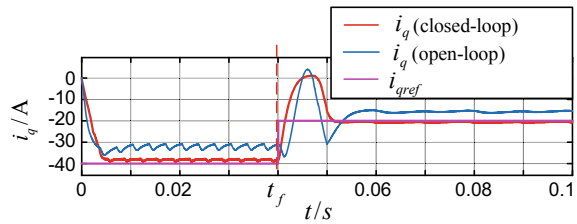


**Table 2** Dynamic and steady-state response indicators under two control modes

Open-circuit fault type	Rise time (s)		Adjustment time (s)		Steady-state error (%)	
	Closed-loop	Open-loop	Closed-loop	Open-loop	Closed-loop	Open-loop
$S_{a1}$	0.0016	0.0058	0.0029	0.0113	2.8	18.7
$S_{a2}$	0.0005	0.0078	0.0010	0.0105	1.12	17.5

The  $q$ -axis current output response curves are shown in Figs. 7 and 8, and the corresponding indicators are shown in Table 2. It can be seen from the graphs and table that the output current of closed-loop system can quickly switch to the new steady-state current, and in the steady-state operation stage, the steady-state error is kept in a small range. Compared with this, the rise time and adjustment time in open-loop FTC system are longer, and the steady-state error is also larger. Hence, the closed-loop active FTC strategy is obviously superior to the open-loop control mode.

## 6 Conclusion

An active FTC strategy of ANPC three-level inverter based on SM control is designed to realize the stable operation of the system under an open-circuit fault of a single switch. Simulation results show that the proposed control strategy is simple in principle, good in stability, and independent of other hardware and has great FTC performance.

## References

1. Hao Q, Feng XY (2014) Research on minimum switch loss modulation strategy of ANPC. *Electr Drive Locomotives* 04:24–27 (in Chinese)
2. Qin CW, Wang QJ, Chen Q et al (2014) Analysis of losses in three-level active clamped inverter based on numerical method. *Power Electron* 48(10):13–25 (in Chinese)
3. Hu KT, Liu ZG, Hu RR et al (2018) A novel model-based diagnosis for open-circuit fault in electric multiple unit traction inverter. *J China Railway Soc* 40(02):31–38 (in Chinese)
4. Zhu QY, Li GH, Wu Y et al (2017) Fault detection and identification for three-level inverter based on state observer. *J Power Supply* 15(5):87–93 (in Chinese)
5. Choi UM, Lee JS, Blaabjerg F et al (2016) Open-circuit fault diagnosis and fault-tolerant control for a grid-connected NPC inverter. *IEEE Trans Power Electron* 31(10):7234–7247
6. Xu S, Zhang J, Hang J (2017) Investigation of a fault-tolerant three-level t-type inverter system. *IEEE Trans Ind Appl* 53(05):4613–4623
7. Anderson VR, Sidelmo MS, Igor AP et al (2014) A new fault-tolerant realization of the active three-level NPC converter. In: ECCE, IEEE, America, pp 3483–3490
8. Liu C, Qian K, Li YH et al (2018) Integrated robust active fault tolerance controller design based on linear matrix inequality. *Control Decis* 33(01):53–59 (in Chinese)
9. Su XJ, Liu XX, Song YD (2018) Fault-tolerant control of multi-area power systems via sliding mode observer technique. *IEEE/ASME Trans Mechatron* 23(01):38–47
10. Shen Q, Yue CF, Goh C et al (2019) Active fault-tolerant control system design for spacecraft attitude maneuvers with actuator saturation and faults. *IEEE Trans Ind Electron* 66(5):3763–3772
11. Santos NMR, Pires VF, Silva JF (2014) Fault tolerant operation of active neutral point clamped multilevel converters using a voltage sliding mode controller. In: 16th International power electronics and motion control conference and exposition, IEEE, Turkey, pp 1072–1077
12. Feng WX, Zhang P, Wang Y et al (2017) Research on fault tolerant control of three-level ANPC converter under open-circuit fault. *Power Electron* 51(03):4–8 (in Chinese)

# A Survey: Learning-Based Energy Management Strategy for Heterogeneous Multi-energy Drive System



Xiaoyu Ren, Xinyue Zhang, Dangwei Duan, and Lijun Diao

**Abstract** The learning-based energy management strategy (EMS) is able to optimize the control of the heterogeneous multi-energy drive system (HMDS) by learning relevant offline data or online data and centralized training, and therefore realizes lower consumption and higher efficiency. Moreover, it is equally of great important for HMDS to select an appropriate drive structure as it is to develop a suitable energy management strategy. In this paper, domestic and overseas development situation of HMDS is discussed. Moreover, it describes the drive structure of the present HMDS and then introduces the research status of two learning-based EMS in HMDS. In addition, the actual implementation prospect and challenges of learning-based energy management strategy are proposed by further analysis.

**Keywords** EMS · HMDS · Neural network · Reinforcement learning · Deep reinforcement learning

## 1 Introduction

The advances in technology and increasing concerns on environmental issues are significantly promoting development of heterogeneous multi-energy drive system (HMDS) in recent years [1]. Nowadays, applications of HMDS have covered more and more fields such as hybrid electric vehicle (HEV), hybrid vessels, rail transport,

---

X. Ren · X. Zhang · L. Diao (✉)

School of Electrical Engineering, Beijing Jiaotong University, Beijing 100044, China  
e-mail: [ljdiao@bjtu.edu.cn](mailto:ljdiao@bjtu.edu.cn)

X. Ren  
e-mail: [18121485@bjtu.edu.cn](mailto:18121485@bjtu.edu.cn)

X. Zhang  
e-mail: [18121544@bjtu.edu.cn](mailto:18121544@bjtu.edu.cn)

D. Duan  
CRRC Changchun Railway Vehicles Co., Ltd., Changchun, Jilin 130062, China  
e-mail: [duandangwei@cccar.com.cn](mailto:duandangwei@cccar.com.cn)

and so on. Evolution from conventional single energy drive system (SEDS) to HMDS has made it possible to realize less consumption and higher efficiency to a considerable extent. As the vital technique of HMDS, the energy management strategy (EMS) has a significant impact on the overall efficiency [2]. The objective of energy management strategy (EMS) for HMDS is to achieve the reasonable energy distribution among various energy sources so as to minimize the energy consumption [3]. However, due to the complex nonlinearity and mutual coupling among the energy sources, it makes very difficult to design an adaptive EMS to optimize the global HMDS. The existing EMS methods can be generally classified into the following three categories [4]: (1) Rule-based strategies that rely on a set of predefined criteria and without a relevant priori knowledge [5]. Although rule-based strategies such as deterministic methods or fuzzy methods can be simple and easy to implement, it could not realize the optimization of the entire system operation [3, 4]. (2) Optimization-based strategies that are based on the known relevant or some predicted information. These strategies such as dynamic programming (DP) can achieve global optimization but it is time-consuming. Therefore, most of these methods are not able to be implemented in real time [6]. (3) Learning-based strategies that apply some intelligence algorithms into solving energy management problem. These control strategies can optimize the power split among the power sources while learning optimal decisions in real time from historical training cycles [7]. To the best of our knowledge, only some reinforcement learning (RL) algorithms and deep reinforcement learning (DRL) algorithms in intelligence algorithms have been implemented to attempt to management HMDS. As a potential and alternative EMS method, researches and explorations on learning-based EMS are of great significance.

## 2 Typical Types of HMDS and Its Structural Components

Before expounding the learning-based EMS, the composition of the present HMDS is briefly introduced. Up to now, the energy source system mainly involves in the following systems: engine-generator unit, fuel cell, battery (charge and discharge), ultra-capacitor, some clean energy sources such as solar or wind, and so on. The so-called HMDS is a combination of two or more the mentioned above energy sources. To change the current energy consumption structure and keep energy supply in the path of sustainable development [1], the power train of transportation facility is also being developed in the direction of HMDS. At present, the widely used HMDS is mainly based on diesel engine and equipped with auxiliary energy sources such as batteries and ultra-capacitors, which would make the engine always work in the high-efficiency zone so as to enhance the fuel efficiency and reduce the emission of harmful substances and mechanical vibration [8]. The HMDS composed of fuel cell and energy storage device (ESD) cannot only make up for the lack of dynamic response of fuel cell, but also decrease the loss of fuel cell and extend its

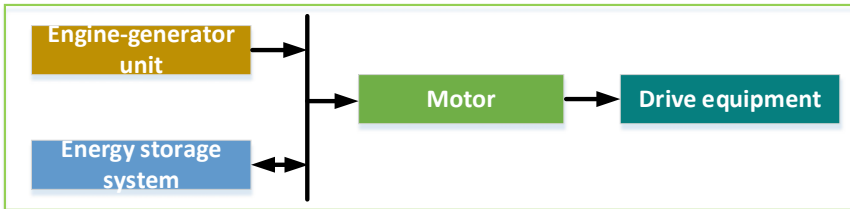


**Fig. 1** Serial structure of HEV

lifetime [7, 9]. Furthermore, combining clean energy sources with the engine has also been gradually applied in vessels, which can achieve energy saving to a certain extent [10].

Whether it is HEV, hybrid vessels, and hybrid locomotive, the power structure of the whole energy system can be roughly divided into three categories: series structure, parallel structure, and hybrid structure [8, 11]. The three power structures of HEV are herein employed to analyze the operation mode of HMDS. For series HEV, the diesel engine is the main power source of the whole vehicle, and battery and other energy storage devices are the auxiliary energy sources. Since the engine is not directly connected to the driving equipment, engine-generator unit and energy storage system can independently drive the motor to provide mechanical energy to the vehicle. Due to simple configuration, the series structure offers more flexibility to system components placement but its energy loss is larger. Serial structure of HEV is depicted in Fig. 1. (The direction of the arrow is the direction of the energy flow).

For parallel HEV, the engine and the motor are connected by coupling devices. The coupling devices which are directly connected with the driving equipment make it possible for them to jointly or independently drive the vehicle. Although the mechanical system of parallel HEV is relatively complex, its energy utilization rate is higher. Reference [11] introduced five configuration schemes of parallel HEV in detail. The typical configuration of parallel HEV is depicted in Fig. 2. Engine driving mode, electric driving mode, and hybrid driving mode are the main three working modes. As for hybrid HEV, their configurations vary from the different

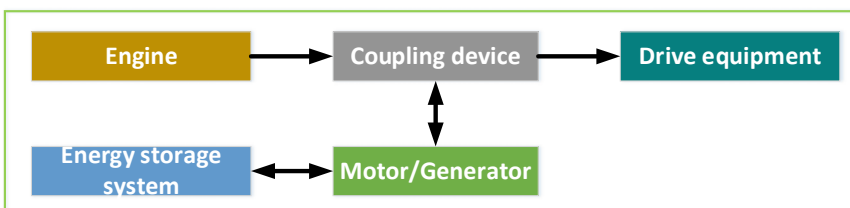


**Fig. 2** Parallel structure of HEV

dynamic coupling configurations. Combined with the characteristics of series and parallel driving pattern, it is easier for hybrid structure to make the whole system work in the high-efficiency area.

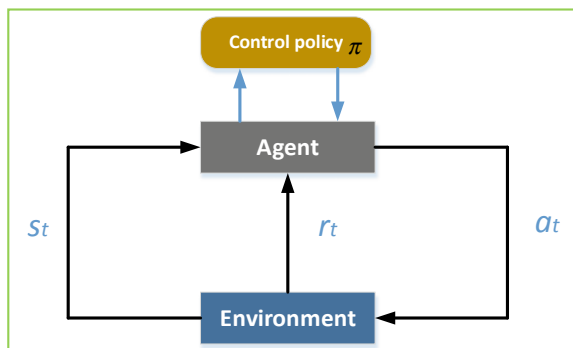
For the HMDS composed by other energy sources such as batteries and ultra-capacitors, or engines and energy storage devices as well as the clean energy source, its drive structure and working mode in practical application are roughly similar to the above three drive structures of HEV.

### 3 Energy Management Strategy Based on Reinforcement Learning

To some extent, the energy management problem of HMDS is actually an optimization problem subjecting to necessary constraints [3]. Meanwhile, it is essentially regarded as the optimal control problem of a dynamic system. Reinforcement learning (RL) algorithms in intelligent algorithms are always implemented to address this optimal control problem. RL is originated from approximate dynamic programming and is designed for incrementally learning optimal control strategy that can maximize a reward function [12]. In a standard reinforcement learning (RL) setup, a learning agent and the environment are two key elements where the agent interacts with the environment in a discretized time space. The concrete RL framework is depicted in Fig. 3.

For HMDS EMS, the EMS represents the environment and the HMDS, as a “decision maker,” is represented by the agent (decision maker) since it generates action on the EMS (input) [7]. Consequently, the HMDS moves to another state. An immediate reward is fed back to the agent (HMDS). The current and previous observations that are used to determine the next action are used to update and form a control policy that maps the current state to an optimal control action [12]. For learning-based EMS, whether adopting EMS based on RL algorithms or EMS based on the following deep reinforcement learning (DRL) algorithms, optimization and control of the whole system is realized by selecting the state variables and

**Fig. 3** RL Framework



action variables of HMDS. Therefore, the selection of different state variables, action variables, and setting different objective functions would have a significant impact on the control effect of the whole system.

In RL, the Q-learning algorithm is widely used. In Ref. [2], connecting Q-learning algorithm with the vehicle speed and position obtained by GPS optimized the output torque of the motor in parallel HEV so as to achieve the purpose of energy saving. Meantime, the experimental results revealed that the Q-learning algorithm was unstable in updating the action-value function in real time. In Ref. [13], a method of combining the reinforcement learning algorithm with the whole vehicle travel distance obtained by GPS was put forward to optimize the management of the oil-electric system in plug-in hybrid vehicle. Compared with the traditional rule-based EMS, the proposed EMS produced relatively larger loss but it has a great advantage in maintaining the SOC balance of the battery. In Ref. [14], Q-learning algorithm and neural dynamic programming method were combined to realize the convergence on fixed or random short-distance routes in HEV and then obtained the optimization strategy. In Ref. [3], two velocity prediction methods for hybrid electric vehicles were proposed, which no longer relied on GPS to obtain the driving speed of the vehicle, and a finite Markov chain was used to discretely represent the real-time power of HEV. The results demonstrated that the EMS based on RL was able to significantly reduce fuel consumption and computational time. In Ref. [15], Pontryagin's minimum principle (PMP) was used to obtain the analytical solution of the energy management problem, and this can help to reduce the iteration time in RL process. In Ref. [7], taking the integral mean square root of battery current in the whole travel time as the objective function with the limitation of the upper and lower limits of the voltage and current of the ultra-capacitor and battery, the RL algorithm was used to control the HMDS in real time only by sampling the battery current. In Ref. [10], an EMS based on the reinforcement learning framework in HMDS composed of solar energy, battery, and engine was proposed, which mainly aimed to keep the SOC of auxiliary battery at a low level and minimize the engine operation in order to reduce fuel consumption. Reference [16] proposed EMS-based RL that could online optimize the energy system of hybrid parallel tracked vehicles under various working conditions.

The stability of RL algorithm also depends on the selection of immediate reward function to some extent. For the HMDS composed of engine and energy storage device, the immediate reward function is always defined as a function of fuel consumption. For other energy storage devices or clean energy systems, different immediate reward functions are set according to the defined objective function, which is not discussed in detail here. Linear function is often used in reinforcement learning to approximate the action-value function. However, the energy management problem of HMDS is a nonlinear problem so that it is sometimes difficult to make the algorithm converge in the training only by using reinforcement learning algorithm, and instability may occur.

## 4 Energy Management Strategy Based on Deep Reinforcement Learning

The recently proposed deep reinforcement learning (DRL) algorithms have been successfully applied to autonomous driving, robot control, and other fields. DRL is an algorithm combining deep neural network and reinforcement learning. When applied to the energy management of HMDS, the Q-learning algorithm itself has great limitations on the dimension of state variables and action variables. Too many dimensions of state and action can cause RL algorithms to produce curse of dimensionality [17]. DRL can avoid curse of dimensionality to a large extent by using the deep neural network and solve the problem of data correlation by using experience replay method. At present, the deep Q-network (DQN) algorithm [18] is used by many scholars to deal with energy management problems of HMDS. In Ref. [17], for parallel HEV, the engine torque was taken as the action variable and then was discretized. The immediate reward function was defined as the function of fuel consumption and battery SOC, and the four-layer neural network was applied to approximate the action-value Q function. The experimental results showed that the EMS based on DQN generated 6% more fuel consumption than the EMS based on dynamic programming but maintained the battery's SOC balance better. In Ref. [19], the EMS based on DQN was proposed to maintain the SOC of each battery pack of electric vehicle, thus prevented the battery from aging in advance and improved its service life. As with reinforcement learning, the setting of immediate reward function in DRL is very important. Reference [12] pointed out that the immediate reward function should be constructed according to the objective function. The EMS is based on DQN in the study that the minimum cumulative power consumption of the whole HEV engine was taken as the objective function, and based on this objective function, a reward function of power was constructed. After comparing with the EMS based on Q-learning and the rule-based EMS, The designed EMS based on DQN first consumed battery energy and reduced fuel consumption compared with the other two strategies under the same conditions. One of the defects of DQN algorithm is that it can only control discrete actions. The EMS based on DQN proposed in Ref. [4] took the engine output torque as the control action, and the output torque of the engine is discretized into 24 equal parts.

In order to control the continuous action space, Ref. [20] introduced a method based on deep deterministic policy gradient (DDPG). On this basis, Ref. [21] applied DDPG algorithm to high-speed train control. Through a long period of training, it enabled high-speed trains to conduct automatic traction and braking so as to reduce system energy loss. In Ref. [22], two energy management strategies based on DQN and DDPG were applied to the energy system of parallel HEV. UDDS and NEDC in advanced vehicle simulator (ADVISOR) in MATLAB were used to simulate the offline and online training of the two strategies. The results indicated that the fuel consumption of EMS based on DDPG is approximately equal to EMS based on DQN. But engine fuel consumption fell 9 percent compared with the rules-based EMS. It also showed that the network trained offline had better

adaptability and better control effect in online test. The DDPG algorithm is more complex than DQN algorithm in algorithm structure, but it is more suitable for the control of continuous variables. For the EMS of HMDS, the structure of EMS based on DQN becomes more complex due to the introduction of neural network. The quality of its control strategy no longer only depends on the selection of state variables, action variables, and the design of immediate reward function. The types of neural network, the number of layers, and the setting of activation function would have an impact on the control effect to some extent.

## 5 Prospect and Conclusion

The successful application of HMDS in HEV, vessels, or locomotives, on the one hand, improves the operational flexibility and safety of transportation facilities; on the other hand, it greatly reduces the emission of pollutants and energy consumption so that it improves the energy utilization efficiency [23, 24]. However, real-time and efficient energy management for HMDS is still an enormous challenge on account of HMDS structure and complex operating conditions. As a new and potential EMS, learning-based EMS is the future development direction of energy management in HMDS. It is also realized that it is difficult to implement learning-based EMS on hardware at present because it needs to store huge parameters of deep neural network and sufficient data for training. In addition, the stability of the intelligent algorithm is affected by many other factors, so that the learning-based EMS is still far from the actual application. Learning-based EMS has gained attention and research in the field of hybrid electric vehicles and locomotives and will be involved in many fields such as hybrid ships in the future. In this paper, the drive structure and working mode of HMDS were analyzed. The research status of EMS based on RL and DRL were introduced. In the final, the challenges in the current practical application of learning-based EMS are briefly described and its application to hybrid vessels and other fields is prospected.

**Acknowledgements** This work is supported by National Key R&D Program of China, No. 2017YFB1201003, Basic Research, No. JCKY2018110C113.

## References

1. Gao LM, Zeng J, Wu J et al (2009) Cooperative reinforcement learning algorithm to distributed power system based on multi-agent. In: 2009 3rd International conference on Power Electronics Systems and Applications PESA, IEEE
2. Song C, Fang Y, Xia B (2015) An energy management strategy for hybrid electric bus based on reinforcement learning. In: Control & Decision Conference, IEEE
3. Liu T, Hu X, Li SE et al (2017) Reinforcement learning optimized look-ahead energy management of a parallel hybrid electric vehicle. IEEE/ASME Trans Mechatron 99:1497–1507

4. Hu Y, Li W, Xu K et al (2018) Energy management strategy for a hybrid electric vehicle based on deep reinforcement learning. *Appl Sci* 8(2):187, 1–15
5. Wu G, Boriboonsomsin K, Barth MJ (2014) Development and evaluation of an intelligent energy-management strategy for plug-in hybrid electric vehicles. *IEEE Trans Int Transp Sys* 15(3):1091–1100
6. Hosseini SM, Majdabadi MM, Azad NL et al (2018) Intelligent energy management of vehicular solar idle reduction systems with reinforcement learning, pp 1–6
7. Abdelhedi R, Lahyani A, Ammari AC et al (2018) Reinforcement learning-based power sharing between batteries and supercapacitors in electric vehicles, pp 1–6
8. Peng D, Zhu L, Han J (2014) Simulation of energy management strategy for fuel cell/battery hybrid ship. *J Sys Simul* 26(11):2797–2802 (in Chinese)
9. Zhu L, Han J, Peng D et al Fuzzy logic based energy management strategy for a fuel cell/battery/ultra-capacitor hybrid ship. In: 2014 International conference on green energy, IEEE
10. Liu H, Xu Y, Pang Y (2016) Research on hybrid energy storage system and its controller in rolling solar ship. In: Power electron motion control conference, IEEE
11. He R, LI J (2018) Survey on power coupling system and energy management strategy for hybrid electric vehicles. 32(10):7–22 (in Chinese)
12. Qi X, Luo Y, Wu G et al (2017) Deep reinforcement learning-based vehicle energy efficiency autonomous learning system. In: 2017 IEEE Intelligent vehicles symposium (IV). Papers (3), pp 1228–1233
13. Liu C, Murphrey YL (2014) Power management for plug-in hybrid electric vehicles using reinforcement learning with trip information. In: 2014 IEEE Transportation Electrification Conference and Expo (ITEC), IEEE
14. Liu C, Murphrey YL (2017) Analytical greedy control and q-learning for optimal power management of plug-in hybrid electric vehicles. In: 2017 IEEE Symposium Series on Computational Intelligence (SSCI), IEEE
15. Zhu Q, Wang QF (2017) Real-time energy management controller design for a hybrid excavator using reinforcement learning. *J Zhejiang Univ Sci A: Appl Phys Eng* 18(11):855–870
16. Liu T, Zou Y, Liu D et al (2015) Reinforcement learning of adaptive energy management with transition probability for a hybrid electric tracked vehicle. *IEEE Trans Ind Electron* 62 (12):7837–7846
17. Song C, Lee H, Kim K et al (2018) A power management strategy for parallel PHEV using deep q-networks, pp 1–5
18. Mnih V, Kavukcuoglu K, Silver D et al (2013) Playing atari with deep reinforcement learning. *Comput Sci*
19. Chaoui H, Gualous H, Boulon L et al (2018) Deep reinforcement learning energy management system for multiple battery based electric vehicles, pp 1–6
20. Lillicrap TP, Hunt JJ, Pritzel A et al (2017) Continuous control with deep reinforcement learning
21. Zhou R, Song S (2018) Optimal automatic train operation via deep reinforcement learning. In: 2018 Tenth International Conference on Advanced Computational Intelligence (ICACI), pp 103–108
22. Hu Y (2018) Research on control system design and energy management strategy of hybrid electric vehicle, pp 1–86 (in Chinese)
23. Zhang Y, Li C, Zhu J (2018) Overview of power plant and energy management of hybrid ship, pp 1–7 (in Chinese)
24. Wirasingha SG, Emadi A (2011) Classification and review of control strategies for plug-in hybrid electric vehicles. *IEEE Trans Veh Technol* 60(1)

# Feed-Forward Compensation Strategy for Suppressing Beat Phenomenon in Railway Traction System



Xueyan Ma, Dongyi Meng, Yaru Xue and Lijun Diao

**Abstract** Due to the characteristics of single-phase converter in the high-speed railway electrical drive system, the fluctuation output of traction inverter will have a terrible effect on the motor control performance, which is beat phenomenon. Furthermore, with traditional modulation, low switching frequency leads to more harmonic at the frequency causing most severe beat phenomenon. The paper proposes a compensation strategy to suppress fluctuation component with the specific harmonic elimination modulation. It gains the accurate DC link voltage using the prediction strategy. The feed-forward compensation is used to correct pulse width and then calculate the switching angles of SHEPWM. The simulation results show that the compensation strategy results in remarkable drops in both current harmonic and torque ripple of motor.

**Keywords** Beat phenomenon · Predictive control · Feed-forward compensation · SHEPWM

## 1 Introduction

The configuration of a single-phase AC–DC converter has been widely applied in high-speed railway electrical drive systems. To maintain the power conservation, the output power of converter pulsates at twice the grid frequency. It leads to waveforms distortion of stator current and electromagnetic torque. Besides, the influence aggravates vibration, noise, and power loss.

In general, a LC filter device installed on the DC link is used to absorb fluctuating power. However, its large volume is bad for power density of system. Reference [1] proposed an approach to increase the DC-side capacitor. But the bulk capacitor leads a security risk. References [2, 3] proposed a new circuit topology of

---

X. Ma · D. Meng · Y. Xue · L. Diao (✉)

School of Electrical Engineering, Beijing Jiaotong University, Beijing 100044, China  
e-mail: [ljdiao@bjtu.edu.cn](mailto:ljdiao@bjtu.edu.cn)

rectifier. In addition to the limitations of the input voltage and the difficulty of changing the topology, it has a significant effect.

References [4–7] are aimed at optimizing control strategy of traction inverter. The feed-forward compensation has advantage on simple principle and easy realization. In [8, 9], feed-forward compensation with prediction control has been proposed. However, SHEPWM is applied to suppress harmonic in high frequency range. These strategies do not target to SHEPWM. The strategy in [10] is complex and needs high sample frequency. Therefore, the target is searching an easily implementable and reliable approach to suppress beat phenomenon in SHEPWM.

## 2 Problem Description

### 2.1 Beat Phenomenon

The AC–DC–AC topology of traction drive system is shown in Fig. 1. Based on the pulse-width modulation theory, the switching function is expressed as

$$\begin{aligned} \begin{pmatrix} S_a(t) \\ S_b(t) \\ S_c(t) \end{pmatrix} &= \begin{pmatrix} u_a^*(t) \\ u_b^*(t) \\ u_c^*(t) \end{pmatrix} \frac{1}{U_{dc}/2} = \begin{pmatrix} U_m \sin \omega_0 t \\ U_m \sin(\omega_0 t - 2\pi/3) \\ U_m \sin(a_0 t + 2\pi/3) \end{pmatrix} \\ \frac{1}{U_{dc}/2} &= \begin{pmatrix} m \sin \omega_0 t \\ m \sin(\omega_0 t - 2\pi/3) \\ m \sin(\omega_0 t + 2\pi/3) \end{pmatrix} \end{aligned} \quad (1)$$

where  $m = U_m/(U_{dc}/2)$ .

The frequency of main ripple  $\omega_r$  is twice of grid frequency. The output of A phase is shown as

$$\begin{aligned} u_a(t) &= S_a \frac{u_{dc}(t)}{2} = m \sin \omega_0 t \cdot \frac{U_{dc} + U_r \sin(\omega_r t + \theta_r)}{2} \\ &= m \frac{U_{dc}}{2} \sin \omega_0 t - m \frac{U_r}{2} \{ \cos[(\omega_0 + \omega_r)t + \theta_r] - \cos[(\omega_0 - \omega_r)t - \theta_r] \} \end{aligned} \quad (2)$$

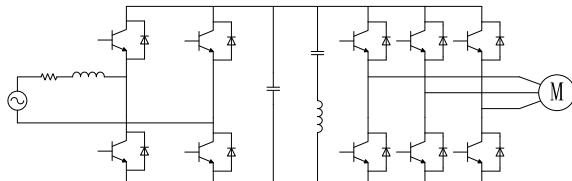


**Fig. 1** AC–DC–AC topology for railway traction system

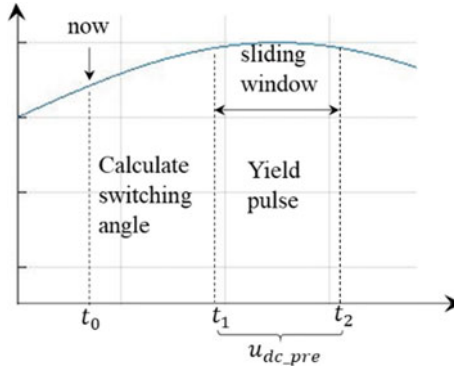


**Fig. 2** Sliding window

The actual DC link voltage  $u_{dc}(t)$  is

$$u_{dc}(t) = U_{dc} + U_r \sin(\omega_r t + \theta_r). \quad (3)$$

As shown in (2), when  $\omega_0$  is in close proximity to  $\omega_r$ ,  $\omega_0 - \omega_r$  approximates zero. In this case, quite small amplitude of beat component can induce severe beat phenomenon. Suppose grid frequency is 50 Hz, the waveform distortion and power loss of motor are severe when  $\omega_0$  is 100 Hz.

$$\begin{pmatrix} S_a(t) \\ S_b(t) \\ S_c(t) \end{pmatrix} = \begin{pmatrix} u_a^*(t) \\ u_b^*(t) \\ u_c^*(t) \end{pmatrix} \frac{1}{U_{dc}/2} = \begin{pmatrix} U_m \sin \omega_0 t \\ U_m \sin(\omega_0 t - 2\pi/3) \\ U_m \sin(\omega_0 t + 2\pi/3) \end{pmatrix} \quad (4)$$

$$\frac{1}{U_{dc}/2} = \begin{pmatrix} m \sin \omega_0 t \\ m \sin(\omega_0 t - 2\pi/3) \\ m \sin(\omega_0 t + 2\pi/3) \end{pmatrix}$$

## 2.2 Feed-Forward Compensation and Its Difficulty

The basic idea of feed-forward compensation is illustrated as follows. In order to relieve the beat phenomenon, modulation depth is determined by the sampling DC voltage  $u_{dc\_s}$ . The corrected modulation depth  $m'$  is

$$m' = m \frac{U_{dc}}{u_{dc\_s}(t)} \quad (5)$$

Substituting (5) into (2), output  $u_a(t)$  is obtained in (6):

$$u_a(t) = S_a \frac{u_{dc}(t)}{2} = m' \sin \omega_0 t \cdot \frac{u_{dc}(t)}{2} = m \frac{U_{dc}}{u_{dc\_s}(t)} \sin \omega_0 t \cdot \frac{u_{dc}(t)}{2} \quad (6)$$

If  $u_{dc\_s}(t) = u_{dc}(t)$ ,  $u_a(t) = u_a^*(t)$ . There is no beat component in the corrected output voltage. In practice, we calculate modulation depth one period ahead to guarantee the correctness of the PWM wave. These reasons lead to error between the sampling DC voltage  $u_{dc\_s}(t)$  and the actual DC voltage  $u_{dc}(t)$ . So  $u_{dc\_s}(t) \neq u_{dc}(t)$  and  $u_a(t) \neq u_a^*(t)$ . Furthermore, low switching frequency of traction drive system and discrete digitizing aggravate the problem above. These can take away from the effect of feedforward. Subsequent paragraphs, however, are indented.

### 3 Control Strategy Description

Owing to the reasons above, predicting the DC voltage is an effective approach to correct the lag. The control diagram of the repetitive prediction proposed in [8] is shown as follow (Fig. 3).

In this paper, the algorithm frequency is set at 1 kHz and the sampling frequency of DC link voltage is set at 10 kHz. Therefore,  $N_c$  is 10 and  $N_r$  is 100.  $u_{dc\_pre}$  is the predicting value. A sliding window whose length is one algorithm period is used to storage  $u_{dc\_pre}$  as shown in Fig. 2.  $u_{dav\_pre}$  is the periodic average of the value in A sliding window. It replaces  $u_{dc\_s}$  in (5) and gets the formula shown as follows.  $u_{dav\_pre}$  is close to the actual DC voltage when the pulse yields. So  $m''$  calculated by (7) is more accurate.

$$m'' = m \frac{U_{dc}}{u_{dav\_pre}} \quad (7)$$

The strategy works effectively in canceling the delay caused by zero-order hold and one period ahead requirement.

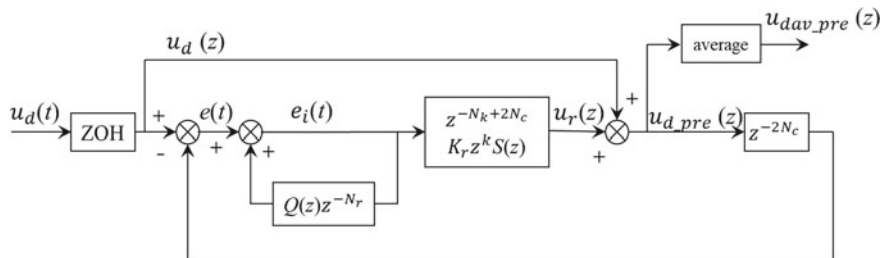


**Fig. 3** Repetitive predictive control diagram [8]

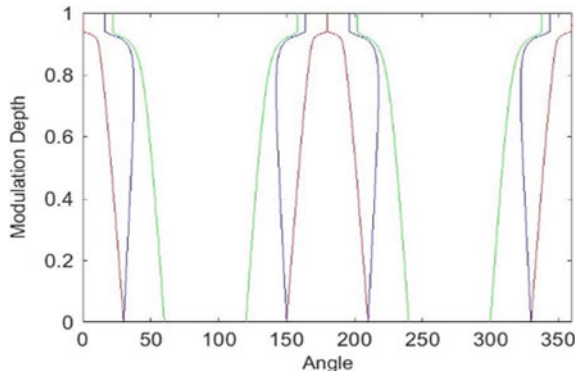


**Fig. 4** Critical angle values versus modulation depth (three critical angles)

SHEPWM can get rid of specified harmonics at the low switching frequency [11]. However, it is complex to obtain the switch angles. Look-up is taken into use generally. It cannot guarantee the continuity of data. Considering the continuity and the difficulty of data storage, this paper adopts the fitting curve to calculate the angles. The curve as shown in Fig. 4 is smooth except to the section in high modulation depth. The section every SHEPWM modes working is so short that the curvature is small. Therefore, fitting polynomial in a low degree can achieve good effect.

$$\text{Angle7\_2} = -10.88 \cdot m^4 + 26.63 \cdot m^3 - 24.55 \cdot m^2 + 10.25 \cdot m - 1.013 \quad (8)$$

Equation (8), which is obtained by the fitting tool in MATLAB, describes the angle shown in Fig. 5 in radian measure. According to analysis above, modulation depth is determined by  $u_{\text{dav\_pre}}$ . We obtain accurate switching angles depending on this modulation depth. The feed-forward compensation achieves better effect and beat phenomenon is suppressed.

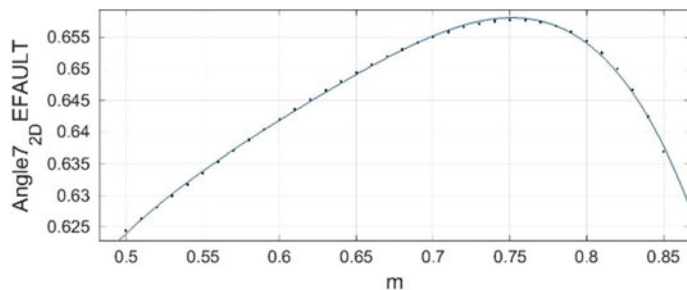


**Fig. 5** Fitting curve about the blue curve in Fig. 4

## 4 Simulation Results

In order to verify the effectiveness of the strategy, a model is established using Simulink. The parameters of the motor are shown in Table 1 and the simulation parameters are set as follows: the simulation is the fixed step and the simulation step is 10  $\mu$ s. The frequency of sampling DC voltage and algorithm is 10 and 1 kHz. Target torque is 1000 N m and load torque is 0 N m.

### 4.1 Contrast of Result

To highlight the control effect, a 1650 V DC source superimposing 50 V/100 Hz AC source supplies power to the inverter. The comparison of the control with feed-forward compensation and without the compensation is shown as follows. Compared with Fig. 6a, the stator current includes more low frequency harmonic and the torque has larger fluctuation range in Fig. 6b around 100 Hz frequency.

The beat phenomenon is most serious at 100 Hz. In theory, beat component mainly yields 0 Hz harmonics in stator current and 100 Hz harmonics in torque. From Fig. 7, the harmonic components of the stator current and output torque around 100 Hz decrease with the strategy in 3. Figures 8 and 9 show the Fourier

**Table 1** Motor parameters

Rated voltage: 1287 V	Stator resistance: 0.223 $\Omega$
Rated power: 160 kW	Rotor resistance: 0.103 $\Omega$
Rated frequency: 84 Hz	Mutual inductance: 43.8 mH
Number of pole pairs: 2	The leakage inductance of stator: 1.58 mH
Inertia: 5 kg m <sup>2</sup>	The leakage inductance of rotor: 2.076 mH

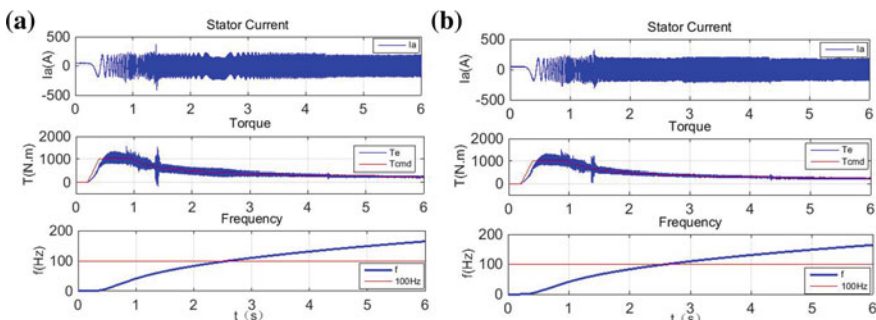


**Fig. 6** Stator current, torque, and frequency **a** without feed-forward compensation and repeat prediction, **b** with feed-forward compensation and repeat prediction

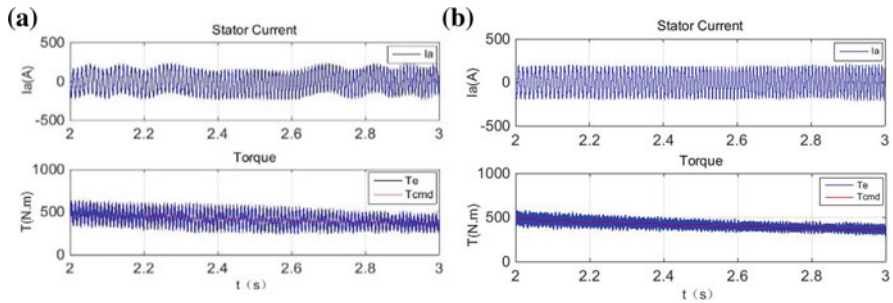


**Fig. 7** Magnification of Fig. 6 around 100 Hz **a** without feed-forward compensation and repeat prediction, **b** with feed-forward compensation and repeat prediction

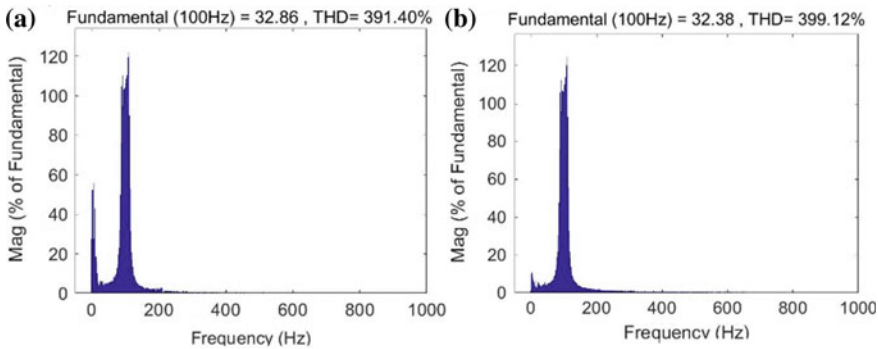


**Fig. 8** Fourier analysis for the stator current in Fig. 7 **a** without feed-forward compensation and repeat prediction, **b** with feed-forward compensation and repeat prediction

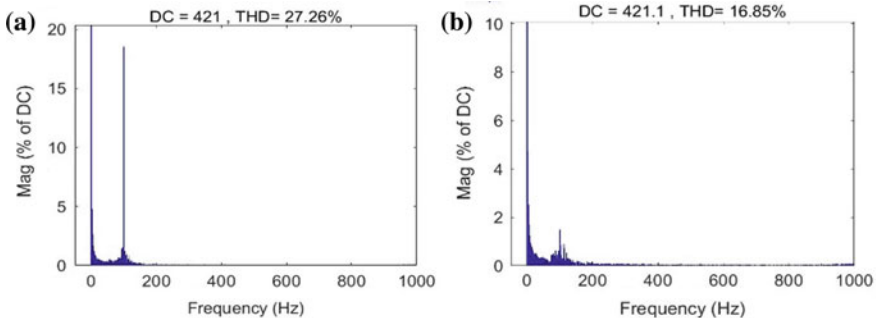


**Fig. 9** Fourier analysis for the torque in Fig. 7 **a** without feed-forward compensation and repeat prediction, **b** with feed-forward compensation and repeat prediction

**Fig. 10** Stator current, torque, and frequency with compensation (fluctuating frequency)

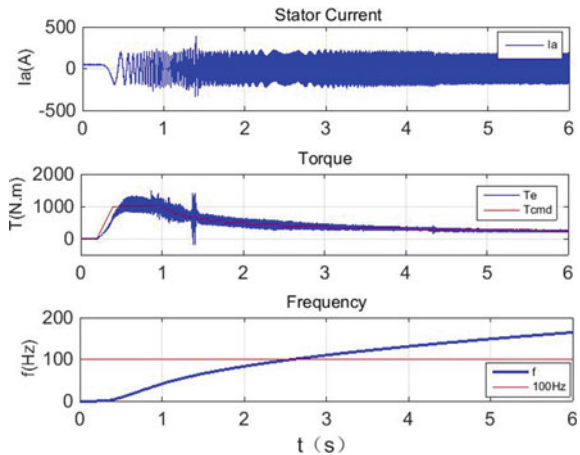
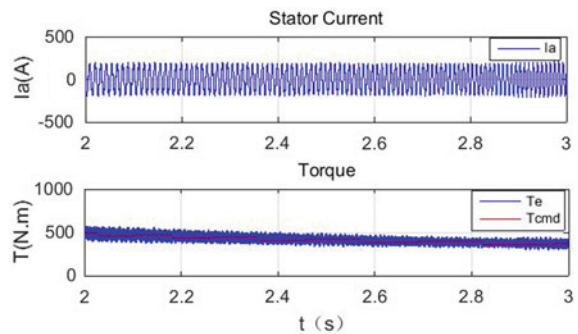


**Fig. 11** Magnification of Fig. 10 around 100 Hz



analysis of the wave in Fig. 7. The 0 Hz harmonic in current and the 100 Hz harmonic in torque decrease significantly. The result verifies a great effect of the strategy.

#### 4.2 Simulation with Fluctuating Frequency

In practice, the converter takes in power from the grid whose frequency fluctuates. To verify the stability of the strategy, the converter, whose input fluctuates in a range from 49.5 to 50.5 Hz, replaces the DC voltage source above. Figure 12, which shows the Fourier analysis of Fig. 11, reveals that the 0 Hz harmonic in current and the 100 Hz harmonic in torque dramatically reduce. The strategy has a good control effect when the frequency fluctuates.

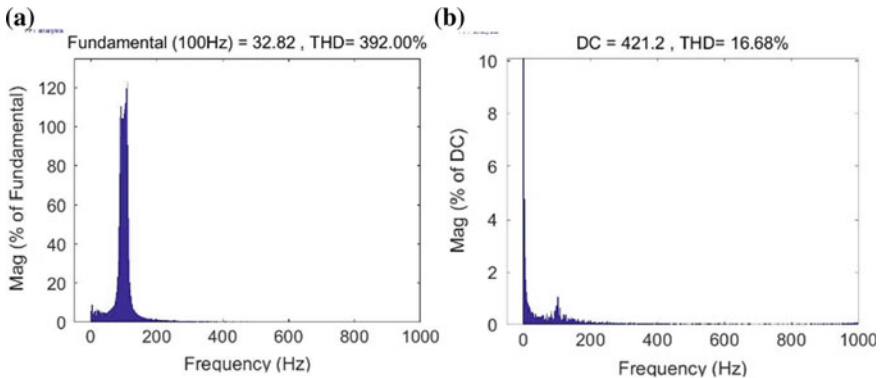


**Fig. 12** **a** Fourier analysis for the stator current and **b** Fourier analysis for the torque in Fig. 11

## 5 Conclusion

The paper described a strategy that aims to suppress beat phenomenon when SHEPWM is taken into use. We established the simulation model of circuit topology and implemented the control algorithm. It is proven that this strategy implemented the function that suppressed harmonic caused by beat component.

## References

1. Dahler P, Knapp G, Nold A (2005) New generation of compact low voltage IGBT converter for traction applications. In: 2005 European conference on power electronics and applications, Dresden, pp 1–9
2. Qi W (2014) Researches on power decoupling problem of single-phase converter. Shandong University, Jinan, China (in Chinese)
3. Jin Y, Shimizu T, Kimura G (1998) DC ripple current reduction on a single phase PWM voltage source converter. In: IECON '98. Proceedings of the 24th annual conference of the IEEE Industrial Electronics Society, vol 1. Aachen, Germany, pp 525–530
4. Maheshwari R, Munk-Nielsen S, Lu K (2013) An active damping technique for small DC-link capacitor based drive system. *IEEE Trans Ind Informatics* 9(2):848–858
5. Dong K (2015) Research on key control techniques and performance optimization of traction drive system for EMUs. Beijing Jiaotong University, Beijing, China (in Chinese)
6. Liu Z (2016) Research on beat-less control with multi-mode PWM method. Beijing Jiaotong University, Beijing, China (in Chinese)
7. Diao LJ, Dong K, Yin SB (2016) Ripple analysis and control of electric multiple unit traction drives under a fluctuating DC link voltage. *J Power Electron* 16(5):1851–1860
8. Ouyang H, Zhang K, Zhang P, Kang Y, Xiong J (2011) Repetitive compensation of fluctuating DC link voltage for railway traction drives. *IEEE Trans Power Electron* 26(8): 2160–2171

9. Funabiki S, Sawada Y (1988) A computative decision of pulse width in three-phase PWM inverter. In: Conference record of the 1988 IEEE Industry Applications Society Annual Meeting, vol 1. Pittsburgh, PA, USA, pp 694–699
10. Zhao SF, Huang XY, Fang YT (2019) DC-link voltage fluctuation compensation for selected harmonics elimination under low switching frequency. *J Zhejiang Univ (Eng Sci)* 53(02): 187–197 (in Chinese)
11. Zhang YC, Zhao ZM, Zhang YC et al (2007) Study on a hybrid method of SVPWM and SHEPWM applied to three-level adjustable speed drive system. *Proc CSEE* 27(16):72–77 (in Chinese)

# Dead-Band Optimization for ZVS in Inductive Power Transfer System



Bing Li, Daomeng Cai, Xuemei Diao, Lei Wang and Lijun Diao

**Abstract** The realization of zero-voltage switching (ZVS) of inverter can reduce the circuit switching loss. It meets the high power density requirements of the inductive power transfer (IPT). To achieve ZVS, it is necessary to consider the matching of impedance properties to dead-band. Therefore, based on the input equivalent impedance and dead-band, the conditions for achieving ZVS are studied in this paper. Firstly, the equivalent input impedance model is established based on secondary-side full compensation and the switching process is analyzed in the case of ZVS. Secondly, based on the above model, the dead-band range of ZVS is derived. Then, the influence of the primary-side compensation capacitor on the ZVS is discussed, which provides a theoretical basis for fine-tuning the compensation capacitor. Finally, the feasibility of the method is verified by simulation.

**Keywords** Inductive power transfer · ZVS · Dead-band optimization · Primary compensation capacitor

---

B. Li · X. Diao · L. Wang (✉) · L. Diao  
Beijing Jiaotong University, Beijing, China  
e-mail: [leiwang@bjtu.edu.cn](mailto:leiwang@bjtu.edu.cn)

B. Li  
e-mail: [17121452@bjtu.edu.cn](mailto:17121452@bjtu.edu.cn)

X. Diao  
e-mail: [17121421@bjtu.edu.cn](mailto:17121421@bjtu.edu.cn)

L. Diao  
e-mail: [ljdiao@bjtu.edu.cn](mailto:ljdiao@bjtu.edu.cn)

D. Cai  
Systems Engineering Research Institute CSSC, Beijing, China  
e-mail: [cmd315@163.com](mailto:cmd315@163.com)

Beihang University, Beijing, China

## 1 Introduction

Wireless power transfer (WPT) technology, as a new type of power transmission mode, overcomes the problems of traditional wire transmission, such as contact sparks, bare wires, occupying surface space and so on. It has important application value in the fields of electric vehicles, biomedical, electronic consumer products and so on [1–3].

Typical wireless charging system includes AC/DC, DC/AC, resonant compensation network, transfer receiving coil, rectifier and so on [4]. In the full-bridge inverter circuit, in order to prevent MOSFETs from passing through, the upper and lower MOSFETs need to have a certain dead-band. Compared with other applications, a reasonable dead-band can not only prevent full-bridge inverter in IPT system from being damaged, but also realize its soft switching. That plays a great role in improving the system efficiency, power density and operating environment. Li et al. [5] proposed an optimal dead-band for a series resonant inverter only for the specific dead-band without analyzing the optimal dead-band range. In [6], based on digital signal processor, the optimal design of series resonance dead-band is analyzed. But, the difficulty of control increases. In [7], the dead-band optimization method of ZVS for series-series (SS) compensated IPT system is studied. However, this method only discusses the dead-band for half-bridge inverter. It is proposed in [8] that the circuit can be perceptual by adjusting the compensation capacitor of the secondary coil. It provides the condition for the realization of ZVS in MOSFETs, but there is no specific design method for dead-band. Based on the analysis above, aimed at SS compensation IPT system, this paper proposes the dead-band optimization method with MOSFETs junction capacitor and primary-side compensation capacitor as variables and provides a theoretical basis for the optimization of dead-band of SS compensation IPT system.

## 2 Equivalent Model and Freewheeling Analysis

Figure 1 shows a simplified circuit diagram of the SS-type IPT system.

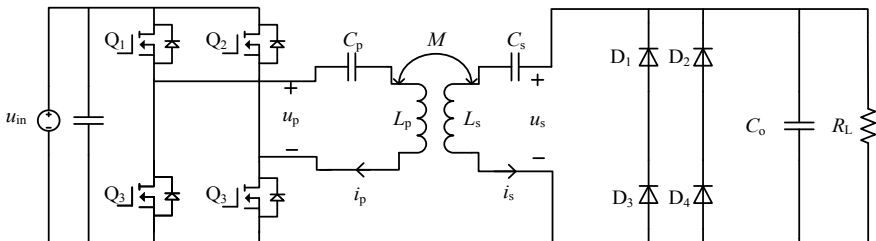


**Fig. 1** Simplified circuit of voltage source IPT system

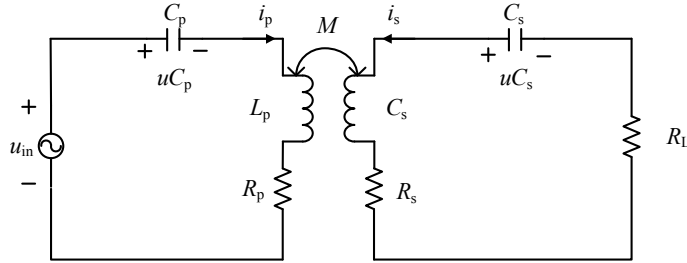


**Fig. 2** SS-type IPT mutual inductance coupling model

The system consists of high-frequency inverter circuit, resonant network, rectifier, filter and load. The inverter circuit inverts the DC voltage into the high-frequency square wave. For easier analysis, the parasitic resistance of the primary-side and secondary-side windings is ignored, and the IPT mutual inductance coupling model is established as shown in Fig. 2.

In Fig. 2, the impedances of the primary-side and secondary-side winding can be expressed as

$$\begin{cases} Z_p = R_p + j\left(\omega L_p - \frac{1}{\omega C_p}\right) \\ Z_s = R_s + R_L + j\left(\omega L_s - \frac{1}{\omega C_s}\right) \end{cases} \quad (1)$$

Considering that the primary-side and secondary-side windings fully resonant and ignoring their internal resistances, it can be obtained

$$Z_{p\_in} = R_p + \frac{(\omega M)^2}{R_L} + j\left(\omega L_p - \frac{1}{\omega C_p}\right) \quad (2)$$

Therefore, the equivalent primary-side impedance angle and impedance can be shown as below

$$\begin{cases} \theta_{p\_in} = \arctan\left(\left(\omega L_p - \frac{1}{\omega C_p}\right)/\left(R_p + \frac{(\omega M)^2}{R_L}\right)\right) \\ |Z_{p\_in}| = \sqrt{\left[R_p + \frac{(\omega M)^2}{R_L}\right]^2 + \left[\omega L_p - \frac{1}{\omega C_p}\right]^2} \end{cases} \quad (3)$$

During the turn-off process of the MOSFETs, the junction capacitor across the drain and source can function as a converter buffer to achieve zero-voltage turn-off; while in the turn-on process, in order to achieve zero-voltage turn-on, the body diode must maintain freewheeling to the previous cycle [9]. This requires the equivalent primary-side impedance angle  $\theta_{p\_in}$  and it must be greater than zero, which means the load is inductive. In practical applications, the angular frequency  $\omega$  is fixed and the primary-side inductance  $L_t$  is wound by the Litz wires, which is

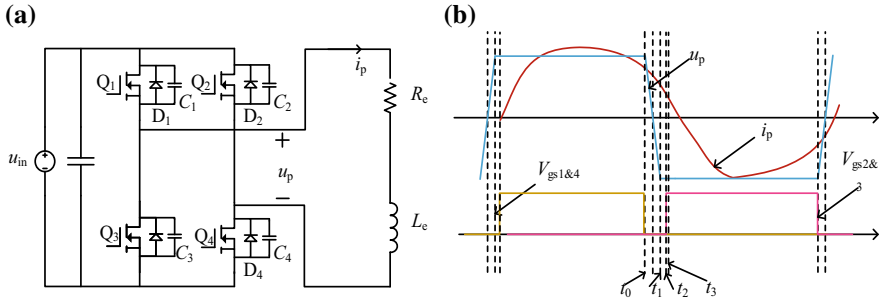


**Fig. 3** Inductive conditions **a** simplified circuit, **b** waveforms

difficult to adjust. Therefore, the inductive equivalent input impedance generally can be realized by fine-tuning the primary-side resonant capacitor  $C_t$ .

Under inductive conditions, Fig. 2 can be equivalent to that shown in Fig. 3a.

The following part analyzes the effect of the MOSFETs junction capacitor ( $C_1, C_2, C_3, C_4$ ) on their ZVS in a nonideal case. Before analysis, it is assumed that  $C_1 = C_2 = C_3 = C_4 = C_{oss}$ . A switching cycle is shown in Fig. 3b.

In Fig. 3b, before  $t_0$ ,  $Q_1$  and  $Q_4$  are turned on, the current is positive; at  $t_0$ ,  $Q_1$  and  $Q_4$  are turned off; since the current is positive,  $C_1$  and  $C_4$  are charged and  $C_2$  and  $C_3$  are discharged.  $Q_1$  and  $Q_4$  are approximately zero-voltage turn-off due to the charging of  $C_1$  and  $C_4$ ; at  $t_1$ , the charging of  $C_1$  and  $C_4$  and discharging of  $C_2$  and  $C_3$  are finished; if  $Q_2$  and  $Q_3$  are turned on after  $t_1$ , zero-voltage turn-on of  $Q_2$  and  $Q_3$  can be realized; after  $t_3$ , current is reversed and  $C_2$  and  $C_3$  are recharging; the voltage across the drain and source  $V_{ds}$  of  $Q_2$  and  $Q_3$  is not zero. If  $Q_2$  and  $Q_3$  are turned on at this moment, zero-voltage turn-on of  $Q_2$  and  $Q_3$  cannot be realized.

### 3 Optimized Design of Dead-Band

According to the analysis above, the optimal dead-band of the MOSFETs to achieve ZVS should ensure the full charge and discharge of the parasitic capacitor and open another two MOSFETs before the end of the body diode freewheeling. Thus, the dead-band  $t_d$  should be satisfied in one cycle

$$0 < t_{Cc} + t_{off} < t_d < t_D < T \quad (4)$$

where  $t_{Cc}$  is the charge and discharge time of the junction capacitor,  $t_{off}$  is the off-time of the MOSFETs,  $t_D$  is the freewheeling time of the body diode and  $T$  is a switching period of the MOSFETs.

### 3.1 Design of Optimal Dead-Band Range

When MOSFETs are turned off, the current of the inverter is  $I_{\text{off}}$ . Since the parasitic capacitor's charge and discharge time is relatively short compared to the conduction time, the current can be approximately constant. Then, it can be obtained

$$t_{\text{Cc}} = (2C_{\text{oss}} + C_{\text{str}}) \frac{U_d}{I_{\text{off}}} \quad (5)$$

where  $C_{\text{oss}}$  is the junction capacitor of MOSFETs and  $C_{\text{str}}$  is a stray capacitor.

Output current of inverter can be expressed as

$$I_p = 2 \frac{U_d}{\pi |Z_{\text{p\_in}}|} \sin(\omega t - \theta) \quad (6)$$

The MOSFETs are turned off at the time of  $t = \pi$ , so the turn-off current is

$$I_{\text{off}} = \frac{2U_d}{\pi |Z_{\text{Tin}}|} \sin \theta \quad (7)$$

Combine (5) and (7), it can be obtained as follows

$$t_{\text{Cc}} = (2C_{\text{oss}} + C_{\text{str}}) \frac{\pi |Z_{\text{p\_in}}|}{2 \sin \theta} \quad (8)$$

Within one cycle, the freewheeling time of the body diode is determined by the primary current  $I_p$ , then

$$I_p = \sqrt{2} I_{\text{rms}} \sin(\omega t_D - \theta) = 0 \quad (9)$$

Because the  $t_D$  is smaller than the switching period  $T$ , the solution is obtained

$$t_D = \frac{\theta}{\omega} \quad (10)$$

According to (4), (8) and (10), the dead-band range should be satisfied

$$(2C_{\text{oss}} + C_{\text{stray}}) \frac{\pi |Z_{\text{Tin}}|}{2 \sin \theta} + t_{\text{off}} < t_D < \frac{\theta}{\omega} \quad (11)$$

From (11), the optimal dead-band is affected by  $C_{\text{oss}}$ ,  $C_{\text{stray}}$  and  $C_t$ . In practical applications, the stray capacitance  $C_{\text{stray}}$  is relatively fixed, so it is necessary to consider the influence of  $C_{\text{oss}}$  and  $C_t$ .

### 3.2 Select Primary-Side Capacitor Based on Dead-Band Range

Based on the analysis above, it is can be seen that the larger a primary-side compensation capacitor is, the longer freewheeling time of the body diode is. This increases the dead-band margin and makes it easier to design the dead-band range. However, an excessive primary compensation capacitor will reduce the output power. Therefore, increasing the compensation capacitor appropriately is significant for optimizing dead-band.

Based on this, this paper defines the dead-band difference as

$$\Delta t_d = t_D - (t_{Cc} + t_{off}) \quad (12)$$

From the analysis above,  $\Delta t_d$  needs to be greater than zero, and in practice, a certain amount of time is needed. It is obtained

$$\Delta t_d \geq t_{mrg} \quad (13)$$

where  $\Delta t_d$  is the margin, which can be selected according to the actual situation. The formula above provides a basis for selecting the primary-side compensation capacitor  $C_p$ .

## 4 Simulation Results

In order to verify the dead-band optimization method and the selection of the MOSFETs junction capacitor and primary-side capacitor proposed in this paper, an IPT model is built in MATLAB. The basic parameters of the calculation are shown in Table 1.

The MOSFETs select IXFH46N65X2. When  $V_{ds}$  is 400 V, the junction capacitor is about 0.1 nF, the off-time  $t_{off}$  is 50 ns, the inverter circuit stray capacitor  $C_{stray}$  is set to 1 nF and the margin time  $t_{mrg}$  is set to 100 ns. The primary-side capacitor  $C_p$  can be selected to be 30 nF according to the (13). Substituting the parameters above into (11), the best dead-band range is calculated as

$$391 \text{ ns} < t_d < 831 \text{ ns} \quad (14)$$

**Table 1** IPT model parameters

Parameter	Value	Parameter	Value
$U_{in}$	500 V	$V_{out}$	24 V
$f_{sw}$	85 kHz	$k$	0.7
$L_p$	180 $\mu\text{H}$	$L_s$	0.8 $\mu\text{H}$
$C_p$	19.5 nF	$C_s$	4.4 $\mu\text{F}$

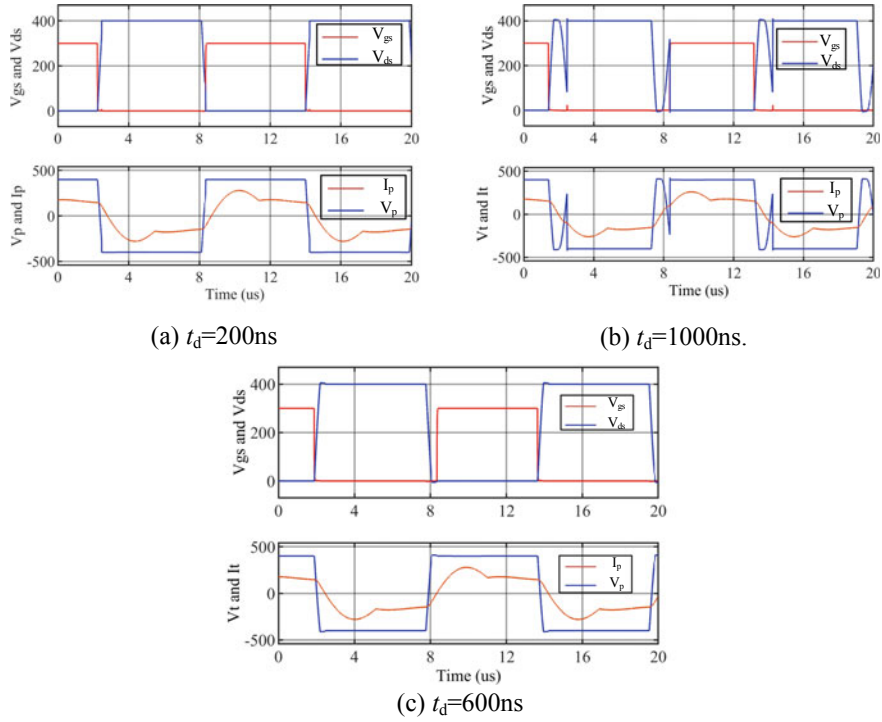


**Fig. 4** Waveforms under different dead-bands

Substituting different dead-band  $t_d$  into the simulation model yields the following waveforms

As shown in Fig. 4a, since the dead-band setting is too small, the MOSFETs junction capacitor is not completely discharged. When  $U_{DS}$  is larger than zero, the MOSFETs are turned on, and the junction capacitor is instantaneously short-circuited, and ZVS cannot be realized. In Fig. 4b, since the dead-band setting is too large, the MOSFETs are turned on when the current is recharged to the MOSFETs junction capacitor after the end of the diode freewheeling. At this time,  $U_{ds}$  is larger than zero, the ZVS cannot be realized. In Fig. 4c, MOSFETs are turned on during the freewheeling of its body diodes. At this moment, the  $U_{ds}$  of the MOSFETs is zero, and ZVS is realized.

## 5 Conclusion

In SS compensation IPT system, the soft switching of inverter is affected by the dead-band and the primary-side compensation capacitor. Based on this, this paper proposes a calculation method of dead-band and compensation capacitance. Firstly,

an equivalent impedance model of the secondary-side full compensation is established. Then, the dead-band range  $t_D$  is derived based on the model, and the range of the primary-side capacitance  $C_p$  is designed. Finally, the theories are verified by simulation. It provides a calculation method and theoretical basis for the soft switch implementation of the SS compensation IPT system.

## References

1. Zhang H, Wang X, Li N, Lei Y, Yang F et al (2016) Analysis of wireless charging hybrid compensation topology circuit for electric vehicle. *Power Sys Autom* 40(16):71–75 (in Chinese)
2. Zhao Z, Liu F, Chen K (2016) A review of the research on wireless charging technology for electric vehicles. *J Electr Technol* 31(20):30–40 (in Chinese)
3. Lu F, Zhang H, Zhu C, Diao L, Gong M, Zhang W et al (2018) A tightly-coupled inductive power transfer system for low-voltage and high-current charging of automatic guided vehicles (AGVS). *IEEE Trans Ind Electron* 1–1
4. Li S (2015) Wireless power transfer for electric vehicle applications. *IEEE J Emerg Sel Top Power Electron* 3(1):4–17
5. Li M, Jiang H, Du Y, Zhang S (2003) Selection of the best dead zone for series resonant inverters. *Power Electron* 37(4):22–24
6. Zhang S, Li M (2004) A series resonant induction heating system with optimal dead-band based on DSP. *Electr Trans Autom* 26(6):23–27 (in Chinese)
7. Lan J, Ma D, Tang H (2014) Optimization of dead-band of ZVS in inductively coupled power transmission system. *J Mot Control* 18(12):50–56 (in Chinese)
8. Li S, Li W, Deng J, Nguyen TD, Mi CC (2015) A double-sided LCC compensation network and its tuning method for wireless power transfer. *IEEE Trans Veh Technol* 64(6):2261–2273
9. Kundu U, Yenduri K, Sensarma P (2016) Accurate ZVS analysis for magnetic design and efficiency improvement of full bridge LLC resonant converter. *IEEE Trans Power Electron* 1–1

# Research on the Improved Fault-Tolerant Control of ANPC Three-Level Converter



**Qinyue Zhu, Chen Wang, Xitang Tan, Pengcheng Zhang  
and Qingwen Fan**

**Abstract** In recent years, the reliability requirements of active neutral-point-clamped (ANPC) three-level converter are getting higher and higher with its large-scale application. In order to overcome the problem of the limited fault-tolerant capability of the basic ANPC three-level converter when compound faults occur, an improved fault-tolerant topology based on component sharing was proposed in this paper. Compared with the basic ANPC three-level converter topology, two bidirectional thyristors and a double-pole double-throw switch are added to each phase, which can realize Fault-Tolerant Control (FTC) for multiple fault types and greatly improve the reliability with small additional costs. The corresponding self-diagnosis FTC algorithm composed of topology reconfiguration module, switch state generation module, and PWM output control module is also put forward. With the real-time generation of switch state, the reconfiguration of fault-tolerant topology is easy to realize and adaptable. Finally, the effectiveness and feasibility of the proposed topology and FTC algorithm are verified by simulation and experimental results.

**Keywords** Active neutral-point-clamped converter · Fault-tolerant control · Self-diagnosis · Topology reconfiguration · Switch state generation

## 1 Introduction

In recent years, NPC three-level converter has been widely used in fields of new energy power generation, high-speed electrified railways, etc. [1]. In order to adapt to higher reliability requirements, FTC has become a hot research issue in domestic and overseas. In general, power switching tube IGBT is the main object of three-level converter for FTC. Researches and applications show that open-circuit

---

Q. Zhu · C. Wang · X. Tan (✉) · P. Zhang · Q. Fan

School of Electronics and Information Engineering, Tongji University, Shanghai 201804,  
People's Republic of China

e-mail: [xtan@tongji.edu.cn](mailto:xtan@tongji.edu.cn)

fault caused by thermomechanical fatigue is the main failure mode of IGBT [2]. Hence, this paper mainly deals with FTC of IGBT open-circuit faults in NPC three-level converter.

At present, FTC methods of NPC three-level converter mainly include switch redundancy type, four-leg type, and ANPC type. Switch redundancy type utilizes the redundant voltage vector [3] to realize FTC. Four-leg type adds an extra three-level leg to replace the faulty phase leg based on the basic topology [4]. ANPC type employs two extra active switches per phase in the original NPC structure to make load current flow bidirectionally in the neutral path, which can overcome specific open-circuit faults [5].

FTC methods mentioned above have a good effect on specific faults, but have limited fault-tolerant capability for compound faults. Therefore, an improved ANPC three-level converter topology and the corresponding self-diagnosis control algorithm are proposed to ensure the performance of the converter when compound faults occur.

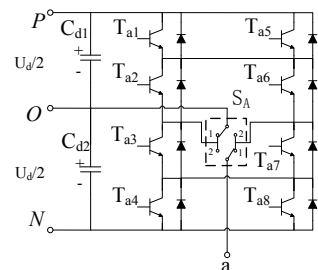
## 2 Improved Fault-Tolerant Topology

### 2.1 Design of the Improved Fault-Tolerant Topology

A self-healing fault-tolerant topology is shown in Fig. 1 which was proposed in Ref. [6]. The bridge arms are completely symmetric, enabling the converter to overcome different faults occurring inside the arm by utilizing its self-redundant resources without affecting the operation of other legs. However, its power device utilization is low.

Based on this self-healing structure, an improved ANPC three-level converter fault-tolerant topology is proposed in this paper. Two bidirectional thyristors and a double-pole double-throw switch are added to each phase in the original ANPC three-level converter, as shown in Fig. 2. Phase A is taken as an example for the convenience of analysis. The output position is selected by the double-pole double-throw switch: When  $S_A$  is at “1” position, power tubes  $T_{a1}$ ,  $T_{a2}$ ,  $T_{a3}$ , and  $T_{a4}$  make up the main leg, and  $T_{a5}$  and  $T_{a6}$  act as clamp tubes; when  $S_A$  is at “2”

**Fig. 1** Phase A leg of self-healing ANPC three-level converter fault-tolerant topology



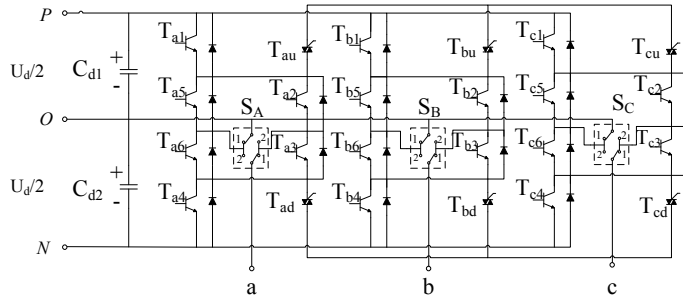


**Fig. 2** Improved ANPC three-level converter fault-tolerant topology

position,  $T_{a1}$ ,  $T_{a5}$ ,  $T_{a6}$ , and  $T_{a4}$  make up the main leg, and  $T_{a2}$  and  $T_{a3}$  are clamp tubes. Bidirectional thyristors  $T_{au}$  and  $T_{ad}$  establish the connection between three phases after external IGBT fault occurs. When an external IGBT fault occurs in phase A, the external IGBT of phase B can act as a backup through the action of the thyristor. This topology has the same performance as the topology shown in Fig. 1, but cost is reduced with improved utilization.

## 2.2 Principle of Fault-Tolerant Topology Reconfiguration

According to the number of IGBTs that are faulty at the same time, the fault is divided into basic fault (single open-circuit fault) and compound faults (multiple open-circuit faults). Basic fault is the simplest and is the basis. Therefore, basic fault that occurs in phase A is taken as an example to show reconfiguration process. As shown in Fig. 3, if an open-circuit fault occurs at the external tube  $T_{a1}$  in the

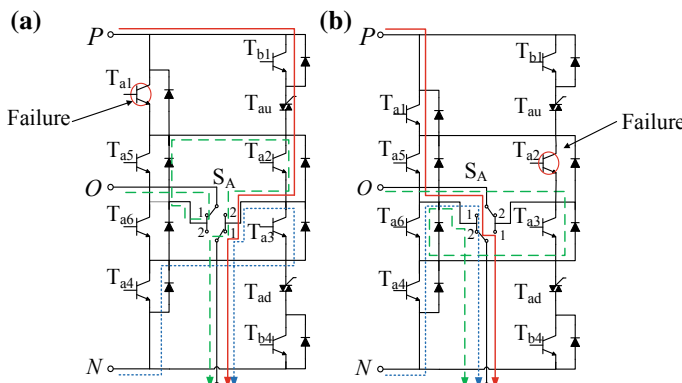


**Fig. 3** Basic fault reconfiguration process

converter, then  $T_{au}$  is triggered to be turned on to make  $T_{b1}$  be used as a backup of  $T_{a1}$ . The reconfiguration process is shown in Fig. 3a. The red, blue, and green dashed lines indicate the current path of the faulty phase leg when outputting positive, zero, and negative levels, respectively. If an open-circuit fault occurs at the internal tube  $T_{a2}$ , the double-pole double-throw switch  $S_A$  will be placed at “2” position to make  $T_{a1}$ ,  $T_{a5}$ ,  $T_{a6}$ , and  $T_{a4}$  become the main leg, the reconfiguration process is shown in Fig. 3b. After the reconfiguration, all the power tubes only need to bear the bus voltage of  $U_d/2$ .

The fault of power tubes at any position will cause the existing current loop to be destroyed. However, it is still possible to overcome the fault as long as there is available redundant resources in the critical current loop, so the condition for judging the success or failure of fault tolerance is whether there is a conflict of the switch state requirements of the IGBT when it simultaneously undertakes the output tasks of two or more current loops. For example, if an open-circuit fault occurs at  $T_{a1}$ , then  $T_{b1}$  will replace  $T_{a1}$  to undertake the output tasks of both phase A and phase B. Therefore,  $T_{b1}$  is required to be turned on when phase A outputs “P” level at a certain time, and  $T_{b1}$  is required to be turned off when phase B outputs “N” level. The two loops have inconsistent requirements on the switching state of  $T_{b1}$ , which creates a conflict. As a result, how to recover current loops through software control or hardware reconfiguration and use redundant resources to resolve conflicts is a key problem to overcome compound faults.

In the fault-tolerant topology proposed in this paper, each external IGBT has two redundant resources (the external IGBTs of the bridge arms of other two phases), and each internal IGBT has one redundant resource (the symmetric clamp tube in the same phase). For example, if an open-circuit fault occurs at  $T_{a2}$ , the redundant resource  $T_{a5}$  is used to replace  $T_{a2}$ , and phase A can still output “P” level. If faults occur simultaneously at  $T_{a5}$  and  $T_{a2}$ , no redundant resources are available, and the “P” level output loop of phase A is destroyed, which makes the converter lose fault-tolerance capability.

### 3 Self-diagnosis Fault-Tolerant Control Algorithm

It can be seen from the above analysis that different fault-tolerant topology reconfiguration programs and PWM control strategies are needed for different fault types. The reconfiguration and PWM control programs for specific fault types are often calculated manually and stored in a matrix which are then implemented by lookup method in traditional FTC. This method is low in cost and convenient to use, but may lose effectiveness when the system fails unexpectedly as the FTC program may not match the actual fault type. Hence, a self-diagnosis FTC algorithm based on combinational logic [7] is proposed to get the optimal fault-tolerant reconfiguration topology and PWM control method in real time according to fault

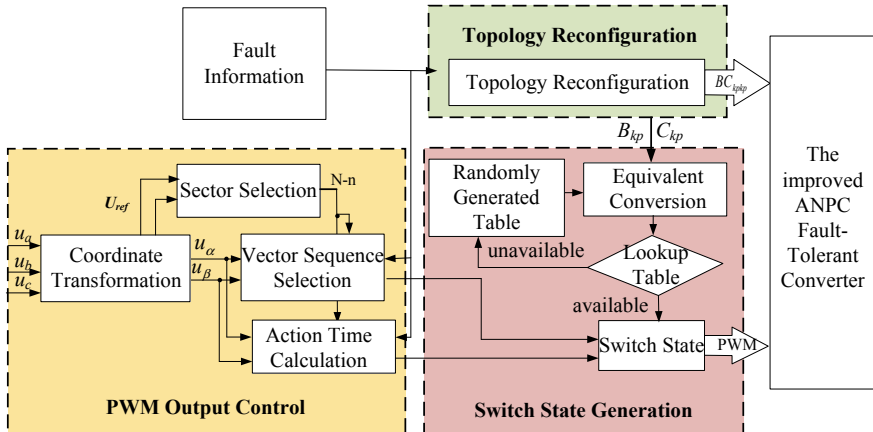


**Fig. 4** Structure of self-diagnosis FTC algorithm

location and fault type, covering the shortcomings of traditional algorithms that are not effective for unexpected faults. Figure 4 shows the structure of the self-diagnosis FTC algorithm.

### 3.1 Topology Reconfiguration Module

The topology reconfiguration program is determined by this module according to fault type. The topology reconfiguration actually corresponds to the determination about the action signal of the contactor and the driving signal of the thyristor.

#### ① Determination of the action signal of the contactor

The status signal  $FIM_k = F_{k2} + F_{k3}$  is taken to indicate whether the internal IGBT is faulty, and  $FIC_k = F_{k5} + F_{k6}$  to indicate whether the clamp IGBT is faulty. Then the fault-tolerant logic is depicted as follows:

$$\begin{aligned} \text{If } FIM_k = 0 & \quad \text{then } C_{k1}C_{k2} = 00, \\ \text{If } FIM_k = 1 \& FIC_k = 0 & \quad \text{then } C_{k1}C_{k2} = 11, \\ \text{If } FIM_k = 1 \& FIC_k = 1 & \quad \text{then } C_{k1}C_{k2} = 10. \end{aligned}$$

Consequently, the logical expressions of  $C_{k1}$  and  $C_{k2}$  can be described as follows:

$$C_{k1} = FIM_k = F_{k2} + F_{k3} \quad (1)$$

$$C_{k2} = FIM_k \cdot \overline{FIC_k} = (F_{k2} + F_{k3}) \cdot \overline{(F_{k5} + F_{k6})} \quad (2)$$

where  $F_{kp}$  is the fault state flag of the  $p$ -th IGBT in phase  $k$ , “1” means fault state, “0” means normal state. The values of  $k$  are specified as 0, 1, 2, 3, and 4 which represent phase C, phase A, phase B, phase C, and phase A, respectively. The values of  $p$  are specified from 1 to 6, which are corresponding to the serial number of the IGBT in each phase as shown in Fig. 3.  $C_{k1}$  represents the position of the upper contactor of the double-pole double-throw switch in phase  $k$ , while  $C_{k2}$  represents the position of the lower contactor, “1” means at position 1, “0” means at position 2.

## ② Determination of the driving signal of the thyristor

If an external IGBT fails, the bidirectional thyristor will be triggered on, then multiple bridge arms will share the same external tube after reconfiguration. It can be classified into two cases as the determination of the driving signal of the thyristor should comprehensively consider the fault conditions of other bridge arms. If we take the bidirectional thyristor of the upper bridge arm as an example, the process of how to derive the logical expression of the switch state is clarified as follows.

*Case1:* If we suppose that the external tube of the upper bridge arm in phase  $k$  occurs an open-circuit fault, at this time the upper external tubes of the other two phases need to be utilized for fault tolerance. Thus, the bidirectional thyristor of phase  $k$  should be turned on, which means  $B_{k1} = 1$ . If the fault occurs at the external IGBT of the lower bridge arm and the external IGBT of the upper bridge arm does not fail, whether the upper external IGBT of the other two phases is faulty should also be considered. If fault occurs, the upper external IGBT of phase  $k$  needs to be used as a redundant resource, that is  $B_{k1} = 1$ . Otherwise,  $B_{k1} = 0$ .

*Case2:* If we assume that the upper external IGBT of phase  $k$  does not fail, whether the  $k$ -phase upper external tube be used as a redundant resource to participate in FTC is determined by the condition of the other two phases. If both upper external IGBTs of the other two phases fail, the upper external IGBT of phase  $k$  is the only redundant resource, then  $B_{k1} = 1$ ; if only one upper external IGBT of the other two phases fails, the upper external IGBT of phase  $k$  will participate in FTC ( $B_{k1} = 1$ ) when the lower external IGBT of phase  $k$  fails or the upper external IGBT of phase  $k-1$  fails.

Above all, the logical expression of  $B_{k1}$  can be described as follows:

$$B_{k1} = F_{k1} + \overline{F_{k1}} \cdot F_{(k-1)1} \cdot F_{(k+1)1} + \overline{F_{k1}} \cdot \overline{F_{k4}} \cdot F_{(k-1)1} + \overline{F_{k1}} \cdot F_{k4} \\ \cdot (F_{11} + F_{21} + F_{31}) \quad (3)$$

where  $B_{k1}$  and  $B_{k2}$  are the driving signal of the upper and lower bidirectional thyristor of phase  $k$ , respectively, “1” means the thyristor is under the on state, and 0 is under the off state. The values of  $k$  are similar as those mentioned above.

### 3.2 Switch State Generation Module

Switch state will change after the converter is reconfigured, which is then calculated by this module according to fault type and reconfiguration program. The specific generation process is as follows: ①A switch state table of the reconfigured topology is randomly generated; ②the switch state table is equivalently converted into a switch state table of the basic ANPC three-level converter according to the fused switch state reconfiguration information; ③whether the switch state table can correctly output the corresponding level is conducted by looking up the basic ANPC switch state table. If not, return to ①.

If we assume that the driving signal of the  $p$ -th IGBT of phase  $k$  of the reconfigured topology is represented by  $S_{Fkp}$ , where “1” means on and “0” means off, the driving signal of the  $p$ -th IGBT of phase  $k$  of the equivalent model is represented by  $S_{Tk_p}$ , “1” is on and “0” is off. Thus, the driving signal  $S_{Tk_p}$  of the external IGBT is affected by  $S_{Fkp}$  of the external IGBT, the bidirectional thyristor switch state, and operation state of the contactor. The equivalent conversion process is depicted as:

$$S_{Tk_p} = ((S_{F1p} \cdot B_{1m} + S_{F2p} \cdot B_{2m} + S_{F3p} \cdot B_{3m}) \cdot B_{km} + S_{Fkp}) \cdot \overline{C_{k1} \oplus C_{k2}}, \quad (4)$$

$$m = 1, 2$$

The driving signal  $S_{Tk_p}$  of the internal IGBT is only affected by  $S_{Fkp}$  of the external IGBT and the contactor operation state. The equivalent conversion process is depicted as:

$$S_{Tk_p} = (S_{Fkp} \cdot \overline{C_{k1} \cdot C_{k2}} + S_{Fk(p+3)} \cdot C_{k1} \cdot C_{k2}) \cdot \overline{C_{k1} \oplus C_{k2}}, \quad p \leq 3 \quad (5)$$

$$S_{Tk_p} = (S_{Fkp} \cdot \overline{C_{k1} \cdot C_{k2}} + S_{Fk(p-3)} \cdot C_{k1} \cdot C_{k2}) \cdot \overline{C_{k1} \oplus C_{k2}}, /, p \geq 3 \quad (6)$$

In general, the given reconfigured topology can be judged available if the equivalent converted switch state is a subset of the switch state table of the basic ANPC three-level converter shown in Ref. [5], otherwise it needs to be re-specified.

### 3.3 PWM Output Control Module

The output mode of PWM pulse generated by this module can be classified into three types according to the performance of the converter after FTC: ①symmetric full-power operation mode (for most faults), where all three phases operate at three-level state, which are controlled by traditional SVPWM strategy [8]; ②asymmetric operation mode ( $T_{k1}$  and  $T_{k3}$  fail simultaneously). The fault phase works at two-level state while the other two phases work at three-level state. An asymmetric three-level SVPWM control strategy is required [9] as the maximum modulation ratio is not decreased; ③derating-power operation mode ( $T_{k2}$  and  $T_{k5}$

fail simultaneously). The fault phase is connected to the neutral point while the other two phases work at three-level state. SPWM control strategy is employed [10] as the maximum modulation ratio is reduced to  $1/\sqrt{3}$  of the original value.

## 4 Simulation and Experimental Verification

In order to verify the validity of the proposed topology and control algorithm, an improved ANPC three-level converter FTC model is built on MATLAB platform.

### 4.1 Simulation Verification

ANPC converter in high-power AC drive system of CRH high-speed EMUs is taken as the object [11]. Phase A is taken as an example due to the symmetry of the three-phase converter. Three different types of open-circuit faults of the power tubes in phase A are simulated. It is supposed that all faults occur at  $t = 0.02$  s, and FTC is conducted at  $t = 0.027$  s. The specific simulation parameters are as follows: load resistor is  $10 \Omega$ , load inductor is  $30 \text{ mH}$ , DC bus capacitor is  $3 \text{ mF}$ , DC voltage is  $3000 \text{ V}$ , fundamental frequency is  $50 \text{ Hz}$ , carrier frequency is  $1250 \text{ Hz}$ , and modulation ratio is 0.8.

#### 4.1.1 Open-Circuit Fault of $T_{a1}$

Figure 5 shows the simulation results after  $T_{a1}$  fails. It can be seen that phase A cannot normally output “P” level during the fault operation period, especially

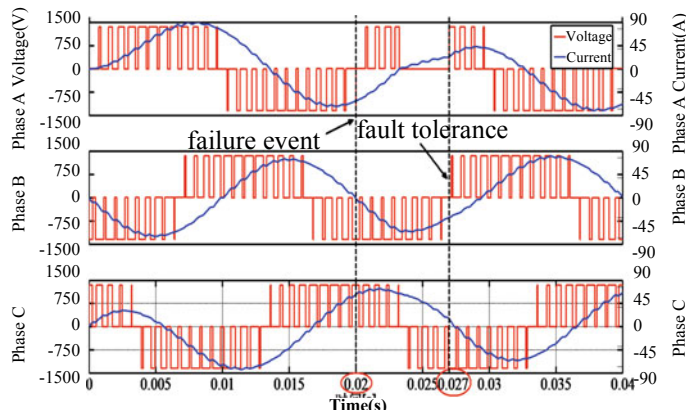


**Fig. 5** Simulation results when  $T_{a1}$  fails

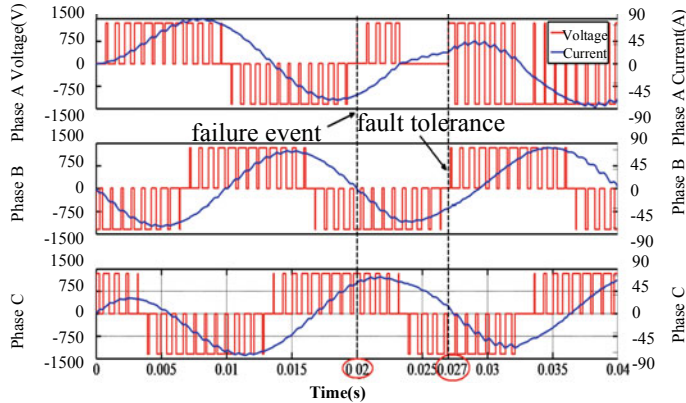


**Fig. 6** Simulation results when  $T_{a1}$  and  $T_{a3}$  fail

when output current crosses zero. The current that should flow from  $T_{a1}$  is forced to flow from  $D_{a5}$ , which makes phase A output “O” level and the three-phase output current unbalanced. The output of phase A is back to normal after FTC without affecting the output of phase B, verifying that the proposed control algorithm can overcome open-circuit faults of external IGBTs.

#### 4.1.2 Open-Circuit Fault of $T_{a1}$ and $T_{a3}$

Figure 6 shows the simulation results after  $T_{a1}$  and  $T_{a3}$  fail. Phase A cannot normally output “P” level during the fault operation period, especially when output current crosses zero, which makes phase A output “O” level. Asymmetric SVPWM control strategy is adopted because FTC under this fault requires proper reduction of output performance, which means phase A operated at two-level state while phases B and C operated at three-level state. The three-phase output current is back to normal after FTC. Although  $T_{b1}$  is shared by phase A and phase B, while  $T_{a5}$  and  $T_{a6}$  replace  $T_{a2}$  and  $T_{a3}$  to become the main leg for output, the proposed control algorithm can overcome open-circuit faults of both external IGBTs and internal IGBTs.

#### 4.1.3 Open-Circuit Fault of $T_{a2}$ and $T_{a5}$

Figure 7 shows the simulation results after  $T_{a2}$  and  $T_{a5}$  fail. Phase A cannot normally output “O” level during the fault period, especially when the output current is negative, which makes phase A output “P” level; phase A also cannot output “P” level when the output current crosses zero, which makes phase A output “O” level and “N” level. The reduction of capacity is needed to perform FTC, which means

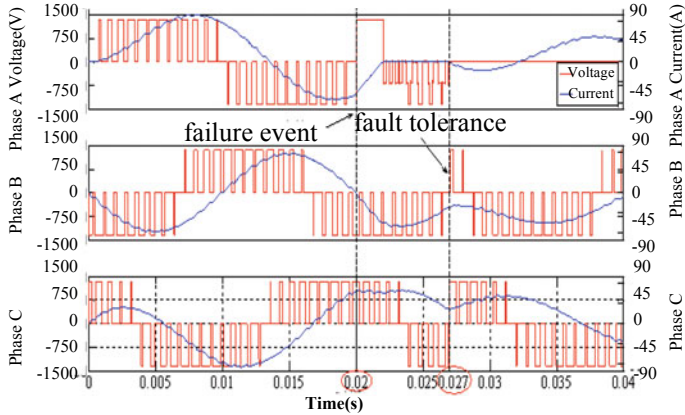


**Fig. 7** Simulation results when  $T_{a2}$  and  $T_{a5}$  fail

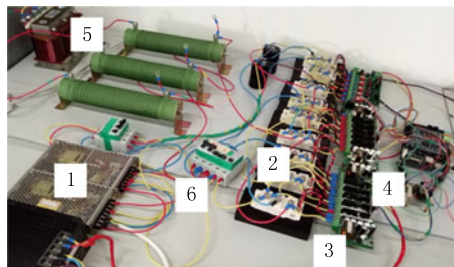
that phase A will be connected to the neutral point to constantly output “O” level, while phase B and C still work at three-level state; thus, the output power will be reduced to  $1/\sqrt{3}$  of the original output power. The three-phase output current is back to normal after FTC, verifying that the proposed control algorithm can overcome open-circuit faults of multiple internal IGBTs.

#### 4.2 Experimental Verification

The low-power experimental system of an improved fault-tolerant ANPC three-level converter is built in order to further verify the effectiveness of the proposed topology and control strategy. The specific experimental parameters are as follows: DC voltage is 48 V, the supporting capacitor is an electrolytic capacitor of 750  $\mu$ F with a bear voltage of 400 V, each power tube unit is an Infineon’s two-unit IGBT module FF75R12RT4, the load resistor is 10  $\Omega$ , and the load inductor is 20 mH. The experimental system is shown in Fig. 8.

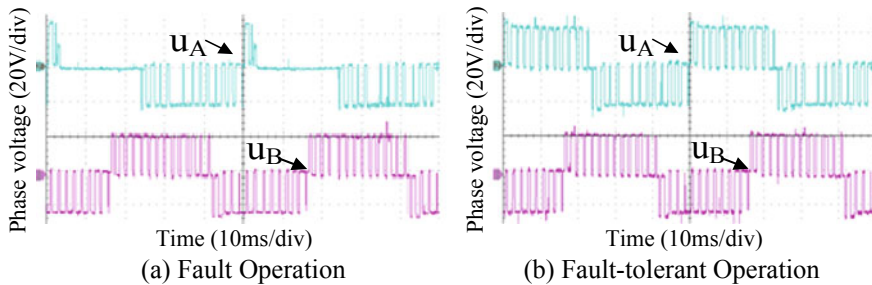
Figure 9 shows the output phase voltage waveforms before and after FTC when  $T_{a1}$  fails. It can be seen that phase A cannot output “P” level normally after the fault. But the output voltage of phase A can return to normal after FTC without affecting phase B, which is basically consistent with the theoretical analysis and the simulation results.

Figure 10 shows the output phase voltage waveforms before and after FTC when  $T_{a1}$  and  $T_{a3}$  fail. The output of phase A is distorted when reference voltage is positive. But the output voltage of phase A can return to normal after FTC without affecting phase B.



1- DC power supplies, 2- main circuit, 3-driving circuit, 4- control circuit, 5- load, 6-fault-tolerant reconfiguration switch of phase A

**Fig. 8** Physical map of experimental system



**Fig. 9** Output phase voltage waveform of phase A and B when  $T_{a1}$  fails

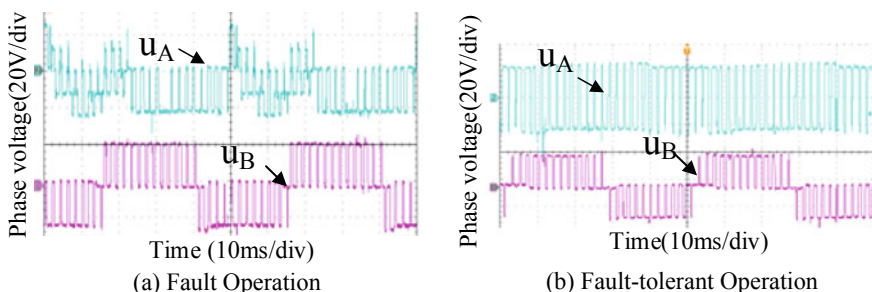


**Fig. 10** Output phase voltage waveform of phase A and B when  $T_{a1}$  and  $T_{a3}$  fail

Figure 11 shows the output phase voltage waveforms before and after FTC when  $T_{a2}$  and  $T_{a5}$  fail. Phase A cannot output normally during the whole fault period. But phase A can output “O” level constantly after FTC without affecting phase B.

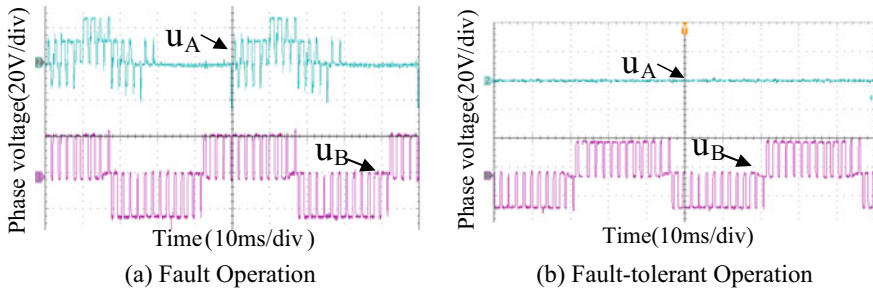


**Fig. 11** Output phase voltage waveform of phase  $A$  and  $B$  when  $T_{a2}$  and  $T_{a5}$  fail

## 5 Conclusion

An improved ANPC three-level converter topology and a self-diagnosis control algorithm are proposed in this paper, which can overcome single open-circuit fault and most of the compound faults without loss of output performance. The topology reconfiguration can be implemented by calculating the corresponding switch state with the proposed algorithm in real time according to the fault position. The FTC method can adapt to various fault modes with practical value. The effectiveness of the proposed topology and control algorithm is verified by simulation and experimental results.

## References

- Findings on Energy Reported by Investigators at Konkuk University (2018) A Harmonic Voltage Injection Based DC-Link Imbalance Compensation Technique for Single-Phase Three-Level Neutral-Point-Clamped (NPC) Inverters. *Energy Weekly News*
- Hui L, Ran Y, Wei L, Hai R, Jinyuan L (2019) Modeling and analysis on overall fatigue failure evolution of press-pack IGBT device. *IEEE Trans Electron Devices* 66(3):1435–1443
- Xulong Z, Feng W, Wen J, Shuyun Q, Yanjing C (2017) Fault tolerant control method for three-level photovoltaic inverter based on redundant voltage space vector. In: 2017 36th Chinese Control Conference (CCC), Dalian, pp 9249–9253
- Qinyue Z, Lei G, Xitang T, Wenlong L, Ling T (2017) Four-leg fault-tolerant control of traction inverter for composite fault. *J Power Supply* 15(02):59–66 (in Chinese)
- Wenxuan F, Peng Z, Yu W et al (2017) Research on fault tolerant control of three-level ANPC converter under open-circuit fault. *Power Electron* 51(03):4–8
- Rocha AV, Silva SM, Pires IA (2014) A new fault-tolerant realization of the active three-level NPC converter. In: Energy Conversion Congress and Exposition, IEEE, pp 3483–3490
- Fengjun L (2007) Multi-level inverter technology and its application. China Machine Press, China (in Chinese)
- Hangpeng X, Quan C, Guoli L, Xiang D (2019) Research on neutral-point voltage balance of three-level NPC inverter based on improved SVPWM. *Mod Electron Tech* 42(04):129–133 (in Chinese)

9. Jun H, Cungang H, Zhongyuan W (2015) Study on SVPWM method based on KL coordinate system for three-level ANPC inverter. In: 2015 IEEE 10th Conference on Industrial Electronics and Applications (ICIEA), Auckland, pp 1637–1640
10. Byong-Gun P, Jae-Woon L, Min-Hyuk A, Soon-Man K, Ji-Won K (2018) Simple fault-tolerant control using unified voltage modulation for Active Neutral Point Clamped (ANPC) three-level inverter. In: 2018 IEEE 18th International Power Electronics and Motion Control Conference (PEMC), Budapest, pp 1031–1037
11. Liu L, Yin J, Jin G, Zhou P (2017) Simulation of traction drive control system of high-speed EMUs. *Electr Drive Autom* 39:12–15 (in Chinese)

# Reliability Analysis of Metro Traction Substation Based on Bayesian Network



Guangtao Cong, Wen Xu and Zongyi Xing

**Abstract** As an important part of urban rail transit system, metro traction power supply system has important significance for ensuring the safe and stable operation of the system. In order to evaluate the reliability of the metro traction substation, the reliability model of the system based on Bayesian network is established, and the initial failure probability of the system is calculated in this paper firstly. Secondly, the dynamic Bayesian network is used to analyze the reliability of the typical metro traction substation in the time dimension, and the curve of system failure probability with time is accurately calculated. Finally, the two-way inference function of Bayesian network is used to find the weak link of the system, so that the reliability analysis of the metro traction substation is realized.

**Keywords** Traction substation · Bayesian network · Reliability

## 1 Introduction

With the rapid development of human society, the prosperity of the city continues to increase in spite of the fact that urban traffic congestion is also growing exponentially. Therefore, subway has become the main way to alleviate traffic congestion in large and medium-sized cities [1] consider to its large transportation capacity, significant energy saving and environmental protection, rapid safety and punctuality [2]. As the increasing development of urban subway lines has greatly facilitated the daily travel of the people, the safe and reliable operation of subway traction power supply system is also facing new challenges.

In this paper, the top event fault rate of the metro traction substation's reliability model is calculated by GeNIE simulation software, which is based on Bayesian network. And for the purpose of the posterior probability order of each node, joint

---

G. Cong · W. Xu · Z. Xing (✉)

School of Automation, Nanjing University of Science and Technology,  
Nanjing, Jiangsu, China  
e-mail: [xingzongyi@163.com](mailto:xingzongyi@163.com)

model is used to calculate the network model [3]. Then, we can quantitatively identify the weak link of the initial state of the system; at the same time, another reliability model of the traction substation is established, which is based on the dynamic Bayesian network to obtain its performance in the time dimension. Through the system's time-varying failure rate curve and a posteriori probability ordering, we can determine the main factors affecting the system's steady-state reliability and provide theoretical support for the next system monitoring and equipment maintenance.

## 2 Bayesian Network

### 2.1 *The Basic Principle of Bayesian Network*

The Bayesian network, also known as the Bayesian reliability network, uses a directed graph to express the probability relationship between system variables to solve the uncertainty caused by the conditional correlation of various components of the system [4].

Probability theory is the basis of the development of Bayesian network theory. Probabilistic knowledge commonly used in computational reasoning using Bayesian network theory includes: conditional probability, Bayesian formula, prior probability, posterior probability, and conditional independence [5].

Let event set be  $E$ ,  $B$  be the sample data of the event set, and  $B = \{B_1, B_2, \dots, B_n\}$  is an independent event group, and  $P(B_i) > 0$ ,  $A$  is any event in  $E$ , and then,

$$P(B_i|A) = \frac{P(A|B_i)P(B_i)}{\sum_{j=1}^n P(B_j)P(A|B_j)} \quad (1)$$

In the above formula,  $P(B_i)$  represents the prior probability, which is generally judged by experts or calculated based on existing historical statistics and is the initial probability value in the network;  $P(B_i|A)$  represents the posterior probability, which can be corrected by the Bayesian formula of the component prior probability;  $P(A|B_i)$  represents the conditional probability, indicating the conditional probability that event  $A$  also occurs under the condition that event  $B_i$  occurs.

Bayesian network graphics are mainly directed acyclic graphs composed of nodes and directed edges, as shown in Fig. 1. The nodes include three types: root node, leaf node, and intermediate node, which represent different random variables in the system and connect nodes. The directed edge represents the logical relationship between nodes, which can be represented by a conditional probability table in detail.

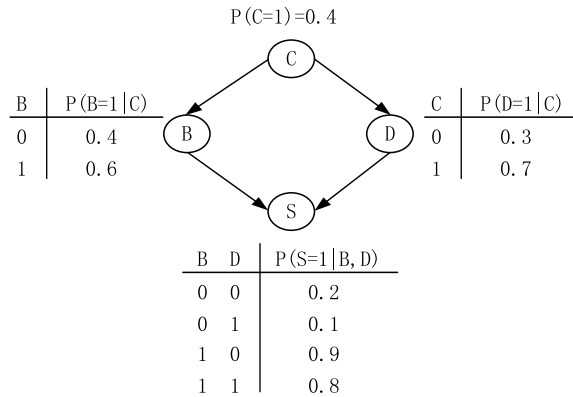


**Fig. 1** Graphical representation of a Bayesian network

Figure 1 is a graphical representation of a Bayesian network containing four nodes and four directed edges,  $P(C = 1) = 0.4$  representing the prior probability of node C, and nodes B, D, and S labeled with their respective conditional probability tables.

## 2.2 The Basic Principle of Dynamic Bayesian Network

Dynamic Bayesian network is based on the extension of static Bayesian network considering time problem, which inherits the advantages of Bayesian network analysis and reasoning, extends the static network structure to the time dimension, and finally forms a network model that can solve the timing problem [6].

When describing the stochastic model of a dynamic system with a dynamic Bayesian network, the first is to obtain the joint probability distribution of the system random variable  $X[1], \dots, X[n]$ . Therefore, when studying complex dynamic system models, it is necessary to simplify the processing based on two constraints: stationary hypothesis and Markov assumption [7]. The joint probability distribution of the stochastic process described by the dynamic Bayesian network can be composed of two parts: a static initial network and a transfer network [8].

The initial network  $B_0$  represents the joint probability distribution of the event in the initial state  $X[0]$ . Transfer network  $B_{\rightarrow}$  represents the transition probability distribution of the event under  $X[t - 1], X[t]$ , denoted as  $P(X[t]|X[t - 1])$ . Given the initial network and the transition network of the dynamic Bayesian network model  $B^*(B_0, B_{\rightarrow})$ , the joint probability distribution of the random variable  $X[1], \dots, X[n]$  can be expressed as:

$$P(X[0], \dots, X[n]) = P_{B_0}(X[0]) \prod_{t=0}^{n-1} P_{B_{\rightarrow}}(X[t+1]|X[t]) \quad (2)$$

It can be obviously known from Formula (2) that the dynamic Bayesian network model describes the probability distribution of the system on the time trajectory in the dynamic random process.

### 3 Reliability Model of Metro Traction Substation

#### 3.1 Representative Main Wiring of Metro Traction Substation

In the reliability study of the subway traction substation, the first thing to consider is the structural composition and operation mode of the system. At the same time, it is necessary to fully understand the reliability model of each component of the system and the characteristics of its fault form. Historical statistics show that the distribution function of failure rate is different for different types of equipment. If you use different failure rate distribution functions when building the reliability model of the entire life cycle of the system, the complexity of reliability modeling and analysis will be greatly increased. In general, the failure rate of the main equipment of the power system is often low, and the reliability parameter error obtained by the statistical method may have a greater impact on the system reliability. Considering the requirements of system calculation accuracy and complexity, and according to the actual situation of a certain line, it is assumed in the calculation process that all components are in the accidental fault zone near the middle of life, that is, the failure rate is constant, and the reliability function of the system components obeys the exponential distribution.

The main wiring of a representative subway traction substation is shown in Fig. 2. The main equipment includes 35 kV AC bus, AC circuit breaker, electric disconnector, manual disconnector, rectifier transformer, rectifier, DC bus, and current transformer. And according to the main wiring form of the traction substation, its operation mode can be divided into normal operation mode and fault operation mode.

#### 3.2 Reliability Model of Representative Metro Traction Substation

##### (1) Bayesian network model

Firstly, based on the Bayesian network model construction method, the basic events and logical relationships in the system main wiring shown in Fig. 2 are converted into nodes in the Bayesian network graph by the GeNIE software. Secondly, according to the hierarchical relationship between the basic events of the metro traction substation, all the nodes in the Bayesian network model are connected by

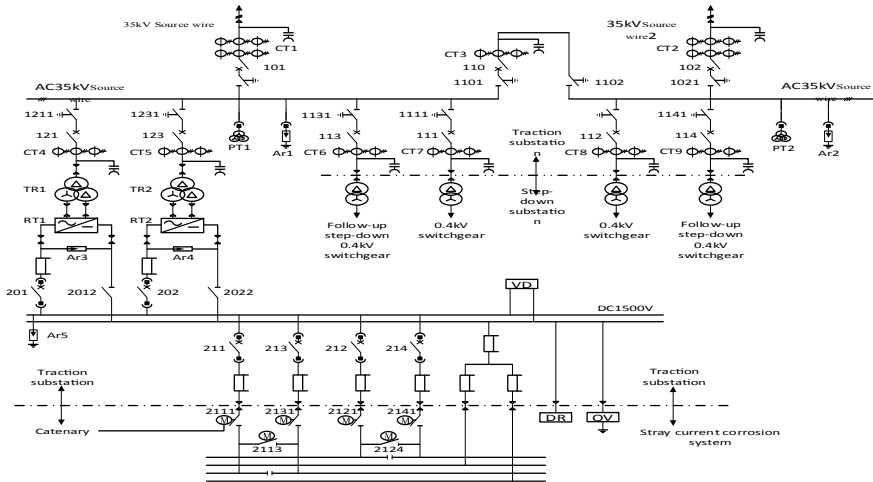


**Fig. 2** Representative main wiring of metro traction substation

the directed edges. Then, set the conditional probability table of part nodes in the Bayesian network and determine the prior probability of the other nodes. Finally, we get the reliability model of the Bayesian network of a typical metro traction substation which is shown in Fig. 3. The fault data of each major device is shown in Table 1, and the correspondence between each node and the basic event in the Bayesian network model is shown in Table 2. ( $S$ ,  $M$ , and  $T$  series node are calculated by  $X$  series basic node).

## (2) dynamic Bayesian network model

The method of establishing a system reliability model using dynamic Bayesian network is similar to that of a static Bayesian network, including graph nodes, directed edges, conditional probability tables, transition probability tables, and prior probability settings. The difference is that the dynamic Bayesian network introduces the time factor, which represents that the conditional transition probability between the current time and the next unit time of the same network node needs to be

**Fig. 3** Bayesian network model of representative metro traction substation

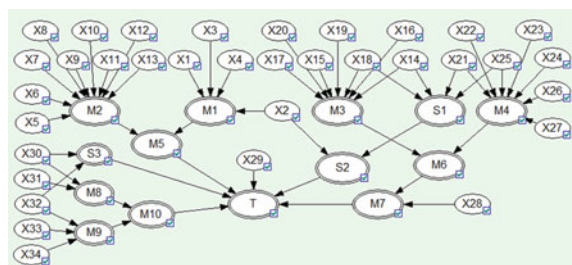


**Table 1** Traction data of each component of the traction substation

Device name	Failure rate (times/year)	Recovery rate ( $\text{h}^{-1}$ )	Probability of failure
35 kV source wire	0.8	0.09091	1.005E-3
35 kV bus bar	0.1	0.33333	3.425E-5
Breaker	0.12	0.33333	4.110E-5
Electric switch	0.08	0.33333	2.740E-5
Isolation switch	0.015	0.33333	5.137E-6
Current transformer	0.015	0.1	1.712E-5
Rectifier transformer	0.09	0.03333	3.082E-4
Rectifier	0.09	0.05	2.055E-4
DC bus	0.065	0.1	7.420E-5
DC circuit breaker	0.12	0.33333	4.110E-5

**Table 2** Meaning of each event node in the Bayesian network model

Number	Event	Number	Event	Number	Event	Number	Event
X1	35 kV source wire 1	X18	Breaker 121	X9	Breaker 102	X26	Current transformer CT5
X2	Breaker 101	X19	Current transformer CT4	X10	Breaker 110	X27	Isolation switch 1231
X3	Current transformer CT1	X20	Isolation switch 1211	X11	Isolation switch 1021	X28	DC bus
X4	Isolation switch 1011	X21	Breaker 202	X12	Isolation switch 1101	X29	35 kV Bus bar 1
X5	35 kV source wire 2	X22	Rectifier 2	X13	35 kV Bus bar 2	X30	Breaker 212
X6	Isolation switch 1102	X23	Isolation switch 2022	X14	Breaker 201	X31	Isolation switch 2121
X7	Current transformer CT2	X24	Rectifier transformer 2	X15	Rectifier 1	X32	Breaker 214
X8	Current transformer CT3	X25	Breaker 123	X16	Isolation switch 2012	X33	Isolation switch 2141
X17	Rectifier transformer 1	X34	Isolation switch 2124				

determined during the establishment of the network model. Since the dynamic Bayesian network is based on the stationary hypothesis and the Markov assumption, we have,

$$P(A(t + \Delta t) = 1 | A(t) = 0) = \int_0^{\Delta t} f_A(t) dt \quad (3)$$

Then, the conditional transition probability between two adjacent time periods of a dynamic Bayesian network can be expressed as,

$$\left\{ \begin{array}{l} P(A(t + \Delta t) = 1 | A(t) = 0) = \int_0^{\Delta t} f_A(t) dt \\ P(A(t + \Delta t) = 1 | A(t) = 1) = 1 - \int_0^{\Delta t} m_A(t) dt \\ P(A(t + \Delta t) = 0 | A(t) = 0) = 1 - \int_0^{\Delta t} f_A(t) dt \\ P(A(t + \Delta t) = 0 | A(t) = 1) = \int_0^{\Delta t} m_A(t) dt \end{array} \right. \quad (4)$$

In the formula, 1 means node  $A$  is invalid; 0 means node  $A$  works normally;  $f_A(t)$  is the failure density function of node  $A$ ; and  $m_A(t)$  is the maintenance density function of  $A$ . Then, the transition probability table between the current time and the next time of node  $A$  is shown in Table 3.

In terms of a dynamic Bayesian network, not only the static network needs to be assigned, but also the assignment of its transfer network. Assuming that the repair rate and failure rate of each major equipment of the system are constant, that is, the equipment life function is exponentially distributed, the failure density function can be expressed as  $f(t) = \lambda e^{-\lambda t}$  and the maintenance density function is  $m(t) = \mu e^{-\mu t}$ . According to the calculation of the transition probability in Table 3, the conditional

**Table 3** Transition probability table of node  $A$

$A$	1	0
1	$1 - \int_0^{\Delta t} m_A(t) dt$	$\int_0^{\Delta t} f_A(t) dt$
0	$\int_0^{\Delta t} m_A(t) dt$	$1 - \int_0^{\Delta t} f_A(t) dt$

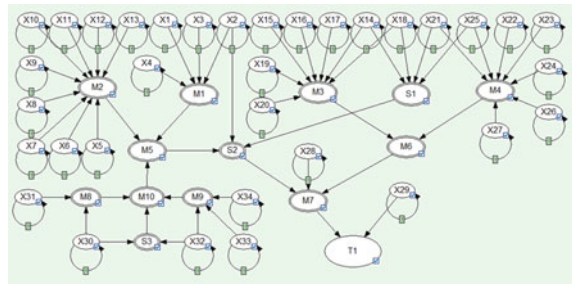
**Table 4** Conditional probability table of node  $X1$  in time slice

X1	Conditional probability
1	0.001005
0	0.998995

**Table 5** Transition probability table of node  $X1$  at adjacent time

$X1(t - 1)$	1	0
1	0.91310072	0.001004495
0	0.086899284	0.99899551

**Fig. 4** Dynamic Bayesian network model of representative metro traction substation



transition probability table of each node in the dynamic Bayesian network can be obtained. For example, Tables 4 and 5 are the conditional probability table and the transition probability table of the node  $X_1$ , respectively.

According to the Bayesian network model of the typical metro traction substation shown in Fig. 3, its dynamic Bayesian network is constructed in GeNIE software as well, whose topology is shown in Fig. 4. Besides, the specific meaning of each node is the same as the static Bayesian network node.

#### 4 Reliability Analysis of Metro Traction Substation

After determining the topology, node prior probability, and conditional probability of the Bayesian network of the traction substation, we obtain the probability that the traction substation cannot supply normal power to the uplink contact network is about 0.015668644%. If the reliability of the system is required to be not less than 0.9, the time interval for preventive maintenance should not exceed 671 h in order to ensure the reliable operation of the metro traction power supply system. After setting the initial probability and transition probability, the system failure rate with the consideration of the maintenance factor in time dimension can be easily obtained, as shown in Fig. 5.

When the system is in steady-state operation for a period of time considering the maintenance factor, it can be found that the failure rate will increase rapidly in the early stage of the traction power supply system operation. However, the system failure rate reaches a steady state after 180 h, and its steady-state failure rate is about 0.14035505%. At the same time, using the backward reasoning function of the Bayesian network, the posterior probability of each component of the system in both static network and dynamic network can be calculated separately, as shown in Table 6.

According to Table 6, the DC bus and 35 kV busbars I in the static Bayesian network have a greater impact on the reliability of the traction substation, and the posterior probability is 47.30% and 21.83%, respectively, which is the weak link of system reliability. The above calculation result is in line with the actual cause of system failure during system operation, which is consistent with the actual situation

**Fig. 5** System failure rate in time dimension

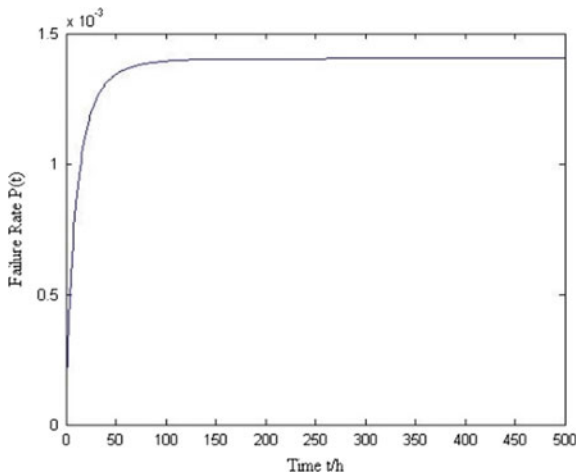


**Table 6** Posteriori probability table of the main nodes

Device name	Static Bayesian network (%)	Dynamic Bayesian network (%)	Device name	Static Bayesian network (%)	Dynamic Bayesian network (%)
DC bus	47.301387	55.507729	35 kV bus bar 2	0.026573367	0.11198961
35 kV Bus bar 1	21.833861	8.607243	CT1	0.014475599	0.17283591
Breaker 101	4.291431	1.819357	CT2	0.013282804	0.16674175
Breaker 123	4.279142	1.836635	CT3	0.013282804	0.16674175
Source wire 1	0.84976499	10.980333	Isolation switch 1102	0.0039856172	0.016798953
Source wire 2	0.77974407	10.593168	Isolation switch 1101	0.0039856172	0.016798953
Rectifier transformer 1	0.15053847	10.057647	Isolation switch 2141	0.0038194255	0.011325897
Rectifier transformer 2	0.15053847	10.057647	Isolation switch 2124	0.0038194255	0.011325897
Breaker 110	0.031888041	0.13438901	Isolation switch 2022	0.0025091373	0.01957268

of DC bus or AC bus disconnection. However, in the dynamic Bayesian network, the posterior probability of DC bus, 35 kV incoming power and rectifier transformer is ranked higher, indicating that the above nodes are weak links after the system is steady. In the maintenance process, it is necessary to strengthen the maintenance of the above components to improve the reliability of each unit to improve the reliability of the power supply zone under the bilateral power supply mode.

At the same time, according to the comparison results of Table 6, it can be seen that the post-test probability of some nodes changes greatly after considering the maintenance factor, indicating that the maintenance rate of the equipment will affect the importance of the node in the system when considering the maintenance factor. For example, transformers and rectifiers are the key equipment of the system. Although the failure rate is low, the posterior probability of system failure is small. However, considering the maintenance factors such as long repair time and low repair rate of the equipment, its impact on the steady-state reliability of the system will be increasingly amplified. Therefore, in addition to reducing the failure rate of the equipment itself, it can also optimize the maintenance strategy of the key equipment and improve its maintenance rate, so that the system can keep a high reliability level for a long time.

## 5 Conclusion

In this paper, firstly, the Bayesian network is used to analyze the reliability of the metro traction substation. The reliability model of the system based on Bayesian network is established by GeNIE simulation software, which helps to calculate the system's failure probability. Secondly, through establishing the dynamic Bayesian network, the system failure rate is analyzed, and the curve of failure rate changes with time is obtained. Finally, using the two-way inference function of Bayesian network, the posterior probability order of each component in the initial state and steady state is calculated, while the weak link of the system is found, which may have significant contribution to the identification of system key nodes, system maintenance, and network structure optimization.

**Acknowledgements** This work is supported by National Key R&D Program of China (2017YFB1201202).

## References

1. Cui H, Ma T (2009) Research on Urban Transportation Sustainable Development Strategy Based on Traffic Demand. *J Wuhan Univ Technol (Social Science Edition)* 22(3):80–84
2. Yang W (2016) Research on reliability analysis method and its application in high speed railway, Southwest Jiaotong University (in Chinese)
3. Karaduman O, Eren H, Kurum H, Celenk M (2013) Interactive risky behavior model for 3-car overtaking scenario using joint Bayesian network. *Intelligent Vehicles Symposium (IV), 2013 IEEE*
4. Zhang L, Wu X, Skibniewski MJ et al (2014) Bayesian-network-based safety risk analysis in construction projects. *Reliab Eng Syst Saf* 131(3):29–39
5. Zhai S, Lin SZ (2013) Bayesian networks application in multi-state system reliability analysis. *Appl Mech Mater* 347–350:2590–2595. Brown B, Aaron M (2001) The politics of nature. In: Smith J (ed) *The rise of modern genomics*, 3rd edn. Wiley, New York

6. Yao J Y, Jiao L, Li H et al (2015) Modeling system based on fuzzy dynamic Bayesian network for fault diagnosis and reliability prediction. In: Reliability & Maintainability Symposium, 2015
7. Wu X, Liu H, Zhang L et al (2015) A Dynamic Bayesian network based approach to safety decision support in tunnel construction. Reliab Eng Syst Saf 134:157–168
8. Cai B, Liu Y et al (2015) Real-time reliability evaluation methodology based on dynamic bayesian networks: a case study of a subsea pipe ram bop system. ISA Transactions, 58, S0019057815001470

# Study on Steady-State Output Characteristics of Three-Level Boost Converter



Chengwei Kang, Wei Wang, Guoqin Zhang and Huiqing Du

**Abstract** The application of the three-level boost converter (TLBC) is able to reduce the voltage stress of power switches and diodes in the back-end circuit, also can reduce the volume and weight of energy storage components, and improve the overall power density of the DC–DC converter system. In this paper, the output characteristics of TLBC used as a voltage stabilizer in high-voltage applications are studied. The topology of TLBC is introduced, and the voltage–current relationship of the converter in five basic switching modes is analyzed with the equivalent circuits. The mathematical models are established for all modes. And then the continuous conduction mode (CCM) of TLBC has been analyzed and derived the voltage gain with different duty ratios in this mode. The working characteristics under CCM mode were analyzed from three aspects including ripple current, ripple voltage and controller design. The output characteristics of TLBC are obtained, which provides a theoretical basis for the design and application of TLBC. Finally, simulation experiments verified the conclusion obtained by analyzing the TLBC steady-state output characteristics.

**Keywords** Three-level boost converter · Output characteristics · Mathematical model

---

C. Kang (✉) · G. Zhang  
CRRC Changchun Railway Vehicles Co., Ltd., Changchun 130062, China  
e-mail: [kcw\\_2014@163.com](mailto:kcw_2014@163.com)

G. Zhang  
e-mail: [zhangguoqin@cccar.com](mailto:zhangguoqin@cccar.com)

W. Wang  
CRRC Qingdao Sifang Rolling Stock Research Institute Co., Ltd.,  
Qingdao 266000, China  
e-mail: [wangwei1809@163.com](mailto:wangwei1809@163.com)

H. Du  
CSSC System Engineering Research Institute, Beijing 100094, China  
e-mail: [huiqingdu@126.com](mailto:huiqingdu@126.com)

## 1 Introduction

DC/DC converter is often used as a front-stage voltage stabilizing circuit in train auxiliary converter to reduce the input voltage variation range, ensure the stability of intermediate DC voltage, provide reliable protection for the DC input voltage of the inverter [1], and prevent the inverter from unreliable working conditions.

Because of its simple topology, continuous input current and high efficiency, the boost converter is often used as a voltage stabilizing circuit for the auxiliary converter [2, 3]. Compared with the two-level topology, TLBC is more suitable for high-voltage and high-power applications. In reference [3], a test platform used for urban railway vehicles is established based on the TLBC topology and its property has been evaluated. And those test results in reference [4–6] have proved that TLBC also can reduce the voltage stress of boost diodes, reduce the loss caused by the reverse recovery, and improve the equivalent switching frequency, which reduces the output voltage harmonic distortion and the size of the energy storage components such as boost inductors and filter capacitors.

In this paper, the output characteristics of TLBC have been analyzed theoretically. Based on the five kinds of converter switching modes, the mathematical model of TLBC is established. Then, the voltage gain, under working conditions of continuous conduction mode (CCM) and discontinuous conduction mode (DCM), is deduced. And this paper summarizes the advantages and disadvantages of TLBC, based on the comparison of working characteristics under different modes. Finally, TLBC simulation model is established to verify the correctness of theoretical analysis.

## 2 Mathematical Model of TLBC

The TLBC is evolved from the floating-capacitor-clamped multilevel inverter. The topology of TLBC is shown in Fig. 1, where  $L_b$  is the boost inductor,  $Q_{b1}$  and  $Q_{b2}$  are the main switches,  $D_{b1}$  and  $D_{b2}$  are the boost diodes,  $C_{b1}$  and  $C_{b2}$  are the filter capacitor,  $u_{Lb}$  is the boost inductor voltage,  $V_{dc}$  is the input voltage,  $i_{Lb}$  is the boost

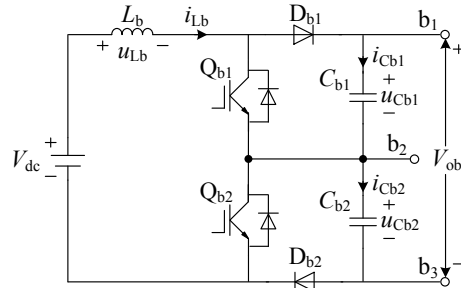


**Fig. 1** Topology of three-level boost converter

inductor current,  $u_{Cb1}$  and  $u_{Cb2}$  are the two filter capacitor voltages,  $i_{Cb1}$  and  $i_{Cb2}$  are the two filter capacitor currents and  $V_{ob}$  is the output voltage.

To facilitate the establishment of mathematical model, some assumptions, approximations and definitions are made:

- (1) All switches, diodes, inductors and capacitors in the circuit are ideal components.
- (2) The converter satisfies the low frequency and the small ripple hypothesis [7].
- (3) Under steady-state conditions, the load of TLBC can be equivalent to two-path resistive load [8], and  $R_{b1} = R_{b2} = R_b/2$ .
- (4) The capacitance values of  $C_{b1}$  and  $C_{b2}$  are large enough and both are  $C_b$ , thus, it can be equivalent to a constant voltage source with voltage  $u_{Cb} = V_{ob}/2$ . And the load current is constant at  $I_{ob} = V_{ob}/R_b$ .
- (5) The switching frequency is  $f_{sb}$ , switching period  $T_{sb} = 1/f_{sb}$ , opening time  $t_{on-b} = D_{on-b}T_{sb}$ ,  $D_{on-b}$  is duty ratio.

There are two main switches  $Q_{b1}$  and  $Q_{b2}$  in TLBC topology, let the switching states be  $S_1$  and  $S_2$ , respectively,  $S = 0/1$ (turn on/turn off). According to its four switching states  $S_{1,2} = 00, 01, 10, 11$ , the converter can be divided into the following four basic states.

According to Kirchhoff's circuit law (KCL) and Kirchhoff's voltage law (KVL), the voltage-current relationship of the four basic states can be obtained, which describes the dynamic characteristics of inductor current and capacitor voltage. And then the steady-state output characteristics of the system can be analyzed.

Mode 1(M1): As shown in Fig. 2a,  $S_{1,2} = 00$ , switches  $Q_{b1}$  and  $Q_{b2}$  turn on at the same time, diodes  $D_{b1}$  and  $D_{b2}$  are reverse biased and whose voltage stress is  $V_{ob}/2$ . The input voltage is applied at  $L_b$ , so the inductor current increases linearly  $i_{Lb} = i_{Lb0} + V_{dc}t/L_b$ . Filter capacitors  $C_{b1}$  and  $C_{b2}$  provide energy to the loads, capacitor current is  $i_{Cb1} = i_{Cb2} = (-I_{ob}) < 0$ .

Mode 2(M2): As shown in Fig. 2b),  $S_{1,2} = 01$ , switch  $Q_{b1}$  turns on and  $Q_{b2}$  turns off, diode  $D_{b1}$  cuts off and  $D_{b2}$  conducts and the voltage stress of  $Q_{b2}$  and  $D_{b1}$  is  $V_{ob}/2$ . Inductor current  $i_{Lb}$  provides energy to  $C_{b2}$  and  $R_{b2}$ ,  $i_{Cb2} = (i_{Lb} - I_{ob}) > 0$ . The change of inductor current  $i_{Lb}$  is related to the  $u_{Cb2}$ . When  $u_{Cb2} < V_{dc}(D_{on-b} < 0.5)$ ,  $i_{Lb}$  increases, while  $u_{Cb2} > V_{dc}(D_{on-b} > 0.5)$ ,  $i_{Lb}$  drops. Capacitor  $C_{b1}$  provides energy to  $R_{b1}$ ,  $i_{Cb1} = (-I_{ob}) < 0$ .

Mode 3(M3): As shown in Fig. 2c),  $S_{1,2} = 10$ , switch  $Q_{b2}$  turns on and  $Q_{b1}$  turns off, diode  $D_{b2}$  cuts off and  $D_{b1}$  conducts, the voltage stress of  $Q_{b1}$  and  $D_{b2}$  is  $V_{ob}/2$ . Stage of the work is consistent with the mode 2, two capacitor currents are, respectively,  $i_{Cb1} = (i_{Lb} - I_{ob}) > 0$ ,  $i_{Cb2} = (-I_{ob}) < 0$ . Mode 4(M4): As shown in Fig. 2d),  $S_{1,2} = 11$ , switches  $Q_{b1}$  and  $Q_{b2}$  turn off at the same time, diodes  $D_{b1}$  and  $D_{b2}$  are conducted. Inductor current  $i_{Lb}$  provides energy to loads, so the inductor current drops linearly  $i_{Lb} = i_{Lb0} - (V_{ob} - V_{dc})t/L_b$ . Current of the capacitors is  $i_{Cb1} = i_{Cb2} = (i_{Lb} - I_{ob}) > 0$ .

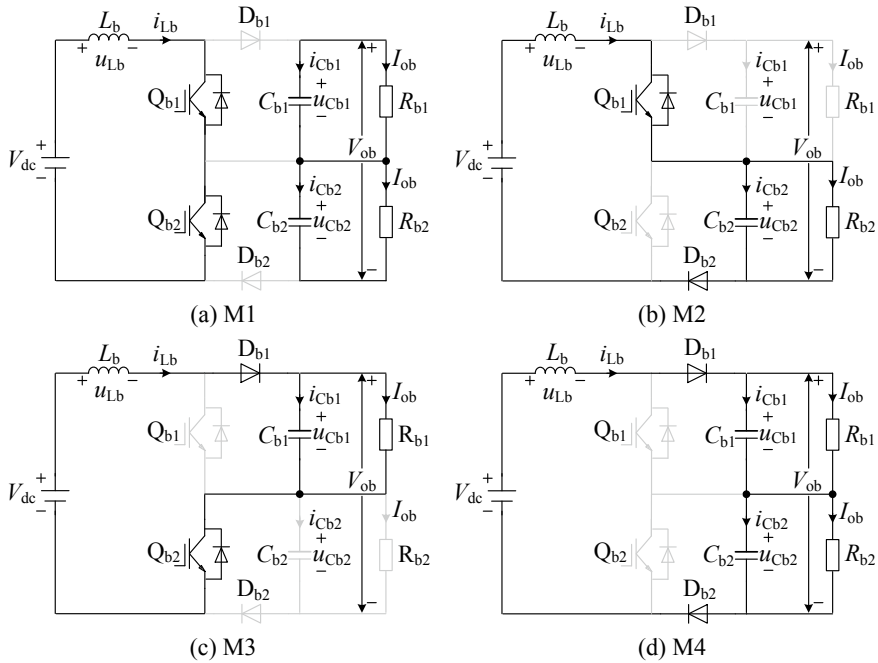


**Fig. 2** Equivalent circuits under four basic switching modes

The voltage–current relationship of modes 1–4 can be integrated into state equations which include the states of the switches:

$$\frac{d}{dt} \begin{bmatrix} i_{Lb} \\ u_{Cb1} \\ u_{Cb2} \end{bmatrix} = \begin{bmatrix} 0 & -S_1/L_b & -S_2/L_b \\ S_1/C_{b1} & -1/(C_{b1}R_{b1}) & 0 \\ S_2/C_{b2} & 0 & -1/(C_{b2}R_{b2}) \end{bmatrix} \begin{bmatrix} i_{Lb} \\ u_{Cb1} \\ u_{Cb2} \end{bmatrix} + \begin{bmatrix} 1/L_b \\ 0 \\ 0 \end{bmatrix} V_{dc} \quad (1)$$

In modes 2 and 3 when \$D\_{on-b} > 0.5\$ and in mode 4, inductor current will drop. If the current drops to 0, there will be another state, which is set as Mode 5(M5): The inductor current drops to 0, thus, the diodes are turned off. And the inductor is disconnected from the load side, which hinders the continuous drop of the inductor current and keeps it at 0 until the next switching states. If it is switched by mode 2/3, voltage stress of \$Q\_{b2}/Q\_{b1}\$ is \$V\_{dc}\$, voltage stresses of \$D\_{b1}/D\_{b2}\$ and \$D\_{b2}/D\_{b1}\$ are \$V\_{ob}/2\$, \$V\_{ob}/2 - V\_{dc}\$, respectively. When switching from mode 4, the voltage stress of \$Q\_{b1}\$, \$Q\_{b2}\$ are \$V\_{dc}/2\$, respectively, and the voltage stress of \$D\_{b1}\$ and \$D\_{b2}\$ is \$V\_{ob}/2 - V\_{dc}\$. Filter capacitor \$C\_{b1}\$ and \$C\_{b2}\$ provide energy to the loads, current of the capacitor is \$i\_{Cb1} = i\_{Cb2} = (-I\_{ob}) < 0\$, the voltage–current relationship of this stage is:

$$\frac{d}{dt} \begin{bmatrix} i_{Lb} \\ u_{Cb1} \\ u_{Cb2} \end{bmatrix} \begin{bmatrix} 0 & 0 & 0 \\ 0 & -1/(C_{b1}R_{b1}) & 0 \\ 0 & 0 & -1/(C_{b2}R_{b2}) \end{bmatrix} \begin{bmatrix} i_{Lb} \\ u_{Cb1} \\ u_{Cb2} \end{bmatrix} \quad (2)$$

In the actual working process, TLBC is regular switched between the above five basic switching modes, namely in the switching state  $S_{1,2} = 00, 01, 10, 11$ . Often we use  $180^\circ$  staggered pulse width modulation: switches  $Q_{b1}$  and  $Q_{b2}$  by pulse width modulation based on the same reference wave, but two carrier signals are having a phase difference by  $180^\circ$ , which makes switching states of  $Q_{b1}$  and  $Q_{b2}$  are having a  $180^\circ$  phase difference too. According to different boost inductor current states in the circuit, TLBC will work in the two kinds of conductive pattern: If the inductor current is always greater than zero, the system works under CCM; if the inductor current has dropped to zero at the end of a switch mode, then it works under DCM [9–11].

### 3 TLBC Under Continuous Conduction Mode

Limited by paper length, this passage mainly analyzes the CCM working pattern of TLBC. It can be seen from the operating characteristics of basic switching modes that the variation of inductor current in mode 2 and mode 3 is affected by duty ratio  $D_{on-b}$ : when  $D_{on-b} < 0.5$ ,  $i_{Lb}$  increases; when  $D_{on-b} > 0.5$ ,  $i_{Lb}$  drops. Typical switching waveforms of TLBC in CCM are shown in Fig. 3 and the switching processes are different under different duty ratios. When  $D_{on-b} < 0.5$ , the switches switch between modes 2, 3 and 4; when  $D_{on-b} > 0.5$ , the switches switch between modes 1, 2 and 3. TLBC in the two cases is analyzed and its output characteristics have been deduced.

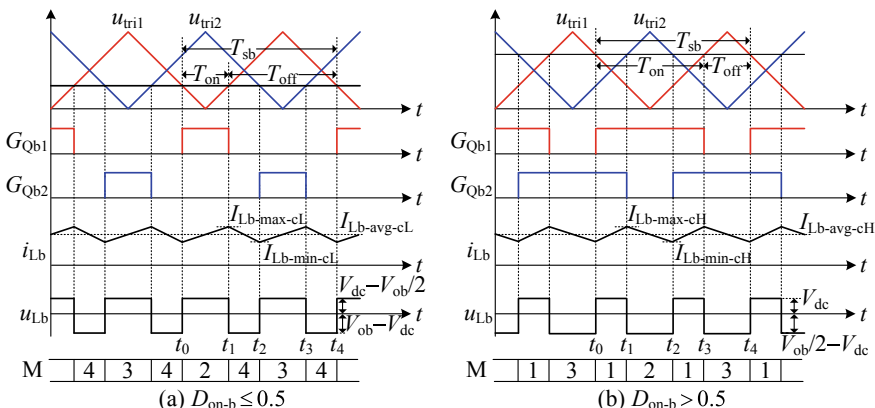


**Fig. 3** Typical switching waveforms of TLBC in CCM

Case (a):  $D_{\text{on-b}} \leq 0.5$ , waveform is shown in Fig. 3a), in a switching cycle  $T_{\text{sb}}$ , the switching mode sequence of the system is: M2 → M4 → M3 → M4. The inductor current variations of modes 2 and 3 are consistent, so the output characteristics can be obtained by only analyzing half a period  $[t_0, t_2]$ .

$[t_0, t_1]$ : The system operates in mode 2, and the inductor voltage is  $V_{\text{dc}} - u_{\text{Cb}2}$ . Since  $u_{\text{Cb}2} \leq V_{\text{dc}}$  when  $D_{\text{on-b}} \leq 0.5$ , the inductor current increases linearly, and the current increment is:

$$\Delta I_{\text{Lb-cL+}} = \frac{V_{\text{dc}} - V_{\text{ob}}/2}{L_b} (t_1 - t_0) = \frac{V_{\text{dc}} - V_{\text{ob}}/2}{L_b} D_{\text{on-b}} T_{\text{sb}} \quad (3)$$

$[t_1, t_2]$ : The system operates in mode 4, and the inductor voltage is  $V_{\text{dc}} - u_{\text{Cb}2}$ . The inductor current drops linearly, and the current decrement:

$$\Delta I_{\text{Lb-cL-}} = \frac{V_{\text{ob}} - V_{\text{dc}}}{L_b} (t_2 - t_1) = \frac{V_{\text{ob}} - V_{\text{dc}}}{L_b} \left( \frac{1}{2} - D_{\text{on-b}} \right) T_{\text{sb}} \quad (4)$$

When the system works under steady state, the variation of inductor current in one cycle is 0, that is, the changes of inductor current of adjacent modes have equal size and opposite phase,  $\Delta I_{\text{Lb-cL+}} = \Delta I_{\text{Lb-cL-}}$ . Thus, it can be obtained that the voltage gain of system under CCM when  $D_{\text{on-b}} \leq 0.5$  is:

$$M_{\text{ob-c}} = \frac{V_{\text{ob}}}{V_{\text{dc}}} = \frac{1}{1 - D_{\text{on-b}}} \quad (5)$$

Case (b):  $D_{\text{on-b}} > 0.5$ , waveform is shown in Fig. 3b), in a switching cycle  $T_{\text{sb}}$ , the switching mode sequence of the system is: M1 → M2 → M1 → M3. The inductor current variations of modes 2 and 3 are consistent, so the output characteristics can be obtained by only analyzing half a period  $[t_0, t_2]$ .

$[t_0, t_1]$ : The system operates in mode 1, and the inductor voltage is  $V_{\text{dc}}$ . The inductor current increases linearly, and the current increment is:

$$\Delta I_{\text{Lb-cL+}} = \frac{V_{\text{dc}}}{L_b} (t_1 - t_0) = \frac{V_{\text{dc}}}{L_b} \left( D_{\text{on-b}} - \frac{1}{2} \right) T_{\text{sb}} \quad (6)$$

$[t_1, t_2]$ : The system operates in mode 2, and the inductor voltage is  $V_{\text{dc}} - u_{\text{Cb}2}$ . Since  $u_{\text{Cb}2} > V_{\text{dc}}$  when  $D_{\text{on-b}} > 0.5$ , the inductor current drops linearly, and the current decrement is:

$$\Delta I_{\text{Lb-cL-}} = \frac{V_{\text{ob}}/2 - V_{\text{dc}}}{L_b} (t_2 - t_1) = \frac{V_{\text{ob}}/2 - V_{\text{dc}}}{L_b} (1 - D_{\text{on-b}}) T_{\text{sb}} \quad (7)$$

When the system works in steady state, the variation of inductor current in one cycle is 0, that is, the changes of inductor current of adjacent modes have equal size

and opposite phase,  $\Delta I_{Lb-cL+} = \Delta I_{Lb-cL-}$ . Thus, it can be obtained that the voltage gain of system under CCM when  $D_{on-b} > 0.5$  is:

$$M_{ob-c} = \frac{V_{ob}}{V_{dc}} = \frac{1}{1 - D_{on-b}} \quad (8)$$

It can be seen that when the system works in CCM, the output voltage gain  $M_{ob-c}$  is only dependent on the duty ratio  $D_{on-b}$  and has nothing to do with the load current, so its output characteristic is good.

## 4 Simulation Study on Output Characteristics

The following is a simulation study of TLBC output characteristics under different conductive modes based on the PSIM/MATLAB co-simulation system. Basic simulation parameters:  $V_{dc} = 1.0$  kV,  $C_{b1} = C_{b2} = 2267 \mu F$ ,  $f_{sb} = 8$  kHz,  $L_b = 62.5 \mu H$ ,  $R_b = 100 \Omega$ . And we set the relative time constant  $\tau_b = 0.005$ . As shown in Fig. 4, it is the simulation waveforms of TLBC with different duty ratios when  $\tau_b = 0.005$ .

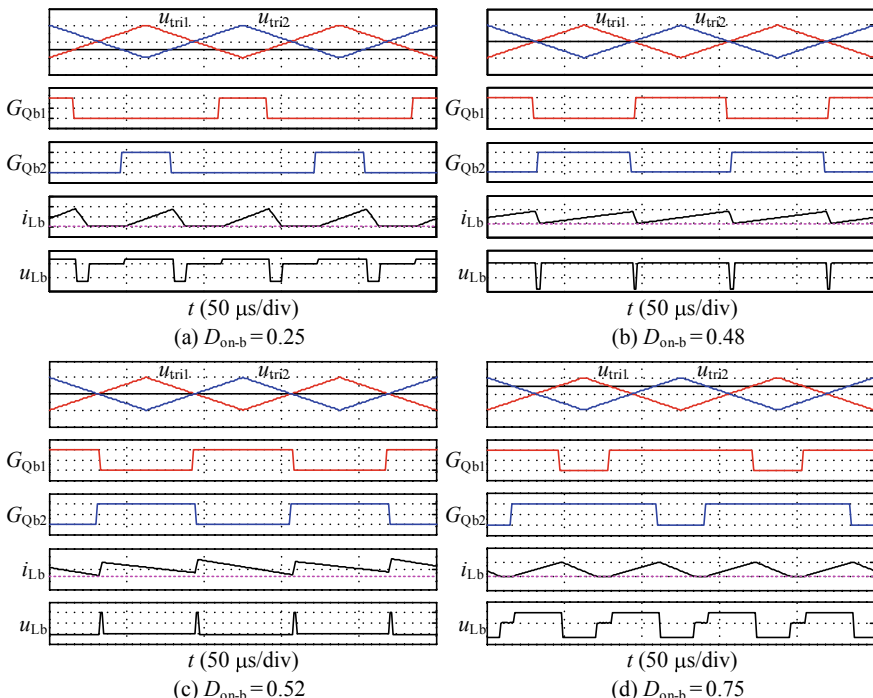


**Fig. 4** Simulation waveforms with different duty ratios when  $\tau_b = 0.005$

**Table 1** Statistical data of output voltage

$D_{\text{on-b}}$	Conduction mode	Output voltage $V_{\text{ob}}/\text{kV}$		
		Simulation results	Theoretical calculation	$V_{\text{dc}}/(1 - D_{\text{on-b}})$
0.25	DCM	1.650	1.654	1.333
0.48	CCM	1.918	1.923	1.923
0.52	CCM	2.075	2.083	2.083
0.75	DCM	4.665	4.674	4.000

The summary of the output voltage under different duty ratios is shown in Table 1.

It can be seen from the table that the output voltage data obtained by simulation are basically consistent with the theoretical calculation results, which fully verify the correctness of the TLBC output voltage gain  $M_{\text{ob-d}}$  under different conduction modes deduced by theory.

## 5 Conclusions

In this paper, we have established the mathematical models of five switching modes of the TLBC. And by using those modes, this paper mainly analyzes TLBC topology under CCM, derives the voltage gain of the converter with different duty ratios, and gets the output characteristics of the TLBC under different operation modes. The comparison result shows that the output characteristics under CCM condition are better than that under DCM condition, so it is better to let the TLBC work under CCM condition.

## References

- Pavlovsky M, De Haan SWH, Ferreira JA (2009) Reaching high power density in multikilowatt DC–DC converters with galvanic isolation. *IEEE Trans Power Electron* 24(3):603–612
- Meleshin VI, Zhiklenkov DV, Ganshin AA (2012) Efficient three-level boost converter for various applications. In: Power electronics and motion control conference. Novi Sad, Serbia, pp DS1e.9-1–DS1e.9-8
- Zhiyuan Y, Meng H, Hongfei W, Yan X (2017) A quasi single-stage power factor correction converter based on a three-level boost converter. In: IECON 2017—43rd annual conference of the IEEE Industrial Electronics Society, Beijing, pp 669–674
- Lijun D, Lei W, Huiqing D, Lu W, Zhigang L, Suleiman MS (2017) AI-HM based zero portion effects and phase-shift optimization for railway auxiliary inverter with pulsating DC-link. *IEEE Access* 5:7444–7453

5. Lijun D, Huiqing D, Zhan S, Yaru X, Mu L, Suleiman MS (2018) A comparative study between AI-HM and SPD-HM for railway auxiliary inverter with pulsating DC-link. *IEEE Trans Ind Electron* 65(7):5816–5825
6. Kwon JM, Kwon BH, Nam KH (2008) Three-phase photovoltaic system with three-level Boosting MPPT control. *IEEE Trans Power Electron* 23(5):2319–2327
7. Gannshin AA, Meleshin VI, Sachkov SA et al (2014) Railway auxiliary power converter operating with 3 kV DC supply line on the basis of 6.5 kV IGBT modules. In: Power electronics and motion control conference and exposition (PEMC), pp 654–660
8. Weiping Z (2008) Modeling and control of switching converter. China Electric Power Press, Beijing
9. Lin BR, Lu HH (2000) A novel PWM scheme for single-phase three-level power-factor-correction circuit. *IEEE Trans Industr Electron* 47(2):245–252
10. Lais AV, Remya K, Deepak ES, Mats L, Sasi KK (2013) Control and implementation of three level boost converter for load voltage regulation. In: Industrial Electronics Society IECON 2013—39th annual conference of the IEEE, pp 561–565
11. Soman DE, Krishna R, Leijon M et al (2014) Discontinuous conduction mode of a three-level boost DC-DC converter and its merits and limits for voltage cross regulation applications. In: Industrial Electronics Society IECON 2014—40th annual conference of the IEEE, pp 4268–4272

# Optimization of Magnetic Coupling for Small and Medium Power Wireless Charging System



Xuemei Diao, Chunhui Miao, Bing Li, Weiyao Mei and Lijun Diao

**Abstract** Aiming at the problem that low coupling coefficient of small and medium power wireless charging system always leads to low charging efficiency, a method improving the coupling coefficient by optimizing magnetic coupling structure was proposed. 3-D finite-element analysis (FEA) has been carried out to compare and analyze the transmission performance of three commonly used magnetic coupling structures. In addition, the coil coupling effects at different lengths and widths were compared under the same coil area to achieve the best coupling performance. The equations about output power and efficiency were derived from the equivalent circuit, and the expressions about coupling coefficient were obtained by analyzing the equivalent magnetic circuit diagrams, which provide the basis for optimizing magnetic core structures. Then, a process of design and optimization of magnetic cores was presented and following the process a retro-shaped core structure was designed for rectangular coil. The simulation results show that compared with the original charging system, coupling coefficient of the wireless charging system using the optimized magnetic coupling structure is improved significantly, thus, verifying the effectiveness of the optimization methodology.

**Keywords** Magnetic coupler · SS compensation · IPT system · Anti-offset capability

---

X. Diao · B. Li · W. Mei · L. Diao (✉)  
Beijing Jiaotong University, Beijing, China  
e-mail: [ljdiao@bjtu.edu.cn](mailto:ljdiao@bjtu.edu.cn)

X. Diao  
e-mail: [17121421@bjtu.edu.cn](mailto:17121421@bjtu.edu.cn)

B. Li  
e-mail: [17121452@bjtu.edu.cn](mailto:17121452@bjtu.edu.cn)

W. Mei  
e-mail: [15291117@bjtu.edu.cn](mailto:15291117@bjtu.edu.cn)

C. Miao  
Systems Engineering Research Institute CSSC, Beijing, China  
e-mail: [mchcat@189.cn](mailto:mchcat@189.cn)

## 1 Introduction

Nowadays, the inductive power transfer (IPT) is recognized as the preferred technology of choice for electric vehicle charging thanks to its expediency, safety and environmental friendliness [1]. The high-frequency switching power converter, magnetic coupler and compensation network are the main components of the IPT system applied to electric vehicles [2]. The optimized design of the magnetic coupler is a core part of evaluating the efficiency and economy of the IPT system for that the energy is transmitted through the mutual inductance of the primary and secondary coils of the magnetic coupler. The optimization of magnetic coupler is mainly concentrated in two aspects, namely the optimization research of magnetic coupler structure and the calculation method of magnetic coupler model. DD, DDQ and overlapping DD pads' configurations of magnetic couplers have been put forward in succession to ameliorate the horizontal misalignment tolerance and interoperable capability [3–5]. However, the complex structures have also led to an increase in the size and cost of IPT systems. Recently, new progress has been made in the theoretical study of magnetic couplers. A method for calculating the distribution parameters of coils and a formula specifically designed to calculate the mutual inductance between two coils have been proposed successively [6, 7]. These theoretical studies have typically focused on calculating a parameter of a magnetic coupler without combining it with a compensation topology, which results in a departure from the practical application.

To address the above issues, the rectangular magnetic structure that satisfies the small and medium power dynamic charging demand is selected. The expressions about coupling coefficient were obtained by analyzing the equivalent magnetic circuit diagrams, which provide the basis for optimizing magnetic core structures for both single coil and double coil couplers. Moreover, a methodology of design and optimization of magnetic cores was presented and following the process a retro-shaped core structure was designed for rectangular coil. A series of simulations have been conducted to evaluate the optimal system design.

## 2 Analysis

### 2.1 System Description and Mathematical Model

Equivalent circuit of magnetic coupler based on SS compensation has been established as shown in Fig. 1.  $L_1$  is the inductance of primary and  $L_2$  is the inductance of secondary.  $k$  is the coupling coefficient of the magnetic coupler and  $M$  is mutual inductance between two coils. The winding resistances of the magnetic coupler primary and secondary can be recognized as  $R_1$  and  $R_2$ . To enhance the power transmission efficiency,  $C_1$  and  $C_2$  are added as compensation capacitors. The analysis of the power and efficiency characteristics of the IPT system derived from

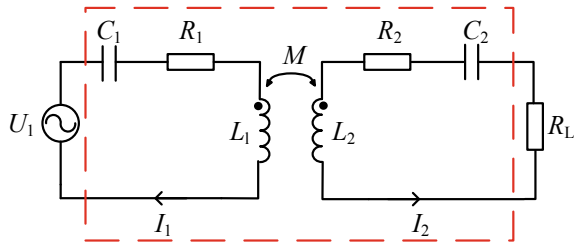


**Fig. 1** Equivalent circuit of magnetic coupler based on SS compensation

the established mathematical model is the theoretical basis for optimizing the magnetic coupler.

$$\begin{bmatrix} U_1 \\ 0 \end{bmatrix} = \begin{bmatrix} R_1 + j\left(\omega_r L_1 - \frac{1}{\omega_r C_1}\right) & -j\omega_r M \\ -j\omega_r M & R_L + R_2 + j\left(\omega_r L_2 - \frac{1}{\omega_r C_2}\right) \end{bmatrix} \begin{bmatrix} I_1 \\ I_2 \end{bmatrix} \quad (1)$$

$$\omega L_1 = \frac{1}{\omega_r C_1}, \quad \omega L_2 = \frac{1}{\omega_r C_2} \quad (2)$$

$$Q_1 = \frac{\omega_r L_1}{R_1} \quad Q_2 = \frac{\omega_r L_2}{R_2} \quad (3)$$

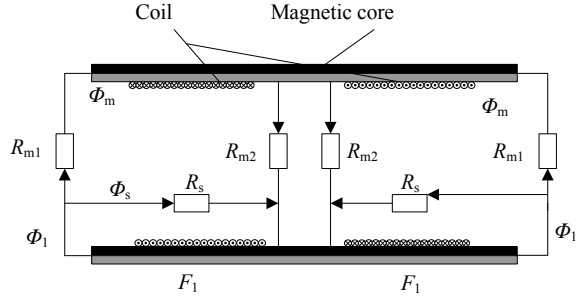
$$\eta_{\max} = \frac{k^2 Q_1 Q_2}{\left(1 + \sqrt{1 + k^2 Q_1 Q_2}\right)} \quad (4)$$

From the above derivation, we can see that the quality factor is proportional to  $\omega_r$  [8]. It also means that increasing the frequency can improve system efficiency, but the increase in frequency has long been limited by the development of thyristor technology. Therefore, the maximization of the coupling coefficient will be the focus of the optimal design of the magnetic coupler.

## 2.2 Magnetic Path Expression of Coupling Coefficient

The magnetic circuit analysis can purposefully reduce the magnetic resistance of the magnetic flux path and clarify the optimization direction of the magnetic core. Assuming that the self-coupling region has a magnetoresistance  $R_s$  and the mutual coupling region has a magnetoresistance  $R_m$ . Then, an equivalent magnetic circuit model is established as shown in Fig. 2.  $\phi_1$  is the total magnetic flux on one side and  $\phi_s$  is the self-coupling part of the magnetic flux.  $\phi_m$  is the mutual coupling part of the magnetic flux and  $F_1$  is the magnetomotive force. Corresponding to Fig. 2, the reluctance of the mutual coupling region 1 is  $R_{m1}$  and the reluctance of the

**Fig. 2** Equivalent magnetic circuit



mutual coupling region 2 is  $R_{m2}$ . The relationship between the magnetic flux and the coupling coefficient can be expressed as:

$$\phi_1 = \phi_s + \phi_m \quad (5)$$

$$k = \frac{\phi_m}{\phi_1} = \frac{R_s // (R_{m1} + R_{m2})}{R_{m1} + R_{m2}} = \frac{1}{1 + \frac{R_{m1} + R_{m2}}{R_s}} \quad (6)$$

It can be seen that to increase the coupling coefficient, it is necessary to reduce  $(R_{m1} + R_{m2})$  and increase  $R_s$  at the same time. That is, the proper placement of the core position can reduce the reluctance of the mutual coupling region while increasing the magnetic resistance of the self-coupling region. Thereby, the coupling coefficient is increased. This part of the work provides a theoretical basis for optimizing the core structure.

### 3 Comparative Analysis and Optimization of Coil Structure

#### 3.1 Comparison and Analysis of Coil Shapes

In ANSYS Maxwell, three coil models with the same diameter and length are established. The simulation diagram of three coil coupling situation and simulation results of the magnetic induction distribution at the same distance directly above the coil is obtained as shown in Fig. 3. Comparing the three shapes of the coil, it can be found that the circular coil has the highest coupling coefficient among the three coils because there is no chamfer and spatially completely symmetrical, but the mutual inductance is the lowest at the same distance. The rectangular coil and the circular coil are more stable in the mutual inductance than the DD type. The mutual inductance changes little under the same air gap fluctuation, which is beneficial to the system control. The DD type has the largest mutual inductance among the three coils, but as the air gap gradually increases, its superiority gradually becomes

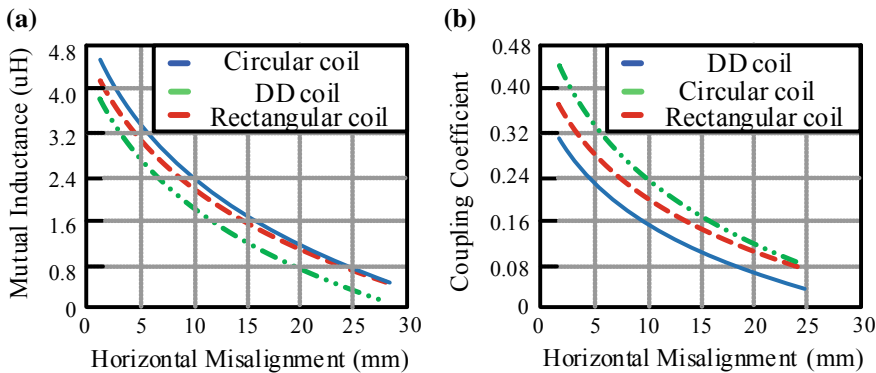


**Fig. 3** Comparison of anti-offset performance of coils with different shapes: **a** mutual inductance vary with air gap fluctuation; **b** coupling coefficient varies with air gap fluctuation

smaller, approaching the rectangular coil. Considering the practical application scenario of inductive power transmission in small and medium power applications, the mutual inductance of the circular coil is too small. Although the mutual inductance of the combined coil is large, the winding is complicated and the area is large. Combining the above considerations, the rectangular coil has a strong overall performance, and the mutual inductance fluctuation is small under the same air gap fluctuation, thus, a rectangular coil is proposed.

### 3.2 Comparison Optimization of Rectangular Coil Dimension

Figure 4 is the simulation data of the coupling coefficient when the rectangular magnetic couplers of the five design dimensions move along the X, Y and Z directions, respectively. Design parameters for different dimensions of magnetic couplers are shown in Table 1. As can be seen from Fig. 4a, c, the longer the magnetic coupler is designed, the higher the coupling coefficient can be achieved when the straight distance is the same. However, when the X direction misalignment occurs, the coupling coefficient will also drop faster. It can be seen from Fig. 4b that the wider the design of the magnetic coupler, the smaller the coupling coefficient that can be achieved under the same vertical distance, and the decrease rate of each size when the misalignment in the Y direction occurs is relatively close. In general, a longer rectangular magnetic coupler can achieve a larger coupling coefficient, but its ability to resist X direction offset is weaker. Therefore, in the design, it is usually combined with the design specifications in the actual application. In this design, the nominal vertical spacing is 10 mm, and the tolerance for

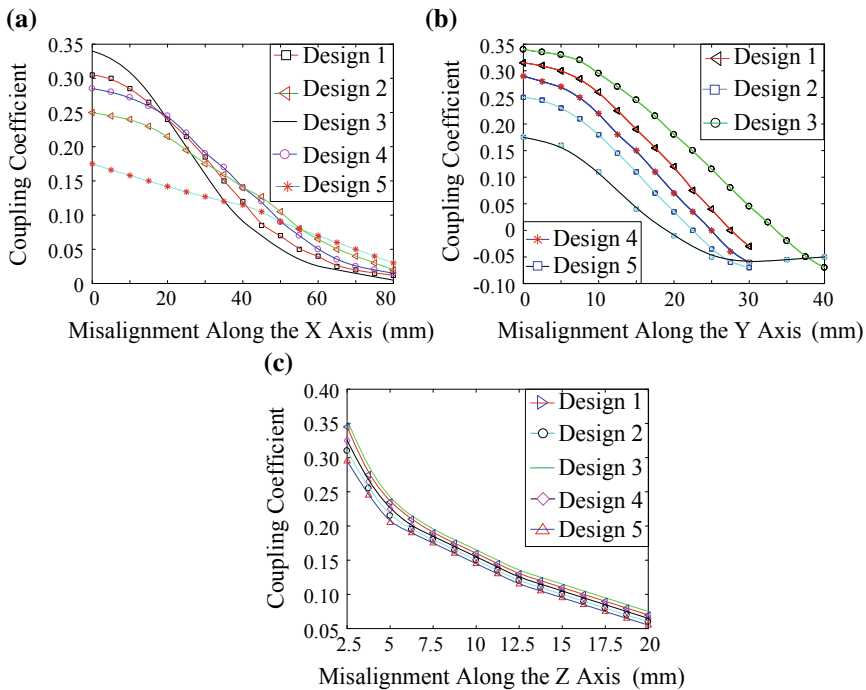


**Fig. 4** Performance comparison of magnetic couplers with different length and width: **a** the variation of the coupling coefficient with the misalignment in the *X* direction; **b** the variation of the coupling coefficient with the misalignment in the *Y* direction; **c** the variation of the coupling coefficient with the misalignment in the *Z* direction

*X* and *Y* offset tolerance is  $\pm 35$  mm and  $\pm 15$  mm, respectively. The coupling coefficient range is required to be around 0.15–0.3, so only  $150 \times 180 \times 4$  mm can meet the design requirements.

#### 4 Design and Optimization of Magnetic Core Structure

For a fixed coupling coil, when the core is used to enhance its coupling performance, the number of cores used can be optimized, so that the self-inductance and mutual inductance of the coupled coil can be maximized with a minimum of cores. The ANSYS simulation software is used to obtain the self-inductance and mutual inductance of the rectangular coil as a function of the number of cores, as shown in Fig. 5a. As can be seen from Fig. 5a, for a rectangular coupled coil, the increment of the mutual inductance of the coupled coil and the increment of the self-inductance of the coupled coil will be different during the increase of the number of cores. The defined balance factor  $E$  is the ratio of the mutual inductance value

**Table 1** Design parameters for different dimensions of magnetic couplers

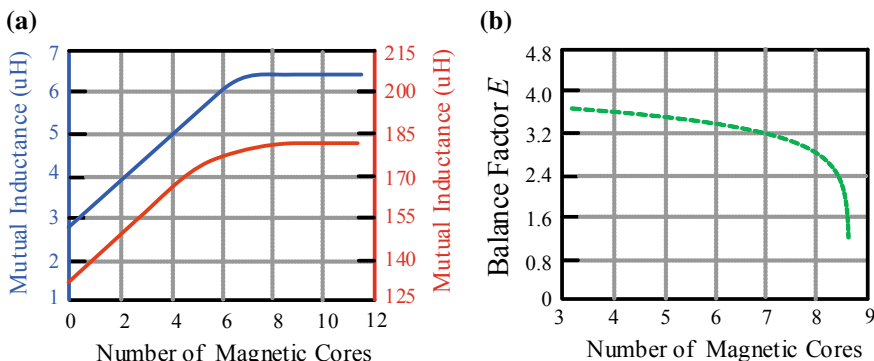
	Design 1	Design 2	Design 3	Design 4	Design 5
Dimension (mm)	150 × 180 × 4	180 × 150 × 4	135 × 200 × 4	164 × 164 × 4	200 × 135 × 4

increment of the coupled coil to the self-inductance value increment of the coupled coil. When the number of cores increases gradually, if the value of  $E$  decreases, it means that the increment of the mutual inductance value of the core is less than the increment of the self-inductance value, so the change of the value can be used to measure the effect of the core on the coil. The curve of the balance factor  $E$  as a function of the number of cores is shown in Fig. 5b.

$$E = \frac{\Delta M}{\Delta L} = \frac{M_n - M_{n-1}}{L_n - L_{n-1}} \quad (2.1)$$

By analyzing the curves of Fig. 5, it can be seen that the balance coefficient  $E$  decreases from the eighth core, that is, the degree of enhancement of the mutual inductance of the coupled coil is sharply decreased with respect to the self-inductance value. Therefore, by the above, it is preferable to select 8 the number of cores and the core is utilized to the utmost extent. The final optimized core structure is shown in Fig. 6.

Figures 7 and 8 show the simulation analysis of the core loss and the analysis of the coupling coefficient in the 2000 W induction power transmission system. As shown in Fig. 7, the loss of the three-type magnetic core structure is 90 W, 70 W and 50 W, respectively, which verifies the effectiveness of the proposed magnetic core structure. As shown in Fig. 8, the optimized magnetic coupler has a 10% improvement in the coupling coefficient compared to the unoptimized magnetic coupling structure.

**Fig. 5** Effect of the number of cores on the coupling performance: **a** self-inductance and mutual inductance change with the number of cores; **b** the balance factor  $E$  varies with the number of cores

**Fig. 6** Optimized core structure

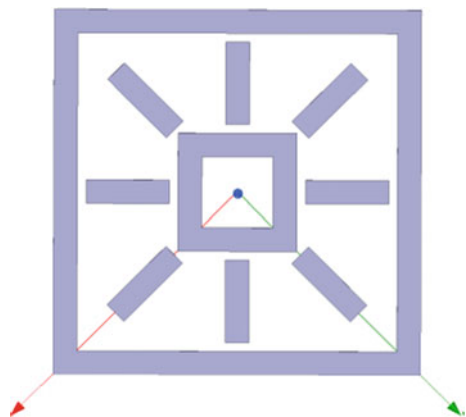


**Fig. 7** Core loss for different core structures

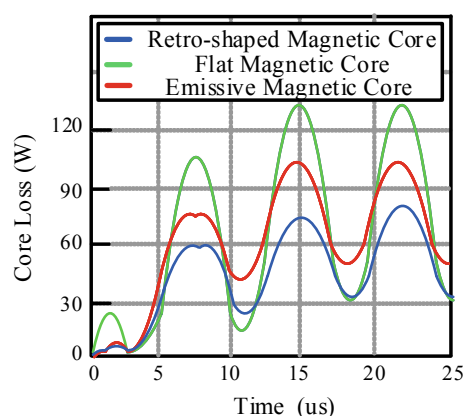
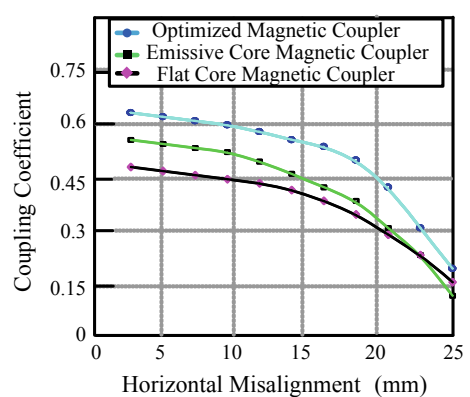


**Fig. 8** Comparison of coupling performance of magnetic couplers with different structures



## 5 Conclusion

Firstly, to achieve the best magnetic field coupling effect under the same coil area, magnetic field simulation was carried out by ANSYS to analyze the coupling characteristics of different shapes of coils. Rectangular magnetic structure that satisfies the small and medium power dynamic charging demand is selected. Then, the coil coupling effects at different lengths and widths were compared under the same coil area, and finally, a set of coil sizes with the best coupling effect was applied. To ensure that the IPT systems are as efficient, cost effective and light as possible, it is critical that the desired coupling between the power pads is achieved with a minimum amount of ferrite. A magnetic structure of retro-shape is proposed by deriving the magnetic circuit expression. The minimum number of cores to achieve the best coupling effect was studied by introducing the balance factor  $E$ . By optimizing the core structure and the number of cores, the core loss is reduced and the system efficiency is improved. The quantitative results presented in this paper form a basis for the proper design of power pads for IPT systems.

## References

1. Kan T, Lu F, Nguyen T-D, Mercier PP, Mi CC (2018) Integrated coil design for EV wireless charging systems using LCC compensation topology. *IEEE Trans Power Electron* 33(11): 9231–9241
2. Li S, Li W, Deng J, Nguyen TD, Mi CC (2015) A double-sided LCC compensation network and its tuning method for wireless power transfer. *IEEE Trans Veh Technol* 64(6):2261–2273
3. Airani KC, Kumaraswamy HV (2016) Analysis of e plane, h plane e-h plane mutual coupling in  $2 \times 2$  antenna formation. In: 2016 Online international conference on green engineering and technologies (IC-GET), pp 1–3
4. Lu B, Yang X (2014) Effects of high frequency on the distributed parameters of the sparse-wound solenoid coils. *IEEE Trans Plasma Sci* 42(1):154–161
5. Durmus F, Karagol S (2018) Mutual inductance calculation formula for planar square coils. In: 2018 2nd international symposium on multidisciplinary studies and innovative technologies (ISMSIT), pp 1–5
6. Li S, Mi CC (2015) Wireless power transfer for electric vehicle applications. *IEEE J Emerg Selected Topics Power Electron* 45:1547–1552
7. Yiming Z, Zhengming Z, Kainan C (2014) Frequency decrease analysis of resonant wireless power transfer. *IEEE Trans Power Electron* 29(3):1058–1063
8. Lu F, Zhang H, Zhu C, Diao L, Gong M, Zhang W et al (2018) A tightly-coupled inductive power transfer system for low-voltage and high-current charging of automatic guided vehicles (AGVs). *IEEE Trans Ind Electron* 1-1

# Dynamic Programming in Energy Management Strategy for Optimizing Multi-energy Drive System



Xinyue Zhang, Xiaoyu Ren, Caihui Zheng, Yue Yuan and Lijun Diao

**Abstract** Transportation industries are incorporating multi-energy drives systems to alleviating environmental pollution. Multi-energy drives systems are currently a transition from traditional power systems to electrical power systems, which are important for fuel economy and emissions reduction. In this paper, a dynamic EMS for power system with a diesel engine and auxiliary batteries model is used to achieve an optimal power allocation between them. Dynamic programming algorithm is proposed for optimization of energy distribution in multi-energy drive systems, which proves better global results even if its dimensionality problems since real-time requirement is not so strict. Results indicate lower fuel consumption levels compared to the rule-based algorithm.

**Keywords** Dynamic programming · Multi-energy drive system · Optimization · Energy management strategy (EMS)

---

X. Zhang · X. Ren · Y. Yuan · L. Diao (✉)

School of Electrical Engineering, Beijing Jiaotong University, Beijing 100044, China  
e-mail: [ljdiao@bjtu.edu.cn](mailto:ljdiao@bjtu.edu.cn)

X. Zhang  
e-mail: [18121544@bjtu.edu.cn](mailto:18121544@bjtu.edu.cn)

X. Ren  
e-mail: [18121485@bjtu.edu.cn](mailto:18121485@bjtu.edu.cn)

Y. Yuan  
e-mail: [16126065@bjtu.edu.cn](mailto:16126065@bjtu.edu.cn)

C. Zheng  
CRRC Changchun Railway Vehicles Co., Ltd., Changchun, Jilin 130062, China  
e-mail: [zhengcaihui@eccar.com.cn](mailto:zhengcaihui@eccar.com.cn)

## 1 Introduction

At present, with the increasing number of urban traffic vehicles, how to control exhaust emissions has become a hot research issue. Power system is an important source of energy [1]. The main advantages of multi-energy drive systems lie in the effective transmission and distribution of power and torque from power source to multi-energy drive system and the reuse of regenerative braking energy. On the basis of satisfying the basic traction performance of vehicles, the energy management strategy (EMS) achieves the optimization of efficiency, emission and power by coordinating various subsystems. Dynamic programming (DP) proposed by R. E. Bellman et al. in the early 1950s is a numerical method for solving decision-making process based on Bellman's superiority principle, which aims at global optimization and often serves as an optimization benchmark in the field of energy management such as electric vehicles and smart grids [2]. Compared with other strategies, dynamic programming can solve the multistage decision-making problem. The complex multi-variable optimization problem is processed step by step, and the optimal solution of each stage is obtained first. Finally, the optimal solution of the complex problem is obtained by using the recursive call algorithm. However, because it needs to know the whole cycle condition in advance, and it can only be used for offline calculation, not for real vehicles. However, useful control rules can be extracted from the optimal results of dynamic programming, which can be used to improve the control strategy of real vehicles [3]. This paper adopts modeling, algorithm controlling and simulation analyzing to get the feasible result of fuel economy compared to the more common rule-based instantaneous power control strategy.

## 2 Modeling of the Multi-energy Drive System

### 2.1 *Multi-energy Drive System Topology*

The series topology of Multi-energy drive system is shown in Fig. 1. It consists of engine, energy storage battery pack, motor and machinery. The engine is connected with the generator. Its advantage is that the engine and the driving device are not combined, so the engine can work at any working point on its universal characteristic curve, and the engine can be constrained in an efficient operating range, which greatly reduces the pollution level of harmful substances.

### 2.2 *Internal Combustion Engine*

The fuel consumption rate and emissions are assumed to be static functions of engine speed and engine torque and can be got through looking up the engine map

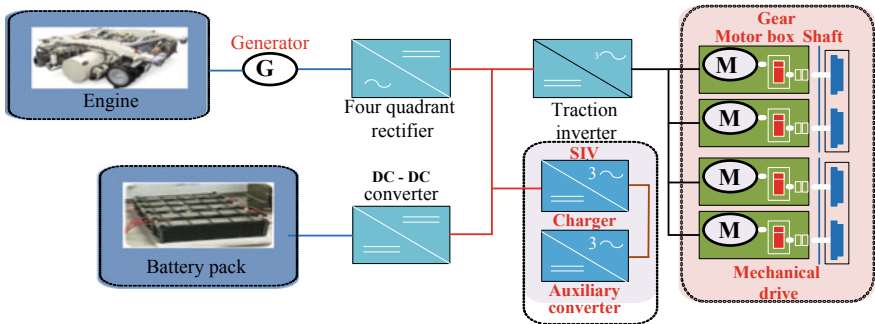


**Fig. 1** Series topology of multi-energy drive system

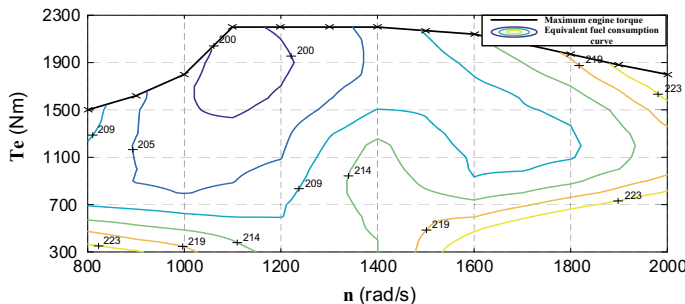


**Fig. 2** Fuel consumption map of the engine

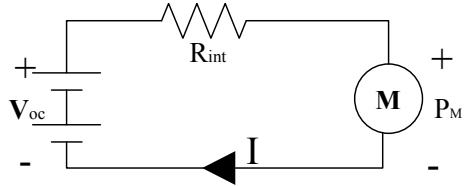
[4]. The following is the modeling based on the data of German Man D2876 series 345 kW engine map with hybrid train configuration. Its universal characteristic curve is shown in Fig. 2 [5].

In the research process, firstly, the diesel generator speed and actual output power are taken as reference values, the fuel consumption curve is divided into net format, and then the current operating state of the diesel generator set is combined to query the instantaneous fuel consumption rate. The quantitative calculation of fuel consumption is realized by the integral method as one of the standards for energy management strategy formulation and evaluation [6].

### 2.3 Battery System

Energy management-oriented power battery modeling mainly adopts simple and practical equivalent model of battery internal resistance, as Fig. 3. The relationship between SOC and current of charge and current of discharge is integral, as Formula (1) and (2), after differential as (3).

**Fig. 3** Internal resistance equivalent model of battery



$$\text{SOC}(t) = \frac{Q(t)}{Q_{\max}} = \frac{\text{SOC}_{\text{init}} \cdot Q_{\max} - \frac{1}{3600} \cdot \int_0^t I_s(t) dt}{Q_{\max}} \quad (1)$$

$$I_s(t) = \frac{V_{\text{oc}} - \sqrt{V_{\text{oc}}^2 - 4P_M \cdot R_{\text{int}}}}{2R_{\text{int}}} \quad (2)$$

$$\frac{d\text{SOC}(t)}{dt} = -\frac{I_s(t)}{3600Q_{\max}} \quad (3)$$

Among them,

$\text{SOC}(t)$	state of charge at time $t$
$Q(t)$	charge of battery at time $t$
$Q_{\max}$	maximum charge of battery
$\text{SOC}_{\text{init}}$	initial state of charge
$V_{\text{oc}}$	open-circuit voltage
$R_{\text{int}}$	inner resistance
$P_M$	power of electrical motor
$I_s(t)$	current of battery at time $t$ .

### 3 Application of DP in Energy Management Strategy

Energy management strategy (EMS) is the focus of multi-energy drive system research and development. Due to the special structure of multi-energy drive system, it is particularly important to allocate the energy flow or energy flow between engine and motor. The key point of realization is the design of dynamic programming controller. Firstly, we need to determine the optimization objectives, state variables, decision control variables and constraints, and then select the network to determine the cost functions and cost matrix.

#### 3.1 The Overall Objective Functions

The core of an ideal control strategy is to optimize the selection of reasonable control algorithm. The main purpose of the control is to optimize the fuel economy

rationally, reduce the emission of toxic and harmful gases and pollutants, obtain good driving performance or reduce the use of some functional components through system control to reduce the cost of vehicle manufacturing.

For series multi-energy drive system, it needs to satisfy power flow as follows,

$$P_{\text{ICE}}(t) + P_{\text{bat}}(t) = P_{\text{req}}(t) + P_{\text{el}}(t) \quad (4)$$

All are during time  $t$ ,

$P_{\text{bat}}(t)$  output power of battery

$P_{\text{ICE}}(t)$  output power of engine and generator set

$P_{\text{req}}(t)$  demand power of the power system

$P_{\text{el}}(t)$  electrical loads like power consumed by lamps, fans, etc.

Since there is no mechanical connection between the engine and the transmission system, at the same power output from the engine, it can operate at different operating points ( $T_{\text{ICE}}, w$ ), allowing the engine to operate at the point where fuel consumption is minimal:

$$f_{\min}(P_{\text{ICE}}) = \min f(T_{\text{ICE}}, w) = \min_{(T_{\text{ICE}}, w) \in \Omega(P_{\text{ICE}})} f(P_{\text{ICE}}|w) \quad (5)$$

$$\Omega(P_{\text{ICE}}) = \{(T_{\text{ICE}}, w) | P_{\text{ICE}} = T_{\text{ICE}} \cdot w\} \quad (6)$$

Among them,

$f$  fuel consumption

$f_{\min}(P_{\text{ICE}})$  minimum fuel consumption at  $P_{\text{ICE}}$

$f(P_{\text{ICE}}|w)$  fuel consumption at  $P_{\text{ICE}}$  and different speed  $w$ .

The goal is to minimize fuel consumption throughout the cycle,

$$\min J(P_{\text{ICE}}) = \min \int_0^T f(P_{\text{ICE}}(t)) dt \quad (7)$$

### 3.2 Basic Constraint Functions

Generally, when designing the energy management strategy of multi-energy drive system, many factors will be synthesized. For example, to optimize the working point and working range of internal combustion engine (ICE); to minimize engine power; to minimize idle time of engine; to optimize the switching time of engine; to maximize regenerative energy; to optimize SOC working range; to consider relevant national emission policies and so on [7].

$$\begin{aligned}
w_{\text{ICE min}} &\leq w_{\text{ICE}}(t) \leq w_{\text{ICE max}} \\
T_{\text{ICE min}}(w_{\text{ICE}}) &\leq T_{\text{ICE}}(t) \leq T_{\text{ICE max}}(w_{\text{ICE}}) \\
P_{\text{ICE min}}(t) &\leq P_{\text{ICE}}(t) \leq P_{\text{ICE max}}(t) \\
V_{s \min}(t) &\leq V_s(t) \leq V_{s \max}(t)
\end{aligned} \tag{8}$$

### 3.3 Algorithm Implementation

The principle of superiority points out that for the optimal strategy of multistage decision-making process, no matter what the initial state and initial decision are, when any of the stages and states are regarded as the initial stage and initial state, the remaining decisions from that stage must be an optimal decision for that stage. Dynamic programming is to decompose the control time, control signal and system state into several sub-problems. The sub-problems are solved first, and then recursively based on time to get the optimal solution of the system.

Divide  $[0 T]$  into  $N$  parts, each length  $\Delta t$  and  $[\text{SOC}_{\min}, \text{SOC}_{\max}]$  into  $M$  parts, each length  $\Delta \text{SOC}$ .

The battery discharge from SOC  $(k, i)$  to SOC  $(k + 1, j)$  through  $I_s(k, i, j)$  after time  $\Delta t$ ,

Formula (7) change as

$$J(P_{\text{ICE}}) = \sum_{k=0}^{N-1} f_{\min}(P_{\text{ICE}}(k)) \Delta t \tag{9}$$

Formula (3) change as

$$\frac{\text{SOC}(k+1, j) - \text{SOC}(k, j)}{\Delta t} = -\frac{I_s(k, i, j)}{3600 Q_{\max}} \tag{10}$$

Among them,

$\text{SOC}(k, i)$   $i$ th SOC in  $k$ th stage

$I_s(k, i, j)$  current from  $i$ th SOC to  $j$ th SOC in  $k$ th stage.

From below parametric analogy Table 1, all index correlations are summarized. The algorithm is depicted in steps in Table 2 [8]. And its optimization principle is shown in Fig. 4a [9].

### 3.4 Simulation Comparison

This paper selects the actual working condition from Jining south station to Hohhot east station. A total of 917 s, or 15.3 min, is taken from the start of the train to the

**Table 1** Parametric analogy

Meaning in DP	Parameter	Representative in EMS
Total number of stages discretized by time	$n$	$n$ time phases
$k$ th stages	$k$	$k$ th time phase
The state variable in the $k$ th stage	$xk$	SOC (state of charge), Treq (torque that system require)
The decision control variable of the $k$ th stage	$uk(xk)$	$T_{ICE}$ (torque that engine provide)
All the possibilities of decision control variable in the $k$ th stage	$Dk(xk)$	All the possibilities of $T_{ICE}$ according to SOC in the $k$ th stage
The decision control variable sequence (from first stage), namely strategy	$P(x1) = \{u1(x1), u2(x2), \dots, un(xn)\}$	$T_{ICE}$ sequence (from first stage to the end)
The transfer function of the nonlinear discrete system	$xk + 1 = Tk(xk, uk)$	From the state of $k$ th to the state of stage $k + 1$
The objective function	$J(u1, u\dots.un, x1, x2\dots xn + 1)$	Total fuel consumption
The cost function	$L(uk, xk)$	Fuel consumption in $k$ th stage
The optimal strategy	$P^* = \{u1^*, u2^* \dots un^*\}$	$T_{ICE}$ sequence that optimize the objective function
The optimal trajectory	$X^* = \{x1^*, x2^* \dots xn + 1^*\}$	All the state variables according to the transfer function in the optimal strategy

stop, and the selected time of the stop condition is 1000 s, or the total length of the working condition is 16.6 min. The time-speed running curve of the train in this working condition is shown in Fig. 4b [10].

In the process of simulating the selected working condition, the waveform of power distribution changing with time obtained by the rule-based instantaneous power control and dynamic programming control is shown in Fig. 5. It can be seen that in the whole working condition, under the control of the dynamic programming algorithm, the power of the diesel generator is small when the SOC of the power battery is high. As the SOC decreases, the power of the diesel generator plays a larger role to ensure that the diesel generator runs at the operating point with higher efficiency as far as possible.

## 4 Conclusion

In recent years, with the rapid development of electrification and intelligent technology of travel vehicles, scholars have proposed a variety of intelligent algorithms for the energy management of multi-energy drive system [11]. In this paper, diesel

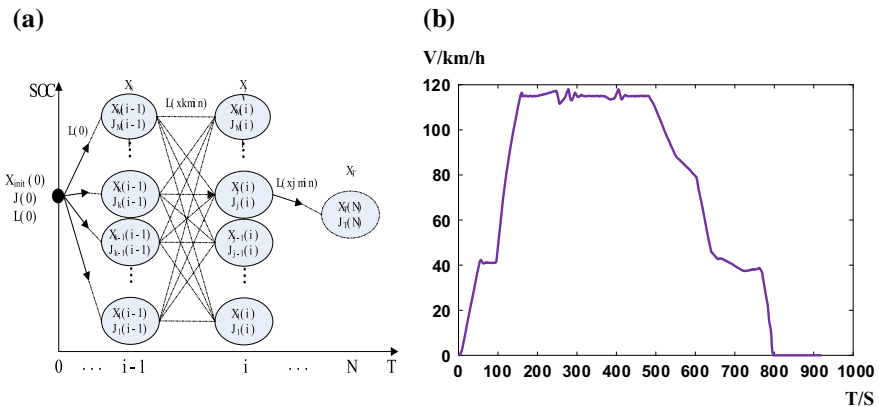


**Fig. 4** **a** Network graph of dynamic programming algorithm, **b** The time-speed operating curve of HEMU

**Table 2** Pseudocode of DP algorithm

1:	{Forward Path Generation}
2:	for $i$ such that $i = 2: N+1$ do
3:	for $j$ such that $j = 1: M$ do
4:	for $k$ such that $k = 1: M$ do
5:	$J(0) = L(0)$
6:	Locate minimum of $J_k(i-1)$
7:	Save index of min Min [ $i-1, k_{min}$ ] for min of $J_k(i-1)$
8:	Compute $L(xk)$
9:	Compute $J_i(i) = J_k(i-1) + L(xk)$
10:	end for
11:	end for
12:	end for
13:	{Backward Path Trace}
14:	for $m$ such that $m = 1: N$ do
15:	Locate Node( $T$ ) = min $J_T(N)$
16:	Locate all Node = Min ( $\cdot, 2$ )
17:	end for

generator and power battery, two core components, are modeled according to the general topology of the multi-energy drive system. Finally, the simulation results show that dynamic programming is a feasible energy optimization strategy compared to the rule-based algorithm.

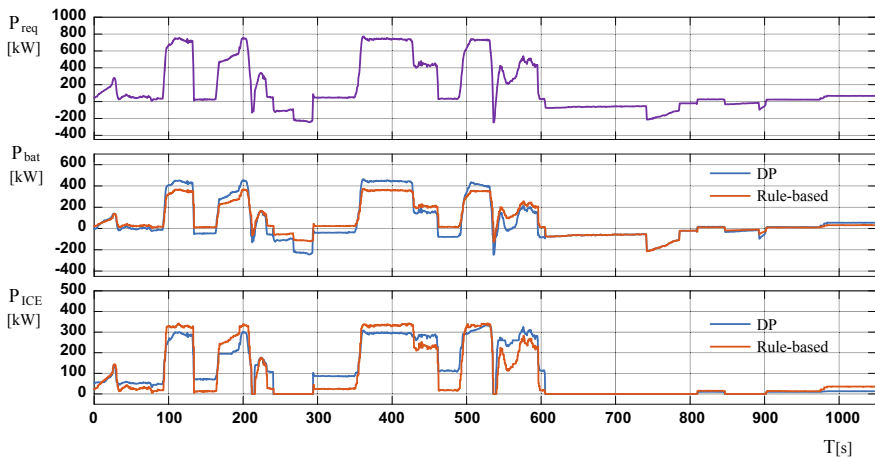


**Fig. 5** Power distribution curve by DP and rule-based algorithm control

**Acknowledgements** This work is supported by National Key R&D Program of China, No.2017YFB1201003, Basic Research, No.JCKY2018110C113.

## References

1. Mansour C, Clodic D (2012) Optimized energy management control for the Toyota Hybrid System using dynamic programming on a predicted route with short computation time. *Int J Autom Technol* 13(2):309
2. Deng T, Han HS, Luo JL (2008) Research on improved ECMS energy management control for hybrid electric vehicles based on dynamic programming algorithm. *China Mech Eng* 29 (03):326–332(in Chinese)
3. Song B (2017) Energy optimization simulation of parallel hybrid electric vehicle based on dynamic programming. *Jilin University*, 2017 (in Chinese)
4. Xu G, Li W, Xu Y, Wang Z (2008) Dynamic energy management for hybrid electric vehicle based on adaptive dynamic programming. In: *IEEE International Conference on Industrial Technology, ICIT 2008*
5. Ye Y (2018) Research on capacity configuration and energy management strategy of diesel-electric multi-energy drive system. *Beijing Jiaotong university*, 2018 (in Chinese)
6. Yu W (2017) Dc side stability research and energy control management of hybrid powertrain. *Beijing Jiaotong university*, 2017 (in Chinese)
7. Liu Y (2018) Research on energy management of hybrid electric vehicles based on adaptive dynamic programming control strategy. *Changchun University of Technology*, 2018 (in Chinese)
8. Fares D, Panik F, Chedid R, Jabr R, Karaki S (2015) Dynamic programming technique for optimizing fuel cell hybrid vehicles. *Int J Hydrogen Energy* 40(24):7777
9. Zhang C (2018) Optimal allocation and control of new energy tram energy storage system. *Beijing Jiaotong University*, 2018 (in Chinese)

10. He R (2019) Research on optimization of Energy management control for DEMU. Beijing Jiaotong University, 2019 (in Chinese)
11. Hu Y (2018) Research on control system design and energy management strategy of hybrid electric vehicle. University of Chinese academy of sciences (shenzhen advanced technology research institute, Chinese academy of sciences), 2018 (in Chinese)

# Research on Principle and Control Method of Totem-Pole PFC



Chunjiang Liu, Chao Li, Weiyao Mei, Chunmei Xu and Lijun Diao

**Abstract** Active power factor correction is an effective method to suppress harmonic current and improve power factor. One of the important developing directions of power factor correction circuit is to improve conversion efficiency. Among various kinds of power factor correction circuits, the Totem-Pole boost power factor correction circuit, as a bridgeless PFC, uses fewer devices and theoretically achieves higher conversion efficiency and better performance. In this paper, the working principle of Totem-Pole PFC is analyzed, a Totem-Pole PFC control scheme is proposed, and the SimCoder simulation tool is used for simulation. The feasibility of the scheme is verified through the simulation results.

**Keywords** Power factor correction · Bridgeless PFC · Totem-Pole · Control method

## 1 Introduction

With the development of power electronic devices and the wide application of power electronics technology in various industries, power electronic switching power supply devices connected to the power grid have gradually become the main source of harmonic injection into the power grid [1]. For example, in the subway station lighting system, due to the use of a large number of LED lighting devices,

---

C. Liu · W. Mei · C. Xu (✉) · L. Diao

School of Electrical Engineering, Beijing Jiaotong University, Beijing 100044, China

e-mail: [chmxu@bjtu.edu.cn](mailto:chmxu@bjtu.edu.cn)

C. Liu

e-mail: [18126106@bjtu.edu.cn](mailto:18126106@bjtu.edu.cn)

W. Mei

e-mail: [15291117@bjtu.edu.cn](mailto:15291117@bjtu.edu.cn)

L. Diao

e-mail: [ljdiao@bjtu.edu.cn](mailto:ljdiao@bjtu.edu.cn)

C. Li

Qingdao Technical College, Qingdao, China

it will produce a large number of harmonic pollution without effective power factor correction. Therefore, the use of low-loss, high-efficiency PFC solutions is of great significance for reducing harmonic pollution and improving the effective utilization of electrical energy. The basic principle of the active power factor correction circuit is to use the control circuit to force the input current waveform to track the input voltage waveform to realize the sinusoidal of the AC input current and synchronize with the AC input voltage [2]. The conventional power factor correction circuit uses a rectifier bridge and has many disadvantages such as a large number of components and a large on-state loss [3–5]. The bridgeless PFC technology can theoretically achieve smaller conduction losses and improve efficiency by removing the rectifier bridge or reducing the number of power devices on the current conduction path. Among the various schemes of bridgeless PFC, the Totem-Pole bridgeless PFC has the advantages of minimum device, lowest conduction loss, high efficiency, and low common mode noise. So it has wide application prospects [6].

This paper analyzes the working principle of Totem-Pole PFC and proposes a Totem-Pole bridgeless PFC control scheme. And then, the feasibility of the scheme proposed is verified through SimCoder.

## 2 The Working Principle of Totem-Pole PFC

Figure 1 shows the circuit topology of the Totem-Pole bridgeless PFC converter.

The circuit topology includes a switching arm and a diode arm. The Totem-Pole PFC is equivalent to the boost circuit in both the positive half cycle and the negative half cycle of the AC power supply, so the output voltage is higher than the input voltage [7, 8]. Among them,  $S_1$  and  $S_2$  are MOSFETs,  $D_1$  and  $D_2$  are diodes, and  $L$ ,  $C$ , and  $R$  are inductance, capacitance, and resistance, respectively.

In the positive half cycle of the alternating current, when  $S_1$  is turned on, as shown in Fig. 2a, the alternating current is charged to the inductor through the inductors  $L$ ,  $S_1$ , and  $D_1$ , and the energy storage of the inductor is increased; when  $S_1$  is turned off, as shown in Fig. 2b, the alternating current forms a loop through the body diodes of  $S_2$ ,  $R$ ,  $C$ , and  $D_1$ . The inductor  $L$  and the power supply  $V_{ac}$  discharge

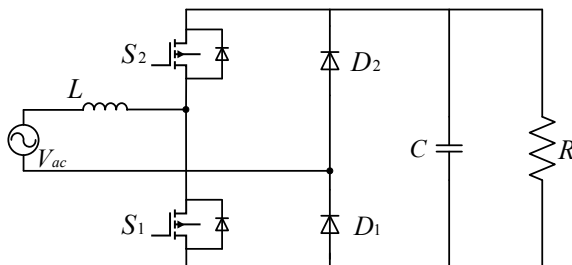


**Fig. 1** Topology of Totem-Pole PFC

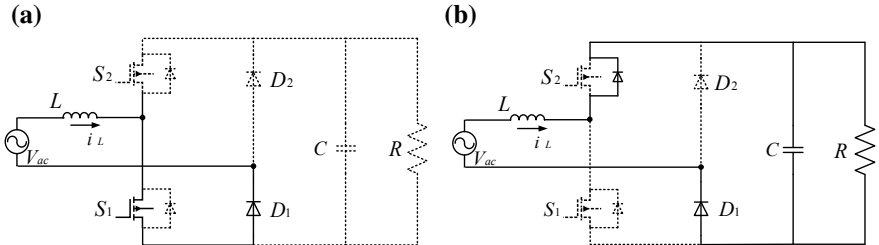


**Fig. 2** Operating condition of a positive half cycle of alternating current

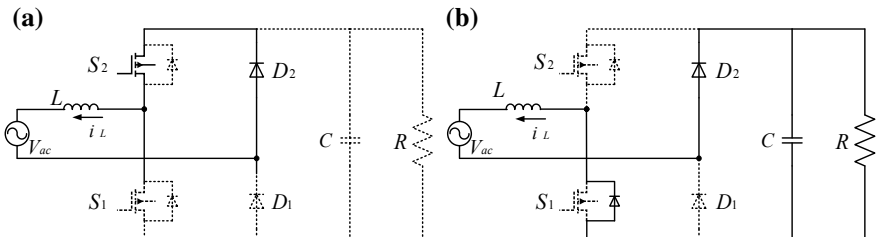


**Fig. 3** Operating condition of an alternating current negative half cycle

the capacitor  $C$  and the resistor  $R$ . Hence, the output voltage is higher than the power supply voltage, and the energy storage of the inductor  $L_1$  is reduced. The body diodes of the switches  $S_1$  and  $S_2$  then form a Boost PFC structure. During the positive half cycle of the sinusoidal alternating current,  $D_1$  is continuously turned on and  $D_2$  is continuously turned off.

The operating state of the AC negative half cycle is similar to that of the positive half cycle.

In the negative half cycle of the power supply, the inductive current is negative,  $D_2$  is continuously on, and  $D_1$  is continuously off, as shown in Fig. 3. The body diodes of  $S_2$  and  $S_1$  constitute boost PFC structure.

The two switches switch functions when the polarity of the input voltage changes. For example, when the voltage becomes negative after crossing zero,  $S_1$  changes from being switched on as the inductance energy storage to its body diode conduction to supply power for the load, while  $S_2$  changes in the opposite function. Therefore, the functions of the two switches are complementary and interchangeable with the change of polarity.

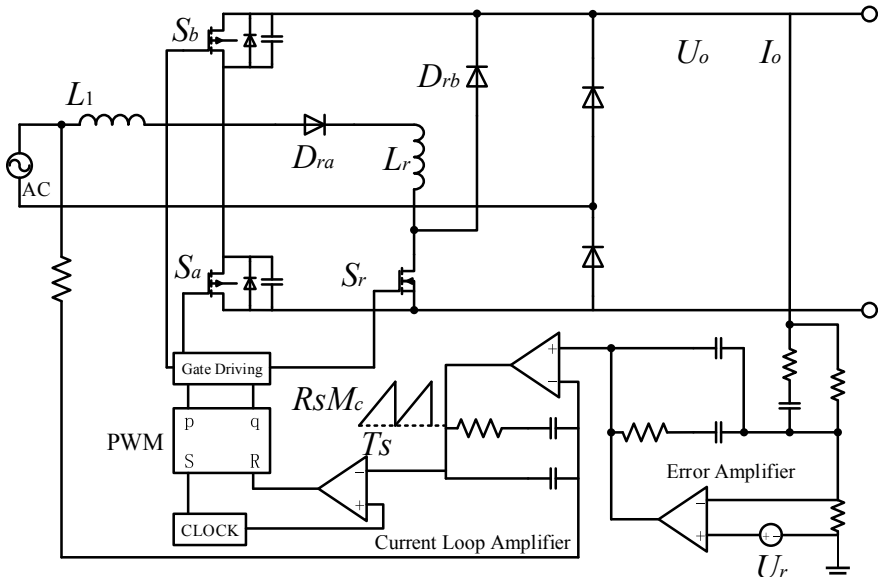
According to the analysis of working principle, the advantages of Totem-Pole PFC are fewer components, less loss, high efficiency, and relatively small EMI effect. It can be seen that the Totem-Pole PFC is a relatively complete and practical bridge-free PFC design scheme.

### 3 Control System Design

Switching converter control mode can be roughly divided into voltage control and current control. In the current control, according to the conduction mode of the inductive current, the working mode of the switching converter is divided into the continuous conduction mode (CCM), the discontinuous conduction mode (DCM), and the critical conduction mode (CRM) [9]. With the appearance and application of GaN high-speed MOS tube and other devices, the Totem-Pole PFC has been able to work in CCM mode. This design adopts CCM mode under average current control. The control of PFC usually adopts double-loop control, the outer loop is the voltage loop for stabilizing the output voltage, and the inner loop is the current loop for limiting the output current and improving the dynamic performance [10].

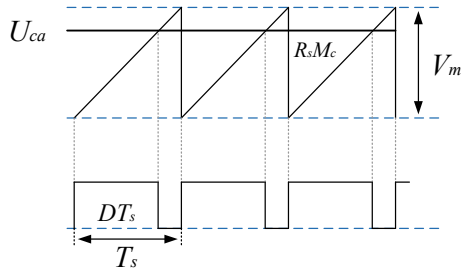
Figure 4 shows the working principle of the average current control mode, the current loop amplifier output signal  $U_{ca}$  compares with PWM modulator constant slope  $R_s M_s$ , and produces control signal duty cycle  $d$ , the  $R_s$  is the internal resistance of equivalent inductance sampling,  $M_s$  slope is PWM ramp signals, voltage signals  $U_{ca}$  is port voltage by partial pressure resistance, compared with a given voltage error voltage and after compensating voltage, and then as a reference voltage of the inner ring.

Figure 5 shows the schematic diagram of generating control signal duty cycle  $d$ , slope  $R_s M_s$  is enables reference signal, its time cycle is equal to the switch signal the time period of  $T_s$ , sampling the voltage error amplifier output signal  $U_{ca}$ , the signals



**Fig. 4** Working principle of the average current control mode

**Fig. 5** Schematic diagram of duty cycle generation



is greater than the slope  $R_s M_s$  time to switch enables the opening of the time, need the time compared to the cycle time is the duty ratio.

## 4 Simulation and Experiment

The design parameters of Totem-Pole PFC converter are as follows:

$$\begin{aligned} P_o &= 115W, V_o/f = 40V/60 Hz, \\ V_d &= 70V, \text{ PWM dead zone time} = 2 \mu s, \\ L &= 1.323 \text{ mH}, C = 330 \text{ F}. \end{aligned}$$

Current loop: This control architecture adopts the double-loop average current control architecture and adopts the type II controller. However, the low-pass part is placed in the sensing loop ( $f_c = 20$  kHz), and the controller itself adopts the proportional integral to control. In addition, a forward control signal is added to the control voltage of PWM.

Voltage circuit: Voltage loop resistance to design with full load,  $R = 49 \Omega$ , and thus, there are

$$H_{dc}(s) = \frac{26.21}{s + 61.84} \quad (1)$$

Set  $f_c = 20$  Hz,  $\omega_c = 125$  rad/s, choose  $p = 180$  rad/s,  $z = 30$  rad/s, then

$$Gv(s) = \frac{30(s + 30)}{s(s + 180)} \quad (2)$$

The SimCoder simulation tool of PSIM is used for simulation, and the simulation waveform is shown in Fig. 6. It can be seen from the simulation results that the input current waveform can well follow the input voltage waveform and be corrected to the standard sine wave. The output also meets the given requirements.

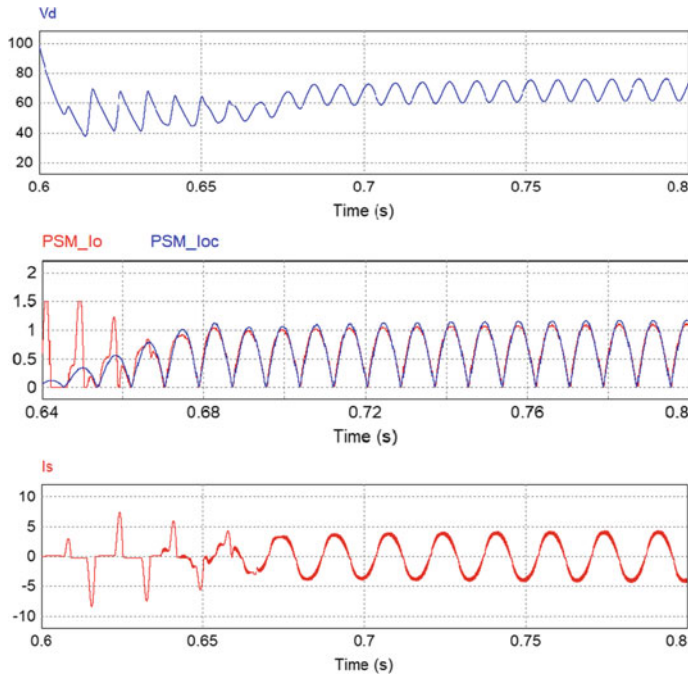


**Fig. 6** Simulation results of Totem-Pole bridgeless PFC SimCoder

## 5 Conclusion

In this paper, the advantages and application value of the Totem-Pole bridge-free PFC have been summarized, the working principle of the Totem-Pole bridge-free PFC has been analyzed, and the working modes of the topology in the positive and negative cycles of alternating current have been expounded. On this basis, the architecture of double-loop average current control in the continuous mode of inductance current has been presented, and the main key technical points are analyzed, and the corresponding solutions are proposed. The correctness and practicability of the scheme are proved by system simulation and experiment.

## References

1. Muhammad KS, DDC, Lu (2012) Two-switch ZCS totem-pole bridgeless PFC boost rectifier. In: 2012 IEEE international conference on Power and Energy (PECon), 2012
2. Kim J-H, Moon G-W, Kim J-K (2012) Zero-voltage-switching totem-pole bridgeless boost rectifier with reduced reverse-recovery problem for power factor correction. In: 2012 7th International Power Electronics and Motion Control Conference (IPEMC), 2012

3. Yao R, Deng W (2017) A totem pole PFC control method and Simulink simulation. J Dalian Jiaotong Univ 38(06):111–114 (in Chinese)
4. Qian S (2017) Analysis and design of continuous conduction mode totem pole bridgeless PFC converter. Southeast University (in Chinese)
5. Li G (2017) Research on high-efficiency high-power totem pole PFC converter. Harbin Institute of Technology (in Chinese)
6. Zhang W, Wang B, Zhang X (2016) Research on two CCM PFC controllers. J Power Supply 14(05):7–14 (in Chinese)
7. Yang C, He K, Jin N, Feng X (2015) Simulation study on a new type of PFC control. Power Technol 39(03):586–587 + 603 (in Chinese)
8. Zhang C, Xie Y (2006) Single-period implementation of Boost PFC circuit of totem pole. Commun Power Technol (03):53–55 (in Chinese)
9. Chen X (2014) Study on totem pole bridge free PFC converter. Zhejiang University, (in Chinese)
10. Wang Y, Xia R (1998) An improved scheme of PFC control technology. Electron Sci Technol 1998(02):32–35; 52(3):701–708 (in Chinese)

# Pure Electric Brake of the Train with Speed Sensorless Vector Control



Qiya Wu, Shaobo Yin, Dangwei Duan, Chunmei Xu and Lijun Diao

**Abstract** In this paper, the pure electric brake of the train and the vector control of the asynchronous motor without speed sensor are studied, respectively. The pure electric brake of the train is controlled by a combination of regenerative brake and reverse brake. The estimation method of the feedback speed is based on the Model Reference Adaptive System (MRAS), and both the traditional MRAS and the improved MRAS are analyzed. In this paper, pure electric brake and MRAS estimation are combined to get a better system. Finally, by using the improved MRAS speed estimation method, a simulation of the pure electric brake with speed sensorless control is established with MATLAB simulation software to verify the study.

**Keywords** MRAS · Pure electric brake · Speed sensorless control · Vector control

## 1 Introduction

Most of the train braking methods of China is a combination of electric brake and air brake, which uses the friction between the brake shaft and the wheel to decelerate the train. But the friction braking force is limited by the brake heat capacity. Prolonged friction will cause wear on the wheel, which increases the maintenance difficulty of mechanical parts and reduces their service life [1]. In addition, the

---

Q. Wu · S. Yin · C. Xu (✉) · L. Diao

School of Electrical Engineering, Beijing Jiaotong University, Beijing, China

e-mail: [chmxu@bjtu.edu.cn](mailto:chmxu@bjtu.edu.cn)

Q. Wu

e-mail: [18121512@bjtu.edu.cn](mailto:18121512@bjtu.edu.cn)

S. Yin

e-mail: [15117395@bjtu.edu.cn](mailto:15117395@bjtu.edu.cn)

L. Diao

e-mail: [ljdiao@bjtu.edu.cn](mailto:ljdiao@bjtu.edu.cn)

D. Duan

CRRC Changchun Railway Vehicles Co., Ltd., Changchun 130000, Jilin, China

response speed of the electric brake is faster than that of the air brake, which means the electric brake has to take a delay measure to cooperate with the air brake [2]. The use of pure electric brake can solve these problems and make the deceleration process more comfortable to passengers.

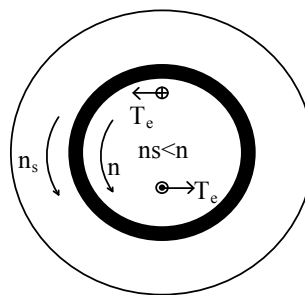
Speed sensorless vector control has advantages of reducing hardware cost and control robustness, and it is one of the important research contents in the field of traction drive. One of the conditions of high-performance control is the accurate acquisition of flux. Therefore, the flux observation is a key technology for speed sensorless vector control. MRAS-based methods are widely used to improve the performance of flux observation. The traditional MRAS speed estimation takes the voltage-type flux observer as a reference model, and the current-type flux observer as an adjustable model and feeds the estimated speed back to the current-type flux observer [3]. When the outputs of two models are consistent, the estimated speed and actual value coincide. But due to the parameter sensitivity and the pure integral part in the voltage-type flux observer, the performance of traditional MRAS method is limited.

In this paper, the improved MRAS observation method is used, which replaces the reference model to a motor model, and the obtained estimated speed is fed back to the vector control part to realize the pure electric brake of the trains with speed sensorless control [4].

## 2 Principle Analysis

### 2.1 Pure Electric Brake

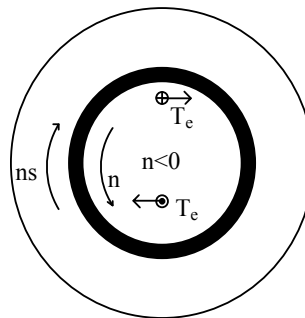
The pure electric brake is composed of regenerative brake and reverse brake [5]. In the region of regenerative brake, the stator current will be controlled to change the frequency of stator. The synchronous speed  $n_s$  is lower than the rotor speed  $n$ , the slip  $s < 0$ , and if the rotor speed is considered to be positive, then the electromagnetic torque  $T_e$  is negative. The motor works as a generator which converts kinetic energy of the train into electrical energy, as shown in Fig. 1.



**Fig. 1** Generator mode of inductor motor

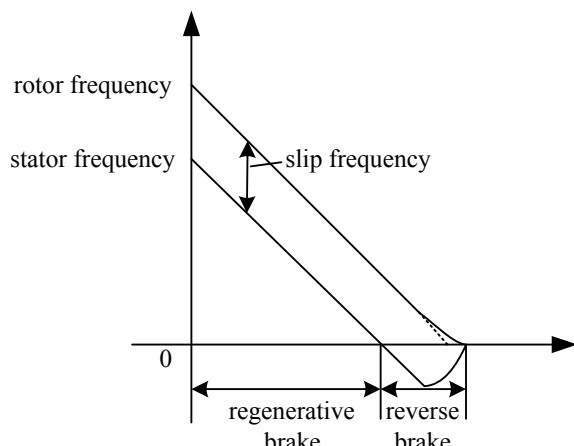
Reverse brake reverses the frequency of stator by changing the phase sequence of the power supply. Then, the rotor speed is considered negative, the slip  $s > 0$ , and the direction of the electromagnetic torque  $T_e$  is the same as that of the synchronous speed  $n_s$ . The motor works at the electromagnetic braking system, as shown in Fig. 2.

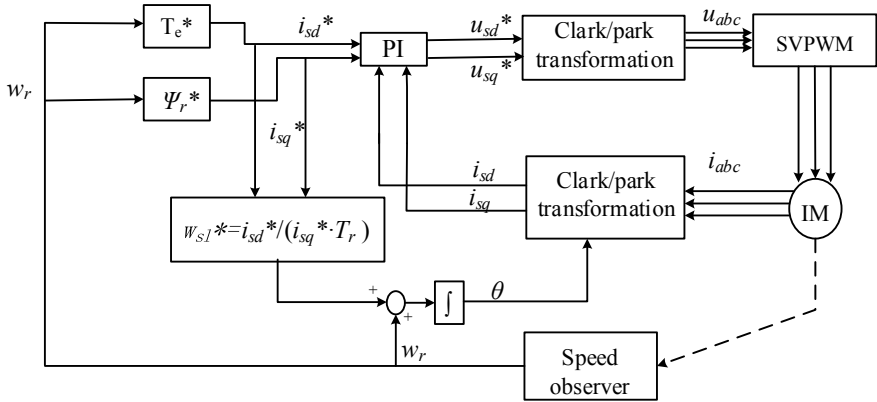
The pure electric brake control is shown in Fig. 3. When the brake starts, regenerative brake is adopted. We change the rotation direction of rotor by reducing the frequency of the rotating magnetic field to generate the braking force. As the rotor speed decreases, the frequency of the rotating magnetic field continuously decreases to zero. When the regenerative brake force is insufficient at low speed, reverse brake is adopted to maintain the electric braking force. And the traction motor is in the reverse traction state, which means that the braking torque of the reverse brake should be removed in time when the train stops, otherwise the train will be pulled backward and cannot be stopped. Therefore, when the speed is lower than a certain value, the reverse traction torque must be gradually reduced until the speed is zero.



**Fig. 2** Electromagnetic brake mode of induction motor

**Fig. 3** Pure electric brake





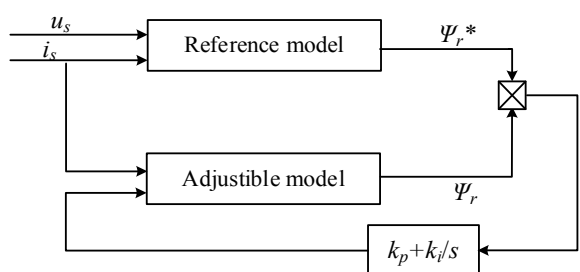
**Fig. 4** Vector control block diagram

Figure 4 shows the block diagram of vector control [6]. Real-time feedback of the speed is required in the control. The accuracy of the speed measurement is directly related to the performance of the system control [7].

## 2.2 Speed Estimation

MRAS is a stability design method with parameter identification adaptive, which makes the identification parameters asymptotically convergent. The MRAS uses two models, the model without unknown parameters is considered as the reference model, and the model containing the estimated parameter is considered as the adjustable model. Then, compare the same parameter obtained with the two models and get the estimated quantity through a certain adaptive rate. It is then fed back to the adjustable model to gradually converge the error. Figure 5 shows the block diagram of the MRAS. When the error of the two models is 0, the estimated speed equals to the actual speed.

**Fig. 5** Principle diagram of MRAS



The traditional MRAS speed estimation takes a voltage-type flux observer as a reference model and a current-type flux observer as an adjustable model. The voltage flux observer formula is:

$$\begin{cases} \Psi_{r\alpha} = \frac{L_r}{L_m} [\int (u_{s\alpha} - R_s i_{s\alpha}) dt - \sigma L_s i_{s\alpha}] \\ \Psi_{r\beta} = \frac{L_r}{L_m} [\int (u_{s\beta} - R_s i_{s\beta}) dt - \sigma L_s i_{s\beta}] \end{cases} \quad (1)$$

It can be known from the equation that the traditional MRAS speed estimation model contains stator resistance and pure integration part, which will cause poor performance at low speed. The improved MRAS method replaces the voltage-type flux observer with the motor model to improve the accuracy of the estimation. Therefore, the easily measured stator current is selected as the parameter to be compared, and the adjustable model is changed to the stator current estimation model. Then

$$\begin{cases} \frac{di_{s\alpha}}{dt} = \frac{L_m}{\sigma L_s L_r T_r} \Psi_{r\alpha} + \frac{L_m}{\sigma L_s L_r} \omega_r \Psi_{r\beta} - \frac{R_s L_t^2 + R_r L_m^2}{\sigma L_s L_r^2} i_{s\alpha} + \frac{u_{s\alpha}}{\sigma L_s} \\ \frac{di_{s\beta}}{dt} = \frac{L_m}{\sigma L_s L_r T_r} \Psi_{r\beta} - \frac{L_m}{\sigma L_s L_r} \omega_r \Psi_{r\alpha} - \frac{R_s L_t^2 + R_r L_m^2}{\sigma L_s L_r^2} i_{s\beta} + \frac{u_{s\beta}}{\sigma L_s} \end{cases} \quad (2)$$

The flux in the formula can be obtained by the current-type flux observer:

$$\begin{cases} \Psi'_{r\alpha} = \frac{1}{1+T_r p} [L_m i_{s\alpha} - T_r \Psi'_{r\beta} \omega_r] \\ \Psi'_{r\beta} = \frac{1}{1+T_r p} [L_m i_{s\beta} + T_r \Psi'_{r\alpha} \omega_r] \end{cases} \quad (3)$$

where  $p$  denotes a differential operator.

According to the Lyapunov's theorem, the speed adaptation rate of the current error is designed to obtain the speed estimation value:

$$\omega'_r = k_p (e_{is\alpha} \Psi'_{r\beta} - e_{is\beta} \Psi'_{r\alpha}) + k_i \int (e_{is\alpha} \Psi'_{r\beta} - e_{is\beta} \Psi'_{r\alpha}) dt \quad (4)$$

In summary, the block diagram of the improved MRAS speed observer is shown in Fig. 6. In practice, in order to make the flux observer and the speed estimation independent of each other, the current-type flux observer uses the estimated current instead of the actual current.

### 3 Simulation Results

A MATLAB simulation is built to verify the principle with a field-oriented control (FOC) induction motor drive. The simulation step is 2e-6 and the switching frequency is 1 kHz. The s-function module in Simulink is used for programming, and

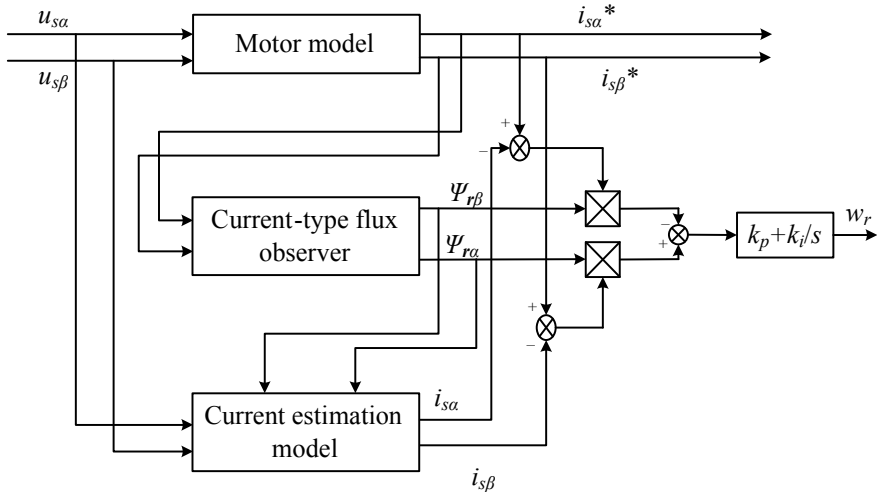


**Fig. 6** Principle diagram of improved MRAS speed estimation

**Table 1** Motor parameters

Symbol	Quantity	Values ( $\Omega$ )	Symbol	Quantity	Values
$R_s$	Stator resistance	0.1148	$P_N$	Rated power	210 kVA
$R_r$	Rotor resistance	0.1148	$I_N$	Rated stator current	60 A
$L_s$	Stator inductance	0.033	$n_p$	Pole pair	2
$L_r$	Rotor inductance	0.033	$f$	Rated stator frequency	60 Hz
$L_m$	Magnetic inductance	0.032	$\Omega$	Rated speed	1800 rpm

the backward Euler transform is used to make the discretization of each module easily. Table 1 shows the motor parameters [8, 9].

Figure 7a shows the speed of the motor with the speed sensor, and Fig. 7b is an enlarged view of the circular portion in Fig. 7a, which shows the brake process combined with regenerative brake and reverse brake. The actual speed and estimated speed of the motor with speed sensorless vector control is shown in Fig. 8. The estimated speed can match the actual speed at low speed. Figure 9 shows the pure electric brake process of the motor with a speed sensorless control, which can achieve smooth deceleration of the train.

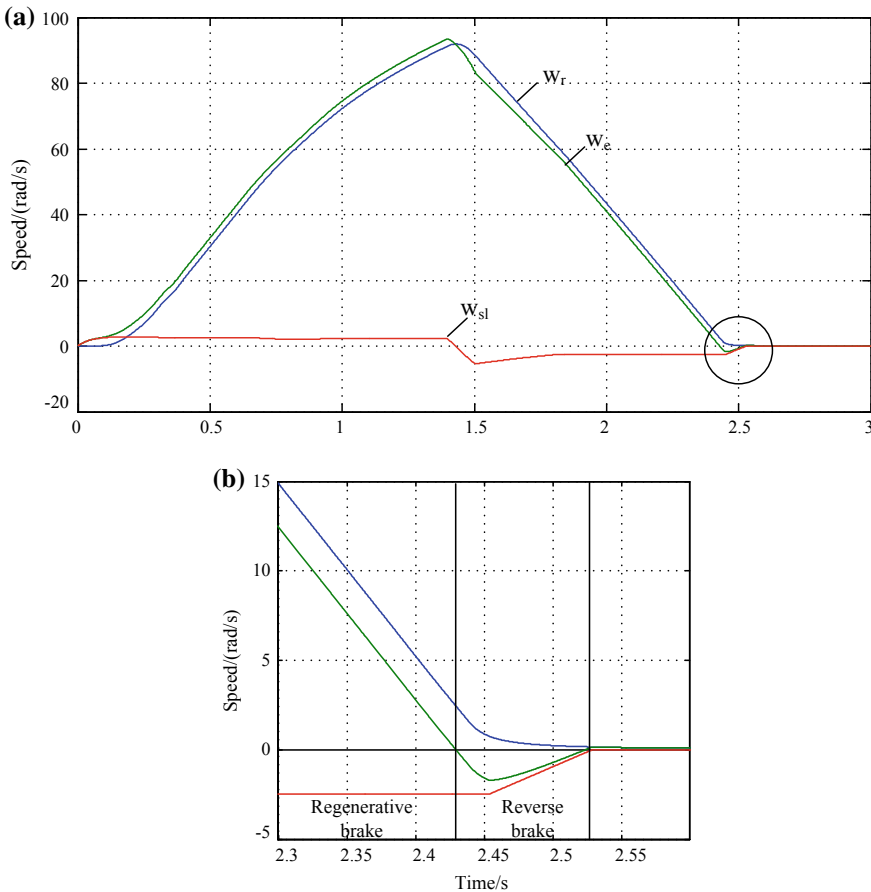


**Fig. 7** Pure electric brake with speed sensor

#### 4 Conclusion

In this paper, the pure electric brake of the train with speed sensor and speed sensorless was simulated, respectively. An improved MRAS-based observer is adopted in the speed estimation. Simulation results prove that pure electric brake of the train with speed sensorless vector control can be realized well.

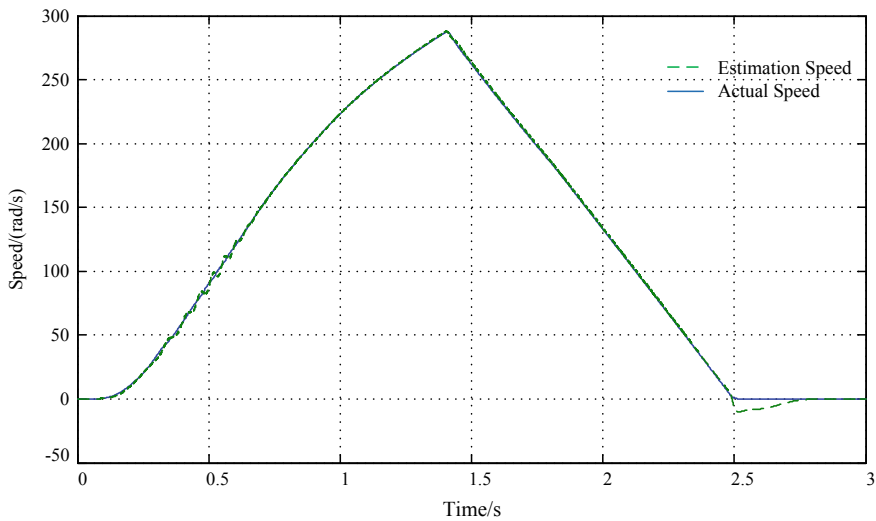
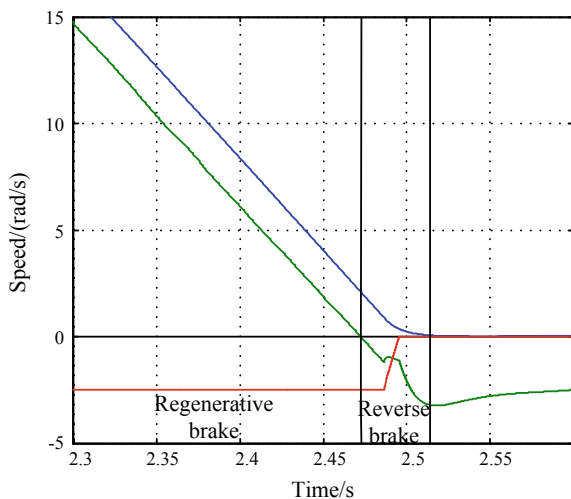


**Fig. 8** Speed of induction motor

**Fig. 9** Pure electric brake with speed sensorless control



## References

1. Zhou M (2011) Research on pure electric brake control strategy of traction linear induction motor. Beijing Jiaotong University, Beijing (in Chinese)
2. Ashiya M, Sone S, Sato Y, Kaga A (2000) Application of pure electric braking system to electric railcars. In: 6th international workshop on advanced motion control (Cat. No.00TH8494), Nagoya, Japan, pp 163–168

3. Benlaloui I, Drid S, Chrifi-Alaoui L, Ouriagli M (2015) Implementation of a new mras speed sensorless vector control of induction machine. *IEEE Trans Energy Convers* 30(2):588–595
4. Bai X (2017) Research on vector control strategy without speed sensor. Beijing Jiaotong University, Beijing (in Chinese)
5. Yi Z (2012) Research on pure electric brake of high speed train based on traction drive simulation platform. Beijing Jiaotong University, Beijing (in Chinese)
6. Sun W (2016) Research on low-speed operation technology of induction motor without speed sensor vector control. Harbin Institute of Technology, Harbin (in Chinese)
7. Wang Y, Yao Y (2005) Pure electric braking. *J Convert Electr Traction* 2005(05):21–22 (in Chinese)
8. Dong W (2015) Research on key technology and system performance optimization of EMU traction inverter control. Beijing Jiaotong University, Beijing (in Chinese)
9. He L, Wang F, Wang J, Rodriguez J (2019) Zynq implemented Lunenberger disturbance observer based predictive control scheme for PMSM drives. *IEEE Trans Power Electron* 35 (2):1770–1778

# Rule-Based Energy Management Strategy for Multi-energy Drive System



Yue Yuan, Rongjia He, Haibo Zhao, Enlong Li, Xuekun Li  
and Chunmei Xu

**Abstract** Energy management plays an important role in improving the fuel economy and reducing emissions of multi-energy drive system. This paper focuses on the rule-based energy management strategy for multi-energy drive system of “diesel generator + battery.” It mainly focused on the optimization of the following three aspects: control of diesel generator sets, control of power battery packs, and load energy management. Moreover, simulation results have verified that the rule-based energy management strategy can operate stably in the multi-energy drive system, realize the power distribution of the two power sources, and make the system run in the low-consumption and high-efficiency area.

**Keywords** Multi-energy · Energy management · Rule-based · Drive system

## 1 Introduction

With the rapid development of China’s railway industry, EMU technology is gradually maturing [1]. However, the traditional EMU train highly depends on the catenary, in which the energy supply mode is single, and its regenerative braking will cause harmonic pollution to the catenary. In recent years, the R&D team of the EMU has borrowed the ideas of new energy vehicles into the research of high-speed trains and proposed the concept of hybrid EMUs [2, 3]. This paper mainly studies the multi-energy drive system composed of “diesel generator + lithium battery.”

---

Y. Yuan · C. Xu (✉)

School of Electrical Engineering, Beijing Jiaotong University, Beijing, China  
e-mail: [chmxu@bjtu.edu.cn](mailto:chmxu@bjtu.edu.cn)

Y. Yuan

e-mail: [16126065@bjtu.edu.cn](mailto:16126065@bjtu.edu.cn)

R. He

China Railway Fifth Survey and Design Institute Group Co., LTD., Beijing, China

H. Zhao · E. Li · X. Li

CRRC Changchun Railway Vehicles Co., LTD., Changchun, China

The energy distribution between diesel generators and lithium batteries depends on the energy management strategy that is mainly divided into energy management control based on rules and energy management control based on optimization. And the energy management control strategy based on optimization can be divided into global optimization and instantaneous optimization. Global optimization has an ideal optimization performance and can achieve global optimization. However, it usually depends on the working cycle and has a large amount of calculation, which is not conducive to real-time control [4]. Instantaneous optimization is usually not restricted by circulating conditions and requires little computation, which enables real-time control, but it cannot guarantee global optimization [5]. The rule-based energy management strategy is established, based on engineering experience and mathematical model [6]. Besides, considering the actual running condition of the train, corresponding rules are formulated in advance. The rule-based energy management strategy has advantages of simple algorithm, strong robustness, and easy implementation [7, 8].

Based on the above analysis and considering that railway traffic has its own unique rules, the rule-based energy management strategy is suitable for multi-energy drive system [9].

## 2 Design of Multi-energy Drive System

The multi-energy drive system consists of a diesel generator set, a power battery pack, and a DC/DC converter. The diesel generator set is connected to the middle DC side by the uncontrolled rectification of the four-quadrant converter, and the power battery pack is connected to the DC side by the DC/DC converter. The block diagram of the system is shown in Fig. 1.

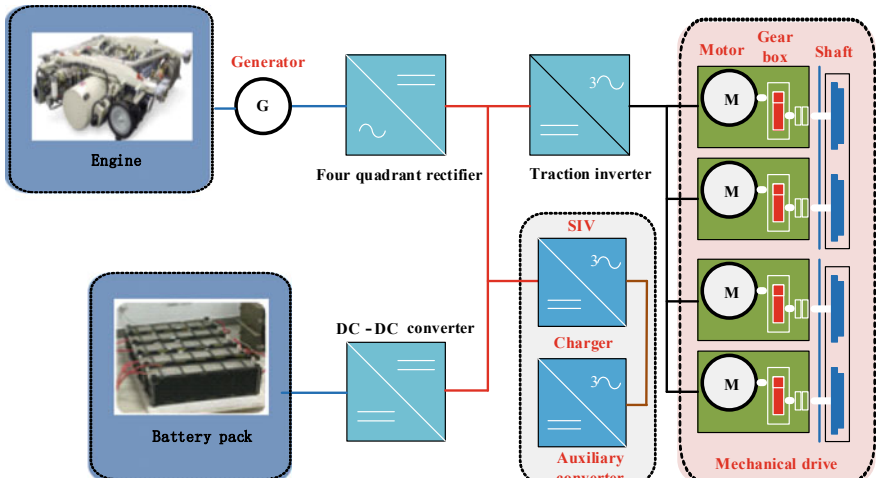


**Fig. 1** Multi-energy drive system block diagram

Permanent magnet synchronous generator (PMSM) is selected as the generator to control the volume and weight of the multi-energy drive system diesel generator. Considering the high power density, high cycle life, low self-discharge rate, and fast charging–discharging performance required in the multi-energy drive system, lithium-titanate battery [10] is selected as the energy source in this paper. The multi-energy drive system uses a bidirectional converter to charge and discharge the battery [11]. The bidirectional buck–boost converter uses a double closed-loop control strategy, which uses the control method of the voltage outer loop current inner loop.

### 3 Rule-Based Energy Management Strategy

The rule-based energy management strategy for multi-energy drive system is used for the power distribution of power battery pack and diesel generator set.

#### 3.1 Control Strategy of Power Battery

According to engineering practice, the upper and lower limits of SOC of power battery pack are set to 85% and 20%, respectively. SOC of power battery has different limits under different working conditions,  $SOC_{\text{dislim}}$  is the lower limit of battery SOC discharge;  $SOC_{\text{cons\_lo}}$  is the lower limit of battery SOC for parking charging;  $SOC_{\text{chglim}}$  is the upper limit of constant speed charging of battery SOC;  $SOC_{\text{cons\_hi}}$  is the upper limit of battery SOC for parking charging;  $SOC_{\text{brklim}}$  is the braking charging upper limit of battery SOC;  $V_{\text{lim}}$  is the speed limit for diesel generator starting.

Table 1 shows the formulation of rules for the instantaneous power based on the comprehensive speed and train operating conditions, where  $P_{\text{tra}}$ ,  $P_{\text{bat}}$ ,  $P_{\text{pp}}$  are the power required by train traction, the output power of power battery pack, and the output power of diesel generator set, respectively.

**Table 1** Power battery pack logic threshold rule

Number	Condition		Control rule
1	$V < V_{\text{lim}}$	$SOC < SOC_{\text{cons\_lo}}$	$P_{\text{pp}} = P_{\text{tra}} + P_{\text{bat}}$
2		$SOC \geq SOC_{\text{cons\_hi}}$	$P_{\text{bat}} = P_{\text{tra}}, P_{\text{pp}} = 0$
3	$0 < V < 120$	$SOC < SOC_{\text{dislim}}$	$P_{\text{pp}} = P_{\text{tra}}, P_{\text{bat}} = 0$
4		$SOC \geq SOC_{\text{dislim}}$	$P_{\text{pp}} + P_{\text{bat}} = P_{\text{tra}}$
5	$0 < V < 120$	$SOC < SOC_{\text{brklim}}$	$P_{\text{bat}} = P_{\text{tra}}, P_{\text{pp}} = 0$
6		$SOC \geq SOC_{\text{brklim}}$	$P_{\text{pp}} = P_{\text{tra}}, P_{\text{bat}} = 0$
7	Idle running condition	$SOC < SOC_{\text{chglim}}$	$P_{\text{pp}} = P_{\text{tra}} + P_{\text{bat}}$
8		$SOC \geq SOC_{\text{chglim}}$	$P_{\text{pp}} = P_{\text{tra}}, P_{\text{bat}} = 0$

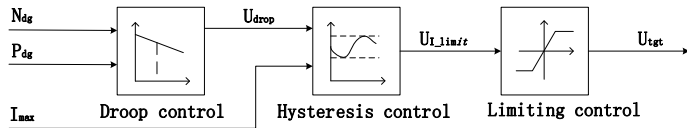


**Fig. 2** Logical block diagram of power battery charge

In order to ensure the stability of DC bus voltage during operation, hysteresis control will be added when the target value of power battery is set. Because of the charge–discharge characteristic of the power battery itself, it is necessary to carry on the limiting control to the power battery.

The logic block diagram of the power battery charge and discharge control based on droop control is shown in Fig. 2.

### 3.2 Control Strategy of Diesel Generator Set

Combined with the actual operating conditions of the train, the vehicle speed, and the SOC value of the power battery pack, the instantaneous power control rules for the speed of the diesel generator set are obtained as shown in Table 2. In the table,  $N_{dg}$  is the speed of diesel generator,  $N_{chg}$  is the rotational speed of the diesel generator when it is charging the power battery pack under the running condition of idling,  $N_{idling}$  is the idling speed of a diesel generator set,  $N_{trac}$  is the rotation speed of diesel generator set under traction condition,  $N_{brk}$  is the rotational speed of the diesel generator set when the power battery absorbs the electric braking energy,  $N_{cons}$  is the rotational speed of a diesel generator set providing traction system

**Table 2** Optimization of working point of diesel generator set

Number	Condition		Control rule
1	$V < V_{lim}$	$SOC < SOC_{cons\_lo}$	Station charging mode, $N_{dg} = N_{chg}$
2		$SOC \geq SOC_{cons\_hi}$	Station pure battery mode, $N_{dg} = N_{idling}$
3	$0 < V < 120$	$SOC < SOC_{dislim}$	Diesel generator mode, $N_{dg} = N_{trac}$
4		$SOC \geq SOC_{dislim}$	Hybrid power mode, $N_{dg} = N_{trac}$
5	$0 < V < 120$	$SOC < SOC_{brklim}$	Pure battery brake mode, $N_{dg} = N_{brk}$
6		$SOC \geq SOC_{brklim}$	Mechanical brake mode, $N_{dg} = N_{cons}$
7	Idle running condition	$SOC < SOC_{chglim}$	Driving charging mode, $N_{dg} = N_{chg}$
8		$SOC \geq SOC_{chglim}$	Diesel generator mode, $N_{dg} = N_{cons}$

energy and auxiliary system energy. In addition, the diesel generator adopts constant speed control in different working conditions to ensure rapid response and stable operation.

## 4 Load Energy Management

The multi-energy drive system is also a multi-load system, and there is also the matching problem between the power supplies and the load. Therefore, it is necessary to manage the load to achieve energy stability.

In this paper, the concept of “power reduction coefficient” is proposed, which is defined as the ratio of available power to load power of the system. In the process of train operation, the maximum output and absorption capacity of the system on the load of the inverter under traction and braking conditions are shown in (1) and (2), respectively.

$$P_{\max} = P_{\text{available}} + I_{\max\_dch} U_{\text{bat}} - P_{\text{aps}} \quad (1)$$

$$P_{\max} = I_{\max\_ch} U_{\text{bat}} + P_{\text{aps}} \quad (2)$$

where  $P_{\text{available}}$  is the maximum available power of the diesel generator set;  $I_{\max\_cha}$ ,  $I_{\max\_dch}$  are the maximum charging and discharging currents of the power battery pack, respectively;  $U_{\text{bat}}$  is the battery voltage;  $P_{\text{aps}}$  is the auxiliary power.

Therefore, the power reduction coefficient  $k_r$  of the load of the hybrid power system is shown in (3), and  $P_{\text{inv}}$  is the power of the inverter.

$$k_r = \frac{P_{\max}}{P_{\text{inv}}} \times 100\% \quad (3)$$

## 5 Simulation Results

The simulation results are shown in Fig. 3. The waveform of the power reduction coefficient and system power is shown in Fig. 4.

It can be seen that the energy management system can correctly judge the starting in the station, hybrid traction, idling charging or electric braking modes of the system. The diesel generator selects the corresponding speed control method according to the operation mode. And it also can be seen from the waveform of the power reduction coefficient and system power that the load power always runs according to the smaller value of the instruction power and the maximum output power, realizing the load energy management, and avoiding the overload of diesel generator or power battery.

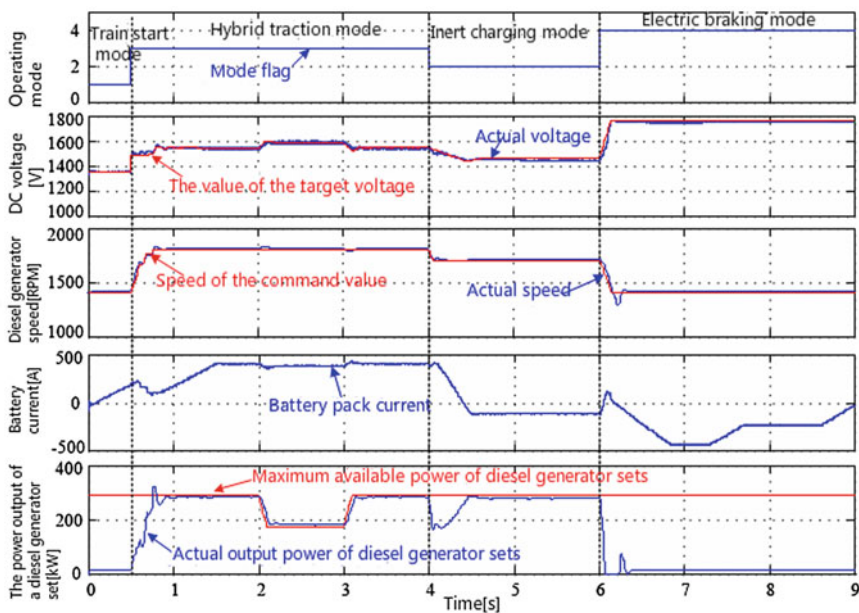


**Fig. 3** Simulation result of the rule-based energy management strategy

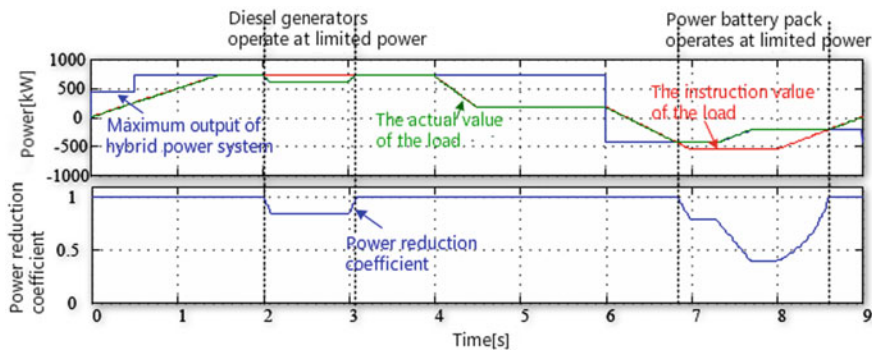


**Fig. 4** Simulation result of load power reduce control

## 6 Conclusion

According to the actual operating conditions and traction characteristics of the multi-energy drive system, this paper selects the rule-based energy management strategy to conduct research and improves the energy management strategy. The diesel generator is controlled by a combination of constant speed control and hysteresis control, and the power battery is controlled by a combination of droop

control-based charge and discharge control and hysteresis control, and the load is managed to achieve energy stability. Moreover, simulation results have verified that the rule-based energy management strategy can run stably in the multi-energy drive system, realize the power distribution of the two kinds of energy, and control the flow direction of the energy.

**Acknowledgements** This work is supported by National Key R&D Program of China (No. 2018YFB1201600) and Basic Research (No. JCKY2018110C113).

## References

1. Li J (2015) China's current situation and development trend of high speed emu research. *J Inform Sci Technol China* 10:105–106. <https://doi.org/10.3969/j.issn.1001-8972.2015.10.041> (in Chinese)
2. Tian R, Kang Y (2012) Development of hybrid locomotives at home and abroad (part 1). *Diesel Locomot* 09:1–3 + 0–1 (in Chinese)
3. Tian R, Kang Y (2012) Development of hybrid locomotives at home and abroad (part 2). *Diesel Locomot* 10:1–4 (in Chinese)
4. Galdi V, Ippolito L, Piccolo A et al Multiobjective optimization for fuel economy and emissions of HEV using the goal-attainment method. In: Proceedings of the 18th international electric vehicle symposium, Berlin, Germany
5. Paganelli G, Ercole G, Brahma A et al (2001) General supervisory control policy for the energy optimization of charge-sustaining hybrid electric vehicles. *JSME Rev* 22(4):511–518
6. Rahman Z, Butler KL, Ehsani MA (2000) Comparison study between two parallel hybrid control concepts. *SAE Paper* 2000-01-0994
7. Ehsani M, Gao Y, Butler KL (1999) Application of electrically peaking hybrid (ELPH) propulsion system to a full-size passenger car with simulated design verification. *IEEE Trans Vehic Technol* 48(6):1779–1787
8. Kimura A, Abe T, Sasaki S (1999) Drive force control of a parallel-series hybrid system. *JSME Rev* 20(3):337–341
9. Zhang X, Mi C (2011) Vehicle power management: modeling, control and optimization. Springer Science & Business Media, Berlin
10. Liu S, Jiang J, Wang Z et al (2014) Research on applicability of lithium titanate battery for low-floor vehicles. In: Proceedings of the 2013 international conference on electrical and information technologies for rail transportation (EITRT2013), vol II. Springer, Berlin, pp 115–125
11. Du Y, Zhou X, Bai S et al (2010) Review of non-isolated bi-directional DC-DC converters for plug-in hybrid electric vehicle charge station application at municipal parking decks. In: Twenty-fifth annual IEEE applied power electronics conference and exposition (APEC). IEEE, pp 1145–1151

# Vector Control Optimization of Traction Motors Based on Online Parameter Identification



Xitang Tan, Dabo Xie, Qinyue Zhu, Zhaoyang Li,  
Wei Dai and Quanpeng Wu

**Abstract** In order to further improve the accuracy of parameter identification under the fluctuation of traction motor speed (torque) and improve the speed control performance of the motor, the vector control strategy of traction motor is optimized. An online identification model of motor parameters based on recursive least squares (RLS) and model reference adaptive method (MRAS) is proposed. The motor stator and rotor parameters identified by RLS are input into MRAS on the basis of the rotor flux observation model. A proportional-integral adaptive law by use of Popov's hyperstability theory is designed to identify the rotor resistance. Through the above optimization, the vector control strategy is optimized to realize effective control of speed regulation characteristics of traction motors in different speed intervals and under different working conditions. Consequently, the effectiveness of the proposed model and control strategy is realized and verified by simulation.

**Keywords** Recursive least squares · Model reference adaptive system · Online parameter identification · Vector control strategy

## 1 Introduction

Due to its good static and dynamic control performance, the induction motor vector control strategy based on rotor field orientation has been widely used in high-speed electric motor units (EMUs) traction drive systems of the traction motor. In actual operations, the traction drive system forms a closed-loop control by feeding back the output current and speed signals of the traction motor, so that the traction inverter outputs a three-phase AC voltage necessary for motor operation. During the closed-loop control process, the rotor flux and speed of the traction motor will follow the target values in real time to achieve AC speed control. The key lies in

---

X. Tan · D. Xie · Q. Zhu (✉) · Z. Li · W. Dai · Q. Wu

School of Electronics and Information Engineering, Tongji University, 201804 Shanghai,  
People's Republic of China  
e-mail: [zqymelisa@tongji.edu.cn](mailto:zqymelisa@tongji.edu.cn)

accurate orientation of the rotor field, that is, to accurately obtain the amplitude and phase of the rotor flux. The observation effect is largely influenced by the motor stator and rotor parameters [1]. In the actual system, when the traction motor is operating at different speeds (from low speed to high speed) and under different loads, the internal stator and rotor parameters will vary accordingly with the motor speed, temperature rise, frequency change, and saturation of the magnetic circuit. Therefore, in order to achieve good speed control in the traction drive process, it is essential to accurately identify the stator and rotor parameters of the traction motor online.

The parameters of the traction motor mainly include stator and rotor resistance, stator and rotor inductance, as well as the mutual inductance. Currently, there are several popular online parameter identification methods: RLS [2], MRAS [3], Kalman filtering method (KF) [4], and Artificial Intelligence algorithm (AI) [5]. Among them, the parameter identification process based on KF is computationally intensive and difficult to apply online. While there is plenty of research on AI, it still needs to be further improved in terms of practicability and feasibility. In contrast, the RLS has found more applications due to its simple calculation process. It transforms the mathematical model of the traction motor into a standard form of the RLS and identifies the motor parameters by measuring the voltage, current, and speed signals. However, it has complicated calculation and a relatively high demand for computer storage space. In view of this, Ref. [6] added a recursive algorithm based on the basic RLS and introduced a forgetting factor, which greatly reduces the amount of data calculation. Nevertheless, when the motor speed is unstable or fluctuating greatly, the accuracy of rotor resistance identification is reduced even though the identification of the inductance parameters is relatively accurate. On account of this, Ref. [7, 8] proposed to use the model reference adaptive system to identify rotor resistance online. Ref. [7] used the whole traction motor as the reference model based on the estimated deviation of the stator current. The MRAS-based identification scheme is designed with the equation containing the parameter to be identified as the adjustable model. Ref. [8] derived the corresponding adaptive law based on the Lyapunov stability theory, designed a stable MRAS identification system, and obtained accurate results. However, for lack of experience, it is fairly difficult to select proper Lyapunov function for a particular MRAS system to design the adaptive law. The identification accuracy of all parameters of the motor stator and rotor cannot be guaranteed either.

This paper proposes a traction motor vector control optimization strategy based on combining the RLS with MRAS, which improves the identification accuracy in case of speed (torque) fluctuations and has better anti-interference performance and realizes effective control of the traction motor speed regulation characteristics in different speed intervals and under different working conditions. Finally, the effectiveness of the proposed optimization model and strategy is verified by simulations.

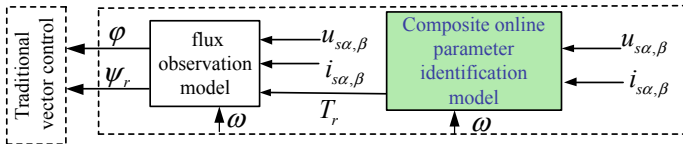


**Fig. 1** Structure of motor vector control optimization system

## 2 The Design Idea of Traction Motor Vector Control Optimization

Based on the traditional vector control system, this paper designs a composite online parameter identification model to improve the original flux feedback portion and optimize the motor vector control strategy so as to enhance the motor control performance. Figure 1 shows the corresponding optimized vector control system structure, which mainly consists of two parts—the traditional vector control part and the composite online parameter identification model. The online parameter identification model is intended for real-time identification of the motor parameters under different operating states by taking advantage of the RLS and MRAS after obtaining the motor voltage, current and speed signals. The identified results are input into the flux observation model to adjust the observed results of the rotor flux in real time. Then, the flux observation model passes the observed flux amplitude and phase to the traditional vector control part.

## 3 Traction Motor Vector Control and Optimization Strategy

When the motor parameter identification based on the RLS is affected by unstable speed or fluctuation, an error of rotor resistance is likely to occur. However, MRAS is effective in eliminating the system disturbance. In this paper, the advantages of the two methods are made use of to achieve accurate identification of motor parameters. First, the parameters related to the stator and rotor of the motor are identified based on the initial values of off-line parameters and the RLS, and then the identified parameters are input into MRAS based on the rotor flux observation model. By using Popov hyperstability theory to design a proportional-integral adaptive law, the rotor time constant can be identified.

### 3.1 Online Identification of Motor Parameters Based on Recursive Least Squares

Currently, the RLS is widely applied to the online identification of traction motor parameters. Although the accuracy of rotor resistance identification is reduced when the motor speed is unstable or fluctuating greatly, the identification of other parameters of the motor is barely affected. So, this paper uses the RLS to identify the motor parameters.

$$\begin{cases} \hat{\theta}(N+1) = \hat{\theta}(N) + K(N+1) [y(n+N+1) - \varphi^T(N+1)\hat{\theta}(N)] \\ K(N+1) = P(N)\varphi(N+1)(1 + \varphi^T(N+1)P(N)\varphi(N+1))^{-1} \\ P(N+1) = [I - K(N+1)\varphi^T(N+1)]P(N) \end{cases} \quad (1)$$

where  $\theta(N)$  is the parameter matrix to be identified,  $K(N)$  is the gain matrix,  $\varphi(N)$  is the observation matrix, and  $P(N)$  is the covariance matrix.

In order to apply the method to identify the stator and rotor parameters of the motor [9], it is necessary to convert the mathematical model of the motor into a standard form that can be used for the RLS. Assuming that the motor speed is stable or fluctuating slightly, in order to avoid the influence of rotor flux on parameter identification, all the rotor flux items should be eliminated in the derivation. Then, according to the mathematical model of the traction motor in the  $d$ - $q$  two-phase rotating coordinate system, the motor parameter identification model based on the standard form of the RLS can be obtained as follows:

$$\begin{cases} \frac{d^2i_{sd}}{dt^2} - \omega \frac{di_{sq}}{dt} = -\left(\frac{R_s}{\sigma L_s} + \frac{1}{\sigma T_r}\right) \frac{di_{sd}}{dt} - \frac{R_s}{\sigma L_s T_r} i_{sd} + \omega \frac{1}{\sigma T_r} i_{sq} + \frac{1}{\sigma L_s} \cdot \frac{du_{sd}}{dt} + \frac{1}{\sigma L_s T_r} u_{sd} \\ \frac{d^2i_{sq}}{dt^2} + \omega \frac{di_{sd}}{dt} = -\left(\frac{R_s}{\sigma L_s} + \frac{1}{\sigma T_r}\right) \frac{di_{sq}}{dt} - \frac{R_s}{\sigma L_s T_r} i_{sq} - \omega \frac{1}{\sigma T_r} i_{sd} + \frac{1}{\sigma L_s} \cdot \frac{du_{sq}}{dt} + \frac{1}{\sigma L_s T_r} u_{sq} \end{cases} \quad (2)$$

where  $u_{sd}$  and  $u_{sq}$  are the components of the stator voltage in the  $d$ - $q$  coordinate system,  $i_{sd}$  and  $i_{sq}$  are the components of the stator current,  $R_s$  and  $L_s$  are stator resistance and inductance, respectively,  $T_r = L_r/R_r$  is rotor time constant,  $\omega$  is the motor speed, and  $\sigma = 1 - L_m^2/(L_s L_r)$  is the motor leakage coefficient.

Defined  $k_1 = R_s/(\sigma L_s) + 1/(\sigma T_r)$ ,  $k_2 = R_s/(\sigma L_s T_r)$ ,  $k_3 = 1/(\sigma T_r)$ ,  $k_4 = 1/(\sigma L_s)$ ,  $k_5 = 1/(\sigma L_s T_r)$ , the RLS algorithm is applied to estimate the parameters to be identified in the model. Finally, the identified values of the parameters of the motor can be obtained:  $R_s = k_2/k_5$ ,  $L_s = k_3/k_5$ ,  $T_r = k_4/k_5$ ,  $\sigma = 1 - k_5/k_3 k_4$ .

### 3.2 *Online Identification of Rotor Resistance Parameters Based on MRAS*

MRAS uses the equation without unknown parameters as a reference model and the equation with the parameters to be identified as an adjustable model. The outputs of the two models have the same physical meaning, and the error between them is utilized to achieve the purpose of system identification by selecting an appropriate adaptive law [10].

In this paper, since the basic voltage-type flux observation model of the traction motor does not contain  $T_r$ , it can be regarded as the reference model. The basic current-type flux observation model contains  $T_r$ , so it is considered as the adjustable model. The actual value  $\psi_r$  and observed value  $\hat{\psi}_r$  of the rotor flux from the two models are input into the adaptive mechanism to form a reference adaptive system. In this system, Popov's hyperstability theory is used to design the adaptive law of MRAS [10]. Assuming all parameters of the traction motor except  $T_r$  are accurate, the error between the identified value  $\hat{T}_r$  and the actual value  $T_r$  of rotor time constant can be considered to be caused by the error of the output rotor flux of the two models in the figure. The online identification of rotor time constant is adjusted according to the rotor flux error. In what follows, we derive its adaptive identification model briefly.

According to the basic voltage-type flux observation model, the rotor flux  $\psi_r$  can be:

$$\psi_r = \frac{L_r}{L_m} \left[ \int (\mathbf{u}_s - R_s \mathbf{i}_s) dt - \sigma L_s \mathbf{i}_s \right] \quad (3)$$

According to the basic current-type flux observation model, with the observed value of rotor time constant being substituted, the observed value of rotor flux  $\hat{\psi}_r$  can be:

$$\hat{\psi}_r = \frac{1}{\hat{T}_r s + 1} \left( L_m \mathbf{i}_s - \omega \hat{T}_r \hat{\psi}_r \right) \quad (4)$$

Here, Eq. (3) is taken as the reference model and Eq. (4) as the adjustable model. According to the designing method of the Popov hyperstability theory, with rotor time constant adaptive law in the proportional-integral link being used, as shown in Eq. (5).

$$\begin{aligned} \frac{1}{\hat{T}_r} = & K_i \int_0^{t_1} \left[ (\psi_{rx} - \hat{\psi}_{rx}) (L_m i_{sx} - \hat{\psi}_{rx}) + (\psi_{r\beta} - \hat{\psi}_{r\beta}) (L_m i_{s\beta} - \hat{\psi}_{r\beta}) \right] dt \\ & + K_p \left[ (\psi_{rx} - \hat{\psi}_{rx}) (L_m i_{sx} - \hat{\psi}_{rx}) + (\psi_{r\beta} - \hat{\psi}_{r\beta}) (L_m i_{s\beta} - \hat{\psi}_{r\beta}) \right] + \frac{1}{\hat{T}_r(0)} \end{aligned} \quad (5)$$

The above MRAS based on Eq. (5) is stable over a wide range. Here, it is proved.

When rotor time constant is the actual value  $T_r$ , the rotor flux obtained by the current model is the same as that obtained by the voltage model, so they are equivalent. We define the generalized error as  $e = \psi_r - \hat{\psi}_r$ , and then

$$\begin{bmatrix} \frac{de_{rx}}{dt} \\ \frac{de_{r\beta}}{dt} \end{bmatrix} = \begin{bmatrix} -\frac{1}{T_r} & -\omega_r \\ \omega_r & -\frac{1}{T_r} \end{bmatrix} \begin{bmatrix} e_{rx} \\ e_{r\beta} \end{bmatrix} - \left( \frac{1}{\hat{T}_r} - \frac{1}{T_r} \right) \begin{bmatrix} L_m \begin{pmatrix} i_{sx} \\ i_{s\beta} \end{pmatrix} - \begin{pmatrix} \hat{\psi}_{rx} \\ \hat{\psi}_{r\beta} \end{pmatrix} \end{bmatrix} \quad (6)$$

It can be simplified as

$$\frac{de}{dt} = A_e e - w \quad (7)$$

Therefore, the adaptive law designed by using Popov's hyperstability theory is

$$F(e, \tau, t) = \int F_1(v, \tau, t) d\tau + F_2(v, t) \quad (8)$$

In order for the system to be stable, the Popov integral inequality should be satisfied.

$$\eta(0, t_1) = \int_0^{t_1} v^T(t) w(t) dt \geq -\gamma_0^2 \quad \forall t_1 \geq 0, \gamma_0^2 > 0 \quad (9)$$

Substituting  $e$  and  $W$  into Eq. (9), we have

$$\eta(0, t_1) = \int_0^{t_1} e^T(t) \left( \frac{1}{\hat{T}_r} - \frac{1}{T_r} \right) \begin{bmatrix} L_m \begin{pmatrix} i_{sx} \\ i_{s\beta} \end{pmatrix} - \begin{pmatrix} \hat{\psi}_{rx} \\ \hat{\psi}_{r\beta} \end{pmatrix} \end{bmatrix} dt \quad (10)$$

According to the adaptive law,  $1/\hat{T}_r$  can be expressed in the proportional-integral form

$$\frac{1}{\hat{T}_r} = \int_0^{t_1} F_1(v, \tau, t) d\tau + F_2(v, t) + \frac{1}{\hat{T}_r(0)} \quad (11)$$

where  $\hat{T}_r(0)$  is the initial value.

Substituting Eq. (11) into Eq. (10), we have

$$\begin{aligned} \eta(0, t_1) &= \int_0^{t_1} e^T(t) \left( \int_0^{t_1} F_1(v, \tau, t) d\tau + \frac{1}{\hat{T}_r(0)} - \frac{1}{T_r} \right) \left[ L_m \begin{pmatrix} i_{sx} \\ i_{s\beta} \end{pmatrix} - \begin{pmatrix} \hat{\psi}_{rx} \\ \hat{\psi}_{r\beta} \end{pmatrix} \right] dt \\ &\quad + \int_0^{t_1} e^T(t) F_2(v, t) \left[ L_m \begin{pmatrix} i_{sx} \\ i_{s\beta} \end{pmatrix} - \begin{pmatrix} \hat{\psi}_{rx} \\ \hat{\psi}_{r\beta} \end{pmatrix} \right] dt \end{aligned} \quad (12)$$

Let  $x = e^T(t) \left[ L_m \begin{pmatrix} i_{sx} \\ i_{s\beta} \end{pmatrix} - \begin{pmatrix} \hat{\psi}_{rx} \\ \hat{\psi}_{r\beta} \end{pmatrix} \right]$ , and then, Eq. (12) can be reduced to

$$\eta(0, t_1) = \int_0^{t_1} x \left( \int_0^{t_1} F_1(v, \tau, t) d\tau + \frac{1}{\hat{T}_r(0)} - \frac{1}{T_r} \right) dt + \int_0^{t_1} x F_2(v, t) dt \quad (13)$$

Thus, Eq. (13) can be divided into the following two inequalities. To prove  $\eta(0, t_1) \geq -\gamma_0^2$ , we can first prove the two inequalities are valid.

$$\eta_1(0, t_1) = \int_0^{t_1} x \left( \int_0^{t_1} F_1(v, \tau, t) d\tau + \frac{1}{\hat{T}_r(0)} - \frac{1}{T_r} \right) dt \geq -\gamma_1^2 \quad (14)$$

$$\eta_2(0, t_1) = \int_0^{t_1} x F_2(v, t) dt \geq -\gamma_2^2 \quad (15)$$

For Eq. (14), let  $df(t)/dt = x$ , and then

$$Kf(t) = \int_0^{t_1} F_1(v, \tau, t) d\tau + \frac{1}{\hat{T}_r(0)} - \frac{1}{T_r} \quad (16)$$

Take derivatives of both sides of Eq. (16), and we have

$$F_1(v, \tau, t) = K_i x = K_i e^T(t) \left[ L_m \begin{pmatrix} i_{s\alpha} \\ i_{s\beta} \end{pmatrix} - \begin{pmatrix} \hat{\psi}_{ra} \\ \hat{\psi}_{r\beta} \end{pmatrix} \right] \quad (17)$$

Since  $\int_0^{t_1} \frac{df(t)}{dt} kf(t) dt = \frac{k}{2} [f^2(t_1) - f^2(0)] \geq -\frac{k}{2} f^2(0)$  ( $k > 0$ ), it is easy to find that for  $K_i > 0$ , the inequality  $\eta_1(0, t_1) \geq -\gamma_1^2$  holds.

For Eq. (15), the inequality is invariably true as long as the function to be integrated on the left side is positive. Here, we take

$$F_2(v, t) = K_p x = K_p e^T(t) \left[ L_m \begin{pmatrix} i_{s\alpha} \\ i_{s\beta} \end{pmatrix} - \begin{pmatrix} \hat{\psi}_{r\alpha} \\ \hat{\psi}_{r\beta} \end{pmatrix} \right] \quad (18)$$

Similarly, we can prove the inequality  $\eta_2(0, t_1) \geq -\gamma_2^2$  holds for  $K_p > 0$ .

From the above analysis, it can be seen that Eq. (13) is valid; namely, the Popov integral inequality is satisfied. By substituting Eqs. (17) and (18) into Eq. (8), we can obtain the rotor time constant identification model as shown in Eq. (5). According to  $T_r = L_r/R_r$ , the identified results of rotor resistance can be found.

## 4 Simulation Verification

In order to prove the composite online parameter identification method is effective in optimizing the traction motor vector control performance, and further study the performance optimization of the vector control system when the traction motor is in different working conditions, a simulation model of the traction drive control system is built with reference to the actual parameters of a certain CRH EMUs [11]. The motor vector control part uses the structure shown in Fig. 1, and the specific simulation parameters are rated power  $P_N = 365\text{kw}$ , rated voltage  $U_N = 2000\text{V}$ , rated frequency  $f_N = 140\text{Hz}$ , DC link voltage  $2600\text{V}$ , support capacitor  $C_{d1} = C_{d2} = 4.25\text{ mF}$ , stator resistance  $R_s = 0.15\Omega$ , rotor resistance  $R_r = 0.16\Omega$ , stator inductance  $L_s = 0.00142\text{ H}$ , rotor inductance  $L_r = 0.0006\text{ H}$ , and mutual inductance  $L_m = 0.0254\text{ H}$ .

### (1) Simulation I

In order to verify the proposed online identification model of rotor time constant in terms of accuracy and dynamic response characteristics, the simulation assumes that the motor is in no-load operational state. It starts at  $t = 0\text{ s}$ , and the given speed is  $1500\text{ r/min}$ . After it is steady, the motor torque increases sharply from  $0$  to  $+50\text{ N}\cdot\text{m}$  at  $t = 0.2\text{ s}$ . The simulation time is  $0.4\text{ s}$ , and the corresponding results are shown in Fig. 2.

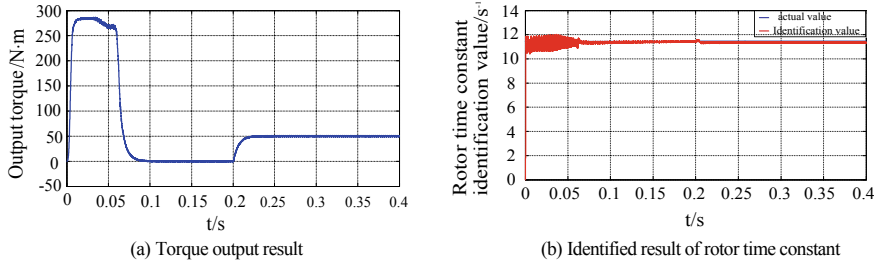


**Fig. 2** Simulation waveforms in the case of motor acceleration and sudden load change

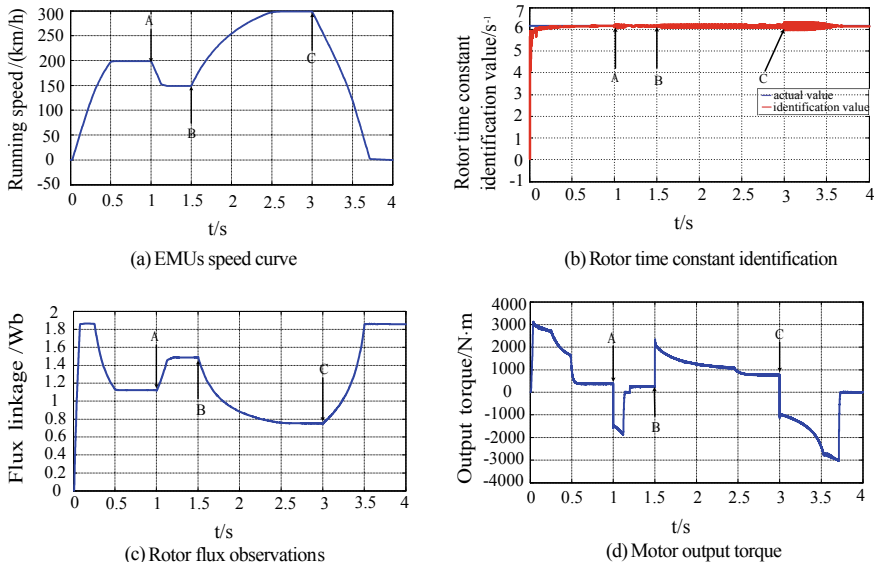


**Fig. 3** Simulation waveforms of EMU's traction motor vector control system under different working conditions

According to the motor parameters, the actual value of the reciprocal of rotor time constant can be obtained;  $1/T_r = R_r/L_r = 11.443$ . It can be seen from Fig. 2 that at  $t = 0 \sim 0.065$  s, the motor is in the acceleration stage and the identified results fluctuate around the actual value, which is largely due to the continuous increase of the motor speed at this time. At  $t > 0.065$  s, the motor runs at a constant speed, and the identified results are basically consistent with the actual values. At  $t = 0.2$  s when a load of  $50 \text{ N} \cdot \text{m}$  is applied suddenly, the corresponding identified results experience short fluctuations at  $t = 0.017$  s and then converge quickly and stabilize at the actual value. Therefore, the above online identification model of parameters has high accuracy, good dynamic response characteristics and effective anti-interference.

## (2) Simulation II

It is assumed that the EMUs run according to the speed curve in Fig. 3a. Specifically, it accelerates from 0 to the given speed of 200 km/h based on the actual average starting acceleration of  $0.38 \text{ m/s}^2$  and maintains a constant speed. At  $t = 1 \text{ s}$ , it starts to brake and the speed is reduced to 150 km/h at  $t = 1.2 \text{ s}$ , and then, it keeps running at a constant speed. At  $t = 1.5 \text{ s}$ , the train starts to accelerate again, but the acceleration decreases gradually. At  $t = 2.5 \text{ s}$ , it accelerates to 300 km/h and keep a constant speed again. At  $t = 3 \text{ s}$ , the EMUs start to brake until it comes to a complete stop. Three time points indicated by A, B, and C in the figure correspond to the three working condition switching points at  $t = 1 \text{ s}$ ,  $1.5 \text{ s}$ ,  $3 \text{ s}$ , respectively. The ratio of the simulation time in the figure to the actual running time is around 1:200, and the switching frequency is set to 2 kHz. Then, the corresponding simulation results of the EMU's traction motor control system under different working conditions can be obtained, as shown in Fig. 3b-d.

It can be seen that during the operation of each working condition, the identified results of rotor time constant and rotor flux of the motor are basically consistent with the actual values, with high accuracy. When switching between different working conditions, as indicated by A, B, and C in the figure, the identified value of rotor time constant will fluctuate due to the sudden increase of the given torque and then gradually becomes stable. The flux observation model can keep good observation effect and dynamic response characteristics, and meanwhile, the vector control system can maintain stable and fast output torque of the traction motor. Therefore, the vector control optimization strategy based on the online identification model of rotor parameters improves the traction motor drive control performance effectively. This strategy also applies to the frequent switching mode of traction motor working conditions.

## 5 Conclusion

In this paper, the traction motor vector control system is taken as the research object, and a vector control optimization strategy based on a composite online parameter identification model is proposed. By combining the RLS with MRAS, an online identification optimization model of motor parameters is proposed, which improves the accuracy of parameter identification in case of fluctuations of speed (torque) and effectively reduces the error caused by the single parameter identification method. It has better anti-interference performance and improves the reliability of system operation. The vector control strategy is optimized through parameter identification method, which realizes effective control of the speed regulation characteristics of the traction motor in different speed intervals and under different working conditions, and enhances the practicability of the control strategy. The effectiveness of the proposed optimization model and strategy has been verified by simulations.

## References

1. Buchholz O, Bocker J (2017) Gopinath-observer for flux estimation of an induction machine drive system. In: IEEE Southern Power Electronics Conference (SPEC), IEEE, Germany, pp 1–7
2. Jing T, Yong HY, Frede B, Jie C, Li JD, Zhi GL (2018) Parameter identification of inverter-fed induction motors: A review. *Energies* 11(9):2194
3. Morey MS, Virulkar VB, Dhomane GA (2016) MRAS based speed identification and online updating of rotor time constant for sensorless field oriented controlled induction motor. In: International Conference on Emerging Trends in Electrical, Electronics and Sustainable Energy Systems (ICETEESES), IEEE, India pp 179–185
4. Hong YL, Qun JW, Fang X (2015) Parameters estimation of IM with the extended Kalman filter and least-squares. In: IEEE 10th Conference on Industrial Electronics and Applications (CIEA), IEEE, New Zealand, pp 1625–1628
5. Ramin N, Mehdi A, Hossein V (2018) Improving performance of sensorless vector control using artificial neural network against parametric uncertainty. In: CPE-POWERENG, IEEE, Qatar, pp 1–6
6. Fahrner W, Vogelsberger MA, Wolbank T (2018) A new technique to identify induction machine rotor parameters during dynamic operation and low speed. In: IEEE 18th international Power Electronics and Motion Control Conference (PEMC), IEEE, Hungary, pp 471–476
7. Bhavnesh K, Trishla G (2018) Investigations on flux estimation methods for stator current based MRAS speed estimator for induction motor drive. In: IEEMA Engineer Infinite Conference (eTechNxT), IEEE, India pp 1–5
8. Aenugu M, Tejavathu R (2015) Rotor-flux based MRAS speed estimator for direct torque and flux control of an induction motor drive. In: IEEE Students Conference on Engineering and Systems (SCES), IEEE, India, pp 1–6
9. Jeong I, Gu BG, Kim J (2015) Inductance estimation of electrically excited synchronous motor via polynomial approximations by least square method. *IEEE Trans Ind Appl* 51 (2):1526–1537
10. Arif I, Mohammed AH (2018) MRAS based sensorless control of induction motor based on rotor flux. In: International Conference on Computational and Characterization Techniques in Engineering & Sciences (CCTES), IEEE, India, pp 152–155
11. Zhu QY, Chen JB, Cheng LK (2015) Simulation research on traction drive control system of high speed EMUs. *Urban Rail Transit Res* 18(2):19–23 (in Chinese)

# T-Type Equivalent Circuit of Double-Sided Long Primary Linear Induction Motor Considering the Backward Traveling Wave



Jiefang Ma, Huijuan Liu and Qian Zhang

**Abstract** In order to calculate the performance of double-sided long primary linear induction motor (DSLPLIM) more accurately and simply, a precise T-type equivalent circuit is derived, where the resistance and magnetization reactance correction coefficients are introduced separately to account for the effect of the backward traveling wave. Then, the electromagnetic thrust characteristic curves of the DSLPLIM are calculated by using the deduced T-type equivalent and finite-element simulation software at different frequencies, respectively, and the results are in good agreement.

**Keywords** Equivalent circuit · DSLPLIM · Backward traveling wave

## 1 Introduction

DSLPLIM has unique advantages in high-speed and high-thrust situations such as electromagnetic launch and space experiments because of its high-thrust density, lightweight of the mover, zero normal resultant force, and large payload [1–3]. At the same time, because of the end effect, its theoretical analysis and characteristic calculation are more complex than that of rotary induction motor. Generally, its operation characteristics are analyzed by electromagnetic field analysis, but the analysis and calculation of electromagnetic field are only applicable to the case where the primary current is known, and it is complex and time-consuming. Equivalent circuit converts complex electromagnetic field calculation into circuit calculation, which reflects the electromagnetic relationship between stator and rotor and the balance of voltage, current, and power. After calculating the equivalent circuit and its parameters, the operation performance of the motor can be further calculated according to the circuit. The unbalanced three-phase impedance of linear

---

J. Ma (✉) · H. Liu · Q. Zhang

School of Electrical Engineering, Beijing Jiaotong University, No.3 Shangyuan Village, Xizhimen, Haidian, Beijing, China  
e-mail: [17121479@bjtu.edu.cn](mailto:17121479@bjtu.edu.cn)

induction motor makes the amplitude of air-gap magnetic field un-evenly distributed along the direction of magnetic field movement. Therefore, the equivalent circuit of linear induction motor cannot be solved by the method of rotary motor. The existing literatures mainly study the equivalent circuit of the short primary linear induction motor [4].

However, few papers present the effect of backward traveling wave attenuated along negative direction. Furthermore, while various studies have reported the traveling waves that attenuate in the longitudinal positive direction in [5, 6]. Actually, it is found that the effect of the backward traveling wave on the air-gap magnetic field of the motor cannot be ignored in the case of non-high speed. In [7], the excitation reactance and primary leakage reactance of the motor are neglected, and the series equivalent circuit of the LIM is obtained from that of the rotary motor. Because many factors are neglected, the accuracy of the motor performance calculated by the equivalent circuit is poor. In [8], the equivalent circuit of DSLPLIM with series type is deduced, but it cannot calculate the current of secondary, which has some limitations in application.

In this paper, a T-type equivalent circuit of DSLPLIM is deduced, taking full account of the backward traveling wave. The correction factors of secondary phase resistance and magnetization reactance can well represent the effect of backward traveling wave. The electromagnetic thrust of the DSLPLIM calculated by the T-type equivalent circuit agrees well with the results of finite-element method.

## 2 T-Type Equivalent Circuit

According to the electromagnetic field theory, the slotted primary core is replaced by a smooth core, and an infinitely thin current layer instead of the primary winding, which is represented by line current density is given by Xialing [9]

$$J_1 = \frac{\sqrt{2}m_1 W_1 k_{w1}}{p\tau} I_1 \quad (1)$$

where  $m_1$  is the number of phases,  $W_1$  is the number of turns in series per pole and phase,  $k_{w1}$  is winding factor,  $p$  is the number of pole pairs,  $\tau$  is the pole pitch, and  $I_1$  is the rms of primary current.

The primary line current density can be expressed as

$$j_1 = J_1 e^{j(\omega t - kx_0)} \quad (2)$$

where  $k = \frac{\pi}{\tau}$ .

Establish the coordinate system with the secondary,  $E_{1z}$  is the intensity of secondary induced electric field, and then, the secondary line current density  $j_2$  can be described by [9]

$$j_2 = \sigma_s E_{1z} \quad (3)$$

where  $\sigma_s$  is the equivalent conductivity of secondary plate.

The complex power transferred to the secondary and air gap is described by

$$S = 2a \int_0^{L_2} \frac{1}{2} [-\vec{j}_1^* \cdot \vec{E}_{1z}] dx = s \cdot (P + jQ) \quad (4)$$

where  $2a$  is the width of primary,  $s$  is the slip, and  $P$  and  $Q$  are the active power and reactive power of the motor.

## 2.1 The Equivalent Circuit Without Considering End Effects

Without considering the end effects, the equivalent circuit of the DSLPLIM is shown as Fig. 1. The complex power generated by the fundamental magnetic field can be expressed as

$$\begin{aligned} S_1 &= s \cdot m_1 I_1^2 \left[ \frac{4\mu_0 f \tau \cdot 2a m_1 (W_1 k_{w1})^2}{\pi \delta p} \right] \frac{j + sG}{1 + s^2 G^2} \\ &= s \cdot m_1 I_1^2 x_{m0} \frac{j + sG}{1 + s^2 G^2} = s \cdot m_1 I_1^2 z_{e0} \\ &= s \cdot (P_3 + Q_3) \end{aligned} \quad (5)$$

where  $z_{e0}$  is the equivalent impedance of secondary plate, and  $S_1$  is the complex power of the fundamental wave obtained with the secondary reference coordinate system. Ignoring the excitation resistance and secondary leakage reactance, convert the parameters to the primary, and then

$$-\vec{E}_1 = I_1 \cdot x_{m0} \frac{j + sG}{1 + s^2 G^2} \quad (6)$$

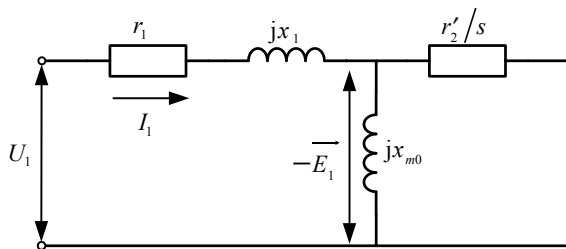


**Fig. 1** T-type equivalent circuits without considering end effects

$$\begin{aligned}
R &= \frac{m_1 | -E_1 |^2}{P_2} = \frac{m_1 \left( I_1 \cdot x_{m0} \frac{\sqrt{1+s^2G^2}}{1+s^2G^2} \right)^2}{m_1 I_1^2 x_{m0} \frac{sG}{1+s^2G^2}} = \frac{x_{m0}}{sG} \\
&= \frac{\frac{4\mu_0 f \tau a m_1 (W_1 k_{w1})^2}{\pi \delta}}{s \cdot \frac{2\mu_0 \sigma_s f \tau^2}{\pi \delta}} = \frac{4am_1 (W_1 k_{w1})^2}{s \cdot p \tau \sigma_s} = \frac{r'_2}{s}
\end{aligned} \tag{7}$$

$$X = \frac{m_1 | -E_1 |^2}{Q_3} = \frac{m_1 \left( I_1 \cdot x_{m0} \frac{\sqrt{1+s^2G^2}}{1+s^2G^2} \right)^2}{m_1 I_1^2 x_{m0} \frac{1}{1+s^2G^2}} = x_{m0} = G \cdot r'_2 \tag{8}$$

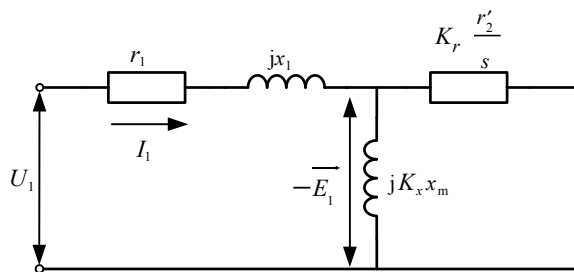
where  $G$  is the quality factor, and  $\delta$  is the air gap.

## 2.2 The Equivalent Circuit Considering Longitudinal End Effect

The longitudinal end effect will affect the distribution of air-gap magnetic density and thus affect the performance of DSLPLIM. The existing equivalent circuit of long primary linear induction motor mostly ignores the influence of the backward component in the air-gap magnetic field, so that this kind of equivalent circuit is only suitable for high-speed linear motor. At medium and low speeds, there is a certain error between the motor performance calculated by the equivalent circuit and the finite-element results. In order to deduce the equivalent circuit of the DSLPLIM with wider application range, the equivalent circuit with the influence of end effects (include backward traveling wave and forward traveling wave) taken into account is shown in Fig. 2

$$\begin{aligned}
-\overrightarrow{E_1} &= \frac{P+jQ}{m_1 \overrightarrow{I_1}} = \frac{m_1 I_1^2 x_{m0} \frac{1}{\sqrt{1+s^2G^2}} \frac{1}{L_2} (C_1 + jC_2)}{m_1 I_1} \\
&= I_1 x_{m0} \frac{1}{\sqrt{1+s^2G^2}} \frac{1}{L_2} [C_1 + jC_2]
\end{aligned} \tag{9}$$

**Fig. 2** T-type equivalent circuits considering longitudinal end effect



$$R_2 = \frac{m_1 \cdot \left| -\overrightarrow{E_1} \right|^2}{P} = \frac{m_1 \cdot \left( I_1 x_{m0} \frac{1}{\sqrt{1+s^2G^2}} \frac{1}{L_2} \sqrt{C_1^2 + C_2^2} \right)^2}{m_1 I_1^2 x_{m0} \frac{1}{\sqrt{1+s^2G^2}} \frac{1}{L_2} C_1} = \frac{r'_2}{s} \cdot K_r \quad (10)$$

$$x_m = \frac{m_1 \cdot \left| -\overrightarrow{E_1} \right|^2}{Q} = \frac{m_1 \cdot \left( I_1 x_{m0} \frac{1}{\sqrt{1+s^2G^2}} \frac{1}{L_2} \sqrt{C_1^2 + C_2^2} \right)^2}{m_1 I_1^2 x_{m0} \frac{1}{\sqrt{1+s^2G^2}} \frac{1}{L_2} C_2} = x_{m0} \cdot K_x \quad (11)$$

where  $L_2$  is secondary length.

The correction factors of longitudinal dynamic end effect with secondary phase resistance and magnetization reactance can be calculated by

$$K_r = \frac{sG}{2p\tau\sqrt{1+s^2G^2}} \frac{C_1^2 + C_2^2}{C_1} \quad (12)$$

$$K_x = \frac{1}{2p\tau\sqrt{1+s^2G^2}} \frac{C_1^2 + C_2^2}{C_2} \quad (13)$$

$$C_1 + jC_2 = e^{j(\arctan \frac{1}{sG})} \left( L_2 - \sqrt{-jsG} \cdot D_F + \sqrt{-jsG} \cdot D_B \right) \quad (14)$$

$$D_B = \frac{e^{-\alpha L_2 + j(k-\alpha)L_2} - 1}{-\alpha + j(k-\alpha)} \quad (15)$$

$$D_F = \frac{1 - e^{-\alpha L_2 - j(k+\alpha)L_2}}{\alpha + j(k+\alpha)} \quad (16)$$

### 3 Simulation and Finite-Element Analysis

Figure 3 is the basic schematic diagram of the double-sided long primary linear induction motor, and its structural parameters are shown in Table 1. The working frequency of the motor is 38.1 Hz, and the rated speed is 11 m/s.

Using this equivalent circuit and the calculation method of its parameters, the electromagnetic thrust and the force caused by the end effect are analyzed. The comparison with the results of finite-element analysis is shown in Figs. 4 and 5.  $F_{em1}$  is the electromagnetic thrust without considering the end effects, and  $F_{em}$  is the thrust with end effect.  $F_{end}$  is the force produced by the end effect.

The forward traveling wave produces an additional thrust, the direction of which is the same as that produced by the fundamental wave. The backward traveling wave produces a braking force, i.e., in opposite direction to the fundamental forces.

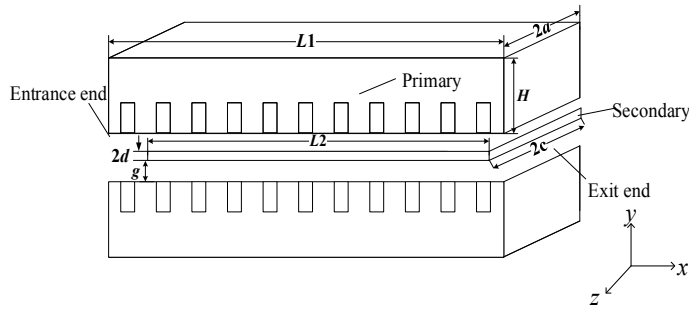
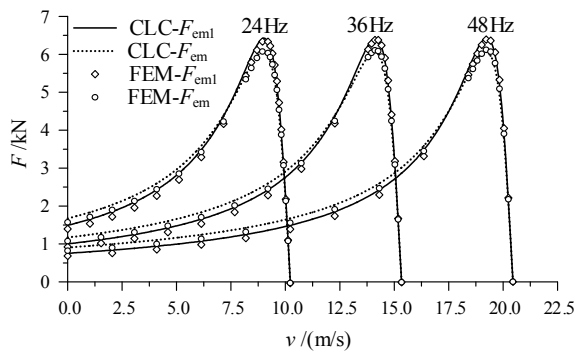


**Fig. 3** A schematic diagram of the longitudinal end effect in DSLIM

**Table 1** Size parameters of motor

Item	Value
Number of poles $2p$	8
Single primary length $L_1/\text{mm}$	1260
Primary width $2a/\text{mm}$	280
Primary height $H/\text{mm}$	100
Secondary length $L_2/\text{mm}$	1260
Secondary width $2c/\text{mm}$	400
Secondary thickness $2d/\text{mm}$	6
Unilateral mechanical air gap $g/\text{mm}$	5

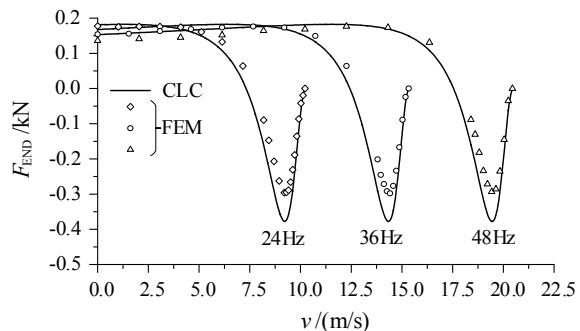
**Fig. 4** Electromagnetic thrust characteristics of motors at different frequencies



## 4 Conclusion

In this paper, the equivalent circuit of DSLPLIM is firstly established, which is based on the relationship of the complex power obtained by one-dimensional electromagnetic field and the equivalent circuit. Secondly, the influence of the longitudinal end effect is considered by adding correction factors to the excitation reactance and secondary resistance. Therefore, the equivalent circuit considering the

**Fig. 5** Force caused by the end effect at different frequencies



longitudinal end effect is obtained. In the derivation above, the effect of the backward traveling wave on the air-gap magnetic field of the motor is fully considered, so that the equivalent circuit can be widely applied to various operating conditions. Finally, the equivalent circuit derived in this paper is used to calculate the performance of the motor, and the results are consistent with those obtained by finite-element simulation. The equivalent circuit can be used to calculate the motor performance more accurately.

## References

1. Zhang Zhihua, Shi Liming, Cai Hua et al (2015) Research on braking characteristics of Long primary double-sided linear induction motor. Proc CSEE 35(11):2854–2861
2. Qin L (2015) Research on control strategy of high speed long primary bilaterally linear induction motor. University of Chinese Academy of Sciences (in Chinese)
3. Boldea I (2013) Linear electric machine, drives, and MAGLEVs handbook. CRC Press, London, UK, pp 55–128
4. Woronowicz K, Safaei A (2014) A novel linear induction motor equivalent-circuit with optimized end-effect model including partially-filled end slots. In: 2014 IEEE Transportation Electrification Conference and Expo (ITEC), 2014, pp 1–5
5. Lu J, Ma W (2011) Research on end effect of linear induction machine for high-speed industrial transportation. IEEE Trans Plasma Sci
6. Sun Z, Ma W, Wu X et al (2019) Electromagnetic parameters calculation for double primaries coupling linear induction motors. Proc CSEE 39(7):1–8 (in Chinese)
7. Li HT (2008) The design of long-primary linear induction motor and research on electromagnetic and thermal field. Harbin University of Science and Technology (in Chinese)
8. Shanghai Technology University (1979) Shanghai Electromotor Factory, linear asynchronous motor. China Machine Press, pp 49–58 (in Chinese)
9. Xialing L (2006) Theory and method of electromagnetic design for linear induction motors. Science Press, Beijing, p 38 (in Chinese)

# Optimal Matching of High-Speed Pantograph Parameters Considering Catenary Suspension Irregular Point and Wind Damping



Yulong Liu, Ying Wang, Li Cao, Xiaoqiang Chen and Zhengqing Hao

**Abstract** Lanzhou–Xinjiang high-speed railway has passed through several wind areas, and it is necessary to study pantograph–catenary coupling under wind environment. In this paper, SS400 + pantograph used in Lanzhou–Xinjiang line is utilized to study the pantograph–catenary parameter matching. Firstly, the sliding vibration law of the pantograph is analyzed considering pantograph–catenary coupling. Secondly, a three-mass pantograph model considering wind damping is established. Then, the Laplace transform is applied to the pantograph model, and the relation between the pantograph–catenary contact force and the pantograph head displacement is established. Finally, under the different pantograph parameters, the optimal amplitude–frequency characteristic matching test is carried out for ensuring the smooth coupling of pantograph–catenary system.

**Keywords** High-speed railway · Pantograph–catenary parameters matching · Wind damping · Amplitude–frequency characteristic

## 1 Introduction

With the rapid development of high-speed railway in China, dynamic coupling characteristics of the pantograph–catenary system have become one of the key factors restricting the high-speed operation of locomotives [1]. In [2], the different catenary models at home and abroad are compared. The pantograph model mainly includes the mass model [3], the rigid body model [4], and the hybrid model [5]. In view of the coupling performance of the pantograph and catenary under wind load, the relationship between wind speed and vibration amplitude of the catenary is deeply studied in [6]. In [7], the wind tunnel test is used to calculate the aerody-

---

Y. Liu · Y. Wang (✉) · L. Cao · X. Chen · Z. Hao

School of Automation & Electrical Engineering, Rail Transit Electrical

Automation Engineering Laboratory of Gansu Province,

Lanzhou Jiaotong University, No.88 West Anning Road, Lanzhou, China

e-mail: [wangying01@mail.lzjtu.cn](mailto:wangying01@mail.lzjtu.cn)

namic coefficient of the contact line under the action of horizontal wind. Pombo et al. [8] adopt Von Karman method of wind spectrum to simulate the horizontal and vertical wind fields and directly calculated the buffeting force of the fluctuation wind on the contact line.

As an extension of the previous work, we will study the matching performance of the pantograph–catenary system from the angle of the pantograph in this paper. Based on the wind environment in which the China Lanzhou–Xinjiang line is located, a mathematical model of the pantograph considering the wind damping is established from the SS400 + pantograph. The parameter amplitude–frequency characteristic matching test between pantograph and catenary droppers is carried out for ensuring smooth coupling of pantograph–catenary system.

## 2 Pantograph Vibration Analysis Considering Coupling

### 2.1 Pantograph–Catenary-Coupled Vibration Mechanism

With the running of the high-speed locomotives, the locomotive-roof pantograph often produces mechanical waves generated by the contact-line fluctuations at the catenary dropper, which affects the coupling contact performance between pantograph and catenary as a whole. The relationship between the vibration amplitude  $|F_p|$  of the pantograph and the mechanical wave amplitude after contact with the contact line can be written as [9]:

$$|F_p| = \omega(1 + \beta)|A| \left| \frac{Z_t Z_p}{Z_t + Z_p} \right| \quad (1)$$

In Formula (1),  $\omega$  is the mechanical wave frequency,  $\beta$  is the mechanical wave refractive index,  $Z_p$  is the mechanical impedance of the pantograph,  $Z_t$  is mechanical impedance of the contact net, and  $Z_t = 2\sqrt{\rho T}$ ,  $\rho$  is the Lanzhou–Xinjiang contact line contact line density ( $\rho = 1.350 \text{ kg/m}$ ),  $T$  is the Lanzhou–Xinjiang contact line tension ( $T = 20000 \text{ N}$ ).

In addition, the amplitude of the mechanical wave after the contact line fluctuates  $|A|$  can be written as [9]:

$$|A| = \left| \frac{1}{1 + (Z_t/Z_p)} \right| \frac{\omega_0 B}{1 - \beta} \quad (2)$$

In Formula (2),  $\omega_0$  is the mechanical wave refraction frequency, and  $\omega(1 - \beta)/B = \omega_0 = 2\pi v/\lambda$ ,  $B$  is half of the amplitude of the mechanical wave,  $\lambda$  is the mechanical wave wavelength, and  $v$  is the sliding speed of the pantograph, that is, the driving speed of the high-speed locomotive.

It can be seen from Formulas (1) and (2) that the fluctuating magnitude  $|F_p|$  is mainly related to the mechanical impedance  $Z_p$  of the pantograph and the mechanical impedance  $Z_t$  of the catenary. The catenary is a complex nonlinear network with mechanical impedances related to tension, contact line density, stiffness, span and dropper, Young's modulus, Poisson's ratio, and structural height. Therefore, this paper focuses on the wind environment in which the China Lanzhou–Xinjiang railway line is located and studies the influence of the mechanical parameters of the pantograph on the vibration amplitude of the catenary, which is the influence of wind damping, that is, the matching relationship between the research  $Z_p$  and  $|F_p|$ .

## 2.2 Mathematical Modeling and Vibration Analysis of Pantograph

The pantograph can be established by a three-mass model that effectively characterizes the vertical motion of the pantograph, as shown in Fig. 1.

In Fig. 1,  $k_1$ ,  $k_2$ , and  $k_3$  represent the stiffness coefficients of the three-mass pantograph model, respectively;  $m_1$ ,  $m_2$ ,  $m_3$ , respectively, represent the pantograph mass, the upper frame mass, and the lower frame mass of the pantograph model;  $c_{11}$ ,  $c_{21}$ , and  $c_{31}$ , respectively, represent the self-damping coefficients of the three-mass model;  $c_{12}$ ,  $c_{22}$ , and  $c_{32}$ , respectively, represent wind damping coefficients considering a three-mass model under wind load;  $F_0$  represents the static lifting force of the pantograph (generally set to 120 N in China);  $F$  represents the dynamic contact force of the pantograph (hereinafter referred to as the pantograph–catenary contact force).

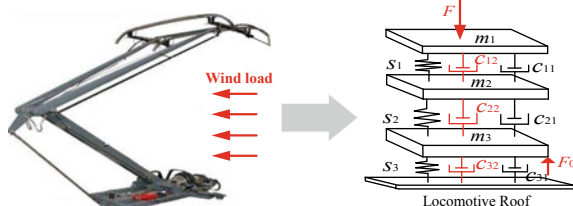
The differential equation of the three-mass pantograph motion under the influence of wind load can be expressed as:

$$m_1\ddot{y}_1 + (c_{11} + c_{12}) \times (\dot{y}_1 - \dot{y}_2) + k_1(y_1 - y_2) = -F \quad (3)$$

$$m_2\ddot{y}_2 + (c_{11} + c_{12}) \cdot (\dot{y}_2 - \dot{y}_1) + k_1(y_2 - y_1) + (c_{21} + c_{22}) \cdot (\dot{y}_2 - \dot{y}_3) + k_2(y_2 - y_3) = 0 \quad (4)$$

$$m_3\ddot{y}_3 + (c_{21} + c_{22}) \cdot (\dot{y}_3 - \dot{y}_2) + k_2(y_3 - y_2) + (c_{31} + c_{32}) \cdot \dot{y}_3 + k_3(y_3 - y_2) = F_0 \quad (5)$$

**Fig. 1** Three-mass pantograph model under wind load



In Formulas (3)–(5),  $y_1$ ,  $y_2$ , and  $y_3$ , respectively, represent the vertical displacements of the pantograph three-mass model.  $\ddot{y}$  is the corresponding acceleration.  $\dot{y}$  is the corresponding speed. It should be pointed out in Formulas (3)–(5) that, unlike the existing three-mass pantograph differential equation of the literature [6], the wind load received during the actual high-speed locomotive operation is considered here. That is the wind damping coefficients  $c_{12}$ ,  $c_{22}$ , and  $c_{32}$  of the three-mass model are added to the three masses of the pantograph.

The Laplace transform is performed on Formulas (3)–(5). The static contact force  $F_0$  is a constant and does not affect the characteristics of the pantograph, so its value can be ignored. Then the transformed formulas are:

$$[m_1 s^2 + (c_{11} + c_{12})s + k_1] Y_1(s) - [(c_{11} + c_{12})s + k_1] Y_2(s) = F(s) \quad (6)$$

$$\begin{aligned} & [m_2 s^2 + (c_{11} + c_{12})s + (c_{21} + c_{22})s + k_1 + k_2] Y_2(s) - [(c_{11} + c_{12})s + k_1] Y_1(s) \\ & - [(c_{21} + c_{22})s + k_2] Y_3(s) = 0 \end{aligned} \quad (7)$$

$$[m_3 s^2 + (c_{21} + c_{22})s + (c_{31} + c_{32})s + k_2 + k_3] Y_3(s) - [(c_{21} + c_{22})s + k_2] Y_2(s) = 0 \quad (8)$$

In Formulas (6)–(8),  $Y_1(s)$ ,  $Y_2(s)$ , and  $Y_3(s)$ , respectively, represent the Laplace transform of the vertical displacement of the three-mass pantograph model.

This paper considers the actual operation of the CRH2 electrical multiple units of Lanzhou–Xinjiang railway line. The type of locomotive-roof pantograph is SS400+. The corresponding specific parameters are shown in Table 1.

In Formulas (6)–(8), the wind damping coefficient of the pantograph three-mass mathematical model under wind damping is [10]  $c_{12} = 0.19$ ,  $c_{22} = 0.8$ , and  $c_{32} = 1.2$ .

The transfer function  $H(s)$  considering the relationship between the pantograph head contact force  $F(s)$  and the pantograph head displacement  $Y_1(s)$  coupled with the catenary can be written as:

$$H(s) = \frac{F(s)}{Y_1(s)} = \frac{A(s) + B(s) + C(s) + D(s) + E(s) + F(s) + G(s)}{H(s) + I(s) + J(s) + K(s) + L(s)} \quad (9)$$

**Table 1** Three-mass model physical parameters of the SS400 + pantograph

Parameter	Equivalent mass (kg)	Parameter	Equivalent stiffness ( $\text{N}\cdot\text{m}^{-1}$ )	Parameter	Equivalent damping ( $\text{Ns}\cdot\text{m}^{-1}$ )
$m_1$	6.1	$k_1$	10400	$c_{11}$	10
$m_2$	10.154	$k_2$	10600	$c_{21}$	0
$m_3$	10.3	$k_3$	0	$c_{31}$	120

In Formulas (9),

$$A(s) = k_1 k_2 k_3;$$

$$B(s) = (c_{11}k_2k_3 + c_{12}k_2k_3 - c_{21}k_1k_2 - c_{22}k_1k_2 + c_{31}k_1k_2 + c_{32}k_1k_2)s;$$

$$\begin{aligned} C(s) = & (-c_{11}c_{21}k_2 - c_{11}c_{22}k_2 + c_{11}c_{32}k_2 + c_{11}c_{31}k_2 + c_{12}c_{31}k_2 \\ & + c_{12}c_{32}k_2 - c_{12}c_{22}k_2 - c_{12}c_{21}k_2 - c_{21}^2k_12c_{21}c_{22}k_1 \\ & - c_{22}^2k_1 + k_1k_2m_1 + k_1k_2m_2 + k_1k_3m_1 + k_1k_2m_3 \\ & + k_1k_3m_2 + k_2k_3m_1)s^2; \end{aligned}$$

$$\begin{aligned} D(s) = & (-c_{11}c_{21}k_2 - c_{11}c_{22}k_2 + c_{11}c_{32}k_2 + c_{11}c_{31}k_2 + c_{12}c_{31}k_2 + c_{12}c_{32}k_2 \\ & - c_{12}c_{22}k_2 - c_{12}c_{21}k_2 - c_{12}c_{21}^2 - c_{12}c_{22}^2 + c_{12}k_2m_2 - 2c_{12}c_{21}c_{22} \\ & + c_{12}k_3m_1 + c_{12}k_2m_3 + c_{12}k_3m_2 + c_{21}k_1m_1 + c_{21}k_1m_2 - c_{21}k_2m_1 \\ & + c_{22}k_1m_1 + c_{22}k_1m_2 - c_{22}k_2m_1 + c_{32}k_1m_1 + c_{31}k_1m_2 + c_{31}k_2m_1 \\ & + c_{32}k_1m_1 + c_{32}k_1m_2 + c_{32}k_2m_1)s^3; \end{aligned}$$

$$\begin{aligned} E(s) = & (c_{11}c_{21}m_1 + c_{11}c_{21}m_2 + c_{11}c_{22}m_1 + c_{12}c_{21}m_1 + c_{11}c_{22}m_2 + c_{12}c_{21}m_2 \\ & + c_{12}c_{22}m_1 + c_{12}c_{22}m_2 + c_{11}c_{31}m_1 + c_{11}c_{31}m_2 + c_{11}c_{32}m_1 + c_{12}c_{31}m_1 \\ & - 2c_{21}c_{22}m_1 + c_{11}c_{32}m_2 + c_{12}c_{31}m_2 + c_{12}c_{32}m_1 + k_1m_1m_3 + k_2k_1m_2 \\ & + k_1k_2m_3 + k_2k_1m_3 + k_3k_1m_2 - c_{21}^2m_1 + c_{12}c_{32}m_2c_{22}^2m_1)s^4; \end{aligned}$$

$$\begin{aligned} F(s) = & (c_{11}m_1m_3 + c_{11}m_2m_3 + c_{12}m_1m_2 + c_{12}m_2m_3 + c_{21}m_1m_2 + c_{22}m_1m_2 \\ & + c_{31}m_1m_2 + c_{32}m_1m_2)s^5; \end{aligned}$$

$$G(s) = m_1m_2m_3; L(s) = m_2m_3s^4; H(s) = k_1k_2 + k_1k_3 + k_2k_3;$$

$$\begin{aligned} I(s) = & (c_{11}k_2 + c_{11}k_3 + c_{12}k_2 + c_{12}k_3 + c_{21}k_1 - c_{21}k_2 + c_{22}k_1 \\ & - c_{22}k_2 + c_{31}k_1 + c_{31}k_2 + c_{32}k_2)s; \end{aligned}$$

$$\begin{aligned} J(s) = & (-c_{21}^2 - c_{22}^2 + c_{11}c_{21} + c_{12}c_{12} + c_{21}c_{22} + c_{11}c_{31} + c_{11}c_{32} \\ & + c_{12}c_{31}2c_{21}c_{22} + c_{12}c_{32} + k_1m_3 + k_2m_2 + k_2m_3 + k_3m_2)s^2; \end{aligned}$$

$$K(s) = (c_{11}m_3 + c_{12}m_3 + c_{21}m_2 + c_{22}m_2 + c_{31}m_2 + c_{32}m_2)s^3.$$

Set  $s = j \cdot 2\pi f$ , then

$$|H(j \cdot 2\pi f)| = \left| \frac{M(j \cdot 2\pi f)}{N(j \cdot 2\pi f)} \right| \quad (10)$$

In Formula (10),  $|H(j \cdot 2\pi f)|$  indicates the amplitude of the vibration of the pantograph up and down when the pantograph–catenary is coupled at this frequency points.

Figure 2 shows that the amplitude–frequency response of pantograph, that is, the mechanical impedance increases with the increase of frequency; but there are two

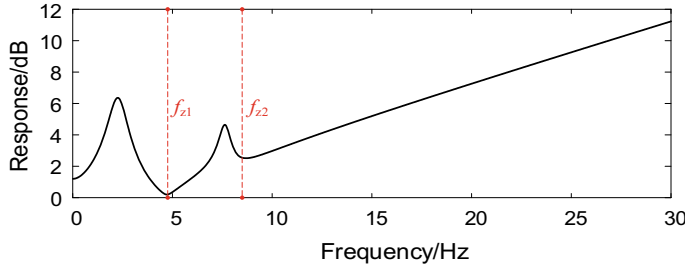


**Fig. 2** Pantograph amplitude frequency curve

minimum values  $f_{z1}$  and  $f_{z2}$ . If the corresponding pantograph parameters can be adjusted, the mechanical impedance of pantograph can be minimized, and the vibration amplitude of the contact force can be effectively reduced.

### 3 Pantograph Parameters Matching

When the pantograph head passes through the catenary droppers, the pantograph uplifts change slightly. After passing the droppers, the pantograph uplifts increase gradually. In the middle of the span, the period of pantograph uplifts is about the vibration period of droppers. Therefore, as long as the pantograph vibration period is close to the dropper vibration period, the pantograph–catenary coupling can be optimized. So, we can optimize the parameters of pantograph and make its frequency  $f_{z1}$  and  $f_{z2}$  close to the dropper frequency  $f_d$ .

The ratio between adjacent dropper distance  $d$  and locomotive speed  $v$  is the time when the pantograph passes through the droppers. The vibration frequency of catenary droppers is defined as  $v/d$ . Changing the pantograph parameters makes the pantograph amplitude–frequency characteristic curve move; thus,  $f_{z1}$  and  $f_{z2}$  approach the dropper frequency  $f_d$ .

In this paper, SS400+ pantograph and CTMH150 catenary of Lanzhou–Xinjiang high-speed railway are studied. The speed of Lanzhou–Xinjiang high-speed railway is  $v = 200$  km/h, and the distance of adjacent catenary droppers is  $d = 5$  m. The calculated dropper frequency is  $f_d = 13.88$  Hz. Through the above analysis, we know that changing the pantograph parameters can change the two turning frequencies  $f_{z1}$  and  $f_{z2}$  of the amplitude–frequency characteristic curve. Next, the variation trends of turning frequency can be obtained through change different pantograph parameters. Figures 3 and 4 show the specific comparison results.

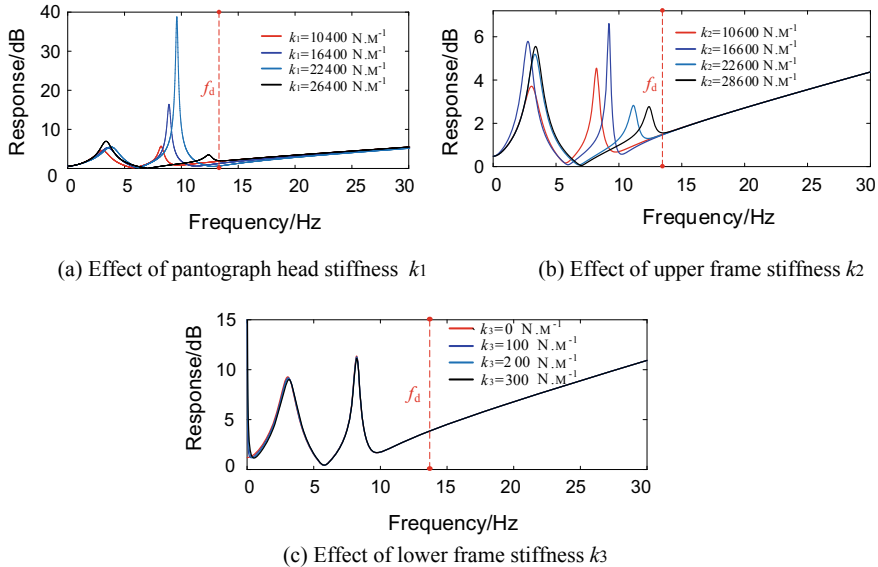


**Fig. 3** Effect of pantograph stiffness on amplitude–frequency characteristics

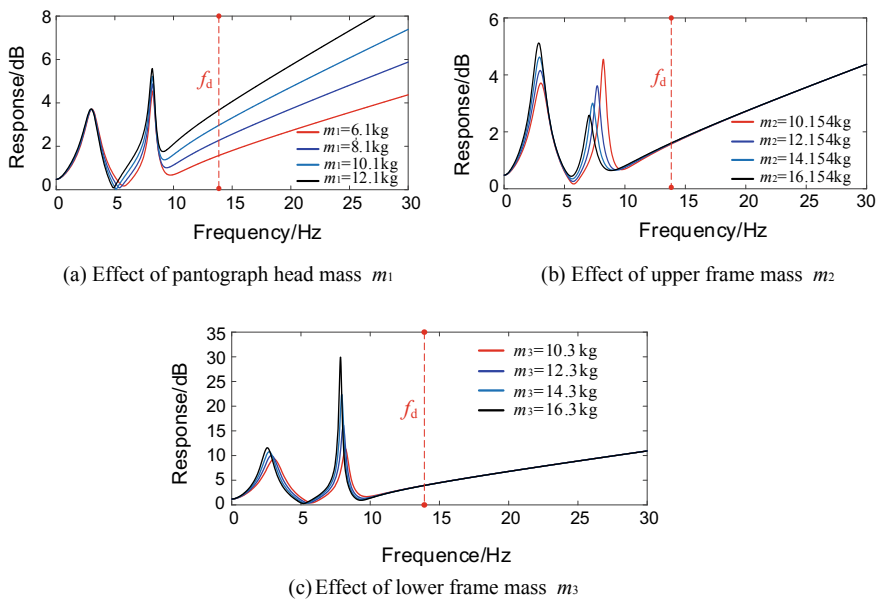


**Fig. 4** Effect of pantograph mass on amplitude–frequency characteristics

By analyzing Figs. 3 and 4, the following conclusions can be drawn:

- (1) With the change of  $k_1$ , the second turning frequency  $f_{z2}$  changes obviously.
- (2) With the change of  $k_2$ , the change of turning frequency  $f_{z2}$  is not obvious than the change of  $k_1$ .
- (3) With the change of  $k_3$ , the curve is basically unchanged.
- (4) When  $m_1$  is changed, the change of turning frequency  $f_{z2}$  is obvious.
- (5) When  $m_2$  is changed, the change of the output curve is not obvious.
- (6) Changing  $m_3$  has a great influence on the first turning frequency  $f_{z1}$  and a little influence on the second turning frequency  $f_{z2}$ .

Through the above analysis, it can be found that  $k_1$  and  $m_1$  have a significant effect on the second turning frequency  $f_{z2}$  and can significantly reduce the amplitude at the dropper frequency  $f_d$ . Compared with  $f_{z1}$  and  $f_{z2}$ ,  $f_{z2}$  is easier to approach dropper frequency  $f_d$  by changing pantograph parameters. Therefore, the following tests mainly consider the relationship between  $f_{z2}$  and  $f_d$ .

## 4 Tests and Discussions

From the above analysis results, it can be seen that the pantograph head stiffness  $k_1$  and the pantograph head mass  $m_1$  have the greatest influence on the second turning frequency  $f_{z2}$ . Therefore, we can analyze the changes of contact force caused by these two variables separately and select the optimal parameters.

As shown in Fig. 5a, changing the value of  $k_1$ , it can be found that with the increase of  $k_1$ , the turning frequency  $f_{z2}$  first approaches the dropper frequency  $f_d$  gradually and finally exceeds the turning frequency  $f_{z2}$ . Therefore, there must be a turning frequency  $f_{z2}$  close to the dropper frequency  $f_d$ . The closer the turning frequency  $f_{z2}$  is to the dropper frequency  $f_d$ , the smaller the amplitude is. Also, in Fig. 5b, changing the value of  $m_1$ , it can be also found that with the increase of  $m_1$ , the turning frequency  $f_{z2}$  first approaches the dropper frequency  $f_d$  gradually.

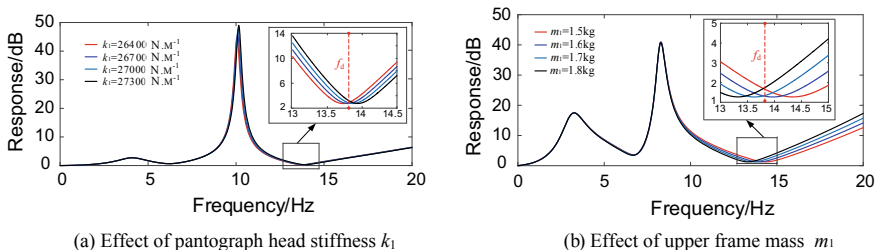


**Fig. 5** Variations of the amplitude–frequency characteristic curve

**Table 2** Turning frequency  $f_{z2}$  under the different stiffness  $k_1$ 

Different stiffness $k_1$ ( $\text{N} \cdot \text{m}^{-1}$ )	Turning frequency $f_{z2}$ (Hz)	Absolute value of frequency difference from $f_d$ (Hz)
26700	13.7959	0.0841
27000	13.8665	0.0135
27300	13.9370	0.0570

**Table 3** Turning frequency  $f_{z2}$  under the different mass  $m_1$ 

Different mass $m_1$ (kg)	Turning frequency $f_{z2}$ (Hz)	Absolute value of frequency difference from $f_d$ (Hz)
1.5	14.3400	0.4600
1.6	13.9668	0.0868
1.7	13.6302	0.2498
1.8	13.3254	0.5546

By changing the pantograph head stiffness  $k_1$ , the absolute value between turning frequency  $f_{z2}$  and dropper frequency  $f_d$  is as shown in Table 2. It can be found that when  $k_1$  is  $26700 \text{ N m}^{-1}$ ,  $f_{z2}$  is closest to  $f_d$ . Also, by changing the different pantograph head mass  $m_1$ , the absolute value between turning frequency  $f_{z2}$  and dropper frequency  $f_d$  is as shown in Table 3. It can be found that when  $m_1$  is 1.6 kg,  $f_{z2}$  is closest to  $f_d$ .

## 5 Conclusions

1. The pantograph–catenary sliding coupling vibration of Lanzhou–Xinjiang high-speed railway is analyzed, and the influence factors of pantograph mechanical parameters on the vibration amplitude of catenary considering the influence of air damping are revealed.
2. The pantograph amplitude–frequency characteristic parameter matching tests are carried out at the catenary droppers of Lanzhou–Xinjiang railway line, and the pantograph–catenary coupling performance under wind load is optimized.

**Acknowledgements** This work was supported by the Science Research and Development Plan of China Railway Corporation (2017J012-A), the National Natural Science Foundation of China (51767013, 51867012), the Natural Science Foundation of Gansu Province Science and Technology Department (18JR3RA111).

## References

1. Ying W, Zhigang L, Xiuqing M et al (2016) An extended Haberdank's equation-based EMTP model of pantograph arcing considering pantograph-catenary interactions and train speeds [J]. IEEE Trans Power Deliv 31(3):1186–1194
2. Bruni S, Ambrosio J, Carnicer A et al (2015) The results of the pantograph catenary interaction benchmark. Veh Syst Dyn 53(3):412–435
3. Lee H, Park W, Oh K et al (2015) Analysis of dynamic interaction between catenary and pantograph with experimental verification and performance evaluation in new high-speed line. Veh Sys Dyn 53(8):1117–1134
4. Jing J, Liu Zhigang, Yang S (2015) Simulation study on dynamic behavior of pantograph-catenary considering the nonlinear characteristics of pantograph. Comput Simul 32(2):170–174 (in Chinese)
5. Abdullah A, Michitsuji Y, Nagai M et al (2010) Integrated simulation between flexible body of catenary and active control pantograph for contact force variation control. J Mech Syst Transp Logistics 3(1):166–177
6. Yanlong S, Ying W, Xiaoqiang C (2018) Wavelength component Analysis of the pantograph-catenary contact force based on EEMD-SPWVD. In: International conference on computational modeling simulation and mathematical statistics, Xian, China, 20–22 October 2018
7. Yucheng L, Zhigang L, Yang S et al (2014) Simulation calculation and wind tunnel test of static aerodynamic parameters of high-speed railway contact line. J China Railway Soc 36 (5):33–38 (in Chinese)
8. Pombo J, Ambrosio J (2013) Environmental and track perturbations on multiple pantograph interaction with catenaries in high-speed trains. Comput Struct 124(1):88–101
9. Aboshi M, Manabe K (2000) Analyses of contact force fluctuation between catenary and pantograph. Q Rep RTRI 41(4):182–187
10. Honglei S (2010) Influence of aerodynamic forces on current-collection of high-speed pantograph, Beijing Jiaotong University, Beijing, vol 36(5), pp 33–38

# Dynamic Power Threshold Control Strategy of Wayside Hybrid Energy Storage System Based on Battery SOC Tracking



Mingcheng Ai, Zhongping Yang, Fei Lin and Qiangqiang Qin

**Abstract** In order to extend battery service life and increase the total revenue of the hybrid energy storage system (HESS), this paper puts forward a dynamic power threshold control strategy (DPTCS). The battery charge and discharge power threshold are adjusted in real time according to the battery state of charge (SOC), and the battery SOC is controlled within a certain range. Firstly, the model of urban rail traction power supply system with HESS is established. Then, the paper uses the intelligent algorithm and urban rail train power supply system simulation platform to optimize the control parameters of DPTCS. Finally, the simulation results show the effectiveness of the proposed control strategy.

**Keywords** Hybrid energy storage system · Battery state of charge · Intelligent algorithm · Battery life · Total energy-saving benefit

## 1 Introduction

With the increase in mileage of urban rail transit operations, the importance of energy-saving and emission reduction work for rail transit has become increasingly prominent. The cost of electricity accounts for about 50% of the total operating cost of the subway, and the energy generated during vehicle braking accounts for about 33% of the vehicle's power consumption [1].

The energy storage system recycles the braking energy of the vehicle, stabilizes the network voltage, and reduces regeneration failure rate, which can effectively reduce the operating cost, achieve energy-saving and emission reduction. So far, batteries, supercapacitors (SC), flywheels, etc., are used as the energy storage components [2–6]. Because a single type of energy storage component cannot meet the demand of urban rail transit well, the hybrid energy storage system of battery and supercapacitor is proposed.

---

M. Ai (✉) · Z. Yang · F. Lin · Q. Qin

School of Electrical Engineering, Beijing Jiaotong University, Beijing, China

e-mail: [17121409@bjtu.edu.cn](mailto:17121409@bjtu.edu.cn)

At present, there is little research on the control strategy of HESS in DC power supply system. A fixed power threshold control strategy (FPTCS) is proposed in [7], which sets a power threshold for the lithium battery. The power requirement within the threshold is provided by the lithium battery, and the rest power is provided by the supercapacitor. This method is highly efficient and has strong engineering applicability. In [8], a filtering strategy decouples the power demand and assigns separately to the supercapacitor and battery. This strategy fails to maintain the battery SOC within the required range, and the engineering applicability is low. Zhang [9] proposed a control strategy for one station corresponding to a ratio of supercapacitors and lithium batteries. Essentially, it is still a fixed threshold strategy.

The organization of this work is as follows: In Sect. 2, the simulation model of traction power supply system with HESS is built; In Sect. 3, the control strategy of dynamic power threshold is introduced; In Sect. 4, the battery life model and optimization objective function are built. In Sect. 5, the control parameters are optimized by genetic algorithm and the validity and rationality of DPTCS are verified through the simulation of an actual line; In Sect. 6, the summary is given.

## 2 Urban Rail Transit Power Supply System Simulation Model

The simulation model includes the train operation module TPS, the DC network power flow simulation module DC-RLS, and HESS module. The TPS is based on the input line parameters, the output vehicle parameter of the position of trains and the electric power. TPS also contains the train braking resistor. The HESS module can set the energy management strategy and capacity configuration scheme. The DC network parameters can be set in DC-RLS. This module is mainly used to simulate the operating conditions of multiple trains on the line. The voltage and current of the substation and the charge and discharge power of HESS are obtained by the power flow analysis (Fig. 1).

HESS includes energy storage component and bidirectional DC/DC converter. The supercapacitor and the lithium battery are, respectively, connected to the DC network through the bidirectional DC/DC converter. The control of the bidirectional DC/DC converter adopts the traditional double-loop control, the outer voltage loop stabilizes the DC network voltage, and the inner current loop adjusts the charge and discharge current of the energy storage component. The specific structure is shown in Fig. 2.  $P_{\text{HESSref}}$  is the total charge and discharge power command of HESS.  $U_{\text{net}}$  is the DC network voltage,  $U_{\text{char}}$  is the charging threshold,  $U_{\text{dis}}$  is the discharging threshold, and  $I_{\text{batref}}$  and  $I_{\text{SCref}}$  are, respectively, the current command of the lithium battery and the supercapacitor. PWM is the IGBT control pulse.

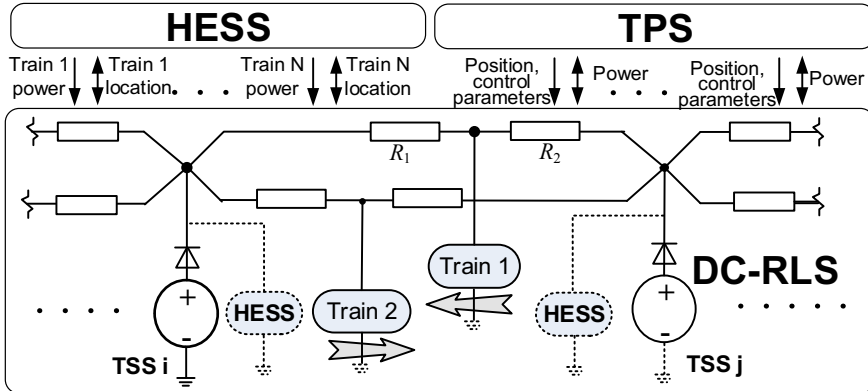


**Fig. 1** Urban rail train power supply system simulation platform

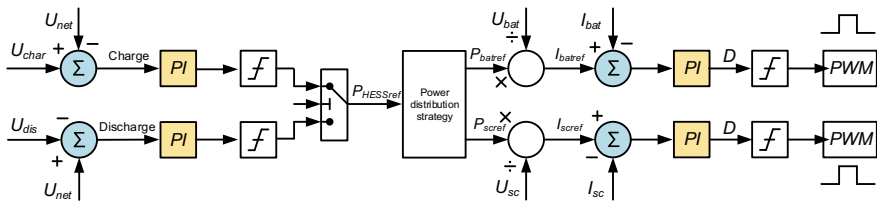


**Fig. 2** Traditional double-loop energy management strategy

### 3 Dynamic Power Threshold Control Strategy (DPTCS)

#### 3.1 Control Logic

Because power threshold under FPTCS is constant, it cannot be adapted to the optimum conditions and battery SOC is uncontrollable. To control the battery SOC, the battery can be charged with small current when SOC is large and discharged with small current when SOC is small under DPTCS. When HESS is charging, and the battery SOC is less than  $SOC_{low}$ , the battery charge power threshold  $P_{chth}$  takes the minimum value  $-P_{bmax}$ ; when it is larger than  $SOC_{low}$ ,  $P_{chth}$  gradually increases until the battery SOC reaches  $SOC_{ceil}$ , and  $P_{chth}$  is 0. When HESS is discharging, and the battery SOC is larger than the  $SOC_{up}$ , the battery discharge power threshold  $P_{disth}$  takes the maximum value  $P_{bmax}$ ; when it is smaller than the  $SOC_{up}$ ,  $P_{disth}$  gradually decreases until the battery SOC reaches  $SOC_{floor}$ , and  $P_{disth}$  is 0. The battery charge and discharge power threshold curve are shown in Fig. 3.

According to the battery power threshold variation, the battery SOC is divided into five areas in Fig. 4: overdischarge prohibited area 1, overdischarge adjustment area 2, reasonable area 3, overcharge adjustment area 4, and overcharge prohibited area 5. The battery charging energy is  $S_1$  under DPTCS during a single traction

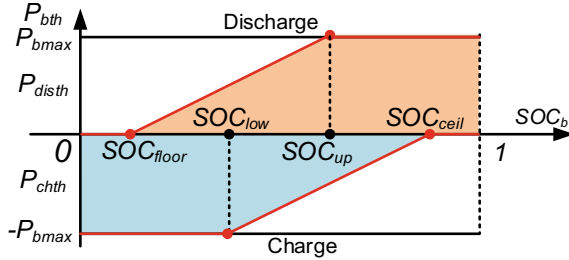


**Fig. 3** Battery charge and discharge power threshold curve

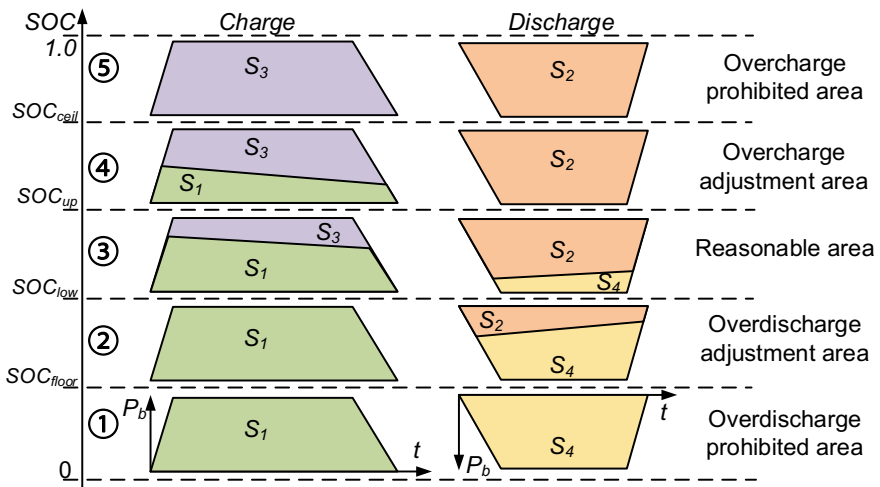


**Fig. 4** Battery SOC division charging and discharging energy of battery in each area

braking process, and the discharging energy is  $S_2$ .  $S_3$  is the difference of battery charging energy between FPTCS and DPTCS. And  $S_4$  is the discharging one. It can be seen from Fig. 4 that as the battery SOC increases,  $S_1$  gradually decreases, and  $S_2$  gradually increases. Compared to the FPTCS, the increase of the battery SOC is well suppressed with larger battery SOC. Conversely, with smaller battery SOC, the battery SOC reduction is suppressed compared to the FPTCS.

### 3.2 Dynamic Power Threshold Calculation

As shown in Fig. 5, the battery charging threshold  $P_{chth}$  is set to 0 in area 5 and  $-P_{bmax}$  in area 1 and 2. In areas 3 and 4, the charging threshold is adjusted by a SOC loop, whose SOC reference value is  $SOC_{ceil}$ ; the battery discharging threshold

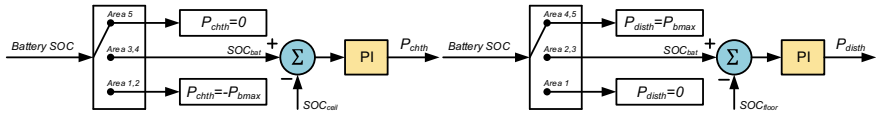


Fig. 5 Battery power threshold calculation

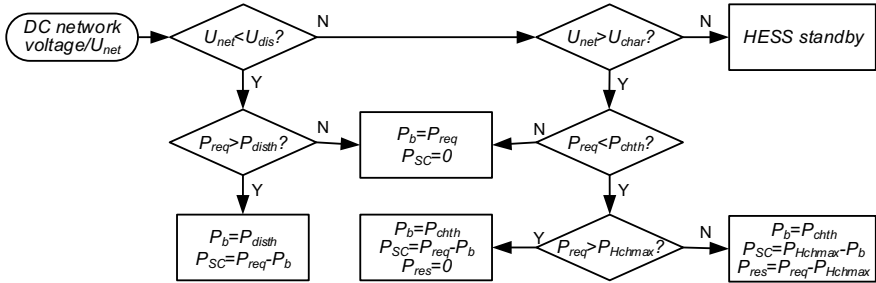


Fig. 6 Dynamic power threshold control strategy block diagram

$P_{disth}$  is set to 0 in area 1 and  $P_{bmax}$  in areas 4 and 5. In areas 2 and 3, the discharging threshold is adjusted by another SOC loop, whose SOC reference value is  $SOC_{floor}$ .

DPTCS block diagram is shown in Fig. 6, where  $P_{Hchmax} = P_{chth} - P_{SCava}$ ,  $P_{Hchmax}$  is the maximum charge power of HESS, and  $P_{SCava}$  is the available power of SC.

## 4 Control Parameter Optimization

### 4.1 Battery Life Prediction Model

Since the battery life is closely related to its charge and discharge current, DOD, and other factors, the battery life model considering the DOD is established to estimate the battery life loss during the actual working process.

The relationship between the maximum charge and discharge times of the battery and the DOD is shown in Eq. 1, where  $D_r$  is the rated DOD and the corresponding number of cycles is  $N_r$ ;  $D_a$  is the DOD of the actual discharge process, and the corresponding cycle number is  $N_a$ ;  $\alpha$  and  $\beta$  are the fitting coefficients.

$$N_a = N_r \left( \frac{D_r}{D_a} \right)^\alpha e^{\beta(1 - \frac{D_a}{D_r})} \quad (1)$$

Since the battery charge and discharge mode are irregular during the actual operation, the DOD changes in real time. Therefore, the rain flow counting method is used to calculate the battery DOD. Assume that the DOD corresponding to each cycle of the battery is  $D_1, D_2 \dots D_k$ , and the corresponding cycle number is  $N_1, N_2 \dots N_k$ , and the battery life calculation formula is shown in Eqs. 2–3, where  $L_b$  is the battery life,  $\text{floor}$  is a round-down function,  $L_{\text{day}}$  is the battery life loss per day,  $\theta$  is the number of cycles, the full cycle takes 1, and the half cycle takes 0.5.

$$L_{\text{day}} = \theta \sum_{i=1}^k 1/N_i \quad (2)$$

$$L_b = \text{floor}(1/L_{\text{day}}) \quad (3)$$

## 4.2 Optimization Objective Function $\text{ObjV}$

In order to quantitatively compare the energy-saving gain difference between DPTCS and FPTCS, we take the total energy-saving return  $E$  as the objective function. According to the change of train departure interval, it is divided into peak, flat peak, and low peak period. The corresponding Beijing electricity price is peak price  $C_p$ , flat peak price  $C_g$ , and low peak price  $C_d$ . Taking the sum of the product of energy saved during each period and the corresponding electricity price, the total energy-saving income of HESS in a day can be obtained, and then, we get the total energy-saving income  $E$  during the service life of HESS.

$$E = e_g * C_p + e_p * C_g + e_d * C_d \quad (4)$$

$$\text{ObjV} = E_{\text{dyn}} - E_{\text{fix}} \quad (5)$$

The total energy-saving benefit under DPTCS is  $E_{\text{dyn}}$ , and benefit under FPTCS is  $E_{\text{fix}}$ , so the objective function is as shown in Eq. 5.

## 5 Case Analysis and Simulation Verification

### 5.1 Genetic Algorithm (GA)

In order to obtain the energy management strategy control parameters under the maximum total energy-saving benefit, this paper uses genetic algorithm to optimize the control parameters and PI parameters of the control strategy.

The optimization variables are as shown in Eq. 6, wherein the first four parameters are the battery charge and discharge SOC loop PI parameters, and the last four parameters are  $SOC_{\text{floor}}$ ,  $SOC_{\text{low}}$ ,  $SOC_{\text{up}}$ , and  $SOC_{\text{ceil}}$ .

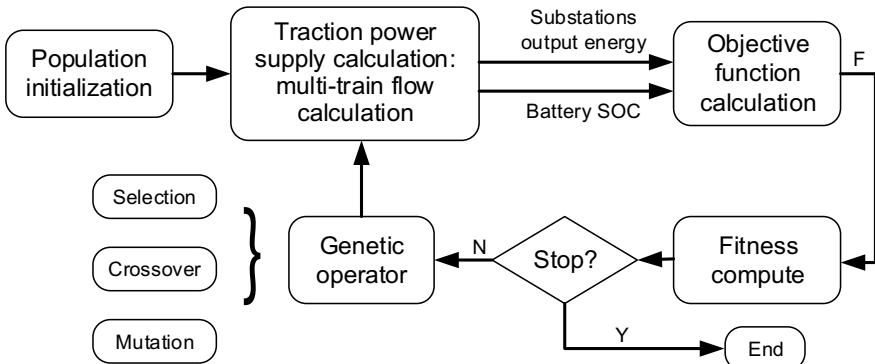
$$X = [K_{p1} K_{i1} K_{p2} K_{i2}, x_1 x_2 x_3 x_4] \quad (6)$$

The genetic algorithm optimization flowchart is shown in Fig. 7. The GA continuously optimizes the variables and inputs them to the simulation platform. After simulation, the corresponding objective function is obtained, and the next-generation optimization is performed. With the continuous increase of genetic generation, the GA can obtain the maximum objective function and obtain the optimal control parameters of the dynamic power threshold control strategy.

In this paper, the optimization of the control parameters is achieved by finding the largest objective function, so the value of the objective function  $\text{ObjV}$  is taken as the fitness value of the individual. The larger the objective function, the larger the individual fitness value, indicating that the individual is better. Since DPTCS is an improvement of FPTCS, in order to prevent the total energy-saving gain from decreasing, the fitness function is as shown in Eq. 7.  $\text{ObjV}[X]$  is the objective function obtained by the parameter group of the  $X$  chromosome for the control parameter.

$$\text{Fitness}[X] = \begin{cases} \text{ObjV}[X], & \text{ObjV}[X] \geq 0 \\ 0, & \text{ObjV}[X] < 0 \end{cases} \quad (7)$$

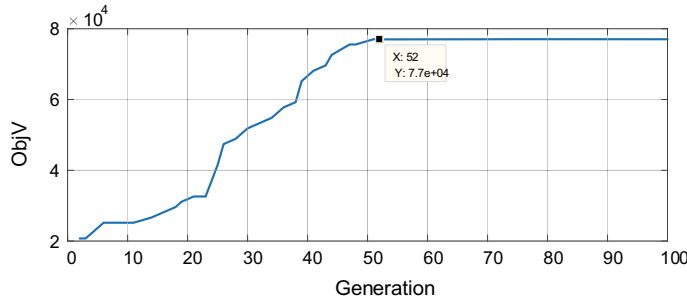
The parameters of GA are set as shown in Table 1, where  $NIND$  is the population size,  $MAXGEN$  is the genetic generation,  $P_c$  is the crossover probability,  $P_m$  is the mutation probability, and  $GGAP$  is the population generation ditch.



**Fig. 7** Block diagram of the control parameter optimization

**Table 1** GA's parameters

<i>NIND</i>	<i>MAXGEN</i>	<i>P<sub>c</sub></i>	<i>P<sub>m</sub></i>	<i>GGAP</i>
20	100	0.7	0.015	0.95

**Fig. 8** Objective function iterative process

In order to prevent the battery from overcharging and overdischarging, and ensuring that the battery has sufficient energy for emergency rescue, the battery SOC must be larger than 0.4 and smaller than 0.8. The supercapacitor SOC range limits 0.25–1.0.

Figure 8 shows the change of the optimal objective function value of each generation under the optimization of genetic algorithm. It can be seen that from the 52th generation, the objective function value which means total energy-saving benefits of HESS within the life span converges to 77,000 ¥, and the corresponding control parameter is the optimal solution.

## 5.2 Simulation Verification

The simulation parameters are shown in Table 2. Control parameters are the aforementioned optimization results. The departure interval is 180 s.

Figure 9 shows the battery current and SOC curve under the two control strategies, respectively, when the initial SOC of the battery is 0.6, which is in area 3. It can

**Table 2** Simulation parameters

Parameters	Value (V)	Parameters	Value	Parameters	Value
$U_o$	836	SOC <sub>floor</sub>	0.4000	SOC <sub>ceil</sub>	0.8000
$U_{\text{char}}$	850	SOC <sub>low</sub>	0.5429	SOC <sub>up</sub>	0.6857
$U_{\text{dis}}$	819	Battery power	200 kW	SC power	800 kW

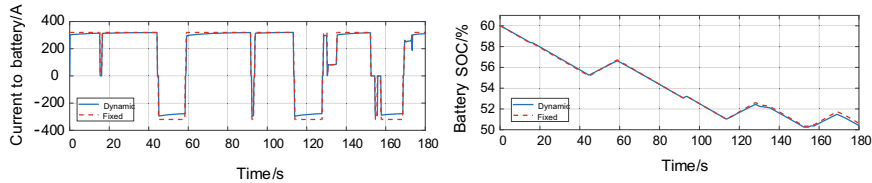


**Fig. 9** Initial battery SOC is 0.6

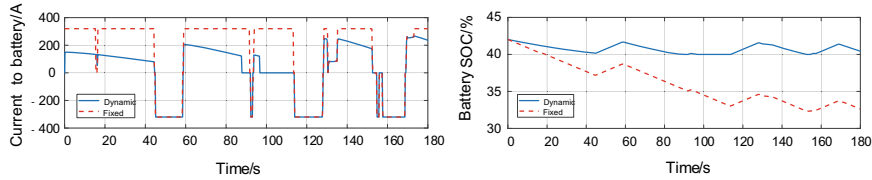


**Fig. 10** Initial battery SOC is 0.42

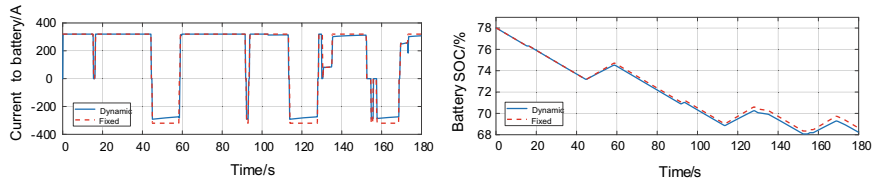


**Fig. 11** Initial battery SOC is 0.78

be seen that the output power of the battery changes dynamically with the SOC of the battery, and the current under DPTCS is reduced compared to the one under FPTCS. And the battery DOD difference between two strategies is small.

Then, we change the initial battery SOC to 0.42, which is in the area 2. The battery current curve shown in Fig. 10 left shows that the discharge current under DPTCS is significantly decreased than FPTCS, and the charge current is the same. Hence, it results in battery SOC curve under DPTCS varies smaller than FPTCS after a departure interval in Fig. 10 right. In other words, the change of battery SOC is effectively suppressed to make it run in a certain range.

At last, we change the initial battery SOC to 0.78, which is in the area 4. The battery current curve shown in Fig. 11 left shows that the charge current under DPTCS is decreased than FPTCS, and the discharge current is the same. The battery under DPTCS charges less than FPTCS after a departure interval. It can be seen that the charging energy of battery is effectively suppressed in Fig. 11 right.

From the simulation results above, we can conclude that DPTCS could effectively adjust the battery power threshold to keep the battery SOC in a certain range. Current under DPTCS is smaller than FPTCS.

## 6 Conclusion

In this paper, the simulation platform of urban rail train power supply system including train and HESS is established. Considering the influence of battery current and DOD on battery life, a DPTCS based on battery SOC tracking is proposed. Based on the actual operating characteristics of the battery, a battery life prediction model was established to calculate the total energy-saving benefit of HESS. Finally, based on the difference between the total energy-saving benefits of the two strategies, a method based on genetic algorithm to optimize the control parameters is proposed. It is verified with the actual line data in the simulation, and it can be a reference to prolong the service life of the battery and improve the total energy-saving benefit of HESS.

## References

1. González-Gil A, Palacin R, Batty P (2015) Optimal energy management of urban rail systems: key performance indicators. *Energy Convers Manag* 90:282–291
2. Chen JF, Lin RL, Liu YC (2005) Optimization of an MRT train schedule: reducing maximum traction power by using genetic algorithms. *IEEE Trans Power Syst* 20(3):1366–1372
3. Ramos A, Peña MT, Fernández A et al (2007) Mathematical programming approach to underground timetabling problem for maximizing time synchronization. *XI Congreso de Ingeniería de Organización* 1395–1405
4. Yang X, Li X, Gao Z et al (2013) A cooperative scheduling model for timetable optimization in subway systems. *IEEE Trans Intell Trans Syst* 14(1):438–447
5. Lixing Yang, Keping Li, Ziyou Gao (2012) Optimizing trains movement on a railway network. *Omega* 40:619–633
6. Watanabe Shoichiro, Koseki Takafumi (2014) Train group control for energy-saving DC-electric railway operation. In: 2014 International Power Electronics Conference, IPEC-Hiroshima-ECCE Asia 2014, pp 1334–1341
7. Carter R, Cruden A, Hall PJ (2012) Optimizing for efficiency or battery life in a battery/supercapacitor electric vehicle. *IEEE Trans Veh Technol* 61(4)
8. Lin S, Song W, Feng Z (2016) Metro hybrid energy storage system and its power dynamic distribution control method. *J Sci Instrum* 37(12):2829–2835 (in Chinese)
9. Chi Zhang (2018) Research on energy management optimization of on-board hybrid energy storage system for modern trams. Beijing Jiaotong University (in Chinese)

# Research on Key Technologies of Energy Storage in Photovoltaic/Battery MicroGrid



Jun Zhou, Tao Yang, Wen Xuan Wang, Yalou Chen and ZhaoRui He

**Abstract** With the increasing scale of power grid and the increasingly high reliability and security requirements of users, energy storage plays an increasingly important role in microgrid. Under the background of national energy saving and emission reduction and vigorously promoting the development of new energy sources, photovoltaic–energy storage combined microgrid has become a research hotspot because it can use the characteristics of energy storage to overcome the impact of photovoltaic grid connected. In this paper, three key technologies of energy storage in optical storage microgrid are studied. They are smooth control of output power, simplified load shifting control, and power supply control when the off-grid operation is realized by utilizing the charging and discharging characteristics of the energy storage system. And their feasibility is verified by simulations and experiments.

**Keywords** The photovoltaic/battery microgrid · Power smoothing · Load shifting off-grid control

---

J. Zhou (✉) · T. Yang · W. X. Wang · Y. Chen · Z. He  
NARI Group Corporation, No. 19, Chengxindadao, Nanjing, Jiangsu, China  
e-mail: [zhoujun@sgepri.sgcc.com.cn](mailto:zhoujun@sgepri.sgcc.com.cn)

T. Yang  
e-mail: [yangtao1@sgepri.sgcc.com.cn](mailto:yangtao1@sgepri.sgcc.com.cn)

W. X. Wang  
e-mail: [wangwenxuan@sgepri.sgcc.com.cn](mailto:wangwenxuan@sgepri.sgcc.com.cn)

Y. Chen  
e-mail: [chenyalou@sgepri.sgcc.com.cn](mailto:chenyalou@sgepri.sgcc.com.cn)

Z. He  
e-mail: [hezhaorui@sgepri.sgcc.com.cn](mailto:hezhaorui@sgepri.sgcc.com.cn)

## 1 Introduction

The conflict between the expanding scale of power grid and the increasing reliability and security requirements of users is becoming increasingly prominent. Therefore, countries around the world have begun to pay attention to environmentally friendly, efficient, and flexible power generation methods—distributed generation. However, there are problems and challenges in the development of distributed generation. Taking solar power generation as a representative, it has the characteristics of randomness and intermittence. It is difficult to provide continuous and stable power, and it is difficult to predict accurately manually. Compared with the traditional power generation mode, the instability of energy output greatly weakens the role of distributed power supply [1].

In microgrid, it is necessary to add energy storage links to adjust the power fluctuation of distributed power supply, to suppress system disturbances, to maintain the dynamic balance of power generation and load, and to maintain the stability of frequency and voltage. Energy storage system is an important and indispensable key part of the microgrid system [2].

This paper researches the photovoltaic–energy storage combined microgrid, focusing on the coordinated optimization control technology and the dual-mode operation capability of the microgrid, using the characteristics of energy storage to overcome the impact of photovoltaic grid connected on the grid [3], and continuing to provide power for the load when the grid fails. The topology and control strategy of energy storage converter are researched, and the energy control strategy of microgrid system is researched. The feasibility of the design is verified by simulation and experiment.

## 2 Research on Key Technologies of Energy Storage in Optical Storage Microgrid

This paper mainly studies the key technologies of energy storage in microgrid system from three aspects: power smoothing control, load shifting control, and off-grid operation control [4].

### 2.1 Power Smoothing Control

The output power of grid-connected photovoltaic power generation system is related to installation inclination, efficiency of photovoltaic array, efficiency of inverters, grid-connected efficiency, and received solar radiation angle. Therefore, the photovoltaic access power fluctuates randomly with the influence of environmental factors such as sunlight [5]. In this paper, the effect of smoothing the output

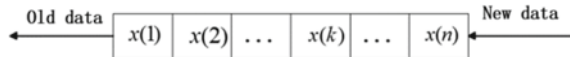


**Fig. 1** Sample data window of moving average filter algorithm

power of microgrid can be achieved by utilizing the charging and discharging characteristics of energy storage system and formulating a reasonable operation strategy. In order to make the input/output power of the access point change slowly, the sliding average method is adopted when the optical storage microgrid system is connected to the grid through a single point based on the power smoothing control of the energy storage system [6].

The sliding average filtering algorithm regards the sampled data as a queue. The length of the queue is fixed to  $n$ , and the value of  $n$  is set by the user himself. Each time new data is sampled, the sampled results are put into the end of the queue, the original data of the head of the queue is deleted, and there are always  $n$  “latest” data in the queue. The sampling schematic diagram is shown in Fig. 1.

In the above sampling data window, when calculating filtering values, as long as  $n$  data in the queue are averaged, new filtering values can be obtained. The direct calculation formula is

$$y(i) = [x(i) + x(i - 1) + \dots + x(i - n + 1)]/n \quad (1)$$

The recurrence formula of sliding filter algorithm is

$$y(i) = y(i - 1) + [x(i) - x(i - n)]/n \quad (2)$$

$x(i)$  is the sampling value,  $x(i - n)$  is the discarded value of this calculation,  $y(i - 1)$  is the last filtering output, and  $y(i)$  is the current filtering output.

When calculating with sliding filtering algorithm, the number of sampling times  $n$  determines the filtering effect, and  $1/n$  can be regarded as the influence factor of each sampling value on the results. If the number of sampling is too small, the influence factor is large, and the smoothing effect is poor. If the number is too large, the influence factor is small, the sensitivity decreases, and it is insensitive to the changing trend of parameters. By observing the output response of sliding average under different  $N$  values,  $n$  values are selected so as to occupy less sampling time and achieve the best filtering effect.

## 2.2 Load Shifting Control

There are periodic variations of day peak and night trough in power load. The difference between peak and trough of load often reaches 30–40% of the output of power generation. The stored energy can be used to store the redundant power of distributed generation when the load is low, and the stored energy can be fed back

to the microgrid at peak load to meet the need of power regulation. In this paper, a simplified load shifting control is adopted, which is realized by adding additional charging and discharging power to the power of battery energy storage system [7].

Under the grid-connected mode, the energy storage system can realize the combined control of power smoothing and load shifting. The control block diagram is shown in Fig. 2. The photovoltaic and energy storage system is connected to the grid through a single point. The energy controller takes the sum of the photovoltaic power collected as the input signal of power smoothing. The power after sliding average filtering is separated by comparing the input power and then superimposes the power generated by load shifting control, which is the power instruction of the energy storage system.

After power smoothing and load shifting algorithm, the power instructions of energy storage system may change frequently between positive and negative. Dead time control can reduce the number of switching and prevent the damage caused by frequency switching between charge and discharge of energy storage converter. At the same time, SOC feedback control can be added to adjust the charging and discharging power according to the remaining capacity of the battery to protect the battery from overcharging and over discharge [8].

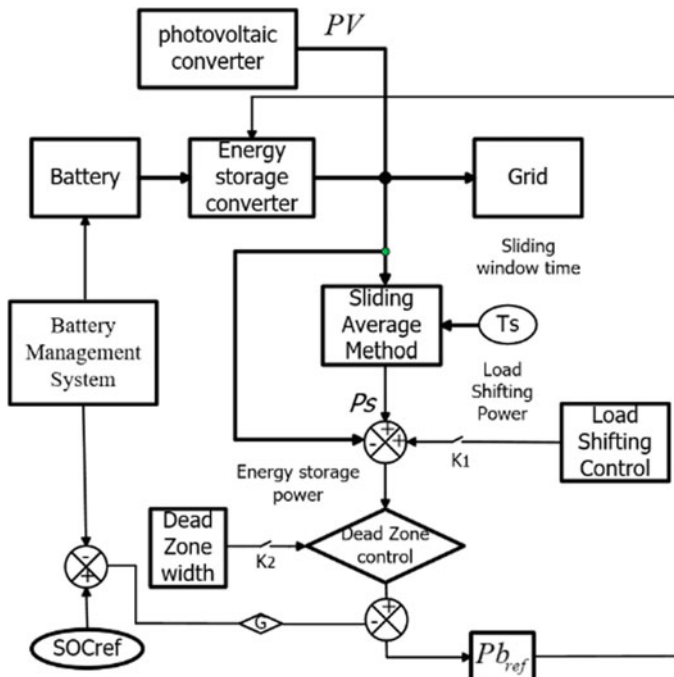


**Fig. 2** Control block diagram of microgrid system

## 2.3 Off-Grid Operation Control

When a fault is detected or the power quality does not meet the grid-connected requirements, the microgrid is disconnected from the main grid and operates independently, which is called island operation. The energy storage system provides power for the load alone.

In order to ensure the supply of important loads, it is required that the output voltage and frequency fully meet the requirements of the power load. Therefore, the energy storage converter works in the voltage source mode [9]. It is better to use parallel voltage model for analysis. Reasonable control of energy storage system can help microgrid transition smoothly in grid-connected/off-grid mode.

## 3 Simulation

In this section, MATLAB simulations are used to verify whether the key techniques mentioned above are available.

### 3.1 Simulation of Sliding Average Algorithms

According to the previous description, the size of sliding window will have a great impact on the filtering results. In order to obtain a reasonable window width, the filtered outputs under different window widths are compared.

The comparison of filter outputs under different window widths is shown in Fig. 3. In the simulation of the photovoltaic system, the sinusoidal signal superimposed harmonics are generated, so the sinusoidal wave is added as the reference in the comparison. It can be seen from the figure that the smaller the window time is, the less obvious the filtering effect is; the larger the window time is, the lag of the

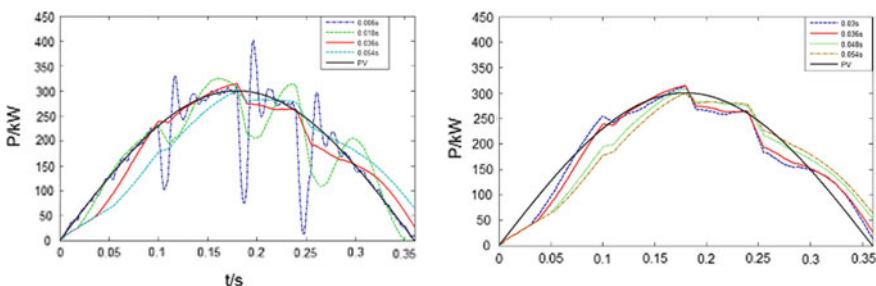


**Fig. 3** Comparison chart of filtering effect under different sliding window time

filtered waveform is larger than that of the sinusoidal waveform curve, resulting in greater difference between the two, which makes the input and output power of the energy storage converter in a larger level.

When the window width is 0.036 s, the output waveform of the filter not only meets the requirements of filtering effect, but also has a small difference with the sinusoidal curve. The simulation time is 0.36 s and the window width is 0.036 s, which is 1/10 of the total time. If the photovoltaic cell board has output power for 10 h in a day, the sliding window width for 1 h is chosen.

### 3.2 Simulation Under off-Grid Mode

In the V/F control mode of DC/AC converter, the inner inductance current loop of AC voltage outer loop is adopted, which not only stabilizes the AC side voltage, but also responds to the power change of microgrid system. The DC/DC converter adopts double closed-loop control to stabilize the DC side voltage. Based on this control strategy, the simulation model of energy storage converter is built in this paper.

In order to test the dynamic performance of V/F control strategy, load dynamic switching is added in the model. Load power changes abruptly at 0.15 s and 0.3 s. Load power changes and power response of converter are shown in Fig. 4. From the figure, it can be seen that the converter can dynamically adjust its power output through PI with closed-loop voltage and current and can follow the change of load power.

The waveforms of voltage and phase current on AC side are shown in Fig. 5. It can be seen that the waveform of voltage on AC side is stable. When the load is switched, the voltage fluctuates, but it can be quickly stabilized by PI through voltage loop. The current amplitude varies with the change of load size and is excessively stable.

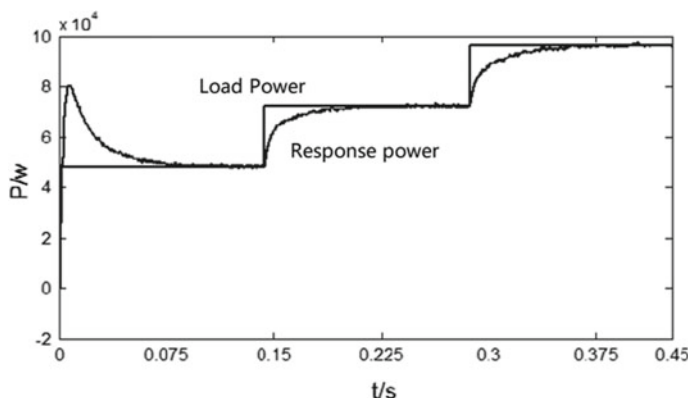


**Fig. 4** Changes in load power and the response of energy power conversion system

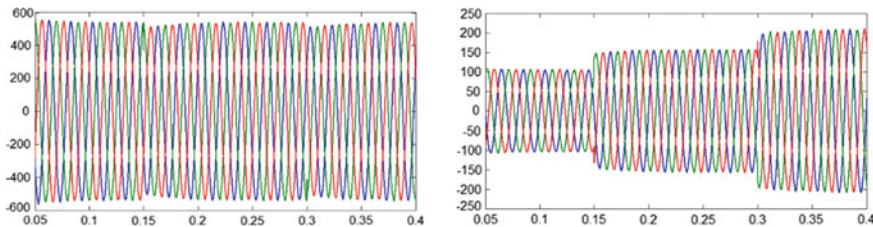


**Fig. 5** Voltage and current waveforms of AC side

## 4 Experiments and Analysis

Through experiments, the feasibility of power smoothing, load shifting, and off-grid handover strategy is verified.

In the experimental system, the total installed capacity of the photovoltaic power generation system is 50 kWp, 224, 225 Wp photovoltaic modules with 14 series and 16 parallel structures are used for the photovoltaic array, and lithium iron phosphate battery with capacity of 0.6 MWh is used for energy storage system. The energy storage converter consists of 75 kW triple DC/DC plus 100 kW DC/AC.

### 4.1 Experiments of Grid Connected to off-Grid

Microgrid works in grid-connected mode. When grid fault is detected or artificial disconnection occurs, energy storage and photovoltaic converters detect under-voltage shutdown on the grid side. The monitoring system disconnects the switch between the microgrid and the grid, and then the energy storage converter starts automatically off the grid. After a stable AC side voltage is established, the load is connected and the load is supplied. The photovoltaic converter detects the start of AC bus voltage and supplies power to the load in combination with the energy storage converter. This is the control process of microgrid system switching from grid-connected operation to off-grid operation. According to this control, the experimental waveform is shown in Fig. 6. It can be seen that the whole switching process is carried out as expected. In off-grid control, the energy storage converter as the synchronous source of the system can maintain the stability of the AC side voltage.

Among them, CH1 is energy storage converter current (phase a), CH2 is energy storage converter current (phase b), CH3 is energy storage converter AC side voltage, and CH4 is grid voltage.

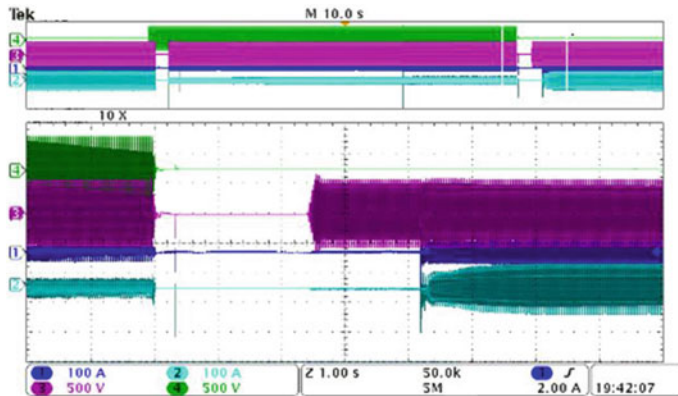


**Fig. 6** Waveform from grid connected to off-grid

#### 4.2 Experiments of off-Grid to Grid Connected

The microgrid system works in the off-grid mode. When the power supply is restored, the energy storage and photovoltaic converter shutdown, the monitoring system controls the switch between the closed microgrid system and the power grid, the load is restored to the power supply, and the photovoltaic converter and the energy storage converter are restored to the grid. The switching experimental waveform is shown in Fig. 7.

Among them, CH1 is energy storage converter current (phase a), CH2 is energy storage converter current (phase b), CH3 is energy storage converter AC side voltage, and CH4 is grid voltage.

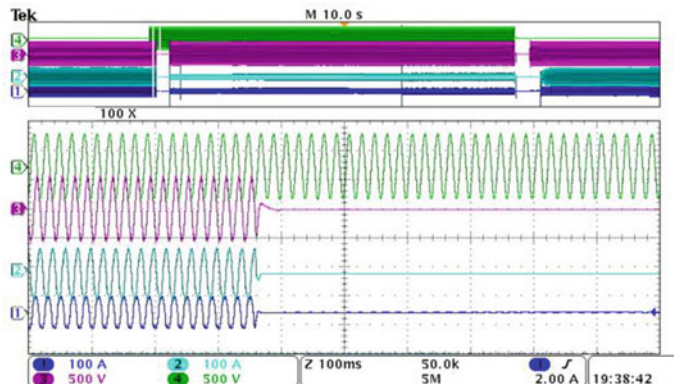


**Fig. 7** Waveform from off-grid to grid connected

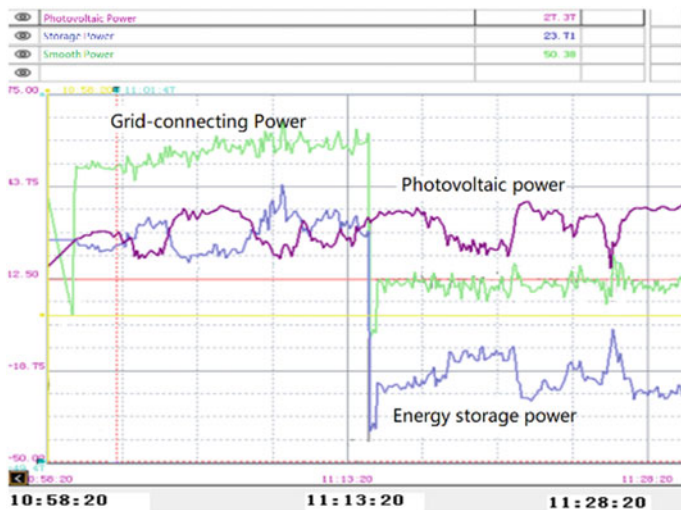


**Fig. 8** Control curve of power smoothing and load shifting

### 4.3 Power Smoothing and Load Shifting Experiments

According to the previous research, the sliding window averaging method is used as power smoothing algorithm in the experiment. According to the idea of power smoothing, the power difference between the filtered curve and the photovoltaic generation curve is taken as the power of the energy storage converter. The measured power smoothing curve in the monitoring and dispatching system is shown in Fig. 8.

It can be seen from the figure that the output power of the energy storage converter can be supplemented by the sliding average algorithm when the photovoltaic power fluctuation occurs, so that the sum of the two is a smooth curve, which achieves the effect of power smoothing. After 11:13:20, the output power of the energy storage converter decreases, that is to say, a certain DC component is added on the basis of smoothing the output current, mainly to verify the feasibility of load shifting function. It can be seen that the power smoothing has not been affected by adding the function of load shifting.

## 5 Conclusion

Energy storage in optical storage microgrid mainly realizes the functions of power smoothing, load shifting, and off-grid operation. This paper focuses on these three functions. Firstly, the control algorithms and methods of energy storage in

microgrid are analyzed. Then, the control strategy of energy storage converter is designed. Finally, the feasibility of the control strategy is verified by experiment. Energy storage in microgrid realizes the expected function.

## References

1. Wang Y, Huang Y et al (2018) Operation optimization in a smart micro-grid in the presence of distributed generation and demand response. *Sustainability*. <https://doi.org/10.3390/su10030847>
2. Abdul H, Hidehito M, Saeed S, Tomonobu S (2018) Design and line fault protection scheme of a dc microgrid based on battery energy storage system. *Energies* 11(7):1823
3. Yaling L, Lei W et al (2016) Effect of distributed PV grid on voltage of distribution net-work. *Chin J Power Sources* 40(6) (in Chinese)
4. Kumar M, Srivastava SC, Singh SN (2017) Control strategies of a dc microgrid for grid connected and islanded operations. *IEEE Trans Smart Grid* 6(4):1588–1601 (in Chinese)
5. Luo J, Hanying H et al (2017) Influence of multiple access points of photovoltaic power supply on distribution network voltage distribution. *Power Electron* 5:40–43 (in Chinese)
6. Wang Z, Ma W, Ruonan H (2017) Power fluctuation stabilization control strategy of micro grid. *Acta Energiae Solaris Sin* 38(9):2344–2348 (in Chinese)
7. Ren Z, Lu J, Wang G, Long X, Xiao Z, Chao L (2016) The charging and discharging balance control strategy of power batteries for hybrid energy storage. In: International symposium on power electronics
8. Baoen LI, Xianwei LI, Bingxin WU, Corporation XG (2017) Research on energy optimal dispatching strategy for microgrid based on battery SOC. *Power Syst Prot Control* 45(11): 108–114
9. Wang L, Zhou X et al (2017) Research on peer to peer control strategy for microgrid based on the improved power loop. *Electr Power* 50(9):171–177 (in Chinese)

# Performance Evaluations of DCAT Position for the Floating DCAT System in DC Railways



Miao Wang, Xiaofeng Yang, Trillion Q. Zheng, Menghan Ni, and Wei Guo

**Abstract** DC auto-transformer (DCAT) traction power supply system has been studied for the stray current and rail potential issues in DC railways, and the solidly grounded DCAT system of equal sections has been analyzed in detail. However, in practice, the floating scheme more tends to be adopted in DC railways, and the sections of DCAT system is hard to achieve complete equality. Therefore, the performance evaluations of DCAT position for the floating DCAT system were proposed in this paper. The performances of floating DCAT system with equal sections were analyzed comparing with the existing system. Then the theoretical analysis and the relationships between DCAT position, rail potential, and stray current were discussed in detail. Finally, the correctness of the proposed analysis was verified by the simulation results.

**Keywords** DC railways · Rail potential · Stray current · DC auto-transformer · Floating scheme

---

M. Wang · X. Yang (✉) · T. Q. Zheng · M. Ni · W. Guo  
School of Electrical Engineering, Beijing Jiaotong University, Beijing, China  
e-mail: [xfyang@bjtu.edu.cn](mailto:xfyang@bjtu.edu.cn)

M. Wang  
e-mail: [wangmiao@bjtu.edu.cn](mailto:wangmiao@bjtu.edu.cn)

T. Q. Zheng  
e-mail: [tqzheng@bjtu.edu.cn](mailto:tqzheng@bjtu.edu.cn)

M. Ni  
e-mail: [nimenghan@bjtu.edu.cn](mailto:nimenghan@bjtu.edu.cn)

W. Guo  
e-mail: [guowei@bjtu.edu.cn](mailto:guowei@bjtu.edu.cn)

## 1 Introduction

Nowadays, the urban rail transit has been gradually utilized in modern cities of the world. Take China as an example, 35 cities have 185 urban rail lines and the total distance has exceeded 5700 km by the end of 2018. The urban rail transit mainly adopts DC traction power supply system, and the metro, for example, usually adopts DC1500 V or DC750 V power supply. However, the running rails are usually used as the return path of the traction current in DC railways. Because the rails are not totally earth-isolated, a part of current leaks into the ground and leads to the stray current and rail potential issues [1, 2]. The stray current causes serious corosions of rails, underground structures, and pipelines, resulting in the huge economic losses. Meanwhile, the high rail potential also endangers human life and the normal operation of traction power supply system [3, 4].

Therefore, in order to solve the stray current and rail potential issues, some measures have been adopted in DC railways, such as strengthening the rail-to-ground insulation, reducing the rail resistance, setting the stray current collection system, and so on [5, 6]. However, these solutions may have some shortcomings, such as the high cost, weak applicability, poor performance, and so on. Therefore, DC auto-transformer (DCAT) was proposed by shifting the traction current from rail to other specific lines. Thus, it may solve the stray current and rail potential issues fundamentally [7–9]. In [7], the rail potential and stray current of solidly grounded DCAT system with equal sections were analyzed in detail. The results showed that the rail potential and stray current of solidly grounded DCAT system are reduced to  $1/N$  and  $1/N^2$ , respectively, comparing with the existing system, and here,  $N$  means the number of equal sections.

However, the solidly grounded scheme is not the only option for the existing traction substations, other grounding schemes also have been adopted in many railway lines, such as the floating scheme, diode-grounded scheme, thyristor-grounded scheme, and so on [10–13]. Especially, the grounding design principle is documented in China national standard such as GB 50157-2013 [14] and GB/T 10411-2005 [15]: the floating scheme is recommended to be used in DC traction power supply system. So the performance analysis of rail potential and stray current in floating DCAT system is essential. Meanwhile, the sections of DCAT system are hard to achieve complete equality in practice.

Therefore, in order to evaluate the performances of DCAT system more accurately, the performance evaluations of DCAT position for the floating DCAT system are analyzed and discussed in detail in this paper. The paper is organized as follows: Sect. 2 analyzes the performances of floating DCAT system with equal sections comparing with the existing system; Sect. 3 presents the relationships between DCAT position, rail potential, and stray current in detail; Sect. 4 shows the simulation results verifying the correctness of the theoretical analysis; finally, Sect. 5 concludes the paper briefly.

## 2 Floating DCAT System

The configuration of DCAT system is shown in Fig. 1, which adds the negative feeder and several DCATs comparing with the existing system. DCATs achieve the voltage balancing between the overhead line (or third rail), the rail, and the negative feeder. DCATs transfer the traction current from the rail to the negative feeder and contact line, thus the rail current of no-train sections is zero. Therefore, DCAT system may solve the stray current and rail potential issues fundamentally.

However, the grounding schemes of traction power supply system mainly include the solidly grounded scheme and the floating scheme. For the solidly grounded scheme, the negative of each substation is grounded to the local ground grid without any intentional impedance. For the floating scheme, the negative return rails are not bonded to the ground at substations. Different from above solidly grounded scheme, the floating scheme increases the rail potential of substations, while decreases the stray current greatly. Therefore, combining the stray current control and the rail potential protection, the floating scheme with the over-voltage protection device (OVPD) has been widely adopted in the new lines [2].

The rail potential comparisons between the solidly grounded scheme and the floating scheme are shown in Fig. 2, when the train is running on the midpoint of the rail. In Fig. 2, the voltage difference between the train and the substations in the floating scheme is consistent with that in the grounding system. Meanwhile, for the floating scheme, the positive area is equal with the negative area, because the rail-to-ground current must be equal with the ground-to-rail current according to the KCL equations. Based on the above theoretical analysis, and referring to the conclusions in the solidly grounded scheme [7], the rail potential of the train and the stray current (i.e., the total leaked current from the rail to the ground) can be obtained as follows:

$$V_E = \frac{(L - x)xRI_o}{2L}, 0 \leq x \leq L \quad (1)$$

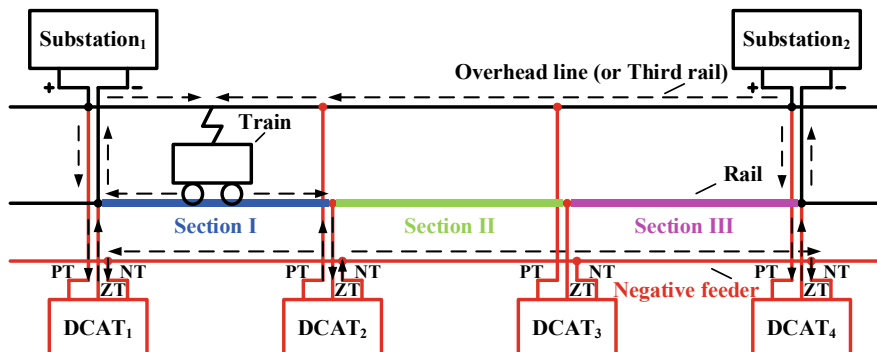


**Fig. 1** Configuration of DCAT system

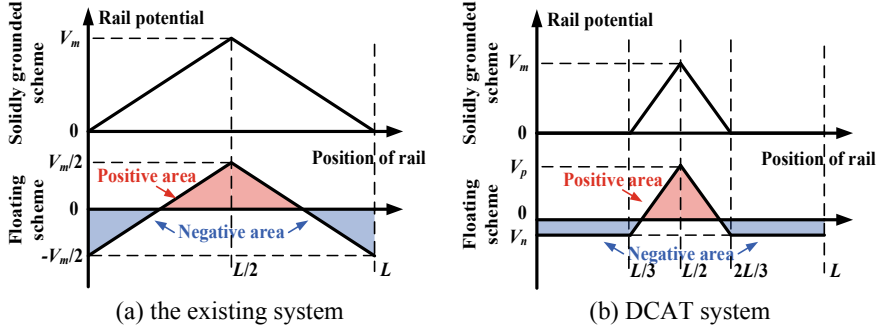


**Fig. 2** Rail potential comparisons between the solidly grounded scheme and floating scheme

$$I_E = \frac{(L - x)xRI_o}{8R_g}, 0 \leq x \leq L \quad (2)$$

$$V_{DCAT} = \frac{(2N - 1)RI_o}{2L} \left[ x - \frac{(P - 1)L}{N} \right] \left( \frac{PL}{N} - x \right), \frac{(P - 1)L}{N} \leq x \leq \frac{PL}{N} \quad (3)$$

$$I_{DCAT} = \frac{(2N - 1)^2 RI_o}{8N^2 R_g} \left[ x - \frac{(P - 1)L}{N} \right] \left( \frac{PL}{N} - x \right), \frac{(P - 1)L}{N} \leq x \leq \frac{PL}{N} \quad (4)$$

where  $L$  is the distance between the substations in kilometers,  $x$  is the distance between the train and the substation<sub>1</sub> in kilometers,  $R$  is the rail resistance in ohms per kilometer,  $R_g$  is the rail-to-ground resistance in ohm kilometers, and  $I_o$  is the train load current in amps. Moreover, the rail of DCAT system is divided into  $N$  sections equally, and the train is running on the section  $P$  ( $P \in \mathbb{Z}, 1 \leq P \leq N$ ).

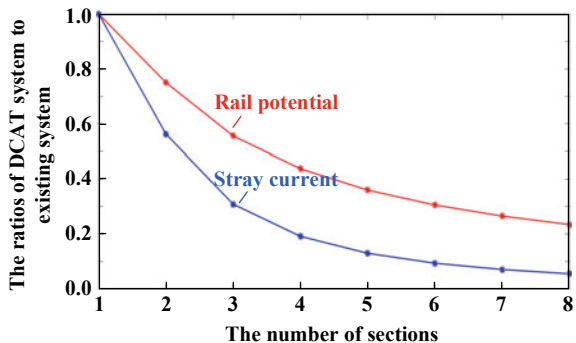
Based on (1)–(4), the maximum and average ratios of the floating DCAT system with  $N$  equal sections to the existing system can be concluded as follows:

$$\frac{V_{E\_max}}{V_{DCAT\_max}} = \frac{V_{E\_av}}{V_{DCAT\_av}} = \frac{2N - 1}{N^2} \quad (5)$$

$$\frac{I_{E\_max}}{I_{DCAT\_max}} = \frac{I_{E\_av}}{I_{DCAT\_av}} = \left( \frac{2N - 1}{N^2} \right)^2 \quad (6)$$

Base on (5) and (6), the ratios of DCAT system to the existing system can be given as shown in Fig. 3. Obviously, with increasing the number of sections  $N$ , the effects of DCAT system on the stray current and rail potential issues will be better. Therefore, with comprehensive consideration of the effects and the cost of DCAT system, the recommended number of sections is 3 to 5 under different substation distance.

**Fig. 3** Ratios of DCAT system to the existing system



### 3 Performance Evaluations of DCAT Position

In order to simplify the analysis, take DCAT system with four DCATs (i.e., three sections) as an example, then the performance evaluations of DCAT position are discussed in detail. As shown in Fig. 1, DCAT<sub>1</sub> and DCAT<sub>4</sub> are installed in substation<sub>1</sub> and substation<sub>2</sub>, respectively, and their positions are unchanged. However, DCAT<sub>2</sub> and DCAT<sub>3</sub> are installed between the substations and their positions are adjustable. Therefore, adjust the position of DCAT<sub>2</sub> and DCAT<sub>3</sub>, then the stray current and rail potential of floating DCAT system can be obtained. The parameters of DCAT system and the existing system are given in Table 1, and the typical cases are listed as follows.

Case I, the existing system; Case II, DCAT system with equal sections (i.e.,  $x_{DCAT2}$  and  $x_{DCAT3}$  are 1 and 2 km, respectively); Case III, DCAT<sub>2</sub> moves 0.1 km to the right, and DCAT<sub>3</sub> moves 0.1 km to the left (i.e.,  $x_{DCAT2}$  and  $x_{DCAT3}$  are 1.1 and 1.9 km, respectively); Case IV, DCAT<sub>2</sub> moves 0.1 km to the left, and DCAT<sub>3</sub> moves 0.1 km to the right (i.e.,  $x_{DCAT2}$  and  $x_{DCAT3}$  are 0.9 and 2.1 km, respectively). Here,  $x_{DCAT}$  is the distance between the DCAT and substation<sub>1</sub>.

Based on the theoretical analysis, the rail potential comparisons between the existing system and DCAT system are shown in Fig. 4, while the rail potential of train and stray current comparisons are shown in Fig. 5. Meanwhile, the maximum and average rail potentials and stray currents are given in Table 2. Comparing with Case I, the rail potential and stray current of Case II, Case III, and Case IV are

**Table 1** Parameters of DCAT system and the existing system

Variable	Description	Value
$V_{in}$	Substations voltage	1500 V
$I_o$	Train load current	1000 A
$L$	Distance between substations	3 km
$R$	Rail resistance	30 mΩ/km
$R_g$	Rail-to-ground resistance	15 Ω km
$N$	Number of sections	3

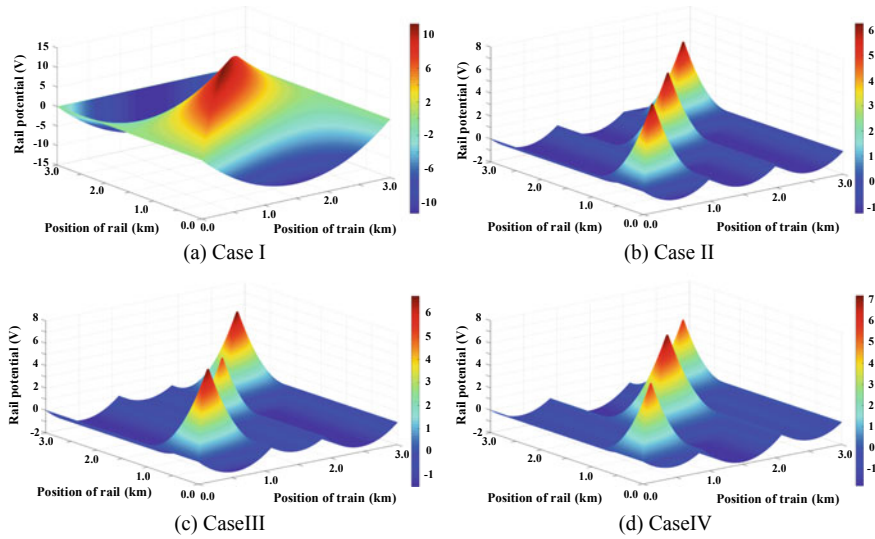


**Fig. 4** Rail potential comparisons between the existing system and DCAT system

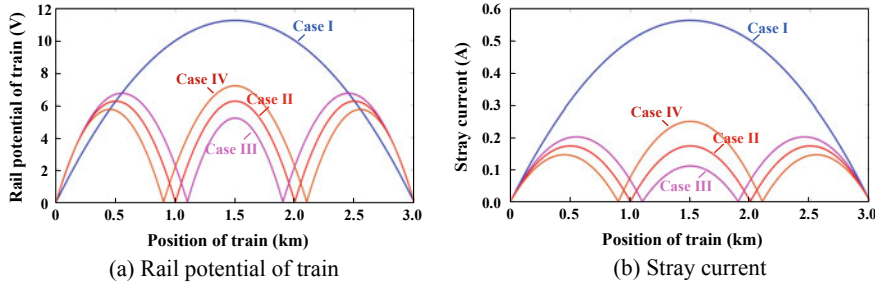


**Fig. 5** Comparisons between the existing system and DCAT system

**Table 2** Maximum and average comparisons of rail potential and stray current

	Rail potential		Stray current	
	Maximum (V)	Average (V)	Maximum (A)	Average (A)
Case I	11.250	7.500	0.563	0.375
Case II	6.250	4.167	0.174	0.116
Case III	6.738	4.218	0.202	0.120
Case IV	7.200	4.215	0.230	0.120

reduced significantly proving the effectiveness of DCAT system on the stray current and rail potential issues. Meanwhile, the average rail potentials of Case III and Case IV increase 1.22 and 1.15% comparing with Case II, while the average stray currents increase 3.45 and 3.45%. Therefore, Case II, Case III, and Case IV are basically consistent in solving the stray current and rail potential issues.

Based on the above analysis, the rail potential and stray current of DCAT system are closely related to the distances of each section. Supposing that the distances of Sect. 1, Sect. 2, and Sect. 3 are  $L_1$ ,  $L_2$ , and  $L_3$ , respectively, the average rail potential and stray current of DCAT system can be derived as follows:

$$V_{av} = \frac{RI_o}{12L^2} [(2L - L_1)L_1^2 + (2L - L_2)L_2^2 + (2L - L_3)L_3^2] \quad (7)$$

$$I_{av} = \frac{RI_o}{48R_g L^3} [(2L - L_1)^2 L_1^3 + (2L - L_2)^2 L_2^3 + (2L - L_3)^2 L_3^3] \quad (8)$$

Change the positions of DCAT<sub>2</sub> and DCAT<sub>3</sub>, then the average rail potential and stray current of different DCAT positions can be obtained as shown in Fig. 6. Clearly, DCAT system with equal sections has the minimum rail potential and stray current. Meanwhile, Fig. 6b, d show that the small-scale movement of DCATs almost has no effect on the rail potential and stray current.

In order to analyze more accurately, define the moving ratio of DCATs  $\lambda$  and the changed ratios of rail potential  $\eta_r$  and stray current  $\eta_s$  to evaluate the performance of DCAT positions, here,  $\lambda$  is the ratio of the moving distance  $X$  to the equal sections distance  $L_N$ . As shown in Fig. 6, the rail potential and stray current have the

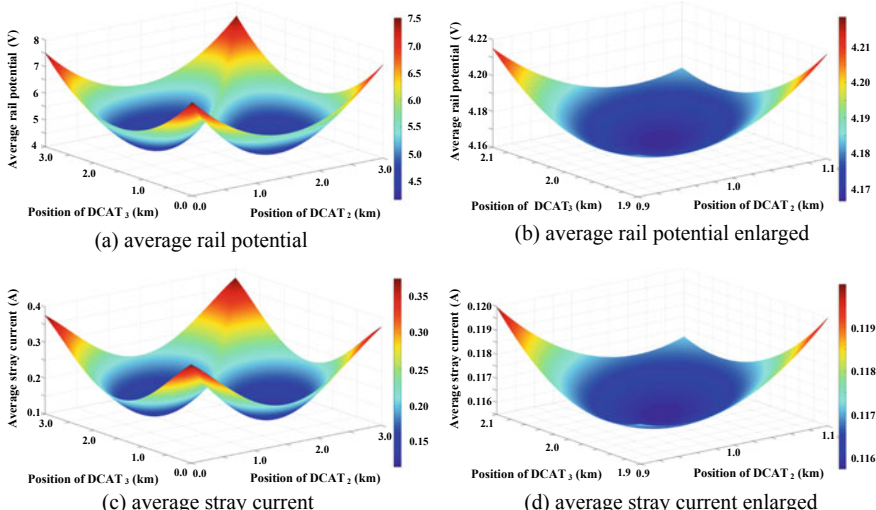
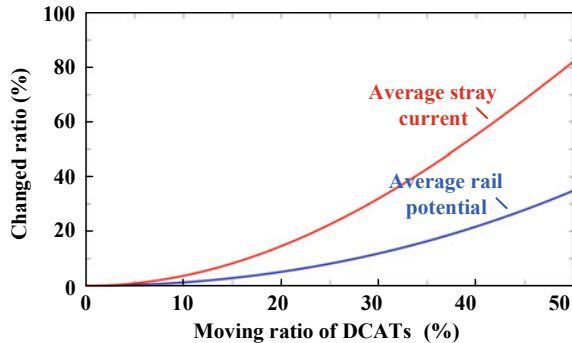


**Fig. 6** Average rail potential and stray current of different DCAT positions

**Fig. 7** Relationship curves between the moving ratio of DCATs and the changed ratios



maximum when DCAT2 moves  $X$  to the right, while DCAT3 moves  $X$  to the left. Therefore, the distances of each section can be obtained as follows:

$$\begin{cases} L_1 = L_3 = (1 + \lambda) \frac{L}{3} \\ L_2 = (1 - 2\lambda) \frac{L}{3} \end{cases} \quad (9)$$

Combining (7)–(9), the changed ratios of rail potential  $\eta_r$  and stray current  $\eta_s$  can be given as follows:

$$\eta_r = \frac{2(5 - \lambda)(1 + \lambda)^2 + (5 + 2\lambda)(1 - 2\lambda)^2 - 15}{15} \times 100\% \quad (10)$$

$$\eta_s = \frac{2(5 - \lambda)^2(1 + \lambda)^3 + (5 + 2\lambda)^2(1 - 2\lambda)^3 - 75}{75} \times 100\% \quad (11)$$

Base on (10)–(11), the relationship curves between the moving ratio of DCATs and the changed ratios are shown in Fig. 7. Obviously, when the moving ratio of DCATs is controlled within 10%, the changed ratio of average rail potential can be limited to 1.24%, and the changed ratio of average stray current can be limited to 3.68%. Therefore, the small-scale movement of DCATs has little effect on the rail potential and stray current of DCAT system, which proves the high adaptability of DCAT positions.

## 4 Simulation Results

To verify the feasibility of above theoretical analysis, DCAT system and the existing system are performed in MATLAB/Simulink. The simulation model adopts the discrete analysis method to simulate the train running on the rail. For the simulation model, the rail is divided into several small intervals, and the rail resistance and rail-to-ground resistance in each interval can be equivalent to three

resistors (i.e.,  $R_{ix1}$ ,  $R_{ix2}$ , and  $R_{ixg}$ ), as shown in Fig. 8. The simulation parameters are listed in Table 3, and all the components are assumed ideal to simplify the analysis.

The comparisons between the theoretical results and the simulation results are shown in Fig. 9, and the comparison results are given in Tables 4 and 5. Obviously,

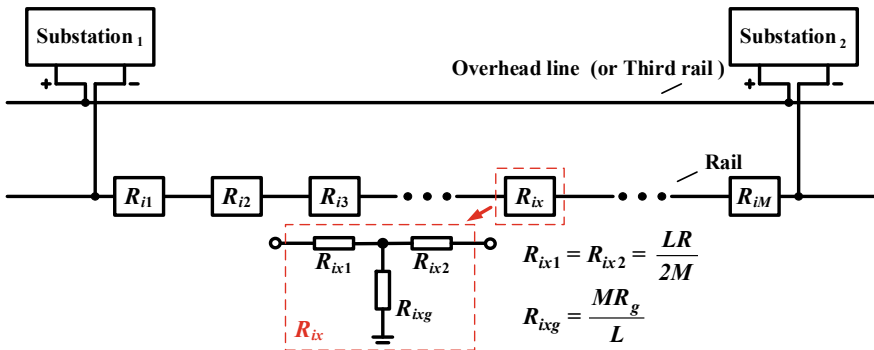


**Fig. 8** Discrete analysis method of the rail resistance and rail-to-ground resistance

**Table 3** Simulation parameters of DCAT system and the existing system

Variable	Description	Value
$V_{in}$	Substations voltage	1500 V
$I_o$	Train load current	1000 A
$L$	Distance between substations	3 km
$R$	Rail resistance	30 mΩ/km
$R_g$	Rail-to-ground resistance	15 Ω km
$N$	Number of sections	3
$M$	Rail intervals number	30
$R_{ix1}, R_{ix2}$	Rail resistors	1.5 mΩ
$R_{ixg}$	Rail-to-ground resistor	150 Ω

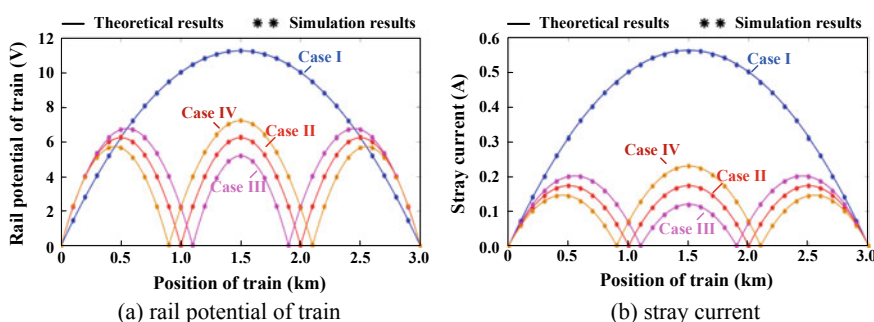


**Fig. 9** Comparisons between the theoretical results and the simulation results

**Table 4** Comparison results of rail potential between DCAT system and the existing system

	Maximum rail potential		Average rail potential		Mean error (%)
	Theoretical (V)	Simulation (V)	Theoretical (V)	Simulation (V)	
Case I	11.250	11.246	7.500	7.246	0.06
Case II	6.250	6.249	4.167	3.991	0.03
Case III	6.682	6.680	4.218	4.042	0.03
Case IV	7.200	7.199	4.215	4.040	0.03

**Table 5** Comparison results of stray current between DCAT system and the existing system

	Maximum stray current		Average stray current		Mean error (%)
	Theoretical (A)	Simulation (A)	Theoretical (A)	Simulation (A)	
Case I	0.563	0.560	0.375	0.361	0.61
Case II	0.174	0.173	0.116	0.110	0.80
Case III	0.202	0.200	0.120	0.114	0.73
Case IV	0.230	0.230	0.120	0.114	0.69

the simulation results are basically agreement with the theoretical results on the maximum rail potential and stray current. But for the average rail potential and stray current, the simulation results are slightly smaller than the theoretical results, because the rail intervals number is not big enough. Meanwhile, comparing all the simulation results with the theoretical results, the mean errors of rail potential are limited in 0.06%, while the mean errors of stray current are limited in 0.80%. Therefore, it can be concluded that the simulation results are consistent with the theoretical results, which prove the correctness of the theoretical analysis effectively.

## 5 Conclusions

The floating DCAT system has been described in this paper, and the rail potential and stray current of floating DCAT system were discussed in detail. Meanwhile, the performance evaluations of DCAT position were analyzed with four typical cases. Then the effectiveness of the theoretical analysis was validated with simulation results. Both the theoretical analysis and the simulation results show that the floating DCAT system may solve the stray current and rail potential issues

effectively, and the small-scale movement of DCATs has little effect on the rail potential and stray current of floating DCAT system. In conclusion, all the results show that DCAT system has a promising application prospect in DC railways.

**Acknowledgements** This work is supported by the State Key Program of National Natural Science of China (No. 51737001).

## References

1. Ibrahim A, Elrayyah A, Sozer Y, Abreu-Garcia J (2017) DC railway system emulator for stray current and touch voltage prediction. *IEEE Trans Ind Appl* 53(1):439–446
2. Xu S, Wang WY (2013) Effects of vehicle running mode on rail potential and stray cur-rent in DC mass transit systems. *IEEE Trans Veh Technol* 62(8):3569–3580
3. Cai Z, Hao C (2019) Evaluation of metro stray current corrosion based on finite element model. *J Eng* 2019(16):2261–2265
4. Xue H, Yang X, Zhou Y, Zheng TQ (2018) Multi-interval DC traction system simulator for stray current and rail potential distribution. In: *IEEE Energy Conversion Congress and Exposition*, Portland, USA
5. Jin J, Allan J, Goodman CJ, Payne K (2004) Single pole-to-earth fault detection and location on a fourth-rail DC railway system. *IEE Proc Electr Power Appl* 151(4):498–504
6. Fotouhi R, Farshad S, Fazel SS (2009) A new novel DC booster circuit to reduce stray current and rail potential in DC railways. In: *Compatibility and power electronics*
7. Wang M, Yang X, Wang L, Zheng TQ (2017) DC auto-transformer traction power supply system for DC railways application. In: *3th international conference on electrical engineering and information technologies for rail transportation*, Wuhan, China
8. Wang M, Yang X, Wang L, Zheng TQ (2018) Resonant switched capacitor converter based DC auto-transformer for urban rail transit. In: *IEEE applied power electronics conference*, San Antonio, USA
9. Wang M, Yang X, Zheng TQ, Gu J (2018) Power analysis on DCAT traction power supply system for urban rail transit. In: *IEEE international power electronics and application conference and exposition*, Shenzhen, China
10. Cotton I, Charalambos C, Aylott P, Ernst P (2005) Stray current control in DC mass transit systems. *IEEE Trans Veh Technol* 54(2):722–730
11. Lee C, Lu C (2006) Assessment of grounding schemes on rail potential and stray currents in a DC transit system. *IEEE Trans Power Del* 21(4):1941–1947
12. Jamali S, Alamuti MM, Savaghebi M (2008) Effects of different earthing schemes on the stray current in rail transit systems. In: *43rd international universities power engineering conference*, Padova, Italy
13. Alamuti MM, Nouri H, Jamali H (2011) Effects of earthing systems on stray current for corrosion and safety behaviour in practical metro systems. *IET Electr Syst Transp* 1(2):69–79
14. Beijing Municipal Commission of Urban Planning: Code for design of metro, GB 50157-2013 (in Chinese)
15. Standardization Administration of China: DC traction power supply system for urban rail transit, GB/T 10411-2005 (in Chinese)

# Negative Impedance Converter for Reducing Rail Potential in Urban Rail Transit



Wei Guo, Xiaofeng Yang, Jingda Gu and Trillion Q. Zheng

**Abstract** In conventional traction power supply system (C-TPSS), the traction current returned to the substation through the running rail. Running rail current leaks into the earth forming stray current, which inevitably causes serious corruptions on the buried metals and endangers personal safety. In order to solve this problem, this paper proposes the negative impedance converter traction power supply system (NIC-TPSS). Based on configuration and operation principle analysis of NIC-TPSS, the working modes of negative impedance converter (NIC) are described in detail. The simulation results show that, compared with C-TPSS, NIC-TPSS can solve the stray current and rail potential problems.

**Keywords** Urban rail transit · Traction power supply system · Negative impedance converter · Rail potential · Stray current

## 1 Introduction

With the ever-increasing urban area and population, urban rail transit has developed rapidly and become an indispensable part of people's lives. In conventional traction power supply system (C-TPSS), the traction current flows through the catenary, train, and running rails in sequence. Eventually, the current returns to the substation with a closed loop. Since the running rails and the earth are not completely insulated, a part of the currents leaks into the earth and is called stray current [1–4]. Stray current causes a

---

W. Guo · X. Yang (✉) · J. Gu · T. Q. Zheng

School of Electrical Engineering, Beijing Jiaotong University, Beijing, China

e-mail: [xfyang@bjtu.edu.cn](mailto:xfyang@bjtu.edu.cn)

W. Guo

e-mail: [guowei@bjtu.edu.cn](mailto:guowei@bjtu.edu.cn)

J. Gu

e-mail: [15117391@bjtu.edu.cn](mailto:15117391@bjtu.edu.cn)

T. Q. Zheng

e-mail: [tqzheng@bjtu.edu.cn](mailto:tqzheng@bjtu.edu.cn)

potential difference between the running rail and the earth, which is called rail potential. In the traction power supply system (TPSS), the running rail current is greatly increased when the train is in traction or braking state. Under the same insulation conditions, the increase in rail potential may exacerbate stray current leakage.

The defects of stray current are mainly manifested in three aspects: (1) corrosion of underground metal pipelines and building structures [5]; (2) affecting the normal operation of transformers in urban grids; and (3) causing frequent actions of the over-voltage protection device (OVPD). Under the long-term corrosion of stray current, the buried metal pipelines, especially which are near the running rails, are perforated, and the underground building structure becomes fragile, which not only causes huge economic losses, but also endangers personal safety [6].

Scholars and researchers have proposed a variety of methods to reduce the stray currents defects. Such methods include (1) reducing the longitudinal resistance of running rail; (2) increasing the rail-to-ground resistance between running rail and earth; (3) increasing the voltage level of substation; (4) shortening the distance between substations; and (5) using the fourth rail as a return path for traction current [7–10]. The first four methods are expensive and difficult to implement. And the stray current and rail potential suppressing performance are limited. The fourth-rail TPSS has been applied in practice in the USA, Canada, Malaysia, etc. However, the fourth-rail TPSS requires extra expensive equipment. And it also requires the modification of existing trains, which is difficult to adopt and promote.

In order to solve the above problems, this paper proposed negative impedance converter traction power supply system (NIC-TPSS) with better efficiency, economy, and reliability. The negative impedance converter (NIC) is installed in the substation to transfer traction current to return cable. This paper verifies the feasibility of NIC-TPSS by mathematical analysis and simulation. Then, it is compared with the C-TPSS. The results show that NIC-TPSS can effectively solve the problems of stray current and rail potential.

## 2 Configuration and Operation Principles of NIC-TPSS

The configuration of NIC-TPSS is shown in Fig. 1, consisting of three parts. The first part is NIC, and its circuit diagram is shown in Fig. 2. The positive output terminal of the NIC is connected to the running rail, and the negative output terminal is connected to the return cable. The second part is the switch unit (SU) installed along the running rails. The third part is the return cable, which provides a path for the traction current returning to the substations through NIC and SUs.

As shown in Fig. 1, the SUs divide the running rail between the substation 1 and the substation 2 into four intervals, namely: Interval I, Interval II, Interval III, and Interval IV. The NIC outputs a negative impedance for offsetting the return cable impedance. The total resistance between the train interval and the substations is zero, and the traction current flows into the return cable through the SUs. The return cable is generally insulated with the earth, so that it can prevent the traction current from leaking into the earth.

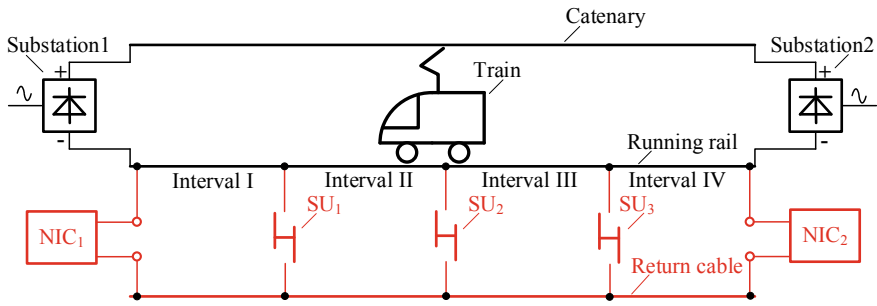
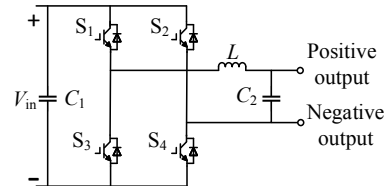


**Fig. 1** Configuration of NIC-TPSS

**Fig. 2** NIC main circuit



Taking the train in the Interval III as an example, Fig. 3 shows the flow direction of the traction current in the NIC-TPSS. The blue dotted line indicates the traction current and the arrow indicates the current direction. Once the train is detected running in Interval III, SU2 and SU3 are turned on, while the remaining SUs are all turned off. It helps provide a path for traction current to the return cable. The running state of the train includes traction, uniform speed, and braking. After detecting the state of the train, the corresponding control strategy is applied to the NIC to make it work in the correct state. The negative impedance provided by NIC1 will offset the return cable impedance between the substation 1 and the SU2. The operation principle is the same when the train is running in other intervals.

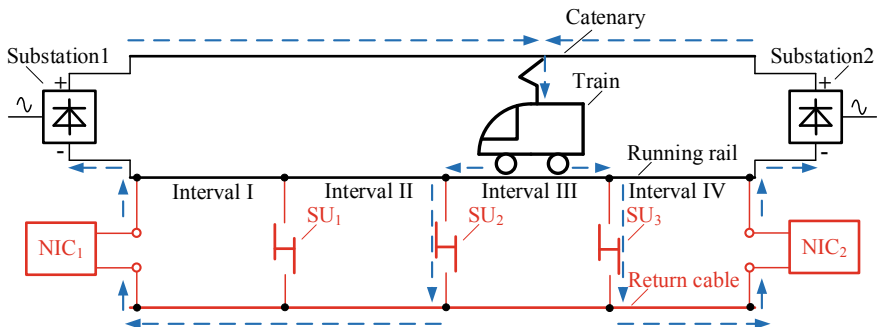


**Fig. 3** Flow direction of traction current

In the NIC-TPSS, only the train interval has a traction current flowing. The current is zero in the no-train intervals and the stray current and rail potential problem can be solved.

### 3 Working Modes and Mathematical Analysis of NIC

The topology of NIC is shown in Fig. 4.  $S_1$ – $S_4$  are IGBTs with anti-parallel diodes.  $C_1$  and  $C_2$  are filter capacitors and  $L$  is a freewheeling inductor.  $R_c$  represents the return cable impedance.

The operating waveforms of the NIC are shown in Fig. 5.  $I_t$  represents the traction current waveform.  $SS_1$ – $SS_4$  represent the control signals of  $S_1$ – $S_4$ , respectively.

$t_0$ – $t_1$ : During this period, the train is in traction state.  $S_1$  is controlled by pulse width modulation (PWM) and  $S_4$  remains normally open, while  $S_2$  and  $S_3$  are both turned off.

**Fig. 4** Simplified structure of NIC-TPSS

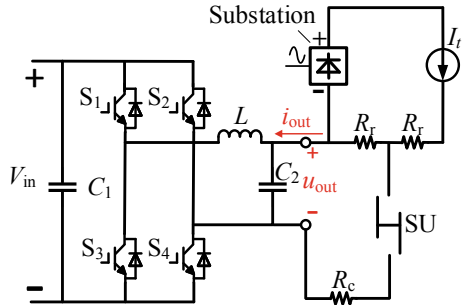
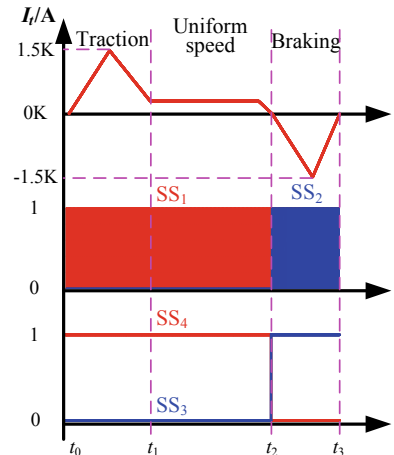


**Fig. 5** Operating waveforms of NIC



$t_1-t_2$ : The train is at uniform speed during this time. The states of  $S_1-S_4$  are also the same as the traction state.

During the period from  $t_0$  to  $t_2$ , the working modes of the NIC include mode 1 and mode 2, which are shown in Fig. 6a, b.

$t_2-t_3$ : The train is in braking state.  $S_2$  is controlled by PWM and  $S_3$  remains normally open, while  $S_1$  and  $S_4$  are both turned off. During this period, the working modes of the NIC include mode 3 and mode 4, which are shown in Fig. 6d, e.

In mode 1 and mode 3, the circuit structure is equivalent to a buck converter. In mode 2 and mode 4, the inductor freewheels the current. The inductor current waveform for traction and uniform speed state are shown in Fig. 6c. The inductor current waveform for the braking state is shown in Fig. 6f. The positive direction of the output voltage and current of NIC have been marked in Fig. 4.

When the NIC is working in mode 1 and mode 3, the equivalent circuit of NIC-TPSS is shown in Fig. 7a, b, respectively. As shown in Fig. 7a, when the train is in traction or uniform speed state, the substation is supplied with power to the train. The output current of the NIC is negative, the output voltage is positive. And the negative impedance of the NIC output offsets the positive return cable impedance. According to the Kirchhoff voltage law (KVL), the relationship between output impedance and return cable impedance is described as

$$V_{\text{in}} - L \frac{di_L(t)}{dt} - u_{\text{out}} = 0 \quad (1)$$

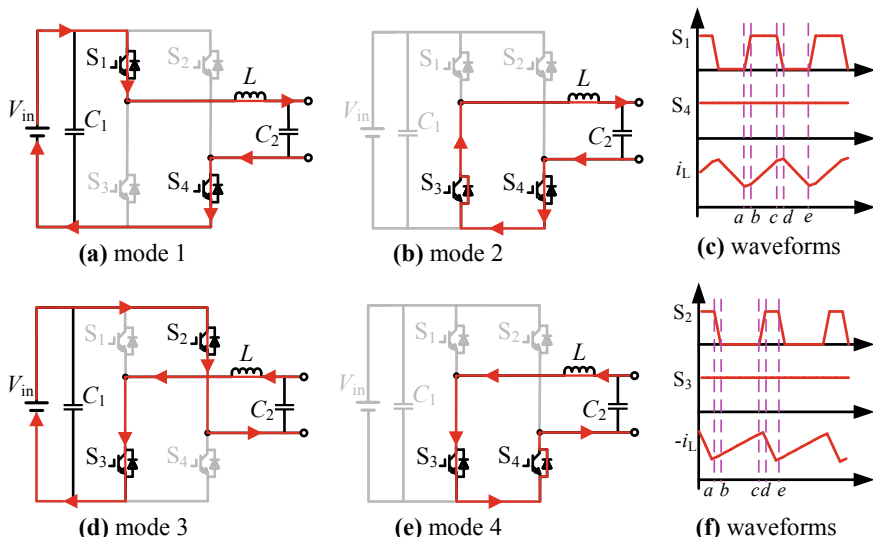
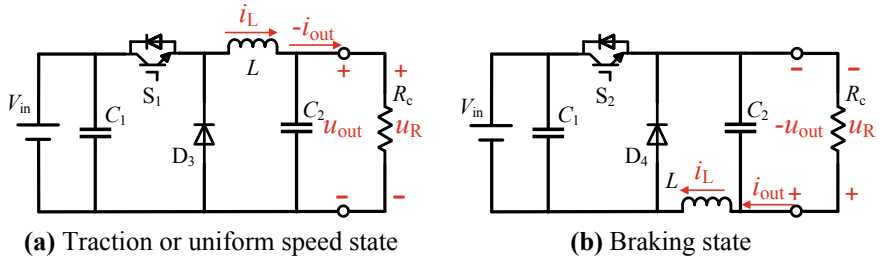


Fig. 6 Working modes of NIC



**Fig. 7** Equivalent circuit of NIC-TPSS

$$u_{\text{out}} = V_{\text{in}} - L \frac{di_L(t)}{dt} = u_R \quad (2)$$

$$R_{\text{out}} = \frac{u_{\text{out}}}{-i_{\text{out}}} \quad (3)$$

$$R_c = \frac{u_R}{i_{\text{out}}} = \frac{u_{\text{out}}}{i_{\text{out}}} = -R_{\text{out}} \quad (4)$$

When the train is in the braking state, the traction current returns to the catenary. The output current is positive, and the output voltage is negative. The negative impedance of the NIC output offsets the positive impedance of the return cable. The relationship between the output impedance and return cable impedance is similar to the traction state.

## 4 Simulation Results

To verify the feasibility of NIC-TPSS, a 2.5 MVA simulation model is performed. The simulation model uses four SUs to divide the track into 5 intervals. This paper mainly concerns on the effects of stray current and rail potential reduction in no-train running intervals. Therefore, simulation results of running rail potential and current are shown. The traction current waveform  $I_t$  is shown in Fig. 5. The main parameters of the simulation models are listed in Table 1.

Figure 8 shows the rail potential at the midpoint of each interval when the train is running from Interval I to Interval V. When the train is running in the traction state in Interval I, the maximum rail potential reduction of no-train intervals is 69.91%. When the train is running in the braking state in Interval V, the maximum rail potential reduction of other intervals is 69.34%. When the train is running in the uniform speed state, the maximum rail potential reduction is 96.31%. The rail potential of the traction and braking states are approximately three times than that of the uniform speed state. Thus, the effect of reducing the rail potential in the traction and braking states is more significant.

**Table 1** Simulation parameters

Implication	Parameters	Value
Input voltage of NIC	$V_{in}$	750 V
Input capacitance of NIC	$C_1$	470 $\mu\text{F}$
Output capacitance of NIC	$C_2$	940 $\mu\text{F}$
Filter inductor	$L$	0.1 mH
Traction substation voltage	$V_t$	1500 V
Return cable resistance	$R_c$	0.075 $\Omega/\text{km}$
Running rail resistance	$R_r$	0.019 $\Omega/\text{km}$
Catenary resistance	$R_l$	0.075 $\Omega/\text{km}$
Rail-to-ground resistance	$R_g$	15 $\Omega \text{ km}$
Length of each interval	$l$	1 km
The number of intervals	$n$	5

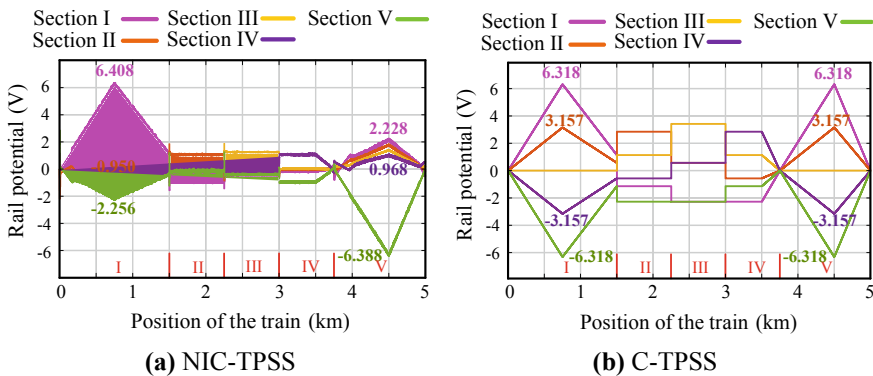
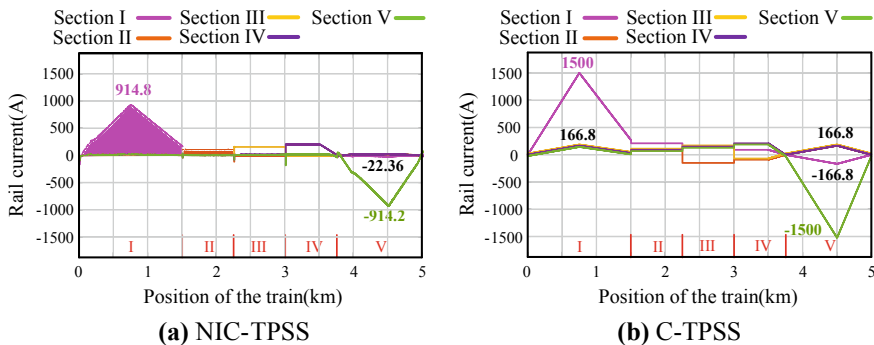
**Fig. 8** Comparison of rail potential between NIC-TPSS and C-TPSS

Figure 9 shows the rail current of each interval when the train is running from Interval I to V. Take the traction and braking states with large current as an example. When the train is running in Interval I in traction state, the maximum rail current of Interval II to Interval V is 23.19 A in NIC-TPSS. In the C-TPSS it is 166.8 A. When the train is running in Interval V in braking state, the maximum rail current of Interval I to Interval IV is -22.36 A in NIC-TPSS. In C-TPSS, the maximum absolute value of the rail current of Interval I to Interval IV is 166.8 A. This indicates that in the NIC-TPSS, the rail current of the no-train running intervals is reduced to approximately 14% of the C-TPSS's. Therefore, the voltage drops of running rails are decreased. The amount of stray current can be greatly reduced.



**Fig. 9** Comparison of rail current between NIC-TPSS and C-TPSS

## 5 Conclusion

NIC-TPSS is proposed to solve the stray current and rail potential problems in this paper. It can suppress the stray current defects in no-train intervals. In terms of rail potential, the NIC-TPSS has control effect in both the train interval and no-train intervals. When the train is in the traction or braking state, it greatly reduces the rail potential of the no-train intervals. These results show that NIC-TPSS can effectively solve stray current and rail potential problems.

**Acknowledgements** This work was supported by the Key Program of National Natural Science Foundation of China (Award Number: 51737001).

## References

1. Jin M, Mu L (2006) A novel on-line monitoring device of stray current in DC rail transit systems. In: 2006 International conference on power system technology. IEEE Press, Chongqing, pp 1–4
  2. Chen Z, Qin C, Zhang Y, Yang, X (2010) Application of a stray current monitoring system base upon virtual instrument. In: 2010 IEEE international conference on automation and logistics. IEEE Press, Hong Kong and Macau, pp 341–344
  3. Roman Š, Pavel S (2014) Analysis of stray currents for traction vehicles. In: 14th International conference on environment and electrical engineering. IEEE Press, Krakow, pp 265–270
  4. Zheng TQ, Yang X, You X (2016) DC auto-transformer based traction power supply system for urban rail transit. *Urban Rapid Rail Trans* 29(3):91–97 (in Chinese)
  5. Aylott PJ, Cotton I, Charalambous CA (2013) Impact and management of stray current on DC rail systems. In: 6th IET professional development course on railway electrification infrastructure and systems. IET, London, pp 210–218
  6. Wang P, Li B, Shi G, Zhou J (2017) Control of stray currents in pipeline system based on Melnikov theory. In: 36th Chinese control conference. IEEE Press, Dalian, pp 1207–1210

7. Niasati M, Gholami A (2008) Overview of stray current control in DC railway systems. In: 2008 International conference on railway engineering—challenges for railway transportation in information age. IET, Hong Kong, pp 1–6
8. Natarajan R, Imece AF, Popoff J, Agarwal K, Meliopoulos PS (2001) Analysis of grounding systems for electric traction. IEEE Trans Power Deliv 16(3):389–393 (2001)
9. Lee C (2005) Evaluation of the maximum potential rise in Taipei rail transit systems. IEEE Trans Power Deliv 20(2):1379–1384
10. Zaboli A, Vahidi B, Yousefi S, Hosseini-Biyouki MM (2017) Evaluation and control of stray current in DC-electrified railway systems. IEEE Trans Veh Technol 66(2):974–980

# Distributed Cooperative Absorption Method of Braking Energy for Urban Rail Transit



Shenyi Liu, Lei Wang, Ming Li, Yanqin Wang and Lei Zhang

**Abstract** The braking energy absorption of urban rail transit has always been an important issue. The use of supercapacitors for energy absorption is an efficient way. In order to make the supercapacitors of each substation better recover the braking energy, the traction substation is equivalent to the voltage source and the virtual impedance, and then the virtual impedance is configured to achieve the average distribution of braking current among the supercapacitor braking energy absorption devices in the adjacent traction substation, or as far as possible. For such voltages and resistances are uncertain, the multivariate online solution is difficult to achieve by traditional methods. In this paper, through the equivalent and simplification of the circuit topology, and the introduction of the genetic algorithm, the simultaneous solution of voltage and resistance is realized. Four different situations are analyzed.

**Keywords** Virtual impedance · Average current distribution · Genetic algorithm

---

S. Liu · L. Wang (✉)

School of Electrical Engineering, Beijing Engineering Research Center  
of Electric Rail Transportation, Beijing Jiaotong University, Beijing 100044, China  
e-mail: [leiwang@bjtu.edu.cn](mailto:leiwang@bjtu.edu.cn)

S. Liu

e-mail: [18126108@bjtu.edu.cn](mailto:18126108@bjtu.edu.cn)

M. Li · Y. Wang · L. Zhang

CRRC Tangshan Locomotive & Rolling Stock Co. Ltd., Beijing, China  
e-mail: [sjc-liming.ts@crrgc.cc](mailto:sjc-liming.ts@crrgc.cc)

Y. Wang

e-mail: [wangyanqin@crrgc.cc](mailto:wangyanqin@crrgc.cc)

L. Zhang

e-mail: [bjc-zhanglei.ts@crrgc.cc](mailto:bjc-zhanglei.ts@crrgc.cc)

## 1 Introduction

At present, the DC traction power supply system of urban rail transit is mainly composed of three parts: traction substation, traction network, and train. The running rail forms part of the traction power supply circuit, and the return line leads the rail backflow to the traction substation [1, 2].

The supercapacitor is a capacitor with a capacitance of several thousand Farads [3]. In the process of absorbing the braking energy from the supercapacitor, the energy distribution problem is of the greatest concern [4]. In order to make the supercapacitor of each substation recover braking energy better, the traction substation is equivalent to a voltage source and virtual impedance. The voltage and virtual impedance of the equivalent voltage source of the traction substation can be changed. These can be realized by controlling the supercapacitor absorption device with program algorithm.

During the braking process, the train will return the braking energy to the nearby traction substation [5]. Because of the impedance of the catenary between two substations, most of the energy is absorbed by the substation on both sides of the train. Therefore, when considering the equivalent topology at the time of braking, only the two traction substations on each side are considered. Based on this consideration, we can be equivalent to the following four situations:

1. Two traction substations on the left side of the train
2. One traction substation on each side of the train
3. Two left sides of the train and one traction substation on the right side
4. Two traction substations on the left and right sides of the train.

## 2 Simple Case Topology Analyses

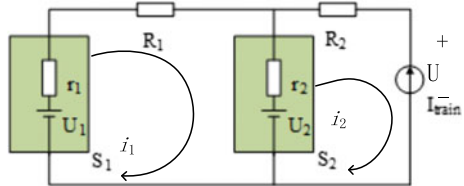
The first two cases of the above four cases only contain two substations, and the analysis is relatively easy.

### 2.1 *Two Substations on the Left Side*

The following is a detailed analysis of the situation of two substations on the left side. In this case, the current flow during train braking is shown in Fig. 1.

As shown in Fig. 1,  $U$  is the traction network voltage at the train;  $i_1$  and  $i_2$  are the loop currents of the circuit at the two traction substations  $S_1$  and  $S_2$  closest to the immediate position of the train,  $I_{\text{train}}$  is the braking current of the train and there is a relationship shown in Eq. (1):

**Fig. 1** Current flow when braking at two substations on the left



$$-i_2 = I_{\text{train}} \quad (1)$$

According to the loop current method, the following equation can be derived:

$$\begin{cases} r_1 i_1 + R_1 i_1 + (i_1 - i_2) r_2 = U_1 - U_2 \\ -i_2 = I_{\text{train}} \end{cases} \quad (2)$$

The train braking currents borne by  $S_1$  and  $S_2$  are  $-i_1$  and  $i_1 - i_2$ ,  
From the constraints, the solution is:

$$\begin{cases} i_1 = \frac{-I_{\text{train}} r_2 + U_1 - U_2}{r_1 + r_2 + R_1} \\ i_2 = -I_{\text{train}} \end{cases} \quad (3)$$

When the traction currents of the two traction substations are equal, i.e.:

$$-i_1 = i_1 - i_2 \quad (4)$$

From Eq. (4),

$$2i_1 = i_2 = -I_{\text{train}} \quad (5)$$

From Eqs. (3) and (5),

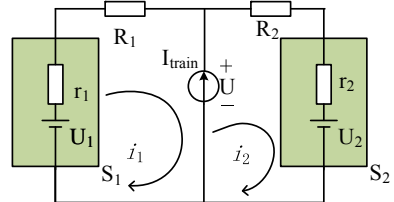
$$I_{\text{train}} = \frac{2(U_2 - U_1)}{r_1 - r_2 + R_1} \quad (6)$$

The above constraint is a complex linear system of equations with four variables ( $r_1, r_2, U_1, U_2$ ) and one external input  $I_{\text{train}}$ , which cannot be solved quickly online.

## 2.2 One Substation on Each of the Left and Right Sides

The current flow in this case during train braking is shown in Fig. 2.

**Fig. 2** Current flow when braking at one substation on the left and right sides



There is a relationship between them as shown in Eq. (7):

$$i_2 - i_1 = I_{\text{train}} \quad (7)$$

According to the loop current method, the following equation can be obtained:

$$(r_1 + R_1)i_1 + (R_2 + r_2)i_2 = U_1 - U_2 \quad (8)$$

The braking currents of the trains of  $S_1$  and  $S_2$  are, respectively,  $-i_1$ ,  $i_2$ , i.e.:

$$\begin{cases} I_{s1} = -i_1 \\ I_{s2} = i_2 \end{cases} \quad (9)$$

Therefore, when  $I_{s1} = I_{s2}$ , the following conditions should be satisfied:

$$-i_1 = i_2 \quad (10)$$

From Eqs. (8)–(10):

$$I_{\text{train}} = \frac{2(U_1 - U_2)}{r_2 - r_1 + R_2 - R_1} \quad (11)$$

### 3 Searching for the Optimal Solution by Genetic Algorithm

In this paper, the genetic algorithm (GA) is introduced to find the optimal solution for multi-variable equality.

GA is an adaptive stochastic method based on natural selection theory and biological genetic theory [6, 7]. The solution to the problem to be solved is regarded as a number of individuals in the population, each individual in the group is coded, expressed in a string form, and then the selection, intersection, and variation between individuals are simulated according to the fitness of the individual. The operation produces a new solution [8]. During the cyclic evolution of the population, the individual gradually evolves to the state of the approximate optimal solution, thus obtaining the optimal solution of the problem [9].

Power supply division	First Power Supply Zone				Second Power Supply Zone			Third Power Supply Zone			
	Dayangtian Station	Chenjianying Station	Dabegeng Station	Datangzi Station	Huochebei Station	Donghua Station	Dashuying Station	Juhuacun Station	Juhua Station	Kunmingdong Station	Maju Station
Station spacing (m)	1500	1002	2295	972	1537	1559	772	940	1526	2522	1532
Distance between traction substations (m)	1500	3297		972	3096		3238			4054	

**Fig. 3** Distribution chart of train section and traction substation

The station section and the traction substation distance are as shown in Fig. 3. It is assumed that the braking energy is recovered when the train is traveling at the Datangzi Station. As shown in Fig. 3, the distance from the train to the traction substation 1 is 4797 m, and the distance from the traction substation 2 is 3297 m.

The unit resistance of 60 kg rail used in the subway is  $0.018 \Omega/\text{km}$ , considering the backflow; two rails are connected in parallel. As a result,  $R_1 = 4.797 \times 0.018 \times 1.5 = 0.130 \Omega$  and  $R_2 = 3.297 \times 0.018 \times 1.5 = 0.089 \Omega$  brought these values into Eq. (6) to obtain:

$$I_{\text{train}} = \frac{2(U_2 - U_1)}{r_1 - r_2 + 0.13} \quad (12)$$

Equation (12) is the objective function of the GA. Since the GA is the minimum of the fitness function, the fitness function should be chosen as:

$$\text{fitness} = 1 / \left( I_{\text{train}} - \frac{2(U_2 - U_1)}{r_1 - r_2 + 0.13} \right) \quad (13)$$

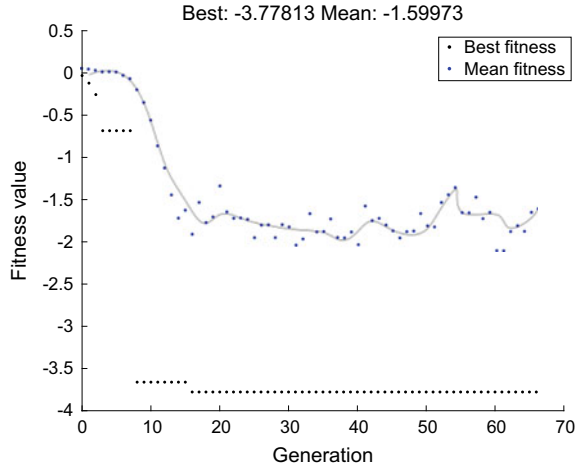
Assume that the braking current of the train is 20 A. The GA is simulated by the GA toolbox of MATLAB, after 66 generations of calculations, the values of the four variables to be sought are  $U_1 = 9.147 \text{ V}$ ,  $U_2 = -4.321 \text{ V}$ ,  $r_1 = 4.688 \Omega$ , and  $r_2 = 6.147 \Omega$ .

Bring in verification:

$$\frac{2(U_2 - U_1)}{r_1 - r_2 + 0.13} = \frac{2 * (-4.321 - 9.147)}{4.688 - 6.147 + 0.13} = 20.26$$

It is basically equal to the assumed train braking current. The relationship between the optimal solution and the number of iterations of each generation of the algorithm is shown in Fig. 4. It can be seen that the algorithm basically converges after 15 generations.

**Fig. 4** Optimal solution curve for each generation



In the situation of there is one substation on each side, it is assumed that the brake energy recovery is carried out when the train is driving at the Maju Station. As shown in Fig. 3, the distance from the train to the traction substation 1 is 2522 m, and the distance from the traction substation 2 is 1532 m.

Therefore,  $R_1 = 2.522 \times 0.018 \times 1.5 = 0.068 \Omega$  and  $R_2 = 1.532 \times 0.018 \times 1.5 = 0.041 \Omega$  brought values into Eq. (11) to obtain:

$$I_{\text{train}} = \frac{2(U_1 - U_2)}{r_2 - r_1 - 0.027} \quad (14)$$

The fitness function should be chosen as:

$$\text{fitness} = 1 / \left( I_{\text{train}} - \frac{2(U_1 - U_2)}{r_2 - r_1 - 0.027} \right) \quad (15)$$

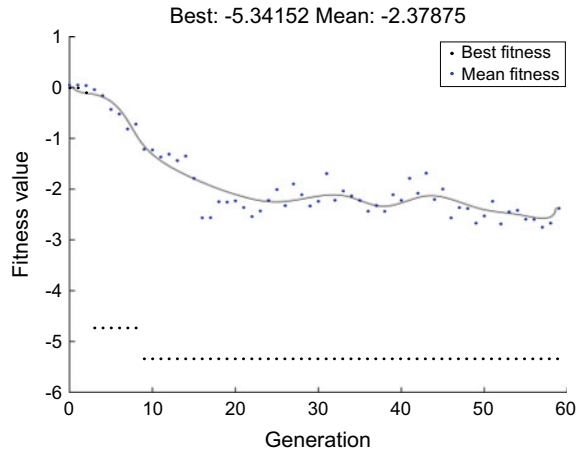
Assume that the braking current is 20 A, after 59 generations of calculations, the values of the four variables to be sought are  $U_1 = -2.401 \text{ V}$ ,  $U_2 = 12.368 \text{ V}$ ,  $r_1 = 26.508 \Omega$ , and  $r_2 = 25.071 \Omega$ .

Bring in verification:

$$\frac{2(U_1 - U_2)}{r_2 - r_1 - 0.027} = \frac{2 * (-2.401 - 12.368)}{26.508 - 25.071 - 0.027} = 20.15$$

The algorithm basically converges after 15 generations as shown in Fig. 5.

**Fig. 5** Optimal solution curve for each generation



## 4 Complexity Topology Analyses and GA Solving

### 4.1 Two Substations on the Left and One Substation on the Right Side

In this case, the current flow during the braking of the train is as shown in Fig. 6.

The relationship is shown in Eq. (15):

$$i_3 - i_2 = I_{\text{train}} \quad (16)$$

After Thevenin equivalence, the circuit of two traction substations on the left is shown as Fig. 7.

According to the deduction in the preceding section, in order to satisfy that the braking current of each substation is equal, the equivalent circuit should satisfy that  $\frac{1}{3}I_{\text{train}}$  flows through  $S_3$  traction substation and  $\frac{2}{3}I_{\text{train}}$  flows through  $S'_1$  substation, according to the loop current method, the following equations can be obtained:

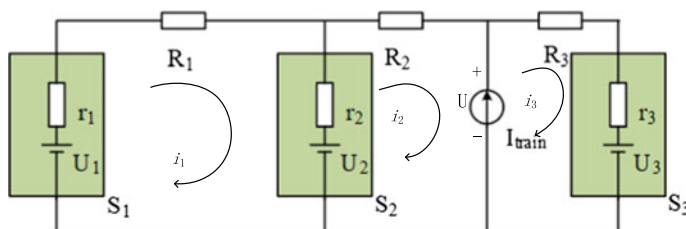
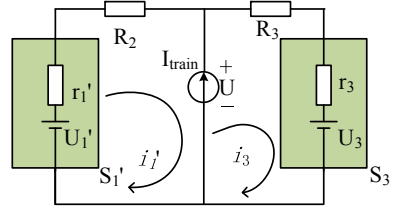


**Fig. 6** Current flow during train braking with two substations on the left and one substation on the right

**Fig. 7** Equivalent circuit diagram



$$(r'_1 + R_2)i'_1 + (R_3 + r_3)i_3 = U'_1 - U_3 \quad (17)$$

$$I_{\text{train}} = \frac{3(U'_1 - U_3)}{R_3 + r_3 - 2(r'_1 + R_2)} \quad (18)$$

At the same time, the equivalent two substations on the left should satisfy the following requirements:

$$\frac{2}{3}I_{\text{train}} = \frac{2(U_2 - U_1)}{r_1 - r_2 + R_1} \quad (19)$$

Suppose that the braking energy is absorbed when the train is running to the Dahegeng Station, as shown in Fig. 3. Thus,  $R_1 = 1.5 \times 0.018 \times 1.5 = 0.041 \Omega$ ,  $R_2 = 1.002 \times 0.018 \times 1.5 = 0.027 \Omega$ , and  $R_3 = 2.295 \times 0.018 \times 1.5 = 0.062 \Omega$ .

Assuming the braking current of the train is 30A. After 153 and 58 generations of calculations, the values of the variables to be sought are  $U'_1 = 8.849 \text{ V}$ ,  $U_3 = 56.111 \text{ V}$ ,  $r_3 = 3.604 \Omega$ ,  $r'_1 = 4.169 \Omega$ ,  $U_1 = 14.241 \text{ V}$ ,  $U_2 = 29.953 \text{ V}$ ,  $r_1 = 5.458 \Omega$ , and  $r_2 = 3.929 \Omega$

Bring in verification:

$$\frac{3(U'_1 - U_3)}{0.062 + r_3 - 2(r'_1 + 0.027)} = \frac{3 * (8.849 - 56.111)}{0.062 + 3.604 - 2 * (4.169 + 0.027)} = 30.001$$

$$\frac{2(U_2 - U_1)}{r_1 - r_2 + 0.041} = \frac{2(29.953 - 14.241)}{5.458 - 3.929 + 0.041} = 20.015$$

It is basically equal to the assumed train braking current. The algorithm basically converges after 100 and 20 generations as shown in Fig. 8.

## 4.2 Two Substations on Each Side

In this case, the current flow during the braking of the train is as shown in Fig. 9.

According to the above, the equivalent circuit should satisfy half of the braking currents on the left and right sides in order to satisfy the equal braking currents of

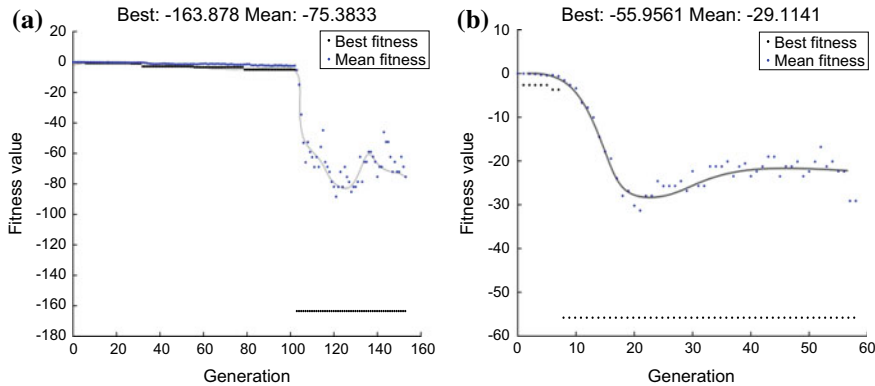


Fig. 8 Optimal solution curve for each generation

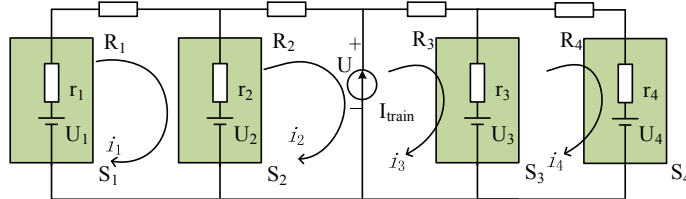


Fig. 9 Current flow direction during braking of two substations on the left and right sides

the substations. Based on this analysis, each side can be equivalent to a case that there are two substations on one side of the train.

Assume that the train is braking at the Dashuying Station for braking energy recovery. Thus,  $R_1 = 3.113 \times 0.018 \times 1.5 = 0.084 \Omega$ ,  $R_2 = 3.096 \times 0.018 \times 1.5 = 0.083 \Omega$ ,  $R_3 = 3.238 \times 0.018 \times 1.5 = 0.087 \Omega$ , and  $R_4 = 4.054 \times 0.018 \times 1.5 = 0.109 \Omega$ .

Assume the braking current at this time is 20 A, after 55 generations of calculations, the values of the four variables to be sought are  $U_1 = 4.047 \text{ V}$ ,  $U_2 = -9.816 \text{ V}$ ,  $r_1 = 5.527 \Omega$ ,  $r_2 = 8.373 \Omega$ ,  $U_3 = 4.205 \text{ V}$ ,  $U_4 = -2.929 \text{ V}$ ,  $r_3 = 7.332 \Omega$ , and  $r_4 = 8.858 \Omega$

Bring in verification:

$$\frac{2(U_2 - U_1)}{r_1 - r_2 + 0.084} = \frac{2 * (-9.816 - 4.047)}{5.527 - 8.373 + 0.084} = 10.038$$

$$\frac{2(U_4 - U_3)}{r_3 - r_4 + 0.109} = \frac{2 * (-2.929 - 4.205)}{7.332 - 8.858 + 0.109} = 10.069$$

Basically equal to the assumed train braking current. The algorithm basically converges after 15 generations as shown in Fig. 10.

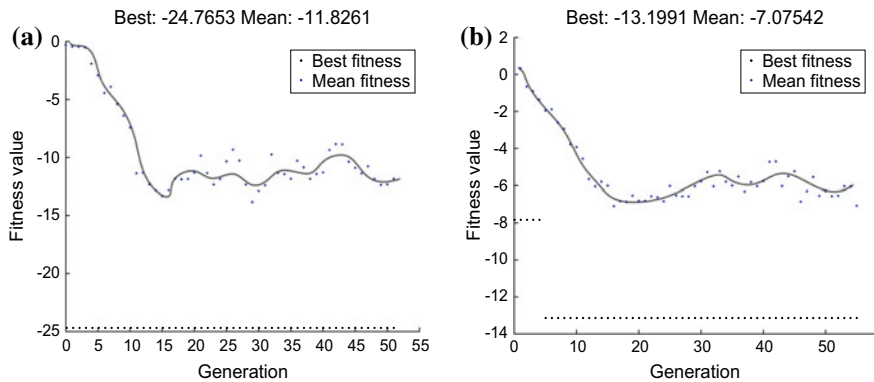


**Fig. 10** Optimal solution curve for each generation

## 5 Conclusions

Through the above analysis of four cases and the deduction of the conditions to be met, the braking current can be equally distributed as far as possible by changing the virtual impedance and controlling the voltage of traction substation in different cases.

The more complicated two cases can be transformed into a combination of two simple cases by the equivalent of the circuit, and the GA can be used to solve it multiple times. The application of GA makes it possible to solve multiple voltages and resistance values simultaneously online. It can be seen that, the optimal solution curves still have some fluctuation after the convergence of the algorithm. This is because the solution of voltage and resistance that satisfies the condition is not unique and the randomness of the GA makes the curve after convergence still fluctuates.

**Acknowledgements** This work is supported by National Key Research and Development Program Projects (2016YFB1200504-C-02).

## References

1. Huang X, Yoichi H, Tosiyuki H (2014) Bidirectional power flow control for battery supercapacitor hybrid energy system for electric vehicles with in-wheel motors. In: 2014 16th International power electronics and motion control conference and exposition (PEMC), pp 1078–1083
2. Wang Y (2017) Research and implementation of key technology of braking energy recovery system for off-highway dump truck, pp 3912–3917
3. Tang L, Wu L (2017) Research on the integrated braking energy recovery strategy based on super-capacitor energy storage. In: 2017 International conference on smart grid and electrical automation (ICSGEA), pp 175–178

4. Lu Y et al (2017) Status analysis of regenerative braking energy utilization equipment in urban rail transit. In: 2017 IEEE transportation electrification conference and expo, Asia-Pacific (ITEC Asia-Pacific), pp 85–90
5. Chen Z et al (2017) Study on Braking energy recovery efficiency of electric vehicles equipped with super capacitor. In: 2017 Chinese automation congress (CAC), pp 7231–7236
6. Pierini S, Aleardi M, Mazzotti A (2019) A method to attenuate genetic drift in genetic-algorithm optimizations: applications to analytic objective functions and two seismic optimization problems. *Geophysics* 84(2): R295–R310
7. Sana SS et al (2019) Application of genetic algorithm to job scheduling under ergonomic constraints in manufacturing industry. *J Ambient Intell Hum Comput* 10(5SI): 2063–2090
8. Campos RS. and L. Lovisolo. (2019) Genetic algorithm-based cellular network optimization considering positioning applications. *IET Commun* 13(7SI): 879–891
9. Jeon B et al (2019) Parametric optimization for energy calibration and gamma response function of plastic scintillation detectors using a genetic algorithm. *Nucl Instrum Methods Phys Res Sect A-Accel Spectrom Detect Assoc Equip* 930:8–14

# Lifetime Prediction Model of IGBT Modules in EMU



Benchao Zhu, Lei Wang , Lei Zhang, Ming Li and Yanqin Wang

**Abstract** The purpose of this paper is establishing the life prediction model of the IGBT modules in traction converter. Firstly, the failure mechanism of IGBTs and the existing life prediction models is described. Then, according to the special working condition of IGBTs inside TC, a bidirectional accelerated aging experiment was designed, and the experiment proved that loss on free-wheeling diode accelerated the IGBT aging. Then, the Weibull distribution was used to fit the data of accelerated aging experiment of IGBTs, and the parameters of the Weibull distribution were solved by the maximum likelihood method and particle swarm algorithm. Finally, the IGBT life prediction model is established according to the Weibull distribution obtained by this experiment.

**Keywords** Fault prediction · Fatigue model · Accelerated fatigue test · IGBT

---

B. Zhu · L. Wang

School of Electrical Engineering, Beijing Engineering Research Center of Electric Rail Transportation, Beijing Jiaotong University, Beijing 100044, China  
e-mail: [leiwang@bjtu.edu.cn](mailto:leiwang@bjtu.edu.cn)

B. Zhu

e-mail: [18126190@bjtu.edu.cn](mailto:18126190@bjtu.edu.cn)

L. Zhang · M. Li · Y. Wang

CRRC Tangshan Co., Ltd., Tangshan, Hebei, China  
e-mail: [sjc-zhanglei.ts@crrcgc.cc](mailto:sjc-zhanglei.ts@crrcgc.cc)

M. Li

e-mail: [sjc-liming.ts@crrcgc.cc](mailto:sjc-liming.ts@crrcgc.cc)

Y. Wang

e-mail: [wangyanqin@crrcgc.cc](mailto:wangyanqin@crrcgc.cc)

## 1 Introduction

Urban railway networks have spread across major cities in China, bringing huge economic benefits. Traction converter (TC) is the core equipment of electric multiple units (EMU) of a subway that provides traction power. IGBT is an important part of traction converter and is more likely to be fatigued than other components in converter. If the lifetime of IGBT was accurately estimated and the IGBT was timely maintained based on the estimated lifetime, the impact of IGBT failure on subway could be minimal.

The internal structure of IGBT is shown in Fig. 1. IGBT composed of multiple layers, each of which composed of different materials that have its own coefficient of thermal expansion (CTE). As presented in Table 1, the different CET will cause different expansion of materials inside the IGBT, and the different expansion between adjacent layers would generate thermal-mechanical stress when IGBT is repeatedly turn on and turn off, which resulting in temperature fluctuate in IGBT module. This thermal-mechanical stress causes plastic deformation and creep deformation of IGBT chips. These deformations cause IGBT to gradually age and eventually fail.

There are two main manifestations of IGBT aging [1]:

First, the solder layers between the chip and the copper layer, the copper layer and the baseplate, as well as the electrical terminals and the copper layer appear hollow and layered. This mainly results from creep deformation. Gao et al. [2] points out that solder layers would crack under the action of cyclic thermal-mechanical stress, and the aging of the solder layer will increase the thermal resistance of IGBT, which will lead to higher thermal stress endured by IGBT, which will accelerate the aging of the solder layer.

Second, the bond wires that connect silicon chips with copper layers lift off and break away from pad because of plastic deformation. When part of bond wires lift off, the remains are under more severe pressure of the current, which cause more wires to lift off [3, 4].

The aging state of IGBT could be observed by some precursor parameters such as threshold voltage, transconductance, and collector-emitter ON voltage ( $V_{ceo}$ ) [5]. Wei et al. [6] considered that the bond wire failure if  $V_{ceo}$  increased by 5% and the solder layer failure if  $R_{th}$  increased by 20% in the aging experiment.

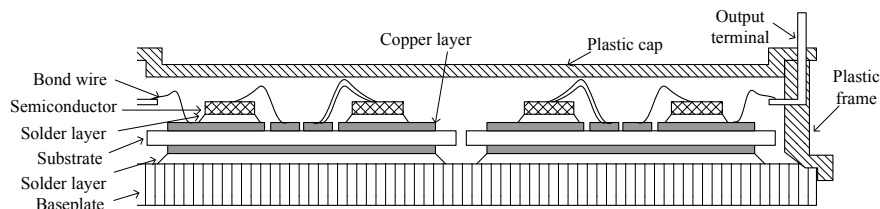


**Fig. 1** Standard IGBT structure

**Table 1** IGBT module material and CTE for each layer

Layer	Material	CTE/(ppm/°C)
Bond wire	Al	22
Semiconductor	Si	3
Solder layer	SnAg	28
Upper copper layer	Cu	17.5
Substrate	Al <sub>2</sub> O <sub>3</sub>	7
Lower copper layer	Cu	28
Solder layer	SnAg	17.5
Baseplate	Cu	17.5

Life prediction of IGBT module refers to the life evaluation of power module under a certain working condition by using life prediction model, that is, the expected residual life value of the module is evaluated through the task curve of the module [7].

IGBT lifetime models can be divided into analytical models and physical models. Analytical models can be obtained by fitting the aging experimental data. In order to obtain expressions of physical models, the aging experimental data and material strain analysis results need to analyse simultaneously.

The commonly applied analytical model is Lesit model [8]. The Lesit model regards the swing of junction temperature ( $\Delta T_j$ ) and average junction temperature ( $T_m$ ) as important parameters determining the aging velocity of IGBTs and introduces Arrhenius factor to express the influence of average operating temperature on the number of cycles to failure. Its expression is given by

$$N_f = A(\Delta T_j)^\alpha e^{\frac{Q}{RT_m}}, \quad (1)$$

with  $R$  is the gas constant (8.314 J/mol K) and  $Q$  is the activation energy equaling to 0.8 eV.  $A$  and  $\alpha$  are obtained by fitting experimental data.

In order to obtain the lifetime model of IGBTs in TC, first, this paper designed a bidirectional accelerated failure test because of the specific work condition of IGBT in TC. Then, the Weibull distribution was used to fit the experimental data, for obtaining the IGBT aging distribution. Finally, the lifetime model of IGBT is derived from the Weibull distribution.

## 2 Bidirectional Accelerated Failure Test Design

Accelerated failure tests (AFT) are usually used to obtain data to study the failure mechanism of IGBTs and to estimate the residual lifetime because the design lifetime of IGBTs is generally more than 20 years. The accelerated failure test

performed in different conditions may cause the failure of IGBTs in a different mechanism. Although there is a lot of research and verification on how to obtain an accurate lifetime model, there is still no general lifetime model suitable for IGBTs in different applications.

In conventional accelerated failure test, the effect of free-wheeling diode (FWD) loss in the aging of IGBT module is not considered generally. Because in general, the IGBT modules under test are experienced higher temperature stress than the FWDs, and the losses of IGBTs are dominant in the IGBT module [4, 9]. Therefore, the accelerated failure test mainly focuses on the influence of the current flow through IGBTs.

But for an IGBT module in a TC used in EMU, the loss generated by the FWD is not negligible. Figure 2 is the topology of TC in EMU. In Fig. 2,  $Q_1-Q_6$  are IGBTs, and  $D_1-D_6$  are FWDs.  $QB$  and  $RB$  constitute the brake energy consumption branch. The  $QB$  and  $DB$  are not used with high frequency, so this paper only considers the aging process of  $Q_1-Q_6$  and  $D_1-D_6$ .

In the EMU braking, electric braking is generally preferred, and air braking is added when electric braking cannot meet the requirements [10]. Electric braking energy has the characteristics of high amplitude and short time and has a great impact on the TC. The power of braking mainly flows through FWD instead of the IGBT, and the loss on FWD will result in the temperature of the IGBT module rapid increase.

Therefore, the thermal stress generated by the current flowing through the FWD cannot be ignored in the design of accelerated failure test.

So, this paper designed a bidirectional accelerated failure test (BAFT) with topology as Fig. 3. In Fig. 3,  $G_1-G_5$  is auxiliary GTO,  $I_1$  is a fatigue current, and  $I_2$  is used to measure  $V_{ceo}$ . There is a linear relationship between junction temperature ( $T_j$ ) and  $V_{ceo}$  [11], which will not change even if the bond wires fail.  $R$  and  $C$  constitute the absorption branch. When  $G_1$  and  $G_5$  turn on,  $I_1$  flows through IGBT. When  $G_2$  and  $G_4$  turn on,  $I_1$  flows through the FWD. The function of  $G_3$  is to provide the free-wheeling route of  $I_1$ .

The ambient temperature of the test is approximately 25 °C. The frequency of  $I_1$  is 12 s with 48% duty cycle. The number of cycles of  $I_1$  flowing through IGBT or FWD is equal. The  $V_{ceo}$  of the IGBT was measured regularly to detect the aging state [12]. So, the cumulative failure rate  $F$  is defined as below:

**Fig. 2** Traction converter topology

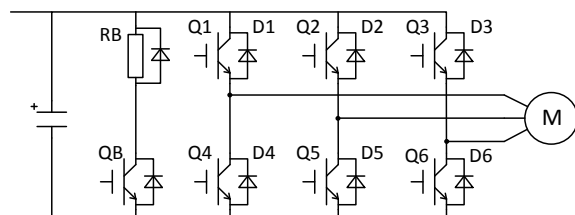
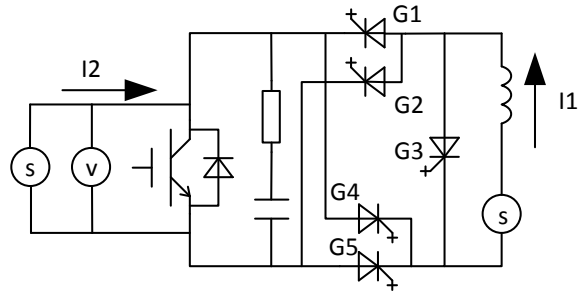


**Fig. 3** Topology of bidirectional accelerated fatigue test



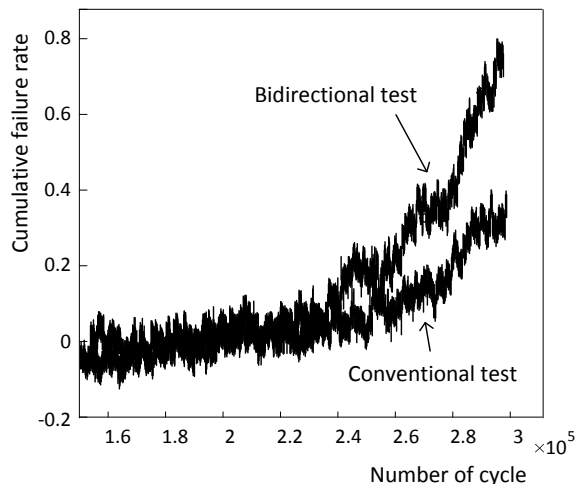
$$F = 5 \times \frac{V_{ceo} - V_{ceo0}}{V_{ceo0}} \quad (2)$$

where  $V_{ceo0}$  is the initial  $V_{ceo}$  of a new IGBT module. When  $V_{ceo} = 1.2V_{ceo0}$ , the  $F$  is equal to 1.

The test was carried out at  $I_1$  equaling to 1500 A. And in order to verify the FWD loss has the effect of accelerating IGBT aging, another test that  $I_1$  only flow through the IGBT as conventional accelerated failure test in the same condition is performed. The cumulative failure rate curve obtained is shown in Fig. 4, where the horizontal axis is the number of cycles, and the vertical axis is the cumulative failure rate.

It can be seen from Fig. 4 that after  $2.2 \times 10^5$  cycles, the cumulative failure rate of IGBT in the bidirectional test is higher than that in the conventional test, and the difference between the cumulative failure rate is increasing with the number of cycles ascending. So, the FWD loss indeed accelerates the aging of the IGBT module.

**Fig. 4** Cumulative failure rate curves obtained under 1500 A



### 3 IGBT Lifetime Distribution

In order to intuitively describe the relationship between the cumulative failure rate and the number of experimental cycles, the experimental data need to be fitted to obtain an analytical model, and the analytical model of IGBT aging is also the basis for the establishment of a lifetime estimation model.

Weibull distribution is usually used to describe the aging status of devices in reliability analysis and lifetime estimation. The Weibull distribution, introduced by Weibull, is commonly used for modeling systems with monotone failure rates. But systems that have failure rates curve as bathtub shape and unimodal shape are common in reliability analysis. In order to improve the generality of Weibull distribution, some improved Weibull distributions are proposed. For example, [13] introduced the exponentiated Weibull distribution; log-Weibull distribution is taken as lifetime distribution in [14, 15] present the generalized modified Weibull (GMW) distribution. These distributions not only can model bathtub and unimodal failure rates but also can provide sufficient support for monotone failure rates. These distributions improve the generality of the distribution model by adding parameters but make the distribution more complex and the parameter fitting more difficult.

This paper only fit the Weibull distribution with two parameters by maximum likelihood method. The probability density function of Weibull distribution is given by (3), and the cumulative distribution function of that is given by (4).

$$f(x; \lambda, k) = \begin{cases} \frac{k}{\lambda} \left(\frac{x}{\lambda}\right)^{k-1} e^{-\left(\frac{x}{\lambda}\right)^k}, & x > 0 \\ 0, & x \leq 0 \end{cases} \quad (3)$$

$$F(x) = \begin{cases} 1 - e^{-\left(\frac{x}{\lambda}\right)^k}, & x > 0 \\ 0, & x \leq 0 \end{cases} \quad (4)$$

If the cumulative failure rate  $F$  and the experimental data ( $x = x_1, x_2, \dots, x_n$ ) obey Weibull distribution, the logarithmic likelihood function is

$$H(\lambda, k) = \ln L(\lambda, k) = N \ln \frac{k}{\lambda} + (k-1) \sum_{i=1}^N \ln \frac{x_i}{\lambda} - \sum_{i=1}^N \left(\frac{x_i}{\lambda}\right)^k \quad (5)$$

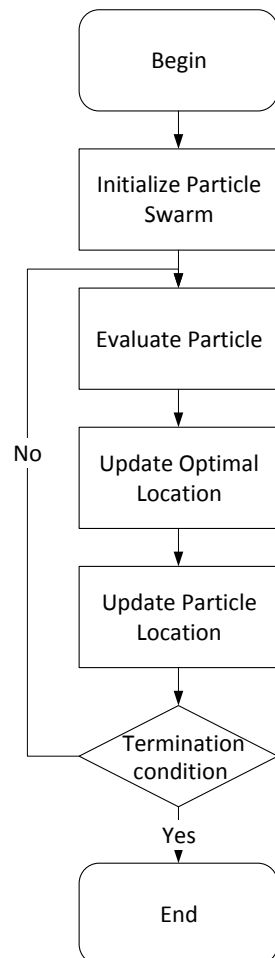
Take the first derivative with respect to the parameter  $\lambda$  and  $k$ , respectively, and set the first derivative to be zero, then the simultaneous equations can be written as

$$\begin{cases} \frac{\partial H(\lambda, k)}{\partial \lambda} = -\frac{N}{\lambda} - N \frac{k-1}{\lambda} + \sum_{i=1}^N k \left(\frac{x_i}{\lambda}\right)^{k-1} \frac{x_i}{\lambda^2} = 0 \\ \frac{\partial H(\lambda, k)}{\partial k} = \frac{N}{k} + \sum_{i=1}^N \ln \frac{x_i}{\lambda} - \sum_{i=1}^N \left(\frac{x_i}{\lambda}\right)^k \ln \frac{x_i}{\lambda} = 0 \end{cases} \quad (6)$$

Formula (6) is a system of nonlinear equations, which can be solved by Newton Iteration method or by some intelligent optimization algorithms. Common intelligent optimization algorithms include genetic algorithm, particle swarm algorithm, simulated annealing algorithm, ant colony algorithm, neural network algorithm, and so on. Particle swarm optimization (PSO) has a simple principle, few parameters, and easy implementation. It has no complex coding and genetic operation of a genetic algorithm. Compared with the ant colony algorithm, PSO can share information about the optimal solution found globally. The equation of Formula (6) is simple, and the dimension is low. It avoids the difficulty of convergence analysis of PSO [16]. Therefore, this paper uses PSO to solve Formula (6).

Figure 5 is the flowchart of PSO. The particle swarm consists of 20 particles, each composed of three two-dimensional vectors, namely

**Fig. 5** Flowchart of PSO



Current position:  $p_i = (p_{i1}, p_{i2}) = (\lambda_i, k_i)$ ;  
Optimal position:  $pb_i = (pb_{i1}, pb_{i2})$ ;  
Velocity:  $v_i = (v_{i1}, v_{i2})$ .

All particles in particle swarm share the best optimal position, written as  $pb_g$ .  
The fitness function is defined as

$$\text{fitness} = \exp \left[ \left( \frac{\partial H(\lambda_{i\text{new}}, k_{i\text{new}})}{\partial \lambda} \right)^2 + \left( \frac{\partial H(\lambda_{i\text{new}}, k_{i\text{new}})}{\partial k} \right)^2 \right] \quad (7)$$

$\lambda_{i\text{new}}$  and  $k_{i\text{new}}$  represent the latest observation values.

The way to change the velocity and position of the particle according to Eqs. (8) and (9)

$$v_{id} = v_{id} + c_1 \cdot \text{rand1}() \cdot (pb_{id} - p_{id}) + c_2 \cdot \text{rand2}() \cdot (pb_{gd} - p_{id}) \quad (8)$$

$$x_{id} = x_{id} + v_{id} \quad (9)$$

In Eq. (8), `rand1()` and `rand2()` are the random functions that return a value between 0 and 1, but the two functions use a different seed to produce random value.  $c_1$  and  $c_2$  are acceleration constant and  $c_1 = c_2 = 2$ . The termination condition of this algorithm is  $\text{fitness} < 1 \times 10^{-3}$ .

Performed the bidirectional accelerated test on the condition that  $I_1$  equals to 900, 1200, and 1500 A separately to obtain experimental data. Then, programming in MATLAB to run this algorithm, get the lifetime distribution model on the condition that  $I_1$  equals to 900, 1200, and 1500 A as (10), (11), and (12), respectively.

$$F_{900}(x) = 1 - e^{-\left(\frac{x}{508734}\right)^{7.95}} \quad (10)$$

$$F_{1200}(x) = 1 - e^{-\left(\frac{x}{918312}\right)^{5.78}} \quad (11)$$

$$F_{1500}(x) = 1 - e^{-\left(\frac{x}{317212}\right)^{12.45}} \quad (12)$$

## 4 IGBT Lifetime Estimation Model

The aging test only adjusts the amplitude of  $I_1$  and keeps its frequency constant. So, the junction temperature swings of IGBT in the aging test can be reflected by the amplitude of  $I_1$ . Therefore, based on the Lesit model as (1), the influence of junction temperature swings on the number of cycles to failure can be expressed by the current of IGBT as below:

$$N_f = f(I_1) e^{\frac{Q}{kT_m}} \quad (13)$$

The mean of Weibull distribution, also called mean time to failure (MTTF), is given by

$$\bar{T} = \eta \cdot \Gamma\left(\frac{1}{\beta} + 1\right) \quad (14)$$

with  $\Gamma$  is the gamma function. According to (14), the MTTFs of 900 A, 1200 A, and 1500 A are 851,462, 479,230, and 304,990, respectively.

According to the aging distribution model of IGBT obtained from three experiments, the analytical model can be obtained by fitting MTTFs of the three Weibull distributions. Using a quadratic function to fit the parameters, the lifetime prediction model of IGBT is

$$N_f = (2.375 \times 10^{-14} \cdot I_1^2 - 7.666 \times 10^{-11} \cdot I_1 + 6.814 \times 10^{-8}) \cdot e^{\frac{7.8 \times 10^4}{8.314 \cdot T_m}} \quad (15)$$

Taking Shenzhen Metro as an example, the annual average temperature in Shenzhen is 23 °C, and the  $I_1$  in a single year is 692 A in the record. So, the expected life of the train is 1,517,123 cycles. A train normally has 204 power cycles per day. Therefore, the life expectancy of a train under that condition is 25 years.

## 5 Conclusions

In this paper, a special accelerated aging test strategy is proposed for the IGBT module used in traction converter. Then, a lifetime prediction model of IGBT is proposed based on the experimental data. The availability of the life model is verified by the actual data of the Shenzhen Metro.

**Acknowledgements** This work is supported by the National Key Research and Development Program of China (No. 2016YFB1200504-C-02).

## References

1. Ciappa M, Castellazzi A (2007) Reliability of high-power IGBT modules for traction applications. In: IEEE, pp 480–485
2. Gao B, Yang F, Chen M et al (2018) Thermal lifetime estimation method of IGBT module considering solder fatigue damage feedback loop. Microelectron Reliab 82:51–61
3. Chen M, Hu A, Liu B (2011) Failure mechanism and life prediction model analysis of insulated gate bipolar transistors. J Xi'an Jiaotong Univ 45:65–71 (in Chinese)
4. Zheng T, Huang M, Liu Y, Zha X (2018) Reliability model of bond wire fatigue for IGBT in MMC with system redundancy consideration. Microelectron Reliab 88–90:1164–1167

5. Patil N, Das D, Goebel K, Pecht M (2008) Identification of failure precursor parameters for Insulated Gate Bipolar Transistors (IGBTs). In: IEEE pp 1–5
6. Wei L, Chen M, Li R, Wang X, Xu S (2015) Failure mechanism analysis of IGBT under aging test conditions. *Proc Chin Soc Electr Eng* 35:5293–5300 (in Chinese)
7. Fang X, Zhou L, Yao D, Du X, Sun P, Wu J et al (2014) Review of IGBT module life prediction model. *J Power Supply* 2014:14–21 (in Chinese)
8. Durand C, Klingler M, Coutellier D, Naceur H (2016) Power cycling reliability of power module: a survey. *IEEE Trans Device Mater Reliab* 16:80–97
9. Ma K, Liserre M, Blaabjerg F, Kerekes T (2015) Thermal loading and lifetime estimation for power device considering mission profiles in wind power converter. *IEEE Trans Power Electr* 30:590–602
10. Xu A (2009) Research on regenerative braking energy utilization technology of urban rail transit. Nanjing University of Aeronautics and Astronautics, Jiangsu. <https://doi.org/10.7666/d.d076127>. (in Chinese)
11. Gachovska TK, Tian B, Hudgins JL, Qiao W, Donlon JF (2015) A real-time thermal model for monitoring of power semiconductor devices. *IEEE Trans Ind Appl* 51:3361–3367
12. Smet V, Forest F, Huselstein J, Rashed A, Richardeau F (2013) Evaluation of  $V_{ce}$  monitoring as a real-time method to estimate aging of bond wire-IGBT modules stressed by power cycling. *IEEE Trans Ind Electron* 60:2760–2770
13. Mudholkar GS, Srivastava DK (1993) Exponentiated Weibull family for analyzing bathtub failure-rate data. *IEEE Trans Reliab* 42:299–302
14. Jiang R, Wang T (2013) Log-Weibull distribution as a lifetime distribution. In: IEEE; pp 813–816
15. Bagheri SF, Bahrami Samani E, Ganjali M (2016) The generalized modified Weibull power series distribution: theory and applications. *Comput Stat Data Anal* 94:136–160
16. Liu J (2009) The basic theory of particle swarm optimization and improvement. In: Central South University, p 120 (in Chinese)

# Research on Medium Voltage MMC Fault-Tolerant Optimized Control Strategy



**Qinyue Zhu, Qingwen Fan, Xitang Tan, Zhaoyang Li,  
Wei Dai and Dabo Xie**

**Abstract** Sub-module (SM) open-circuit fault is a common type of fault in modular multilevel converter (MMC). To solve the problem of low utilization rate and limited fault-tolerant capability of SMs in existing SM fault-tolerant control strategies, the improved neutral-point shift fault-tolerant control strategy is studied in this paper. With the segmentation modulation idea, the phase voltage vectors are reconstructed through the neutral-point shift control in different stages to achieve symmetric output of line voltages after the fault. Due to the increasing of the circulating current after fault-tolerant, the harmonic extraction is performed on the circulating current and suppressed by PR controller. By designing the switching controller to correct the corresponding modulation wave parameters during different stages, the optimized suppression of the circulating current is completed, so that the MMC system has better running results under the fault-tolerant operation. Finally, the effectiveness and feasibility of the optimized control strategy are verified by simulation and experiment.

**Keywords** Modular multilevel converter · Sub-module fault · Fault-tolerant control · Circulating current suppression

## 1 Introduction

Modular multilevel converter (MMC) has been widely used in fields of high voltage direct current transmission, traction power supply and high-power AC drive. However, a large number of cascading sub-modules (SMs) also pose a safety hazard. With the appearance of sub-module (SM) faults, the control objectives become more complicated. It is necessary to consider the problems of SM utilization, difficulty in control, and circulating current suppression after fault-tolerant control [1].

---

Q. Zhu · Q. Fan · X. Tan (✉) · Z. Li · W. Dai · D. Xie  
School of Electronics and Information Engineering, Tongji University,  
Shanghai 201804, People's Republic of China  
e-mail: [xtan@tongji.edu.cn](mailto:xtan@tongji.edu.cn)

MMC non-redundancy SM fault-tolerant control methods do not increase the cost of system and only need to adjust modulation strategy after SM fault. Therefore, they have received wide attention in recent years. So far, the researches on SM non-redundancy fault-tolerant control strategies have focused on energy balance [2], zero-sequence voltage injection [3] and neutral-point shift control [4]. Among them, neutral-point shift control has more obvious effect. The traditional neutral-point shift control reconstructs phase voltage vectors by moving original neutral-point position after fault under asymmetrical maximum output of three-phase voltage. The related algorithm is complex in this method. Adjustment parameters need to be stored after offline calculation and then obtained after table look-up. Based on this, Ref. [4] adopts partial symmetrical-bypass method. The voltage vectors are reconstructed by moving neutral-point through the direction of fault phase voltage vector. Although the algorithm in this method is simpler, there are still some shortcomings such as the failure of achieving SM maximum utilization and limited number of fault-tolerant SMs.

When faulty SM is isolated and the above control is input, stable output can be maintained. However, due to the asymmetrical structure, capacitor voltage fluctuation is further aggravated, thereby causing an increase in circulating current and device loss [5]. In view of circulating current suppression of asymmetric system, the strategies mainly include superimposing harmonic suppressor in control [6], bridge arm current decoupling control [7] and adjusting capacitor voltage while changing switching frequency [8]. But all of the above strategies still have some shortcomings such as long dynamic process of suppression and complicated control structure.

In this paper, for MMC system under Phase Disposition PWM (PDPWM) [5], an improved neutral-point shift fault-tolerant control strategy is proposed to solve the problem of limited fault-tolerant capability. On this basis, the circulating current optimized strategy is designed to suppress circulating current after fault-tolerant. Finally, the effectiveness of proposed strategies is verified by simulation and experiment.

## 2 Improved Neutral-Point Shift Fault-Tolerant Control

### 2.1 *MMC Basic Principles*

The typical MMC main circuit and SM topology are shown in Fig. 1. AC side output is closely related to the output voltage of SMs. In each SM, output voltage can be made zero or capacitor voltage by controlling the switching tubes T1 and T2. In order to maximize DC side voltage and maintain its stability, the number of turn-on SMs of each phase is always N. The desired output can be obtained by changing the distribution of turn-on SMs on the upper and lower bridge arms.

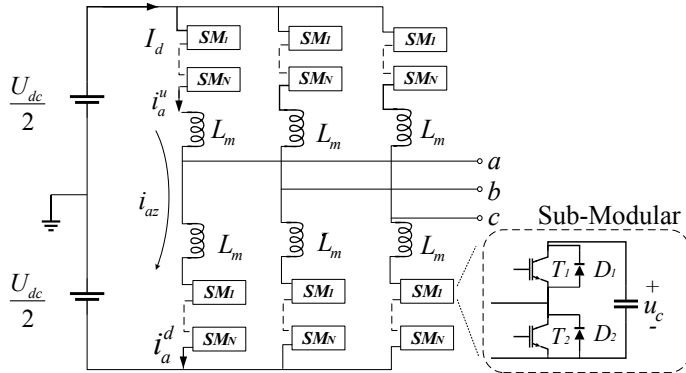


**Fig. 1** MMC main circuit and its sub-modular structure

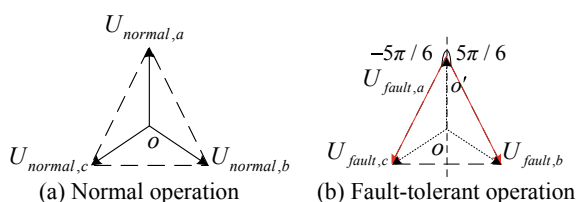
## 2.2 Improved Neutral-Point Shift Fault-Tolerant Control Strategy

Under MMC system normal operation, the modulation signal is expressed in Eq. (1). Where  $S_{\text{normal},j}$  ( $j = a, b, c$ ) is the modulation wave,  $\theta_{\text{normal},j}$  is its initial phase,  $m$  is the modulation ratio,  $\omega$  is the angular frequency of output voltage. For the convenience of description, we assume that in normal operation  $\theta_{\text{normal},a}$ ,  $\theta_{\text{normal},b}$  and  $\theta_{\text{normal},c}$  are equal to 0,  $-2\pi/3$  and  $2\pi/3$ , respectively. Phase voltages are symmetric outputs under PDPWM modulation. The amplitude is the same, and the initial phase differs by  $2\pi/3$  sequentially. The phase voltage vector diagram is shown in Fig. 2a.

$$S_{\text{normal},j} = m \sin(\omega t + \theta_{\text{normal}}^j) \quad (1)$$

When SM faults occur, fault phase voltage output capability decreases as the number of fault SM increases while non-fault phase voltage output capability is unchanged. According to neutral-point shift control principle, the reconstruction of modulation waves after fault is essentially corresponding to the adjust of modulation ratios and initial phases aiming at output line voltages to be constant and as large as possible. The neutral-point shift in fault phase direction is achieved by

**Fig. 2** Vector diagram of phase voltage



continuously reducing modulation ratio [5]. This fault-tolerant method can complete symmetrical output of line voltages after fault. When the number of faulty SMs in single bridge arm gradually increases to  $N/2 - 1$  ( $N$  is the SM number per bridge arm), the decreasing fault phase modulation ratio makes MMC system unable to achieve fault-tolerant [9].

In order to further improve SM utilization rate and fault-tolerant capability, simplify the algorithm, the basic idea of neutral-point shift control proposed in this paper is as follows. When SM fault occurs and faulty SM is isolated, MMC adopts the segmented method to output different phase voltage in different stages. Correspondingly, the symmetric output of line voltages is achieved by neutral-point shift control in different stages. Without loss of generality, the following takes an SM open-circuit fault on a-phase upper bridge arm as an example to illustrate the fault-tolerant control strategy proposed in this paper. The principle is the same no matter where SM fault occurs.

As shown in Fig. 3, when faulty SM is isolated, its maximum amplitude of phase voltage is reduced to  $U_{\text{fault},a}^{\max}$ . In this way, each basic period of phase voltage can be divided into two stages, named limited stage  $T_{\text{limited}}$  and uptime stage  $T_{\text{uptime}}$ . In two different stages, the control method is described as follows. ① During  $T_{\text{limited}}$ : Firstly, let a-phase voltage output a limited and fixed amplitude  $U_{\text{fault},a}^{\max}$ . Then, the neutral-point position can be moved along the direction of a-phase voltage vector. At this time, the length of fault phase voltage vector is adjusted to zero, and the neutral-point position will be moved from “o” to the vertex of a-phase voltage vector “o”. Thus, line voltage vectors unchanged by reconstructing b-phase and c-phase voltage vectors. ② During  $T_{\text{uptime}}$ : The output phase voltages of three-phase are the same as those in normal operation. Accordingly, the neutral-point position does not move.

According to the above, reconstruction after fault includes the following steps.

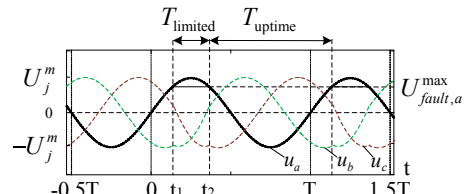
### (1) Calculation of Maximum Output Phase Voltage of Fault Phase

Maximum output phase voltage of fault phase can be expressed in Eq. (2) after fault.

$$U_{\text{fault},a}^{\max} = (N - 2n_{\text{fault}}) \cdot U_{\text{dc}} / 2N \quad (2)$$

where  $n_{\text{fault}}$  is the number of faulty SMs in a-phase.

**Fig. 3** Phase voltage diagram



## (2) Determination of Different Modulation Stages in Each Basic Period

As shown in Fig. 3, it is assumed that in a basic period  $[0 \sim T]$  of output phase voltage, the start and the end time of the limited stage are  $t_1$  and  $t_2$ , respectively. According to the sinusoidal variation law of output phase voltage,  $t_1$  and  $t_2$  can be expressed as:

$$\begin{aligned} t_1 &= \arcsin\left(\frac{U_{\text{fault},a}^{\max}}{U_{\text{normal},a}^m}\right)/\omega, \\ t_2 &= \left[\pi - \arcsin\left(\frac{U_{\text{fault},a}^{\max}}{U_{\text{normal},a}^m}\right)\right]/\omega \end{aligned} \quad (3)$$

where  $U_{\text{normal},a}^m$  is the voltage amplitude during normal operation.

Therefore, in each period of the output voltage,  $T_{\text{limited}}$  refers the stage  $[t_1, t_2]$ ,  $T_{\text{uptime}}$  refers the stage  $[0, t_1] \cup [t_2, T]$ .

## (3) Calculation of Phase Voltage Amplitude and Initial Phase of Non-fault Phases

After determining the specific stages of segmented output, phase voltages are the same as those in normal operation during  $T_{\text{uptime}}$ . During  $T_{\text{limited}}$ , the reconstructed phase voltages maintain the vector triangle unchanged. When a-phase limiting outputs  $U_{\text{fault},a}^{\max}$ , the length of a-phase voltage vector is zero. So, from Fig. 2b, the amplitude and initial phase of non-fault phase voltages after fault can be expressed as Eqs. (4) and Eq. (5).

$$U_{\text{fault},j}^m = \sqrt{3}U_{\text{normal},j}^m \quad (4)$$

$$\theta_{\text{fault},b} = -5/6\pi, \theta_{\text{fault},c} = 5/6\pi \quad (5)$$

where  $U_{\text{fault},j}^m$  and  $\theta_{\text{fault},j}$  are the amplitude and initial phase of non-fault phases voltages after fault, respectively.

Since there is a DC bias voltage  $U_{\text{fault},a}^{\max}$  in fault phase during  $T_{\text{limited}}$ , the same DC bias should be present in non-fault phase voltages to ensure three-phase symmetry.

## (4) Calculation of Fault-Tolerant Initial Phase

Due to the randomness of fault occurrence, it is necessary to determine the initial phase of modulation wave at the start of fault-tolerant. We need to sample phase voltage of a-phase and calculate the initial phase at fault-tolerant start time:

$$\theta_{\text{fault}} = \arcsin(u_{\text{fault},a}/U_{\text{normal},a}^m), t_{\text{fault}} = \theta_{\text{fault}}/\omega \quad (6)$$

where  $u_{\text{fault},a}$  is the phase voltage of a-phase at fault-tolerant start time,  $t_{\text{fault}}$  is the fault-tolerant start time and  $\theta_{\text{fault}}$  is the corresponding initial phase.

### (5) Determination of Modulation Wave

Combing the calculation of part (1)–(4) and neutral-point shift fault-tolerant control strategy, three-phase voltages after fault-tolerant are obtained. After the normalization of phase voltages, three-phase modulation waves can be expressed as Eq. (7).

$$\begin{cases} S_{\text{fault},a}^{T_{\text{uptime}}} = m \sin(\omega t + \theta_{\text{fault}}) \\ S_{\text{fault},b}^{T_{\text{uptime}}} = m \sin(\omega t - 2/3\pi + \theta_{\text{fault}}) \\ S_{\text{fault},c}^{T_{\text{uptime}}} = m \sin(\omega t + 2/3\pi + \theta_{\text{fault}}) \end{cases} \quad \begin{cases} S_{\text{fault},a}^{T_{\text{limited}}} = S_{\text{fault},a}^{\max} \\ S_{\text{fault},b}^{T_{\text{limited}}} = S_{\text{fault},a}^{\max} + m_{\text{fault}} \sin(\omega t + \theta_{\text{fault},b} + \theta_{\text{fault}}) \\ S_{\text{fault},c}^{T_{\text{limited}}} = S_{\text{fault},a}^{\max} + m_{\text{fault}} \sin(\omega t + \theta_{\text{fault},c} + \theta_{\text{fault}}) \end{cases} \quad (7)$$

where  $m_{\text{fault}} = 2U_{\text{fault},j}^m / U_{\text{dc}}$  is the modulation ratio after fault-tolerant,  $S_{\text{fault},j}^{T_{\text{uptime}}}$  and  $S_{\text{fault},j}^{T_{\text{limited}}}$  are modulation waves in  $T_{\text{uptime}}$  and  $T_{\text{limited}}$  ( $j = a, b, c$ ),  $S_{\text{fault},a}^{\max} = 2U_{\text{fault},a}^{\max} / U_{\text{dc}}$  is maximum amplitude of a-phase modulation wave.

When  $t_{\text{fault}}$  and  $\theta_{\text{fault}}$  are determined, three-phase modulation waves are determined and cycled in a period of  $2\pi/\omega$ .

## 3 Circulating Current Control Optimized Strategy

### 3.1 Analysis of Circulating Current Generation Mechanism

Circulating current  $i_{jz}(j = a, b, c)$  in MMC is combined with DC component  $i_{jz,\text{dc}}$ , AC component  $i_{jz,\text{ac}}$  and harmonic components  $i_h$  [7]. The presence of circulating current further affects capacitor voltage, which in turn causes arm voltage to fluctuate.

After using the improved strategy to achieve fault-tolerant control, the sum of SM voltages on upper and lower bridge arms can be expressed as Eq. (8) [10]:

$$\begin{aligned} u_{\text{fault}}^u \sum_j &= \begin{cases} n_u[i_{jz,\text{dc}}t + I_j \cos(\omega t + \varphi)/2\omega]/2C \sum N + u_{hu}, t \in T_{\text{limited}} \\ n_u[i_{jz,\text{dc}}(t - m \cos(\omega t)/\omega) + I_j m \cos(2\omega t + \varphi)/4\omega]/2C \sum N + u_{hu}, t \in T_{\text{uptime}} \end{cases} \\ u_{\text{fault}}^d \sum_j &= \begin{cases} n_d[i_{jz,\text{dc}}t - I_j \cos(\omega t + \varphi)/2\omega]/2C \sum N + u_{hd}, t \in T_{\text{limited}} \\ n_d[i_{jz,\text{dc}}(t + m \cos(\omega t)/\omega) - I_j m \cos(2\omega t + \varphi)/4\omega]/2C \sum N + u_{hd}, t \in T_{\text{uptime}} \end{cases} \end{aligned} \quad (8)$$

where  $u_{\text{fault}}^u \sum_j$  and  $u_{\text{fault}}^d \sum_j$  are the sum of SM voltages per arm;  $n_u$  and  $n_d$  are the numbers of normal SMs per arm;  $I_j$  is the bridge arm current amplitude, and  $\varphi$  is the initial phase;  $u_{hu}$  and  $u_{hd}$  are the higher harmonics;  $u$  and  $d$  stands for upper and lower arm;  $C \sum$  is the sum of SM capacitance per phase;  $j = a, b, c$ ;  $h = 1, 2, \dots, \infty$ .

It can be seen from the above analysis that due to the segmented modulation after fault, the difference in circulating current between two different stages is mainly reflected in the amplitude of harmonics, while the harmonic components are identical. The main harmonics are fundamental and second frequency component. When system uses neutral-point shift control after fault, bridge arms are asymmetrical ( $n_u \neq n_d$ ). So, harmonics of output voltage cannot be canceled and circulating current further increases. If harmonics are suppressed, circulating current can be effectively reduced.

### 3.2 Circulating Current Suppression Optimized Strategy

#### (1) Extraction of Harmonic Components

Since circulating current mainly contains fundamental and second frequency component, remaining harmonics can be negligible. Therefore, the band-stop filter (BSF) is designed to quickly filter out the fixed frequency harmonic components  $i_{BSF(k)}$ . The extracted harmonic components are as shown in Eq. (9).

$$i_{h(k)} = i_{jz} - i_{BSF(k)} \quad k = 1, 2 \quad j = a, b, c \quad (9)$$

The extraction of harmonics requires real-time tracking and meeting dynamic requirements. In this paper, the Chebyshev II type filter, which has a fast attenuation in the transition zone and can quickly extract harmonic components, is selected.

#### (2) Principle of Circulating Current Suppression

In this paper, PI and proportional-resonance (PR) controller are chosen to adjust modulation wave by feedback harmonics of circulating current and SM capacitor voltage. The strategy based on PR controller has obvious advantages. It can suppress multiple frequencies components under different SM fault types and is easy to implement [7].

Based on the above method, the optimized fault-tolerant control model of MMC system is designed. As shown in Fig. 4, the model mainly includes two parts: fault-tolerant control module and circulating current optimized suppression module.

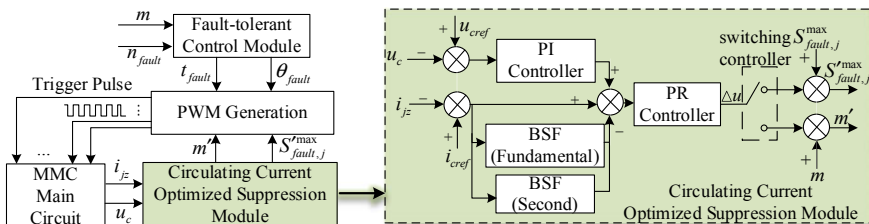


**Fig. 4** Optimized fault-tolerant control model of MMC system

The fault-tolerant control module is based on the improved neutral-point shift control. The module takes modulation ratio and number of faulty SM as inputs, calculates and outputs the fault moment and the initial fault phase for reconstructing.

The circulating current optimized suppression module includes harmonics extraction and suppression controller. The module takes capacitor voltage and circulating current as inputs, superimposes controller output on modulation parameters. The strategy uses switching controller to select different parameters in different stages. It can ensure directly suppression during the segmented adjustment process.

- (1) When the system is running until  $T_{\text{limited}}$ , switching controller selects  $S_{\text{fault},j}^{\max}$  as adjustment object and introduces feedback to obtain  $S'_{\text{fault},j}^{\max}$  with circulating current suppression effect.  $S'_{\text{fault},j}^{\max}$  can be expressed as:

$$S'_{\text{fault},j}^{\max} = S_{\text{fault},j}^{\max} + \Delta u = 1 - 2n_{\text{fault}}/N + \Delta u \quad (10)$$

- (2) When the system is running until  $T_{\text{uptime}}$ , switching controller selects  $m$  as the adjustment object and combines with the feedback value to obtain  $m'$  with circulating current suppression effect.  $m'$  can be expressed as:

$$m' = m + \Delta u \quad (11)$$

where  $\Delta u$  is the harmonic feedback determined by PI and PR controllers. Different parameters in different stages can be feedback-adjusted. This enables circulating current suppression for unbalanced MMC system.

- (3) The outputs  $t_{\text{fault}}, \theta_{\text{fault}}, m', S'_{\text{fault},j}^{\max}$  are jointly input to PWM generation module, and MMC main circuit is controlled by the output signals of PWM.

## 4 Simulation Verification

In order to verify the effectiveness of fault-tolerant control strategy and optimized circulating current suppression strategy proposed in this paper, the medium voltage MMC traction converter in high-power AC drive system of CRH high-speed EMUs is taken as object [11]. An MMC simulation model is built in MATLAB. The specific simulation parameters are as follows: DC bus voltage is  $U_{\text{dc}} = 3000$  V,  $2N = 8$ ,  $L_m = 3$  mH, load resistance is  $10 \Omega$ , load inductance is 3 mH, carrier

frequency is 2 kHz, base frequency of output is 50 Hz,  $m = 0.56$ ,  $k_p=2$ ,  $k_r=5$ ,  $k_{r2}=3$ ,  $\omega_c=15$  rad/s,  $\omega=100\pi$ .

Assume that when system runs to  $t = 0.3$  s, the open-circuit fault occurs on SM1 and SM2 on a-phase lower bridge arm. When  $t = 0.32$  s, bypass faulty SMs and input improved neutral-point shift fault-tolerant control strategy and circulating current suppression optimized strategy. The output voltages before and after fault-tolerant are shown in Fig. 5. The circulating current under different suppression strategies after fault-tolerant is shown in Fig. 6.

As shown in Fig. 5, in fault operation, output voltages have a certain degree of distortion. Under fault-tolerant operation, the limited output and uptime output are obvious, which is consistent with the improved neutral-point shift fault-tolerant control. Line voltages are basically symmetrical during fault-tolerant process; system can operate stably and achieve reliable fault tolerance of two faulty SMs under control. Comparing with fault-tolerant control by reducing modulation ratio, which the maximum number of SMs that can be fault-tolerant per bridge arm is only  $N/2 - 1 = 1$  in the same situation. It is clear that the improved strategy has better fault-tolerant capability.

As shown in Fig. 6, the circulating current is about 50 A under traditional strategy, while it is significantly reduced to 20 A after using optimized strategy. The result verifies the effectiveness of the proposed circulating current suppression strategy.

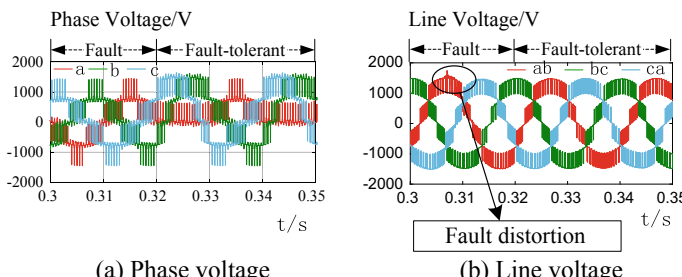


**Fig. 5** Three-phase output voltages

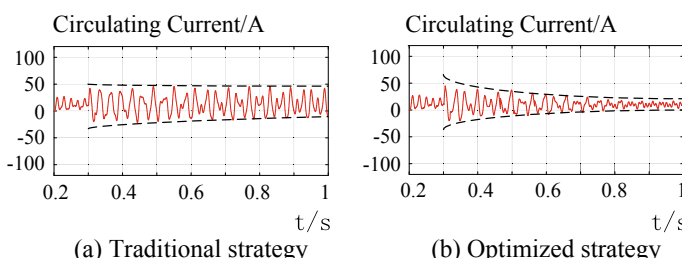


**Fig. 6** Circulating current

## 5 Experimental Verification

In order to further verify the validity of theoretical analysis and simulation results, a low-power MMC experimental system was built as shown in Fig. 7. Each SM is an Infineon's two-unit IGBT module FF75R12RT4. The control circuit uses a joint control module consisting of DSP + FPAG, where the DSP type is TMS320F28335 and FPGA is Spartan 6 XC6SLX16. The specific experimental parameters are as follows:  $U_{dc} = 96$  V,  $2N = 4$ ,  $L_m = 3$  mH, load resistance is  $20 \Omega$ , load inductance is  $20$  mH, carrier frequency is  $2$  kHz, base frequency of output is  $50$  Hz, and  $m = 0.56$ .

Figure 8 shows output voltage in normal operation. As shown in Fig. 8a, phase voltage is three levels and the voltage of each level is in the order of  $48$  V. Figure 8b is line voltage. The voltage is five levels, and the phases differ by  $120^\circ$ .

The above experimental results indicate that the experimental system can achieve three-phase MMC normal operation, the hardware circuit design is correct, and the software control strategy employed is in line with relevant requirements.

Figure 9 shows output current and line voltage after fault-tolerant control. The corresponding experimental results are the outputs of conditioning circuit. It can be seen from Fig. 9a that under fault-tolerant operation, the current outputs stably and its amplitude is consistent with theoretical value  $(96 \times 0.56)/20 = 2.688$  A. Difference between current phases of a-phase and b-phase is  $1/3$  period. It also can be seen from Fig. 9b that line voltage after fault is basically unchanged compared

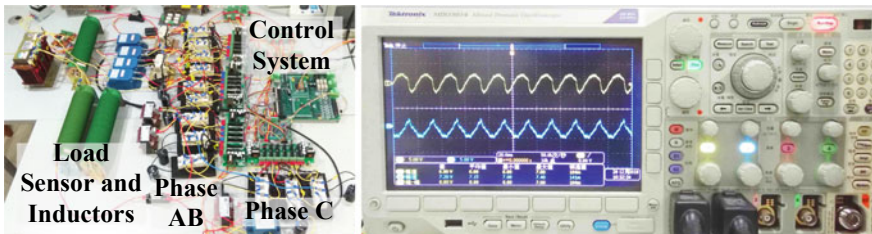


**Fig. 7** Physical map of the experimental system

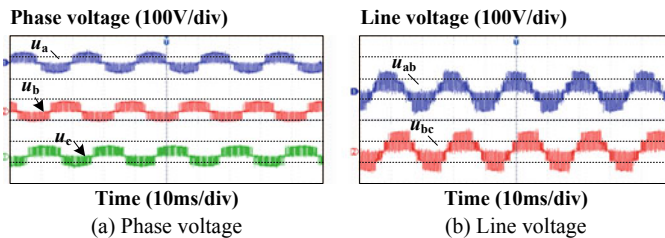


**Fig. 8** Outputs in normal operation

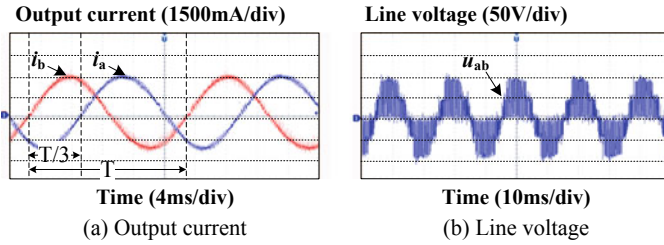


**Fig. 9** Outputs under fault-tolerant control

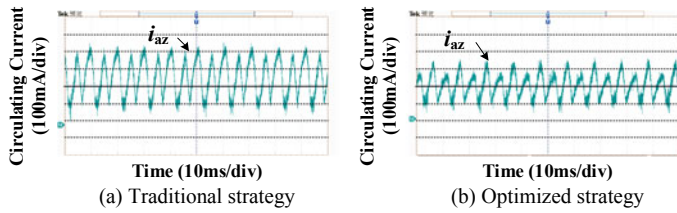


**Fig. 10** Circulating current under different suppression strategies in fault-tolerant operation

with that shown in Fig. 8b. The experimental results are basically consistent with theoretical analysis, which indicates the validity of the proposed fault-tolerant control strategy.

As shown in Fig. 10, the system has a stable circulating current value of about 200 mA under traditional suppression strategy, while circulating current amplitude is only about 100 mA when adopting optimized strategy, which is 50% of the value in using traditional strategy. It is clear that the proposed optimized circulating current suppression strategy has a significant effect.

## 6 Conclusion

This paper, with modular multilevel converter as research object, an improved neutral-point shift fault-tolerant control strategy is proposed. The strategy ensures the maximum utilization of the SMs, and the improvement of fault-tolerant capability.

Based on fault-tolerant control, a circulating current suppression optimized strategy is proposed to make the suppression effect more obvious by directly adjusting modulation wave in different stages. The effectiveness of the proposed strategies is verified by simulation and experimental results.

## References

1. Amin G, Yasser Abdel-Rady IM (2016) A resilient framework for fault-tolerant operation of modular multilevel converters. *Trans Ind Electron IEEE* 63(5):2669–2678
2. Kai L, Zhengming Z, Yuan L, Sizhao L (2017) Control Strategy based on the energy balance for reducing sub-module capacitor voltage fluctuation of modular multilevel converter. *Trans China Electrotechnical Soc* 32(14):17–26
3. Ke S, Jianze W, Mingfei B, Yanchao J, Xingguo C (2014) Fault tolerant control for modular multilevel converter based on zero-sequence voltage injection. *Autom Electr Power Syst* 38(5):96–102
4. Wen W, Xuezhi W, Long J, Kejin L, Shuai W, Xiaoxing W (2016) Fault-tolerant control strategy of neutral point shift for sub-module faults of modular multilevel converters. *Autom Electr Power Syst* 40(21):20–26
5. Kejun L, Zhengfa Z, Zhijie L, Xiaowu Q, Xiaoyan Y, Zhuodi W (2016) Asymmetric characteristics analysis of MMC in Arm Asymmetrical operation and control strategy under submodule fault. *High Voltage Eng* 42(10):3059–3067
6. Yuebin Z, Daozhuo J, Jie G, Yiqiao L, Pengfei H (2012) Analysis of sub-module capacitor voltage ripples and circulating currents in modular multilevel converters. *Proc CSEE* 32(24): 8–14 + 4
7. Zhihua F, Shihong M, Ziwen L, Kaiyun C, Yilong K (2018) Modular multilevel converter sub-module fault characteristics analysis and decoupling control strategy. *Trans China Electrotechnical Soc* 33(16):3707–3718
8. Lili J, Wenzhong M, Linhuan L, Tiantian S, Shukun W (2014) A fault-tolerant control strategy of modular multi-level converters. *Power Syst Technol* 38(8):2497–2503
9. Qinyue Z, Wei D, Lei G, Xitang T, Zhaoyang L, Dabo X (2019) A fault-tolerant control strategy of modular multilevel converter with sub-module faults based on neutral point compound shift. *Energies* 12(5):876–898
10. Jun W, Han X, Hao M, Zhihong B (2018) Analysis and injection control of circulating current for modular multilevel converters. *IEEE Trans Ind Electron* 1–1
11. Liu L, Yin J, Jin G, Zhou P (2017) Simulation of traction drive control system of high-speed EMUs. *Electr Drive Autom* 39:12–15

# Energy Storage System Design for Catenary Free Modern Trams



Li Wang, Qinghua Zhao, Hongliang Duan and Changqing Liu

**Abstract** Modern trams use pure electric to drive. Trams are currently new popular railway transportation products. They are convenient and environment friendly, comfortable and efficient. But since the overhead power network in some particular environment or section has an adverse impact on the landscape, it brings some difficulties to the line planning. With the development of new energy storage technology, research and development of catenary free low floor tram are to adapt to the current market demand of the technology development direction. In this chapter, the supercapacitor-based energy storage system is used to achieve full range of catenary free tram design, and the feasibility of this scheme is checked and verified by the traction calculation.

**Keywords** Catenary free · Energy storage · Low floor tram · Supercapacitor

## 1 Introduction

The modern tram which is green, convenient, comfortable, less investment and simple approval has been favored in many cities. Application of catenary free technology in the modern trams removes bad influence of the catenary on the city landscape “visual pollution.” The modern tram has become a beautiful landscape in the city [1]. Types of power supply catenary are various, such as supercapacitor, electric double layer capacitor, lithium batteries, hydrogen fuel cells and inductive power supply.

Supercapacitor is a capacitor between batteries and electrostatic storage devices with high power density and suitable for short time output power source. It has the

---

This work was supported in part by the China National Science and Technology Support Program under Grant 2017YFB1201005.

---

L. Wang (✉) · Q. Zhao · H. Duan · C. Liu  
CRRC Changchun Railway Vehicles Co. Ltd., Changchun, China  
e-mail: [13689813910@163.com](mailto:13689813910@163.com)

advantages of high specific power, high specific energy, high amount of once energy storage and so on. It can smooth power battery charge and discharge current. The battery life will be prolonged greatly. This feature determines that the supercapacitor can absorb electrical braking feedback energy and achieve the effect of energy conservation [2–7].

To solve technical problems of the catenary free application on trams, this chapter will introduce the design scheme of supercapacitor-based energy storage system application on 100% low floor modern tram, achieving the full mesh, the high efficiency of supercapacitor power supply-charging mode, finally passed the actual loading test [8, 9]. The successful implementation of the supercapacitor energy storage system is a good example for all catenary free tram application.

## 2 Main Technical Parameters of Vehicles

The basic configuration of 100% low floor trams is five-car module; the whole train has two motor bogies and one trailer bogie.

The vehicle shall meet the track parameters in Table 1.

On the mainline and in the depot, the trams use supercapacitor to provide power. The charging device for the supercapacitor is arranged in the base station and vehicle.

And the train traction and brake performance parameters are as follows in Table 2.

Note: in the AW2 load and wheel wear state and semidry, clean and straight rail and the rated voltage (DC750V).

The train traction system adopts VVVF inverter. The electric brake adopts regenerative brake. The brake energy will be feedback to the supercapacitors.

**Table 1** Track parameters

Item		Figure
The minimum radius of plane curve	The mainline (interval)	20 m
	Yard line	20 m
The minimum radius of vertical curve		350 m
Maximum gradient		60‰

**Table 2** Traction and brake performance

Item	Parameter
The maximum train running speed	70 km/h
Starting acceleration (0–40 km/h)	$\geq 1.0 \text{ m/s}^2$
The average acceleration (0–70 km/h)	$\geq 0.7 \text{ m/s}^2$
The maximum equivalent braking deceleration (70 km/h ~ 0)	$\geq 1.2 \text{ m/s}^2$

Train traction system main circuit adopts voltage type DC–AC inverter circuit. When the supercapacitor voltage is within the range of DC616V~820V, the traction system can work normally.

### 3 Design of Energy Storage System

According to the requirements of vehicle parameters, supercapacitor is used as energy storage element. Considering the train configuration of 100% low floor tram, roof installation space and vehicle energy consumption demand, two kinds of supercapacitor boxes are designed in the five-module vehicle. The related system parameters are described as follows.

#### 3.1 Parameters of SuperCapacitor Box

Type I, II supercapacitor box parameters are shown in Tables 3 and 4.

#### 3.2 Energy Consumption Calculation

##### General Calculation

For brake energy feedback of the supercapacitor energy storage system on trams, simulation calculation can be carried out as follows.

The system consists of two type I supercapacitor boxes and two type II supercapacitor boxes. The maximum recovery current of the whole energy storage system is:

$$I = 2 \times (560 + 840) = 2800 \text{ A} \quad (1)$$

**Table 3** Performance parameters of type I supercapacitor box

Parameter name	Parameter values
The nominal capacity (F)	256
The working voltage range (V)	616~820
The effective energy storage of working voltage range (kWh)	9.5
Standard charging current (A)	280
The maximum charging current (A)	560 (20S)
The standard discharge current (A)	$\leq 280$
The maximum discharge current (A)	560 (20S)
20S charging energy (kWh)	0.8
Electric brake upper limit voltage (V)	850

**Table 4** Performance parameters of type II supercapacitor box

Parameter name	Parameter values
The nominal capacity (F)	389
The working voltage range (V)	616 ~ 820
The effective energy storage working voltage range (kWh)	14.3
Standard charging current (A)	420
The maximum charging current (A)	840 (20S)
The standard discharge current (A)	$\leq 420$
The maximum discharge current (A)	840 (20S)
20S charging energy (kWh)	1.2
The electric brake line voltage (V)	850

The maximum current can last up to 20 s.

The total capacity of the energy storage system is:

$$C_{\text{总}} = 2 \times (C_1 + C_2) = 2 \times (256 + 389) = 1290F \quad (2)$$

Assuming 80% SOC is the starting point of maximum recovery calculation, the voltage  $u1 = 783$  V. At this time, the recyclable power is:

$$P_{\text{MAX}} = U_1 \times I = 783 \times 2800 = 2192.4 \text{ kW} \quad (3)$$

Then, the recovery energy in 20 s is:

$$E = P_{\text{MAX}} \times 20/3600 = 12.18 \text{ kWh} \quad (4)$$

In the calculation of 0% SOC, the voltage  $u2 = 616$  V.

At this time, the recyclable power is:

$$P_{\text{MIN}} = U_2 \times I = 616 \times 2800 = 1724.8 \text{ kW} \quad (5)$$

At this time, the recovery energy in 20 s is:

$$E = P_{\text{MIN}} \times 20/3600 = 9.58 \text{ kWh} \quad (6)$$

According to the calculation result, the energy storage system can realize the braking energy recovery of 9.58–12.18 kWh in 20 s in theory.

### Total Energy and Working Energy

The supercapacitor energy storage system is composed of two sets of type I supercapacitor box and two sets of type II supercapacitor box. The total storage energy of the supercapacitor system is 47.6 kWh, and the actual working total energy is also 47.6 kWh.

## Available Energy Calculation

The working voltage range of supercapacitor box is:

$$U_{\min} = 6 \times 36 \times 2.85 = 615.6 \text{ V} \quad (7)$$

$$U_{\max} = 6 \times 36 \times 3.8 = 820.8 \text{ V} \quad (8)$$

The available energy is calculated as follows:

For type I supercapacitor box, the available energy is:

$$E_1 = \frac{\frac{1}{2}C \frac{(U_{\max})^2 - (U_{\min})^2}{3600}}{1000} = \frac{\frac{1}{2} \times 256 \times \frac{(820)^2 - (616)^2}{3600}}{1000} = 10.46 \text{ kWh} \quad (9)$$

For type II supercapacitor box, the available energy is:

$$E_2 = \frac{\frac{1}{2}C \frac{(U_{\max})^2 - (U_{\min})^2}{3600}}{1000} = \frac{\frac{1}{2} \times 389 \times \frac{(820)^2 - (616)^2}{3600}}{1000} = 15.89 \text{ kWh} \quad (10)$$

The total available energy storage of supercapacitor system is:

$$E = 2E_1 + 2E_2 = 52.7 \text{ kWh} \quad (11)$$

The above calculation is only theoretical calculation. The actual output energy will be influenced by the resistance of the supercapacitor. According to the 100 A monomer charging and discharging test, each single monomer will actually release energy of 22 Wh. The number of monomers assembled on the vehicle energy storage system is 2160. Therefore, the actual energy storage is 47.6 kWh.

## Fully Regenerative Braking Power Absorption of Traction System

When 100% low floor tram brakes, the electric braking of traction system will be used in priority. Traction motor will produce regenerative braking energy, and this energy will be feedback to the main circuit through the IGBT diode to the supercapacitor for absorption. According to Tables 3 and 4, the charging energy from one type I and one type II supercapacitor will be supplied to a traction inverter. The nominal currents are 280 and 420 A, a total of 700 A. The maximum charging currents are 560 A (20 s) and 840 A (20 s), a total of 2800 A (20 s). According to the traction calculation, the maximum braking current is less than 1600 A. Therefore, the supercapacitor can absorb all the electrical regenerative braking energy.

Fully absorbed of braking energy on the one hand can increase the additional energy for the supercapacitor, on the other hand, can also eliminate the braking resistance and reduce wear of brake shoe. It has big contribution for energy saving and environment friendly.

## 4 Design Verification

For calculation, the following parameters are chosen: The wheel diameter of the train is 540 mm, gear ratio is 6.0294 and the efficiency of traction system is 0.98. In order to calculate the equivalent mass of train, we assume the inertial coefficient of motor train is 10%; inertia coefficient of the trailer train is 5%.

The total weight of the train is shown in Table 5.

As shown in Figs. 1 and 2, in DC750V and AW2 loads, the maximum traction torque for each motor is about 964.6 Nm. The maximum adhesion coefficient is 0.174. The maximum traction motor power is 179.5 kW. The train is at a maximum speed of 80 km/h. The maximum motor speed is 4738.8r/min. Then, the total current of the vehicle super capacitance is up to 1050.5 A (assuming the converter efficiency is 98%).

As shown in Figs. 3 and 4, in DC825V and AW2 loads, the maximum braking torque for each motor is about 964.7 Nm. The maximum adhesion coefficient is 0.183. The maximum motor braking power train is 290.2 kW. The maximum

**Table 5** Weight of the train

Working condition	Train weight (T)
AW0	52.2
AW2	70.2
AW3	75

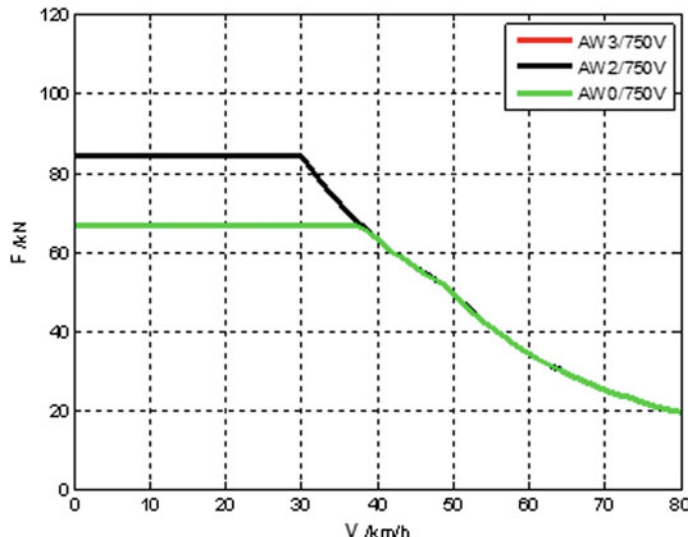


**Fig. 1** Traction force and speed curve (AW2, DC750V)

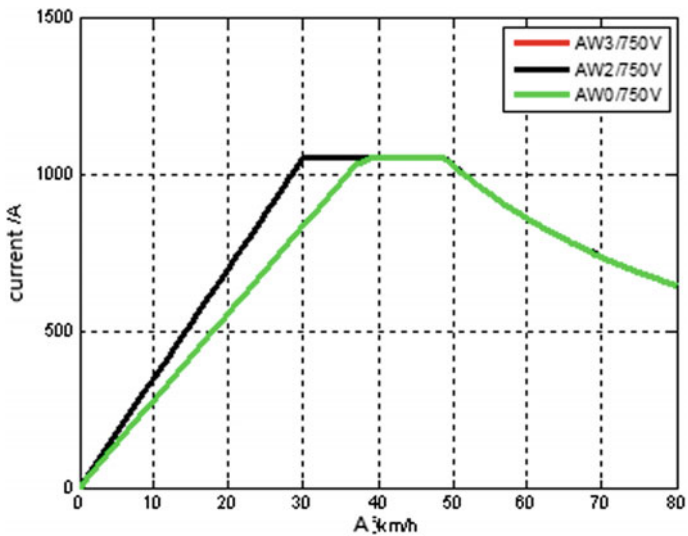


Fig. 2 Current and speed curve (AW2, DC750V)

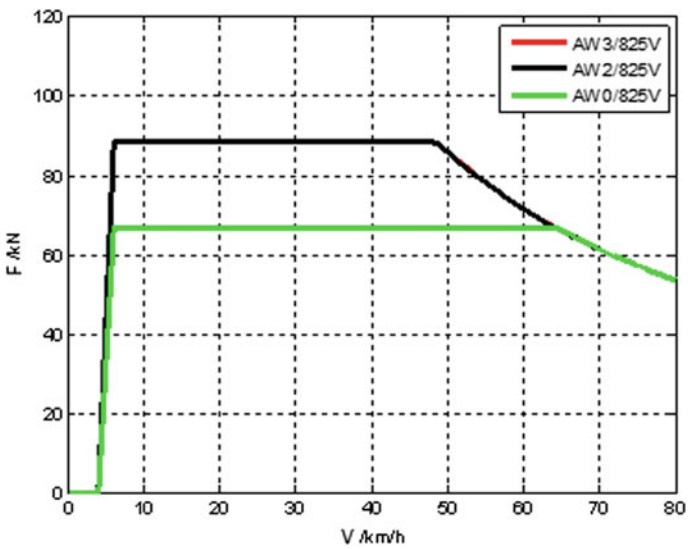
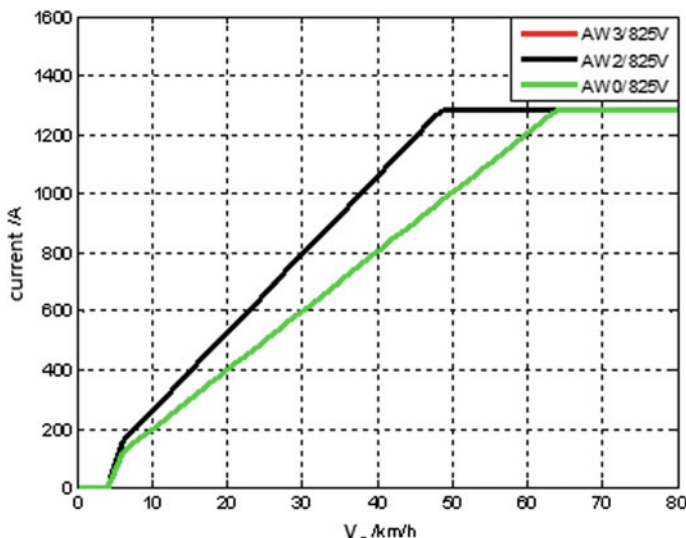


Fig. 3 Traction force and speed curve (AW2, DC825V)



**Fig. 4** Current and speed curve (AW2, DC825V)

operating speed is 80 km/h. The maximum speed of motor is 4738.8 r/min. The supercapacitor current is up to 1282.6 A (assuming the converter efficiency is 98%).

## 5 Conclusion

On the basis of the research on the energy storage system of catenary free trams, the technology of on-board energy storage, high current charging and discharging and capacity management system has been broken through. The trams with the energy storage system have been assembled and have completed the relative type tests. The energy storage system on the trams has been convinced to meet the requirements of catenary free tram network for both at home and abroad. This technology improves the technical level of domestic tram development greatly and promotes the development of China's rail tram industry.

## References

1. Tongfang D (2016) Analysis on the key points of electrical wiring for metro vehicles. Eng Tech (10):252
2. Jianguo C (2015) Development of a new type vehicle energy storage system for urban railtransit. Res Urban Rail Transit (7):18

3. Bo P, Fang W (2013) Research on charging and discharging control strategy of supercapacitor. *Ind Control Comput* 12:138–139
4. Bose BK (2002) Modern power electronics and AC drives. Prentice-Hall, America, pp 22–25
5. Atmaja TD, Amin (2015) Energy storage system using battery and ultracapacitor on mobile charging station for electrical vehicle. *Energy Proc* 68:429–437
6. Farzanehfard H, Beyragh DS, Adib E (2008) A bidirectional soft switched ultracapacitor interface circuit for hybrid electric vehicles. *Energy Convers Manage* 49:3578–3584
7. Uzunoglu M, Alam MS (2007) Dynamic modeling, design and simulation of a PEM fuel cell/ultra-capacitor hybrid system for vehicular applications. *Energy Convers Manage* 48:1544–1553
8. Vazquez JM (2010) Energy storage system for transport and grid applications. *IEEE Trans Electron* 57(12):3881–3895
9. Iannuzzi D, Pagano E, Tricoli P (2013) The use of energy storage systems for supporting the voltage needs of urban and suburban railway contact lines. *Energies* 1802–1820

# Modeling and Simulation of Multi-Vehicle DC Traction Power Supply System Based on MATLAB/Simulink



Hui Liu, Zhenhai Sun, Jinping Fang and Zihui Hao

**Abstract** DC traction power supply system is an important part of urban rail transit. The modeling of it is not only the basis of safe operation of urban rail transit, but also provides theoretical basis for failure mechanism analysis. In order to solve the problems caused by high traffic density and long power supply distance of suburban lines in the rush hours of urban rail transit, this paper established the integrated model of rectifier units-traction network-vehicle simulation on MATLAB/Simulink platform. Taking bilateral power supply mode as an example, the starting current of multi-vehicle in different locations and times in DC traction power supply system is analyzed. By comparing the simulation results, the characteristics are distinguished between multi-vehicle starting current and remote short-circuit current effectively to protect the DC traction power supply system reliably.

**Keywords** Rectifier unit · Traction network · Multi-vehicle · MATLAB simulation · Protection application

## 1 Introduction

The safety and reliability of DC traction power supply system are the keys to the safe and smooth operation of urban rail transit. With the rapid development of urban rail transit, some new problems arise, such as the high traffic density during peak hours and the long power supply distance between suburban lines and so on [1, 2]. Therefore, the research and analysis of simulation modeling of multi-vehicle DC traction power supply system are of great significance in the actual urban rail operation.

---

H. Liu (✉) · Z. Sun · J. Fang  
Beijing Subway Operation Technology Centre, Beijing, China  
e-mail: [630288235@qq.com](mailto:630288235@qq.com)

Z. Hao  
School of Electrical Engineering, Beijing Jiaotong University, Beijing 100044, China  
e-mail: [17121439@bjtu.edu.cn](mailto:17121439@bjtu.edu.cn)

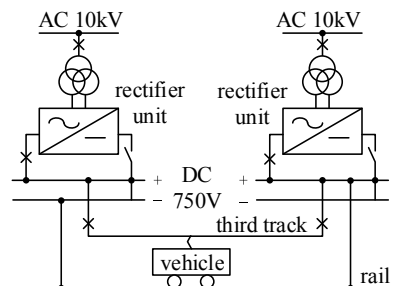
DC traction power supply system is a huge and complex system, which usually consists of traction substation, traction network and vehicle. Rectifier units of DC traction power supply system which is replaced by Thevenin equivalent circuit are established in Ref [3, 4]. The authors calculate the external characteristics of rectifier units and analyze the steady-state operation of the system. Tingzhi [5] introduces the modeling and calculation methods of inductance, DC resistance of running rail and contact rail under the mode of third rail power supply. In reference [6], an approximate calculation method of DC resistance and inductance in DC transient process is proposed. Xiaohong [7] simplifies the vehicle model as impedance to simulate the starting and passing insulation of the vehicle. The AC drive system of vehicle which based on vector decoupling control is modeled and analyzed by MATLAB/Simulink in Ref [8, 9]. It also proposes a method to identify the remote short-circuit current by combining the rise rate of wavelet transform. Most previous literatures only consider simplified vehicle models or modeling and protection of DC traction power supply system under single-vehicle condition, but few studies have been done on simulation and protection under multi-vehicle starting conditions.

Aiming at the above problems, this paper conducts the simulation study of DC traction power supply system for multi-vehicle operation. This paper is structured as follows: Sect. 2 establishes the model of DC traction power supply system on MATLAB/Simulink simulation platform, analyzes the working characteristics of 24-pulse rectifier unit, simplifies the vehicle as DC motors and establishes rectifier units-traction network-vehicle based on parameters of actual metro lines; in Sect. 3, we analyze the characteristics of vehicle starting current under bilateral power supply mode on the basis of simulation model; in Sect. 4, based on the simulation results, a method to distinguish multi-vehicle starting current from remote short-circuit fault current is proposed, so that DC traction power supply system protection becomes more comprehensive and reliable.

## 2 Modeling of DC Traction Power Supply System

DC traction power supply system provides running power of vehicle. China adopts two voltage systems, 1500 V DC and 750 V DC. Taking the third rail power supply system of 750 V DC as an example, its structure is shown in Fig. 1. It mainly

**Fig. 1** DC traction power supply system



includes DC traction substation and traction network, what is more, rectifier unit is the core equipment of traction substation.

## 2.1 Rectifier Unit Modeling

In order to improve the utilization ratio of transformer and reduce the harmonic content of AC side, 24-pulse rectifier unit has gradually replaced 12-pulse rectifier unit in China. 24-pulse rectifier unit is modeled and simulated on MATLAB/Simulink platform.

**Operating Principle of 24-Pulse Rectifier Unit.** The rectifier unit includes rectifier transformer and rectifier. The 24-pulse rectifier unit consists of two axial double-split four-winding traction rectifier transformers and four groups of three-phase full-wave rectifier bridges.

Each rectifier transformer's secondary winding is connected to two groups of rectifier bridges with Y connection and D connection, respectively. The two windings can be connected in parallel to form 12-pulse rectifier units. The primary winding of the rectifier transformer is phase-shifted  $\pm\pi/24$  with the same capacity and connection mode. The DC side outputs 24 pulses after step-down and rectification. The main principle diagram is shown in Fig. 2.

When the load on the DC side is no-load or light-load, the actual output voltage on the DC side of the rectifier is called ideal no-load DC voltage. The calculation equation is shown as follows (Eq. 1).

$$\begin{aligned} U_{d0} &= \frac{12}{\pi} \int_{-\frac{\pi}{24}}^{\frac{\pi}{24}} \sqrt{6}U \cos(\omega t) d(\omega t) \\ &= \frac{24\sqrt{2}}{\pi} \sin \frac{\pi}{24} U_{2N} \\ &= 1.41 U_{2N} \end{aligned} \quad (1)$$

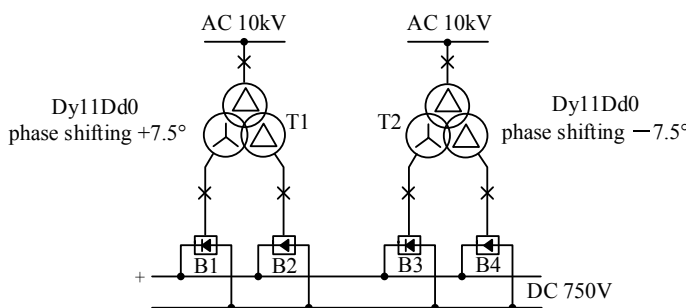


**Fig. 2** Schematic diagram of 24-pulse rectifier unit

where  $U_{2N}$  is rated line voltage of secondary side of rectifier transformer.

**Simulation Model of 24-Pulse Rectifier Unit.** When the 24-pulse rectifier unit is modeled in MATLAB/Simulink, because of the immutability of the connection mode of the primary side of three-phase three-winding transformer, phase-shifting transformer is introduced to realize phase change. Phase-shifting transformer can be located in the primary or secondary side of three-winding transformer. The two cases are simulated and analyzed separately; the models are shown in Fig. 3.

All the modules in these two models are set to the same parameters. The power supply frequency is 50 Hz, the capacity of the rectifier transformer is 3360 kA, and the ratio of the primary side voltage to the secondary side voltage is 10/0.59 kV. The waveforms of the voltage at load side in a period under no-load condition are shown in Fig. 4.

Figure 4 shows that the DC output voltage waveform fluctuates 24 times in one cycle. When no-load, the average DC output voltage of phase-shifted transformer at the primary side of rectifier transformer is 821.57 V, but at the secondary side of rectifier transformer is 816.75 V. According to Eq. (1), the ideal no-load DC voltage  $U_{d0}$  is 831.9 V. So the simulation model of phase-shifted transformer at the primary side of rectifier transformer is more accurate.

## 2.2 Traction Network Modeling

In this paper, the traction network is equivalent to a  $\pi$ -type equivalent circuit. The upper and lower rails are merged into one, and the module is encapsulated. The traction network between the two adjacent substations is considered to be divided into two segments by vehicle starting position or the short-circuit fault position. Assuming that the quality of catenary rail and rail is uniform and the distribution distance between lines remains unchanged. The corresponding relationship between distance and unit impedance is established, so the length of traction network can be set by changing the length variable.

The “PI Section Line” module in Simulink module library is used to model traction network. The model is shown in Fig. 5. The parameters of it are shown in Table 1 [10].

## 2.3 Vehicle Modeling

According to the traction control technology of different traction motors, metro vehicles can be divided into two categories: DC motors controlled by cam or DC chopper voltage regulation, and AC motors controlled by voltage and frequency regulation. The working principle of the metro vehicle is shown in Fig. 6.

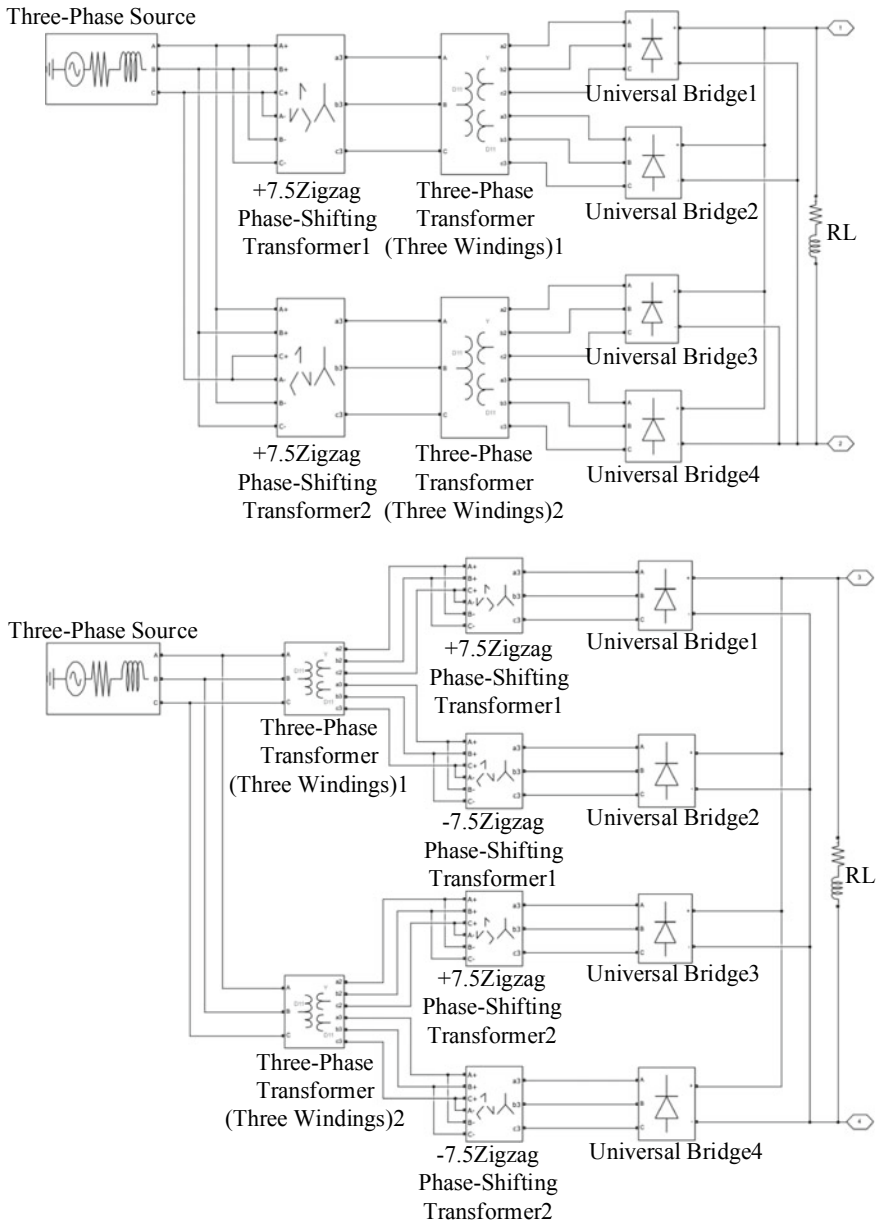


**Fig. 3** Simulation model of 24-pulse rectifier unit in two positions of phase-shift transformer. (top) Simulation model of 24-pulse rectifier unit with phase-shifting transformer in front of three-winding transformer, (bottom) Simulation model of 24-pulse rectifier unit with phase-shifting transformer after three-winding transformer

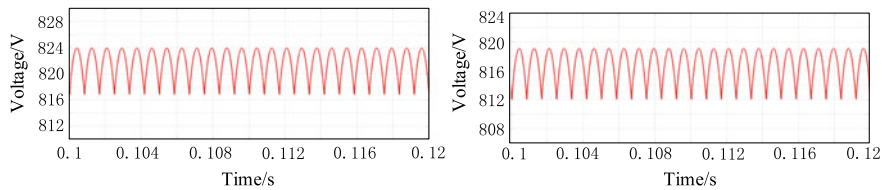


**Fig. 4** Waveform of DC output voltage. (left) Voltage waveform of phase-shifted transformer in front of three-winding transformer. (right) Voltage waveform of phase-shifted transformer after three-winding transformer

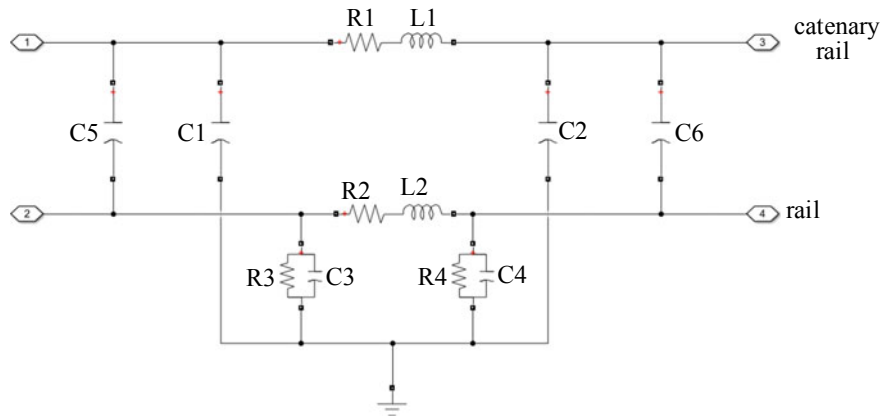


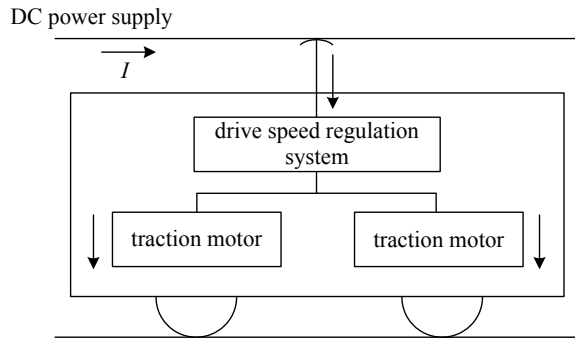
**Fig. 5** Simulation model of catenary rail and rail

**Table 1** Parameters of traction network

Name	Label	Value
Resistance of catenary rail ( $\Omega/\text{km}$ )	$R_1$	0.02
Parallel resistance of two rails ( $\Omega/\text{km}$ )	$R_2$	0.019
Transition resistance of two rails in parallel connection ( $\Omega/\text{km}$ )	$R_3, R_4$	3
Inductance of catenary rail ( $\text{mH}/\text{km}$ )	$L_1$	1.07
Parallel inductance of two rails ( $\text{mH}/\text{km}$ )	$L_2$	0.65
Capacitance of catenary rail to ground ( $\text{nF}/\text{km}$ )	$C_1, C_2$	6.02
Capacitance of rail to ground ( $\text{nF}/\text{km}$ )	$C_3, C_4$	26.5
Capacitance of catenary rail to rail ( $\text{nF}/\text{km}$ )	$C_5, C_6$	7.07

Actually, the starting process of metro vehicles is very complex, which is often composed of multiple starting modes and multiple motors. In this paper, the starting process of metro vehicle is simplified as the starting process of DC motor. The main modules of vehicle starting are modeled and simulated to simplify the complex control module.

**Fig. 6** Metro vehicle schematic



In this paper, the DC motor controlled by cam resistance regulation is selected to simulate the starting process of vehicle on MATLAB/Simulink platform. Four parallel DC motors are used to simulate the starting process of vehicle. The third-order resistances are  $5.5 \Omega$ ,  $2.45 \Omega$  and  $1.11 \Omega$ , respectively [11]. The vehicle model and speed waveform are shown in Figs. 7 and 8, respectively.

It can be seen from Fig. 8 that the motor can start smoothly by gradually cutting off the resistance step by step to ensure sufficient starting torque after starting the motor.

### 3 Simulation Result

The simulation model of DC traction power supply system under bilateral power supply mode is built on MATLAB/Simulink platform in Fig. 9. The simulation running time  $T$  is 1 s and the sampling frequency  $T_s$  is  $10^{-6}$ s.

As shown in Fig. 9: Source A and Source B are external power supply modules; Substation A and Substation B are rectifier unit modules; L1, L2 and L3 are DC traction network modules, whose length parameters can be changed to adjust the length of traction network; Vehicle 1# and Vehicle 2# are vehicle starting modules; Step 1 and Step 2 pulse generators can simulate vehicle starting time and the occurrence time of short-circuit between catenary rail and rails, respectively. The parameters of L2 and L3 can change the distance between vehicle starting point or short-circuit point with two traction substations, and the distance between two vehicles can be changed by adjusting L3 parameters.

Figures 10 and 11 show the feeder current waveforms of two vehicles starting one after another at different distances and at different times under the same distance between two traction substations, respectively. With the increase of the interval distance between two vehicles, the main influence on the starting current is that the peak value decreases; with the increase of the interval time between two vehicles, the peak value of the vehicle starting current decreases and the time delay occurs.

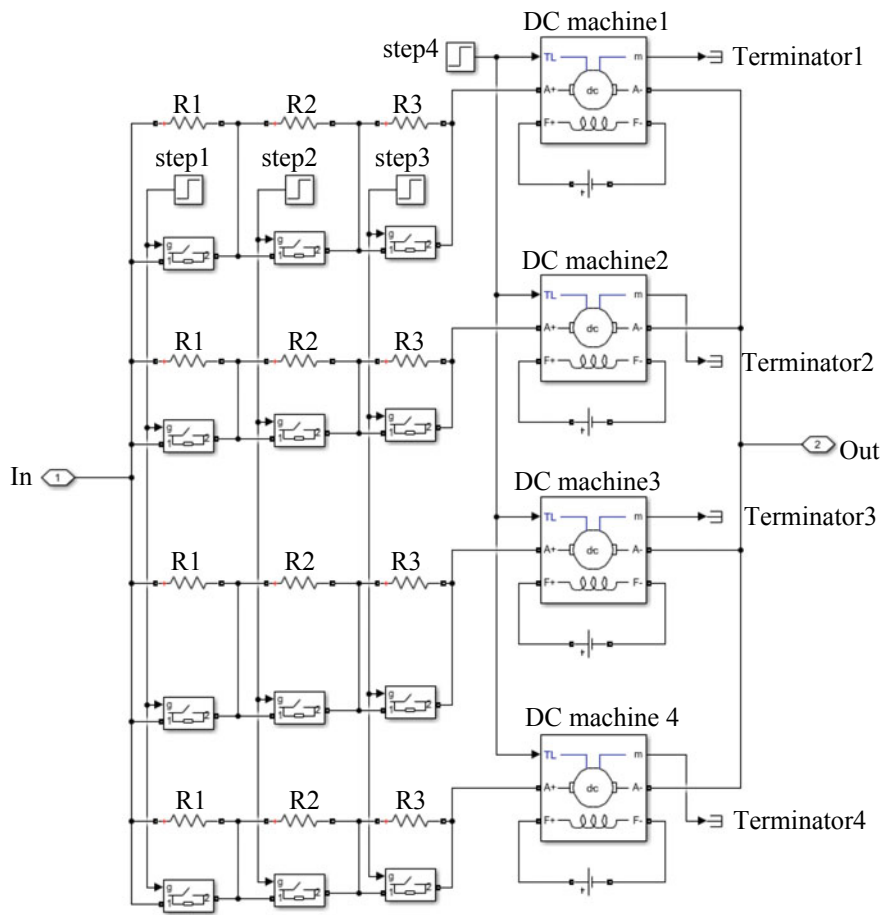


**Fig. 7** Model of metro

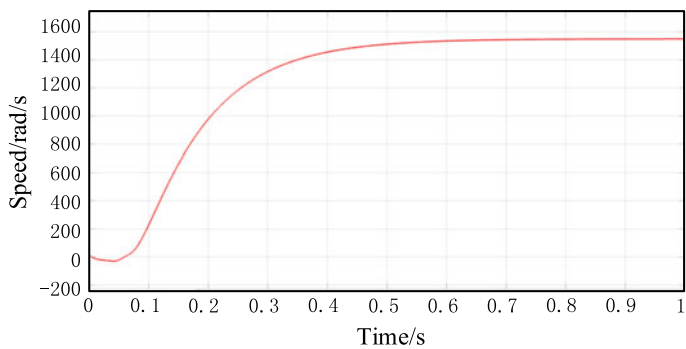


**Fig. 8** DC motor speed waveform

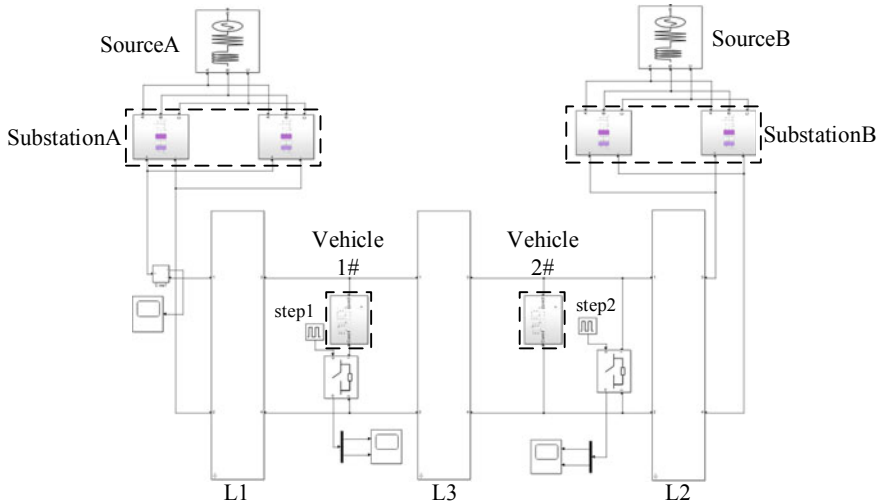


**Fig. 9** Simulation model of DC traction power supply system

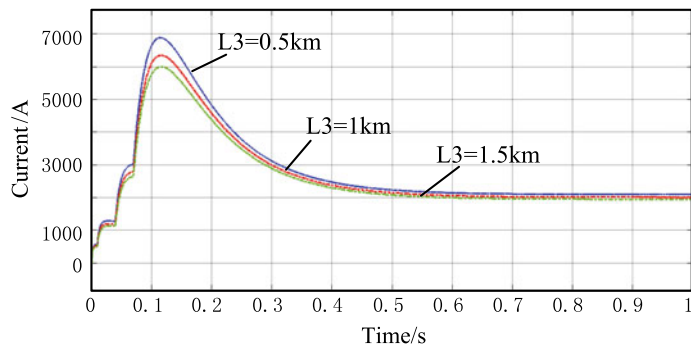


**Fig. 10** When  $L = 2\text{ km}$ , the two vehicles are 0.5, 1 and 1.5 km away from each other, the current waveform of Substation A feeder started at the same time

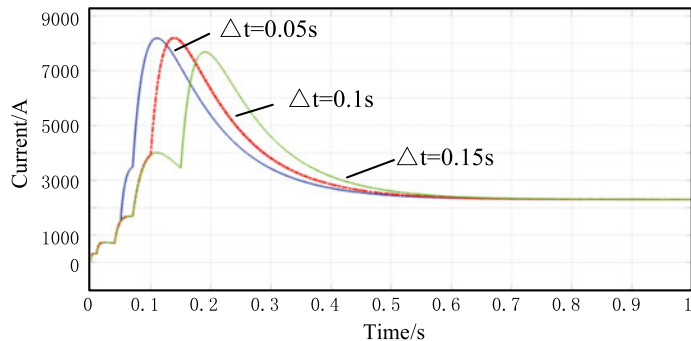


**Fig. 11** When  $L = 2\text{ km}$ , the feeder current waveform of Substation A when the two vehicles start successively from 0.05, 0.1 and 0.15 s

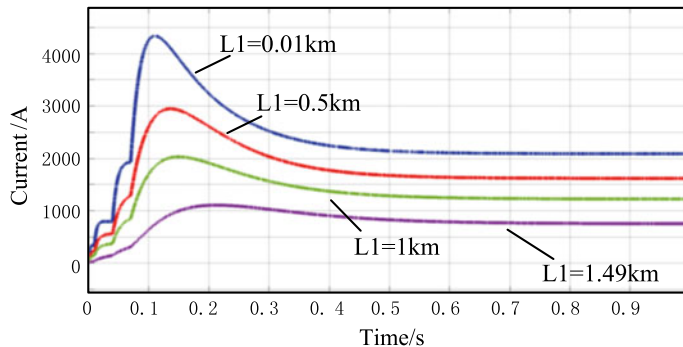


**Fig. 12** When  $L = 2$  km, the distance between two vehicles is 0.5 km, and the distance between Vehicle 1# and Substation A is 0.01, 0.5, 1 and 1.5 km, the waveform of feeder current in Substation A

Figure 12 shows the change of position of starting current from near to far away from Substation A. The distance between two substations is 2 km, and the starting distance between two vehicles is fixed at 0.5 km at the same time. It can be seen that when the starting distance between two vehicles is fixed, the peak value of starting current, the change rate of starting current and the current stability value gradually both decrease with the increase of the distance from the substation.

#### 4 Multi-Vehicle Starting Protection

The safe and reliable operation of DC traction power supply system needs to cooperate with quick-break protection, current rising rate and current incremental (DDL) protection and definite time overcurrent protection. However, the traditional

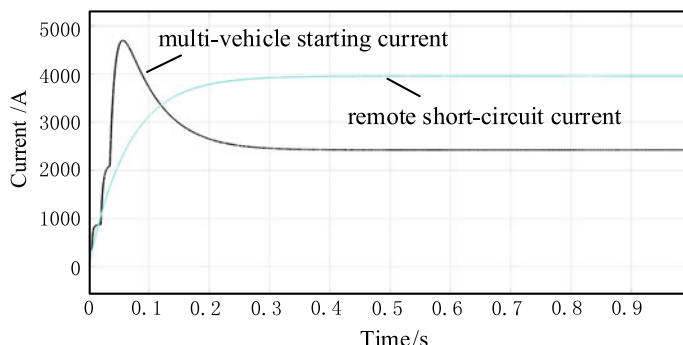


**Fig. 13** When  $L = 4$  km, the waveform of feeder current of Substation A starting current of Vehicle 1# and Vehicle 2# at the same time and short-circuit of Substation A at the far end of Substation A

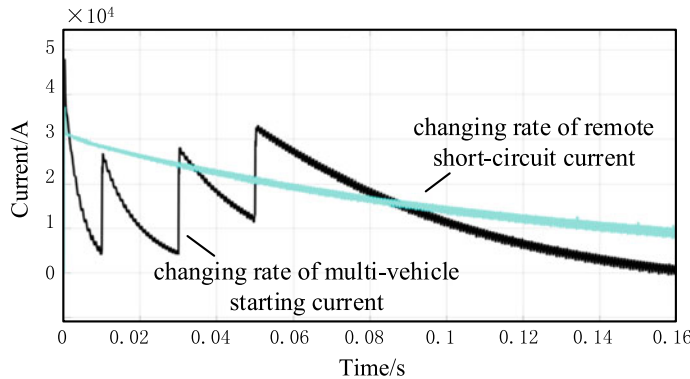


**Fig. 14** When  $L = 4$  km, the change rate waveform of feeder current of Substation A starting current of Vehicle 1# and Vehicle 2# at the same time and short-circuit of Substation A at the far end of Substation A

protection methods often fail to distinguish the multi-vehicle starting current from the remote short-circuit current. Figures 13 and 14 are the comparative figures of the current and current change rates of two vehicles under the same power supply arm starting at the same time and the remote short-circuit, respectively.

The traditional protection method of DC traction power supply system is to distinguish vehicle starting current from short-circuit current by combining current change rate, current increment and delay time. But when two vehicles start at the same time, as shown in Figs. 13 and 14, the increment of starting current and the change rate of current are similar to the short-circuit current at the far end. Traditional protection methods, such as quick-break protection and DDL protection, may misjudge the situation of two vehicles starting at the same time, which affects the safe operation of DC traction power supply system.

This special case can be identified according to the characteristics of the starting current and short-circuit current of vehicle. From Figs. 13 and 14, it can be seen that of both the amplitude and the rate of change of vehicle starting current decrease rapidly after the peak value of staged starting is reached, while the level of short-circuit current will not decrease after the peak value is reached, and the rate of change will decrease rapidly after the peak value is reached. Therefore, the current integral value and the average value can be used as the setting value. Although the peak value of starting current and short-circuit current is close at the beginning, the current integral value is quite different in a certain period of time. At the same time, the ratio of the average value of starting current to the maximum value is smaller than that of the far-end short-circuit. The setting value can also be adjusted according to the actual operation condition of the system to meet the safety needs of metro traffic.

## 5 Conclusion

In this paper, the simulation model of multi-vehicle DC traction power supply system is built on MATLAB/Simulink platform, and the current characteristics of multi-vehicle starting at different locations and at different times under bilateral power supply mode are analyzed. According to the simulation results of simultaneous starting current and remote short-circuit current of multi-vehicle, current integral value and average value are setting values to protect the DC traction power supply system with multi-vehicle starting, so that to improve the reliability of DC system protection.

**Acknowledgements** This work is supported by research project of Beijing Subway Operation Company Limited in 2018, “Development of Data Analysis and Computing Software for Subway Power Supply System” (No. 2018000504000002). Hui Liu is the corresponding author.

## References

1. Liangwei L (2007) The study of short circuit fault on the direct current side of urban rail transit (in Chinese)
2. Xiaojun S (2007) On-line monitoring technology of direct current feeder cable of urban mass transit (in Chinese)
3. Liangwei L, Qunzhan L, Wei L (2007) Simulation and application of external characteristics curve of 24-pulse rectifier in urban rail transit. Res Urban Rail Transit 10(10):52–55 (in Chinese)
4. Wei L, Qunzhan L, Liangwei L (2008) Steady-state short-circuit calculation of DC traction supply system based on polygonal external characteristic. Electric Drive Locomotives 208(1):61–64 (in Chinese)
5. Tingzhi G (2009) Study on mathematical model and short-circuit current calculation of DC traction power supply system (in Chinese)
6. Hill RJ, Carpenter DC (1991) Determination of rail internal impedance for electric railway traction system simulation. IEE Proc B Electric Power Appl 138(6):311–321
7. Xiaohong W (2002) The research of DC feeder protection of subway (in Chinese)
8. Moxue L (2010) Modeling for DC traction power supply system and development of protection algorithm based on discrimination of current characteristic quantity (in Chinese)
9. Yunhai C (2005) Manufacture of the feeder microprocessor-based protection equipment in DC traction system (in Chinese)
10. Junting Z (2017) Modeling and simulation of AC/DC power supply system for urban rail transit based on MATLAB/Simulink (in Chinese)
11. Chi M (2012) Design on protection device of subway DC power system (in Chinese)

# Research on Eddy Current Braking Control Strategy of 600 km/h High-Speed Maglev Train



Hongfeng Qi, Wenjin Hao and Jianqiang Liu

**Abstract** As an important guarantee for maglev trains in emergency, eddy current braking system and its control strategy are essential for the safety of high-speed maglev trains. In this paper, the principle of eddy current braking and the characteristics of safety braking force of 600 km/h high-speed maglev train are analyzed. An eddy current braking control strategy for ideal braking curve tracking control is proposed according to the target of safety braking control. This strategy uses a fuzzy controller to determine the eddy current braking level and achieves the target of stopping the train in the target parking area through closed-loop tracking control of the actual train position. The effectiveness of this proposed eddy current braking control strategy is verified by the simulation model built by MATLAB.

**Keywords** High-speed maglev train · Eddy current braking · Ideal braking curve · Fuzzy control

## 1 Introduction

As a new type of rail vehicle, the high-speed maglev train maintains a certain air gap between the train and the track during the running process. And, there is no contact friction between the train and the track, so it can run at very high speeds. At present, the maximum speed setting of the electrical magnetic system (EMS) high-speed maglev train has reached 600 km/h. As the maximum speed increases, the safety

---

H. Qi (✉)

Technical Research Department, CRRC Industry Research Institute Co., Ltd.,  
Beijing, China  
e-mail: [qihongfeng@errgc.cc](mailto:qihongfeng@errgc.cc)

W. Hao · J. Liu

School of Electrical Engineering, Beijing Jiaotong University, Beijing, China  
e-mail: [17121438@bjtu.edu.cn](mailto:17121438@bjtu.edu.cn)

J. Liu

e-mail: [liujq@bjtu.edu.cn](mailto:liujq@bjtu.edu.cn)

performance of the train has become a primary concern. When the train is in a sudden emergency or train failure, the operation control system can immediately cut off the traction system and rely on the eddy current braking system to provide braking force to stop the train. Due to the characteristics of the maglev train and the special structure of the maglev track, the train is required to be parked in the target parking area. Therefore, it becomes the focus of research that how to control the braking force of the eddy current braking system to achieve the target of stopping the train in the parking area.

As one of the key technologies for the safety operation of maglev trains, there have been a lot of researches on eddy current braking systems. However, there are relatively few studies on eddy current braking control. A method of applying fuzzy controller to eddy current braking control is proposed in [1]; however, it is only used in the control of rotary eddy current brake. A method for judging the safety braking level of the train is proposed in [2], but an effective control strategy is not proposed to achieve the tracking control of the train position.

This paper analyzes the principle of eddy current braking and the characteristics of safety braking force of 600 km/h high-speed maglev train and proposes an eddy current braking control strategy for ideal braking curve tracking control according to the target of safety braking control, which uses a fuzzy controller to determine the eddy current braking level and achieves the target of stopping the train in the target parking area through closed-loop tracking control of the actual train position. Then, it verifies the effectiveness of this proposed eddy current braking control strategy by the simulation model built by MATLAB.

## 2 Principle of Eddy Current Braking

It is known from the electromagnetic field theory that the moving electric field interacts with the magnetic field to suppress the change of the magnetic field or electric field [3].

For the maglev train, when the train is stationary, as shown in Fig. 1a, the magnetic flux is generated by the excitation coil. This magnetic flux generates a magnetization current on the rail surface, and the magnetization current interacts with a magnetic field generated by the excitation coil to form a magnetic field force  $F$ . When the train is running, the eddy current brake is starting as shown in Fig. 1b. For the front end of the train moving direction, the magnetic flux has a tendency to strengthen, so that eddy current will be induced to cancel the increased magnetic flux on the rail surface; thus, the magnetic field is weakened in the air gap. For the back end of the train moving direction, the situation is exactly the opposite of the front end. In this way, the magnetic induction line in the air gap leans toward the horizontal direction, and the magnetic field force forms an angle with the horizontal direction. This magnetic field force can be divided into two forces, the normal direction is the electromagnetic attraction force  $F_A$ , and the horizontal direction is the eddy current braking force  $F_B$  [4–6].

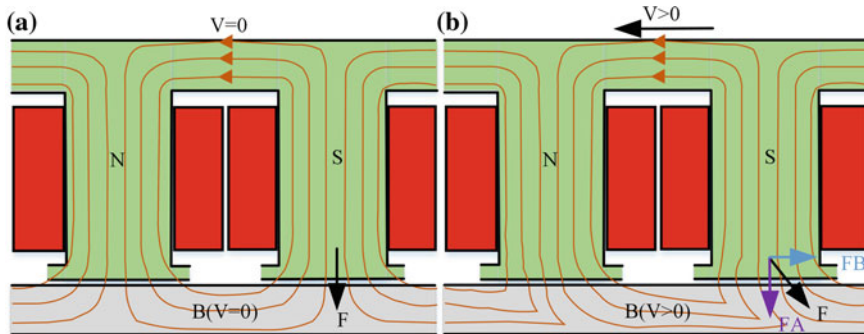


**Fig. 1** Principle of eddy current braking: **a** The train is stationary. **b** The train is running

### 3 Control Strategy of Safety Braking

#### 3.1 Analysis of Safety Braking Force

When the braking failure of the train traction system or other emergency occurs, train operation control system first cuts off the train traction system and then starts the safety braking system. In the initial braking stage, the train speed is relatively high, the normal force is small, and the electromagnet is not in contact with the wear plate. Therefore, the eddy current braking system only generates horizontal eddy current braking force. With the decrease of the train speed, the normal force increases, eventually causing the electromagnet to contact with the wear plate to generate friction. When the train speed drops to 10 km/h, the skids are released and the eddy current braking system is turned off. The train is released from suspension, and the skids are used to brake the train to the target parking point. Also, during the braking process, the guiding electromagnet produces eddy current induction to generate braking force, which acts on the train together with the braking force generated by the eddy current braking system. In addition, the train is also affected by air resistance, additional ramp resistance and other disturbance forces during braking [4]. Therefore, in the process of safety braking, the resultant force on the train is given by (1).

$$F_T = F_A + F_e + F_w + F_a + F_C + F_G + F_R \quad (1)$$

where  $F_A$  is the air resistance,  $F_e$  is the eddy current braking force,  $F_w$  is the skid friction,  $F_a$  is the copper plate friction,  $F_C$  is the guiding electromagnet resistance,  $F_G$  is the additional resistance of ramp, and  $F_R$  is the disturbance force.

### 3.2 Research on Safety Braking Control Strategy

In the process of safety braking, if the braking force of the eddy current braking system is set to the maximum value, the speed-distance curve of the train braking process in this case is called the upper limit speed curve of safety braking. If eddy current braking force is not applied and only the kinetic energy and potential energy of the train act, the speed-distance curve of the train braking process in this case is called the lower limit speed curve of safety braking.

Safety braking requires that the train can be parked in the parking area accurately. However, if the position and speed of the train are not monitored in real time during braking, the following may occur:

1. When the train is braking with the maximum eddy current braking force, the parking position will still exceed the target parking area.
2. When the train is braking with the minimum eddy current braking force, the parking position will still do not reach the target parking area.

In order to avoid the above situation, the train operation control system, in the control process, is required to monitor the train speed and position information in real time to ensure that the train always runs in the safety protection area composed of the upper speed curve of safety braking and the lower speed curve of safety braking. At the same time, when the safety braking system starts, the operation control system needs to adjust the value of the safety braking force in real time to ensure that the train can be safely and accurately parked at the target parking area.

**Generation and Tracking Control of Ideal Braking Curve.** In the process of safety braking, due to the cutting of the traction system, only the train dynamic model is considered in the control process, as given in Eq. (2).

$$\begin{cases} \frac{ds}{dt} = v \\ \frac{dv}{dt} = F_T/M \end{cases} \quad (2)$$

where  $s$  is the distance of train braking,  $v$  is the train speed,  $F_T$  is the total braking force, and  $M$  is the total weight of the train.

*Ideal Braking Curve.* Ideally, it is assumed that there is no error between the eddy current braking force obtained by Eq. (1) and the braking force generated by the actual eddy current braking system, and the train has no disturbance, i.e.,  $F_R = 0$  in Eq. (1).

When the safety braking is started, the train speed-distance curve is solved by using the train dynamics model according to the initial braking speed and weight of the train in the vehicle safety computer, as given in Eq. (2). The eddy current braking of 600 km/h high-speed maglev train is divided into 7 braking levels, and the corresponding excitation currents are 61.6 A, 52.8 A, 44 A, 35.2 A, 26.4 A, 17.6 A and 8.8 A, respectively. The vehicle safety computer (VSC) first calculates the train speed-distance curve  $v_0(s)$  at the braking level of 0 and determines the

relationship between the position  $P_0$  at which the train speed is 0 and the target parking point  $P$ . If  $P_0$  does not exceed the target point  $P$ , then continue to calculate the speed-distance curve  $v_1(s)$  of the next braking level and determine whether the parking position  $P_1$  exceeds the target parking point  $P$ . According to this rule, the calculation is carried out step by step until  $P_k > P$  is established, and the level of  $k$  and  $k - 1$  is taken as the safety braking level of the train. Then, the speed-distance curve  $v_k(s)$  corresponding to the  $k$  braking level is shifted to the target parking point  $P$  to obtain the new speed-distance curve  $v_{kp}(s)$ , as shown in Fig. 2. The intersection point  $P_c$  obtained by calculating the two speed-distance curves  $v_{kp}(s)$  and  $v_{k-1}(s)$  is the switching point of eddy current braking.

*Tracking Control.* Since there are some random disturbances in the actual safety braking process, if the train still uses the  $k - 1$  braking level before  $P_c$  point and switches to the  $k$  braking level when reaching  $P_c$  point, it may not be able to stop at the target parking point. Therefore, in the process of the actual safety braking control, the ideal braking speed-distance curve is calculated according to the initial braking speed and the target parking distance to obtain the ideal braking distance  $S_{ref}$  at the current moment, and then, the train position is monitored in real time and compared with the target parking point to obtain the actual braking distance  $S$  at the current moment. After that, the eddy current braking level controller sets the eddy current braking level of the train according to the position deviation  $\Delta S = S_{ref} - S$  and obtains the corresponding excitation current value according to the braking level to calculate the eddy current braking force of the train to achieve the purpose of tracking the ideal braking curve [7]. The tracking control block diagram is shown in Fig. 3.

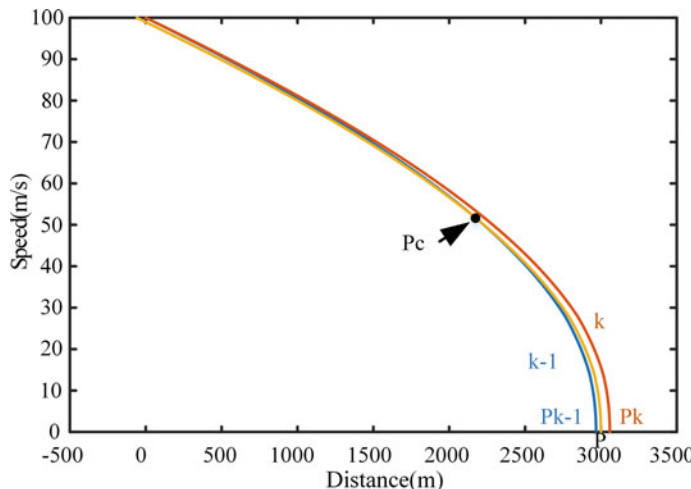
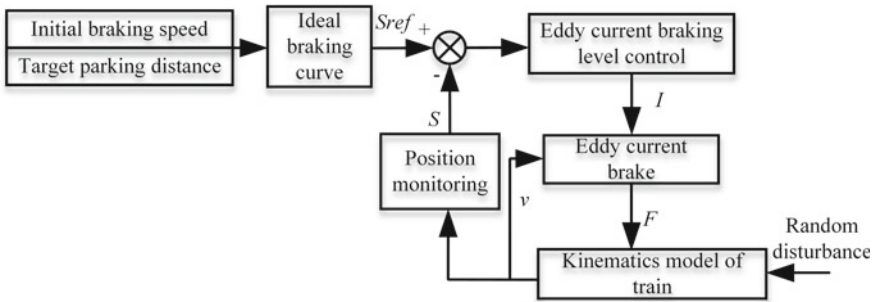


Fig. 2 Ideal braking curve



**Fig. 3** Block diagram of braking control

### 3.3 Eddy Current Braking Level Control

Due to the nonlinearity of the eddy current braking system and the discreteness of the eddy current braking level, the safety braking model of the maglev train becomes a nonlinear system. The traditional PI control cannot fully achieve the control target. Therefore, the fuzzy controller is selected to control the eddy current braking level.

Fuzzy control is a kind of nonlinear intelligent control based on fuzzy set theory, fuzzy language and fuzzy logic. It is usually expressed in the form of “if condition, then result”, and the core part is the fuzzy controller, as shown in Fig. 4. The fuzzy controller used in the eddy braking level control has two input variables  $e$  and  $e^*$ , which, respectively, represent the deviation between the ideal and actual braking distance of the train, and the rate of change of the deviation  $E$  and  $EC$  are fuzzy sets reflecting the braking distance deviation and deviation change after the fuzzification.  $IF$  is the fuzzy control output variable, and  $if$  is the output accurate quantity obtained by the defuzzification. The two parameters  $k_e$  and  $k_{ec}$  at the input and the parameter  $k_u$  at the output are called the quantization factor and the proportion factor, which are used to achieve the fuzzification of the input and the defuzzification of the output. When  $e$  is large, a large value of  $k_e$  and  $k_u$  is conducive to eliminating the error and ensuring the rapidity of the system. When  $e$  is small, the system will approach the steady state. If  $k_{ec}$  is large and  $k_u$  is small, the overshoot can be avoided and the system can enter the steady-state accuracy range as soon as possible.

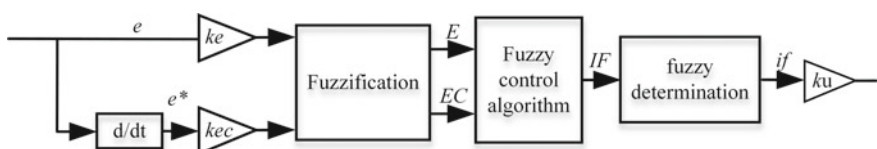


**Fig. 4** Fuzzy controller

The length of a single maglev train is about 25 m. According to the characteristics and requirements of the maglev train, the stopping error of the train should be half of the length of the single train, that is, the allowable error is  $[-12, 12]$ . Therefore, the fuzzy set range of braking distance deviation  $e$  and deviation change  $e^*$  can be set as  $X = \{-6, -5, -4, -3, -2, -1, 0, 1, 2, 3, 4, 5, 6\}$ , the quantization factor  $k_e$  can be set as 0.5, and the quantization factor  $k_{ec}$  can be set as 0.25. The eddy current brake includes 7 braking levels of 8.8, 17.6, 26.4, 35.2, 44, 52.8 and 61.6 A. Therefore, the fuzzy set of the fuzzy controller output  $U$  can be set as  $\{-6, -5, -4, -3, -2, -1, 0, 1, 2, 3, 4, 5, 6\}$ , and the proportion factor  $k_u$  can be set as 8.8. By rounding the accurate output  $u$ , 7 braking levels can be obtained completely. The calculation formula is given in Eq. (3).

$$I = \begin{cases} 8.8 & 61.6 + u_r k_u < 8.8 \\ 61.6 + u_r k_u & 8.8 \leq 61.6 + u_r k_u \leq 61.6 \\ 61.6 & 61.6 + u_r k_u > 61.6 \end{cases} \quad (3)$$

where  $u_r$  is the value of the exact output  $u$  rounded off,  $k_u$  is the proportion factor, and  $u_r k_u$  is the adjustment quantity of excitation current.

According to the setting of the input and output range of the eddy current braking system, three input and output variables  $e$ ,  $e^*$  and  $u$  are taken in each range to take 7 linguistic variables, which are positive big, positive medium, positive small, zero, negative small, negative medium and negative big, and the membership functions are all triangular.

In the actual eddy current braking control process, when the braking distance is less than the ideal braking distance, the actual braking deceleration is greater than the ideal braking deceleration, and the braking force should be reduced to make the actual and ideal braking distances equal. According to the control principle as described above, the control rules of the fuzzy controller are designed as given in Table 1.

**Table 1** Fuzzy control rules

EC	E							
	NB	NM	NS	ZE	PS	PM	PB	
NB	PB	PB	PB	PB	PM	ZE	ZE	
NM	PB	PB	PB	PB	PM	ZE	ZE	
NS	PM	PM	PM	PM	ZE	NS	NS	
ZE	PM	PM	PS	ZE	NS	NM	NM	
PS	PS	PS	ZE	NM	NM	NM	NM	
PM	ZE	ZE	NM	NB	NB	NB	NB	
PB	ZE	ZE	NM	NB	NB	NB	NB	

## 4 Simulation

### 4.1 Simulation Results and Analysis

We conduct the simulation in the following three conditions:

- When safety braking starts, the initial speed of braking is 166.7 m/s and the target distance of safety braking is 17,000 m. The train runs on a straight track without random disturbance. The simulation results are shown in Fig. 5.

By analyzing the simulation waveform, it can be seen that in the ideal braking process, as shown in Fig. 5a, the train uses 1 braking level at the beginning. When it reaches 9776 m, the braking level will be switched to level 2 to continue braking. In the actual braking process, as shown in Fig. 5c, the distance error between the actual braking distance and the ideal braking distance is within the tolerance of  $[-12, 12]$ , and the final distance error is stable at 1.998 m. Therefore, the control strategy is considered to be effective for the maglev train running on a straight track without random disturbance.

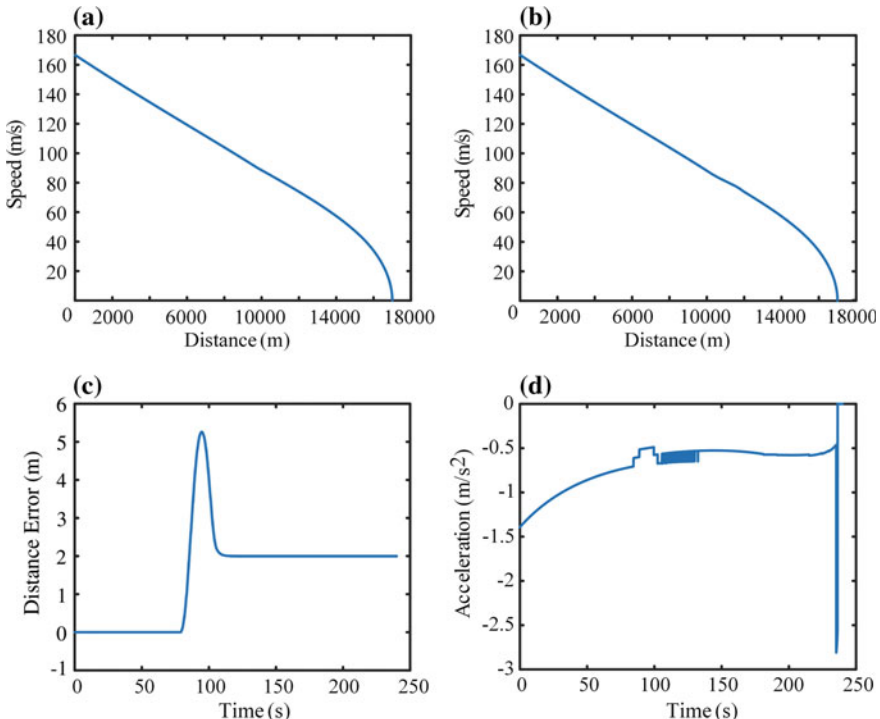


**Fig. 5** Simulation results of condition one: **a** The ideal braking curve. **b** The actual braking curve. **c** The distance error. **d** The braking acceleration

2. When safety braking starts, the initial speed of braking is 166.7 m/s and the target distance of safety braking is 17,000 m. There is a ramp from 4 to 6 km ahead of the train braking with a slope of  $\pm 5\%$ , and there is a disturbance error of 20%. The simulation results are shown in Fig. 6.

By analyzing the simulation waveform, it can be seen that in the ideal braking process, as shown in Fig. 5a, the train uses two braking levels for braking. But in the actual braking process, as shown in Fig. 6a, the braking level of the train is constantly changing, which can be reflected by the change of the acceleration as shown in Fig. 6b. In this condition, the actual braking can also track the ideal braking curve. The final distance error between the actual braking distance and the ideal braking distance is stable at 2.046 m as shown in Fig. 6c. Compared with the case of a straight track without random disturbance, although the error is increased, it is still within the error tolerance range. Therefore, it is considered that the control strategy is still effective in the case of adding  $\pm 5\%$  ramp and 20% random disturbance error.

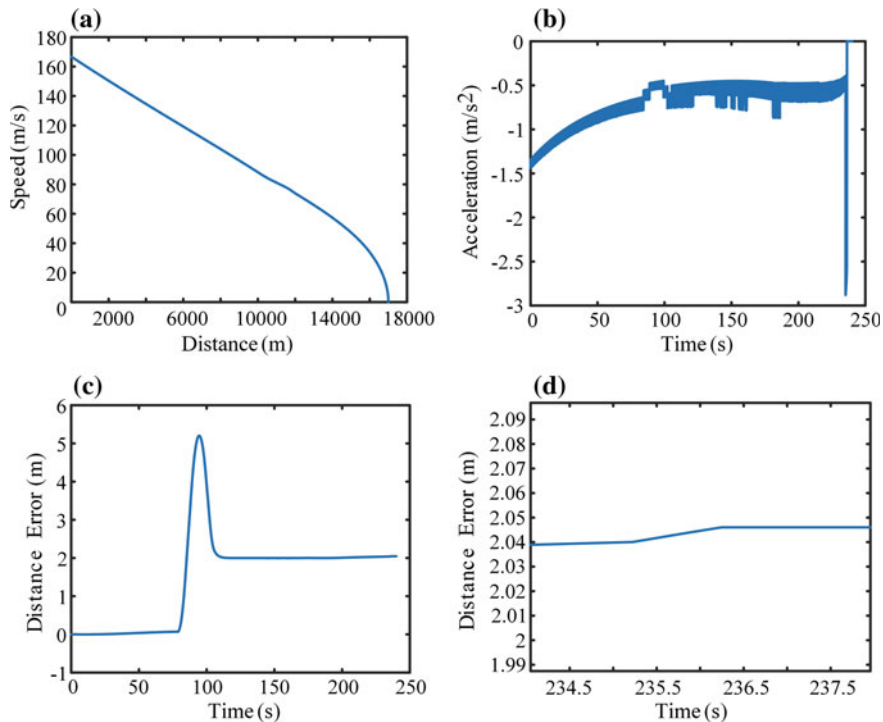


**Fig. 6** Simulation results of condition two: **a** The actual braking curve. **b** The braking acceleration. **c** The distance error. **d** The error magnification

## 5 Conclusion

This paper proposes an eddy current braking control strategy for tracking the ideal braking curve by analyzing the generation principle of eddy current braking force and the safety braking force of maglev train. Based on the theoretical analysis of control strategy, the safety braking process of maglev train is realized by MATLAB. By comparing the simulation results under different braking conditions, it can show that the train can track the ideal braking curve and stop at the target stopping point safely and accurately, which verifies the accuracy of eddy current braking control strategy proposed in this paper.

**Acknowledgements** This work is supported by the National Key Research and Development Program of China (2016YFB1200602-29).

## References

1. Zhu W, Tang J, He R (2006) Application of on-line rule of self-regulation stepping fuzzy control to eddy current retarder. *J Jiangsu Univ (Natural Science Edition)* 1(02):126–129 (in Chinese)
2. Luo T, Guo Q (2006) Study on high-speed Maglev safely braking control based on Eddy Current Brake (ECB). *Railway Locomotive Car* 1(05):41–43 (in Chinese)
3. Yan G, Fang Y, Zhang F (2010) Design and analysis of hybrid excitation rail eddy current brake system of high-speed train. *J Mech Electr Eng* 27(08):19–22 (in Chinese)
4. Li H, Zhan P, Ding F et al (2015) Simulating analysis of braking force characteristics of linear Eddy Current Brake. *Railway Locomotive Car* 35(06):25–27+31 (in Chinese)
5. Jang S-M, Lee S-H, Jeong S-S et al (2002) The characteristics analysis of eddy current brake system using the linear Halbach array. In: 2002 IEEE International Magnetics Conference (INTERMAG). IEEE, Amsterdam, The Netherlands, pp FT6
6. Kou B, Jin Y, Zhang H et al (2014) Analysis and design of hybrid excitation linear Eddy Current Brake. *IEEE Trans Energy Convers* 496–506
7. Zamani A (2014) Design of a controller for rail eddy current brake system. *IET Electr Syst Transp* 4(2):38–44

# Extended Kalman Filter Observer Based on the Induction Motor Model Considering Iron Loss



Leiting Zhao, Chengguang Huang, Shaobo Yin, Dongyi Meng,  
and Kan Dong

**Abstract** The traditional induction motor equivalent circuit defects due to the neglect of iron loss. This paper analyzes the equivalent circuit of the induction motor considering iron loss and derives the basic equations of the motor in the two-phase stationary reference frame and the two-phase rotating reference frame. On this basis, an extended Kalman filter observer based on the model of induction motor considering iron loss is designed to observe the speed and rotor flux of induction motor. Besides, a speed sensorless vector control system is realized, and the performance of Kalman filter observer and speed sensorless technology is verified by theoretical and experimental results.

**Keywords** Induction motor · Iron loss · Extended Kalman filter · Speed sensorless control

## 1 Introduction

In the industrial application of induction motor, the speed information is essential in the control process such as traditional FOC and DTC [1, 2]. The method of obtaining speed information mainly involves installing the speed sensor on the motor shaft. However, this measuring method brings about many drawbacks, such as increased system complexity, high cost and application scenario limitation.

To solve these problems, researchers have focused on the speed sensorless technology of induction motor, and the accurate observation of the speed is the most important part. Among the existing observation methods, extended Kalman filter (EKF) observer has been widely used due to its randomness suitable for

---

L. Zhao (✉) · C. Huang · K. Dong  
China Academy of Railway Sciences Corporation, 100018 Beijing, China  
e-mail: [18117037@bjtu.edu.cn](mailto:18117037@bjtu.edu.cn)

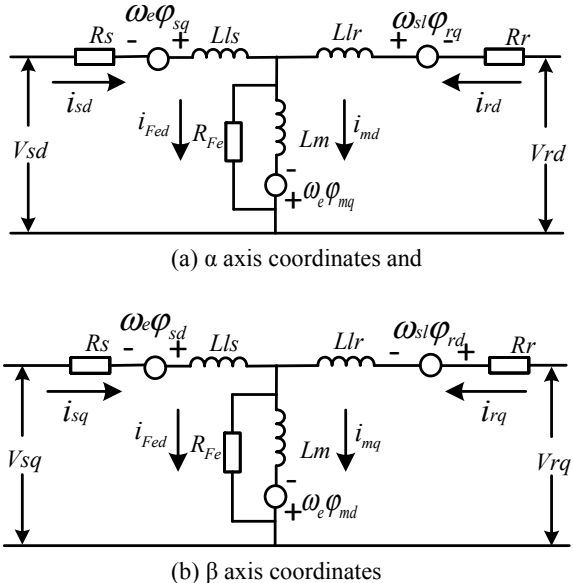
S. Yin · D. Meng  
School of Electrical Engineering, Beijing Jiaotong University,  
No.3 Shang Yuan Cun, Hai Dian District, 100044 Beijing, China

uncertainties and nonlinearities inherent in induction motor models, high observation precision, strong parameter robustness and so on [3–5]. In terms of motor modeling considering iron loss, there are currently two main types, one is the series model, and the other is the parallel model where the iron loss resistor and excitation branch are in parallel. Since the  $d$ -axis current deduced by the series model in the two-phase rotating coordinate system is not zero, it is not suitable for rotor orientation vector control [6–8]. Therefore, this paper uses paralleling model considering the iron loss of the motor to analyze the speed senseless technology.

## 2 The Induction Motor Model Considering Iron Loss

In order to obtain the motor model considering iron loss, one needs to start with the T-type equivalent circuit of the motor, get the equivalent circuit of the motor model considering iron loss and then derive the mathematical model of the motor according to the equivalent circuit. It is assumed that the winding of the motor is three-phase symmetric, and the air-gap flux of the motor is distributed evenly in space; the magnetic circuit of the motor is unsaturated, and the self-inductance and mutual inductance of the winding are linear. Based on the assumptions above, the T-type equivalent circuit considering the iron loss of the motor in the two-phase static coordinate system can be obtained, as shown in Fig. 1.

**Fig. 1** Motor model considering iron loss in two-phase static coordinate system



According to the equivalent circuit, the voltage equation of the motor considering iron loss can be obtained as follows:

$$\begin{cases} 0 = R_r i_{rd} - \omega_{sl} \varphi_{rq} + p \varphi_{rd} \\ 0 = R_r i_{rq} + \omega_{sl} \varphi_{rd} + p \varphi_{rq} \end{cases} \quad (1)$$

where  $\omega_{sl}$  is the slip frequency;  $\varphi_{sd}$ ,  $\varphi_{sq}$  are stator flux linkage of  $d$ - and  $q$ -axis, respectively;  $\varphi_{rd}$ ,  $\varphi_{rq}$  are rotor flux linkage of  $d$ - and  $q$ -axis, respectively;  $\varphi_{md}$ ,  $\varphi_{mq}$  are main flux linkage of  $d$ - and  $q$ -axis, respectively;  $i_{Fed}$ ,  $i_{Feq}$  are the winding currents of  $d$ - and  $q$ -axis, respectively, based on equivalent iron loss.

Neglect the stator and rotor leakage inductance and adapt the rotor magnetic field orientation. Then, the flux linkage of system steady state can be described:

$$\begin{cases} \varphi_{sq} = \varphi_{rq} = \varphi_{mq} = 0 \\ \varphi_{sd} = \varphi_{rd} = \varphi_{md} = \varphi_r = i_{sd} L_m \\ p \varphi_{rd} = p \varphi_{rq} = 0 \end{cases} \quad (2)$$

Combine (1) and (2), we can get

$$i_{rd} = 0, i_{rq} = -(\omega_{sl} \varphi_r) / R_r \quad (3)$$

Since each current variable is represented as direct current in the two-phase rotating coordinate system and the voltage drop on  $L_m$  is 0, the voltage equation of the excitation loop in Fig. 1 can be obtained as follows:

$$\begin{cases} R_{Fe} i_{Fed} + \omega_e \varphi_{mq} = 0 \\ R_{Fe} i_{Feq} - \omega_e \varphi_{md} = 0 \end{cases} \quad (4)$$

Combining (2) and (4), the expression of the branch current of iron loss can be obtained as follows:

$$i_{Fed} = 0, i_{Feq} = (\omega_e \varphi_r) / R_{Fe} \quad (5)$$

Ignore the stator and rotor leakage inductance of the motor, and according to (3) and (5), the equivalent circuit considering iron loss in Fig. 1 can be simplified as follows:

It can be seen from Fig. 2 that the iron loss will cause the rotor current and flux linkage of the motor in operation to interfere with each other. If the iron loss of the motor is not taken into account in the vector control, the decoupling of the  $d$ - and  $q$ -axis components will be incomplete, which will lead to the orientation deviation of the flux and reduce the dynamic response performance of the motor. However, if the iron loss of the motor is considered, the accuracy of motor flux observation and the control performance of the system can be improved.

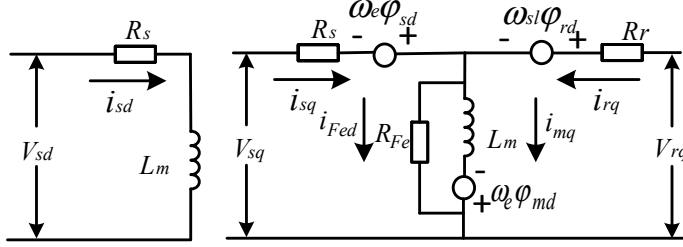


**Fig. 2** Simplified equivalent circuit of motor model considering iron loss

### 3 Extended Kalman Filter Observer

Due to the strong anti-interference ability of the extended Kalman filter, the high observation accuracy, the small influence of the motor parameters and the good robustness [9–11], this paper combines the motor model considering the iron loss and the extended Kalman filter in order to observe the speed and flux linkage of the motor and implement vector control without a speed sensor.

In the two-phase rotating reference frame,  $x = [i_{sx}, i_{s\beta}, \varphi_{rx}, \varphi_{r\beta}]^T$  is selected as state variable; the stator voltage  $u = [u_{sx} u_{s\beta}]^T$  is input variable, and  $y = [i_{sx}, i_{s\beta}]^T$  is the output variable. In order to observe the rotational speed, a speed variable is added as the state variable on the basis of the original state equation, and a five-order augmented motor model is required. At this point, the state variable of the motor can be described:

$$x_a = [i_{sx} i_{s\beta} \varphi_{rx} \varphi_{r\beta} \omega_r]^T \quad (6)$$

The corresponding state equation of the augmented motor model is as follows:

$$\frac{dx_a(t)}{dt} = A_a x_a(t) + B_a u(t) \quad (7)$$

$$y(t) = C_a x_a(t) \quad (8)$$

where  $T_r = L_r/R_r$ ,  $\xi = L_m/(\sigma L_s L_r)$ ,  $\sigma = 1 - L_m^2/(L_s L_r)$

$$A_a = \begin{bmatrix} -R_s/(\sigma L_s) - \xi L_m/T_r & 0 & \xi/T_r & \xi(\omega_r - (R'_F e L_m^2 \omega_e)/(T_r L_r)) & 0 \\ 0 & -R_s/L_r - \xi L_m/T_r & -\xi(\omega_r - (R'_F e L_m^2 \omega_e)/(T_r L_r)) & \xi/T_r & 0 \\ L_m/T_r & 0 & -1/T_r & -\omega_r + (R'_F e L_m^2 \omega_e)/(T_r L_r) & 0 \\ 0 & L_m/T_r & \omega_r - (R'_F e L_m^2 \omega_e)/(T_r L_r) & -1/T_r & 0 \\ 0 & 0 & 0 & 0 & 0 \end{bmatrix}$$

$$B_a = \begin{bmatrix} 1/(\sigma L_s) & 0 & 0 & 0 & 0 \\ 0 & 1/(\sigma L_s) & 0 & 0 & 0 \end{bmatrix}^T, C_a = \begin{bmatrix} 1 & 0 & 0 & 0 & 0 \\ 0 & 1 & 0 & 0 & 0 \end{bmatrix}$$

The above-augmented matrix contains the rotational speed and parameters of the motor. When the sampling period is small, the speed can be regarded as approximately constant within a sampling period, which can be considered as  $p\omega_r = 0$ . After discretization of (7) and (8), the errors caused by approximation and discretization are treated as system noise, and the discretization equations obtained by adding system noise and measurement noise are as follows:

$$x(k+1) = A_d x(k) + B_d u(k) + V(k) \quad (9)$$

$$y(k) = C_d x_d(k) + W(k) \quad (10)$$

where  $A_d$ ,  $B_d$  and  $C_d$  are the discretized matrix;  $V(k)$  is the system noise,  $W(k)$  is the measurement noise. Regard  $Q$ ,  $R$  as the covariance matrix of  $V(k)$ ,  $W(k)$ ,  $P$  as covariance matrix of system state vector, then  $Q$ ,  $R$  and  $P$  can determine the statistics and measurement of noise. Besides, value coupled with the “~” is the predicted value, and “^” is the estimated value. Then, the Jacobi matrix of the discrete augmented motor model is

$$F(k) = \frac{\partial}{\partial x} (A_d x + B_d u) \Big|_{x=\tilde{x}(k)} = \begin{bmatrix} 1 - \left(\frac{R_e}{\sigma L_s} + \xi \frac{L_m}{T_r}\right)T & 0 & \frac{\xi}{T_r} T & \xi \left(\omega_r - \frac{R'_e L_m^2 \omega_e}{T_r L_r}\right) T & \xi \tilde{\varphi}_{rq}(k) T \\ 0 & 1 - \left(\frac{R_e}{\sigma L_s} + \xi \frac{L_m}{T_r}\right)T & \xi \left(-\omega_r + \frac{R'_e L_m^2 \omega_e}{T_r L_r}\right) T & \frac{\xi}{T_r} T & -\xi \tilde{\varphi}_{rd}(k) T \\ \frac{L_m}{T_r} T & 0 & 1 - \frac{1}{T_r} T & \left(-\omega_r + \frac{R'_e L_m^2 \omega_e}{T_r L_r}\right) T & -\tilde{\varphi}_{rq}(k) T \\ 0 & \frac{L_m}{T_r} T & \left(\omega_r - \frac{R'_e L_m^2 \omega_e}{T_r L_r}\right) T & 1 - \frac{1}{T_r} T & \tilde{\varphi}_{rd}(k) T \\ 0 & 0 & 0 & 0 & 1 \end{bmatrix} \quad (11)$$

$$H(k) = \frac{\partial}{\partial x} C_d x \Big|_{x=\tilde{x}(k)} = \begin{bmatrix} 1 & 0 & 0 & 0 & 0 \\ 0 & 1 & 0 & 0 & 0 \end{bmatrix} \quad (12)$$

The implementation of extended Kalman filter observer can be divided into two phases: prediction phase and filtering phase. In the prediction stage, the predicted value  $\tilde{x}(k+1)$  of the next state is calculated according to the motor model and the state at the last state, and the system state vector covariance matrix  $P$  is calculated through the covariance matrix  $Q$ :

$$\tilde{x}(k+1) = A_d \tilde{x}(k) + B_d u(k) \quad (13)$$

$$\tilde{P}(k+1) = f(k+1) \tilde{P}(k) F^T(k+1) + Q \quad (14)$$

In filtering stage, the first step is to calculate the Kalman gain matrix of motor,

$$K(k+1) = \tilde{P}(k+1)H^T(k+1)[H(k+1)\tilde{P}(k+1)H^T(k+1) + R]^{-1} \quad (15)$$

Then, by increasing the error correction term, the next state estimation value can be obtained from the state predicted value, and at the same time, the state error covariance matrix can be updated:

$$\hat{x}(k+1) = \tilde{x}(k+1) + K(k+1)[y(k+1) - H(k+1)\hat{x}(k)] \quad (16)$$

$$\hat{P}(k+1) = \tilde{P}(k+1) - K(k+1)H(k+1)\tilde{P}(k+1) \quad (17)$$

By substituting (9)–(12) into (13)–(17), the Kalman filter iterative formula is obtained, and the motor flux can be observed, while the motor speed is identified.

## 4 Experimental Implementation of Speed Sensorless Control

Considering the iron consumption motor model, the vector control system implementation based on the extended Kalman filter is shown in Fig. 3. During the operating process, only DC bus voltage and a, b phase currents of the inverter are collected, and motor speed is observed through the designed EKF observer.

The experiment adopts the digital control system with TI company dual-core TMS320F28377D and Xilinx Sparatan6 series FPGA as the core. A photoelectric encoder is reserved for the motor on the experimental platform, which can be used to measure the real-time speed of the motor. Through the DA output channel reserved on the main control board, internal data variables can be displayed in real time. Moreover, the motor parameters of the experimental platform are shown in Table 1.

Firstly, the performance of the extended Kalman filter based on the iron consumption model is tested. From the waveforms in Fig. 4, observed rotor flux has sinusoidal waveforms at both high and low speeds. In the full speed range, the extended Kalman filter can still accurately obtain the rotor flux signal, which provides a foundation for the operation of no speed sensor in the full speed range.

Then, the speed observation performance of the extended Kalman filter is verified. As shown in Fig. 5, the motor starts and accelerates from zero to 90 Hz. From the waveform of the observed speed and the actual speed, the observed speed is almost consistent with the actual speed. When the observed speed is brought into the vector control, the stator current does not have divergency and other unstable phenomena, and the motor runs smoothly in the whole acceleration process.

Through the above experimental results, it can be found that the extended Kalman filter based on the iron consumption model can accurately observe the rotor flux at low and high speeds and estimate the motor speed. As a result, it can run

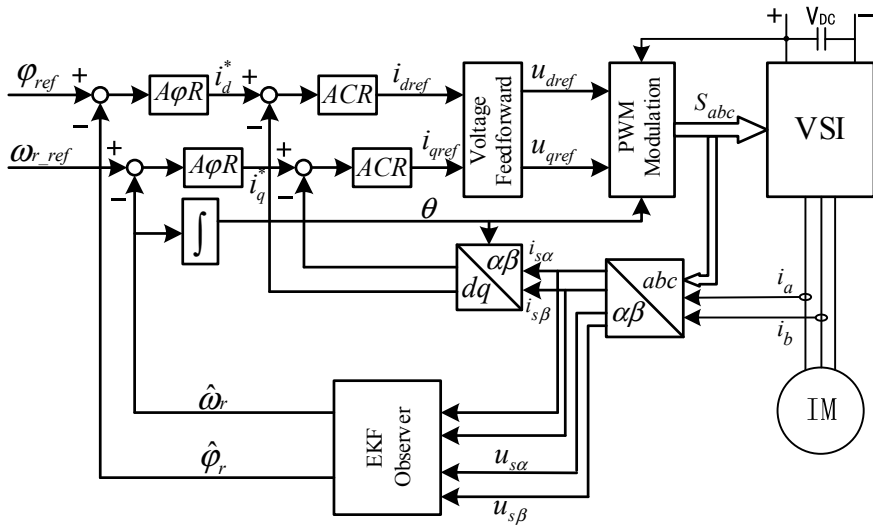


**Fig. 3** Speed sensorless vector control system

**Table 1** Table captions should be placed above the tables

Rated voltage/frequency: 1287 V/84 Hz	Stator resistance: 0.223 Ω
Rated current: 88A	Rotor resistance: 0.103 Ω
Rated power: 160 kW	Mutual inductance: 0.0438 H
Rated speed: 2520 r/min	The leakage inductance of rotor: 0.002076 H
Number of pole-pairs: 2	Rated efficiency: 93%
Rated flux: 1.41 Wb	Power factor: 0.86

stably even under the condition that there are a large number of harmonics in the stator current and large noises in the measurement results. So far, the excellent performance of the observer designed in this paper has been verified.

## 5 Conclusion

This paper has analyzed the mathematical model of the iron loss asynchronous motor. Besides, the extended Kalman observer based on the iron loss motor model has improved the control precision of the sensorless vector control system. The experimental results show that the designed observer has good observation performance and can achieve satisfactory dynamic and static performance in a wide speed range, which provides a reference for the realization of sensorless vector control.

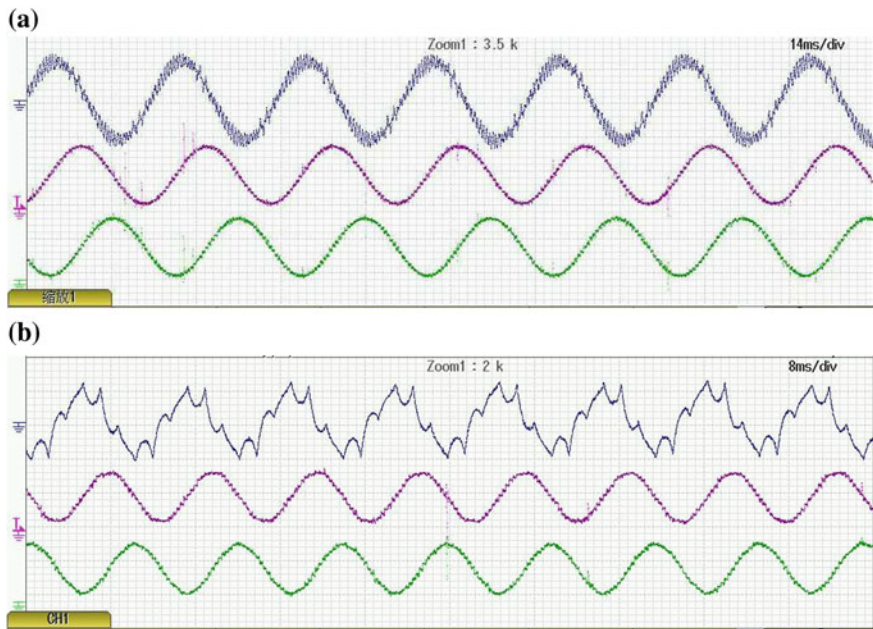


Fig. 4 Flux linkage observation waveform of motor running at both low and high speed

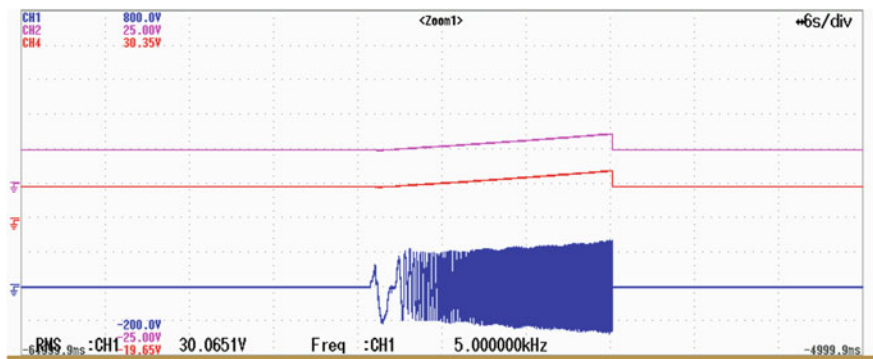


Fig. 5 Actual speed and estimated speed

**Acknowledgements** This work was supported by Foundation of China Academy of Railway Sciences (2017YJ017) and project 18ZHWF0309

## References

1. Diao LJ, Sun DN, Dong K et al (2013) Optimized design of discrete traction induction motor model at low-switching frequency. *IEEE Trans Power Electron* 28(10):4803–4810
2. Feng X (2009) Electric traction AC drive and its control system. Higher Education Press (in Chinese)
3. Zhao X, Tong R, Wang S et al (2016) A speed-sensorless direct torque control based on the extended Kalman. *J Anhui Agric Sci* (6):303–308
4. Min X, Liu B (2018) Application of extended Kalman filter in the sensorless vector control system of synchronous motor. *Ind Control* 25(08):61–63
5. Li Y, Diao L (2016) Parallel model of induction motor considering iron consumption and its influence on vector control. *New Electr Electr Technol* 35(01):13–18 (in Chinese)
6. Moulahoum S et al (2007) Induction machine modeling with saturation and series iron losses resistance. In: IEEE international electric machines & drives conference
7. Liu X, Li H, Tan X (2008) Vector control of induction motor based on series iron loss. *J Naval Univ Eng* (02):71–74
8. Li J, Du X, Song H, Zhong Y (2014) Experimental evaluation of induction machine parameter identification considering iron loss. *Trans China Electro-Technical Soc* 29(03):89–95
9. Zhang Y, Zhang H, Li Z (2015) Speed sensorless high performance control technology for asynchronous motor. Machinery Industry Press (in Chinese)
10. Du T, Vas P, Stronach AF et al (1994) Application of Kalman filters and extended Luenberger observers in induction motor drives. In: Intelligent motion proceedings
11. Bose BK (2002) Modern power electronic and AC drives. Prentice Hall, Upper Saddle River, NJ

# Online Fault Protection Method and Its Implementation Based on Control Bus for Electromechanical Composite Transmission Bench Test System



Lei Guo, Gen Zeng and Yaoheng Li

**Abstract** At present, the faults of the electromechanical composite transmission bench test system are presented in a complex and diverse manner, and the fault handling is mostly manual; its safety performance is reduced, and it is easy to cause delay and secondary failure. This paper aims at the safety of the system, guarantees that the fault can be handled in the shortest time after the fault occurs, proposes an online fault protection method for the electromechanical composite drive system based on control bus, and applies the method to the test bench. The method is oriented to the fault diagnosis of the electromechanical composite transmission bench test system and can provide a dynamic real-time protection mechanism for the system, and when a system-level alarm or fault occurs during the system operation, the system performs the protection program according to the preset protection logic. In order to ensure system safety and fault coordination, it can provide an information-based means of “reliability prediction” for fault diagnosis and health management of an electromechanical composite transmission.

**Keywords** Electrical composite transmission · Fault diagnosis · Reliability · Electromechanical compound transmission control

## 1 Introduction

In the process of fault diagnosis of the electromechanical composite transmission test system for special vehicles, the system fault detection method mostly uses sensors to connect the monitoring components. The sensor can monitor the working parameters of each component in real time and set the protection limit value if each

---

L. Guo (✉) · G. Zeng · Y. Li  
China North Vehicle Research Institute, Beijing 100072, China  
e-mail: [guodeji@126.com](mailto:guodeji@126.com)

protection limit is triggered to remind the staff in time, and the staff can use the experience to process the obstacle online. This method lacks flexibility, and its fault diagnosis technology monitors the individual components and cannot achieve the synergistic logic protection of the monitoring data. The electromechanical composite transmission system has the characteristics of faster response time than the traditional mechanical transmission, and more real-time fault coordination is needed; in the current processing mode, there is a certain delay when manually processing the fault, which often causes a secondary fault of the system. Nowadays, with the application of communication network technology in vehicles, high-speed real-time control networks such as FlexRay, TTE, TTCAN, and other communication networks have emerged, making the electromechanical composite drive bench test system better for real-time online detection of faults by controlling the way the bus is transmitted and by setting the fault protection logic. So that when the fault occurs, the fault co-processing protection is protected and the safety of the personnel is protected [1].

## 2 Electromechanical Composite Transmission Bench Test System Structure

At present, the main devices of the special vehicle electromechanical composite transmission bench test system include generator, generator rectifier controller, left drive motor, left power inverter controller, right drive motor, right power inverter controller, electromechanical composite transmission control unit, coupling mechanism and dynamometer loading unit, dynamometer power unit, and so on [2]. The controllers communicate with each other through the control bus to complete coordinated control between the drive motor, the generator and the dynamometer loading unit, and the dynamometer power unit. The CAN bus has a maximum transmission rate of 1 Mbps. Because of its unique design, high reliability, and good performance, it is widely used in special vehicle electromechanical compound transmission control systems.

Electromechanical composite transmission structure is shown in Fig. 1. It can be seen from the figure that the electromechanical composite transmission system is composed of a control network, a data monitoring network, and a equipment network; the control network realizes communication with the electromechanical composite transmission system, the industrial computer, and the control monitoring interface through the CAN bus. The data monitoring network monitors the data uploaded by the electromechanical composite transmission through the CAN bus in real time; the equipment network is used for data processing and forwarding between the uploaded data and the human-computer interaction interface.

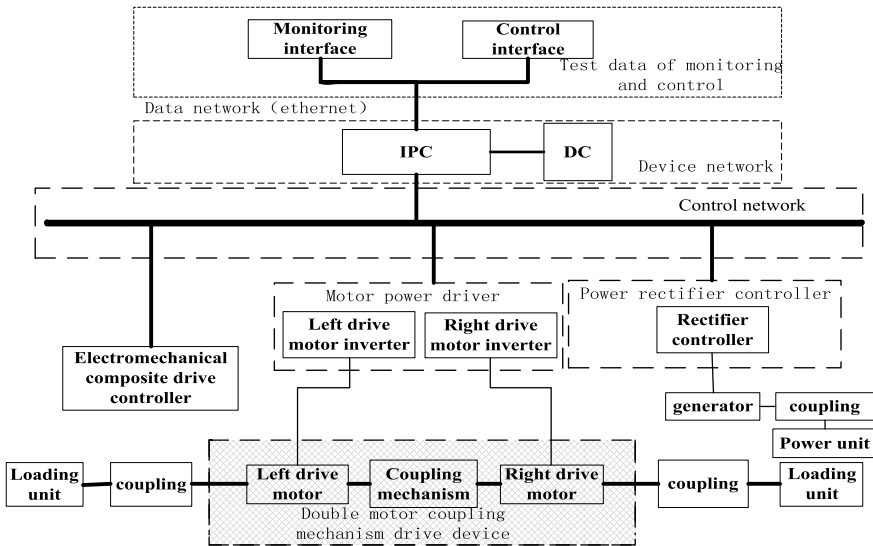


**Fig. 1** Schematic diagram of electromechanical composite transmission bench test system

### 3 Technical Implementation

#### 3.1 Test Project Mode Selection

On the basis of the electromechanical composite transmission bench test system architecture, considering the functional requirements during the test, the electromechanical composite drive system can be decomposed into three parts: generator subsystem, electromechanical composite drive, and generator joint adjustment subsystem.

The generator subsystem comprises of a generator, a generator rectifier controller, and a power unit; the generator subsystem can convert the generated alternating current into a DC 900 V through the generator rectifier controller to supply power to the busbar, thereby converting the electrical energy into mechanical energy through the electromechanical composite transmission; if the generator subsystem is operated separately, it is converted into DC 900 V and then passed through the DC power cabinet and absorbed by the DC power cabinet. The electromechanical composite transmission subsystem includes the electromechanical composite transmission control unit and the loading unit, wherein the electromechanical composite transmission includes the left drive motor and the left drive motor inverter, right drive motor, right drive motor inverter, and coupling mechanism; electromechanical composite drive subsystem can convert DC power supplied by DC power supply system into AC drive through left drive motor inverter and right drive motor inverter, thereby driving the operation of the motor, converting electrical energy into mechanical energy; the electromechanical

composite transmission and generator coupling subsystem integrate the generator subsystem and the electromechanical composite transmission subsystem; the DC 900 V, that can be inverted by the generator passed through the left drive motor inverter and right drive motor inverter and converted to AC to drive the motor operation, converts electrical energy into mechanical energy; and power of the motor and the loading motor provided loading function.

The three subsystems correspond to three working modes; the required modes can be selected according to the needs of the test, and different fault protections are completed according to the different modes. The mode distinction is selected through the mode selection control of the control interface and is sent to the electromechanical composite through the CAN bus and controls the operation of each other control device through the electromechanical composite transmission control unit.

### **3.2 Test Item Sub-Mode Selection**

After the test project mode is determined, the test project mode is abstracted as an input to the test project sub-mode, and the test project sub-mode is selected.

The generator subsystem includes a sub-mode: 1. dynamometer power unit is speed control mode, DC power supply is the current mode, and generator rectifier controller is voltage regulation mode.

The electromechanical composite transmission subsystem includes three sub-modes: (1) dynamometer loading unit is torque mode, and left drive motor and right drive motor are speed modes; (2) dynamometer loading unit is speed mode, and left drive motor and right drive motor are torque modes; (3) dynamometer load unit is torque mode, and left drive motor and right drive motor are torque modes.

The electromechanical composite drive and generator joint adjustment subsystem include three sub-modes: (1) generator rectifier controller is voltage regulator mode, dynamometer power unit is speed mode, left drive motor and right drive motor are speed modes, and dynamometer load unit is torque mode; (2) generator rectifier controller is voltage regulator mode, dynamometer power unit is speed mode, left drive motor and right drive motor are torque modes, and dynamometer load unit is speed mode; (3) generator rectifier controller is voltage regulator mode, dynamometer machine power unit is speed mode, left drive motor and right drive motor are torque modes, and dynamometer load unit is torque mode.

### **3.3 Fault Protection Processing Logic**

After determining the test project mode and the test project sub-mode, the corresponding subsystem test can be carried out. According to the target mode and the

fault degree, the fault state can be divided into different types. Comprehensive consideration of target models divides the fault into light faults and serious failure.

According to the classification of fault states, different faults need to be handled. The fault protection processing logic is further divided into fault condition monitoring and fault protection.

Fault condition monitoring means that after a slight fault occurs in the system, the device is protected by establishing upper and lower limit protections on each of the underlying data channels. For set values and read values, the system will do different processing. For the set value, the system internally limits the set value to a certain range according to the test bench equipment standard. At the same time, when the value manually output by the worker is close to the limit working condition, the system will give an alarm reminder.

For the read value, when the physical quantity of a channel read back is closed to the limit condition, the system will perform a fault alarm to remind the test personnel; and the upper and lower limit alarm values of each channel can be manually modified on the monitoring page, otherwise the system default [3].

Fault protection means that when a serious fault occurs in the system, the fault detection loop will trigger a stop command. After receiving the stop signal, the system will make fault protection shutdown according to the test status given by the equipment. The fault protection scheme is shown in Tables 1, 2, 3, and 4.

Table shows the monitoring set value and the monitoring read value. The DC electrical interface between the power generation rectifier and the left drive motor inverter and the right drive motor inverter are connected with a 900 V high voltage DC power bus (referred as a DC bus). Electrical power coupling is achieved via a DC bus. The upper and lower limits of the voltage setting value in the generator are generally limited to 750–1000 V. When the bearing temperature of the generator exceeds 120 °C, an alarm will be triggered. When the winding temperature exceeds

**Table 1** Set value and read value of each device fault condition monitor

Device	Set point of monitoring	Read value of monitoring
DC	Voltage, electric current, power	Voltage, electric current, power
Motor power	Velocity, torque	Velocity, torque, power
Loading motor	Velocity, torque	Velocity, torque
Generator	DC	DC, torque, velocity, generator rectifier controller/winding temperature/bearing temperature
Electric motor	Velocity, torque	Velocity, torque, voltage, left drive motor inverter controller/right drive motor inverter controller/winding temperature

**Table 2** Target mode for the fault protection logic of the generator subsystem

Sub-target mode	Power supply	Faulty equipment	Stop mode
Power motor speed mode, generator voltage regulation mode, DC power supply current mode	Generator power generation, DC power absorption power	Power motor	The power motor fails to stop, the tested generator is disabled, and the DC power supply stops after the voltage is lower than 700 V
		Generator	The power motor speed drops to zero, the generator fails to stop, and the DC power supply stops after the voltage is lower than 700 V
		DC	Power failure protection, the generator power is disabled when less than 20 kW, then the power motor speed is reduced to 0

**Table 3** Target mode for the fault protection logic of the electrical composite transmission subsystem

Sub-target mode	Power supply	Faulty equipment	Stop mode
Load motor torque mode, motor speed mode	DC power supply	Load motor	In load motor failure, torque is 0; command is sent; tested motor speed is reduced to 0
		Motor	The load motor torque is set to 0, and the tested piece is shut down
		DC	The tested motor is disabled. The load motor first reduces the torque to 0, then turns to the speed control, and reduces the speed to 0
Load motor speed mode, motor torque mode	DC power supply	Load motor	Load motor is disabled; the torque of the tested motor drops to 0
		Motor	The tested motor is stopped, and the load motor speed is reduced to 0
		DC	The tested motor is disabled, and the load motor speed is reduced to 0
Load motor torque mode, motor torque mode	DC power supply	Load motor	In load motor failure, torque is 0 command; the tested motor is switched to speed control, and speed drops to 0
		Motor	The load motor is switched to speed control; the speed is reduced to 0; the tested motor is fault protected
		DC	The load motor is switched to speed control, and the speed drops to 0; the torque of the tested motor is reduced to 0

**Table 4** Target mode for electrical composite transmission and generator joint subsystem fault protection logic

Sub-target mode	Power supply	Faulty equipment	Stop mode
Generator voltage regulation mode, power motor speed mode, motor speed mode, load motor torque mode	Generator power supply	Power motor	Power motor failure to stop the generator is disabled and stops generating electricity; the motor under voltage protection stops the load motor and torque drops to zero and stops working
		Generator	The tested motor is disabled; load motor is disabled; generator is disabled, after that the voltage is lower than 700 V, the speed of the power motor drops to zero
		Load motor	In load motor failure, torque zero command is sent; power motor speed is reduced to zero; generator is disabled. After the voltage is lower than 700 V, the speed of the power motor drops to zero
		Motor	Motor failure to stop, load motor torque set to zero; generator is disabled. After the voltage is lower than 700 V, the speed of the power motor drops to zero
Generator voltage regulation mode, power motor speed mode, motor torque mode, load motor speed mode	Generator power supply	Power motor	Power motor failure to shutdown, generator is disabled and stops generating electricity; the motor under voltage protection stops, and the load motor torque drops to zero and stops working
		Generator	Motor is disabled, and load motor is disabled; generator is disabled; after the voltage is lower than 700 V, the speed of the power motor drops to zero
		Load motor	Load motor is disabled; power motor torque drops to zero; generator is disabled. After the voltage is lower than 700 V, the speed of the power motor drops to zero
		Motor	Motor failure to stop the load motor speed drops to zero; generator is disabled. After the voltage is lower than 700 V, the speed of the power motor drops to zero

(continued)

**Table 4** (continued)

Sub-target mode	Power supply	Faulty equipment	Stop mode
Generator voltage regulation mode, power motor speed mode, motor torque mode, load motor torque mode	Generator power supply	Power motor	Motor failure to stop the load motor torque drops to zero; generator is disabled. After the voltage is lower than 700 V, the speed of the power motor drops to zero
		Generator	The tested motor is disabled; load motor is disabled; generator is disabled. After the voltage is lower than 700 V, the speed of the power motor drops to zero
		Load motor	In load motor failure, torque zero command is sent; the tested motor is switched to speed control, the speed is reduced to zero; generator is disabled. After the voltage is lower than 700 V, the speed of the power motor drops to zero
		Motor	The load motor is switched to speed control, and the speed is reduced to zero; the tested motor is fault protected. Generator is disabled. After the voltage is lower than 700 V, the speed of the power motor drops to zero

220 °C, an alarm will be triggered. Other monitoring settings can be set according to the specific values of the speed and torque, and the voltage, current, and power of the DC power supply loaded in the test project [4].

The basic steps for implementing a fault protection [5, 6] are as follows:

- (1) If the power motor or the load motor fails, the fault status flag will be sent through the field bus. The host receives the fault status flag, first forwards the fault status flag to the electromechanical composite drive control unit, and determines the current operating status. According to the current operating state, the power motor, the loading motor, and the DC power supply are processed according to the control strategy; at the same time, after receiving the fault status flag forwarded by the host, the electromechanical compound transmission controls the generator and motor according to the control strategy and the current system operating state.
- (2) If the DC power supply fails, the industrial computer sends a fault status flag through the control bus. The host receives the fault status flag, first forwards the fault status flag to the electromechanical composite drive control unit,

and determines the current operating status. According to the current operating state, the power motor, the loading motor, and the DC power supply are processed according to the control strategy; at the same time, after receiving the fault status flag forwarded by the host, the electromechanical compound transmission control unit controls and processes the generator and the motor according to the current system operation state and the control strategy in the table.

- (3) If the motor or generator fails, the fault status flag is sent through the control bus. After receiving the fault status flag, the electromechanical composite drive control unit first forwards the fault status flag to the host and determines the current operating status. According to the current operating state, the generator and the motor are processed according to the control strategy; at the same time, after receiving the fault status flag forwarded by the electromechanical composite transmission control unit, according to the current system operating state, the power motor, the loading motor, and the DC power source are controlled according to the control strategy in the table.

## 4 Method Implementation and Test

### 4.1 Method Implementation

The technical implementation method above-proposed is implemented for the fault protection logic. The implementation is based on the current electromechanical composite transmission control unit, the top layer implementation builds the bench test model through MATLAB and automatically generates the code of the underlying implementation through freescale microcontroller. After the top layer is released, the automatically generated code is embedded in the electromechanical compound drive control unit and run. The model built is shown in Figs. 2, 3, and 4. The software development environment of freescale is CodeWarrior [7, 8].

Figure 2 shows the overall framework and input and output interfaces of the model built for fault protection logic; Figure 3 shows three test project modes that can be entered into their respective modes by choose logic; Figure 4 shows the model diagram of the third test project model. In the model, there is a choice of sub-modes for test project, and there are three sub-modes for the third test project. Other test project sub-modes are no longer listed one by one. Figure 5 shows the software development environment.

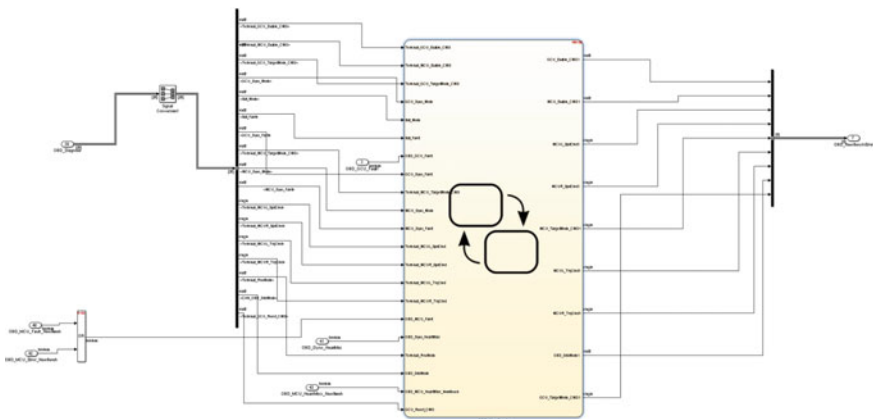


**Fig. 2** Fault protection module

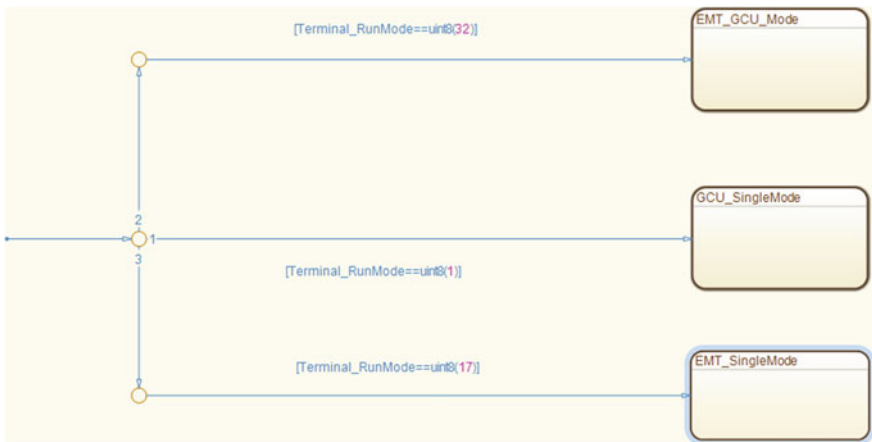


**Fig. 3** Fault protection project mode

## 4.2 Test

The test is divided into two parts: one is the testing of the single component of the electromechanical composite transmission control unit; the other is joint testing that between the electromechanical composite transmission control unit and IPC, the generator rectifier controller, the left power inverter controller, the right power inverter controller. System joint testing can be performed after testing of individual components. The test effect chart is shown in Fig. 6. After the test is passed, the test

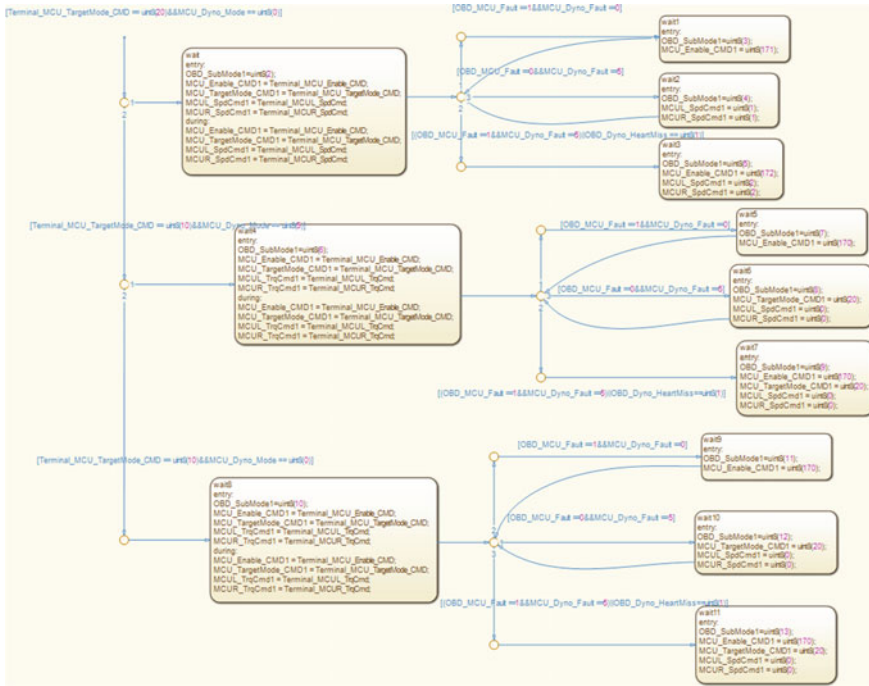
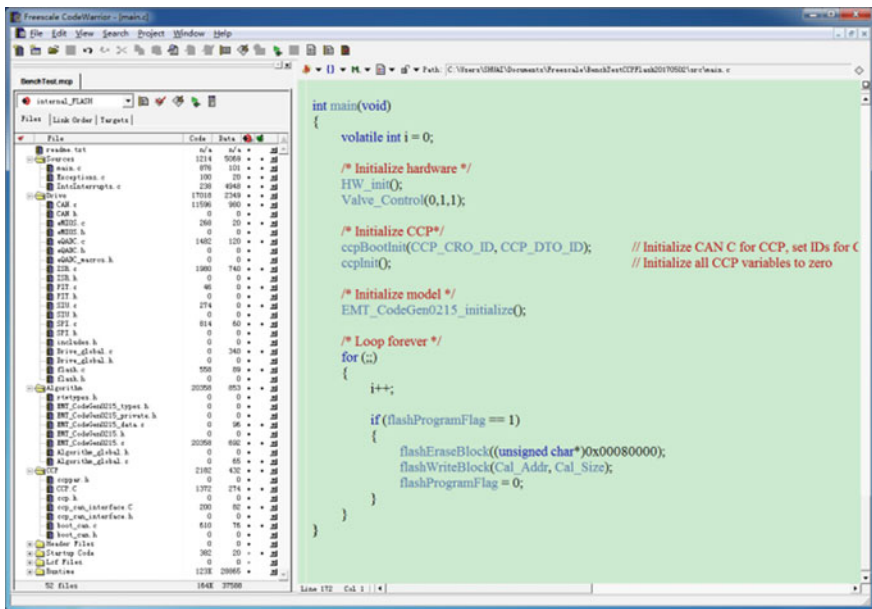


Fig. 4 Fault protection electrical composite transmission subsystem mode

of the real test can be carried out, and the actual test results are shown in Fig. 7. The real test running time is about 5 h. The actual test data is shown in Table 5.

Table 5 shows the test data during the test of the mode three electromechanical composite drives and generator joint adjustment subsystems. The test uses an electromechanical composite drive control unit to control the speed and load the motor control torque, continuous operation for 5 h. Due to the stable operation, the fault alarm is unlikely to occur for a long time, so the load motor uses a human injection fault alarm. It can be seen from the table that the left motor speed, the right motor speed, and the left motor torque continue to operate stably. When the left motor is set to 2000 r/min, the load motor has a fault alarm, and then the left motor speed is reduced to 500–15 r/min until it stops., the right motor speed is reduced to 502–20 r/min until it stops. It can be seen from the table that the fault protection logic is triggered by the load motor fault alarm, so that the left and right motor speeds down to zero, and the load motor also stops running. The test data for other projects is no longer listed.



**Fig. 5** CodeWarrior 2.10 Software structure in an integrated development environment

## 5 Conclusion

As a means of predicting “reliability,” fault protection solves the problem of relying on manual intervention. Through the pre-judgment of the fault condition in the electromechanical composite transmission system, the software configures the fault protection logic to realize the coordinated protection of the fault. Continuous simulation test and real test are carried out for the software. The test results show that the fault coordination can be better realized in the case of single-component and system-level faults.

The electromechanical composite transmission system will have a large number of fault alarm messages in a short period of time. Due to the complexity and diversity of faults, it is difficult to quickly take countermeasures based on manual and software fault protection and may even cause misjudgment. At present, the methods for fault diagnosis include expert system based on expert knowledge, fault diagnosis system based on neural network, fault diagnosis system based on the combination of expert knowledge and neural network [9]. In the future, facing complex systems, it requires a high degree of adaptability, faster response, and more accurate fault diagnosis technology. The adaptive intelligent fault diagnosis system has become the future development direction.

Time	Chn	ID	Name	Event Type	Dir	DLC	D...	Data
594...	CAN 2	CFO1...		CAN Frame	Rx	8	8	AA 00 00 00 00 00 00 E6
594...	CAN 2	CFO2...		CAN Frame	Rx	8	8	00 00 00 01 00 02 00 00
594...	CAN 2	CFE1...		CAN Frame	Rx	8	8	00 00 00 F2 00 00 00 00
594...	CAN 2	18FO...		CAN Frame	Rx	8	8	22 00 02 00 00 C8 14 14
594...	CAN 2	18FO...		CAN Frame	Rx	8	8	B5 12 B2 4C 00 79 31 31
594...	CAN 1	CFI1...	VCU_MCU	CAN Frame	Rx	8	8	55 00 14 10 27 10 27 85
	~	MCU_Enable				85	55	
	~	MCU_Reset				0	0	
	~	MCU_TargetMode				20	14	
	~	MCU_TrqCmd				0	2710	
	~	MCU_N_TrqCmd				0	2710	
	~	VCU_Life				133	85	
594...	CAN 1	CFO1...		CAN Frame	Rx	8	8	AA B0 BC 10 27 10 27 85
594...	CAN 2	18FO...		CAN Frame	Rx	8	8	E8 03 D4 00 21 01 00 00
594...	CAN 1	CFI1...	VCU_MCU_SPD	CAN Frame	Rx	4	4	C8 32 3B 1B
	~	MCU_SpdCnd				3000	32C8	
	~	MCU_SpdCnd				-3000	1B58	
594...	CAN 1	18FO...		CAN Frame	Rx	8	8	10 27 10 27 2E 03 00 00
594...	CAN 2	18FO...		CAN Frame	Rx	8	8	00 00 7A 00 01 00 14 00
594...	CAN 2	18FO...		CAN Frame	Rx	8	8	00 00 00 00 BC 24 61 29
594...	CAN 1	CFO0...	MCUR_VCU_1	CAN Frame	Rx	8	8	78 55 1B 05 27 1B 27 0B
	~	MCUR_FaultState				0	0	
	~	MCUR_ModeStatus				2	2	
	~	MCUR_PowerStatus				1	1	
	~	MCUR_MG_Status				1	1	
	~	MCUR_SelfCheck				1	1	
	~	MCUR_EnableLock				0	0	
	~	MCUR_Spd				-2997	1B58	
	~	MCUR_Trq				"11	2705	
	~	MCUR_Power				1.4000	271E	
	~	MCUR_EnableCmdFbk				1	1	
	~	MCUR_EnableStatus				1	1	
	~	MCUR_ModeCmdFbk				2	2	
	~	MCUR_ResetCmdFbk				0	0	
	~	MCUR_ResetStatus				0	0	
594...	CAN 2	18FO...		CAN Frame	Rx	8	8	00 00 00 00 00 80 3E 00
594...	CAN 2	18FO...		CAN Frame	Rx	8	8	0F 27 0F 27 10 27 00 00
594...	CAN 2	18FO...		CAN Frame	Rx	8	8	42 27 42 27 C4 22 64 64
594...	CAN 2	18FO...		CAN Frame	Rx	8	8	F7 2A 29 23 31 27 D1 26

**Fig. 6** CANoe tool test renderings**Fig. 7** Test site

**Table 5** Test test data sheet

Electromechanical composite drive controller control speed of load motor control torque										
Left motor set speed	Right motor set speed	Load motor 2 set torque	Load motor 1 set torque	Left motor speed	Left motor torque	Left torque meter torque	Right motor speed	Right motor torque	Right torque meter torque	Load motor 2 speed
500	500	499	501.03	494	60	527.1	495	51	532.8	-45.76
500	500	999	1000.43	500	90	1014.5	492	100	1006.2	-45.6
500	500	1500	1501.27	495	146	1519.6	494	137	1512.9	-45.28
500	500	1999	2000.68	502	185	2027.5	492	189	1997.8	-45.76
1000	1000	499	501.03	997	55	522.7	993	52	522.6	-91.36
1000	1000	999	1000.43	992	100	1016.3	998	93	1005.4	-91.36
1000	1000	1500	1501.27	996	141	1516.7	1001	134	1514.4	-91.2
1000	1000	1999	2000.68	1002	198	2021.2	998	182	2015.1	-91.68
1500	1500	499	501.03	1495	58	520.5	1498	48	513.3	-137.28
1500	1500	999	1000.43	1493	97	1019.4	1500	92	1017.9	-137.12
1500	1500	1500	1501.27	1495	149	1528.4	1500	138	1524.8	-137.44
1500	1500	1999	2000.68	1499	182	2037.1	1503	136	2031.9	-137.6
2000	2000	499	501.03	1999	59	531.5	1999	50	528	-183.36
2000	2000	999	1000.43	1995	106	1033.2	2002	94	1027.6	-183.36
2000	2000	1500	1501.27	500	143	1537.9	502	131	1537.8	-83.36
2000	2000	1999	2000.68	15	20	2050.2	20	18	2044	-18.36

## References

1. Chuanjun W, Huaizhen L, Jinsheng Y (2016) Research on fault diagnosis expert system of electric vehicle motor and controller. *Motor Control Appl* 43(5) (in Chinese)
2. Bo M, Jinji G, Zhinong J (2017) Multi-dimensional fault diagnosis method based on expert thinking. *J Mech Eng* 23(53):32–38 (in Chinese)
3. Hualiang P, Shulong S, Jun L (2019) Fault diagnosis expert system design based on fault tree. *Control Eng China* 26(3) (in Chinese)
4. Qiang Z, Changfeng SH, Huibin W (2018) Turbogenerator fault diagnosis expert system based on rule and case reasoning. *Electric Power Sci Eng* 34(6) (in Chinese)
5. Yan CF, Ma SM (2013) Fault diagnostic expert system of rolling element bearing based on CLIPS. *J Inf Comput Sci* 10(10):3053–3062
6. Narasimhan S, Biswas G (2007) Model-based diagnosis of hybrid systems. *IEEE Trans Syst Man Cybern-Part A: Syst Humans* 37(3):348–360
7. Ruwedel M (2013) A qualitative and quantitative functional modelling method for PHM system design. *Chem Eng Trans* 33:223–228
8. Chaohui Y, Huiyu W, Zhihe H (2018) Research on software fault diagnosis and repair method based on expert system. *Inf Commun* 11:138–139 (in Chinese)
9. Xin W, Di C, Yu Q (2018) Domestic neural network fault diagnosis technology and its application in spacecraft. *J Shenyang Aerosp Univ* 35(3) (in Chinese)

# Research on Transformer Core Loosening Fault Diagnosis Based on VMD



Yuzhi Liu, Kuankuan Zhai, Xiaorui Kang, Wei Guo  
and Xinyu Zhang

**Abstract** In order to accurately extract the characteristic frequency of the vibration signal of the transformer core, a fault diagnosis method based on variational mode decomposition (VMD) and sparse decomposition is proposed for the non-linear, non-stationary and low signal-to-noise ratio of the vibration signal of transformer core. The fundamental frequency (100 Hz) and some frequency doubling component are included in the vibration signal of the transformer core. After the failure of the transformer core, the characteristic frequency in the vibration signal of the core also changes. Firstly, the signal is sparsely decomposed and denoised, and the noise-reduced signal is subjected to VMD decomposition. Then, the characteristic components are selected from the decomposed components for spectrum analysis. Finally, the state of the core is detected.

**Keywords** Characteristic frequency · Sparse decomposition · Core fault · VMD

## 1 Introduction

Large-scale power transformers are the most important primary electrical equipment in the power grid, which directly affects the safe and stable operation of power systems. According to statistics, the fault caused by the transformer core accounts for a large proportion of the total accident of the transformer. Therefore, a method for accurately determining the state of the core of the power transformer is needed [1].

In recent years, many scholars have been working on monitoring transformer faults on transformer vibration signals. Compared with the traditional method, the vibration method has no electrical connection with the entire power system and can safely and reliably monitor the state of the power transformer, so it has good application prospects [2].

---

Y. Liu (✉) · K. Zhai · X. Kang · W. Guo · X. Zhang  
Shijiazhuang Tiedao University, Shijiazhuang, China  
e-mail: [610659996@qq.com](mailto:610659996@qq.com)

Vibration analysis method collects the vibration signal of transformer surface by vibration sensor, analyzes the change of the signal when the transformer works. Time-frequency analysis methods commonly used for transformer vibration signals include short-time Fourier transform (STFT) [3], wavelet transform (WT) [4], empirical mode decomposition (EMD) [5], ensemble empirical mode decomposition (EEMD), local mean decomposition (LMD), etc. [6]. Among them, the STFT and the WT have defects such as poor time-frequency resolution and weak aggregation; the EMD has some disadvantages in signal processing, such as modal aliasing and endpoint effect, the EEMD adopts the idea of adding Gauss white noise to eliminate the modal aliasing problem in EMD, and although some results have been achieved, the parameters such as noise amplitude and noise number directly affect the decomposition effect of EEMD; LMD method is also difficult to get rid of the bondage of modal aliasing and endpoint effect [7].

In view of the above situation, Dragomiretskiy and Zosso [8] proposed a new signal preprocessing method in 2014, variational mode decomposition (VMD). VMD decomposition has the advantages of high robustness and fast convergence and can realize the effective separation of intrinsic mode function (IMF) of signals. This paper combines the VMD method with the dilution decomposition method to decompose the vibration signal into IMF components of different time scales through VMD, and each IMF component obtained by VMD decomposition is used to sparse decompose and noise reduce. Finally, the characteristic components of core fault are selected for analysis to complete the fault diagnosis of transformer core.

Magnetostriction of silicon steel sheet causes transformer core vibration. Considering the linear relationship between the loading voltage and the flux density and the relationship between the magnetostrictive deformation and the square of flux density is approximately linear, it can be seen that there is a square relationship between the vibration force caused by magnetostriction and the loading voltage. That is to say,

$$F \propto U^2 \quad (1)$$

Formula (1):  $F$  is the core vibration force,  $U$  is the loading voltage. At the same time, it can be deduced that the fundamental frequency of core vibration is twice that of loading voltage, that is, 100 Hz.

In addition, due to the strong nonlinearity of the magnetostrictive phenomenon of the core and the different length of the magnetic path along the inner frame and outer frame of the core, the vibration of the transformer core is more complex. Besides the fundamental frequency signal (100 Hz), the core also includes high-order harmonic components.

## 2 Sparse Decomposition Algorithm

Since Mallat et al. [9] introduced the idea of matching pursuit algorithm (MP) for the first time, MP algorithm has been a research hot spot of sparse decomposition. In this paper, MP algorithm is used to select the optimal atom.

Let  $D = \{g_r\} \gamma \in \Gamma$  be the over-complete library and  $g_r$  be the atom defined by the parameter group  $\gamma$ . Normalization of atoms, that is  $g_r = 1$ , where  $\Gamma$  is the collection of parameter group  $\gamma$ . According to the over-completeness of the library, the number of parameter group  $\gamma$  should be much larger than the length of the signal, that is, if  $P$  is used to represent the number of atoms in the over-complete library  $D$ , then  $P$  should be much larger than the length of the signal  $N$ . The signal decomposition process of MP method is as follows: Firstly, the atom  $g_{r0}$  matching the decomposed signal is selected from the over-complete library, which satisfies the following conditions.

$$|\langle fg_{r_0} \rangle| = \sup_{\gamma \in f} |\langle fg_{\gamma} \rangle| \quad (2)$$

Thus, the signal can be decomposed into two parts: components and residues on optimal atom  $g_{r0}$ , that is to say,

$$f = \langle fg_{r_0} \rangle g_{r_0} + R^1 f \quad (3)$$

Among them,  $R^1 f$  is the residual signal after optimum matching. Continue residual signal decomposition,

$$R^k f = \langle R^k f g_{r_k} \rangle g_{r_k} + R^{k+1} f \quad (4)$$

$g_{r_k}$  satisfies  $|\langle R^k f g_{r_k} \rangle| = \sup_{\gamma \in f} |\langle R^k f g_{\gamma} \rangle|$ .

From formulas (3) and (4), the signal is decomposed into formula (5) after  $n$ -step decomposition.

$$f = \sum_{k=0}^{n-1} \langle R^k f g_{r_k} \rangle g_{r_k} + R^n f \quad (5)$$

Among them, the linear combination of  $n$  atoms is  $R^n f$  by decomposing the original signal, which is usually used to represent the error caused. In each step of decomposition, the selected best atom satisfies equation (5), so as the decomposition proceeds, the residue decreases rapidly. It can be proved that the exponent of  $|R^n f|$  decreases to 0 with the increase of  $n$  under the condition that the signal satisfies the finite length  $n$ . Generally speaking, a small number of atoms (compared with the length of the signal) can be used to represent the main components of the signal, that is to say,

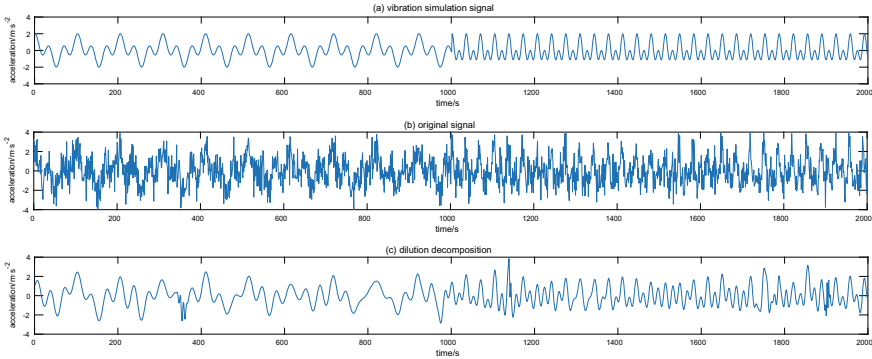


**Fig. 1** Vibration simulation signal and noise adding and denoising results

$$f \approx \sum_{k=0}^{n-1} \langle R^k f g_{\gamma_k} \rangle g_{\gamma_k} \quad (6)$$

Among them,  $n \ll N$ . Formula (6) and condition  $n \ll N$  embody the central idea of dilution.

According to the characteristics of core vibration signals, a set of simulation signals are constructed.

$$f(x) = \begin{cases} \cos(2 \times \pi \times 100 \times t) + \cos(2 \times \pi \times 300 \times t) & 0 < t < 0.1 \\ \cos(2 \times \pi \times 300 \times t) + \cos(2 \times \pi \times 600 \times t) & 0.1 < t < 0.2 \end{cases} \quad (7)$$

On the basis of the simulation signal, random noise is added, and the wavelet soft threshold decomposition, morphological filter and sparse decomposition are used to reduce the noise. The vibration simulation signal, the noise-added signal and the noise-reduced signal are shown in Fig. 1.

Figure 1a is the vibration simulation signal, Fig. 1b is the vibration signal after adding random noise, and Fig. 1c is the vibration signal after MP sparse decomposition. It can be seen that MP sparse decomposition can denoise the signal.

### 3 Variational Modal Decomposition

Variational mode decomposition (VMD) is a new adaptive time–frequency analysis method with strict mathematical basis. Its decomposition process is essentially an iterative solution process of a special variational model [10]. VMD decomposes multicomponent signal  $f$  into a series of bandwidth-limited intrinsic mode functions (IMFs) by adaptive quasi-orthogonal transformation. That is to say,

$$u_k(t) = A_k(t) \cos(\varphi_k(t)) \quad (8)$$

$A_k(t)$  is the instantaneous amplitude of  $u_k(t)$  in formula (8),  $w_k(t)$  is the instantaneous frequency of  $w_k(t)$ ,  $w_k(t) = d\varphi(t)/dt$ ;  $u_k(t)$  is a set of discrete sub-signals. The bandwidth sparsity of each sub-signal is different in the spectral domain.

Each modal component is closely concentrated near the central frequency  $w_k$ . Gauss smoothing migration signal  $H^1$  can be used to estimate its bandwidth. Because VMD decomposition is sparse, it can be considered as a constrained variational problem when K-order decomposition is performed.

$$\min_{\{u_k\} \cdot \{w_k\}} \left\{ \sum_k \left\| \partial_t \left[ \left( \sigma(t) + \frac{j}{\pi t} \right) u_k(t) \right] e^{i-jw_k t} \right\|_2^2 \right\} \quad (9)$$

$u_k$  satisfies

$$\sum_{k=1}^K u_k = f \quad (10)$$

$\{u_k\} = \{u_1, \dots, u_k\}$  represents the K IMF components obtained by the decomposition in formula (8);  $\{w_k\} = \{w_1, \dots, w_k\}$  represents the frequency center of each IMF. The following introduces the augmented Lagrange function to obtain the optimal solution of the above constrained variational problem, that is to say,

$$L(\{u_k\}, \{w_k\}, \lambda) = \alpha \sum_k \left\| \partial_t \left[ \left( \sigma(t) + \frac{j}{\pi t} \right) u_k(t) \right] e^{i-jw_k t} \right\|_2^2 + \left\| f(t) - \sum_k u_k(t) \right\|_2^2 + \left\langle \lambda(t), f(t) - \sum_k u_k(t) \right\rangle \quad (11)$$

In formula (11),  $\alpha$  is the penalty factor and  $\lambda$  is a Lagrange multiplier.

The point of the augmented Lagrange function is obtained by using the alternating direction multiplier algorithm, which is the optimal solution of the variational model constrained by formula (9). Thus, the original signal  $f$  is decomposed into  $K$  narrowband IMF components. The implementation process is as follows:

1. Initialize  $\{u^1\}$ ,  $\lambda^1$  and  $n$  to 0.
2. Let  $n = n + 1$ , start the iteration cycle.
  - Let  $k = k + 1$  until  $k = K$ , update  $u_k$  according to formula  $u_k^{n+1} = \arg \min_{u_k \in X} L_{u_k \in X} \{ \{u_i^{n+1}\}, \{u_{i \geq k}^n\}, \{w_i^n\}, \lambda^n \}$
  - Let  $k = k + 1$  until  $k = K$ , update  $w_k$  according to formula  $w_k^{n+1} = \arg \min_{w_k \in X} L_{w_k \in X} \{ \{u_i^{n+1}\}, \{w_{i < k}^{n+1}\}, \{w_{i \geq k}^n\}, \lambda^n \}$
  - Update  $\lambda$  according to formula  $\lambda^{n+1} = \lambda^n + \tau(f - \sum_{k=1}^{n+1} u_k)$

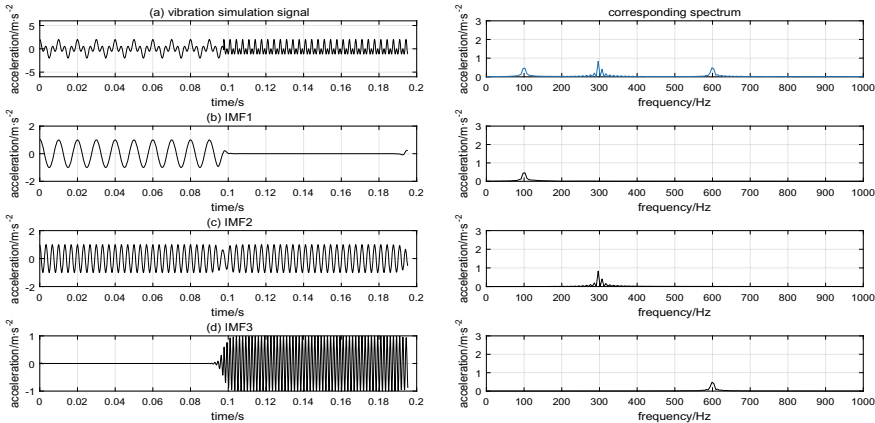


**Fig. 2** Vibration simulation signal and VMD decomposition results

3. Repeat step 2. For a given discriminant accuracy  $\varepsilon > 0$ , if  $\sum_k \|u_k^{n+1} - u_k^n\|_2^2 / \|u_k^n\|_2^2 < \varepsilon$ , the iteration is stopped, and the decomposition is completed.

VMD decomposition is performed using the simulation signal constructed by formula (10), and the results are shown in Fig. 2.

In Fig. 2, the left (b)–(d) is the component of VMD decomposition, (a) is the vibration simulation signal, and the right is the corresponding spectrum. From Fig. 2, it can be seen that the VMD algorithm can decompose the vibration signal effectively without noise interference. It can be clearly seen that there are 100 and 300 Hz signals between 0 and 0.1 s, 300 and 600 Hz signals between 0.1 and 0.2 s.

## 4 Simulation Signal Analysis

According to the analysis of the vibration mechanism of the transformer core, the vibration frequency of the transformer core is 100 Hz, and there are some higher harmonic components. According to the characteristics of the vibration signal of the transformer core, the noise is added on the basis of the constructed simulation signal (7), after noise reduction by MP sparse decomposition, the result is shown in Fig. 3

Figure 3a is the vibration simulation signal of the structure, Fig. 3b is the random noise with the amplitude of 1 added, (c) and (d) in Fig. 3 are the noise reduction results of the wavelet hard threshold processing and the flat structure morphological filter. Figure 3e is the MP sparse decomposition result. It can be seen that the denoising effect of MP sparse decomposition is better than the wavelet hard threshold processing and the flat structure morphological filter. Moreover, the wavelet hard threshold method has better noise reduction effect only when the selected wavelet base has a similarity with the original signal, but the wavelet base is

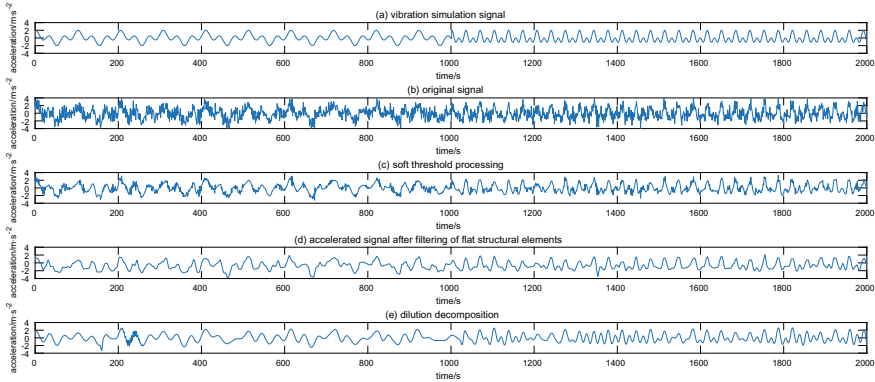


**Fig. 3** Vibration simulation signal and its MP sparse decomposition

difficult to select. The morphological filter also needs to select a suitable filter structure. Therefore, it is more effective to use MP sparse decomposition to reduce noise.

On the basis of the original signal plus random noise, the original signal is decomposed by EMD algorithm, wavelet decomposition algorithm and MP combined with VMD. The EMD decomposition selects the first six layers of effective information, and the wavelet selects db5 wavelet base for four-layer decomposition. VMD setting decomposition layer number  $K = 3$ , secondary penalty factor  $\alpha = 2000$ . The decomposition results are shown in Figs. 4, 5 and 6. The results show that the EMD anti-noise performance is poor, and the similar frequencies cannot be accurately separated, resulting in modal aliasing in the decomposition result. In IMF2, the components of 300 Hz should have been overlapped in waveforms that originally contained only 600 Hz components, which leads to the problem of aliasing in IMF3 and IMF4 in the subsequent decomposition, and decomposition has some false components unrelated to the simulated signal, which

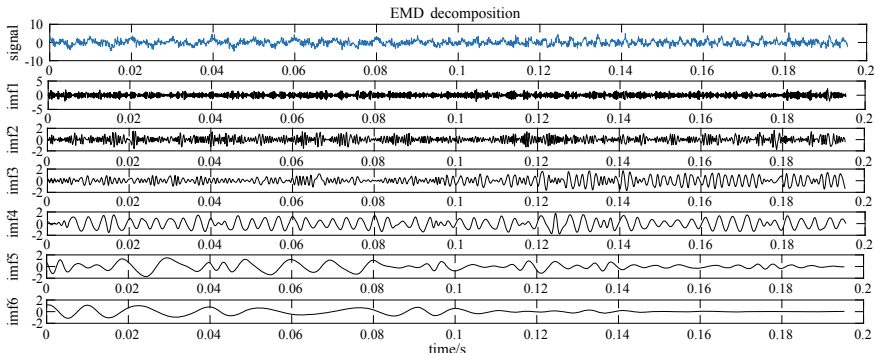


**Fig. 4** EMD decomposition results

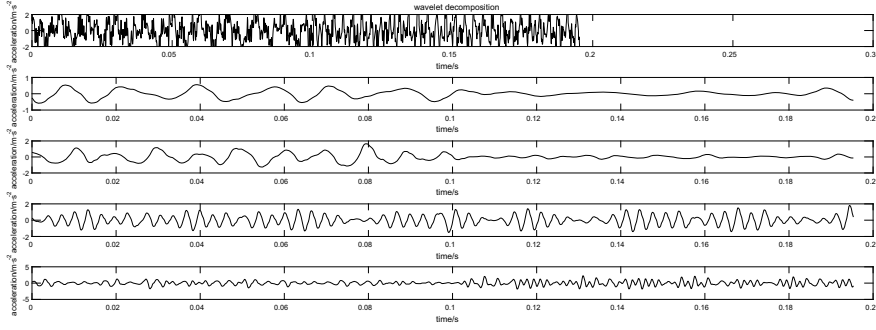


**Fig. 5** Wavelet decomposition results

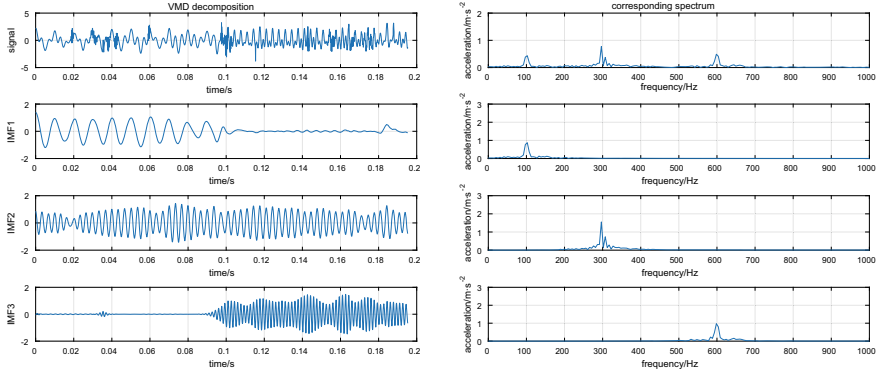


**Fig. 6** MP combined with VMD decomposition results

interferes with the signal processing results; wavelet decomposition decomposes two components of 300 and 600 Hz on d4, and the problem of waveform distortion occurs at the same time. The frequency is effectively distinguished, the waveform is very good, and the decomposition effect is obviously better than EMD and wavelet.

## 5 Application of VMD-Based Algorithm in Transformer Core Fault Diagnosis

In this paper, the fault of the transformer core is studied. In order to make the vibration signal of the transformer surface unaffected by the vibration of the winding, this test is completed under the no-load condition of the transformer. Since the vibration of the winding is caused by the electric power in the coil, the load current is zero at no load, the electric power between the transformer windings is

zero, and the winding vibration is too small to be neglected. Therefore, the vibration characteristic of transformer fuselage is the vibration characteristic of transformer core in no-load condition.

The IEPE acceleration sensor is used to collect the vibration signal of the transformer under no-load conditions. The sensor is adsorbed on the surface of the three-phase transformer box of Su-1600/10 of Jinxing Transformer Factory. By loosening the iron core fastening bolt and set the transformer core fault, vibration signal collected by sensor is converted to digital signal by acquisition card and transmitted to PC. The software sets the sampling frequency to 10,240 Hz and the sampling point to 81,920. The data of the collected transformer normal condition and the loose state of the core are analyzed by MATLAB.

The time domain waveforms are shown in Fig. 7. On the left is transformer normal and on the right is core failure.

In Fig. 7, it can be seen that the amplitude of the transformer core decreases when it fails. However, it is not possible to determine that the transformer has failed. VMD combines the dilution decomposition algorithm for signal processing.

Firstly, the signal is denoised by MP sparse decomposition, and then, the VMD is used to decompose the vibration signals in normal and faulty. Because the amount of data is too large, the decomposition time is long, so 21,920 points are intercepted for processing. According to the paper [10], the maximum relevance minimum redundancy criterion (mRMR) is used to adaptively select the parameter K in the VMD, and the signal is decomposed into four layers. The decomposed IMF component is shown in Figs. 8 and 9.

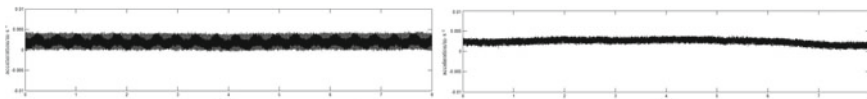


**Fig. 7** Time domain waveforms

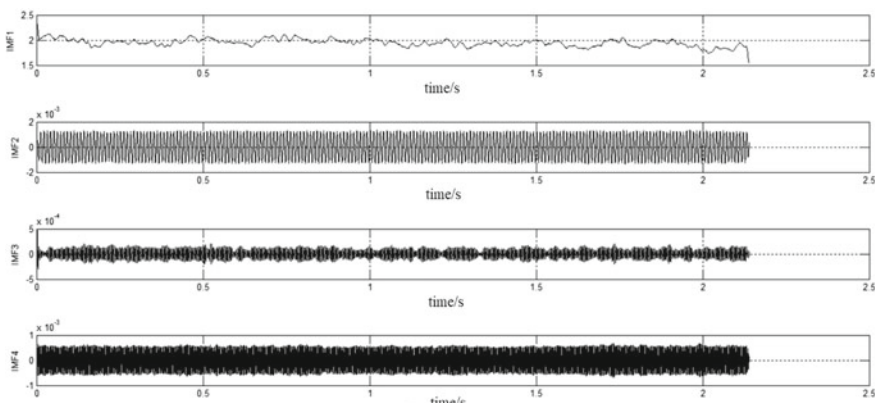


**Fig. 8** VMD decomposition waveform after MP denoising when the transformer is normal

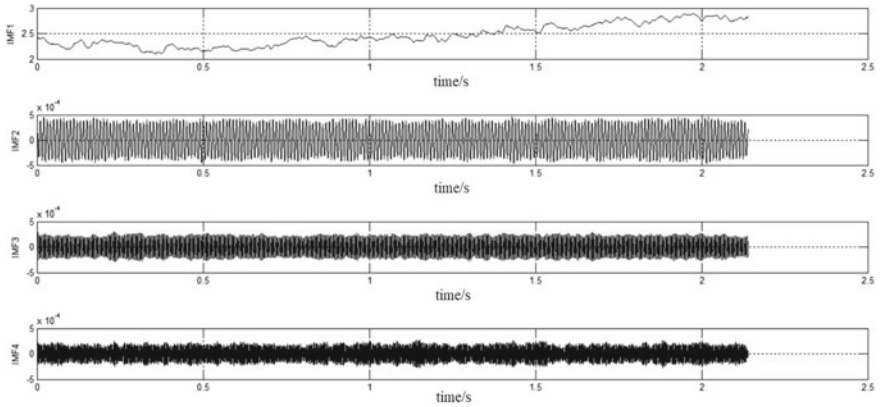


**Fig. 9** VMD decomposition waveform after MP denoising in transformer core failure

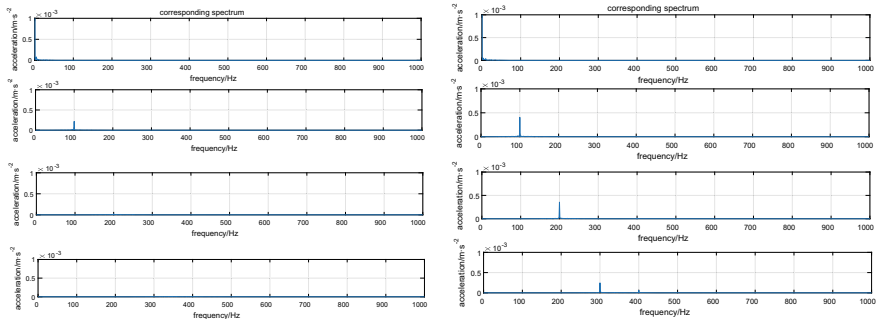


**Fig. 10** Spectrum of the signal after dilution and decomposition

It can be seen from Figs. 8 and 9 that the VMD decomposes the transformer normal signal and the transformer core fault vibration signal into four layers of IMF components, respectively, the frequency increases from IMF1 to IMF4, and the frequency domain figure is obtained by the IMF component. Figure 10 is the spectrum of the signal after dilution and decomposition.

As shown in Fig. 10, the transformer vibration signal contains four characteristic frequencies, and the IMF1 component after VMD decomposition is low frequency component below 100 Hz. According to the vibration mechanism analysis of the transformer, this frequency is mainly generated by peripheral devices such as a cooling system. The IMF2 component has the largest amplitude and is the fundamental frequency (100 Hz) vibration. IMF3 and IMF4 are the frequency doubling components caused by the nonlinear vibration of the transformer core silicon steel sheet. The IMF3 is 200 Hz frequency component, and the IMF4 is 300 Hz frequency component.

Comparing the spectrum diagram under the normal condition of the transformer and the looseness of the transformer core, it can be found that the amplitude of the fundamental frequency is the largest among the frequencies decomposed by the VMD, the fundamental frequency amplitude is significantly smaller when the transformer core fails, and the vibration intensity below 100 Hz is basically unchanged; the fundamental frequency (100 Hz) vibration intensity becomes smaller; the 200 Hz frequency vibration intensity becomes larger; the 300 Hz frequency vibration also increases. Therefore, by comparing the vibration intensities of 100, 200 and 300 Hz, the looseness of the transformer core can be judged.

## 6 Conclusion

- (1) By comparing the VMD and wavelet and EMD decomposition results, the superiority of VMD in decomposing different frequency domain signals is verified and introduced into the vibration fault diagnosis of transformers for the first time.
- (2) The transformer core fault diagnosis method based on the variational mode decomposition (VMD) and dilution decomposition can effectively extract the fault feature frequency. The VMD algorithm solves the modal aliasing problem of EMD and wavelet algorithm. The denoising effect of MP algorithm is better than that of wavelet threshold.
- (3) The vibration signal of normal transformer and core fault is analyzed under no-load conditions. The vibration changes at the fundamental frequency (100 Hz), 200 and 300 Hz can indicate the looseness of the transformer core.

**Acknowledgements** This work is partially supported by the National Natural Science foundation of China (No. 51807124), Natural Science foundation of Hebei Province (No. E2018210144) and Distributed Energy Application Center of Hebei Province (No. SG20182050).

## References

1. Wang C, Geng Z, Ma H et al (2015) Fault diagnosis of transformer core loosing based on vibration. *High Voltage Electr Appl* 51(12):59–65 (in Chinese)
2. Zhang H (2015) Transformer winding fault analysis based on short-time Fourier transform. *Yunnan Power Technol* 43(S1):53–55 (in Chinese)
3. Zhang D (2011) Study on vibration signal characteristics of power transformer based on wavelet theory. North China Electric Power University, Beijing (in Chinese)
4. Xiong W (2006) Empirical mode decomposition method and its application in transformer condition monitoring. Zhejiang University, Hangzhou (in Chinese)
5. Meng Y, Zhongbo, Jia S (2005) Application and development of vibration analysis in the condition monitoring of electrical equipment. *High Voltage Electr Appl* 41(6):461–465 (in Chinese)

6. Xiang L, Yan X (2014) Performance contrast between LMD and EMD in fault diagnosis of turbine rotors. *J Power Eng* 12:945–951 (in Chinese)
7. Yujuan Chen, Huanna Li (2016) Rolling bearing fault diagnosis method based on VMD and Teager energy enhanced spectrum. *Mach Tools Hydraul Press* 44(15):178–183 (in Chinese)
8. Konstantin D, Dominique Z (2014) Variational mode decomposition. *IEEE Trans Signal Process* 62(3):531–544
9. Mallat SG, Zhang Z (1993) Matching pursuit with time-frequency dictionaries. *IEEE Trans Signal Process* 41(12):3397–3415
10. Zhang Y, Zhang P, Wang H, Yang Y (2017) Feature extraction and state recognition for sliding bearing friction faults based on variational mode decomposition. *Int Combust Engine Eng* 38(04):89–96 (in Chinese)

# Braking Energy Harvesting Strategy of High-Speed Maglev System



Dong Yang, Rong Wei and Pengkun Sun

**Abstract** Compared with traditional transportation means, the high-speed maglev train has incomparable advantages. In high-speed maglev transportation system, speed control is an important part. The speed control is related to the performance index of the maglev train, the passengers' travel experience, and the energy control of the converter. In the traction process of the train, the speed of the train is constantly changing. When the train is in a deceleration braking process, the train's kinetic energy is converted into electrical energy and returned to the converter. Due to the high speed of maglev train and the huge energy brought by deceleration braking, it needs to be absorbed and fed back to avoid energy waste and impact on the power grid. In the high-speed maglev transportation system, further analysis and experiments are needed to maximize the energy utilization rate and maximize the safety performance.

**Keywords** High-speed magnetic levitation · Speed control · Deceleration braking · Energy feedback

## 1 Introduction

In recent years, with the acceleration of China's development, traditional transportation has been unable to meet the demand and has become an important factor restricting the rapid economic development. Therefore, as a new type of transportation between railway and airplane, high-speed maglev train has attracted more and more attention. High-speed maglev trains are pulled along by linear motors

---

D. Yang · P. Sun

School of Electronic, Electrical and Communication Engineering,  
University of Chinese Academy of Sciences, Beijing, China

D. Yang · R. Wei (✉) · P. Sun

Key Laboratory of Power Electronics and Electric Drive,  
Institute of Electrical Engineering, Chinese Academy of Sciences, Beijing, China  
e-mail: [weirong@mail.iee.ac.cn](mailto:weirong@mail.iee.ac.cn)

with greater traction, higher efficiency, less resistance and therefore can run more smoothly at higher speed. So in the high-speed maglev transportation system, traction control system plays a very important role.

When the train is decelerating and braking, the energy conversion of the train is different from that of traction, so it is necessary to analyze and select an appropriate braking control strategy [1].

In the subway transportation, the general application of braking schemes is electrical and air braking [2]. Among them, the air brake will generate a lot of heat, which shortens the service life of the brake shoe, and is unconducive to maintenance, so electrical braking is used in the high speed, and air braking is used at a low speed. When the vehicle is under electrical braking, the traction motor is converted from an electric motor to a generator, and the energy is converted from the kinetic energy of the train to electric energy. The feedback energy can affect the traction power supply system. However, the rectifier that takes energy from the power grid in the subway traction system is unidirectional rectifier and has no energy feedback ability [3].

At present, the regenerative braking energy absorption technology of subway mainly includes energy dissipation type, energy storage type, and energy feedback type, among which energy dissipation type is the most widely used because of its simple structure and low equipment manufacturing cost, while energy storage type and energy feedback type are relatively few in practice [4].

In high-speed railway, researches on feedback type and energy storage type are also carried out around the recovery of regenerative braking energy.

The feedback type is feeding back the regenerative energy to other voltage level power supply network, such as lighting supply and signal system, through the feedback equipment [5]. Energy storage type is to establish energy storage device in the traction power supply system and to store the excess regenerative braking energy, which is then supplied to traction load or other loads for use.

Different from subway and high-speed rail traction systems, the high-speed maglev system oriented at 600 km/H adopts back-to-back ANPC converter topology of 24 MVA, shown in Fig. 1. Topology diagram of the back-to-back ANPC converter is shown in Fig. 1. The ANPC converter has four-quadrant operation ability [6]. The DC bus voltage of the ANPC converter is higher, and the power of the converter is greater. And it can carry on the energy feedback.

## 2 Analysis of Maglev Motion Process

The semi-physical simulation platform is used to simulate the train running process and monitor the train and traction system through various variables. The speed of maglev train is controlled under the traction system. The energy and velocity waveforms in the whole movement process are shown in the figure, and the active and reactive power is calculated as below (Fig. 2):

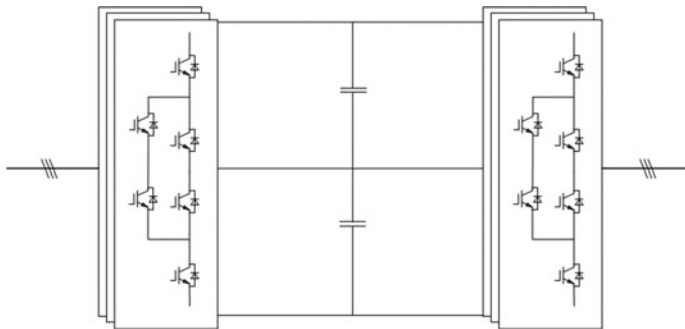


**Fig. 1** Topology diagram of the back-to-back ANPC converter

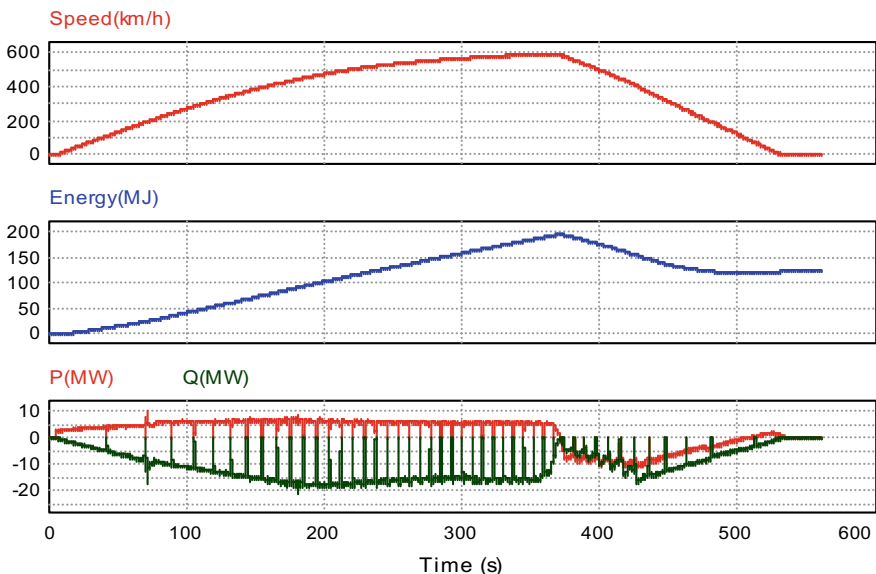


**Fig. 2** Energy and speed changes during traction

$$\begin{aligned} P &= \frac{3}{2} (u_{sd} i_d + u_{sq} i_q) \\ Q &= \frac{3}{2} (u_{sq} i_d - u_{sd} i_q) \end{aligned} \quad (1)$$

Through the analysis of waveform, when the highest speed is 600 km/h, acceleration/deceleration for  $-4 \text{ m/s}^2$ , the maximum active power of feedback energy in the process of the maglev train braking is 11.8 MW. If this part of the energy is not processed, it will make the bus voltage over-voltage [7]. And if all

this part of the energy feedback to the grid, because of its tremendous power, it will make the grid side voltage fluctuate and other adverse condition happen [8].

## 2.1 Strategy of Energy Controlling

In the high-speed maglev traction system with a speed of 600 km/h, brake resistor is selected to release the feedback energy during braking [9].

Instantaneous power model of rectifier:

$$P_{\text{in}} - P_{\text{out}} - P_{\text{brake1}} = CU_d \frac{dU_d}{dt} \quad (2)$$

where

$P_{\text{in}}$  the input power of the rectifier

$P_{\text{out}}$  the output power of the inverter

$P_{\text{brake}}$  the power of the brake module.

At steady state:

$$P_{\text{in}} - P_{\text{out}} - P_{\text{brake}} = 0 \quad (3)$$

where

$$P_{\text{in}} = U_d i_d \quad (4)$$

$$U_d i_d = P_{\text{out}} + P_{\text{brake}} \quad (5)$$

In order to make no energy feedback to the grid side, then  $i_d = 0$ , and the braking module consumes the same load power:

$$-P_{\text{out}} = P_{\text{brake}} \quad (1.6)$$

where

$$P_{\text{out}} = U_{\text{dl}} i_{\text{dl}} + U_{\text{ql}} i_{\text{ql}} \quad (7)$$

## 3 Simulation and Experiment

When the braking module is not used, the feedback power of train braking is returned to the power grid through the rectifying end, which causes great pressure on the power grid and bus capacitance. As can be seen from Fig. 3, when the train

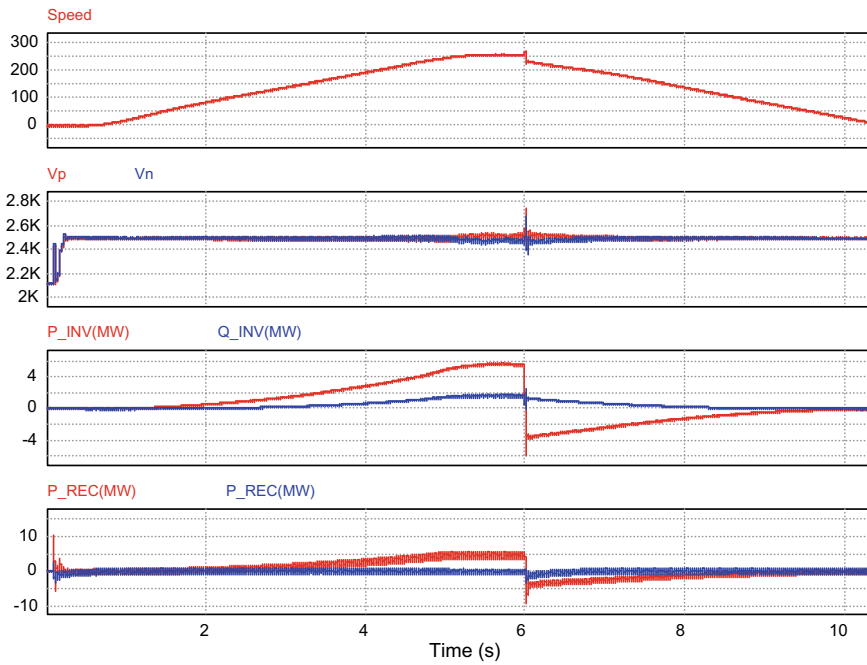


**Fig. 3** Waveform of voltage and power during train movement with full power feedback

is braking, the direction of the active power on the inverter side and the rectifier side changes, and the energy is converted from kinetic energy to electric energy in the power grid.

After the braking module is added, it can be seen from Fig. 4 that the energy generated by braking does not enter the rectifier side, but is released through the braking resistance, so it will not affect the bus capacitance and the power grid side.

As shown in Fig. 5, combining using the braking module and energy feedback, it can combine the advantages of both.

## 4 Conclusion

Using brake resistor for brake control, the control strategy is more reliable, but there is a disadvantage of energy waste, and complete energy feedback will cause a big impact on the power grid. Therefore, the application of brake resistance to release strong impact energy, and at the same time to steadily feed back most of the energy, can not only achieve the purpose of energy conservation, but also reduce the power grid pressure, and brake resistance is too large. The simulation results achieved the expected target.

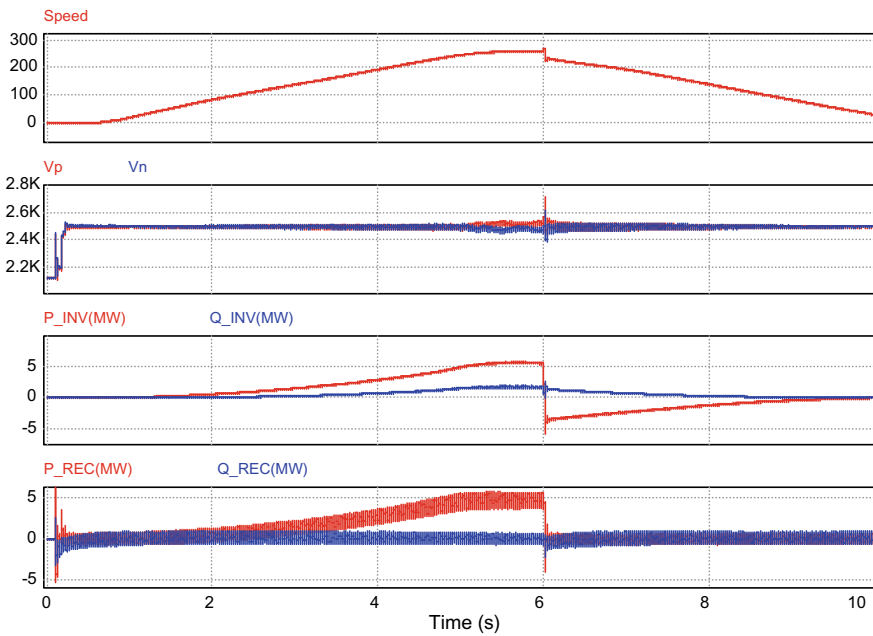


**Fig. 4** Waveform of voltage and power during train movement with resistance energy consumption

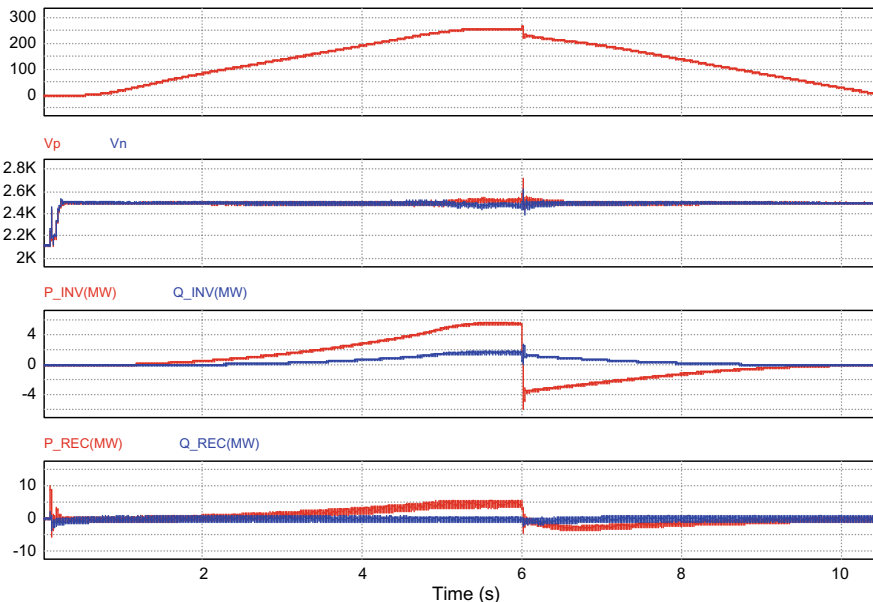


**Fig. 5** Waveform of voltage and power during train movement with resistance energy consumption

## References

1. Jiang Y, Liu J, Tian W, Shahidehpour M et al (2014) Energy harvesting for the electrification of railway stations: getting a charge from the regenerative braking of trains. *A. IEEE Electrif Mag* 2(3):39–48
2. Scheepmaker GM, Goverde RMP (2016) Energy-efficient train control including regenerative braking with catenary efficiency. In: *IEEE international conference on intelligent rail transportation*. IEEE. (2016)
3. Hayashiya H, Kikuchi S, Matsuura K, Hino M, Tojo M, Kato T et al (2013) Possibility of energy saving by introducing energy conversion and energy storage technologies in traction power supply system. In: *European conference on power electronics & applications*. IEEE
4. Bouhali O, Rizoug, N, Mesbahi T, Francois B (2014) Modeling and control of the three-phase NPC multilevel converter using an equivalent matrix structure. In: *7th IET international conference on power electronics, machines and drives (PEMD 2014)*, Manchester, pp 1–6 (2014)
5. Guo A, Xu P, Zhou Y, He X, Shu Z (2015) The modulation techniques in 3L-NPC cascade converter. In: *2015 IEEE 2nd international future energy electronics conference (IFEEC)*, Taipei, pp 1–6 (2015)
6. Wang W et al (2014) A novel energy management strategy of onboard supercapacitor for subway applications with permanent-magnet traction system. *IEEE Trans Veh Technol* 63 (6):2578–2588
7. Sebastian DLT, Sanchez-Racero AJ et al (2015) Optimal sizing of energy storage for regenerative braking in electric railway systems. *IEEE Trans Power Syst* 30(3):1492–1500
8. Yang Z et al (2017) Improved control strategy of energy storage system considering train operation states. In: *2017 IEEE 20th international conference on intelligent transportation systems (ITSC)*
9. Allegre A et al (2010) Energy storage system with supercapacitor for an innovative subway. *IEEE Trans Industr Electron* 57(12):4001–4012

# Research on the Improved Time-Sharing Control Strategy with MPPT Algorithm



Yi Fan , Fan Lu, Tao Yang, Wenxuan Wang and Mingxiang Liu

**Abstract** An improved time-sharing control strategy was presented for the two-stage grid-tied PV inverter. To provide a stable reference voltage for the MPPT algorithm, a kind of digital notch filter for low frequency ripple was adopted. A kind of calculation of input decoupling capacitance was provided, and meanwhile, system loss analysis of two control strategies was given in detail. Finally, two prototypes were built, and the experimental results demonstrate the feasibility of the improved time-sharing control strategy and show the merits and drawbacks of these two control strategies.

**Keywords** Grid-tied PV inverter · Maximum power point tracking · Time-sharing control strategy · Low frequency ripple · Loss analysis

## 1 Introduction

With the severe energy shortage and environmental pollution, solar energy is widely used because of the wide distribution and direct utilization [1–3]. As the core part of energy conversion, grid-connected photovoltaic inverter plays an important role in the performance of the whole system [4, 5]. Two-stage non-isolated topology is chosen as the research object in this paper [6, 7].

---

Y. Fan  · F. Lu · T. Yang · W. Wang · M. Liu  
NARI Group Corporation, No. 19 Chengxindadao, Nanjing, Jiangsu, China  
e-mail: [sgr\\_fanyi@126.com](mailto:sgr_fanyi@126.com)

F. Lu  
e-mail: [lufan1@sgepri.sgcc.com.cn](mailto:lufan1@sgepri.sgcc.com.cn)

T. Yang  
e-mail: [yangtao1@sgepri.sgcc.com.cn](mailto:yangtao1@sgepri.sgcc.com.cn)

W. Wang  
e-mail: [wangwenxuan@sgepri.sgcc.com.cn](mailto:wangwenxuan@sgepri.sgcc.com.cn)

M. Liu  
e-mail: [liumingxiang@sgepri.sgcc.com.cn](mailto:liumingxiang@sgepri.sgcc.com.cn)

Based on the principle and structure of time-sharing dual-mode control strategy [8], a novel control scheme with MPPT algorithm is proposed in this paper. The fundamental cause of the secondary voltage ripple on the PV side and the suppression method are analyzed. Furthermore, the optimal design of input decoupling capacitor based on time-sharing dual-mode control strategy is given.

Finally, combined with the loss analysis and calculation, conventional control strategy and novel time-sharing dual-mode control strategy of two-stage grid-tied photovoltaic inverter are compared and analyzed in detail. Meanwhile, the simulation analysis is carried out by using MATLAB/Simulink software, and two prototypes are built for experimental verification. The experimental result shows that the improved time-sharing dual-mode control strategy has the advantages of less loss, higher efficiency, and smaller volume than the traditional control strategy under the same power level, but the THD of grid-tied current is worse than the traditional control strategy.

## 2 Time-Sharing Dual-Mode Control Strategy with MPPT Algorithm

### 2.1 Analysis and Suppression of Secondary Voltage Fluctuation on PV Side

As shown in reference [8], the inverter contains an extra bypass diode  $D_b$  in the first power processing stage compared with the conventional one. And the bus capacitor has the advantage of a smaller volume than the conventional strategy because of not used as power decoupling. The analysis of grid-tied current loop and small-signal modeling for “Buck” and “Boost” modes under time-sharing control strategy have been deduced in detail in reference [9].

A secondary pulsation of the output voltage of PV array will disturb the maximum power point tracking algorithm and lead to misjudgment depending on using the voltage above as real-time feedback signal of MPPT outer loop. Therefore, it is necessary to suppress the voltage ripple by adding a resonant controller.

Figure 1 shows the structure of the grid-tied photovoltaic inverter, where the power factor of it is close to 1. Firstly, it is assumed that the PV array works at the

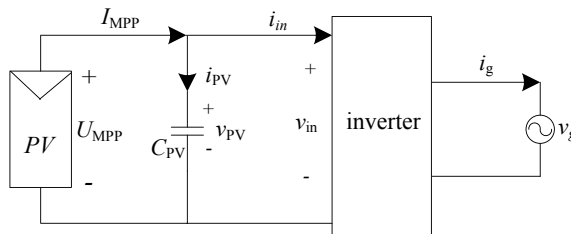


**Fig. 1** Schematic diagram of time-sharing control strategy

maximum power point and the voltage of the input capacitor  $C_{PV}$  is a constant DC value. Secondly, according to the power conservation and neglecting the energy loss in the circuit. Meanwhile, the amplitude of voltage fluctuation of  $C_{PV}$  is  $\hat{u} = 0.5 \times \Delta v_{PV}$  ( $\Delta v_{PV}$  is the peak value of voltage fluctuation). It is shown in (1) that the voltage waveform will reach its maximum value when  $\omega_o t = \pi/4$ .

$$\tilde{u}_c = U_{MPP} + \frac{I_{MPP}}{2\omega_o C_{PV}} \sin(2\omega_o t) = U_{MPP} + \hat{u} \sin(2\omega_o t) \quad (1)$$

In order to prevent the secondary fluctuation of input voltage from misjudging MPPT algorithm, a resonant controller (second harmonic notch filter) [10] is needed between input voltage sampling and voltage feedback of MPPT loop. The pulsation frequency of output voltage of PV array is twice the grid voltage angular frequency (100 Hz).

## 2.2 Implementation of an Improved Time-Sharing Dual-Mode Control Strategy with MPPT Algorithm

An improved time-sharing control strategy with MPPT algorithm is proposed in this paper. Input power sampling and power control are used as outer-loop control to ensure maximum power transmission from photovoltaic system to grid, and grid voltage/current sampling and SPWM modulation are used as inner-loop control to ensure excellent grid-tied current quality. The control block diagram is shown in Fig. 2.

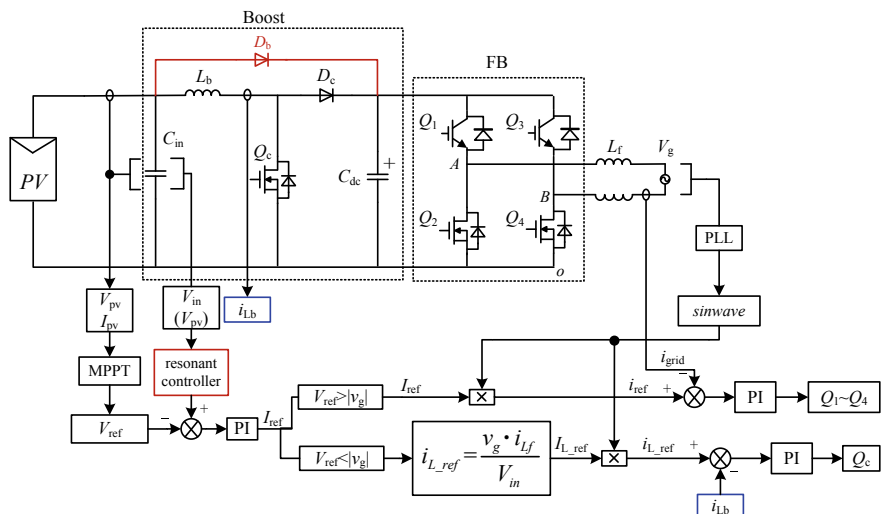


**Fig. 2** Control diagram of grid-tied PV inverter on time-sharing control strategy

### 2.3 Optimal Design of Power Decoupling Capacitor on PV Side of Time-Sharing Control Strategy

The output power of PV arrays with voltage fluctuation will be lower than that of PV arrays without one. The formula of decoupling capacity can be deduced as (2) according to (1). Among which,  $P_{\text{MPP}}$  and  $U_{\text{MPP}}$  can be obtained from the photovoltaic module application manual.

$$C_{\text{PV}} = \frac{P_{\text{MPP}}}{2\omega_o \cdot U_{\text{MPP}} \cdot \hat{u}} \quad (2)$$

The relationship between output voltage fluctuation and utilization ratio of photovoltaic module is given by reference [11], and  $\hat{u}$  is related to utilization ratio and parameters of PV array. The photovoltaic product in this paper is chosen as follows: Hanhua SF220 Poly X-tra 235 wp module (polycrystalline silicon) for 1 kW photovoltaic system. According to Eq. (2), the output side decoupling capacitance of PV array at 1 kW power level is obtained as  $C_{\text{PV}} = 872 \mu\text{F}$ .

The input current of the converter consists of two parts: corresponding to the “Buck” and “Boost” modes, respectively (without considering the current ripple). Under the assumption that the output current of PV array is a DC current  $I_{\text{pv}}$ , the RMS of input capacitive current  $i_{\text{cin}}$  under time-sharing control in one cycle can be obtained as  $I_{\text{cin}} = 4.52 \text{ A}$ . Among which,  $\theta_1 = 28.8\pi/180$ ,  $\theta_2 = 115.2\pi/180$ ,  $V_{\text{in}} = 150 \text{ V}$ .

### 3 Analysis and Comparison of System Loss Between Improved Time-Sharing Dual-Mode Control Strategy and Conventional Control Strategy

Loss analysis of converter has an important significance in improving system efficiency and power density [8, 13, 14]. The loss analysis method proposed mentioned in reference ignores the interaction between switching devices, so there are still some shortcomings. Thus, the system loss analysis is carried out in this paper by using the method proposed in reference [15].

The relevant parameters of the circuit are shown as follows: input voltage  $V_{\text{in}} = 150 \text{ VDC}$ , bus voltage  $V_{\text{bus}} = 380 \text{ VDC}$ , grid voltage  $V_g = 220 \text{ V(rms)}$ , output power  $P = 1 \text{ kW}$ , grid frequency  $f_o = 50 \text{ Hz}$ , switch frequency  $f_s = 20 \text{ kHz}$ .

The parameters of the components of the inverting system are shown as follows. Boost bypass diode: IXYS-DESI30, Boost diode: IXYS-DSEP60\_06A, Full bridge reverse diode: IXYS-DSEP29\_06A, MOSFET of Boost/full bridge: IXYS-IXKH7N60C5, IGBT of full bridge: IXYS-IXGH72N60A3, Input inductance: Boke NPF300060 MPP cores, Bus capacitance: Jianghai electrolytic capacitor CD29L(conventional)/EACO film capacitance(time-sharing), Output filter inductance: Boke NPF306060 MPP cores.

### 3.1 Loss Analysis of Conventional Control Strategy

Figure 3 shows the switch loss of front-end chopper, switch loss of back-end inverter, and loss of energy storage components on conventional control strategy. The total loss of circuit on conventional control strategy is 46.7 W.

### 3.2 Loss Analysis of Time-Sharing Dual-Mode Control Strategy

Figure 4 shows the switch loss of “Buck” mode, switch loss of “Boost” mode, and loss of energy storage components on time-sharing control strategy. The total loss of circuit on time-sharing control strategy is 36.08 W.

### 3.3 System Efficiency Comparison of Two Control Strategies

In terms of switch loss, each part of the circuit in time-sharing control strategy is lower than that of the conventional one.

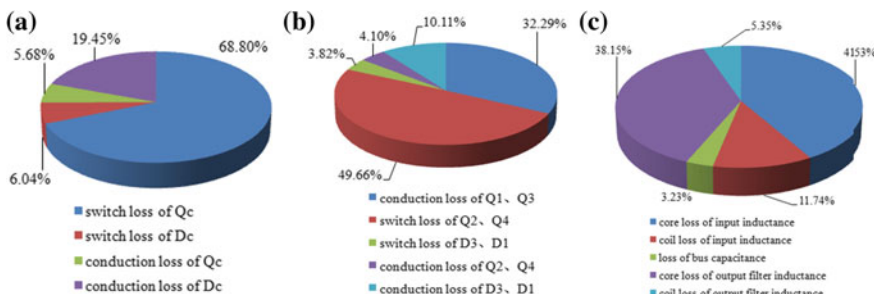


Fig. 3 Loss of circuit on conventional control strategy

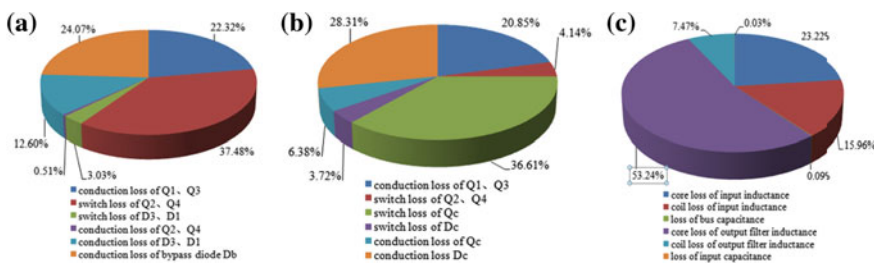


Fig. 4 Loss of circuit on time-sharing control strategy

In terms of energy storage components loss, the input inductance loss of time-sharing control strategy is lower than that of conventional one. Meanwhile, the bus capacitor in the time-sharing control strategy optimizes the electrolytic capacitor to the film capacitor, which results in a smaller parasitic resistance, so the corresponding loss is also much smaller. In addition, although one more input capacitance exists in the improved time-sharing control strategy, this loss is small.

## 4 Simulation and Experimental Analysis

### 4.1 System Simulation Research

Figure 5 shows the voltage waveform of the sampling signal of the output voltage of the PV array before and after the resonant controller and the given voltage  $V_{\text{ref}}$  waveform of the MPPT algorithm. From the simulation waveform, it can be seen that an obvious second harmonic component is contained in the voltage signal sampled of real time, and the second harmonic in the voltage waveform of the resonant controller is basically filtered out. By using the filtered voltage, signal can eliminate the interference of the second fluctuation component of the input voltage in MPPT algorithm. Thereby, it can effectively prevent the misjudgment of MPPT algorithm and improve the tracking efficiency.

### 4.2 System Experimental Verification

Experimental waveform of driving, grid-tied voltage/current on improved time-sharing control strategy (a) and conventional control strategy (b) are the

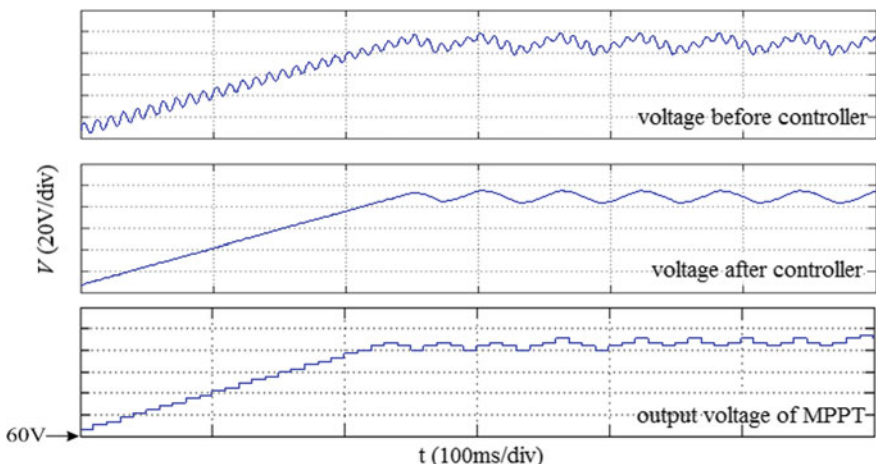


**Fig. 5** Simulation waveform before/after resonant controller on time-sharing control strategy

relevant experimental waveforms, which correspond to waveform of MPPT dynamic tracking, waveform of Boost inductance current  $i_{Lb}$ , waveform of bus capacitance voltage  $V_{bus}$ , waveform of inter-bridge voltage  $V_{AB}$ , waveform of drive/grid voltage/grid current under conventional control and time-sharing control strategy, respectively. The experimental waveform shows that the improved time-sharing control strategy can realize MPPT algorithm and lead to a good quality of the grid-tied current (Figs. 6, 7, 8 and 9).

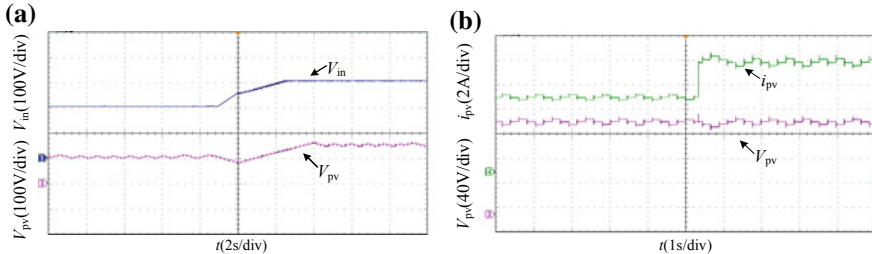


**Fig. 6** Dynamic process of MPPT on improved time-sharing control strategy

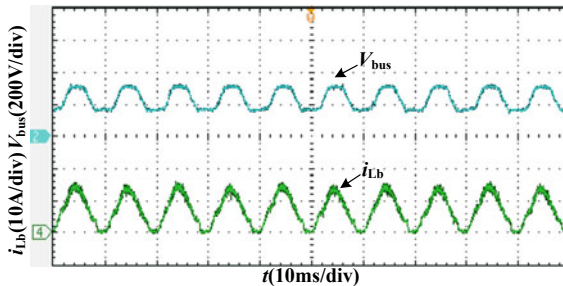


**Fig. 7** Experimental waveform of input inductance current and bus voltage on improved time-sharing control strategy

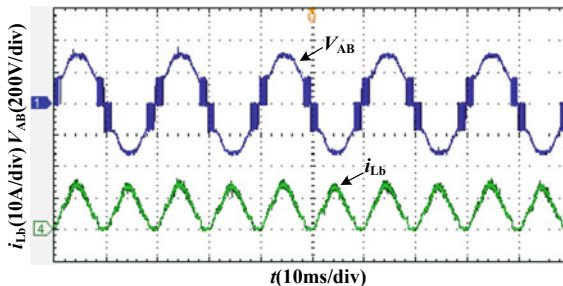


**Fig. 8** Experimental waveform of bridge voltage and input inductance current on improved time-sharing control strategy

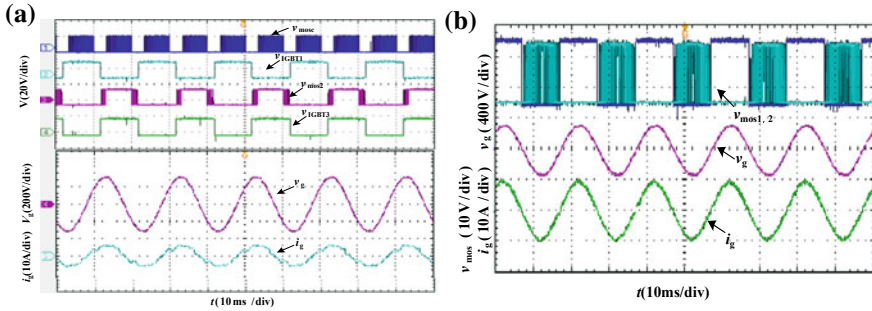


**Fig. 9** Experimental waveform of driving, grid-tied voltage/current on improved time-sharing control strategy (a) and conventional control strategy (b)

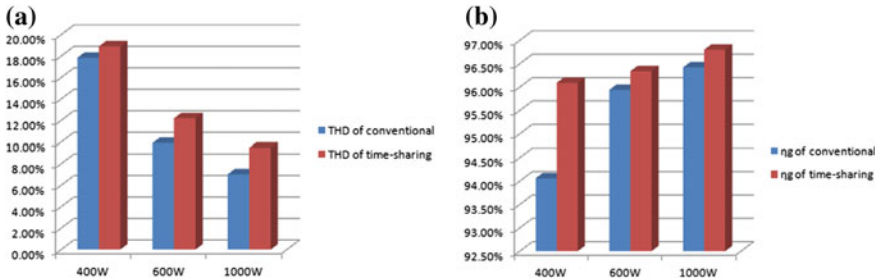


**Fig. 10** Experimental data of both control strategies

Figure 10 presents the experimental data of photovoltaic grid-tied system based on conventional and improved time-sharing control strategy. It is presented that an improved time-sharing control strategy is beneficial to improve the efficiency of grid-tied photovoltaic inverter.

## 5 Conclusion

In this paper: (1) Based on the time-sharing control principle of two-stage grid-tied inverter, an improved scheme with MPPT algorithm is proposed. (2) The cause of secondary voltage ripple on PV side and its suppression method are analyzed, and the optimal design of decoupling capacitor of input side is presented. (3) The loss analysis of the improved time-sharing control strategy and the conventional control strategy is carried out in detail. (4) The simulation model of MATLAB/Simulink is built to simulate the control strategies proposed in this paper. On this basis, a sound experimental verification platform is established. Both of the results verify the correctness and validity of the improved control strategy in this paper.

(5) The comparison of the two strategies shows that the improved time-sharing control strategy has the advantages of less loss, higher efficiency, and smaller volume than the conventional one at the same power level. Meanwhile, the THD of grid-tied current is slightly worse than the conventional control strategy.

## References

1. Tang S (2017) The research of fuzzy control strategy and digital design technology for the photovoltaic grid-connected inverter system. Donghua University, Shanghai (in Chinese)
2. Mahdi Moosavian S, Abd Rahim N, Selvaraj J (2011) Photovoltaic power generation: a review. In: 2011 IEEE first conference on clean energy and technology, pp 359–363
3. Wang J, Dou A (2019) Research on two-stage PV grid-connected inverter system. In: The world of Inverters, pp 91–96 (in Chinese)
4. Zhang X, Zhou M, He J et al (2018) Development of novel photovoltaic grid-connected inverter based on DSP. Tech Explor 9(1):60–67 (in Chinese)
5. Li J (2018) Research on grid-connected control strategy of photovoltaic system. Lanzhou University of Technology, Lanzhou (in Chinese)
6. Schimpf F, Norum LE (2008) Grid connected converters for photovoltaic, state of the art, ideas for improvement of transformerless inverters. In: Nordic workshop on power and industrial electronics
7. Qiu B (2016) Study of the electrical characteristics of grid-connected PV inverter. South China University of Technology, Guangdong (in Chinese)
8. Ogura K, Nishida T, Hiraki E et al (2004) Time-sharing boost chopper cascaded dual mode single-phase sine wave inverter for solar photovoltaic power generation system. In: Proceeding IEEE Power Electronics Specialists Conference (PESC), Germany, pp 4763–4767
9. Fang L, Zhang J, Fan Y (2016) Research on time-shared compound control strategy for two-stage grid-connected inverter. Mod Electron Tech 38(15):112–116 (in Chinese)
10. Deng X, Wei Z, Gong C et al (2011) A novel technique for low frequency input current ripple reduction in two-stage DC-AC inverter. Proc CSEE 31(30):24–29 (in Chinese)
11. Kjaer SB (2005) Design and control of an inverter for photovoltaic applications. Aalborg University, Denmark
12. Chen J, Chen J, Gong C (2011) Method to enhance the short-circuit running reliability of current-controlled two-stage inversion power supply. IET Power Electron 4(4):407–413
13. Yuan Y, Hu G, Mao K et al (2018) Loss analysis of front circuit of two stage inverters under two control method. Power Electron 52(8):86–89 (in Chinese)
14. Qiu Z (2018) Research on changeable drive technology and loss of power switch. East China Jiaotong University, Nanchang (in Chinese)
15. Hong F, Shan R, Wang H et al (2008) Analysis and calculation of inverter power loss. Proc CSEE 28(15):72–78 (in Chinese)

# Research on Power Conversion System Based on Multiple DC/DC Converter



Wenxuan Wang , Tao Yang, Jun Zhou, Yi Fan and Zhaorui He

**Abstract** With the increasing scale of energy storage system, the demand for high-power energy storage converter is more and more intense. The multiple DC/DC converter is introduced into the topology of high-power energy storage converter. Through the analysis of its characteristics, it is found that the multiple DC/DC converter has significant advantages in current ripple and harmonics. When researching the control strategy of energy storage converter, droop control is added. The experiment results of the topology and control strategy show that the designed energy storage converter has excellent performance.

**Keywords** Multiple DC/DC converter · The photovoltaic/battery microgrid system · Power conversion system · Droop control

## 1 Introduction

There are some problems and challenges in the development of distributed generation, such as the randomness and intermittence of wind energy and solar energy, which make it difficult to predict accurately manually, and the instability of energy output greatly weakens the role of distributed generation [1].

---

W. Wang · T. Yang · J. Zhou · Y. Fan · Z. He  
NARI Group Corporation, No. 19 Chengxindadao, Nanjing, Jiangsu, China  
e-mail: [wangwenxuan@sgepri.sgcc.com.cn](mailto:wangwenxuan@sgepri.sgcc.com.cn)

T. Yang  
e-mail: [yangtao1@sgepri.sgcc.com.cn](mailto:yangtao1@sgepri.sgcc.com.cn)

J. Zhou  
e-mail: [zhoujun@sgepri.sgcc.com.cn](mailto:zhoujun@sgepri.sgcc.com.cn)

Y. Fan  
e-mail: [fanyi@sgepri.sgcc.com.cn](mailto:fanyi@sgepri.sgcc.com.cn)

Z. He  
e-mail: [hezhaorui@sgepri.sgcc.com.cn](mailto:hezhaorui@sgepri.sgcc.com.cn)

Microgrid is an autonomous system that can realize self-control, self-protection and self-management. As an important part of smart grid, it is generally composed of distributed power supply, energy storage device, power conversion device, load, monitoring system and protection device. Microgrid can be regarded as a controllable unit in large power grid to meet the needs of external transmission and distribution network. It can also provide an uninterrupted power supply, maintain local voltage stability, reduce feeder losses and increase reliability [2, 3]. To achieve these functions, the selection of the structure, topology and control strategy of the energy storage converter is very important.

Energy storage converter can be divided into single stage and double stage according to whether there are DC/DC links or not. Compared with single-stage energy storage converter, the two-stage topology has more advantages than single-stage energy storage converter because of its shortcomings such as narrow battery voltage range, low reliability and large impulse current. However, in high-power applications, the small capacity of a single energy storage converter will lead to the parallel connection of multiple converters. According to the current research, the power of a single DC/AC inverter can be very large, even up to MW level, while the capacity of a single DC/DC converter is limited by such factors as power electronic power devices and the capacity limit of the batteries connected. Therefore, a two-stage multi-DC/DC parallel energy storage converter with multi-battery access capability emerges as the times require.

## 2 Multiplex DC/DC Converter

The structure of the two-stage multi-DC/DC parallel energy storage converter with multi-battery access capability is shown in Fig. 1.

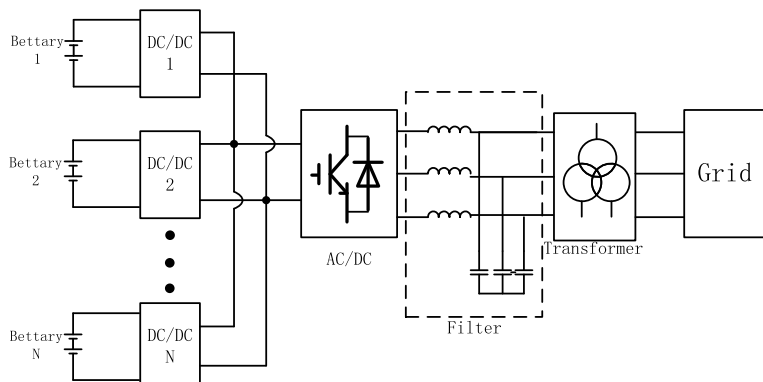


**Fig. 1** Energy storage converter structure with multiple batteries connected

In this figure, the access of large number of small capacity DC/DC modules will increase the system loss, further reduce the energy conversion efficiency, and the coordination control will become more complex. Therefore, number of modules can be reduced by maximizing the power of each DC/DC module and optimize the control in the stage of fixed total capacity.

The design scheme of multi-DC/DC module is adopted. Several buck-boost converters with the same structure are used to construct another kind of composite [4–6] by phase staggered. The topology of main circuit of the multi-DC/DC converter is presented in Fig. 2.

For the current analysis of  $m$  DC/DC modules, the switching period of unit converter is  $T_S$ , the switching frequency is  $f_S$ , and the DC component of inductance current  $i_L$  is  $I_0$ . PWM modulation mode is adopted, and the start time of the switch is  $T_S/m$ . The inductance currents  $i_{L1}(t), i_{L2}(t), i_{L3}(t) \dots i_{Lm}(t)$  of each circuit own the same pulsating current with phase difference  $T_S/m$  and identical waveform, if the duty cycle  $D$  of switching devices in  $m$  converting units is the same in a switching cycle  $T_S$ . Total current  $i_{mL}$  is the sum of inductance currents of  $m$  units. Taking triple topology as an example, the current waveform is presented in Fig. 3.

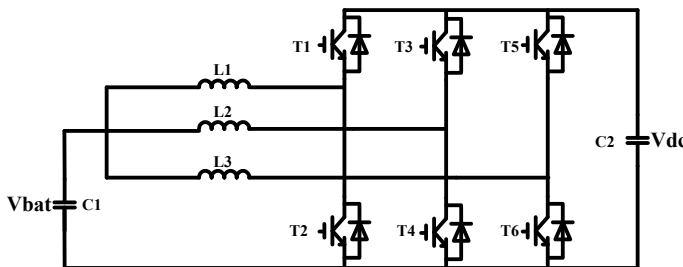


**Fig. 2** Three-phase interleaved bi-directional DC/DC converter

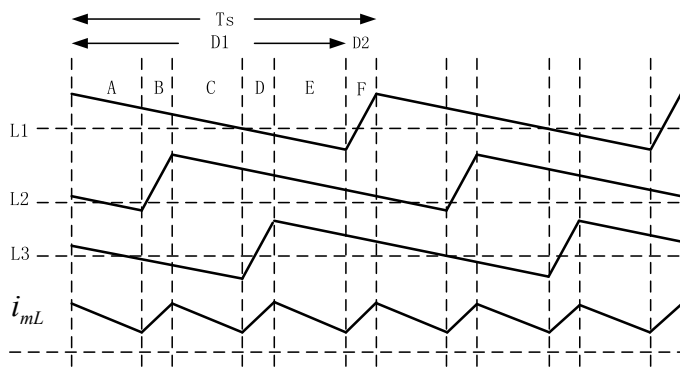


**Fig. 3** Current waveform

### 3 Research on Control Strategy

#### 3.1 Control Strategy in Grid-Connected Mode

Under the grid-connected mode, energy storage takes on the functions of power smoothing and peak cutting and valley filling in the microgrid. It is necessary to respond to the power instructions of the microgrid system in time so that the system can reach a stable state.

Therefore, in grid-connected mode, DC/AC converter is in rectifier or inverter state, which is responsible for controlling the constant voltage of DC side while interacting with the power grid. DC/DC single-current loop control responds to the given instructions by controlling the impulse and discharge power of storage battery.

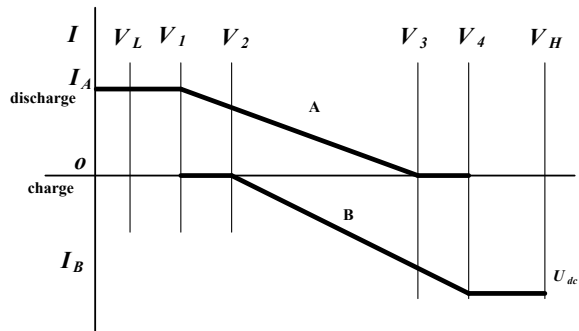
In this mode, DC/DC adopts single-current closed-loop, each current is given the same, the first pulse signal regulated by PI maintains its original state, the second signal delays  $2\pi/3$  switching cycles, and the third signal delays  $4\pi/3$  switching cycles. The delayed three signals are used to trigger the switching device separately, so that the actual current can track the instruction current and make the current on each inductor satisfy the requirements at the same time.

DC/AC converter adopts voltage-oriented control (VOC) based on grid side voltage. Voltage orientation control adopts the double closed-loop structure of DC voltage outer loop and network side current inner loop. Voltage outer loop can maintain the stability of middle DC side voltage, and current inner loop can control current. Through the double closed-loop control of voltage and current, the grid side unit power factor can be connected to the grid.

#### 3.2 Control Strategy in Offline Mode

In the off-grid mode, DC/AC converter acts as a power source to stabilize the amplitude and frequency of AC side voltage. Therefore, the  $V/f$  control [7] can be used. The AC voltage outer loop can stabilize the AC side voltage. The output of the voltage outer loop responds to the power change of the system under the current inner loop. The DC/AC converter of energy storage converter no longer has ability to stabilize the intermediate DC side voltage. DC side voltage needs to be stabilized by DC/DC converter. Considering the factors of automatic current sharing and circulating current suppression of each module, droop control is introduced into the control of DC/DC converter [8].

The principle of droop control is to write “DC side voltage  $V_{dc}$ -inductance current  $I_L$ ” droop curve in DC/DC control strategy, so that the given value of inductance current  $I_L$  responds to the given power according to the set droop curve of DC side voltage  $V_{dc}$ . Drop control includes two modes: droop charging mode and droop discharging mode. The set droop curve is shown in Fig. 4.

**Fig. 4** Droop control graph

The sag control is modified to make the voltage range of charging mode and discharging mode multiplexed, which greatly reduces the required voltage regulation range. The working curve can be determined only by the joint determination of the charging and discharging state of the system.

#### (1) Dropping discharge mode (Curve A)

When  $V_{dc} > V_4$ , continued discharge may cause the voltage to continue to rise and trigger protection, and the system will automatically switch to charging mode.

When  $V_3 < V_{dc} < V_4$ , this is the dead zone of sagging discharge, which can prevent frequent switching of charge and discharge caused by voltage jitter.

When  $V_1 < V_{dc} < V_3$ , the DC/DC module operates according to the sag curve. The relationship between the current value and DC side voltage is as follows (1). When the load power increases, the DC/AC discharge power increases, which will cause the DC side voltage to drop. According to the curve, the discharge current increases, the DC side voltage is supplemented, and the balance of the system is maintained, and vice versa.

$$I_{ref} = \frac{U_{dc} - V_1}{V_3 - V_1} (I_0 - I_A) + I_A \quad (1)$$

When  $V_{dc} < V_1$ , the module operates according to the maximum discharge current, which is the reference current of the sagging discharge curve.

#### (2) Dropping charging mode (Curve B)

When  $V_{dc} > V_4$ , the module operates according to the maximum charging current, which is the reference current of the sagging charging curve.

When  $V_2 < V_{dc} < V_4$ , DC/DC module operates according to sag curve, in which the relationship between current value and DC side voltage is expressed as (2). When the power of DC/AC rectifier increases, the DC side voltage will rise.

According to the curve, the charging current will increase, the DC side voltage will be reduced, and the balance of the system will be maintained, and vice versa.

$$I_{\text{ref}} = \frac{V_4 - U_{\text{dc}}}{V_4 - V_2} (I_0 - I_B) + I_B \quad (2)$$

When  $V_1 < V_{\text{dc}} < V_2$ , the dead zone of sagging charging can prevent frequent switching of charge and discharge caused by voltage jitter.

When  $V_{\text{dc}} < V_1$ , charging may cause the voltage to continue to drop and trigger protection, and the system will automatically switch to discharge mode.

## 4 Experimental Analysis

In order to verify the feasibility of the above control strategy, a functional experimental platform of energy storage converter is built as shown in Fig. 5. The energy storage converter consists of three 75 kW triple DC/DC converters and one 500 kW DC/AC converter. Because of the large battery capacity and limited conditions, a 500 kW converter is used to replace the battery pack. The DC source adopts double closed-loop control, and the DC side voltage is stable. It is used as a battery pack with a stable voltage. The parallel and offline operation of energy storage converter can be realized by switching the state of circuit breaker  $Q_2$  and  $Q_3$ .

When the battery is discharged, the energy flows from left to right, the DC source works in the rectifying state, and the converter works in the inverting state.

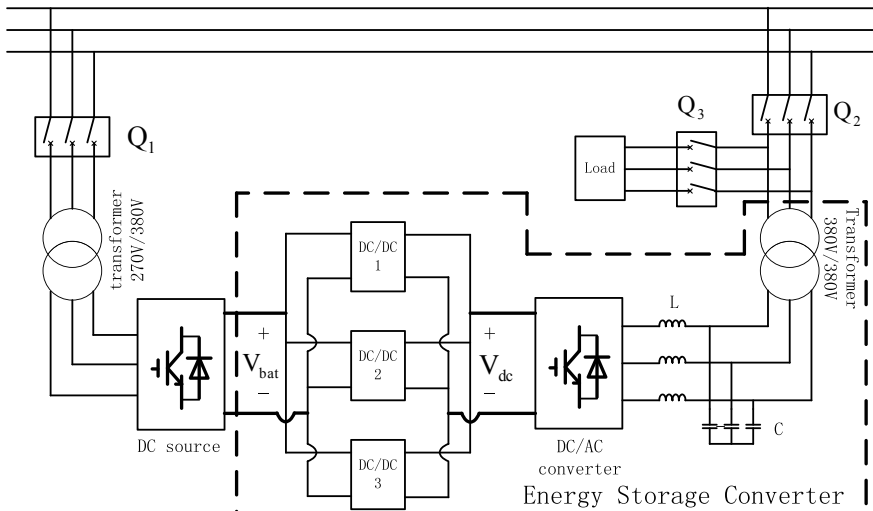


**Fig. 5** Experimental platform of storage converter

When the battery is charged, the energy flows from right to left, the DC source works in the inverting state, and the converter works in the rectifying state.

#### 4.1 Grid-Connected Experiment

When connected to the grid, close circuit breakers  $Q_1$  and  $Q_2$ , disconnect  $Q_3$ , and the converter is connected to the grid.

##### (1) Full power charging experiment of single DC/DC module

DC source is set to double closed-loop control, and battery side voltage is 500 V; DC/DC full power operation, charging current is set to  $-150$  A (charging is negative); DC/AC converter is operated in double closed-loop, and DC side voltage is set to 600 V. The experimental waveforms of DC/DC are shown in Fig. 6a, b. In Fig. 6a, CH1: battery side voltage, CH2: DC side voltage, CH3: battery side capacitive current, CH4: sum of three inductance currents. In Fig. 6b, CH1–CH3 is three inductance currents of DC/DC module, CH4: synthesis current of three inductance.

The DC side voltage is stable at 600 V, which is consistent with the given voltage. The double closed-loop of DC/AC converter plays the role of stabilizing the DC side voltage; the three inductance currents are basically distributed equally; the ripple is greatly reduced. The total current value is 151 A, which is basically the same as the given one. The charging current traces the current instructions well.

##### (2) DC/DC full power constant current discharge test

In the discharge experiment, the battery side voltage is set to 500 V; DC/AC converter operates in double closed-loop mode with 700 V DC side voltage; DC/DC operates at full power with 150 A discharge current. The experimental waveforms of DC/DC are shown in Fig. 7.

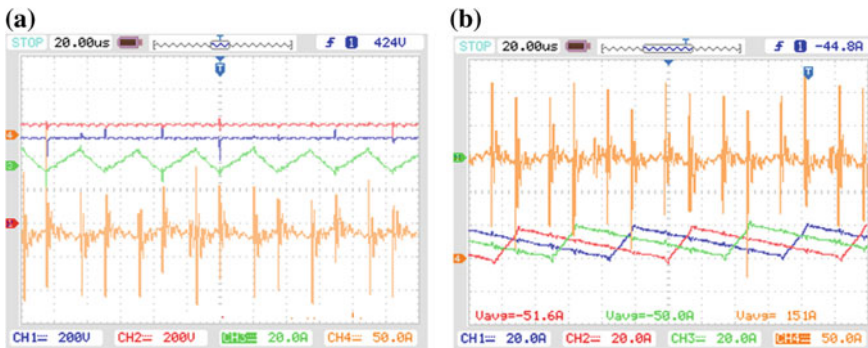


**Fig. 6** Experimental waveforms at full power charge

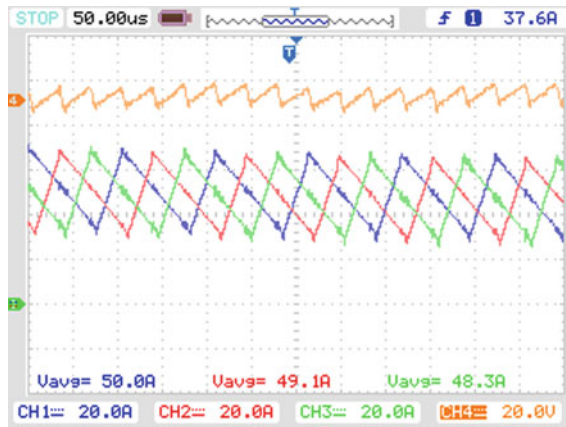


**Fig. 7** Experimental waveforms at full power discharge

CH1–CH3 are three inductance currents of DC/DC module, CH4: composition of three current.

### (3) DC/AC converter grid-connected experiment

Set the energy storage converter to discharge state and charging state, respectively, the power is given to 100 kW, and the DC side voltage is set to 800 V. The measured DC/AC converter voltage and current waveform are shown in Fig. 8a, b. CH1 (200 V per grid): the phase voltage; CH2 (200 V per grid): DC side voltage; CH3 (200 A per grid): the phase current. Regard the current from DC side to AC side as the positive direction.

The DC side voltage is stable at 800 V, which is the same as the setting. In the discharge state, the voltage and current have the same phase, and the power factor is about +1; in the charging mode, the voltage and current phase are opposite, and the power factor is about -1.

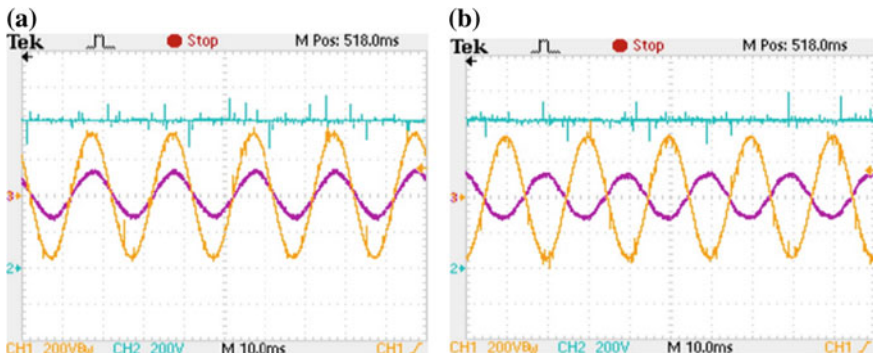


**Fig. 8** Grid side voltage and current

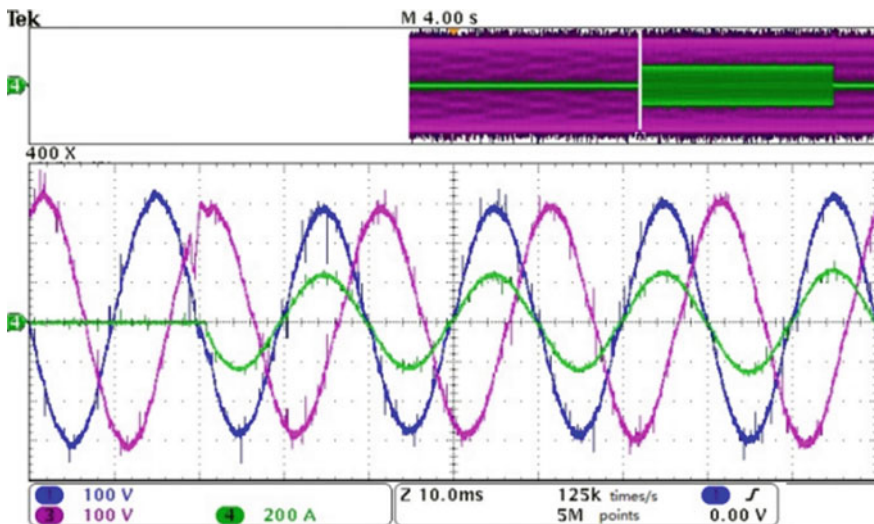


**Fig. 9** Network side voltage and current under off-grid mode

#### 4.2 Offline Experiment

Close circuit breakers  $Q_1$  and  $Q_3$ , disconnect  $Q_2$ , and the converter operates off-grid, providing separate power supply for the load.

In off-grid mode, DC/DC converter adopts droop control, and DC/AC converter adopts V/f control. The waveform obtained by the test is shown in Fig. 9.

CH1 (100 V/grid): the phase voltage; CH2 (100 V/grid): B phase voltage; CH3 (200A/grid): the phase current.

The phase voltage of AC side is stable at 220 V when the converter is offline and no-load operation; after putting 120 kW load into operation, the voltage of AC side falls and returns to normal after 2–3 cycles of regulation.

### 5 Conclusion

With the rapid development of battery energy storage technology, the power level of energy storage converter is also expanding rapidly. The traditional converter topology cannot meet the requirements, so a two-stage multi-DC/DC parallel topology is adopted. Each DC/DC module adopts multiple designs to optimize the current ripple and its harmonics, and the inverter uses a three-phase voltage source PWM rectifier with simple principle and easy realization. The corresponding control strategy is formulated by studying the functions of energy storage converter under different conditions of grid-connected/off-grid, and droop control is introduced into the control.

## References

1. Cuo Z, Yan X, Yang DZ (2018) Probability-weighted robust optimization for distributed generation planning in microgrids. *IEEE Trans Power Syst* 1–1
2. Guopeng Z, Xinwei Z, Hongwei Y, Feng XU (2018) Droop control based seamless transfer strategy for three- phase converter in microgrid. In: IOP conference series earth and environmental science, vol 192, p 012028
3. Kotra S, Mahesh KM (2019) Design and stability analysis of DC microgrid with hybrid energy storage system. *IEEE Trans Sustain Energ* 1–1
4. Son HS, Kim JK, Lee JB, Moon SS, Park JH, Lee SH (2017) A new buck-boost converter with low voltage stress and reduced conducting components. *IEEE Trans Ind Electron* 1–1
5. Faisal A, Hasan S, Suherman (2018) Simulation comparison of proportional integral derivative and fuzzy logic in controlling AC-DC buck boost converter. *J Phys Conf Ser* 978(1):012074
6. Lai CM, Cheng YH, Hsieh MH, Lin YC (2018) Development of a bidirectional dc/dc converter with dual-battery energy storage for hybrid electric vehicle system. *IEEE Trans Veh Technol* 67(2):1036–1052
7. Hong-Liang LI, Jian-Guo J, Zhong-Zheng Z (2017) V/f control method of induction motor's starting and oscillation in a certain frequency band. *Electr Mach Control*
8. Woo DY, Park SJ, Kim CS (2016) Bi-directional DC-DC converter For ESS using the Droop Control. In: 2016 IEEE Transportation Electrification Conference and Expo, Asia-Pacific (ITEC Asia-Pacific). IEEE

# Simulation Analysis and Experimental Verification of High-Speed Train Electromagnetic Disturbance



Jun Yu

**Abstract** Electromagnetic compatibility of high-speed railway system with military facilities, civil equipment and aviation equipment has been a research hotspot in recent years. The electromagnetic disturbance of high-speed train to the external environment is one of the important factors that affect the electromagnetic compatibility of high-speed railway system with other systems. Equipment and devices including inverters, wireless communication devices, high-power electrical equipment and electrical connection cables as well as circuit boards are all sources of electromagnetic disturbance to the external environment of the train. The type test of the whole train was carried out after installation of all devices and cables. The rectification will waste a lot of manpower and material resources if external electromagnetic disturbance exceeds the standards. Hence, in this study, the influencing factors of external electromagnetic disturbance of high-speed train are analyzed to identify the source and propagation path. The peak of electromagnetic disturbance is extracted and identified by means of simulation, so as to propose an improvement scheme of electrical design. The effectiveness of the simulation analysis is verified through the vehicle test, which provides a guiding reference for the electrical design and manufacture of the high-speed train.

**Keywords** Electromagnetic compatibility · High-speed train · Simulation analysis · EMI

---

J. Yu (✉)

Locomotive and CAR Research Institute, China Academy of Railway Sciences Corporation Limited, Beijing, China  
e-mail: [yjhj0803@163.com](mailto:yjhj0803@163.com)

J. Yu

Beijing Zongheng Electro-Mechanical Technology Co., Ltd., Beijing, China

## 1 Introduction

The railway system is a distributed system, where the transmission field depends on the location of the moving train and the current load capacity [1]. The electromagnetic environment of rail transit is a complex, superimposed electromagnetic environment involving light industry, civil, commercial and heavy industrial applications. Electrified railways require high output power systems and power electronics characterized by large changes in voltage and current during its whole operation and special current distribution generated by moving load. Electric multiple unit (EMU), an important moving equipment of high-speed rail, converts 15 kV/16.67 Hz or 25 kV/50 Hz electric energy into mechanical energy through AC drive system. Broadly speaking, an AC drive system consists of a pantograph, a transformer, a converter, a motor, a gearbox and wheels. Electromagnetic disturbance of the entire EMU can be generated at any stage of electric power conversion and transmission [2].

The electromagnetic conduction disturbance equivalent model of traction system of high-speed EMU established and analyzed in [3] is used to predict the electromagnetic conduction disturbance of high-speed EMU, but its validity has not been verified with field test data. Reference [4] analyzes the impact of electromagnetic interference (hereinafter referred to as “EMI”) generated by pantograph–catenary disconnection on the speed sensor of EMU CRH380BL, theoretically analyzes the interference value by means of mechanism analysis and formula derivation, identifies the out-of-limit frequency point of 10 MHz and verifies the same with test. However, the electromagnetic interference model is not analyzed during the whole process. In [5, 6], the EMI mechanism of EMU is analyzed, a circuit simulation model of EMI of the entire train is established, and real train test is performed. But the simulation result differs greatly from the field test result (Fig. 1).

As a tool that effectively predicts EMI characteristics, simulation identifies abnormal frequency points at the design stage, guides circuit design and improves the verification efficiency of any corrective measure taken in the rectification

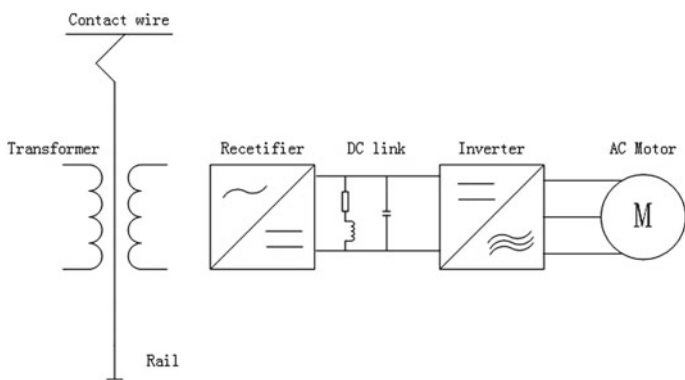


**Fig. 1** Block diagram of AC drive system

process after test data exceeds the limit of applicable standard. Moreover, simulation and experimental verification combines with and complements each other to enhance EMC design and verification capabilities of EMU.

## 2 EMI Test of EMU

### 2.1 Test Procedure

References [7] and [8] serve as the basis for EMI test of the entire train of EMU. During the test, an antenna was erected 10 m away from the center of the track to test the external radio frequency disturbance ranging from 9 kHz to 1 GHz generated by the EMU. The antenna was erected before the EMU ran, and tests were performed in static, traction and regenerative brake conditions of EMU.

In static condition, the entire train was stationary, the pantograph was raised, the main breaker was closed, and all auxiliary units such as air conditioning, vehicle radio, signaling and lighting systems were energized and operated properly.

In dynamic condition, the EMU moved at a speed of  $50 \pm 10$  km/h and accelerated or decelerated at approximately 1/3 of its maximum traction over a given speed range. Data was collected during a full test cycle marked by the pass of the entire train through the antenna.

### 2.2 Test Result

The red line is limit line in Figs. 2 and 3. The white line or purple line represents EMI amplitude of the whole train, while the yellow line represents background noise. Test value exceeding the limit occurs in 720 kHz, 830 kHz and 900 kHz approximately. The explanation of this phenomenon specified in EN50121-3-1 was “If at specific frequencies or in specific frequency ranges the ambient noise is higher than the limitless 6 dB, the measurements at these frequencies need not be considered. These frequencies shall be noted in the test report.” Actually, 720 and 830 kHz are the frequency of AM broadcast rather than the deliberate EMI of the train. As shown in Figs. 2 and 3, the test result indicates that EMI of the EMU exceeds the required limit at 900 kHz in both traction condition and electronic brake conditions.

### 2.3 EMI Disturbance Sources

Any of the four-quadrant rectifier, output of traction invertor or converter, auxiliary inverter, auxiliary loads (e.g., air conditioner, charger, fan, inverter power supply,

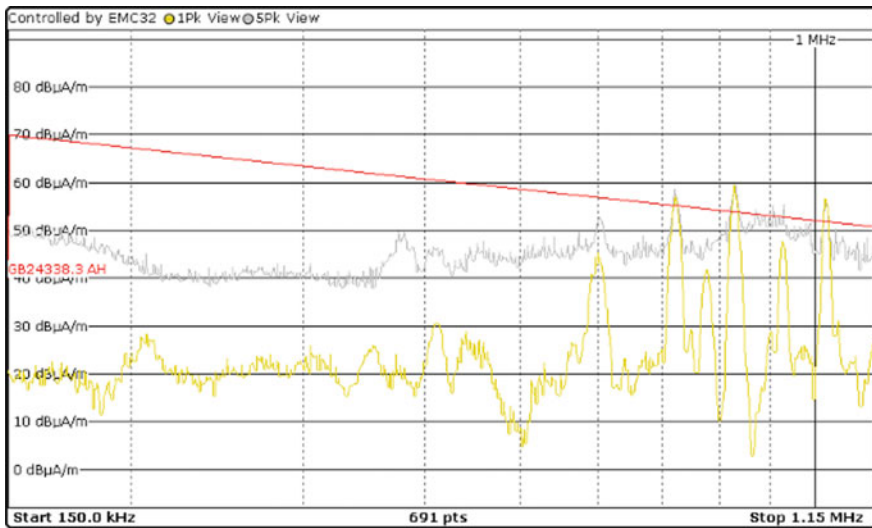


**Fig. 2** External EMI of the entire EMU at 150 kHz–1.15 MHz (in traction condition)

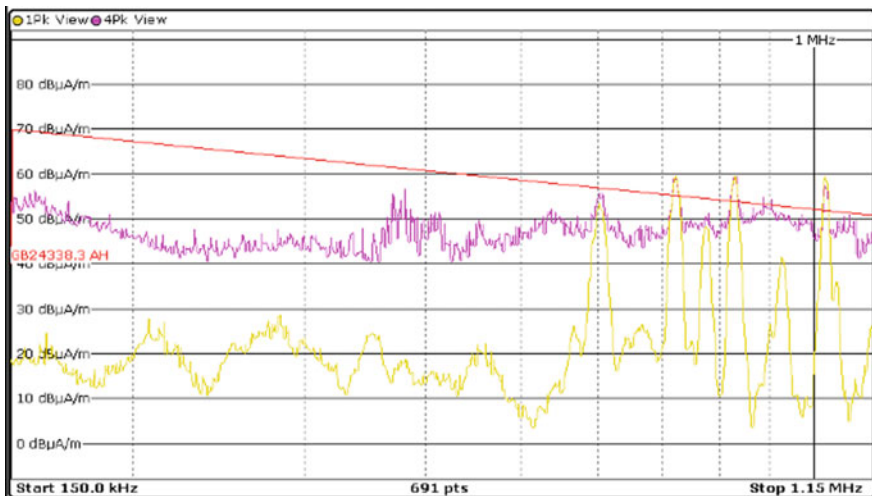


**Fig. 3** External EMI of the entire EMU at 150 kHz–1.15 MHz (in regenerative brake condition)

compressor, lighting or passenger information) of EMU can be a source of EMI. According to the waveform, the nonconforming frequency band takes the form of a step wideband rather than a narrowband pulse exceeding limit at a single frequency point. Taking the EMU as a whole, the out-of-limit radio frequency disturbance is caused by the synthetic action of the whole system.

Comparison between waveforms of static and dynamic tests shows that RF disturbance in dynamic condition is much greater than that in static condition. All auxiliary units were activated in static and dynamic conditions. The difference lies in that the AC drive system composed of transformers, converters and motors entered the running state in dynamic condition. Hence, the AC drive system can be identified as the main source of external EMI of the EMU.

## 2.4 EMI Transmission Path

The EMI radiated by the EMU to the external environment has a frequency of greater than 9 kHz, and harmonic component within such frequency range is negligible. In practical applications, system-level EMI is primarily generated from electromagnetic disturbances of cables, including common mode and differential mode disturbance. The traction converter is equipped with a differential mode filter, and the area of differential mode circuit is much smaller than that of common mode circuit. The component of differential mode interference of AC drive system is generally small. The common mode disturbance is generated as high-frequency common mode current flows through the cable and constitutes a circuit with the earth, producing an “antenna effect,” and it is proportional to the circuit area.

Insulated gate bipolar translator (IGBT) characterized as high current density and switching speed is the important component of converter. The high speed and instantaneous switching process of IGBT produces high  $dv/dt$  and  $di/dt$  to form EMI. Following aspects can be described the EMI source generated by IGBT: The distributed capacitance of converter circuit can be charge or discharge by the jumping of voltage. The switching process produces induced voltage on the stray inductance, and LC oscillation circuits generate electromagnetic waves in the charging and discharging process between capacity and inductance. Pulse-width modulation (PWM), an inverter control method, produces higher harmonic whose frequency can reach several hundred Hz, and harmonic frequency can reach several kHz. High-frequency harmonic is also the source of EMI.

According to Fig. 5, the cable connecting the traction transformer to the converter has a distributed capacitance to the ground. Both of the DC bus of traction converter and the cable of traction motor have a distributed capacitance to the ground. A current of 50 Hz cannot pass through the circuit formed by them. The common mode current constitutes a circuit when its frequency exceeds hundreds kHz, and the entire circuit emits EMI to the external environment (Fig. 4).

## 2.5 EMI Circuit Model

As shown in Fig. 5, the common mode circuit is modeled and simulated with the Simpower toolkit of MATLAB. As shown in Figs. 5 and 6, FFT analysis is

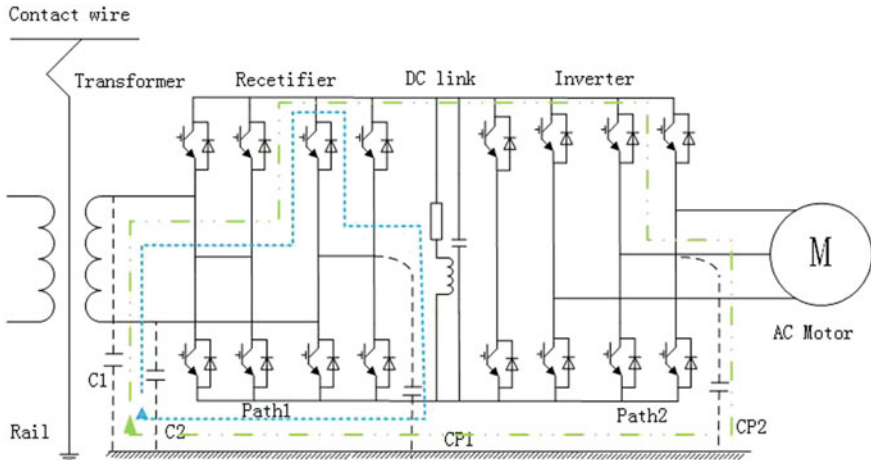


**Fig. 4** Common mode EMI transmission path of the EMU traction system

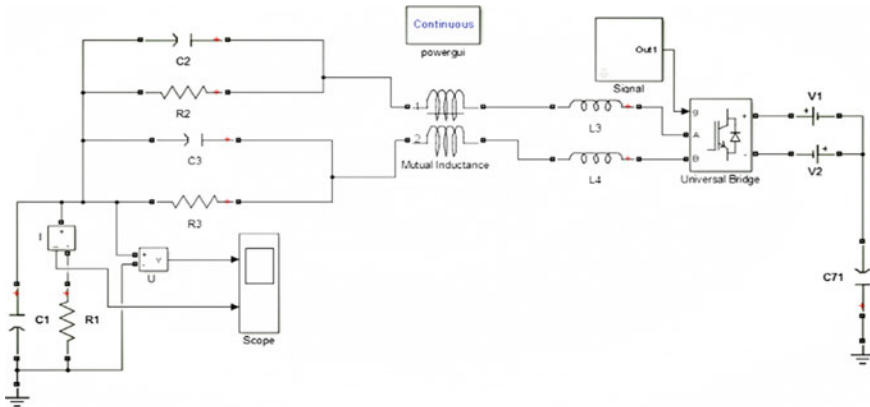


**Fig. 5** Traction system circuit model

conducted for the common mode voltage. The result indicates that the common mode voltage can reach 800 V at 900 kHz, which is consistent with the real train test at 900 kHz.

Figure 6 shows simulation waveform of common mode voltage which can motivate the EMI of the train to outside space. Figure 7 shows the spectrum of common mode voltage based on FFT. It is worth noting that frequency of extreme point is around 900 kHz.

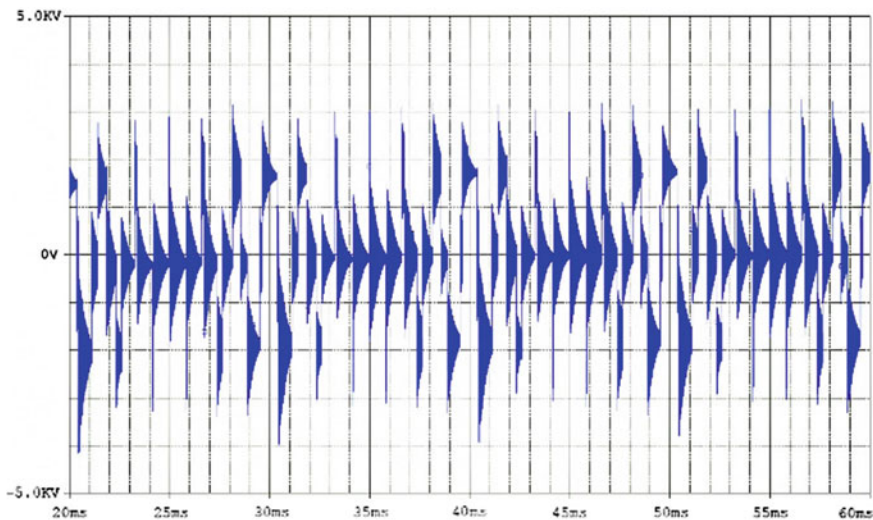


Fig. 6 Simulation waveform of common mode voltage

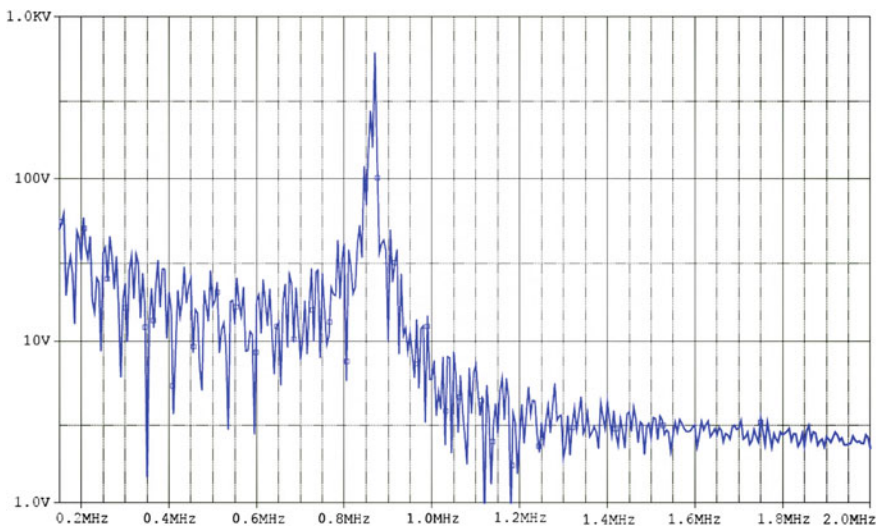
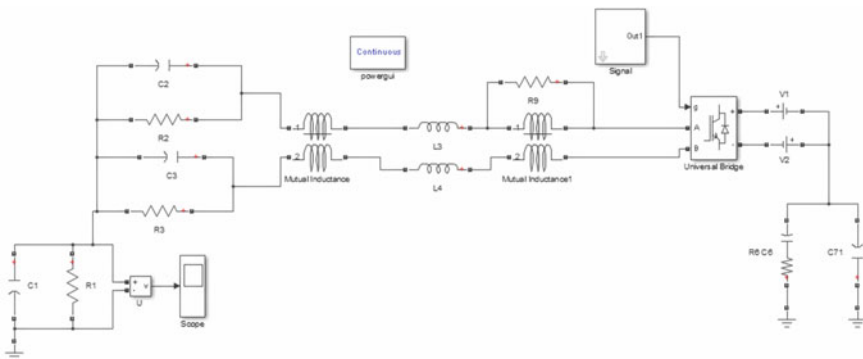


Fig. 7 FFT waveform of common mode voltage

### 3 EMI Model Optimization and Implementation of Rectification of EMU

Further verification was made with the above model by providing a common mode magnetic ring (with a frequency of 1 MHz, an impedance of  $10 \Omega$  and a common mode inductance of  $10 \mu\text{H}$ ) in the cable between the transformer and the converter. The simulation result shows that the peak EMI at 900 kHz is significantly weakened (Figs. 8, 9).



**Fig. 8** Model of the common mode circuit provided with common mode magnetic ring

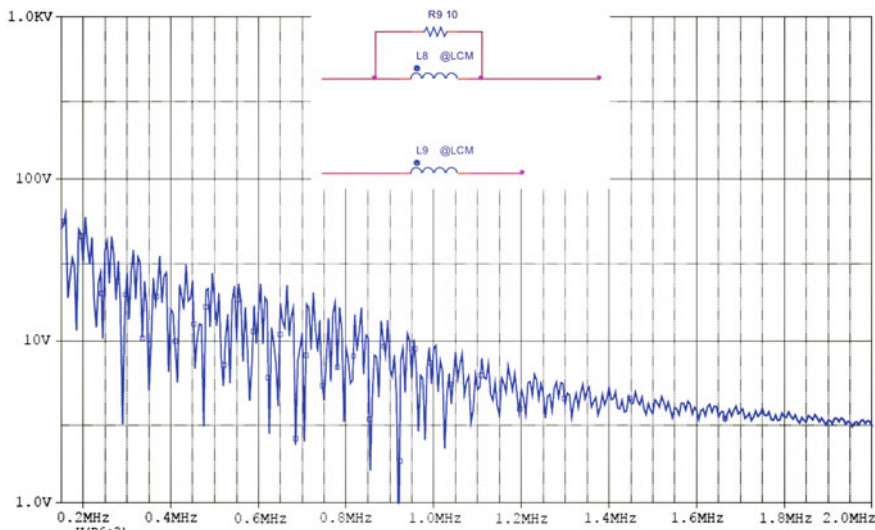


**Fig. 9** Simulation result at 900 kHz of common mode circuit provided with magnetic ring

#### 4 Experimental Verification

The EMU was rectified by providing a common mode magnetic ring of the same parameters between the transformer and the converter. Field tests show that the common mode magnetic ring significantly restrains the EMI of the entire train at 900 kHz and the test value is smaller than the limit (Figs. 10, 11).

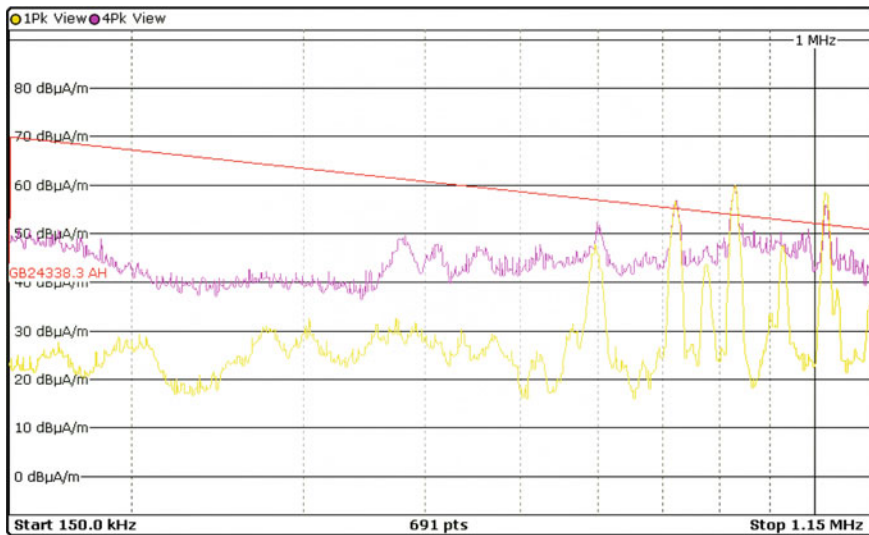


**Fig. 10** External EMI of the entire EMU at 150 kHz–1.15 MHz (in traction condition field test)

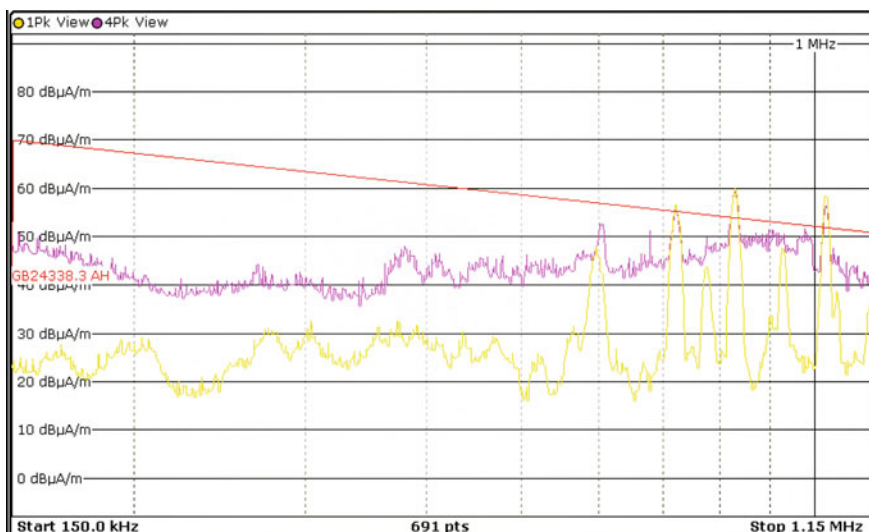


**Fig. 11** External EMI of the entire EMU at 150 kHz–1.15 MHz (in regenerative brake condition of field test)

## 5 Conclusion

This study uses the simulation analysis that verifies the corrective measure effectively in combination with the experimental verification to provide a means for optimizing EMC design of EMU.

**Acknowledgements** This work is supported by Joint Funds of the National Natural Science Foundation of China (No. U1734203) and 2018 Talent Lifting Project of China Association for Science and Technology. Jun Yu is the corresponding author.

## References

1. Ogunsola A (2012) Electromagnetic compatibility in railways: analysis and management. Springer, Genoa
2. Sun J, Yu J (2017) The experimental study and optimized countermeasures on EMI characteristics of 400 km/h China standardized high-speed train. In: IECON 2017-43rd Annual conference of the IEEE Industrial Electronics Society, Beijing, pp 7046–7051
3. Yang Z, Li H, Feng C, Jiang Y, Lin F, Yang Z (2018) Survey on electromagnetic interference analysis for traction converters in railway vehicles. In: 2018 International Power Electronics Conference (IPEC-Niigata 2018-ECCE Asia), pp 2058–2065
4. Xiong D, Liu X, Chen X (2018) Optimization design of anti-strong magnetic interference for intelligent miniature circuit breaker. In: 2018 2nd IEEE Conference on energy internet and energy system integration (EI2), pp 1–5
5. Ji J, Liu Y, Chen W, Li J, Yang X (2018) Modeling and simulation on overall-train EMI of china standardized high-speed train. In: 2018 IEEE International symposium on electromagnetic compatibility and 2018 IEEE Asia-pacific symposium on electromagnetic compatibility (EMC/APEMC), Singapore, pp 953–955
6. Jeschke S, Tsapenko S, Hirsch H (2015) Investigations on the shaft currents of an electric vehicle traction system in dynamic operation. In: 2015 IEEE International symposium on electromagnetic compatibility (EMC), Dresden, pp 696–701
7. CENELEC.EN50121-3-1-2017 (2017) Railway-applications electromagnetic compatibility part 3-1: rolling stock-train and complete vehicle. Technical Committee GEL/9, Brussels
8. CENELEC.EN55016-2-3-2014 (2014) Specification for radio disturbance and immunity measuring apparatus and methods part 2-3: methods of measurement of disturbances and immunity-radiated disturbance measurements. Technical Committee A1, Brussels

# Research on a PMSM Control Method Based on Model Prediction Control



Yalou Chen, Jun Zhou, Wenzuan Wang, Tao Yang, and Zhaorui He

**Abstract** The model predict control (MPC) algorithm is based on the desired reference trajectory and the model of the control object to establish a prediction model, calculate the current period predicted value and then use the prediction error of the previous cycle to correct the predicted value, and the optimal control increment is obtained by rolling optimization based on cost function, then obtaining the optimal control increment accumulated in time. The MPC algorithm is introduced into the speed loop of PMSM field-oriented control to design speed loop controller, and then establish simulation model to prove that the PMSM field-oriented control based on MPC has fast and accurate response and better robustness then the PMSM field-oriented control based on PI.

**Keyword** MPC · PMSM · Field-oriented control

## 1 Introduction

The PMSM is a complex, strongly coupled and nonlinear system [1]. The traditional PMSM field-oriented control based on PI that has some shortcomings, such as the difficulty of setting parameters and the difficulty of achieving higher control performance requirements, poor parameter robustness is increasingly difficult to

---

Y. Chen (✉) · J. Zhou · W. Wang · T. Yang · Z. He

NARI Group Co. Ltd. (State Grid Electric Power Research Institute), Nanjing, China

e-mail: [chenyalou@sgepri.sgcc.com.cn](mailto:chenyalou@sgepri.sgcc.com.cn)

J. Zhou

e-mail: [zhoujun2@sgepri.sgcc.com.cn](mailto:zhoujun2@sgepri.sgcc.com.cn)

W. Wang

e-mail: [wangwenxuan@sgepri.sgcc.com.cn](mailto:wangwenxuan@sgepri.sgcc.com.cn)

T. Yang

e-mail: [yangtao1@sgepri.sgcc.com.cn](mailto:yangtao1@sgepri.sgcc.com.cn)

Z. He

e-mail: [hezhaorui@sgepri.sgcc.com.cn](mailto:hezhaorui@sgepri.sgcc.com.cn)

meet the meet of the actual site [2–4]. And the performance of control loops of PMSM mostly lies on the performance of speed loop, and the current loop is able to respond to the output of the performance of speed loop, so in recent years, many advanced algorithms are introduced into the speed control loop in order to improve the performance of the hole loops [5–7].

The MPC algorithm is introduced into the speed loop of PMSM field-oriented control to design speed loop controller by establishing an angle speed prediction model and then calculating the current period predicted angle speed value to obtain the optimal control increment accumulated in time.

## 2 Model of PMSM

The current field-oriented diagram of PMSM in two-phase rotating coordinate system ( $d$ - $q$  coordinate system) is shown in Fig. 1 [8, 9].

The straight-axis current  $i_d$  and the cross-axis current  $i_q$  are the  $i_s$  components along the  $d$ -axis and  $q$ -axis, respectively, in the  $d$ - $q$  coordinate system. The  $\theta$  is the angles between the rotating  $d$ -axis and the static  $A$ -axis. The stator voltage equation is presented as Eq. (1) [10].

$$\begin{bmatrix} u_d \\ u_q \end{bmatrix} = \begin{bmatrix} R + L_d \frac{di_d}{dt} & -\omega L_q \\ R + L_q \frac{di_q}{dt} & \omega L_d \end{bmatrix} \begin{bmatrix} i_d \\ i_q \end{bmatrix} - \begin{bmatrix} 0 \\ \psi_f \omega \end{bmatrix} \quad (1)$$

$\omega = P_n \omega_r$ ,  $P_n$  is the polar logarithm of PMSM,  $\omega_r$  is the mechanical angular velocity of PMSM,  $\psi_f$  is the rotor flux of PMSM,  $u_d$  and  $u_q$  is the component of molecular voltage on  $d$ - and  $q$ -axes, respectively,  $L_d$  and  $L_q$  is the stator inductance on  $d$ - and  $q$ -axes, respectively.

Electromagnetic torque equation  $T_e$  of PMSM as Eq. (2).

$$T_e = \frac{3}{2} p_n [\psi_f i_q + (L_d - L_q) i_d i_q] \quad (2)$$

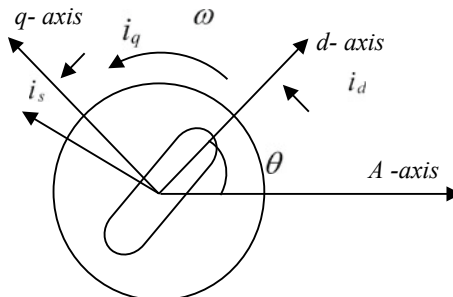


**Fig. 1** Current field-oriented diagram of PMSM in  $d$ - $q$  coordinate system

According to the Eq. (2),  $\psi_f$ ,  $L_d$ ,  $L_q$ , and  $p_n$  are constants, and the value changes of  $T_e$  is only related to  $i_d$ ,  $i_q$ .

The mechanical equation of PMSM as Eq. (3).

$$\frac{d\omega_r}{dt} = (T_e - T_L - B\omega_r)/J \quad (3)$$

The  $J$  is the moment of inertia,  $B$  is adhesion coefficient, and  $T_L$  is the load torque.

### 3 Loop Controller Design

The field-oriented control loop of permanent magnet synchronous motor based on MPC consists of a speed loop and two current loops as shown in Fig. 2. The current loop corresponds to the  $d$ -axis current loop and the  $q$ -axis current loop, respectively. The controller is designed by PI. The parameters of the  $d$ -axis current controller are consistent with those of the  $q$ -axis current controller. And the speed controller is designed by introducing MPC algorithm.

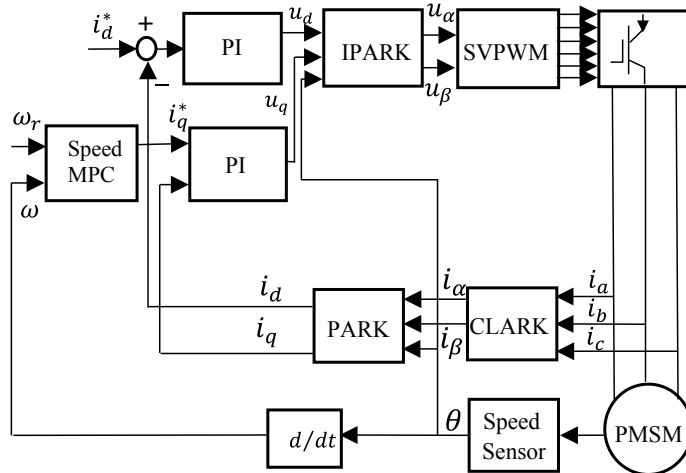


**Fig. 2** Field-oriented control loop of PMSM based on MPC

### 3.1 Speed Loop Controller Design

The design of speed controller is mainly divided into speed model prediction, prediction feedback correction, reference trajectory and rolling optimization thus four steps. The controller input is the angular velocity reference given and the actual angular velocity feedback, and the output is the  $q$ -axis current reference given.

#### (1) Speed prediction model.

The load torque is discretized from the mechanical equation Eq. (3) of PMSM and the electromagnetic torque equation to obtain the difference equation.

$$\begin{cases} \omega(k) = ai_q(k-1) - b\omega(k-1) \\ \omega(k+1) = ai_q(k) - b\omega(k) \end{cases} \quad (4)$$

The discrete equation of the prediction model of angular velocity is obtained by subtracting the two equations.

$$\omega_p(k+1) = a\Delta i_q(k) - (b-1)\omega(k) + b\omega(k-1) \quad (5)$$

Where  $a = K(1 - e^{-TB/J})$ ,  $b = -e^{-TB/J}$ ,  $K = n_p\psi_f$ .

#### (2) Prediction feedback correction

It is impossible to accurately calculate the actual error of the predicted value of the current sampling period relative to the next sampling period in the current sampling period. However, the sampling period is very short, and thus, the prediction error of the current time can be replaced to correct the prediction value by the prediction error of the previous time.

$$\begin{cases} \omega_e(k+1) = \omega_p(k+1) + e(k) \\ e(k) = \omega(k) - \omega_p(k) \end{cases} \quad (6)$$

#### (3) Reference trajectory

The first-order exponential function  $y_r(k+1)$  is selected as a given reference function for enabling the input and output of MPC speed controller smooth, as similar to the exponential function,

$$y_r(k+1) = c\omega_e(k+1) + (1-c)\omega_r(k) \quad (7)$$

$c = e^{-T/\tau}$  is the proportional constant, the smaller the value of  $\tau$ , the faster the reference value, if the value is not appropriate, there will be a larger overshoot.

#### (4) Optimization criteria.

There are usually three kinds of optimization functions for making the output of the model approximate to the reference trajectory as much as possible: quadratic performance index function, one-norm performance index function and infinite-norm performance index function.

$$H = \min \left\{ \lambda [\omega_e(k+1) + y_r(k+1)]^2 + \beta [\Delta i_q^*]^2 \right\} \quad (8)$$

$\lambda$  and  $\beta$  are the proportion parameters that need to be configured. The increment of the output  $\Delta i_q^*(k)$  of the speed controller is obtained by deriving Eq. (8) from both sides.

$$\Delta i_q^*(k) = -\frac{\lambda a}{\lambda a^2 + \beta} [(b-1)\omega_r(k) + b\omega_r(k-1) + e(k) - y(k+1)] \quad (9)$$

Then, the output value of speed controller as the reference input value of  $q$ -axis current controller:

$$i_q(k) = \Delta i_q^*(k) + i_q(k-1) \quad (10)$$

### 3.2 Current Loop Controller Design

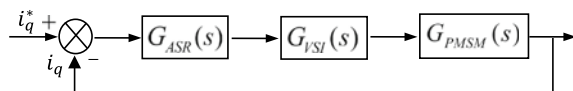
Figure 3 shows the equivalent loop of the current loop.

The transfer function  $G_{PMSM}(s)$  is an equivalent transfer function of voltage source inverter equivalent transfer function of PMSM. Permanent magnet synchronous motor (PMSM) can be regarded as a first-order inertia link, which can be expressed as

$$G_{PMSM}(s) = \frac{i_q(s)}{u_q(s)} = \frac{1}{R + L_q s} = \frac{1/R}{1 + sL_q/R} \quad (11)$$

The transfer function of PI controller is obtained by Laplace transform on both sides of Eq. (8):

**Fig. 3** Equivalent loop of the current loop



$$G_{\text{ASR}}(s) = \frac{U(s)}{E(s)} = K_p \left( 1 + \frac{1}{\tau_i s} \right) = K_{p\text{ACR}} + \frac{K_{i\text{ACR}}}{s} \quad (12)$$

$$K_{p\text{ACR}} = K_p, K_{i\text{ACR}} = K_p/\tau_i.$$

Because of its high switching frequency and small inertia time, voltage source inverters can be a first-order inertia link which has a very small time constant that can be expressed as

$$G_{\text{VSI}}(s) = \frac{1}{1 + T_{\text{pwm}} s} \quad (13)$$

$T_{\text{pwm}}$  is the value of the cycle the voltage source inverter.

Open-loop transfer function of current loop

$$G_{\text{ACR}}(s) = K_{p\text{ACR}} + \frac{K_{i\text{ACR}}}{s} = K_{p\text{ACR}} \left( \frac{\tau_{\text{ACR}} s + 1}{\tau_{\text{ACR}} s} \right) \quad (14)$$

The zero of PI controller's transfer function is used to eliminate the large time constant poles of the open-loop transfer function. At this time, the open-loop transfer function of the loop is

$$G_K(s) = \frac{K_i}{s(1 + T_{\text{pwm}} s)} \quad (15)$$

$$K_i = K_{p\text{ACR}}/L_q.$$

In the formula, the natural oscillation frequency and the damping ratio are selected according to the typical design method of the Tan-type system.

$$K_{p\text{ACR}} = \frac{L_q}{T_{\text{pwm}}}, \quad K_{i\text{ACR}} = \frac{L_q^2}{R T_{\text{pwm}}} \quad (16)$$

## 4 Simulation

According to the PMSM field-oriented control based on MPC block diagram shown in Fig. 2, the simulation model is constructed by using MATLAB, as shown in Fig. 4. It mainly consists of PMSM simulation model, coordinate transformation module, SVPWM module, MPC controller module and PI controller module, and the control loop consists of speed loop and current loop.

According to the construction method of MPC speed controller, the simulation model of the speed controller based on MPC is established as shown in Fig. 5.

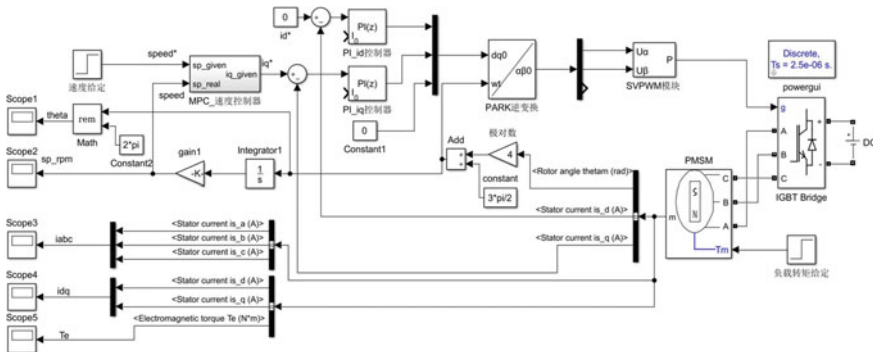


Fig. 4 Simulation model of the PMSM field-oriented control based on MPC

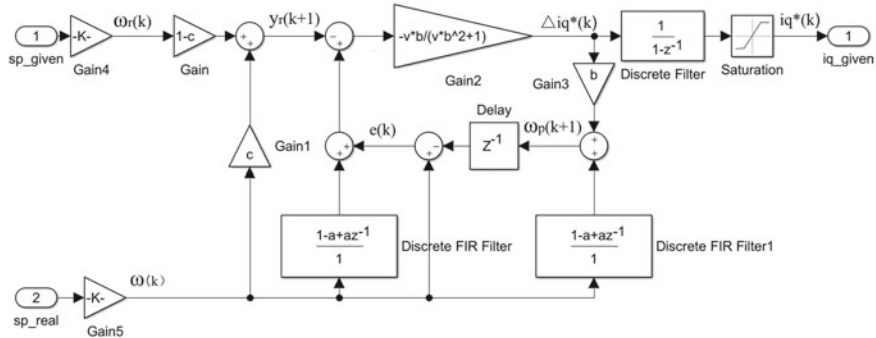


Fig. 5 Simulation model of the speed controller based on MPC

Table 1 Parameters table of loop controllers

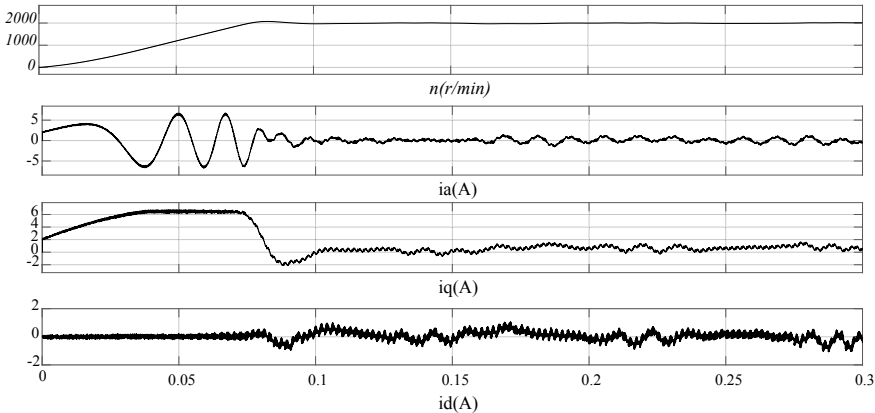
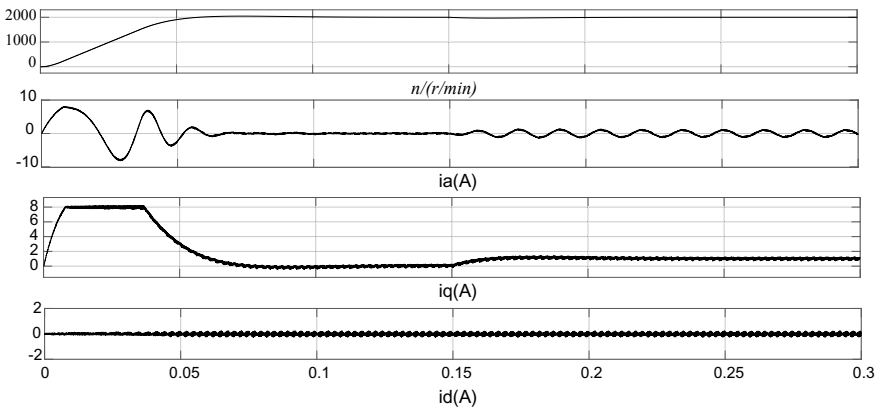
MPC controller	$v = \alpha : \beta$	$T$	$\tau$
30		0.0001	0.05
$a = n_p \psi_f (1 - e^{-TB/J})$		$b = -e^{-TB/J}$	$c = e^{-T/\tau}$
0.0795		-0.9999	0.9998
PI current controller	$K_p ACR = L_q/T$	$K_i ACR = L_q^2/RT$	
1.49573		122.3	

The MPC speed loop controller and PI current controller are configured according to Table 1, and motor parameters are configured according to Table 2. The simulation time is 0.3 s, the motor is started with no load, and step load is added to 0.15 s. The simulation results are shown in Figs. 6 and 7.

According to the simulation result of Figs. 6 and 7, the PMSM field-oriented control based on MPC can make faster response and less overshoot than the latter

**Table 2** Parameters table of PMSM

$R_s$ ( $\Omega$ )	$L_d, L_q$ (mH)	$\psi_f$ (Wb)	$B$	$J$ ( $\text{kg/m}^2$ )
0.2	8.5	0.175	0.500	0.089

**Fig. 6** Simulation result based on MPC**Fig. 7** Simulation result based on PI

also has better robustness in load mutation and has better static stability, such as the balance of electric current, small fluctuation and good sinusoidal waveform of motor. And that  $i_d$  is basically zero indicates  $d$ -axis and  $q$ -axis decoupled completely.

## 5 Conclusion

The MPC algorithm is introduced into the speed loop of PMSM field-oriented control to design speed loop controller by establishing an angle speed prediction model and then calculate the current period predicted angle speed value to obtain the optimal control increment accumulated in time. The simulation result of PMSM field-oriented control system based on MPC shows that PMSM field-oriented control based on MPC has better dynamic and static characteristics and robustness than based on PI.

## References

1. Zhang D, Xu S (2017) Application of ADRC in permanent magnet synchronous motor control. *Motor Control Appl* 44(04):70–73 (in Chinese)
2. Wang H, Zhu F, Tian Y (2019) Event-triggered optimal reset control of hard disk drive head-positioning servo systems. *Proc Inst Mech Eng, no 5* (in Chinese)
3. Zhang T, Yu H, Shen T, Leilei, Chen M (2016) Two-degree-of-freedom permanent magnet synchronous motor control based on neural network. *Micromotor* 49(12):41–45 (in Chinese)
4. Mohamed YARI (2007) Design and implementation of a robust current-control scheme for a PMSM field-oriented drive with a simple adaptive disturbance observer. *IEEE Trans Ind Electron* 54(4):1981–1988
5. Kim H, Son J (2011) Lee of a PMSM J. A high-speed sliding-mode observer for the sensorless. *IEEE Trans Ind Electron* 58(9):4069–4077
6. Liu Y (2012) Application status and prospect of fuzzy control in electric drive. *Ind Technol Forum* (12):94–95 (in Chinese)
7. LI H (2015) Research on control strategy of permanent magnet synchronous motor based on neural network. Doctoral dissertation of Northeastern University (in Chinese)
8. Wang Q, Zhang X, Zhang C (2014) Speed identification of double sliding mode reference adaptive system for permanent magnet synchronous motor field-oriented control. *J Electr Eng China, no (06)* (in Chinese)
9. Hebert SR, Jesus LF, Carlos GR et al (2014) On the control of the permanent magnet synchronous motor: an active disturbance rejection control approach. *IEEE Trans Control Syst Technol*
10. Cai M, Zhao C (2014) Genetic optimized neural network control of permanent magnet linear synchronous motor. *Micromotor, no (09)* (in Chinese)

# Research of the Three-Phase Input High Efficiency and Low Harmonic Battery Charging Power Supply



Chunhui Miao, Jie Yang, Sen Yang, Yu Yao, Zhijie Zhang, Fei Li and Wei Yang

**Abstract** This paper presents a circuit structure for lead–acid battery. The AC-DC stage employs VIENNA rectifier not only to achieve AC/DC conversion but also realizes low input current THD. To convert DC voltage to 44–64 V, meanwhile to improve the output current capability and efficiency of the converter, an improved phase-shift full-bridge (PS-FB) ZVS PWM double current synchronous rectifier converter is adopted. The VIENNA rectifier utilizes the triple harmonic injection double ramp comparison SPWM (DRC-SPWM) control method to decrease input current THD. The improved DC-DC converter adopts peak current control mode to improve the dynamic response speed of the system. Performance of the proposed circuit is verified by experimental results.

**Keywords** Three-phase · Low input THD · Lead–acid battery charger · VIENNA rectifier · ZVS PWM · Double current synchronous rectifier converter · Soft-switching

---

C. Miao · J. Yang  
Naval University of Engineering, Wuhan, Hubei, China

C. Miao · J. Yang · S. Yang · Z. Zhang (✉)  
CSSC Systems Engineering Research Institute, Haidian, Beijing, China  
e-mail: [07zhangzhijie@163.com](mailto:07zhangzhijie@163.com)

Y. Yao  
Shandong Vocational College of Industry, Zibo, China

F. Li  
Zibo Electric Power Company. Shandong Electric Power Company, Zibo, China

W. Yang  
School of Electrical Engineering and Automation, Harbin Institute of Technology,  
Harbin, China

## 1 Introduction

Lead-acid batteries play a major role in the development of microgrids, electric vehicles, shipbuilding industry and rail transport industry [1, 2]. The input sources of the charging power supply should be single or three-phase grid input. For the high-power output charger, three-phase grid input sources should be utilized.

According to the charging requirement, the three-phase grid input battery charger has some special qualities such as high efficiency, low-cost and low harmonic content. For the AC-DC stage, the traditional converter is composed of diode or thyristor [3]. However, its AC side power factor is low. With the in-depth research, three-phase PWM rectifier has been widely used in medium- and high-power applications with its high power factor and high efficiency advantages [4, 5]. However, due to the large stress of the device, the application of this topology has limitations in the case of high reliability and high power density requirements. In the recent past, multi-level topology has solved the problem of device stress [6]. And among which, the VIENNA rectifier has the advantage of low switch stress and less number of switches. Based on this advantage, it has significance to study VIENNA rectifier.

For the DC-DC stage, in order to improve power density, switch frequency should be increased. However, with the increase of switching frequency, over-voltage and overcurrent should occur during switching process. The soft-switching technology can solve this disadvantage [7]. In high output current applications, rectifier losses of the full-bridge converter have become an important issue. To reduce the on-state loss of the full-bridge converter, synchronous rectification technology is introduced [8].

This paper presents a circuit structure for lead-acid battery. The AC-DC stage employs VIENNA rectifier to realize low input current THD. To improve the output current capability and efficiency, improved PS-FB ZVS PWM double current synchronous rectifier converter is adopted. Controllers of the converter are designed. Performance of the proposed circuit is verified by a 1.5 kw prototype.

## 2 Charger Configuration

Figure 1 shows the circuit topology of the charger system. VIENNA rectifier is used to achieve AC/DC conversion. An improved PS-FB ZVS PWM double current synchronous rectifier converter is employed to regulate the output DC voltage. The leakage inductance of the transformer, the resonant inductor and the junction capacitance of MOSFET are utilized to achieve ZVS.

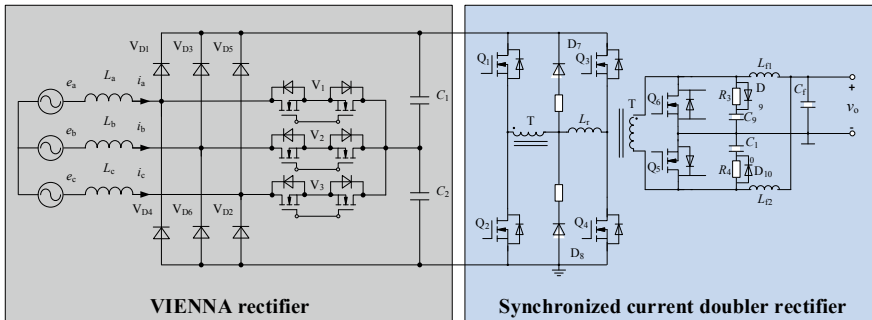


**Fig. 1** Topology of the charger system

### 3 System Operation Principle

In order to facilitate the analysis of the working principle of VIENNA rectifier, the DC-DC converter is eliminated from Fig. 1. Meanwhile, the sinusoidal power frequency cycle is divided into six sectors; each sector is  $60^\circ$  as shown in Fig. 2, and sector 2 is taken as an example. In Fig. 1, each switch in VIENNA rectifier has two states of turnoff and turnon, in which “0” means turnoff state, and “1” means turnon state. There are eight state combinations in each sector. The eight state combinations are listed in Table 1. The switch state of the other sectors is similar to sector 2.

To facilitate the analysis of the working principle of the DC-DC converter, the VIEENA converter is eliminated from Fig. 1.

Figure 3 shows the main waveforms of the converter in phase shifting.

**Fig. 2** Division of power frequency periodic working sector

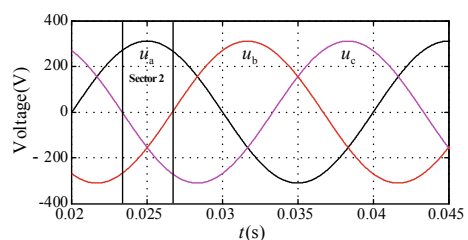
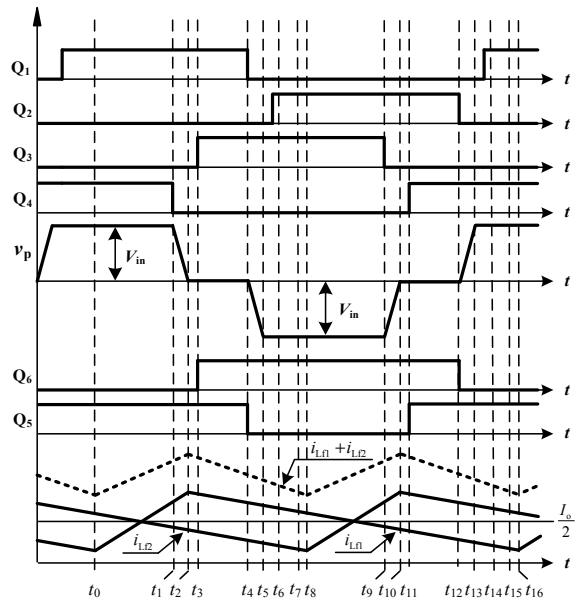


**Table 1** Eight switching state of sector 2

Power switch	Switch state							
$V_1$	1	1	1	1	0	0	0	0
$V_2$	1	1	0	0	0	1	1	0
$V_3$	1	0	0	1	1	1	0	0

**Fig. 3** Main waveforms of the converter in phase shifting



## 4 Controller Design of the Converter

### 4.1 VIENNA Rectifier Small-Signal Model

Assuming all devices are ideal devices and circuit losses are neglected, the basic equation of VIENNA rectifier can be listed as follows:

$$\begin{cases} L \frac{di_a}{dt} = u_a - Ri_a - u_{aN} \\ L \frac{di_b}{dt} = u_b - Ri_b - u_{BN} \\ L \frac{di_c}{dt} = u_c - Ri_c - u_{cN} \end{cases} \quad (1)$$

$$\begin{cases} u_a = U_m \cos(\omega_0 t) \\ u_b = U_m \cos(\omega_0 t - 120^\circ) \\ u_c = U_m \cos(\omega_0 t + 120^\circ) \end{cases} \quad (2)$$

where  $u_a, u_b, u_c$  are input voltage;  $u_m$  is voltage amplitude;  $\omega_0$  is power frequency;  $i_a, i_b, i_c$  are the inductance current;  $L_a = L_b = L_c = L$  are inductance value;  $R$  is the equivalent resistance;  $u_{aN}, u_{BN}, u_{cN}$  are voltage between bridge arm and neutral point  $N$ .

Switch function of the converter is listed as

$$\begin{cases} S_{a,b,c} = 1 & \text{turn off} \\ S_{a,b,c} = 0 & \text{turn on} \end{cases} \quad (3)$$

The expression of bidirectional switch voltages can be obtained as follows:

$$\begin{cases} u_{aM} = u_o / 2 \operatorname{sgn}(i_a) S_a \\ u_{bM} = u_o / 2 \operatorname{sgn}(i_b) S_b \\ u_{cM} = u_o / 2 \operatorname{sgn}(i_c) S_c \end{cases} \quad (4)$$

where  $u_{c1}, u_{c2}$  are output capacitor voltage;  $u_o = u_{c1} + u_{c2}$  is the output voltage, and  $\Delta u = u_{c1} - u_{c2}$  is differential voltage between  $C_1$  and  $C_2$ .

Assuming  $C_1 = C_2 = C$ , the basic equation can be listed as follows:

$$\begin{cases} C^{\frac{du_{c1}}{dt}} = i_p - u_o / R_L \\ C^{\frac{du_{c2}}{dt}} = i_n - u_o / R_L \end{cases} \quad (5)$$

Small signal disturbance is imposed on VIENNA rectifier as follows:

$$\begin{cases} \langle i_j \rangle = I_j + i_j \\ \langle u_j \rangle = U_j + u_j \\ \langle u_o \rangle = U_o + u_o \\ d'_j = D'_j + d'_j \quad j = a, b, c \\ \langle \Delta u_o \rangle = \Delta U_o + \Delta u_o \\ \Delta d_o = \Delta D_o + \Delta d_o \end{cases} \quad (6)$$

According to the above formula, the small-signal model of VIENNA rectifier is shown in Fig. 4.

## 4.2 Controller Design of VIENNA Rectifier

VIENNA rectifier usually uses double ramp comparison, which is called DRC-SPWM (double ramp comparison) method. In [9], it is pointed out that injecting third harmonic into the modulation wave can reduce THD. DRC-SPWM control block diagram after third harmonic injection is shown in Fig. 5, where  $K_I(s)$  controls the inductor current in phase with the input voltage, while the output voltage controller  $K_V(s)$  controls the output voltage to maintain a constant value.

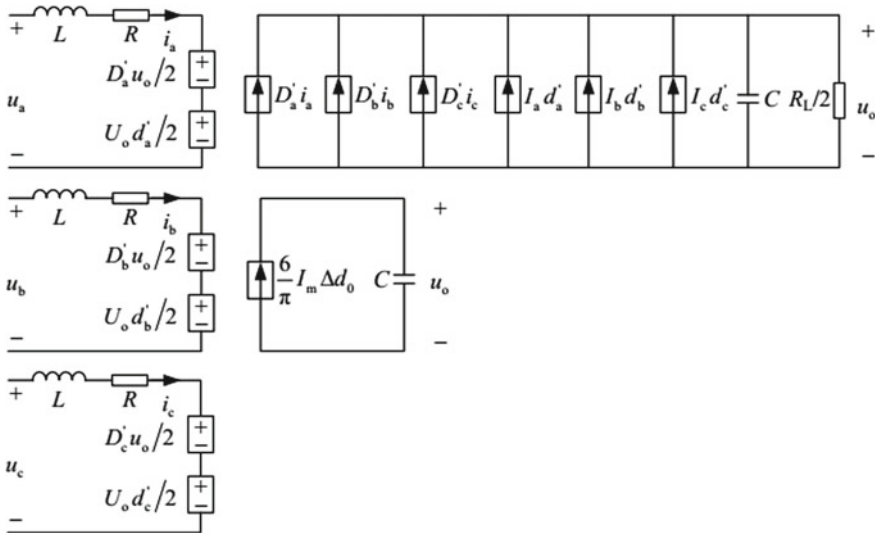
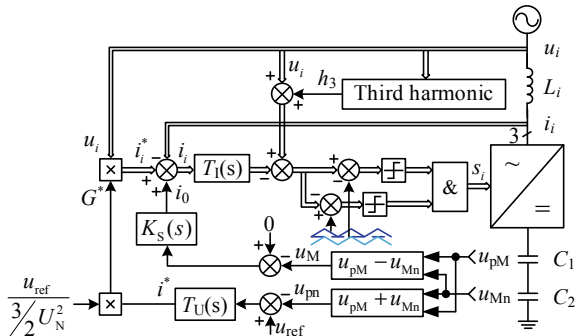


**Fig. 4** Small-signal model of VIENNA rectifier

**Fig. 5** DRC-SPWM control block diagram of VIENNA rectifier



PI controller is used for voltage and current controller of the VIENNA rectifier which is shown as follows:

$$\begin{cases} T_I(s) = k_{I\_p} + \frac{k_{I\_I}}{s} \\ T_U(s) = k_{U\_p} + \frac{k_{U\_I}}{s} \end{cases} \quad (7)$$

According to the principle of zero-pole compensation,  $k_{I\_p} = 12.6$ ,  $k_{I\_I} = 240$ ,  $k_{U\_p} = 4.2$ ,  $k_{U\_I} = 64$  can be obtained. And the compensated open-loop Bode diagram of the current controller and voltage controller are shown in Fig. 6.

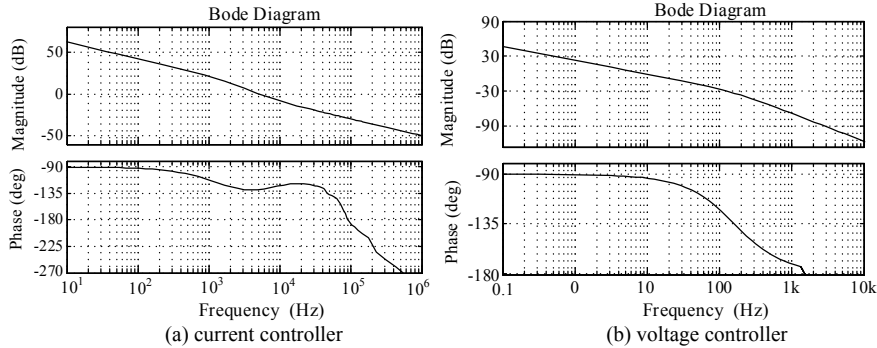


**Fig. 6** Compensated open-loop Bode diagram of the current and voltage controller

### 4.3 Controller Design of the DC-DC Converter

The average circuit model for converters can be described as follows:

$$v_{pc} = d/nv_{ac} - 2(L_r + L_{lk})f_s i^2/n^2 \quad (8)$$

$$i_a = d/n i_p - 2(L_r + L_{lk})f_s i_p^2/n^2 v_{ac} \quad (9)$$

According to (8 and 9), average circuit model can be obtained as follows.

According to Fig. 7, the open-loop transfer function of the peak current control mode DC-DC converter is obtained as follows:

$$G(s) = F_v(s)G_c(s)K_{vof} \frac{G_{od}(s)}{1 + F_i(s)G_{id}(s)} \quad (10)$$

where

$$G_{od}(s) = \frac{\hat{v}_o(s)}{\hat{d}(s)} = \frac{V_{in}/n}{LC_f s^2 + (C_f R_1 + L/R_2)s + R_1/R_2 + 1} \quad (11)$$

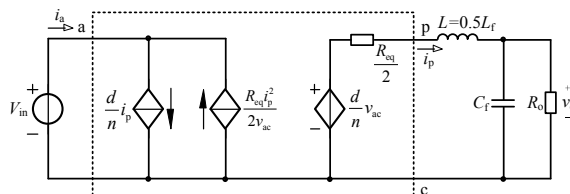


**Fig. 7** Average model of PS-FB ZVS PWM double current synchronous rectifier converter

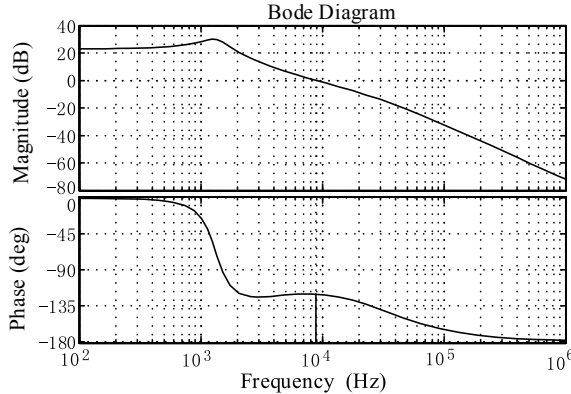


**Fig. 8** Compensated open-loop Bode diagram of the output voltage controller

$$G_{id}(s) = \frac{[LC_f s^2 + (C_f R_1 + L/R_2)s + 1]V_{in}/(nR_2)}{LC_f s^2 + (C_f R_1 + L/R_2)s + R_1/R_2 + 1} \quad (12)$$

PI controller is used for output voltage controller which is shown as follows:

$$T_V(s) = k_{V\_p} + \frac{k_{V\_I}}{s} \quad (13)$$

According to the principle of zero-pole compensation,  $k_{V\_p} = 2.2$ ,  $k_{V\_I} = 42$  can be obtained. And the compensated open-loop Bode diagram of the output voltage controller is shown in Fig. 8.

## 5 Experiment Results

The 1.5 kW prototype is built in which the frequency of VIENNA rectifier and DC/DC converter is 50 kHz. Figure 9 shows the input current waveform and the power quality of the input current. It can be seen that the phase difference of the current meets the results of theoretical analysis and the THD of the input current is 4.71%, less than 5%.

Figure 10 shows the output current waveform and the efficiency of the converter. It can be seen that the efficiency of the converter is greater than 93% in full load range. And maximum efficiency is higher than 95.5%.

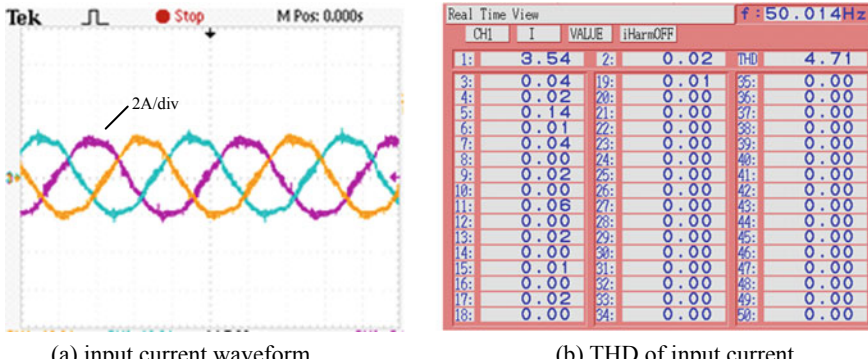


Fig. 9 Waveforms of input current

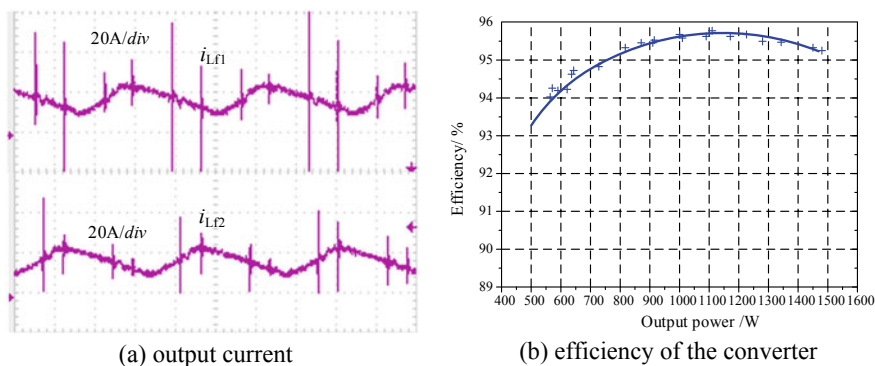


Fig. 10 Output current and efficiency of the converter

## 6 Conclusion

Through theoretical analysis and experiments, the charging converter with the presented circuit topology and control method has some advantages: (1) The VIENNA rectifier with the third harmonic injection DRC-SPWM control method can decrease the input current THD less than 5%. (2) The improved PS-FB ZVS PWM double current synchronous rectifier converter can improve the output current capability. (3) With the VIENNA rectifier and improved DC-DC converter which has peak current control mode, the efficiency of the converter is greater than 93% in full load range and maximum efficiency is higher than 95.5%.

## References

1. Razi R, Asaei B, Nikzad MR (2017) A new battery charger for plug-in hybrid electric vehicle application using back to back converter in a utility connected micro-grid. In: IEEE Power Electronics, Drive Systems & Technologies Conference (PEDSTC), Mashhad, Iran, pp 13–18
2. Kamble AS, Swami PS (2018) On-board integrated charger for electric vehicle based on split three phase induction motor. In: IEEE International Conference on Emerging Trends and Innovations In Engineering and Technological Research (ICETIETR), Ernakulam, India, pp 1–5
3. Sidorov VE, Zharkov ME, Korobkov DV, Balagurov MV, Volkov AG (2017) Applying the estimation system for synchronization of thyristor rectifier operating from the permanent magnet synchronous machine. In: International conference of young specialists on micro/nanotechnologies and Electron Devices (EDM), Erlagol, Russia, pp 579–583
4. Tahiri FE, Chikh K, El Afia A, Lamterkati J, Khafallah M (2017) Simulation and experimental validation of VOC and hysteresis control strategies of unit power factor three-phase PWM rectifier. In: IEEE International Conference on Electrical and Information Technologies (ICEIT), Rabat, Morocco, pp 1–6
5. Afsharian J, Xu DD, Wu B, Gong B, Yang Z (2017) Improved eight-segment PWM scheme with non-equally distributed zero-vector intervals for a three-phase isolated buck matrix-type rectifier. In: IEEE Energy Conversion Congress and Exposition (ECCE), USA, pp 3415–3419
6. Saleh SA, Onge XFS, McGivney XM, McLeod JD (2017) A new multi-level AC-DC power electronic converter for applications in PMG-based WECSs. In: IEEE industrial and Commercial Power Systems technical conference (I&CPS), Canada, pp 1–9
7. Chiranjeevi S, Patnaik S, Singh VP (2018) Partial soft switched DC-DC converter with constant voltage control. In: IEEE transportation electrification conference and expo, Asia-Pacific (ITEC Asia-Pacific), Bangkok, Thailand, pp 1–5
8. Li H, Chen S, Fang J, Tang Y (2018) Synchronous rectification-based phase shift keying communication for wireless power transfer systems. In: IEEE Southern Power Electronics Conference (SPEC), Singapore, pp 1–4
9. Kolar JW, Drolenik U, Minibock J, Ertl H (2000) A new concept for minimizing high-frequency common-mode EMI of three-phase PWM rectifier systems keeping high utilization of the output voltage. In: IEEE Applied Power Electronics Conference and Exposition (APEC), USA, pp 519–527

# Analysis and Suppression of Bearing Electric Erosion in the Metro Traction Motors



Erle Yang<sup>ID</sup>, Ruifang Liu<sup>ID</sup>, Qincong Zhao<sup>ID</sup> and Zhiwei Zheng

**Abstract** The pulse-width modulation (PWM) inverter variable voltage variable frequency speed control systems are widely applied to the modern subway vehicles. The bearing electrical corrosion problems due to the variable frequency power supply have caused serious dangers to the subway operation. In this paper, the bearing current problem of Beijing Metro Line 10 traction motors was analyzed. The common mode equivalent circuit of the motor bearing current was established, and the influence of the ground resistance on bearing current was analyzed. The simulation results showed that the poor earthen condition of motor frame is the reason for the bearing electric erosion. Finally, the new bearing current suppression method was proposed. The appropriate stator ground resistance of the traction motor was determined by the shaft ground resistance and the motor stray capacitances, which could eliminate the bearing current.

**Keywords** Traction motor · Bearing current · Stray capacitance · Ground resistance

## 1 Introduction

With the improvement of the power electronic devices and the development of motor control strategies, the new subways and high-speed trains use the vector controlled high-frequency insulated gate bipolar transistor (IGBT) variable frequency variable voltage asynchronous traction speed regulation system. Due to the PWM inverter power supply, there is a common mode voltage to ground at the neutral point of the

---

E. Yang · R. Liu (✉) · Q. Zhao

School of Electrical Engineering, Beijing Jiaotong University,  
Haidian, Beijing 100044, China  
e-mail: [rliu@bjtu.edu.cn](mailto:rliu@bjtu.edu.cn)

Z. Zheng

Beijing Urban Construction Design & Developement Group Co. Limited,  
Beijing 100037, China

inverter which outputs three-phase voltage [1, 2]. Under the action of the stray capacitance coupling of the motor, there is the bearing voltage appeared between the inner and outer rings of the bearing [3]. There is an oil film between the bearing raceway and the balls. The thickness of the bearing oil film varies with the motor speed, oil film temperature and the type of grease [4]. When the bearing voltage exceeds the bearing oil film threshold voltage, it will break down the oil film and generate the discharge bearing current. Then, there is a large amount of heat releasing in a short period of time, which will cause different degrees of damage to the inner and outer raceways of the bearings, as well as the balls or rollers. This damage is different from the normal mechanical abrasions. The electrochemical corrosion of the discharge current to the bearing surface will increase the vibration and noise of the motor and threaten the reliability of the motor operation. People gradually discover the problem of bearing corrosion under variable frequency power supply on the subway and railway running lines. Many scholars have done a lot of researches on the harm of the common mode voltage, such as the relationship among the common mode voltage, bearing current and bearing erosion [5], the calculation of the high-frequency coupling parameters in the motor [6], the generation mechanism [7], suppression measures of the internal circulation bearing current of the motor [8] and the time-frequency characteristics of common current [9]. However, the analysis on the bearing current mainly are based on the ideal circuit model, that is, the motor frame is well grounded, as well as it is an open-circuit state between the shaft and the ground, ignoring the influence of the ground impedances on the bearing current. Thus, it still lacks in-depth study of the influence of the ground impedance on the bearing current.

In this paper, the bearing electric erosion of the traction motor of DKZ15 on the Beijing Metro Line 10 was analyzed. First, the traction motor bearing current generation mechanism was researched and the equivalent circuit was established. Then, the effect of ground resistance on the bearing currents was studied by MATLAB. Finally, the bearing current suppression was proposed.

## 2 Bearing Current Model of the Traction Motor

### 2.1 Common Voltage

The AC traction motor of the DKZ15 traction system is powered by the three-phase IGBT inverter. There exists the common voltage in the output voltage of the inverter. When the inverter adopts the two-level pulse-width modulation mode, the switching tube (IGBT) of the upper and lower bridge arms of the inverter is combined to turn on and off, and the inverter outputs a series of pulse voltage with the equal values and unequal widths. And the common mode voltage  $V_{com}$  is the average of these pulse voltages described by the following formula:

$$V_{\text{com}} = \frac{V_a + V_b + V_c}{3} \quad (1)$$

where  $V_a$ ,  $V_b$ ,  $V_c$  are the output phase voltages of the inverter.

Due to the three-phase voltage asymmetry, there exists a common mode voltage which is not zero. Thus, the common mode voltage is a series of step waves with four levels and the frequency of carrier frequency. The common mode voltage generated by the system of the real variable frequency drive motor superimposes the sinusoidal voltage at the midpoint of the DC bus. The common mode voltage is divided by the parasitic coupling capacitance in the motor to induce the bearing voltage on the motor shaft [3].

## 2.2 Stray Capacitances

There exist the coupling capacitances in the motor. It mainly includes three types of capacitances, the capacitance  $C_{wf}$  between the stator winding and the frame, the capacitance  $C_{wr}$  between the stator winding and the rotor, and the capacitance  $C_{rf}$  between the rotor and the frame. The stray capacitances at high frequencies provide a path for the common mode current generated by the common voltage. The stray capacitances can be acquired through the finite element calculation or the measurement [6, 10].

## 2.3 Bearing Equivalent Electrical Parameters

The equivalent bearing circuit consists of a capacitance  $C_b$  parallel with a resistance  $R_b$ . In the actual motor running state, there is an oil film between the bearing raceway and the balls among which consist of the equivalent capacitance of the bearing. For the bearing equivalent resistance, a rotating bearing resistance is not constant, whose magnitude is megohm level before oil film is breakdown and a few ohms after breakdown [11]. When the resistance is megohm level, it can be considered that the resistance branch is open. Thus, there is a switch in series with the breakdown resistance  $R_b$  and then in parallel with the capacitance  $C_b$ .

## 2.4 Ground Resistances

Ideally, the stator frame of the motor should be grounded. However, due to improper procession and installation, the stator frame is poorly grounded sometimes. Thus, there exists the ground resistance  $R_{fg}$  between the stator frame and the

ground. On the other hand, the shaft of the traction motor is connected to the gearbox, then to the ground via the axle box bearings which connect the wheels. There also exists a ground resistance  $R_{rg}$  between the shaft and the ground. The source of the bearing voltage is not only the voltage divider of the common mode voltage, but also related to the ratio of the stator frame to the ground resistance and the shaft to ground resistance.

## 2.5 Bearing Current Model

According to the above analysis, the equivalent circuit of the motor under the PWM inverter power supply operation is shown in Fig. 1, where  $R$  is the sum of the motor stator resistance and the cable line resistance per phase.  $L$  is the motor leakage inductance per phase, and  $R_{rg}$  is the ground resistance between the shaft to the ground.  $R_{fg}$  is the stator frame to the ground resistance. The cables connect the inverter and the motor.  $U_d$  is the DC bus voltage.  $V_{com}$  is the common voltage between the stator winding neutral point and the ground.  $V_b$  is the bearing voltage between the bearing inner and outer races.  $i_{com}$  is the common current, and  $i_b$  is the bearing current.

If the values of  $C_{wf}$ ,  $C_{wr}$ ,  $R_{fg}$  and  $R_{rg}$  do not meet the balance relationship, the common mode voltage induces the bearing voltage through parasitic couplings and then causes the bearing voltage. When the bearing voltage exceeds the threshold voltage of the lubricating oil film, the oil film will be broken down and the switch is closed. When the bearing voltage does not exceed the threshold voltage of the lubricating oil film, the oil film is integrated and the switch  $k$  is opened.

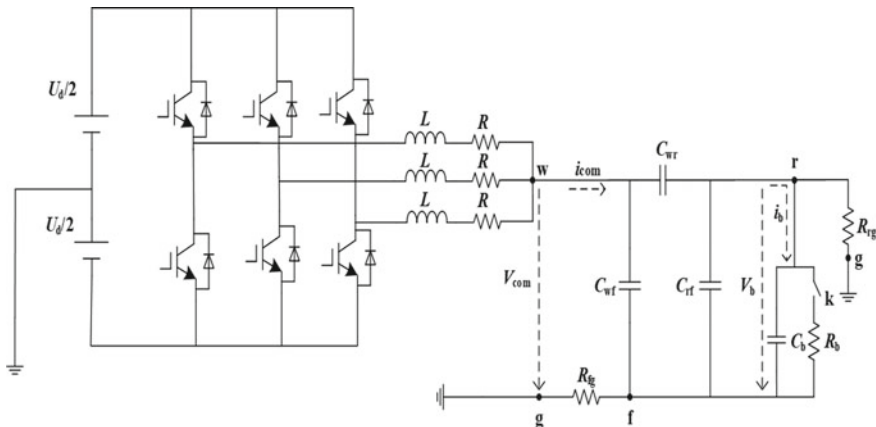


**Fig. 1** Bearing current model

### 3 Influence of Ground Resistances on Bearing Current

#### 3.1 Bearing Current Simulation Under Poor Grounding State

The traction motor of Beijing Metro Line 10 had noise and vibration during operation. When the fault bearings of the traction motors were extracted for disintegration, the bearing electrical corrosion was found. After analysis, it was found that the grounding connection of the stator frame was poor, and the simulation analysis of bearing current was in this state. The circuit of Fig. 1 was simulated with MATLAB. In the simulation circuit, the threshold voltage of the bearing oil film is set as 25 V. The main parameters in Fig. 1 were shown in Table 1, and the calculation results were shown in Fig. 2.

As shown in Fig. 2, the common mode voltage presents its own stepped waveform. Due to the three-phase voltage asymmetry, the common mode voltage is not zero. The voltage on the bearing is very high, which exceeds the threshold

**Table 1** Main parameters of the simulation circuit

Parameter	Value	Parameter	Value
DC voltage	750 V	$C_{wf}$	13835.2 pF
$R$	10 $\Omega$	$C_{wr}$	69.8 pF
$L$	9 $\mu\text{H}$	$C_{rf}$	648.0 pF
$R_{fg}$	1 M $\Omega$	$C_b$	140 pF
$R_{rg}$	20 $\Omega$	$R_b$	20 $\Omega$

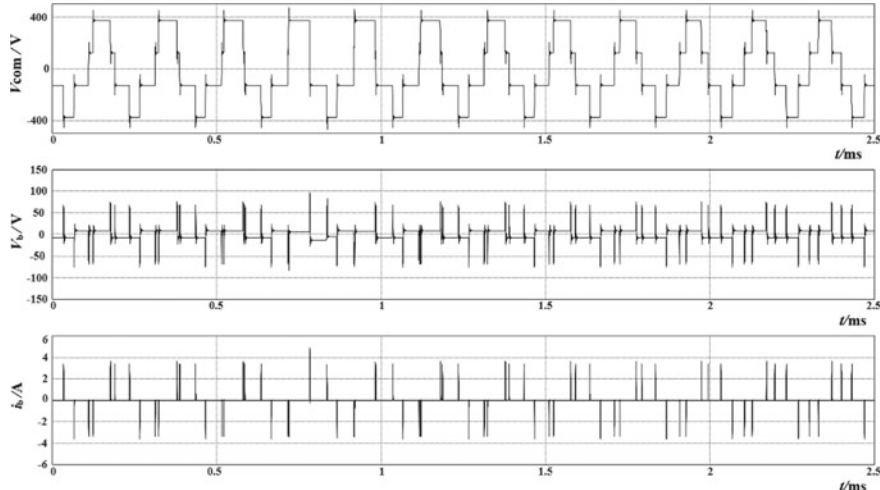


**Fig. 2** Waveforms of common mode voltage, bearing voltage and bearing current under bad earthen condition

voltage of the oil film, and there is the large discharge current, which reaches 4.81 A. On the one hand, the traction motor frame is poorly grounded, and the ground resistance  $R_{fg}$  is very large, which raises the electric potential of the motor frame. On the other hand, the rotating shaft is grounded through the gearbox and other parts. The resistance  $R_{rg}$  is small, pulling down the potential of the shaft. At very high bearing voltage, bearing current pulses also occur frequently, which constantly damage the bearing and endanger the safe operation. Thus, the bad earthen condition of motor frame is the reason for the bearing problem in the Line 10 traction motor.

### 3.2 Bearing Current Simulation with the Different Ground Resistances

To study the effect of the values of the stator ground resistance  $R_{fg}$  on the bearing current, the circuit of Fig. 1 was simulated with different  $R_{fg}$  by the MATLAB. Other parameters keep unchanged. The values of different stator ground resistances and corresponding values of bearing current are shown in Table 2.

It can be seen from Table 2 that there is a critical resistance in the simulation circuit that makes the bearing current zero. In this case, the critical resistance is  $0.1 \Omega$ . If the stator frame ground resistance is less than the critical resistance, the bearing current will increase with the stator frame ground resistance decreasing. When the stator frame ground resistance is greater than the critical resistance, the bearing current will increase with the stator frame ground resistance increasing. It is not that the smaller the stator frame ground resistance, the smaller the bearing current. The presence of stator frame ground resistance and shaft ground resistance affects the potential of the inner and outer rings of the bearing and then affects the bearing current. There is a relationship among the capacitance  $C_{wf}$ , the capacitance  $C_{wr}$ , the resistance  $R_{fg}$  and the resistance  $R_{rg}$  that affects the magnitude of the bearing current. Therefore, it is necessary to carefully analyze the bearing current equivalent circuit.

**Table 2** The values of bearing current  $i_b$  corresponding to different stator ground resistance  $R_{fg}$

$R_{fg} (\Omega)$	$i_b$	$R_{fg}$	$i_b$ (A)
0.001	0.185 mA	$100 \Omega$	2.445
0.01	0.168 mA	$1 \text{ k}\Omega$	2.979
0.1	0 A	$10 \text{ k}\Omega$	3.208
1	1.59 mA	$100 \text{ k}\Omega$	3.573
10	1.155 A	$1 \text{ M} \Omega$	4.814

## 4 Analysis and Suppression of Bearing Current

As shown in Table 2, there exists the critical stator frame ground resistance making the bearing current zero. Thus, the bearing current suppression of selecting the appropriate resistance is proposed. The selection of this resistance depends on the analysis of the bearing current equivalent circuit and determination of the relationship among the bearing current, the capacitance  $C_{wf}$ , the capacitance  $C_{wr}$ , the resistance  $R_{fg}$  and the resistance  $R_{rg}$ .

The circuit is shown in Fig. 3 after rearranging the circuit of Fig. 1. It is the typical Wheatstone bridge circuit by observing Fig. 3. According to the balance condition of the Wheatstone bridge circuit, the condition that the value of the bearing voltage is 0 V is

$$\begin{cases} |j\omega C_{wf}| |R_{fg}| = |j\omega C_{wr}| |R_{rg}| \\ \varphi_1 + \varphi_3 = \varphi_2 + \varphi_4 \end{cases} \quad (2)$$

where  $\omega$  is the angular frequency,  $\varphi_1$  is the impedance phase angle of  $C_{wf}$ ,  $\varphi_2$  is the impedance phase angle of  $C_{wr}$ ,  $\varphi_3$  is the impedance phase angle of  $R_{rg}$ , and  $\varphi_4$  is the impedance phase angle of  $R_{fg}$ .

$$R_{fg} = R_{rg} \frac{C_{wr}}{C_{wf}} \quad (3)$$

Put the data in Table 1 into (3), the critical resistance  $R_{fg}$  can be obtained, appropriately 0.1  $\Omega$ .

Good grounding is required from a security perspective. However, poor grounding not only brings insecurity but also causes serious bearing electrical corrosion. To eliminate the bearing current, the stator ground resistance  $R_{fg}$  should be selected according to (3). It means  $R_{fg}$  should be equal to  $R_{rg}$  multiplied by the

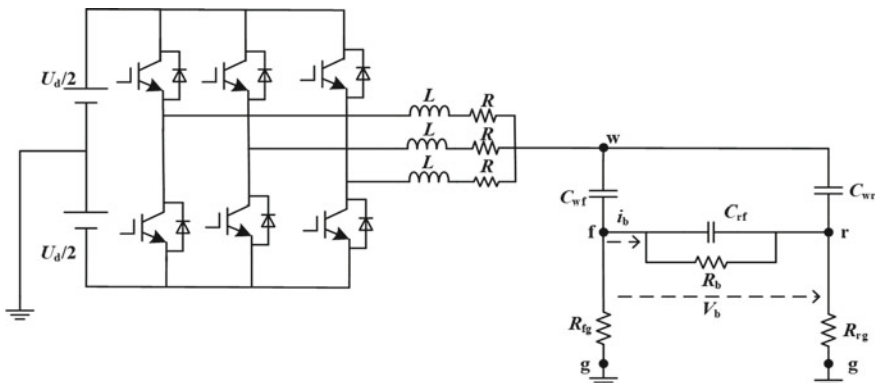


**Fig. 3** Rearranged circuit of Fig. 1

ratio of  $C_{wr}$  to  $C_{wf}$ , which is the so-called critical ground resistance. Under this condition, the bearing voltage and the bearing current could be zero. In general,  $C_{wr}$  is much smaller than  $C_{wf}$  in the induction motors. The ratio of  $C_{wr}$  to  $C_{rf}$  is 0.005 in this case, and then, the critical  $R_{fg}$  is quite small, namely 0.1 Ω.

## 5 Conclusion

This paper introduced the bearing current model of the traction motor and analyzed the reason for the traction motor bearing current of the Beijing subway, finding that the poor grounding of the stator leads to the serious bearing electrical corrosion. Theoretical derivation found the bearing voltage was not only the voltage divider of the common mode voltage, but also related to the ratio of the stator ground resistance and the shaft ground resistance. Based on the theoretical analysis, a bearing current suppression method was proposed to solve this problem. When the shaft is connected to the ground through the gearbox and the wheel, the shaft ground resistance  $R_{rg}$  is inevitably formed. If the stator ground resistance  $R_{fg}$  meets the critical resistance condition, which value equals to  $R_{rg}$  multiplied by the ratio of  $C_{wr}$  to  $C_{wf}$ , the bearing current could be eliminated.

**Acknowledgements** This work was supported by the National Natural Science Foundation of China under Grant 51777008.

## References

1. Chee S, Kim H, Ko S, Sul S (2015) Common-mode voltage reduction of three-level four-leg PWM converter. *IEEE Trans* 51(5):4006–4016
2. Arora TG, Renge MM, Aware MV (2017) Effects of switching frequency and motor speed on common mode voltage, common mode current and shaft voltage in PWM inverter-fed induction motors. In: 12th IEEE Conf Ind Electron Appl (ICIEA), Siem Reap 2017
3. Kalaiselvi J, Srinivas S (2015) Bearing currents and shaft voltage reduction in dual-inverter-fed open-end winding induction motor with reduced CMV PWM methods. *IEEE Trans Ind Electron* 62(1):144–152
4. Gattermann S, Kriese M, Poll G et al (2010) Capacitances and lubricant film thicknesses of motor bearings under different operating conditions. In: The XIX International Conference on Electrical Machines (ICEM), Roma 2010
5. Busse D, Erdman J, Kerkman RJ, Schlegel D, Skibinski G (1997) Bearing currents and their relationship to PWM drives. *IEEE Trans Power Electron* 12(2):243–252
6. Byrtus M, Hruska K, Kindl V et al (2016) Calculation of induction machine parasitic capacitances using finite element method. In: 11th International Conference on ELEKTRO, Strbske Pleso, High Tatras, Slovakia, 2016
7. Fan ZX, Shi Y, Yan GL et al (2016) Research of bearing voltage and bearing current in induction motor drive system. In: 7th Asia-Pacific International Symposium on Electromagnetic Compatibility (APEMC), Shenzhen, China, 2016

8. Wu WM, Jiang YM, Liu Y et al (2016) A new passive filter design method for overvoltage suppression and bearing currents mitigation in a long cable based PWM inverter-fed motor drive system. In: 8th IEEE International Power Electronics and Motion Control Conference (IPEMC-ECCE) Asia, Hefei, 2016
9. Cao SR, Huang XY, Niu F et al (2019) Time-frequency characteristics research of common mode current in PWM motor system. *IEEE Trans Power Electron* 35(2):1450–1458
10. Sang BQ (2016) Analysis and measurement of bearing current of variable frequency power supply AC motor. Master's thesis, Jiaotong University, Beijing (in Chinese)
11. Prashad H (1987) Effect of operating parameters on the threshold voltages and impedance response of non-insulated rolling element bearings under the action of electrical currents. *Wear* 117(2):223–240

# Hardware-in-the-Loop Real-Time Simulation Platform Design for Electric Rail Traction System



Zhen Zhao, Jialu Liu, Leiting Zhao and Weizhi Liu

**Abstract** Due to the complex structure, nonlinear and time-varying characteristics of the train traction drive system, the product development cycle is long and the design verification is difficult. In order to reduce the difficulty of development and debugging and improve the efficiency of product development, this paper designed a hardware-in-the-loop real-time simulation platform suitable for the simulation test of electric rail traction system, which based on HiGale hardware-in-the-loop (HIL) simulation platform. It provides a perfect software and hardware platform for product field verification, fault reproduction and regression test, and a convenient environment for product software and hardware pre-research and development.

**Keywords** Traction drive system · Real-time simulation · Hardware-in-the-loop · HiGale

## 1 Introduction

The traction system of the electric rail train has a complicated structure, which consists of pre-charging circuit, main circuit breaker, flat-wave reactor, traction converter, traction motor, brake resistance, ground detection circuit, backflow circuit, grounding circuit, pantograph and cable, etc., and has the characteristics of

---

Z. Zhao (✉) · L. Zhao · W. Liu

Locomotive & Car Research Institute, China Academy of Railway Sciences Corporation Limited, Haidian, Beijing, China  
e-mail: [zhaozhen@zemt.cn](mailto:zhaozhen@zemt.cn)

L. Zhao  
e-mail: [zhaoileiting@zemt.cn](mailto:zhaoileiting@zemt.cn)

W. Liu  
e-mail: [liuweizhi@zemt.cn](mailto:liuweizhi@zemt.cn)

Z. Zhao · J. Liu · L. Zhao · W. Liu  
Beijing Zongheng Electro-Mechanical Technology Co., Ltd., Haidian, Beijing, China  
e-mail: [liujiaolu@zemt.cn](mailto:liujiaolu@zemt.cn)

nonlinear and time-varying. So product development cycle is long, the system reliability requirements are high, especially including multiple high-power devices, and analysis and verification is very difficult [1–3]. In order to realize the design and verification of EMU TCU system level, real-time simulation technology, as a fast, safe and reliable technology, has been widely used in recent years. This technology greatly shortens the development cycle, reduces the design cost, improves the system reliability, and it is an indispensable auxiliary design verification method [4–6].

In order to realize the fast and reliable design and verification of traction drive system, we designed a hardware-in-the-loop real-time simulation platform based on HiGale simulator. In this paper, the overall system architecture, simulation model construction and system data acquisition and display will be carried out to establish a complete real-time simulation platform for traction drive system. Finally, the effectiveness of the designed simulation platform is proved by comparing the simulation results with the actual test waveform.

## 2 System Architecture

The real-time simulation system used HiGale, which is developed independently by Hengrun Technology. Aimed at the requirements of traction system test and characteristics research and development, the hardware-in-the-loop real-time simulation platform of traction drive system is developed based on the model (Fig. 1).

The real-time simulation system, including six HiGale real-time simulator, interface and real-time simulation software, can meet the real-time simulation processing and IO requirements of four models of EMU or urban rail at most. It is controlled by the experiment management system based on high-speed Ethernet. Data between each real-time simulator is synchronized by reflective memory.

## 3 Key Simulation Model Building

Real-time model is the core of semi-physical simulation. The hardware-in-the-loop simulation platform of traction drive system designed in this paper built the models of traction rectifier, traction inverter, traction motor, traction transformer, the dynamics of the body, wheel/rail, bow net flow, auxiliary system, the air brake system, network interface and network control logic and circuit. These models are built based on system generator, an open-source software of Xilinx. In this section, several key simulation models are researched and the simulation models are built by calculation.

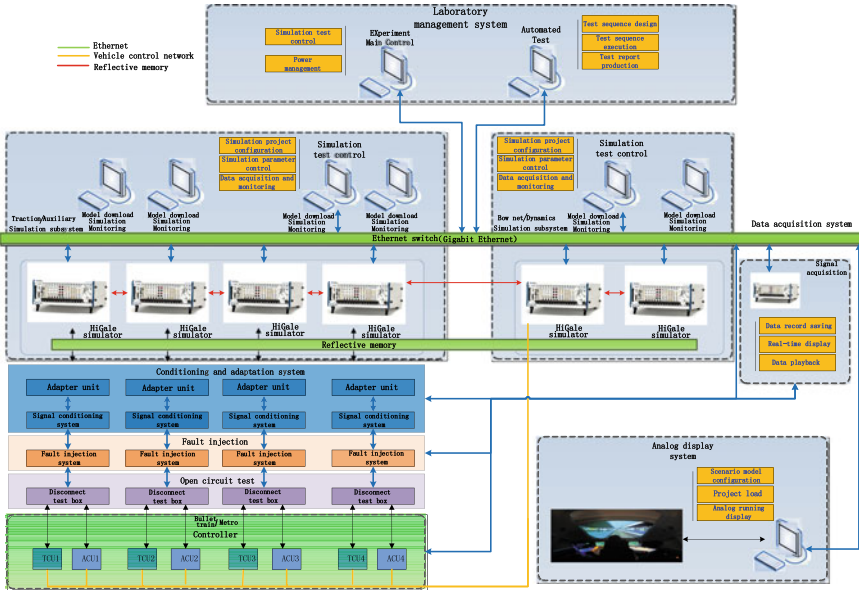


**Fig. 1** Traction system real-time simulation platform architecture

### 3.1 DC Link Model

DC link circuit is the converter intermediate link. The model simulates the DC link capacitor, LC secondary filter circuit, ground detection circuit, slow down resistance and overvoltage chopper circuit. Considering the stray inductance of capacitor, the circuit topology can be simplified into capacitor load, LC secondary filter and chopper circuit. The topology of chopped and DC link circuits is shown in Fig. 2.

The equation of capacitive load circuit is:

$$i_c = C \frac{dU_o}{dt} \quad (1)$$

$$I_c(s) = CsU_o(s)$$

The copper circuit judges whether  $g_{chop}$  is high when  $U_o$  is positive. If  $g_{chop}$  is high, the equal resistor is  $R_z$ . On the contrary, it is zero. When  $U_o$  is negative, the equal resistor is  $(R_z/R_d) + R_d$ .

For the models of LC quadratic filter and chopper circuit and other models, the same method can be used. The equation of LC secondary filter can be deduced as follows:

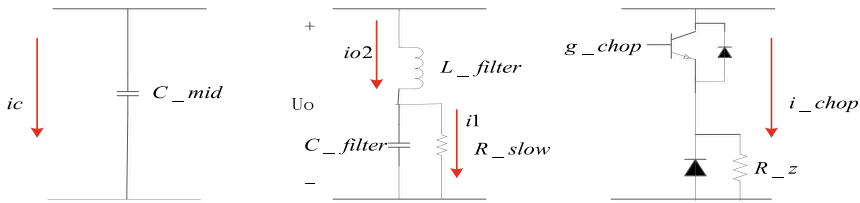


**Fig. 2** Topology of chopped and intermediate DC circuits

$$\begin{aligned}
 U_o &= L_{\text{filter}} \frac{di_{o2}}{dt} + R_{\text{slow}} i_1 \\
 i_{o2} &= i_1 + C_{\text{filter}} \frac{R_{\text{slow}} i_1}{dt} \\
 U_o(s) &= sL_{\text{filter}} I_{o2}(s) + R_{\text{slow}} I_1(s) \\
 I_{o2}(s) &= I_1(s) + sC_{\text{filter}} R_{\text{slow}} I_1(s)
 \end{aligned} \tag{2}$$

The model of LC secondary filter is built by discretizing the equation above.

### 3.2 Model of IGBT and DC-AC Converter

The half-bridge consisting of IGBT is the core and basic of converter circuit. It implements converter relying on IGBT switch. The model consists of IGBT semiconductor junction and internal side-by-side diode and simulates two-level IGBT half-bridge circuit. It is controlled by TCU signal by IO and feedback the trouble signal. The topology is shown in Fig. 3. This model can combine the models of rectifier and DC-AC converter.

g1-g6 are gate control signals of IGBT. These were usually controlled by 6-channel PWM wave of three phase. The three-phase output voltage is judged by the direction of three-phase current. Take VT1 and VT2 as examples, whose logical

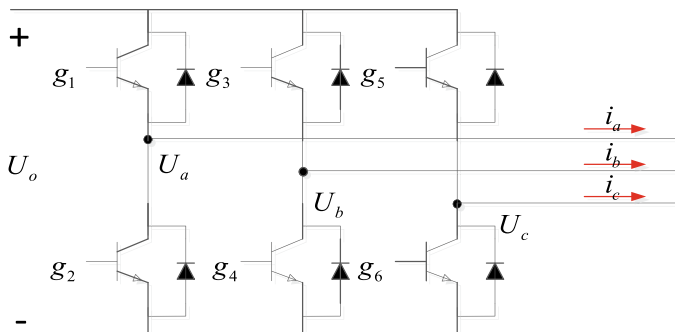


**Fig. 3** Topology of DC-AC converter

**Table 1** Influence of gate control signal and current direction on IGBT state

Direction of $ia$	$g1$	$g2$	State
+	1	0	VT1 turns on and VT2 turns off, $U_a = U_o$
+	0	1	VT1 turns off and VT2 turns on, $U_a = 0$
-	1	0	VT1 turns on and VT2 turns off, $U_a = U_o$
-	0	1	VT1 turns off and VT2 turns on, $U_a = 0$

relationship is shown in the table below; if the gate control signal is greater than the threshold, the conduction state is 1, otherwise it is 0 (Table 1).

The three line voltages  $U_{ab}$ ,  $U_{bc}$ ,  $U_{ca}$  have corresponding outputs by superimposed the output three-phase voltage.

### 3.3 Model of Traction Motor

Traction motor is an important part of the electric transmission system, and its electrical and mechanical characteristics are very important. Traction motor models are divided into stator flux solution model, rotor flux solution model, current solution model and electromagnetic torque solution model [7–9].

The stator flux linkage solution model is obtained by the voltage equation and flux linkage equation:

$$\begin{aligned}\psi_{s\alpha} &= \int (u_{sa} - R_1 i_{s\alpha}) dt \\ \psi_{s\beta} &= \int (u_{s\beta} - R_1 i_{s\beta}) dt\end{aligned}\quad (3)$$

The solution model of rotor flux is obtained by the voltage equation and flux equation:

$$\begin{aligned}0 &= P\psi_{r\alpha} + \omega_r \psi_{r\beta} + R_2 i_{r\alpha} \\ 0 &= P\psi_{r\beta} - \omega_r \psi_{r\alpha} + R_2 i_{r\beta}\end{aligned}\quad (4)$$

For the electromagnetic torque calculation module, it can be directly obtained from the torque equation of the motor equation:

$$T_e = n_p L_m (i_{s\beta} i_{r\alpha} - i_{s\alpha} i_{r\beta}) \quad (5)$$

The solution model of current is obtained by the flux model:

$$\begin{pmatrix} i_{s\alpha} \\ i_{s\beta} \\ i_{r\alpha} \\ i_{r\beta} \end{pmatrix} = \begin{pmatrix} \frac{L_r}{L_r L_s - L_m^2} & 0 & \frac{-L_m}{L_r L_s - L_m^2} & 0 \\ 0 & \frac{L_r}{L_r L_s - L_m^2} & 0 & \frac{-L_m}{L_r L_s - L_m^2} \\ \frac{-L_m}{L_r L_s - L_m^2} & 0 & \frac{L_s}{L_r L_s - L_m^2} & 0 \\ 0 & \frac{-L_m}{L_r L_s - L_m^2} & 0 & \frac{L_s}{L_r L_s - L_m^2} \end{pmatrix} \begin{pmatrix} \psi_{s\alpha} \\ \psi_{s\beta} \\ \psi_{r\alpha} \\ \psi_{r\beta} \end{pmatrix} \quad (6)$$

The above models are the mathematical models of traction motor. We build simulation model by discretizing the mathematical models.  $L_m$  is the mutual inductance between stator and rotor winding.  $L_s$ ,  $L_r$  are the self-inductance of two-phase stator and rotor.  $R_1$ ,  $R_2$  are the stator and rotor resistance.

## 4 Data Acquisition and Display

In order to perceive the information inside the simulation system in real time during debugging, a set of data acquisition and display system is designed (Fig. 4).

The data acquisition system is composed of chassis, discrete data acquisition board, analog data acquisition board, processor and digital data acquisition software. After the collected data is processed, it is uploaded to the test data display module through the bus for display, which is convenient for debugging personnel to observe.

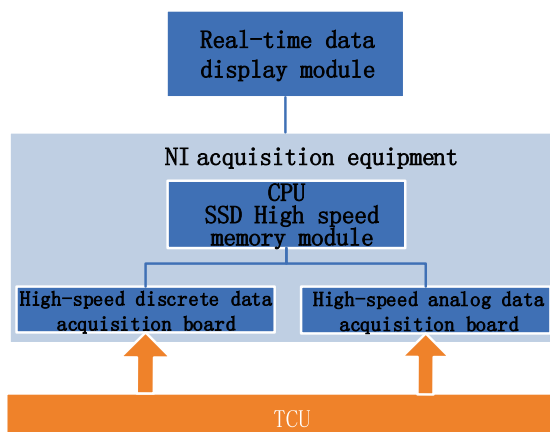


**Fig. 4** Data acquisition and display system

## 5 Simulation Verification

In order to verify the effectiveness of the hardware-in-the-loop real-time simulation system, this section compares the simulation results with the actual experimental results.

Figure 5 is the simulation and actual experimental waveform of traction characteristic curve scanning, Fig. 6 is the simulation and experimental waveform of running condition changing from traction state to braking state. It can be seen from the comparison that the real-time simulation platform of traction drive system designed can simulate the actual running state of traction system, which fully proves the effectiveness of the simulation platform designed.

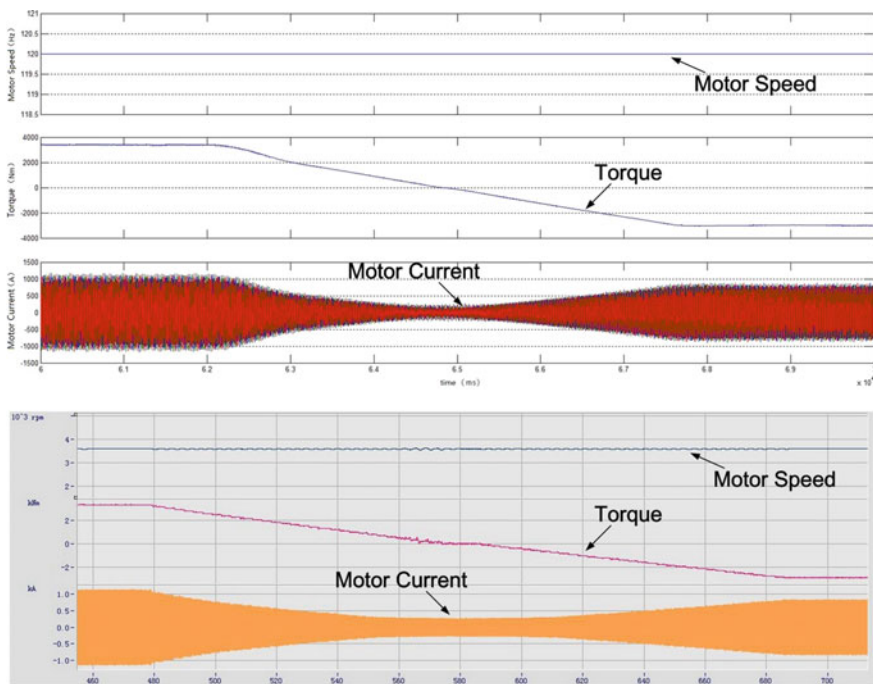


**Fig. 5** Traction characteristic curve scanning waveform

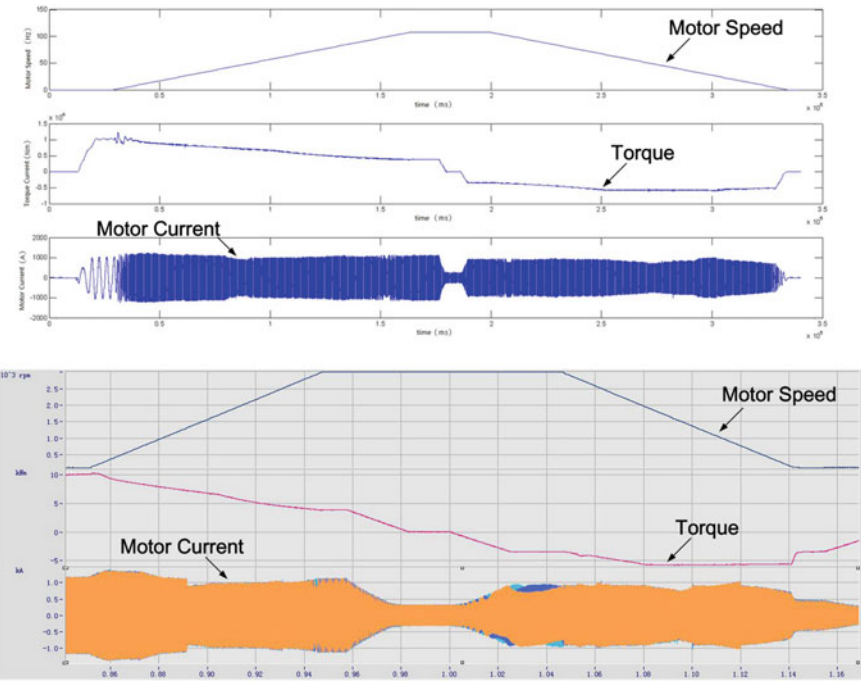


**Fig. 6** Traction—brake condition conversion waveform

## 6 Conclusion

This paper takes the traction drive system of trains as the research object. In order to reduce the development difficulty and improve the development efficiency, a set of real-time simulation system suitable for traction drive system simulation test of EMU and metro trains is designed. The overall architecture of system design, the establishment of key simulation model and the acquisition and display of system data are introduced in detail. The simulation results are compared with the actual experimental waveform, which proves the effectiveness of the designed simulation platform. This provides a good simulation test platform for the development and test of train traction drive system, greatly reducing the dependence of designers on the field test environment and fully reducing the test risk and debugging cycle.

**Acknowledgements** This work was supported by Foundation of China Academy of Railway Sciences (2017YJ012) and project 1751ZH1202.

## References

1. Wei Qin, Wei Zhang (2012) Industrial transformation and upgrading plan (2011–2015) series interpretation of the next gold mine of intelligent manufacturing equipment. *Equip Manuf* 6:52–55 (in Chinese)
2. Huili Zhen, Jianning Han, Rong Lian et al (2018) Research on semi-physical simulation model of train traction permanent magnet synchronous motor based on FPGA. *Modern Ind Econ Inf* 3:8 (in Chinese)
3. Tavana NR, Dinavahi V (2015) Real-time FPGA-based analytical space harmonic model of permanent magnet machines for hardware-in-the-loop simulation. *IEEE Trans Magnet* 51(8): 8106609
4. Song J, Gao X, Guo W et al (2016) Research on semi-physical simulation of CRH3 emu traction system. *Chinese High-tech Enterp* 6:13–14 (in Chinese)
5. Keller T, Wenk H, Scheiben E (1998) Hardware-in-the-loop simulation of rail-vehicles at Adtranz. The Eurosime, Espoo, Finland
6. Liu C, Guo X, Ma R et al (2018) A system-level FPGA-based hardware-in-the-loop test of high-speed train. *IEEE Trans Transport Electr* 4(4):912–921
7. Bose BK (2013) Modern power electronics and ac transmission. China Machinery Industry Press
8. Zhao L (2014) Research on key control technology and performance optimization of subway traction electric transmission system. Beijing Jiaotong University (in Chinese)
9. Diao L, Sun D, Dong K, Zhao LT, Liu ZG (2013) Optimized design of discrete traction induction motor model at low-switching frequency. *IEEE Trans Power Electron* 28(10): 4803–4810

# Control Strategy of Rail Transit High-Power Permanent Magnet Synchronous Motor and Verification of Semi-physical Platform



Zhenzhong Liang, Qubo Xie and Xuepu Li

**Abstract** Owing to its advantages of energy saving and emission reduction, the high-power permanent magnet synchronous motor (PMSM) has been widely used in the field of rail transit. Based on the operation characteristics of the PMSM, the control strategy is designed in the full-speed range. Based on the rotor magnetic field orientation model of the PMSM, a control algorithm based on the maximum torque/current ratio is proposed in the rated speed range, and a power angle control algorithm is employed above the rated speed. The correctness and effectiveness of the proposed control strategy of the PMSM are verified on HIGALE.

**Keywords** High-power permanent magnet synchronous motor · Power angle control · Maximum torque current ratio · Semi-physical simulation

## 1 Introduction

Compared with the asynchronous motor traction systems with high-performance controller widely used in the traditional rail transit field [1–4], the permanent magnet synchronous motor (PMSM) has higher efficiency and higher power density because there is no winding on the rotor and the loss is small. Therefore, adopting high-power PMSM as the power output is more suitable for the future traction drive system [5], and the research on the control technology of the high-power PMSM on the traction drive system is gradually put on the agenda.

The semi-physical simulation platform technology, as an effective means of train control system testing, is widely used by companies such as Bombardier, ABB and Zhuzhou Times with its flexibility and low cost. The platform is able to simulate the train vehicle and test environment, and the traction system can be tested online to verify the feasibility of the control scheme, saving R&D costs and improving speed and design accuracy. The permanent magnet system with the PMSM application as

---

Z. Liang (✉) · Q. Xie · X. Li  
CRRC Datong Co., Ltd., No. 1 Qianjin Street, Datong, Shanxi, China  
e-mail: [liangzhenzhong.dt@crccgc.cc](mailto:liangzhenzhong.dt@crccgc.cc)

the core has begun to attract extensive attention in the world and be gradually applied in the field of traction drive and power generation. It has huge development space, but the whole technology is still in the growth stage. Thus, it is extremely urgent to apply the semi-physical simulation technology to the PMSM drive system and establish an effective and credible comprehensive simulation design platform for permanent magnet electric drive system.

This paper proposes control architecture for the full-speed range of high-power PMSMs. According to different speed ranges, the MTPA control algorithm and the power angle control algorithm are adopted, and their feasibility and effectiveness are verified on the PMSM simulation platform based on HIGHELE.

## 2 High-Power PMSM Control Technology

### 2.1 MTPA Control Strategy

The motor adopts the MTPA control strategy in the rated speed to ensure that the motor can output the maximum torque under the given current condition. At the same time, in order to ensure the motor can work reliably under the voltage fluctuation condition, the excitation current is adjusted according to the bus voltage fluctuation. The current loop adopts a double closed-loop current control strategy to control the torque current  $i_q$  and the excitation current  $i_d$  by decoupling the current.

The torque of a PMSM is mainly composed of two parts. One part is the electromagnetic torque generated by the interaction of magnetic field of the permanent magnet and the motor current, and it plays a major role. The other part is reluctance torque generated by the interaction of magnetic field of motor stator current and the motor current. The reluctance torque is generated due to the asymmetry of the magnetic circuit of the motor, resulting from the sinusoidal SPWM modulation. When the electromagnetic torque of the motor is in the positive direction, the current vector of the motor  $i_s$  is located in the second quadrant of the  $d-q$  synchronous rotating coordinate system [6, 7], as shown in Fig. 1. According to the torque equation of the PMSM, when the value of the  $|i_s|$  remains unchanged, change the value of the  $\lambda$  and the electromagnetic torque of the motor will reach the maximum value at a specific position in the range of  $90^\circ \leq \lambda \leq 135^\circ$ . On the other hand, when the electromagnetic torque is negative, which means that the motor runs in the brake condition, the MTPA principle is the same.

Torque equation of PMSM is described as follows:

$$T_e = \frac{3}{2} p \psi_f i_s \sin \lambda + \frac{3}{4} p (L_d - L_q) i_s^2 \sin 2\lambda \quad (1)$$

In order to force the motor to always operate in the MTPA state, the key is to achieve a maximum torque-to-current ratio. This control strategy essentially seeks

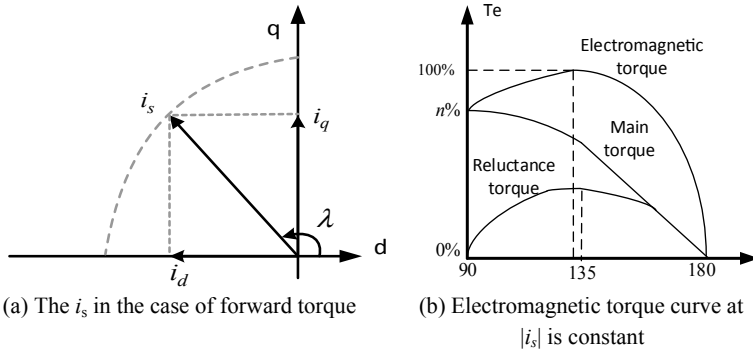


**Fig. 1** PMSM current vector and electromagnetic torque

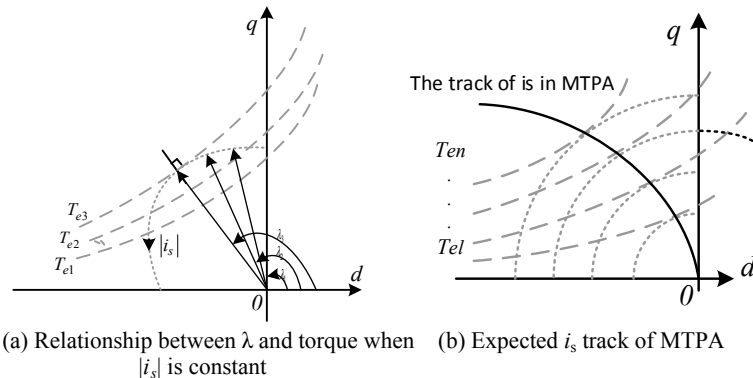


**Fig. 2** Current vector and MTPA principle

to the optimal allocation of  $i_s$ ,  $i_d$ ,  $i_q$  at any given torque [8]. As shown in Fig. 2a, when the given torque is positive, the value of  $|i_s|$  remains unchanged and different values of  $\lambda$  are taken; the intersection of the end point of  $i_s$  and the electromagnetic torque curve express the current running state of the motor [9, 10]. If and only if the  $i_s$  vector and the motor torque curve are perpendicular and the foot is the  $i_s$  end point, that is, the circle where the  $i_s$  vector track is located and the torque curve of the motor is tangent, then the motor electromagnetic torque reaches the maximum and the PMSM runs in the state of MTPA, and there is  $di_s/d\lambda = 0$  at this time. Figure 2 shows the stator current track of MTPA at different torques. It can be seen that as the torque increases,  $\lambda$  also increases. Therefore, if we want to run the PMSM in the MTPA state at any given torque, only control  $i_d$  and  $i_q$  so that the end track of  $i_s$  follows the expected MTPA curve.

## 2.2 Power Angle Control Strategy

The power angle control strategy is adopted when the motor speed is above rated value, and the switching frequency of power module increases with the increase of speed. To reduce the switching loss of the device, the square wave control phase is entered. At this time, the voltage exerted by the inverter on the motor is uncontrollable. Only the excitation and torque of the motor can be adjusted by controlling the power angle of it. Then, the  $d$ -axis current of the motor is controlled, and the output of the PI regulator controls the power angle to control the PMSM above the fundamental frequency. The block diagram of the power angle control is shown in Fig. 3.

In order to verify the validity of the aforementioned hybrid pulse-width modulation strategy, we use HiGale hardware-in-the-loop simulation platform equipped with four FPGA boards to test it with a nanosecond simulation step size.

The main parameters of the traction inverter are set as follows: Rated input voltage is DC 1500 V, three-phase AC output voltage is 0–1130 V, and output frequency is 0–280 Hz. The main parameters of the traction motor are: rated power 180 kW, rated voltage 1000 V, rated current 116.4 A, pole number 8, rated torque 859.4 N m, rated frequency 133.3 Hz, and rated speed 2000 r/min.

## 3 Simulation Analysis

The low-speed physical simulation waveform is as follows, when the motor is running in the SPWM modulation state. The waveform is in turn the bus voltage, the motor line voltage, the motor two-phase current, the motor torque, and two pulses. It can be seen from the figures that the motor torque is relatively stable, the current sinusoidal is fine, the switching frequency of the switching tube is gradually reduced with the increase of the speed, and the maximum switching frequency is less than 1 kHz (Fig. 4).

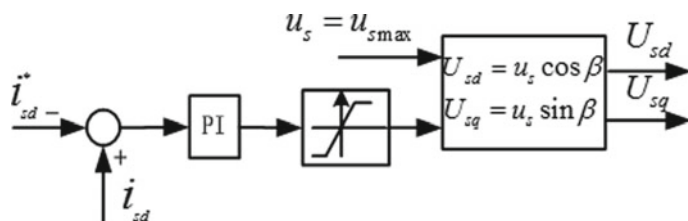


**Fig. 3** Power angle control strategy

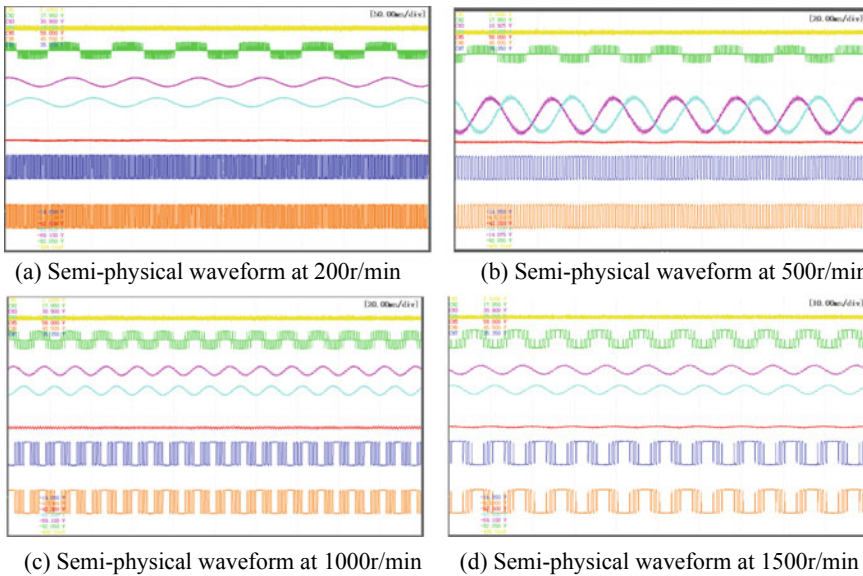


**Fig. 4** Simulation waveform at low speed

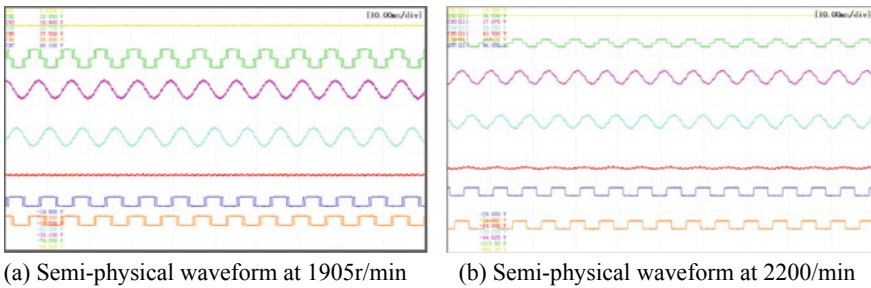


**Fig. 5** Simulation waveform near rated speed

When the motor runs near the rated speed, the waveform is as shown in Fig. 5. At 2200 r/min, the motor enters the square wave mode. Under the power angle control strategy, the motor torque can still achieve closed-loop tracking.

When the motor is running near the high speed, the waveform is as shown in Fig. 6. At 4000 r/min, the motor can still achieve closed-loop tracking under the power angle control strategy, but there are obvious fluctuations.

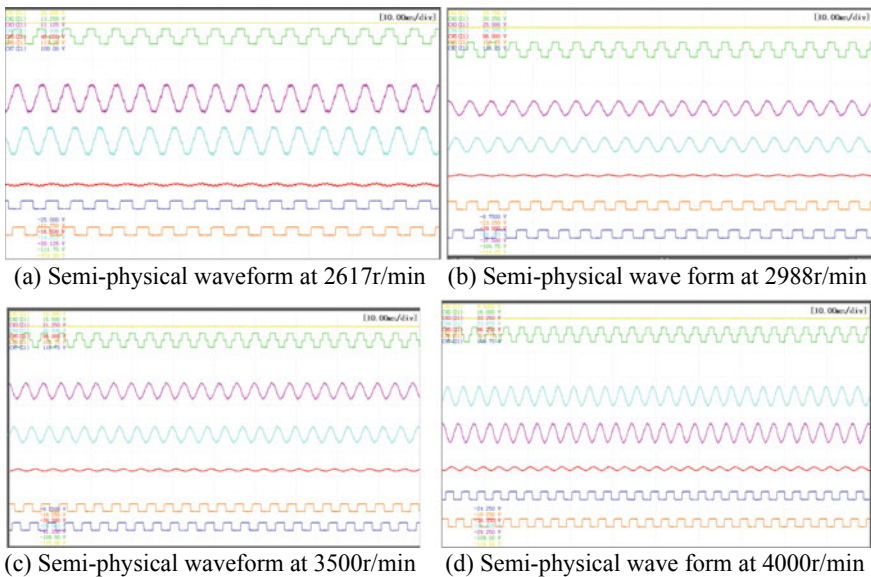


**Fig. 6** Simulation waveform at high speed

## 4 Conclusion

This paper designs a control strategy for high-power PMSM over the full-speed range. The semi-physical simulation of PMSM based on HIGALE shows that the control strategy of the high-power PMSM in the full-speed range obtained by the paper obtains the accurate tracking control of current torque, achieving a wide range of 0–4000 r/min speed.

## References

1. Diao L, Sun D, Dong K et al (2013) Optimized design of discrete traction induction motor model at low-switching frequency. *Trans Power Electron* 28(10):4803–4810
2. Diao L, Tang J, Loh PC et al (2018) An efficient DSP-FPGA-based implementation of hybrid PWM for electric rail traction induction motor control. *IEEE Trans Power Electron* 33(4): 3276–3288
3. Yin S, Huang Y, Xue Y et al (2019) Improved full-order adaptive observer for sensorless induction motor control in railway traction systems under low-switching frequency. *IEEE J Emerg Sel Top Power Electron*
4. Xue Y, Meng D, Yin S et al (2019) Vector-based model predictive hysteresis current control for asynchronous motor. *IEEE Trans Ind Electron* 66(11):8703–8712
5. Xue H, Xue H (2019) Design of permanent magnet synchronous motor speed control system. *Shandong Ind Technol* (08):178 (in Chinese)

6. Dianov A, Young-Kwan K, Sang-Jeon L et al (2008) Robust self-tuning MTPA algorithm for IPMSM drives
7. Li Y, Liu J (2011) Implementation of MTPA control for permanent magnet synchronous motor vector control system. *Electric Drive Autom* 33(4):9–11
8. Krishnan R (2012) Permanent magnet brushless motor and its driving technology. In: Chai F et al (eds) Mechanical Industry Press, Beijing, pp 23–28
9. Lin K (2014) Research on control method of permanent magnet motor under low switching frequency. Beijing Jiaotong University
10. Bao W (2015) Research on IPMSM control system based on maximum torque-to-current ratio. Wuhan University of Technology

# Research on PWM Modulation Strategy of High-Power Permanent Magnet Synchronous Traction System



Qubo Xie, Zhenzhong Liang and Wen Wang

**Abstract** For high-power permanent magnet synchronous traction system, the inverter generally uses high-voltage and high-current switching devices, and the switching frequency is low. Aiming at the problem of switching frequency limitation of high-power permanent magnet synchronous traction system, the segmentation modulation method is used to study the switching conditions between different modulation modes, and the smooth switching between asynchronous modulation SVPWM, synchronous modulation SHEPWM, and square wave is realized. The semi-physical simulation of permanent magnet synchronous motor verifies the correctness and effectiveness of the above modulation strategy.

**Keywords** High-power permanent magnet synchronous traction system · Segment modulation · Semi-physical simulation

## 1 Introduction

The permanent magnet synchronous traction system has been closely watched by the rail transit industry for its high efficiency and energy saving [1–3], which is the development direction of the traction system in the future. Therefore, it is necessary to study the control strategy of high-power permanent magnet synchronous motor (PMSM).

High-power permanent magnet synchronous traction systems generally use IGBTs as switching devices. High-power systems are subjected to switching losses and system heat dissipation [4]. The switching frequency of IGBTs is generally designed at hundreds of hertz. In practical applications, the carrier ratio of the PMSM has a wide range of variation, and a reasonable PWM modulation strategy must be adopted to meet the control requirements in different speed ranges [5]. The commonly used over-modulation strategy can improve the utilization of the bus

---

Q. Xie (✉) · Z. Liang · W. Wang  
CRRC Datong Co., Ltd., No. 1 Qianjin Street, Datong, Shanxi, China  
e-mail: [xiequbo.dt@crccgc.cc](mailto:xiequbo.dt@crccgc.cc)

voltage, and then, there are higher low-order harmonics. Besides, the intermediate  $60^\circ$  modulation strategy is easy to implement, but the motor torque ripple is large and is not suitable for the traction system. Therefore, this paper adopts the segmentation modulation strategy to meet the control requirements in different speed ranges. At low speed, the asynchronous modulation method is adopted to make full use of the switching frequency. After the speed increases, the carrier ratio gradually decreases, and synchronous SPWM is adopted to maintain the three-phase symmetry and harmonics which are suppressed. When the carrier ratio is further reduced, specific harmonic cancellation modulation is employed to reduce the performance impact of low harmonics on the high-power permanent magnet synchronous traction system. When the PMSM operates above the fundamental frequency, it adopts SHEPWM modulation to transition smoothly to the square wave phase.

## 2 Control Structure of High-Power PMSM Traction System

According to the traction motor torque control (traction/electric braking characteristic control) and idle, sliding control [4, 6, 7], under the condition of the uncertainty, the motor control instruction is drawn by collecting, analyzing and processing the information of motor speed, motor torque and so on. Then, the given motor torque  $T_e^*$  is sent to motor control system. This allows the train to operate close to the current maximum adhesion coefficient of the line, thereby obtaining the maximum adhesion utilization ratio while avoiding idling/sliding.

The control structure of PMSM is shown in Fig. 1. The high-power permanent magnet synchronous traction system adopts the control structure of the outer ring of torque, and the rotor position information  $\theta$  obtained by the rotating transformer and the motor speed or obtained by the differentiation of  $\theta$  serve as the feedback quantity of control. The reference torque is decomposed into reference torque current  $i_{sq}^*$  and reference excitation current  $i_{sd}^*$  by MTPA module. The current  $i_u$  and current  $i_v$  measured by the sensor are converted into current  $i_{s\alpha}$  and current  $i_{s\beta}$  through  $3s/2r$  transformation. Current  $i_{s\alpha}$  and current  $i_{s\beta}$  are converted into excitation current  $i_{sd}$  and torque current  $i_{sq}$  by  $2s/2r$  transformation. Reference torque current  $i_{sq}^*$ , feedback torque current  $i_{sq}$ , reference excitation current  $i_{sd}^*$  and feedback excitation current  $i_{sd}$  can get reference torque voltage  $U_{sq}$  and reference excitation voltage  $U_{sd}$  by double-PI decoupling control; then,  $U_{sq}$  and  $U_{sd}$  generate 6-channel PWM signal to control the three-phase inverter through the PWM generation part, thus driving the motor to run.

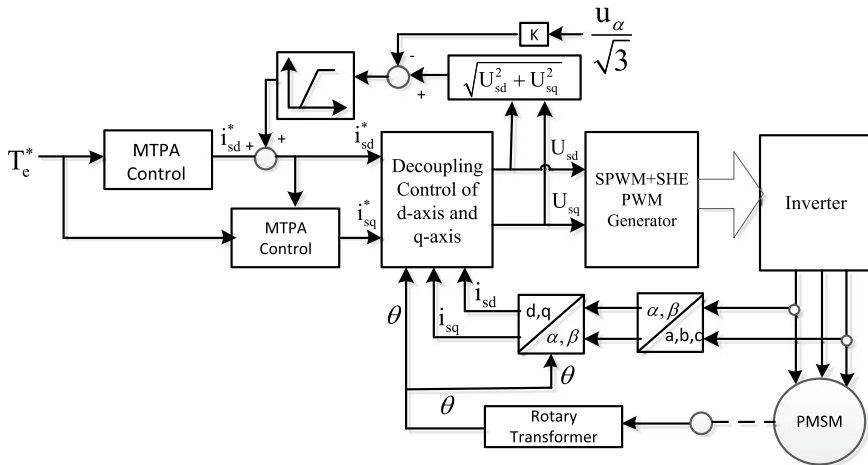


**Fig. 1** Diagram of high-power PMSM control system

### 3 Control Process of High-Power PMSM Traction System

#### 3.1 Segmented Pulse Modulation Strategy

Due to the low switching frequency of the high-power permanent magnet system, the system adopts the segmented PWM modulation mode [5], which is composed of asynchronous SPWM modulation, synchronous SHEPWM modulation and square wave modulation. As the motor speed increases, the PWM modulation pulse number is successively: asynchronous modulation → 9-pulse synchronous modulation → 7-pulse synchronous modulation → 3-pulse synchronous modulation → square wave modulation.

In low-speed startup phase, the use of asynchronous modulation strategy, in this case, the frequency of the modulation signal rise, carrier ratio decreased. When the carrier ratio is reduced to a certain extent, the problem of positive and negative half-cycle asymmetry caused by asynchronous modulation will no longer be able to be ignored, and the three-phase output symmetry will become worse, at which time the synchronous modulation mode needs to be transferred. When the modulated signal frequency reaches 87 Hz, the carrier is relatively low. In order to eliminate the adverse effects of the low harmonics, such as the 7th and 5th harmonics, and to accurately control the actual output fundamental wave voltage of PMSM, specific harmonic elimination modulation strategy is adopted. At the same time, when the modulated signal frequency reaches 133 Hz, the phase voltage driving pulse of the 3-pulse optimized synchronous SHEPWM modulation adopted by the system is close to the square wave pulse, so that the smooth transition from the specific harmonic elimination modulation to the square wave condition can be achieved.

In the traction and braking conditions, the relationship between switching frequency, modulation rate and output frequency is shown in Fig. 2a and b, respectively.

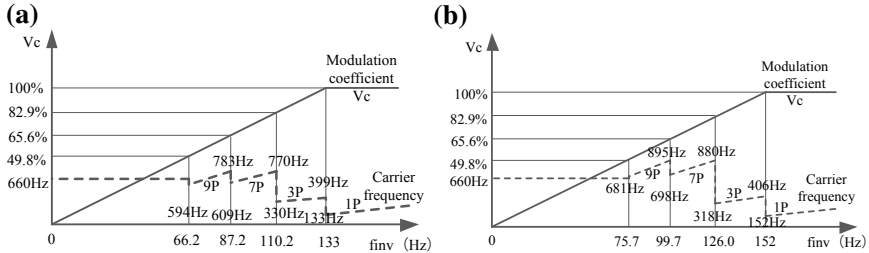


**Fig. 2** Relation during **a** traction and **b** braking

### 3.2 Selective Harmonics Elimination (SHE) Modulation Strategy

The selective harmonics elimination (SHE) modulation strategy can effectively eliminate some harmonics [7, 8]. The output voltage waveform acquired from the SHE modulation method has the characteristics of half period and quarter period symmetry. The following two figures show the typical output waveforms of SHEPWM method. In general, when  $N$  is odd, waveform in Fig. 3a is adopted, and when  $N$  is even, waveform in Fig. 3a is adopted. In Fig. 3b, the initial state of waveform is a low level, while in Fig. 3b is a high one.

Waveform in Fig. 3a, b can be uniformly expressed by Fourier series as,

$$u(\omega t) = \sum_{n=1}^{\infty} [a_n \cos(n\omega t) + b_n \sin(n\omega t)] \quad (1)$$

where  $a_n = \frac{1}{\pi} \int_0^{2\pi} U_0(t) \cos(n\omega t) d\omega t$  and  $b_n = \frac{1}{\pi} \int_0^{2\pi} U_0(t) \sin(n\omega t) d\omega t$ .

Because the fundamental wave from SHEPWM has axial symmetry at  $\pi/2 + k\pi$  and point symmetry at  $k\pi$ , the mathematical expressions are

$$\begin{aligned} u(\omega t) &= -u(\omega t + \pi) \\ u(\omega t) &= u(\pi - \omega t) \end{aligned} \quad (2)$$

Introduce  $a_n$ ,  $b_n$  into expressions above, let  $a_n = 0$ , when  $n$  is even;  $b_n = 0$ , when  $n$  is odd,

$$b_n = (-1)^N \frac{2U_d}{n\pi} \left[ 1 + 2 \sum_{k=1}^N (-1)^k \cos(n\alpha_k) \right] \quad (3)$$

where  $\alpha_k$  represents the  $k$ th of  $N$  switching angles in the interval  $[0, \pi/2]$  and  $n$  represents harmonic order.

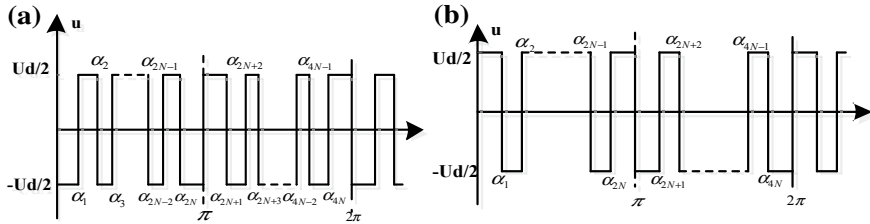


**Fig. 3** a SHEPWM when  $N$  is odd and b SHEPWM when  $N$  is even

For the three-phase symmetric system, when the number of harmonic order is integer multiples of three, the harmonic voltages will not generate harmonic current and will not affect the motor torque. Therefore,  $n = 6k \pm 1$  and SHE equations can be listed as follows, based on the mentioned above.

$$\begin{cases} U_{01} = b_1 = (-1)^N \frac{2U_d}{\pi} \left[ 1 + 2 \sum_{k=1}^N (-1)^k \cos(\alpha_k) \right] \\ b_n = (-1)^N \frac{2U_d}{n\pi} \left[ 1 + 2 \sum_{k=1}^N (-1)^k \cos(n\alpha_k) \right] = 0 \end{cases} \quad n = 6k \pm 1 \quad (4)$$

There are  $N$  variables in the elimination equations, namely  $\alpha_1, \alpha_2, \alpha_3, \dots, \alpha_v$ , setting the fundamental amplitude  $U_{01}$  to a specified value. The latter  $N - 1$  equations construct a mathematical model of a selective harmonic elimination technique in which  $N$  switching angles are used to eliminate  $N - 1$  selective harmonics in a quarter of a period. When  $N$  is odd, the maximum number of harmonics elimination  $n$  is  $3N - 2$ , that is, the  $N$  switching angles calculated can eliminate  $3N - 2$  harmonics at most. And when  $N$  is even,  $n$  is  $3N - 1$  at most.

Using the existing mathematical algorithm toolbox and functions in MATLAB, compose systematic transcendental equations solving software. With this software,  $N$  switching angles at different modulation ratios can be obtained. Moreover, the calculation results under different modulation ratios are shown in the figures below (Fig. 4).

## 4 Simulation Results

In order to verify the effectiveness and correctness of the proposed control strategy, this paper adopts HiGale hardware-in-the-loop simulation (HILS) platform for testing. The parameters set in the HILS system are basically the same as the actual conditions.

The waveforms of bus voltage, phase-to-phase motor voltage, two-phase motor current, motor torque and two channel pulse, when the motor speed rises from

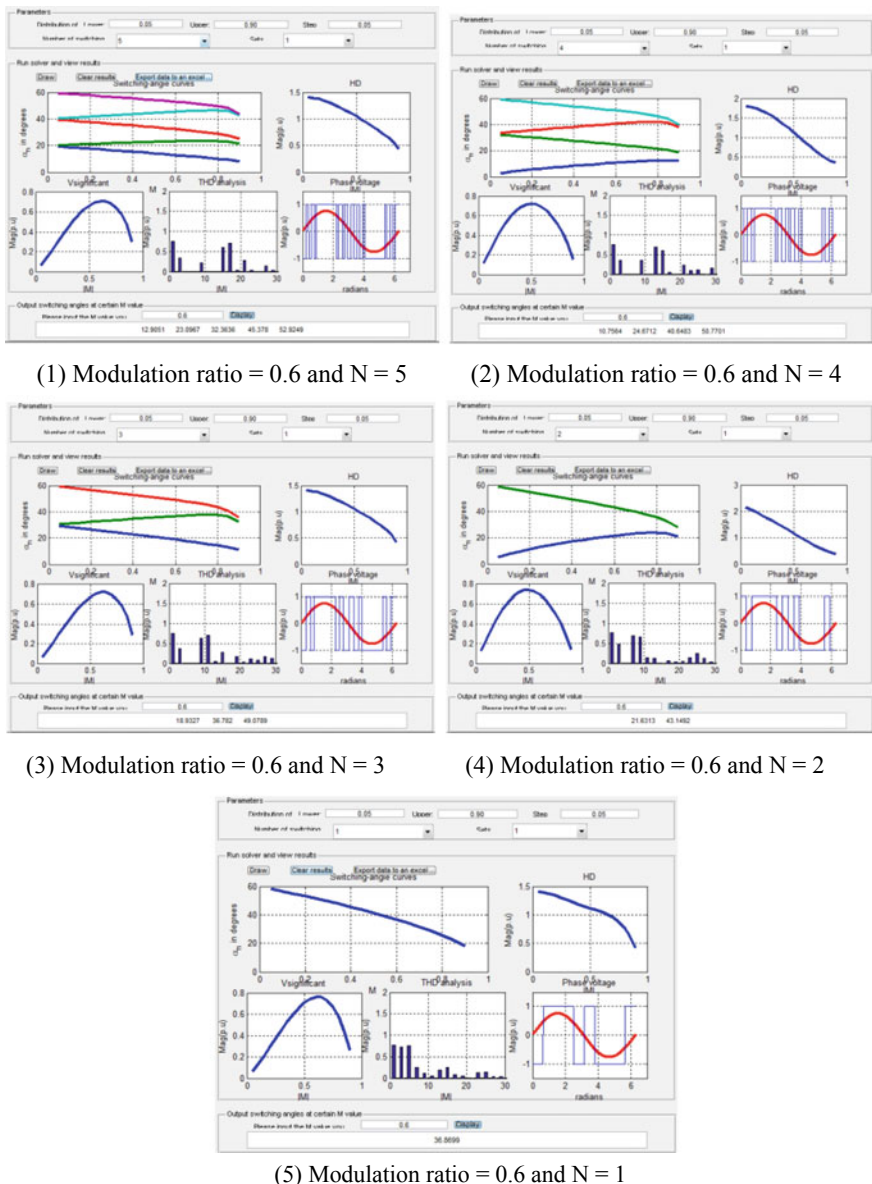
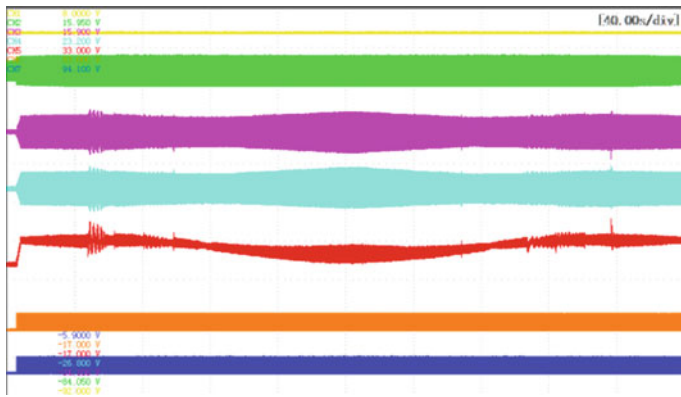


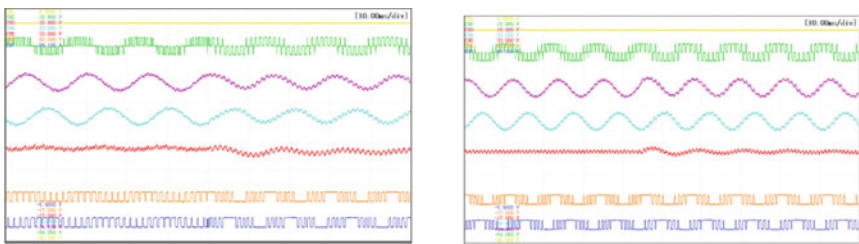
Fig. 4 Calculation results under different  $N$

200 r/min to 4000 r/min and then decreases to 200 r/min, are as follows, respectively (Fig. 5).

The waveforms of motor before and after each switching point under traction condition are shown as follows (Fig. 6).

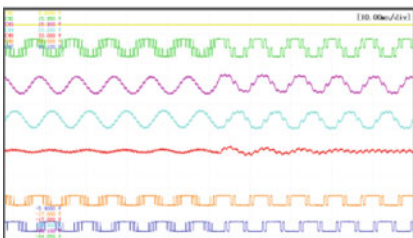


**Fig. 5** Waveforms during motor acceleration and deceleration

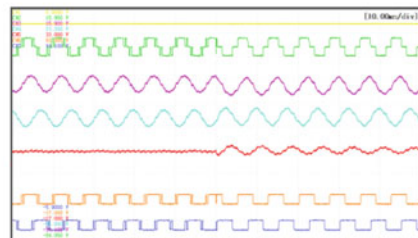


(a) AM to SM of 9 pulses

(b) SM of 9 pulses to AM of 7 pulses



(c) SM of 7 pulses to SM of 3 pulses



(d) SM of 3 pulses to square-wave modulation

**Fig. 6** State diagrams of motor under different modulation strategies (AM—asynchronous modulation; SM—synchronous modulation)

The HILS results show that, within the range of full speed, it has good output characteristics under various modes of modulation and achieves a smooth transition between the modes, with a small current impact before and after the switching point. Especially in the same mode, there is almost no current shock when switching between 7-pulse SHEPWM modulation and 5-pulse SHEPWM

modulation, or between 5-pulse SHEPWM modulation and 3-pulse SHEPWM modulation, and a natural smooth transition between 3-pulse SHEPWM modulation and square wave modulation is also realized.

## 5 Conclusion

Based on the analysis of existing modulation strategies, this paper proposes a hybrid pulse width modulation strategy. The results show that the proposed modulation strategy can achieve a smooth transition between different modes. When the stator current of the motor is stable relative to the switching point, the current transition is relatively stable, and it can operate reliably within the entire speed regulation range. The torque ripple of the motor is small, which is suitable for the permanent magnet synchronous traction system with high power and low switching frequency.

## References

1. Qingyuan C (2017) Modeling and simulation of permanent magnet traction system for urban rail transit. Chang'an University (in Chinese)
2. Bolognani S, Peretti L, Zigliotto M (2011) Online MTPA control strategy for DTC synchronous-reluctance-motor drives. *IEEE Trans Power Electron* 26(1):20–28
3. Sun T, Wang J, Chen X (2014) Maximum torque per ampere (MTPA) control for interior permanent magnet synchronous machine drives based on virtual signal injection. *IEEE Trans Power Electron* (99):1–11
4. Diao L, Sun D, Dong K et al (2013) Optimized design of discrete traction induction motor model at low-switching frequency. *Trans Power Electron* 28(10):4803–4810
5. Diao L, Tang J, Loh PC et al (2018) An efficient DSP-FPGA-based implementation of hybrid PWM for electric rail traction induction motor control. *IEEE Trans Power Electron* 33 (4):3276–3288
6. Shangkun Z, Jianhu Y, Kai Y (2017) Drive control system of embedded permanent magnet synchronous motor for electric vehicle based on improved maximum torque-current ratio control. *Electr Control Appl* 44(11):12–17
7. Jiafeng F, Zhuwei X, Hongcheng H (2015) Analysis of emergency traction function of autonomous 120 km/h subway train. *Mot Electr Drive* (5):69–71 (in Chinese)
8. Kezhen L (2014) Study on control method of permanent magnet motor under low switching frequency. Beijing Jiaotong University (in Chinese)

# Optimization Control of Energy-Efficient Driving for Trains in Urban Rail Transit Based on GA-PSO Algorithm



Lidan Zhao, Junqin Peng, Jiaxing Wang and Yonghua Zhou

**Abstract** In recent years, as the development of urban rail transit has effectively slowed down the congestion of urban traffic, more and more cities have focused on promoting the development of urban rail transit. But those trains of urban rail transit have also generated more and more energy consumption. In order to alleviate the energy shortage and promote energy conservation and emission reduction, it is of great significance to reduce the energy consumption of subway trains. The optimization control of energy-efficient driving is to reduce the energy consumption of trains when operating and improve the operation efficiency. The traditional particle swarm optimization algorithm is easy to fall into the local optimum and the global performance is not so good. In this paper, the genetic particle swarm optimization algorithm (GA-PSO) is used, combining the advantages of genetic algorithm and particle swarm algorithm, to optimize the energy consumption of trains. And MATLAB is used to carry out modeling and simulation analysis. Compared with the traditional particle swarm and genetic algorithm, the optimized algorithm is verified that it can effectively reduce the energy consumption of trains. The results show that the energy cost is reduced by 18.8%, which verifies the effectiveness of the developed algorithm.

**Keywords** Particle swarm algorithm · GA-PSO algorithm · Energy-efficient optimization

## 1 Introduction

In recent years, urban rail transit has developed rapidly, and energy-efficient and efficient urban rail transit control optimization has become an important research direction in the field of rail transit. Many domestic and foreign scholars have

---

L. Zhao (✉) · J. Peng · J. Wang · Y. Zhou

School of Electronic and Information Engineering, Beijing Jiaotong University,  
Beijing 100094, China

e-mail: [17120299@bjtu.edu.cn](mailto:17120299@bjtu.edu.cn)

conducted in-depth research on energy-saving control of rail transit. Energy-efficient problem was extensively explored using the maximum principle [1–4]. Genetic algorithm (GA) was used to calculate the coasting position during the process of train operation, in advance, to reduce energy consumption [5–7]. Wang and Hou [8] proposed a train control strategy considering uniform motion state and adopted an improved genetic annealing algorithm to solve the problem. Fan [9] studied the control strategy using ant colony algorithm about train running curves. Huang et al. [10] proposed to optimize the train running curve based on the algorithm of particle swarm optimization (PSO), so as to reduce energy consumption. These algorithms have their own advantages and disadvantages. For example, the global performance of GA is good, but the convergence rate is slow. Thus, the optimal control of train energy conservation needs to be studied further.

PSO algorithm is inspired by the behavior characteristics of the biological population and used to solve complex optimization problems. The individual diversity of particle population in the late iterations of traditional PSO algorithm is small, and after a certain number of iterations, globally optimal and locally optimal positions and particle positions are equal, which may lead to the situation of local optimality, and its global performance is poor. In this paper, the GA, having good global performance, and particle swarm algorithm are combined to make up for the shortcomings of particle swarm algorithm, so as to better solve the train running speed curve.

## 2 Energy-Efficient Control Problem of Trains

The energy-efficient problem of a single train is described and analyzed [1–4]. According to the train running state and Newton's second law, we can obtain the differential equations as follows.

$$\begin{cases} \frac{dv}{dx} = \frac{\mu_f f(v) - \mu_b b(v) - w_0(v) - g(x)}{v} \\ \frac{dt}{dx} = \frac{1}{v} \end{cases} \quad (1)$$

where  $f(v)$  is the maximum traction force at the corresponding speed  $v$ ,  $b(v)$  is the maximum braking force,  $w_0(v)$  represents the unit basic resistance of the train,  $g(x)$  represents the resistance along a rail line, and  $\mu_b$  and  $\mu_f$  are the braking and traction control variables, respectively.

In the actual train operation process, suppose the length of the train operation interval is  $S$ , the train starts from the origin, reaches the destination after time  $T_s$ , and the arrival speed is zero. Then, the boundary conditions should meet the following conditions:

$$\begin{cases} t(S) - t(0) = T_S \\ v(0) = v(s) = 0 \end{cases} \quad (2)$$

At the same time, the traction force and braking force must not exceed their maximum value, and the two forces cannot exist simultaneously. And according to the speed limit requirements along a rail line, there are the following constraints:

$$\begin{cases} \mu_b, \mu_f \in [0, 1] \\ \mu_f \cdot \mu_b = 0 \\ v(x) \leq V_{\max}(x) \end{cases} \quad (3)$$

According to the energy-efficient control scheme, the traction energy consumption of a train is:

$$\min : A = \frac{1}{\eta} \int_0^S \mu_f f(v) dx \quad (4)$$

where the coefficient  $1/\eta$  will change due to the different electromechanical efficiency of the transmission system of different rail vehicles, but it does not change with the control mode of a train. Thus, after simplifying the solution, the objective function can be expressed as:

$$\min : A = \int_0^S \mu_f f(v) dx \quad (5)$$

The Hamiltonian function is constructed according to the maximum principle, and the costate equation is solved, introducing the adjoint matrix of velocity:

$$\beta = \frac{\beta_2}{v} \quad (6)$$

According to the condition of maximum value of Hamiltonian function in the optimal curve, the relations between adjoint variables and several train control strategies are obtained in [1–4], as shown in Table 1.

**Table 1** Relations between adjoint variables and train manipulation strategies

Adjoint variables	Control variables	Corresponding working conditions
$\beta < 0$	$\mu_f = 0, \mu_b = 1$	MB (maximum braking)
$0 < \beta < 1$	$\mu_f = 0, \mu_b = 0$	C (cruising)
$\beta = 1$	$\mu_f \in [0, 1], \mu_b = 0$	PP (partial power)
$\beta > 1$	$\mu_f = 1, \mu_b = 0$	MP (maximum power)

The general energy-efficient manipulation strategy adopts the three-stage manipulation strategy of ‘MB-C-MP.’

### 3 Optimization Control of Energy-Efficient Driving for Trains Based on GA-PSO Algorithm

#### 3.1 Division Strategy of Inter-station Rail Line Intervals

According to different slope types and conversion conditions of different working conditions, the inter-station lines are divided into small areas to ensure there are the same line condition and the same speed limit in the same section. Meanwhile, the corresponding velocity of the interval is also divided into  $n$  parts. That can be represented as follows.

$$\begin{cases} X = \{X_1, X_2, \dots, X_{n-1}, X_n\} \\ V = \{V_1, V_2, \dots, V_{n-1}, V_n\} \end{cases} \quad (7)$$

where  $X$  is the set of distances of subintervals divided,  $V$  is the set of corresponding target velocity,  $X_i$  represents the distance of the  $i$ th subinterval,  $V_i$  represents the target velocity corresponding to the  $i$ th distance. Different target speed sequences correspond to different running strategies, and the corresponding energy consumption and time of duration are also different.

According to the strategy of inter-station rail line interval division, a set of velocity sequences with the lowest energy consumption and meeting the time requirements are solved by the optimization algorithm, which is the required target velocity curve.

#### 3.2 Basic PSO

PSO is a kind of parallel heuristic random search method. Compared with other intelligent algorithms, it has the advantages of simple calculation and strong global search ability. For the optimization curve of train energy conservation, according to the requirements of energy conservation operation strategy and comfort, the basic process of PSO [11] in the simulation is described as follows.

- (1) Population initialization. According to the rail line constraints, randomly generated  $n$  particles, and each particle location is a candidate solution to solve the problem. Generally, the number of particles is 20–40, and we choose 30 as the initial number.

- (2) The applicability function value of individuals in the particle swarm is calculated, and the minimum value is recorded as the local optimal value  $p_{\text{best}}$  of corresponding individuals and the global optimal value  $g_{\text{best}}$  in the overall comparison.
- (3) Update particle location and speed according to PSO, and judge whether the rail line constraint condition is satisfied to ensure that the population of particles is the feasible solution and the number is complete. The updating mode of velocity of each particle is expressed as:

$$V'_{im} = \omega V_{im} + c_1 \text{rand}() (P_{i,p_{\text{best}}} - X_{im}) + c_2 \text{rand}() (P_{g_{\text{best}}} - X_{im}) \quad (8)$$

where  $V_{im}$  is the velocity of the  $i$ th particle in the  $m$ th dimension,  $c_1$  and  $c_2$  are the parameters that regulate  $P_{i,p_{\text{best}}}$  and  $P_{g_{\text{best}}}$ , respectively, normally  $c_1$  is equal to  $c_2$  with the value of  $0 \sim 4$ .  $P_{i,p_{\text{best}}}$  is the optimal position that the  $i$ th particle has reached, and  $P_{g_{\text{best}}}$  is the optimal position that the whole particle swarm has reached.  $\omega$  is the inertia weight, which controls how much of the previous velocity is retained in each generation of particle velocity update, and usually takes the value among  $0.4 \sim 1.2$ .

The particle position update formula is:

$$X'_{im} = X_{im} + V'_{im} \quad (9)$$

- (4) Judge whether the iteration number requirements are met. If so, then output the results. If not, return to (3) and repeat the process until the end.

### 3.3 Genetic Algorithm-Particle Swarm Optimization (GA-PSO)

Although PSO has advantages like few parameters and simple calculation, premature convergence often occurs. However, the global performance of the GA is good, and the crossover mutation of chromosomes can increase the diversity of particles. Add the idea of crossover mutation in the GA into the PSO which can avoid the phenomenon of premature convergence into local optimality. The basic process of the GA-PSO in the simulation, which combines the advantages of PSO and GA, is represented as follows.

- (1) Population initialization. Randomly generate  $n$  particles and satisfy rail line constraints.
- (2) The applicability function value of individuals in the particle swarm is calculated, and the minimum value is recorded as the local optimal value  $p_{\text{best}}$  of corresponding individuals and the global optimal value  $g_{\text{best}}$  in the overall comparison.

- (3) The old population is retained, and particle locations and velocities are updated according to PSO Eqs. (9) and (10).
- (4) Update the inertia weight  $\omega$ . The parameter  $\omega$  of the fundamental particle swarm remains unchanged. However, when  $\omega$  is large, the local search ability is weak due to the strong global search ability, and when  $\omega$  is small, the local search ability is strong due to the weak global search ability. Therefore, the value of  $\omega$  is set as a function decreasing with time, and the expression is:

$$\omega = \omega \times \left(1 - \delta \frac{n}{N}\right) \quad (10)$$

where  $\delta$  is a constant coefficient,  $n$  is the current number of iterations, and  $N$  is the total number of iterations.

- (5) Reorder the particles by fitness. For half of the particles with poor fitness, the crossover operation of GA is carried out to generate new particles, and the elite retention strategy with parent particles is adopted to retain the half particles with high fitness. The crossover operation formulas of GA are as follows.

$$\begin{cases} \text{NewParticle}_1(x_i) = \alpha \text{OldParticle}_1(x_i) + (1 - \alpha) \text{OldParticle}_2(x_i) \\ \text{NewParticle}_2(x_i) = \alpha \text{OldParticle}_2(x_i) + (1 - \alpha) \text{OldParticle}_1(x_i) \end{cases} \quad (11)$$

where  $\alpha$  is a random number between [0, 1], usually set as 0.2.

- (6) Half of the particles with good fitness are implemented as elite reservation, and the particles with high fitness are selected to form a new population with the particles.
- (7) Judge whether the iteration number requirements are met. If so, then output the results. If not, return to (3) and repeat the process until the end.

### 3.4 Simulation and Results

The GA-PSO is used to simulate the energy-efficient problem in Beijing subway Yizhuang line and optimize the control according to the actual line data and actual train parameters. This paper mainly uses the proposed algorithm to optimize the inter-station line between Wanyuan street and Rongjingdong street and compares it with the basic PSO algorithm. The interval length is 1280 m, the planned running time is 103 s, and the train weight is 194 t. According to the speed limit and ramp curve from Wanyuan street to Rongjingdong street, the four-stage method is adopted to solve the target speed curve under the minimum running time, as shown in Fig. 1.

Target velocity curve and corresponding energy consumption are solved by two algorithms, respectively, as shown in Fig. 2. Figure 2a is the train target velocity curve solved by the basic PSO algorithm, and the energy consumption per unit

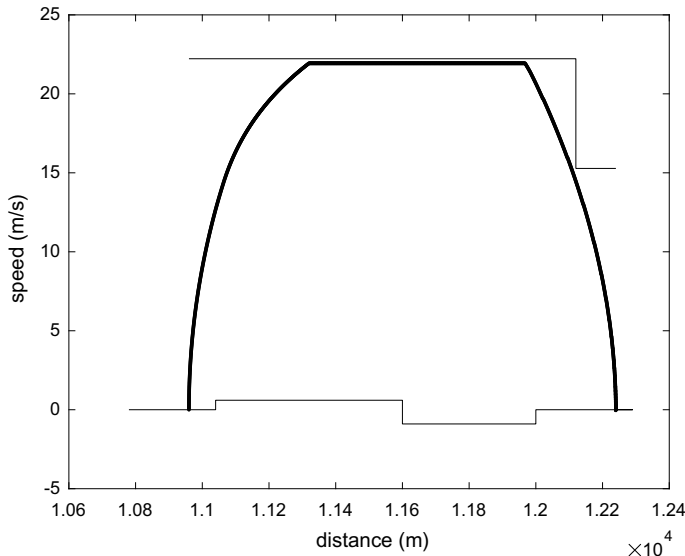


**Fig. 1** Speed limit and gradient information for Wanyuan Street—Rongjingdong Street

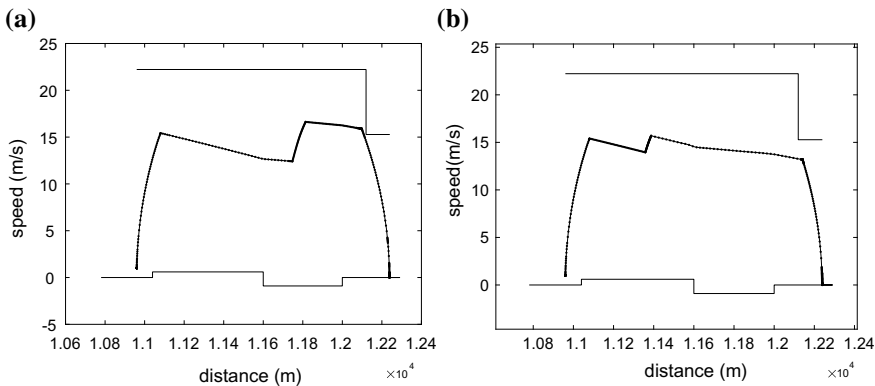


**Fig. 2** Target-velocity curves after the optimization based on two algorithms

mass is 187.46 J/t. Figure 2b is the train target velocity curve solved by the GA-PSO. It can be seen that the curve is smoother than the other curve, and the energy consumption per unit mass is 152.45 J/t, namely, the energy consumption is reduced by 18.8%.

In the process of simulation solution, fitness function curves of the two algorithms are obtained. Under the premise of not exceeding the speed limit and reducing the stopping error, both the GA-PSO algorithm and the basic PSO algorithm can find the conditions that meet the requirements. In Fig. 3b, the fitness

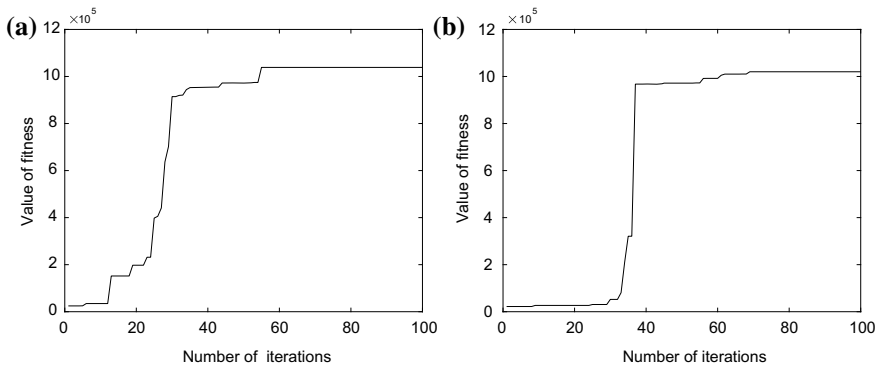


**Fig. 3** Fitness function curves of two algorithms

function of the GA-PSO algorithm has become stable after about 40 times iteration, but in Fig. 3a, the fitness function of the basic PSO is not stable at this time, indicating that the GA-PSO can better find the optimal solution.

## 4 Conclusions

To sum up, aiming at the problem of energy consumption of urban rail transit trains, this paper designs a method to solve the problem of train optimization by combining the idea of GA and PSO. At the same time, the parameters of PSO are improved, and the GA-PSO after fusion increases the diversity of particles so as to improve the search ability of global optimal value of particles and avoid the particle to fall into the local optimal value. The optimal driving strategy obtained by the GA-PSO is compared with that obtained by the basic PSO, and the results show that the GA-PSO algorithm can effectively reduce energy consumption. Due to the differences between the actual situation and theoretical analysis about the rail line, rail vehicles, and other factors, the ATO operation curve obtained should be compared and adjusted with the actual test results, so as to approach the actual operation effects and ensure to meet the actual requirements of the train energy-efficient operation.

**Acknowledgements** This work was financially supported by the National Natural Science Foundation of China (Grant No. 61673049).

## References

1. Howlett P (1990) An optimal strategy for the control of a train. *J Aust Math Soc Ser B Appl Math* 31(4):454–471
2. Cheng J, Howlett P (1992) Application of critical velocities to the minimisation of fuel consumption in the control of trains. *Automatica* 28(1):165–169
3. Khmelnitsky E (2000) On an optimal control problem of train operation. *IEEE Trans Autom Control* 45(7):1257–1266
4. Liu R, Golovitcher IM (2003) Energy-efficient operation of rail vehicles. *Transp Res Part A* 37(10):917–932
5. Chang CS, Sim SS (1997) Optimising train movements through coast control using genetic algorithms. *IEEE Proc Electr Power Appl* 144(1):65–73
6. Han SH, Byen YS, Baek JH et al (1999) An optimal automatic train operation (ATO) control using genetic algorithms (GA). In: Proceedings of the IEEE region 10 conference. TENCON 99.
7. Acikbas S, Soylemez MT (2008) Coasting point optimization for mass rail transit lines using artificial neural networks and genetic algorithms. *IET Electr Power Appl* 2(3):172–182
8. Wang Z, Hou Z (2014) Research on energy-saving optimization control of urban rail transit train based on MGASA. *Appl Res Comput* 31(12):3575–3579
9. Fan L (2016) Optimization of train recommendation speed curve based on ant colony algorithm. Beijing Jiaotong University, Beijing
10. Huang Y, Shaofeng G, Yuan C et al (2016) Energy-saving driving optimization model of urban rail train based on particle swarm optimization algorithm. *J Traffic Transp Eng* 16(2): 118–124
11. Eberhart R, Kennedy J (1995) A new optimizer using particle swarm theory. In: MHS'95. Proceedings of the sixth international symposium micro machine and human science, Institute of electric and electronic engineer

# Impact of Inverter's DC Virtual Resistance on Braking Energy Flow in Urban Rail Transit



Dongsheng Xu, Gang Zhang, Fengjie Hao and Yong Wang

**Abstract** Braking energy inverter has been widely used in urban rail transit traction power system due to obvious energy-saving effect. Its DC side virtual resistance, also known as DC resistance, can have a significant impact on the DC side energy flow of traction power supply system (TPSS). This paper introduces the definition and implementation method of the virtual resistance and analyzes its effect on the TPSS. The simulation model of traction power supply system is established, and the rectified energy and inverted energy under different virtual resistance values are compared by simulation. The simulation results show that the virtual resistance can change the path of regenerative braking energy flow and the overall energy consumption of the TPSS.

**Keywords** Traction power supply system · DC resistance · Railway simulation · Energy consumption

---

D. Xu (✉) · G. Zhang · F. Hao

School of Electrical Engineering, Beijing Engineering Research Center of Electric Rail Transportation, Beijing Jiaotong University, Beijing 100044, China  
e-mail: [17121514@bjtu.edu.cn](mailto:17121514@bjtu.edu.cn)

G. Zhang  
e-mail: [gzhang@bjtu.edu.cn](mailto:gzhang@bjtu.edu.cn)

F. Hao  
e-mail: [16117396@bjtu.edu.cn](mailto:16117396@bjtu.edu.cn)

Y. Wang  
Institute of Standards and Metrology, China Academy of Railway Sciences Group Co., Ltd, Beijing 100081, China  
e-mail: [15210261167@163.com](mailto:15210261167@163.com)

## 1 Introduction

Compared with friction braking, regenerative braking is widely used in urban rail transit. Regenerative braking can not only reduce noise and brake shoe wear, but also convert the kinetic energy of trains into electrical energy [1]. However, if regenerative braking energy cannot be completely absorbed, it will cause the DC network voltage rise and regenerative braking failure. Generally, in order to make better use of the regenerative braking energy, energy storage equipment and braking energy inverter are employed in TPSS [2–4]. Energy storage equipment, including supercapacitor, fly wheel and lithium battery, can store energy when trains are braking and release energy when trains are in traction. Braking energy inverter can invert the regenerative energy back to AC bus for further use [5–7], shown in Fig. 1. Due to the higher cost and shorter life of energy storage equipment [8], braking energy inverters are increasingly employed.

Constant voltage control strategy is commonly used in braking energy inverter to stabilize the DC voltage. But, this strategy may cause excessive power in one substation and return energy back to the power grid [9].

The literature [10] uses the droop control strategy and proposes the concept of virtual inner resistance, which solves this problem. However, that paper does not analyze the energy flow on the DC side in detail. Therefore, this paper will further study the impact of DC resistance on the DC side regenerative braking energy flow of the traction power supply system.

## 2 DC Resistor of Inverter

### 2.1 Introduction of DC Resistor

The main circuit of braking energy inverter is a three-phase voltage source grid-connected inverter, shown as Fig. 2. The inverter is paralleled with the diode rectifier, so that the regenerative braking energy can be reused on the AC side.

**Fig. 1** Application of  
braking energy inverter in  
TPSS

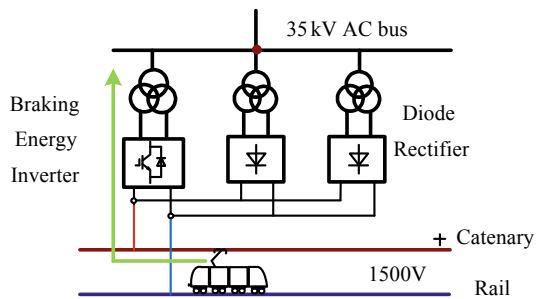


**Fig. 2** Main circuit of braking energy inverter

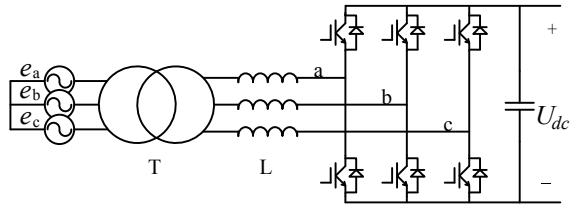
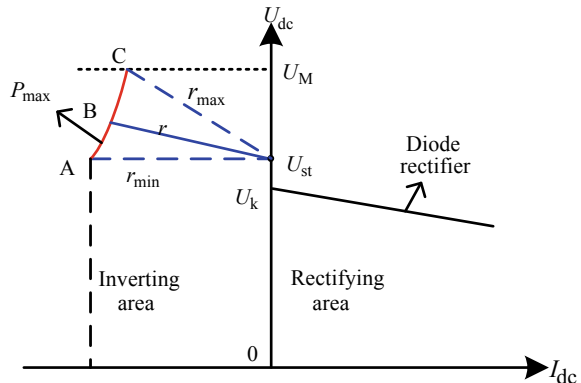


**Fig. 3** Substation operating characteristics



Substation operating characteristics are shown in Fig. 3. The braking energy inverter operates in the inverting area.  $U_k$  is the no-load voltage of the diode rectifier.  $U_{st}$  is the starting voltage of the inverter, which means the inverter operates when the voltage is higher than  $U_{st}$ .  $U_M$  is the maximum voltage of the inverter. The curve ABC is the maximum power of the inverter. Therefore, inverter operating characteristics can be divided into two regions:

- (1) Voltage rises linearly (or does not change) with the increase of current when the power is smaller than the maximum, and we call it linear region.
- (2) Voltage rises along the curve ABC when the power equals to the maximum, and we call it constant power region.

The inverter can be equivalent to a voltage source  $U_{st}$  in series with a resistor  $r$  in linear region. Actually, the resistor does not exist, so it is called virtual resistor. The range of  $r$  can be concluded from the figure, as shown in Formula (1).

$$0 \leq r \leq \frac{U_M \cdot (U_M - U_{st})}{P_{\max}} \quad (1)$$

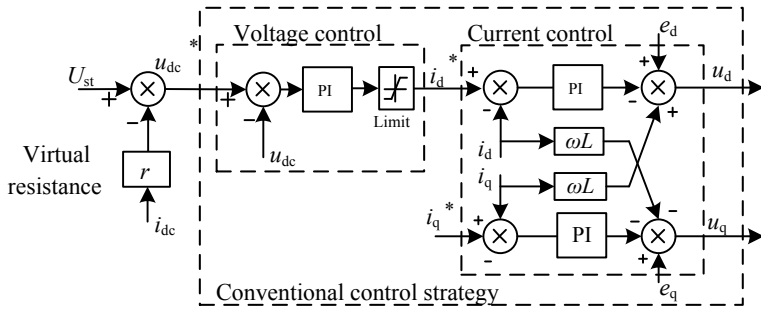


**Fig. 4** Control strategy with virtual resistor

## 2.2 Implementation of DC Resistor

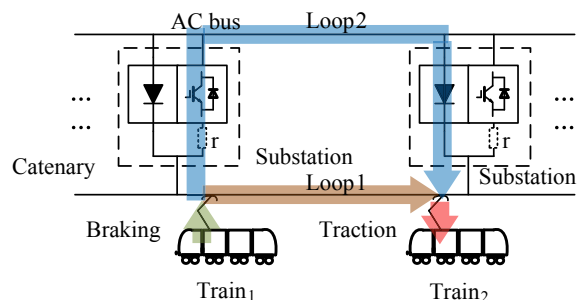
New control strategy with DC resistor is shown in Fig. 4.  $u_{dc}^*$  is DC voltage reference, which is no longer given directly [11]. It will change dynamically with DC current  $i_{dc}$ . DC resistance can be approximately expressed as Formula (2) in this strategy [12].

$$Z_{dc} = -\frac{\Delta u_{dc}}{\Delta i_{dc}} \approx r \quad (2)$$

## 2.3 Impact of DC Resistor

Regenerative braking energy can be absorbed by other trains when they are in traction. The energy can be used through the DC traction network directly. Meanwhile, it can also flow to other substations through the inverter and the AC bus and can be used through the diode rectifier, shown as Fig. 5. Apparently, the energy flowing through these two paths is related to their impedance. The path of regenerative braking energy can be changed by changing the inverter DC resistance. The

**Fig. 5** Diagram of regenerative braking energy flow



impedance of path 2 will increase with the increasing of virtual resistance and the more energy are absorbed through the DC traction net. Thus, the inverter DC resistance has a huge impact on the energy flow in TPSS. In order to quantify this “impact,” it is necessary to model the TPSS to calculate the power flow.

### 3 Modeling of Traction Power Supply System

Typical DC traction power supply system consists of traction substations, traction network and trains. The mathematical model will be built for them in the following, respectively.

#### 3.1 Traction Substation

Traction substation operating characteristics are shown in Fig. 3. Diode rectifier operates in rectifying area, which can be equivalent to a voltage source  $U_k$  in series with a resistor  $r_d$ . Braking energy inverter operates in inverting area, which can be equivalent to a voltage source  $U_{st}$  in series with a resistor  $r$  in linear region and a power source in constant power region, shown as Fig. 6.

#### 3.2 Traction Network

Metro traction network consists of catenary, rail and return line. The catenary and rail are assumed to be homogeneous. The circuit model is shown as Fig. 7 [13], where  $R_c$  and  $R_r$  are the equivalent resistance of catenary and rail, respectively, and  $Y_r$  is the equivalent admittance against the ground.

**Fig. 6** Circuit model of traction substation

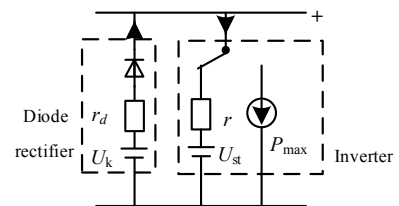


**Fig. 7** Circuit model of catenary and rail

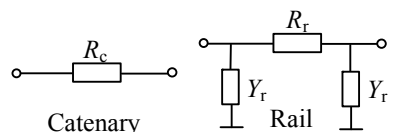
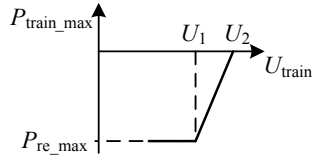


**Fig. 8** Maximum regenerative braking power of train



### 3.3 Train

Train can be equivalent to power source, and its instantaneous power and position can be calculated by traction calculation. It is worth noting that train will reduce the regenerative braking power to prevent overvoltage protection when the pantograph voltage is too high and start using the brake shoes to ensure sufficient braking power, shown as Fig. 8, where  $U_1$  is the reducing power voltage of train,  $U_2$  is the maximum voltage of train and  $P_{re\_max}$  is the maximum regenerative braking power of train.

The maximum regenerative braking power can be expressed as Formula (3).

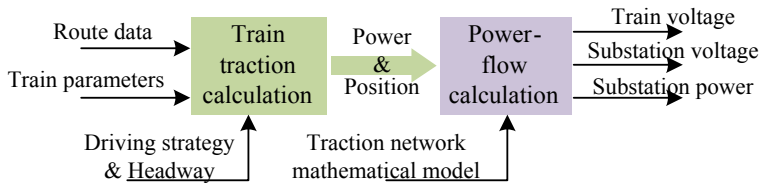
$$P_{train\_max} = \begin{cases} P_{re\_max} & U_{train} < U_1 \\ P_{re\_max} \cdot \frac{U_2 - U_{train}}{U_2 - U_1} & U_1 \leq U_{train} \leq U_2 \\ 0 & U_{train} > U_2 \end{cases} \quad (3)$$

### 3.4 Simulation System

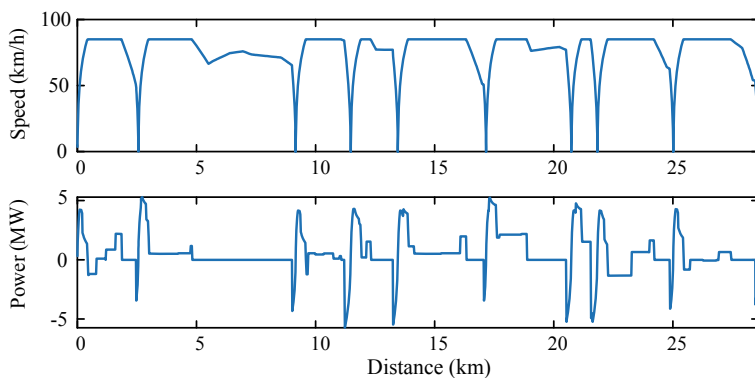
The simulation system is composed of traction calculation and power flow calculation, as shown in Fig. 9. Train traction calculation can calculate the power and position information of each train in the system at each time, which will be used as the input of power flow calculation. The mathematical model of traction network is transformed into node admittance matrix by power flow calculation, and the voltage, current and power of each node are solved by iteration calculation and Newton–Raphson method [14].

## 4 Simulation Study

The length of the metro line in simulation system is 28.5 km with 11 traction substations. The parameters of the system are shown in Table 1, and the traction calculation result is shown in Fig. 10.

**Fig. 9** Structure of simulation system**Table 1** System parameters

Parameter	Value	Parameter	Value
Headway (s)	300	No-load voltage of rectifier (V)	1650
Maximum traction power (kW)	7000	Rectifier equivalent resistance ( $\Omega$ )	0.05
Maximum braking power (kW)	-7000	Starting voltage of inverter (V)	1650
Maximum speed (km/h)	85	Maximum voltage of inverter (V)	2000
Train mass (t)	264	Capacity of inverter (kVA)	2000
Catenary resistivity ( $\Omega/\text{km}$ )	0.014		

**Fig. 10** Traction calculation result

#### 4.1 Traction Power Supply System Simulation

Trains' position and power can be calculated based on the traction calculation result and headway. The simulation time is 300 s, and the DC resistance of inverters is set to 0. The substation voltage and power are shown in Fig. 11. The maximum inverting power is 2 MW, and the maximum rectifying power is 1.918 MW. The highest voltage is 1.688 kV, and the lowest voltage is 1.579 kV. Voltage drops

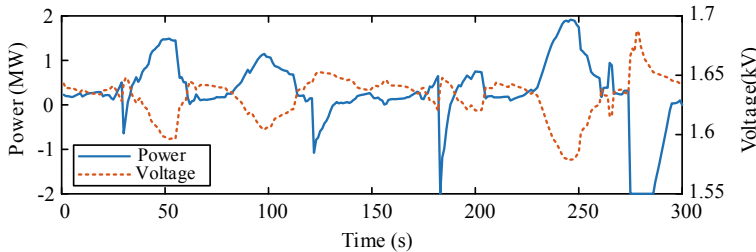


**Fig. 11** Substation power and voltage

when the substation operates in rectifying area, and voltage can be maintained at around 1.65 kV in inverting area before the inverting power reaches 2 MW, which verifies the model and calculation method are correct.

## 4.2 Simulation with DC Resistor

TPSS is simulated separately with different virtual resistances. The range of  $r$  is 0–0.175 according to Formula (1), and the simulation time is 300 s.

The total inverted energy and the total regenerative braking energy are shown in Fig. 12. With the increase of virtual resistance, the inverting energy decreases from 128.4 to 85.9 kW·h, while the regenerative braking energy is almost constant. This means that virtual resistor causes more regenerative braking energy (about 40 kWh) to be absorbed by other trains through the traction network instead of substation and AC bus, which increases the utilization rate of energy in traction network and reduces the burden on traction substations.

The energy consumed on DC side of the system is as shown in Fig. 13. As the virtual resistance increases, DC energy consumption increases from 298.7 to 301.4 kW·h. This is because more energy is flowing on the traction net and the power loss is larger.

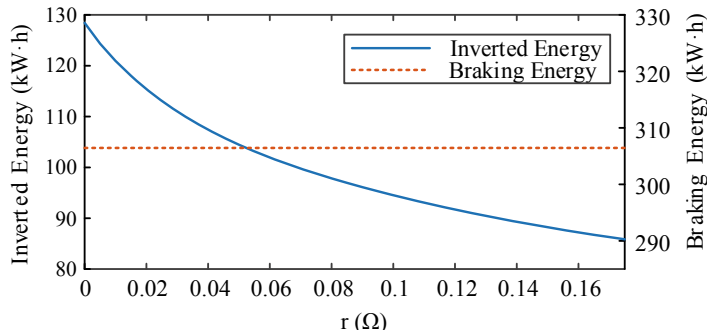


**Fig. 12** Total inverted energy and regenerative braking energy

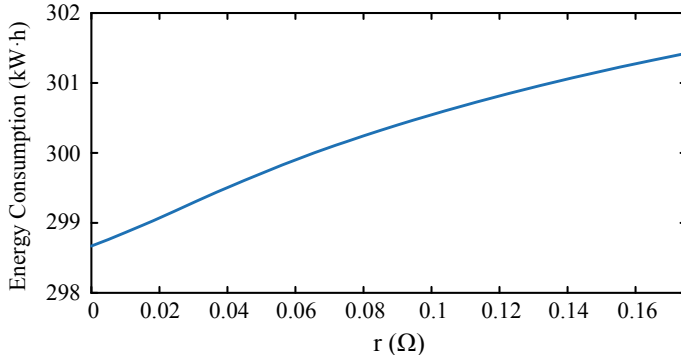


Fig. 13 DC energy consumption of the system

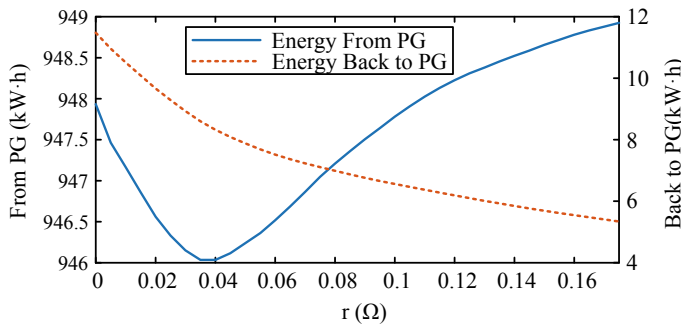


Fig. 14 Energy from power grid and energy back to power grid

The energy obtained from power grid and the energy fed back to power grid are shown in Fig. 14. With the increase of virtual resistance, the energy of the system feedback back to power grid decreases gradually, which makes the energy obtained from power grid decrease when  $r < 0.04$ . Meanwhile, the loss of the system increases, so the energy obtained from the power grid increases when  $r > 0.04$ .

## 5 Conclusion

This paper introduces the virtual resistance and its implementation method and establishes the model of traction power supply system. The correctness of the model and algorithm is verified by simulation, and the impact of virtual resistance on regenerative braking energy flow is analyzed. The following conclusions can be drawn:

- (1) Virtual resistor can change the flow path of the regenerative braking energy of the train. The larger virtual resistance is, the more regenerative braking energy flows inside the traction network.
- (2) The DC energy consumption decreases with the decrease of virtual resistance.
- (3) As the virtual resistance increases, the energy obtained from power grid decreases first and then increases.

**Acknowledgements** This research was supported by the National Key Research and Development Program (2016YFB1200502-04).

## References

1. T S (1982) DC power-supply system with inverting substations for traction systems using regenerative brakes. *IEE Proc B Electr Power Appl* 129(1):18–26
2. Yii Shen T, Ruay-Nan W, Nanming C (1998) Electric network solutions of DC transit systems with inverting substations. *IEEE Trans Veh Technol* 47(4):1405–1412
3. Huan X (2017) Hierarchical control and capacity allocation optimization of supercapacitor energy storage system for urban rail transit. Beijing Jiaotong University (in Chinese)
4. Gee AM, Dunn RW (2015) Analysis of trackside flywheel energy storage in light rail systems. *IEEE Trans Veh Technol* 64(9):3858–3869
5. de la Sebastián T, Antonio José S, José Antonio A, Manuel R, Oliver M (2015) Optimal sizing of energy storage for regenerative braking in electric railway systems. *IEEE Trans Power Syst* 30(3):1492–1500
6. Daniel C (2010) Efficient recovery of braking energy through a reversible dc substation. In: Electrical systems for aircraft, railway and ship propulsion. IEEE, Bologna, pp 1–9
7. Gang Z, Zhongbei T, Huiqing D, Zhigang L (2018) A novel hybrid DC traction power supply system integrating PV and reversible converters. *Energies* 11(7):1661
8. Lingli X (2017) Optimal system design of inverter feedback device for urban rail. Southwest Jiaotong University (in Chinese)
9. Bin T (2018) Research on distributed cooperative control of urban rail transit traction power supply system. Beijing Jiaotong University (in Chinese)
10. Gang Z, Zhongbei T, Pietro T, Stuart H, Yong W, Zhigang L (2019) Inverter operating characteristics optimization for DC traction power supply systems. *IEEE Trans Veh Technol* 68(4):3400–3410
11. Jung-Won K, Hang-Seok C, Bo Hyung C (2002) A novel droop method for converter parallel operation. *IEEE Trans Power Electron* 17(1):25–32
12. Zhigang L, Fengjie H, Jie C, Gang Z (2019) Optimization method of train-ground coordination parameters for urban traction power supply system. *J Beijing Jiaotong Univ* 43 (1):79–87 (in Chinese)
13. Zhongbei T, Paul W, Ning Z, Stuart H, Clive R, Lei C (2017) System energy optimisation strategies for metros with regeneration. *Transp Res Part C Emerg Technol* 75:120–135
14. Jinghan H, Zhicheng L, Xiaojun W, Yuyu X (2016) Power flow algorithm for DC grid considering various control modes. *Power Syst Technol* 40(3):712–718 (in Chinese)

# Grey Prediction Method for Cylinder Wear Extent of Automobile Engine



Zheng-Wei Fan

**Abstract** This paper adopts the grey system to study the basic methods of formulating engine cylinder wear extent forecasting model. The results show that the GM (1,1) grey model can forecast cylinder wear extent accurately and the grey model can be used to forecast the wear extent and repair the cylinder in practice.

**Keywords** Automobile engine · Cylinder wear extent · Grey model · Forecasting

## 1 Introduction

The cylinder is an important part of the engine, and its wear rate directly affects the clearance between the piston, piston ring and cylinder liner, which is related to the life of the engine. Engine cylinder wear is influenced by many factors such as engine load, lubrication oil quality, engine speed, oil temperature and starting times [1–4]. Because of the influence of many factors, it is difficult to predict the wear of the cylinder. For the purpose of better studying the engine cylinder wear, taking into account that engine cylinder wear has few measurements and high uncertainty, this paper adopts the grey system to study the basic methods of formulating engine cylinder wear extent forecasting model.

## 2 Basic Methods of Grey Forecasting

Grey prediction is a practical method to predict the future development of the system by using the known system data, using the grey modelling method and using the established grey model. The GM (11) model [5–8] can be used in grey forecasting

---

Z.-W. Fan (✉)

Bengbu Automobile NCO Academy of PLA, Bengbu 233011,  
Anhui, People's Republic of China

because there is only one variable in engine cylinder wear extent forecasting. The basic steps are as follows.

## 2.1 The First Step: Regenerate the Raw Data

Building data

$$X^{(0)} = \{x^{(0)}(1), x^{(0)}(2), \dots, x^{(0)}(n)\}$$

Make an accumulation of  $X^{(0)}$

$$x^{(1)}(k) = \sum_{i=1}^k x^{(0)}(i); \quad k = 1, 2, \dots, n$$

The resulting sequence is

$$X^{(1)} = \{x^{(1)}(1), x^{(1)}(2), \dots, x^{(1)}(n)\}$$

## 2.2 The Second Step: Modelling with GM (1,1)

GM (1,1) whitening differential equation for  $x^{(0)}(k)$ :

$$\frac{dx^{(1)}}{dt} + ax^{(1)} = u \quad (1)$$

The  $A$  and  $u$  are the undetermined parameters, and the upper expression is discretized

$$\Delta^{(1)}(x^{(1)}(k+1)) + az^{(1)}(x(k+1)) = u \quad (2)$$

where  $\Delta^{(1)}(x^{(1)}(k+1))$  is  $x^{(1)}$  in the  $(k+1)$  Iago time sequence

$$\begin{aligned} \Delta^{(1)}(x^{(1)}(k+1)) &= \Delta^{(0)}[x^{(1)}(k+1)] - \Delta^{(0)}[x^{(r)}(k)] = x^{(1)}(k+1) - x^{(1)}(k) \\ &= x^{(0)}(k+1) \end{aligned} \quad (3)$$

$z^{(1)}(x(k+1))$  is background value at  $(k+1)$  moments (that is, the value of the  $X$  corresponding to that moment)

$$z^{(1)}(x(k+1)) = \frac{1}{2}(x^{(1)}(k+1) + x^{(1)}(k)) \quad (4)$$

Bring (3) and (4) into (2):

$$x^{(0)}(k+1) = a \left[ -\frac{1}{2}(x^{(1)}(k) + x^{(1)}(k+1)) \right] + u \quad (5)$$

Unfold (5)

$$\begin{bmatrix} x^{(0)}(2) \\ x^{(0)}(3) \\ \vdots \\ x^{(0)}(n) \end{bmatrix} = \begin{bmatrix} -\frac{1}{2}(x^{(1)}(1) + x^{(1)}(2)) & 1 \\ -\frac{1}{2}(x^{(1)}(2) + x^{(1)}(3)) & 1 \\ \vdots & \vdots \\ -\frac{1}{2}(x^{(1)}(n-1) + x^{(1)}(n)) & 1 \end{bmatrix} \begin{bmatrix} a \\ u \end{bmatrix} \quad (6)$$

$$\text{Suppose } Y = \begin{bmatrix} x^{(0)}(2) \\ x^{(0)}(3) \\ \vdots \\ x^{(0)}(n) \end{bmatrix}$$

$$B = \begin{bmatrix} -\frac{1}{2}(x^{(1)}(1) + x^{(1)}(2)) & 1 \\ -\frac{1}{2}(x^{(1)}(2) + x^{(1)}(3)) & 1 \\ \vdots & \vdots \\ -\frac{1}{2}(x^{(1)}(n-1) + x^{(1)}(n)) & 1 \end{bmatrix},$$

$\Phi = [a \ u]^T$  is the parameter vector to be identified. Then, (6) can be written  

$$Y = B\Phi \quad (7)$$

The parameter vector  $\Phi$  can be obtained by the least square method:

$$\hat{\Phi} = [\hat{a}, \hat{u}]^T = (B^T B)^{-1} B^T Y \quad (8)$$

Find its discrete solution as

$$\hat{x}^{(1)}(k+1) = \left[ x^{(0)}(1) - \frac{\hat{u}}{\hat{a}} \right] e^{-\hat{a}k} + \frac{\hat{u}}{\hat{a}} \quad (9)$$

Restore to raw data

$$\hat{x}^{(0)}(k+1) = \hat{x}^{(1)}(k+1) - \hat{x}^{(1)}(k) = (1 - e^{\hat{a}}) \left[ x^{(0)}(1) - \frac{\hat{u}}{\hat{a}} \right] e^{-\hat{a}k} \quad (10)$$

(9) and (10) are called the time corresponding function models of GM (1,1), and it is the concrete formula of grey prediction of GM (1,1) model.

### 2.3 The Third Step: Model Checking

Suppose the known data for the  $K$  moment is  $x^{(0)}(k)$ . Model calculated value is  $\hat{x}^{(0)}(k)$ .

The absolute residual is:  $(q(k) = x^{(0)}(k) - \hat{x}^{(0)}(k))$ .

Relative residual is:  $\varepsilon(k) = \frac{q(k)}{x^{(0)}(k)} \times 100\%$ .

The residual value and relative residual are calculated to test whether the predicted value of the prediction model meets the requirement of accuracy.

## 3 Engine Cylinder Wear Extent Forecasting Model

The measurement data of EQ1118GA diesel engined car and its first cylinder wear at different mileages are shown in Table 1.

Since the measured data is a range value, two methods can be used in the calculation of data. One is to calculate the average value of the wear and tear, and then grey modelling and prediction according to the average value. The other is to process the data of each measurement point, i.e. to establish two sequences. One is the lower bound of the wear rate, and the other is the upper limit of the amount of wear, which is modelled and calculated, respectively [9]. At the end of the processing, we can get a range of predicted values of wear data. Since the two sequences are closer to the actual measurement value, the method of modelling and calculation is adopted in this paper.

**Table 1** Actual mileage and cylinder wear

Mileage/(km)	5000	10,000	15,000	20,000	25,000
Wear extent/( $\mu\text{m}$ )	30–33	50–60	70–80	100–120	120–150

### 3.1 Model Building

Building Engine cylinder wear extent data module (Take Lower limit accumulation series for example).

Lower limit series of wear:

$$X^{(0)} = (x^{(0)}(1), x^{(0)}(2), \dots, x^{(0)}(5)) = (30, 50, 70, 100, 120)$$

Make an accumulation of  $X^{(0)}$

$$x^{(1)}(k) = \sum_{m=1}^k x^{(0)}(m) \quad (k = 1, 2, \dots, 5)$$

$$X^{(1)} = (x^{(1)}(1), x^{(1)}(2), \dots, x^{(1)}(5)) = (30, 80, 150, 250, 370)$$

Construct data matrix  $B$  and data vector  $Y$ :

$$\begin{cases} z^{(1)}(2) = \frac{1}{2}[x^{(1)}(1) + x^{(1)}(2)] = 55 \\ z^{(1)}(3) = \frac{1}{2}[x^{(1)}(2) + x^{(1)}(3)] = 115 \\ z^{(1)}(4) = \frac{1}{2}[x^{(1)}(3) + x^{(1)}(4)] = 200 \\ z^{(1)}(5) = \frac{1}{2}[x^{(1)}(4) + x^{(1)}(5)] = 310 \end{cases}$$

So, we can get

$$Y = \begin{bmatrix} x^{(0)}(2) \\ x^{(0)}(3) \\ x^{(0)}(4) \\ x^{(0)}(5) \end{bmatrix} = \begin{bmatrix} 50 \\ 70 \\ 100 \\ 120 \end{bmatrix}, B = \begin{bmatrix} -Z^{(1)}(2) & 1 \\ -Z^{(1)}(3) & 1 \\ -Z^{(1)}(4) & 1 \\ -Z^{(1)}(5) & 1 \end{bmatrix} = \begin{bmatrix} -55 & 1 \\ -115 & 1 \\ -200 & 1 \\ -310 & 1 \end{bmatrix}$$

Parameter list is estimated by least square method

$$\Phi = [a \quad u]^T$$

$$\hat{\Phi} = [\hat{a}, \hat{u}]^T = (B^T B)^{-1} B^T Y = \begin{bmatrix} -0.2776 \\ 37.8163 \end{bmatrix}$$

So, we can get

$$\hat{a} = -0.2776, \hat{u} = 37.8163$$

### Model building

$$x^{(0)}(k) + -0.2776z^{(1)}(k) = 37.8163$$

The solution time response sequence is

$$\begin{aligned}\hat{x}^{(1)}(k+1) &= \left[ x^{(0)}(1) - \frac{\hat{u}}{\hat{a}} \right] e^{-\hat{a}k} + \frac{\hat{u}}{\hat{a}} \\ &= (30 + 136.25) e^{-0.2776k} + 136.25\end{aligned}$$

Bring  $k = 1, 2, 3, 4, 5$  into the time response function.

Take  $\hat{x}^{(1)}(1) = \hat{x}^{(0)}(1) = x^{(1)}(1) = 30$

$$\begin{aligned}\hat{x}^{(0)}(k+1) &= \hat{x}^{(1)}(k+1) - \hat{x}^{(1)}(k) = (1 - e^{\hat{a}}) \left[ x^{(1)}(1) - \frac{\hat{u}}{\hat{a}} \right] e^{-\hat{a}k}, \\ \text{Restore value } &\hat{X}^{(0)} = (\hat{x}^{(0)}(1), \hat{x}^{(0)}(2), \dots, \hat{x}^{(0)}(6)) \\ &= (30, 53.1823, 70.1950, 92.6499, 122.2897, 161.4017)\end{aligned}$$

### 3.2 Model Checking

Comparison of predicted values and actual lower wear values of cylinder is shown in Table 2.

Similarly, the same calculation can be done using the upper limit data for cylinder wear.

The model calculation value and relative error of the upper limit of the cylinder wear are shown in Table 3.

Based on the above data, the final results are sorted into Table 4.

The above calculation results show that the prediction has high accuracy. Except one point, the model predictions of the other points are very close to the actual

**Table 2** Comparison of predicted values and actual lower wear values of cylinder

Serial number	Mileage/(km)	Wear extent/(\mu m)	Model calculation value/(\mu m)	Residual	Relative error
1	5000	30	30	0	0
2	10,000	50	53.1823	-3.1823	-6.3646%
3	15,000	70	70.1950	-0.1950	-0.2785%
4	20,000	100	92.6499	7.3501	7.3501%
5	25,000	120	122.2897	-2.2897	-1.9066%
6	30,000		161.4071		

**Table 3** Comparison of predicted values and actual upper wear values of cylinder

Serial number	Mileage/(km)	Wear extent/(\mu m)	Model calculation value/(\mu m)	Residual	Relative error
1	5000	33	33	0	0
2	10,000	60	61.0112	-1.0112	-1.6853%
3	15,000	80	82.5398	-2.5398	-3.1748%
4	20,000	120	111.6651	8.3349	6.9458%
5	25,000	150	151.0676	-1.0676	-1.9066%
6	30,000		204.3738		

**Table 4** Actual wear and predicted value of cylinder

Mileage/(km)	Wear extent/(\mu m)	Model calculation value/(\mu m)	Remarks
5000	30–33	30–33	
10,000	50–60	53.1823–61.0112	
15,000	70–80	70.1950–82.5398	
20,000	100–120	92.6499–111.6651	
25,000	120–150	122.2897–151.0676	
30,000		161.4071–204.3738	Predicted value

values. It shows that the response function established by the grey model is reliable. It can better reveal the inherent regularity of the change of the cylinder's wear volume with the change of mileage.

The above example analysis shows that the grey prediction method is characterized on the short-term data prediction has higher prediction accuracy. The relationship between the amount of wear and the mileage obtained by the grey model is not the linear relationship obtained by least square regression. In terms of the actual application and wear mechanism of the internal combustion engine, the predicted values obtained by grey prediction may be closer to the real situation. Because once the clearance between the cylinder liner and the piston ring and the piston clearance exceeds the optimum fit clearance, the wear will increase rapidly.

The grey prediction method uses GM (1.1) to predict the cylinder wear of the vehicle engine. The results are very close to the actual measured values. It can be used in the prediction of engine cylinder wear and has good application prospect. We can use this method to predict the wear of the engine cylinder according to the mileage of the vehicle. It is convenient for vehicle users to arrange engine maintenance plan flexibly according to their running characteristics, so as to effectively prevent the decline of engine dynamic performance and reduce the number of sudden failures caused by engine cylinder wear.

## 4 Conclusion

The wear of the engine cylinder is related to many factors in the actual use of the engine. As can be seen from the calculation data, the response function established by the GM (11) model of grey theory can predict the wear of the cylinder accurately. The calculated results are in good agreement with the existing data. The method has higher practical application value for the repair and replacement of the engine cylinder.

## References

1. Wei Z, Qin S, Wang J (2011) Non-probabilistic reliability assessment and anti-wear life prediction. *Mach Des Manuf* 7:194–196 (in Chinese)
2. He X, Yang S-Q, Zhang K, Jiang G-W (2018) Life loss mechanism of heavy duty diesel engine for real vehicle application. *J Sci Technol Eng* 18(14):141–146
3. Rao X, Sheng C-X, Guo Z-W (2018) Research on the friction and wear properties of diesel engine cylinder liner with different surface textures. *J Acta Armamentarii* 39(2):356–363. <https://doi.org/10.3969/j.issn.1000-1093.2018.02.019> (in Chinese)
4. Fu J, Papadopoulos KD, Lu Y et al (2007) Ostwald ripening: a decisive cause of cylinder corrosive wear. *Tribology Lett* 1(1):21–24
5. Luo Y (2001) Grey system theory and its application in mechanical engineering. National University of Defense Technology Press, Beijing 93–102 (in Chinese)
6. Zeng B, Liu S F, Xie NM et al (2010) Prediction model for interval grey number based on grey band and grey layer. *Control Decis* 25(10):1585–1588 + 1592
7. Baidu W, <https://wenku.baidu.com/view/2e9533ec65ce050877321342.html>. 2018/06/28
8. CSDN, <https://blog.csdn.net/qq547276542/article/details/77865341/>. 2017/09/06
9. Shoudao L, Zhaohui ZLW (2000) Forecasting diagnosis of rolling bearing by GM model. *Lubr Eng* 2:38–39. <https://doi.org/10.3969/j.issn.0254-0150.2000.02.014>. (in Chinese)

# Modeling Analysis and Control of Bidirectional DC/DC Converter in Hybrid EMU System



Wang Li, Miaoxin Jin and Libing Fan

**Abstract** The application of hybrid power system in EMU not only has the characteristics of low consumption and emission reduction but also can improve the reliability of power supply. The stability of the bidirectional DC/DC converter, which is connected with the energy storage device and the intermediate DC link, greatly affects the charging and discharging process of the energy storage device. In this paper, the mathematical model of the bidirectional DC/DC converter in the hybrid EMU system is studied. The modeling and transfer function analysis of Buck mode and Boost mode converters in detail are carried out by means of switching element average method. Moreover, the voltage and current double closed-loop control strategy of bidirectional DC/DC converter and the influence of DC capacitor C are introduced, which lays a foundation for further study on the stability of the whole hybrid EMU system.

**Keywords** Bidirectional DC/DC converter · EMU · Energy storage devices

## 1 Introduction

With the application of vast energy storage equipment in emu, automobile and vessels, the high-power bidirectional DC/DC converter for energy buffering has received a lot of attention and research [1]. For EMU, the bidirectional DC/DC converter, as the driving equipment of energy storage devices (ESD), is applied to different levels of voltage conversion, energy flow control and the stabilization of the intermediate DC link voltage [2]. Therefore, the stability of bidirectional DC/DC converter has an enormous impact on the normal operation of the whole hybrid EMU system [3]. Relevant hybrid power system is depicted in Fig. 1. The bidirectional DC/DC converter is a nonlinear and time-varying system whose dynamic analysis is complex [4].

---

W. Li (✉) · M. Jin · L. Fan

The State Key Laboratory of Heavy Duty AC Drive Electric Locomotive Systems Integration, CRRC Zhuzhou Locomotive Co., Ltd., Zhuzhou 412001, Hunan, China  
e-mail: [hunanliwang@126.com](mailto:hunanliwang@126.com)

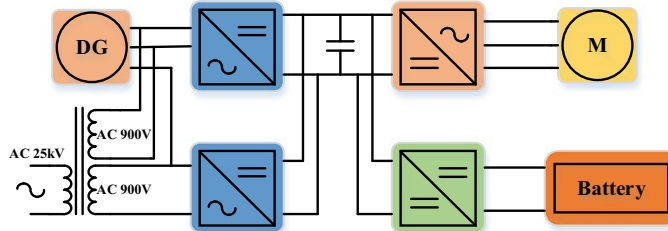


**Fig. 1** Structure of hybrid EMU system

In order to complete the stability analysis of bidirectional DC/DC converter in the near future, its mathematical model must be established [5]. This paper conducts mathematical modeling of the half-bridge bidirectional Buck–Boost DC/DC converter, respectively, by using the switching element average method [6] and then obtains the corresponding transfer function expressions. In addition, the voltage and current double closed-loop control system of bidirectional DC/DC converter is analyzed.

## 2 Modeling of Bidirectional DC/DC Converter

At present, non-isolated half-bridge bidirectional Buck–Boost converter with small size and convenient integration is widely used in hybrid EMU system [7]. The circuit topology is seen in Fig. 2.

### 2.1 Model of Boost Mode Bidirectional Converter

Take the ideal Boost converter as an example, as seen in Fig. 3.

The small-signal AC modeling about the half-bridge bidirectional Boost circuit is carried out and then obtains its small-signal model diagram by separating and disturbing the average variables of voltage and current. Relevant small-signal model diagram is described as Fig. 4.

**Fig. 2** Topology of the proposed bidirectional DC/DC converter

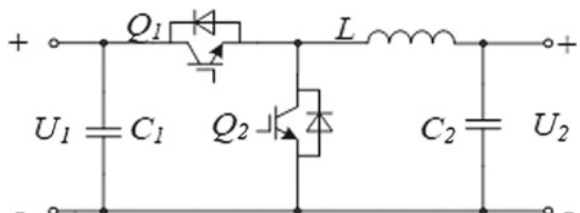


**Fig. 3** Circuit topology of an ideal Boost converter

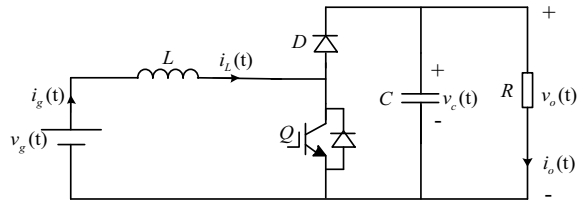
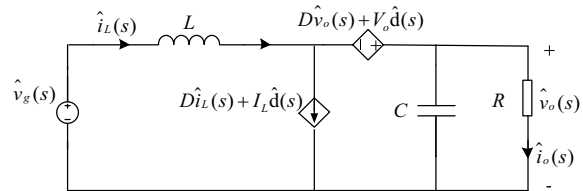


**Fig. 4** AC small-signal equivalent circuit topology of ideal Boost converter



According to the equivalent model of AC small signal shown in Fig. 4, the KVL and KCL circuit equations of the circuit are as follows:

$$\begin{cases} \hat{v}_g - \hat{i}_L \cdot sL + (D\hat{v}_o + V_o \hat{d}) - \hat{v}_o = 0 \\ \hat{i}_L - (D\hat{i}_L + I_L \hat{d}) - \hat{v}_o(sC + 1/R) = 0 \end{cases} \quad (1)$$

where  $D$  represents the duty cycle of the switch.

Then, settle the above equation and get the ideal Boost converter transfer function as follows:

$$G_{vg}(s) = \frac{\hat{v}_o(s)}{\hat{v}_g(s)}|_{\hat{d}(s)=0} = \frac{D'}{D'^2 + \frac{L}{R}s + LCs^2} \quad (2)$$

$$G_{vd}(s) = \frac{\hat{v}_o(s)}{\hat{d}(s)}|_{\hat{v}_g(s)=0} = \frac{V_g(1 - sL/D'^2R)}{D'^2 + \frac{L}{R}s + LCs^2} \quad (3)$$

where  $G_{vg}(s)$  is the transfer function of output voltage  $\hat{v}_o(s)$  to input voltage  $\hat{v}_g(s)$  and  $G_{vd}(s)$  is the transfer function of output voltage  $\hat{v}_o(s)$  to control variable  $\hat{d}(s)$  and  $D' = 1 - D$ .

Considering the circuit, inductance and the equivalent resistance  $r$  of power battery, it is only necessary to change the KVL and KCL equations slightly [8]. The modified transfer function is as follows:

$$G_{vg}(s) = \frac{\hat{v}_o(s)}{\hat{v}_g(s)}|_{\hat{d}(s)=0} = \frac{D'}{(D'^2 + \frac{r}{R}) + (\frac{L}{R} + rC)s + LCs^2} \quad (4)$$

$$G_{vd}(s) = \frac{\hat{v}_o(s)}{\hat{d}(s)} \Big|_{\hat{v}_g(s)=0} = \frac{(-(sL+r)/D'R+D')V_0}{LCs^2 + s(\frac{L}{R} + Cr) + (D'^2 + \frac{r}{R})} \quad (5)$$

$$G_{iLd}(s) = \frac{\hat{i}_L(s)}{\hat{d}(s)} \Big|_{\hat{i}_o(s)=0} = \frac{V_g}{RD'} \frac{(2+RCs)}{LCs^2 + s(\frac{L}{R} + Cr) + (D'^2 + \frac{r}{R})} \quad (6)$$

## 2.2 Model of Buck Mode Bidirectional Converter

In Buck converter mode, inverter motor is regarded as the input source and battery pack is regarded as the load. Take the ideal Buck converter as an example (see Fig. 5).

The small-signal AC modeling about the half-bridge bidirectional Buck circuit was carried out and then obtained its small-signal model diagram by separating and disturbing the average variables of voltage and current. Relevant small-signal model diagram is shown in Fig. 6.

According to the equivalent model of AC small signal shown in Fig. 6, the KVL and KCL circuit equations of the circuit are as follows:

$$\begin{cases} (D\hat{v}_g + V_g\hat{d}) - \hat{i}_L \cdot sL - \hat{v}_o = 0 \\ \hat{i}_L - \hat{v}_o(sC + 1/R) = 0 \end{cases} \quad (7)$$

where  $D$  represents the duty cycle of the switch and  $D = 1 - D'$

Then, settle the above equation and get the ideal Buck converter transfer function as follows:

**Fig. 5** Circuit topology of an ideal Buck converter

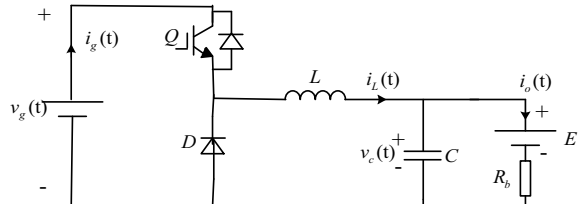
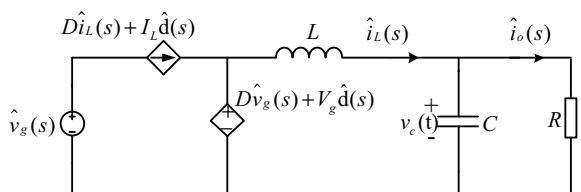


**Fig. 6** AC small-signal equivalent circuit topology of ideal Buck converter



$$G_{vg}(s) = \frac{\hat{v}_o(s)}{\hat{v}_g(s)}|_{\hat{d}(s)=0} = \frac{D}{1 + \frac{L}{R}s + LCs^2} \quad (8)$$

$$G_{vd}(s) = \frac{\hat{v}_o(s)}{\hat{d}(s)}|_{\hat{v}_g(s)=0} = \frac{V_g}{1 + \frac{L}{R}s + LCs^2} \quad (9)$$

where  $G_{vg}(s)$  is the transfer function of output voltage  $\hat{v}_o(s)$  to input voltage  $\hat{v}_i(s)$  and  $Y_i(s)$  is the open-loop input admittance.

Considering the circuit, inductance and the equivalent resistance  $r$  of power battery, it is only necessary to change the KVL and KCL equations slightly. The modified transfer function is as follows:

$$G_{vg}(s) = \frac{\hat{v}_o(s)}{\hat{v}_g(s)}|_{\hat{d}(s)=0} = \frac{D}{LCs^2 + s(\frac{L}{R} + Cr) + 1 + \frac{r}{R}} \quad (10)$$

$$G_{vd}(s) = \frac{\hat{v}_o(s)}{\hat{d}(s)}|_{\hat{v}_g(s)=0} = \frac{V_{dc}}{LCs^2 + s(\frac{L}{R} + Cr) + 1 + \frac{r}{R}} \quad (11)$$

$$G_{ild}(s) = \frac{\hat{i}_L(s)}{\hat{d}(s)}|_{\substack{\hat{v}_g(s)=0 \\ \hat{i}_o(s)=0}} = \frac{V_g}{R} \frac{1 + RCs}{LCs^2 + s(\frac{L}{R} + Cr) + 1 + \frac{r}{R}} \quad (12)$$

### 3 Double Closed-Loop Control System for Bidirectional DC/DC Converter

The common control methods of bidirectional DC/DC system are single-voltage loop control and double-voltage current loop control. The single-loop control structure is simple and easy to design [8]. However, when the system is disturbed, the regulating action lags behind which is suitable for the occasions of low demand on the output dynamic performance. Double-loop control has great regulation performance and fast dynamic response and can realize over-current protection, which is suitable for occasions with high requirements on system's output performance. In this paper, the input current inner loop (ICIL) control methods are adopted in the research process [9, 10]. The Buck converter and Boost converter share a PI control system, which can achieve the natural commutation of positive and negative duty ratios. The on and off state of the upper and lower tubes of the IGBT bridge arm can be switched naturally. Figure 7 is the double closed-loop control block diagram.

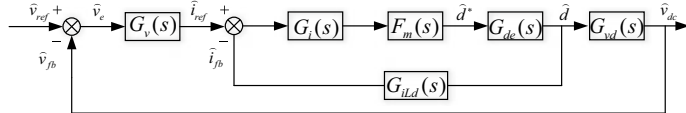


**Fig. 7** Double closed-loop control block diagram of bidirectional DC/DC converter

where the transfer function of current inner loop PI controller is as follows:

$$G_i(s) = \frac{k_{ip}s + k_{ii}}{s} \quad (13)$$

The transfer function of voltage outer loop PI controller is as follows:

$$G_v(s) = \frac{k_{vp}s + k_{vi}}{s} \quad (14)$$

The delay link transfer function is as follows:

$$G_{ge}(s) = e^{-sT_s} \quad (15)$$

Ignoring the influence of the delay link, the open-loop transfer function  $G_{io}(s)$  and closed-loop transfer function  $G_{ic}(s)$  of the current inner loop are as follows:

$$G_{io}(s) = G_i(s)G_{iLd}(s) \quad (16)$$

$$G_{ic}(s) = \frac{\hat{d}}{\hat{i}_{ref}} = \frac{G_i(s)}{1 + G_i(s)G_{iLd}(s)} \quad (17)$$

If the current inner loop is expressed by its closed-loop transfer function  $G_{ic}(s)$ , the double closed-loop control model can be simplified into the single-loop control model shown in Fig. 8.

The voltage controller  $G_v(s)$  and the closed-loop transfer function  $G_{ic}(s)$  of the current inner loop in the model in Fig. 8 are unified and combined. Take  $G_c(s) = G_v(s)G_{ic}(s)$ , then the double closed-loop control model can be equivalent to the single-voltage loop regulation system as shown in Fig. 9, so as to facilitate the necessary design and analysis of the control link.

**Fig. 8** Simplified single-loop control block diagram of bidirectional DC/DC converter

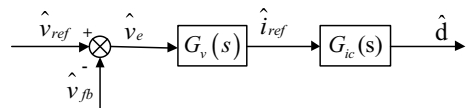
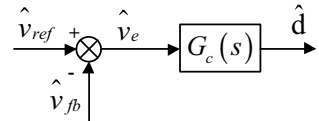


**Fig. 9** Simplified voltage current double closed-loop equivalent control block diagram of bidirectional DC/DC converter



## 4 Design of Double Closed-Loop Control System for Boost Converter

Double closed-loop control system of Buck converter is similar to the control strategy of Boost converter. Therefore, this paper takes double closed-loop control system of Boost converter as an example. As for the double closed-loop control design of Buck converter, there is no more discussion. The relevant design parameters of Boost converter are shown in Table 1.

Substitute the system parameters into the above formula  $G_{vd}(s)$  and  $G_{iLd}(s)$ , and the expression of them are as follows:

$$G_{vd}(s) = \frac{1997(1 - 0.0023s)}{1 + 0.00296s + 0.0000617s^2} \quad (18)$$

$$G_{iLd}(s) = \frac{1698.4(1 + 0.01408s)}{1 + 0.00296s + 0.0000617s^2} \quad (19)$$

The Bode diagram of the above two transfer functions is shown in Figs. 10 and 11, respectively, and its Nyquist curve is shown in Figs. 12 and 13, respectively.

According to Fig. 11, the amplitude margin of the current inner ring is infinite, and the phase angle margin is  $90^\circ$ , so the current inner ring is stable. The voltage loop transfer function is a non-minimum phase system, and the stability cannot be judged by the Bode diagram. It can be seen from the Nyquist curve that there is an unstable closed-loop pole, so the controller needs to be designed to make it stable. Adding the current loop controller  $G_i(s)$ , we can get the Bode diagram, the closed-loop transfer function  $G_{ic}(s)$  of the current loop in Fig. 14 and Nyquist curve of  $G_{ic}(s)$  in Fig. 15 where  $K_{ip} = 1/100$ ,  $K_{ii} = 1/1000$ .

**Table 1** Relevant design parameters of Boost converter

Parameter	Parameter values
IGBT rated parameters	3300 V/1500 A
Switch frequency	1 kHz
Inductance L	4 mH
Capacitance C	8 mF
Low-voltage side voltage	1100 V
High-voltage side voltage	1500 V/1750 V

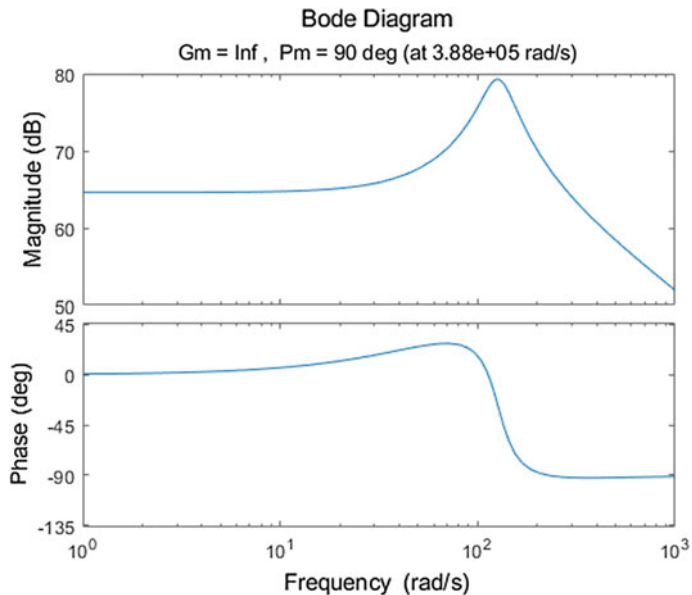


**Fig. 10** Bode diagram of  $G_{vd}(s)$

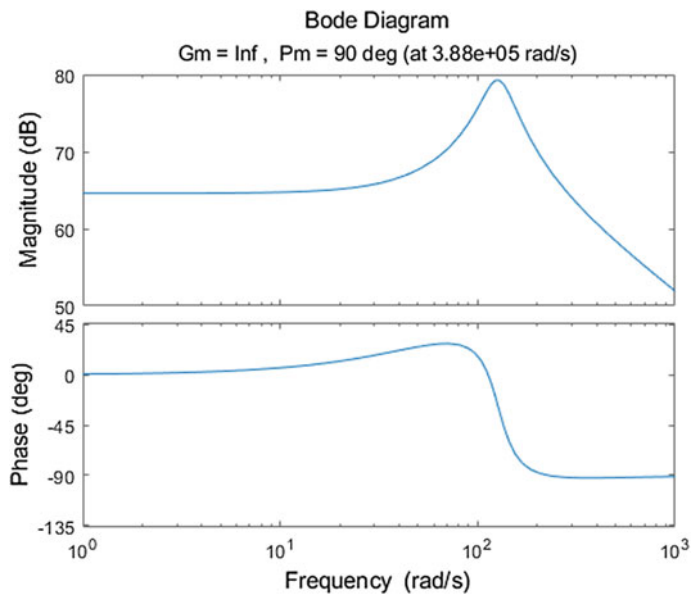


**Fig. 11** Bode diagram of  $G_{il,d}(s)$

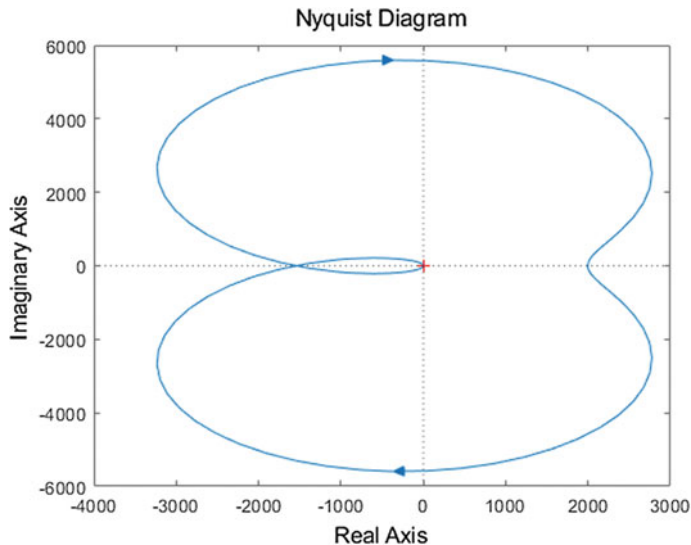


**Fig. 12** Nyquist curve of  $G_{vd}(s)$

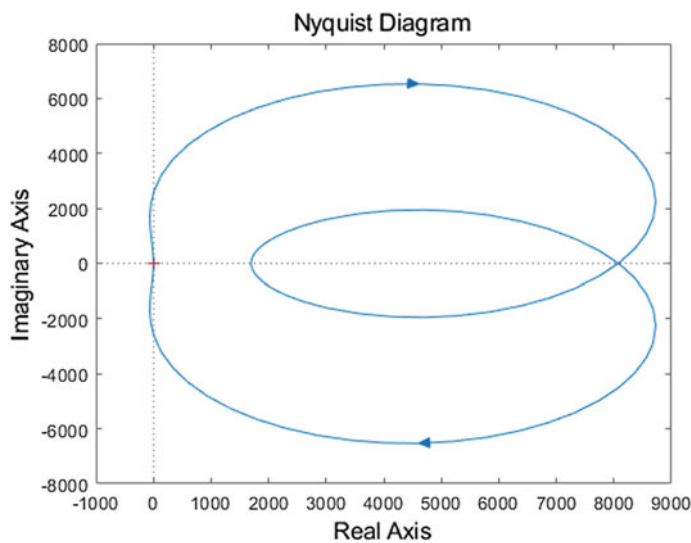


**Fig. 13** Nyquist curve of  $G_{iLd}(s)$

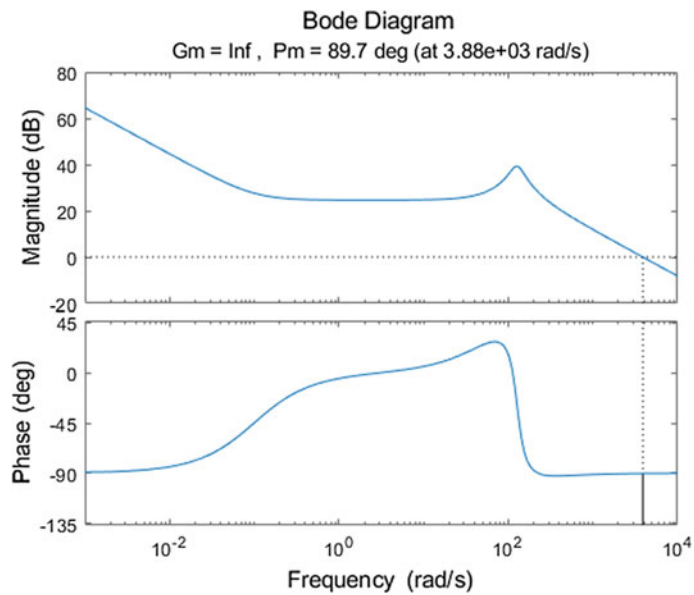


**Fig. 14** Bode diagram of  $G_{ic}(s)$

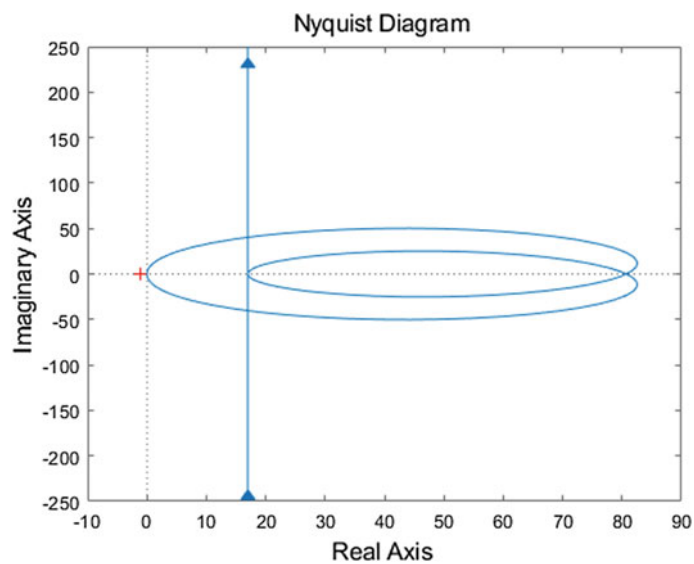


**Fig. 15** Nyquist curve of  $G_{ic}(s)$

According to Fig. 14, the amplitude margin is infinite, and the phase angle margin is  $89.7^\circ$ . The Nyquist curve does not include the point  $(-1, j0)$ , so the control system is stable.

Furthermore, this function can be approximately equivalent to a proportional link, which is used as part of the voltage loop to participate in the calculation. The expression of the open-loop transfer function  $G_{vo}(s)$  of Boost converter voltage outer ring is as follows:

$$G_{vo}(s) = G_c(s)G_{vd}(s) = G_v(s)G_{ic}(s)G_{vd}(s) \quad (20)$$

The Bode diagram and Nyquist curve of the open-loop transfer function  $G_{vo}(s)$  of the current loop are depicted in Figs. 16 and 17 where  $K_{vp} = 1/1200$ ,  $K_{vi} = 1/50$ .

It can be seen from Fig. 16 that the amplitude margin is 35.2 db, the phase angle margin is  $89.6^\circ$  and the Nyquist diagram does not include  $(-1, j0)$ . The system is stable. Compared with the current loop, the response speed of the voltage loop is slow, and the overall double closed-loop system is stable.

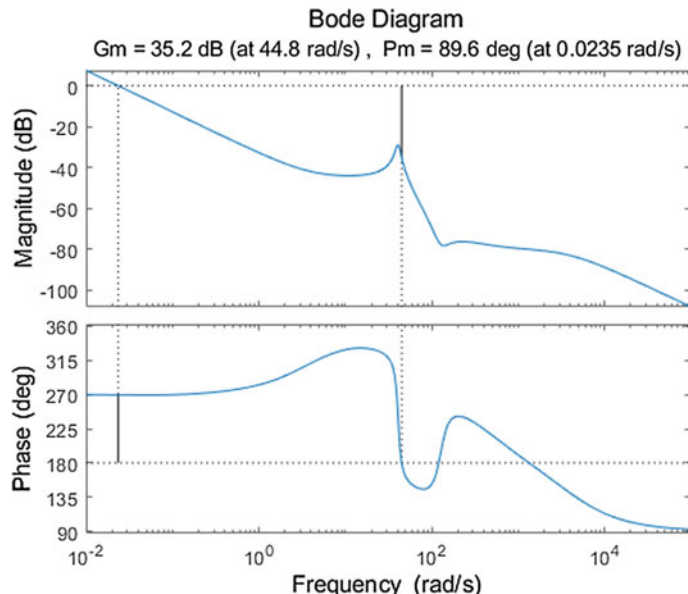


**Fig. 16** Bode diagram of  $G_{vo}(s)$

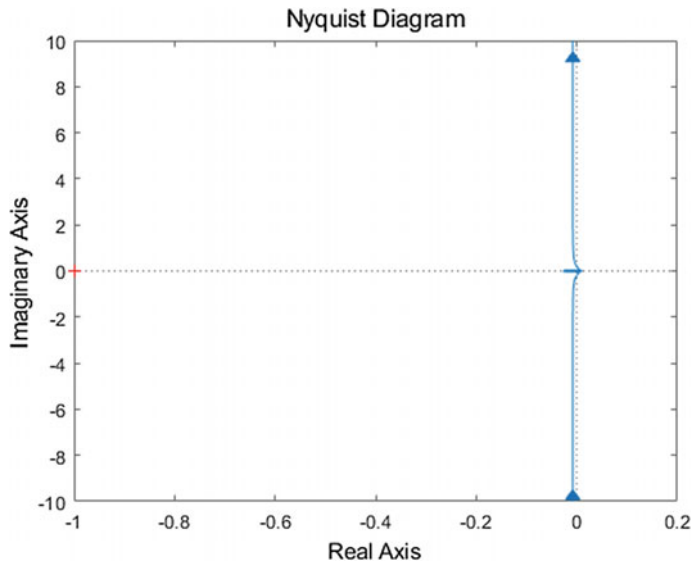


**Fig. 17** Nyquist curve of  $G_{vo}(s)$

## 5 The influence of DC capacitor C on closed-loop stability in Boost mode

Keep the inductance value  $L = 4\text{mH}$ , and the capacitance  $C$  (unit: mF) take 4, 8, 16, and 32 respectively. The corresponding input and output impedance Bode diagram and Closed loop impedance ratio Nyquist diagram are as follows (Fig. 18):

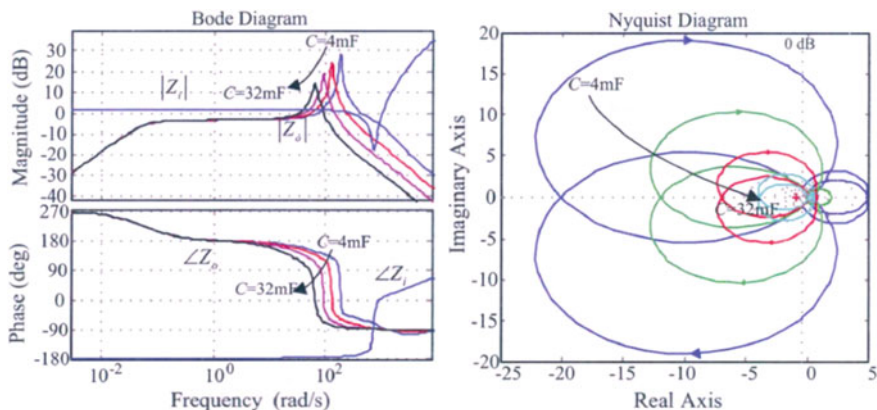


**Fig. 18** Closed-loop output impedance input/output impedance diagram and Closed loop impedance ratio Nyquist diagram

According to the impedance Bode diagram, as the capacitance C becomes larger, Amplitude-frequency curve of the closed-loop output impedance of the Boost con-verter and the curve resonance frequency decreases and amplitude decreases. The area where it intersects with Z becomes smaller and Closed loop impedance ratio Nyquist diagram moving to the right gradually means that the capacitance value increases and the cascade system tends to be stable.

## 6 Conclusion

In this paper, a half-bridge bidirectional Buck–Boost DC/DC converter is taken as the main research object. It mainly completes the mathematical modeling of Boost and Buck modes of bidirectional DC/DC converter. Moreover, the analysis of the open-loop and closed-loop design in Boost mode of bidirectional DC/DC converter is completed, and the results show that the designed double closed-loop control constitutes a control system with fast response speed in the inner loop and stable performance in the outer loop. Finally, analyze the influence of DC capacitor C on closed-loop stability in Boost mode the closed-loop stability of the system using the Bode diagram and Nyquist diagram of the closed-loop impedance.

## References

1. Phetphimoon W, Bhumkittipich K (2016) Modeling and simulation of bidirectional half bridge dc-dc converter. In: International conference on electrical engineering/electronics. IEEE
2. Cheng X (2009) Modeling and simulation of nonideal DC-DC converter. HeFei University of Technology, pp 1–77 (in chinese)
3. Gong J, Liu W, Xie S (2010) Modeling and stability analysis of bidirectional DC/DC. Comput Sci 27(10):263–267 (in chinese)
4. Wang YX, Qin FF, Kim YB (2015) Bidirectional DC-DC converter design and implementation for lithium-ion battery application. 2014 IEEE PES Asia-Pacific power and energy engineering conference (APPEEC). IEEE, 2015
5. Ouyang C (2004) Analysis and study on modeling of DC-DC switching converter. Nanjing University of Aeronautics and Astronautics, pp 1–172 (in chinese)
6. Luo Y (2013) Research on the bidirectional DC/DC converter and the battery energy management system. Huazhong University of Science and Technology, pp 1–72 (in chinese)
7. Kumar BV, Singh RK, Mahanty R (2017) A modified non-isolated bidirectional DC-DC converter for EV/HEV's traction drive systems. In: IEEE international conference on power electronics. IEEE, 2017
8. Liang X (2018) Research on control strategy of multiple bidirectional Buck/Boost Converter. North China University of Technology, pp 1–96 (in chinese)
9. Zhifu W, Yupu W et al (2016) Design of closed-loop control system for a bidirectional full bridge DC/DC converter. Appl Energy 194
10. Diao L, Du H, Shu Z, Xue Y, Li M, Sharkh SM (2018) A Comparative study between AI-HM and SPD-HM for railway auxiliary inverter with pulsating DC link. IEEE Trans Ind Electron 65(7):5816–5825

# Research on Energy Configuration and Characteristics of Hybrid EMU Power System



Yunxin Fan, Wang Li, Miaojin Jin and Qingmin Qin

**Abstract** From the perspective of the whole vehicle, this paper introduces the main technical parameters, operation characteristics, analyzes energy requirements of the system through traction calculation, carries out the capacity allocation of hybrid power and selection of key components and configures the capacity of two core components of the system, diesel generator set and power battery pack. Then, according to the structure, output characteristics and fuel consumption of diesel generator set, the uniform function of drooping output voltage and fuel consumption curve at different speed and power of diesel generator set are established. The parameters, characteristics and SOC zonal operation diagram of power battery pack are briefly introduced.

**Keywords** Hybrid EMU · Diesel generator set · Power battery pack

## 1 Introduction

With the increasing awareness of sustainable development, the research on new rail transit vehicles is deepening [1, 2]. The concept of hybrid power first appeared in the automotive industry. Since the 1990s, this concept has been used for reference in the field of rail transit. In the mainstream conceptual design of the hybrid EMU, the hybrid power system is composed of diesel generator set and energy storage components. At the same time, the maximum fuel economy and optimal energy recycling are realized by means of the optimal management and rational distribution of energy. For hybrid power systems, reasonable energy calculation and capacity allocation are important prerequisites for system design and economic operation. In addition, in-depth study on the characteristics of key components will help to adopt

---

Y. Fan (✉) · W. Li · M. Jin · Q. Qin

The State Key Laboratory of Heavy-Duty AC Drive Electric Locomotive Systems Integration, CRRC Zhuzhou Locomotive Co., Ltd., Zhuzhou 412001, Hunan, China  
e-mail: [fan\\_yunxin@126.com](mailto:fan_yunxin@126.com)

appropriate energy management and coordination strategies according to the characteristics of each subsystem, so as to achieve the overall optimization of efficiency, energy consumption and environmental protection.

## 2 Energy Configuration of Hybrid EMU

### 2.1 Operation Characteristics of Hybrid EMU

Hybrid EMU adopts the form of two-motor-one-trailer (2M1T). Each motor vehicle is equipped with a set of hybrid power system including power battery pack and diesel generator set, a set of traction converters and four motors. Each trailer is equipped with dual auxiliary converters. The major technical indicators are shown in Table 1 [3].

From the start-stop process, the operation of the train can be divided into three stages according to the traction state, which are traction, idling and braking. The typical operation diagram is shown in Fig. 1.

### 2.2 Energy Requirements of Hybrid EMU

In order to make a reasonable energy configuration of hybrid power, the energy requirements of the system should be firstly defined. According to the main performance indexes and characteristic curves of the train, the traction calculation is carried out by using EXCEL sheet. The calculation step length is 0.01 s, and the power and energy requirements of the vehicle in traction, idling and braking

**Table 1** Major requirements and parameters of hybrid EMU

Requirements	Parameters
Group form	2M1T
Car weight	240t
Design speed	120 km/h
Maximum traction	106 kN
Maximum braking force	105 kN
Maximum motor power	160 kW*4*2
Motor efficiency	0.9
Inverter efficiency	0.98
Unidirectional DC-DC efficiency	0.95
Rated capacity of auxiliary converter	100 kVA*2
Station spacing reference value	15 km

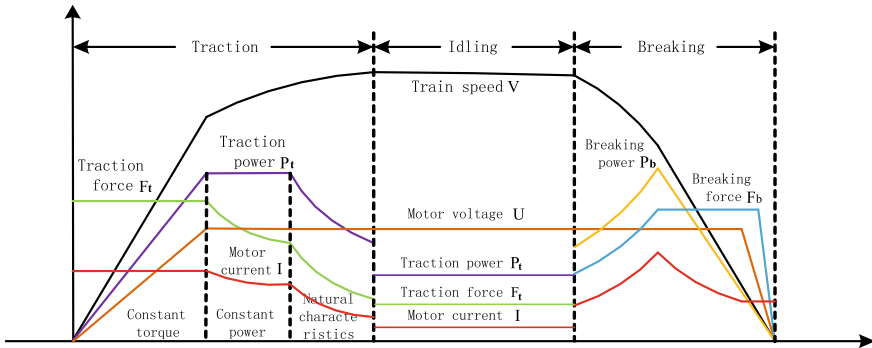


**Fig. 1** Operating characteristics curve of hybrid EMU

**Table 2** Energy requirements in different operating cycle of hybrid EMU

Performance indexes	Parameters			
	Traction	Idling	Breaking	Station stop
Energy source	Diesel generator set/power battery pack	Diesel generator set/power battery pack	Regenerative braking energy	Power battery pack/diesel generator set
Peak power	838.72 kW	212.16 kW	-509.13 kW	85 kW
Operation time	120.37 s	340.05 s	66.67 s	120 s
Running mileage	2.554 km	11.335 km	1.111 km	0
Total energy consumption in the process	24.12 kWh	21.02 kWh	-7.78 kWh	2.83 kWh

operation interval and when stopping at the station can be obtained. By calculation, the energy requirements of each stage of the vehicle operation interval are shown in Table 2. The corresponding formulas are as follows:

$$F_r = 0.000755 * m * g + 120.344 * (v + v_w) + (v + v_w)^2 \quad (1)$$

$$P_o = P_{SIV} + \frac{4P_m}{\eta_m \eta_{inv}} = P_{SIV} + \frac{4F_m V}{\eta_m \eta_{inv}} \quad (2)$$

$$P'_o = \eta_{dcdc} (\eta_m \eta_{inv} P_{brk} - P_{SIV}) \quad (3)$$

where,  $F_r$  is the train running resistance,  $m$  is the train weight,  $v$  is the current train speed,  $v_w$  is the upwind speed of EMU, 15km/h,  $P_o$  is the output power of Hybrid power system,  $P_{SIV}$  is the power of auxiliary converter, 85kw,  $F_m$  is the traction force,  $V$  is the current speed,  $\eta$  is the efficiency of motor inverter and DC/DC converter,  $P'_o$  is the power absorbed by energy storage system,  $P_{brk}$  is the regenerative braking power.

### 2.3 Capacity Configuration of Hybrid EMU

Usually, the power and energy requirements of hybrid EMU in the operating interval are defined by traction calculation. In the energy allocation between the sources of hybrid power system, the rated power of the diesel generator set is required to meet Eq. (1) according to the principle that the energy of the energy storage system in the cyclic operating interval (without considering the stop) is generally unchanged.

$$P_{\text{gen}} \geq k \times \frac{W_T}{t_{\text{gen}}} = 1.2 \times \frac{39.36 \text{ kWh}}{477.08 \text{ s}} = 338 \text{ kW} \quad (4)$$

Where  $P_{\text{gen}}$  refers to the rated power of the diesel generator set,  $k$  is the power margin, 1.2,  $W_T$  means total energy consumption of the train in a single cycle,  $t_{\text{gen}}$  is the operation time of diesel generator set in a single cycle.

According to the traction calculation, and considering the complexity of the actual running conditions of the train, when the battery capacity is configured, it is necessary to consider four times the braking energy margin and two times the traction energy margin, so that the minimum capacity of the power battery pack is 50.3 kWh, and the maximum charging and discharging power is about 510 kW. The capacity and power requirements of the power battery pack are shown in Table 3.

## 3 Research on Characteristics of Diesel Generator Set

### 3.1 Basic Structure of Diesel Generator Set

The diesel generator set studied in this paper adopts a permanent magnet synchronous generator and uses a diode uncontrolled rectifier bridge to rectify and output DC voltage. They form the diesel generator power supply system, and its structure is shown in Fig. 2.

With a rated power of 345 kW, a continuous running power of 200–330 kW, and an engine speed of 600–2000 RPM (Round Per Minute), the RailPack 400DE of German VOITH company is used as a diesel generator set. The effective output voltage is 500–1350 V, which meets the system requirements.

**Table 3** Power and energy requirements of battery

Design requirements	Parameters
Maximum charging power	-509.13 kW (66.67 s)
Maximum discharging power	507.14 kW (120 s)
Minimum capacity requirement	50.3 kWh

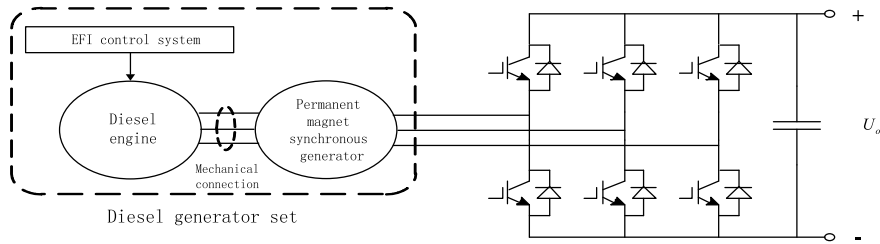


**Fig. 2** Schematic diagram of diesel generator power supply system

### 3.2 Drooping Output Characteristics of Diesel Generator Set

The no-load voltage and maximum available power of DC side at different rotational speeds are obtained through the characteristic experiment of diesel generator set. The experimental data are plotted as a curve as shown in Fig. 3. The following two conclusions are drawn:

1. The DC side no-load output voltage of diesel generator set is approximately proportional to the diesel engine speed.
2. The maximum available power of diesel generator set is approximately proportional to the square of diesel engine speed.

In this paper, indirect control of output power is carried out by using droop characteristics of diesel generator set. The droop characteristic is that the DC output voltage decreases with the increase of the output power, which can be described by the following formula,

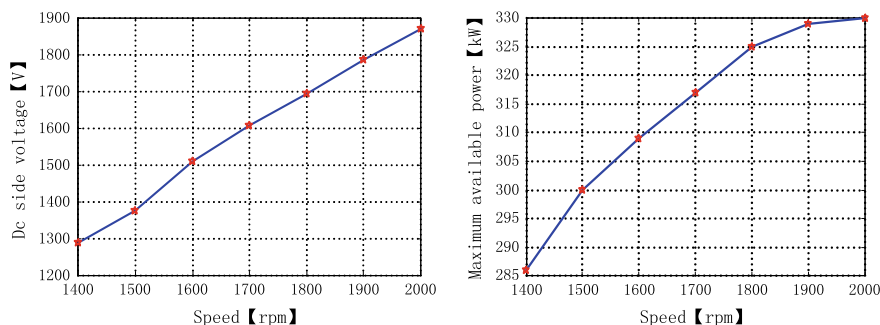


**Fig. 3** No-load voltage and power limit versus speed of diesel generator set

$$U_{dc} = U_{dco} - k_{dp} \cdot P_{dc} \quad (5)$$

where  $U_{dco}$  is the no-load voltage on dc side,  $k_{dp}$  is the drooping slope,  $P_{dc}$  is the output power on rectifier bridge side.

After comprehensive consideration, the uniform function of the fitting voltage droop curve is,

$$U_{dc} = U_{dco-2000 \text{ rpm}} \times \frac{\text{Speed}}{2000} - k_{dp}P_{dc} \approx 1832 \times \frac{\text{Speed}}{2000} - 0.4P_{dc} \quad (6)$$

Referring to the expression of voltage droop curve, the DC voltage at a certain power output can be predicted. Similarly, the output power at the current speed of the diesel generator set can be roughly calculated from the DC voltage. This principle can be used for subsequent energy management, and the output power of the diesel generator can be indirectly controlled by controlling the DC link voltage in the middle.

### 3.3 Fuel Consumption Analysis of Diesel Generator Set

The fuel consumption of diesel generator set is affected by its speed, torque and output power, etc., so it is necessary to estimate the fuel consumption according to its fuel consumption characteristic curve. We analyze the working state and fuel consumption under different working conditions, evaluate its power performance index and economic index, and seek the best operating interval according to the design of the working condition [4]. The fuel consumption curve of diesel generator set used in this paper is shown in Fig. 4.

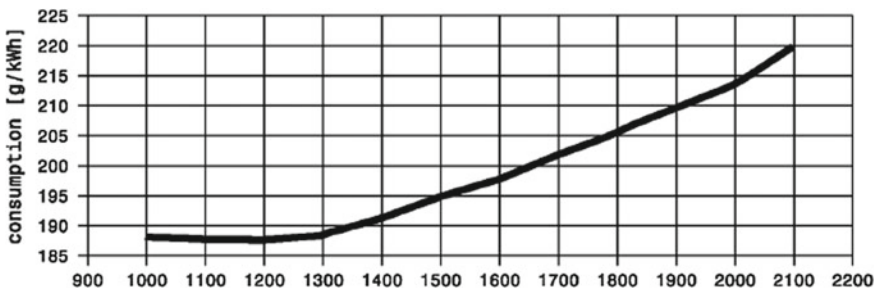


Fig. 4 Fuel consumption curve of diesel generator set

## 4 Research on Characteristics of Power Battery Pack

### 4.1 Selection and Grouping Parameters of Power Battery Pack

Combined with the requirements of high-power density, high cycle life span and quick charging and discharging performance of the energy storage system, lithium titanate battery was selected as the energy storage device of hybrid power. In practical application, this paper selects the way of 6P440S (6 in parallel and 440 in series), the minimum capacity of the battery pack is 51 Ah [5, 6]. The main technical parameters of lithium titanate battery are shown in Table 4.

### 4.2 Characteristics of Lithium Titanate Battery

After selecting the lithium titanate battery pack as the energy storage device of the hybrid EMU, the characteristics of the lithium titanate battery should be studied to establish the simulation model of the battery pack and facilitate the follow-up research work [7]. In the research process of this paper, the battery module built in MATLAB/Simulink was used to build the simulation model of lithium titanate battery pack. The actual performance parameters of lithium titanate power battery were selected as the simulation parameters, and the external characteristics of the battery pack were obtained as shown in Fig. 5.

**Table 4** Main parameters of lithium titanate battery

Indicators	Parameters
Battery pack configuration	6P440S (6 in parallel and 440 in series)
Rated voltage (V)	1012
Battery pack rated capacity (Ah)	51
Battery pack rated energy (kWh)	51.6
Energy density (Ah/kg)	80
Operating temperature (°C)	-25 to 50 °C
Nominal voltage	2.3 V
Charging cut-off voltage	2.8 V
Discharging cut-off voltage	1.5 V
Energy density	80 Wh/kg
Self-discharging rate	5%/month
Working temperature	-25 ~ 50 °C
Cycle times	≥ 10000

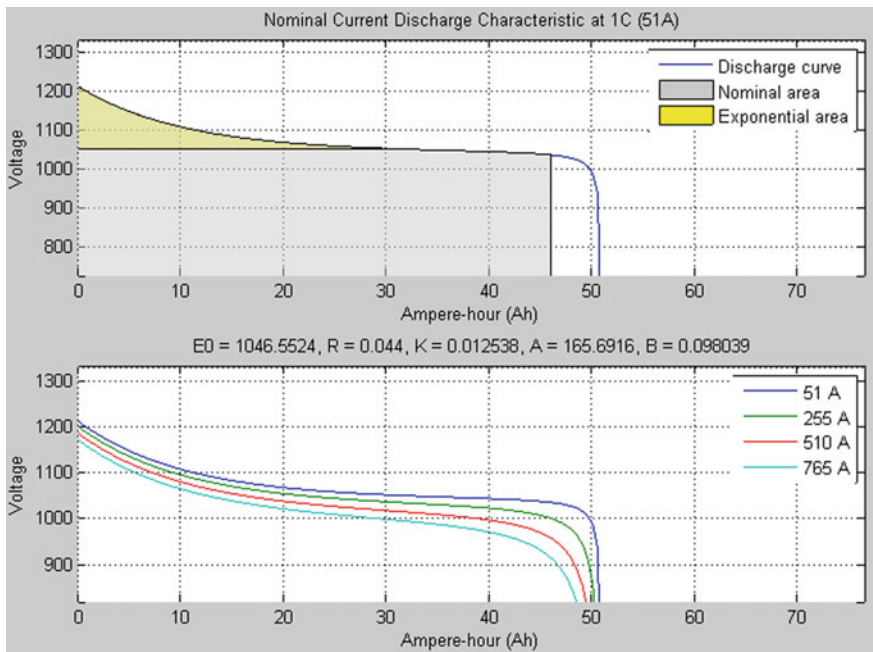


**Fig. 5** Characteristic curves of simulation model built in MATLAB/Simulink

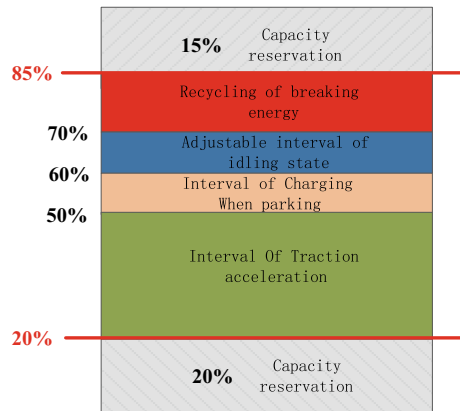
### 4.3 Analysis of Battery Working Mode

Known from the analysis of the lithium titanate battery characteristics above, when SOC of the lithium titanate battery is too low or too high, the terminal voltage changes violently and power of charging and discharging decreases rapidly, to ensure the operation stability and extend battery life, this article set the upper and lower limits of the battery pack's SOC in the process of research in advance and on the basis of maintaining the balance of battery SOC, combined with traction calculation and battery characteristics, we give the usage range for SOC a general reasonable planning. Firstly, the changes of main parameters of the power battery pack in each stage of vehicle operation are analyzed, as shown in Table 5.

**Table 5** Energy variation of hybrid EMU battery bank in different operating cycle

Operation conditions	Current (A)	Power (kW)	Change rate of SOC (%)
Hybrid traction	500	506	-25
Breaking	500	505	+14
Station stop	88	90	-5
Idling	85	86.4	+16

**Fig. 6** SOC operating zone of hybrid EMU battery pack



In practical operation, 15 and 20% allowance are reserved in the high and low SOC area of the lithium titanate battery pack, respectively, that is, to control battery pack work within the range of 20–85% SOC, and the upper and lower limit protection thresholds are 20 and 85% [8]. According to the SOC changes of battery packs in each stage of train operation in Table 5, the schematic diagram of battery SOC operation zones is shown in Fig. 6.

## 5 Conclusion

The main content of this paper is the research on the energy configuration and system characteristics of hybrid EMU. Firstly, the power and energy demand of the hybrid EMU in a single cycle operation interval is determined by traction calculation, and on this basis, the capacity configuration of the diesel generator set and the power battery pack is carried out. Then, the droop output characteristics and fuel consumption characteristics of diesel generator set are studied by selecting appropriate models and establishing simulation models. Finally, the selection and grouping parameters of the power battery pack are introduced. According to its charge-discharge characteristics and temperature characteristics, the SOC zonal operation diagram in line with the battery characteristics is developed to facilitate the further development of energy management and control strategy.

## References

1. Yinan K, Rui T (2012) Development of hybrid locomotives at home and abroad (part 1). Diesel Locomot 09:1–3 + 0–1 (in Chinese)
2. Yinan K, Rui T (2012) Development of hybrid locomotives at home and abroad (part 2). Diesel Locomot 10:1–4 (in Chinese)

3. Jia X (2015) Research on application of lithium battery energy storage system in hybrid emu. Beijing Jiaotong University (in Chinese)
4. Sun Y (2013) Research and simulation of coordinated control method of hybrid power crane based on PSCAD. Wuhan University of Technology (in Chinese)
5. Yanwei S, Xiaoguang T, zhou D-H et al (2012) The development of the power battery status quo and application. Value Eng 31(14):33–34. <https://doi.org/10.3969/j.issn.1006-4311.2012.14.018> (in Chinese)
6. Li H, Li Q, Wen J et al (2005) The application and development trend of power battery. J Henan Univ Sci Technol (Nat Sci Ed) 26(6):35–39. <https://doi.org/10.3969/j.issn.1672-6871.2005.06.011> (in Chinese)
7. Jin Z (2015) Research on energy flow control strategy of power system of hybrid powertrain. Beijing Jiaotong University (in Chinese)
8. Liu Y (2014) Research on stability control technology of dc bus interconnection of power electronic converter. Harbin Engineering University (in Chinese)

# Dynamic Imitation Real Platform of Urban Rail Transit Traction Power Supply System for PHM



Jianmin Wen, Kaikang Wang, Fei Ye, Bin He and Jiangtao Wu

**Abstract** Considering the importance of traction power supply system in urban rail transit, it is difficult to carry out prognostic and health management (PHM) experiments in traction power supply system. Therefore, a simulation platform of traction power supply system is constructed in this paper. The platform simulates various operating conditions and fault states of the traction power supply system by building a physical model of the traction power supply system of low-power rail transit. This paper mainly introduces the main structure and system design of the dynamic simulation platform, and by using the upper computer monitoring software to realize the function of vehicle-ground wireless communication, the train group in the system can run under different working conditions.

**Keywords** Urban · Rail transit · Traction power supply · Traction calculation · Simulation

## 1 Introduction

In order to conduct dynamic real-time simulation and fault simulation for train operation and scheduling [1], more and more universities and research institutes improve their research and design level by establishing the semi-physical simulation system of urban rail transit. For example, Junwei Qiu of Zhejiang University [1] and Luyao Li of Southwest Jiaotong University [2] have designed and implemented the hardware-in-the-loop simulation platform of train communication network control, and they studied the train's TCN network, gate control system, and traction system. Runze Zhang and Fei Lin et al. established a semi-physical real-time simulation experiment platform for the traction power supply system based on dSPACE-Xsim [3], which can simulate the running state of trains on

---

J. Wen (✉) · K. Wang · F. Ye · B. He · J. Wu

China Railway Siyuan Survey and Design Group Co., Ltd., 745 Peace Avenue, Yangyuan, Wuchang, Wuhan, Hubei Province, China

traction power supply system in real time and prepare for the development of train algorithm. It is an important tool for the reliability design and development of urban rail transit to simulate and test the actual or envisaged system online with the system model [4, 5].

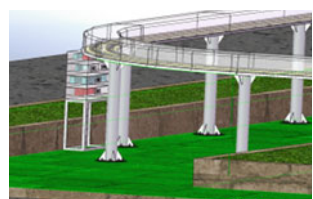
## 2 Design of Test Platform

The semi-physical simulation system has promoted the continuous development of the application field of urban rail transit to a certain extent [6], but it is unable to carry out system-level simulation test for the complex urban rail transit system, which is limited to a certain extent, and the simulation effect is slightly different from the actual system [7]. In addition, the semi-physical platform has difficulties in programming and integration of software and hardware platforms, so it can only verify the reliability of the control strategy and cannot judge the correctness of the new control strategy. The dynamic imitation real simulation platform for traction power supply of urban rail transit established in this paper is completely materialized in design, and it is designed in a certain proportion to the actual subway traction power supply system in terms of voltage level, power, transformer parameters, etc. The establishment of a low-power urban rail transit traction power supply system can provide a test platform for the control algorithm and further improve the accuracy of the simulation system.

### 2.1 System Composition of Platform

The scale of the dynamic imitation real platform is shown in Fig. 1. The conductor rails in the system are used for power supply, and there are five current rails on the track. The two most outwards are positive and negative DC voltage rails drawn from the traction substation, and the middle three are three-phase AC voltage rails drawn from the onboard transformer of the train group, as shown in Fig. 2. When the train group is running, electric energy is obtained from the DC conductive rail by means of brush, and the transformed AC energy is connected to the ground transformer through traction transformer and vehicle-mounted transformer, and finally connected to the AC power grid to form an energy ring network.

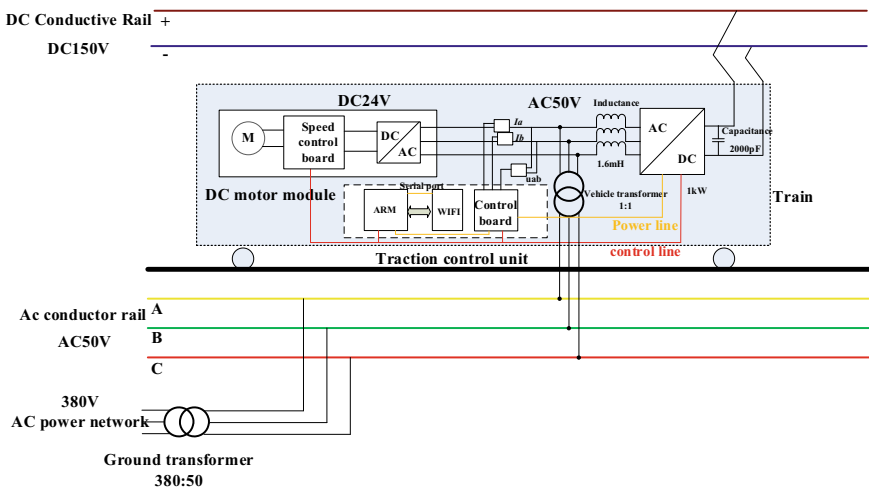
**Fig. 1** Scale of platform construction



**Fig. 2** Train conductor rail

### 2.1.1 Train Group System

The main substation, traction substation, and vehicle-mounted converter of the dynamic simulation platform for traction power supply of urban rail transit follow the design principles of consistent structure and equal proportion. The main substation of the platform is connected with 380 V voltage, and the medium voltage ring network voltage of 380 V traction power supply system is obtained through a transformer with a transformation ratio of 1:1 to supply power to the traction substations of the subway, wherein each traction substation consists of a rectifier unit module and an energy feeder module, and 150VDC voltage is output through voltage reduction and rectification to the subway contact network to realize direct current traction. The train group in the dynamic imitation real system adopts the way of grouping three carriages, and the system structure is shown in Fig. 3.

**Fig. 3** Diagram of train set with dynamic imitation true system

### 2.1.2 Vehicle-Ground Network Monitoring System

The schematic diagram of the vehicle-ground wireless communication platform of the system is shown in Fig. 4, which is mainly composed of a control computer, a traction control/communication module with ARM as the core, and a DC motor module. The traction control/communication module with ARM as the core in the dynamic simulation real system integrates STM32F103ZET6 processor, WIFI232 module, digital potentiometer, relay, and other key components, and the DC motor module consists of uncontrollable AC/DC converter, DC motor speed regulating board, DC motor, etc.

The upper computer software written on the control computer can realize continuous, fast, and large-capacity two-way data transmission between the lower computer control equipment with Wi-fi module based on vehicle-ground wireless communication. The upper computer software as the server sends train control instructions and traction calculation simulation results (train speed and traction power) to the development board with ARM as the core based on TCP/IP protocol. Through receiving train control instructions and train speed, the start-stop and up-down control of the train group of the dynamic simulation real system is realized, so that the train runs at different speeds. The received traction power is sent to the DSP control board in the train traction control unit through the serial port to obtain the corresponding traction current value, and the dynamic imitation real system judges the current running condition of the train according to the positive and negative values of the traction current and controls the rectification/inversion of the onboard converter, thus simulating the energy flow of the actual urban rail transit traction power supply under different working conditions.

### 2.1.3 Upper Computer Software Monitoring System

The PC software based on Visual C# has the following specific functions: According to the existing input conditions such as train information, passenger capacity, travel distance, and road conditions, and the simulation of train traction operation and the calculation of energy consumption are completed based on the comprehensive optimization control strategy of the train and output in the form of

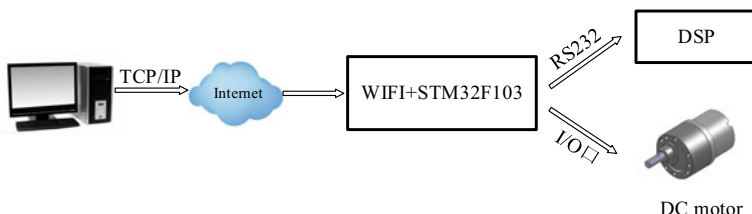


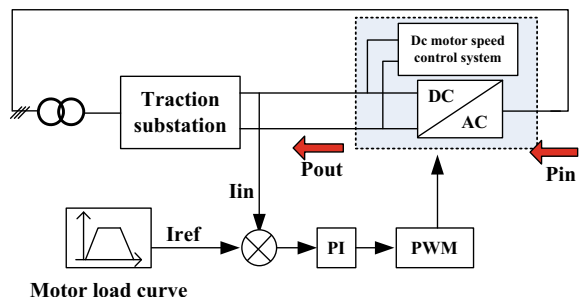
**Fig. 4** Schematic diagram of communication platform

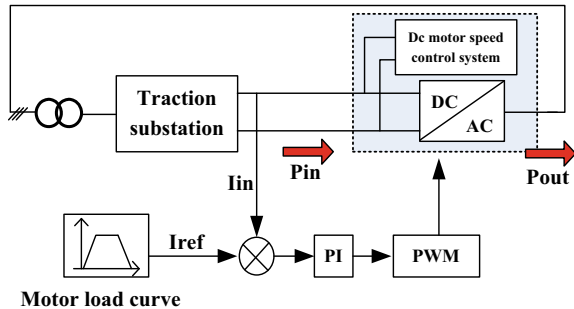
charts, with the function of data storage and result reproduction. At the same time, the train control instructions and traction calculation simulation results are sent to the lower computer control equipment based on TCP/IP protocol to control the start-stop and forward-reverse of the motor and make the motor run at different speeds to realize intelligent control of the real platform train group and simulate the energy flow of the traction power supply system of the actual urban rail transit under various working conditions (traction, inertia, and braking). The upper computer interface displays the dynamic position and road section of train group with dynamic simulation platform in real time, as well as the running condition, speed, and traction power of the current train. In addition, the train operation monitoring interface based on vehicle-to-ground wireless communication can realize two-way data transmission between vehicles and ground, receive and display voltage and current changes in key parts of main substation and traction substation, and form perfect human-computer interaction software. The specific functions of traction calculation and vehicle-to-ground wireless communication on the upper computer monitoring software are detailed in the third section of this paper.

#### 2.1.4 Simulation of Traction Power Supply System

In the power supply system of urban rail transit, there are three typical working conditions of trainload: traction, braking, and idling. The dynamic imitation real platform uses a three-phase four-quadrant converter to simulate the trainload. Under the traction conditions, the traction current is positive and the four-quadrant converter is inverted. The trainload current is fed back to the AC power grid by the four-quadrant converter, as shown in Fig. 5. Under the braking condition, the traction current is negative, the four-quadrant converter rectifies, and the energy flows from the four-quadrant converter to the DC traction network. The regenerative braking is simulated. The medium voltage energy feeder is started, and the energy is fed back to the AC network, as shown in Fig. 6.

**Fig. 5** Traction condition

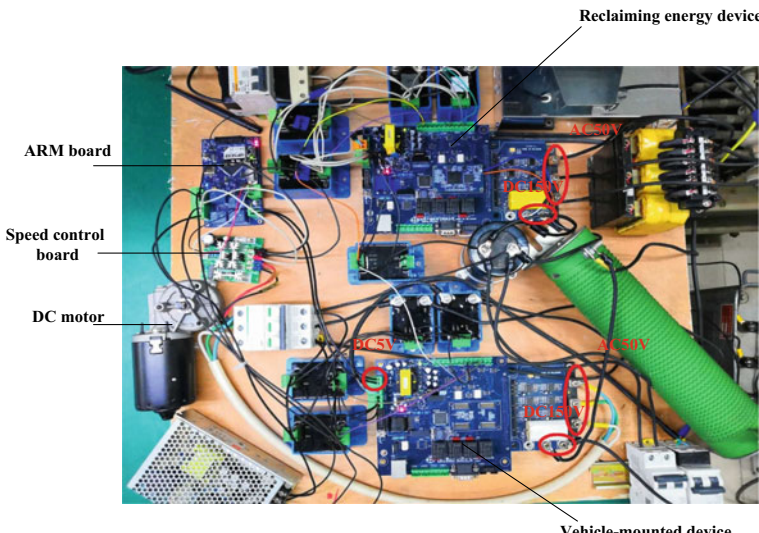


**Fig. 6** Braking condition

### 3 Platform Building

#### 3.1 Test Platform

The whole hardware circuit of the dynamic simulation real system is built as shown in Fig. 7. When the traction current sent by the upper computer software is positive and the train is in traction condition, the four-quadrant converter in the vehicle-mounted device converts the input voltage of DC150V on the conductive rail into AC50V output and supplies power to the DC motor through the inductor through the uncontrollable rectification output DC24V. The load current of the train is fed back to the AC grid by the four-quadrant converter, and energy flows into the locomotive from the traction grid. When the traction current is negative and the train is in braking condition, the four-quadrant converter of the onboard device

**Fig. 7** Hardware circuit platform

rectifies and the medium voltage energy feeder of the traction substation starts, the DC150V of the conductive rail is inverted into AC50V, the medium voltage ring network voltage of the 380 V traction power supply system is obtained through transformer boosting, and finally, the energy is fed back to the AC power grid, and the energy flows from the locomotive to the traction network. In terms of hardware design, both the vehicle-mounted device and the energy-fed device are four-quadrant converters, which can realize the two-way flow of energy, depending on the running condition of the train.

### **3.2 Upper Computer Software**

The upper computer monitoring software mainly has two major functions: traction calculation and train operation monitoring function based on wireless communication between the vehicle and the ground.

#### **3.2.1 Traction Calculation**

The train traction calculation function is mainly divided into three modules in design: data input module, calculation simulation module, and result processing module. According to the input information, the calculation and simulation of traction force, speed, and power during train traction operation are realized.

The data input of traction calculation mainly includes road information and train data, and the interface display is shown in Fig. 8. The software written has two login modes: administrator and user. If you log in as an administrator, you have the right to modify parameters.

The train traction calculation adopts a comprehensive optimization control strategy, and the operation principle is as follows. When the train is started, the maximum traction is adopted for traction and acceleration operation. When the speed of the train reaches the upper speed limit of the current road section, the train enters an intermediate stage, so that the train moves between the upper speed limit and the lower speed limit. When the train arrives at the station, the maximum braking force is used to decelerate the arrival.

The simulation results of traction calculation mainly include train speed, traction force, and traction power. The calculation output of the software has four output modes, and the specific output effects are shown in Fig. 9, respectively.

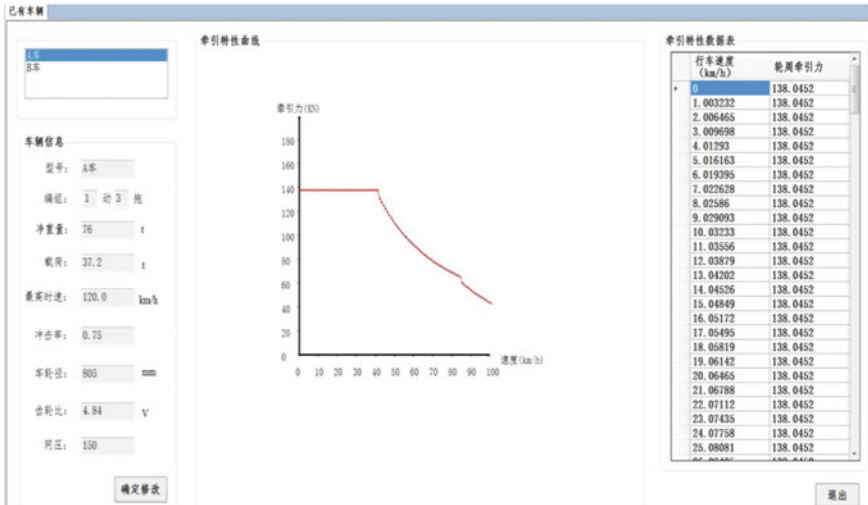
#### **3.2.2 Vehicle-Ground Wireless Communication**

The main interface of the upper computer software can be used to control the train group of the dynamic simulation real system, and the interface display is shown in Fig. 10. Select the running direction of the train on the interface, and click the

线路描述						
ID	行别	起点里程	坡度	长度	曲线半径	线路允许速度
1	上	0.000	-12.7	462.00	0.0	100.0
2	上	0.462	-3.0	22.00	0.0	100.0
3	上	0.484	-3.0	968.00	0.0	100.0
4	上	1.452	5.0	1122.41	0.0	100.0
5	上	2.574	5.0	379.59	2204.0	100.0
6	上	2.953	5.0	198.00	2204.0	100.0
7	站2	3.152	0.0	1.00	0.0	0.0
8	上	3.153	9.0	2700.00	2204.0	100.0
9	上	5.853	9.0	808.06	0.0	100.0
10	站3	6.661	0.0	1.0	0.0	0.0
11	上	6.662	11.5	1347.00	0.0	100.0
12	上	8.009	11.5	1182.36	2200.0	100.0
13	站4	9.191	0.0	1.0	0.0	0.0
14	上	9.192	12.7	1915.0	2200.0	100.0
15	上	11.107	12.7	138.45	0.0	100.0
16	上	11.246	12.7	282.06	2800.0	100.0
17	上	11.528	12.7	338.00	2800.0	100.0
18	上	11.866	12.7	455.00	2800.0	100.0
19	站5	12.321	0	1	0.0	0.0
20	上	12.322	12.6	817	0.0	80.0
21	上	13.139	12.6	1092.79	2000.0	80.0
22	上	14.232	12.6	302.66	0.0	80.0
23	上	14.535	12.6	1605.99	1605.5	80.0
24	站6	16.141	0	1	0	0.0
25	上	16.142	6.5	617	0.0	80.0
26	上	16.759	6.5	416.23	12000.0	80.0
27	上	17.175	6.5	135.75	0.0	80.0
28	上	17.311	5.1	475.20	0.0	80.0

打开文件  
 线路参数  
 路段: 路段1  
 里程: 0.484  
 坡度: -3.0  
 长度: 968.00  
 曲线半径: 0.0  
 线路允许速度: 100.0  
 确定修改  
 取出

(a) Line description interface



(b) Train information interface

Fig. 8 Data input module

“start” button, the train model on the track starts to run dynamically, and the table on the right shows the changes of electrical parameter values during the running of the train and the specific route information currently running in real time. At the same time, the traction calculation simulation results are sent to the lower computer control equipment based on socket network communication, so that the DC motor operates at different speeds, the rectification/inversion state of the traction converter is controlled, and the simulation function of urban rail transit traction p-power supply under different working conditions is realized.

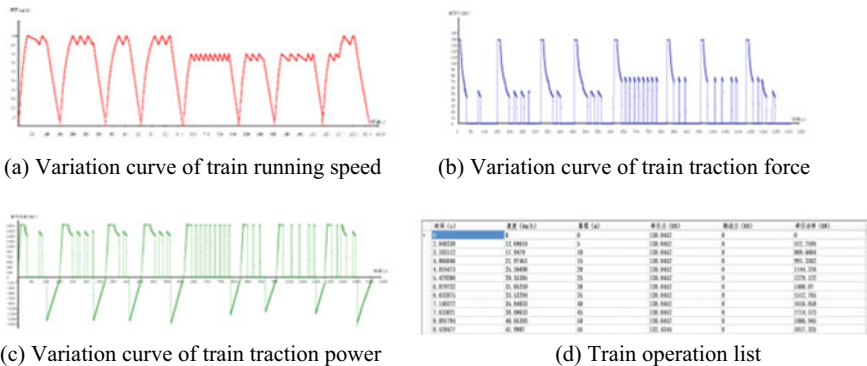


Fig. 9 Output of calculation results

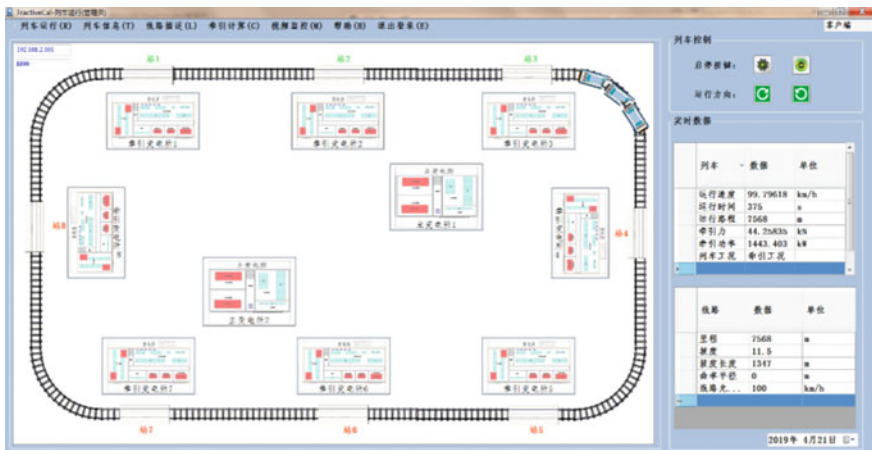


Fig. 10 Main interface

## 4 Conclusion

The dynamic simulation platform built in this paper is completely physical in design, which makes up for the deficiency of the hardware-in-the-loop simulation system and improves the accuracy of the simulation system. Through the coordination of the ground train control center, train model, traction power supply system, and the compiled upper computer software, it can completely simulate the urban rail train operation and station control and dispatching. Based on the train and line parameters, it can carry out dynamic simulation and fault simulation on the train operation and simulate various operating conditions and fault states of the actual traction power supply system of urban rail transit.

## References

1. Xu S (2017) Analysis of the development status and trend of traction control for rail transit vehicles. *Sci Technol Inf* 15(32):84–85 (in Chinese)
2. Guo Q, Kang J, Feng J et al (2017) Development status and trend of traction control for rail transit vehicles. *J Power Supply* 15(02):40–45 (in Chinese)
3. Yang Z (2013) Design of high-speed data acquisition and processing module based on CPCI bus. University of Electronic Science and Technology (in Chinese)
4. Yuan J (2005) Design and implementation of A/D module based on CPCI bus. *Comput Digital Eng* 129–133 (in Chinese)
5. Wei J (2018) Design and implementation of CPCI system based on FPGA. *Appl Electron Technol* 44(11):50–52+56 (in Chinese)
6. Wu R, Chou J, Liu T (2012) Development and application of Loongson 2GJ-based CPCI-bus board. In: Second international conference on Instrumentation, Measurement, Computer, Communication and Control (IMCCC)
7. Wang R, Zhang Y, Chen Y et al (2010) Design of CPCI interface based on data acquisition card of FPGA. *Electron Technol* 37(02):35–37 (in Chinese)

# Design Method of Fuzzy Controller for Speed Control of Heavy-haul Train



Jiao Dong, Youneng Huang and Huazhen Yu

**Abstract** The state of heavy-haul train in operation is variable because of some constraints, such as train weight, marshaling length, neutral section and so on; therefore, it is difficult for drivers to ensure the safety of train. To solve this problem, a design method of fuzzy controller is proposed to control the operation of heavy-haul train on gentle section. This method focuses on the structural characteristics of heavy-haul train and studies the influence of neutral section and line condition on train speed. Then, based on control theories and on-site driver's experience, a fuzzy PID controller is designed to better adapt to the changes of system parameters during train operation. Finally, the performance of controller is verified by simulation based on the actual line data and train marshaling information. The results prove that the controller is feasible and can control the heavy-haul train to run more securely and placidly.

**Keywords** Heavy-haul train · Speed controller · Fuzzy PID · Neutral section

## 1 Introduction

In China, one part of the heavy-haul railway line is in gentle section while the other part is in mountainous section with large longitudinal change. The difficulty of controlling the train on the gentle section increases because of series of restrictions such as the train weight, marshaling length, speed limits and neutral sections, a slight negligence may lead to overspeed, and so the driver works intensively. While on the mountainous section, the driver must implement air braking for several times

---

J. Dong (✉) · Y. Huang · H. Yu

School of Electronic and Information Engineering, Beijing Jiaotong University,  
Beijing, China

e-mail: [jiaodong@bjtu.edu.cn](mailto:jiaodong@bjtu.edu.cn)

Y. Huang

National Engineering Research Center of Rail Transportation Operation and Control System,  
Beijing Jiaotong University, Beijing, China

to prevent the train from overspeeding. However, the nonlinear characteristics of air braking pose a great challenge to ensure the safety of train. Therefore, it is of great significance to study the speed control strategy of heavy-haul train to lighten the labor intensity of drivers and ensure the driving safety.

At present, the researches on heavy-haul train mainly focus on the optimization of operation [1, 2], braking characteristics [3, 4] and longitudinal dynamics [5–7], while there are few researches on the speed tracking control. At the same time, compared with high-speed train and urban rail train, the heavy-haul train has obvious differences. In terms of structure, heavy-haul train has heavy load and long length. In the braking mode, air braking and electric braking are commonly used. In addition, its operation lines are long and the conditions are poor, and the train is also greatly affected by the neutral section. Consequently, the existing speed control methods of high-speed train [8, 9] and urban train [10] are difficult to directly apply to the heavy-haul train.

In this paper, the speed control of the heavy-haul train on gentle section is studied. The longitudinal movement model of train on gentle section is established by simplifying each locomotive and vehicle into a particle. Considering the influence of line condition and neutral section, a design method of fuzzy controller is proposed, and the validity of the controller is verified based on actual railway line.

## 2 Dynamic Model of the Heavy-haul Train

The heavy-haul train is composed of a series of locomotives and vehicles. Along the running direction, the train is subjected to traction force, braking force and operation resistance. If we simplify each locomotive and vehicle into a particle, the following equation can be established by the force analysis.

$$\begin{cases} m_1\ddot{x}_1 = F_{d1} - F_{h1} - F_{z1} \\ m_2\ddot{x}_2 = F_{d2} + F_{q2} - F_{h2} - F_{z2} \\ \vdots \\ m_n\ddot{x}_n = F_{dn} + F_{qn} - F_{hn} - F_{zn} \\ \vdots \\ m_N\ddot{x}_N = F_{dN} + F_{qN} - F_{zN} \end{cases} \quad (1)$$

where  $N$  is the total number of locomotives and vehicles,  $m_n\ddot{x}_n$  is the resultant force of the  $n$ th vehicle,  $F_{dn}$  is the traction/electric braking force of the  $n$ th vehicle,  $F_{qn}$  is the action force of the  $n-1$ th vehicle on the  $n$ th vehicle, namely the front coupler force,  $F_{hn}$  is the rear coupler force and  $F_{zn}$  is the operation resistance of the  $n$ th vehicle that mainly includes basic resistance, additional resistance of slope, additional resistance of curve and additional resistance of tunnel.

In the longitudinal movement model,  $F_d$  represents the traction/electric braking force that acts merely on the locomotive. Its size is related to the traction force and electric braking characteristic curve, and it is decided by the current speed of the locomotive and the level of the joystick (or the using coefficient of traction/electric braking force), i.e.,

$$F_d = f(\eta, v) \quad (2)$$

where  $\eta$  is the level of the joystick or the using coefficient of traction/electric braking force and  $v$  is the running speed of the locomotive.

If the locomotive speed is  $v_t$  at time  $t$  and the using coefficient of traction force is  $\eta_t$ , the calculation formula of traction force is as follows:

$$F_{dt} = \eta_t \cdot \left( F_1 + \frac{(v_t - v_1)(F_2 - F_1)}{v_2 - v_1} \right) \quad (3)$$

where  $(v_1, F_1)$  and  $(v_2, F_2)$  are two points on the tractive characteristic curve and  $(v_t, F_{dt})$  is located between them.

The unit's basic resistance is:

$$f_0 = a + bv + cv^2 \quad (4)$$

where  $a$ ,  $b$  and  $c$  are the basic resistance coefficients that depend on the type and structure of vehicle.

The additional resistance varies with the change of train's location:

$$f_a = \frac{\sum i_i l_i + 600 \sum \frac{l_{cp}}{R_{cp}} + \sum w_{sq} l_{sq}}{L} \quad (5)$$

In the above equation,  $L$  is the length of the train,  $i_i$  and  $l_i$  are the slope and length of the  $i$ -th ramp covered by the train, respectively,  $R_{cp}$  and  $l_{cp}$  are the radius and length of the  $p$ -th curve, and  $w_{sq}$  and  $l_{sq}$  are the unit additional resistance and length of the  $q$ -th tunnel.

### 3 Research Method

#### 3.1 Influence Factors of Train Operation

The heavy-haul train is affected by many external factors in operation, so the state of the train changes greatly. Combined with the structure and operation characteristics of heavy-haul trains, the following influencing factors should be taken into account in the design of the controller.

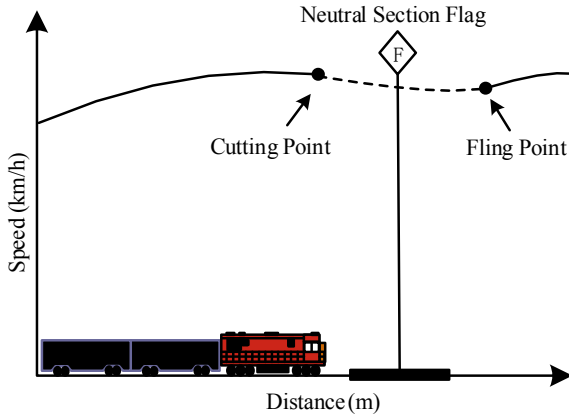


**Fig. 1** Diagram of heavy-haul train passing through the neutral section

### (1) Neutral section

Figure 1 shows the manipulation process of heavy-haul train passing through the neutral section. Before entering the neutral section, the current of the train is cut off to release the traction force and electric braking force. That is to say, the controller stops exporting the corresponding control quantity when the train is in the neutral section. After coasting through the neutral section and regaining the current, the controller is required to restore the steady state in time and continue to control the heavy-haul train to run at the exit speed of the neutral section.

### (2) Line condition

Due to the heavy load and long length, in addition to the traction force and electric braking force, the line slope also has a great influence on the train. Therefore, this vital factor should be taken into account in the design of the speed controller.

## 3.2 Design of the Fuzzy PID Controller

The speed of heavy-haul train is affected by the line slope, neutral section and other interference factors. If we want to get better control effect of the speed, the controller must have good adaptive ability. In this section, we design a fuzzy adaptive PID controller, the parameters of which can be adjusted dynamically with the change of train state.

Figure 2 illustrates the structure of the fuzzy PID controller, where the input of the PID controller includes the deviation  $e$  between the target speed and the actual speed, as well as the adjustment quantities  $\Delta K_p$ ,  $\Delta K_i$  and  $\Delta K_d$  of fuzzy controller to

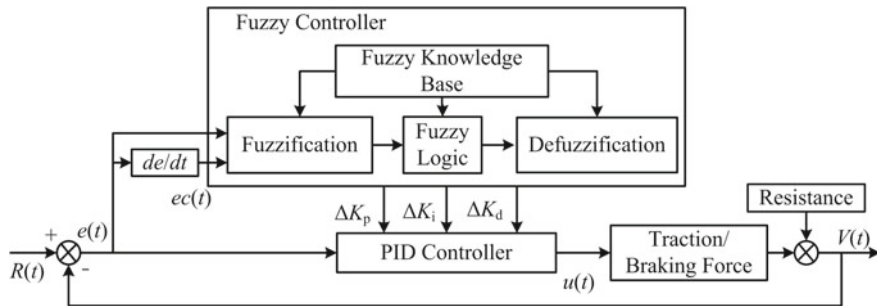


**Fig. 2** Structure diagram of the fuzzy PID controller

the proportional coefficient, integral coefficient and differential coefficient of the PID controller. The output  $u$  is the using percentage of traction/electric braking force.

The inputs  $e$  and  $ec$  of the fuzzy controller are firstly converted into fuzzy quantities by fuzzification, then the fuzzy sets of outputs  $\Delta K_p$ ,  $\Delta K_i$  and  $\Delta K_d$  are obtained by fuzzy logic, and finally, the clear values of three coefficient increments are obtained by defuzzification. Here, the domains of input quantities are set as  $[-3, 3]$ , and the domains of output quantities are  $[-10, 10]$ . The fuzzy subsets of the inputs and the outputs are set as {negative big ( $NB$ ), negative medium ( $NM$ ), negative small ( $NS$ ), zero ( $ZO$ ), positive small ( $PS$ ), positive medium ( $PM$ ), positive big ( $PB$ )}, and the types of membership functions are trimf. For instance, the membership function of  $e$  is shown in Fig. 3.

According to the requirements for the stability and rapidity of the control system of heavy-haul train, the main goal of the system is to eliminate the speed error when the error is relatively large, and in order to avoid overshoot, the system should give priority to maintaining stability when the error is small. Based on this principle and combined with the driving experience of on-site drivers, the fuzzy inference rules are summarized. Taking  $\Delta K_p$  as an example, its fuzzy control rules are given in Table 1.

**Fig. 3** Membership function of  $e$

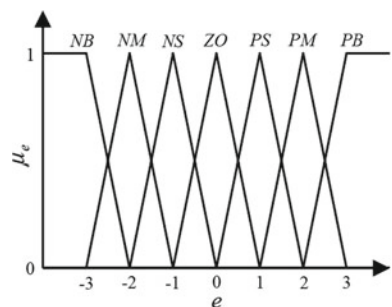


**Table 1** Fuzzy rules for adjusting  $\Delta K_p$ 

$\Delta K_p$		ec						
		NB	NM	NS	ZO	PS	PM	PB
<i>e</i>	NB	PB	PB	PM	PM	PS	ZO	ZO
	NM	PB	PB	PM	PS	PS	ZO	NS
	NS	PM	PM	PM	PS	ZO	NS	NS
	ZO	PM	PM	PS	ZO	NS	NM	NM
	PS	PS	PS	ZO	NS	NS	NM	NM
	PM	PS	ZO	NS	NM	NM	NM	NB
	PB	ZO	ZO	NM	NM	NM	NB	NB

After setting the target speed, the error  $e$  and the error rate  $ec$  are fed into the controller. By continuously monitoring the changes of  $e$  and  $ec$ , the fuzzy rules adjust the values of three parameters,  $K_p$ ,  $K_i$  and  $K_d$  of the PID controller in real time, so as to change the level of joystick or the using coefficient of traction/braking force to control the movement of the train. Finally, the using percentage of traction/electric braking force output by the controller is expressed as:

$$u(t) = K_p e(t) + K_i \sum_{j=0}^t e(j) + K_d [e(t) - e(t-1)] \quad (6)$$

where velocity errors  $e(t)$  and  $e(t-1)$  are obtained by the  $t$ -th and  $t+1$ -th sampling, respectively,  $e(t) = R(t) - V(t)$ ,  $R(t)$  is the target speed, and  $V(t)$  is the tracking speed.

Moreover, the parameters of the PID controller adjusted by the fuzzy controller are as follows.

$$\begin{cases} K_p = K_{p0} + \Delta K_p \\ K_i = K_{i0} + \Delta K_i \\ K_d = K_{d0} + \Delta K_d \end{cases} \quad (7)$$

in which  $K_{p0}$ ,  $K_{i0}$  and  $K_{d0}$  are the proportional, integral and differential coefficients of the pre-adjustment PID controller, respectively,  $\Delta K_p$ ,  $\Delta K_i$  and  $\Delta K_d$  are increments of these three parameters.

## 4 Case Study

### 4.1 Data Input

To verify the validity of the speed controller designed in this paper, we first establish the model of the speed tracking control system of heavy-haul train based on PID control method and fuzzy PID control method, respectively, by using the

**Table 2** Speed limit and slope information

Start position (m)	Slope (%)	Slope length (m)	Speed limit (km/h)	Start position (m)	Slope (%)	Slope length (m)	Speed limit (km/h)
0	-1.5	1650	45	16,150	3	600	80
1650	0	650	45	16,750	-2	800	80
2300	-0.5	950	45	17,550	3.5	1000	80
3250	-1	550	80	18,550	-4	520	80
3800	-2.5	800	80	19,070	-3	600	80
4600	1.5	750	80	19,670	0	850	80
5350	-2	650	80	20,520	-1	1080	80
6000	0	500	80	21,600	-2	910	80
6500	1	500	80	22,510	2	700	80
7000	0	500	80	23,210	-1	810	80
7500	-4	510	80	24,020	0	2190	80
8010	0	3100	80	26,210	-2.8	990	80
11,110	1.9	490	80	27,200	0	800	80
11,600	0.5	650	80	28,000	-2	1150	80
12,250	4	650	80	29,150	-0.5	600	80
12,900	0	1500	80	29,750	-2.5	500	80
14,400	-3	1200	80	30,250	1.5	700	45
15,600	-1	550	80	30,950	0	2640	45

simulation software. Then, the simulation test is carried out with the driving guidance curve from station A to station B as the tracking target. The speed limit and slope information of the line are given in Table 2.

## 4.2 Results Analysis

Input the driving guidance curve, speed limit, slope and neutral section information of the above line into control systems, the tracking effect is obtained as shown in Fig. 4, and the change rate of train acceleration is shown in Fig. 5.

It can be seen from Figs. 4 and 5 that the PID controller has a large tracking deviation in the cruise stage, and the change rate of train acceleration is large during the whole trip, which results in the large change of the longitudinal force inside the train and easily leads to the coupler fracture. By contrast, the fuzzy PID controller can track the target curve well in the traction stage, the cruise stage and the braking stage. Meanwhile, the train runs steadily throughout the whole process, which is conducive to reducing the longitudinal impulse inside the train and conforms to the on-site driver's control strategy.

For the further verification of the effectiveness of the fuzzy PID controller, we calculate the maximum absolute error ( $E_1$ ), the average absolute error ( $E_2$ ) and the

**Fig. 4** Tracking result of control system to target curve

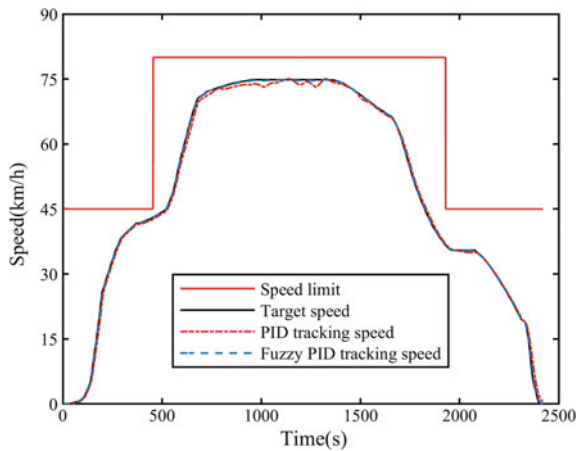
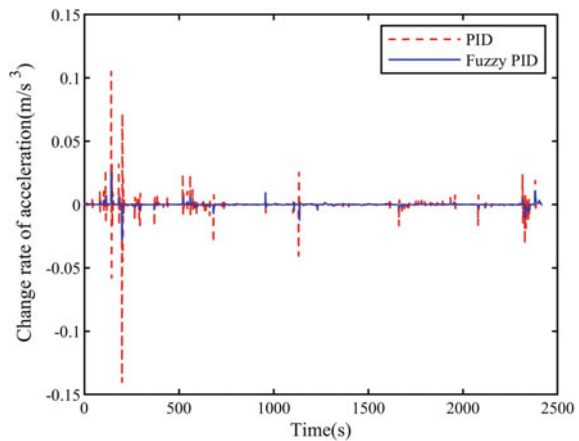


**Fig. 5** Change rate of train acceleration



root-mean-square error ( $E_3$ ) of two controllers, and Table 3 is a comparison of the differences between two controllers. From the table, under the control of the fuzzy PID controller,  $E_1$ ,  $E_2$  and  $E_3$  are 0.28 m/s, 0.02 m/s and 0.03 m/s, respectively. Compared with the PID controller, they are reduced by 0.82 m/s, 0.11 m/s and 0.14 m/s, respectively. Therefore, it can be seen that the control effect of the fuzzy PID controller is better.

**Table 3** Key performance indicators of controller

Indexes	PID controller	Fuzzy PID controller
$E_1$ (m/s)	1.1	0.28
$E_2$ (m/s)	0.13	0.02
$E_3$ (m/s)	0.17	0.03

## 5 Conclusion

Aiming at the speed control of heavy-haul train under the given target curve, a design method of fuzzy controller is proposed in this paper. Firstly, the structural characteristics of heavy-haul train are analyzed, the longitudinal movement model of train on gentle section is built by simplifying each locomotive and vehicle into a particle, and the traction force, electric braking force and running resistance are described mathematically. After that, the fuzzy PID controller is designed by considering the operation characteristics and the influence of neutral section and line condition on the train. Finally, combined with the results in Sect. 4, it can be seen that the controller designed in this paper meets the requirements, which provides technical support for the steady operation of heavy-haul train and better guarantee the driving safety of train.

**Acknowledgements** This work was supported by the China Railway Corporation Science and Technology Research and Development Project under Grant P2018X011, the scientific research projects of Shuohuang Railway Development Co. in 2019 and the Beijing Municipal Science and Technology Plan projects under Grant Z181100003918006.

## References

1. Huang Y, Tan L, Chen L, Tang T (2016) A neural network driving curve generation method for the heavy-haul train. *Adv Mech Eng* 8(5):1–14
2. Yang J, Jia LM, Lu SF, Li ZY (2016) Energy-efficient operation of electric freight trains-part I: speed profile optimization. *J China Railway Soc* 38(4):22–31 (in Chinese)
3. Wei W, Hu Y, Wu Q, Zhao X et al (2017) An air brake model for longitudinal train dynamics studies. *Veh Syst Dyn* 55(4):517–533
4. Afshari A, Specchia S, Shabana AA, Caldwell N (2013) A train air brake force model: car control unit and numerical results. *Proc Inst Mech Eng Part F: J Rail Rapid Transit* 227(1):38–55
5. Wu Q, Cole C, Luo S, Spiriyagin M (2014) A review of dynamics modelling of friction draft gear. *Veh Syst Dyn* 52(6):733–758
6. Chang C, Guo G, Wang J, Ma Y (2017) Study on longitudinal force simulation of heavy-haul train. *Veh Syst Dyn* 55(4):571–582
7. Sun SL, Ding JJ, Zhou ZY, Li F et al (2017) Analysis and test of heavy haul train longitudinal impulse dynamics. *J Mech Eng* 53(8):138–146 (in Chinese)
8. Dong HR, Gao B, Ning B, Zhang YX (2010) Fuzzy-PID soft switching speed control of automatic train operation system. *Control Decis* 25(5):794–796, 800 (in Chinese)
9. Ganesan M, Ezhilarasi D, Benni J (2017) Second-order sliding mode controller with model reference adaptation for automatic train operation. *Veh Syst Dyn* 55(1):1–23
10. Li ZQ, Yang H, Liu MJ, Liu JM (2016) Modeling and tracking control for braking process of high speed electric multiple unit. *China Railway Sci* 37(5):80–86 (in Chinese)

# Design of Wireless Data Transmission System for Vehicle Energy Storage Components Based on STM32



An Zhang, Yan kun Li, Yan ru Zhang, and Ding hong Chen

**Abstract** The calculation of the characteristics of energy storage components requires a large amount of historical data support, so it is necessary to store data for a long time and perform a large number of calculations; and the existing management system pursues high-precision, extremely simplified technical indicators, which cannot meet the demand. This design is based on ARM's STM32F105RCT6 interconnect chip, which is used as the core part of the embedded device. It is equipped with the GPRS module of SIM900 for the device networking communication part, realizing the function of transferring the data of the energy storage system to the background remotely and solving a large amount of data transmission, storage, calculation problems.

**Keywords** STM32F105 · GPRS · SIM900 · Embedded · Wireless transmission

## 1 Introduction

With the promotion and popularization of new energy technologies, a large number of new energy applications have emerged in the industrial field, in which energy storage components are an indispensable and important part, and monitoring of energy storage components has become necessary. In view of the decline of energy storage components and the calculation of failure modes, a large amount of data is

---

A. Zhang · Y. k. Li  
CRRC Qingdao Sifang Co., Ltd., Qingdao 266111, China  
e-mail: [zhangan.sf@crrcgc.cc](mailto:zhangan.sf@crrcgc.cc)

Y. k. Li  
e-mail: [liyankun.sf@crrcgc.cc](mailto:liyankun.sf@crrcgc.cc)

Y. r. Zhang · D. h. Chen (✉)  
School of Electrical Engineering, Beijing Jiaotong University, Beijing 100044, China  
e-mail: [17117408@bjtu.edu.cn](mailto:17117408@bjtu.edu.cn)

Y. r. Zhang  
e-mail: [yr\\_zhang@bjtu.edu.cn](mailto:yr_zhang@bjtu.edu.cn)

required, and the existing energy storage component management system (mainly battery management system, BMS) cannot store a large amount of data. Therefore, a GPRS wireless data transmission-embedded terminal device based on STM32 processor is designed. According to the Beijing standardization guidance technical document “DB11/Z 993.3-2013 Technical specifications of remote service and management system for electric vehicles Part 3: Communication protocol and data format of vehicle terminal” requirements, the data of the energy storage component is transmitted to the background server remotely, solving a large number of data transmission, storage, calculation problems [1, 2], and at the same time, the stability of the terminal is also realized, the disconnection is automatically reconnected, and the data is reissued [3–5].

The STM32 chip is one of ST’s mainstream products based on the ARM Cortex-M3 core designed for embedded applications requiring high performance, low cost and low power consumption. The STM32F105RCT6 is one of the interconnected chips and is the first in the STM32 family to integrate two CAN2.0B controllers, enabling developers to develop gateway devices that can connect two industry-standard Controller Area Network (CAN) buses. It is currently widely used in the industrial field. The SIM900 is a quad-band GSM/GPRS module in SMT package. The performance is stable, the appearance is small, the cost of data transmission is cost-effective, and it can meet the various needs of customers and is favored by engineers [6, 7].

This design is to realize the remote transmission of data through the use of STM32 microprocessor carrying SIM900 GPRS module, and the background server is equipped with the corresponding WEB monitoring interface to achieve real-time data monitoring.

## 2 System Design

The wireless data transmission system consists of an embedded terminal device and a background server. The embedded terminal device is mainly controlled by STM32, which realizes two functions of battery management system (BMS) data acquisition and remote data transmission. MCU will process the received BMS data and send it to the SIM900 module. SIM900 will package the data to be sent into a TCP/IP data packet, connect to the server on the Internet through the GPRS network and send the data to the server database [8]. The overall design block diagram of the system is shown in Fig. 1.

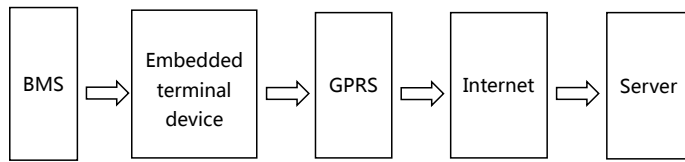


**Fig. 1** Schematic diagram of the system design scheme

### 3 Embedded Device Design

#### 3.1 Hardware Design

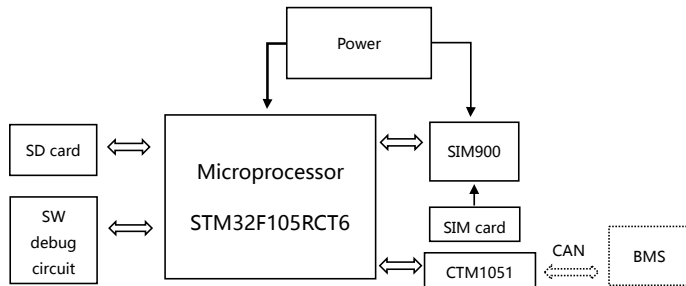
This design uses STM32F105RCT6 interconnected chip as the core processor of the device. SIM900 is used as the networking communication device, and CTM1051 isolated CAN transceiver of Zhiyuan Electronics Co., Ltd. is used to receive messages about the energy storage system information sent by the battery management system (BMS) from the CAN network. After the analysis and processing of the MCU, the data of the energy storage system shall be in accordance with the requirements of the Beijing standardization guidance technical document “DB11/Z 993.3-2013 Technical specifications of remote service and management system for electric vehicles Part 3: Communication protocol and data format of vehicle terminal”. It is packaged and uploaded to the background server through SIM900. The data of the energy storage component can be monitored in real time through the matching WEB interface or WeChat public number. If the energy storage component fails, the WEB monitoring interface and the WeChat public account will remind you and the SIM900 module can also send a text message to the preset mobile phone number to notify the relevant staff to process.

In addition, considering the application of the embedded terminal device and the energy storage system in the transportation field, the embedded terminal device is also equipped with an SD card, when the terminal device with the vehicle running to a place where there is no network signal or the network signal is weak, the energy storage component data can be stored locally, and the data is reissued to the server after waiting for the network to recover.

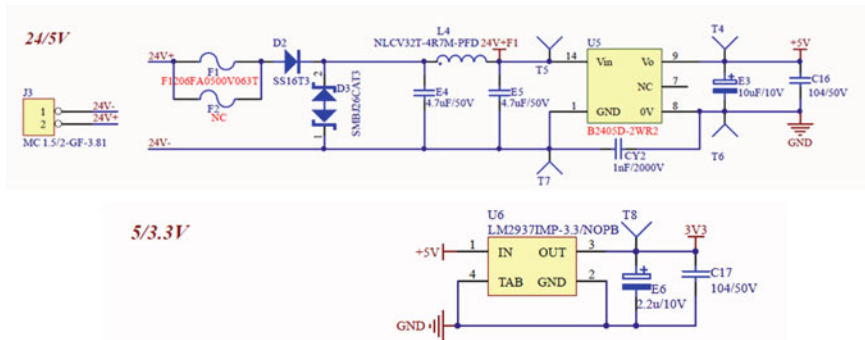
The overall hardware structure is shown in Fig. 2.

The dotted line indicates that the external device is connected to the terminal and is not a part of the terminal device (Fig. 3).

**Power module.** Considering that the power supply voltage of the embedded terminal in the vehicle environment is 24 V, but the STM32 microprocessor requires a 3.3 V supply voltage, and the SIM900 module operates at a voltage of 3.2–4.8 V, devices such as SIM cards and MOSFETs require a 5 V supply voltage, so it is necessary to supply power to each module separately. First, the 24 V vehicle power supply is stepped down to 5 V through the capacitor filter input B2405D, and then the 5 V voltage is converted to 3.3 V via the LM2937. The power supply circuit is as shown below:



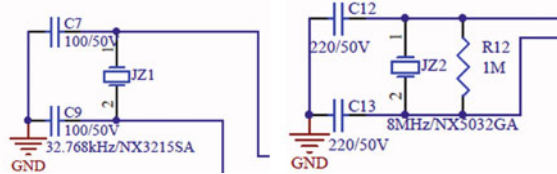
**Fig. 2** Embedded terminal device architecture



**Fig. 3** Power supply circuit diagram

**Microprocessor module.** For the processor of embedded terminal device, we adopt the STM32F105RCT6 chip, a high-performance, low-cost, low-power microcontroller based on the Cortex-M3 core. This type of MCU is an interconnected series in the STM32 family to integrate two CAN2.0B controllers, enabling developers to develop gateway devices that can connect two industry-standard CAN buses, which is suitable for this design scenario. Its pin package is LQFP64 package, the clock frequency is up to 72 MHz, it can realize high-speed operation, embed up to 256 KB flash memory, 64 KB static random access memory (SRAM), and peripherals are rich, there are four 16-bit timers, one 16-bit PWM timer, 2 watchdog timers and a 24-bit system time timer. It also has two I<sub>2</sub>C interfaces, 3 SPI interfaces, 5 USART serial ports and 2 CAN channels. The interface meets the requirements of this design.

The microprocessor relies on the 3.3 V output of the above LM2937 for power supply, and the external 32.768 kHz crystal oscillator is used for the RTC. The external 8 MHz crystal oscillator is used as the system clock and the PLL phase-locked loop input, which are, respectively, connected to the 3, 4 and 5, 6 pin of the chip. The clock circuit is shown in Fig. 4.

**Fig. 4** Clock circuit

According to the reference manual of STM32 [9], there are three start-up modes for the chip, as shown in the following Table 1.

When we burn the program, BOOT0 is 1 and BOOT1 is 0. After the program is programmed, BOOT0 is required to be 0, and BOOT1 can be arbitrarily 1 or 0 at this time. Therefore, BOOT1 is always grounded to simplify the circuit design; the start-up circuit is shown in Fig. 5.

The design uses the SWD download circuit to download and debug the software. The circuit is shown in Fig. 6.

Considering the use environment of the terminal device, the function may not be realized by using software reset. Therefore, the mode of button reset is adopted. To implement the reset function, the chip's NRST pin is required to be kept at a low level of not less than 20 microseconds, and its reset circuit is as shown in Fig. 7.

In conclusion, the circuit design of microprocessor STM32F105RCT6 is completed.

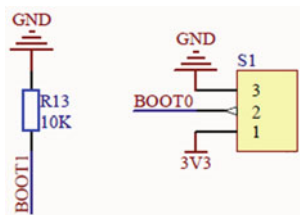
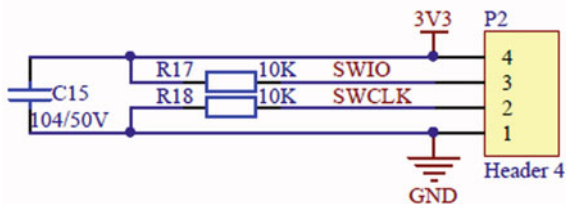
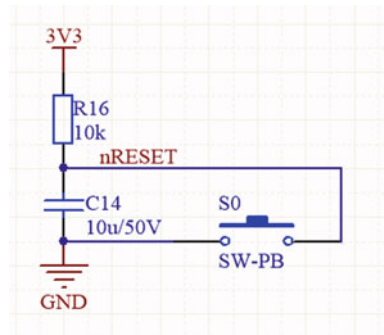
**SIM900 module.** This design uses SIM900 module of SIMCom company as a networked communication device. The SIM900 is a quad-band GSM/GPRS module that enables low-power voice, data and information transmission. It is small in size and relatively low in price. Through the AT command control operation, establish a TCP connection to the remote server, and send the corresponding AT command through the STM32 MCU to realize the control of the SIM900, so that the device can be remotely monitored.

The SIM900 module is mainly connected to the 15 and 16 pin of the microcontroller (i.e., USART2\_RX and USART2\_TX pin) via pin 9, 10 (i.e., TXD and RXD pin). The 10 pin (RXD) of SIM900 is used to receive data from the STM32 and send it through its antenna.

Considering that the SIM900's operating voltage is 3.2–4.8 V and the typical value is 4 V, the MP1593 chip of MSP is adopted in the design to supply 4 V DC separately for it, after weighing the practical and cost-effective. The MP1593 is a

**Table 1** Microprocessor start-up mode configuration

BOOT0	BOOT1	Start-up mode	Explain
0	X	User flash memory	Also known as flash start
1	0	System memory	For serial download
1	1	SRAM	For debugging code in SRAM

**Fig. 5** Start-up circuit**Fig. 6** Download circuit**Fig. 7** Reset circuit

step-down voltage stabilizer with internal power MOSFET. It achieves 3A continuous output current at a wide input power supply (4.75–28 V) to meet the SIM900's 2A peak current requirement. The schematic diagram of the circuit is shown in Fig. 8.

This design uses SIM card to connect with SIM900; the main use is the power line, data line, clock line and reset line of SIM card. The SIM card is powered by the SIM900, where the DATA line has been pulled up in the module, and its connection circuit is shown in Fig. 9.

**CAN module.** Controller Area Network (CAN) is a serial communication protocol bus used in real-time applications. It was first proposed and established by BOSCH in Germany in the 1980s and is used exclusively in the automotive industry.

The terminal device communicates with BMS through the CAN bus and receives the BMS message. On the CAN bus, the message is transmitted through the differential signal. Therefore, the CAN transceiver is needed. The performance of the CAN transceiver directly affects the communication quality of the system.

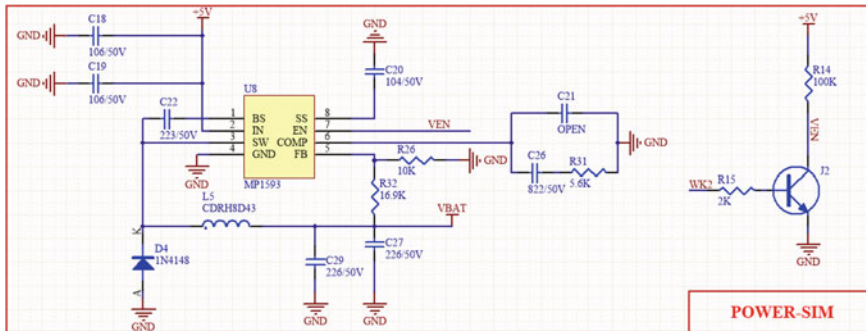
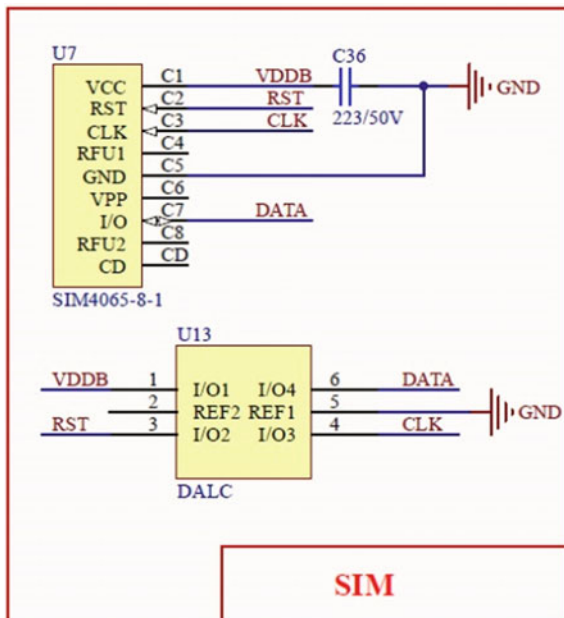


**Fig. 8** SIM900 power supply circuit

**Fig. 9** SIM card connection circuit



Considering that the terminal application is in the complex electromagnetic environment of electric vehicles and rail transit, this design uses the CTM1051 isolated CAN transceiver from Zhiyuan Electronics Co., Ltd. to improve the differential transmission capability of the bus and the differential acceptance capability of the CAN, thereby ensuring the accuracy and reliability of the data received by the terminal equipment; this is what design scheme in the existing literature does not have. The schematic diagram of the circuit is shown in Fig. 10.

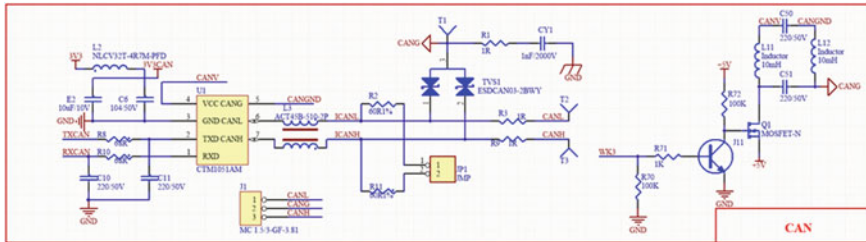


Fig. 10 Isolated CAN Transceiver

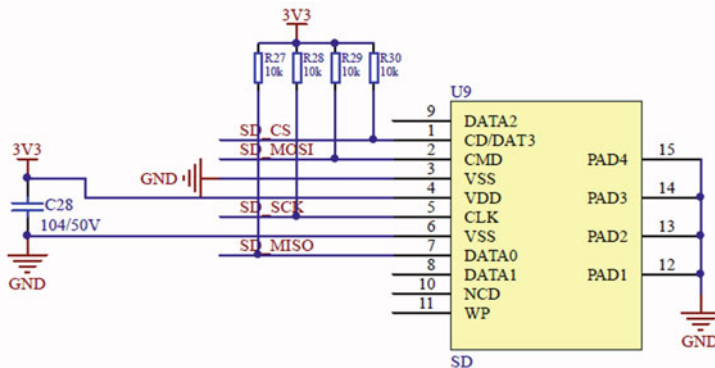
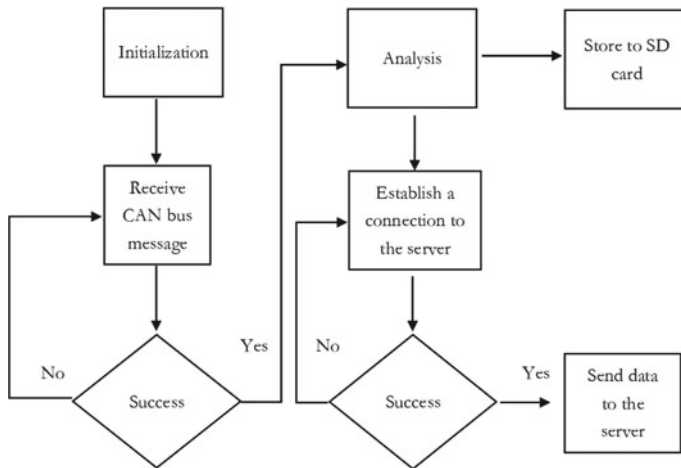


Fig. 11 SD card connection circuit

**SD card storage module.** Considering that the terminal equipment travels with the vehicle to a place where the network signal is poor or there is no network signal, the terminal cannot establish a connection with the background server at this time, and data loss occurs. However, the existing literature [1–4] lacks solution of the problem. Therefore, in the design, the SD card storage module is added to the terminal device, so that the terminal device can upload the data to the background server in time when the network communication state is good and can simultaneously save the data on the SD card, in order to prevent data loss when network communication is abnormal, and data can be reissued to the server when network communication is restored. When the SD card storage space is full, the new data will cover the data in the farthest time, and there is no need to manually clear the SD card. The SD card and the microprocessor are communicated through the four-wire SPI mode. Therefore, the 20–23 pin on the microprocessor are PA4 (used as the chip select pin CS), PA5 (using its SPI1\_SCK function) and PA6 (using SPI1\_MISO function), and PA7 (using SPI1\_MOSI function) is connected to the corresponding 4-wire of the SD card. The schematic diagram is shown in Fig. 11.



**Fig. 12** Embedded terminal software flow chart

### 3.2 Software Design

The software design of the embedded terminal device mainly includes the development of the library using the STM32 microcontroller, and the development of some AT commands for the operation of the SIM900 module. The terminal software development is written in the Keil uVision4 compiler environment using C language. Because the software code is complex and has many functions, the whole software flowchart is given here as shown in Fig. 12.

Through the flowchart, we can know the workflow of the software as follows: the initialization and interruption of each module are completed after the terminal is powered on; STM32 receives the CAN bus message of the BMS through CTM1051. After successfully receiving the data, the data is parsed according to the BMS communication protocol. While the data is stored to the local SD card, the synchronous control GPRS module establishes a network connection with the background server. After the connection is successful, the data is transparently transmitted to the server according to the communication protocol. STM32 also monitors the GPRS network connection. If there is a network communication error, the microprocessor will continuously request to reconnect to the background, and mark the data when the line is disconnected. When connecting to the background again, it will continue to send the current time data, and read the data when the terminal is disconnected from the SD card and reissue it to the background server to realize the disconnection reconnection and data reissue function, and there is no data loss.

At present, the terminal is operating stably in rail vehicles.

## 4 Conclusion

In order to save the long-term data of the energy storage system, this paper designs a wireless data transmission system. By adding an SD card, it can satisfy the requirements of data local storage and uploading to the server at the same time. It can also realize data compensation when the device is offline, which solves the problem that the existing wireless data transmission system will have incomplete data. And the corresponding background data monitoring interface can be used to monitor the data in real time and view the historical data. Through the experimental verification, the whole content of the design is realized, and it is widely applied to the actual, and truly solves a large number of energy storage system data transmission, storage and calculation problem. The system has high development efficiency and low cost and can be widely applied in the field of new energy transportation, adding a layer of guarantee for the safety of energy storage components.

**Acknowledgements** This work is supported by the National Key Research and Development Program (2017YFB1201004-15).

## References

1. Wang Y (2017) Design and application of alarm system based on ARM and GPRS. Technol Wind 6:13–15 (in Chinese)
2. Tao H, Jia Zt (2014) Wireless communication module's design and implementation based on STM32 and SIM900A. Electr Des Eng 22(17):106–110 + 114 (in Chinese)
3. Cai Hj, Zhai S, Cai M (2013) Design of smart home control system based on GSM and STM32. Tech Autom Appl 32(8):37–40 (in Chinese)
4. Xu J, Qian J, Peng X (2019) Design of wireless data controller based on GPRS. Fireworks Technol Market 03:220 (in Chinese)
5. Lin Jh, Lin Em (2019) Design and implementation of intelligent home control system on the strength of STM32 wireless network. J Panzhihua Univ 36(02):35–39 (in Chinese)
6. Liang M-l, Yin L-s, Chen L-j (2019) Design of wearable health monitoring system based on Cortex-M3 and SIM900A. J Shandong Agric Univ (Nat Sci Ed) 50(3):445–448 (in Chinese)
7. Liu Fl, Sheng Yf, Min J, Kong Xx (2018) Research and design of air quality monitoring system based on STM32. Technol Wind 22:103 + 116 (in Chinese)
8. Li T, Yy Ma, Yang D (2012) Design of GPRS remote monitoring terminal based on STM32. Electron World 11:126–127 (in Chinese)
9. Yiu J The definitive guide to the ARM Cortex-M3. Beihang University Press, Beijing, China

# The Charging Control Scheme of On-board Battery Energy Storage System in Tram



Dangwei Duan, Caihui Zheng, Zhanguo Wang and Fulai An

**Abstract** Pure battery-driven trams often use battery packs in parallel due to power and energy requirements. Because there is no isolation between each group, current circulation is prone to occur during battery use. The multi-stage constant-current charging method causes a lot of trouble, because the charging current of the parallel branch cannot be controlled, and it is easy to cause the charging current to exceed the limit of each branch. This paper introduces a battery system charging control method in which multiple battery packs are connected directly in parallel, which can limit the charging current of each battery pack and ensure that it does not exceed the limit.

**Keywords** On-board battery system · Charging control · Parallel · Tram

## 1 Introduction

The modern tram system is an important part of urban public transport and has been widely developed around the world. In order to reduce the adverse impact of the power supply network on the urban landscape and the problem of large line loss and limited braking energy recovery, modern trams in some cities use on-board energy storage technology. The common on-board energy storage technologies include

---

D. Duan (✉) · C. Zheng  
CRRC Changchun Railway Vehicles Co., Ltd., Changchun, China  
e-mail: [duandangwei@cccar.com.cn](mailto:duandangwei@cccar.com.cn)

C. Zheng  
e-mail: [zhengcaihui@cccar.com.cn](mailto:zhengcaihui@cccar.com.cn)

Z. Wang · F. An  
National Active Distribution Network Technology Research Center,  
Beijing Jiaotong University, Beijing, China  
e-mail: [zhgwang@bjtu.edu.cn](mailto:zhgwang@bjtu.edu.cn)

F. An  
e-mail: [17117422@bjtu.edu.cn](mailto:17117422@bjtu.edu.cn)

flywheel energy storage, battery energy storage, capacitor energy storage, and fuel cell energy storage. The flywheel energy storage technology is not mature enough at present, and the safety and rotation force problems restrict the flywheel energy storage technology in the tram [1]. The application of fuel cells has the inability to recover regenerative braking energy and requires the installation of special hydrogen storage tanks in the tram and the construction of a hydrogen charging station in the depot. The capacitor energy storage system has a higher power density than the battery energy storage system, which reversely limited by the influence of its energy density, resulting in a short distance between stations when applied in tram [2]. Battery energy storage system with good energy density and power density characteristics is currently the preferred choice for on-board energy storage system.

Compared with the current popular pure electric vehicles, the pure battery-driven tram has higher demand for energy and power. This often requires the battery to be grouped in parallel and series, and then, the battery packs are connected in parallel to improve the battery system capacity. The grouping method of this system is complicated, because each battery pack is connected directly in parallel through the high-voltage contactor without any isolation. The battery system is difficult to ensure balance during charging and discharging, between which the current circulation is easy to generate. That causes great trouble for charging the entire battery system, because the traditional multi-stage constant-current charging method can only control the total charging current in parallel, and the charging current of each branch is depending on internal resistance. The current distribution rule cannot guarantee that the charging current of each battery pack does not exceed the charging current limit of the battery. Long-term use of over-limit current to charge the battery will cause damage to the battery and shorten the service life of the battery [3].

For the above charging current of parallel battery packs which cannot guarantee that the charging current of each battery pack does not exceed the limit, this paper introduces a charging method based on total charging voltage control for the consideration that the total voltage values of each parallel battery pack are the same. The required charging voltage of each battery pack can be obtained from the required charging current of the battery pack, and the minimum value of these required charging voltages can be used as the actual charging voltage to realize the actual charging current that does not exceed the limit of the required charging current.

The remainder of the paper is organized as follows. A commonly used battery charging current limit calculation method is introduced in Sect. 2. A charging control method based on total charging voltage is depicted in Sect. 3. The experiment and evaluation for the proposed charging control approach are illustrated in Sect. 4. Finally, the conclusion is presented in Sect. 5.

## 2 A Commonly Used Battery Charging Current Limit Calculation Method

The maximum chargeable current of battery is characterized by the charging SOP value, which is affected by the internal electrochemical kinetics and thermodynamics of the battery, and reflects the maximum current value that can be absorbed by the battery in the current state. It is related to the voltage, temperature, available capacity, and SOC.

When considering the maximum chargeable current of the battery, the SOC and voltage of the battery are important limiting factors for ensuring the safety and durability of the entire system while the operating temperature and available capacity of the battery are known. Among them, the voltage limitation is difficult to satisfy, and the SOC limit is not adopted due to its simplicity compared with the voltage limitation. As a key constraint in calculating the maximum chargeable current of the battery, the result is a current limiting problem under the calculation of the voltage limit.

So far, the most common method for calculating the maximum chargeable current in different states of the battery is the hybrid pulse power characteristic method (HPPC) [4], which is based on the Rint model, as shown in Fig. 1. The upper and lower cut-off voltages of the battery are used to calculate the maximum chargeable current.

The terminal voltage of each cell can be expressed in (1).

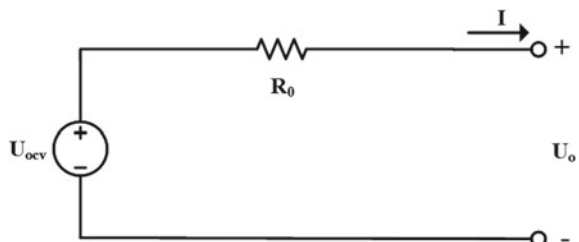
$$U_O(t) = U_{OCV}[\text{SOC}(t)] + R_0 I(t) \quad (1)$$

where  $U_O(t)$  is the external voltage of the cell.  $U_{OCV}[\text{SOC}(t)]$  is the open-circuit voltage when the state of charge is  $\text{SOC}(t)$ .  $I(t)$  is the charging current of which the value is positive when the cell is charging.  $R_0$  is the internal resistance which is related to the temperature, SOC, and aging condition.

Considering the terminal voltage of the battery is limited by the upper and lower limits, it can be seen that the maximum chargeable current value of the cell is shown in (2).

$$I_{\text{chg}} = \frac{U_{\max} - U_{OCV}[\text{SOC}]}{R_{\text{chg}}} \quad (2)$$

**Fig. 1** Rint equivalent circuit model of battery



where  $U_{\max}$  is the charging cut-off voltage.  $R_{\text{chg}}$  is the internal resistance of the cell under the charging condition, and the value is generally obtained from the mixed pulse test under different temperature, SOC, and aging conditions in the laboratory.  $I_{\text{chg}}$  is the maximum chargeable current obtained by the HPPC test.

When considering the battery system, assume that the battery pack is made up of  $m$  series and  $n$  parallels. The maximum chargeable current value of the battery pack can be expressed in (3).

$$I_{\text{chg}}^{\max} = n \min_{l \in [1, m]} (I_{\text{chg}}^l) \quad (3)$$

where  $l$  represents a cell in the battery pack.

### 3 A Charging Control Method Based on Total Charging Voltage

When the battery energy storage system uses multiple battery packs in parallel, it is difficult to ensure balance between the battery packs during charging and discharging. Current circulation is prone to occur which causes great trouble for charging the entire battery system, because the charging method of total charging current control cannot guarantee that the charging current of each battery pack does not exceed the charging current limit [5]. In the above case, considering the total voltage is the same for the parallel battery pack, the better way to control the charging current is to control the total charging voltage. The maximum chargeable current of each battery pack varies according to the battery state. The voltage calculated from the limit current will be different. The lowest of the multiple voltage values can be used as the charging voltage to make the charging current not to exceed the limit current requirements.

During the charging process, the battery management system calculates the maximum chargeable current of each battery pack according to the method in Sect. 2. At the same time, the actual charging current value can be measured. To achieve closed-loop control, it is necessary to rely on the wireless communication system establishing communication between the battery management system in tram and the charger on ground. The battery management system transmits the maximum chargeable current value and the actual charging current value of each battery pack to the charger, and the charger will calculate and control the total charging voltage of the DC bus [6] as shown in Fig. 2.

During the charging process, the charger charges the parallel battery packs according to the maximum chargeable current value and the actual charging current value of each battery pack based on the principle of voltage control, which uses the

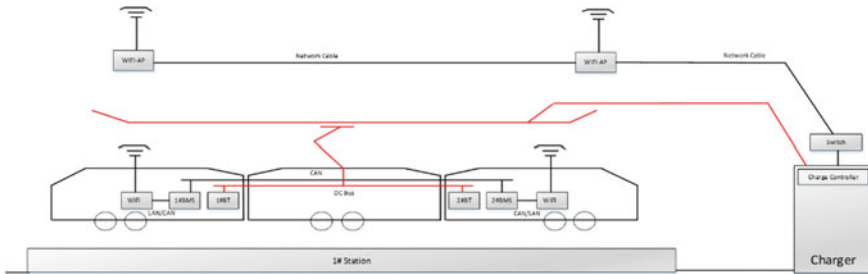


**Fig. 2** Charging network diagram of tram

PI control method to control the total charging voltage of the DC bus as shown in Fig. 3. When charging, the required charging current of each battery pack is set to be the maximum chargeable current of the battery pack. There is a deviation between the required charging current and the actual charging current, and the PI control method can be used to eliminate the static deviation between them. To a certain extent, the proportional-integral term calculated from the deviation can be regarded as the difference between the total charging voltage and the total required charging voltage [7]. Taking two battery packs for example, there exist two initial charging voltages and two proportional-integral terms. The total charging voltages of the battery packs can be obtained from the initial value of the charging voltages plus the corresponding proportional-integral terms, in which the smaller one can be the final charging voltage of the DC bus. When the smaller of the two total charging voltage is converted from one battery pack to another, the two initial charging voltage values are updated as the voltage value of the DC bus and the proportional-integral term are cleared to zero. The calculation of PI control is restarted.

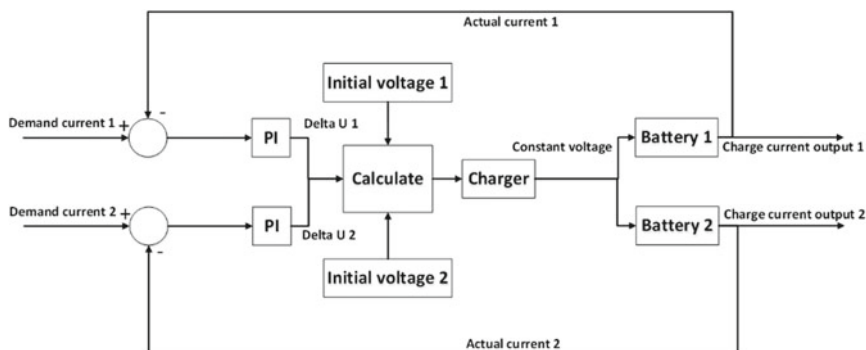


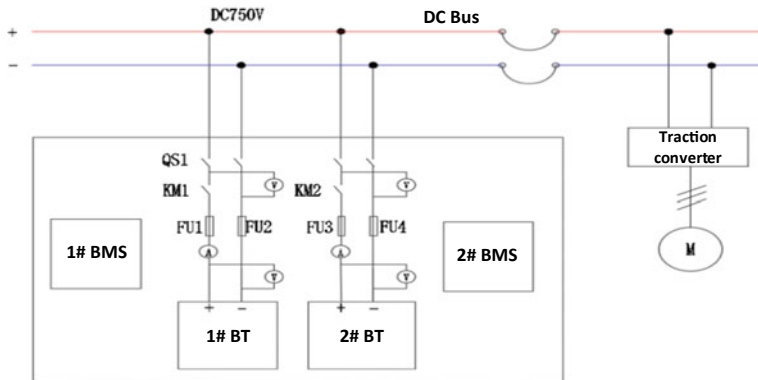
**Fig. 3** Schematic diagram of charging control

## 4 The Experiment and Evaluation

The electrical structure diagram of the on-board battery energy storage system of a tram is shown in Fig. 4. The battery system is composed of two battery packs, and the two battery packs are connected to the DC bus by direct parallel connection [8]. There is no isolation between them. In the charging process, the communication between the battery management system and the charger is established by means of wireless communication to ensure the charging control of the battery system.

Each battery pack of the on-board battery energy storage system includes 324 series and 4 parallels. The capacity of the lithium titanate battery is 10 Ah. In the actual charging process, a battery pack is placed under a certain temperature condition. The maximum chargeable current is related to the state of charge. The specific parameters are given in Table 1.

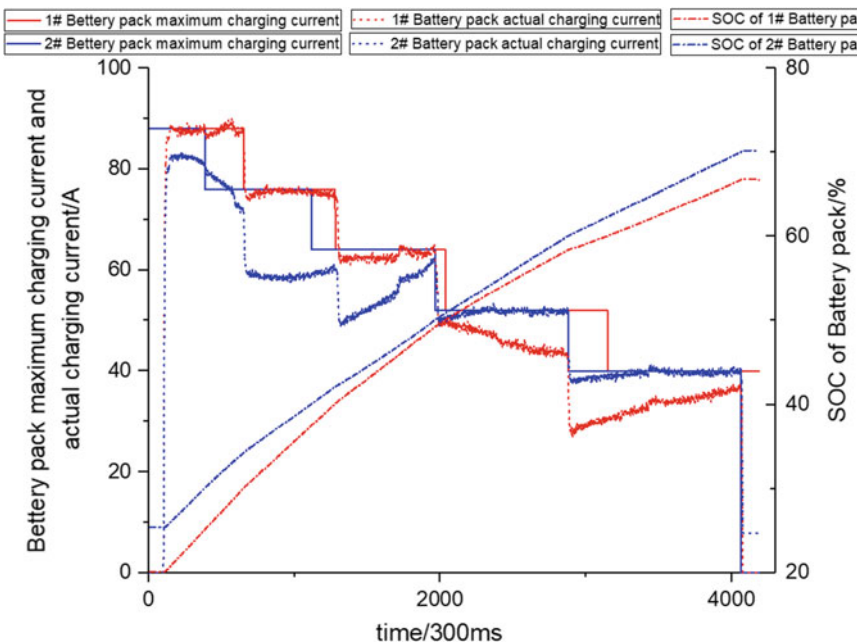
The two battery packs are charged according to the maximum chargeable current value under different SOC conditions, and the initial SOC of the two packs is 20.1% and 25.4%, respectively. The charging current and SOC can be obtained as shown in Fig. 5. It can be seen from the curve that during the charging process, the actual charging current of the two battery packs does not exceed its maximum chargeable current limit. In this process, only one battery pack can reach its charging current limit value. When reaching the charging current limit is switched from one battery pack to another, there is no large and long-time overshoot charging current. During the end of charging, the maximum chargeable current value rapidly drops to 0, and the actual charging current can quickly keep up and almost drops to zero at the same time. From the above results, the method of voltage control can ensure that the charging current of each battery pack does not exceed its maximum charging current, and the charging time is shortened, which satisfies the charging requirement of the existing battery packs in parallel.



**Fig. 4** Electrical structure diagram of on-board battery energy storage system

**Table 1** Maximum chargeable current in different SOCs

SOC (%)	Maximum chargeable rate (C)	Maximum chargeable current (A)
<20	2.4	96
20–30	2.2	88
30–40	1.9	76
40–50	1.6	64
50–60	1.3	52
60–70	1	40
>70	0	0

**Fig. 5** Current and SOC of two battery packs in charging process

## 5 Conclusion

A charging control method for a battery energy storage system based on wireless communication, characterized in that on-board battery energy storage system, is grouped by battery packs connecting in parallel without any isolation. During the charging and discharging process of the battery system, it is difficult to ensure balance between the battery packs. The current circulation is likely to occur, which causes great trouble for charging the entire battery system. This is because the traditional multi-stage constant-current charging method can only control the total

charging current in parallel, and the charging current of each branch is depending on branch internal resistance. The current distribution rule cannot guarantee that the charging current of each battery pack does not exceed the charging current limit of the battery. The long-term use of the over-limit current to charge the battery will cause damage to the battery and shorten the service life of the battery. Considering that the total charging voltages are the same for the battery pack in parallel, the better way to control the charging current of each battery pack is to use the method of voltage control. The maximum chargeable current of each battery pack varies according to the battery state. The voltage calculated from the limit current will be different. The lowest of the multiple voltage values can be used as the charging voltage to make the charging current not to exceed the limit current requirements.

**Acknowledgements** The authors are grateful for financial support via the National Key R&D Program of China (2017YFB1201003-006).

## References

1. Richardson MB (2002) Flywheel energy storage system for traction applications. *Power Electron Mach Drives* 275–279 (in Chinese)
2. Wang X (2010) Study the control strategy of energy saving system with super capacitor on-board of railway vehicle for urban mass transit. Beijing Jiaotong University, Beijing (in Chinese)
3. Gao Y, Jiang J (2017) Lithium-ion battery aging mechanisms and life model under different charging stresses. *J Power Sources* 360:180–188
4. Idaho National Engineering & Environmental Laboratory (2010) Battery test manual for plug-in hybrid electric vehicles. Assistant Secretary for Energy Efficiency and Renewable Energy (EE) Idaho Operations Office: Idaho Falls, ID, USA
5. Okui A, Hase S, Shigeeda H (2010) Application of energy storage system for railway transportation in Japan. *Power Electronics Conference (IPEC), 2010 International. IEEE*, 2010, pp 3117–3123
6. Cai B, Li X (2015) On contactless traction power supply for modern trams. *Urban Railway Transit Res* 72–77 (in Chinese)
7. Li J (2014) Research on pure electric vehicle charging system stability and harmonic characteristic. Beijing Jiaotong University, Beijing (in Chinese)
8. Xu J (2018) The running and power supply simulation system of energy storage tram. Southwest Jiaotong University, Chengdu (in Chinese)

# SOC Estimation of All-Vanadium Redox Flow Battery via Parameters Identification and UKF Algorithm



Guobin Sun, Yufu Hao, Zhenghao Li, Li Wang and Kun Fang

**Abstract** The accurate estimation of the state of charge (SOC) under the nonlinear model of all-vanadium redox flow battery (VRB) is studied in this paper. Based on the VRB equivalent circuit model, the recursive least squares (RLS) algorithm is used to identify the model parameters and verify the correctness of the model in the constant current charging process. Then, unsupervised Kalman filter (UKF) algorithm is used to estimate SOC and compared with the extended Kalman filter (EKF) estimation results. Simulation experiments show that the UKF algorithm can accurately estimate the SOC faster, with an error less than 2%. In addition, analyzing the influence of initial value of SOC verifies the convergence and anti-interference ability of the algorithm.

**Keywords** Vanadium redox flow battery · State of charge · Parameter identification · Unsupervised Kalman filter · Recursive least squares

## 1 Introduction

Confronted with the growing energy crisis and environmental problems, the development of new energy rail transit is an important measure to implement sustainable development in cities. At present, vanadium redox flow battery (VRB) has widely attracted extensive attention of researchers due to the excellent performances beyond lithium batteries [1, 2]. Therefore, efficient energy management and control have important sense to VRB. State of charge (SOC) estimation of VRB is the core problem in this process. Not only the service life of VRB can be prolonged through accurately estimating SOC, but also the efficiency of power utilization can be improved, and the stability and security of the system can be enhanced.

---

G. Sun · Y. Hao · Z. Li (✉)

CRRC Qingdao Sifang Rolling Stock Research Institute Co., Ltd., Qingdao 266031, China  
e-mail: [lzhhfut@163.com](mailto:lzhhfut@163.com)

L. Wang · K. Fang

CRRC Changchun Railway Vehicles Co., Ltd., Changchun 130062, China

At present, SOC estimation methods include ampere-hour method, open-circuit voltage method, neural network method, Kalman filter method and so on. However, large accumulated errors could be caused by the ampere-hour method with the accumulation of time [3]. Though open-circuit voltage method is relatively simple, inevitably, the battery terminal voltage deviation is easy to occur due to the motionlessness of the settling time after charging and discharging, so that it can only be applied to the initial stage and the end of charging and discharging [4]. Highly dependent on the number of data and training methods, the accuracy of neural network method can not be guaranteed [5], since high model-dependence, Kalman filtering algorithm [6] is limited to applying to linear time-varying systems. Paradoxically, linearization will decline the estimation accuracy due to the high nonlinear strength of battery model.

With the strong nonlinearity of VRB and the difficulty in measuring of the model parameters, the general filtering method can not guarantee the accuracy of estimation. Unsupervised Kalman filter (UKF) algorithm is used to estimate SOC in [7, 8], and the result is satisfactory. However, the operation process of batteries can not be reflected well with relatively simple model. Therefore, in order to solve the above problems, RLS and UKF algorithms are used in this paper to achieve accurate estimation for SOC of VRB.

The paper is organized as follows: In Sect. 2, the model of vanadium redox flow battery system is presented with RLS. An UKF estimator is described in detail in Sect. 3. In Sect. 4, simulations are conducted to verify the effectiveness of the proposed parameters' identification and estimation strategy. Finally, the conclusion of this paper is drawn in Sect. 5.

## 2 Modeling

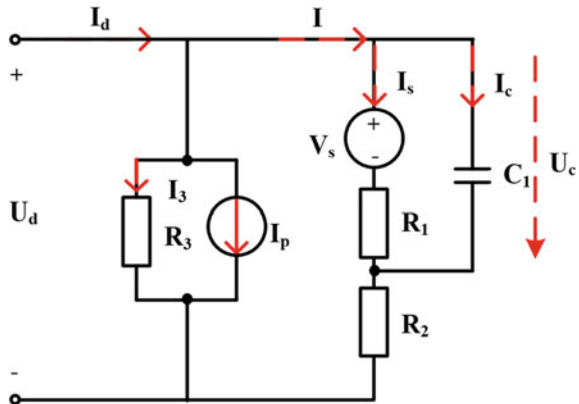
### 2.1 Mathematical Modeling of VRB

Equivalent circuit model and its improved optimization based on loss assumption for VRB have been widely used in recent years. In this paper, the equivalent circuit model [9, 10] based on the principle of VRB is shown in Fig. 1.

According to Kirchhoff's current and voltage law, the circuit equation is written as follows:

$$\left\{ \begin{array}{l} U_c = V_s + I_s \times R_1 \\ U_d = U_c + I \times R_2 \\ I_d = I_3 + I_p + I \\ I_3 = \frac{U_d}{R_3} I \\ I = I_s + I_c \\ I_c = C_1 \frac{dU_c}{dt} \end{array} \right. \quad (1)$$

**Fig. 1** Equivalent circuit model of VRB



where  $U_d$  is terminal voltage of VRB,  $I_d$  is charging–discharging current (charging direction be defined as positive direction),  $V_s$  is open-circuit voltage,  $I_p$  is pump loss, expressed by constant current source,  $R_1$  and  $R_2$  are internal impedances of batteries including dynamic equivalent impedance, diaphragm impedance, solution impedance, mass transfer impedance, bipolar plate impedance and electrode impedance,  $R_3$  is parasitic loss,  $C_1$  is electrode capacitance and  $U_c$  is capacitor voltage.

The SOC model is shown as:

$$\text{SOC} = \text{SOC}_0 + \frac{1}{C_N} \int_0^{\tau} I_d dt \quad (2)$$

where  $C_N$  is rated capacity of VRB, the value between 24 and 34.5 Ah [11],  $\tau$  is charging-discharging time. Followed with Nernst equation, it can be got as follow:

$$V_s = \left( V_e + \frac{2RT}{F} \ln \frac{\text{SOC}}{1 - \text{SOC}} \right) \times N \quad (3)$$

where  $R = 8.314 \text{ J/(K} \cdot \text{mol)}$  is the ideal gas constant,  $T$  is temperature,  $F = 96500 \text{ C/mol}$  is Faraday constant,  $N$  is number of batteries in series connection and  $V_e = 1.4 \text{ V}$  is standard electrode potential of battery.

Combining (1–3), the state equation of VRB can be rewritten as:

$$\begin{cases} \frac{dU_c}{dt} = \left[ -\frac{R_1 + R_2 + R_3}{R_1(R_2 + R_3)C_1} \right] U_c + \frac{R_3}{(R_2 + R_3)C_1} (I_d - I_p) + \frac{N}{R_1 C_1} \left( V_e + \frac{2RT}{F} \ln \frac{\text{SOC}}{1 - \text{SOC}} \right) \\ \frac{d\text{SOC}}{dt} = \frac{1}{C_N} I_d \end{cases} \quad (4)$$

And, system output is written as:

$$U_d = \frac{R_2 R_3}{(R_2 + R_3)} (I_d - I_p) + \frac{R_3}{(R_2 + R_3)} U_c \quad (5)$$

Ordering  $\lambda = \frac{R_1 + R_2 + R_3}{R_1(R_2 + R_3)C_1}$ , the discrete-time equation of (4–5) can be rewritten as:

$$\left\{ \begin{array}{l} U_c(k) = e^{-\lambda T_s} U_c(k-1) - \frac{1}{\lambda} (e^{-\lambda T_s} - 1) \\ \quad \times \frac{N}{R_1 C_1} \left( V_e + \frac{2RT}{F} \ln \frac{\text{SOC}}{1 - \text{SOC}(k-1)} \right) \\ \quad + \frac{1}{\lambda} (e^{-\lambda T_s} - 1) \frac{R_3}{(R_2 + R_3) C_1} \\ \quad \times (I_d(k-1) - I_p(k-1)) \\ \text{SOC}(k) = \text{SOC}(k-1) + \frac{1}{C_N} I_d T_s \end{array} \right. \quad (6)$$

$$U_d(k) = \frac{R_2 R_3}{(R_2 + R_3)} (I_d(k) - I_p(k)) + \frac{R_3}{(R_2 + R_3)} U_c(k) \quad (7)$$

where  $R_1$ ,  $R_2$ ,  $R_3$  and  $C_1$  are identification parameters.

## 2.2 Parameter Identification Based on RLS

The new measurement value based on RLS is used to modify the last time estimation result. With the modification of the parameter estimation result, the estimation result consistent with the accuracy is presented. From (4–5), the difference equation of the model for parameter identification can be obtained, as shown as follows:

$$U_d(k) = a U_d(k-1) + c (I_d(k) - I_p(k)) + b V_s(k) + d (I_d(k-1) - I_p(k-1)) \quad (8)$$

$$\left\{ \begin{array}{l} a = e^{-\lambda T_s} \\ b = \frac{R_3}{R_1 + R_2 + R_3} (1 - e^{-\lambda T_s}) \\ c = R_2 R_3 / (R_2 + R_3) \\ d = \frac{R_1 R_3^2}{(R_1 + R_2 + R_3)(R_2 + R_3)} - \frac{(R_1 + R_2) R_3}{(R_1 + R_2 + R_3)} e^{-\lambda T_s} \end{array} \right. \quad (9)$$

where  $a$ ,  $b$ ,  $c$  and  $d$  are parameters of the discrete-time model and those relationship between  $R_1$ ,  $R_2$ ,  $R_3$  and  $C_1$  in the continuous model is shown in (9). The value of the under-identified parameters can be deduced by separating the identification parameter's vector  $(a, b, c, d)$ .

### 3 UKF Estimate Algorithm

With adopting Kalman linear filtering framework in UKF, it is unrequired for nonlinear system's state equation and observation equation to be linearized into linear system [12, 13], and unscented transformation (UT) is used to approximate the probability density distribution of the nonlinear function, to improve the calculation accuracy. Supposing that the state equation and observation equation of a nonlinear system are as follows:

$$\begin{aligned} X(k+1) &= \phi[X(k), w(k), k] \\ Z(k+1) &= h[X(k+1), v(k+1), k+1] \end{aligned} \quad (10)$$

where  $k$  is the current time,  $X$  is the state equation,  $Z$  is the observation equation and  $w(k)$  and  $v(k)$  are the process noise and the measurement noise with covariance of  $Q$  and  $R$ . The algorithm steps are as follows:

(1) Setting initial value

$$\begin{cases} \hat{X}(0) = E[X(0)] \\ P(0) = E\left\{\left[X(0) - \hat{X}(0)\right]\left[X(0) - \hat{X}(0)\right]^T\right\} \end{cases} \quad (11)$$

(2) Generating sigma point and weighting coefficient

$$\begin{cases} X^{(0)} = \bar{X} \\ X^{(i)} = \bar{X} + (\sqrt{n+\lambda}\bar{P})_i, i = 1, 2, \dots, n \\ X^{(\bar{i})} = \bar{X} - (\sqrt{n+\lambda}\bar{P})_i, i = n+1, \dots, 2n \end{cases} \quad (12)$$

where  $n$  is the system dimension,  $\bar{X}$  and  $\bar{P}$  are the mean and covariance, respectively.

$$\begin{cases} \omega_m^{(0)} = \frac{\lambda}{\lambda+n} \\ \omega_c^{(0)} = \frac{\lambda}{\lambda+n} + (1-\alpha^2 + \beta) \\ \omega_c^{(\bar{i})} = \omega_m^{(\bar{i})} = \frac{\lambda}{2(\lambda+n)}, i = 1, \dots, 2n \end{cases} \quad (13)$$

where  $\omega_c^{(i)}$  is the weight of variance,  $\omega_m^{(i)}$  is the weight of mean,  $\alpha$  is the scaling factor of a small positive constant,  $\beta$  is a non-negative weight coefficient and  $\lambda = \alpha^2(n+k) - n$  is a proportional parameter.

## (3) Time update

$$\begin{aligned}
x(k/k-1) &= \phi[x(k-1)] \\
\bar{x}(k) &= \sum_{i=0}^{2n} W_i^m x_i(k/k-1) \\
\bar{P}(k/k-1) &= \sum_{i=0}^{2n} W_i^p [x_i(k/k-1) - \bar{x}(k)] [x_i(k/k-1) - \bar{x}(k)]^T \\
z(k/k-1) &= H[x(k/k-1)] \\
\bar{z}(k) &= \sum_{i=0}^{2n} W_i^m z_i(k/k-1)
\end{aligned} \tag{14}$$

## (4) Measurement update

$$\begin{aligned}
P_{\bar{z}(k)\bar{z}(k)} &= \sum_{i=0}^{2n} W_i^p [z_i(k/k-1) - \bar{z}(k)] [z_i(k/k-1) - \bar{z}(k)]^T \\
P_{\bar{x}(k)\bar{z}(k)} &= \sum_{i=0}^{2n} W_i^p [x_i(k/k-1) - \bar{x}(k)] [z_i(k/k-1) - \bar{z}(k)]^T \\
K(k) &= P_{\bar{x}(k)\bar{z}(k)} P_{\bar{z}(k)\bar{z}(k)}^{-1} \\
\hat{x}(k) &= \bar{x}(k) + K(k) [z(k) - \bar{z}(k)] \\
P(k) &= \bar{P}(k) - K(k) P_{\bar{z}(k)\bar{z}(k)} K^T
\end{aligned} \tag{15}$$

Firstly,  $U_c$  and SOC are iterated by (12) and (13), and then, the one-step prediction mean  $x(k/k-1)$  and covariance matrix  $\bar{P}(k/k-1)$  are obtained by combining (6) and (14). With the mean value of one-step prediction be transformed into two-step traceless transformation, the covariance  $P_{\bar{x}(k)\bar{z}(k)}$ ,  $P_{\bar{z}(k)\bar{z}(k)}$  and mean value  $\bar{z}(k)$  of the system prediction are calculated combining (7), (14) and (15). In the same time, the Kalman gain  $K(k)$  can be calculated by (15). Finally, the state and covariance are updated according to the actual voltage value  $z(k)$ ,  $K(k)$  at  $k$  time, and the state quantity at  $k+1$  time can be obtained.

## 4 Analysis of Simulation and Experimental Results

### 4.1 Parameters Identification Based on RLS

In order to identify the VRB model parameters by RLS and verify the correctness, a 5 kW/30 kWh VRB energy storage system experiment platform is built as shown

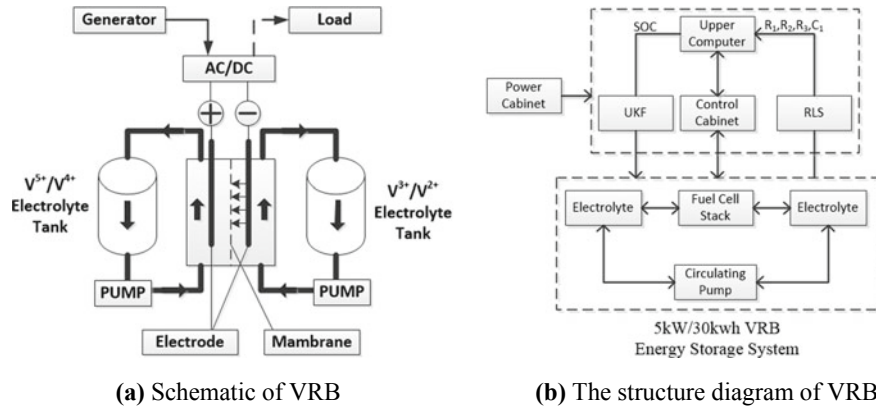


**Fig. 2** VRB energy storage system

in Fig. 2. The battery is charged at a constant current of 105 A, until be charged at the cut-off voltage of 60 V.

Charging data in one-hour constant current charging process is selected to identify the model by RLS. The initial identification value  $[R_1, R_2, R_3, C_1]$  is set as  $[10^{-5}, 10^{-5}, 10^{-5}, 10^{-5}]$ , the initial identification state  $P$  is a  $4 * 4$  unit matrix of module 106, and the sampling time is 0.01 s. The identification results are shown in Fig. 3.

It can be seen that the identification accuracy is poor in the early stage, due to the selection of initial value and the less input data. With the identification processing, the final identification results  $[R_1, R_2, R_3, C_1]$  tend to be  $[0.045, 0.03, 13.89, 0.15]$ . According to the identification results, the mathematical model is established. Comparing the current and voltage data in the charging simulation by constant current using identification model with experiment, the curves are shown in Fig. 4.

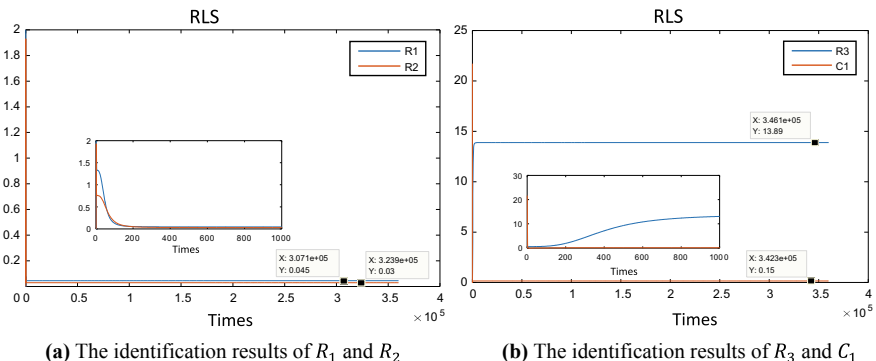
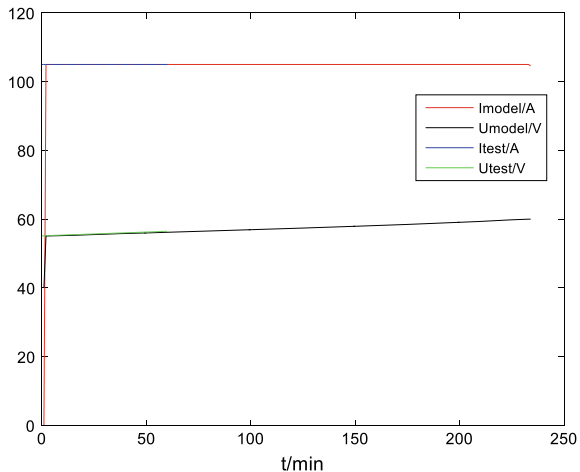


**Fig. 3** Identification results of VRB model parameters by RLS

**Fig. 4** Comparison of identification model and experimental data



It can be known that the current and voltage generated by the battery are basically consistent with generated by the battery model, verifying the correctness of the identification parameters and model.

#### 4.2 SOC Estimation Based on UKF Algorithm

Combined with the battery's mathematical model and UKF algorithm, the SOC is estimated by comparing with EKF algorithm in the charging process. The algorithm parameters are given in Table 1.

The simulation values are compared with the theoretical value obtained from the battery mathematical model in Fig. 5. It can be seen that EKF algorithm can only achieve the first-order linearization approximation and ignores the high-order term in Taylor expansion since the strong nonlinearity of VRB, resulting in low accuracy that the error fluctuates between 2 and 3%. UKF can more accurately track SOC changes and has faster convergence speed with the 1% stability estimation error.

**Table 1** Parameters of 5 kW/30 kWh VRB

Parameter	Value
$P$	$[10^{-4}, 0, 0, 10^{-4}]$
$Q$	$[10^{-6}, 0, 0, 10^{-6}]$
$R$	0.1
$SOC_0$	0.2
$t$	1
$[R_1, R_2, R_3, C_1]$	$[0.045, 0.03, 13.89, 0.150]$

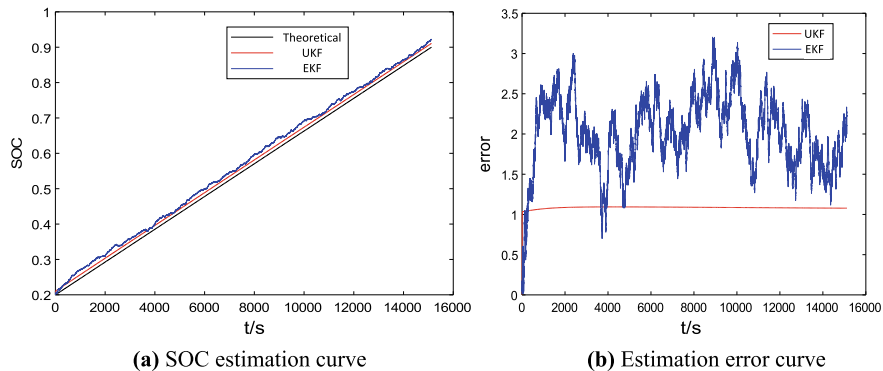


**Fig. 5** SOC and error estimation curves

#### 4.3 The Influence of SOC Initial Value on Estimation Results

Considering the measurement data deviation caused by environment and equipment interference noises, the initial value of SOC may not be obtained accurately. Therefore, it is necessary to further verify the convergence of UKF algorithm with the initial value as inaccurate. The estimated curves when the initial SOC values are set as 0.1 and 0.35 are shown in Fig. 6.

It can be known that UKF algorithm can continuously correct the estimated SOC through Kalman gain when there is a large error in the initial value and finally stabilize the error at about 1% after about 300 s of oscillation. It is verified that there is good convergence property on UKF algorithm with RLS.

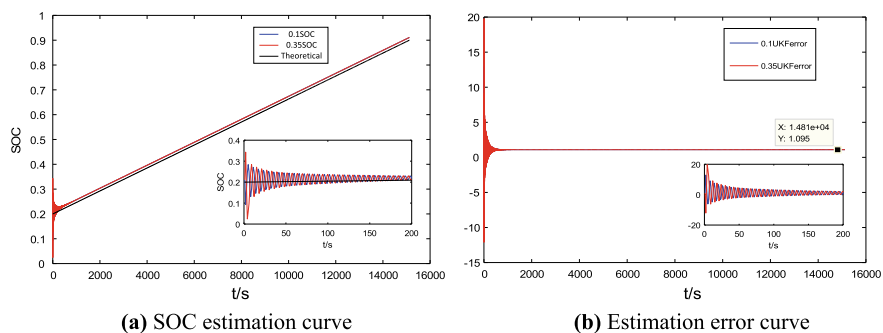


**Fig. 6** SOC and error estimation curves on different initial values

## 5 Conclusion

In this paper, the equivalent circuit model is established according to the principle of VRB, and the RLS algorithm is used to identify the model parameters and verify the correctness of the model. Then, compared with EKF algorithm, UKF algorithm is used to estimate SOC with faster convergence speed and better stability. Considering that the vulnerable to external interference in actual operation of VRB, the influence of SOC initial value on the estimation results is analyzed by giving different initial values. Therefore, UKF algorithm has a broad application prospect in SOC estimation. The great extension of the UKF to VRB control engineering in this paper has successfully demonstrated that the UKF based on RLS technique can be perfectly used to improve the SOC estimation performance.

**Acknowledgements** This work is supported by National Key R&D Program of China (No. 2017YFB1201003-006).

## References

1. Barote L, Marinescu C, Georgescu M (2009) VRB modeling for storage in stand-alone wind energy systems. In: 2009 IEEE bucharest powertech. IEEE
2. Skyllas-Kazacos M, Kazacos M (2011) State of charge monitoring methods for vanadium redox flow battery control. *J Power Sources* 196(20):8822–8827
3. Rodrigues S, Munichandraiah N, Shukla AK (2000) A review of state-of-charge indication of batteries by means of a.c. impedance measurements. *J Power Sources* 87(1–2):12–20
4. Ramadan HS, Becherif M, Claude F (2017) Extended Kalman filter for accurate state of charge estimation of lithium-based batteries: a comparative analysis. *Int J Hydrogen Energy*
5. Hussein AA (2015) Derivation and comparison of open-loop and closed-loop neural network battery state-of-charge estimators. *Energy Procedia* 75:1856–1861
6. Plett GL (2004) Extended Kalman filtering for battery management systems of LiPB-based HEV battery packs: part 2. modeling and identification. *J Power Sources* 134(2):262–276
7. Konatowski S, Kaniewski P, Matuszewski J (2016) Comparison of estimation accuracy of EKF, UKF and PF filters. *Ann Navig* 23(1):69–87
8. Yang B, Jin J (2012) Comparison on EKF and UKF for geomagnetic attitude estimation of LEO satellites. *Chinese Space Science & Technology*
9. Chahwan J, Abbey C, Joos G (2007) VRB modelling for the study of output terminal voltages, internal losses and performance. In: 2007 IEEE electrical power conference montreal: IEEE, pp 387–392
10. Barote L, Marinescu C, Georgescu M (2009) VRB modeling for storage in stand-alone wind energy systems. In: 2009 IEEE power tech. Bucharest: IEEE, pp 1–6
11. Xiong R, Sun F, Gong X et al (2014) A data-driven based adaptive state of charge estimator of lithium-ion polymer battery used in electric vehicles. *Appl Energy* 113:1421–1433
12. Partovibakhsh M, Liu G (2015) An adaptive unscented Kalman filtering approach for online estimation of model parameters and state-of-charge of lithium-ion batteries for autonomous mobile robots. *IEEE Trans Control Syst Technol* 23(1):357–363
13. Liu S, Cui N, Zhang C (2017) An adaptive square root unscented Kalman filter approach for state of charge estimation of lithium-ion batteries. *Energies* 10(9):1345–1358

# The Control Strategy of Hybrid Energy Storage System of Tramcar Based on Parallel Interleaving Bidirectional DC/DC Converter



Zhexu Zhang, Yang Cui, Qinkun Zhao, Bin Zhou and Zhenghao Li

**Abstract** A hybrid energy storage system of tramcar based on PI control strategy for parallel interleaved control bidirectional DC/DC converter is proposed in this paper. Firstly, the bidirectional DC/DC converter with parallel interleaving control is designed for the hybrid energy storage system. At the same time, the mathematical model of DC/DC converter is carried out, and the control strategy of the bidirectional DC/DC converter is proposed. In addition, the capacity configuration parameters of the energy storage components are calculated based on the actual line data. Finally, simulation results that the feasibility of the parallel interleaved control bidirectional DC/DC converter design and control strategy.

**Keywords** Tramcar · Hybrid energy storage · Parallel interleaved control · Bidirectional DC/DC converter · PI controller

## 1 Introduction

With the continuous increase of the city population, more and more tremendous pressure has been brought on urban rail transit. As a medium-traffic rail transit mode, modern tramcar has been numerous studied since the short construction period, small investment, environmental protection, and beautiful appearance [1]. Among them, the hybrid energy storage tramcar, using energy storage components, such as supercapacitors or lithium-ion batteries to supply power to the train and absorb braking energy, eliminates the requirement for infrastructure such as contact nets and braking energy absorption devices.

---

Z. Zhang (✉) · Y. Cui · Z. Li  
CRRC Qingdao Sifang Rolling Stock Research Institute Co., Ltd.,  
Qingdao 266031, China  
e-mail: [zhangzhexu.ss@crrcgc.cc](mailto:zhangzhexu.ss@crrcgc.cc)

Q. Zhao · B. Zhou  
CRRC Changchun Railway Vehicles Co., Ltd., Changchun 130062, China

There are high requirements on energy density and power density of energy storage systems for hybrid energy storage trams. Compared to the supercapacitor with the high power density and low energy density, lithium-ion battery has higher energy density, but the power density is low. In addition, the operation efficiency of the train could be affected by the slow charging and discharging speed for lithium-ion battery [2, 3]. Therefore, it is necessary to make full use of the advantages of different energy storage components of hybrid energy storage system. A hybrid energy storage system with lithium battery and supercapacitor as energy storage elements is proposed for electric vehicles in [4–7] studied the hybrid energy storage system of tramcar.

This paper introduces the topology structure of the onboard hybrid energy storage system and proposes an interleaving control strategy based on the parallel bidirectional DC/DC converter for the main circuit topology. The model of the hybrid energy storage system is established, and the effectiveness of the system topology and control strategy is verified by simulation.

The rest of the paper is structured as follows: Sect. 2 mainly studies the topology of the onboard hybrid energy storage system of the tram; the bidirectional DC/DC converter with parallel interleaving control and the control strategy based on mathematical model of DC/DC converter is designed in Sect. 3. In Sect. 4, the capacity configuration parameters of the energy storage components of the hybrid energy storage system based on the actual line data of the tramcar are calculated, and a hybrid energy storage system is built and simulated. Finally, the conclusion of this paper is described in Sect. 5.

## 2 Topological Structure of Hybrid Energy Storage System

In order to obtain the high energy density and power characteristics, a hybrid energy storage topology is proposed in this paper combined battery and capacitor. The topological structure of the trolley-type hybrid energy storage system is shown in Fig. 1. The topology consists of traction drive system and hybrid energy storage system. The hybrid energy storage system is mainly composed of a lithium battery module, a supercapacitor, and a bidirectional DC/DC converter.

## 3 Interleaved Parallel Bidirectional DC/DC Converter

As shown in Fig. 2, the hybrid energy storage system is directly connected to the grid with a single DC/DC converter and the supercapacitor using two bridge arms in parallel. The charging ripple and the size of the inductor can be reduced by pulse interleaving control for interleaved parallel bidirectional DC/DC converter. At the same time, the heat dissipation pressure can be shared and system reliability can be improved by the two power units.

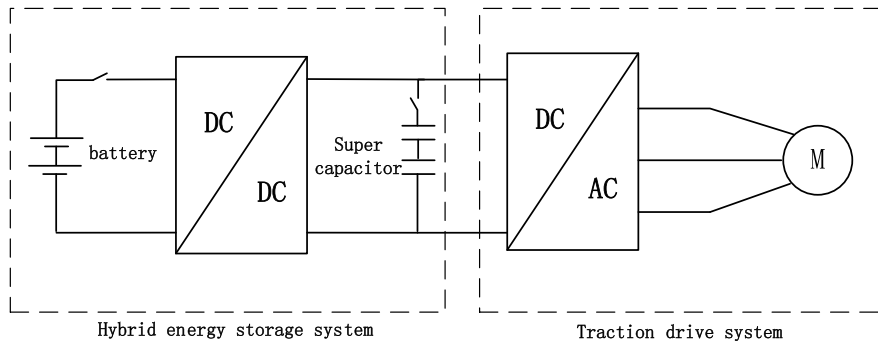
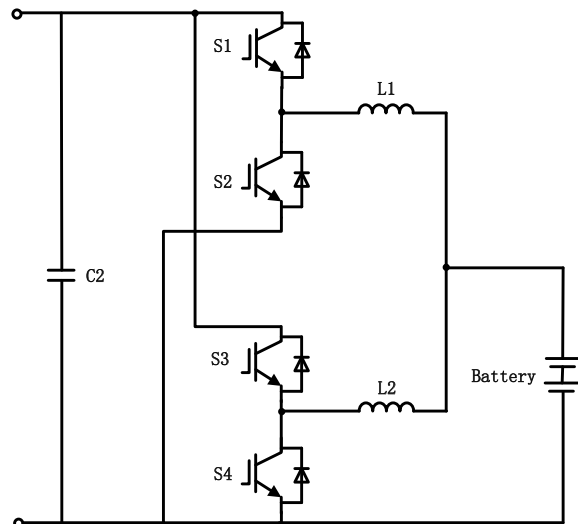


**Fig. 1** Topology of onboard hybrid energy storage system for tram

**Fig. 2** Interleaved parallel bidirectional DC/DC converter main circuit



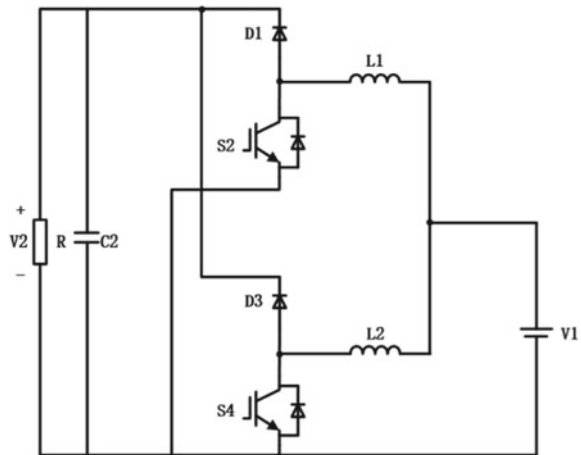
### 3.1 Modeling of Interleaving and Parallel Bidirectional DC/DC Converter

#### (1) Boost circuit modeling

The output side is equivalent to the load resistance  $R$ , and the voltage at both ends is  $V$  [8, 9]. The equivalent circuit of boost converter is shown as Fig. 3.

When the switches  $S_2$  and  $S_3$  are turned on, the voltage across the inductors  $L_1$  and  $L_2$  is:

**Fig. 3** Equivalent circuit of boost



$$v_{L_1}(t) = L_1 \frac{di_{L_1}(t)}{dt} = v_1(t) \quad (1)$$

$$v_{L_2}(t) = L_2 \frac{di_{L_2}(t)}{dt} = v_1(t) \quad (2)$$

When the switches  $S_2$  and  $S_3$  are turned off, the voltage across the inductors  $L_1$  and  $L_2$  is:

$$v_{L_1}(t) = L_1 \frac{di_{L_1}(t)}{dt} = v_1(t) - v_2(t) \quad (3)$$

$$v_{L_2}(t) = L_2 \frac{di_{L_2}(t)}{dt} = v_1(t) - v_2(t) \quad (4)$$

The input and output voltages can be approximated as an average value in one switching cycle since the continuation with little variance. Therefore, the average voltages of  $L_1$  and  $L_2$  during one switching cycle are written as:

$$\langle v_{L_1}(t) \rangle_{T_s} = \frac{1}{T_s} \left[ \int_0^{d_1 T_s} v_{L_1}(t) dt + \int_{d_1 T_s}^{T_s} v_{L_1}(t) dt \right] = \langle v_1(t) \rangle_{T_s} - (1 - d_1) \langle v_2(t) \rangle_{T_s} \quad (5)$$

$$\langle v_{L_2}(t) \rangle_{T_s} = \frac{1}{T_s} \left[ \int_0^{d_3 T_s} v_{L_2}(t) dt + \int_{d_3 T_s}^{T_s} v_{L_2}(t) dt \right] = \langle v_1(t) \rangle_{T_s} - (1 - d_3) \langle v_2(t) \rangle_{T_s} \quad (6)$$

After average processing, it can be rewritten as:

$$\langle v_{L_1}(t) \rangle_{T_s} = L_1 \frac{d\langle i_{L_1}(t) \rangle_{T_s}}{dt} \quad (7)$$

$$\langle v_{L_2}(t) \rangle_{T_s} = L_2 \frac{d\langle i_{L_2}(t) \rangle_{T_s}}{dt} \quad (8)$$

where  $\langle i_{L_1}(t) \rangle_{T_s}$  and  $\langle i_{L_2}(t) \rangle_{T_s}$  are the average values of the currents of the inductor during  $T_s$ . Combined with (5) and (6), it can be shown as:

$$L_1 \frac{d\langle i_{L_1}(t) \rangle_{T_s}}{dt} = \langle v_1(t) \rangle_{T_s} - d'_1 \langle v_2(t) \rangle_{T_s} \quad (9)$$

$$L_2 \frac{d\langle i_{L_2}(t) \rangle_{T_s}}{dt} = \langle v_1(t) \rangle_{T_s} - d'_3 \langle v_2(t) \rangle_{T_s} \quad (10)$$

where  $d' = 1 - d$ .

According to Kirchhoff's current law, the average value of the current of the filter capacitor in  $T_s$  is:

$$\langle i_c(t) \rangle_{T_s} = C \frac{d\langle v_2(t) \rangle_{T_s}}{dt} = d'_1 \langle i_{L_1}(t) \rangle_{T_s} + d'_3 \langle i_{L_2}(t) \rangle_{T_s} - \frac{\langle v_2(t) \rangle_{T_s}}{R} \quad (11)$$

When the DC/DC converter is operating in a steady state,  $D_1 = d_1$ ,  $D_3 = d_3$  the input variable at steady state:  $V_1 = \langle v_1(t) \rangle_{T_s}$ ,  $V_2 = \langle v_2(t) \rangle_{T_s}$  inductor current:  $I_{L_1} = \langle i_{L_1}(t) \rangle_{T_s}$ ,  $I_{L_2} = \langle i_{L_2}(t) \rangle_{T_s}$ .

The volt-second balance principle and the charge balance principle are applied to the inductor voltage and the capacitor current, respectively:

$$V_1 = D'_1 V_2 \quad (12)$$

$$V_1 = D'_3 V_2 \quad (13)$$

$$\frac{V_2}{R} = D'_1 I_{L_1} + D'_3 I_{L_2} \quad (14)$$

The small-signal model is applied for the disturbance at the steady-state operating point:

$$\langle v_1(t) \rangle_{T_s} = V_1 + \widehat{v_1(t)} \quad (15)$$

$$d = D + \hat{d} \quad (16)$$

$$\begin{cases} \langle v_2(t) \rangle_{T_s} = V_2 + \widehat{v_2(t)} \\ \langle i_{L_1}(t) \rangle_{T_s} = I_{L_1} + \widehat{i_{L_1}(t)} \\ \langle i_{L_2}(t) \rangle_{T_s} = I_{L_2} + \widehat{i_{L_2}(t)} \end{cases} \quad (17)$$

Substituting (15–17) into (10):

$$\begin{cases} L_1 \frac{d(I_{L_1} + \widehat{i_{L_1}(t)})}{dt} = (V_1 + \widehat{v_1(t)}) - (D'_1 - \widehat{d}_1)(V_2 + \widehat{v_2(t)}) \\ L_2 \frac{d(I_{L_2} + \widehat{i_{L_2}(t)})}{dt} = (V_1 + \widehat{v_1(t)}) - (D'_3 - \widehat{d}_3)(V_2 + \widehat{v_2(t)}) \end{cases} \quad (18)$$

Substituting (12) and (13) into (18):

$$\begin{cases} L_1 \frac{d \widehat{i_{L_1}(t)}}{dt} = \widehat{v_1(t)} - D'_1 \widehat{v_2(t)} + V_2 \widehat{d}_1 \\ L_2 \frac{d \widehat{i_{L_2}(t)}}{dt} = \widehat{v_1(t)} - D'_3 \widehat{v_2(t)} + V_2 \widehat{d}_3 \end{cases} \quad (19)$$

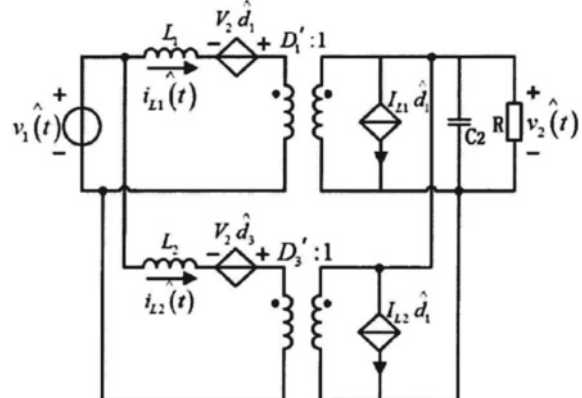
Similarly, the output capacitor can be written as:

$$C_1 \frac{d \widehat{V_2(t)}}{dt} = D'_1 \widehat{i_{L_1}(t)} - I_{L_1} \widehat{d}_1 + D'_3 \widehat{i_{L_2}(t)} - I_{L_2} \widehat{d}_3 - \frac{\widehat{v_2(t)}}{R} \quad (20)$$

A small-signal equivalent model of the staggered parallel boost circuit is established with the controlled current source, controlled voltage source, and ideal transformer model as shown in Fig. 4.

Assuming that the parallel switch parameters are identical, there are:  $L_1 = L_2 = L$ ,  $I_{L_1} = I_{L_2}$ ,  $\widehat{d}_1 = \widehat{d}_3 = \widehat{d}$ ,  $\widehat{i_{L_1}(t)} = \widehat{i_{L_2}(t)} = \widehat{i_L(t)}$ , and  $D_1 = D_3 = D$ .

**Fig. 4** Small-signal equivalent model of interleaved parallel boost circuit



The Laplace transform is performed on Eqs. (19) and (20) to obtain the frequency domain equation.

$$L_s \widehat{i_L(t)} = \widehat{v_1(s)} - D' \widehat{v_2(s)} + V_2 \widehat{d} \quad (21)$$

$$C_2 s \widehat{v_2(s)} = 2D' \widehat{i_L(s)} - 2I_L \widehat{d(s)} - \frac{\widehat{v_2(s)}}{R} \quad (22)$$

After simplification of Eqs. (21) and (22), the sensor function can be obtained:

$$G_{vi}(s) = \frac{2RD'^2 - L_s}{C_2 RSD' + 2D'}.$$

## (2) Buck circuit modeling

In this mode, the traction side energy or the charging pile energy of the traction converter flows to the battery module. The equivalent circuit of the buck converter is shown in Figs. 5 and 6.

**Fig. 5** Equivalent circuit of buck

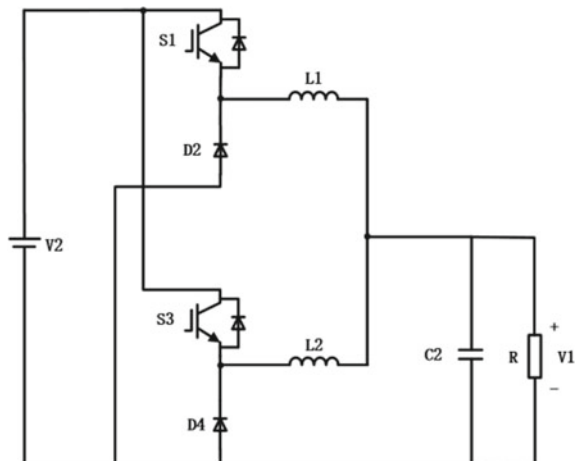
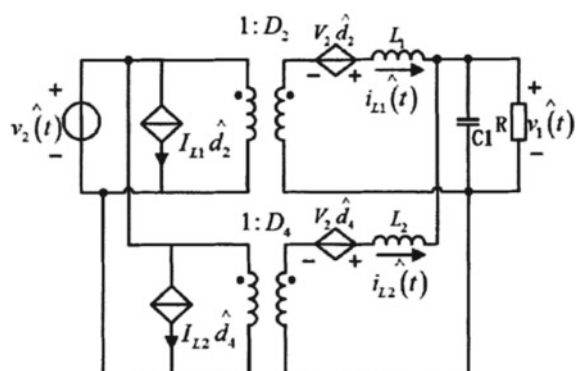


**Fig. 6** Small-signal equivalent model of interleaved buck circuit



Similarly, the small-signal equivalent model of the interleaved parallel buck circuit is shown in the figure below, and the sensor function can be obtained:  $G_{vi}(s) = \frac{2}{C_1 s + \frac{1}{R}}$ .

### 3.2 Control Strategy of Hybrid Energy Storage System

The block diagram of the hybrid energy storage system control algorithm is shown in Fig. 7.

When the bidirectional DC/DC operates in the boost mode, the lithium battery provides power to the traction converter through the bidirectional DC/DC converter by determining the total power of the traction or the current of the super capacitor side [10]. At this time, the lithium battery side reference current signal  $i_{bat}^*$  obtained by calculating the required power of traction is set as the reference current of current loop through the energy distribution strategy. After making difference between  $i_{bat}^*$  and the lithium battery side current signal  $i_{bat}$ , the pulse signal is obtained by PI controller to control the turning states of the  $S_2$  and  $S_4$  tube.

When the bidirectional DC/DC operates in the buck mode, the lithium battery absorbs power from the traction converter through the bidirectional DC/DC converter by determining whether the traction converter is operating in the braking or charging state. Similarly, the turning states of the  $S_1$  and  $S_3$  tube can be obtained.

## 4 Simulation of Hybrid Energy Storage System

### 4.1 Requirement Analysis

In order to verify the effectiveness of the topological structure and control algorithm of the onboard hybrid energy storage system of the tram, the demand analysis is carried out for three domestic tram lines, and the operation of the three trams is

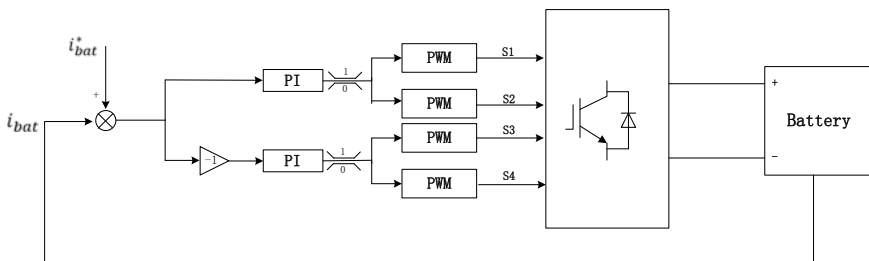


**Fig. 7** Control algorithm block diagram

**Table 1** Demand analysis table

		Line A	Line B	Line C
Normal operation	Longest interval	Station 1 to station 2 (1.37 km)	Station 3 to station 4 (2.09 km)	Station 5 to station 6 (1.35 km)
	Traction + auxiliary loss/kWh	12.13	14.5	21.05
	Braking energy/kWh	5.89	5.52	10.87
	Total energy consumption/kWh	6.24	8.89	10.14
Charging station failure	Charging failure site	Station 2 (2.11 km)	Station 3 (3.42 km)	Station 6 (2.11 km)
	Traction + auxiliary loss/kWh	19.03	27.56	33.14
	Braking energy/kWh	9.95	10.68	17.04
	Total energy consumption/kWh	9.08	16.88	16.10
Traffic jam 15 min	Auxiliary energy consumption/kWh	15	15	15

shown in the table below. When the charging station of the Station 3 of Line B is blocked for 15 min, the maximum energy consumption is 31.88 kWh, so the minimum energy storage of the energy storage system should be greater than 32 kWh (Table 1).

According to the existing charging station configuration and line requirements, the minimum energy storage of the energy storage system shall not be less than 32 kWh; the maximum continuous power of the energy storage system shall be greater than 489 kW, and the peak power shall be greater than 1000 kW.

In order to verify the effectiveness of the topological structure and control strategy of the hybrid energy storage system, the system simulation model is established in Simulink. The specific parameters of the energy storage components and the line simulation are configured according to the actual line simulation as shown in Tables 2 and 3.

**Table 2** Configuration of energy storage elements

	Supercapacitor	Lithium battery
Capacity/Ah	4.4	60
Voltage/V	500–900	324–486
Energy/kWh	3.17	24.8
Continuous power/kW	200	100
Instantaneous power/kW	1150	500

**Table 3** Specific parameters of line simulation

Traction network pressure (V)	750
Filter inductance $L_1$ (mH)	0.15
Chopper inductance $L_2/L_3$ (mH)	1
Filter capacitor $C$ (mF)	2
PI controller parameters	$K_p = 0.008; K_i = 0.1$

## 4.2 Simulation Verification

According to the actual circuit design, the circuit and its control algorithm are simulated by MATLAB. The simulation results are as follows.

Among them, the total power curve of traction converter and the power curve of lithium battery are given. The total power curve of the traction converter includes three conditions: traction acceleration, coasting, and braking. The ratio of lithium battery and supercapacitor power configuration is 3:7. That is, the lithium battery curve takes 0.3 times the total power of the traction converter, and the supercapacitance curve and the lithium battery curve contain current, SOC, and voltage values. The simulation results show that the current ripple is about 9%, and the curve trend of supercapacitor and lithium battery is consistent with the given power. The simulation results show that the designed circuit conforms to the actual circuit model of energy storage system, and the device selection parameters are reasonable. At the same time, according to the simulation results, the control strategy proposed in this paper meets the requirements of accuracy, robustness, and engineering needs (Figs. 8, 9 and 10).

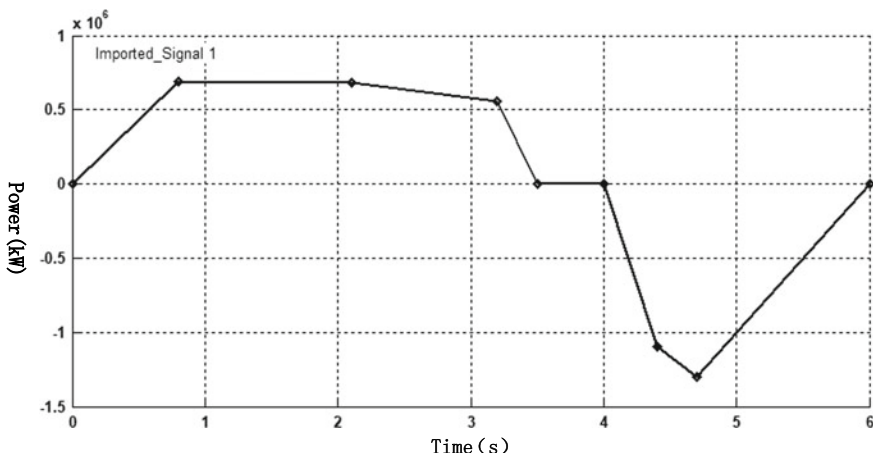


**Fig. 8** Total power curve of traction converter

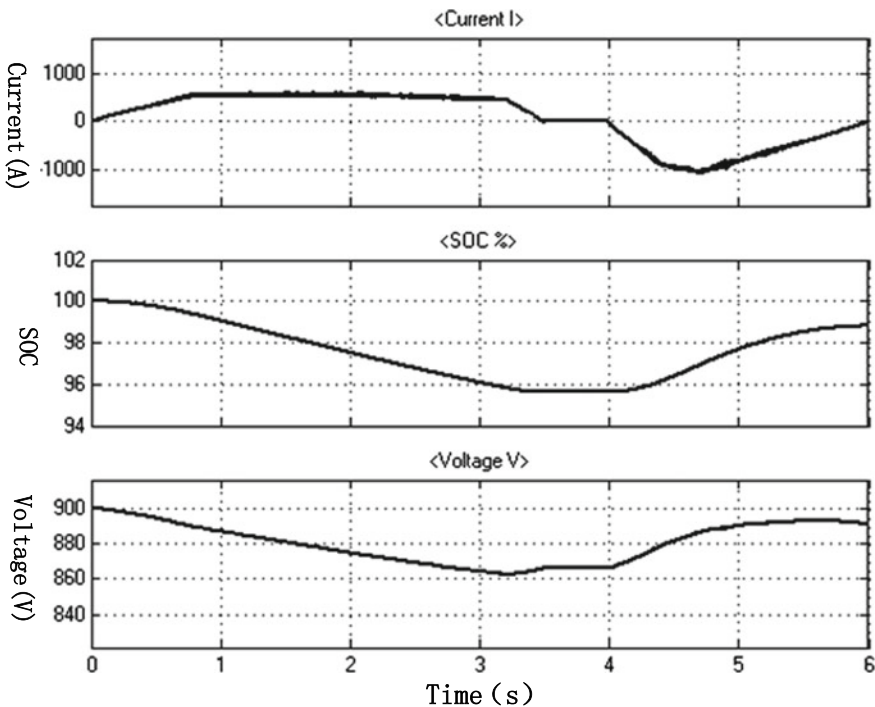


**Fig. 9** Current, SOC, and voltage curve of supercapacitor

## 5 Conclusion

Combined with the actual situation of the tramcar, this paper studies the topological structure of the hybrid energy storage system, the working mode and control strategy of the interleaved and parallel controlled bidirectional DC/DC converter. Finally, it analyzes the line requirements of three actual tram lines, obtains the simulation parameters of the hybrid energy storage system, and finally, according to the simulation model, it carries out simulation verification. The simulation results show that the circuit design, device selection parameters, and control algorithm of the vehicle-mounted hybrid energy storage system based on the tram are reasonable and meet the engineering application.

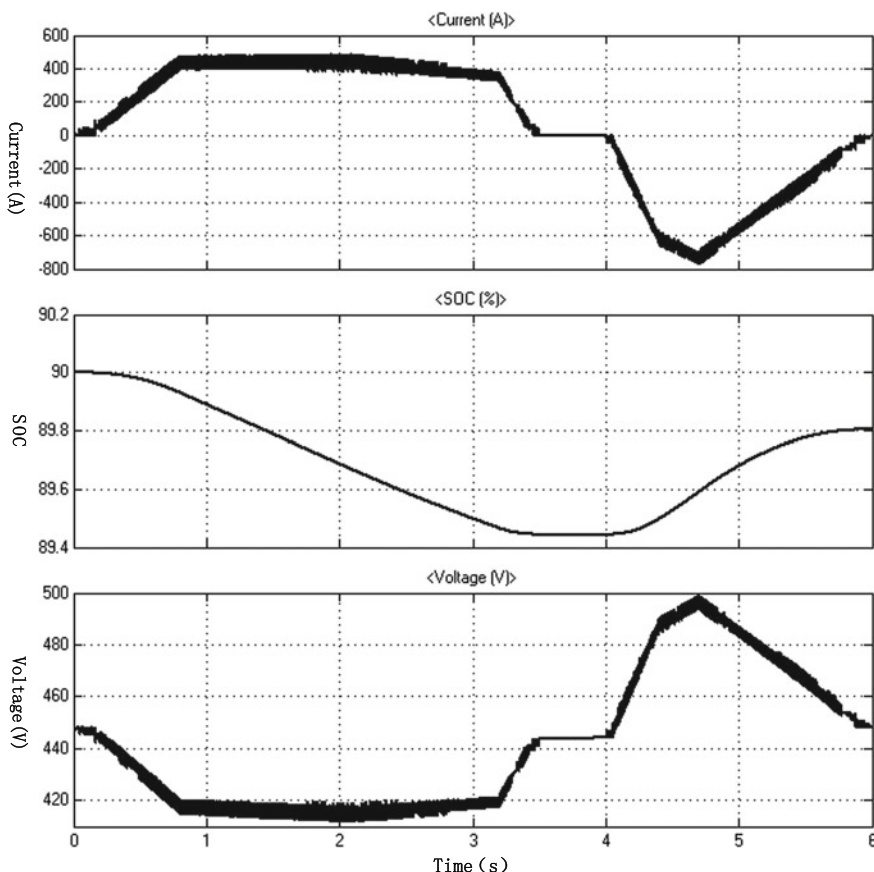


**Fig. 10** Current, SOC, and voltage curve of lithium battery

**Acknowledgements** This work is supported by National Key R&D Program of China (No. 2017YFB1201003-006).

## References

1. Wang J, Ren C (2017) Research of energy storage technology for urban rail transit vehicle. *Urban Mass Trans* 20(1):124–127 (in Chinese)
2. Sang B, Tao Y, Zheng G (2014) Research on supercapacitor-battery hybrid energy storage topology and control strategy. *Power Syst Prot Control* 42(2):1–6 (in Chinese)
3. Xu Q, Hui J (2017) The research on hybrid energy storage system of super capacitor and battery. *Commun Power Technol* 34(1):53–55 (in Chinese)
4. Li H, Fang Z, Lawler JS (2003) A natural ZVS medium-power bidirectional DC-DC converter with minimum number of devices. *IEEE Trans Ind Appl* 2(2)

5. Yang G (2012) Research on staggered parallel bidirectional DCDC converter based on DSP. Southwest Jiaotong University (in Chinese)
6. Zheng C (2016) Research and implementation on hybrid energy storage system of rail transit. *Mach Electron* 34(11):44–47 (in Chinese)
7. Herrera VI, Gaztañaga H, Milo A et al (2016) Optimal energy management and sizing of a battery- supercapacitor-based light rail vehicle with a multiobjective approach. *IEEE Trans Ind Appl* 52(4):3367–3377
8. Chen X (2018) Design of bidirectional DC/DC converter based on interleaved parallel. *Rail locomotive and motor car* 3:4–8 (in Chinese)
9. Wang Z (2018) Study on energy management strategy of mixed energy storage tram based on fuzzy control. Beijing Jiaotong University (in Chinese)
10. Dang Y (2017) Optimization of control strategy and modularization of bidirectional DC/DC converter. Harbin Institute of Technology (in Chinese)

# Vehicle Propulsion System of New MBTA Orange Line Trains



Caihui Zheng, Hang Yin, Haifeng Hong and Changqing Liu

**Abstract** This paper describes the propulsion system of new MBTA Orange Line trains. The new train is supplied by 600 VDC 3rd rail power and adopts three-phase asynchronous traction motor instead of the DC traction motor. The paper covers the train configuration, performance requirement, and overview of the propulsion system. The propulsion functions, including powering and braking control, friction brake interface control, and diagnostics and VMS interface, are given here. Some functions, such as line voltage limit, dynamic braking control, brake blending and holding brake control, slide control, snow brake control, roll back control, and so on, are provided in details here. The designed propulsion system fulfilled MBTA technical requirement.

**Keywords** Propulsion system · Orange line · PCU · FBCU · VMS

## 1 Introduction

CRRC was awarded the contract from the Massachusetts Bay Transportation Authority (MBTA) for the design and manufacture of 284 Boston Orange and Red Line Heavy Rail Subway cars in October, 2014 [1]. It is the first Chinese company to enter the US rail car manufacturing market.

The new trains with advanced AC motor propulsion system will replace the old trains with DC motor system, which is preferred for safety, efficiency, and economic benefits [2].

This paper will introduce the propulsion system based on Orange Line cars.

---

C. Zheng (✉) · H. Yin · H. Hong · C. Liu  
CRRC Changchun Railway Vehicle Co., Ltd., No. 435 Qingyin Road,  
Changchun, China  
e-mail: [zhengcaihui@cccar.com.cn](mailto:zhengcaihui@cccar.com.cn)

C. Liu  
Beijing Jiaotong University, No. 3 Shangyuancun, Beijing, China

## 2 General Information [3]

- Train configuration: 3 Married Pair train (C–NC = C–NC = NC–C)  
C car: Cab car, NC car: Non-cab car, = : auto-coupler
- One propulsion inverter box per car includes two propulsion inverters. Each propulsion inverter manages two AC motors in parallel on the same truck
- Gross mass of train: AW0 = 443,775 lb, AW2 = 571,185 lb, and AW3 = 660,000 lb
- Nominal voltage: 600 VDC (range from 400 to 800 VDC)
- Maximum design speed: 70 mph
- Initial acceleration rate (from 0 to 16.3 mph): 2.75 mphps up to AW2
- Deceleration rate with dynamic brake only (from 42 to 3 mph): 3 mphps up to AW3
- Deceleration rate with blended brake (from 65 to 0 mph): 3 mphps up to AW3
- Powering and dynamic braking performance curves are as shown in Figs. 1 and 2.

## 3 Propulsion System Overview

The propulsion system is designed to operate on 600 VDC 3rd rail power and provides powering and dynamic braking efforts (Fig. 3).

A “Three-phase Drive” with variable voltage and variable frequency (VVVF) control is applied for the propulsion control system. The VVVF inverter is a pulse width modulation (PWM) type using insulated gate bipolar transistors (IGBT). Two independent inverter circuits provide control on a per truck basis. This inverter can perform variable voltage and variable frequency control of the number of rotations of the traction motor (i.e., the speed of the train) over a wide range. It can switch between powering/dynamic braking operation and forward/reverse operation without switching the main circuit. This is accomplished by slip frequency and output phase permutation controls, i.e., only by control of the IGBT gate signals.

## 4 Propulsion Functions

See Fig. 4.

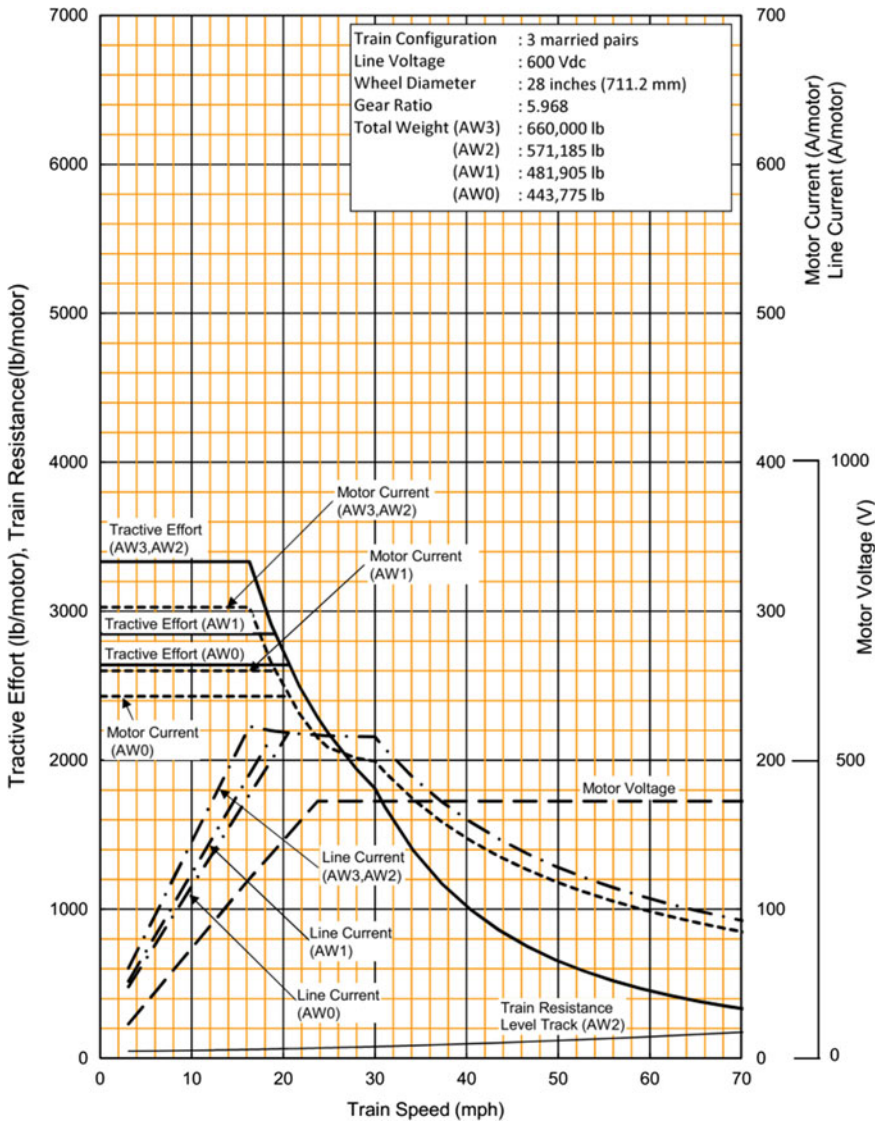


**Fig. 1** Powering performance curve for MBTA orange line

#### 4.1 Powering and Braking Control

The propulsion system controls the tractive effort and brake effort in response to the PWM command, and hybrid mode is used [5]. Powering or braking control is determined by power/brake mode trainline [6].

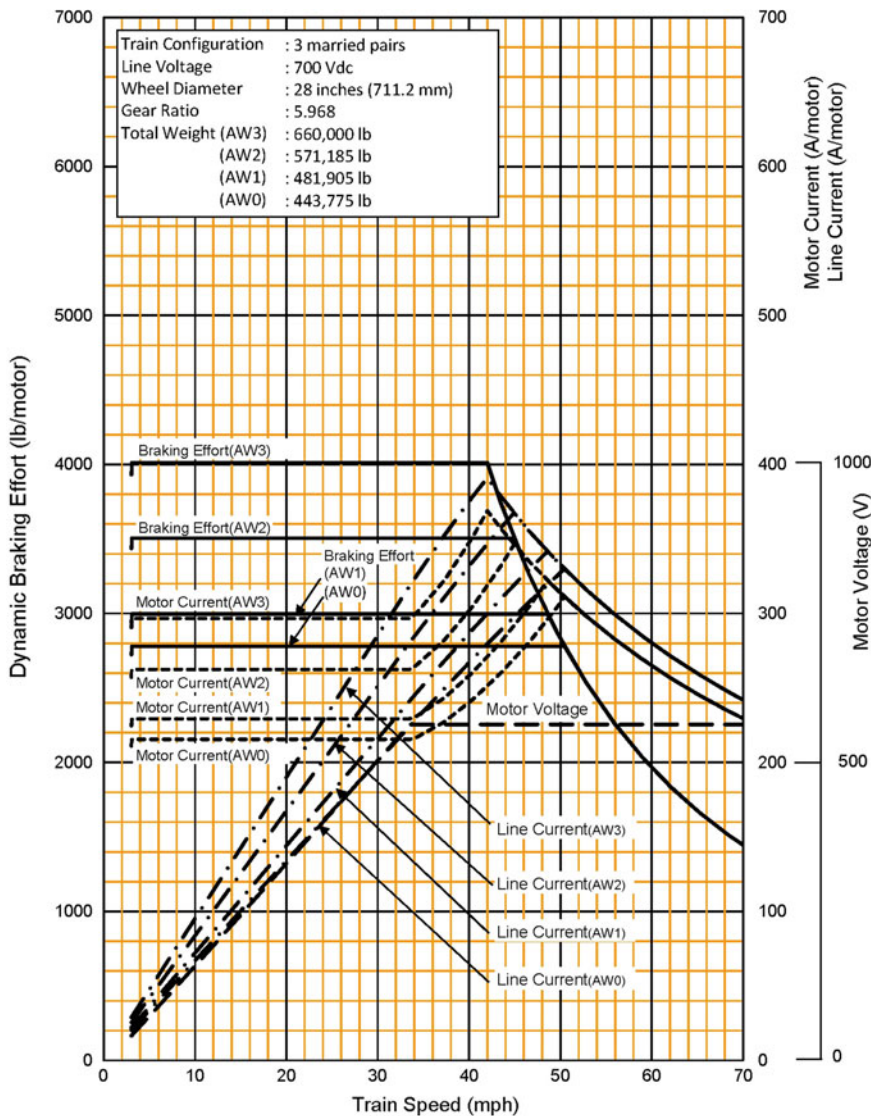


**Fig. 2** Dynamic braking performance curve for MBTA orange line

#### 4.1.1 Line Voltage Limit

The maximum acceleration performance is achieved whenever the line voltage is above 600 V with the base speed of 16.3 mph. When the line voltage is between 600 and 400 V, the base speed is reduced in proportion to the line voltage. The maximum acceleration rate is achieved up to the base speed (Fig. 5).

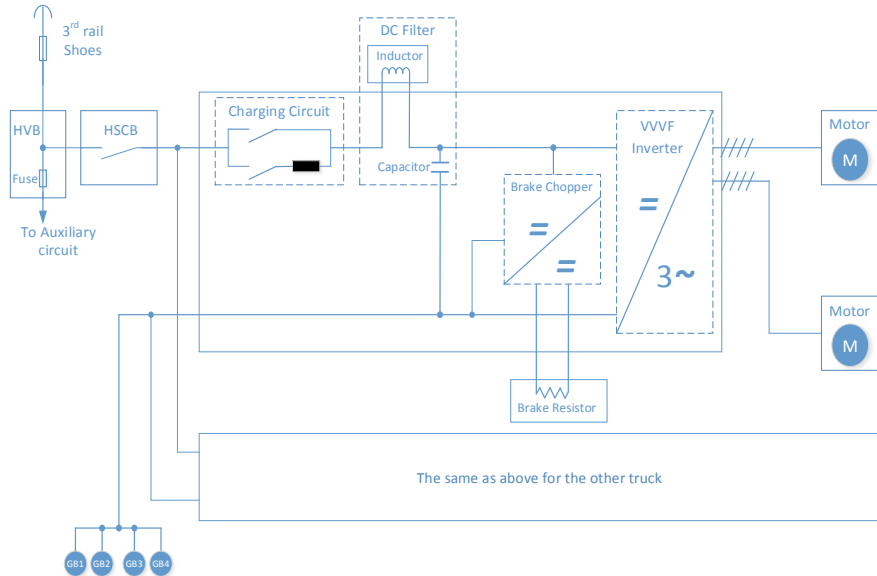


**Fig. 3** Propulsion system block diagram [4]

The maximum dynamic braking performance is achieved whenever the line voltage is above 700 V (no more than 800 V) with the base speed of 42 mph. When the line voltage is lower than 700 V, the base speed is reduced in proportion to the line voltage (Fig. 6).

#### 4.1.2 Load Weight Compensation

The powering performance is compensated by load weights between AW0 and AW2. There is no compensation for car weight above AW2. The tractive effort will be limited at the AW2 level.

The braking performance is compensated by load weights between AW0 and AW3. There is no compensation for the car weight above AW3. The braking effort will be limited at the AW3 level.

#### 4.1.3 Dynamic Braking Control

Dynamic braking is controlled by using rheostatic braking and/or regenerative braking.

1. Dynamic braking will be provided regardless of the status of the 3rd rail, once the proper braking effort has been initiated.

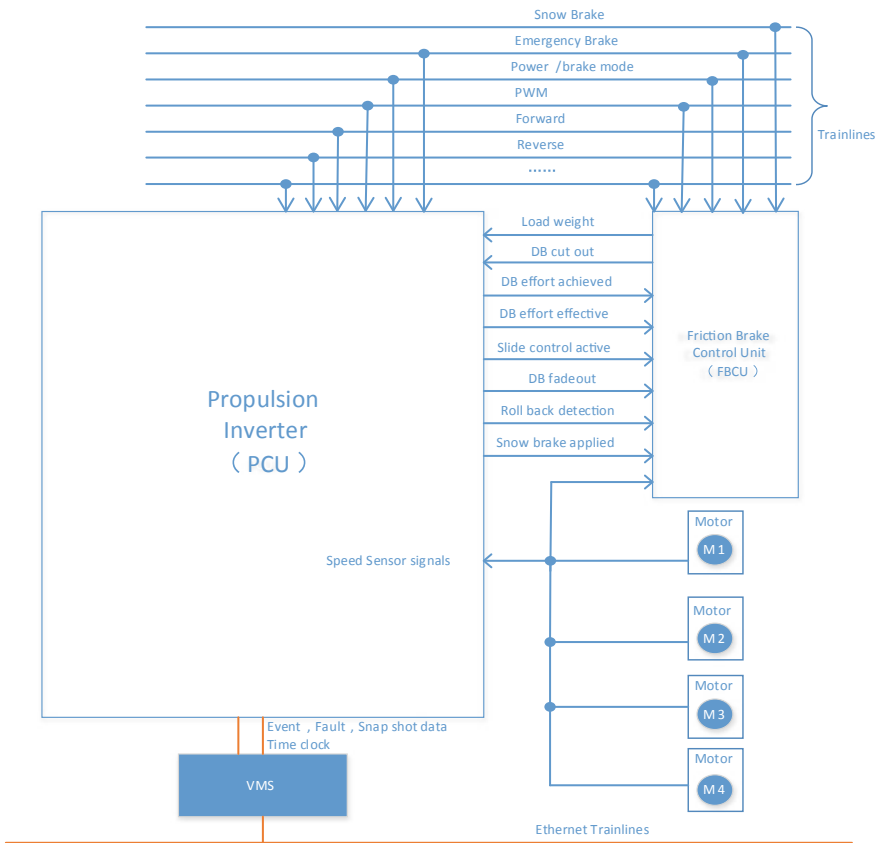


**Fig. 4** Overview of propulsion system interface

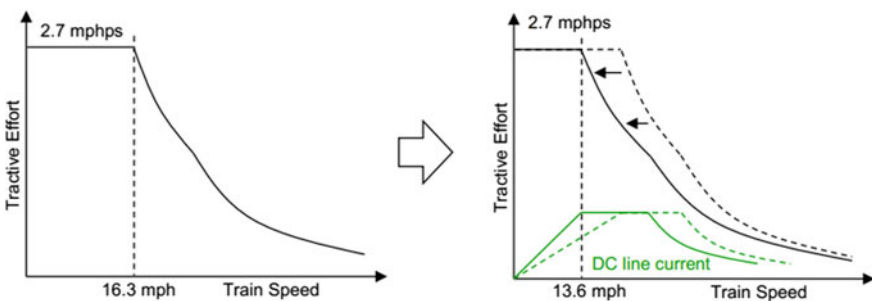


**Fig. 5** Tractive effort/speed based on line voltage between 600 and 400 V

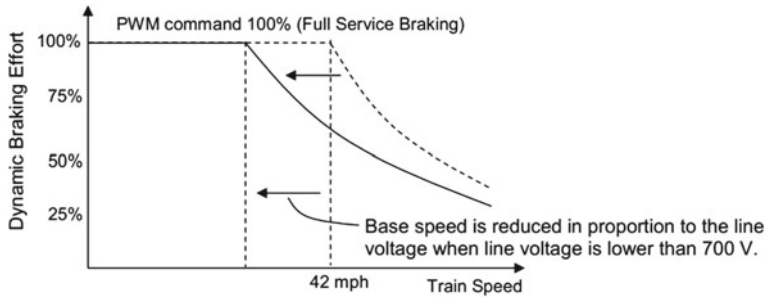


**Fig. 6** Dynamic braking effort/speed based on line voltage

2. The output braking torque is calculated by the output of the PWM command and the load weight from FBCU. The calculated braking torque is limited by dynamic braking performance (Fig. 2).
3. Blending of regenerative and rheostatic braking is applied when the auxiliary loads and/or the 3rd rail are not sufficiently receptive. This function is realized by maintaining the filter capacitor voltage at reference voltage by utilizing the brake chopper (Fig. 7).

## 4.2 Friction Brake Interface

### 4.2.1 Brake Blending and Holding Brake Control

Dynamic braking will be applied in priority. Normally, friction brake is only compensating for high speed above 42 mph and low-speed dynamic brake fade.

The operation of the friction brake and the dynamic brake blending at low speed is described in the following steps (Fig. 8).

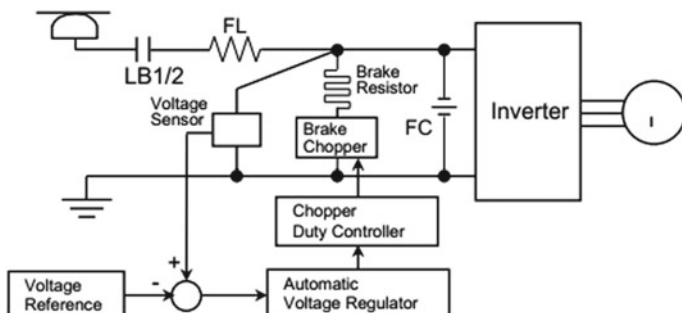


**Fig. 7** Block diagram for brake chopper control

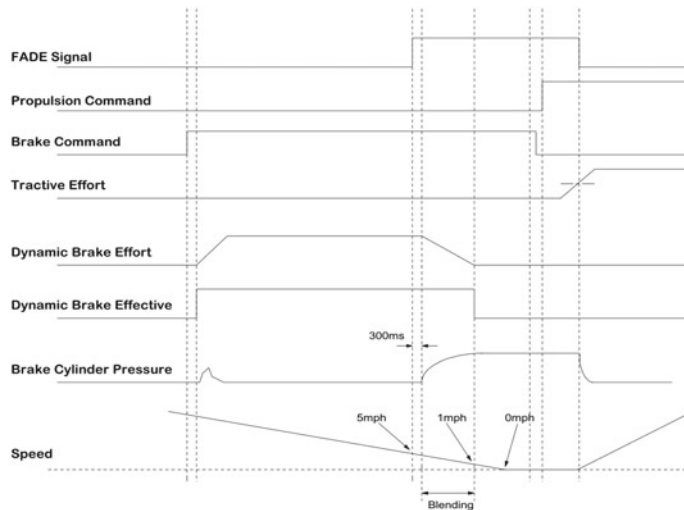


**Fig. 8** Brake blending and holding brake control scheme

1. At a speed of approximately 5 mph, the PCU outputs the dynamic brake fadeout (FADE) signal to the FBCU. After approximately 300 ms, the dynamic brake effort fades out and the friction brake takes over the dynamic brake with the same gradient.
2. In the event that the FBCU does not receive the FADE signal at a predetermined low speed (2 mph) while in a braking mode, the FBCU automatically applies the friction brake.
3. When the propulsion command is applied from a standstill and the PCU confirms that there is sufficient tractive effort to prevent the train from moving backward, the PCU resets the FADE signal. The FBCU will then release the holding brake.
4. The FBCU releases the holding brake after 3 s from the propulsion command is applied for the event of a FADE signal stuck high.

#### 4.2.2 Other Control Functions

##### (1) Slide control

As shown in Fig. 4, Each PCU and FBCU detects speed sensor signals from four axles [7].

During the PCU applies slide corrective control, the PCU outputs the slide control active signal (SLCA). When the FBCU receives this signal, the FBCU does not increase the friction brake even though the dynamic brake effort is reduced.

During wheel slide control by the propulsion inverter, if the FBCU detects uncontrolled wheel slide, the FBCU sends the dynamic brake cut out (DBCO) command to the PCU, which disables dynamic brake for the duration of the stop. If the PCU determines that it cannot adequately control a slide, the DBE signal is removed and the DBA signal is reduced to zero. The FBCU will then apply friction brake to meet the demand.

#### (2) Emergency brake

When the inverter detects emergency brake applied, PCU will immediately cuts off the line contactors and the inverter operation is inhibited, and the traction power is removed within 100 ms by stopping the IGBT gate signal.

#### (3) Snow brake

When snow brake trainline is active, a light pressure will be applied by FBCU at all tread brakes to prevent the buildup of ice and snow on the wheels and brake shoes.

When the PCU receives snow brake active signal, the PCU increases tractive effort within the powering performance curve and decreases braking effort to compensate tractive and braking effort.

#### (4) Rollback

When the rollback exceeds 25% of wheel rotation, the PCU detects it and outputs the rollback detection signal to the FBCU. The FBCU will apply full-service brake to prevent the train from rollback (Fig. 9).

### ***4.3 Diagnostics and Vehicle Monitoring System (VMS) Interface***

The diagnostics system is a function within the propulsion controller of each inverter. The diagnostics system is to record faults, status, snapshots, and to implement the self-test [8].

Each PCU is communicating with VMS through two Ethernet connections (dual homing) for redundancy. The information from PCU diagnostic system is sent to VMS to assist in diagnosis and maintenance of the propulsion equipment.

## **5 Conclusion**

The propulsion system of new MBTA Orange Line trains was designed according to the technical requirement. The train passed all system level and train level static and dynamic tests. The train went to revenue service on August 14, 2019.

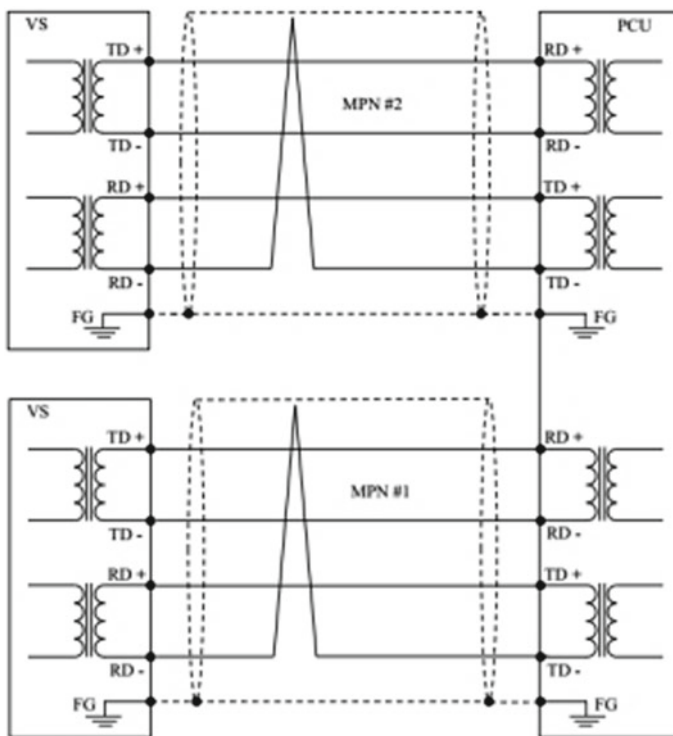


Fig. 9 VMS dual homing interface

## References

- Wenlong Z (2014) CNR exported 284 metro vehicles to the United States. *J Mod Urban Transit* (6):100 (in Chinese)
- Takamitsu Y (2019) The latest research trend of main circuit and traction system of railway vehicles. *J Foreign Diesel Locomotive* (2):6–13 (in Chinese)
- MBTA Red/orange line new vehicle technical specification (2014), T2–T16
- Xiaoyan G, Bo Z, Jin H (2013) Study on traction system integration technology of metro train. *J Railway Locomotive Car* 33(3):56–62 (in Chinese)
- Diao L, Tang J, Loh PC et al (2018) An efficient DSP-FPGA-based implementation of hybrid PWM for electric rail traction induction motor control. *IEEE Trans Power Electron* 33 (4):3276–3288
- IEEE 1475: (2012). The function of interfaces among propulsion friction brake, and train-borne master control on rail rapid transit vehicles, pp 16–32
- Diao LJ, Zhao LT, Jin ZM, Wang L, Sharkh SM (2017) Taking traction control to task: high-adhesion-point tracking based on a disturbance observer in railway vehicles. *IEEE Ind Electron Mag* 11(1):51–62
- Hanqing T (2012) Design of train electrical traction system of first—phase project of Kunming Metro. *J Railway Eng Soc* 12:85–89 (in Chinese)